NATO
OTAN

R&T
ORGANIZATION

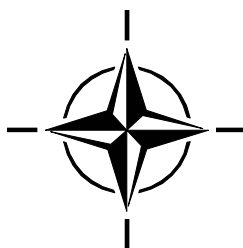AC/323(AVT-113)TP/246

www.rto.nato.int

RTO TECHNICAL REPORT

TR-AVT-113

Understanding and Modeling Vortical Flows to Improve the Technology Readiness Level for Military Aircraft

(Compréhension et modélisation des flux de
vortex pour améliorer le niveau de maturité
technologique au profit des avions militaires)

Summary Report of Task Group AVT-113.

Published October 2009

Distribution and Availability on Back Cover

RTO TECHNICAL REPORT

TR-AVT-113

Understanding and Modeling Vortical Flows to Improve the Technology Readiness Level for Military Aircraft

(Compréhension et modélisation des flux de
vortex pour améliorer le niveau de maturité
technologique au profit des avions militaires)

Summary Report of Task Group AVT-113.

The Research and Technology Organisation (RTO) of NATO

RTO is the single focus in NATO for Defence Research and Technology activities. Its mission is to conduct and promote co-operative research and information exchange. The objective is to support the development and effective use of national defence research and technology and to meet the military needs of the Alliance, to maintain a technological lead, and to provide advice to NATO and national decision makers. The RTO performs its mission with the support of an extensive network of national experts. It also ensures effective co-ordination with other NATO bodies involved in R&T activities.

RTO reports both to the Military Committee of NATO and to the Conference of National Armament Directors. It comprises a Research and Technology Board (RTB) as the highest level of national representation and the Research and Technology Agency (RTA), a dedicated staff with its headquarters in Neuilly, near Paris, France. In order to facilitate contacts with the military users and other NATO activities, a small part of the RTA staff is located in NATO Headquarters in Brussels. The Brussels staff also co-ordinates RTO's co-operation with nations in Middle and Eastern Europe, to which RTO attaches particular importance especially as working together in the field of research is one of the more promising areas of co-operation.

The total spectrum of R&T activities is covered by the following 7 bodies:

- AVT   Applied Vehicle Technology Panel
- HFM   Human Factors and Medicine Panel
- IST   Information Systems Technology Panel
- NMSG   NATO Modelling and Simulation Group
- SAS   System Analysis and Studies Panel
- SCI   Systems Concepts and Integration Panel
- SET   Sensors and Electronics Technology Panel

These bodies are made up of national representatives as well as generally recognised 'world class' scientists. They also provide a communication link to military users and other NATO bodies. RTO's scientific and technological work is carried out by Technical Teams, created for specific activities and with a specific duration. Such Technical Teams can organise workshops, symposia, field trials, lecture series and training courses. An important function of these Technical Teams is to ensure the continuity of the expert networks.

RTO builds upon earlier co-operation in defence research and technology as set-up under the Advisory Group for Aerospace Research and Development (AGARD) and the Defence Research Group (DRG). AGARD and the DRG share common roots in that they were both established at the initiative of Dr Theodore von Kármán, a leading aerospace scientist, who early on recognised the importance of scientific support for the Allied Armed Forces. RTO is capitalising on these common roots in order to provide the Alliance and the NATO nations with a strong scientific and technological basis that will guarantee a solid base for the future.

Table of Contents

Chapter 8 – Numerical Solutions for the CAWAPI Configuration on Unstructured Grids at EADS-MAS, Germany   8-1
by W. Fritz

Chapter 9 – Numerical Solutions for the CAWAPI Configuration on Unstructured Grids at USAFA, United States   9-1
by S. Morton, D.R. McDaniels and R.M. Cummings

Chapter 10 – Numerical Solutions for the CAWAPI Configuration on Unstructured Grids at KTH/FOI, Sweden – Part I   10-1

by S. Görtz and A. Jirásek

Chapter 15 – Numerical Solutions for the CAWAPI Configuration on Unstructured Grids at NASA LaRC, United States

by J.E. Lamar and K.S. Abdol-Hamid

Chapter 16 – What was Learned from Numerical Simulations of F-16XL (CAWAPI) at Flight Conditions

Chapter 22 – Experimental Investigations on the VFE-2 Configuration at Glasgow University, United Kingdom   22-1

by F.N. Coton, S.B. Mat and R.A.McD. Galbraith

Chapter 33 – Semi-Empirical Prediction of Vortex Onset on the VFE-2 Configurations

by R.K. Nangia

Chapter 34 – Lessons Learned from the Numerical Investigations on the VFE-2 Configuration

by W. Fritz and R.M. Cummings

Chapter 35 – Final Results of the International Vortex Flow Experiment – Resumé and Outlook   35-1
by D. Hummel

List of Figures

CHAPTER 9

CHAPTER 22

CHAPTER 23

CHAPTER 25

CHAPTER 26

CHAPTER 29

CHAPTER 31

APPENDIX A3.3

APPENDIX A3.5

List of Tables

Common Notations

Abbreviations

AVT	Applied Vehicle Technology (one of seven technical panels within the RTO)
BART	Basic Aerodynamic Research Tunnel
BL	butt line on airplane, in., positive on right wing (See Chapter 3 – Figure 3-2)
CAWAP	Cranked Arrow Wing Aerodynamics Project
CAWAPI	Cranked Arrow Wing Aerodynamics Project International
CFD	Computational Fluid Dynamics
EFD	Experimental Fluid Dynamics
ESP	Electronic Scanning Pressure
ET	Exploratory Team
FC	Flight Condition
FS	fuselage station on airplane, in., positive aft (See Chapter 3 – Figure 3-2)
HUD	heads-up display
HSCT	High Speed Civil Transport
HSR	High Speed Research
HWA	Hot Wire Anemometry
IR	Infra Red (technique)
ITAR	International Traffic in Arms Regulations
LaRC	Langley Research Center
LE	leading edge
NASA	National Aeronautics and Space Administration
NATO	North Atlantic Treaty Organisation
PIV	Particle Image Velocimetry
PSF	Performance, Stability & Control and Fluid Physics – one of the standing Technical Committees of the AVT Panel
PSP	Pressure Sensitive Paint
RTB	Research and Technology Board
RTO	Research and Technology Organisation – Scientific Arm of NATO
TSP	Temperature Sensitive Paint
VFE-2	Vortex Flow Experiment-2
VL	Virtual Laboratory
WL	waterline on airplane, in., positive up (See Chapter 3 – Figure 3-2)

CAWAPI Chapters (3 – 16) Nomenclature

CFL3D	name of structured grid flow solver developed at NASA Langley
C_p	surface static pressure coefficient
c_f	local skin friction coefficient
F-16XL-1	an extensively modified version of the single-seat F-16A aircraft which is longer and has a cranked arrow wing instead of a trapezoidal wing with leading-edge strake
h	airplane altitude, ft
iges	Initial Graphics Exchange Specifications –> geometry descriptor
i,j,k	grid indices
M_∞	free-stream Mach number
R_n	Reynolds number, based on aircraft reference chord of 24.7 ft
V/V_{RE}	ratio of velocity magnitude in boundary layer to that at the Rake Extreme total-pressure tube
T	absolute temperature, °R
x/c	fractional distance along the local chord, positive aft
y	normal distance above the surface at a rake location, in.
y^+	Reynolds number like term for flat-plate turbulent boundary layer (See Chapter 3 – Ref. [3-1])
α	angle of attack, deg
β	angle of sideslip, deg
$2y/b_l;\eta$	fractional distance along the wing local semispan, positive toward the right wing tip

Subscripts

avg	average value
l, loc	local
nom	nominal value

VFE-2 Chapters (17 – 35) Nomenclature

A	wing aspect ratio
b	wing span
b_{loc}	local span
c	root chord
$\overline{c}$	mean aerodynamic chord
C_m	pitching moment coefficient, reference point at 2c/3; $= M/q_\infty S \overline{c}$
C_N	normal force coefficient; $= N/q_\infty S$
C_T	tangential force coefficient; $= T/q_\infty S$
C_p	pressure coefficient; $= (p - p_\infty)/q_\infty$
q_∞	free stream dynamic pressure

r	streamwise leading edge radius
R	free stream Reynolds number, based on root chord
R_{mac}	free stream Reynolds number, based on mean aerodynamic chord
S	wing area
x, y, z	wing apex fixed coordinates (x downstream, y spanwise, z upwards)
Λ	leading edge sweep angle
ξ, η, ζ	wing apex fixed dimensionless coordinates; $\xi = x/c$, $\eta = 2y/b_{loc}$, $\zeta = 2z/b_{loc}$

Acknowledgements

Understanding and Modeling Vortical Flows to Improve the Technology Readiness Level for Military Aircraft
(RTO-TR-AVT-113)

Executive Summary

The Task Group AVT-113 was established to produce a better understanding and modelling of **vortical flows** in order to improve the technology readiness level of Computational Fluid Dynamics (CFD) for military aircraft. As this problem is so large, the approach chosen was to divide it up into two sub-parts or facets, one that dealt with a complete and representative fighter aircraft with all its complicated geometry – in particular the F-16XL, and one that dealt with an analytically defined delta-wing model on which some wind-tunnel data had already been collected. Both of these slender wings developed vortical flows and this combinational approach to the problem at two different scales was thought to offer the best opportunity to gain the needed insight for improving the CFD tools.

A unique published set of unclassified, flight flow-physics data existed for the F-16XL aircraft, along with CFD and wind-tunnel results. The missing piece was at least one other CFD solution that might explain some noted published anomalies between the predicted and measured flight surface-flow data. Due to the uniqueness of this flight data, three airframe companies – two in the USA and one in Europe – joined this effort along with two governmental laboratories, and four university led efforts. Membership in the latter two groups was evenly split between the USA and European organizations.

The analytically designed delta wing model needed other types of measurements than had been collected and published, both on- and off-the-surface, or in- and out-of-the-boundary-layer to generate a complete data set. An existing model from the USA, along with four new models fabricated in Europe, were employed to generate the needed data. Two of these models were tested in three wind-tunnels in Germany, three models were tested in France, and two in Turkey and one in the U.K. Moreover, CFD solutions were obtained in Germany, Sweden, Turkey, USA and the U.K. in support of this effort. In particular, one set of CFD solutions obtained in Germany was key to an experimental off-surface test focusing its equipment in the proper location.

Studying the resulting vortical flows from these two scale- and shape-perspectives together has provided new insight and led to an increased understanding of the dominant flow physics which exists on- and off-the-surface, or in- and out-of-the-boundary-layer. Researchers from Belgium, the Czech Republic, France, Germany, Italy, Slovenia, Sweden, The Netherlands, Turkey, the United Kingdom and the United States of America – representing the commitment of air-frame manufacturers, government laboratories and universities – contributed to the work of this task group.

It is interesting that the vortical flow problem at transonic speeds was the most complex and difficult problem for both facets. Though some progress has been made, there are still unanswered questions for vortex-dominated flows at transonic speeds.

Compréhension et modélisation des flux de vortex pour améliorer le niveau de maturité technologique au profit des avions militaires
(RTO-TR-AVT-113)

Synthèse

Le groupe de travail AVT-113 a été mis en place pour fournir une meilleure compréhension et une meilleure modélisation des **flux de vortex** afin d'améliorer le niveau de maturité technologique de la Mécanique des Fluides Numériques (MFN) pour les avions militaires. Le sujet étant très étendu, l'approche choisie a été de diviser en deux sous-parties ou facettes, une facette sur l'étude d'un avion de chasse représentatif et complet avec toute sa géométrie complexe – en particulier le F-16XL, une autre facette sur l'étude d'un modèle de voilure delta analytiquement défini sur lequel quelques données de soufflerie avaient été déjà récupérées. Ces deux ailes effilées ont développé des flux de vortex et nous pensons que cette approche combinée du problème à deux échelles différentes était de nature à offrir la meilleure opportunité d'obtenir l'éclairage nécessaire pour améliorer les outils MFN.

Une publication exceptionnelle de données non classifiées sur la physique des flux en vol existait pour l'avion F-16XL, incluant des résultats de données sur le MFN et en soufflerie. La pièce manquante était au moins une autre solution MFN qui puisse expliquer quelques anomalies remarquées dans les publications sur les données prévues et les données mesurées sur la surface d'écoulement en vol. Du fait du caractère exceptionnel de ces données de vol, trois fabricants de cellules – deux aux Etats-Unis et un en Europe – ont rejoint cette activité avec deux laboratoires gouvernementaux et quatre actions universitaires. L'appartenance aux deux derniers groupes provenait à part égale d'organisations des Etats-Unis et d'Europe.

Le modèle de voilure delta conçu analytiquement nécessitait d'autres types de mesures qui ont été récupérées et publiées, à la fois sur la surface et hors-surface, et d'autre part dans et en dehors de la couche limite afin de fournir un ensemble complet de données. Un modèle existant aux Etats-Unis avec quatre nouveaux modèles fabriqués en Europe furent utilisés pour obtenir les données nécessaires. Deux de ces modèles ont été testés dans trois souffleries en Allemagne, trois modèles ont été testés en France, deux en Turquie et un au Royaume-Uni. De plus, pour soutenir cette activité, des solutions MFN ont été obtenues en Allemagne, en Suède, en Turquie, aux Etats-Unis et au Royaume-Uni. En particulier, un ensemble de solutions MFN obtenu en Allemagne a été la clé d'un essai expérimental hors-surface concentrant ses équipements au bon endroit.

L'étude des flux de vortex résultant à ces deux échelles et sous ces deux formes a fourni un nouvel éclairage et a conduit à une meilleure compréhension de la physique des flux dominants qui existent sur la surface et hors-surface ou dans et en dehors de la couche limite. Des chercheurs de Belgique, de la République Tchèque, de France, d'Allemagne, d'Italie, de Slovénie, de Suède, des Pays-Bas, de la Turquie, du Royaume-Uni, et des Etats-Unis d'Amérique – représentant l'engagement des fabricants de cellules, des laboratoires gouvernementaux et des universités – ont apporté leur contribution au travail réalisé par le groupe de travail.

Ce qui est intéressant est que, pour chaque facette, le problème le plus complexe et le plus difficile fut celui du flux de vortex aux vitesses transsoniques. Bien que des progrès aient été faits, il subsiste toujours des questions sans réponses sur les flux de vortex dominants aux vitesses transsoniques.

Chapter 1 – OBJECTIVES AND OVERVIEW

by

John E. Lamar *(Retired)* **and Dietrich Hummel** *(Retired)*

1.1   SUMMARY

The RTO Task Group AVT-113 "Understanding and Modeling Vortical Flows to Improve the Technology Readiness Level for Military Aircraft" was established in April 2003. Two facets of the group, "Cranked Arrow Wing Aerodynamic Project International (CAWAPI)" and "Vortex Flow Experiment-2 (VFE-2)", worked closely together. However, because of the different requirements of each part, the CAWAPI facet concluded its work earlier (December 2006) than the VFE-2 facet (December 2007). In this first chapter of the Final Report of the Task Group an overview on its work is given, and the objectives for the Task Group are described.

1.2   INTRODUCTION

This task group was established to look at two particular problems highlighted at the RTO AVT-072 *Symposium on Advanced Flow Management: Part A – Vortex Flows and High Angle of Attack for Military Vehicles* in 2001 [1-1],[1-2]. These problems had in common a need to revisit leading-edge vortical flows with a view toward understanding and modeling them so that critical flow features could be measured; thereby, providing an improved basis for CFD prediction. The later is tied in with increasing the technology readiness level (TRL) of the CFD solvers for this type of flow. To that end, published flight-test and wind-tunnel model data were examined on configurations that generate significant amounts of vortical flows, along with data collected from new wind-tunnel model tests.

Surface flow measurements on the F-16XL-1 aircraft at a variety of Mach numbers and angles of attack/sideslip comprise the flight-test data set. This airplane, shown in Figure 1-1, has a cranked leading edge with 70°/50° sweep angles and a cropped tip. The CFD studies for this aircraft were performed under the name of **Cranked Arrow Wing Aerodynamics Project International** (**CAWAPI**), and it is one facet of AVT-113.

Figure 1-1: The F-16XL Aircraft in Flight with Tuft and Video Targets on the Left Wing.

Wind-tunnel surface-pressure test results for an analytically defined 65° delta wing-sting combination at a variety of Mach and Reynolds numbers are available at two model scales and form the basic experimental data sets. Both models were tested at NASA Langley Research Center, one in the National Transonic Facility (NTF) [1-3] (see Figure 1-2) and the other in the Low Turbulence Pressure Tunnel (LTPT) [1-4]. Also, both models were designed/fabricated to accommodate four different full-span leading-edge pieces, each of which produced a model bluntness change. These experimental data sets were expanded by task group members using the LTPT and new models in a variety of international wind-tunnels to provide additional data details that will facilitate and enhance comparisons with CFD codes. The results of the experimental and computational studies for this configuration were performed under the name of **Vortex Flow Experiment-2** (**VFE-2**) and it is the other facet of AVT-113.

Figure 1-2: The 65° Delta Wing-Sting Combination in the NASA NTF.

1.3   OVERVIEW AND OBJECTIVES DISCUSSION

1.3.1   CAWAPI Facet

1.3.1.1   Overview

This facet resulted from a cancelled effort by the NASA High Speed Research Program to generate high lift/drag in the terminal environment using a modified F-16XL cranked wing aircraft and to understand its flow physics. The planned modifications primarily included flying with a calibrated engine and adding full-span leading-edge flaps to enhance the lift/drag during take-off and landing at flight conditions compatible with those of the proposed High Speed Civil Transport. When this project was cancelled, the aircraft modifications were not made and the flight restrictions on speed and angle of attack not implemented. Alternate funding was provided by NASA Langley and Dryden to continue the characterization of the **basic aircraft** flow physics in a project named **Cranked Arrow Wing Aerodynamics Project** (**CAWAP**). Some preliminary flights were performed at Langley but the bulk of the flights were conducted at Dryden in a joint effort and included both subsonic, transonic and low supersonic flight speeds using an uncalibrated engine at a

variety of angles of attack, up to ~20°, and sideslip angles of 0° & ±5°. The published results of the **CAWAP** flight test are contained in [1-5] and summarized in [1-1]. During exploratory team meetings of AVT ET-026, set up to advise the AVT on the need for subsequent vortical flow activity beyond the AVT-072 Symposium, the proposals contained in [1-1] and [1-2] were merged into one which emphasized the military nature of aircraft vortical flows. This lead to the establishment of AVT-113 and the results obtained during its tenure are the subject of this report. With several nations interested in performing computations of this aircraft in order to validate the flow physics modeling in their codes, **CAWAP** was expanded to **CAWAPI**.

As the F-16XL geometry is subject to ITAR restrictions, means of facilitating the sharing of this data lead to international agreements and the need to establish a Virtual Laboratory, as discussed in Chapter 2. EADS-M of Germany, KTH/FOI of Sweden, University of Glasgow/Liverpool University of Great Britain, TUSAS/TAI of Turkey, VUB of Belgium and the NLR of The Netherlands joined this aircraft computational effort from Europe. In the USA, there was a corresponding response from the USAFA at Colorado Springs, Lockheed Martin Aeronautics Company at Ft.Worth, Boeing-St.Louis, University of Tennessee/Chattanooga-SimCenter, University of Wyoming at Laramie, and NASA Langley. However, due to non-technical issues, not all were able to sustain their interest to the conclusion of this facet.

1.3.1.2   Objectives

The objectives of this effort are straightforward in that the flight data is to be used to help establish best computational practice for the use of each participant's code. (See Chapter 3 for a discussion.) In particular, this is to occur by computing results for selected flight conditions that contain significant interest and/or flight data using common grids, one for the structured solvers and one for the unstructured solvers (See Chapter 4 for a geometry and grid discussion). A total of seven flight conditions (FC) were chosen, five at a nominal $\beta = 0°$ for a variety of Mach numbers and α's, and two at subsonic speeds at β of ~±5°. The intent was to have as the only variables the solver and its turbulence model for each solver class at each FC; however, it turned out that some solvers required the grid to be tailored for its own particular use, so the results are not as clean as hoped. (See Chapters 5 to 15 for the details.)

The most numerous comparisons available are those made with surface pressures and flows (tufts), but there are limited comparisons of boundary layer and skin friction data at some FCs. No force or moment flight data exists to compare with CFD predictions but code-to-code comparisons are possible for these quantities and are summarized in Chapter 16.

1.3.2   VFE-2 Facet

1.3.2.1   Overview

This facet resulted from the comprehensive review on vortical flows given in [1-2]. In this paper, it was pointed out that current numerical methods for the calculation of vortical flows are available which use the RANS equations with various turbulence models. However, not enough detailed measurements exist of vortical flow fields to properly validate these numerical methods for the large number of available turbulence models.

Therefore, new measurements were proposed in [1-2] to meet the demands for a proper validation of the numerical methods. Following a similar program of VFE-1 in the 1980's, the new experiments were now performed under the name **Vortex Flow Experiment-2 (VFE-2)**. The NASA delta wing (See Figure 1-2) was proposed in [1-2] as a suitable configuration for the additional tests. This configuration has a simple geometry,

which is given analytically for wing and sting support and thus can easily be reproduced elsewhere in order to build new wind-tunnel models. In addition, the configuration comprises four different leading edge shapes, one sharp edged and three rounded ones, having different leading edge radii. Within the framework of VFE-2 new experiments on this configuration should add to the existing data sets ([1-3],[1-4]), with the main emphasis being to obtain flow field data for comparison with CFD results.

A wind-tunnel model that was 75% the size of the NTF model was tested in the NASA/LTPT tunnel and the results made available by NASA for facet members' use. In addition, they shipped this model – designated model (1) – to Europe for testing by means of pressure sensitive paint (PSP) and particle image velocimetry (PIV) at the DLR in the Transonic Wind-Tunnel Goettingen, Germany, and by force balance and PIV at ONERA Lille, France. A new wind-tunnel model (2) was built at the Technical University Munich, Germany, in order to perform surface oil-flow investigations, pressure distribution measurements as well as flow field surveys by means of the PIV and the hot-wire techniques. The same wind-tunnel model has also been tested by the DLR in the cryogenic wind tunnel KKK at Cologne, Germany, using the temperature sensitive paint (TSP) technique for laminar/turbulent transition detection. Another wind-tunnel model (3) has been built and tested through unsteady balance, pressure distribution and flow field studies at University of Glasgow, GBR. Two other new wind-tunnel models (4 and 5) have been built by ONERA Lille, France, in order to carry out balance measurements, and these two models were shipped to Turkey in order to investigate the laminar/ turbulent transition at TUBITAK-SAGE, Ankara.

From its very beginning numerical investigations were an important part of the VFE-2. The purpose for calculations of the flow field around the simple delta wing configuration was threefold:

1) Validation of the available codes;

2) Tuning of new experimental setups by means of CFD results; and

3) Synergistic effects through the possibility of test runs on a simple configuration prior to expensive calculations for a complete aircraft, such as in the CAWAPI facet.

1.3.2.2   Objectives

For the chosen configuration pressure distribution measurements as well as normal force and pitching moment data were already available from NASA for wide ranges of Mach number and Reynolds number. The new experiments should complete these measurements by adding drag data, and the main emphasis was to obtain flow field data, mainly by PIV and hot-wire techniques. For delta wings the status of the boundary layers underneath the vortex system is poorly known, and a more detailed knowledge about this matter would be very useful either for the validation of related prediction methods or for the adaptation of numerical calculations to the experimental status. Therefore attempts have been made to determine the laminar and the turbulent regions on the upper surface of the wing.

Before VFE-2, most experimental investigations on delta wings have been for sharp leading edges with the flow separation fixed to the leading edge. Therefore, the new experiments were aimed mainly at an understanding of the vortex formation for the wing with a rounded leading edge, and the experimental and numerical results were to be compared with the well known sharp leading edge case. Most of the new experiments were carried out at low speed, as the possibilities for tests at higher Mach numbers were limited.

Concerning the angle of attack, the configurations with sharp and rounded leading edges have been investigated at different regimes:

1) At low angles of attack for studies of the onset of vortex shedding on the configuration with rounded leading edge;

2) At moderate angles of attack with large primary vortices, but still without vortex breakdown; and

3) At large angles of attack with large primary vortices including vortex breakdown.

1.4 CONCLUDING REMARKS

In both facets of AVT-113 multiple numerical calculations were carried out. In the **CAWAPI** facet the flow around a complete aircraft configuration has been calculated. On structured as well as on unstructured grids, the computational expense with respect to grid size and CPU time was enormously large and the corresponding calculations were extremely expensive. On the other hand, the **VFE-2** configuration was relatively simple and the amount for numerical investigations was comparatively small. From this contrast resulted considerable synergistic effects within AVT-113. Prior to future expensive calculations for a full aircraft geometry, the codes and the various turbulence models could be checked using the much simpler VFE-2 configuration. Some members were active in both facets of AVT-113, and the discussions within the task group during its semi-annual meetings on the experiences of the members supported the anticipated synergistic effects.

1.5 REFERENCES

[1-1]   Lamar, J.E.: *Cranked Arrow Wing (F-16XL-1) Flight Flow Physics with CFD Predictions at Subsonic and Transonic Speeds*, Presented at RTO AVT Symposium on "Advanced Flow Management; Part A – Vortex Flow and High Angle of Attack", Paper Number 44, in Loen, Norway, during May 7-11, 2001.

[1-2]   Hummel, D. and Redeker, G.: *A New Vortex Flow Experiment for Computer Code Validation*, Presented at RTO AVT Symposium on "Advanced Flow Management; Part A – Vortex Flow and High Angle of Attack", Paper Number 8, in Loen, Norway, during May 7-11, 2001.

[1-3]   Chu, J. and Luckring, J.M.: *Experimental Surface Pressure Data Obtained on 65° Delta Wing Across Reynolds Number and Mach Number Ranges*, NASA TM 4645 (1996).

[1-4]   Luckring, J.M.: Unpublished Data from the NASA Langley LTPT.

[1-5]   Lamar, J.E., Obara, C.J., Fisher, B.D. and Fisher, D.F.: *Flight, Wind-Tunnel, and Computational Fluid Dynamics Comparison for Cranked Arrow Wing (F-16XL-1) at Subsonic and Transonic Speeds*, NASA/TP-2001-210629, February 2001.

Chapter 2 – NECESSITY AND UTILITY OF A VIRTUAL LABORATORY IN AVT-113

by

John E. Lamar *(Retired)* **and James M. Luckring**

2.1 SUMMARY

The Virtual Laboratory (VL) was to be an integral part of the database service that NASA provided to the international community, and for a brief period the VL was fully operational in the CAWAPI facet of the AVT-113 task group. This chapter details how one can construct a VL and also some of the lessons learned along the way that required changes to be made. The VL was to support both the CAWAPI and VFE-2 facets but due to the lack of funding and sufficient Information Technology (IT) support people with the right skills, the VFE-2 facet only reached the advanced planning stage with little software in place. However, both efforts point out the value of a VL in a task group like AVT-113 and illustrate that there needs to be a budgeted item for the IT effort to bring the VL to full operational status in each application.

2.2 INTRODUCTION

Applied Vehicle Technology (AVT) panel chairmen have reiterated at Research and Technology Organisation (RTO) Symposia over the past several years the need for task groups to operate in a virtual laboratory (VL or VLAB) environment. There appear to be at least three valid reasons why they have encouraged the groups to do so. The first is that VLs have become increasingly used in many fields of study, as noted in a literature survey of recent citations summarized in [2-1] which include: education, space science, molecular science/mechanics, physics, structures and materials, environment monitoring, computer science (VL improvement), simulations, mechanics, medical, aerodynamics and a range of other fields. (Some of the preceding reference citations, including those for simulation, aerodynamics and 'range of other fields', involve real-world applications.) A second is that the AVT and RTO are organizations seek to be on the cutting edge of technology and the VL technology is one in which they are not fully vested; and a third is that task groups functioning within a VL environment are anticipated to realize increases in efficiency and collaboration.

Moreover, the Research and Technology Agency (RTA) has established within its Information Management Committee (IMC) an emphasis of developing such a capability for its own and task group use. One product that has been created is the 'Science, Technology and Research Network' (STARNET). "The purpose of this network is to facilitate access to information elements existing worldwide, in terms of science, technology and overall research; it is a database of Web-based data sources, which will allow comprehensive and sophisticated searches. STARNET is designed as a virtual library to provide a "one stop" information resource for policy makers, program managers, scientists, engineers and researchers. It has been designed as a system that can be adapted to address specific information needs as they arise within the NATO community" [2-2]. In addition to these organizational encouragement efforts, individual task groups have identified similar and other needs during the same time frame.

To that end the AVT Panel, through its executive, organized a meeting in Williamsburg, VA during the June 2004 Spring Symposium for those task group chairmen and others interested in VLs to exchange information.

The needs identified at that meeting were reported by its chairman [2-3] to the AVT Panel and include:

1) Tools for collaborative interactions – person/person in a closed group;

2) Team workspace (interactive with team – show documents on computer);

3) Electronic meetings;

4) Electronic library (team data, hyperlinks to other data);

5) Ability to have interactions/workspace for the team both during and after the task group's work is completed; and

6) Firewalls on computer.

The NATO tools of RTO Forum and STARNET were identified as being available and new ones, such as Web Information Services Environment (WISE) [2-4] and the Aerospace Materials Technology Consortium Environment (AMTCE) [2-5], were highlighted as offering real possibilities to many task groups. (After the meeting it was learned that the "… RTO Forum was first developed by the RTA Staffs in June 2002 as a first generation collaborative environment for the RTO Scientific Community. The system was taken off line in November 2004 where it was replaced by the RTO WISE Collaborative Environment.") [2-6].

However, none of these VL tools completely addressed the needs of AVT-113 whose topic is the "Understanding and Modeling Vortical Flows to Improve the Technology Readiness Level for Military Aircraft". In particular, the VL needed by this task group must be able to handle restricted data subject to the 'International Traffic in Arms Regulations' (ITAR), as the geometrical data for the F-16XL aircraft, expressed in either its IGES description or by computational grid files, fall in this category. In addition, these data are only releasable by NASA to those NATO/PfP member nation organizations that have signed Memorandum of Agreements (MOAs) in place regarding the data usage. Moreover, in order for this VL to be truly collaborative, it must allow designated members from those organizations to upload results from CFD solutions to a mass storage and retrieval system for download by other members. Since the VL is hosted at NASA Langley, the preceding created a problem because the upload of data by foreign nationals to the Langley mass store system was not allowed when this effort commenced. Lastly, the VL must be able to accommodate more than one set of users, one with restrictions and one without, as there are two facets of work within AVT-113. In particular, one set will use CFD to predict the F-16XL flight measurements of [2-7] in the Cranked Arrow Wing Aerodynamics Project International (CAWAPI) facet, and the other set will obtain new data for a 65° delta-wing model or use CFD to predict it, along with existing data, in the Vortex Flow Experiment-2 (VFE-2) [2-8] facet. (This multi-user-set feature could be expanded – with appropriate funding and support – to include other international groups who need relational database storage and retrieval as a part of their collaborative efforts.)

The following sections address how the AVT-113 requirements were taken into account and resolved, as well as provide examples of VL content and usage. Due to funding shortfalls and lack of critical IT staff, the VL plans for VFE-2 were not implemented, thus only the thinking and planning for this facet are reported here.

2.3 NECESSITY AND UTILITY DISCUSSION

2.3.1 CAWAPI Facet

As the VL requirements of the CAWAPI facet were more advanced than those of the VFE-2 facet, they are addressed first and depicted in Figure 2-1 by a primitive solution. This depiction highlights many key

elements, including the recognition that only international organizations with MOAs in place with NASA can participate. It works as follows: All data requests and transmissions between members must first pass through the NASA point of contact (POC). Data and its associated meta-data are sent to the POC, who would turn this information over to the database manager for encryption and placement in the mass storage system. Likewise, a data request sent to the POC results in a request to the database manager who would retrieve the data, decrypt it, and put it on a CD for the POC to forward. However, if geometry or grid data are requested, the POC must obtain the approval of the Export Control Officer (ECO) before completely fulfilling the request. Subsequently, the ECO sends a periodic report to the State Department on those export-controlled items transmitted within a specified time period.

Figure 2-1: Primitive AVT-113 Solution: Original Process.

Details of the process used to develop and implement a VL for AVT-113 have been documented [2-9] and these include the various personnel, actions and coordination that were required across multiple areas of expertise. A portion of the report is highlighted here. "The initial requirements for the system were defined by the researcher/aerodynamicist, and molded into an initial application design by the web and database application personnel. This design was then presented to security personnel, who added specific additional system and data security requirements. Since some of the data archived in the system are considered ITAR, the export control personnel were consulted and specific reporting requirements were added. Once a complete set of requirements was defined, networking personnel implemented the De-Militarized Zone (DMZ) network and the necessary rule sets." [2-9] A hardware platform was chosen and installed on the DMZ by system administration personnel who were also responsible for the installation of system software, such as the web server. The result of the preceding is that the VL web server platform is located outside of and electronically isolated from the NASA Langley network, except through a secure port or shell (SSH). "Database administration personnel were required to install the relational database engine, and provide connectivity between the database server and the web server. Additional security personnel were utilized to obtain Public

Key Infrastructure (PKI) certificates used in the encryption of data designated as needing to be protected. Database application developers defined the data schema and implemented structured query language for the database interface, while the web application developers defined and implemented the user-interface. Mass storage personnel were consulted for file storage requirements and backup procedures." [2-9]

Once all these requirements were turned into a viable hardware/software set, the resulting system architecture looks like that shown in Figure 2-2 and consists of a user's desktop, a web server located in the DMZ, a database server and a mass storage system which are connected to the web server by a secure link, shell or port. The associated web pages – see Figure 2-3 as an example – allow authorized members to enter the CAWAPI system and perform the following functions:

- Add a CFD Test and associated meta-data to the archive

- Add a CFD Run and associated meta-data to the archive

- Update meta-data and add new files associated with an existing CFD Run

- Search the archive for CFD data files based on a set of test conditions

- Search the archive for Flight Test data files based on a set of test conditions

- Search the archive for geometry/grid files used in archived CFD Runs

- Upload new geometry grid files to archive

- Download non-ITAR data files

- Download ITAR data files to verified users and Report Activity to Export Control Officer [2-9]
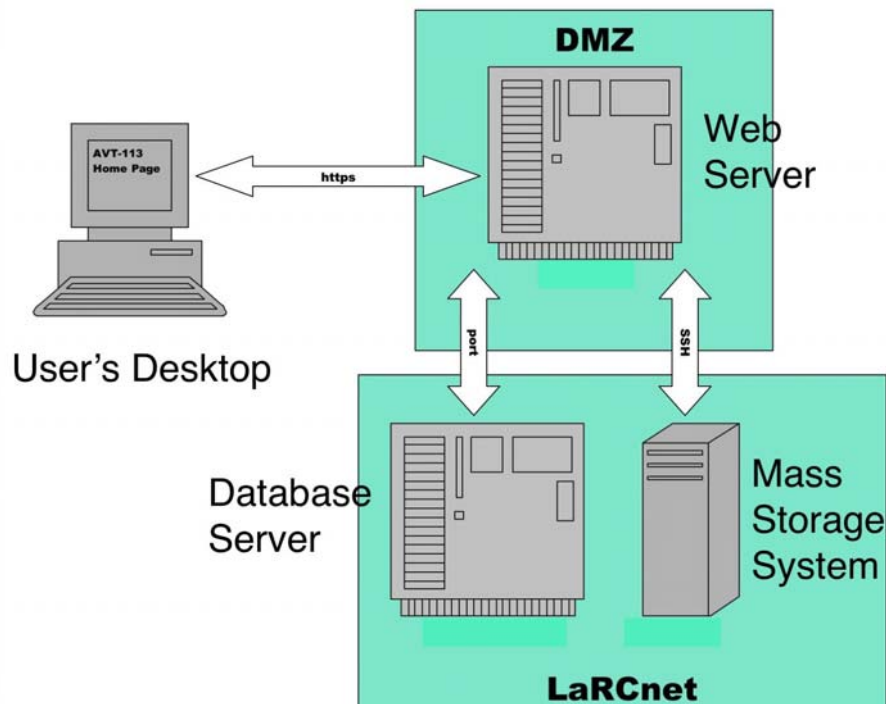
Figure 2-2: Components Needed to Create a Virtual Laboratory Solution for AVT-113, Plan 2003/2004.
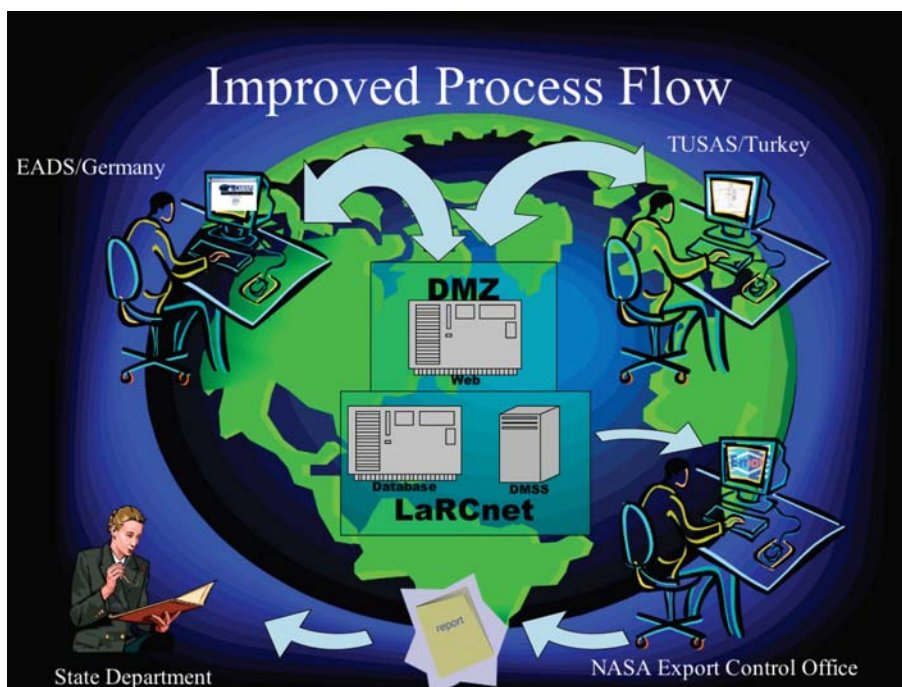
Figure 2-3: Replacement of Primitive Solution with Virtual Laboratory: Improved Process.

Figure 2-4 shows how this VL functions as a replacement for the primitive system.
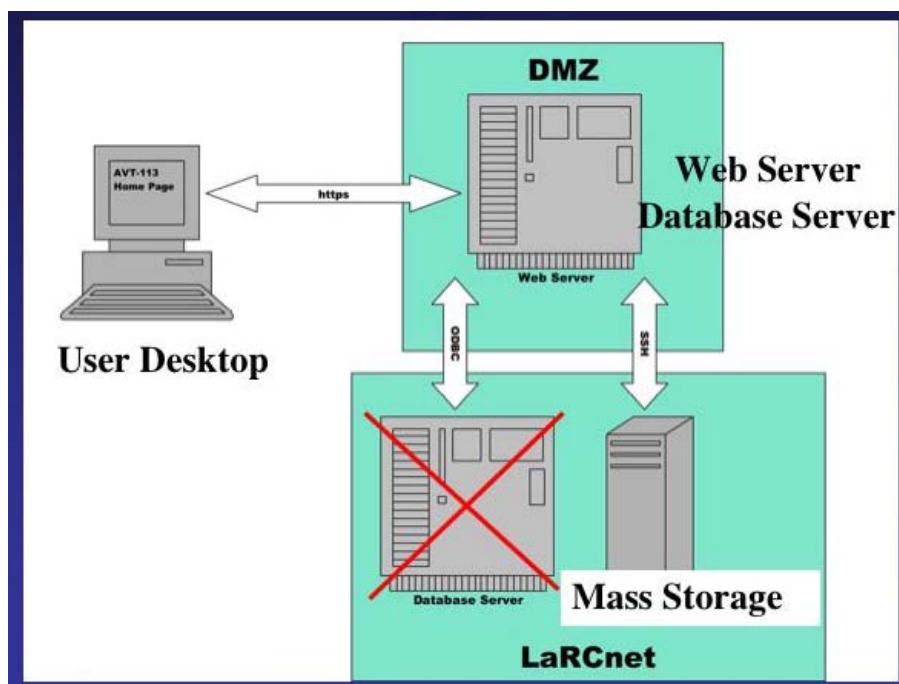
Figure 2-4: Planned Upgrade Virtual Laboratory for AVT-113 to Satisfy Reduced Annual Cost, 2005.

2.3.2   VFE-2 Facet

The VL for CAWAPI facet was extended to include the VFE-2 facet; however, more than a simple extension was performed. This facet also makes use of other database products developed for wind-tunnel data archiving and transmission. The final result is that database searches can be made on additional data types for both wind-tunnel and CFD, and the keywords used for searching have been significantly extended to cover both CFD and wind-tunnel associated defining parameters. Moreover, this database structure is general enough to accommodate other projects by simply changing the defining parameters.

2.3.3   Web Server Access

The VL has three web servers member groups, AVT-113, CAWAPI and VFE-2. All members have access to the their own web server group and AVT-113, but those in CAWAPI also have access to VFE-2, as it is unrestricted to task group members.

2.3.4   Data Types Supported by AVT-113 VL

Any data type for which the relational database schema with defining appropriate meta-data has been prepared is acceptable. This includes a large range of experimental and computational data. In addition, any associated information that can be put on a Web page, such as documents, meeting notes, presentations, etc., can also be accommodated. Since unsteady data collections or predictions result in many large files, this type of VL could potentially be used in that scenario due to its ability to deal with such files.

2.4   SURPRISES AND ADJUSTMENTS

Once the VL was developed and others began to use it, some surprises became apparent with respect to its functionality and sustainability. In particular, there were two issues that had to be addressed expeditiously and they are detailed in the following sections.

2.4.1   File Size

Based on some previous studies for a structured grid, it was anticipated that the maximum file size would be no larger than about 100 MB. However, it was soon learned that unstructured grid files could be ~1 GB and the structured grids could also be larger than first thought. This led to restricted downloading from the VL due to having insufficient space on the Web server to hold both the encrypted and decrypted files in memory simultaneously prior to responding to the request. The consequence of this was that complete files were not available, an unacceptable result. In other instances, the time to download such large files over the internet was excessive for non-USA participants and that led to incomplete files being received.

The adjustments made to accommodate this problem were twofold. First there were IT changes made by both NASA and non-USA participants to address the download time problem. This lead to the download of files that were ~300 MB file in ~ 20 minutes, of which 6 minutes is decryption time on the web-server and is common for any file size. The second change was to implement the use of the CGNS [2-10] format for grids. This change led to file size reductions from 880 MB to 254 MB and the smaller size has already been demonstrated to be downloadable in a reasonable amount of time. Of course, there will always be the need for some users to create pre-processors to read CGNS formatted files and to put them into a format readable by their particular solver.

2.4.2   Out-Years Maintenance Cost

The cost of sustaining such a VL was not given much thought when this effort began or during its development because NASA was under one set of financial accounting; however, as full cost accounting became the standard, the situation changed. The estimate for sustaining the effort based on its initial system layout (Figure 2-2) was $40 – 50K/yr. – a value not even sustainable under the old financial system – and included system administrator (SA) services for the web and database servers, as well as the annual license renewal fee for the relational database software.

The adjustments made to accommodate this problem were also twofold. First, move the database server function onto the web-server platform. This resulted in only one machine needing maintenance and that could be done by a part-time SA for ~$10K/yr. The second involved rewriting a small portion of code in order to use **free** relational database software, thus avoiding the annual fee. These adjustments led to the current configuration for the AVT-113 VL as shown in Figure 2-5.
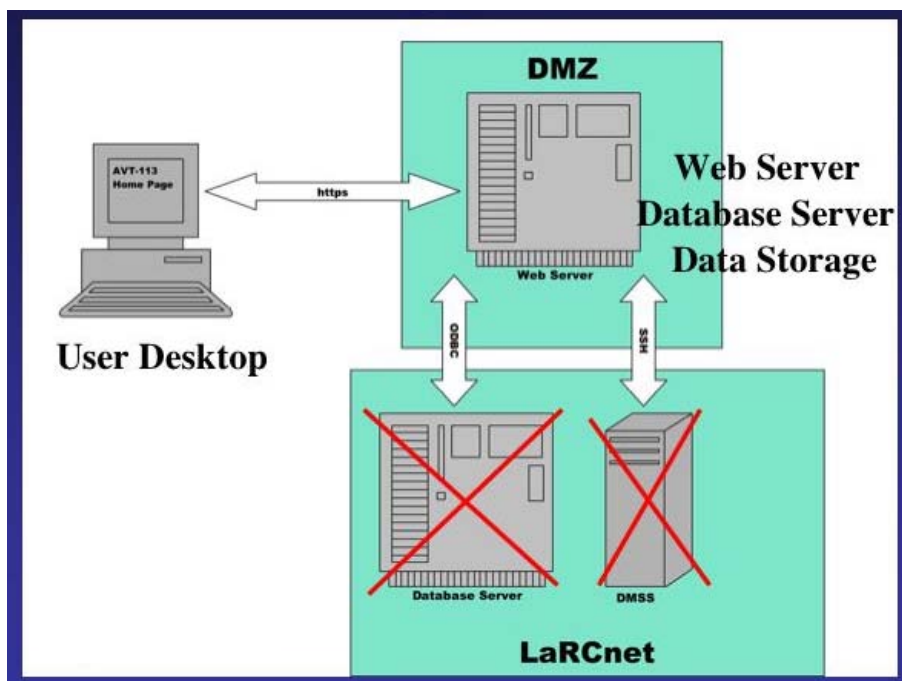
Figure 2-5: Necessitated Upgrade to Virtual Laboratory to Satisfy Loss of Mass Storage System, 2005.

2.5   COLLABORATIVE CAWAPI RESEARCH EXAMPLES

Three collaborative research examples follow:

1) The original purpose;

2) Structural grid generation by partners; and

3) A place to upload large files.

2.5.1 Original Purpose

The purpose for the creation of this VL was to allow CAWAPI members to share CFD results, computer images, comparisons and data files in a secure environment while meeting all the restrictions associated with ITAR data. This purpose has been accomplished as attested to by the number of solutions added to the database since the effort started. Moreover, the use of a common data format has facilitated the creation of data comparisons added to the database. Figure 2-3 shows the list of 'CAWAPI Data Archive' options available to the members and Figure 2-6 illustrates the user process envisioned by the developers; wherein a member downloads geometry/grids and other data from the archive to obtain a solution and subsequently uploads the CFD grid/solution/results and data comparisons back into the archive.
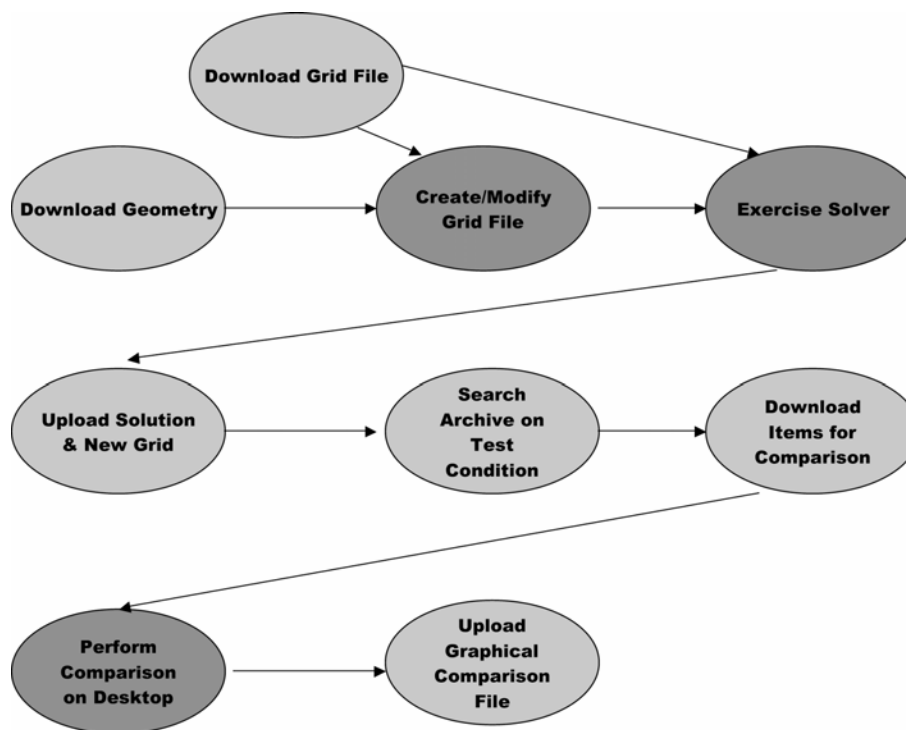
Figure 2-6: Virtual Laboratory Process as Envisioned for CAWAPI Facet.

2.5.2 Structured Grid Creation

Space was provided in the VL so that two members of the CAWAPI facet – one at the Netherlands National Aerospace Laboratory (NLR) and the other at the U.K. University of Glasgow (UGlasgow) – could collaborate in the development of the structured grid for their own use as well as for others. This is a risky endeavor even if the developers are co-located or on the same hall, but certainly more-so if they are in two different countries and having to rely on the VL for all grid exchanges. The plan was for the NLR to produce the blocking strategy with implementation and for UGlasgow to adjust the grid spacing, as needed. Alternatively, NLR could produce and test the grid then UGlasgow would perform a second test on the grid before its general release to the facet. In either case, both would use and support the same grid file. For this problem, it turned out that the alternate plan was the one implemented due, in part, to the difficulties experienced with the transfer of large files, noted previously, from this newly developed VL.

2.5.3 Large File Storage

Because the collaborative work area existed, it served another purpose and that was the location to which members could store large files. There were two occasions in which it has proven useful in this regard. The first was the storage of CGNS formatted files for others to download and use in their solvers, but for which no solution existed and therefore not uploadable into the 'Archive a New CFD Run' provided area. The second was the storage of the minutes and presentations from one of the task group meetings. Once the NASA team learned that the zipped file containing this information was stored on the VL, it was downloaded, unzipped and the components placed in their proper location on the VL for access by all facet members, one file at a time.

2.6 COLLABORATIVE VFE-2 RESEARCH EXAMPLES

Two collaborative research examples are available for this facet in advance of its planned data archive system being implemented. They are cited here because the VL was used to transmit needed grid data for this unclassified model between facet members. The fist is the structured grid developed in the USA that was used by Pressure Sensitive Paint experimenters in Germany; and the second is an unstructured grid, also developed in the USA, but reformatted in Sweden and placed on the VL for download by others.
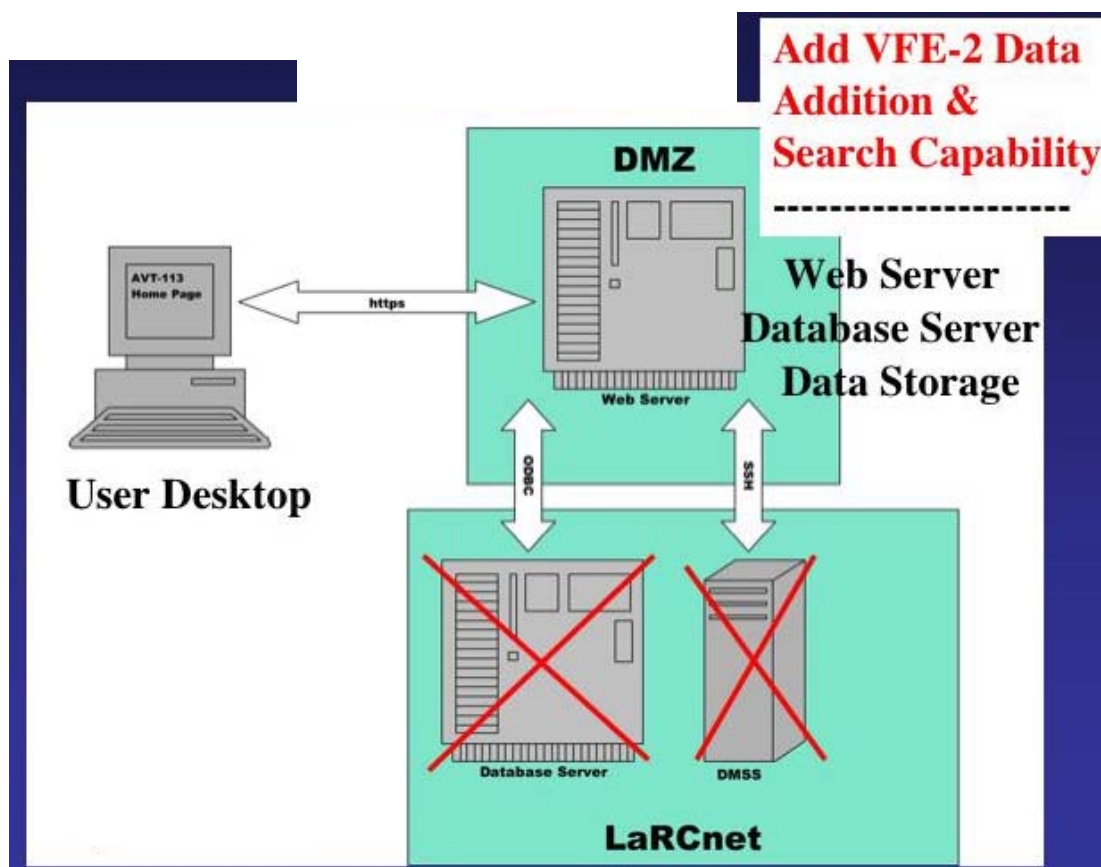
Figure 2-7: Virtual Laboratory Including VFE-2 Facet Capability.

2.7   CONCLUDING REMARKS

The Virtual Laboratory (VL) was to be an integral part of the database service that NASA provided to the international community, and for a brief period the VL was fully operational for the CAWAPI facet. However, the capabilities contained in that version were not fully implemented in the mandated replacements of software and hardware which resulted in a VL that lacked full operational capability. Moreover, due to the lack of funding and sufficient Information Technology (IT) support people with the right skills, the VFE-2 facet only reached the advanced planning stage with little software in place. However, both efforts point out the value of a VL in a task group like AVT-113 and illustrate that there needs to be a budgeted item for the IT effort to bring the VL to full operational status in each application.

2.8   REFERENCES

[2-1]   Lamar, J.E., Cronin, C.K. and Scott, L.E.: *Virtual Laboratory Enabling Collaborative Research in Applied Vehicle Technologies*, In AVT-123 Symposium on "Flow Induced Unsteady Loads and the Impact on Military Applications", Keynote 2, Budapest, Hungary, April 25-29, 2005.

[2-2]   Staff of the RTA. http://starnet.rta.nato.int/ Accessed 11/30/04.

[2-3]   Waldman, J.: Unpublished Charts Presented to the AVT Panel in Williamsburg, VA, USA, on June 11, 2004.

[2-4]   Staff of the Allied Command Transformation. http://open.act.nato.int/ Accessed 12/01/04 with username: openuser; and password: Open2all – WISE link is in Product Projects area.

[2-5]   Staff of the AMTCE. www.asm-philadelphia.com/ Accessed 11/30/04.

[2-6]   Reed, P.: Personal e-mail to first author dated 12/17/04.

[2-7]   Lamar, J.E., Obara, C.J., Fisher, B.D. and Fisher, D.F.: *Flight, Wind-Tunnel, and Computational Fluid Dynamics Comparison for Cranked Arrow Wing (F-16XL-1) at Subsonic and Transonic Speeds*, NASA/TP-2001-210629, February 2001.

[2-8]   Hummel, D. and Redeker, G.: *A New Vortex Flow Experiment for Computer Code Validation*, Presented at RTO AVT Symposium on "Advanced Flow Management; Part A – Vortex Flow and High Angle of Attack", Paper Number 8, in Loen, Norway, during May 7-11, 2001.

[2-9]   Lamar, J.E., Cronin, C.K. and Scott, L.E.: *A Review of Steps Taken to Create an International Virtual Laboratory at NASA Langley for Aerodynamic Prediction and Comparison*, Progress in Aerospace Sciences, Vol. 40/3, April 2004, pp. 163-172.

[2-10] CGNS Steering Committee. http://www.cgns.org. Accessed 11/29/04.

Chapter 3 – THE CRANKED ARROW WING AERODYNAMICS PROJECT (CAWAP) AND ITS EXTENSION TO THE INTERNATIONAL COMMUNITY AS CAWAPI: OBJECTIVES AND OVERVIEW

by

John E. Lamar *(Retired)* [*] **and Clifford J. Obara**[†]

3.1 SUMMARY

This paper provides a brief history of the F-16XL-1 aircraft, its role in the High Speed Research (HSR) program and how it was morphed into the Cranked Arrow Wing Aerodynamics Project (CAWAP). Various flight, wind-tunnel and Computational Fluid Dynamics (CFD) data sets were generated during the CAWAP. These unique and open flight datasets for surface pressures, boundary-layer profiles and skin-friction distributions, along with surface flow data, are described and sample data comparisons given. This is followed by a description of how the project became internationalized to be known as Cranked Arrow Wing Aerodynamics Project International (CAWAPI) and is concluded by an introduction to the results of a 5-year CFD predictive study of data.

3.2 INTRODUCTION

This paper provides a brief history of the F-16XL-1 aircraft, its role in the High Speed Research (HSR) program and how it was morphed into the Cranked Arrow Wing Aerodynamics Project (CAWAP). Various flight, wind-tunnel and Computational Fluid Dynamics (CFD) data sets were generated during the CAWAP [3-2]. These are described and sample data comparisons given. This is followed by a description of how the project became internationalized and is concluded by an introduction to the results of a 5-year CFD predictive study of data collected at flight conditions.

3.2.1 CAWAP History

3.2.1.1 F-16XL Airplane

The F-16XL-1 airplane is a single-place, fighter-type prototype aircraft developed by the General Dynamics Corporation – Ft. Worth Division (now Lockheed Martin Aeronautics Company – Fort Worth) by stretching the fuselage of a Full-Scale Development F-16A and adding a cranked-arrow wing, a modified fuel system, and a modified flight control system. There were two F-16XL aircraft built, the -1, which was used in the CAWAP, and a two-place version, the -2. Consequently, the terms F-16XL and F-16XL-1 are used interchangeably in this paper. Both aircraft had scheduled leading-edge flaps, elevons, and ailerons on the wing for control. The technical specifications for the airplane are given in Table 3-1, which is reconstructed from reference [3-2]. Details on the construction of the aircraft and its intended missions are given in references [3-3]-[3-5].

---

[*] CAWAP Principal Investigator, Configuration Aerodynamics Branch *(Retired)*, MS 499.

[†] CAWAP Project Engineer, Experimental Research Services, MS 237.

Table 3-1: F-16XL-1 Airplane Specifications

Feature	Value
Wing Span	32.4 ft
Height	17.606 ft
Length	54.155 ft
Reference Chord	24.7 ft
Theoretical Root Chord	41.75 ft
Wing Area	646.37 ft^2
Reference Wing Area	600 ft^2
Reference Aspect Ratio	1.75
Typical Takeoff Weight	35,000 lb
Engine; Max Thrust	Pratt & Whitney F100-PW-200; 23,830 lb

The design of the cranked-arrow wing was a cooperative effort of the General Dynamics Corporation and the NASA Langley Research Center. The new wing, common for both the -1 and -2 versions, was designed to provide the F-16 aircraft with improved supersonic performance while maintaining comparable transonic performance to that provided by the current F-16 design. Low-speed wind-tunnel data [3-2] confirm the basic neutral pitch-stability of the aircraft and its cranked-arrow wing planform should limit aerodynamic center movement with increasing Mach number. This leads to flights at 1-g in which the need for trailing-edge control deflections is kept to a minimum. As shown in Figure 3-1 and Figure 3-2, the resultant design had a leading-edge (LE) sweep angle of 70° inboard and 50° outboard of the crank. At the juncture of the wing leading edge with the fuselage, an "S-blend curve" was placed in the leading edge to alleviate a pitch instability that was found to occur at high angles of attack in wind-tunnel tests. All flight test data reported in reference [3-2] were collected with the air dams – upper-surface fences mounted near the wing leading-edge crank – and wing-tip missiles installed, as shown in these figures.

Figure 3-1: F-16XL-1 Aircraft with Missiles, Tufts, Modified Flow-Visualization Paint Scheme, and Video Targets at NASA Dryden Flight Research Center (NASA Photo EC96-43508-2).
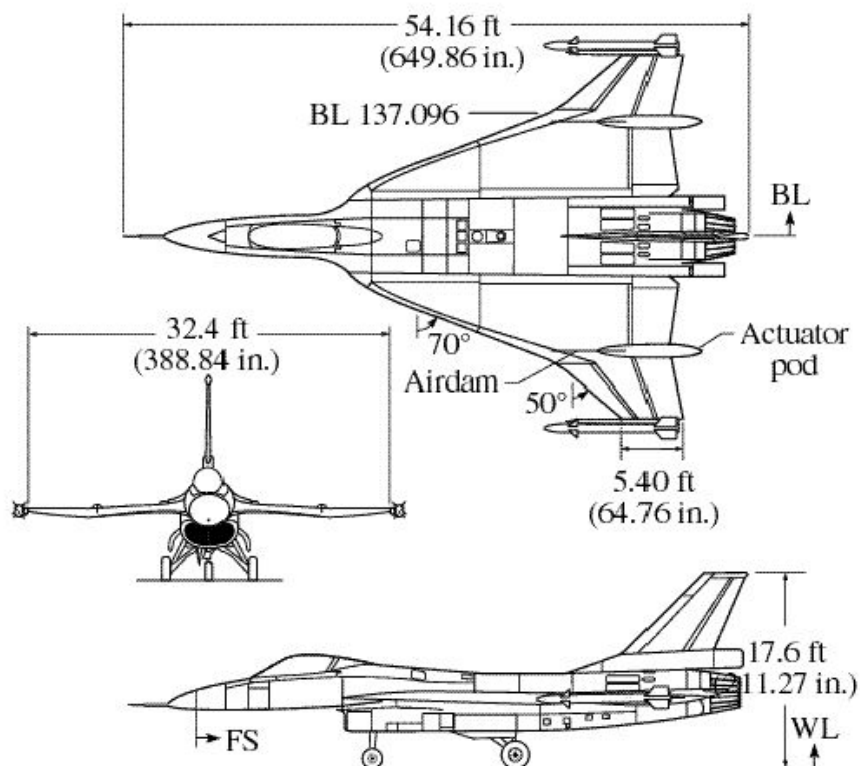
Figure 3-2: Three-View Drawing of F-16XL-1 Airplane. Linear dimensions are in feet (inches).

3.2.1.2   HSR Program Overview

This program was started in 1990 to develop the technologies that would result in a supersonic passenger jet that would fly 300 passengers at more than twice the speed of sound while maintaining comparable ticket prices to current subsonic transports. As envisioned by the government and industrial partners, the high speed civil transport (HSCT) would cross the Atlantic or Pacific oceans in half the time of modern subsonic jets using new technologies for airframe manufacturing, propulsion systems, aerodynamics, and reduced environmental impacts. By 1995, based on several industry design concepts, computer modeling, and wind tunnel tests, a Technology Concept Airplane was selected as a common reference point in furthering the technology development process. This single concept was to have improved aerodynamic performance and operational characteristics while also meeting environmental goals for emissions and noise pollution. The HSCT concept is depicted in Figure 3-3.
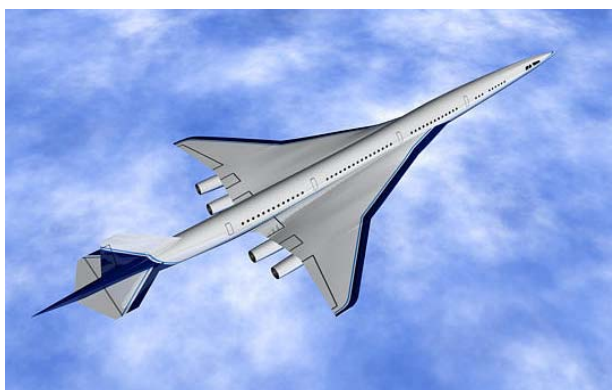
Figure 3-3: High-Speed Civil Transport Concept.

Due to economic constraints, the program was phased out in fiscal year 1999. Despite the cancellation, the program still managed to meet or exceed many of the original HSR program goals. New high-temperature composite materials and structural concepts were developed to keep weight and manufacturing costs down while maintaining the strength and durability that would be required for the aircraft. NASA engineers developed new vision systems for the pilots that maintained safety and performance capabilities while eliminating the need for a drooped nose similar to the Concorde. Another critical element to the program was the development of a propulsion system that would not harm the environment both in atmospheric effects as well as mitigating the noise, while providing the performance and durability required to keep the aircraft economically viable.

3.2.1.3   F-16XL Flight Overview / Planning for HSR

Early in the development of the HSR program, it was determined that improved aerodynamic performance, while reducing the noise at high-lift conditions during take-off and landing, was a critical element to the program. The availability of the F-16XL aircraft with its cranked wing configuration, which was similar to the HSCT concept, provided a unique opportunity for CFD correlation and code validation with flight and wind-tunnel data. The project was divided into three phases based on the required geometry changes to the basic aircraft. The phases are depicted schematically in Figure 3-4 relative to the aircraft modification required. Phase 1 was the basic airplane with no modifications. This phase would serve as a baseline for the future modifications. Phase 2 required the removal of the "S" curve in the apex region of the wing. This second configuration was

more representative of the HSCT cranked wing. The third and final phase would incorporate a high-lift device along the entire leading edge of the aircraft. The exact configuration of the high-lift device would be determined from wind-tunnel experiments and CFD predictions. The high-lift configuration would be representative of the HSCT in a take-off or landing configuration.
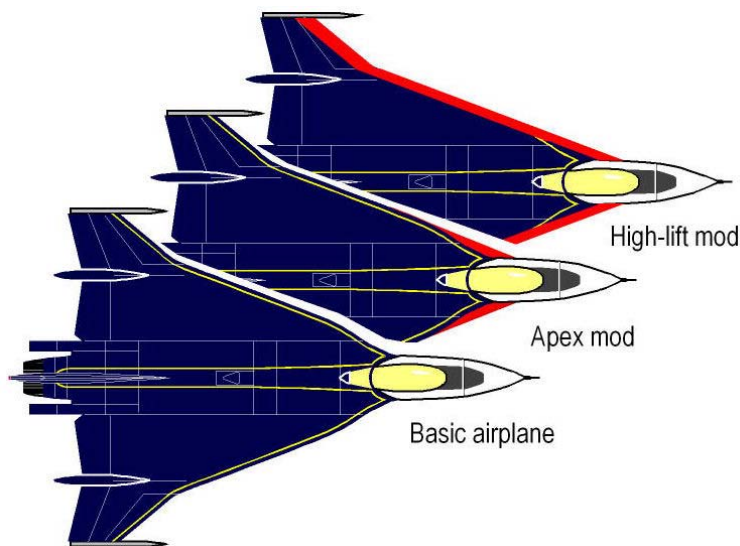
Figure 3-4: F-16XL-1 Research Aircraft Modifications.

The primary objective of the flight test project was to verify the performance of high-lift concepts while ensuring compliance with community noise standards. The first step was to establish a ground to flight correlation for the cranked-arrow wing planform. All three configurations as described would be flight-tested and the data would be used as a calibration of the design analysis tools as well as the noise prediction codes. In addition, advanced operating procedures for take-off and landing would be evaluated. The final objective was to assess integration and "real-world" operation of high-lift devices. A schematic of the ground to flight correlation is shown in Figure 3-5.
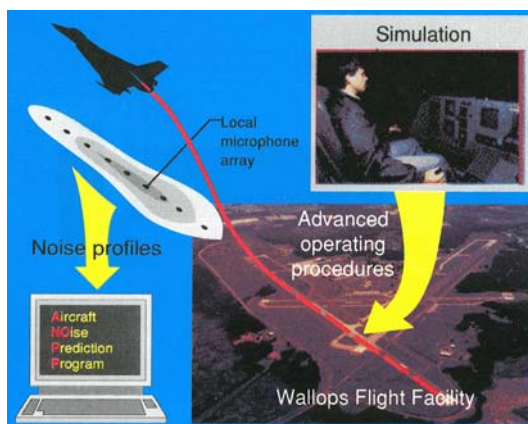
**Figure 3-5: Schematic of Ground to Flight Correlation for Assessing the
Impact of Aerodynamic and Operational Concepts on Noise Profiles.**

3.2.1.4   CAWAP

During the Phase 1 experiments on the baseline F-16XL aircraft in the spring of 1994, the remainder of the project as planned was cancelled due to funding limitations. Sufficient funding was provided to complete the first phase of the project, with a slight change to the objectives. This was the start of the CAWAP as it is known today. The revised objectives were to document upper-surface flow physics at high-lift and transonic test conditions and to characterize the stability and control of the aircraft. The original intent of a flight, wind-tunnel, and CFD correlation experiment would be maintained, albeit for the baseline F-16XL configuration only. Table 3-2 illustrates the extensive set of planned comparisons between flight, wind-tunnel and CFD, and Table 3-3 provides the actual set of comparisons made. (These two tables are reconstructed and *modified* from Ref. [3-2].)

Table 3-2: Planned F-16XL CAWAP Data Comparisons

Item	Data Comparison	Data Type/Instrument	Data Source
1	On and off surface flow	Tufts Static pressures in a row Vapor screen Particle traces	Flight Flight Flight CFD
2	Surface flow and pressure	Oil flow Pressure sensitive paint (PSP)	Wind tunnel Wind tunnel
3	Surface pressure	Pressure sensitive paint Calculations	Wind tunnel CFD
4	Vortex core location	Vapor screen Particle traces	Wind tunnel CFD
5	Vortex core location	Vapor screen Particle traces	Flight, wind tunnel CFD
6	Surface flow	Oil flow Tufts Liquid Crystals	Flight Flight Flight
7	Surface flow	Oil flow Tufts Particle traces	Flight Flight CFD
8	Surface flow	Oil flow Particle traces	Flight, wind tunnel CFD
9	Surface pressure	Pressure sensitive paint Particle traces	Wind tunnel Wind tunnel
10	Off surface flow	Vapor screen Five-hole probe	Flight, wind tunnel Wind tunnel
11	On and off surface flow	Oil flow Vapor screen Particle traces	Flight Flight CFD
12	On and off surface flow	Oil flow Vapor screen Five-hole probe	Flight, wind tunnel Flight, wind tunnel Wind tunnel
13	Surface flow	Oil flow Tufts Liquid Crystals Propylene-glycol-methyl-ether traces	Flight Flight Flight Flight
14	Surface flow	Oil flow Tufts Particle traces Propylene-glycol-methyl-ether traces	Flight CFD Flight Flight

Table 3-2: Planned F-16XL CAWAP Data Comparisons (cont'd)

Item	Data Comparison	Data Type/Instrument	Data Source
15	Vortex core location	Vapor screen Dye traces Particle traces	Wind tunnel Water tunnel CFD
16	Surface pressure contours	Static pressures Calculations	Flight, wind tunnel CFD
17	Surface pressure	Pressure sensitive paint Static pressure in a row	Flight Flight, wind tunnel
18	Surface pressure	Pressure sensitive paint Static pressures in a row Static-pressure surface	Flight Flight, CFD CFD
19	On and off surface flow contours	Tufts Particle traces Stagnation pressure	Flight CFD CFD
20	Boundary-layer profile	Rake Velocities	Flight CFD
21	*Skin-friction distribution*	*Modified Preston tube* *Equation*	*Flight* *CFD*
22	*Leading-edge boundary layer*	*Hot-film gauges*	*Flight*

Table 3-3: Actual F-16XL CAWAP Data Comparisons

Item*	Data Comparison	Data Type/Instrument	Data Source
3	Surface pressure contours	Pressure sensitive paint Calculations	Wind tunnel CFD
6	Surface flow	Oil flow Tufts Liquid Crystals	Flight Flight Flight
12a	On and off surface flow	Oil flow Vapor screen	Wind tunnel Wind tunnel
16a	Surface pressure contours	Static pressures Calculations	Flight CFD
17a	Surface pressure	Static pressure in a row	Flight, wind tunnel
18a	Surface pressure	Static pressures in a row Static-pressure surface	Flight, CFD CFD
19	On and off surface flow	Tufts Particle traces Stagnation pressure contours	Flight CFD CFD
20	Boundary-layer profile	Rake Velocities	Flight CFD
21	*Skin-friction distribution*	*Modified Preston tube* *Equation*	*Flight* *CFD*
22	*Leading-edge boundary layer*	*Hot-film gauges*	*Flight*

* The "a" in the item number signifies a reduction in the actual number of items being compared versus the planned number.

Note that in Table 3-2 an attempt was to be made to perform off-surface laser-vapor-screen data using seeded material, and to develop surface streaklines using propylene-glycol-methyl-ether. However, these two types of data were not obtained due to the lack of funding and higher priority datasets that needed to be collected.

Moreover, consideration was given to perform PSP in flight; however, it quickly became apparent that the timing and cost of the technological development was beyond the scope of this project. The concept was to use the laser light-sheet in combination with a surface coating to obtain the pressure data, but it only reached the idea stage in a discussion between NASA Langley researchers and key personnel from the airframe industry. In addition, since the laser system was not funded to completion, this idea had to be abandoned.

3.3   DATA AVAILABLE FROM CAWAP

Seven different types of flight data were collected, as per Table 3-3, and four are shown schematically in Figure 3-6. Three were pressure based – surface static pressures, boundary-layer rakes, and modified Preston tubes [3-6]; three were video-recording based – surface tufts, surface oil and surface liquid-crystals; and one was hot-film data. The pressure- and surface-flow-data are used for the purpose of establishing the effects of variation in Mach number on the local flow. These data serve as the basis for comparison with other data sets. The hot-film data are used to establish whether boundary-layer transition occurs and under what test conditions. Geometry data of the airplane upper surface was also obtained, using photogrammetry, and compared with the numerical surface description (See Ref. [3-2]).
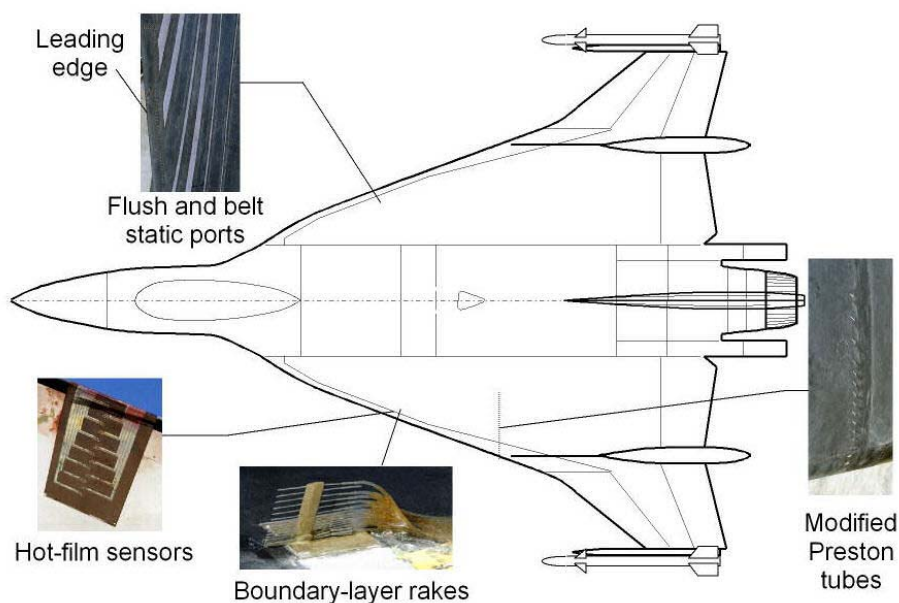
Figure 3-6: General Layout of Pressure and Hot-Film Instrumentation Suite on the F-16XL-1 Aircraft.

3.3.1   Pressure Suite

Figure 3-6 and Figure 3-7 detail the complete pressure instrumentation system layout on the aircraft, including the distribution of the static ports by type, belt or flush, and boundary-layer rakes or modified Preston tubes. These static ports are connected to internally mounted Electronically Scanning Pressure (ESP) modules through tubes. Each pressure-tube in the belt was used to measure two separate values of pressure. This was accomplished by sealing each tube about halfway along its length, thereby making provision for one forward and one aft port. The actual number of static ports associated with each belt are displayed in Figure 3-7 imbedded along the belt nominal Butt Line (BL).
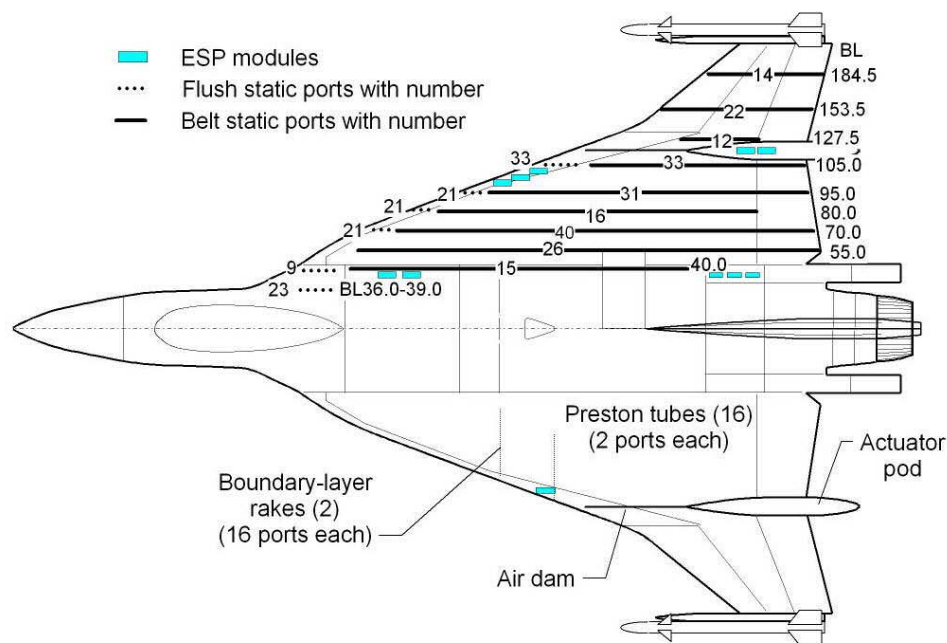
Figure 3-7: Details of Complete-Pressure-Instrumentation Suite and Layout on the Airplane.

The flight surface pressures and boundary-layer rake data are available in ASCII format, along with the associated parameter names, in [3-7] and cited as Appendix 2 of this RTO report. The pressures are ordered by flight number/test point and related to a particular flight condition through an accompanying table from Ref. [3-2]. Corresponding flight-tuft-images are also located there.

The right-wing surface pressures – mostly upper surface – were measured using 337 static ports, both flush (LE region) and in streamwise belts, through eleven 32-port ESP transducers – also called modules. Of these 337 ports, only 326 proved to be reliable and the distribution was 280 on the upper surface and 46 on the lower. The ports were arranged so that there would be a sufficient number at a given BL or Fuselage Station (FS) for cross plotting, as well as for covering other regions of special interest; i.e., the apex and ahead of/and behind the hinge-lines of the trailing-edge control-surfaces.

Boundary-layer measurements were made using two, two-inch high, rakes at a time at four different positions on the left wing and the most inboard one was always used as a control. Each rake used 16 active tubes – 15 total pressures and one static pressure – of the 23 available. These two rakes were connected to one 32-port ESP module located inside that wing. When mounted on the aircraft, each rake was oriented into the local flow at an average angle over its height based on initial CFD predictions from the CFL3D code [3-8], [3-9]. The flow conditions were for the complete aircraft (half-aircraft modeled with symmetry assumed) at $\alpha = 13°$, $M_\infty = 0.29$ and $R_n = 46.1 \times 10^6$; i.e. **nominal values for** Flight Condition (FC) 7. (See Table 3-4 and Table 3-5 for a listing of the FCs of interest in the current study and the associated flight and engine parameters, including the **actual values for** FC7.)

Figure 3-8 shows the four boundary-layer locations chosen – one well inboard of the shed vortex systems (#3), one underneath the primary vortex (#4), and two associated with the secondary vortex. One of the latter is located underneath that vortex (#5) and the other (#7) at its separation point; all are at a nominal position of FS

295. The average of the local flow at- and slightly off-the-surface were used to establish the rake orientation angles for FC7. This figure also shows the relative locations of the modified Preston tubes. They were to be located at the same fuselage station as the boundary-layer rakes, but a more aft position for the tubes was necessitated due to easier aircraft installation and to avoid the flow off a step in the leading-edge region.
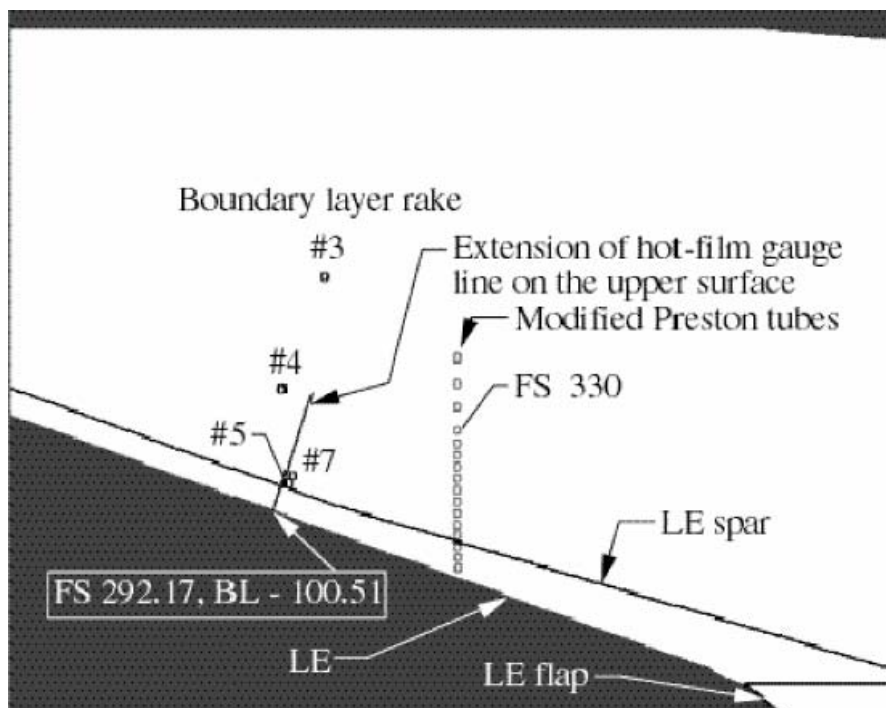
Figure 3-8: General Arrangement of Rake and Modified Preston Tube Relative Locations on F-16XL-1 Left Wing; Pressure Instruments Oriented for M_∞ = 0.29, α = 13° and R_n = 46.1 x 10^6.

The 16 modified Preston tubes (See Figure 3-6 and Figure 3-8) – the modification to each Preston tube is the integration of a static pressure port with the total pressure tube – are used to determine local skin friction across the left wing near FS 330. These 32 pressures use the same ESP as the rakes but not on the same flight. The tubes were aligned with the local flow using the same initial CFL3D solution at FC7. The equation used to generate the EFD c_f values comes from reference [3-5] and relates, through a process of calibration, the pressure change between the total and static tubes to the local skin friction.

3.3.2   Video Suite

Video data was recorded with up to six external cameras; two mounted atop the vertical tail, one on either side of the fuselage behind the canopy, and one in the nose of each dummy missile. An internally mounted HUD camera was also used on occasion. Figure 3-9 shows the camera locations on the aircraft. The time was added to each image by a time-code inserter so that the images could be compared to form a composite and so that the flight test conditions could be established. Images of interest were digitized in a 512 by 480 pixel format for further processing in order that quantifiable video data be developed. In addition to the images, the other input quantities needed for the processes are the video targets and the position and calibration characteristics of each camera/lens combination.
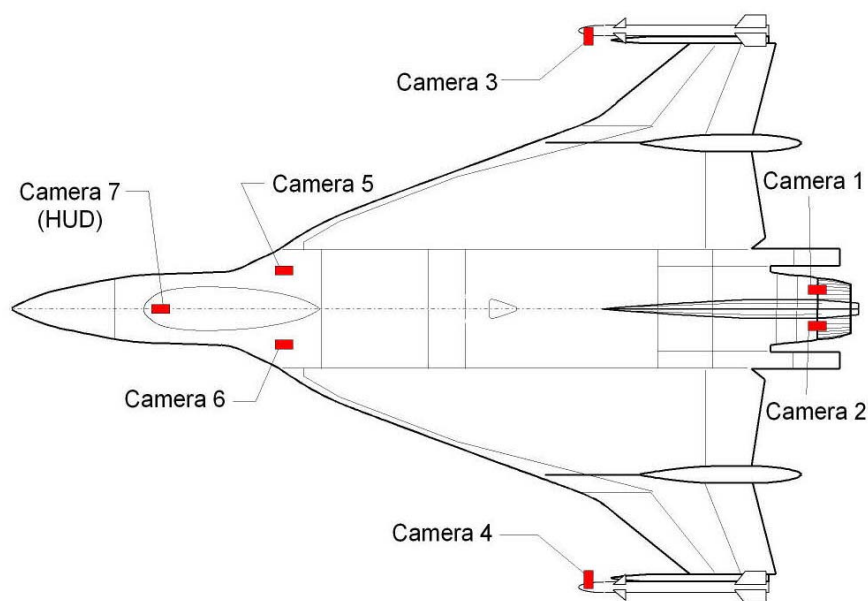
Figure 3-9: Locations of the Video Suite on the F-16XL-1 Airplane.

3.3.3   Wind Tunnel

The second major source of data was from wind-tunnel tests with a variety of model scales. Some of these wind tunnel tests were conducted on the F-16XL configuration prior to the HSR program and others were done in direct support. These tests encompassed a variety of configurations at various Mach and Reynolds numbers. Since some of the tests were conducted with the air dams not installed, they were not applicable for comparison with flight data. The following three wind tunnel tests were primarily used for the flight and CFD comparisons.

1) A test on a 0.11-scaled model was conducted in the NASA Ames 11-Foot Tunnel prior to the start of the flight project. The test is described in reference [3-10], while the actual data is tabulated in reference [3-11]. This model was specifically built to estimate the airloads for the airplane from M = 0.60 to 2.0 using 190 pressure ports distributed on the left-wing upper surface and the right-wing lower surface. The Reynolds numbers tested were 2.3 x 10^6 and 2.75 x 10^6, while the angle of attack varied from -1.94° to 28.75°. The ports were located in streamwise rows that did not nominally match the airplane. Because of data release restrictions, no direct comparisons were made with flight or CFD results. However, un-scaled transonic pressure coefficient contours were used for comparison purposes in reference [3-2].

2) The test for the 0.18-scaled model was conducted in the NASA Langley 30-by 60-Foot Tunnel at a Mach number of less than 0.08 and a Reynolds number of 2.1 x 10^6. The angle of attack varied from -5° to 30° and the angle of sideslip varied from -20° to +20°. In addition to force/moment and pressure data, some vapor screen images were captured. A set of pressure results was published [3-2] and the force/moment results were published in an earlier paper [3-12]. The basic model has 30 right-wing, flush upper surface ports located to yield pressures for both streamwise and spanwise rows. The ports are nominally duplicated on the airplane for comparison. Only two runs were utilized from this test for comparison. One was a force/moment and the other a pressure, both at 0° sideslip.

3) The third wind-tunnel test used for comparison was a 0.04-scaled model in the NASA Langley Basic Aerodynamic Research Tunnel (BART). The test conditions included Mach numbers less than or equal to 0.165, Reynolds numbers less than 1.12 x 10^6, and an angle of attack variation from 5° to 20°. This model had 82 pressure ports divided between the right upper wing surface and the left lower wing surface. The pressure ports correlated with the 0.18-scaled model as well as being nominally duplicated on the airplane. Selected results from the BART test appear in reference [3-13], where they have been compared with Euler code predictions.

3.3.4   CFD Modeling

The last major source of data was that generated by CFD [3-2]. The flow solver CFL3D was run in the Navier-Stokes mode with a turbulent boundary-layer employing the Baldwin-Lomax with the Degani-Schiff turbulence model (in the *j-k* directions) on a multiblock, patched grid over a variety of wind-tunnel and flight test conditions (See Refs. [3-8], [3-9]). Two separate grids were used to model half the aircraft configuration (with undeflected control surfaces) and external flow field. The initial grid had 36 blocks and was used with version 3 of the flow solver to produce the initial results upon which the locations and orientations of the surface instrumentation were set. The current grid had only 30 blocks and was used with version 5 of the flow solver to obtain the comparative solutions reported herein. The current grid was needed for two reasons; namely, to have the grid more closely conform to the actual fuselage and wing geometries, and to improve the grid layout on the wing and fuselage surfaces. The missile- and missile-rail-grids were effectively the same with either grid. For the current grid, the inner region of the aircraft was modeled by 16 blocks, the outer region by 14 blocks, and all 30 blocks are shown schematically in Figure 3-10. The boundary conditions were symmetry, solid wall for the outer mold lines, flow into the duct-inlet but the exhaust-face was faired over, and Riemann-type conditions at the far-field boundaries. A total of 1,372,096 cells (1,707,117 node points) were used to obtain solutions at specified test conditions (M_∞, α, grid R_n, T, etc.). To maximize computer resource allotments, the minimum number of cells was used. The resulting grid spacing normal to the numerical surface led to a value of y^+ of 2 at wind-tunnel R_n, whereas at flight R_n the average value was y^+ of 82. In an effort to compensate for the insufficient grid spacing at flight conditions, the "wall function" option was used to augment the turbulence model in CFL3D. The "wall function" is defined as that boundary-layer growth rate expected from a turbulent mean flow near the wall [3-14].

(a) Inner
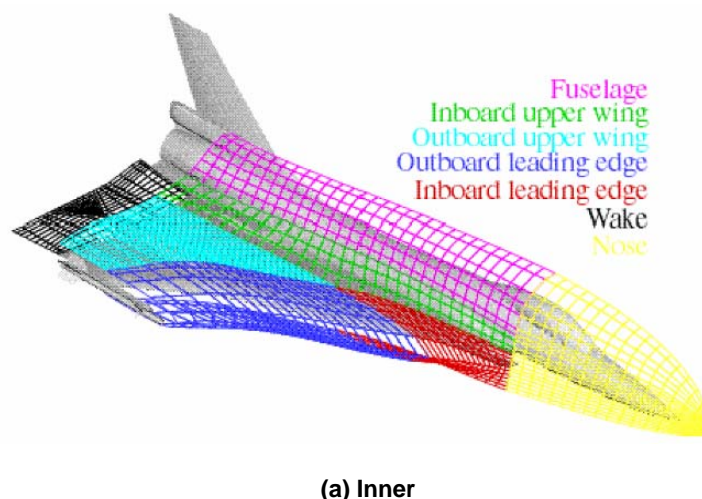
Figure 3-10: CFD Block Structure Layout for F-16XL-1.
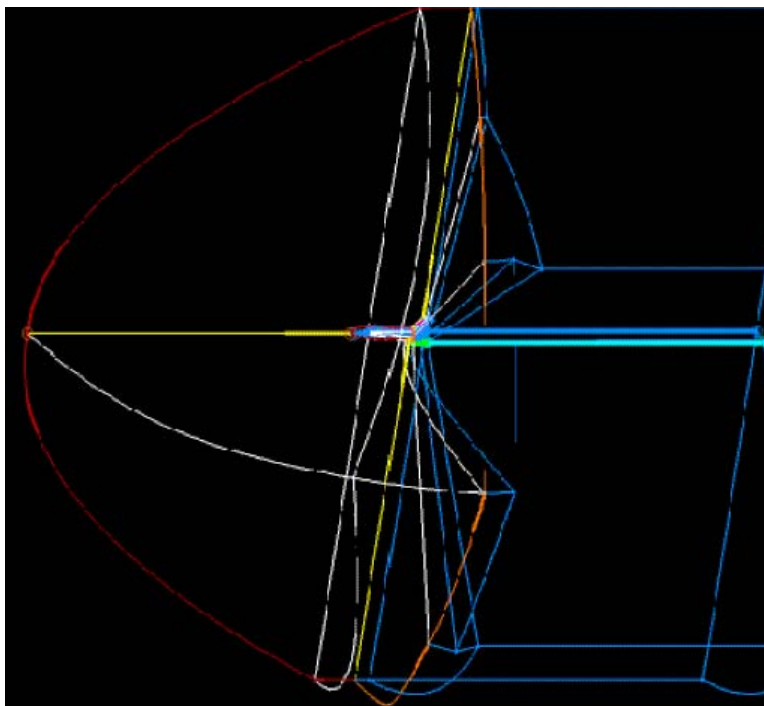
(b) Outer

Figure 3-10: Continued.

3.3.5   Database of Results

A database was set up, as described in Appendix B of reference [3-2], to facilitate data comparison between the various CAWAP sources; i.e. flight, wind-tunnel and CFD. The data types used for comparison were local surface pressures between the three sources, and boundary-layer and skin friction between the flight data and CFD predictions. Moreover, the database stores administrative information about the tests (meta-data) and the full, mass storage, path name of the resulting data files. For the Experimental Fluid Dynamics (EFD) measurements, the data stored are files of pressure, force/moment, still photographs, and two-dimensional images digitized from videotape (both instantaneous and time averaged); for CFD predictions, the grid and solution files are stored as well as C_p data at selected FSs and BLs. The F-16XL-1 database also supports the viewing of 3-D renderings of the 2-D flight images through computer software tools. Queries for selected pressure data and 2-D flight image data were available to internet users by completing an appropriate on-line form on this unclassified/unlimited server. The web service was functional at the publication time of reference [3-2] and shortly thereafter, but has since been discontinued due to changes in policies and available resources.

3.3.6   Sample CAWAP Comparisons

Selected figure samples from the CAWAP report [3-2] are repeated as Figure 3-11 to Figure 3-14. Following each set of figures is an associated commentary provided for completeness. Note that these figures may contain a legend signifying which flight and test point (run number) served as a source for the flight data; for example, **Flt144.Run3b, up**. These dataset associations are not the same as the FC but each one shown has a FC equivalent, as per the figure caption.
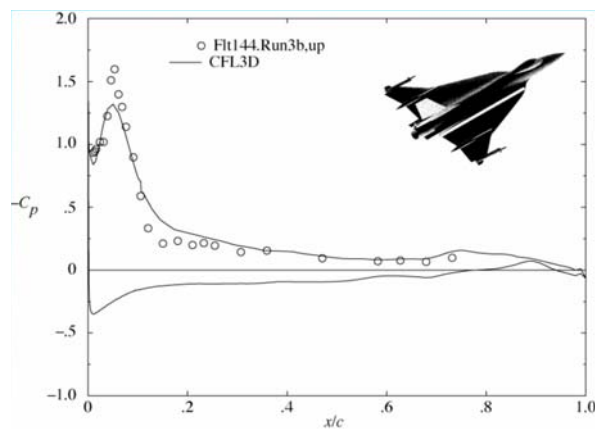
(a) BL 55
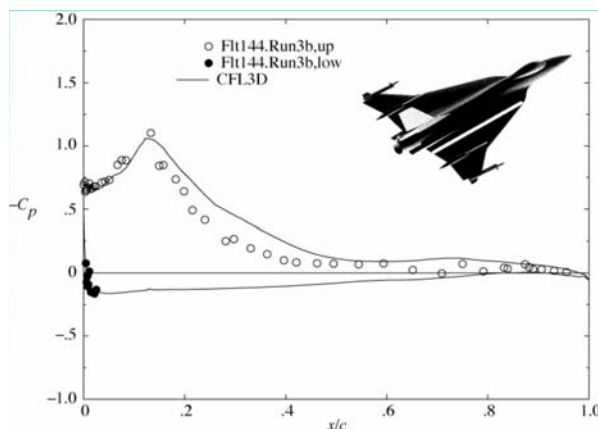
(b) BL 70
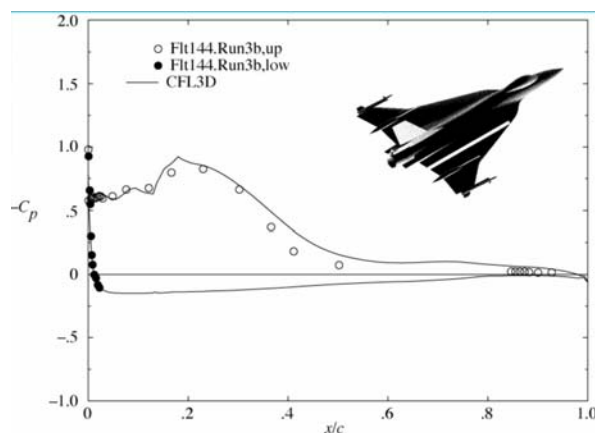
(c) BL 80
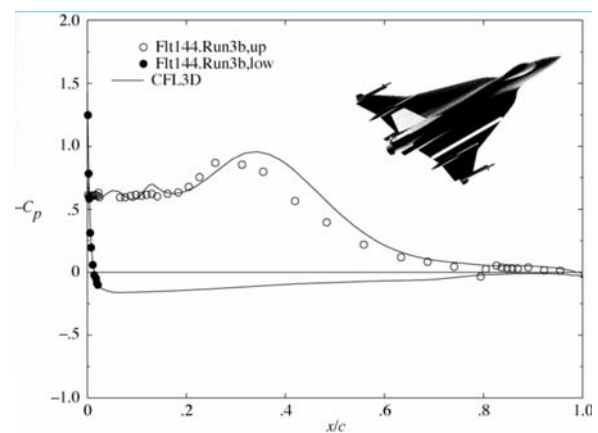
(d) BL 95
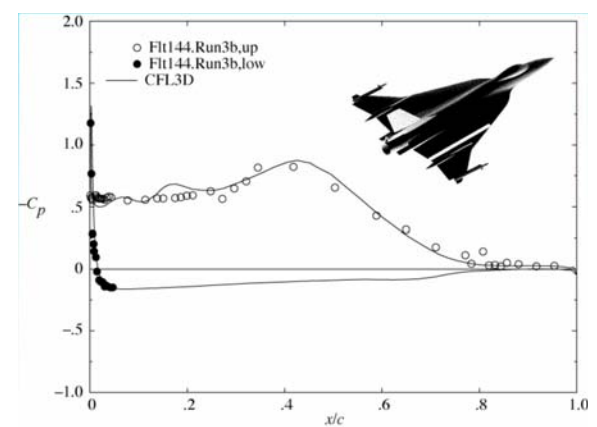
(e) BL 105
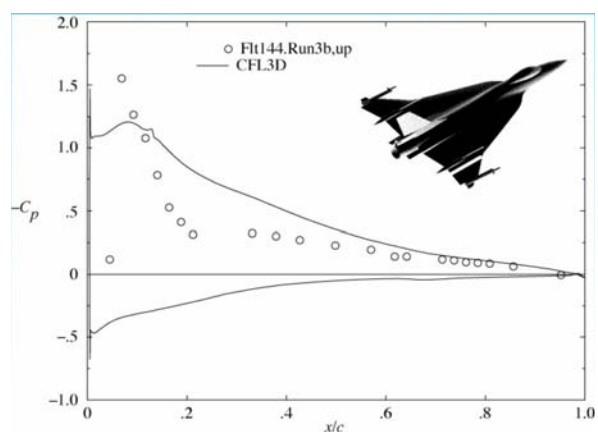
(f) BL 153.5

Figure 3-11: CFD (CFL3D) and Measured C_p at FC46 ($M_\infty = 0.527$, $\alpha = 10.4°$, $R_n = 46.9 \times 10^6$) from Ref. [3-2].
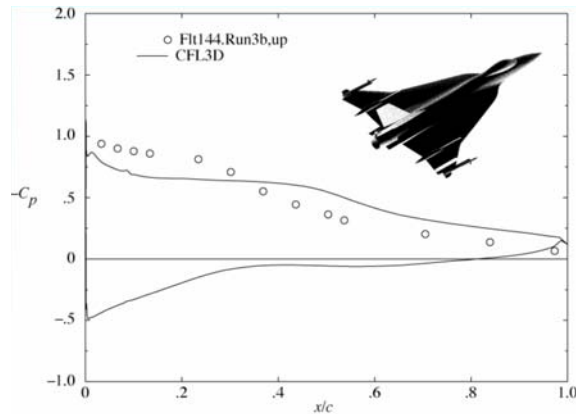
(g) BL 184.5
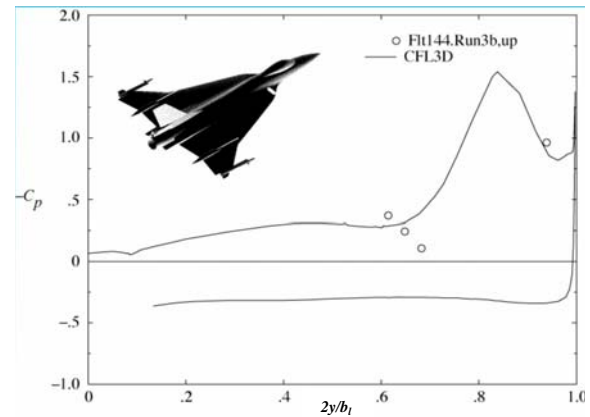
(h) FS 185
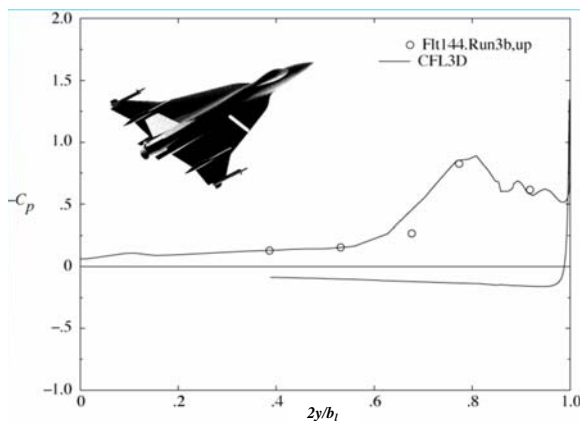
(i) FS 300
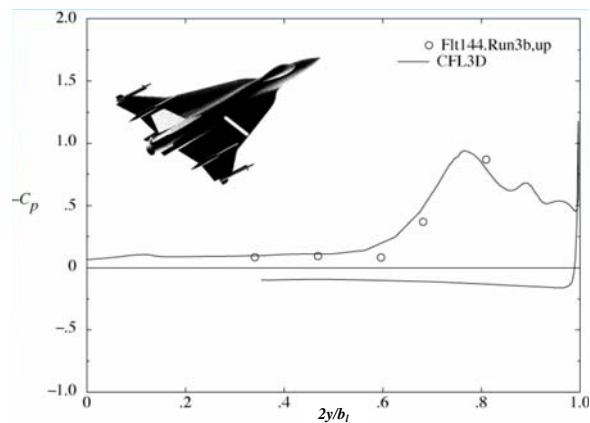
(j) FS 337.5
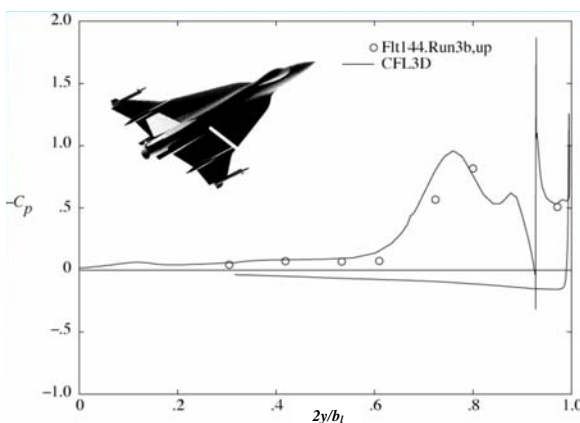
(k) FS 375
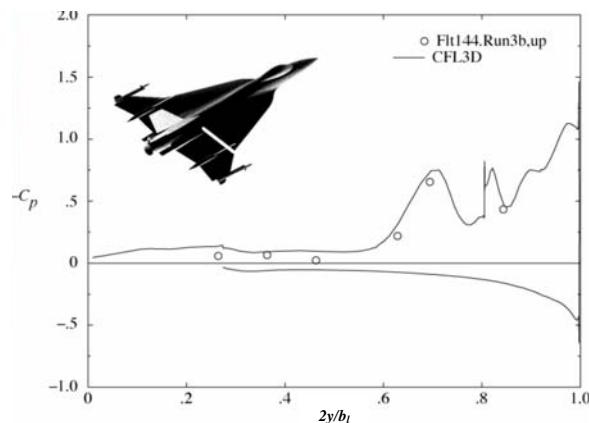
(l) FS 407.5

Figure 3-11: Continued.
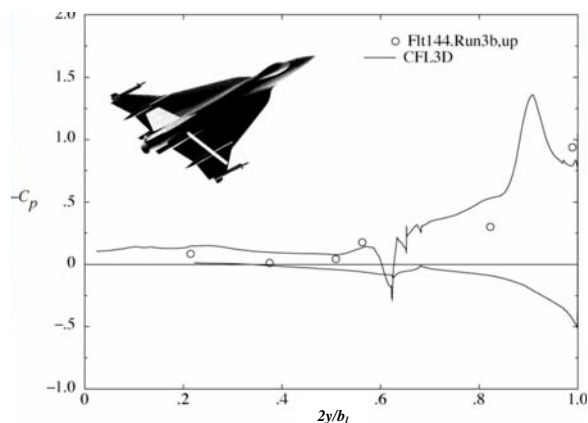
(m) FS 450
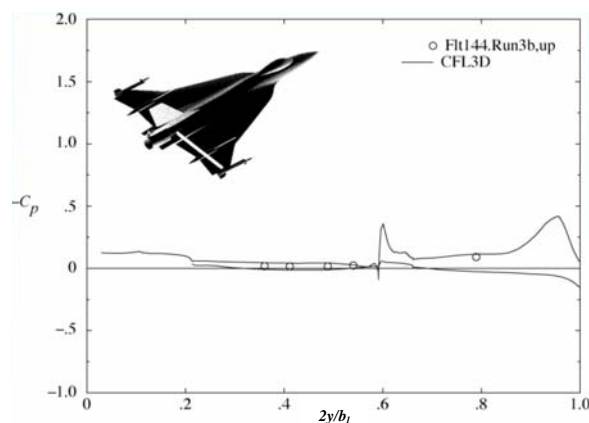
(n) FS 492.5
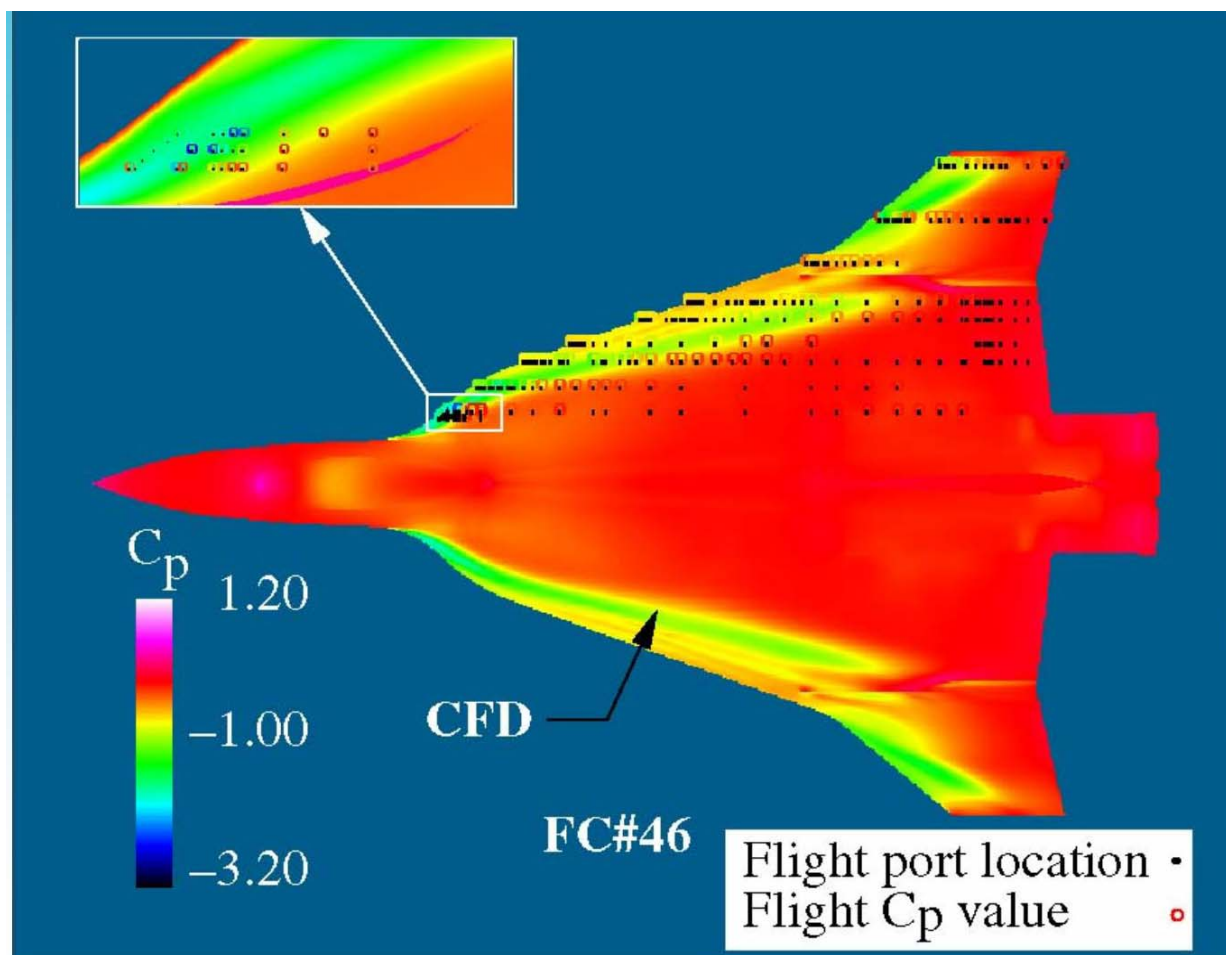
(o) Upper Surface C$_p$ Distribution

Figure 3-11: Concluded.

Figure 3-11 (a) to Figure 3-11 (n) show good overall agreement between the measured and predicted results at this flight condition. There are, however, three notable exceptions. The first is that the primary vortex effect on the suction peak at BL 55, the most inboard location, is under-predicted. The second is at BL 153.5 where the measured data has its primary-vortex suction-peak more forward than predicted and is followed by a more rapid compression downstream. Lastly, is the unusual and uncharacteristic variation near $2y/b_l = 0.6$ for FS 185. The associated ports for the latter are located in and towards the aft-end portion of the S-blend curve part of the airplane, a region where the flow is very sensitive. Even with this unusual behavior of C_p, these results are retained because they do bracket the predicted data at this FC.

Figure 3-11 (o) provides an overview of the upper surface C_p comparison where the black dots represent the location of the flight ports and the associated color of the surrounding bubble indicate the measured value. Where the color of the bubble is the same as the background CFD solution, only the black dot is noted. Generally good overall agreement is seen except in the S-blend region where the measured pressures are more negative, but elsewhere the differences are such that the measured values are more positive.

Figure 3-12 shows the fusion (overlaying) of surface tuft images from the three left-side cameras (tail, missile-nose and fuselage-apex) with CFD surface streamlines and vortex-core representation for FC46. [The white circles are video targets used for camera registration.] In particular, Figure 3-12 (a) presents the camera combination obtained by using the video targets with camera location and orientation angles. Figure 3-12 (b) shows that the CFD surface streamlines compare well with the flow depicted by the surface tufts. Figure 3-12 (c) shows the addition of the stagnation pressure iso-surfaces – at a value of 0.78 representing the locations and extent of the various airplane vortex systems – with transparency. As expected from the results of the surface comparison, the vortex system is well located with respect to the flight tufts [3-2].
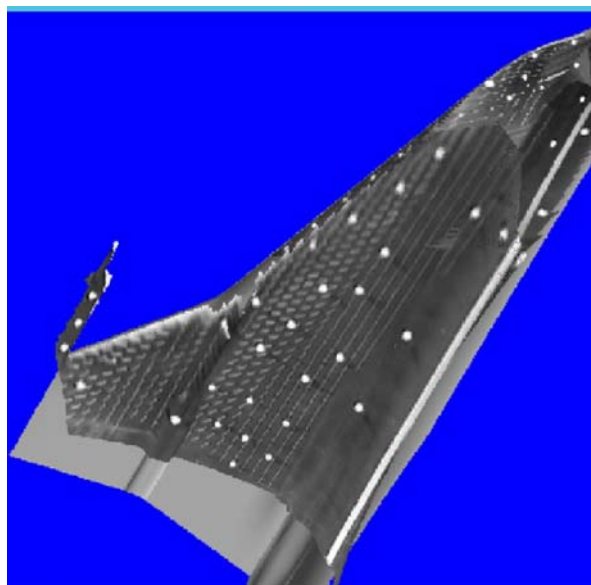
**(a) Tuft Images Projected from Three
Cameras onto Aircraft Grid**
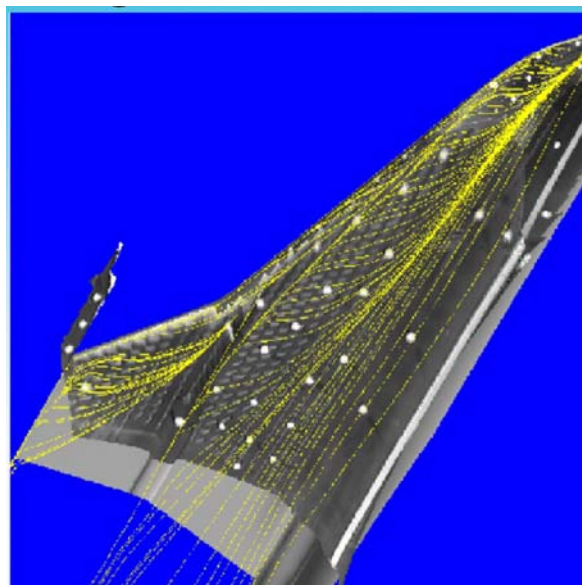
**(b) Combination of Tuft Images
and CFD Surface Streamlines**

**Figure 3-12: Flight Tuft Data from Three Cameras on F-16XL-1 Airplane and
CFD Solution at FC46 ($M_\infty = 0.527$, $\alpha = 10.4°$, $R_n = 46.9 \times 10^6$) from Ref. [3-2].**
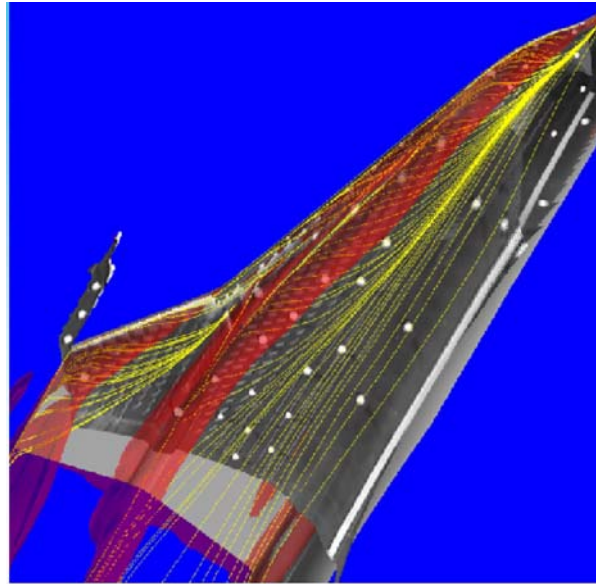
(c) Combination of Tuft Images, Streamlines, and Vortex Systems

Figure 3-12: Concluded.

Figure 3-13 shows the boundary-layer profiles of measured and predicted data. The profile for B.L. rake #3 is seen in Figure 3-13 (a) to be that of a classical, streamwise flow and this location was measured on all such flights to be used as a control. This figure shows good data repeatability and that the predictions agree well with them away from the wall. The data presented in Figure 3-13 (b) for B.L. rake #4, underneath the primary vortex, shows that the predicted trends are seen in the measured data, including the y location for the onset of 'jet-like' flow followed by a reduction from there to the rake extreme. Figure 3-13 (c) and Figure 3-13 (d) are associated with the secondary vortex, one underneath the core (#5) and one along the secondary separation line (#7). Two points are highlighted with respect to these two rakes data sets: the predicted values do not match the measured ones but do show how the anticipated flows would impact the boundary layer profiles; and for all practical purposes the two measured data sets are the same with a profile that does not asymptote to the boundary-layer rake extreme value.
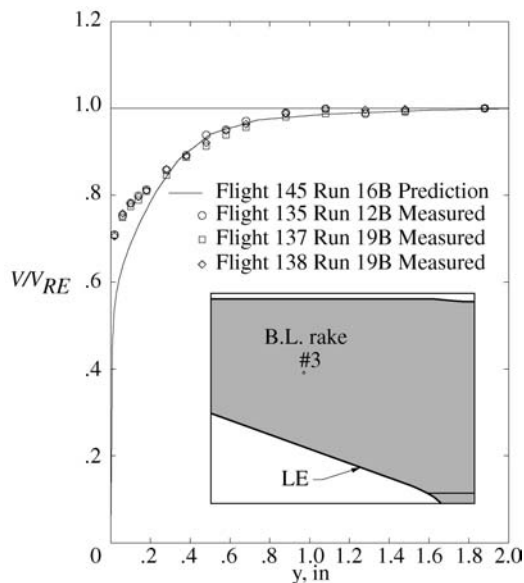
(a) Rake 3: FS 302.17, BL –52.93
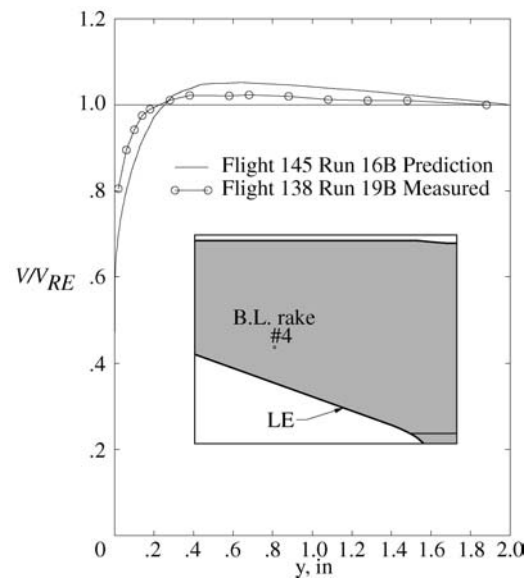
(b) Rake 4: FS 293.45, BL –76.22
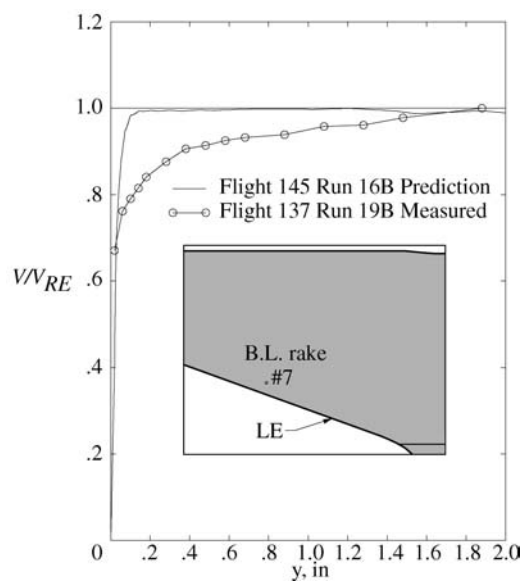
(c) Rake 7: FS 295.52, BL –94.33
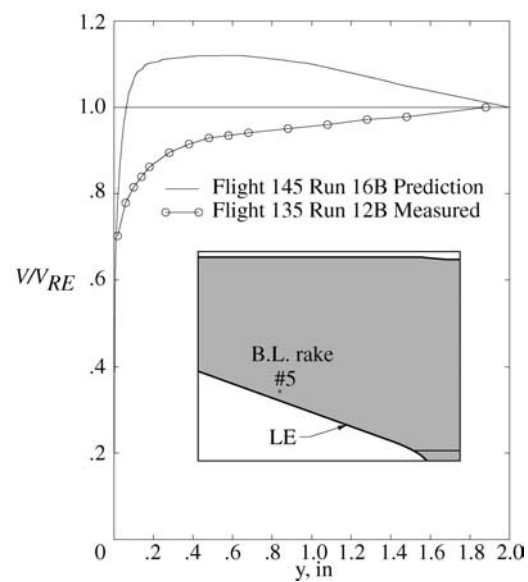
(d) Rake 5: FS 294.59, BL –96.06

Figure 3-13: Predicted and Measured Velocity Profiles for Boundary-Layer Rakes on F-16XL-1 Airplane for FC7 (M_∞ = 0.304, α = 11.89°, β_{nom} = 0°, h = 5000 ft, R_n = 44.4 x 10^{6}) from Ref. [3-2].

Figure 3-14 shows the predicted and measured local skin-friction coefficient at FS 330 for FC7 and FC19, respectively, as these FCs were quite close. High skin-friction peaks are an indication that a vortex system is present above the surface. Both sets of data show at least two such peaks. The predicted values for the primary (inboard) vortex have a different trend and reach a lower value than the measured data, and the vortex location is predicted more inboard than that measured – ~BL -90; however, the solution does a somewhat better job in estimating the peak value and location of the secondary vortex, albeit with two unexplained oscillations which trail toward the LE (BL~ -116).
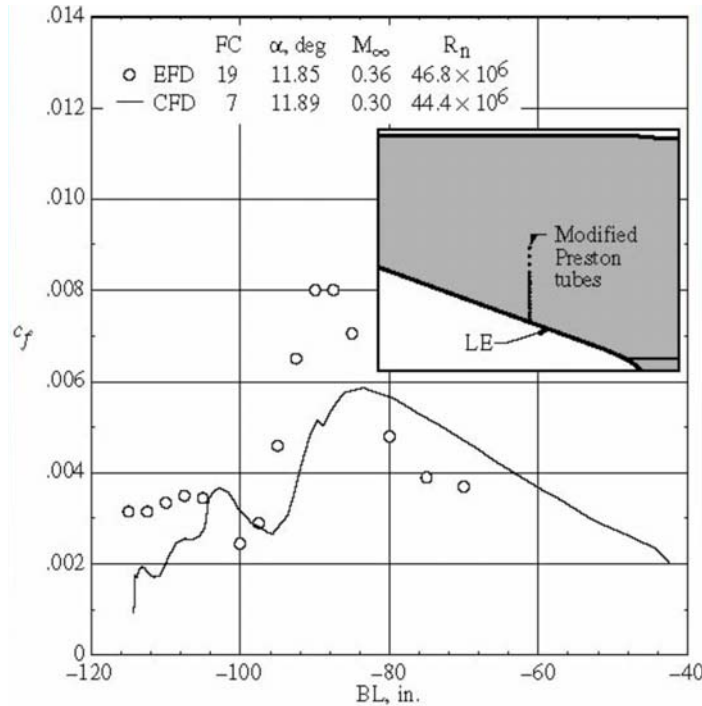
**Figure 3-14: Predicted and Measured c_f on F-16XL-1 Airplane at FS 330 for FC19/FC7
(M_{avg} = 0.33, α_{avg} = 11.9°, β_{nom} = 0°, $R_{n,avg}$ = 45.6 x 10^6) from Ref. [3-2].**

3.4   CAWAPI – ORGANIZATION/FEATURES/PRESENTATIONS

3.4.1   Organization

At the Spring 2000 Research and Technology Organization/Applied Vehicle Technology (RTO/AVT) Symposium week held in Braunschweig, Germany, this international group was asked whether there was interest in predicting the flight results around the F-16XL aircraft – as the report [3-2] documenting the work was in the process of being readied for publication. As a consequence, the Performance, Stability & Control and Fluid Physics (PSF) Technical Committee established an Exploratory Team (ET) to assess interest among the member nations on this and related topics. During the ensuing year, a team was constituted and, at their first meeting in Loen, Norway, in the spring of 2001, they examined a variety of vortical flow topics that could lead to task groups or symposia. A total of five topics were offered for consideration. Some went forward individually, while others were combined in order to gain AVT Panel recommendation for acceptance and Research and Technology Board (RTB) approval.

In particular, two topics presented at the Loen Symposium on "Vortex Flows and High Angle of Attack", during the 2001 spring RTO meeting week, were put forward separately for further study. They were the CAWAP [3-15] and the Vortex Flow Experiment – Number 2 (VFE-2) [3-16] – both of which dealt with vortical flows around slender wings. In the fall of 2002, these two topics were merged into a single proposal that the AVT Panel could recommend for approval by the RTB. Success was achieved in the spring of 2003 when the RTB granted approval for AVT-113 and authorized its first meeting to commence during the upcoming RTO/AVT Symposium week. The title of the task group is "Understanding and Modeling Vortical Flows to Improve the Technology Readiness Level for Military Aircraft". Even though integrated, each topic had its own facet lead, and these leaders became the co-chairmen of the task group. The title for the expansion of CAWAP activity to the International aerodynamics community within the RTO was denoted as CAWAPI. This name was crafted in advance in anticipation of approval and involved using a Virtual Laboratory (VL) at NASA Langley for facilitating secure data storage and transmission (See Refs. [3-17], [3-18]).

3.4.2   Features

The features of the CAWAPI are contained in the foundational document for the task group known as the "Terms of Reference" – an internal RTO/AVT panel document. In particular, there are basically three objectives to be performed under this task among the participants. They are detailed as follows:

1) Assessing various CFD codes against F-16XL-1 flight, and perhaps wind-tunnel, data sets in order to increase the Technology Readiness Level of the respective codes to a value of 5 ("Component and/or breadboard verification in a relevant environment").

2) Developing best practices for each code based on the data sets.

3) Incorporating appropriate or upgraded turbulence models into the respective codes to provide for improved agreement.

These were to be accomplished by having each of the participating groups be responsible for certain aspects of the work. For example, each participating group will use their best efforts, consistent with program priorities and funding, to perform the agreed upon detailed tasks, and to be responsible for providing its own resources for the completion of this task. In particular, NASA agreed to do the following:

1) Supply export-controlled geometry in various formats (iges, structured grid and unstructured grid) of the F-16XL-1 aircraft to participating partners once formal Memorandum-of-Agreements are in place.

2) Make available flight pressures, images, skin-friction and boundary layer measurements to the team.

3) Supply data format to and coordinate database services needed by the group.

4) Coordinate the various efforts and arrange for meetings each 6 months in conjunction with RTO Symposium.

5) The completion date of this task should be a maximum of 3 years after all approvals are granted. The initial ending date was set for December 2005, but this was later extended to December 2007, due to a variety of factors.

The fact that the aircraft geometry was restricted by 'International Traffic in Arms Regulations' (ITAR) complicated the process of NASA fulfilling its obligations until it was realized that a Virtual Laboratory, housed in an electronically secure DeMilitarized Zone, was a solution for geometry and grid transfers among participants. Details about this have been documented [3-17], [3-18]. Accessibility to both old and new data was provided through the VL to the participants. After the conclusion of the task group, it was anticipated that

portions of the database would be made widely available via the VL, but that is highly unlikely given the current environment.

The CAWAPI facet work was facilitated by having well-known and highly respected organizations/ researchers as members of this international effort working under the RTO "umbrella". These organizations appear in the following list grouped according to their basic function. They include four airframe companies – Boeing-St. Louis Phantom Works (USA), EADS-Munich (Germany), Lockheed Martin Aeronautics Company – Fort Worth (USA), and Turkish Aircraft Industries (Turkey); two government research laboratories – NASA Langley (USA) and NLR (The Netherlands); and six university led efforts – KTH/FOI (Sweden), United States Air Force Academy (USA), University of Glasgow/Liverpool University (United Kingdom), University of Tennessee-Chattanooga/SimCenter (USA), University of Wyoming (USA), and Vrije Universiteit Brussels (VUB)/NUMECA (Belgium). Unfortunately, not all of these were able to continue to the end of this facet, and some optioned to continue in the VFE-2 facet instead.

3.4.3 Introduction to Following Chapters

The original CAWAP solutions were obtained using a structured grid solver, based on a documented iges file with refinements, compared with measured flight data, and reported in reference [3-2] for the F-16XL-1 aircraft. It was anticipated that the new solutions would employ both structured and unstructured grids. Rather than just use the same iges file as before, it was decided to reinvestigate the geometry, find the best iges file available, and make certain that it was equally suitable for both solver types. The new iges file is only slightly different from the previous one, but it satisfied both 'grid' communities. The process of obtaining grids for both structured, as well as unstructured, solvers from this iges file is detailed in reference [3-19] and Figure 3-15 is a sample from that paper.
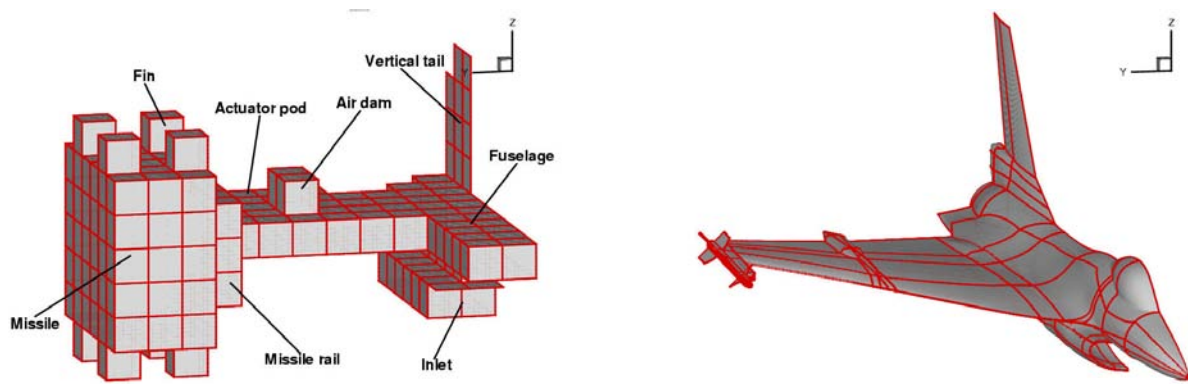
**Figure 3-15: Abstraction of the Surface Geometry (left) and Projected Abstraction (right) for
the F-16XL Half-Span Model from Boelens, et al. [3-19]. [Structured (pictured) and
unstructured grid development from the iges file is discussed in this paper.]**

When the CAWAPI computational effort commenced, the majority of those performing computations planned to do so using structured grid solvers; however, in the ensuing years that trend has reversed and now the majority are using unstructured grid solvers. A partial reason for this movement has been the improvements made in these solvers that include the potential and actualization of breaking a solution down into components for parallel processing, and the potential for automatic grid generation. Both of these can lead to significant time reductions from geometry specification to solver results. In the listing of papers that follow, authors have utilized their

solvers – structured [3-20] to [3-22] or unstructured [3-23] to [3-29] – in order to determine the best practices for each code and type of flow combination and then made comparisons with either other predictions or flight data as they deemed appropriate. Each of these papers has its own focus, but also contains common comparisons. For example, reference [3-20] emphasizes surface streamlines and understanding the relation with the off-surface flow, as shown by the sample Figure 3-16. A variety of aircraft modeling studies were performed in reference [3-21] with the results for the complete aircraft shown in Figure 3-17. References [3-22], [3-25], and [3-29] emphasize the effects of various turbulence models and are shown by sample Figure 3-18, Figure 3-19, Figure 3-20, respectively. Figure 3-20 [3-29] also shows, for comparison, the flight data represented by small circles surrounding the pressure port locations, shown as black dots, and colored by the CFD C_p scale. Reference [3-23] emphasizes solution adaptive grids, as shown by the sample Figure 3-21. References [3-24] and [3-26] highlight time-accurate and time-dependent solutions, as well as time averaged, and are illustrated in Figure 3-22 and Figure 3-23, respectively. Figure 3-24 [3-27] shows Mach 1 iso-surface colored by total pressure at FC70. Figure 3-25 [3-28] shows streamlines and the x-vorticity component for FC50 where β = +5.31°. Lastly, reference [3-30] provides a summary of the "Lessons Learned" as a result of this computational effort, including its impact on the Technology Readiness Level of the examined current solvers.
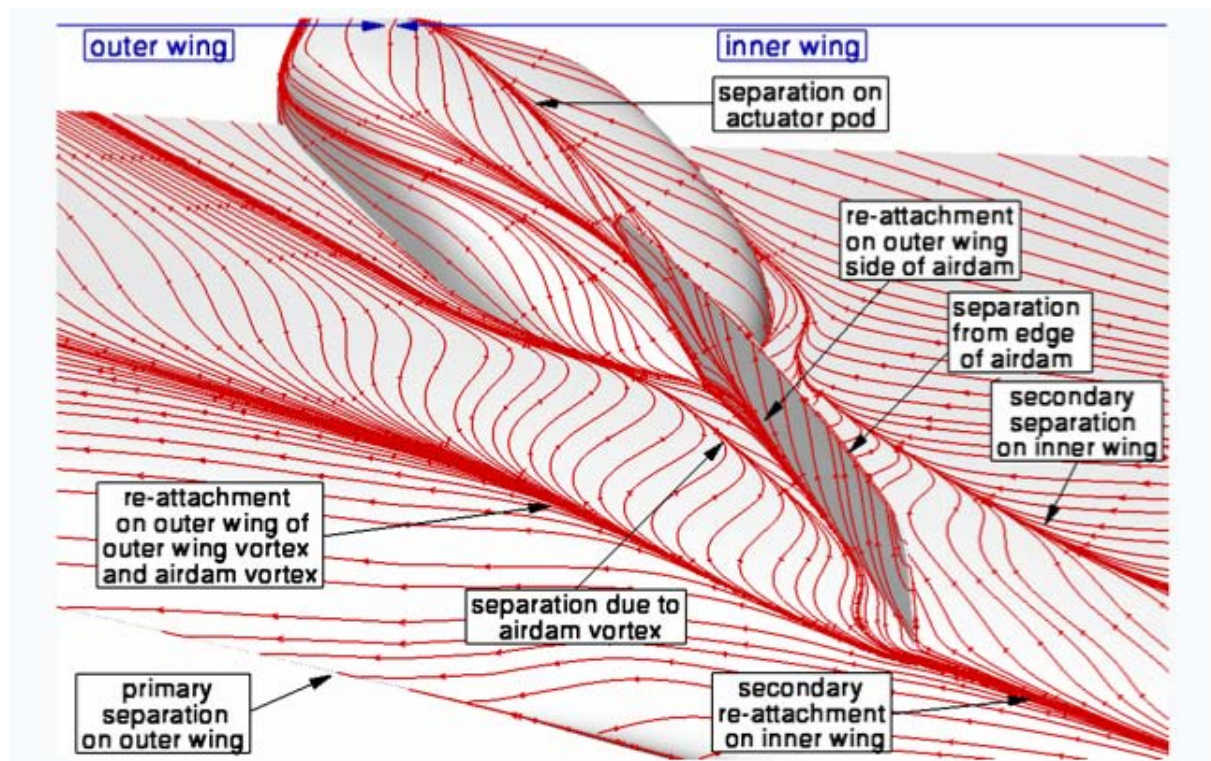
**Figure 3-16: Surface Streamlines with Interpretation for
FC7 with ENSOLV Solver from Boelens, et al. [3-20].**
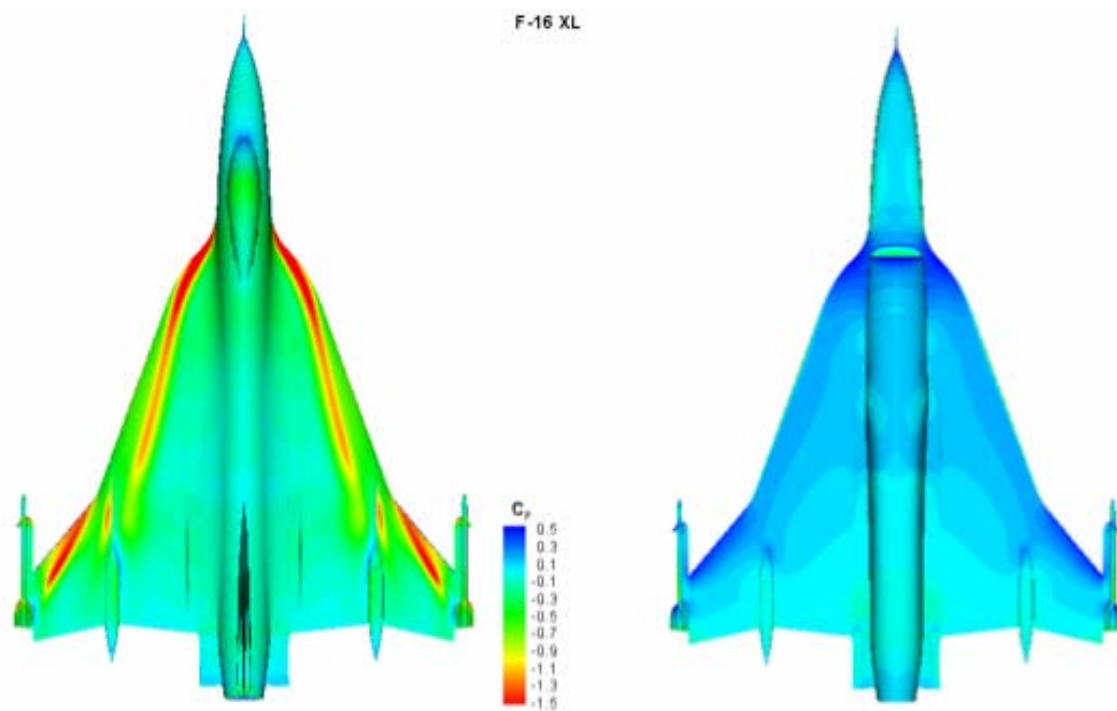
Figure 3-17: Upper and Lower Surface C$_p$ Results for FC7 with PMB Solver from Badcock [3-21].
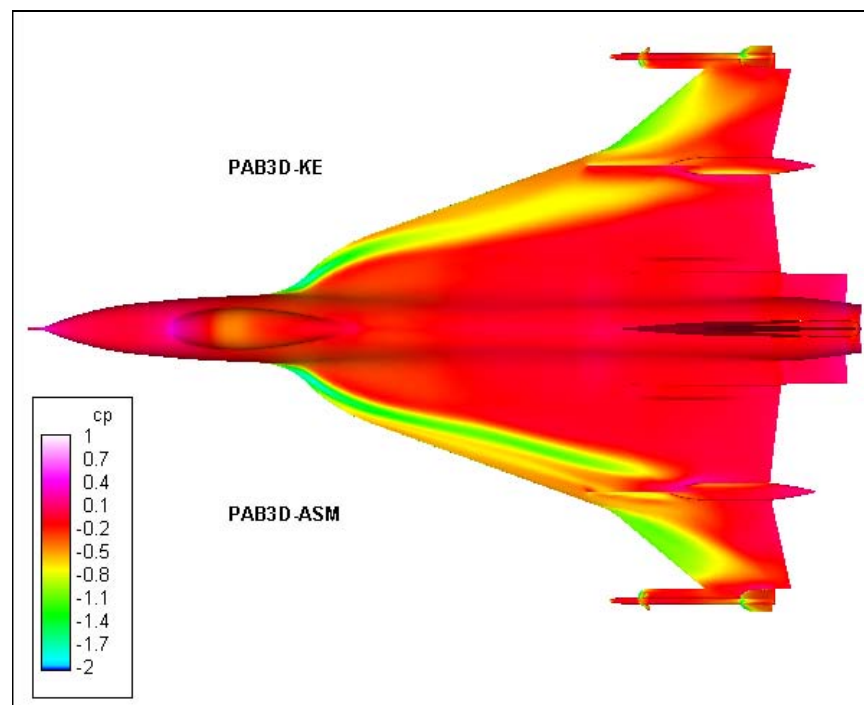
Figure 3-18: Turbulence Modeling Effect on C$_p$ for FC46 with PAB3D Solver from Elmiligue, et al. [3-22].
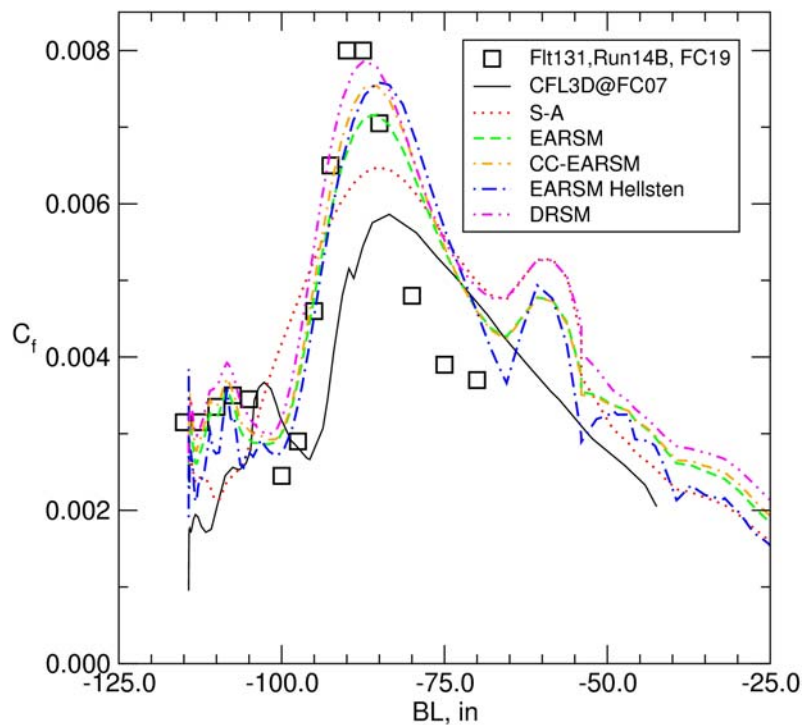
Figure 3-19: Turbulence Modeling Effect on C_p for FC19 with Edge Solver from Goertz, et al. [3-25].
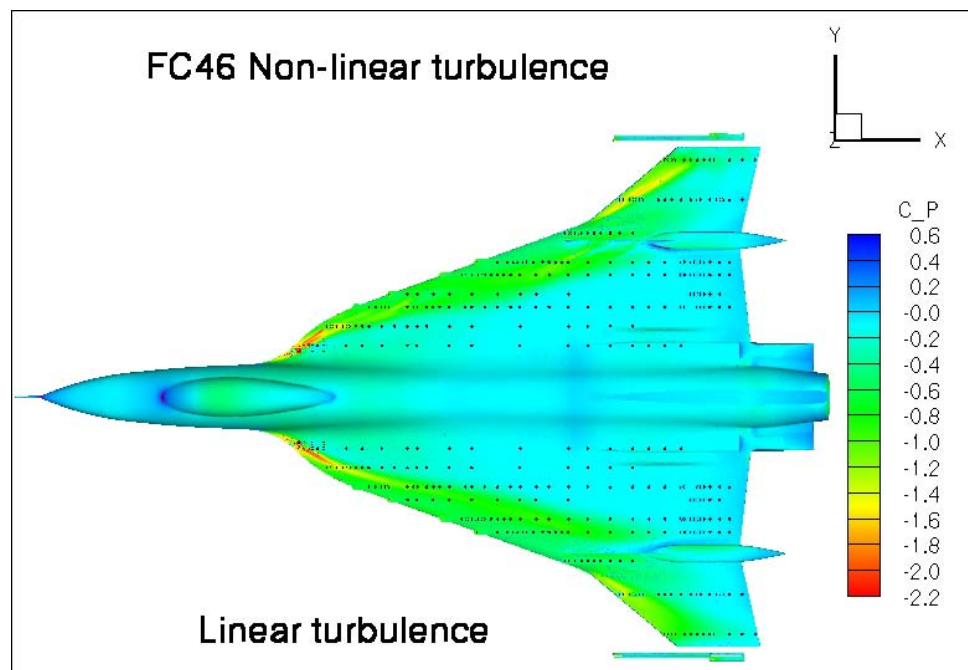
Figure 3-20: Turbulence Modeling Effect on C_p for FC46 with USM3D Solver from Lamar, et al. [3-29]. (Flight data represented by small circles surrounding the pressure port locations, shown as black dots, are colored by the CFD C_p scale. Agreement between the two sets is good when no discernable color difference is noted.)
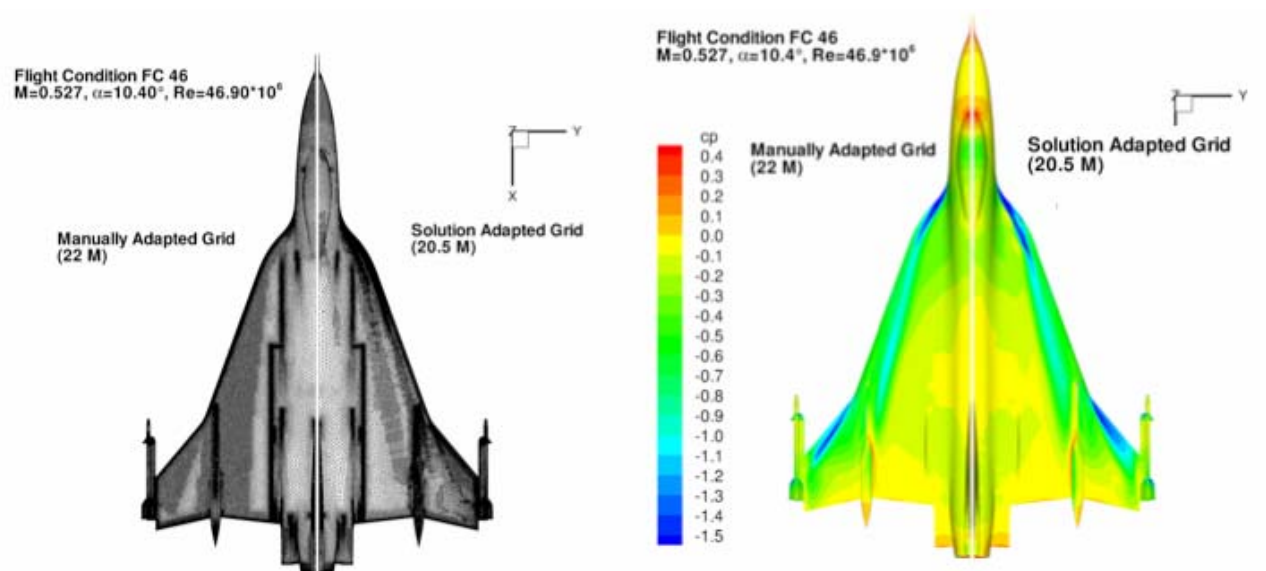
Figure 3-21: Solution Adaptive Grid Effect for FC46 with TAU Solver from Fritz [3-23].
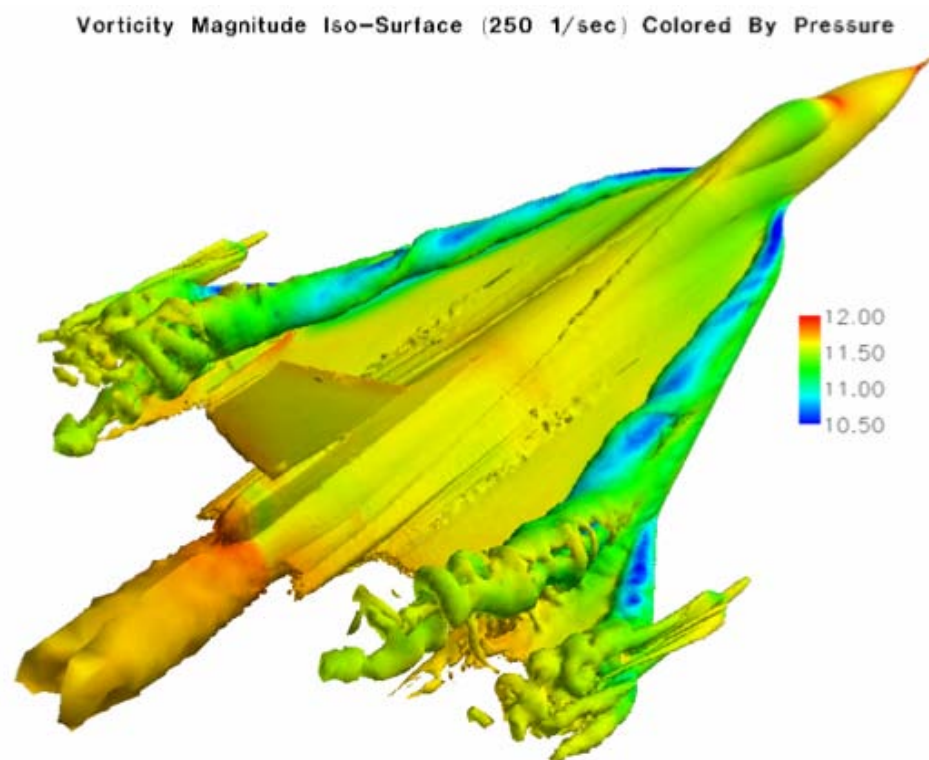
Figure 3-22: Time Accurate Solution for FC19 with Cobalt Solver from Morton, et al. [3-24].
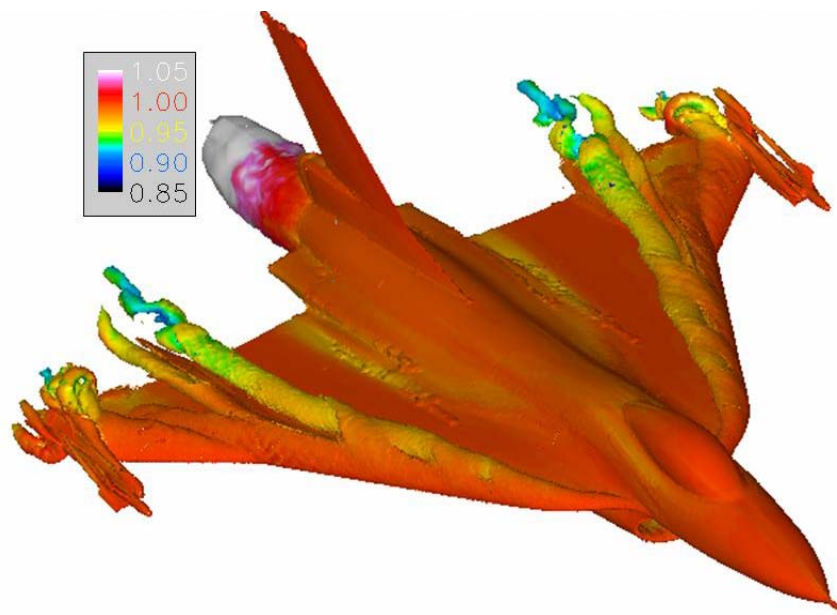
Figure 3-23: Time Dependent Solution for FC7 with BCFD Solver from Michal, et al. [3-26].
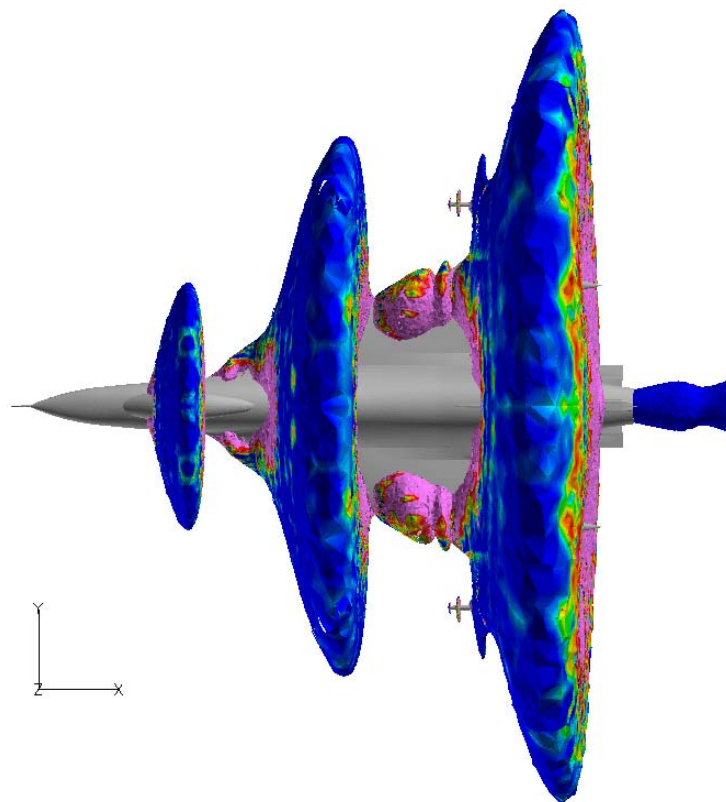
Figure 3-24: Mach 1 Iso-Surface Colored by Total Pressure at FC70 with Falcon v4 Solver from Davis, et al. [3-27].
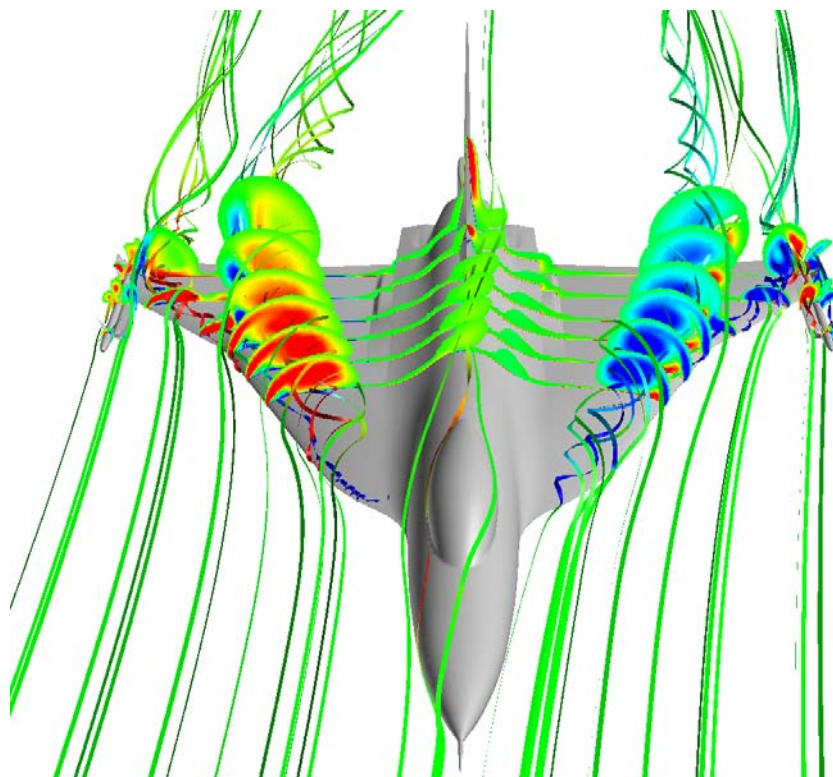
**Figure 3-25: Pressure-Colored Streamlines and x-Vorticity Component
for FC50 with TENASI Solver from Karman, et al. [3-28].**

An initial group of four flight conditions with either vortex-dominated or transonic flows were adopted by this facet for prediction and comparison. These were later expanded to seven and included two sideslip conditions (See Table 3-4). Associated with each was a set of pressure/temperature/Mach number values for a generic engine (See Table 3-5).

Table 3-4: Seven Flight Conditions to be Examined

Flight Condition	Actual Mach No.	Actual α, degs	Actual β, degs	Actual Reynolds No.
FC7	0.304	11.89	-0.133	44.4E+06
FC19	0.36	11.85	+0.612	46.8E+06
FC46	0.527	10.4	+0.684	46.9E+06
FC70	0.97	4.37	+0.310	88.77E+06
FC25	0.242	19.84	0.725	32.22E+06
FC50	0.434	13.56	+5.31	39.41E+06
FC51	0.441	12.89	-4.58	38.95E+06

Table 3-5: Associated Engine Parameters* for these Flight Conditions

Flight Condition	Free Stream Altitude, ft	Free Stream Mach	Inlet Duct Exit Static Temp., degs R	Inlet Duct Exit Static Press., psia	Inlet Duct Exit Velocity, ft/sec	Inlet Duct Exit Mach	Mixing Plane Total Temp., degs R	Mixing Plane Total Press., psia
FC7	5000	0.304	498	11	379.6	0.347	1050	23
FC19	10000	0.36	485.8	10.2	345.8	0.32	1050	21.5
FC46	24000	0.527	443.6	5.85	404.3	0.39	1045	14.8
FC70	22300	0.97	519	10.65	464.7	0.416	1200	30
FC25	10000	0.242	470.1	8.72	474.8	0.447	1209	26.3
FC50	24000	0.434	440	5.16	483.3	0.47	1154	16.95
FC51	24000	0.441	431.8	5.19	468.6	0.46	1146	16.74

* The numbers in this table do not represent any particular engine.

3.5   CONCLUDING REMARKS

Aircraft companies, government laboratories, and universities have access to database sets that may include flight data, but many of these sets are considered proprietary and are only used by them to assess and improve their codes. They hold this information in a closed environment so as to maintain a competitive advantage. The CAWAP dataset, being open, allowed researchers in these organizations to predict flight data in a cooperative manner under the RTO "umbrella" and facilitate doctoral studies.

There is interest in the international aeronautical community (airframe companies, government laboratories and universities) in being able to predict the flow physics measured on a fighter aircraft.

An international team of experts can be assembled with enough patience and institutional support when there is a focused common problem of mutual interest that can provide positive payoff for each organization.

The efforts expended by the participating organizations/researchers described here have led to the development of improved use or best practices for their flow solvers for the F-16XL aircraft. Moreover, an improvement in the ability (Technology Readiness Level) of organizations/researchers to predict complete fighter aircraft flow physics at real flight conditions has occurred, in part, due to their participating in this shared and open environment.

The preceding leads to the **observation** that focused datasets should be collected on aircraft configuration(s) of international aeronautical community interest **without geometrical restriction** under the RTO umbrella for similar CFD solver improvement.

This paper has traced the F-16XL-1 aircraft and the flight flow-physics data from a NASA-only activity to encompass others in the NATO community interested in predicting these data. The Cranked Arrow Wing

Aerodynamics Project (CAWAP) has been internationalized under the auspices of the scientific arm of NATO and the Technology Readiness Level of computational tools has been increased. Sample results obtained by CAWAPI facet members have been highlighted to show the breadth of work to be presented by them in their own papers.

3.6 ACKNOWLEDGEMENTS

3.7 REFERENCES

[3-1] Bertin, J.J. and Smith, M.L.: *Aerodynamics for Engineers*, Second ed. Prentice-Hall, Inc., 1989, p. 146.

[3-2] Lamar, J.E., Obara, C.J., Fisher, B.D. and Fisher, D.F.: *Flight, Wind-Tunnel, and Computational Fluid Dynamics Comparison for Cranked Arrow Wing (F-16XL-1) at Subsonic and Transonic Speeds*, NASA/ TP-2001-210629, February 2001.

[3-3] Hillaker, H.J.: *F-16XL Flight Test Program Overview*, AIAA Paper 83-2730, November 1983.

[3-4] Bower, J.N. and Scott, S.R.: *The F-16XL Flight Test Program*, Soc. of Flight Test Engrs, 15th Ann. Symp. Procs., August 1984, pp. 9-1 to 9-5.

[3-5] Talty, P.K. and Caughlin, D.J.: *F-16XL Demonstrates New Capabilities in Flight Test at Edwards Air Force Base*, J. Aircraft, Vol. 25, No. 3, March 1988, pp. 206-215.

[3-6] Bertelrud, A.: *Total Head/Static Measurements of Skin Friction and Surface Pressure*, AIAA Journal, Vol. 15, No. 3, March 1977, pp. 436-438.

[3-7] Lamar, J.E., Obara, C.J., Fisher, B.D. and Fisher, D.F.: *Flight, Wind-Tunnel, and Computational Fluid Dynamics Comparison for Cranked Arrow Wing (F-16XL-1) at Subsonic and Transonic Speeds*, NASA/ TP-2001-210629/Supplement, June 2008.

[3-8] Thomas, J.L., Anderson, W.K. and Krist, S.T.: *Navier-Stokes Computations of Vortical Flows over Low-Aspect-Ratio Wings*, AIAA Journal, Vol. 28, No. 2, February 1990, pp. 205-212.

[3-9] Thomas, J.L., Weston, R.P., Luckring, J.M., Walters, R.W., Reu, T. and Ghaffari, F.*: A Patch-Grid Algorithm for Complex Configurations Directed Towards the F-18 Aircraft*, AIAA Paper 89-0121, 1989.

[3-10] Spellman, M.W.: *Model and Test Information Report 1/9-Scale F-16E Force and Loads Model*, Rep. No. 400PR026, General Dynamics Corp., August 1981.

[3-11] Elbers, W.K.: *Wind Tunnel Data Report 1/9-Scale F-16E Pressure Model NASA Ames Research Center Tests 517-1-11 and 517-1-97*, Rep. No. 400PR037, Vol. II, General Dynamics Corp., December 1981.

[3-12] Hahne, D.E.: *Low-Speed Aerodynamic Data for an 0.18-Scale Model of an F-16XL with Various Leading-Edge Modifications*, NASA/TM-1999-209703, 1999.

[3-13] Lessard, W.B.: *Subsonic Analysis of 0.04-Scaled F-16XL Models Using an Unstructured Euler Code*, NASA TP-3597, 1996.

[3-14] White, F.M.: *Viscous Fluid Flow*, McGraw-Hill Inc., pp. 474-476, 1974.

[3-15] Lamar, J.E.: *Cranked Arrow Wing (F-16XL-1) Flight Flow Physics with CFD Predictions at Subsonic and Transonic Speeds*, Presented at RTO AVT Symposium on "Advanced Flow Management; Part A – Vortex Flow and High Angle of Attack", Paper Number 44, in Loen, Norway, during May 7-11, 2001.

[3-16] Hummel, D. and Redeker, G.: *A New Vortex Flow Experiment for Computer Code Validation*, Presented at RTO AVT Symposium on "Advanced Flow Management; Part A – Vortex Flow and High Angle of Attack", Paper Number 8, in Loen, Norway, during May 7-11, 2001.

[3-17] Lamar, J.E., Conin, C.K. and Scott, L.E.: *A Review of Steps Taken to Create an International Virtual Laboratory at NASA Langley for Aerodynamic Prediction and Comparison*, Prog Aerospace Sci, Vol. 40, pp. 163-172, 2004.

[3-18] Lamar, J.E., Cronin, C.K. and Scott, L.E.: *Virtual Laboratory Enabling Collaborative Research in Applied Vehicle Technologies*, In AVT-123 Symposium on "Flow Induced Unsteady Loads and the Impact on Military Applications", Keynote 2, Budapest, Hungary, April 25-29, 2005.

[3-19] Boelens, O.J., Görtz, S., Morton, S.A., Fritz, W. and Lamar, J.E.: *Description of the F-16XL Geometry and Computational Grids Used in CAWAPI*, AIAA Paper 2007-0488, To be presented at 45th AIAA Aerospace Sciences Meeting and Exhibit, Reno, NV, January 8-11, 2007.

[3-20] Boelens, O.J., Spekreijse, S.P., Sytsma, H.A. and de Cock, K.M.J.: *Comparison of Measured and Simulated Flow Features for the Full-Scale F-16XL Aircraft*, AIAA Paper 2007-0489, To be presented at 45th AIAA Aerospace Sciences Meeting and Exhibit, Reno, NV, January 8-11, 2007.

[3-21] Badcock, K.J.: *Evaluation of Results from a Reynolds Averaged Multiblock Code Against F-16XL Flight Data*, AIAA Paper 2007-0490, To be presented at 45th AIAA Aerospace Sciences Meeting and Exhibit, Reno, NV, January 8-11, 2007.

[3-22] Elmiligue, A.A., Abdol-Hamid, K.S. and Massey, S.J.: *PAB3D Simulations for the CAWAPI F-16XL*, AIAA Paper 2007-0491, To be presented at 45th AIAA Aerospace Sciences Meeting and Exhibit, Reno, NV, January 8-11, 2007.

[3-23] Fritz, W.: *Hybrid Grid RANS Solutions for the CAWAPI F-16XL*, AIAA Paper 2007-0492, To be presented at 45th AIAA Aerospace Sciences Meeting and Exhibit, Reno, NV, January 8-11, 2007.

[3-24] Morton. S.A., McDaniels, D.R. and Cummings, R.M.: *F-16XL Unsteady Simulations for the CAWAPI Facet of RTO Task Group AVT-113*, AIAA Paper 2007-0493, To be presented at 45th AIAA Aerospace Sciences Meeting and Exhibit, Reno, NV, January 8-11, 2007.

[3-25] Görtz, S. and Jirásek, A.: *Unstructured Steady/Unsteady Solutions with Edge for CAWAPI F-16XL at KTH/FOI*, AIAA Paper 2007-0678, To be presented at 45th AIAA Aerospace Sciences Meeting and Exhibit, Reno, NV, January 8-11, 2007.

[3-26] Michal, T., Oser, M., Mani, M. and Roos, F.: *BCFD Unstructured-Grid Predictions on the F-16XL (CAWAPI) Aircraft*, AIAA Paper 2007-0679, To be presented at 45th AIAA Aerospace Sciences Meeting and Exhibit, Reno, NV, January 8-11, 2007.

[3-27] Davis, M.B., Reed, C. and Yagle, P.: *Hybrid Grid Solutions on the (CAWAPI) F-16XL Using Falcon v4*, AIAA Paper 2007-0680, To be presented at 45th AIAA Aerospace Sciences Meeting and Exhibit, Reno, NV, January 8-11, 2007.

[3-28] Karman, S., Mitchell, B. and Sawyer, S.: *Unstructured Grid Solutions of CAWAPI F-16XL by UT SimCenter*, AIAA Paper 2007-0681, To be presented at 45th AIAA Aerospace Sciences Meeting and Exhibit, Reno, NV, January 8-11, 2007.

[3-29] Lamar, J.E. and Abdol-Hamid, K.S.: *USM3D Unstructured Grid Solutions for CAWAPI at NASA LaRC*, AIAA Paper 2007-0682, To be presented at 45th AIAA Aerospace Sciences Meeting and Exhibit, Reno, NV, January 8-11, 2007.

[3-30] Rizzi, A., Badcock, K.J., Jirásek, A. and Boelens, O.J.: *What was Learned from Numerical Simulations of F-16XL (CAWAPI) at Flight Conditions*, AIAA Paper 2007-0683, To be presented at 45th AIAA Aerospace Sciences Meeting and Exhibit, Reno, NV, January 8-11, 2007.

Chapter 4 – F-16XL GEOMETRY AND GRIDS

by

**Okko J. Boelens, Stefan Görtz, Scott Morton, Willy Fritz, Steve L. Karman Jr.,
Todd R. Michal and John E. Lamar** *(Retired)*

4.1   SUMMARY

The objective of the Cranked-Arrow Wing Aerodynamics Project International (CAWAPI) was to allow a comprehensive validation of Computational Fluid Dynamics methods against the CAWAP flight database. A major part of this work involved the generation of high-quality computational grids. Prior to the grid generation an IGES file containing the air-tight geometry of the F-16XL aircraft was generated by a cooperation of some of the CAWAPI partners. Based on this geometry description both structured and unstructured grids have been generated. The baseline structured (multi-block) grid (and a family of derived grids) has been generated by the National Aerospace Laboratory (NLR). The baseline all-tetrahedral and hybrid unstructured grids were generated at the NASA Langley Research Center and the U.S. Air Force Academy, respectively. To provide more geometrical resolution, additional unstructured grids were generated at EADS-MAS, the UTSimCenter, and Boeing Phantom Works. All the grids generated within the framework of CAWAPI will be discussed.

4.2   INTRODUCTION

The objective of the CAWAPI was to allow a comprehensive validation and evaluation of CFD methods against the CAWAP flight database (see Chapter 3 and [4-1]). Part of the work involved the generation of high-quality computational grids.

In order to allow high-quality grid generation, the available CAD geometry description of the F-16XL aircraft was scrutinized. Issues encountered during this process are discussed in Section 4.3.

At the beginning of the project the task group members recognized the need to use common grids around this complex geometry to eliminate most of the uncertainties related to grid. The original plan was to have two common grids, one structured (multi-block) and one unstructured (tetrahedral). However, whereas all partners using structured CFD methods performed their simulation on a common structured multi-block grid generated at Netherlands National Aerospace Laboratory NLR (see Section 4.4), most partners using unstructured CFD methods have generated their own unstructured grid during the course of the project or have adapted existing grids (see Section 4.5). A section with conclusions completes the chapter.

4.3   GEOMETRY DESCRIPTION

The geometry of the F-16XL aircraft is based on the Full-Scale Development F-16A. It was obtained from this aircraft by stretching the fuselage and adding a cranked-arrow wing, which has a leading-edge sweep angle of 70° inboard and 50° outboard of the crank. An 'S-blend curve' was placed in the leading edge at the juncture of the wing leading edge with the fuselage. During all CAWAP flight tests the aircraft was equipped with an air dam upstream of the actuator pod and wing-tip missiles. The F-16XL aircraft has been described in detail in Chapter 3.

At the beginning of CAWAPI two IGES files of the F-16XL aircraft were available, one from Lockheed-Martin Aeronautics Company and one from NASA Langley. The latter was obtained by measuring the actual aircraft in the NASA hangar, where a numerical surface description (NSD) was obtained through photogrammetric targets. This measurement was performed in the framework of the HSR program (see Chapter 3 and [4-1]). Using both surface descriptions and additional CATIA models for the inlet up to the compressor face and for the nozzle up to the turbine face, an updated IGES file was generated by Lockheed-Martin Aeronautics Company. It should be noted that for the configuration used the control surfaces were not deflected. This IGES file contained a better characterization of the actual aircraft surfaces and the leading edges, but was still not suitable for further grid generation purposes. It was found that the geometry description contained multiple overlaying surfaces. This was corrected at EADS-MAS, where a single set of describing surfaces was generated. The resulting description also included some refinements in the wing leading-edge region to improve future grid generation in this region. It was recognized by the CAWAPI members that this surface description needed some further adjustments to facilitate the generation of a structured grid. The following modifications were applied:

- The gap between the launcher and the missile was closed. Other details of the missile, such as the fins, were unmodified.

- The gap between the nozzle and the trailing-edge flap was closed.

- The environmental control system (ECS) inlet was simplified.

- A step in the longitudinal progression of the nose-boom outer diameter was smoothed out.

These modifications were made at the NASA Langley Research Center. Finally, the modified surface description was checked for water tightness and corrected, where necessary, using the CAD tool 'CADfix' [4-16]. The IGES file containing the air tight geometry description (see Figure 4-1) was used for both the structured and unstructured grid generation.
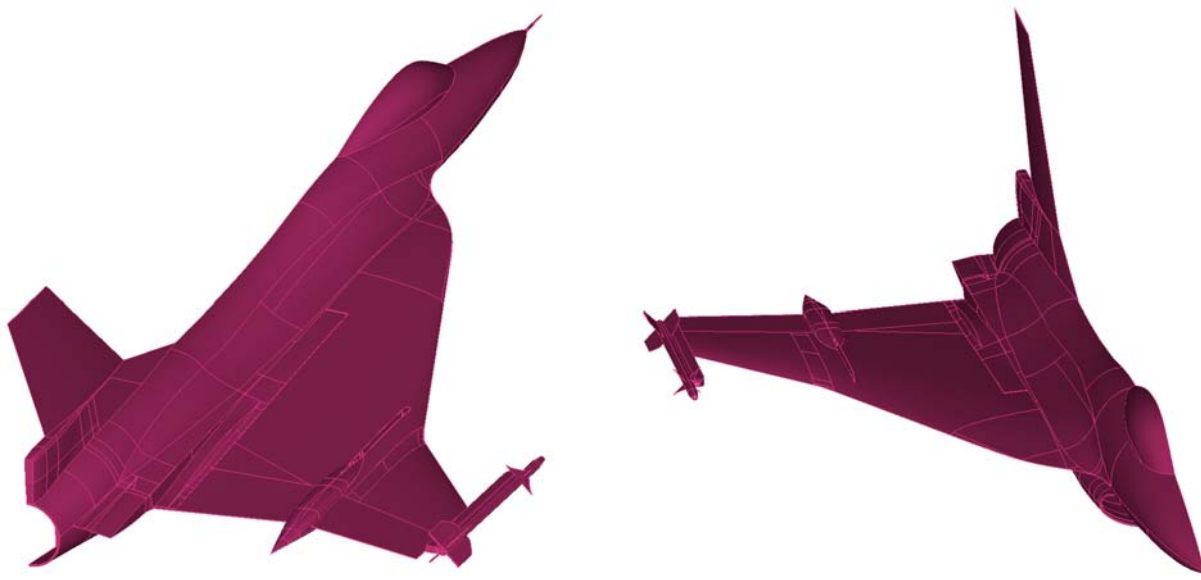
Figure 4-1: CAD Geometry Representation of the F-16XL Aircraft.

4.4 STRUCTURED GRID

4.4.1 Background

During CAWAP a structured grid had been generated at NASA Langley Research Center [4-1]. This grid was based on a prior IGES file and exhibited an average value of y^+ of 82 at flight Reynolds numbers. Simulations on this grid were performed using the 'wall function' option in the turbulence model to compensate for the insufficient grid spacing. It was, therefore, decided that for CAWAPI purposes a new structured grid had to be generated.

The plan, as detailed in [4-10], was for "two members of the CAWAPI − one at the Netherlands National Aerospace Laboratory (NLR) and the other at the U.K. University of Glasgow (UGlasgow) −" to "collaborate in the development of the structured grid for their own use as well as for others. This is a risky endeavor even if the developers are co-located or on the same hall, but certainly more-so if they are in two different countries and having to rely on the Virtual Laboratory (VL) for all grid exchanges. The plan was for the NLR to produce the blocking strategy with implementation and for UGlasgow to adjust the grid spacing, as needed. Alternatively, NLR could produce and test the grid then UGlasgow would perform a second test on the grid before its general release to the facet. In either case, both would use and support the same grid file. For this problem, it turned out that the alternate plan was the one implemented due, in part, to the difficulties experienced with the transfer of large files…from this newly developed VL."

4.4.2 Grid Generation Algorithm

The structured grid has been generated at the Netherlands National Aerospace Laboratory NLR using a Cartesian grid mapping technique. The (semi-automatic) grid generation algorithms are developed at NLR and are part of NLR's ENFLOW flow system [4-2]. Most of these algorithms had become available just before CAWAPI and had only been applied to a clean (no external loads) F-16 configuration. Being the first realistic case to which these tools were applied and bearing in mind that a limited experience with their use existed, it was estimated that six weeks would be needed to generate the complete structured (multi-block) grid.

The Cartesian grid generation technique used by the Netherlands Aerospace Laboratory NLR can be subdivided in the following steps:

1) *Imagine/construct a Cartesian abstraction of the geometry description.* In such an abstraction, the geometry including all details is represented by a set of Cartesian blocks. The abstraction of the half-span full-scale model of the F-16XL used in CAWAPI is shown in Figure 4-2 (a). In this figure, it can be seen that each fin of the wing tip missile for example is represented by a single block. Note furthermore that in this abstraction the engine duct and the nozzle have been closed.

2) *Project the abstraction onto the real geometry description.* The projected abstraction of the half-span full-scale model of the F-16XL is shown Figure 4-2 (b).

(a)   **(b)**
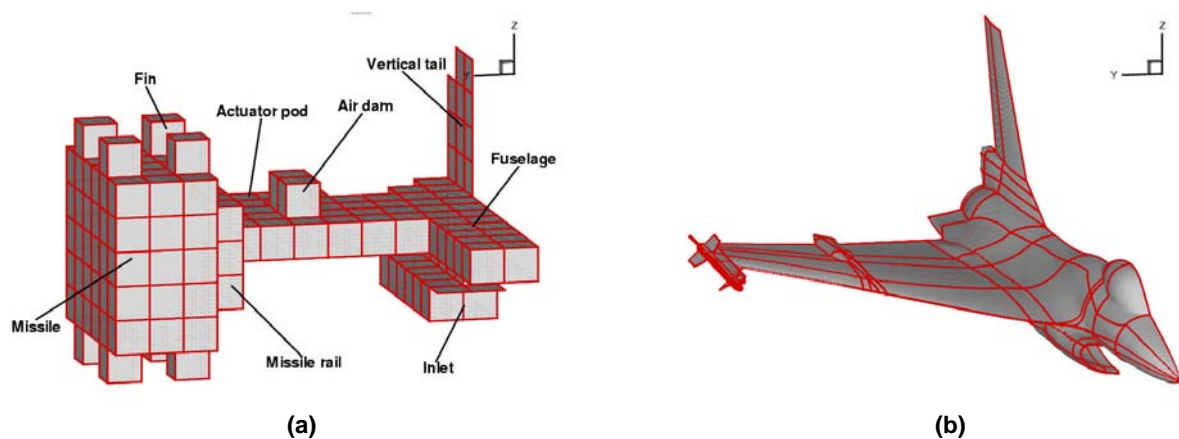
Figure 4-2: Abstraction of the Surface Geometry (a) and Projected
Abstraction (b) for the F-16XL Half-Span Model.

3) *Generate the so-called Navier-Stokes blocks.* This first layer of blocks around the geometry including the engine duct and the nozzle is generated by a simple blow-up technique. The surface patches are translated along the outward normal to the geometry using the corners of the patches as control points. The algorithm used accounts for symmetry planes and only needs the off-set of the blocks as input. The generated layer of blocks has an O-O-type topology. During this step also the blocks to fill up the engine duct and the nozzle are inserted interactively.

4) *Generate the field blocks in the Cartesian space.* The faces of the Navier-Stokes blocks opposite to the geometry combined with the faces at the engine duct inlet and nozzle exit display the same Cartesian structure as the abstraction shown in Figure 4-2 (a). In the Cartesian space the field blocks are generated automatically. As is evident from Figure 4-2 (a), the blocks in the Cartesian space are simple cubical blocks.

5) *Generate the field blocks in the physical space.* The simple cubical blocks in the Cartesian space are automatically mapped to the physical space using a grid deformation technique [4-3]. The algorithm accounts for symmetry planes. Finally, so-called far-field blocks are added to the topology interactively, see Figure 4-3. The far-field boundaries are located several reference wing chords away from the model.

6) *Set the (Euler) grid dimensions.* Each edge is assigned a grid dimension. The minimum number of cells used along an edge is eight, to ensure three levels of multi-grid. In the Navier-Stokes blocks, eight cells were used in the surface normal direction.

7) *Automatically connect the edges.* The grid spacing in the grid is set automatically. For each set of adjoining edges the grid point density is adjusted such that a smooth transition of the grid is obtained. In general, this means that the grid point density of the edge with the larger grid spacing is linked to that of the edge with the smaller grid spacing.

8) *Improve the grid quality by an elliptical smoothing algorithm.* An elliptical smoothing algorithm is applied to the grid. As a result of this algorithm the quality in terms of grid smoothness is improved significantly.

9) *Increase the resolution in the Navier-Stokes blocks.* To provide for sufficient boundary layer resolution the number of grid points in the surface normal direction is increased. In addition a redistribution of the grid points with a specified stretching away from the geometry is applied. The algorithm used accounts for a smooth transition to the grid in the outer blocks.
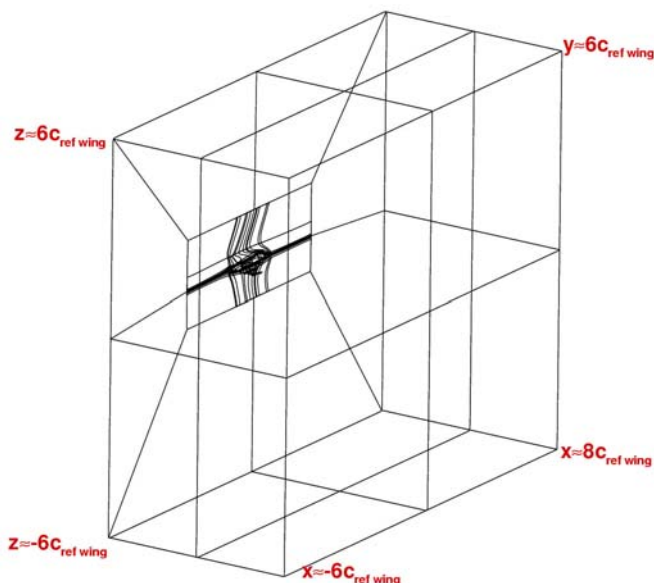
Figure 4-3: Topology on the Geometry, the Symmetry Plane and the Far-Field Boundaries.

Within NLR's ENFLOW CFD system further algorithms exist to:

- Merge blocks within a grid to reduce the total number of blocks.

- Mirror a grid with respect to a symmetry plane to obtain a full-configuration grid from a half-configuration grid.

- Convert the grid from NLR's native ENFLOW format to several other formats, such as Plot3D or CGNS [4-9].

The characteristics of the structured grid obtained using this Cartesian grid mapping technique are described in the next section. Instead of the six weeks estimated prior to the project, the structured grid was generated well within four weeks.

4.4.3   Characteristics of the Grid

During the structured grid generation process the following small modifications to the surface description were made to further facilitate the generation of a structured grid:

- A small 'step' or 'plate' on the wing upper surface was removed.

- The end part of the vertical tail base was slightly rounded off.

The following family of structured grids has been used in CAWAPI:

- The baseline structured grid around the half-span full-scale model of the F-16XL consisting of 1903 blocks, 14,750,720 grid cells and 17,014,119 grid points.

- The above described baseline structured grid with the far-field blocks divided into smaller blocks so that only a one-to-one connection between block faces exists. This version was used by the University of Liverpool.

- The baseline structured grid with a reduced number of blocks. The first merging step was performed at NLR reducing the number of blocks from 1903 to 216. A further small reduction was accomplished at NASA Langley Research Center which yielded a grid with only 200 blocks.

- A structured grid around the full-scale model of the F-16XL consisting of 3806 blocks, 29,501,440 grid cells and 34,028,238 grid points. This grid has been generated by mirroring the baseline structured grid around the half-span full-scale model of the F-16XL with respect to the symmetry plane. This grid has only been used by NLR.

Some details of the baseline structured grid around the half-span full-scale model of the F-16XL are summarized in Table 4-1.

Table 4-1: Details of the Baseline Structured Grid

Number of blocks	1903
Number of boundary layer blocks	367
Number of far-field blocks	20
Number of points in Navier-Stokes blocks in surface normal direction	32
First normal distance from the wall, Δs_1 [m]	6.0×10^{-6} (7.9×10^{-7} $c_{\text{ref wing}}$)
Viscous grid layer geometric progression parameter, $\Delta s_2 / \Delta s_1$	1.1
x_{min}, x_{max}[m]	-45, 60 (-5.97 $c_{\text{ref wing}}$, 7.96 $c_{\text{ref wing}}$)
y_{min}, y_{max}[m]	0 , 45 (0, 7.96 $c_{\text{ref wing}}$)
z_{min}, z_{max}[m]	-45, 45 (-5.97 $c_{\text{ref wing}}$, 5.97 $c_{\text{ref wing}}$)

The upper surface grid is shown in Figure 4-4. In Figure 4-5, the grid is shown in both a plane approximately normal to the flow direction (FS is constant) and in a plane approximately parallel to the flow direction (BL is constant). Finally, the resulting y^+ distribution over the upper surface is shown in Figure 4-6. From this figure, it is evident that the grid spacing normal to the surface has a desired value of y^+ less then one, except for the regions below the vortical structures.
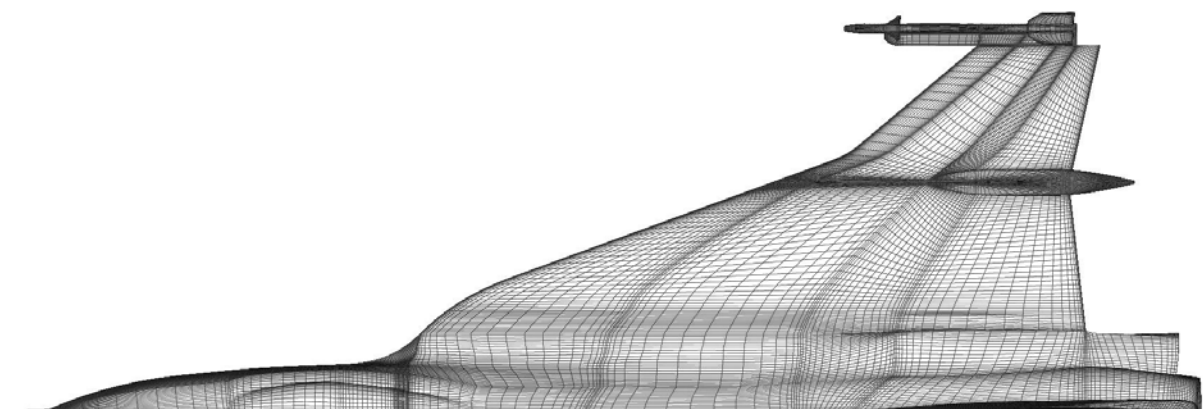
Figure 4-4: Upper Surface Grid for the Structured Grid.

(a)   (b)
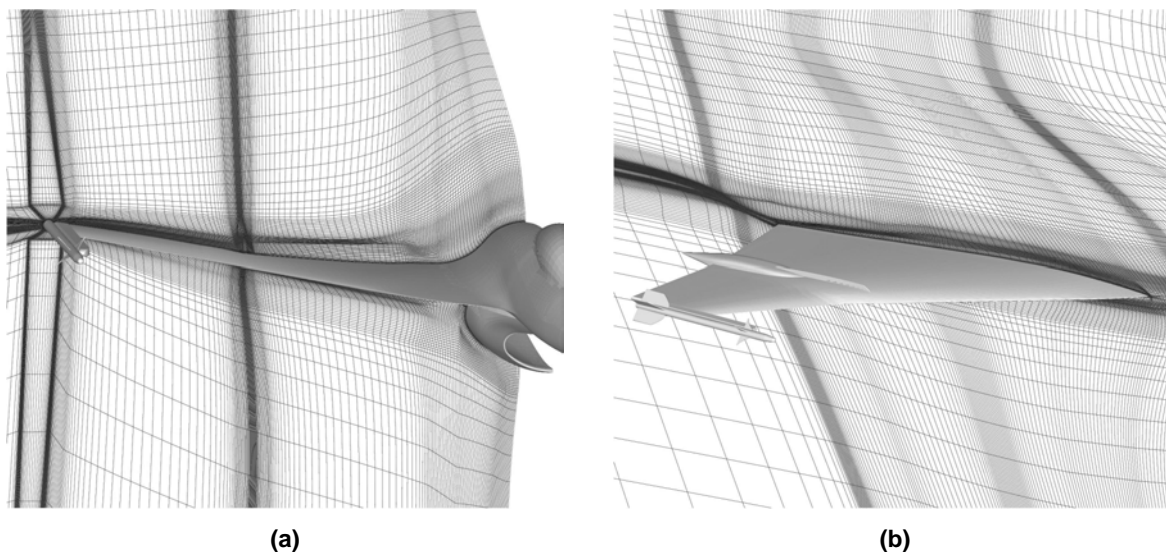
Figure 4-5: Grid Planes Showing the Grid Density Off the Aircraft Surface in a Plane Approximately Normal to the Flow Direction (FS is constant) (a) and in a Plane Approximately Parallel to the Flow Direction (BL is constant) (b).
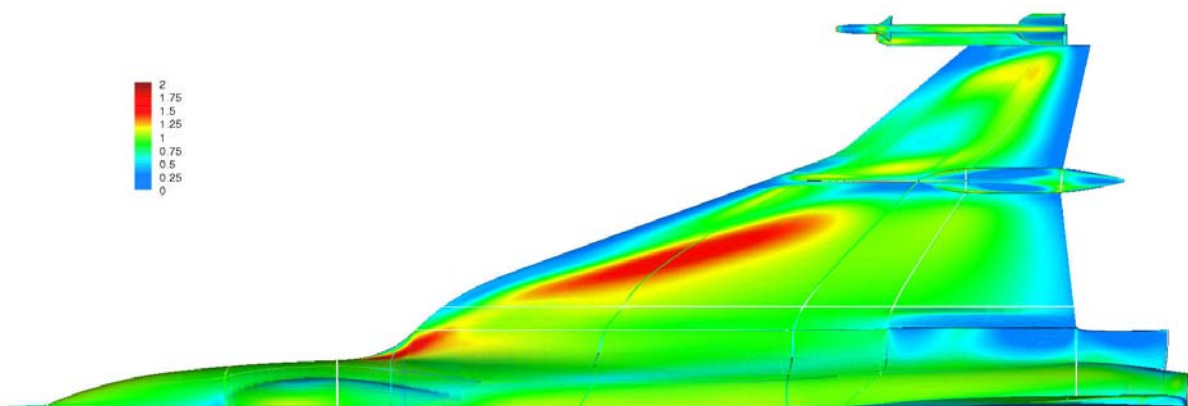
Figure 4-6: Levels of y^+ on the Upper Surface for Flight Condition 19 (TNT k-ω Turbulence Model with Correction for Vortical Flows).

4.5   UNSTRUCTURED GRIDS

4.5.1   Baseline Unstructured Grid

The baseline unstructured 3D all-tetrahedral viscous grid with 2,534,132 nodes, corresponding to 14,802,429 cells, was generated for a half-span full-scale model of the F-16XL-1 (control surfaces not deflected) at the NASA Langley Research Center using the grid generation packages GridTool [4-4] and VGRIDns [4-5].

This grid was converted to a hybrid baseline unstructured grid in Cobalt [4-6] format at the U.S. Air Force Academy using the commercial grid management utility Blacksmith from Cobalt Solutions, LLC. Blacksmith

reduced the cell count to a total of 11,928,103, corresponding to 2,535,842 nodes, by combining highly stretched tetrahedral cells into prismatic cells. The program generated 9 layers of prismatic cells, corresponding to 1,442,394 prisms. The reason the grid had only 9 prismatic layers is that pyramids would be needed as "end caps" for layers that are not complete. Rather than adding another cell type it was decided to accept 9 layers. The transition between the prismatic layers and the tetrahedral grid is very smooth. The surface of the half-span model of the F-16XL is discretized with 160,266 triangular elements. The upper surface grid is shown in Figure 4-7.
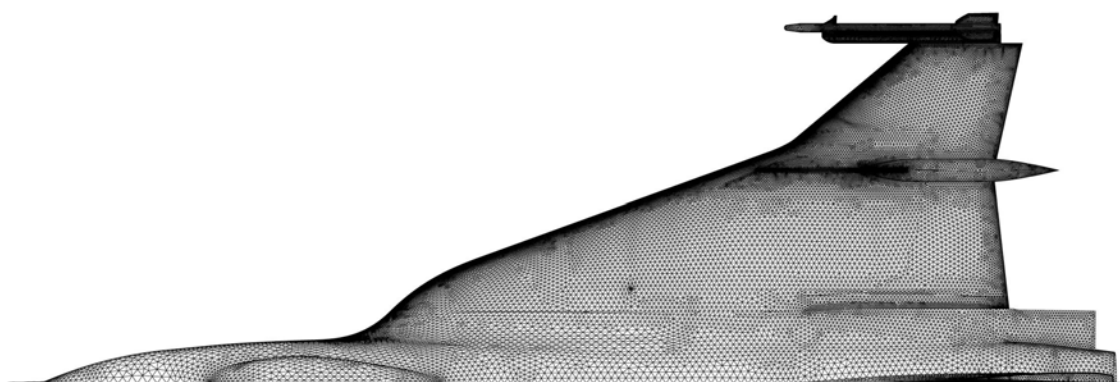
**Figure 4-7: Surface Grid of the Hybrid Baseline Unstructured
Grid for the F-16XL-1 Half-Span Model (160,226 Faces).**

The resolution of the boundary layer requires the grid to be clustered in the direction normal to the surface with the spacing of the first grid point off the wall to be well within the laminar sub-layer of the boundary layer. For turbulent flows, the first point off the wall should exhibit a y^+ value of less than 1.0. Here, the spacing of the first grid point normal to the solid wall is 5.0×10^{-6} m (6.6×10^{-6} c). Away from the wall, the spacing increases by a ratio $\Delta s_2/\Delta s_1$ of 1.2. The resulting y^+ distribution over the upper surface of the aircraft model is shown for flight condition 19 in Figure 4-8. It can be seen that the grid spacing normal to the surface led to an average value of y^+ of less than one and a maximum y^+ of about two under the primary wing vortex, demonstrating that the grid is fine enough at the wall boundaries.
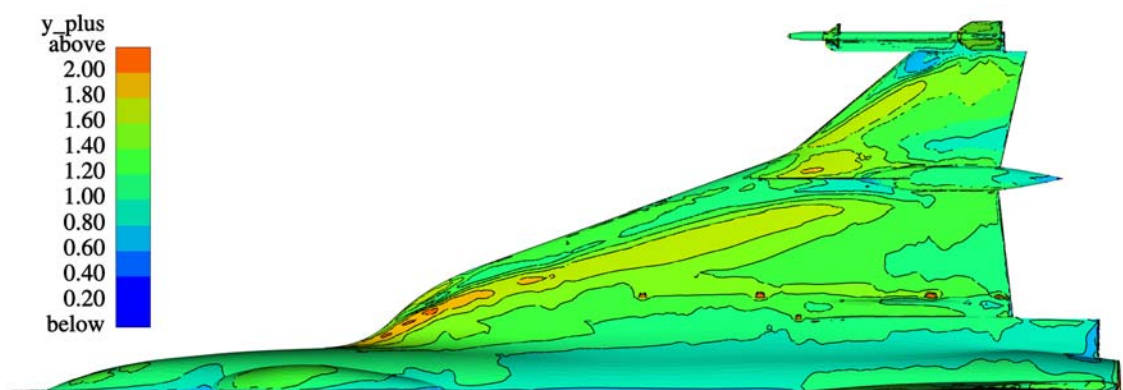
**Figure 4-8: Levels of y^+ on the Upper Surface for the Hybrid
Baseline Unstructured Grid for Flight Condition 19 (EARSM).**

The engine duct is meshed all the way to the inlet duct exit plane. The nozzle is meshed from the engine mixing plane, see Figure 4-9. The grid density off the aircraft surface is shown in Figure 4-10, which depicts a wrinkly cutting plane through the grid at FS496 (fuselage station on airplane in inches, positive aft), close to the trailing edge.
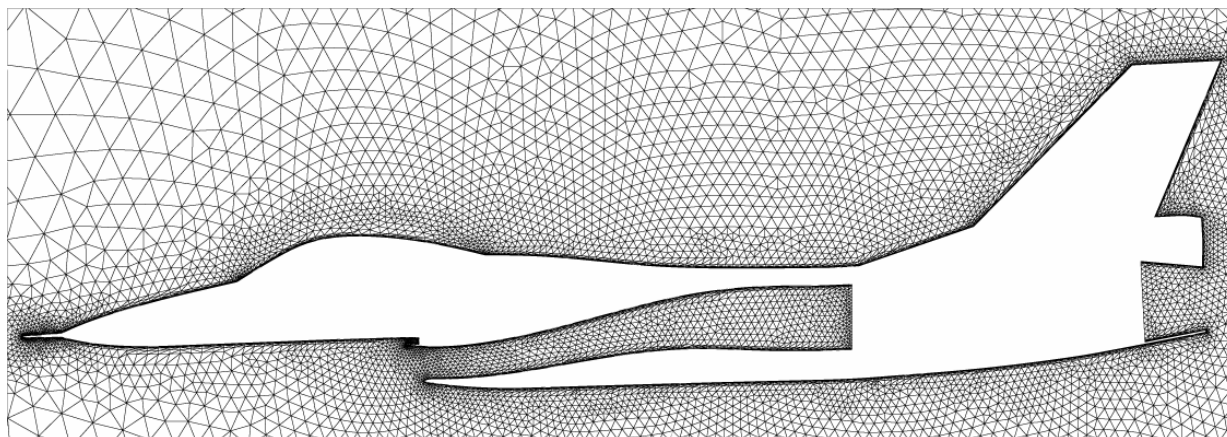
**Figure 4-9: Symmetry Plane of the Hybrid Baseline Unstructured
Grid Showing the Meshed Inlet Duct and Nozzle.**
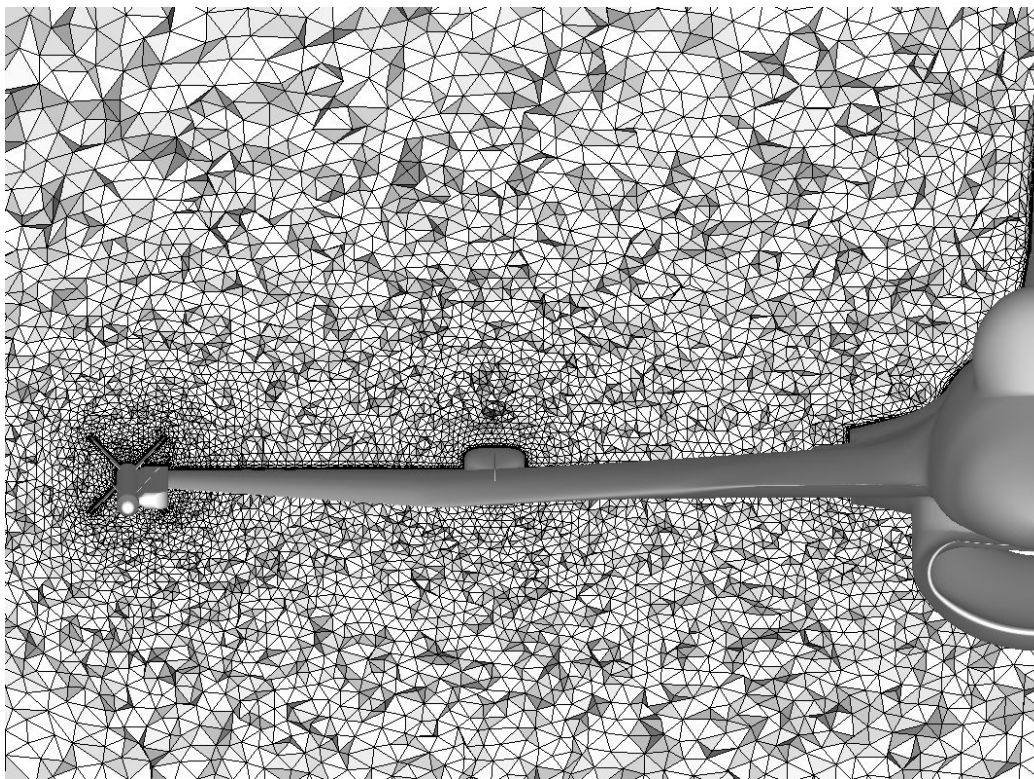
**Figure 4-10: Wrinkly Cutting Plane at FS496 Showing the Grid Density
Off the Aircraft Surface Close to the Trailing Edge of the Wing.**

Next, the group at KTH converted the hybrid grid from Cobalt format to the "Flexible Format Architecture" (FFA) [4-7], the native format of the Swedish CFD code Edge [4-8]. In this conversion step, all grid dimensions were converted from inches to meters.

Finally, KTH researchers converted the FFA-format grid to the CFD General Notation System (CGNS) [4-9] library version 2.3. The resulting CGNS file was uploaded to the Virtual Laboratory (VL) [4-10] at NASA Langley Research Center to be used by other researchers in CAWAPI.

4.5.2   Other Unstructured Grids

4.5.2.1   EADS-MAS

At EADS-MAS the adaptation technique, which is included in the DLR-TAU code [4-11], was used for the CAWAPI CFD simulations (see also Chapter 8). Starting point was a so called initial grid, which subsequently is adapted four times during the flow simulations. This starting grid was a hybrid grid with 10,496,522 nodes in total for the half-span full-scale model of the F-16XL. It has a prismatic layer of 15.6 million prisms in the near wall region and 13.5 million tetrahedra in the outer region. The thickness of the first prismatic layer is 4.0e-06 m and a geometric progression parameter $\Delta s_2/\Delta s_1$ of 1.3 is used for the other 29 viscous layers. In critical regions the prismatic layers are chopped and transition elements such as pyramids and tetrahedra are created. The surface of the aircraft is resolved by 749,742 triangles.

This initial grid was generated using the CentaurSoft grid generator [4-12], which enables the generation of hybrid grids with minimal user interaction. Starting from the air tight geometry description, the grid generation process is split up into surface triangulation, prismatic grid generation and tetrahedral grid generation. Point clustering is achieved by automatic clustering based on geometric features and by user-controlled clustering placing so called sources. This user controlled clustering has been used for a rough adaptation of the grid to the expected vortical flow structure. The surface triangulation works patch-oriented, which results in a not always needed high resolution of all small surface patches. (The geometry definition of the F-16XL contains several such mini-patches). As the adaptation algorithm of the TAU code uses the surface grid as geometry base, the surface triangulation of this initial grid was already relative fine to ensure a sufficient resolution of all geometric details. The tetrahedral grid however was kept somewhat coarse and was expected to be refined by the adaptation.

This grid was used as initial grid for all symmetric flight conditions and during the simulations it was adapted in four steps for each flight condition. In the adaptation feature of the TAU code the edges of the primary grid are bisected, depending on a refinement sensor. The refinement sensor bases on the differences of the flow variables velocity, density, total pressure and helicity. During the adaptation, points can be added and removed, but only previously added points can be removed. The adaptation algorithm can be started after the computation of a flow solution on a certain grid. It then generates a new grid and interpolates the solution into this grid. The maximum increase of grid points for each of the 4 adaptation loops was limited to 25%. Grid points have been added in the surface grid and in the tetrahedral grid. The new surface points have been included in the prismatic grid, but number and thickness of the prismatic layer have not been changed. (The initial prismatic layer was designed such, that it was suitable for a much finer grid).

With this adaptation procedure the final adapted grid (for example flight condition 25) obtained 1,462,096 surface triangles, 32,375,977 prisms, and 25,871,331 tetrahedra. Compared to the initial grid, these elements roughly have been doubled, resulting in a total number of 21,149,945 nodes. Figure 4-11 shows a comparison of the initial and the final adapted surface grid. New grid points mainly have been added along the leading

edge (leading edge suction), inboard and outboard of the suction peak of the primary vortex (pressure gradient) and in the tip section of the rearward wing. In space, new points have been added in regions with vortical flow above the wing (total pressure, helicity) and in the wake region behind the wing.
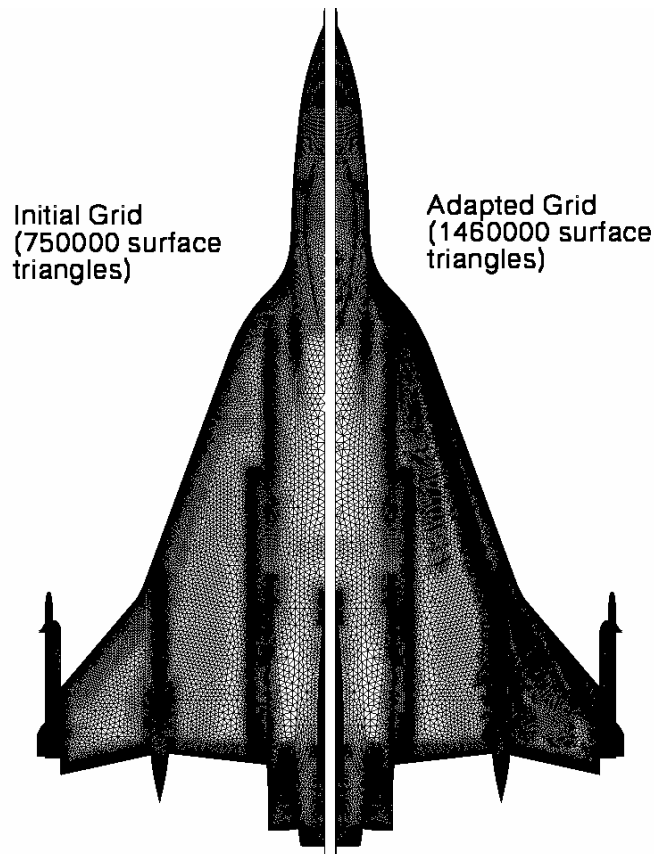
Figure 4-11: Initial EADS-MAS Surface Grid and Final Adapted Grid for Flight Condition 25 (α = 19.84°, M = 0.242).

4.5.2.2   UTSimCenter

One of the more unique grid systems was produced by researchers at the University of Tennessee at Chattanooga Sim Center (UTSimCenter) (see also Chapter 14). Two separate mesh generation programs were used to generate the viscous meshes for these analyses. The first program was a commercially available mesh generation package known as Gridgen [4-13]. Gridgen was used to create an inviscid unstructured mesh. The second mesh generation program was developed in-house at the SimCenter and was used to insert viscous layers in the inviscid mesh.

4.5.2.2.1   Inviscid Mesh

Gridgen was used to create an unstructured inviscid mesh, comprised of mostly tetrahedral [4-13]. Surface meshes, consisting of triangular elements, were created on the geometry defined by the IGES file. Care was

taken to ensure proper resolution of pertinent geometric features such as the leading and trailing edge of the wing. The high curvature of the leading and trailing edges needed fine resolution in the chord-wise direction to resolve the shape. The unstructured triangular surface meshing in Gridgen imposes nearly isometric triangular elements. In order to provide the desired resolution in the chord-wise direction and not have an excessive number of elements in the span wise direction a structured grid was used along the leading and trailing edges of the wing. The aspect ratio of the quadrilateral elements was imposed to be no larger than 15. The resulting structured quadrilateral surface mesh was then converted to an unstructured triangular mesh by subdividing the quadrilateral elements into two triangles. Figure 4-12 shows a section of the leading edge where the converted structured mesh domain meets the unstructured mesh domains. A view of the mesh on the symmetry plane is shown in Figure 4-13.
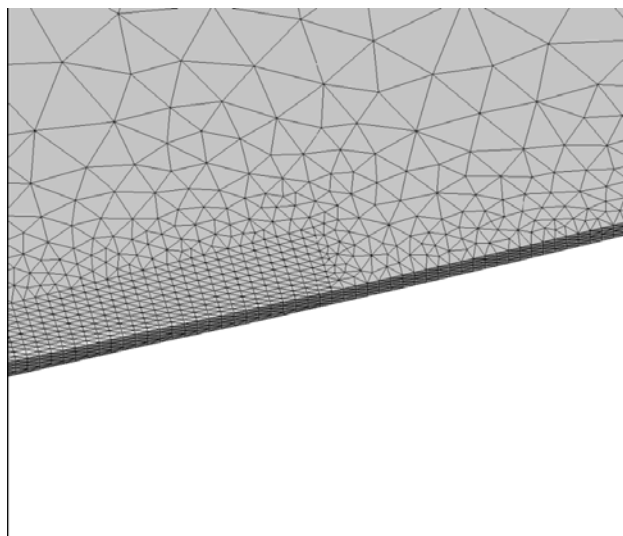
Figure 4-12: Leading Edge Mesh Showing the Converted Structured Mesh Domain Next to an Unstructured Mesh Domain.
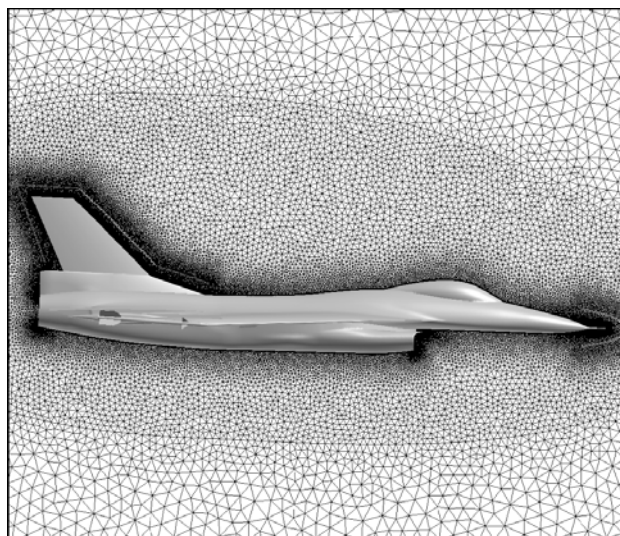
Figure 4-13: Symmetry Plane Mesh.

Baffle surfaces were used to control the spacing of the volume mesh, resulting in a hybrid unstructured inviscid mesh. The quadrilateral elements shown in the figure around the nose and tail are a result of these baffles. Additional baffles were created around the leading edge and trailing edge of the wing and at a near field boundary within a body length of the aircraft.

4.5.2.2.2   *Viscous Layer Addition*

A second in-house developed mesh generation program was used to insert layers of triangular prismatic elements at the no-slip surfaces of the geometry [4-14]. This method uses a Linear-Elastic mesh-smoothing scheme to push the existing mesh away from the surface, making room for the viscous elements. The term normally used to define Young's Modulus in the Linear-Elastic relations is defined using a combination of element aspect ratio and corner angles to provide stiffness in regions of tight grid spacing. Poisson's ratio was set to a constant of 0.25. Only one layer of points is added at a time in reverse order; the top layer is added first and the final layer near the wall is added last. Points are only added where the local mesh spacing is larger than the desired spacing for the current layer. As a result, the number of triangular prismatic elements in a column varies over the surface. Figure 4-14 and Figure 4-15 show the varying number of elements per

column for the mesh at the inlet. This capability allows the outer layer of prisms to match the spacing of the local tetrahedral elements without forcing each column to have unnecessary layers, which could result in kinking or buckling of the outer viscous layers.
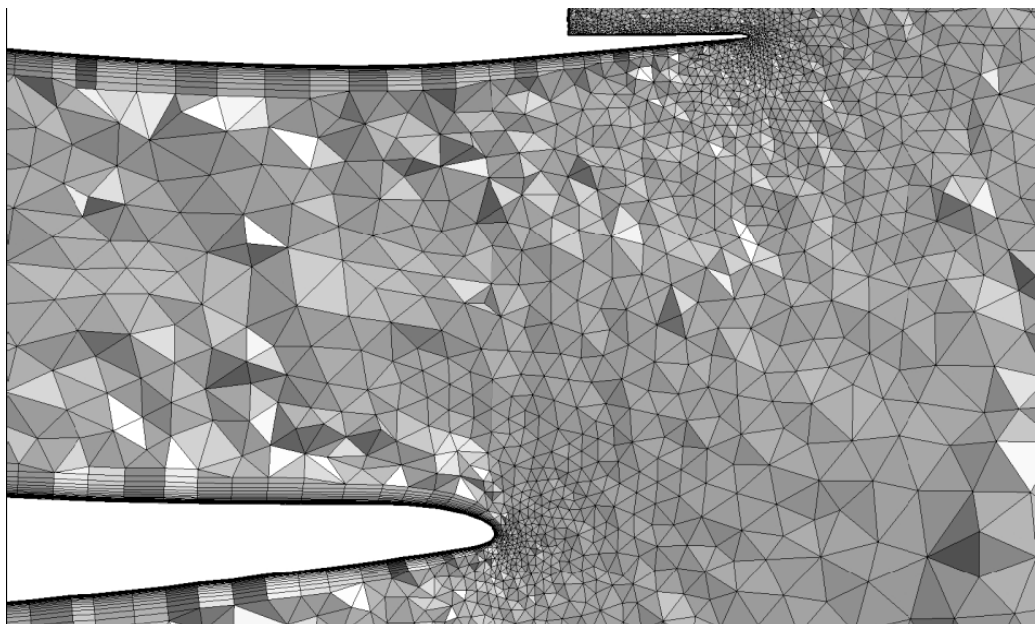
Figure 4-14: Crinkle Cut of Mesh Near the Symmetry Plane at the Inlet.
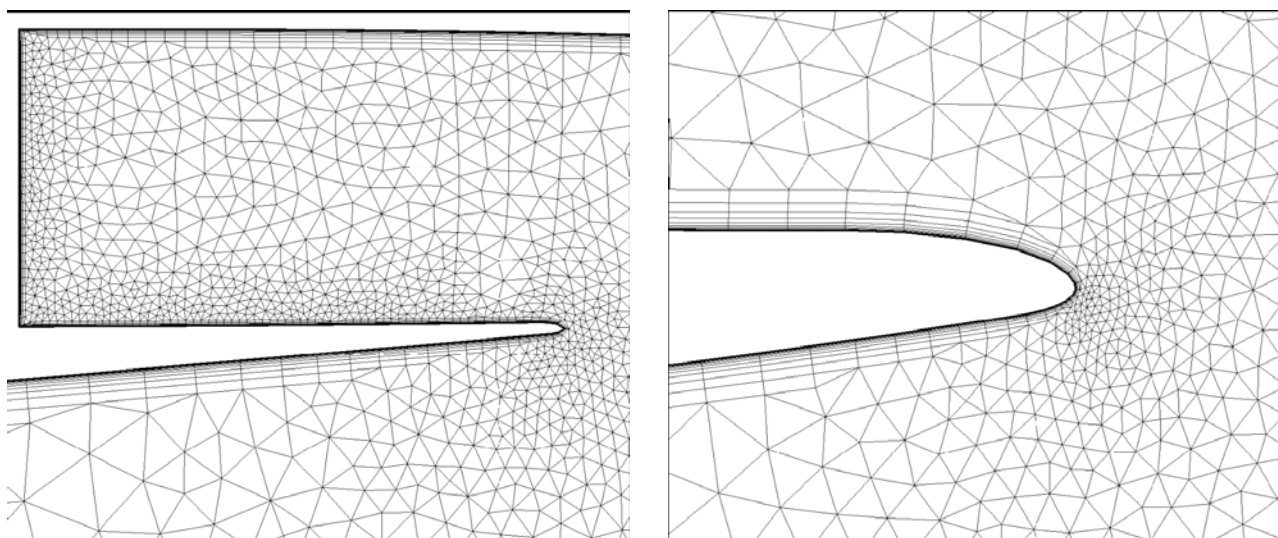
**Figure 4-15: Magnified Views of Symmetry Plane Mesh at
the Upper Inlet Lip (left) and the Lower Inlet Lip (right).**

A total of 25 layers were requested for the viscous region. The initial spacing was specified to correspond to an approximate y^+ value of 1. The height of the subsequent layers increases according to a geometric progression

parameter $\Delta s_2/\Delta s_1$ of 1.15 and a geometric growth rate of 1.02. A view of the viscous layers for the tip missile fins is shown in Figure 4-16. Finer resolution tetrahedra can be seen in the gap region between the fin and the missile rail. The layer insertion strategy matched the normal spacing of the layers with the existing local tetrahedral mesh. The half-model viscous mesh contained 13,906,708 nodes, 32,395,936 tetrahedra, 166,230 pyramid and 15,770,674 prisms.
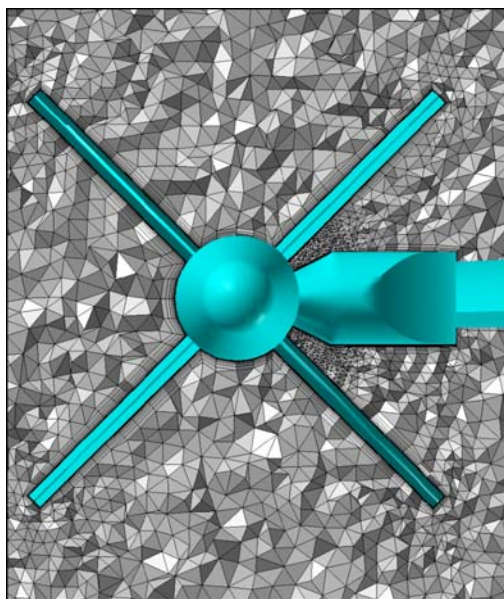
Figure 4-16: Magnified View of Axial Cut Through Tip Missile Fins and Wing.

4.5.2.3   Boeing Phantom Works

The grids used by researchers from the Boeing Phantom Works (see also Chapter 12) were generated using the Boeing Modular Aerodynamic Computational Analysis Process (MADCAP). MADCAP was developed at Boeing as a modular framework to in-house grid generation capabilities from a variety of sources. MADCAP contains a fully automated surface mesh generation capability. In addition to the automated approach, the user can interactively control resolution and mesh element type through the selection of control nodes, edges and surfaces. Unstructured mesh algorithms can be selected from Boeing developed libraries and/or from the Advancing Front with Local Reconnection (AFLR) library [4-15]. Surface meshes can contain a combination of quadrilateral and triangular faces. The volume meshes used in this study were developed with the AFLR code using a combination of element types. Near the wall, advancing layers are used to place highly anisotropic prismatic elements across the boundary layer. Outside the boundary layer, isotropic tetrahedral elements are utilized. A smooth transition between the prismatic and tetrahedral elements is provided by growing each column of the boundary layer mesh until the element at the outside edge is nearly isotropic. The boundary layer resolution is controlled by specification of the initial spacing near the wall, an initial growth rate, a growth stretching and a maximum growth rate. In addition, the extent of the boundary layer thickness can be specified or an estimate of the boundary layer thickness for a turbulent flat plate can be used to extend the prismatic layers beyond the estimate. Control of the resolution of the tetrahedral portion of the mesh is provided by a linear interpolation from the surface mesh. Alternatively, the user can specify a geometry growth rate to control the stretching of resolution in the tetrahedral region. Sources in the form of individual nodes, curves or surfaces can be specified to control the off body resolution of the tetrahedral mesh.

A mesh with higher-resolution than hybrid baseline unstructured grid was constructed in MADCAP to try and improve solution accuracy. In particular, the mesh was concentrated near the wing leading edge to try and improve the prediction near the secondary vortex. Mesh resolution was increased at the leading edge by introducing high aspect ratio quadrilateral elements into the surface mesh. The maximum aspect ratio of the quadrilateral faces is 25. The circumferential resolution at the leading edge is 0.05 inches inboard of the wing crank transitioning to 0.01 inch spacing near the wing tip. The quadrilateral elements were subdivided into triangles in the final mesh. A comparison of the Boeing and common meshes at the wing leading edge is shown in Figure 4-17. The resolution of the Boeing surface mesh is about double that of the common mesh in the immediate proximity of the wing vortices.

(a)   (b)
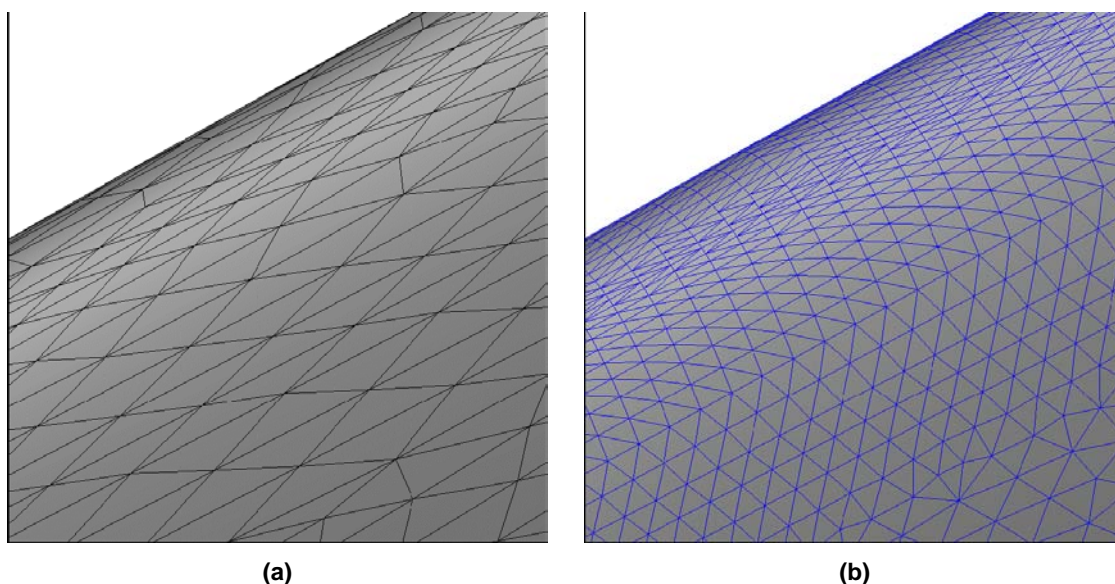
**Figure 4-17: Comparison of Surface Meshes Near the Wing Leading Edge:
(a) Hybrid Baseline Unstructured Grid; (b) Boeing Grid.**

The volume portion of the Boeing mesh was generated in AFLR and consists of a semi-structured boundary layer extrusion connected to an isotropic tetrahedral grid. The extrusion used a 0.0003 inch initial spacing at the wall to yield a y+ of approximately 1. The initial spacing grew geometrically with an initial geometric progression parameter $\Delta s_2/\Delta s_1$ of 1.2 ending at a 1.8 maximum growth ratio. Extrusion terminated when the prisms achieved an aspect ratio near unity. The combination of the initial viscous spacing, growth rate parameters, and surface spacing produced approximately 15 prism layers. The resulting volume grid had 19.3 million cells.

Feature-based grid adaptation has been used to improve the quality of the grid of the Boeing grids (see Chapter 12).

4.6   CONCLUSIONS

In the framework of CAWAPI both structured and unstructured grids have been generated. Prior to the grid generation an IGES file containing the air tight geometry description of the F-16XL aircraft which could be used for both the structured and unstructured grid generation was created.

The baseline structured grid was generated by NLR using in-house developed (semi-automatic) grid generation algorithms. A family of grids including grids with a reduced number of blocks have been derived from this baseline grid. Although most of the algorithms used had become available just before CAWAPI and thus only a limited experience with their application to such a complex configuration as the F-16XL was available, a grid of good quality was generated within a reasonable amount of time. The best practices established during CAWAPI have resulted in a significant reduction of the grid generation time for future projects.

Several unstructured grids have been generated within CAWAPI. The baseline all-tetrahedral and hybrid unstructured grids were generated at NASA Langley Research Center and the U.S. Air Force Academy, respectively. Despite their rather moderate cell count, the baseline all-tetrahedral and hybrid unstructured grids provided sufficient geometrical resolution. However, several CAWAPI members needed grids with more geometrical resolution. Additional unstructured grids were generated at EADS-MAS, the UTSimCenter, and Boeing Phantom Works.

4.7   ACKNOWLEDGEMENTS

The authors gratefully acknowledges the support provided by Lockheed Martin Aeronautics Company – Fort Worth in providing a refined iges geometry file. In addition, the authors gratefully acknowledges the geometrical work performed by Mr. Edward B. Parlette of Vigyan, Inc. in generating unstructured grids from the iges file.

4.8   REFERENCES

[4-1]   Lamar, J.E., Obara, C.J., Fisher, B.D. and Fisher, D.F.: *Flight, Wind-Tunnel, and Computational Fluid Dynamics Comparison for Cranked Arrow Wing (F-16XL-1) at Subsonic and Transonic Speeds*, NASA TP-2001-210629, 2001.

[4-2]   *ENFLOW: A Computer Code System for Accurate Simulation of Three-Dimensional Flows*, URL: http://www.nlr.nl/documents/flyers/f222-01.pdf [cited 12 December 2006].

[4-3]   Spekreijse, S.P., Prananta, B.B. and Kok, J.C.: *A Simple, Robust and Fast Algorithm to Compute Deformations of Multi-Block Structured Grids*, NLR-TP-2002-105, 2002.

[4-4]   Samareh, S.: *GridTool: A Surface Modeling and Grid Generation Tool*, In Proceedings of the Workshop on "Surface Modeling, Grid Generation, and Related Issues in CFD Solutions", NASA CP-3291, May 9-11, 1995.

[4-5]   Pirzadeh, S.: *Progress Toward a User-Oriented Unstructured Viscous Grid Generator*, AIAA-96-0031, 1996.

[4-6]   Strang, W.Z., Tomaro, R.F. and Grismer, M.J.: *The Defining Methods of Cobalt: A Parallel, Implicit, Unstructured Euler/Navier-Stokes Flow Solver*, AIAA-99-0786, 1999.

[4-7]   Wallin, S.: *Standardized Data Format, The Aeronautical Research Institute of Sweden (FFA)*, FFAP-A-950, Stockholm, Sweden, 1992.

[4-8]   Eliasson, P.: *EDGE, a Navier-Stokes Solver for Unstructured Grids*, Proc. To Finite Volumes for Complex Applications III, ISBN 1 9039 9634 1, pp. 527-534, 2002.

[4-9]   Legensky, S.M., Edwards, D.E., Bush, R.H., Poirier, D.M.A., Rumsey, C.L., Cosner, R.R. and Towne, C.E.: *CFD General Notation System (CGNS): Status and Future Directions*, AIAA-2002-0752, 2002.

[4-10] Lamar, J.E., Cronin, C.K. and Scott, L.E.: *A Review of Steps Taken to Create an International Virtual Laboratory at NASA Langley for Aerodynamic Prediction and Comparison*, Progress in Aerospace Sciences, Vol. 40, No. 3, pp. 163-172, April, 2004.

[4-11] Gerhold, T., Friedrich, O., Evans, J. and Galle, M.: *Calculation of Complex Three-Dimensional Configurations Employing the DLR-Tau Code*, AIAA-97-0167, 1997.

[4-12] CentaurSoft Grid Generator, http://www.centaursoft.com [cited 19 DMarch 2007].

[4-13] Pointwise, Inc., Gridgen User Manual, Version 15, http://www.pointwise.com/ [cited 19 DMarch 2007].

[4-14] Karman, S. Jr.: *Unstructured Viscous Layer Insertion Using Linear-Elastic Smoothing*, AIAA Journal, Vol. 45, No. 1, pp. 168-180, January 2007.

[4-15] Marcum, D.L.: *Advancing-Front/Local-Reconnection (AFLR) Unstructured Grid Generation,* Computational Fluid Dynamics Review, World Scientific – Singapore, 1998, p. 140.

[4-16] TranscenData, http://www.transcendata.com [cited 19 DMarch 2007].

Chapter 5 – NUMERICAL SOLUTIONS FOR THE CAWAPI CONFIGURATION ON STRUCTURED GRIDS AT NLR, THE NETHERLANDS

by

**Okko J. Boelens, Stephanus P. Spekreijse,
Harmen A. Sytsma and Koen M.J. de Cock**

5.1   SUMMARY

Accurate and cost-effective Computational Fluid Dynamics (CFD) methods play an increasingly important role, even in the support of fighter aircraft operations. Prior to the deployment of such CFD methods they should be well validated and evaluated against state-of-the-art wind-tunnel and/or flight test data. The Cranked-Arrow Wing Aerodynamics Project (CAWAP) provided the CFD community with an excellent database for validation and evaluation. Initiated by NASA, the Cranked-Arrow Wing Aerodynamics Project International (CAWAPI) was started as a follow-on project of CAWAP. The National Aerospace Laboratory NLR participated in this project using the in-house developed flow simulation system ENFLOW, which includes both grid generation tools and a flow solver. NLR applied (semi-automatic) grid generation tools to generate a structured (multi-block) grid. Steady flow simulations for all seven CAWAPI flight conditions are performed employing the flow solver ENSOLV. Results obtained for flight condition 7, 19 and 25 are discussed. The focus of this discussion is on a comparison of the measured and simulated flow features. It is shown that the understanding of NLR's structured (multi-block) grid generation algorithm and the confidence in the application of its flow simulation method to complex fighter configurations increased significantly by participating in CAWAPI.

5.2   INTRODUCTION

Application of Computational Fluid Dynamics (CFD) methods to support the operation of fighter aircraft requires sufficient accuracy (fidelity) and cost-effectiveness of these methods compared to alternatives such as wind-tunnel tests or flight tests. Two envisaged applications are the assessment of stability and control characteristics and the assessment of changes in aircraft loads due to new store configurations. By using CFD methods the number of flight conditions that need to be flown in a flight test certification program can be optimized and potentially dangerous flight conditions can be identified beforehand. To enable application of CFD methods for such purposes with confidence, the methods should be well validated and evaluated against state-of-the-art wind tunnel and/or flight test data.

The Cranked-Arrow Wing Aerodynamics Project (CAWAP) (see Chapter 3 and [5-1]) provided the CFD community with an excellent database for validation and evaluation purposes. This project focused on the understanding of flow phenomena encountered on a cranked-arrow wing relevant to advanced supersonic fighter and transport aircraft. Initiated by NASA, the Cranked-Arrow Wing Aerodynamics Project International (CAWAPI) was started as a follow-on project.

The National Aerospace Laboratory NLR participated in this task group using the in-house developed flow simulation system ENFLOW, which includes both grid generation tools and a flow solver. The application of the NLR ENFLOW flow simulation system to the CAWAPI test cases is the main subject of this chapter. Based on the IGES file containing the water tight geometry description of the F-16XL (see Chapter 4),

a structured (multi-block) grid was generated at NLR using a grid mapping technique. The grids used in simulations will be discussed in Section 5.3 (see also Chapter 4). Section 5.4 will discuss the important features of the flow solver ENSOLV, which is part of the simulation system ENFLOW. Section 5.5 will discuss some of the results obtained at NLR. The focus will be on a comparison of the measured and simulated flow features. A section with conclusions (Section 5.6) completes this chapter. Both the grid generation process and the flow simulation process employed by NLR will be assessed with respect to their Technology Readiness Level.

5.3 GRID

At the Netherlands National Aerospace Laboratory NLR a family of structured (multi-block) grids has been generated using a Cartesian grid mapping technique. The following grids which are part of this family of structured (multi-block) grids have been used by NLR in CAWAPI:

- The baseline structured grid around the half-span full-scale model of the F-16XL consisting of 1903 blocks, 14,750,720 grid cells and 17,014,119 grid points.

- The baseline structured grid with a reduced number of blocks. The merging step resulted in a reduction of the number of blocks from 1903 to 216.

- A structured grid around the full-scale model of the F-16XL consisting of 3806 blocks, 29,501,440 grid cells and 34,028,238 grid points. This grid has been generated by mirroring the baseline structured grid around the half-span full-scale model of the F-16XL with respect to the symmetry plane.

Further details on the grid generation method and the baseline structured grid around the half-span full-scale model of the F-16XL can be found in Chapter 4.

5.4 FLOW SOLVER

5.4.1 General Description

The flow solver ENSOLV, which is part of NLR's flow simulation system ENFLOW [5-2], is capable of solving the Euler and Navier-Stokes equations on multi-block structured grids for arbitrary configurations. The configuration can be either fixed or moving relative to an inertial reference frame, and can be either rigid or flexible.

The flow equations are cast into a full conservation form employing the density ρ, the components of the momentum vector $\rho\mathbf{u}$ and the total energy per unit volume ρE as dependent variables. The equations are non-dimensionalized using the free-stream static pressure, the free-stream density, the free-stream temperature and a reference length (for example the reference wing chord).

The equations in full conservation form are discretized in space by a second-order accurate, cell-centred, finite-volume method, using multi-block structured grids, central differences, and matrix artificial diffusion. The artificial diffusion consists of a blending of second-order and fourth-order differences with a Jameson-type shock sensor for the basic flow equations and a TVD discontinuity sensor for the turbulence model equations.

For steady flow simulations, the discretized time-dependent system of equations is integrated toward the steady-state solution using a five-stage explicit Runge-Kutta scheme. Local-time stepping, implicit residual averaging and multi-grid acceleration techniques are applied.

For time-accurate simulations, the flow solver uses the dual-time stepping scheme, where for each time-step the time-dependent flow equations are integrated in pseudo-time toward a steady-state solution in a similar way as in the steady flow simulation using the same acceleration techniques.

5.4.2   Turbulence Model

Several turbulence models are present in the flow solver ENSOLV, including the Turbulent Non-Turbulent (TNT) k-ω model [5-4] [5-5], the EARSM model [5-5] and a hybrid RANS-LES model for eXtra-Large Eddy Simulation (X-LES) [5-6] [5-7].

For all simulations in the present study, the TNT k-ω model, which is a variant of the Wilcox k-ω model, is employed. The equations of the model are slightly modified by the introduction of a 'cross diffusion' term [5-3]. This modification has been introduced to resolve the dependency of the free-stream-valued of ω. The model is also extended with a global correction for vortical flows [5-4] [5-5]. It is well known that the standard model, as with most other two-equation models, over predicts the eddy viscosity within the vortex core which leads to exaggerated diffusion of vorticity. As a consequence the details of the vortex core are lost and low suction peaks with wide vortex bases are a characteristic of the solution. The enhanced model[18] controls the production of turbulent kinetic energy and hence eddy viscosity through an increase in the production of dissipation (ω) within regions of highly rotational flow. A suitable sensor has been used to distinguish between shear layers and vortex cores. This sensor is the ratio between the magnitude of strain-rate and vorticity tensor. In shear layers, the velocity gradient is dominated by the gradient in the normal direction, which results in a ratio of approximately one, while in vortex cores, where the flow experiences pure rotation, the ratio is much less than one. This approach has proven to be effective in producing surface pressure profiles on simple delta wings in good agreement with those of experimental data [5-4] [5-5].

In addition, to remove the singular behaviour of ω at solid boundaries, the equations of the k-ω model are reformulated such that instead of ω the quantity $\tau = 1/(\omega + \omega_0)$ is used. Here ω_0 is a positive constant (default value $\omega_0 L_{ref}/u_\infty = 20$, with U_∞ the free-stream velocity and L_{ref} the reference length). Finally, the source terms in the k-ω equations are treated explicitly, while a separate time-step is used for the k-ω equations to enhance the efficiency of the scheme.

At the solid boundaries, both k and τ are set to zero. To prevent unphysical high values of k near stagnation points, the production term in the k-equation has been limited to a maximum of 20 times the dissipation term in the k-equation.

At the 'inflow' parts of the far-field boundary, the free-stream values of the turbulent variables are computed from the free-stream turbulent Reynolds number (0.01 in the present simulations) and the free-stream dimensionless turbulent kinetic energy ($k/u_\omega^2 = 10^{-6}$ in the present simulations).

All simulations were run in fully turbulent mode.

5.4.3   Boundary Conditions

At the F-16XL geometry, a no-slip viscous flow condition (Navier-Stokes adiabatic solid wall) has been employed. For the upstream, top, bottom and side far-field faces, a free-stream boundary condition based on Riemann invariants of the locally linearized one-dimensional Euler equations has been used. Since the flow at these faces is subsonic, the value of the 'incoming' Riemann invariants is computed using the free-stream values. The remaining invariants are extrapolated from the computational domain. A free-stream boundary condition

based on the extrapolation of the pressure has been used at the downstream far-field boundary. For the simulations on the grid around the half-span full-scale model of the F-16XL a symmetry boundary condition has been used at the symmetry plane. For this boundary condition the grid does not necessarily need to be orthogonal to the symmetry plane. Finally, at the inlet duct exit plane (engine inlet) a boundary condition with a prescribed normalized static pressure p/p_∞ is used, whereas at the mixing plane (engine exit) a boundary condition with a prescribed normalized total pressure $p_t/p_{t,\infty}$ and total temperature $T_t/T_{t,\infty}$ is applied.

5.4.4 Details of Simulations

All simulations were performed as steady flow simulations. A Full Multi-Grid (FMG) scheme (grid sequencing) was used to compute the solution on the three grid levels. The solution on a coarse level is used as initial solution on the next-finer level. The number of iterations on each grid level is shown in Table 5-1. The Full Approximation Storage (FAS) multi-grid scheme is used to compute the solution on a specific grid level. Two FAS multi-grid levels were used. The simulations were performed on two processors of NLR's NEC SX5/8B vector computer. Four orders of convergence were obtained for the root mean square norms. Computational details of the simulations are shown in Table 5-1.

Table 5-1: Computational Details of the Simulations

	Number of Grid Cells	Number of Iterations	Computational Wall-Clock Time (Use 2 processors of NLR's SX5/8B)	
			Baseline Structured Grid (see Section 5.3)	Baseline Structured Grid with a Reduced Number of Blocks (see Section 5.3)
4h-grid level	230,480	1500	4h55m	1h00m
2h-grid level	1,843,840	900	12h18m	2h41m
h-grid level	14,750,720	1200	45h31m	12h50m
Total			62h44m	16h33m

Note that, since larger block dimensions result in an increase of the vector length, merging the blocks resulted in a significant reduction of the required computational time. The computation time obtained with the baseline grid with a reduced number of blocks allowed the computation of all flight conditions well within one weekend.

5.5 COMPARISON OF THE MEASURED AND SIMULATED FLOW FEATURES

5.5.1 Flight Test Cases

At NLR simulations have been performed for all flight conditions on the grid around the half-span full-scale model, except for flight condition 50 and 51 for which the grid around the full-scale model was employed.

The data obtained during the flight tests (see Chapter 3 and [5-1]) comprised surface pressure measurements, both along butt lines (BL) and fuselage stations (FS), boundary layer measurements at four positions on the left wing, skin friction measurements at the FS330 station on the left wing and surface flow visualizations using tufts. The data available for each flight condition is shown in Table 5-2.

Table 5-2: Flight Test Data (A = Available, NA = Not Available)

Flight Condition	Surface Pressure Measurements	Boundary Layer Profiles	Skin Friction Measurements	Surface Flow Visualization
7	NA (Use flight condition 35 and flight condition 49 [5-1])	A	NA	A
19	NA	NA	A	A
25	A	NA	NA	A
46	A	NA	NA	A
50	A	NA	NA	A
51	A	NA	NA	A
70	A	NA	NA	A

Based on the data availability and the notion that flight condition 7 and flight condition 19 are practically identical, the assessment of the results presented here will be based on these two flight conditions. By combining the data of these two flight conditions, a fairly complete picture of the flow features can be drawn. In addition, for completeness a comparison of surface pressure measurements and the surface flow visualizations using tufts will be presented for flight condition 25.

The results of other flight conditions such as the transonic flow case (flight condition 70) are presented in Chapter 16.

The engine parameters associated with these flight conditions (see Chapter 3) are displayed in Table 5-3. The table also shows the parameters for the engine boundary conditions (see Section 5.4.3), which are used in the simulations.

Table 5-3: Engine Parameters

Flight condition	Inlet duct Exit					Mixing plane			
	T_s, °R	p_s, psia	u, ft/s	M	p/p_∞	T_t, °R	p_t, psia	$T_t/T_{t,\infty}$	$p_t/p_{t,\infty}$
7	498.0	11.00	379.6	0.347	*0.900*	1050.0	23.00	*2.058*	*1.764*
19	485.8	10.20	345.8	0.320	*1.009*	1050.0	21.50	*2.119*	*1.945*
25	470.1	8.72	474.8	0.447	*0.863*	1209.0	26.30	*2.474*	*2.498*
46	443.6	5.85	404.3	0.390	*1.026*	1045.0	14.80	*2.285*	*2.148*
50	440.0	5.16	483.3	0.470	*0.905*	1154.0	16.95	*2.567*	*2.611*
51	431.8	5.19	468.6	0.460	*0.910*	1146.0	16.74	*2.546*	*2.568*
70	519.0	10.65	464.7	0.416	*1.736*	1200.0	30.00	*2.299*	*2.675*

5.5.2   Assessment of the Results

Before looking in detail to the results, first the large-scale vortical flow structure above the wing is discussed. Figure 5-1 shows an iso-surface of the vorticity magnitude for flight condition 7. The level of the vorticity magnitude equals 250 Hz. The vortical flow structure consists of several vortices, i.e.:

   i)   The inner wing primary vortex originating from the wing leading edge inboard of the crank;

ii) Outer wing vortex originating from the wing leading edge outboard of the crank;

iii) The air dam vortex originating form the air dam at wing upper surface;

iv) The missile vortices originating from the missile fins; and

v) The fuselage vortex.
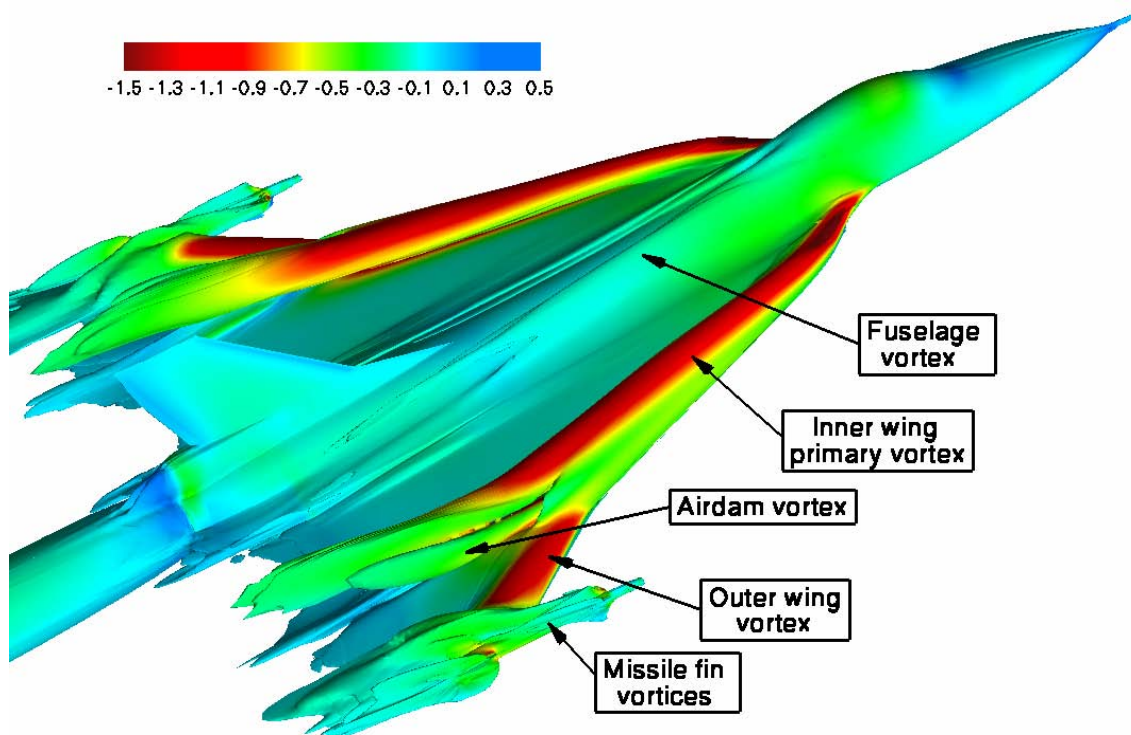
Figure 5-1: Iso-Surface (Level Equals 250 Hz) of Vorticity Magnitude for Flight Condition 7
(α = 11.89°, M = 0.304 and Re = 44.40 x 10^6). The vortices are colored by the pressure coefficient C$_p$.

In addition to these vortices other vortical structures, such as for example the inner wing secondary vortex, are present. All flight conditions characterized by vortical flow exhibit a similar vortical flow structure, although the strength and location of the vortices may differ. As can be seen in Figure 5-1, both the inner wing primary vortex and the outer wing vortex result in a region of high suction downstream of the leading edge.

This behaviour is also evident in the figures showing the sectional surface pressure coefficient at different butt line and fuselage stations. Figure 5-2 shows the sectional surface pressure coefficient for flight condition 25, whereas Figure 5-3 shows this coefficient for flight condition 7 as well as flight condition 19. For the flight condition 25 the simulation data is compared with the actual flight test data for this flight conditions. Since, however, for both flight condition 7 and flight condition 19 no surface pressure data is available, it was agreed within CAWAPI to use data from two neighbouring flight conditions, which are also recommended for comparison in [5-1]. These flight conditions are flight condition 34 (α = 13.50°, M = 0.370 and Re = 40.05 x 10^6) and flight condition 49 (α = 13.00°, M = 0.420 and Re = 38.97 x 10^6).
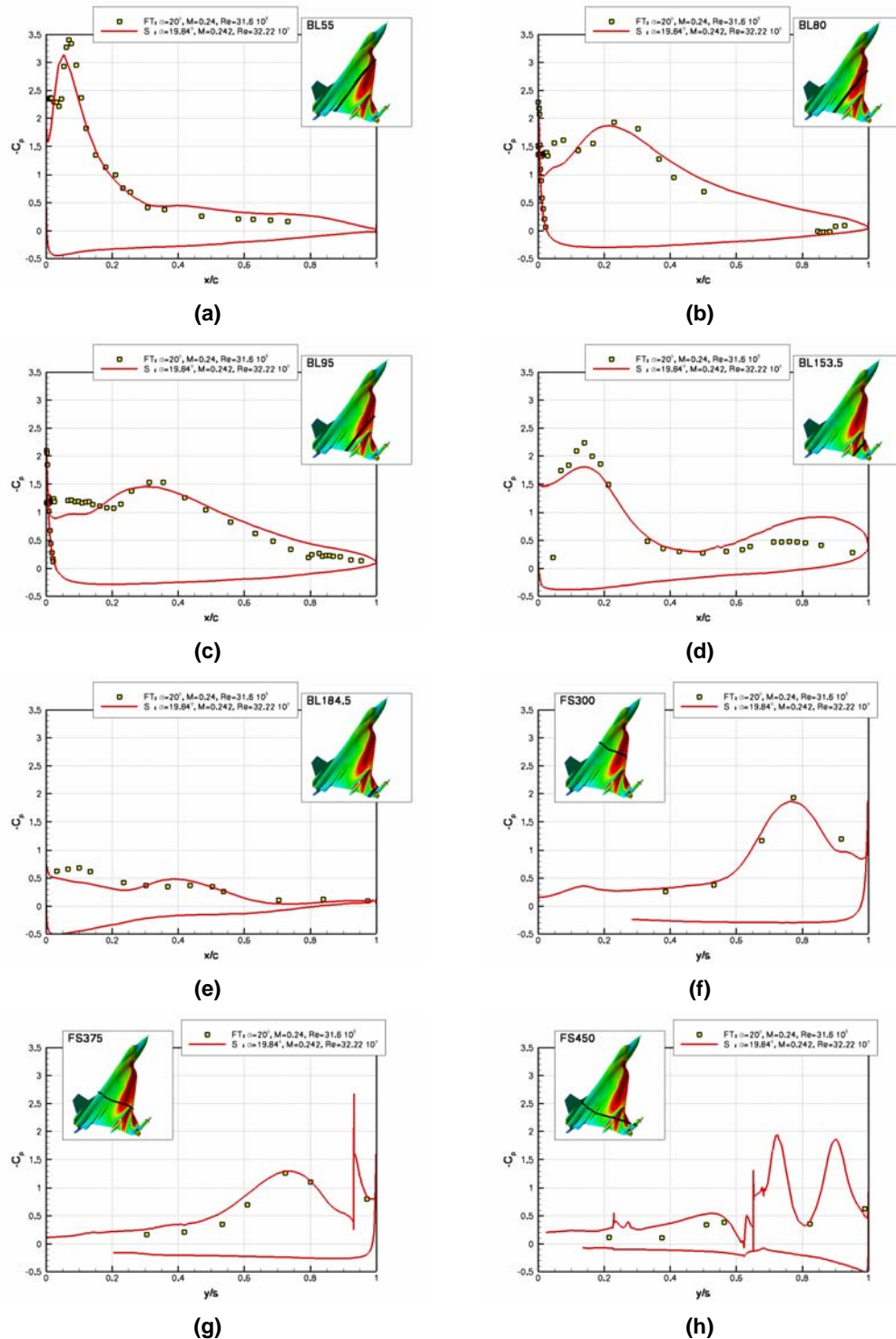
Figure 5-2: Surface Pressure Coefficient for Flight Condition 25 (α = 19.84°, M = 0.242 and Re = 32.22 x 10^6) along Butt Lines: (a) BL55; (b) BL80; (c) BL 95; (d) BL153.5 and (e) BL184.5; and Fuselage Stations: (f) FS300; (g) FS375; and (h) FS450.

(a)

(b)

(c)

(d)

(e)

(f)

(g)

(h)
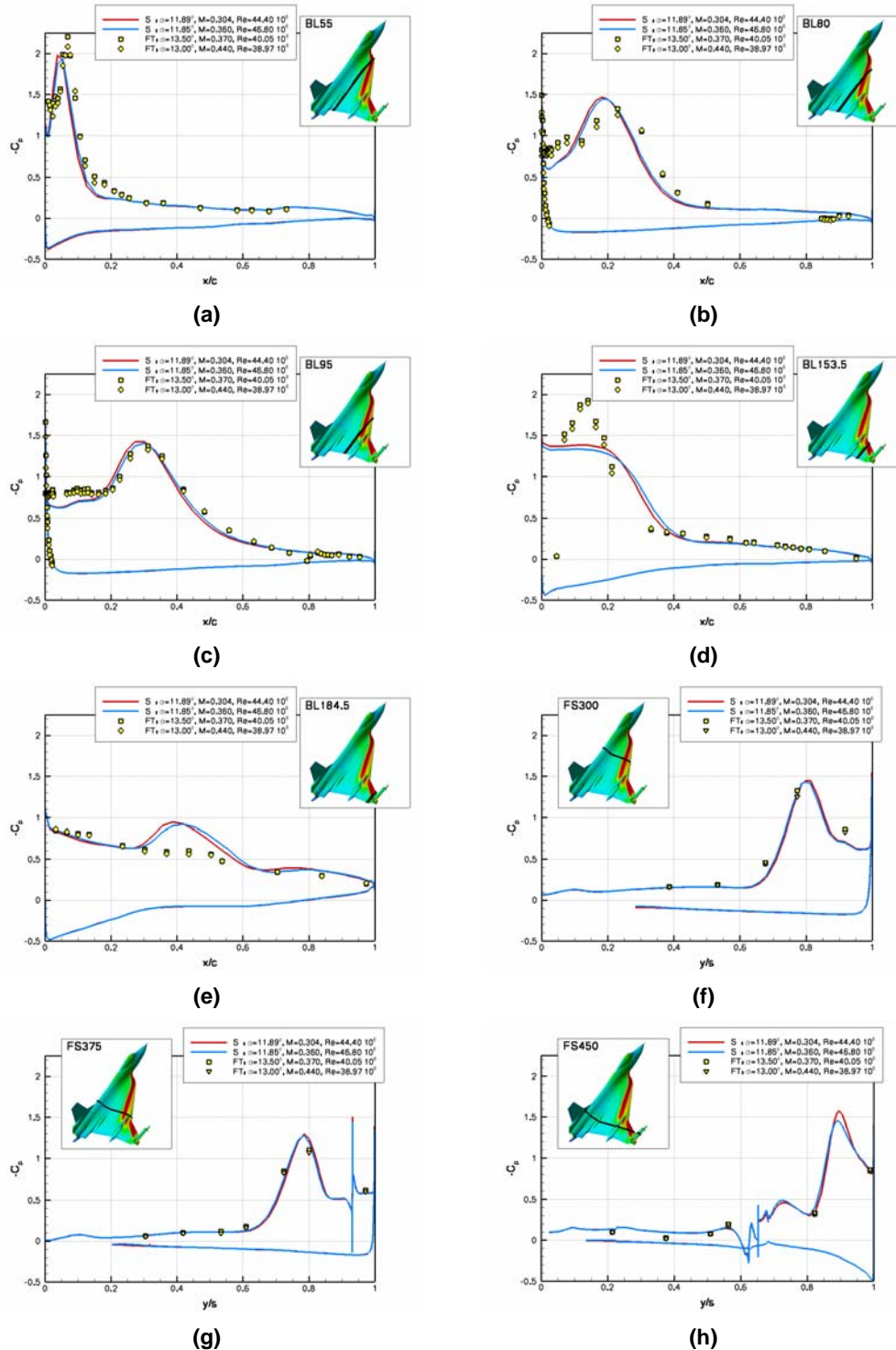
**Figure 5-3: Surface Pressure Coefficient for Flight Condition 7 (α = 11.89°, M = 0.304 and Re = 44.40 x 10^6) and
Flight Condition 19 (α = 11.85°, M = 0.360 and Re = 46.80 x 10^6) along Butt Lines: (a) BL55; (b) BL80;
(c) BL 95; (d) BL153.5; and (e) BL184.5; and Fuselage Stations: (f) FS300; (g) FS375; and (h) FS450.**

Surface pressure measurements are performed using 326 static pressure ports, both flush and in stream wise belts. 337 pressure ports are plumbed in the aircraft structure. These ports are arranged along butt lines and fuselage stations. During the flight tests, only 280 ports on the upper surface and 46 ports on the lower surface proved reliable.

Figure 5-2 and Figure 5-3 show that the agreement between flight tests and simulations is generally good. In addition, Figure 5-3 shows that the difference in surface pressure coefficient for flight condition 7 and flight condition 19 is small, as expected.

For all flight conditions the suction peak associated with inner wing primary vortex is predicted well, see Figure 5-2 (a), (b), (c), (f) and (g) and Figure 5-3 (a), (b), (c), (f) and (g). Since the flight test data is obtained at a higher angle of attack, a lower suction peak is to be expected in the simulations. The peak obtained by the simulations is also slightly more forward on the wing than the peak observed during the flight tests. The suction peak of the inner wing secondary vortex is, however, under predicted. This vortex also starts some distance downstream of the wing apex. The formation of the inner wing secondary vortex is postponed by the relatively coarse grid in the wing apex region.

On the part of the wing outboard of the crank, for flight condition 25 a pressure peak associated with the air dam vortex is observed. This vortex gives rise to a much higher pressure peak than observed during the flight tests; see Figure 5-2 (d) on the aft part of the wing. In addition, a pressure peak associated with the outer wing vortex is present. This pressure peak is under predicted in the simulations; see Figure 5-2 (d). Going outboard the difference between the simulation and the flight test becomes less pronounced; see Figure 5-2 (e). The agreement between the simulation and the flight test is good for all fuselage stations.

For flight condition 7 and flight condition 19, the pressure peak associated with the air dam vortex is much smaller; see Figure 5-3 (h). No influence of the air dam vortex is visible on the aft part of the wing; see Figure 5-3 (d). The outer wing vortex also results in a suction peak. Whereas in the flight tests a clear peak is observed, the simulations show a pressure peak that is rather flat in the part of the wing just outboard of the crank; see Figure 5-3 (d). Going outboard the pressure peak associated with the outer wing vortex, however, is over predicted; see Figure 5-3 (e). Once more, the agreement between the simulation and the flight test is good for all fuselage stations.

With respect to the turbulence model, it should be noted that the global correction for vortical flows (see Section 5.4.2) has primarily been validated for the primary vortex on simple sharp-edged delta wings [5-4] [5-5]. For the inner wing primary vortex, originating from the relatively sharp leading edge, the model results in a good prediction of the suction peak. However, the inner wing secondary vortex originates from a more complex boundary layer separation underneath the inner wing primary vortex. Despite the correction for vortical flows, which switches on in all vortical flow structures, the suction peak associated with the inner wing secondary vortex is under predicted. Inspection of the grid showed that in the region where the secondary vortex resides the grid is relatively coarse. This grid coarseness, especially in the apex region, is most probably the reason for the weaker agreement between the flight tests and the simulations for the inner wing secondary vortex. Finally, the modelling of turbulence also plays an important role in the complex vortical structures on the part of the wing outboard of the crank. The present turbulence model may not be best suited for the complex unsteady vortical structures found in this region.

For flight condition 7 boundary layer measurements were performed at four positions on the left wing (see Chapter 3 and [5-1]). The locations are summarized in Table 5-4. Note that in Figure 5-4 the corresponding positions of the measurement locations on the right wing are shown.

Table 5-4: Boundary-Layer Rake Locations

Boundary Layer Rake	Fuselage Station (FS), in	Butt Line (BL), in
3	302.17	-52.93
4	293.45	-76.22
5	294.59	-96.06
7	295.52	-94.33

(a)

(b)

(c)

(d)
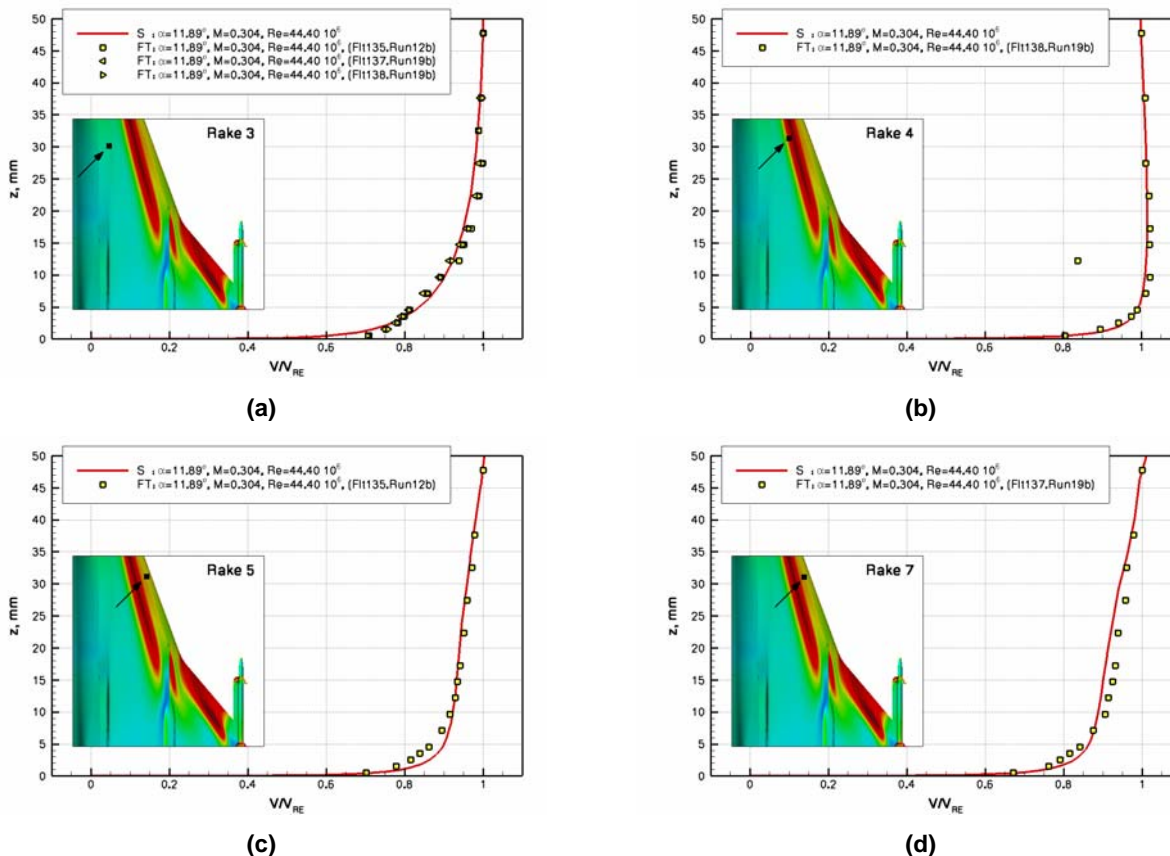
Figure 5-4: Boundary Layer Profiles for Flight Condition 7 ($\alpha = 11.89°$, M = 0.304 and Re = 44.40 x 10^6).

These location were chosen so that one rake is located well inboard of the inner wing primary vortex (rake 3), one is located underneath the inner wing primary vortex (rake 4) and two are located at the secondary vortex, both underneath (rake 5) and at its separation point (rake 7). Of the 23 available tubes on a rake, 16 active tubes were used for pressure measurements (15 for total pressure measurements and one for static measurements). The ultimate tube was located 2 inches above the surface. The rakes were aligned with the local flow according to an average angle over its height. CFD predictions from the CFL3D code[1] were used to determine this angle.

In Figure 5-4 the boundary layer profiles for flight condition 7 are shown. Note that in this figure the corresponding positions of the measurement locations on the right wing are shown. The agreement between the flight test and the simulation is generally good, especially well inboard of the inner wing primary vortex

(rake 3) and underneath the inner wing primary vortex (rake 4). For the rake locations associated with the inner wing secondary vortex (rake 5 and rake 7), the difference between the flight test and the simulation is slightly larger.

Although in the surface pressure coefficient the presence of a secondary vortex was not that clear, the local velocity seems to be in fairly good agreement in this region. Note also that the deviation between the flight test and the simulation is consistent for the rake locations associated with the inner wing secondary vortex.

Local skin friction measurements were performed for flight condition 19. These local skin friction measurements were performed across the left wing near FS330 using 16 modified Preston tubes (see Chapter 3 and [5-1]). Each total-pressure tube was integrated with a static-pressure port. The tubes were aligned with the local flow based on predictions by the CFL3D code [5-1]. The skin friction values are obtained by relating the pressure change between the total- and static-pressure tubes to the local skin friction. For more details see [5-1].

Figure 5-5 shows the local skin friction coefficient. Note once more that in this figure the corresponding positions of the measurement locations on the right wing are shown. The skin friction coefficient is shown both at the fuselage station used for the flight measurements (FS330) and at approximately the fuselage station where the boundary-layer rakes are located (FS300). At FS330 a good agreement between the flight test and the simulation is shown underneath the inner wing primary vortex, whereas the skin friction coefficient is over predicted underneath the inner wing secondary vortex. At FS300 a similar local skin friction distribution is observed. This distribution is in agreement with the boundary-layer measurements shown in Figure 5-4. In Figure 5-4, one can see that when approaching the surface the slope $d(V/V_{RE})/dz$ of the simulation is larger than the slope of the flight test at rake 5 and rake 7, whereas for rake 4 both agree well. Since the tangential component of the total stress tensor is directly proportional to this slope $d(V/V_{RE})/dz$ and the local skin friction coefficient C_f is the non-dimensional form of the magnitude of this tangential component, a good agreement is to be expected underneath the inner wing primary vortex (rake 4). Correspondingly an over prediction of the local skin friction coefficient is to be expected for the rake locations associated with the inner wing secondary vortex (rake 5 and rake 7).
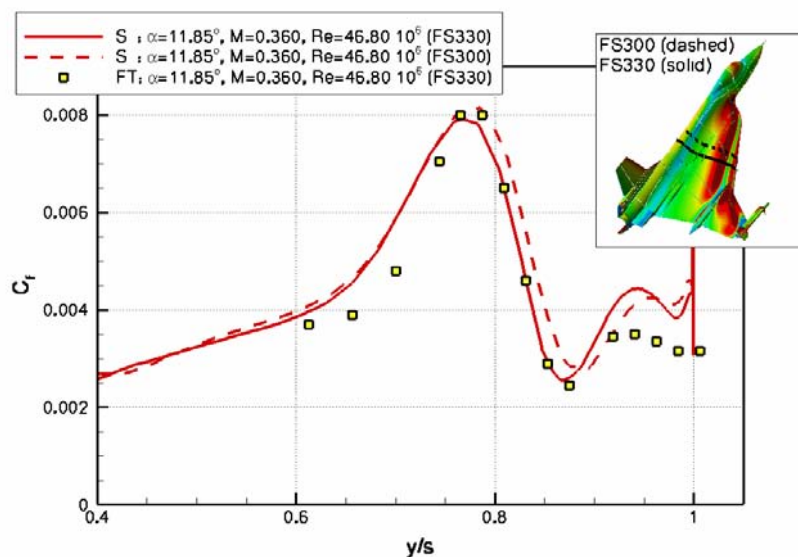
Figure 5-5: Local Skin Friction Coefficient for Flight Condition 19 (α = 11.85°,
M = 0.360 and Re = 46.80 x 10^{6}) at FS300 (dashed line) and FS330 (solid line).

Tufts were used to visualize the surface flow tubes (see Chapter 3 and [5-1]). Six cameras, two mounted atop the vertical tail, one on either side of the fuselage behind the canopy and one in the nose of each dummy missile, were used for recording the tufts data. The time was added to each image by a time-code inserter so that the images could be compared to form a composite and flight test conditions could be established. Images of interest were digitized in a 512- by 480-pixel format for further processing to develop quantifiable video data.

In Figure 5-6, the surface streamlines superimposed on the negative of the original tuft image are shown for flight condition 7 and flight condition 25. The black dots on the wing are video targets that were used for calibrating the images.

(a)   (b)
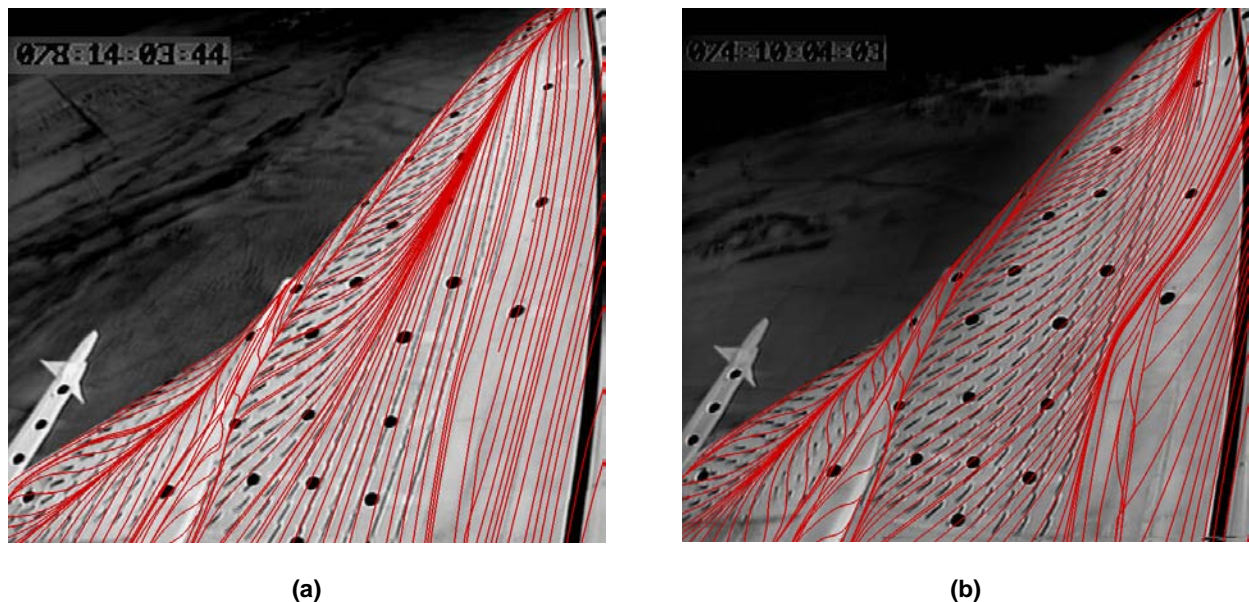
Figure 5-6: Surface Streamlines Superimposed on the Negative of the Tuft Image for (a) Flight Condition 7
(α = 11.89°, M = 0.304 and Re = 44.40 x 10^6), Flight 145, Run 16b, Video (yr, 1996), 078:14:03:44
(Day:hr:min:sec) and (b) Flight Condition 25 (α = 19.84°, M = 0.242 and Re = 32.22 x 10^6),
Flight 144, Run 16b, Video (yr, 1996), 074:10:04:03 (Day:hr:min:sec).

On the part of the wing inboard of the crank the agreement in the flow direction as indicated by the tufts and surface streamlines is good for both flight conditions. Clearly visible are the re-attachment line of the inner wing primary vortex and the separation line of the inner wing secondary vortex.

The agreement in the flow direction as indicated by the tufts and surface streamlines on the part of the wing outboard of the crank is also good for flight condition 25; see Figure 5-6 (b). Note that this flight condition is characterized by a high angle of attack and a strong air dam vortex. For flight condition 7; see Figure 5-6 (a) a less satisfactory agreement is obtained. For both cases, but especially flight condition 7, the tufts have a blurred character on this part of the wing, indicating local unsteadiness of the flow. For both flight conditions a re-attachment line is present.

Finally, the surface streamline pattern obtained for flight condition 7 was further scrutinized; see Figure 5-7. All flight conditions characterized by vortical flow show a surface streamline pattern comparable to that of flight condition 7, although the location of the specific features may differ.

(a)

(b)

(c)

(d)
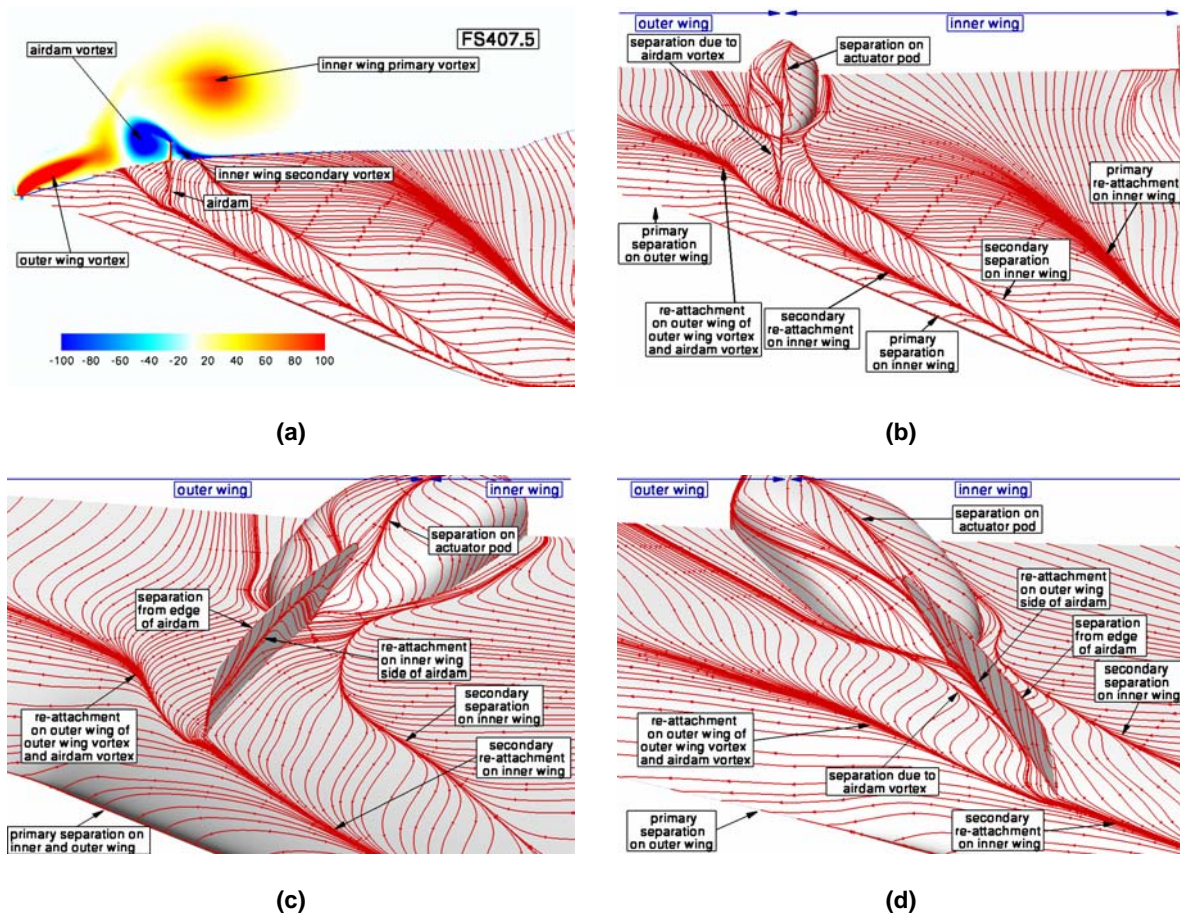
**Figure 5-7: Surface Streamline Pattern for Flight Condition 7 (α = 11.89°, M = 0.304 and Re = 44.40 x 10^6):
(a) Surface Streamlines with Non-Dimensional Vorticity Magnitude on a Cross-Sectional Plane at
FS407.5; (b) Overview of the Surface Streamline Pattern; (c) Detail of the Surface Streamline
Pattern on the Part of the Wing Inboard of the Crank; and (d) Detail of the Surface
Streamline Pattern on the Part of the Wing Outboard of the Crank.**

In Figure 5-7 (a) the vortical flow structures, such as the inner wing primary vortex, the inner wing secondary vortex, the air dam vortex and the outer wing vortex, are shown by means of the non-dimensional vorticity magnitude on a cross-sectional plane at FS407.5. In Figure 5-7 (b), the associated surface streamline pattern is displayed. In Figure 5-7 (c) and Figure 5-7 (d), details on the in board side and the out board side in the air dam region are shown respectively. The surface streamline pattern is composed of the following main elements:

a) *The primary separation on the inner and outer wing*. The flow separates on the wing leading edge. On the part of the wing in board of the crank this separation results in the inner wing primary vortex, whereas on the part of the wing out board of the crank the outer wing vortex is formed.

b) *The primary re-attachment on the inner wing*. At this line the vortical flow associated with the inner wing primary vortex re-attaches on the wing surface. Note that for the present case the inner wing primary vortex lifts off of the surface, resulting in a fanning out of the re-attachment line.

c) *The secondary separation on the inner wing.* Underneath the inner wing primary vortex the flow separates resulting in the inner wing secondary vortex. This separation line starts some distance downstream of the apex of the wing and is present up to the wing trailing edge.

d) *The secondary re-attachment on the inner wing.* At this line the vortical flow associated with inner wing secondary vortex re-attaches to the wing surface. This re-attachment line extends until the leading edge of the air dam.

e) *The re-attachment on the inner wing side of the air dam.* After reaching the air dam the vortical flow resulting from the inner wing secondary vortex re-attaches to the inner wing side of this air dam. Note that this re-attachment line is a continuation of the secondary re-attachment line on the inner wing. When the air dam changes to the actuator pod this re-attachment line stops to exist, and the vortical flow associated with the inner wing secondary vortex re-attaches in the junction between the actuator pod and the wing.

f) *The separation from the edge of the air dam.* The flow separates from the upper edge of the air dam. This separation results in the air dam vortex.

g) *The separation on the actuator pod.* The flow separates from the upper side of the actuator pod. Note that this separation starts before the intersection of the air dam and the actuator pod. The air dam vortex is fed further by the flow coming from this separation.

h) *The re-attachment on the outer wing of the outer wing vortex and the air dam vortex.* At this line the vortical flows associated with both the outer wing vortex and the air dam vortex re-attach.

i) *The separation due to the air dam vortex.* Due to the air dam vortex the flow separates just outboard of the air dam. This separation results in a small vortex in the outboard junction region between the air dam and the wing surface.

j) *The re-attachment on the outer wing side of the air dam.* The vortical flow associated with the small vortex described in (i) re-attaches to the air dam at this line.

Without the presence of the air dam and the actuator pod the vortical flow structure would simply consist of an inner wing primary and secondary vortex and an outer wing vortex. The presence of the air dam and actuator pod significantly complicates the vortical flow structure by introducing a range of other vortices.

5.6   CONCLUSIONS

In the framework of CAWAPI NLR has performed an assessment of NLR's ENFLOW flow simulation system using the F-16XL-1 flight test data. Both the grid generation process and the flow simulation process employed by NLR were part of this assessment.

NLR applied in-house developed (semi-automatic) grid generation algorithms to generate a structured (multi-block) grid. Although most of the algorithms used had become available just before CAWAPI and thus only a limited experience with their application to such a complex configuration as the F-16XL was available, a grid of good quality was generated within a reasonable amount of time. The best practices established during CAWAPI have resulted in a significant reduction of the grid generation time for future projects. At present, once the clean IGES file containing a water tight geometry description of an equally complex configuration is available, a structured (multi-block) grid can be generated in a short period of time. NLR's in-house developed structured (multi-block) grid generation algorithms combine a high grid quality and low through-put time and establish therefore a unique capability in the structured (multi-block) grid generation community.

Steady flow simulations for all seven flight conditions are performed employing the flow solver ENSOLV, which is part of NLR's flow simulation system ENFLOW. All seven flight conditions are simulated within one weekend on NLR's NEC SX5/8B vector computer.

In this chapter only the results obtained for flight condition 7, 19 and 25 are assessed against flight test data, consisting of surface pressure measurements, boundary layer profiles, skin friction measurements and surface flow visualization. Results for the other flight conditions can be found in Chapter 16. The present approach of steady flow simulations utilizing the TNT k-ω model with correction for vortical flows in general predicts the flow well. It should, however, be noted that this turbulence model, primarily validated for the primary vortex on simple sharp-edged delta wings, can be improved for the complex unsteady vortical structures encountered on the F-16XL aircraft. This is suggested by the simulation results for the complex vortical structures on the part of the wing outboard of the crank. In addition, as was seen for the inner wing secondary vortex, grid resolution also plays an important role. To more realistically resolve the complex vortical flow in the region near and outboard of the air dam and actuator pod the introduction of unsteady effects, as was indicated by the tufts images, and the application of more advanced turbulence models that are validated against well-controlled experiments such as performed in the Vortex Flow Experiment II (VFE-II) is required.

CAWAPI has provided NLR with an excellent platform to evaluate its ENFLOW flow simulation system. Through the participation in CAWAPI the grid generation algorithms and the flow algorithms used at NLR have reached a higher Technology Readiness Level for complex fighter configurations.

5.7   REFERENCES

[5-1]   Lamar, J.E., Obara, C.J., Fisher, B.D. and Fisher, D.F.: *Flight, Wind-Tunnel, and Computational Fluid Dynamics Comparison for Cranked Arrow Wing (F-16XL-1) at Subsonic and Transonic Speeds*, NASA TP-2001-210629, 2001.

[5-2]   *ENFLOW: A Computer Code System for Accurate Simulation of Three-Dimensional Flows*, URL: http://www.nlr.nl/documents/flyers/f222-01.pdf [cited 12 December 2006].

[5-3]   Kok, J.C.: *Resolving the Dependence on Free-Stream Values for the k-ω Turbulence Model*, NLR-TP-99295, 1999.

[5-4]   Brandsma, F.J., Kok, J.C., Dol, H.S. and Elsenaar, A.: *Leading Edge Vortex Flow Computations and Comparison with DNW-HST Wind Tunnel Data*, NLR-TP-2001-238, 2001.

[5-5]   Dol, H.S., Kok, J.C. and Oskam, B.: *Turbulence Modeling for Leading-Edge Vortex Flows*, AIAA-2002-0843, 2002.

[5-6]   Kok, J.C., Dol, H.S., Oskam, B. and van der Ven, H.: *Extra-Large Eddy Simulation of Massively Separated Flows*, NLR-TP-2003-200, 2003.

[5-7]   de Cock, K.M.J., Kok, J.C., van der Ven, H., Soemarwoto, B.I., Boelens, O.J. and Oskam, B.: *Extra-Large Eddy Simulation for Delta Wings and Space Launchers*, Presented on the 24th International Congress of the Aeronautical Sciences, Yokohama, Japan, August 29 – September 3, 2004.

Chapter 6 – NUMERICAL SOLUTIONS FOR THE CAWAPI CONFIGURATION ON STRUCTURED GRIDS AT UNIVERSITY OF GLASGOW/LIVERPOOL UNIVERSITY, UNITED KINGDOM

by

Ken J. Badcock

6.1 SUMMARY

Comparisons made within the framework of the RTO task group AVT-113 for RANS predictions of the flow around the F-16XL aircraft are shown. The computations were made on a block structured grid generated by NLR, and used the flow code PMB. The k-ω turbulence model with a rotation correction was used for the computations. The comparison for vortical flows was generally good for the prediction of the primary inboard vortex. Discrepancies for the primary outboard vortex were seen, and it is suggested that this is due either to the behaviour of the turbulence model for the region of high shear between the inboard and outboard vortices, or to unsteady flow in this region. The predictions for a transonic flight condition were consistent with other computations, but showed considerable discrepancy with flight measurements, some of which could perhaps be explained by uncertainty over the flap settings.

6.2 INTRODUCTION

The F-16XL-1 aircraft was produced to improve on the supersonic performance of the F-16. A description of its design and intended mission can be found in references [6-1] and [6-2]. The wing was designed by Langley Research Center and General Dynamics Corporation. It has a 70 degree sweep inboard of the crank, and a 50 degree sweep outboard. An S-blend was used to join the wing leading edge to the fuselage.

The Cranked-Arrow Wing Aerodynamics Project (CAWAP) exploited the F-16XL-1 aircraft to study the flow physics on a cranked wing relevant to future supersonic fighters or transport aircraft [6-3]. Flight tests [6-4] were carried by out NASA, using an aircraft on loan from the US Air Force F-16 Special Projects Office. Wingtip missiles and an air dam on the wing upper surface were both included for all flight tests. A range of measurements were made, including surface pressure measurements, boundary layer rakes and hot film data. The resulting database, which includes careful documentation of the aircraft geometry, is useful for the validation of CFD predictions.

The Cranked-Arrow Wing Aerodynamics Project International (CAWAPI) was started by NASA to allow a comprehensive comparison of several CFD codes with the CAWAP flight test database. This project was incorporated, along with the Vortex Flow Experiment 2 (VFE-2), in the NATO RTO task group AVT-113, under the co-chairmanship of John Lamar and Dietrich Hummel. CAWAPI had several contributions from structured codes (NLR, University of Liverpool, NASA Langley) and unstructured codes (US Air Force Academy, NASA Langley, EADS, FOI/KTH). The intention is to understand the capability and limitations of current CFD codes through comparisons with measurements and between codes.

There are a number of features which are interesting for the current study. First, all but one of the flight conditions have vortical flow. The computation of vortices has advanced significantly in recent years, demonstrated for example in collaborative validation exercises for delta wings [6-5]. Two main approaches have

appeared. The first uses a rotation correction to modify the production of turbulence in vortices for standard linear eddy viscosity type models [6-6]. The second uses Detached Eddy Simulation to switch to large eddy simulation in regions likely to include leading edge vortices [6-7]. CAWAPI provides an opportunity to test these approaches for a full aircraft test case which has a detailed database for validation.

Secondly, the geometry is very complex, featuring the wingtip missile, an air dam, the intake and a number of small details over the aircraft. The handling of the CAD file, and the generation of a grid (structured or unstructured) poses a significant challenge for current methods. For the work reported in this paper these issues were dealt with by NLR [6-8].

Thirdly, the flight Reynolds' numbers are an order of magnitude higher than most delta wing wind tunnel tests. In one respect this simplifies the computations in that it was reported based on hot film measurements that the flow on the aircraft was fully turbulent at the leading edge, removing any question of transition. The flow is assumed fully turbulent in the current work.

Fourthly, the vortical flow is complicated by the presence of the crank (giving two leading edge vortex systems) and the air dam (which interacts with the main vortex). Finally, the transonic cases feature a complex pattern of shock waves.

The current chapter describes the efforts at the University of Liverpool[1] to contribute to CAWAPI. First, the multiblock flow solver is described. Next, the test cases selected for computation are described. Then the grid generated at NLR (see Chapter 4) is discussed and a wing only grid used for evaluating some details is described. Results are then presented for five flight conditions and finally conclusions are drawn.

6.3   FORMULATION

6.3.1   Flow Solver

The Euler and RANS equations are discretised on curvilinear multi-block body conforming grids using a cell-centred finite volume method which converts the partial differential equations into a set of ordinary differential equations. The convective terms are discretised using Osher's upwind method [6-9]. Monotone Upwind Scheme for Conservation Laws (MUSCL) variable extrapolation (see Van Leer [6-9]) is used to provide second-order accuracy with the Van Albada limiter to prevent spurious oscillations around shock waves. Following Jameson [6-11], the spatial residual is modified by adding a second order discretisation of the real time derivative to obtain a modified steady state problem for the flow solution at the next real time step, which is solved through pseudo time. This pseudo time problem is solved using an unfactored implicit method, based on an approximate linearisation of the residual. The linear system is solved in unfactored form using a Krylov subspace method with Block Incomplete Upper Lower (BILU) preconditioning. The preconditioner is decoupled between blocks to allow a high efficiency on parallel computers with little detriment to the convergence of the linear solver. For the Jacobian matrix of the CFD residual function, approximations are made which reduce the size and improve the conditioning of the linear system without compromising the stability of the time marching.

This formulation is implemented in the flow code Parallel Multiblock (PMB). The equations are solved on block structured grids. A wide variety of unsteady flow problems, including cavity flows, aerospike flows, delta wing aerodynamics, rotorcraft problems and transonic buffet have been studied using this code. More details on the flow solver can be found in Badcock et al [6-12].

---

[1]   and previously when the author was at the University of Glasgow.

The RANS equations are solved and the 2-equation k-ω turbulence model is used for closure. It is well known that most linear 2-equation turbulence models over-predict the eddy viscosity within vortex cores, thus causing too much diffusion of vorticity [6-13]. This weakens the strength of the vortices and can eliminate secondary vortices, especially at low angles of attack where the vortices are already weak. The modification suggested by Brandsma et al [6-6] was therefore applied to the standard model k-ω of Wilcox [6-14] to reduce the eddy-viscosity in vortex cores, by limiting the production of turbulent kinetic energy k, as:

$$P_k = \min\{P_k^u, (2.0 + 2.0 \times \min\{0, r-1\})\rho\beta^* k\omega\}$$

Here P_k^u is the unlimited production of k and r is the ratio of the magnitude of the rate-of-strain and vorticity tensors. When k is over-predicted in the vortex core, it will be limited to a value relative to the dissipation in that region. After comparison with experiment [[6-5],[6-6],[6-15]] this modification was found to improve predictions compared with the standard k-ω turbulence model.

No engine boundary conditions were available in the PMB solver. Initial calculations set the engine face and jet exit planes as far field boundaries. Results for the flow on the wing obtained through this approximation agreed well with other calculations which used a more correct representation of the engine. No effort was therefore made to implement an engine boundary treatment, and all results presented in this paper were obtained using the far field treatment.

The calculations presented in this paper were carried out on PC commodity clusters. The one owned by the CFD Laboratory at Liverpool has 130 DELL PCs with an Intel Pentium 4 3.4 GHz processor, with 1 Gb of memory per node, connected by an HP Procurve 5300XL series using a 100Mb/s Fast Ethernet switch.

6.3.2 Test Case Description

The aircraft geometry is that of the F-16XL-1 as described in reference [6-1]. A tour of some of the features is presented in Figure 6-1. The data for the flight conditions considered in the current paper was collected at stabilized flight conditions for 30 seconds. The claimed accuracy of the quoted flight state is 0.003 for the Mach number, 0.3 degrees for the angle of attack and 0.5 degrees for the angle of sideslip [6-1].
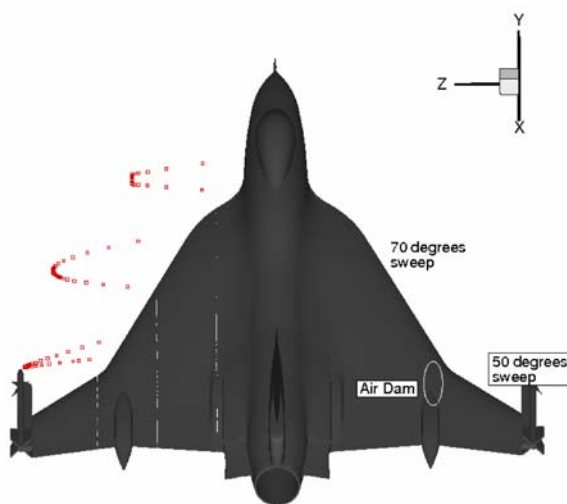
Figure 6-1: Geometry and Leading Edge Details.

Comparison is made with pressure and boundary layer measurements. Electronically scanning pressure transducers were arranged, flush and in streamwise belts. 337 ports were plumbed in the aircraft structure, arranged along Butt lines (BL) and Fuselage stations (FS). Boundary layer measurements were made at four locations using two rakes. Each rake uses 16 pressure measurements (15 total pressure and one static pressure). Each rake is 2 inches long and was oriented based on CFD calculations. The locations of the pressure and rake measurements which are used for comparison are illustrated in Figure 6-2. Note that the BL location is given in inches from the centreline, and the FS is in inches from a reference point just after the nose.
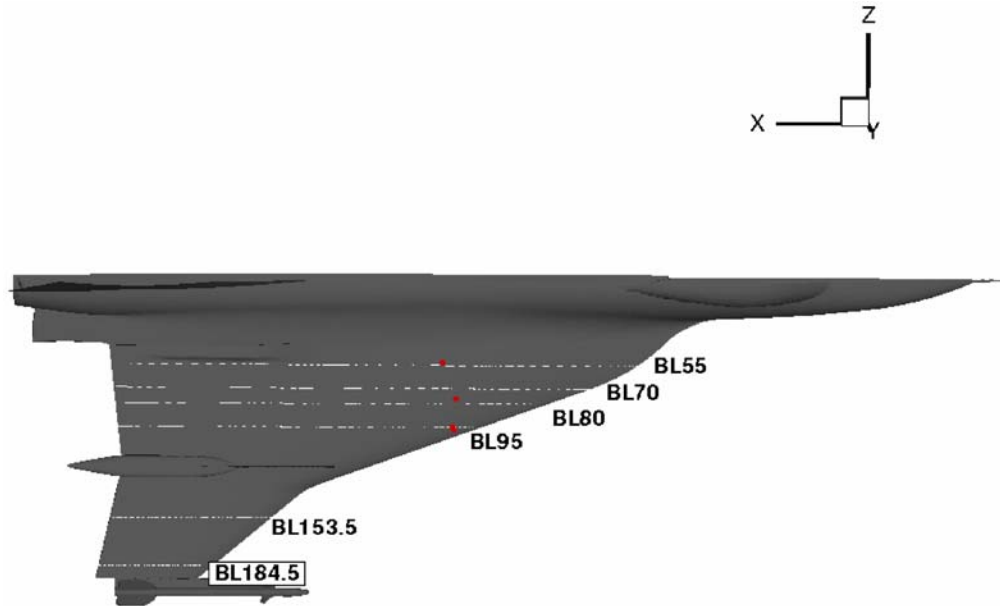
Figure 6-2: Measurement Locations Used for Comparisons.

The reference length used when preparing the CFD grids was 24.7 ft, the reference wing chord. Reynolds' numbers are quoted using this as the length scale. Four flight conditions were chosen as mandatory for the CAWAPI exercise. A further three flight conditions were defined as optional. The four mandatory cases and one of the optional cases have zero sideslip and were calculated as symmetric. The conditions for these cases, which were computed for the current paper, are given in Table 6-1. The two optional cases at sideslip were not computed.

Table 6-1: Summary of Test Cases

Flight Condition	α	M_∞	Re
FC7	11.89	0.304	44.40 million
FC19	11.85	0.360	46.80 million
FC25	19.84	0.250	32.22 million
FC46	10.40	0.527	46.90 million
FC70	4.37	0.970	88.10 million

6.4 GRIDS

6.4.1 Common Grid for Full Geometry

A multiblock grid was generated by NLR [6-8] using their in-house ENFLOW software (see Chapter 4). The original grid has 1903 blocks and over 17 million cells. A major achievement in CAWAPI was the generation of this quality grid within a short time.

For use in PMB two pre-processing steps had to be carried out. First, the original grid, whilst having matched points at block faces, does not have one-to-one matching for the faces themselves, as required by the PMB flow solver. Secondly, the native PMB topology had to be generated. To deal with these two points, the grid file supplied by NLR was initially converted into Plot3D format. This file was then read into ICEMCFD (Version 4.3) mesh editor MED. The mesh editor converted the grid into an unstructured format which could be read into the HEXA mesh generator. The block topology (with one-to-one surface matching) was then reconstructed in HEXA. Finally, the grid (with multiblock topology in an internal format), was loaded back into MED where surface boundary conditions could be marked and then the grid written out in a number of formats. The generic *multiblock-info* format was chosen, because a program already existed to convert to PMB format. The final grid in PMB format has 2610 blocks. A view of the surface grid is shown in Figure 6-3.
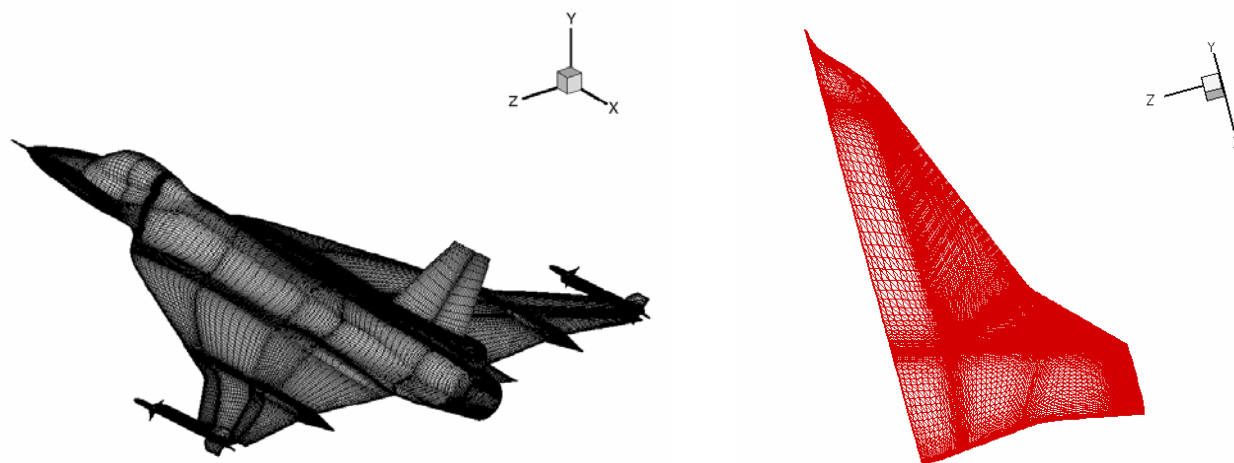
Figure 6-3: View of the Surface Mesh for the Full and Wing Only Configurations.

6.4.2 Wing-Only Grid

To allow testing on a simpler configuration a wing only grid was generated in ICEM HEXA. The surface grid is shown in Figure 6-3. This grid has 3 million points in 72 blocks. There is an O-topology around the wing leading edge, and points are concentrated in the regions where vortices are expected to be present. The wing tip missile launcher and missile, and the air dam were removed. As shown in Figure 6-1 the wing leading edge on the aircraft is formed by a strip towards the apex, is rounded in the centre portion, and then is very sharp outboard of the crank. The wing only grid was made with a sharpened leading edge to allow interpretation from experience with sharp edged delta wings.

6.5   RESULTS FOR FULL CONFIGURATION

6.5.1   Calculation Details

The calculations were made on the Liverpool University CFD Laboratory cluster. FC07 was computed using 48 processors and the other flight conditions using 96. A number of modifications were made to the flow solver prior to the calculations. PMB has a data-structure which is designed to allow general multiblock mesh movement for aeroelastic calculations. This structure extracts the block faces, edges and vertices and computes how these are all connected. The information for the whole grid was previously stored on each processor. For the F-16XL grid, which has a large number of blocks and points, the memory required to store this information, which is not needed since the aircraft is assumed rigid and static, was around 0.5 Gb, comparable with the memory required for storing the grid, solution and Jacobian on each processor. An option was programmed to allow the calculation and storage of this data structure to be skipped if not required.

Secondly, the format of the grid file was altered to allow the grid to be read block by block to speed up the input phase. A utility was written to convert the old PMB grid format into this new one. This utility also computes the block movement data structure as a preprocessing step, although this is not required for the current case. With these minor modifications the flow solver executed first time on the NLR grid.

The main difficulty with the calculations was the small CFL number required to avoid divergence. For difficult cases involving large gradients it is usual to run with a CFL number of 5. However, the current calculations required a CFL number of 1 or 2, leading to a large number of iterations required (10 – 20 thousand). The calculations required around 2 days of processing on 96 CPU's. Check files were used to allow restarting after a specified number of iterations. One reason for the relatively poor performance is the flow behind the rocket, which appeared to be unsteady.

In each case, as is standard practice with the PMB solver, a small number of explicit steps were calculated to smooth the solution from the starting freestream conditions. For the transonic FC70, a number of implicit steps were calculated using the first order spatial scheme. After the initialisation, the full second order spatial discretisation was switched on.

6.5.2   Vortical Flow Cases

The flight conditions 7,19,25 and 46 all feature vortical flow and will be considered together in this section. The surface pressure coefficients are shown in Figure 6-4. They each show the suction from the leading edge vortices inboard and outboard of the crank. This suction is significantly higher for FC25 due to the larger angle of incidence. In addition there is an interaction of the inboard leading edge vortex with the air dam, which is most clearly seen for FC25.

FC7

FC19

FC46

FC25
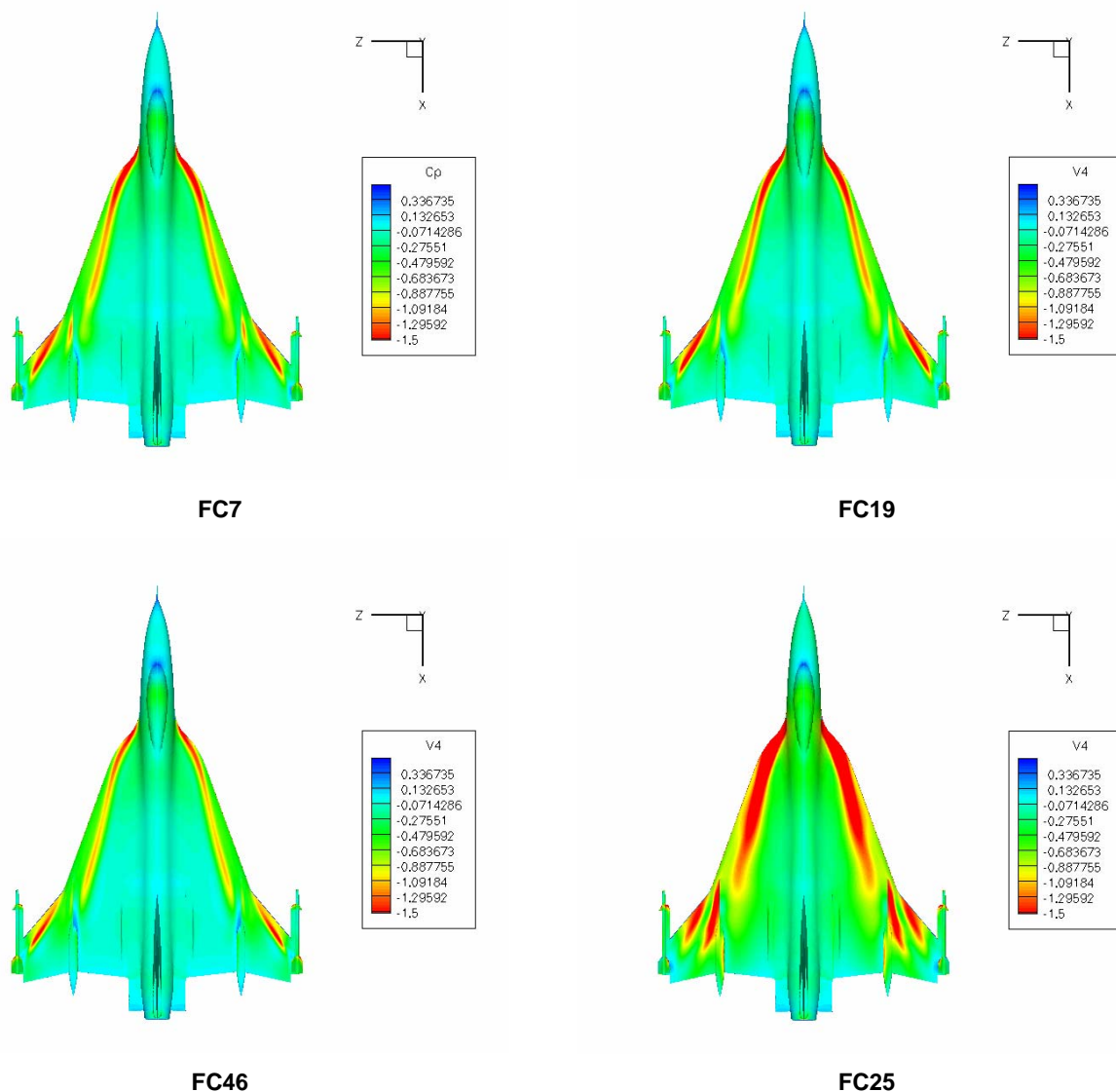
Figure 6-4: Surface Pressure Coefficients.

The comparison of the pressure coefficient with the flight measurements for 6 BL's is shown in Figure 6-5, Figure 6-6 and Figure 6-7. For FC07 the inboard vortex suction is underpredicted close to the fuselage and is then well predicted as the stations move outboard. Initially the secondary separation (indicated by the flat plateau in the distribution near the leading edge, is absent in the computations, but by BL 95 is present. The strength of the outboard leading edge vortex is significantly under-predicted (BL 153.5). For FC 25 the story is similar. FC46, which is at a similar incidence but a higher Mach number, shows different behaviour. The inboard leading edge vortex strength is lower in the computations than for the measurements. Again for inboard stations the secondary separation is absent. The outboard leading edge vortex suction is more in agreement, but the peak is more downstream in the computation.

BL 55

BL 70

BL 80
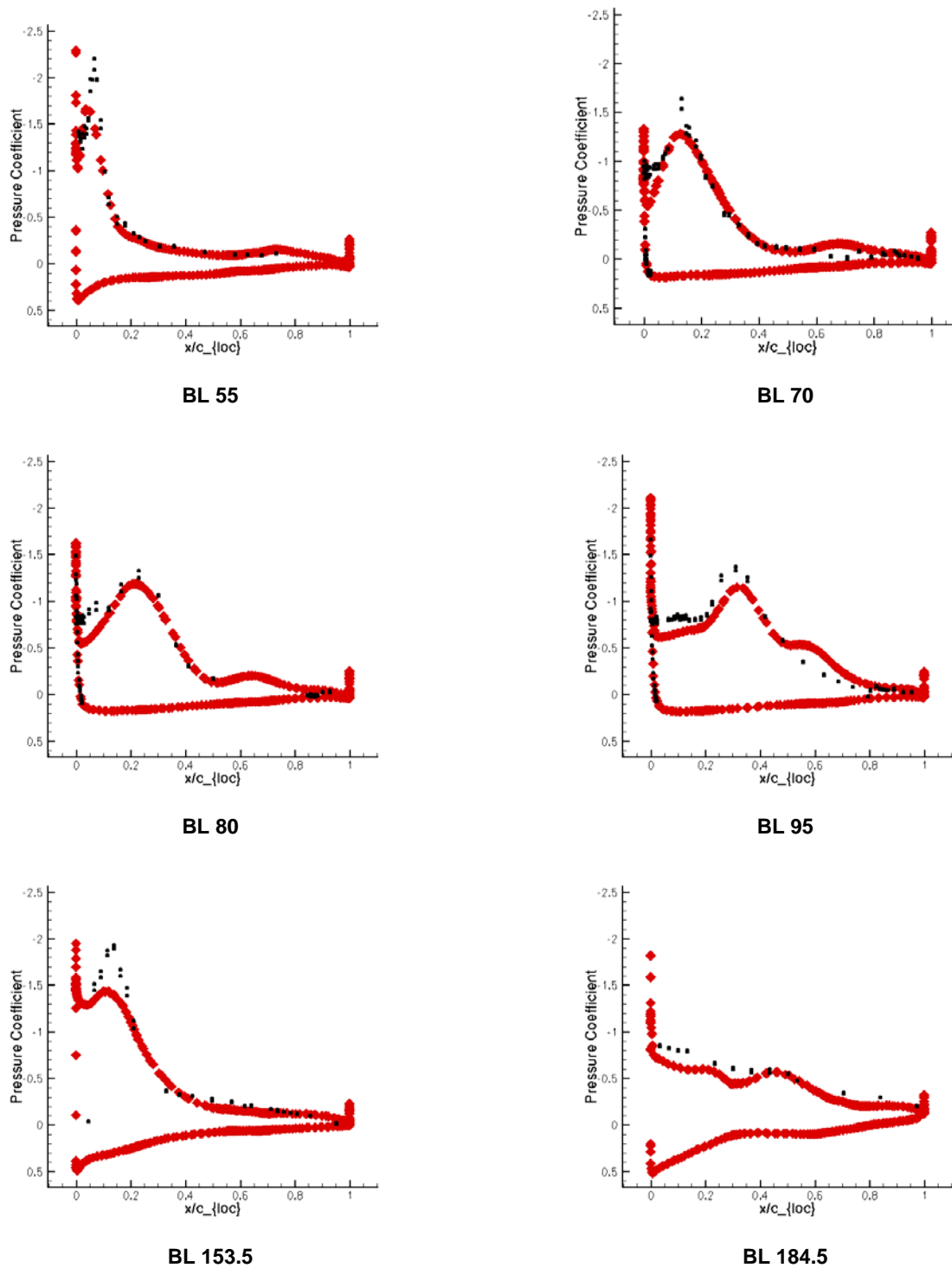
BL 95

BL 153.5

BL 184.5

Figure 6-5: Comparison of Computations (red) with Flight Measurements (black) for FC07. The experimental data is from Flt 144, Run 9b, α = 13.5°, M∞ = 0.37, Re = 40.06 million.
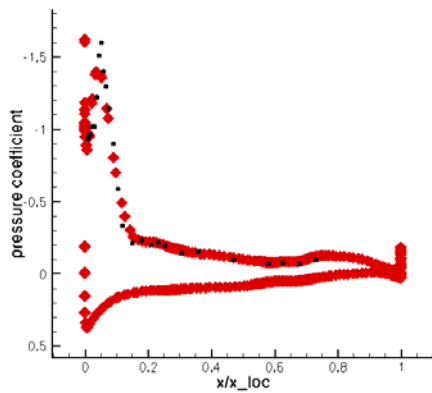
BL 55
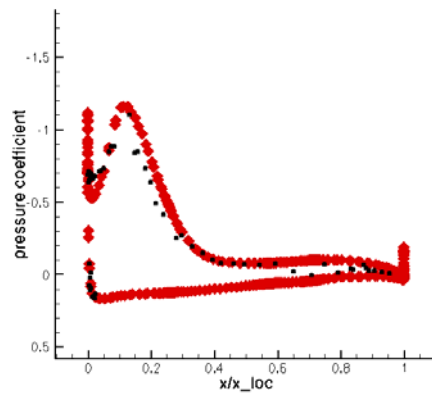
BL 70
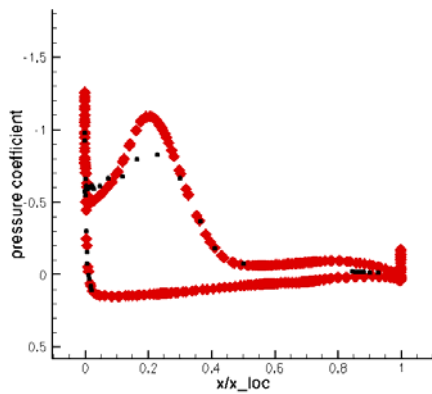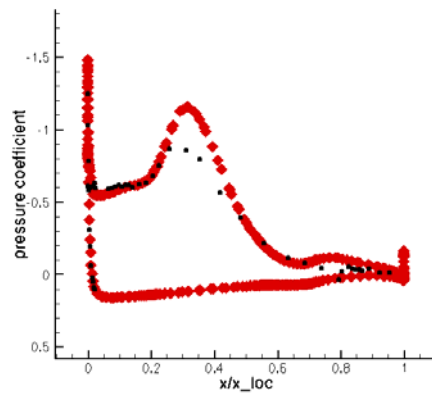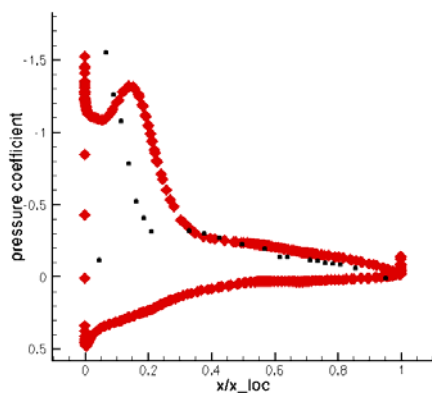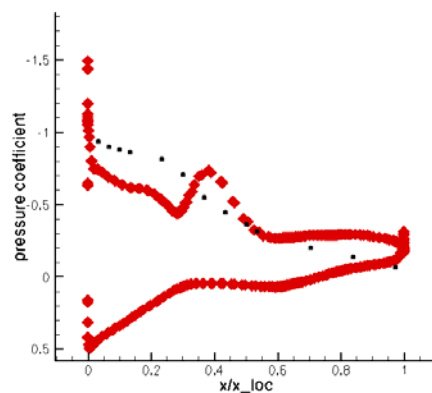
BL 80

BL 95

BL 153.5

BL 184.5

**Figure 6-6: Comparison of Computations (red) with Flight Measurements (black) for FC46.
The experimental data is from Flt 144, Run 3b, α = 10.0°, M∞ = 0.51, Re = 43.7 million.**
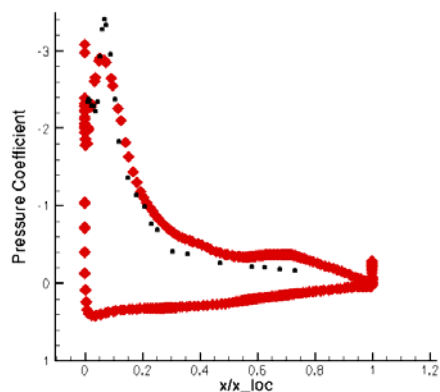
BL 55
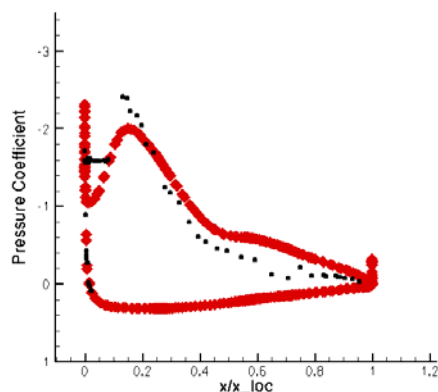
BL 70
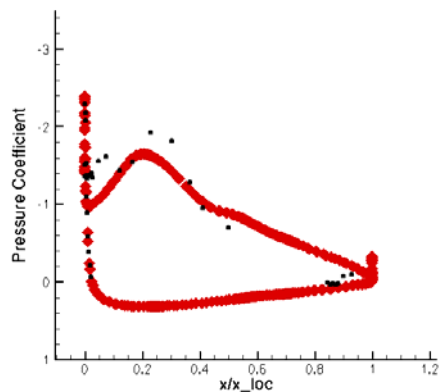
BL 80
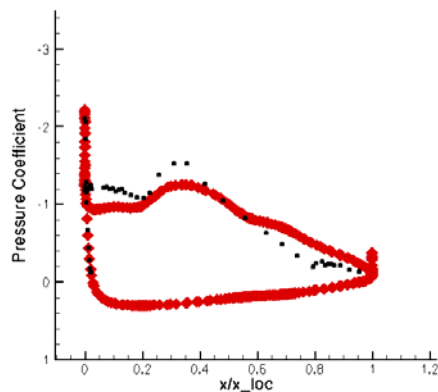
BL 95
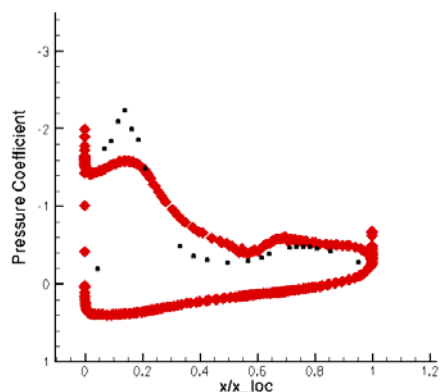
BL 153.5
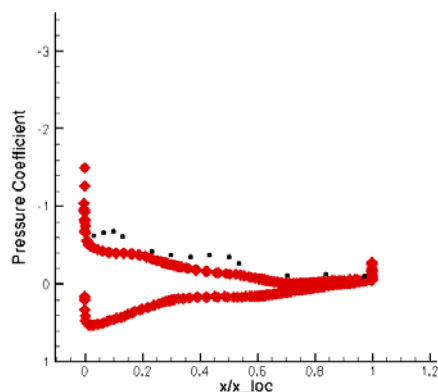
BL 184.5

Figure 6-7: Comparison of Computations (red) with Flight Measurements (black) for FC25.
The experimental data is from Flt 144, Run 16b, α = 20°, M∞ = 0.24, Re = 31 million.

Finally, the boundary layer comparison is shown for FC7 in Figure 6-8. The agreement is generally good, with the computed boundary layers being slightly more turbulent.
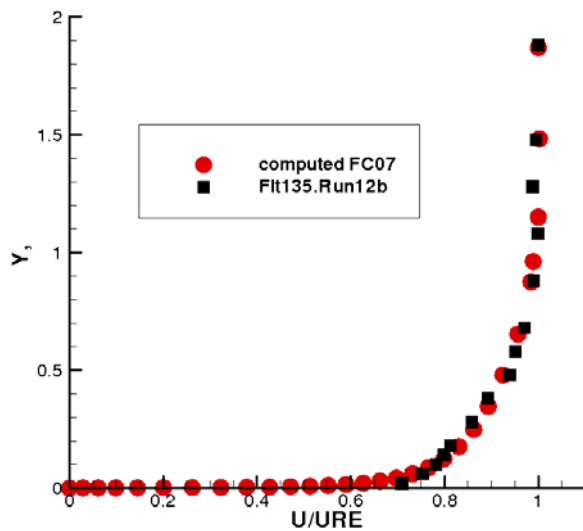
Rake 3 (302.17,52.93)
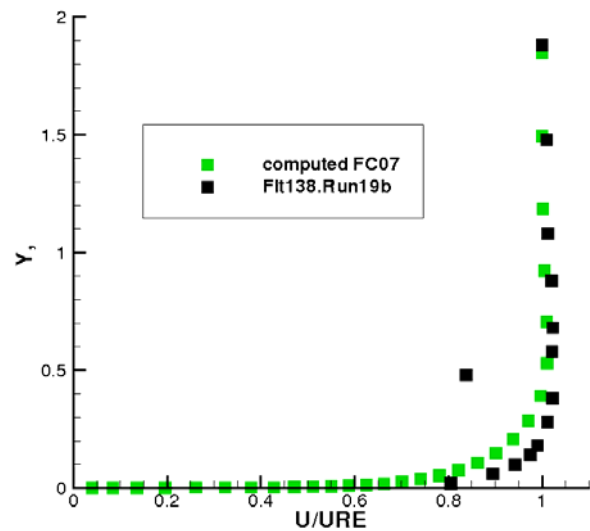
Rake 4 (293.45,76.22)
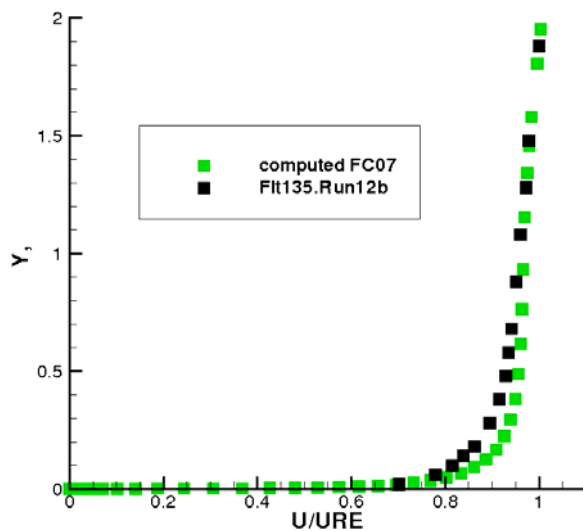
Rake 7 (295.52,94.33)
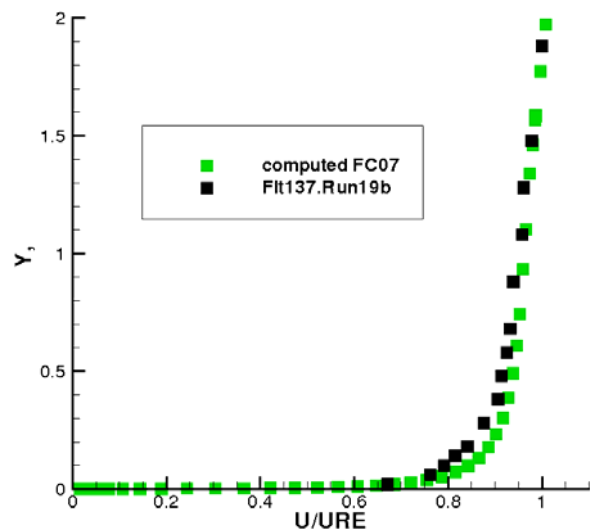
Rake 5 (294.59,96.06)

**Figure 6-8: Comparison of Boundary Layer Profiles with Flight Measurements (black)
for FC07. The experimental data is from Flight 135, Run 12b and 19b.**

6.5.3   Transonic Case

The surface pressure coefficient for FC70 is shown in Figure 6-9. A shock wave is located at about 30% of the chord and bends slightly downstream approaching the leading edge. A second shock on the wing is apparent just before the trailing edge.
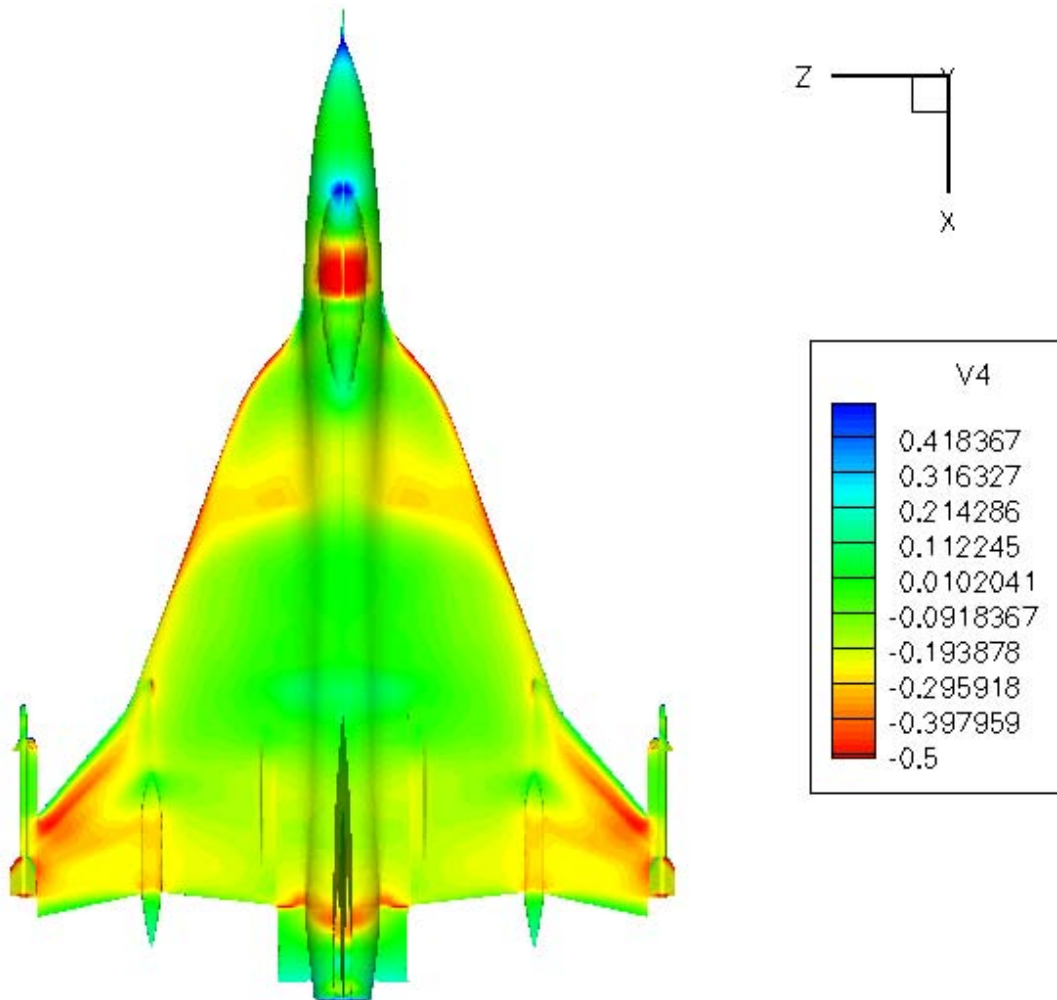
Figure 6-9: Surface C$_p$ for FC70.

The comparison with the measurements is shown in Figure 6-10. It should be noted that there was some doubt about the setting for the leading edge flap outboard of the crank, which could have been deflected up by as much as 9 degrees. There is also considerable scatter in the measurements at some BL stations. The agreement between the measured and computed profiles is close at BL55, where the shock location and strength are in agreement. However, moving to BL70, the computed shock is early compared with the measured one and the agreement after this is poor. This is particularly the case outboard of the crank. These discrepancies are consistent with other computed results in the exercise.

BL 55

BL 70

BL 80

BL 95

BL 153.5

BL 184.5
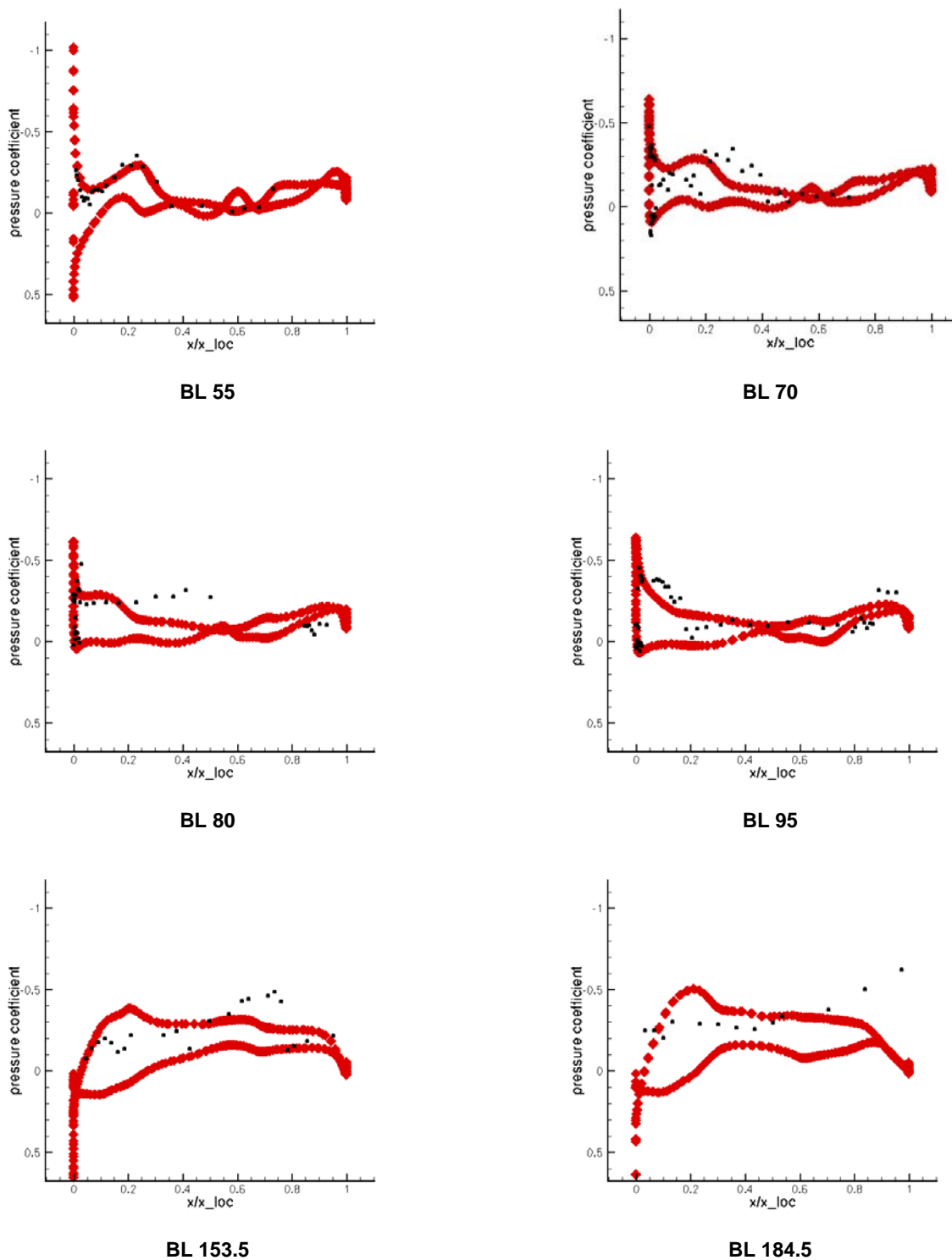
Figure 6-10: Comparison of Computations (red) with Flight Measurements (black) for FC70.

6.6   EVALUATION

The comparisons presented above raise several questions. These are considered in the present section.

Wing only results using several turbulence models for FC07 were obtained. The k-ω, k-ω with rotation correction and a nonlinear version of the k-ω model were used. A similar structure is seen for the location of vortices, but the suction peaks are a little lower than in the full configuration. This is possibly due to the better resolution of the secondary separation for the wing only grid, which shifts the primary vortex higher above the wing. The lower suction peaks are shown in Figure 6-11 where the distributions along the BL's are compared with measurements. The resolution of the secondary separation, particularly at BL70 is indicated by the plateau close to the leading edge. The lack of suction under the vortex outboard of the crank is also clear (BL 153.5), as in the full configuration.

The turbulent Reynolds number distributions (i.e. the eddy viscosity divided by the molecular viscosity) are shown for a spanwise cut before and after the crank for the full configuration and wing grids. The general form of these plots is expected to show low levels of turbulence in the vortices themselves, where turbulence production is suppressed by the limiter. High levels are expected where there is large shear. First, the lack of a secondary separation ahead of the crank is show in Figure 6-12 (a) and it is clear that the grid is coarse in the important region. The wing only grid does resolve a secondary separation (the small blue dot to the left of the primary vortex) and the grid resolution is higher in this region.

When evaluating the primary vortex suction against the measurements, it should be remembered that the calculations and measurements were obtained at different angles of attack. By looking at measurements at different angles, and taking FC07 as an example, this could account for a drop in pressure coefficient of around 0.3. The primary inboard leading edge vortex is considered to be well predicted.

More fundamentally, a deficiency in the full configuration prediction of the outboard primary vortex was highlighted above. The wing only configuration gives an opportunity to evaluate this further since it does not include the air dam which complicates the flow structure in the region of the crank. The structure of the flow for the full configuration is shown in Figure 6-12 (c) where the interaction of the primary inboard vortex with the air dam is apparent. The production limiter leads to a separated region of laminar flow outboard of the air dam. The outboard primary vortex by contrast has very high levels of turbulence in its core, reducing its strength (and hence the suction). The wing only solution shown in Figure 6-12 (d) also shows high levels of turbulence in the outboard primary vortex. There is no air dam vortex present in this case.

The vorticity correction has been successful in predicting leading edge vortices on delta wings. The origins of this success are illustrated in Figure 6-12 (a) where the vortex cores are made laminar by the suppression of the production term in the k-ω model. Note that the maximum level of the turbulent Reynolds number is around 300 in this plot. However, looking to the case where the inboard and outboard primary vortices are present the turbulence levels are an order of magnitude higher. The reason for this is possibly the shear between the two vortices which will generate turbulence. Some of this is convected into the outboard vortex. A second possibility for the poor prediction of the outboard vortex is that the system of multiple vortices might be expected to be unsteady [6-16].
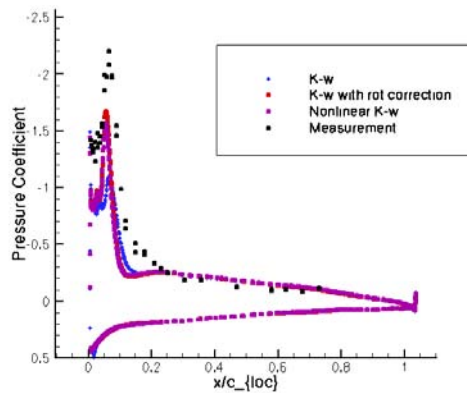
BL 55
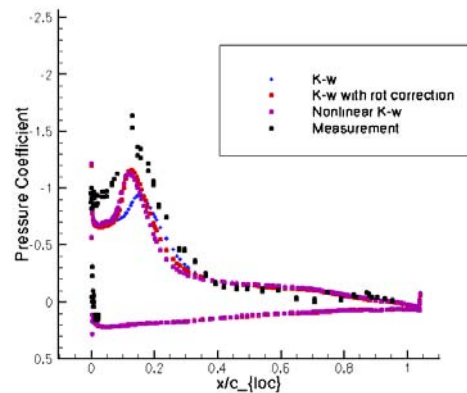
BL 70
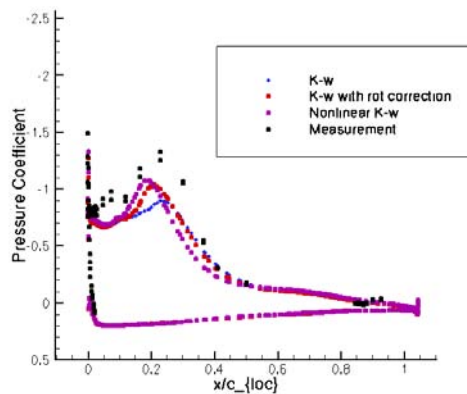
BL 80
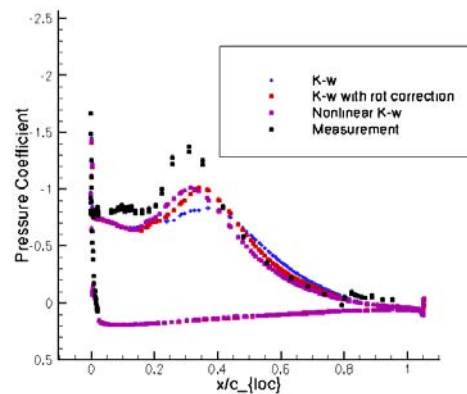
BL 95
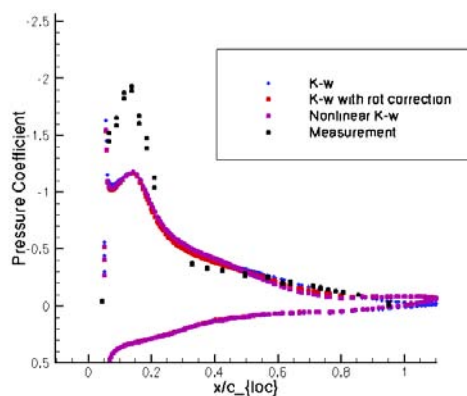
BL 153.5
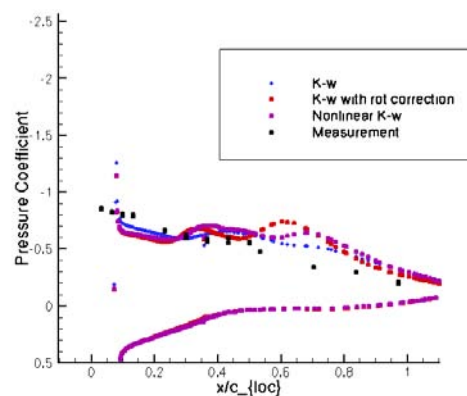
BL 184.5

Figure 6-11: Comparison of Computations (red) with Flight Measurements (black) for FC07.
The experimental data is from Flt 144, Run 9b, α = 13.5°, M∞ = 0.37, Re = 40.06 million.
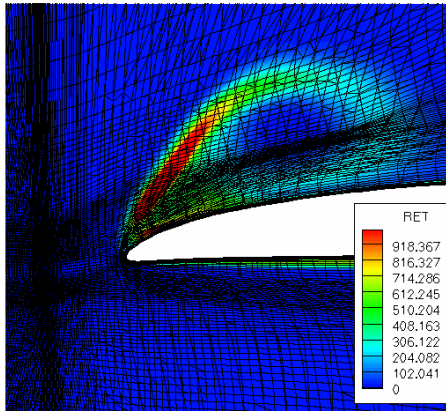
(a) Full – Pre-Crank
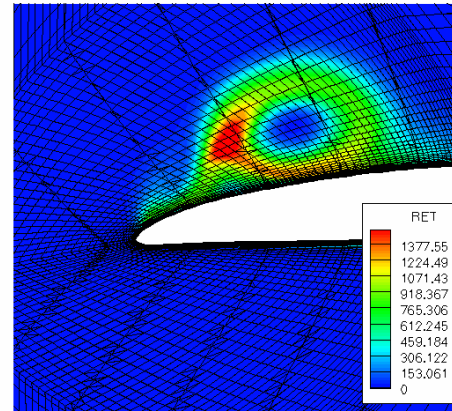
(b) Wing – Pre-Crank
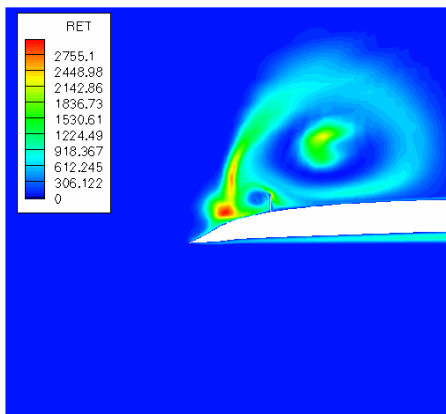
(c) Full – After-Crank
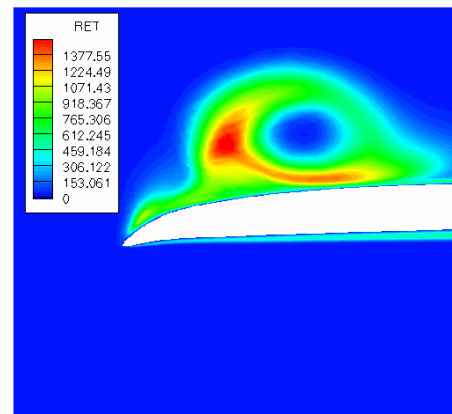
(d) Wing –- After-Crank

Figure 6-12: Evaluation of Full and Wing Solutions for FC07.

6.7 CONCLUSIONS

The predictions of a multiblock code have been compared with flight measurements for the F-16XL aircraft. Turbulence modelling with a rotation correction have been used and generally good agreement was obtained with the measurements.

The convergence of the implicit flow solver was not as good as expected, based on previous performance. This is the subject of further investigation.

For the vortical flow cases, the prediction of the primary vortex before the crank was generally good. However, after the crank the vortex was significantly under-predicted in strength. A possible explanation for

this is the high shear generated between the two primary vortices, and the subsequent behavior of the turbulence models in this region. This requires more careful investigation on a simpler generic configuration, ideally with field data.

The transonic case showed good agreement with measurements for the shock location on the inboard part of the wing. However, this agreement soon disappeared. Note that the computations in CAWAPI were in close agreement. Outboard of the crank the comparison is polluted by doubt over the leading edge flap setting.

6.8   ACKNOWLEDGEMENTS

6.9   REFERENCES

[6-1]   Hillaker, H.J.: *F-16XL Flight Test Program Overview*, AIAA-83-2730, November, 1983.

[6-2]   Talty, P.K. and Caughlin, D.J.: *F-16XL Demonstrates New Capabilities in Flight Test at Edwards Air Force Base*, Journal of Aircraft, 25(3), 206-215, 1988.

[6-3]   Lamar, J.E., Obara, C.J., Fisher, B.D. and Fisher, D.E.: *Flight, Wind-Tunnel, and Computational Fluid Dynamics Comparison for Cranked Arrow Wing (F-16XL-1) at Subsonic and Transonic Speeds*, NASA/TP-2001-210629, 2001.

[6-4]   Anders, S.G. and Fischer, M.C.: *F-16XL-2 Supersonic Laminar Flow Control Flight Test Experiment*, NASA/TP-1999-209683, 1999.

[6-5]   Soemarwoto, B., Boelens, O.J., Fritz, W., Allan, M., Ceresola, N. and Bütefisch, K.: *Towards the Simulation of Unsteady Maneuvers Dominated by Vortical Flow*, AIAA Paper 2003-3528, 2003.

[6-6]   Brandsma, F.J., Kok, J.C., Dol, H.S. and Elsenaar, A.: *Leading Edge Vortex Flow Computations and Comparison with DNW-HST Wind Tunnel Data*, RTO/AVT Vortex Flow Symposium, Loen, Norway, 2001.

[6-7]   Mitchell, A.M., Morton, S.A., Forsythe, J.R. and Cummings, R.M.: *Analysis of Delta-Wing Vortical Substructures using Detached-Eddy Simulation*, AIAA Journal, 44(5), pp 964-972, 2006.

[6-8]   Boelens, O.J., Spekreijse, S.P., Sytsma, H.A. and de Cock, K.M.J.: *Comparison of Measured and Simulated Flow Features for the Full Scale F-16XL Aircraft*, AIAA Paper 2007-0489, 45th Aerospace Sciences Meeting and Exhibit, Reno, NV, January 8-11, 2007.

[6-9]   Osher, S. and Chakravarthy, S.: *Upwind Schemes and Boundary Conditions with Applications to Euler Equations in General Geometries*, Journal of Computational Physics, Vol. 50, pp. 447-481, 1983.

[6-10]   Van Leer, B.: *Towards the Ultimate Conservative Difference Scheme II: Monotonicity and Conservation Combined in a Second Order Scheme*, Journal Computational Physics, Vol. 14, 361-374, 1974.

[6-11]   Jameson, A.: *Time Dependent Calculations using Multigrid, with Applications to Unsteady Flows Past Airfoils and Wings*, AIAA Paper 91-1596, 1991.

[6-12]   Badcock, K.J., Richards, B.E. and Woodgate, M.A.: *Elements of Computational Fluid Dynamics on Block Structured Grids using Implicit Solvers*, Progress in Aerospace Sciences, Vol. 36, 2000, pp. 351-392.

[6-13]   Gordnier, R.E.: *Computational Study of a Turbulent Delta-Wing Flowfield Using Two-Equation Turbulence Models*, AIAA 96-2076, 1996.

[6-14]   Wilcox, D.C.: *Turbulence Modelling for CFD*, DCW Industries, Inc., La Canada, California, 1993.

[6-15]   Allan, M.: *A CFD Investigation of Wind Tunnel Interference on Delta Wing Aerodynamics*, Ph.D. Thesis, University of Glasgow, Glasgow, UK, October 2002.

[6-16]   Morton, S.A., McDaniels, D.R. and Cummings, R.: *F-16XL Unsteady Simulations for the CAWAPI Facet of RTO Task Group AVT-113*, AIAA Paper 2007-0493, 45th Aerospace Sciences Meeting and Exhibit, Reno, NV, January 8-11, 2007.

Chapter 7 – NUMERICAL SOLUTIONS FOR THE CAWAPI CONFIGURATION ON STRUCTURED GRIDS AT NASA LaRC, UNITED STATES

by

Alaa A. Elmiligui, Khaled S. Abdol-Hamid and Steven J. Massey

7.1 SUMMARY

In this chapter numerical simulations of the flow around F-16XL are performed as a contribution to the Cranked Arrow Wing Aerodynamic Project International (CAWAPI) using the PAB3D CFD code. Two turbulence models are used in the calculations: a standard k-ε model, and the Shih-Zhu-Lumley (SZL) algebraic stress model. Seven flight conditions are simulated for the flow around the F-16XL where the free stream Mach number varies from 0.242 to 0.97. The range of angles of attack varies from 0° to 20°. Computational results, surface static pressure, boundary layer velocity profiles, and skin friction are presented and compared with flight data. Numerical results are generally in good agreement with flight data, considering that only one grid resolution is utilized for the different flight conditions simulated in this study. The Algebraic Stress Model (ASM) results are closer to the flight data than the k-ε model results. The ASM predicted a stronger primary vortex, however, the origin of the vortex and footprint is approximately the same as in the k-ε predictions.

7.2 INTRODUCTION

The CAWAPI utilized the F-16XL aircraft as part of a basic research project planned in support of the High Speed Research Program (HSRP). Review of the project and how it evolved over the years is given by Lamar & Obara [7-1]. Flight, wind-tunnel and computational studies were conducted, and various data sets were generated, analyzed, and compared [7-2], [7-3]. The Virtual Laboratory (VL) environment and common data standards to store the data were established. The Virtual Laboratory was housed in an electronically secure area; details about VL have been documented in References [7-4] and [7-5].

CAWAPI objectives were to validate new methodologies and to evaluate a number of predictive methods against available flight test data at high Reynolds numbers, and to check the Technology Readiness Level of Computational Fluid Dynamics (CFD) codes for a military aircraft. Military requirements result in a need for a better understanding of the aircraft characteristics before full-scale production. For this purpose, new and existing CFD codes have to be validated, and their Technology Readiness Level checked and/or increased. To meet these objectives, several numerical studies [7-6] to [7-14] have been conducted to compute and compare predicted flow around the F-16XL with flight data. CAWAPI members embraced the idea of engaging in a cooperative venture. The benefits from validated CFD codes are enhanced analysis of system performance prior to flight, as well as tools to aid in the understanding of unexpected flight behavior.

In the present chapter, PAB3D CFD code is used in conjunction with two-equation k-ε turbulence closure and nonlinear algebraic Reynolds stress models to simulate flow around F-16XL. PAB3D is a structured, multiblock, parallel, implicit, finite-volume solver of the three-dimensional Unsteady Reynolds Averaged Navier-Stokes (URANS) equations; advanced turbulence models are available in the code. PAB3D is widely used for internal and external flow applications by NASA and by the US aerospace industry. PAB3D has several built-in timesaving routines including grid sequencing and customized computer memory requirements that permit the

user to quickly obtain a converged solution. There are several state-of-the-art two-equation and algebraic Reynolds stress turbulence models implemented in the PAB3D code. PAB3D has been well-tested and documented for the simulation of aero-propulsive and aerodynamic flows involving separation, mixing, and other complicated phenomena [7-18]. PAB3D is ported to a number of platforms and offers a combination of good performance and low memory requirements. In addition to its advanced pre-processor, which can handle complex geometries through multi-block general patching, PAB3D has a runtime module capable of calculating aerodynamic performance on the fly as well as a post processor [7-19] used for follow-on data analysis.

This chapter describes and analyzes a series of CFD test cases performed as a contribution to the CAWAPI project. The organization of this chapter is as follows:

1) The description of PAB3D features (Section 7.3);

2) The governing equations and the turbulence models used in this study (Sections 7.4 and 7.5);

3) A brief description of the F-16XL geometry and the computational grid (Section 7.6);

4) Presentation of the numerical results along with discussion and comparison to flight data (Section 7.7); and

5) The concluding remarks (Section 7.8).

7.3 COMPUTATIONAL FLUID DYNAMICS SIMULATION

In this study, PAB3D is used in conjunction with two-equation k-ε turbulence closure and nonlinear algebraic Reynolds stress models to simulate flow around F-16XL. PAB3D solves the simplified Reynolds-averaged Navier-Stokes equations in conservative form. Viscous models include coupled and uncoupled simplified Navier-Stokes and thin layer Navier-Stokes options. Roe's upwind scheme is used to evaluate the explicit part of the governing equations, and van Leer's scheme is used for the implicit part. Diffusion terms are centrally differenced, inviscid terms are upwind differenced, and two finite volume flux-splitting schemes are used to construct the convective flux terms. PAB3D is third-order upwind biased accurate in space, and second-order accurate in time.

7.4 GOVERNING EQUATIONS

The governing equations solved in this study are the time-averaged Reynolds Averaged Navier-Stokes (RANS). The perfect gas law is chosen to represent the air properties.

$$
\frac{\partial \rho}{\partial t} + \frac{\partial \rho u_i}{\partial x_i} = 0
$$

$$
\frac{\partial \rho u_i}{\partial t} + \frac{\partial (\rho u_i u_j + p \delta_{ij})}{\partial x_j} = \frac{\partial (\tau_{ij} - \overline{\rho u_i u_j})}{\partial x_j}
\tag{1}
$$

$$
\frac{\partial \rho e_0}{\partial t} + \frac{\partial (\rho e_0 u_i + p u_i)}{\partial x_i} = \frac{\partial (\tau_{ij} u_j - \overline{\rho u_i u_j} u_j)}{\partial x_i} - \frac{\partial (q_i + C_P \rho \overline{u_i \theta})}{\partial x_i} + \frac{\partial}{\partial x_i} \left[\left(\mu_l + \frac{\mu_t}{\overline{\sigma}_k} \right) \frac{\partial k}{\partial x_i} \right]
$$

7.5   RANS CLOSURE

Two turbulence models are used in the current study to model turbulence: a standard k-ε model, and Shih-Zhu-Lumley (SZL) algebraic stress model [7-20].

7.5.1   Two Equation k-ε Model

To close the RANS equations, the two-equation (k-ε) turbulence model is given by:

$$\frac{\partial \rho k}{\partial t} + \frac{\partial \rho u_j k}{\partial x_j} = -\rho \overline{u_j u_i} \frac{\partial u_i}{\partial x_j} + \frac{\partial}{\partial x_j}\left[\rho\left(v_l + \frac{c_\mu k^2}{\overline{\sigma}_k \varepsilon}\right)\frac{\partial k}{\partial x_j}\right] - \rho \varepsilon$$

$$\frac{\partial \rho \varepsilon}{\partial t} + \frac{\partial \rho u_j \varepsilon}{\partial x_j} = -C_{\varepsilon 1}\rho \overline{u_j u_i}\frac{\partial u_i}{\partial x_j}\frac{\varepsilon}{k} + \frac{\partial}{\partial x_j}\left[\rho\left(v_l + \frac{c_\mu k^2}{\overline{\sigma}_\varepsilon \varepsilon}\right)\frac{\partial \varepsilon}{\partial x_j}\right] - f_2 \tilde{C}_{\varepsilon 2}\rho \frac{\varepsilon}{k}\left[\varepsilon - v_l \left(\frac{\partial \sqrt{k}}{\partial x_j}\right)^2\right] \qquad (2)$$

$$C_\mu = 0.09, C_{\varepsilon 1} = 1.44$$
$$\overline{\sigma}_k = \sigma_k = 1.4, \overline{\sigma}_\varepsilon = \sigma_\varepsilon = 1 \; and \; \overline{C_{\varepsilon 2}} = C_{\varepsilon 2} = 1.92$$

The turbulent stress components are formulated as:

$$-\rho\overline{u_i u_j} = \tau_{ij}^L + \tau_{ij}^{NL} \qquad (3)$$

The linear contribution to the stress is

$$\tau_{ij}^L = -2\rho v_t S_{ij} + \frac{2}{3}\delta_{ij}\,\rho k \qquad (4)$$

where, $S_{ij} = \frac{1}{2}\left[\frac{\partial u_i}{\partial x_j} + \frac{\partial u_j}{\partial x_i}\right] - \frac{1}{3}\delta_{ij}\frac{\partial u_k}{\partial x_k}$ $\qquad (5)$

For the purpose of this paper, RANS turbulent viscosity is defined as

$$v_t^{RANS} = f_\mu C_\mu \frac{k^2}{\varepsilon} \qquad (6)$$

In the case of a linear RANS simulation

$$v_t = v_t^{RANS} and C_\mu = 0.09$$

7.5.2 Algebraic Reynolds Stress

C_μ is 0.09 for the linear model and is a function of vorticity and strain tensors for the nonlinear models and

is equal to: $C_\mu^* = \dfrac{1}{\left(6.5 + A_s^* \dfrac{U^* k}{\varepsilon}\right)}$ where

$$A_s^* = \sqrt{6}\cos(\phi)$$

$$\phi = \frac{1}{3}\cos^{-1}(\sqrt{6}W^*)$$

$$W^* = S_{ij}^* S_{jk}^* S_{ki}^* / (S^*)^3$$

$$U^* = \sqrt{S_{ij}^* S_{ij}^* + \Omega_{ij}^* \Omega_{ij}^*}$$

$$S^* = \sqrt{S_{ij}^* S_{ij}^*}$$

$$S_{ij}^* = S_{ij} - \frac{1}{3} S_{kk} \delta_{ij}$$

$$\Omega^* = \sqrt{\Omega_{ij}^* \Omega_{ij}^*}$$

$$\Omega_{ij}^* = \Omega_{ij} = \frac{1}{2}\left(\frac{\partial u_i}{\partial x_j} - \frac{\partial u_j}{\partial x_i}\right) = -\Omega_{ij}$$

In the SZL nonlinear model [7-20], the turbulent stresses are given by:

$$-\overline{u_i u_j} = 2\nu_t S_{ij} - \frac{2}{3}\delta_{ij} k - 2\beta \frac{k^3}{\varepsilon^2}(W_{ik} S_{kj} - S_{ik} W_{kj})$$

where $\quad \beta = \dfrac{\sqrt{1 - 9C_\mu^2\left(\dfrac{S^* k}{\varepsilon}\right)^2}}{\left(1 + 6\dfrac{S^* k}{\varepsilon}\dfrac{\Omega^* k}{\varepsilon}\right)}$ (7)

Algebraic stress models give inherently better results than the linear stress model because of the explicit modeling of effects such as relaxation and the specific inclusion of nonlinear anisotropic effects from the mean flow strain and vortices. A compilation of the parameters used in the turbulence models can be found in Reference [7-21].

7.6 COMPUTATIONAL DOMAIN AND BOUNDARY CONDITIONS

The F-16XL airplane is a single-place fighter-type prototype aircraft developed by the General Dynamics Corporation, Fort Worth Division (now Lockheed Martin Aeronautics Company – Fort Worth). The design of the cranked-arrow wing was a cooperative effort of the NASA Langley Research Center and the General Dynamics Corporation. Figure 7-1 shows a picture of the F-16XL airplane in flight. The technical specifications for the airplane are given in Table 7-1.

**Figure 7-1: Missiles, Tufts, Modified Flow-Visualization Paint Scheme, and Video
Targets on Airplane at Dryden Flight Research Center (AIAA Paper 2007-0487).**

Table 7-1: Airplane Specifications (from Lamar & Obara [7-1])

Feature	Value
Wing Span	32.4 ft
Height	17.606 ft
Length	54.155 ft
Reference Chord	24.7 ft
Theoretical Root Chord	41.75 ft
Wing Area	646.37 ft^2
Reference Wing Area	600 ft^2
Reference Aspect Ratio	1.75
Typical Takeoff Weight	35,000 lbs
Engine; Max Thrust	Pratt & Whitney F100-PW-200; 23,830 lbs

Description of the F-16XL geometry and computational grids used in CAWAPI are given in Reference [7-15]. The computational grid used in this study consisted of 14.7 million cells and 200 blocks, and is shown in Figure 7-2. The original grid reported in [7-15] had almost 1903 blocks that were subsequently combined and reduced to 216; this number of blocks were further merged to 200 blocks to enhance efficiency during parallel computations. The angles of side-slip β for FC7, FC19, FC 25, FC 46, & FC 70 were all less than 1, and hence one half of the aircraft was simulated with plane of symmetry boundary condition imposed at the symmetry plane. A no-slip boundary condition was applied to all solid surfaces, and a Riemann invariant characteristic type boundary condition was applied to far field boundaries. Constant total values were specified for the nozzle inlet, and constant pressure boundary condition was specified at the nozzle exit. For FC 50 and FC 51 the side-slip angle, β, is approximately 5° and the flow around the full aircraft was simulated. The computational grid consisted of 400 blocks and 29.5 million cells and was generated by mirroring the modified grid around the symmetry plane. On average, the grid first cell height was approximately $y^+<1.2$. The far field boundaries extend six root chords to far field.
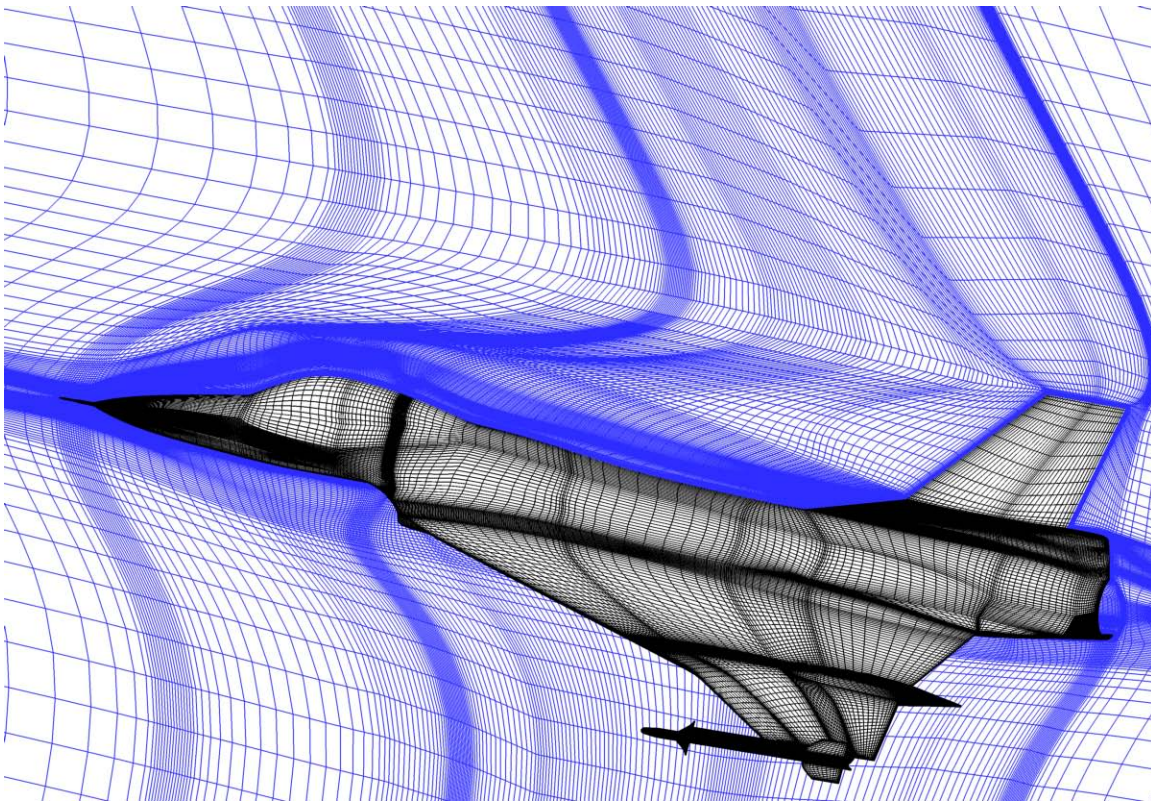
Figure 7-2: Computational Grid on Wing-Fuselage.

7.7   COMPUTATIONAL RESULTS

The flow field was computed using PAB3D [7-16] for seven flight conditions that were published in [7-17]. Two turbulence models were used to model turbulence: the standard k-ε model, and the SZL algebraic stress model (ASM). Table 7-2 and Table 7-3 list the seven flight conditions modeled in this study.

Table 7-2: Seven Flight Conditions (from Lamar & Obara [7-1])

Flight Condition	Actual Mach No.	Actual α	Actual β	Actual Reynolds No.
FC7	0.304	11.89	-0.133	44.4E+06
FC19	0.36	11.85	+0.612	46.8E+06
FC46	0.527	10.4	+0.684	46.9E+06
FC70	0.97	4.37	+0.310	88.77E+06
FC25	0.242	19.84	0.725	32.22E+06
FC50	0.434	13.56	+5.31	39.41E+06
FC51	0.441	12.89	-4.58	38.95E+06

Table 7-3: Associated Engine Parameters* for these Flight Conditions (from Lamar & Obara [7-1])

Flight Condition	Free Stream Altitude, ft.	Free Stream Mach	Inlet Duct Exit Static Temp., degs. R	Inlet Duct Exit Static Press., psia	Inlet Duct Exit Velocity, ft/sec.	Inlet Duct Exit Mach	Mixing Plane Total Temp., degs. R	Mixing Plane Total Press., psia
FC7	5000	0.304	498	11	379.6	0.347	1050	23
FC19	10000	0.36	485.8	10.2	345.8	0.32	1050	21.5
FC46	24000	0.527	443.6	5.85	404.3	0.39	1045	14.8
FC70	22300	0.97	519	10.65	464.7	0.416	1200	30
FC25	10000	0.242	470.1	8.72	474.8	0.447	1209	26.3
FC50	24000	0.434	440	5.16	483.3	0.47	1154	16.95
FC51	24000	0.441	431.8	5.19	468.6	0.46	1146	16.74

*The numbers in this table do not represent any particular engine.

Grid sequencing was used to accelerate convergence by solving 1/4 then 1/2 of the grid in each of the three computational directions. To insure convergence, all the simulations performed in this study ran 5,000 iterations at each of the coarse grid levels and 10,000 iterations on the fine grid level. Figure 7-3 shows convergence history of FC 7 using both turbulence models. All simulations ran on a 2.8 GHz PC cluster, at the Configuration Aerodynamics Branch of NASA Langley Research Center. For FC7, FC19, FC 25, FC 46, & FC 70, only half of the aircraft was modeled and 56 processors were used while the full aircraft was modeled for FC 50 & FC 51, and 113 processors were used. A typical run for the fully converged solution at the fine grid level on a 14.7 million cell grid and 200 blocks required 51 wall clock hours on 56 PC nodes, with the solver running in parallel at a speed on the order of 1.12 μsec/cell for k-ε calculations and 1.24 μsec/cell for ASM calculations. Surface pressure distributions for FC 46, boundary layer profiles for FC 7, and skin friction are presented. This is followed by comparison between PAB3D, the unstructured grid solver USM3D [7-14], and flight data for FC 50. Finally, surface pressure distribution for FC 70 is presented.
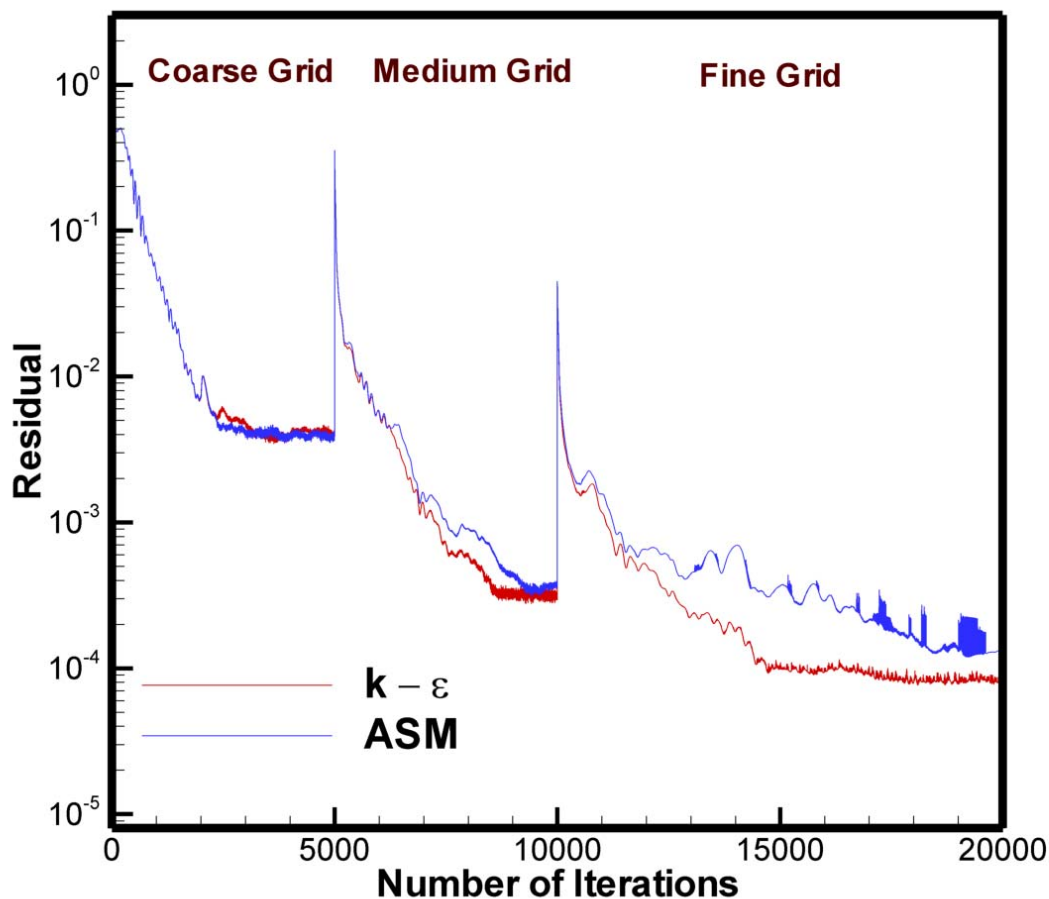
Figure 7-3: Convergence History for FC 7 (M = 0.304, α = 11.89°, R_n = 44.4 x 10^6).

Figure 7-4 (a) to (n) shows comparison between computed results and flight data for FC 46. There is a general overall agreement between computed results and PAB3D predictions. On the suction peak at BL 55, k-ε results under-predicted the primary vortex effect. The ASM over predicted flight data at BL 70 through BL 105 and under predicted flight data at BL 153.5. Figure 7-5 shows that the vortex predicted with the ASM is stronger than that predicted with the k-ε model and also shows that the k-ε model failed to accurately predict the secondary vortex. Figure 7-4 (i) through 4(o) also shows that the k-ε model failed to predict the secondary vortex. Figure 7-6 shows the grid distribution on the upper surface of the wing and the vortex core location for both the k-ε and ASM models. The vortex origin and footprint are approximately the same for both sets of computations. The reason for the slight discrepancy between predicted values and flight data is due to the coarse nature of the grid on the upper surface, as shown in Figure 7-6. To better resolve the flow field on the upper surface of the wing, more points are needed in both the chord wise and in the span wise directions. Areas where a finer grid can render a better prediction are pointed out on Figure 7-6. The vortex core location superimposed on C_p contours is shown Figure 7-7 for both the ASM and k-ε models. Although the ASM predicted a stronger vortex, as shown in Figure 7-7, the vortex origin and footprint is approximately the same.

(a) BL 55

(b) BL 70

(c) BL 80

(d) BL 95

(e) BL 105

(f) BL 153.5
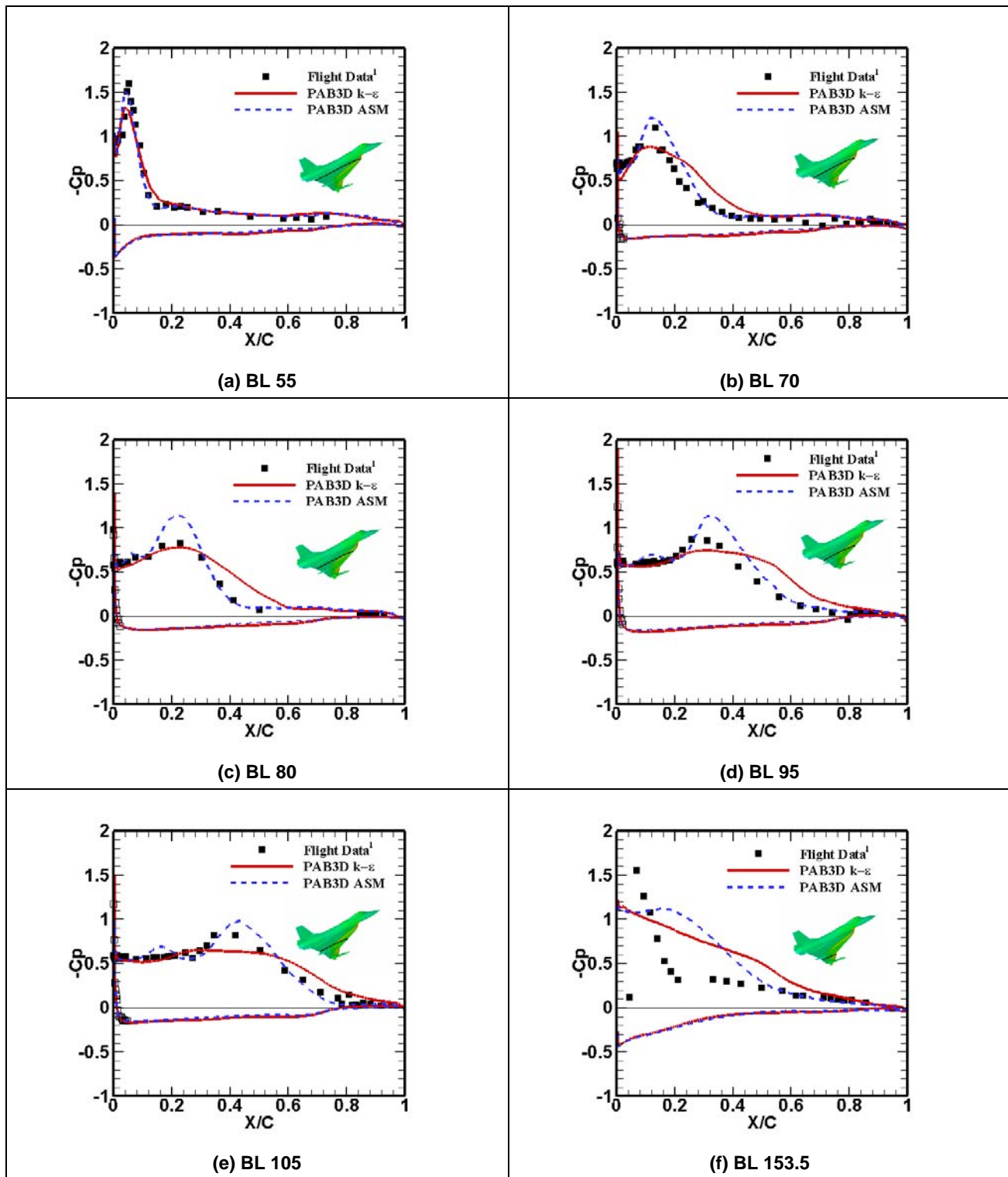
Figure 7-4: Computed and Measured Flight C_p at FC 46 (M = 0.527, α = 10.4°, R_n = 46.9 x 10^6).

(g) BL 184.5

(h) FS 185

(i) FS 300

(j) FS 337.5

(k) FS 375

(l) FS 407.5

Figure 7-4: Continued.

(m) FS 450

(n) FS 492.5
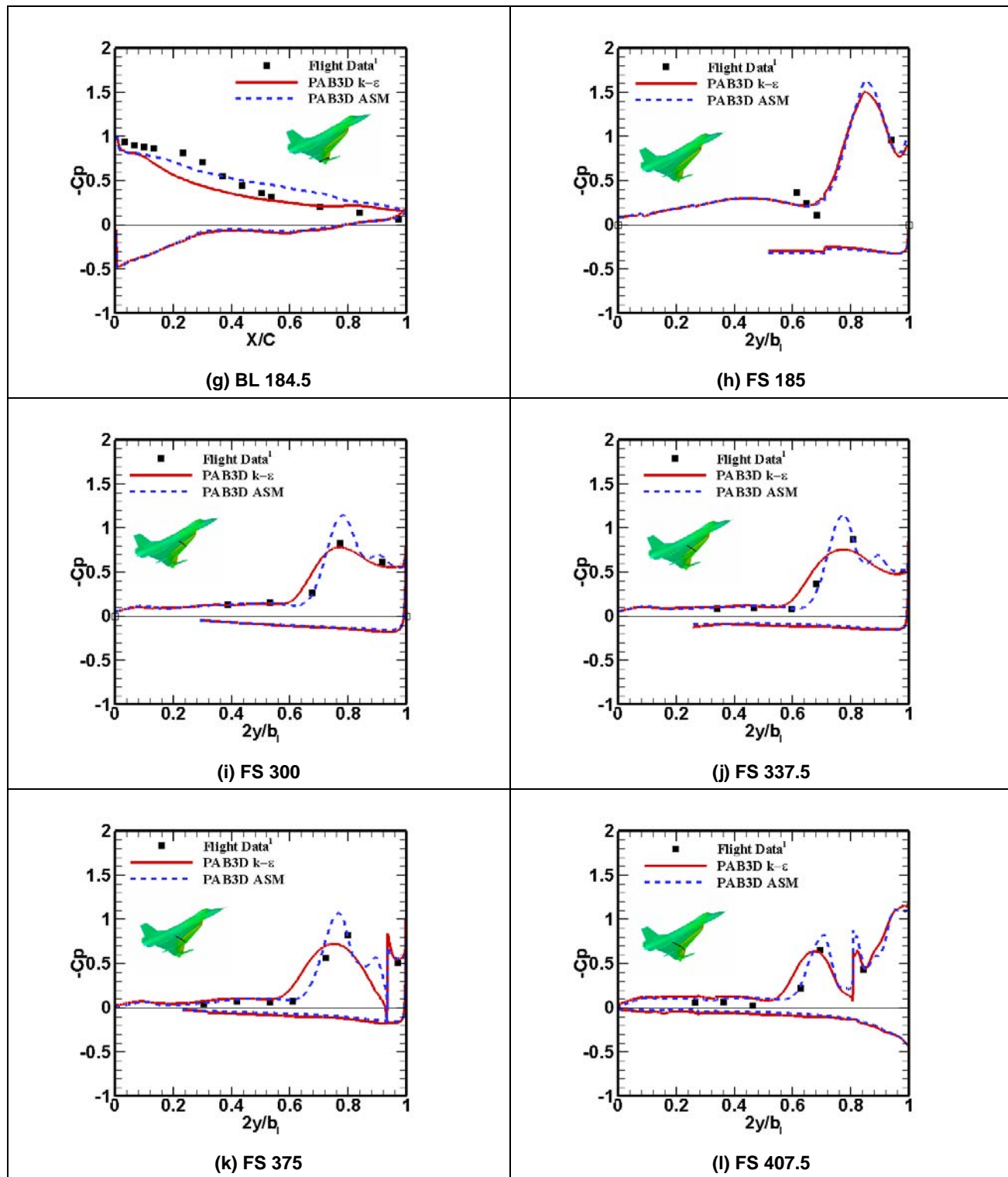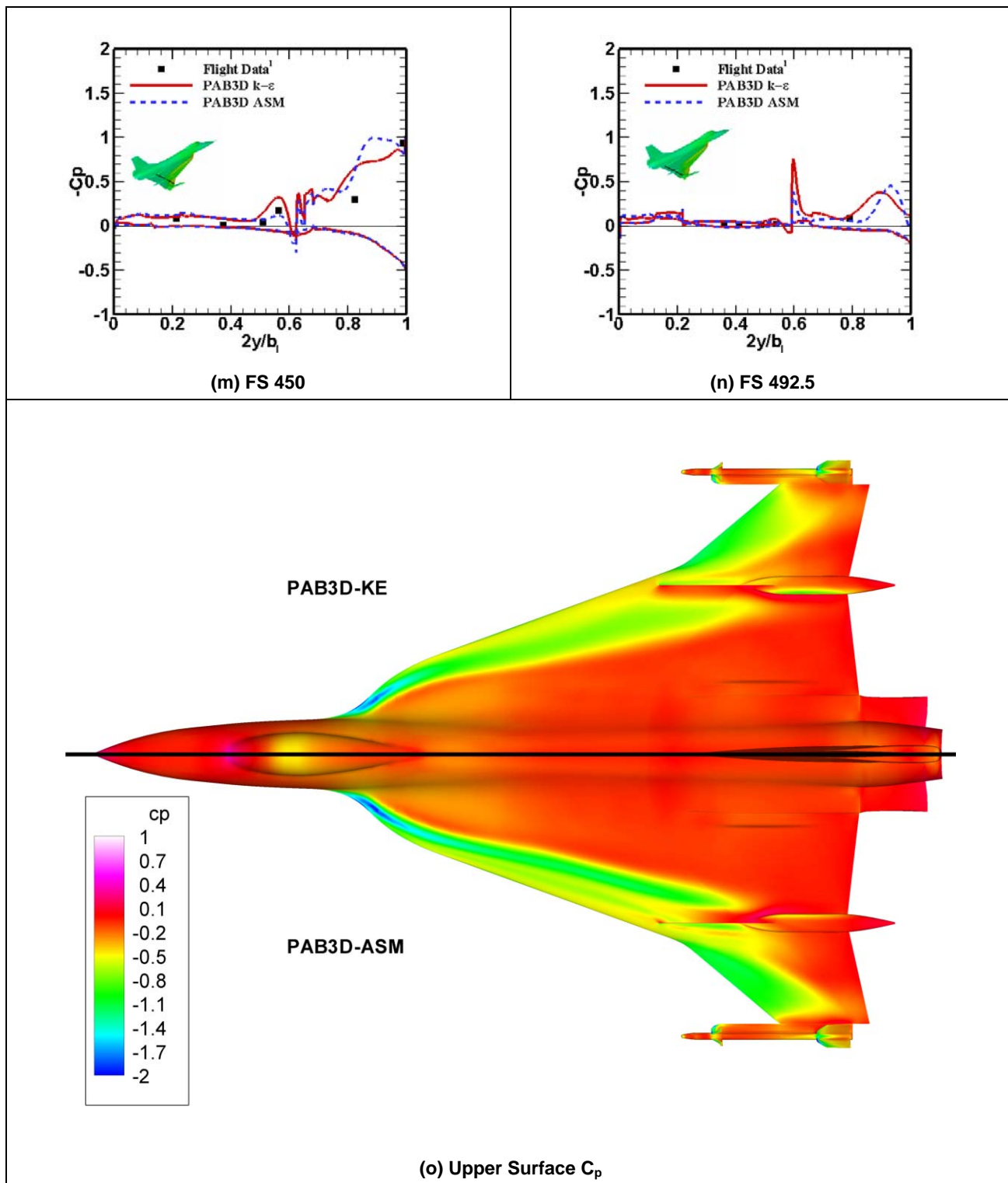
(o) Upper Surface C_p

Figure 7-4: Concluded.
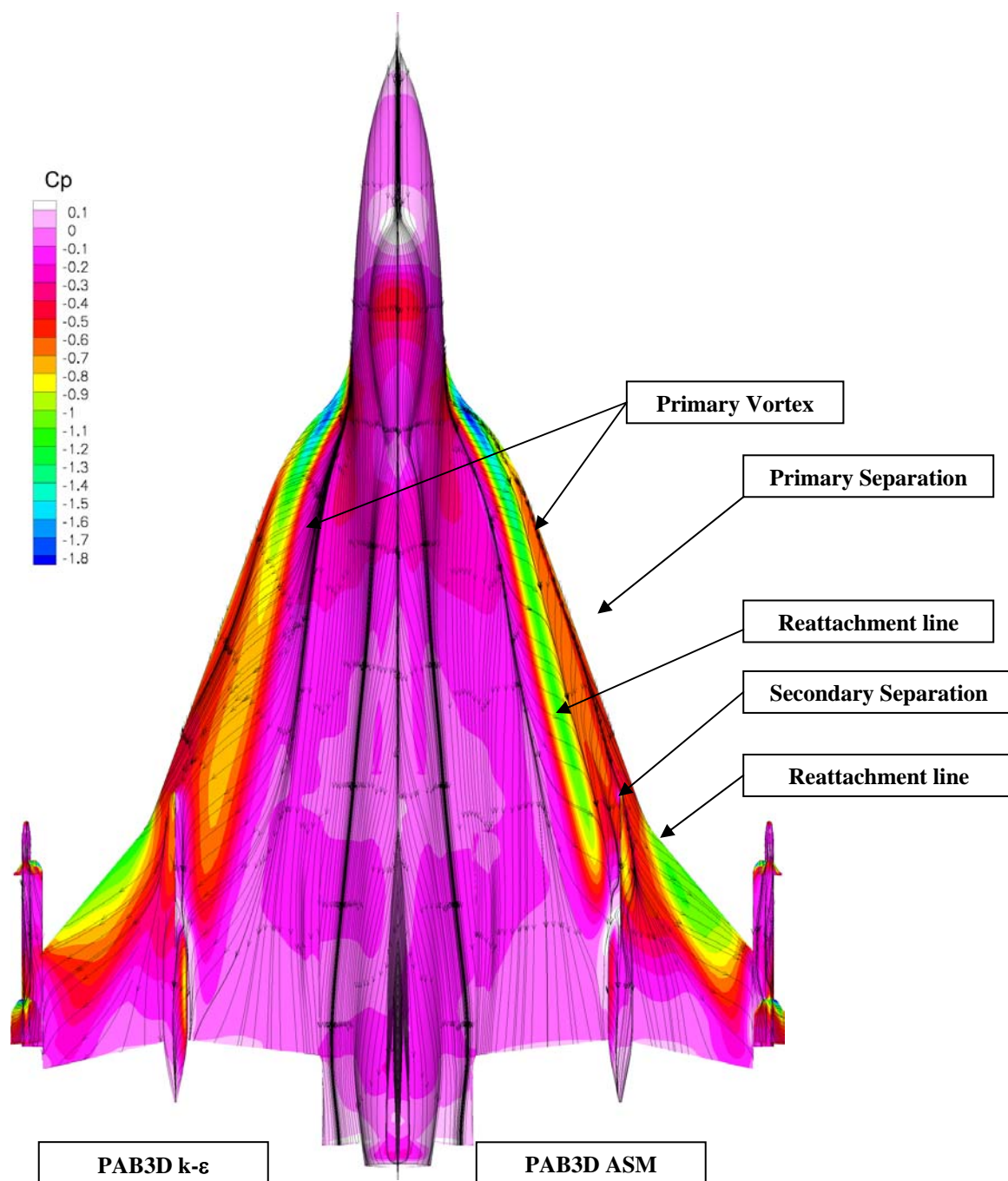
Figure 7-5: Upper Surface Pressure Distribution with Streamlines
FC 46 (M = 0.527, α = 10.4°, Rₙ = 46.9 x 10⁶).

More grid is needed in these areas

Vortex Core location for PAB3D k-ε

Vortex Core location for PAB3D ASM
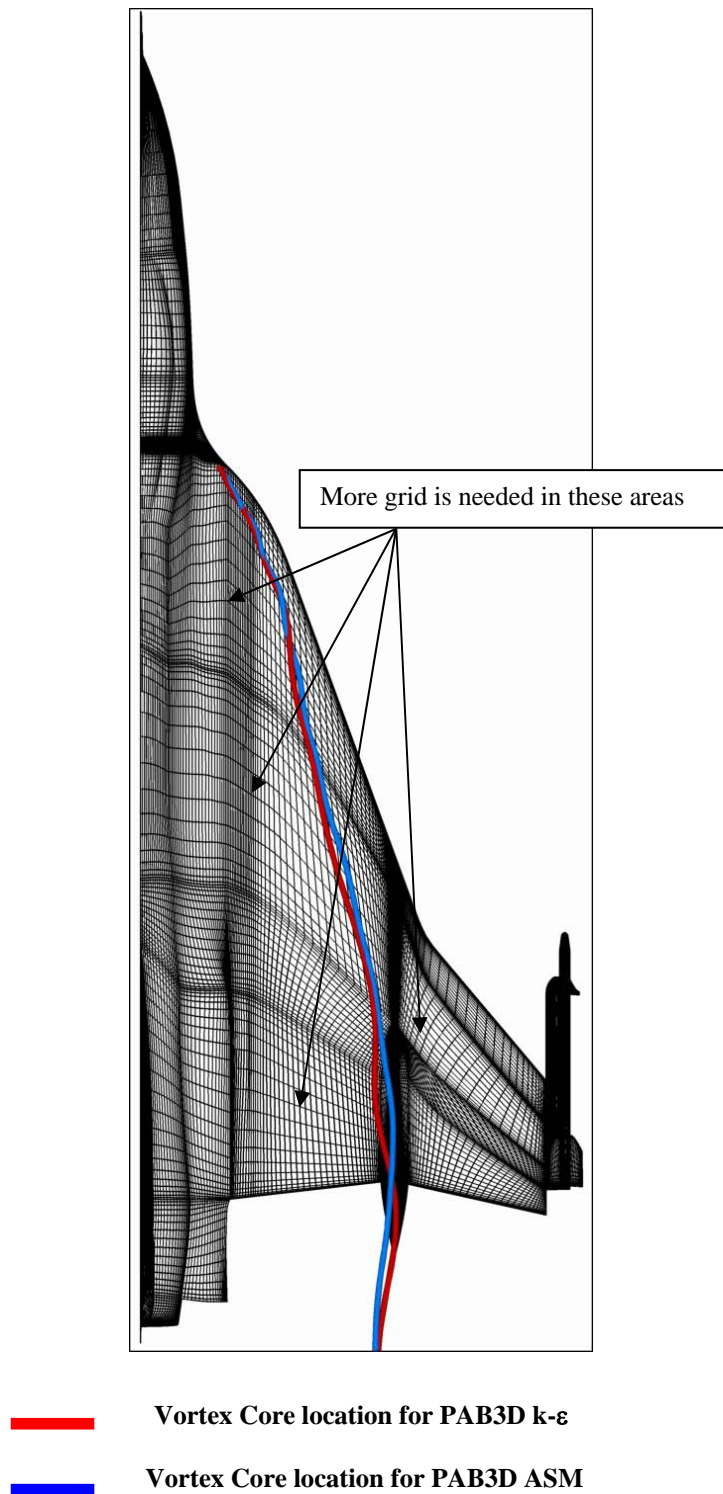
Figure 7-6: Surface with Vortex Core Location for FC 46 (M = 0.527, α = 10.4°, R_n = 46.9 x 10^6).
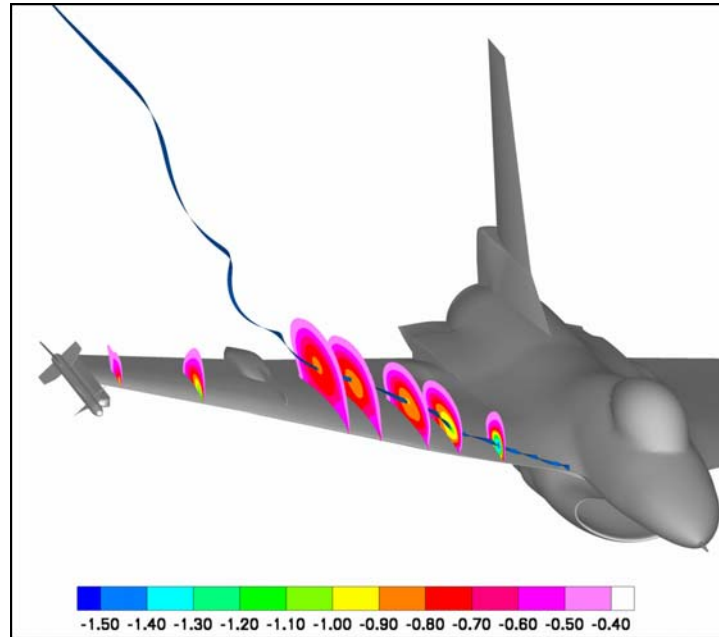
(a) PAB3D k-ε
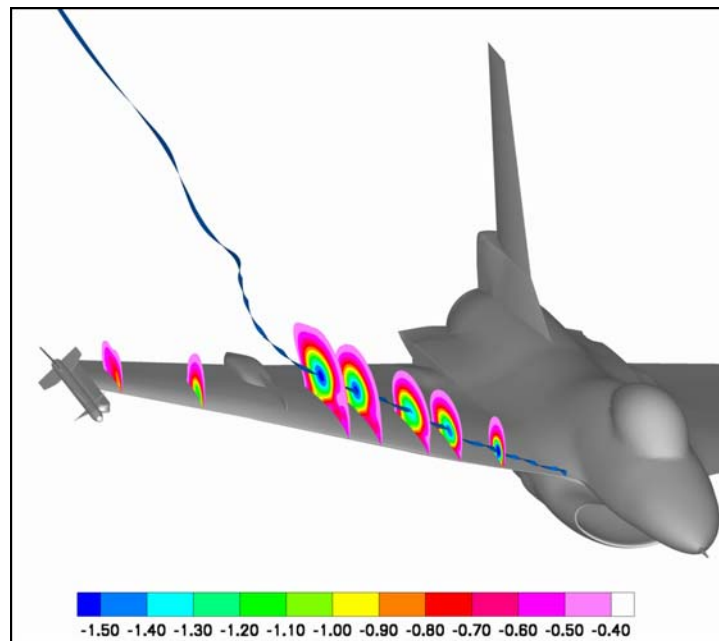
(b) PAB3D ASM

Figure 7-7: C_p Contours with Vortex Core Representation FC 46 (M = 0.527, α = 10.4°, R_n = 46.9 x 10^6).

The computed and flight boundary layer profiles for FC 7 are shown in Figure 7-8. The horizontal axis in Figure 7-8 is the normalized velocity magnitude which is defined as ratio of the velocity magnitude in boundary layer to that at the last rake position. The results for rake 3, FS 302.17, and BL -52.93 are shown in Figure 7-8

(a), where the flow is nearly in the stream wise direction. Both turbulence models show qualitative good agreement with the flight data, with the k-ε model giving a slightly better prediction than the ASM. However, Figure 7-8 (b) shows that the ASM gives better quantitative agreement with flight data than the k-ε model. Figure 7-8 (c) shows results for rake 5, where the k-ε model gives better comparison with flight data than the ASM, which over predicts the flight data. For rake 7, the k-ε model underestimates the flight data while the ASM over predicts it. Figure 7-8 (c) and Figure 7-8 (d) show that the flight data and numerical predictions are not asymptotic at the rake extreme, which is indicative that the edge of the boundary layer has not been captured. Contours of the upper surface C_p for FC 7 are shown in Figure 7-9. Both models predict C_p better inboard and along the leading edge. The ASM predicted a stronger vortex compared to the k-ε predictions.

(a) Rake 3; FS .302.17, BL -52.93

(b) Rake 4; FS 293.45, BL -76.22

(c) Rake 5; FS 295.52, BL -94.33

(d) Rake 7; FS 294.59, BL -96.06
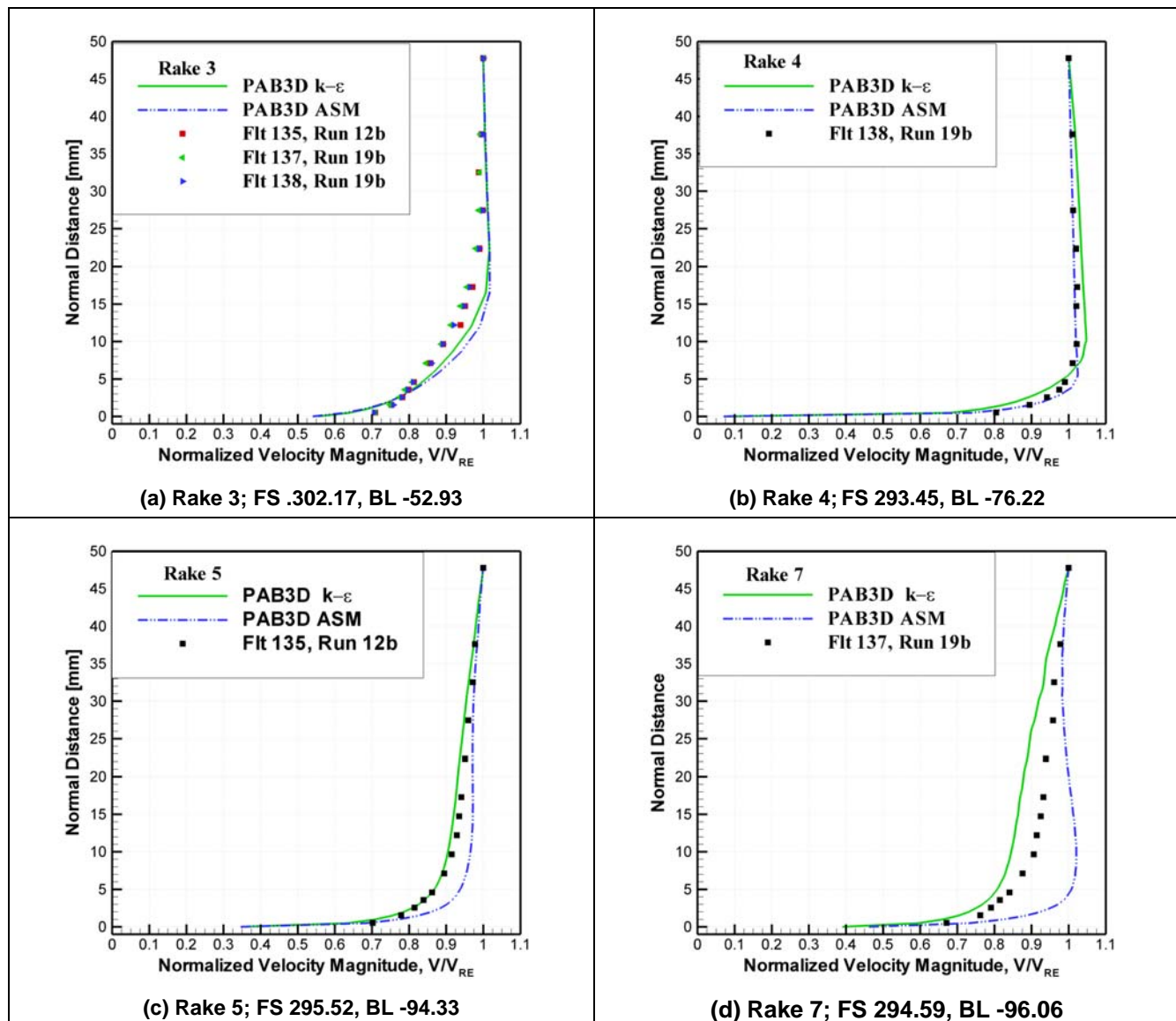
**Figure 7-8: Velocity Profiles for Boundary Layer Rakes on
F-16XL for FC 7 (M_∞ = 0.304, α = 11.89°, R_n = 44.4 x 10^6).**
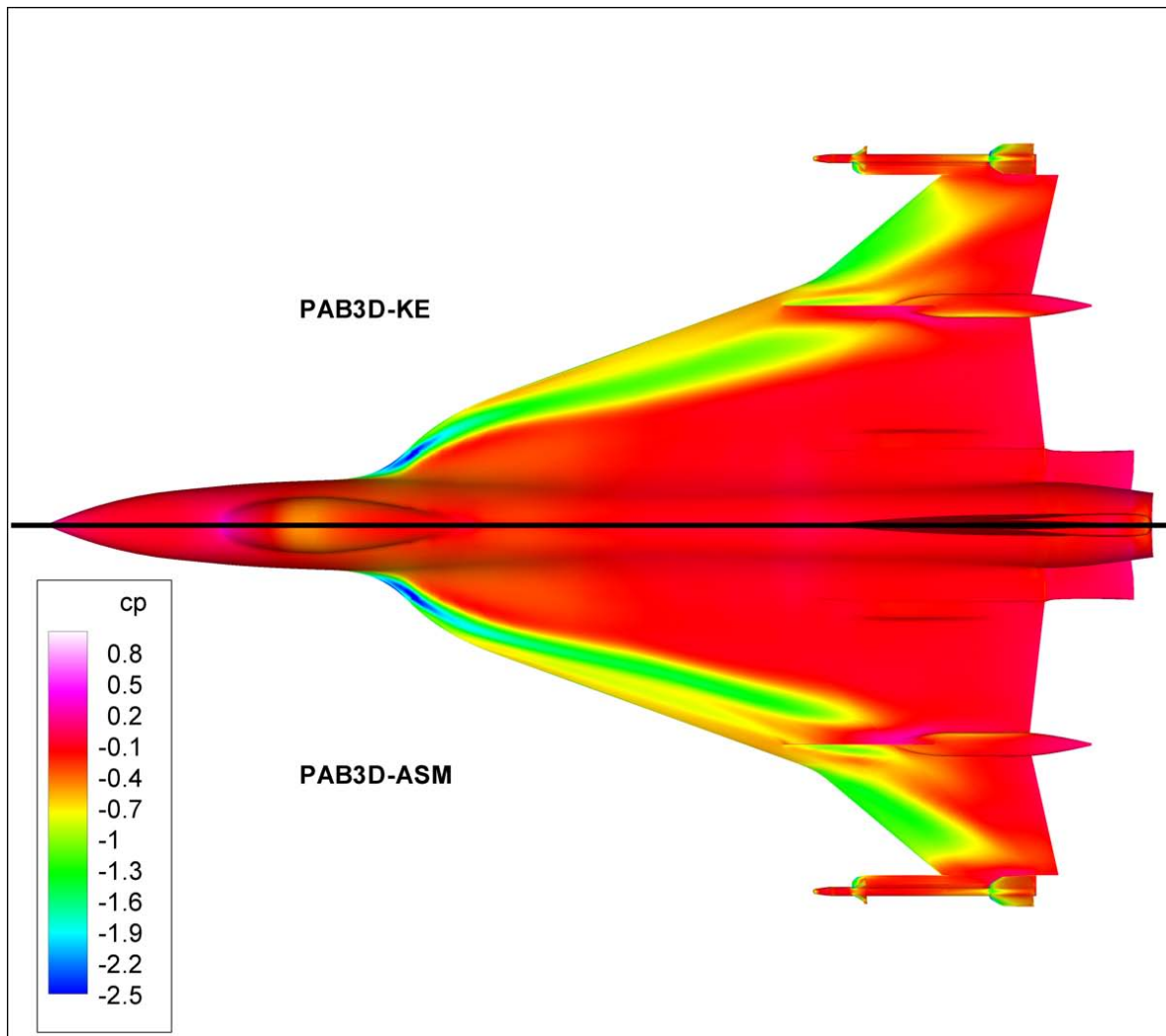
Figure 7-9: Upper Surface Pressure Distribution for FC 7 (M_∞ = 0.304, α = 11.89°, R_n = 44.4 x 10^6).

Figure 7-10 shows a comparison between the computed PAB3D, USM3D [7-14], and measured local skin friction at FS 330 for FC 19. Computed and flight data show good qualitative agreement. Both sets of data capture the two suction peaks, which are an indication of a primary and secondary vortex being present above the wing surface. The USM3D k-ε solution over-predicts the peak of the primary vortex by 7.5% while the PAB3D k-ε model under predicts flight data by 9.4%. The PAB3D ASM model matches the flight data better than the USM3D k-ε and the PAB3D k-ε model, even though that high suction peak of the ASM model under predicts flight data by 15%.
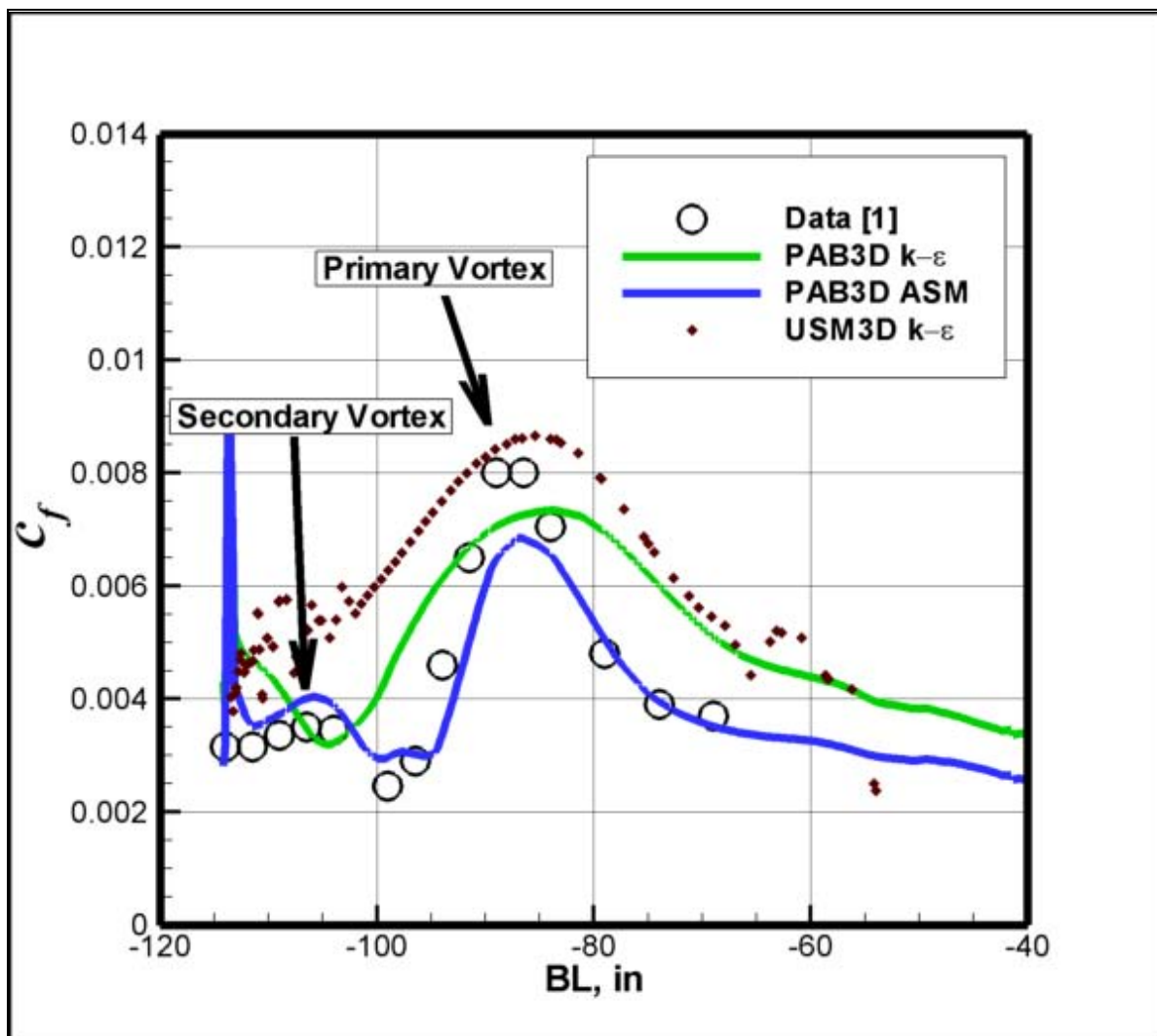
Figure 7-10: Skin Friction on F-16XL Aircraft at FS 330 for FC 19 (M_∞ = 0.36, α = 11.85°, R_n = 46.8 x 10^6).

Figure 7-11 shows the computed upper surface C_p contours for FC 19. Similar to FC 7, the ASM predicted a stronger vortex compared to the k-ε model predictions. The k-ε model failed to accurately predict the secondary vortex.
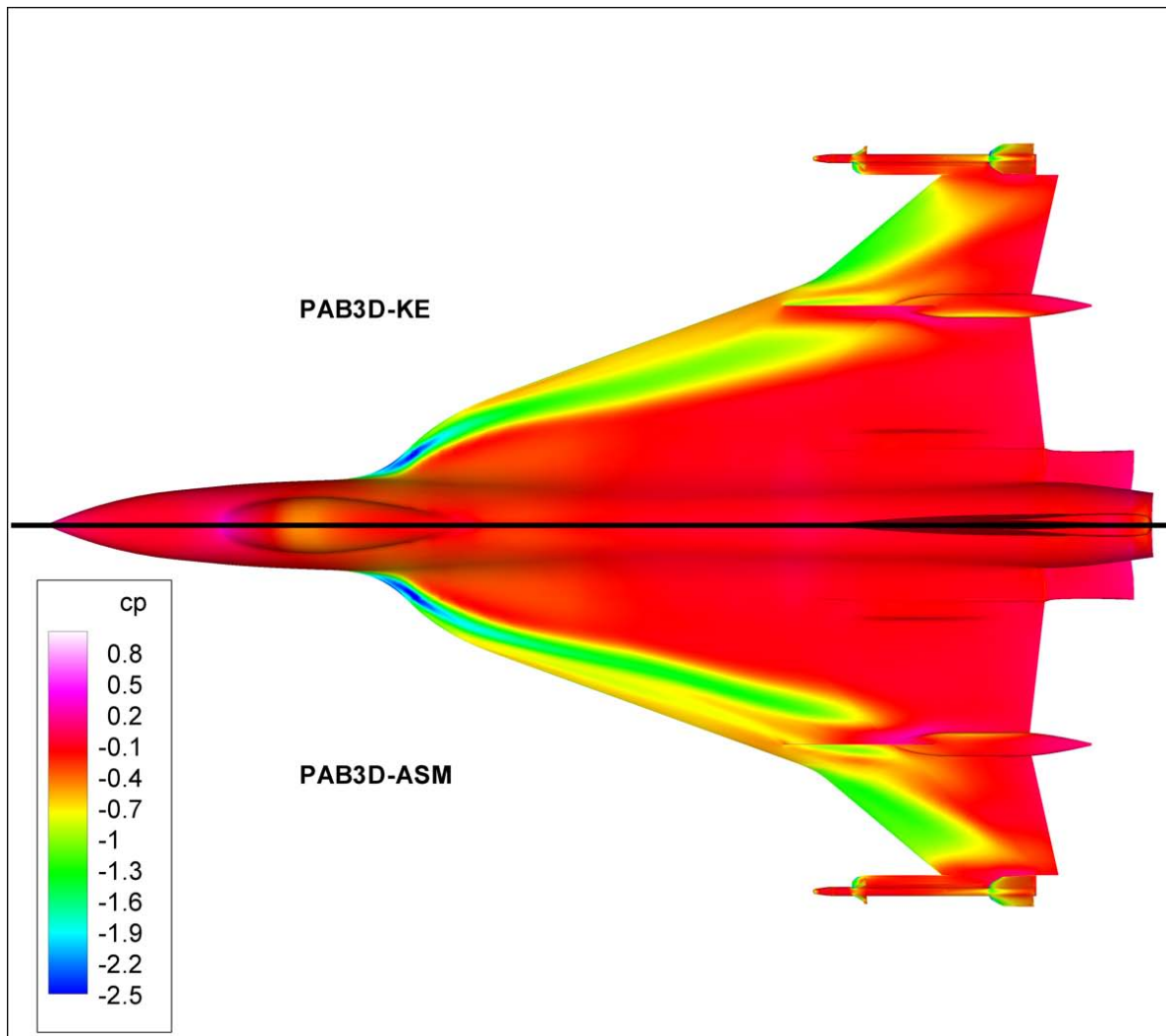
Figure 7-11: Upper Surface Pressure Distribution for FC 19 (M_∞ = 0.36, α = 11.85°, R_n = 46.8 x 10^6).

For FC 50 and FC 51, the flow around the full aircraft was simulated. For FC 50, the side-slip angle, β, is +5.31° while for FC 51, the side-slip angle, β, is -4.58°. Figure 7-12 and Figure 7-13 show C_p contours using ASM for FC 50 and FC 51 respectively. Figure 7-14 shows comparison between computed PAB3D, USM3D [7-14], and flight data for FC 50. All three models compare well with flight data. The USM3D k-ε model captures the suction peak better than PAB3D on the inner wing for BL 55. PAB3D ASM indicated the presence of a secondary vortex for BL 70, BL 80, & BL 95, while the k-ε model for both PAB3D and USM3D failed to predict the secondary vortex. The suction rise and peak were also higher for the ASM case. All models failed to accurately capture compression on the upper surface. As pointed out in the previous section, more points are needed on the upper surface to accurately capture the compression on the upper surface. All three models predicted the lower surface well. A detailed comparison for the effect of turbulence modeling for F-16Xl USM3D predictions is given in reference [7-14].
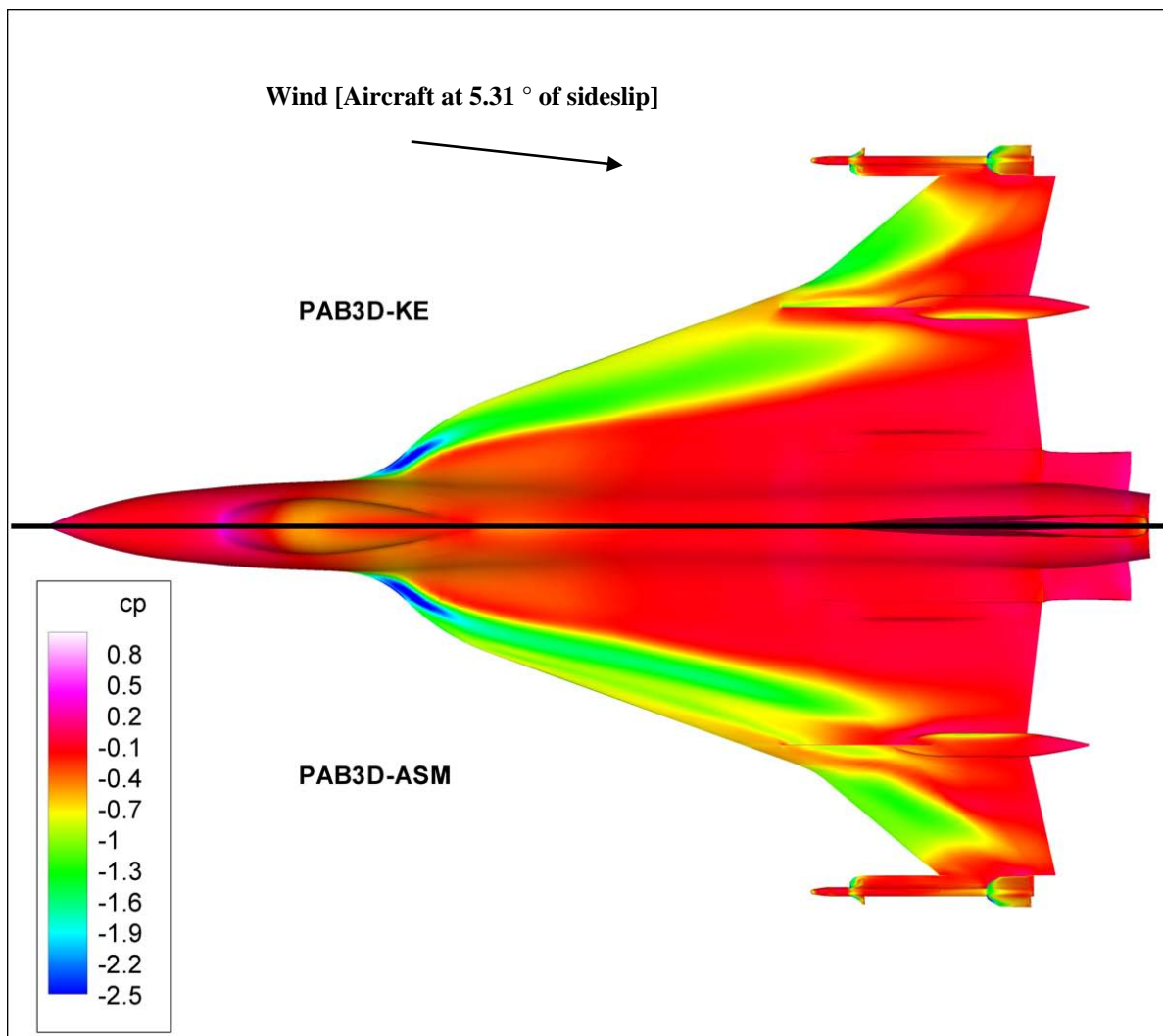
**Figure 7-12: Upper Surface Pressure Distribution for FC 50
(M = 0.434, α = 13.56°, β = +5.31, R_n = 39.4 x 10^6).**
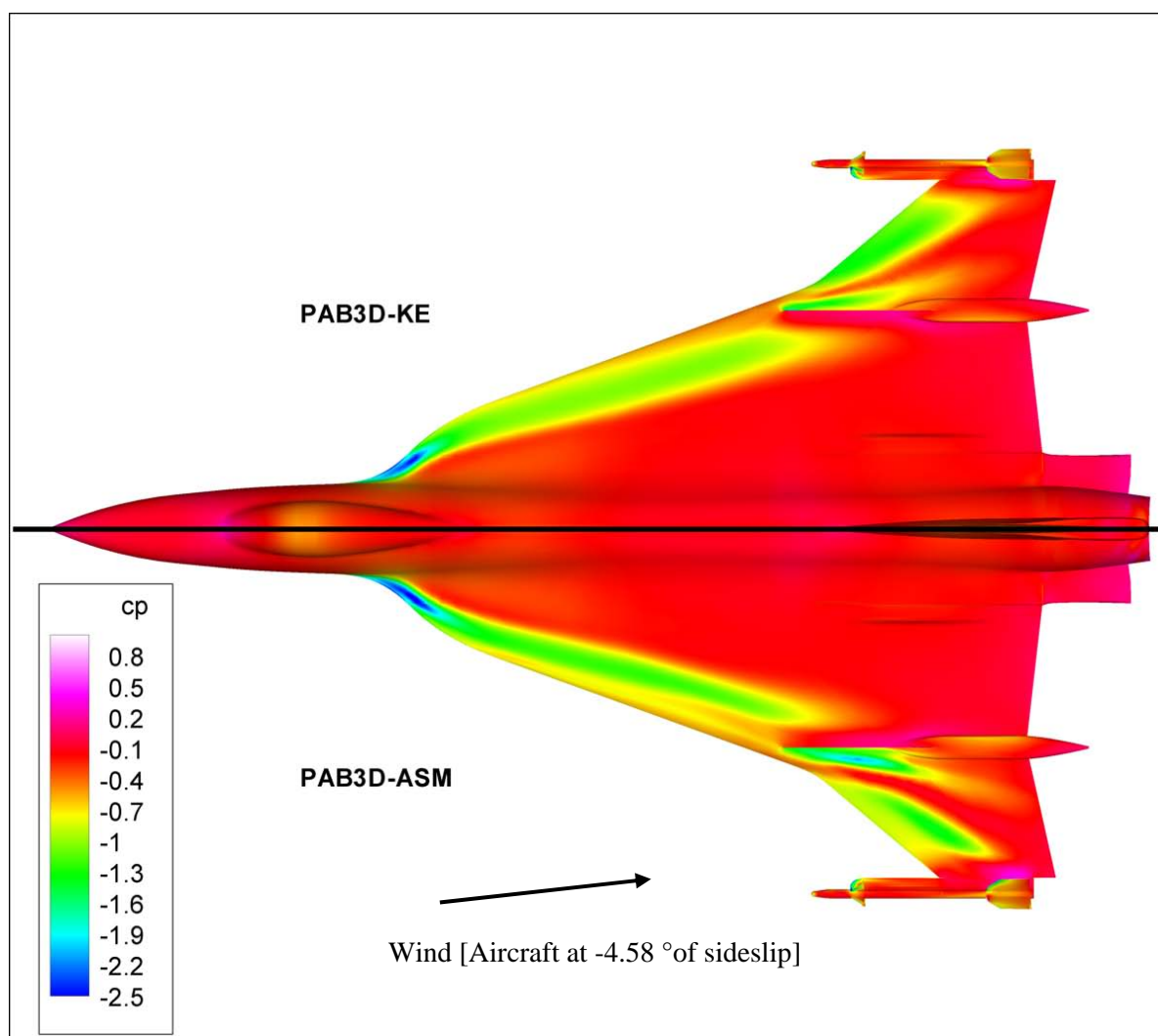
Figure 7-13: Upper Surface Pressure Distribution for
FC 51 (M = 0.441, α = 12.89°, β = -4.58, R_n = 38.9 x 10^6).
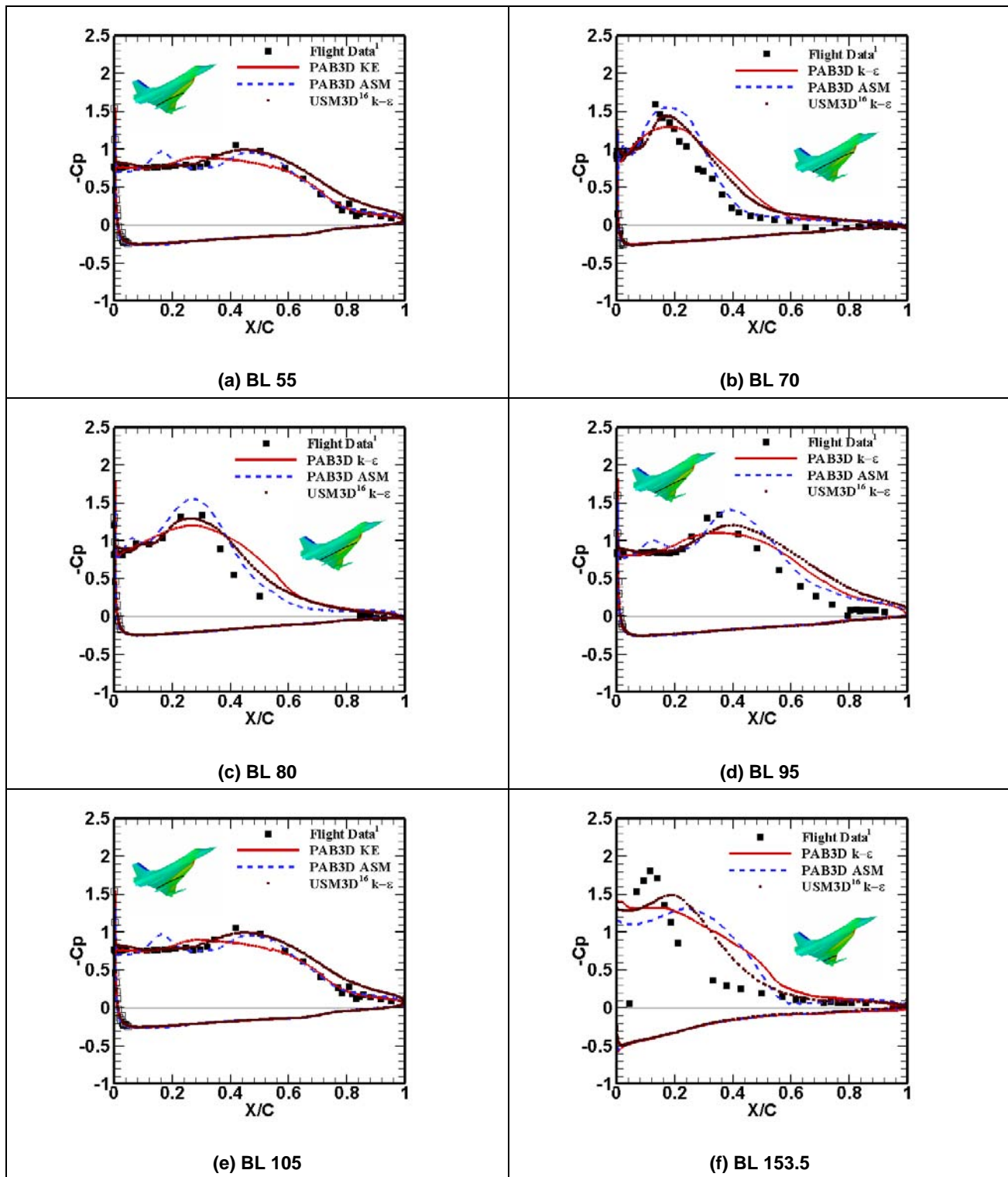
Figure 7-14: Comparison between PAB3D and USM3D C_p for FC 50 (M = 0.434, α = 13.56°, β = +5.31, R_n = 39.4 x 10^6).

(g) BL 184.5

(h) FS 185

(i) FS 300

(j) FS 337.5

(k) FS 375

(l) FS 407.5
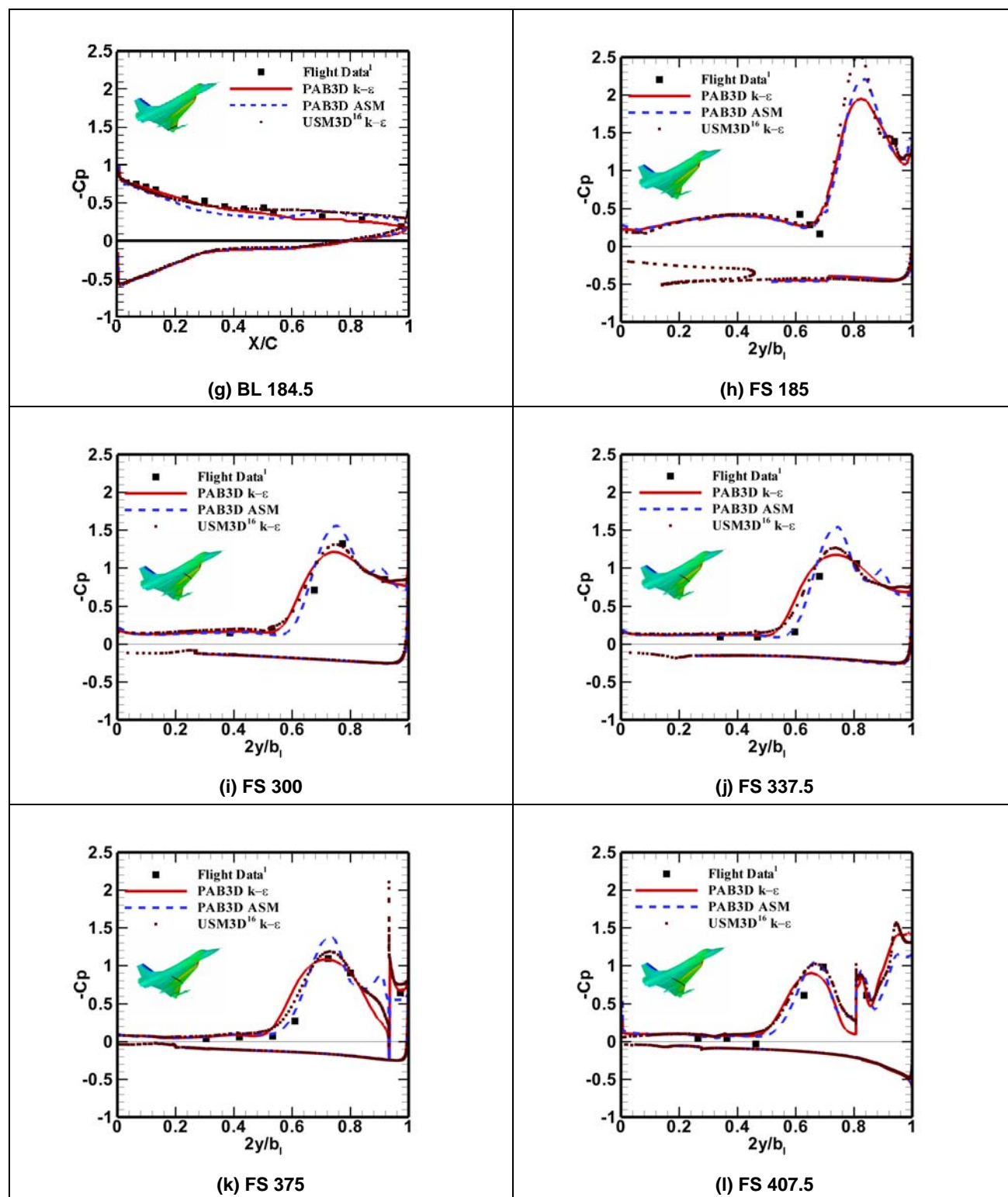
Figure 7.14: Concluded.

Figure 7-15 (a) through (n) shows comparison between PAB3D computed results and flight data for the transonic flight condition (FC 70). Figure 7-15 (o) shows comparison between PAB3D ASM and k-ε calculations of upper surface C_p contours for FC 70. Figure 7-15 shows that calculated results deviate from the flight data, similar behavior was reported by CAWAPI researchers [7-6]-[7-14], for FC 70. Figure 7-15 indicates that the effect of the turbulence model is negligible for this flight condition.

(a) BL 55

(b) BL 70

(c) BL 80

(d) BL 95

(e) BL 105

(f) BL 153.5
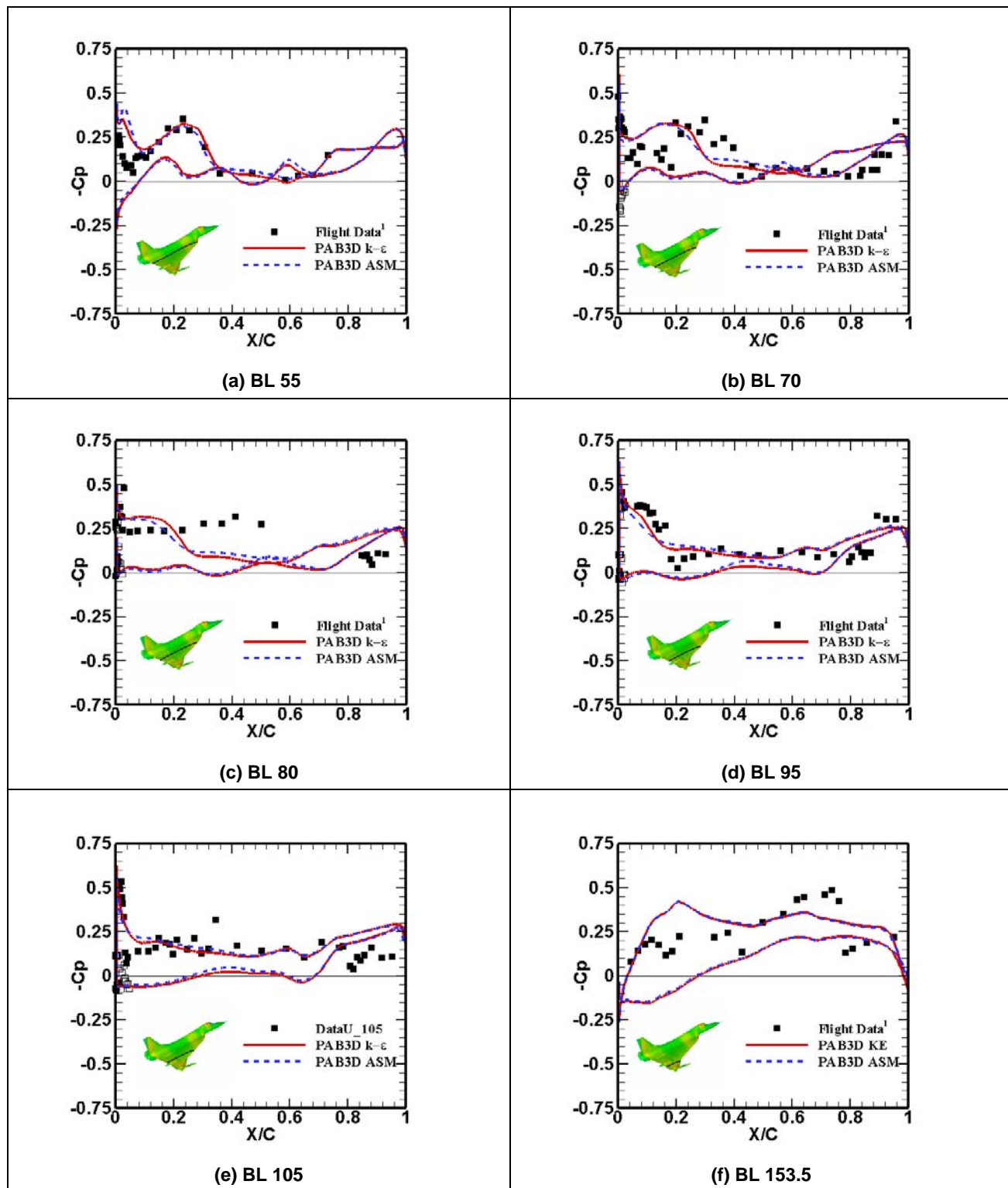
Figure 7-15: Computed and Measured Flight C_p at FC 70 (M = 0.97, α = 4.37°, R_n = 88.77 x 10^6).

(g) BL 184.5

(h) FS 185

(i) FS 300

(j) FS 337.5

(k) FS 375

(l) FS 407.5

Figure 7-15: Continued.

(m) FS 450

(n) FS 492.5

(o) Upper Surface C_p
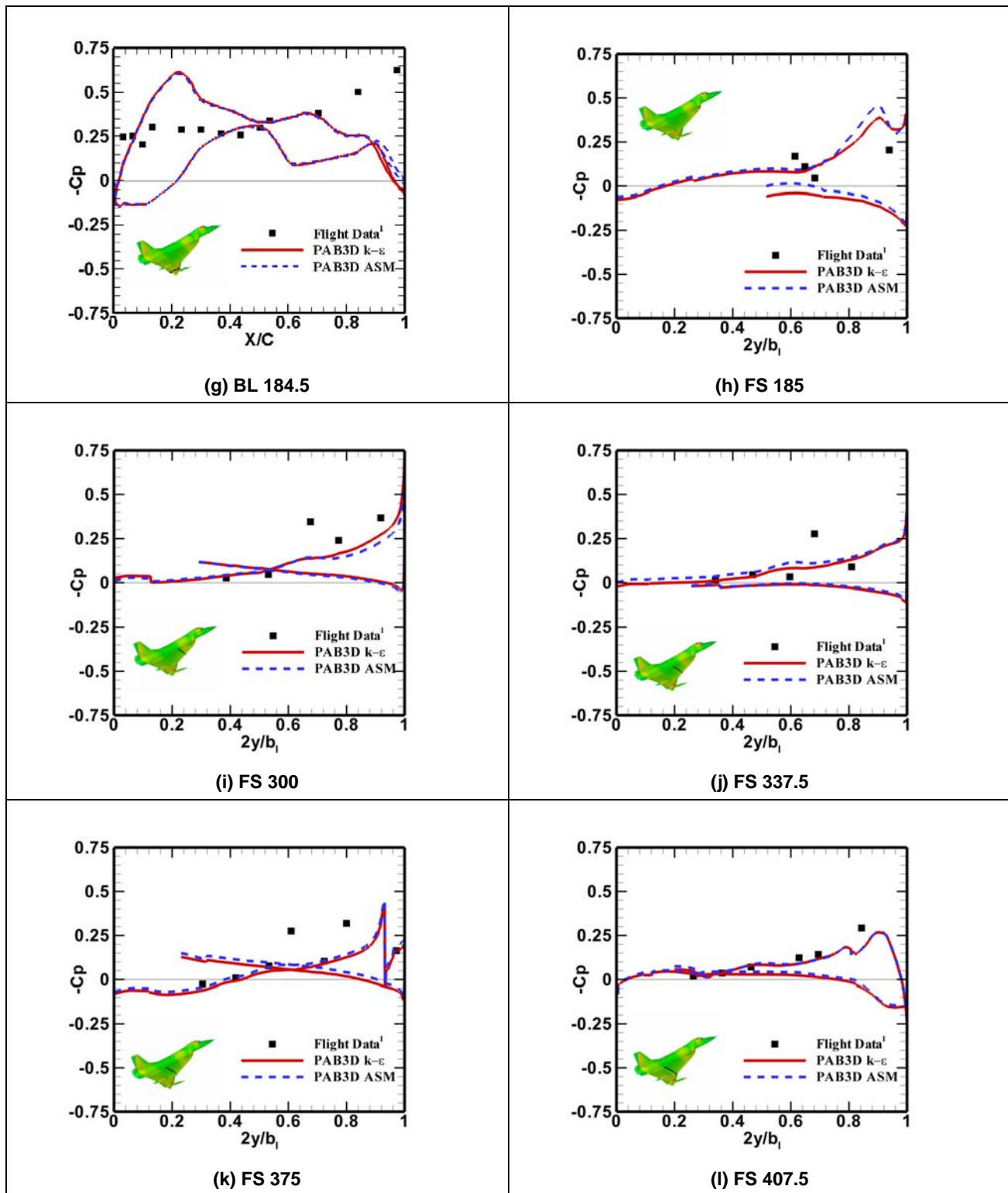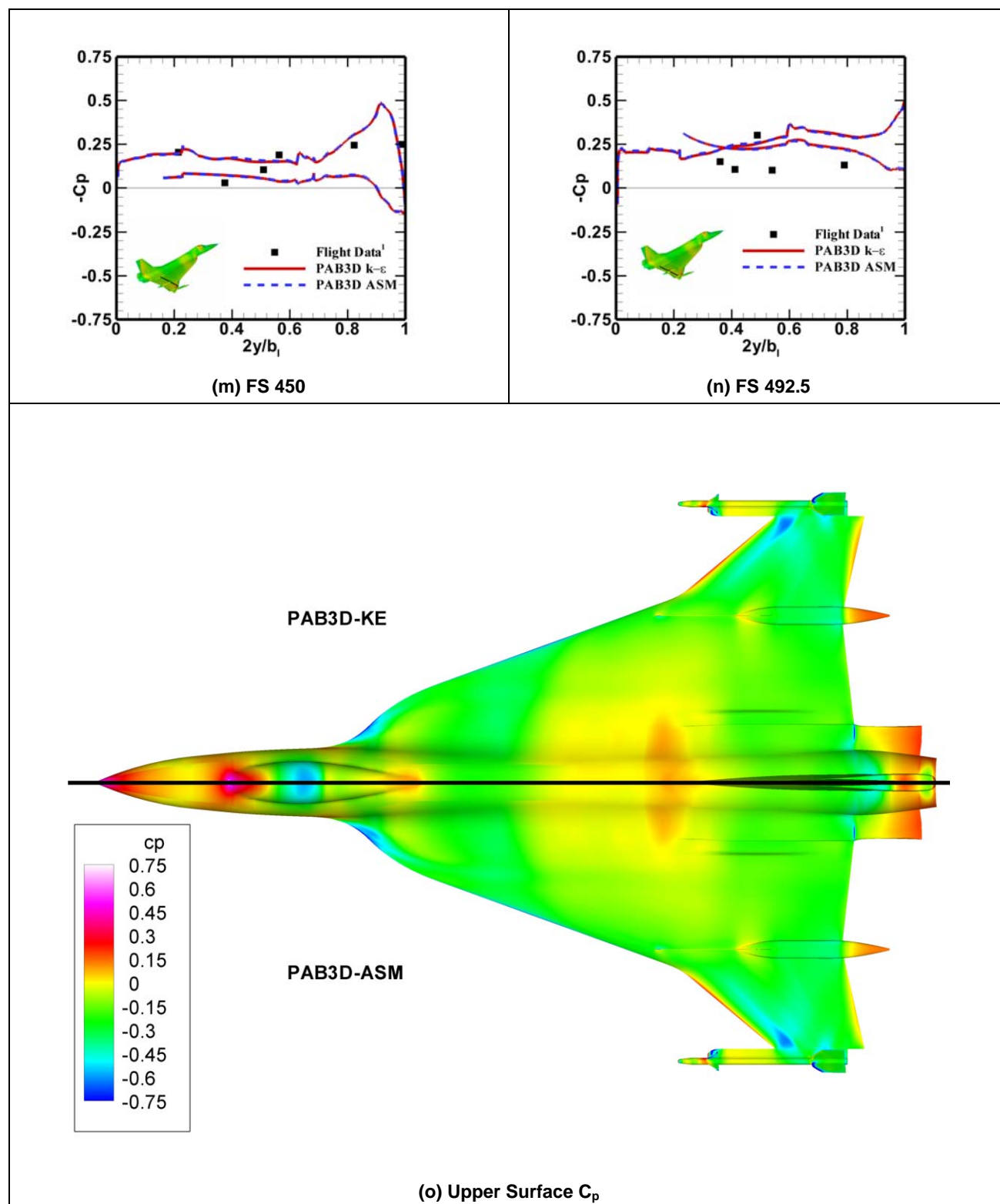
Figure 7.15: Concluded.

7.8   CONCLUDING REMARKS

Numerical simulations of the flow around F-16XL were performed as a contribution to the CAWAPI using the PAB3D CFD code. The flow field was computed for seven flight conditions. Two turbulence models were used in the calculations: a standard k-ε model, and Shih-Zhu-Lumley (SZL) algebraic stress model [7-20]. Surface static pressure, boundary layer velocity profiles, and skin friction were presented and compared to flight data. There is a general good agreement between computed results and flight data. The ASM results are closer to the flight data than the k-ε model results. The ASM predicted a stronger primary vortex, however, the origin of the vortex and the footprint is approximately the same as in the k-ε predictions. The reason for the slight discrepancy between predicted values and flight data is due to the coarse nature of the grid on the upper surface. Comparison with USM3D results, for FC 50, shows good agreement. Results emphasized the conclusion that the algebraic stress models give inherently better results than the linear stress model because of the explicit modeling of effects such as relaxation, and the specific inclusion of nonlinear anisotropic effects from the mean flow strain and vortices. Future work would involve generating a new grid with a y+ <1, and increasing the number of grids in the boundary layer and concentrating grid points on the upper surface in regions where high flow gradients occur.

7.9   ACKNOWLEDGEMENTS

The authors wish to thank Dr. John Lamar for his help and the long hours of fruitful discussions.

7.10   REFERENCES

[7-1]   Lamar, J.E. and Obara, C.J.: *Review of Cranked-Arrow Wing Aerodynamics Project: Its International Aeronautical Community Role*, AIAA Paper 2007-0487, Presented at 45th AIAA Aerospace Sciences Meeting and Exhibit, Reno, NV, January 8-11, 2007.

[7-2]   Lamar, J.E., Obara, C.J., Fisher, B.D. and Fisher, D.F.: *Flight, Wind-Tunnel, and Computational Fluid Dynamics Comparison for Cranked Arrow Wing (F-16XL-1) at Subsonic and Transonic Speeds*, NASA/ TP-2001-210629, February 2001.

[7-3]   Lessard, W.B.: *Subsonic Analysis of 0.04-Scale F-16XL Models Using an Unstructured Euler Code*, NASA TP 3597, October 1996.

[7-4]   Lamar, J.E., Conin, C.K. and Scott, L.E.: *A Review of Steps Taken to Create an International Virtual Laboratory at NASA Langley for Aerodynamic Prediction and Comparison*, Prog Aerospace Sci, Vol. 40, pp. 163-172, 2004.

[7-5]   Lamar, J.E., Cronin, C.K. and Scott, L.E.: *Virtual Laboratory Enabling Collaborative Research in Applied Vehicle Technologies*, In AVT-123 Symposium on "Flow Induced Unsteady Loads and the Impact on Military Applications", Keynote 2, Budapest, Hungary, April 25-29, 2005.

[7-6]   Boelens, O.J., Spekreijse, S.P., Sytsma, H.A. and de Cock, K.M.J.: *Comparison of Measured and Simulated Flow Features for the Full-Scale F-16XL Aircraft*, AIAA Paper 2007-0489, Presented at the 45th AIAA Aerospace Sciences Meeting and Exhibit, Reno, NV, January 8-11, 2007.

[7-7]   Badcock, K.J.: *Evaluation of Results from a Reynolds Averaged Multiblock Code Against F-16XL Flight Data*, AIAA Paper 2007-0490, Presented at the 45th AIAA Aerospace Sciences Meeting and Exhibit, Reno, NV, January 8-11, 2007.

[7-8]   Fritz, W.: *Hybrid Grid RANS Solutions for the CAWAPI F-16XL*, AIAA Paper 2007-0492, Presented at the 45th AIAA Aerospace Sciences Meeting and Exhibit, Reno, NV, January 8-11, 2007.

[7-9]   Morton. S.A., McDaniels, D.R. and Cummings, R.M.: *F-16XL Unsteady Simulations for the CAWAPI Facet of RTO Task Group AVT-113*, AIAA Paper 2007-0493, Presented at the 45th AIAA Aerospace Sciences Meeting and Exhibit, Reno, NV, January 8-11, 2007.

[7-10] Görtz, S. and Jirásek, A.: *Unstructured Steady/Unsteady Solutions with Edge for CAWAPI F-16XL at KTH/FOI*, AIAA Paper 2007-0678, Presented at the 45th AIAA Aerospace Sciences Meeting and Exhibit, Reno, NV, January 8-11, 2007.

[7-11] Michal, T., Oser, M., Mani, M. and Ross, F.: *BCFD Unstructured-Grid Predictions on the F-16XL (CAWAPI) Aircraft*, AIAA Paper 2007-0679, Presented at the 45th AIAA Aerospace Sciences Meeting and Exhibit, Reno, NV, January 8-11, 2007.

[7-12] Davis, M.B., Reed, C. and Yagle, P.: *Hybrid Grid Solutions on the (CAWAPI) F-16XL Using Falcon v4*, AIAA Paper 2007-0680, Presented at the 45th AIAA Aerospace Sciences Meeting and Exhibit, Reno, NV, January 8-11, 2007.

[7-13] Karman, S., Mitchell, B. and Sawyer, S.: *Unstructured Grid Solutions of CAWAPI F-16XL by UT SimCenter*, AIAA Paper 2007-0681, Presented at the 45th AIAA Aerospace Sciences Meeting and Exhibit, Reno, NV, January 8-11, 2007.

[7-14] Lamar, J.E. and Abdol-Hamid, K.S.: *USM3D Unstructured Grid Solutions for CAWAPI at NASA LaRC*, AIAA Paper 2007-0682, Presented at the 45th AIAA Aerospace Sciences Meeting and Exhibit, Reno, NV, January 8-11, 2007.

[7-15] Boelens, O.J., Görtz, S., Morton, S.A., Fritz, W. and Lamar, J.E.: *Description of the F-16XL Geometry and Computational Grids Used in CAWAPI*, AIAA Paper 2007-0488, Presented at the 45th AIAA Aerospace Sciences Meeting and Exhibit, Reno, NV, January 8-11, 2007.

[7-16] PAB3D Code Manual Originally developed by the Propulsion Aerodynamics Branch, now under cooperative program between the Configuration Aerodynamics Branch, NASA Langley Research Center and Analytical Services & Materials, Inc. Hampton, VA, See http://www.asm-usa.com/software/pab3d.html.

[7-17] Elmiligue, A.A., Abdol-Hamid, K.S. and Massey, S.J.: *PAB3D Simulations for the CAWAPI F-16XL*, AIAA Paper 2007-0491, Presented at the 45th AIAA Aerospace Sciences Meeting and Exhibit, Reno NV, January 8-11, 2007.

[7-18] Abdol-Hamid, K., Pao, S.P., Hunter, C., Deere, K.A., Massey, S.J. and Elmiligui, A.: *PAB3D: Its History in the Use of Turbulence Models in the Simulation of Jet and Nozzle Flows*, AIAA-2006-489, Presented at the 44th AIAA Aerospace Sciences Meeting and Exhibit, Reno, Nevada, January 9-12, 2006.

[7-19]   Massey, S.J.: *POST Code Manual*, See http://www.asm-usa.com/post/.

[7-20]   Shih, T.H., Zhu, J. and Lumley, J.L.: *A New Reynolds Stress Algebraic Equation Model*, NASA TM-106644, August 1994.

[7-21]   Elmiligui, A., Abdol-Hamid, K. and Hunter, C.: *Numerical Investigation Flow in an Over-Expanded Nozzle with Porous Surfaces*, AIAA Paper 2005-4159, Tucson, Arizona, 2005.

Chapter 8 – NUMERICAL SOLUTIONS FOR THE CAWAPI CONFIGURATION ON UNSTRUCTURED GRIDS AT EADS-MAS, GERMANY

by

Willy Fritz

This chapter presents some essential results which were obtained within the Cranked Arrow Wing Aerodynamics Project International (CAWAPI). In the CAWAPI, flight test data of the F-16XL aircraft were exploited as test cases for the verification and validation of CFD codes. The chapter focuses on the use of solution adapted hybrid grids with the DLR TAU code. Results for four different flight conditions (FC) will be presented and discussed. Comparisons with flight test data are shown for surface pressure distributions, boundary layer data and surface skin friction coefficients. The results show, that also for a complex configuration, solution adapted grids can fix the grid dependency of the numerical solution.

8.1   NOMENCLATURE

FT	=	flight test
tpl	=	total pressure loss
v/v_e	=	ratio of velocity magnitude in boundary layer to that at the rake extreme total-pressure tube
x/c_{local}	=	fractional distance along the local chord, positive aft
$2y/b_{local}$	=	fractional distance along the local semi span, positive towards the right wing tip
$y+$	=	dimensionless sublayer scale, $u_\tau y/\nu$

8.2   INTRODUCTION

The evolution of Computational Fluid Dynamics (CFD) and the rapidly increasing computational resources have enabled the aeronautical industry to simulate the aerodynamic behavior of realistic configurations. Nowadays this simulation is no longer limited to the computation of steady aerodynamic control characteristics, but also high-fidelity coupled multidisciplinary applications like the simulation of maneuvering fighter aircraft [8-1], [8-2] are possible. With the unstructured approach, the complexity of the geometry is also no longer a severe limitation. Within these coupled multidisciplinary applications (unsteady aerodynamics/flight mechanics/ aeroelastics coupling) the accuracy of the computed aerodynamic characteristics is very often the vital factor for the success of the simulation. So even at times of multidisciplinary applications validation of CFD codes with respect to accuracy and efficiency is still an important theme.

Typical validation data are obtained by wind tunnel measurements on generic configurations. Such data are commonly open to the community, but they are influenced by scaling effects, Re-number effects, and wind-tunnel blockage effects.

The validation of CFD for vortical flows was the purpose for the establishment of the RTO AVT-113 working group. One facet of this working group was the "Cranked Arrow Wing Aerodynamics Project International"

(CAWAPI). This project was started by NASA to allow a comprehensive comparison of several CFD codes with the flight test database of the F-16XL aircraft [8-3]. A more detailed overview on the CAWAPI is given by Lamar et al in Ref. [8-4].

The F-16XL flight test data base includes surface pressure measurements, boundary layer rakes data, and hot film data. This experimental data and the detailed geometry definition were provided by NASA for the use within the CAWAPI. Many of the flight conditions have vortical flow conditions and are thus representative for high performance fighter aircraft.

By this, CAWAPI was an excellent opportunity for EADS-MAS to test the CFD tools with respect to accuracy and computational effort on a realistic configuration at realistic flow conditions. Validation could be done not only by comparison with flight test data, but also by comparison of numerical results obtained by different codes. The main interest of EADS-MAS in this project was however not only to produce a flow solution in a certain grid, but also to get experience and guidelines for the handling of complex configurations with respect to grid generation. In order to realize this by grid refinement and finally by solution based grid adaptation, EADS-MAS had to generate own hybrid grids and did not use any common grid.

The chapter reports on the numerical simulations contributed by EADS-MAS to the CAWAPI and concentrates on the four flight conditions ("FCs") FC 7 ($M_\infty = 0.304$, $\alpha = 12°$, $Re = 44.4 \times 10^6$), FC 19 ($M_\infty = 0.36$, $\alpha = 12°$, $Re = 46.8 \times 10^6$), FC 25 ($M_\infty = 0.25$, $\alpha = 19.84°$, $Re = 32.22 \times 10^6$) and FC 70 ($M_\infty = 0.97$, $\alpha = 4.37°$, $Re = 88.77 \times 10^6$). It shows in detail the effect of the grid adaptation on the numerical solution by a comparison of results obtained in different hybrid grids.

8.3   GEOMETRY

The geometry used in the CAWAPI project was the F-16XL aircraft. It was obtained from the Full-Scale F-16A aircraft by stretching the fuselage and adding a cranked-arrow wing. The wing has a leading edge sweep of 70° inboard and 50° outboard of this crank. At the wing apex, an "S-blend curve" is used to join the wing leading edge to the fuselage. Some essential details of the geometry are the airdam (upper surface fence mounted near the wing leading edge crank) and the tip missile with its rail. Both details were present during the test flights. A detailed description of the aircraft geometry is given in Refs. [8-3], [8-4] and in Chapters 3 and 4. The aircraft geometry was available as an IGES file, which was generated by Lockheed-Martin Aeronautics Company. In this geometry definition file the inlet up to the compressor face and the nozzle up to the turbine face were included but all control surfaces were not deflected. More details about the generation of the IGES file and other geometry preparing can be seen in [8-5] and Chapter 4. The file still contained multiple overlaying surfaces, which have been corrected at EADS-M, where a single set of describing surfaces was generated. Furthermore the gap between the Nozzle and the wing trailing edge flap was closed. All other geometric details (airdam, gap between launcher and missile, step at rear end wing fuselage junction) were kept for the grid generation. Finally the dimension of the geometry has been transferred from inches into meters. Figure 8-1 shows the resulting surface geometry as it was used for the grid generation. (The figure shows a solid model of the final surface grid which was used for the CFD simulations).
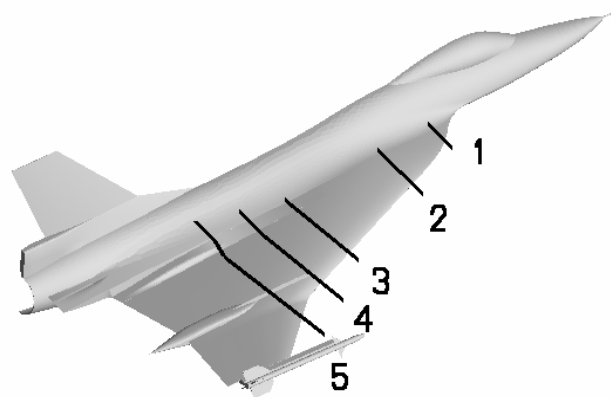
Figure 8-1: Surface Geometry of the F-16XL Aircraft Used in the CFD-Simulations.

A further interesting detail of the geometry is the shape of the leading edge. At the apex (position 1 in Figure 8-1), the wing starts with a kind of cropped sharp leading edge, which merges towards a round leading edge (position 2). At position 3 there is again a transition towards a sharp leading edge and the outer part of the wing finally has a sharp leading edge.

8.4   TEST CASES

Seven different test cases (Flight Conditions, FC) have been selected from the flight test database ([8-3], [8-4]) for the use in the RTO/AVT-113 task group. The present chapter will show results for four of those test cases, which have also been calculated by all the other members of the task group (Refs. [8-10]-[8-18] and Chapters 5 through 15). They are shown in Table 8-1.

Table 8-1: Calculated Flight Conditions

Flight Condition	Actual Mach Number	Actual Alpha (degrees)	Actual Beta (degrees)	Actual Reynolds Number
FC 7	0.304	11.89	-0.133	44.4E+06
FC 19	0.36	11.85	+0.612	44.8E+06
FC 25	0.242	19.84	+0.725	32.22E+06
FC 70	0.97	4.37	+0.310	88.77E+06

For all the above flight conditions a sideslip angle of 0 degrees was assumed thus they were calculated as symmetric. FC 7 was chosen, as boundary layer data (velocity profiles) from flight test were available and for FC 19 there exist surface skin friction data. Flight Condition 25 is that with the highest angle of attack. These 3 FCs all should have a vortical flow field. Finally FC 70 is a transonic test case with a very low angle of attack. For FC 7, FC 25, and FC 70 the calculations were started with a common initial grid and then continued with 4 individual solution based grid adaptation steps for each flight condition. As the conditions for FC 7 and FC 19 were very close, the final adapted grid of FC 7 was also used for FC 19. Each of the four flight conditions was also calculated in the so called "manually adapted" grid of Figure 8-4.

8.5   GRID GENERATION

8.5.1   General Remarks

As it was not sure whether a common unstructured grid could be used by all participants (specific requirements of the different flow solvers) and as also a systematic grid refinement study was planned, EADS-MAS decided to generate an own hybrid grid right from the start. For this the commercial hybrid grid generator from "CentaurSoft" was used [8-6]. This grid generation tool is based on the advancing front method and enables the generation of hybrid grids with minimal user interaction. Starting from the "air-tight" geometry, the grid generation process is split up into surface triangulation, prismatic grid generation and tetrahedral grid generation. Point clustering is achieved by automatic clustering based on geometric features and by user-controlled clustering, placing so called sources. This user controlled clustering has been used for a rough adaptation of the grid to the expected vortical flow structure. The surface triangulation works patch-oriented, which results in a not always needed high resolution of all small surface patches. (The geometry definition of the F-16XL aircraft contains several such mini-patches).

First flow calculations with such "manually adapted" grids were however not very satisfactory. Especially for the test cases with vortical flow structure the leeward suction peaks due to the leading edge vortices were under predicted and even grids with up to 22 million grid points were no guarantor for proper flow solutions. So it was clear, that the point distribution in the field was not always optimal. In order to overcome this problem, a solution based grid adaptation was used for all further calculations.

8.5.2   Solution Based Grid Adaptation

The solution based grid adaptation was realized by the use of the adaptation technique, which is included in the DLR-TAU Code (Refs. [8-7]-[8-9]). The adaptation algorithm needs a hybrid grid and a matching flow solution. With the aid of refinement sensor functions it is determined which edges of the primary grid have to be bisected. As sensor functions the differences of the flow variables between the edge points along an edge were applied, and as flow variables the magnitude of the velocity, the density, the total pressure, and the helicity were used. During the adaptation points can be added and removed, but only points which have been previously added can be removed. The adaptation is a static grid refinement, which can be started after the computation of a flow solution on a certain grid. It then generates a new primary grid and interpolates the solution onto this grid. This procedure can be repeated several times in order to get a final adapted grid.

The starting grid for the solution based grid adaptation was generated by the "CentaurSoft" grid generator [8-6] as described above. This initial grid had 10496522 nodes in total for the half-span full-scale model of the F-16XL. It had a prismatic layer of 15.6 million prisms in the near wall region and 13.5 million tetrahedra in the outer region. The thickness of the first prismatic layer was 4.0e-06 m and a geometric progression parameter of 1.3 was used for the other 29 viscous layers. In critical regions the prismatic layers were chopped and transition elements such as pyramids and tetrahedra were created. The surface of the aircraft was resolved by 749742 triangles.

This grid was adapted in 4 steps for each flight condition. The maximum increase of grid points for each of the 4 adaptation loops was limited to 25%. Grid points have been added in the surface grid and in the tetrahedral grid. The new surface points have been included in the prismatic grid, but number and thickness of the prismatic layer have not been changed. (The initial prismatic layer was designed such, that it was suitable for a much finer grid).

With this adaptation procedure the final adapted grid (for example FC 25) obtained 1462096 surface triangles, 32375977 prisms, and 258771331 tetrahedra. Compared to the initial grid, these elements roughly have been doubled, resulting in a total number of 21149945 nodes. Figure 8-2 shows the development of the surface grid during the 4 adaptation steps. New grid points mainly have been added along the leading edge (leading edge suction), inboard and outboard of the suction peak of the primary vortex (pressure gradient) and in the tip section of the rearward wing.

| (a) First Adaptation Step | (b) Second Adaptation Step |
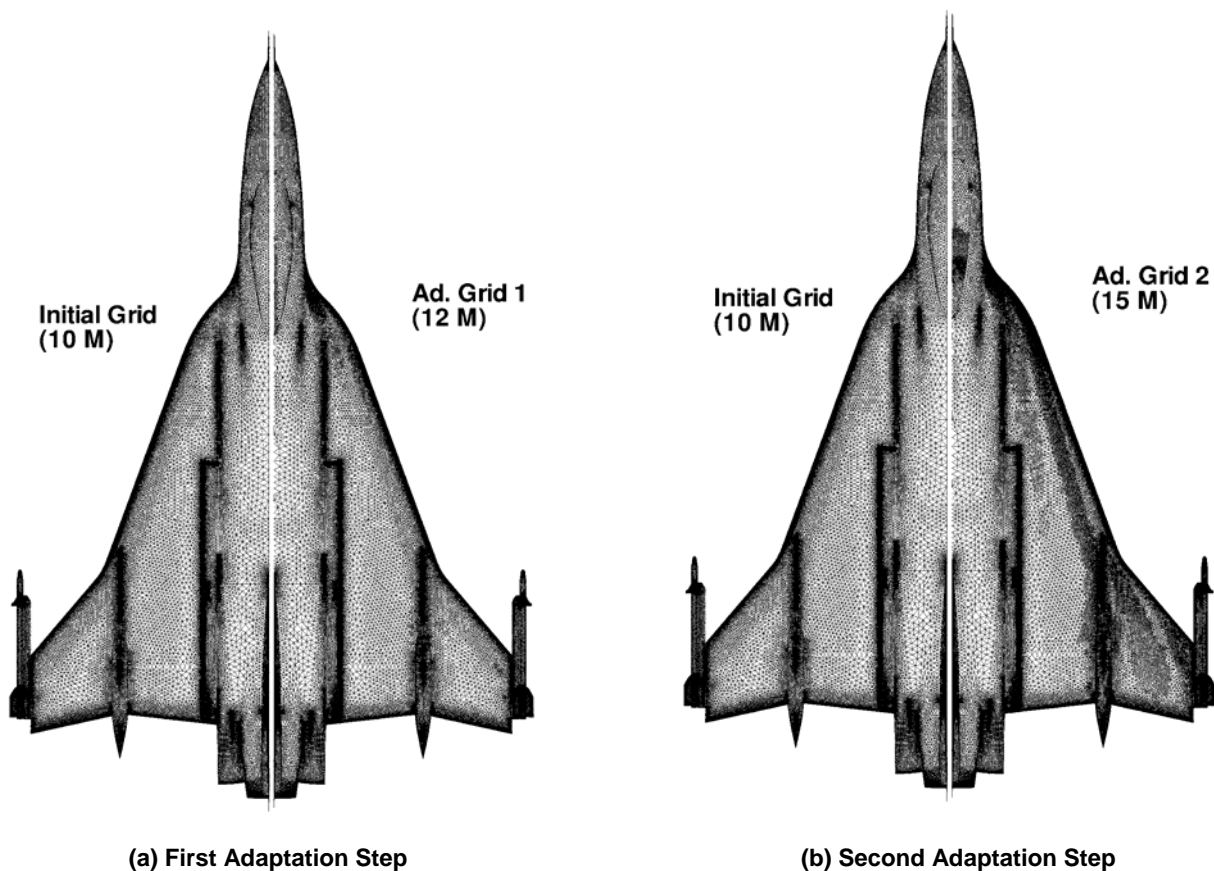
Figure 8-2: Surface Grid Adaptation for FC 25 (M_∞ = 0.242, α = 19.84°, Re = 32.22 x 10^6).

(c) Third Adaptation Step **(d) Fourth Adaptation Step**
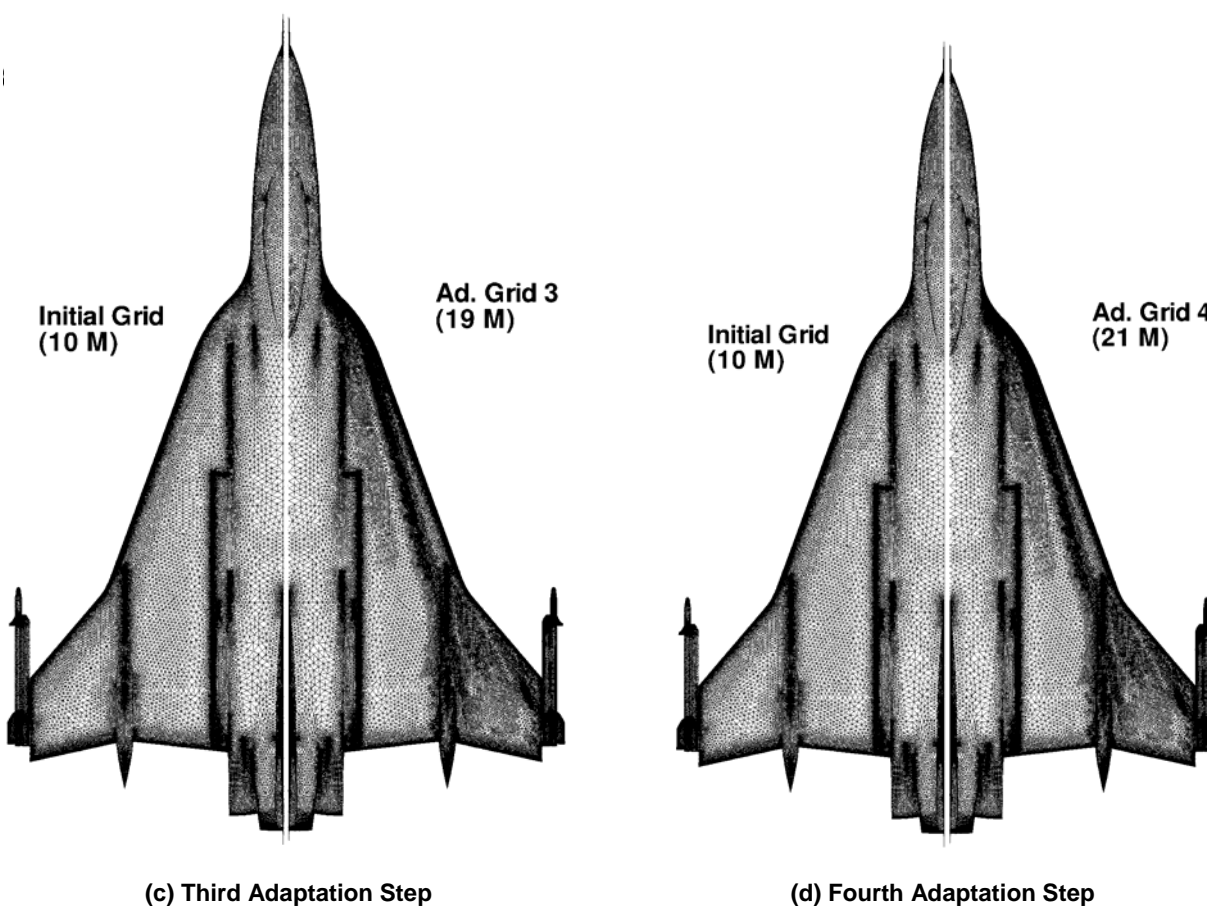
Figure 8-2: Concluded.

In space, new points have been added in regions with vortical flow above the wing (total pressure, helicity) and in the wake region behind the wing, as it is demonstrated in Figure 8-3 for FC 25 at two different cross sections.
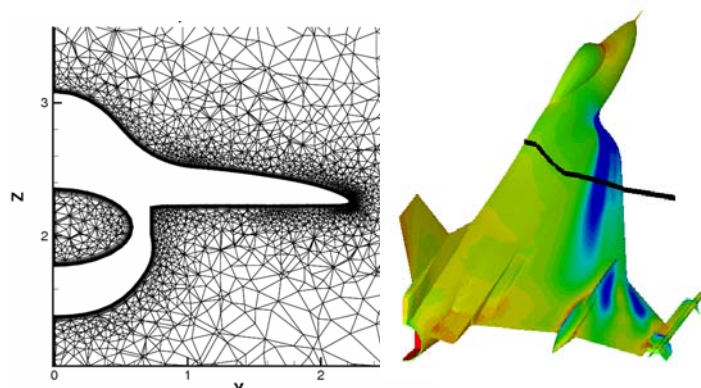
(a) Initial Grid
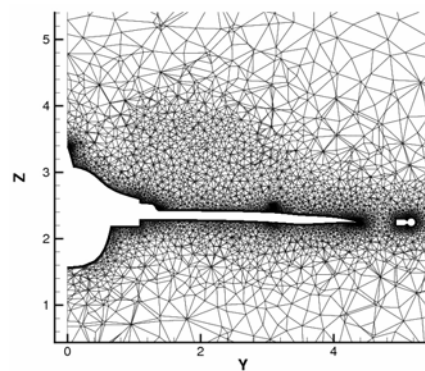
(b) Initial Grid
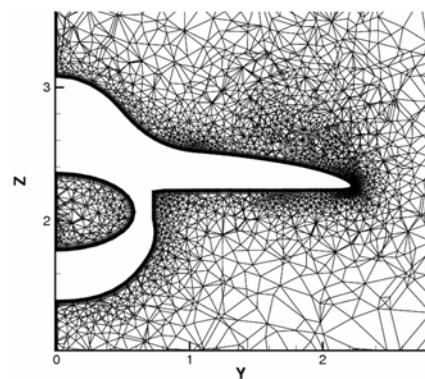
(c) First Grid Adaptation
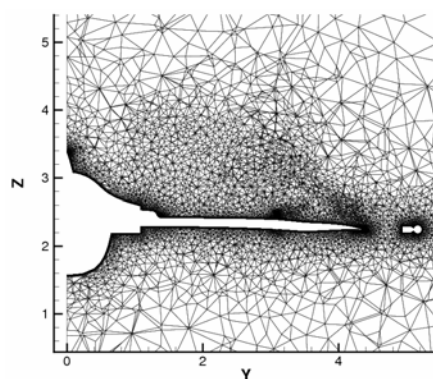
(d) First Grid Adaptation
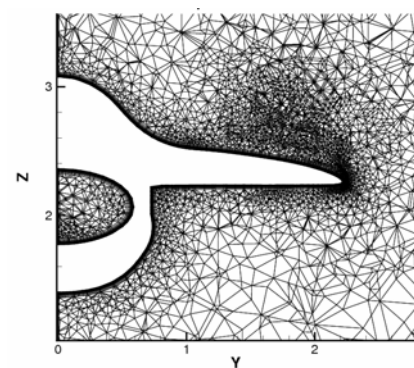
(e) Second Grid Adaptation
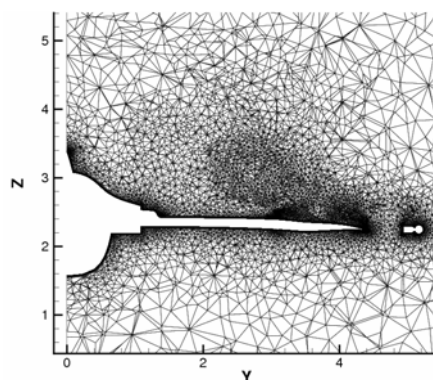
(f) Second Grid Adaptation

Figure 8-3: Field Grid Adaptation for FC 25 (M_∞ = 0.242, α = 19.84°, Re = 32.22 x 10^6).
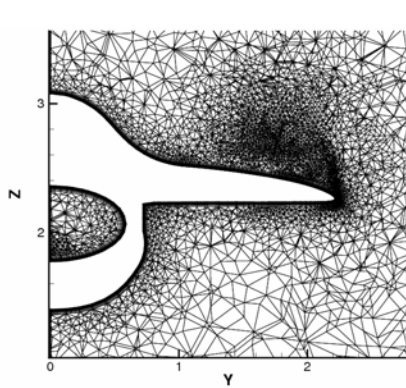
(g) Fourth (Final) Adaptation
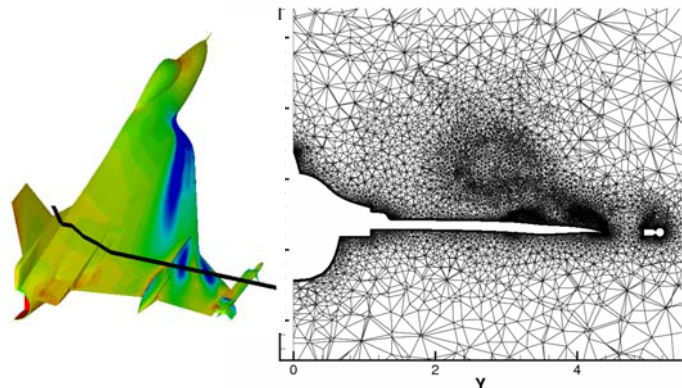
(h) Fourth (Final) Adaptation

Figure 8-3: Concluded.

Figure 8-4 shows a comparison between a so called "manually adapted" grid (left hand) and the final solution adapted grid for FC 25. In the manually adapted grid the grid points are concentrated in regions where a priori vortices were expected.

Manually adapted grid 22 x 10^6 points, 1.48 x 10^6 surface triangles

Solution adapted grid 21 x 10^6 points, 1.46 x 10^6 surface triangles

Total Pressure Contours

(b) Manually Adapted Grid at x = 11 m

Total Pressure Contours
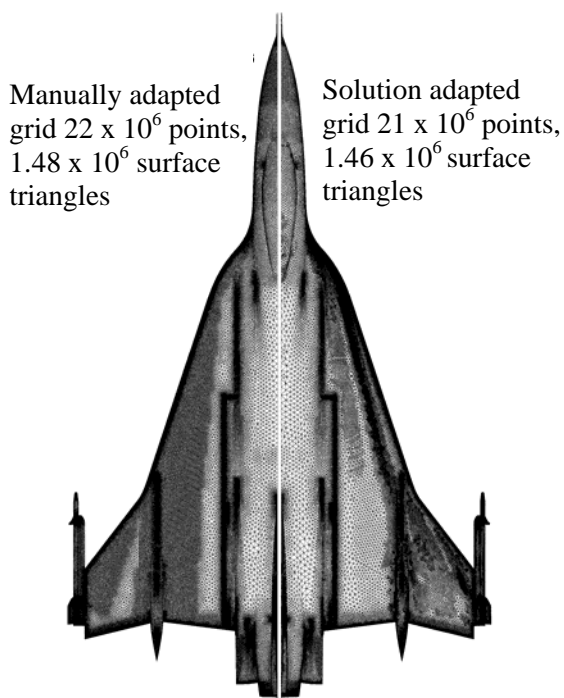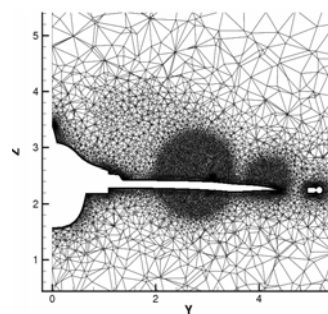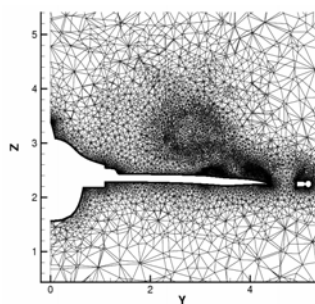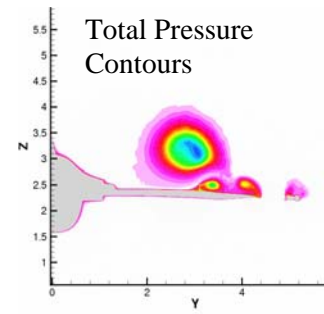
(a) Surface Grid

(c) Solution Adapted Grid at x = 11 m
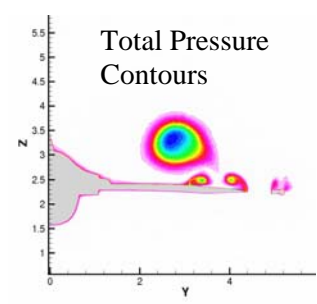
Figure 8-4: Manually and Solution Adapted Grid for FC 25 (M$_\infty$ = 0.242, α = 19.84°, Re = 32.22 x 10^6).

Both grids have approximately the same grid size and also nearly the same number of surface triangles, but the point distribution is completely different. In the flow solution for FC 25 it turned out, that the leading edge vortex moved outside of the high resolution region of the grid (Figure 8-4 (b)) and smeared out. By this the leading edge suction peaks were under predicted in the calculation. With the solution adapted grid, the vortices were caught by the grid which resulted in much more compact vortices (Figure 8-4 (c)).

Figure 8-5 illustrates the convergence of the surface pressure distribution during the four adaptation steps at two different wing sections for FC 25. Obviously the pressure distributions shift towards a final distribution. As there is nearly no difference between the result of the third adaptation and the fourth adaptation, it can be concluded, that the results after the fourth adaptation can be considered as final results.
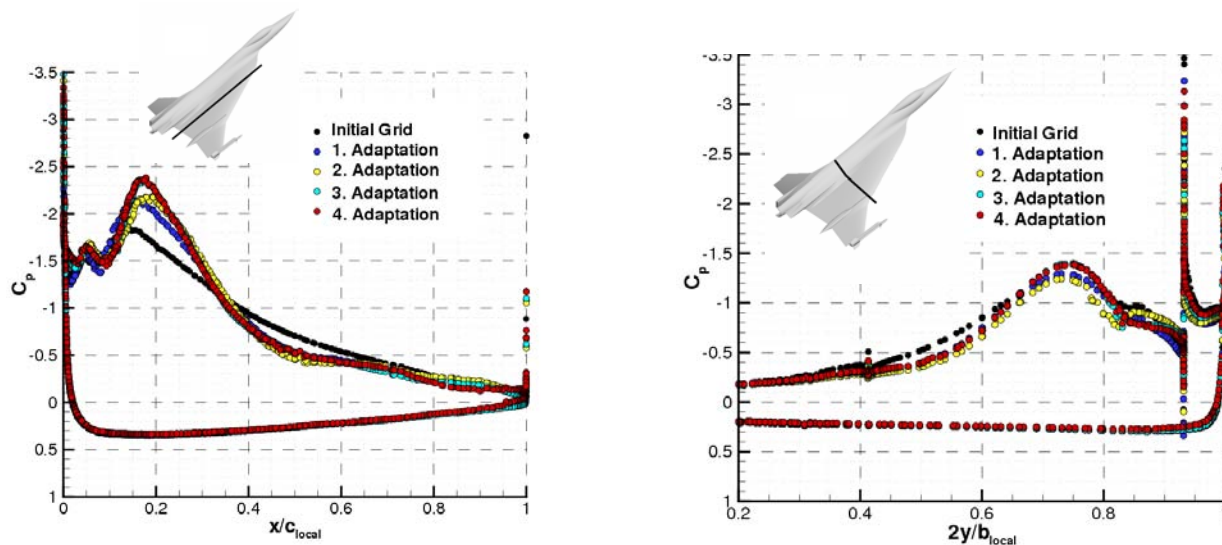
**Figure 8-5: Convergence of Surface Pressure Distribution during the
Grid Adaptation for FC 25, (M$_\infty$ = 0.242, α = 19.84°, Re = 32.22 x 10^6).**

8.6 FLOW SOLUTION

All flow solutions were obtained by the use of the DLR flow solver TAU (Refs. [8-7], [8-8]).The TAU-code is a software system consisting of several separate modules for the prediction of viscous and inviscid flows about complex geometries employing hybrid unstructured grids. In the actual calculations, the modules for pre-processing (computation of the dual grid, metrics, and connectivity), the flow solver and the adaptation module have been used. The pre-processing had to be run for each new primary grid, i.e. also after each adaptation step. The flow solver module uses an edge-based dual cell approach, where the inviscid terms are computed either by a second-order central scheme or a variety of upwind schemes. For the time integration various explicit Runge-Kutta schemes or the explicit LU-SGS (Lower-Upper Symmetric Gauss-Seidel) scheme can be employed. Convergence acceleration is achieved by a multi-grid algorithm based on agglomerated coarse grids. To allow for turbulence, different one- and two-equation turbulence models as well as DES are available.

In the actual flow calculations, the flow solver was applied with the AUSMDV upwind scheme, backward Euler implicit time integration (solved by LU-SGS), SAE one-equation turbulence model, and a 3W multi-grid convergence acceleration. For the initial solution 8000 multi-grid cycles were run and additional

4000 cycles after each adaptation step. The flow solutions were run on 32 processors of a 128/2 Linux cluster (2.6 GHz/CPU). This resulted in a CPU-time of 13h per 1000 MG-cycles and in a turnaround time of 2 – 3 weeks for each test case (starting from scratch, 4 grid adaptations, including all trial and error loops).

Some test calculations using the rotational correction of the turbulence model (SARC) have shown a considerable effect on the eddy viscosity distribution but no effect on the global flow characteristics (pressure distribution, total pressure distribution, vortical flow structure). Other experiences at EADS-MAS with similar configurations have shown that in fine grids the rotational correction limits the eddy viscosity too much, so that the solution can become unstable and has to be stabilized by high artificial viscosity. By this reason the SAE and not the SARC turbulence model was used for the calculations.

8.7   RESULTS AND DISCUSSION

8.7.1   Flight Condition 7

Figure 8-6 shows the surface pressure contours obtained in the manually adapted grid and in the final solution adapted grid (Figure 8-6 (b)). In Figure 8-6 (a) the two different grids are represented. Both grids are of similar size, but the point distribution is very different.

Manually adapted grid 22 x 10^6 points, 1.48 x 10^6 surface triangles

Solution adapted grid 20.5 x 10^6 points, 1.37 x 10^6 surface triangles

Manually adapted grid

Solution adapted grid

cp
0.30
0.20
0.10
0.00
-0.10
-0.20
-0.30
-0.40
-0.50
-0.60
-0.70
-0.80
-0.90
-1.00
-1.10
-1.20
-1.30
-1.40
-1.50

(a) Surface Grids

(b) Surface Pressure Contours
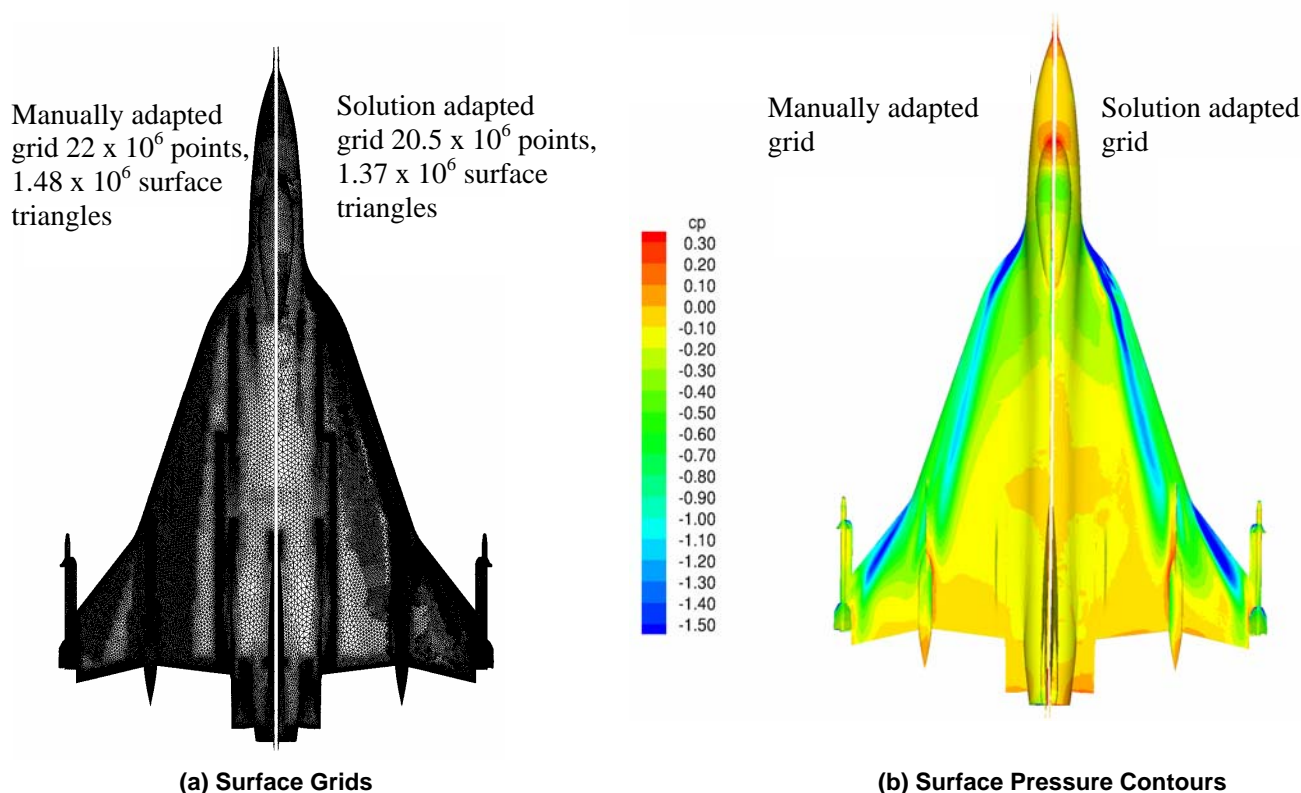
Figure 8-6: Surface Grids and Surface Pressure Contours
for FC 7 (M$_\infty$ = 0.304, α = 11.89°, Re = 44.4 x 10^6).

The solution based grid adaptation has concentrated the grid points at the wing apex, along the leading edge and inboard and outboard of the leading edge suction peak. The reason for the concentration at the wing apex

is the cropped sharp leading edge of the wing, which induces high values of the sensor function for the adaptation (at the surface and in the field).

The pressure contours of the solution adapted grid indicate stronger and more compact leading edge vortices inboard and outboard of the crank. In the apex region of the wing, the solution adapted grid shows two additional small suction peaks between the leading edge and the main leading edge vortex. This may be related to the shape of the leading edge in this region. The cropped sharp leading edge produces pressure disturbances and the finer the grid resolution, the more such disturbances appear in the solution. Or those disturbances are damped out by a high natural or numerical viscosity, as it is indicated by Figure 8-7.
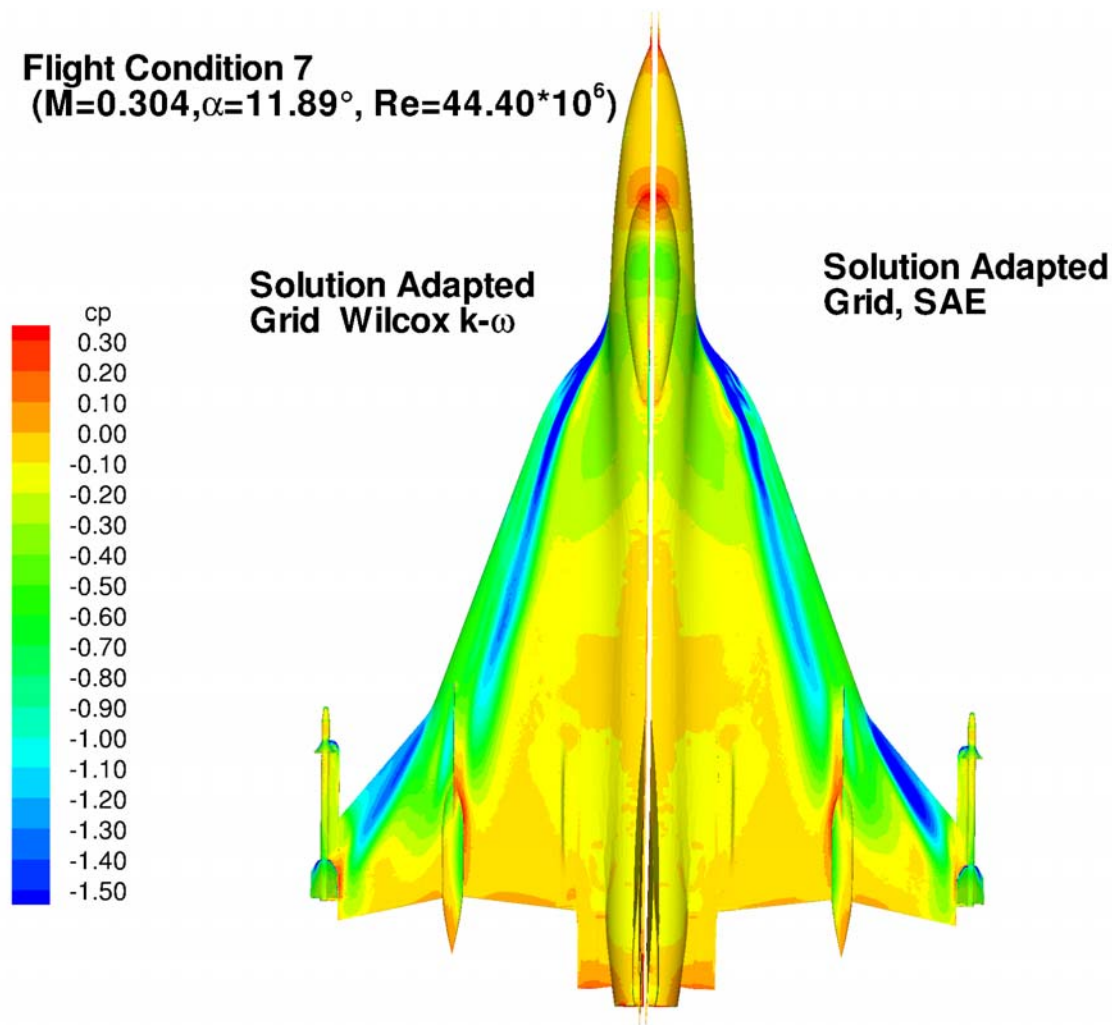
Figure 8-7: Effect of Turbulence Model on Surface Pressure Distribution at FC 7.

A solution with the Wilcox k-ω turbulence model (which is more dissipative than the SAE-model) does not show these pressure disturbances in the apex region of the wing. The k-ω model gives also a weaker leading edge vortex outboard of the crank, whereas the suction peak inboard of the crank sows no substantial difference to the SAE solution.
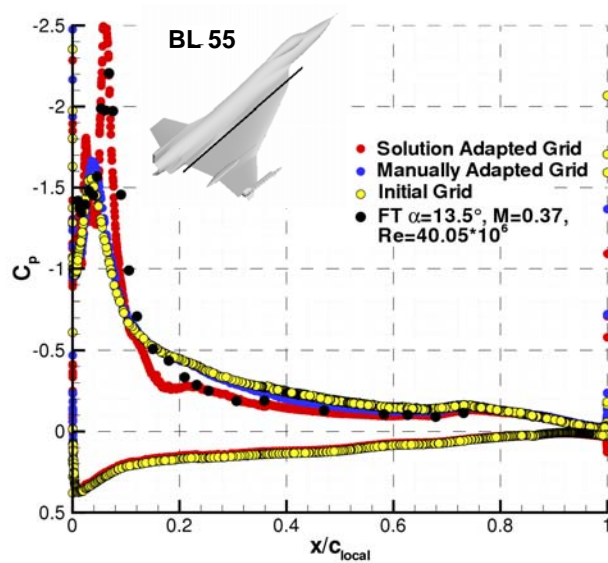
(a) BL 55
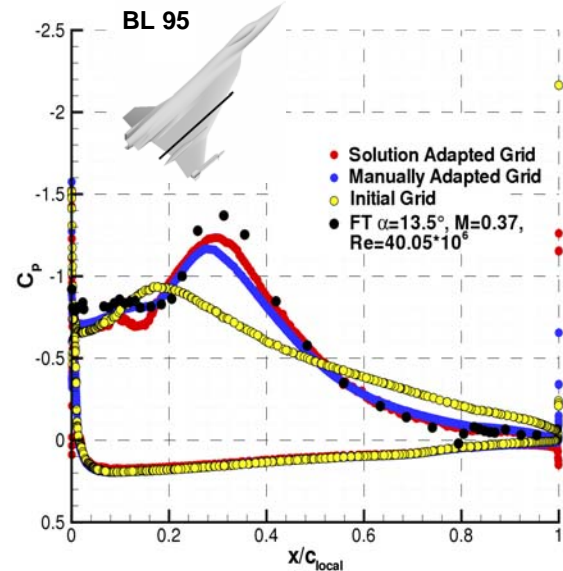
(b) BL 95
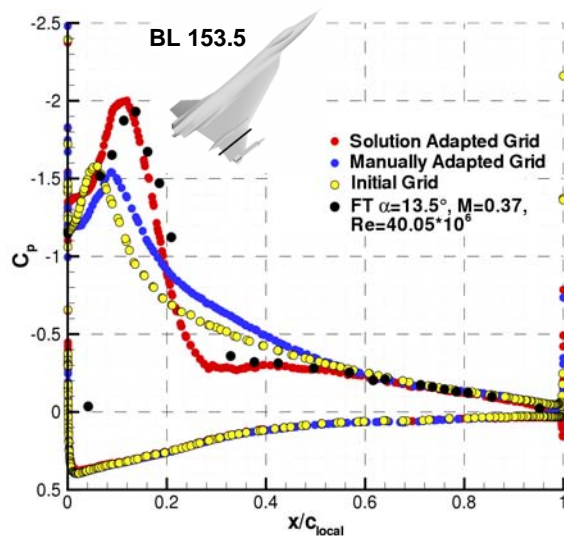
(c) BL 153.5
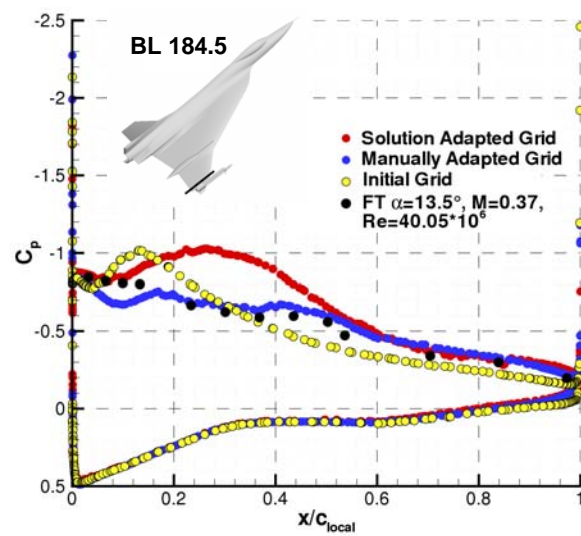
(d) BL 184.5

Figure 8-8: Surface Pressure Distributions at Wing Sections
y = constant for FC 7 (M$_\infty$ = 0.304, α = 11.89°, Re = 44.4 x 10^6).

It should be mentioned, that for FC 7 only boundary layer data but no pressure data from flight test were available. The numerical results in Figure 8-8 are therefore compared with a flight condition, which is very close to FC 7 (the substantial difference is the angle of attack, which is in the flight test 1.5 degrees higher than in the calculation). Figure 8-8 shows the results of 3 different computational grids: the initial grid (yellow symbols), the manually adapted grid of Figure 8-4 (blue symbols), and the solution based adapted grid (red

symbols). Except at the most outboard wing section, the agreement of the results oft the solution adapted grid with the flight test data is pretty good. There is a clear difference between the results of the initial grid and those of the solution adapted grid. At the section BL 95 (Figure 8-8 (b)) the results of the manually adapted grid and of the solution adapted grid are very close, but in all other sections there are considerable differences. At the section BL 55 the solution adapted grid shows this above mentioned second peak very close to the leading edge, which is not present in the flight test data.

The surface pressure distributions in two cross-sections x = constant are given in Figure 8-9. Unfortunately the flight test data points are not very dense, but Figure 8-9 indicates, that the results of the solution adapted grid give the correct position and the correct level of the leading edge suction peak. Remarkable is the clear difference between the two fine grids and the initial grid.

(a) FS 337.5   (b) FS 375
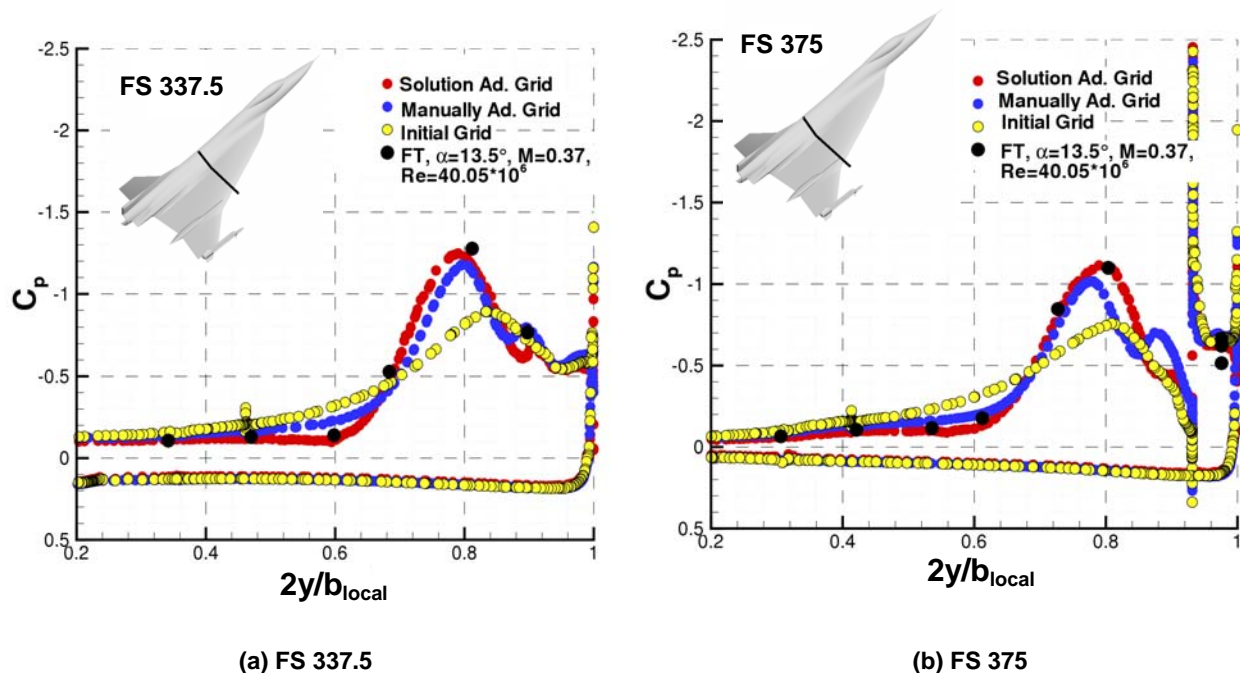
**Figure 8-9: Surface Pressure Distributions at Cross-Sections
x = constant for FC 7 (M_∞ = 0.304, α = 11.89°, Re = 44.4 x 10^6).**

Figure 8-10 shows the boundary layer comparison between the measured and predicted data at 4 different positions. (v_e is the velocity at the rake extreme total pressure tube). Rake 3 (Figure 8-10 (a)) is inboard of the primary vortex and should be in basically stream wise flow. Here the predicted data show the effect of too much turbulence and this effect is independent of the two different turbulence models. Rake 4 is beneath the primary vortex (Figure 8-10 (b)) and the agreement between experiment and numerical predictions is pretty good. The k-ω solution shows the effect of somewhat more turbulence compared to the SAE solution and the experimental results. Rake 5 and rake 7 are both outboard of the primary vortex and very close to each other. (Rake 5 is a little bit more outboard than rake 7). Whereas rake 5 shows a very good agreement between numerical and experimental data, there is a considerable defect in the predicted velocity profiles at rake 7.
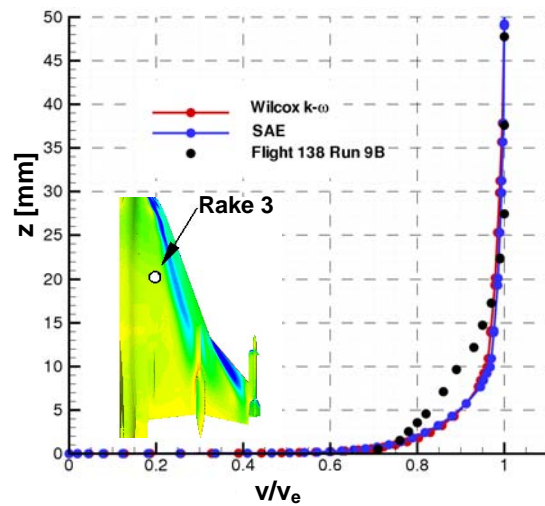
(a) Rake 3
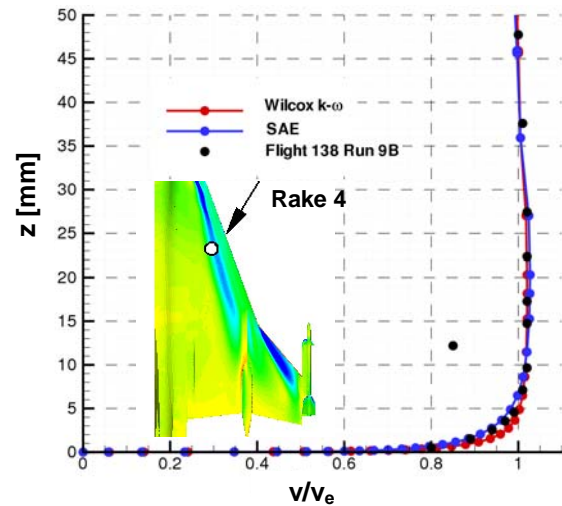
(b) Rake 4
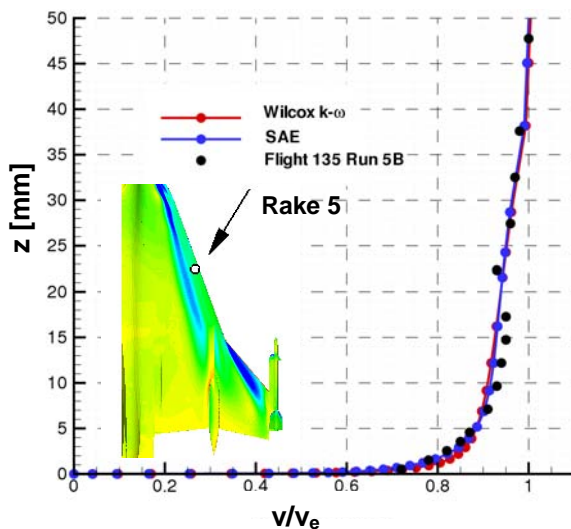
(c) Rake 5
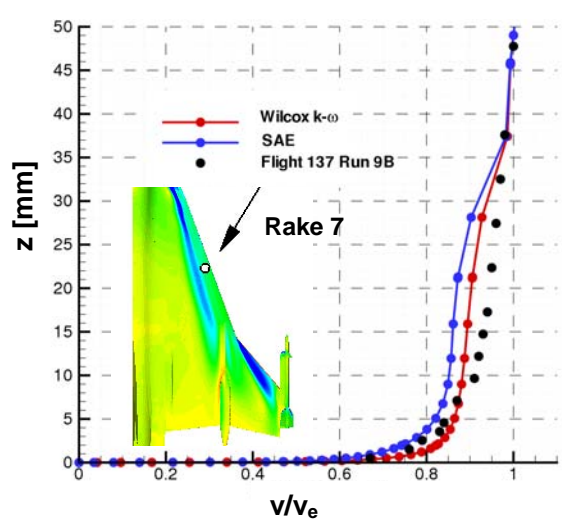
(d) Rake 6

Figure 8-10: Comparison of Boundary Layer Profiles with Flight Measurements
for FC 7 (M_∞ = 0.304, α = 11.89°, Re = 44.4 x 10^6, Solution Adapted Grid).

8.7.2   Flight Condition 19

FC 19 is very close to the previous FC 7 and thus the final adapted grid of FC 7 was also used for FC 19. Figure 8-11 shows a comparison of computed and measured local skin friction coefficient at the cross-section x = constant.
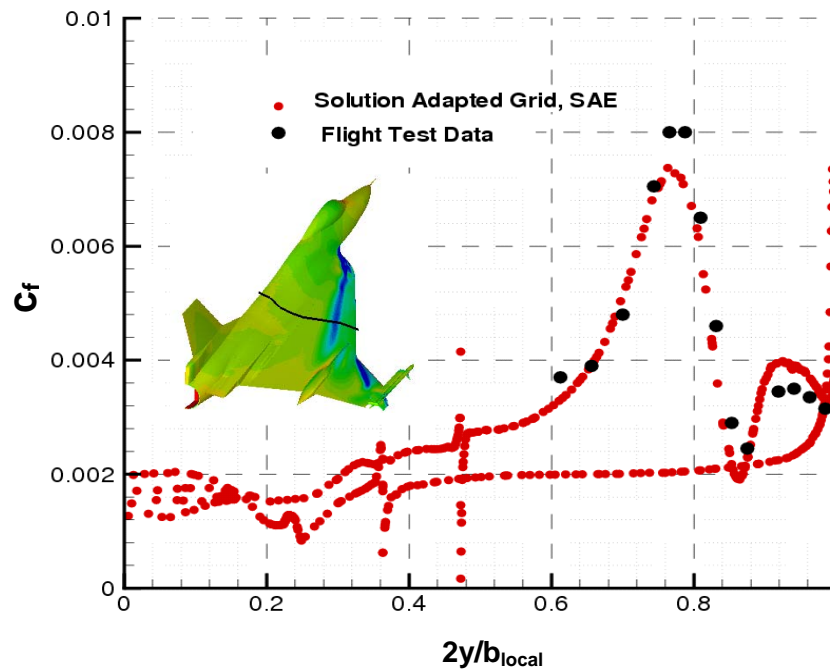
**Figure 8-11: Comparison of Predicted and Measured
c_f for FC 19 ($M_\infty = 0.36$, α = 11.85°, Re = 46.8 x 10^6).**

There are two peaks in the skin friction distribution. The smaller one, close to the leading edge, indicates the presence of a secondary vortex and the higher one indicates the presence of a primary vortex above the surface. The level associated with the primary vortex is not exactly reached by the calculation, but the span wise location is perfectly matched. The second peak is slightly over predicted.

8.7.3   Flight Condition 25

FC 25 is the flight condition with the highest angle of attack and thus a challenging test case. For this FC pressure data from flight test were available. The grids which have been used for this FC are described in the section IV.B (Solution based grid adaptation) and are shown in details in Figure 8-2, Figure 8-3, and Figure 8-4. Figure 8-12 shows the surface pressure contours obtained in the manually adapted and in the solution based adapted grid.
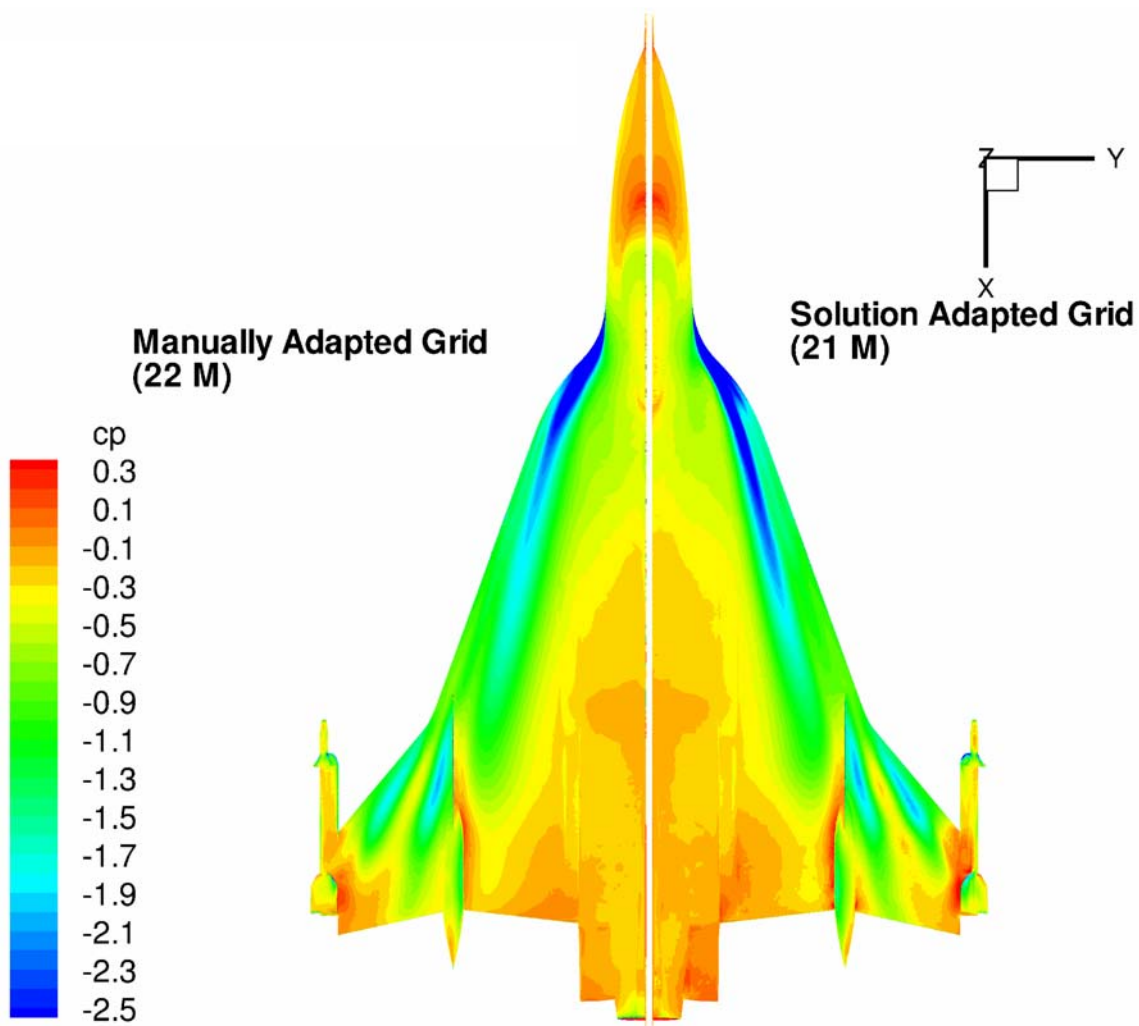
Figure 8-12: Surface Pressure Contours for FC 25 (M_∞ = 0.242, α = 19.84°, Re = 32.22 x 10^6).

The tendency is similar as it was observed for FC 7: in the solution adapted grid there is a stronger and more compact primary vortex at the inner wing. There is also a rather strong effect of the airdam. At the inboard side of the airdam and the actuator pod, there is deceleration of the flow and at the outboard side, a new vortex is generated. Considering the main primary vortex, it can not be concluded from the surface pressure contours, whether there is vortex break down or not.

Figure 8-13 shows a comparison of predicted and measured surface pressure distributions for different wing sections (BL) and cross sections (FS).
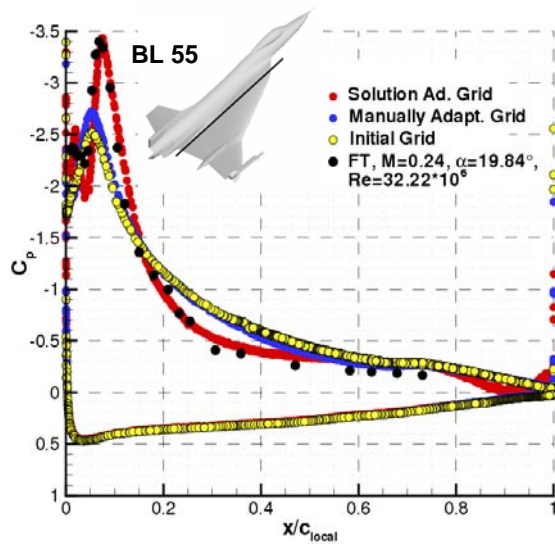
(a) BL 55
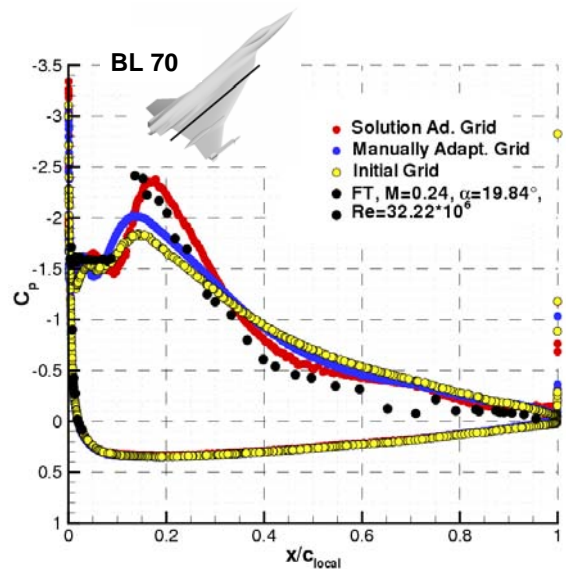
(b) BL 70
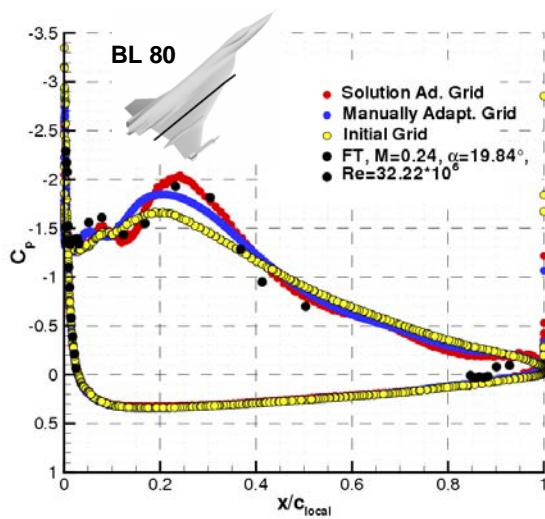
(c) BL 80
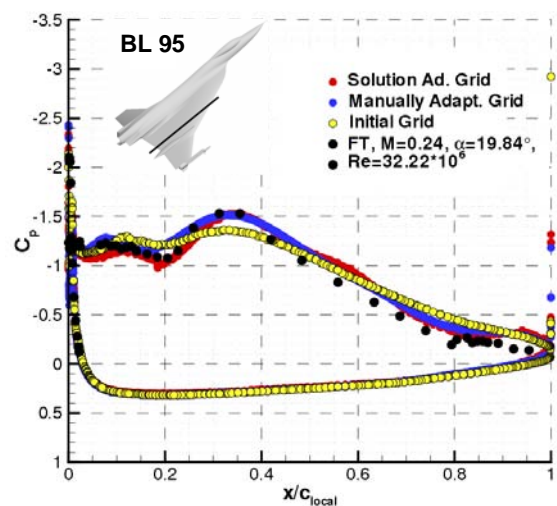
(d) BL 95

Figure 8-13: Computed and Measured Surface Pressure Distribution
at FC 25 (M_∞ = 0.242, α = 19.84°, Re = 32.22 x 10^6).
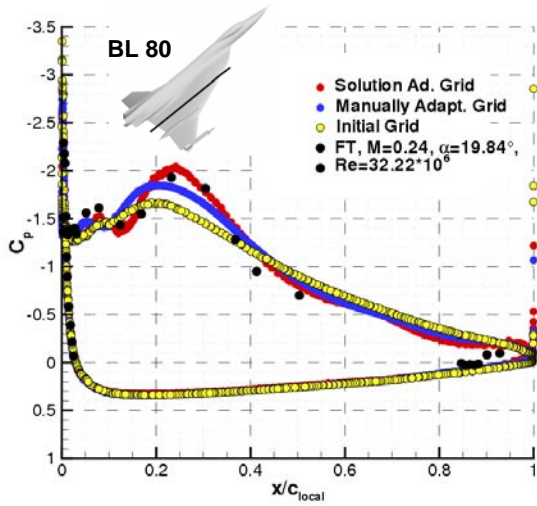
(d) BL 80
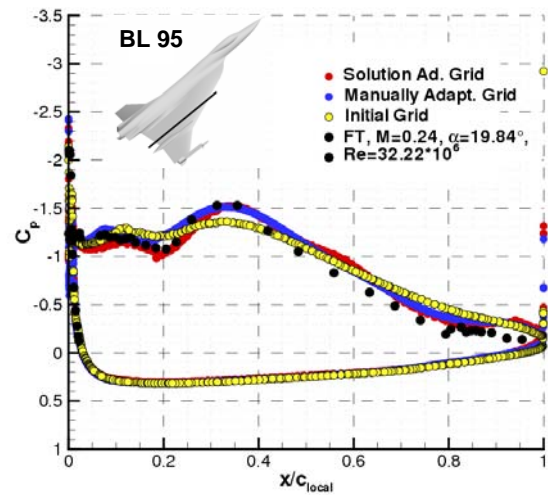
(e) BL 95
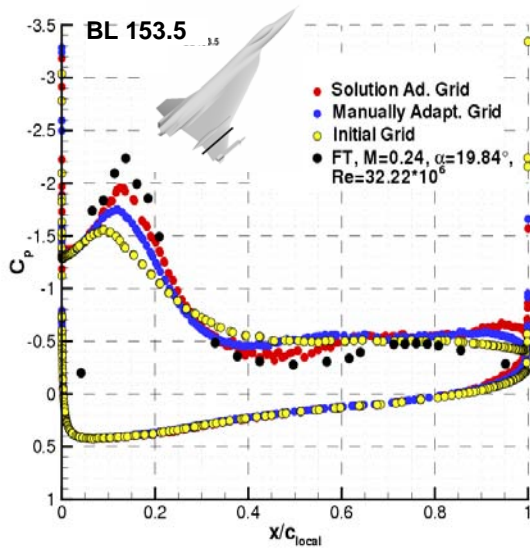
(f) BL 153.5
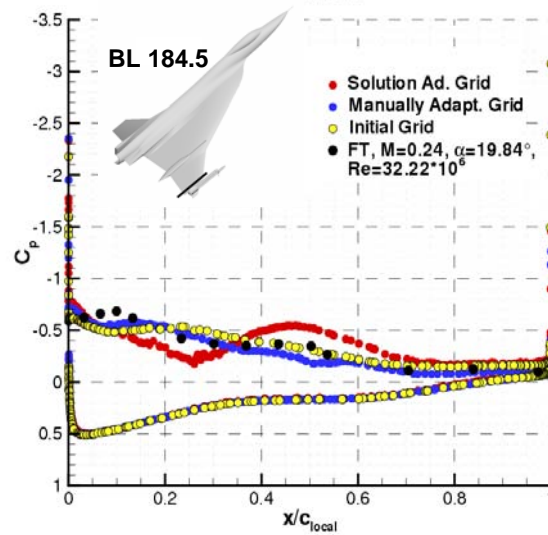
(g) BL 184.5

Figure 8-13: Continued.

(g) FS 300

(h) FS 337.5

(i) FS 375

(j) FS 450
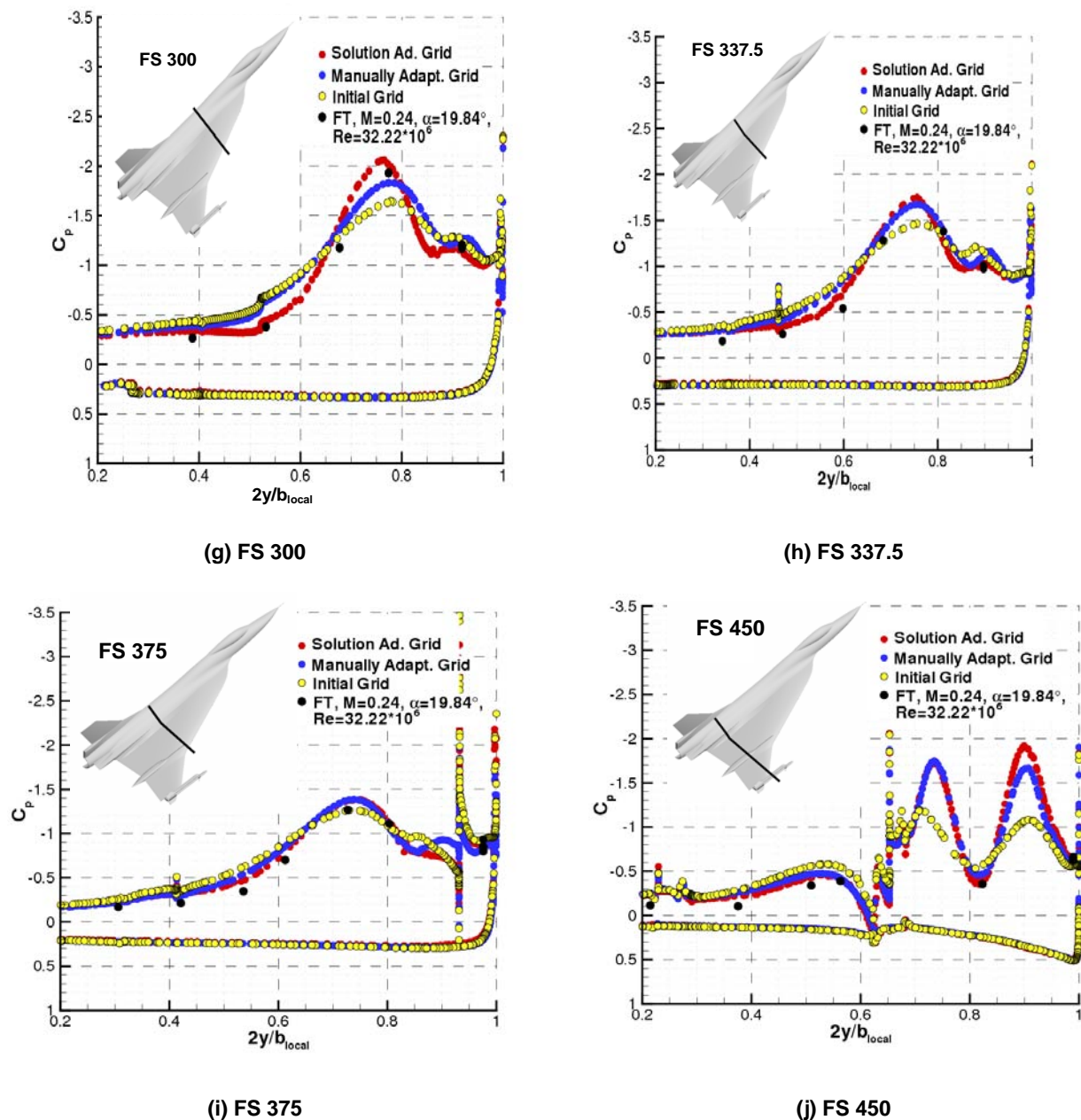
Figure 8-13: Concluded.

As can be seen, the results of the solution adapted grid show a very good agreement with the measured data. Only at BL 153.5 (Figure 8-13 (e)) there is a slight under prediction of the suction peak. The secondary vortex is also very well predicted. There are clear differences between the solution adapted grid and the other grids. The initial grid is of course not fine enough, but also the manually adapted grid with its 22 million grid points was not suitable for this FC. The reason for it is given in Figure 8-4: the leading edge vortices move outside of the high resolution region of the grid. By this the vortices weaken, which results in an under prediction of the suction peaks. In the solution adapted grid, the vortices were caught; they keep compact and are not smeared out.

The pressure distributions in the cross sections (Figure 8-13 (g), Figure 8-13 (h), and Figure 8-13 (i) show very clearly the presence of a primary and secondary vortex until to the beginning of the airdam. With the beginning of the airdam there are 3 vortices. Inboard of the airdam there is the remainder of the primary vortex, which is no longer fed by the leading edge and thus it weakens more and more. The two outboard vortices, which can also be recognized in the surface pressure contours (Figure 8-12), are induced by the airdam and by the crank in the wing.

Figure 8-14 shows the total pressure loss contours and gives some insight into the vortical structure of the flow field. At the apex of the wing a primary vortex develops, which moves inboard and upward of the wing when going in stream wise direction. Thereby the vortex core moves more and more away from the leading edge and the feeding of the vortex by the leading edge becomes weaker and weaker. With the beginning of the airdam, the primary vortex loses the connection to the leading edge and is no longer fed by it. As a consequence the primary vortex becomes weaker and dissipates downstream of the wing, but it does not look like vortex break down. (There is a continuous decrease of the total pressure loss in the vortex core, but the vortex core seems to remain compact). Due to the sidewash of the primary vortex, there is outboard directed flow at the airdam. This outboard directed flow crosses the airdam and induces a new vortex, which turns in opposite direction as the wing primary vortex. At the crank, the sharp leading edge of the outer wing induces a new primary vortex, which turns in the same direction as the wing primary vortex. Upstream of the airdam there is a secondary vortex beneath the primary vortex. Between the secondary vortex and the wing leading edge, there is another vortex. It has the same rotational direction as the primary vortex and can be considered as an elementary part of the feeding sheet of this primary vortex. Behind the wing, the airdam vortex, the outboard wing leading edge vortex and the missile induced vortices merge into one common vortex.
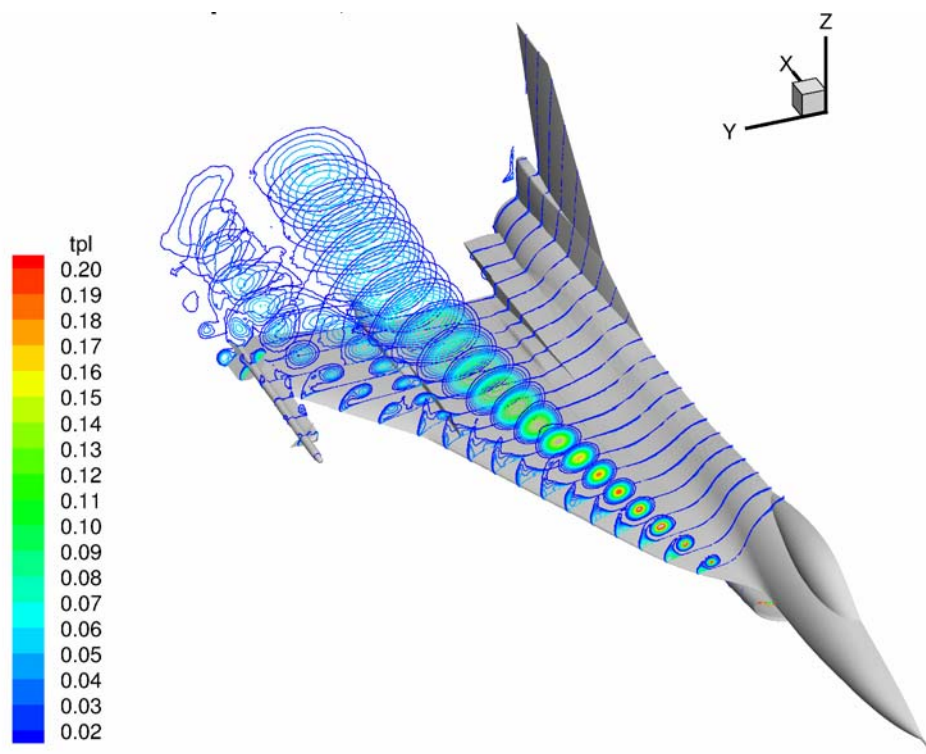
Figure 8-14: Total Pressure Loss Contours at FC 25 (M$_\infty$ = 0.242, α = 19.84°, Re = 32.22 x 10^6).

Figure 8-15 shows some more details of the flow structure at the airdam and at the actuator pod. Upstream of the airdam, the primary vortex and the secondary vortex as well as the small vortex between secondary vortex and leading edge with their separation and attachment lines can be found very clearly in the skin friction lines. Figure 8-15 also shows the interaction of the secondary vortex with the airdam more detailed. The airdam divides the secondary vortex into a small outboard part and into a main part, which remains inboard of the airdam. The outboard part merges into the airdam vortex, whereas the inboard part serves the outboard directed flow as a ramp to ease the crossing of the airdam.
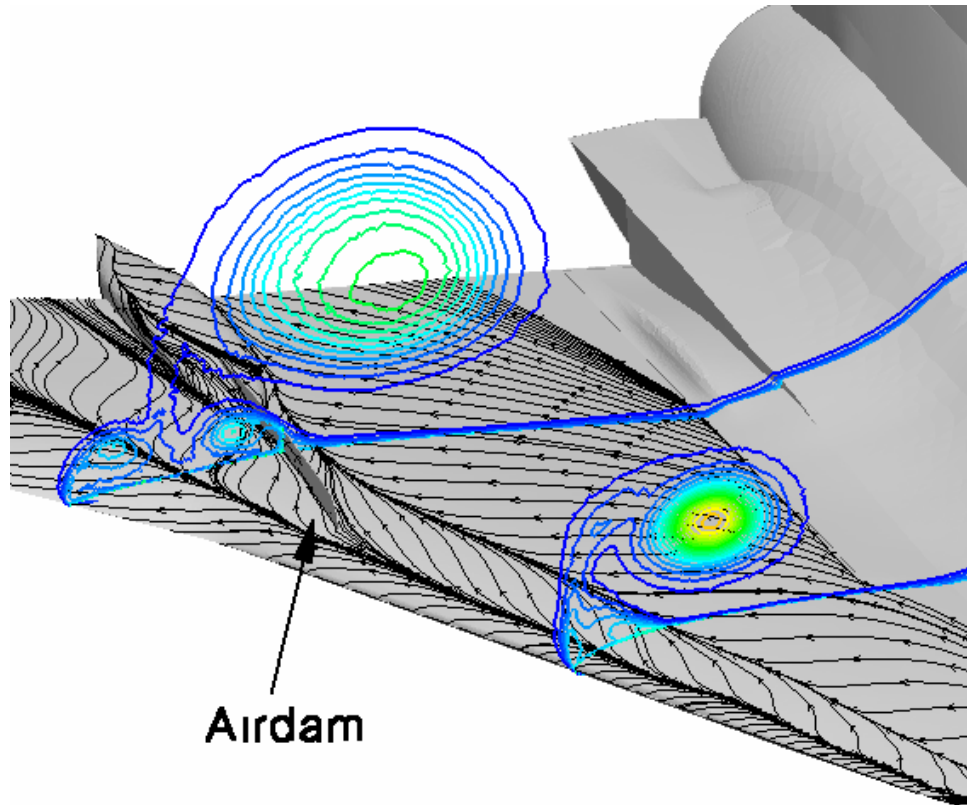
**Figure 8-15: Surface Skin Friction Lines and Total Pressure Loss
Contours at FC 25 (M$_\infty$ = 0.242, α = 19.84°, Re = 32.22 x 10^6).**

8.7.4   Flight Condition 70

This flight condition is characterized by a high, transonic Mach number, but low incidence. Thus no dominating vortical flow characteristics but transonic flow with shocks are to be expected for this test case. Also for this test case the manually adapted grid and the solution adapted grids have been employed in the calculations. The manually adapted grid and the initial grid for the adaptation are the same as for the other flight conditions. Figure 8-16 gives a comparison of the manually adapted grid and the final solution adapted grid.

Manually adapted
grid 22*10^6 points,
1.48*10^6 surface triangles

Solution adapted
grid 18.5*10^6 points,
1.35*10^6 surface triangles
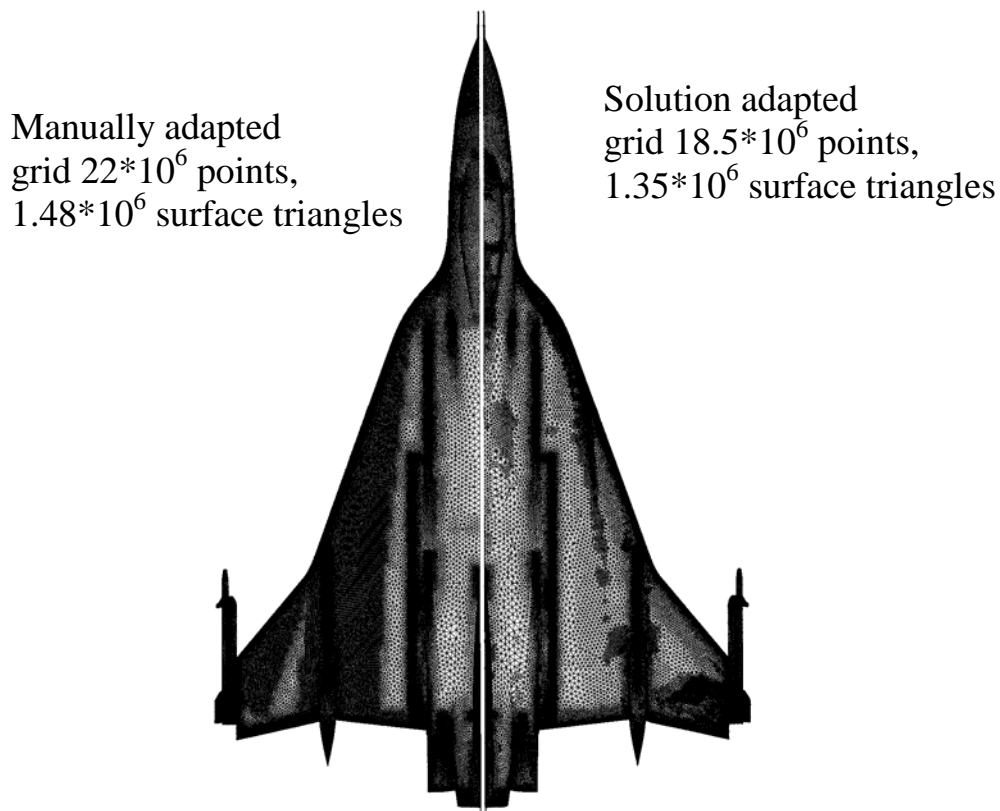
Figure 8-16: Grids for FC 70 (M$_\infty$ = 0.97, α = 4.37°, Re = 88.77 x 10^6).

The final adapted grid (right hand in Figure 8-16) does not show specific transonic flow characteristics. Points have been added in the wing apex region, along the wing leading edge, along the airdam and the actuator pod, and in the region close to the missile. Only at the canopy there is a shock-wave type concentration of grid points.

The surface pressure contours of Figure 8-17 show a surprising result: although the 3 grids are very different, there is no substantial difference in the surface pressure contours. There is a shock wave at the canopy and after the first third of the wing; both are present in the solutions of all grids. In the first third of the wing there is also the footprint of a very weak leading edge vortex. In the solution of the manually adapted grid (Figure 8-17 (b)) this vortex crosses the shock wave clearly, in all other solutions it indeed crosses the shockwave, but then it dissipates.

(a) Initial and Solution Adapted Grid

(b) Manually and Solution Adapted Grid
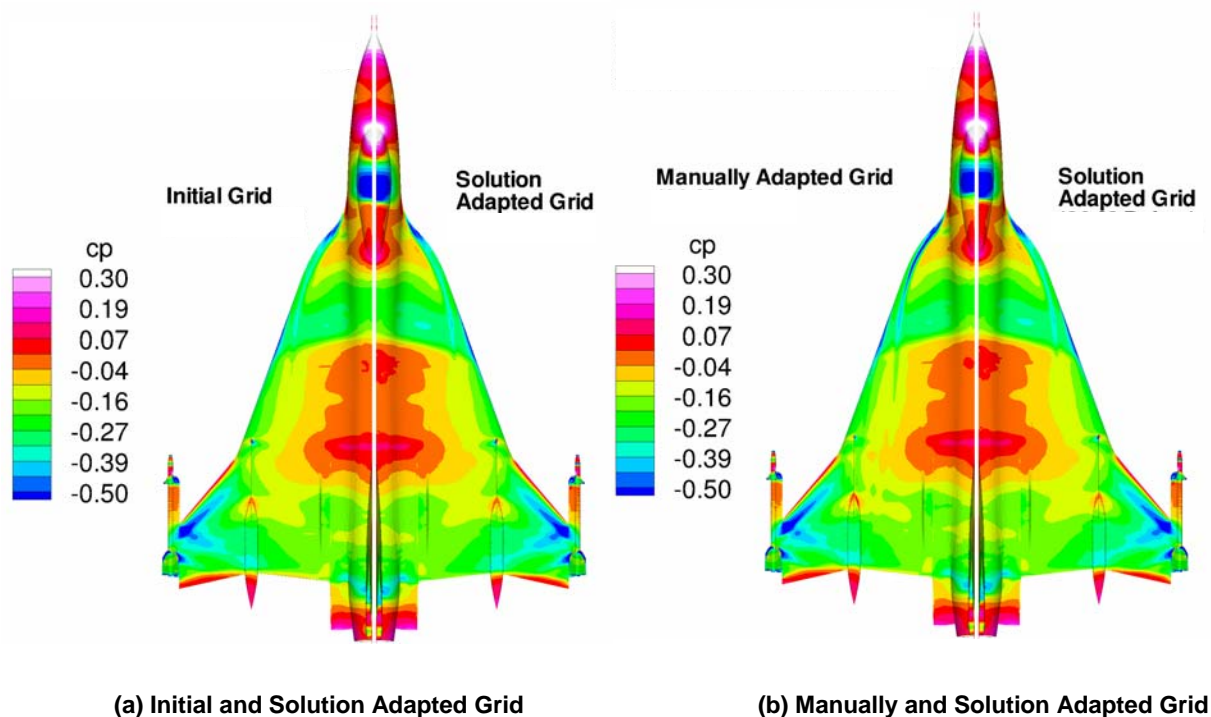
**Figure 8-17: Computed Surface Pressure Contours in Different
Grids at FC 70 (M$_\infty$ = 0.97, α = 4.37°, Re = 88.77 x 10^6).**

Figure 8-18 shows a comparison of computed and measured surface pressure distributions. It is obvious, that the pressure distributions obtained in the different grids are more or less identical and it is also obvious that except at BL 55 (Figure 8-18 (a)), the numerical data do not match the measured data. In the numerical results there is the above mentioned shock wave at the end of the first third of the wing. This shock wave can be seen in the pressure distributions at BL 55 (Figure 8-18 (a)), BL 70 (Figure 8-18 (b)), BL 80 (Figure 8-18 (c)), and BL 95 (Figure 8-18 (d)). In the measurements however a pressure rise due to a shock wave is present at BL 55 (Figure 8-18 (a)) and at BL 95 (Figure 8-18 (d)) in a more downstream position. It is not present at the intermediate sections BL 70 and BL 80 (Figure 8-18 (b), Figure 8-18 (c)). At the outer wing sections (Figure 8-18 (e) and Figure 8-18 (f)) the measured pressure distributions are very different from the computed pressure distributions. The same effect was seen in a comparison of the results of the other participants of the AVT-113 task group ([8-19] and Chapter 16): all the numerical results, although obtained in different grids and by different codes (structured, unstructured) were very close but different to the measurements. These results and the fact, that the grid adaptation has shown no substantial effect on the results indicate that there is no grid effect on the disagreement between computed and measured results.
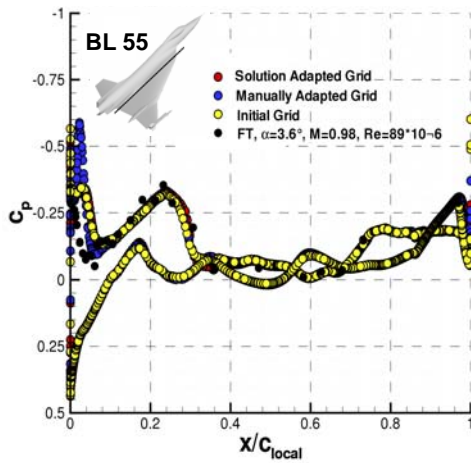
(a) BL 55
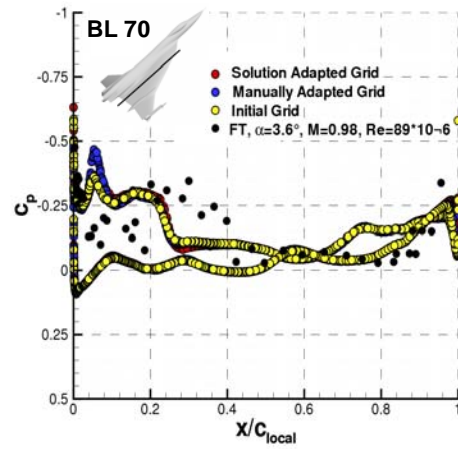
(b) BL 70
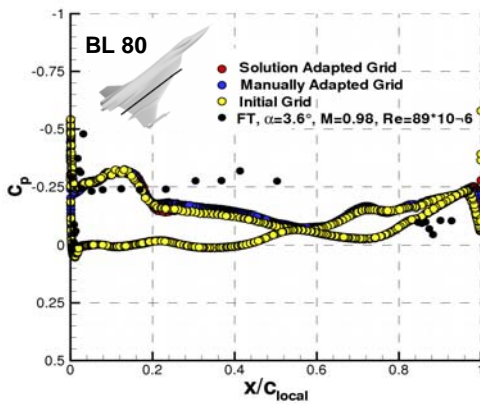
(c) BL 55
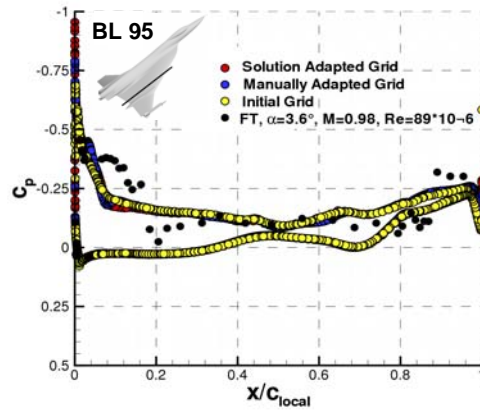
(d) BL 95
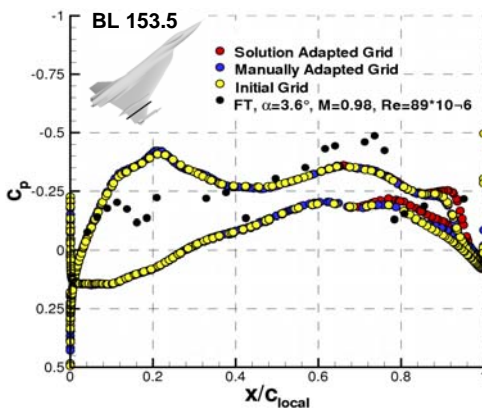
(e) BL153.5
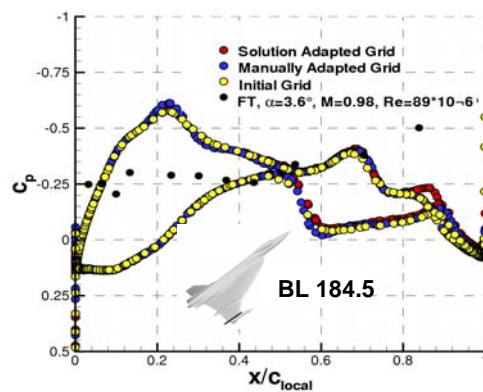
(e) BL184.5

**Figure 8-18: Computed and Measured Surface Pressure Distributions
at FC 70 (M$_\infty$ = 0.97, α = 4.37°, Re = 88.77 x 10^6).**

Figure 8-19 shows the y^+ distribution along the upper surface for FC 70. They are also in an acceptable range (values of $y^+ < 3$ are fine for the SAE turbulence model). So a defect of the grid resolution can be excluded. A defect of the flow solver can also be excluded, as all the different codes of the other participants show the same behavior for this flight condition (Ref. [8-19] and Chapter 16).
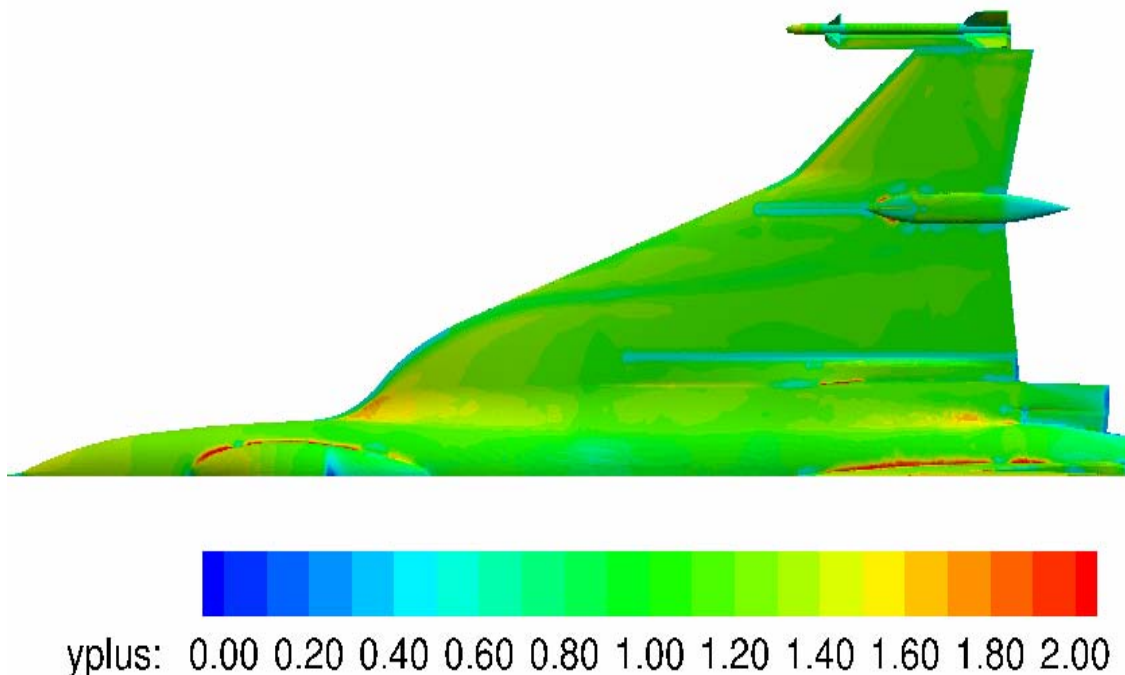
Figure 8-19: y^+ Distribution at Wing Upper Surface for FC 70 (M_∞ = 0.97, α = 4.37°, Re = 88.77 x 10^6).

8.8   CONCLUSIONS

With the framework of CAWAPI, it has been demonstrated, that flow field data measured on the F-16XL fighter aircraft can be predicted by CFD. The presented results underline, that all essential data like pressure distribution, velocity profiles, and skin friction coefficients can be predicted within a satisfactory accuracy (except for FC 70).The results also demonstrate, that that the solution based grid adaptation is a very powerful tool in order to get an optimum grid for a complex configuration and in order to fix grid dependencies in the solution.

But the static, sequential grid adaptation (computing the flow solution, adapting the grid, new pre-processing, new flow solution, etc.) as it was applied in the present study, is a very tedious task and requires some experience and several trial and error loops. For extensive numerical studies at complex configurations (e.g. computation of the aerodynamic control characteristics of a complete fighter aircraft) this kind of grid adaptation is not very suitable, as it requires a complicated solution- and grid bookkeeping and the necessary manual work leads to long turn-around times.

But in any case the solution based grid adaptation can help to generate an optimal pre-refined grid for a certain configuration, which then can be used for a wide range of flow conditions.

8.9   ACKNOWLEDGEMENTS

8.10   REFERENCES

[8-1]   Fournasier, L., Rieger, H., Tremel, U. and van der Weide, E.: *Time-Dependent Aeroelastic Simulation of Rapid Manouevring Aircraft*, AIAA Aerospace and Sciences Meeting and Exhibit, 2002, Reno, NV, CP949.

[8-2]   Sørensen, K.A., Tremel, U., Rieger, H. and Hitzel, S.M.: *Simulation of Manoeuvring Fighter Aircraft with the Unstructured Chimera Approach*, AIAA-2007-0123, Presented at 45th AIAA Aerospace Sciences Meeting and Exhibit, Reno, NV, January 8-11, 2007.

[8-3]   Lamar, J.E., Obara, C.J., Fisher, B.D. and Fisher, D.F.: *Flight, Wind-Tunnel and Computational Fluid Dynamics Comparison for Cranked Arrow Wing (F-16XL-1) at Subsonic and Transonic Speeds*, NASA TP-2001-210629, 2001.

[8-4]   Lamar, J.E. and Obara, C.J.: *Review of Cranked-Arrow Wing Aerodynamics Project: Its International Aeronautical Community Role*, AIAA-2007-487, Presented at 45th AIAA Aerospace Sciences Meeting and Exhibit, Reno, NV, January 8-11, 2007.

[8-5]   Boelens, O.J., Görtz, S., Morton, S., Fritz, W. and Lamar, J.E.: *Description of the F-16XL Geometry and Computational Grids Used in CAWAPI*, AIAA-2007-488, Presented at 45th AIAA Aerospace Sciences Meeting and Exhibit, Reno, NV, January 8-11, 2007.

[8-6]   CentaurSoft Grid Generator, http://www.centaursoft.com (cited 10 June 2008).

[8-7]   Gerhold, T., Friedrich, O., Evans, J. and Galle, M.: *Calculation of Complex Three-Dimensional Configurations Employing the DLR-TAU Code*, AIAA-97-0167, 1997.

[8-8]   Schwamborn, D., Gerhold, T. and Kessler, R.: *The DLR-TAU Code – an Overview*, ONERA-DLR Aerospace Symposium, CP ODAS 99, 21-24 June 1999, Paris, France.

[8-9]   Alrutz, T. and Rütten, M.: *Investigation of Vortex Breakdown over a Pitching Delta Wing Applying the DLR TAU-Code with Full, Automatic Grid Adaptation*, AIAA-2005-5162.

[8-10]   Boelens, O.J., Spekreijse, S.P., Systma, H.A. and de Cock, K.M.J.: *Comparison of Measured and Simulated Flow Features for the Full-Scale F-16XL Aircraft*, AIAA Paper 2007-0489, Presented at 45th AIAA Aerospace Sciences Meeting and Exhibit, Reno, NV, January 8-11, 2007.

[8-11]   Badcock, K.J.: *Evaluation of Results from a Reynolds Averaged Multiblock Code Against F-16XL Flight Data*, AIAA Paper 2007-0490, Presented at 45th AIAA Aerospace Sciences Meeting and Exhibit, Reno, NV, January 8-11, 2007.

[8-12]   Elmiligue, A.A., Abdol-Hamid, K.S. and Massey, S.J.: *PAB3D Simulations for the CAWAPI F-16XL*, AIAA Paper 2007-0491, Presented at 45th AIAA Aerospace Sciences Meeting and Exhibit, Reno, NV, January 8-11, 2007.

[8-13] Morton, S.A., McDaniels, D.R. and Cumming, R.M.: *F-16XL Unsteady Simulations for the CAWAPI F-16XL Facet of RTO Task Group AVT-113*, AIAA Paper 2007-0493, Presented at 45th AIAA Aerospace Sciences Meeting and Exhibit, Reno, NV, January 8-11, 2007.

[8-14] Görtz, S. and Jirásek, A.: *Unstructured Steady/Unsteady Solutions with Edge for CAWAPI F-16XL at KTH/FOI*, AIAA Paper 2007-0678, Presented at 45th AIAA Aerospace Sciences Meeting and Exhibit, Reno, NV, January 8-11, 2007.

[8-15] Michal, T., Oser, M., Mani, M. and Ross, F.: *BCFD Unstructured-Grid Predictions on the F-16XL (CAWAPI) Aircraft*, AIAA Paper 2007-0679, Presented at 45th AIAA Aerospace Sciences Meeting and Exhibit, Reno, NV, January 8-11, 2007.

[8-16] Davis, M.B., Reed, C. and Yagle, P.: *Hybrid Grid Solutions on the (CAWAPI) F-16XL Using Falcon v4*, AIAA Paper 2007-0680, Presented at 45th AIAA Aerospace Sciences Meeting and Exhibit, Reno, NV, January 8-11, 2007.

[8-17] Karman, S., Michell, B. and Sawyer, S.: *Unstructured Grid Solutions of CAWAPI F-16XL by UT SimCenter*, AIAA Paper 2007-0681, Presented at 45th AIAA Aerospace Sciences Meeting and Exhibit, Reno, NV, January 8-11, 2007.

[8-18] Lamar, J.E. and Abdol-Hamid, K.S.: *USM3D Unstructured Grid Solutions for CAWAPI at NASA LaRC*, AIAA Paper 2007-0682, Presented at 45th AIAA Aerospace Sciences Meeting and Exhibit, Reno, NV, January 8-11, 2007.

[8-19] Rizzi, A., Badcock, K.J., Jirásek, A. and Boelens, O.J.: *What was Learned from Numerical Simulations of F-16XL (CAWAPI) at Flight Conditions*, AIAA Paper 2007-0683, Presented at 45th AIAA Aerospace Sciences Meeting and Exhibit, Reno, NV, January 8-11, 2007.

Chapter 9 – NUMERICAL SOLUTIONS FOR THE CAWAPI CONFIGURATION ON UNSTRUCTURED GRIDS AT USAFA, UNITED STATES

by

Scott Morton, David R. McDaniels, Russell M. Cummings

9.1 SUMMARY

This work represents the USAF Academy portion of a culmination of three years of cooperative research in the Cranked Arrow Wing Aerodynamics International (CAWAPI) RTO Task Group, AVT-113. The objective of the group was to compute high resolution CFD simulations of a subset of the conditions created in the CAWAP flight test program managed by NASA Langley researchers and others. Seven flight conditions were chosen with four of them at symmetric conditions of medium to high angle of attack and subsonic Mach numbers, one symmetric condition at a transonic low angle of attack condition, and two conditions at medium angle of attack and subsonic Mach number but with positive and negative sideslips. The emphasis of the USAF Academy team was to explore unsteady effects and the ability of current methods to predict them. Very good agreement with flight test was found in almost all cases and the unsteadiness was documented with flowfield visualization and unsteady surface pressure coefficient data.

9.2 INTRODUCTION

The Cranked-Arrow Wing Aerodynamics Project (CAWAP) provided the computational fluid dynamic (CFD) community with an excellent database for complex aerodynamic validation and verification [9-1][9-2]. A number of researchers simulated the flowfield of the F-16XL at a variety of flight test conditions using different numerical approaches, including structured, block, and unstructured grids, as well as various turbulence models and numerical algorithms. This type of full-scale aircraft configuration provides many challenges to state-of-the-art CFD flow prediction, including the ability to accurately predict unsteady flowfields at flight Reynolds numbers.

While advances have taken place in areas such as grid generation and fast algorithms for solutions of systems of equations, CFD has remained limited as a reliable tool for prediction of inherently unsteady flows at flight Reynolds numbers. Current engineering approaches to prediction of unsteady flows are based on solution of the Reynolds-averaged Navier-Stokes (RANS) equations. The turbulence models employed in RANS methods necessarily model the entire spectrum of turbulent motions. While often adequate in steady flows with no regions of reversed flow, or possibly exhibiting shallow separation, it appears inevitable that RANS turbulence models are unable to accurately predict flows characterized by massive separation. Unsteady, massively separated flows are characterized by geometry-dependent and three-dimensional turbulent eddies. These eddies, arguably, are what defeat RANS turbulence models from predicting flows of any complexity.

To overcome the deficiencies of RANS models for predicting massively separated flows, Spalart et al. [9-3] proposed Detached-Eddy Simulation (DES) with the objective of developing a numerically feasible and accurate approach combining the most favorable elements of RANS models and Large Eddy Simulation (LES). The primary advantage of DES is that it can be applied at high Reynolds numbers, as can Reynolds-averaged techniques, but DES also resolves geometry-dependent, unsteady three-dimensional turbulent

motions as in LES. The unstructured finite-volume solver Cobalt [9-4] has been used in conjunction with DES successfully on a number of complex problems, including a supersonic base flow [9-5], delta wing vortex breakdown [9-6][9-7], the F-15E at high angle of attack [9-8], the F/A-18E with unsteady shock buffet [9-9], and the F/A-18C with tail buffet [9-10].

The specific aim of this work is to perform time accurate calculations for flow over the F-16XL at full-scale flight Reynolds numbers, and to document the effects of applying DES at conditions consistent with complex flow phenomenon. Understanding the unsteady flowfield can lead to improved knowledge about the flight characteristics of aircraft that can be overlooked by steady RANS or unsteady RANS (URANS) calculations. While unsteady CFD predictions of full-scale aircraft are relatively expensive to perform, their value has been shown to be important in many of the studies referenced above. Abrupt wing stall [9-9], for example, could not have been predicted using a URANS CFD approach, and the aerodynamics of maneuvering aircraft cannot be adequately predicted without the use of a hybrid RANS/LES approach. A brief overview of the turbulence models and numerical methods used is presented, as is a detailed look at the determination of the appropriate time steps for the unsteady calculations. Results show that there are several flow features of the F-16XL that are predicted correctly using an unsteady approach.

9.3   SOLUTION METHOD

9.3.1   Flow Solver

Computations were performed using the commercial flow solver *Cobalt* [9-4]. *Cobalt* is a cell-centered, finite volume CFD code. It solves the unsteady, three-dimensional, compressible Reynolds Averaged Navier-Stokes (RANS) equations on hybrid unstructured grids. Its foundation is based on Godunov's first-order accurate, exact Riemann solver. Second-order spatial accuracy is obtained through a Least Squares Reconstruction. A Newton sub-iteration method is used in the solution of the system of equations to improve time accuracy of the point-implicit method. Strang et al [9-4] validated the numerical method on a number of problems, including the Spalart-Allmaras model, which forms the core for the Detached Eddy Simulation (DES) model available in *Cobalt*. Tomaro et al [9-11] converted the code from explicit to implicit, enabling CFL numbers as high as 10^6. Grismer et al [9-12] parallelized the code, with a demonstrated linear speed-up on as many as 4,000 processors. The parallel Metis (ParMetis) domain decomposition library of Karypis et al [9-13] is also incorporated into *Cobalt*. New capabilities include rigid-body and 6 DOF motion, equilibrium air physics, and overset grids. A coupled aeroelastic simulation capability is also being developed.

9.3.2   Numerical Grid and Boundary Conditions

The baseline unstructured grid was generated by researchers at the NASA Langley Research Center using the grid generation packages *GRIDTOOL* [9-14] and *VGRIDNS* [9-15]. The grid is a half-span all-tetrahedral mesh with a viscous inner region made up of high aspect ratio cells and a nearly isotropic outer inviscid region. The grid has 2,534,132 nodes and 14,802,429 cells and is based on a CAD representation of the full-scale model of the F-16XL-1 with all control surfaces set to zero deflection. The surface of the half-span model of the F-16XL is discretized with 160,266 triangular elements (see Figure 9-1).
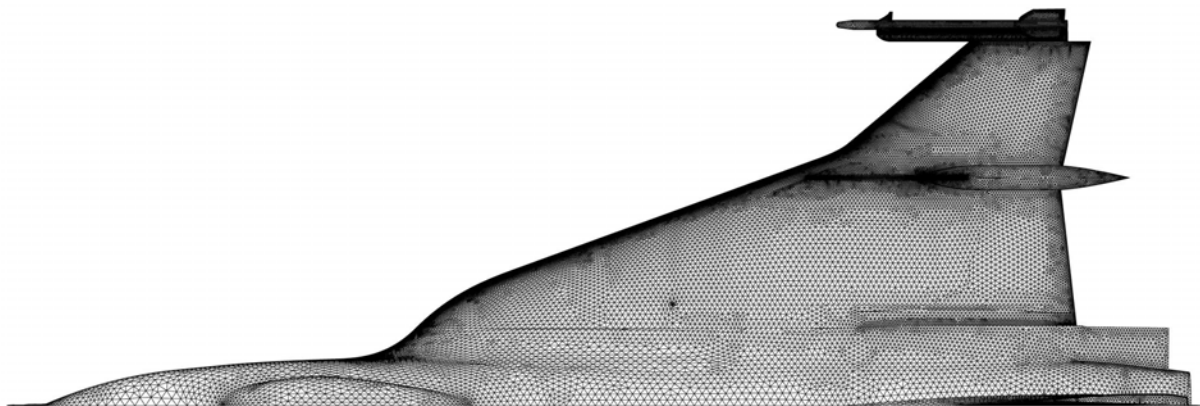
Figure 9-1: F-16XL-1 Half-Span Model Surface Grid (160,266 Faces).

Many flow solvers require the initial layers of cells off of the surface to be prisms or hexahedra to improve numerics. The all tetrahedral grid was converted to a hybrid mesh with inner layers of prisms by recombining the highly stretched inner layers of tetrahedra into prisms. The software used to convert the initial mesh into a hybrid grid was the utility program BLACKSMITH [9-16] from Cobalt Solutions, LLC. BLACKSMITH reduced the cell count to a total of 11,928,103, corresponding to 2,535,842 nodes, by combining highly stretched tetrahedral cells into prismatic cells. The program generated 9 layers of prismatic cells, corresponding to 1,442,394 prisms. Although there are additional layers of cells in the viscous region, these layers are not complete around the entire aircraft and would require "end caps" of pyramids to match up with the tetrahedral cells of the outer region.

To allow simulation of engine effects at the inlet and nozzle exit, the engine duct is meshed all the way to the compressor face plane and the nozzle is meshed from the engine mixing plane (see Figure 9-2). The grid density off the aircraft surface is shown in Figure 9-3, which depicts a crinkle cutting plane through the grid at FS496 close to the trailing edge.
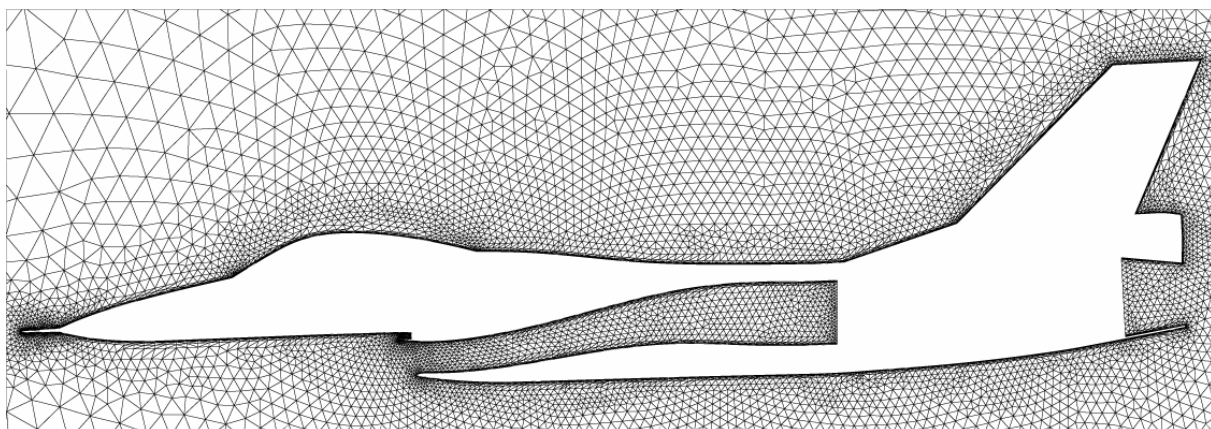
Figure 9-2: Symmetry Plane of the F-16XL-1 Baseline Unstructured Grid.

Figure 9-3: Crinkle Cut Plane through the Grid at FS496
(Fuselage Station on Airplane in Inches, Positive Aft).

The boundary conditions for the half-span computations are symmetry, adiabatic solid wall for the aircraft surface and the engine inlet duct, and modified Riemann invariants for the far-field boundaries. A source boundary condition based on Riemann invariants is used to create an inflow condition at the engine exhaust. A sink boundary condition is used at the engine compressor face to model the mass flow into the engine.

9.4   RESULTS

There are seven CAWAP flight conditions chosen by the CAWAPI RTO Task Group as candidates for comparison (summarized in Table 9-1). Flight conditions 7, 19, 25, 46, and 70 are assumed to be symmetric conditions and only half-span grids are used in the computations, although there is up to a +0.725 and -0.133 degree sideslip error in the assumption as noted in Table 9-1. Flight conditions 7, 19, and 46 are medium angle-of-attack conditions at various subsonic Mach numbers and altitudes, whereas, flight condition 70 is a low angle of attack condition at a transonic Mach number of 0.97. Although the Reynolds number essentially doubles (to 88.8 million) for flight condition 70, the normal spacing of the grid points above the surface in the viscous region is still within a y+ of one for the grid developed for all of the flight conditions. Flight conditions 50 and 51 are medium angle-of-attack conditions at sideslips of +5.31 and -4.58 degrees, respectively, and a mirrored full-span grid created from the baseline grid was used.

Table 9-1: Subset of CAWAP Flight Conditions Chosen for CAWAPI

CAWAPI Flight Conditions						
FC#	**Mach**	**Altitude (ft)**	**AOA (deg)**	**Beta Actual (deg)**	**Beta Comp (deg)**	**Re#**
7	0.304	5,000	11.89	-0.133	0	4.44E+07
19	0.36	10,000	11.85	0.612	0	4.68E+07
25	0.242	10,000	19.84	0.725	0	3.22E+07
46	0.527	24,000	10.4	0.684	0	4.69E+07
70	0.97	22,300	4.37	0.310	0	8.88E+07
50	0.434	24,000	13.56	5.310	5.31	3.94E+07
51	0.441	24,000	12.89	-4.580	-4.58	3.90E+07

All solutions were computed using the software *Cobalt* version 3.0 from Cobalt Solution L.L.C. installed on the Department of Defense High Performance Computing Modernization Program computer systems. Steady-state solutions and initiation of time-accurate solutions were computed using the Reynolds-Averaged Navier-Stokes (RANS) turbulence model of Spalart-Allmaras with Rotation Corrections (SARC), 1st order-accuracy in time, and a time step commensurate with a CFL number of one million. Time accurate solutions were computed with the Detached-Eddy Simulation hybrid RANS-Large Eddy Simulation turbulence model with SARC as the underlying RANS model. A time-step study was conducted to determine the proper time step for the flight condition and grid combination used for this study and is the subject of the next section.

All of the computations were run on 128 to 256 CPUs on two different supercomputing systems at the Aeronautical Systems Center Major Shared Resource Center (ASC MSRC) at Wright-Patterson Air Force Base in Ohio. The initial solutions (mainly FC7) were accomplished on "hpc9", a Compaq SC-45 with 836 Alpha EV6.8 processors running at 1 GHz and running the True64 UNIX operating system. A total of 836 GB of distributed memory was available, and each processor has access to 8 TB of hard disk space. This machine was decommissioned on September 30th, 2006. The balance of the solutions were accomplished on "falcon", a 2,048-processor AMD Opteron (2.8 GHz) cluster with 1,024 XC Compute Nodes (2 processors/node) connected with Infiniband Interconnect. Each node has 4GB of memory (4TB total) with access to 97 TB of local disk space. The machine has a peak performance of 11.5 TeraFLOPS.

Nominally, each solution (corresponding to a flight condition from Table 9-1) was initialized by accomplishing 3,000 flow solution iterations with 2nd order spatial accuracy, 1st order time accuracy with the time step size determined by the global minimum CFL number, and 1 Newton subiteration per time step. For the half-span solutions, this required 17.6 seconds per iteration on hpc9 (880 CPU hrs, 6.88 hrs of wall clock time on 128 procs) and 10.2 seconds per iteration on falcon (510 CPU hrs, 3.98 hrs of wall clock time on 128 procs). From these initial solutions, at least 6,000 additional iterations were performed with a specified time step size and 2nd order spatial and temporal accuracy with 3 Newton subiterations. These runs required 38.9 seconds per iteration on hpc9 and 20.9 seconds per iteration on falcon for the half-span solutions. The full span solutions (FC50/51) required 42.3 seconds per iteration on falcon. These timings varied depending on whether or not time-accurate flow solution files were requested. Typically, the last 2,000 iterations of each run were time-averaged to compute the average solution values in the results, and time-accurate flow solution files were exported every

5 time steps during this time period. The unsteady bounds shown in the results were determined by interrogating these flow solution files.

There are several major features of the F-16XL that contribute to the aerodynamic phenomena to be discussed in this section. The wing is a cranked arrow wing with a leading edge sweep of 70 degrees prior to the crank and 50 degrees in the post crank outer wing region. The wing leading edge is blended to the fuselage with an s-curve shape to aid in high angle of attack pitch characteristics [9-1]. There is also an actuator pod just inboard of the crank and an air dam protruding forward of the actuator pod. Finally, there is an AIM-9 missile attached to the wing-tip pylon.

In the subsequent sections, data will be presented with the nomenclature of butt line (BL) and fuselage stations (FS). The coordinate system used for analyzing the flight and CFD data is x measured aft, y measured out the right wing, and z measured up, with an origin near the nose of the aircraft. The BL is an x-z plane at a constant y coordinate and the numerical designation gives the distance from the symmetry plane to the BL plane measured in inches. The FS is a y-z plane at a constant x coordinate and the numerical designation gives the distance from the nose region to the FS plane measured in inches.

9.4.1   Time Step Study

In order to accurately predict unsteady flows about the F-16XL, both a good grid and a proper time step is required. Of course, "good" and "proper" are relative terms that need to be examined in light of the flow features of interest. If the computation is trying to resolve vortical flow features, the grid of a particular fineness coupled with a specific time step may be adequate. If the computation is trying to resolve smaller turbulent structures, then a finer grid with a smaller time step may be necessary. Figure 9-4 shows the various Strouhal numbers (dimensionless frequency defined as $Sn = fc/U_\infty$) that regularly occur in aerodynamic flowfields [9-17], which can aid in finding a good "starting" time step, based on the flow feature of interest.
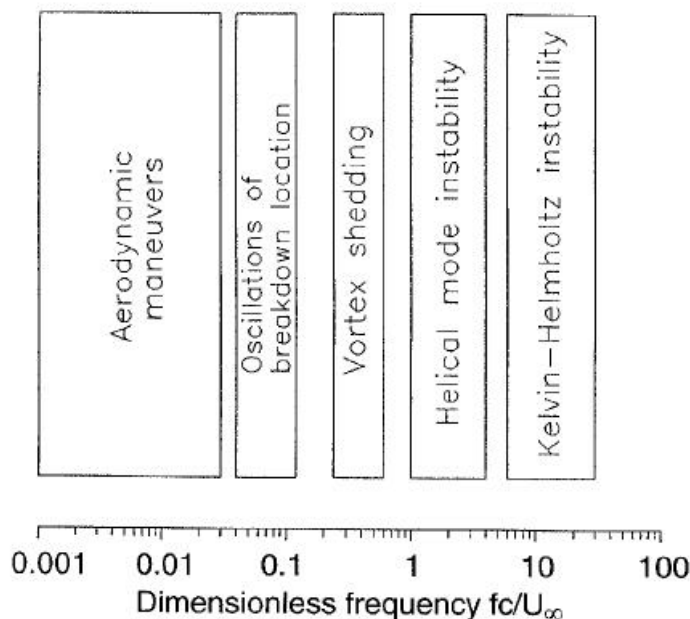
Figure 9-4: Spectrum of Unsteady Flow Phenomena (Ref. [9-17]).

In order to determine the appropriate time step for the numerical simulations of the F-16XL, a study was carried out for the unsteady flowfield above the wing. Figure 9-5 shows the variation of power spectral density of the normal force on the aircraft as a function of time at seven time steps, Δt = 0.00500, 0.00250, 0.00100, 0.00050, 0.00010, and 0.00005 seconds. These time steps were chosen based on the rule of thumb that aerodynamic features of interest are usually "visible" at non-dimensional time steps of approximately $\Delta t^* = 0.01$ ($\Delta t^* = \Delta t\, U_\infty / c$).
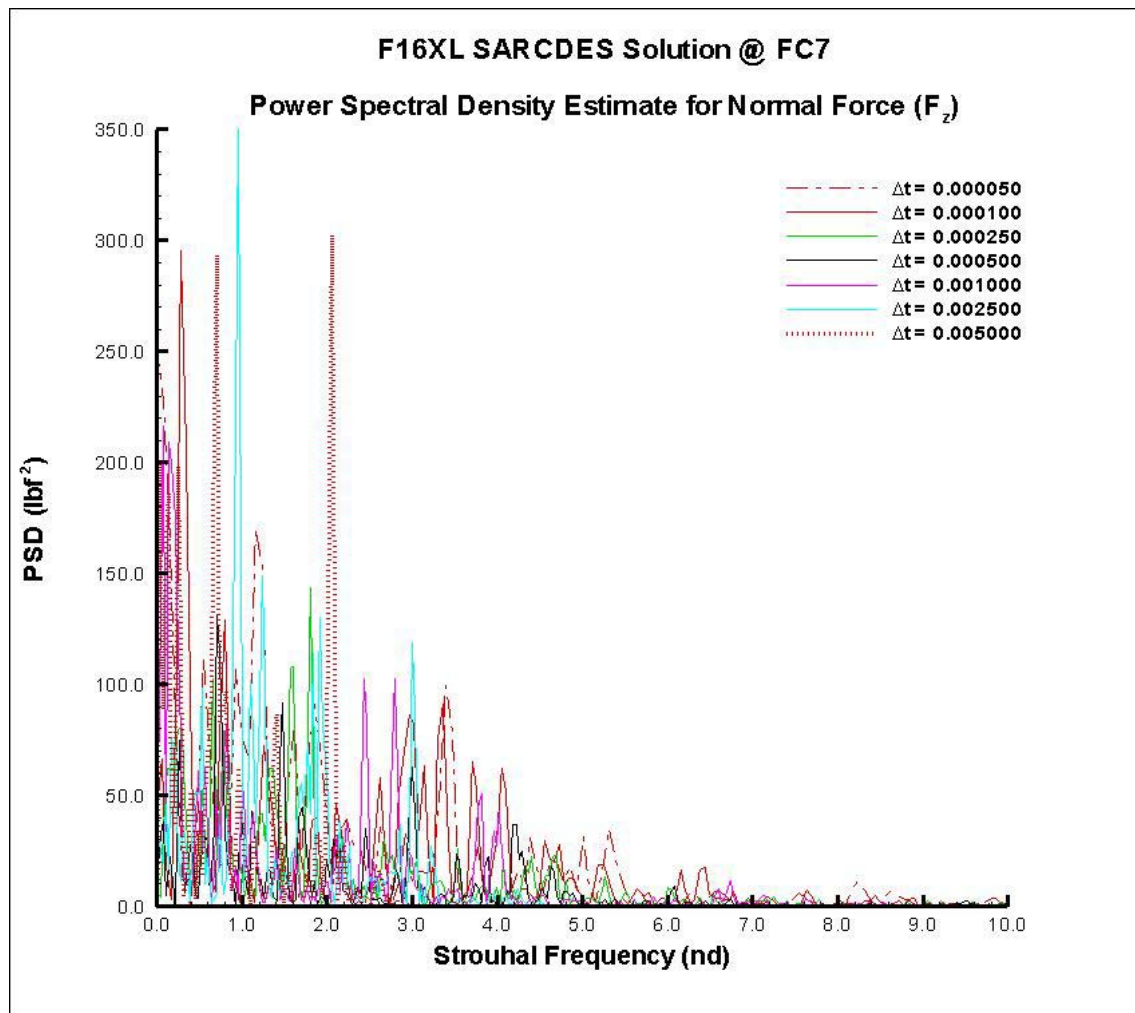
Figure 9-5: PSD of Normal Force Variation with Time at Various Time Steps.

The computations were all performed for the same physical time (1.0 second) by varying the number of iterations for each time step, and each computation was completed with three Newton sub-iterations. An additional side study was accomplished at a time step of 0.005 seconds to determine if simulating the flow field for a longer physical time (up to 3.0 seconds) affected the frequency content of the flow. No significant changes in the power spectral density results were evident. As shown in Figure 9-5, the resulting dominant Strouhal number does not show a definite trend with time step: if the dominant frequency were "converging" with decreasing time step then a lower time step would be required. However, in this case, there is no definite

trend with time step. Based on our experience in predicting these flows [9-18], this trend leads to the conclusion that the integrated normal force is "masking" a number of different flow features that are all contributing to the frequency content shown in Figure 9-5 (multiple vortices, possible vortex breakdown, flow separation regions, etc.). Because of this, we have found that taking detailed flow "measurements" within the flowfield region of interest is the only way to properly determine the primary frequencies and appropriate time steps. Therefore, a series of "pressure taps" were located in the flow, as shown in Figure 9-6, as well as Table 9-2. Figure 9-6 shows the complexity of the flowfield in the region of interest, where a primary leading-edge vortex intersects with the air dam vortex, as well as the creation of another leading-edge vortex at the wing crank. Figure 9-4 shows the pressure tap locations used in the time step study.

(a)   (b)
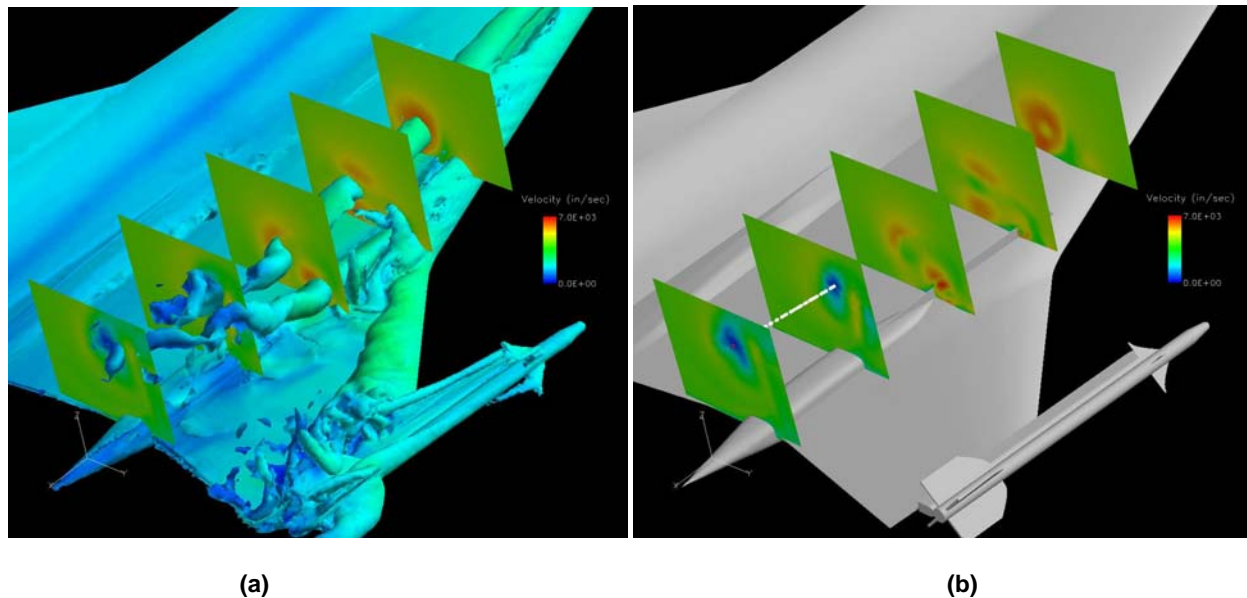
**Figure 9-6: (a) Iso-Surfaces of X-Vorticity and Velocity Cutting Planes;
(b) Velocity Cutting Planes and Pressure Tap Locations (white dots).**

Table 9-2: Pressure Tap Location in Region of Interest

Tap #	X (in)	Y (in)	Z (in)
1	470	124	125
2	475.39	123.326	125.135
3	480.11	122.736	125.253
4	484.941	122.132	125.374
5	491.13	121.359	125.528
6	495.509	120.811	125.638
7	499.788	120.277	125.745
8	504.74	119.657	125.869
9	510	119	126

Each time step was run with the pressure tap locations "collecting" data as a function of time. These pressures were then used to perform PSD calculations for each time step. A representative set of results is shown in Figure 9-7, which is the power spectral density at pressure tap #1. As can be seen, as the time step is decreased, the primary frequency begins to take place at a common frequency, which we consider time step "convergence." Similar results take place at pressure tap #2, but as the more aft pressure taps were evaluated, the flow became much less coherent, without any obvious primary frequencies (as can be seen in Figure 9-7 for tap #1).
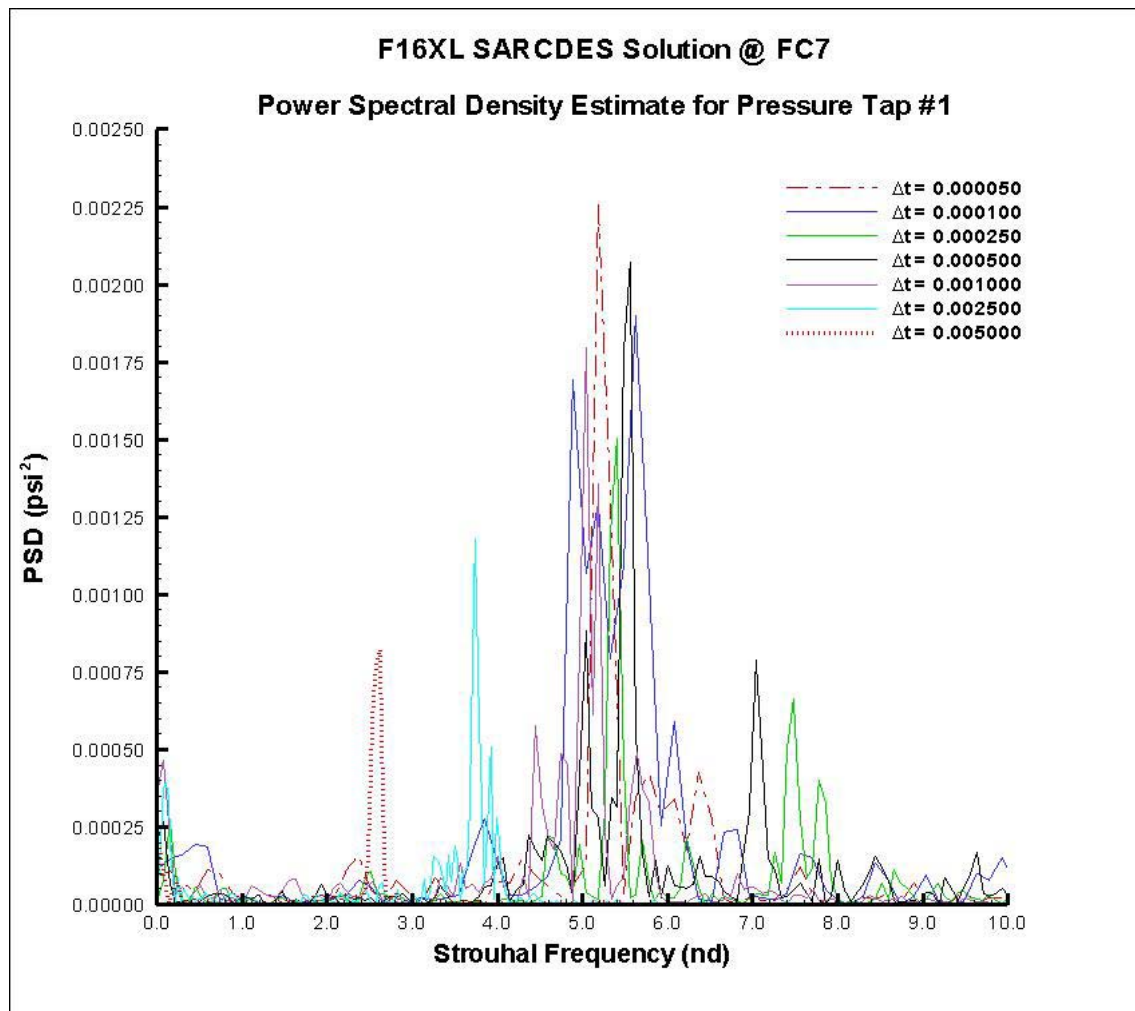
Figure 9-7: Power Spectral Density Results for Pressure Tap #1.

The results for pressure tap #1 are consolidated and shown as a function of time step and wave number in Figure 9-8. As can be clearly seen, the primary wave number is converging to a constant value as the time step decreases, with a wave number of approximately 0.19 reached when the physical time step is below $\Delta t = 0.001$ sec. While a converged time step has been attained at $\Delta t = 0.001$ sec, a smaller time step may be desirable for accurate flow prediction. It is also clear that the Strouhal frequency for the primary flow feature is somewhere in the range of 5, which corresponds to a helical mode instability in Figure 9-4.
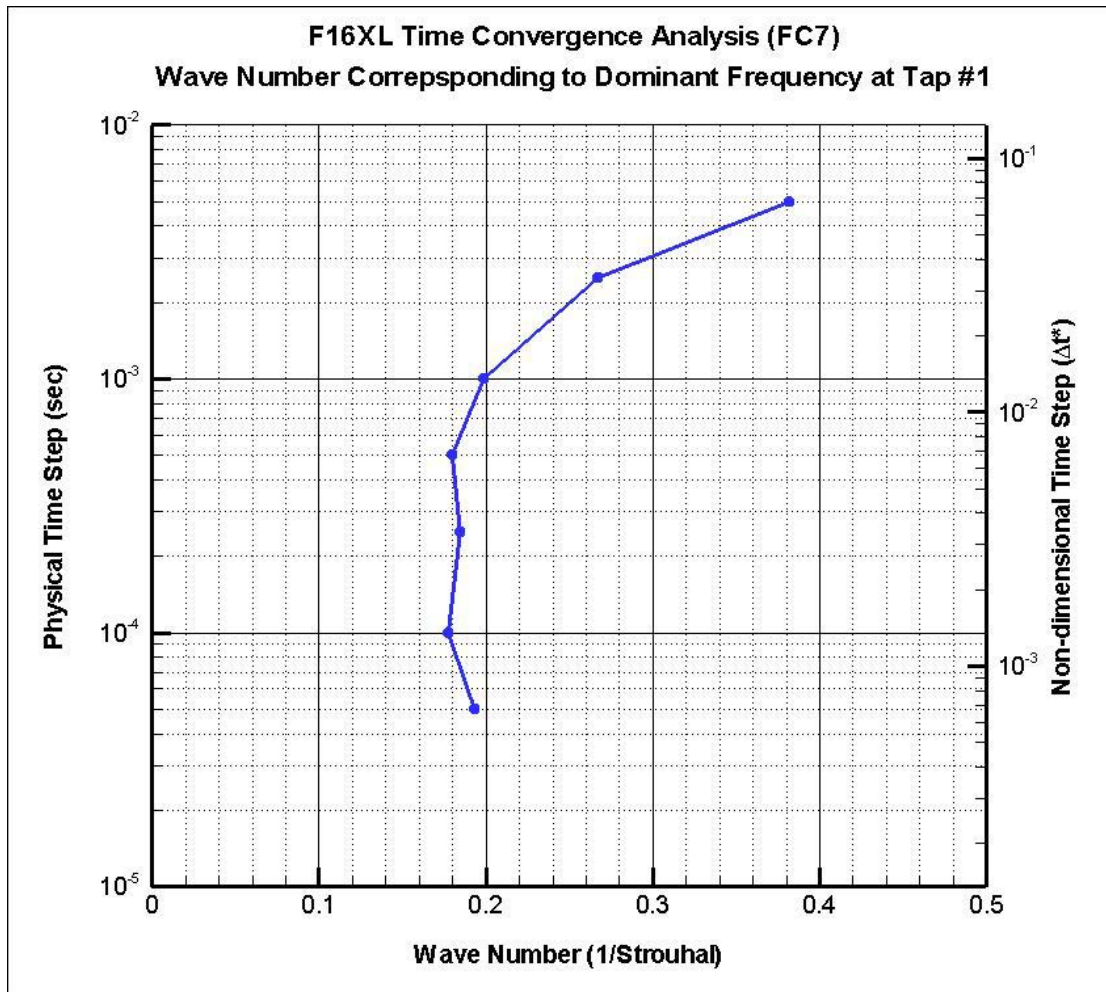
Figure 9-8: Wave Number Variation with Time Step for Pressure Tap #1.

While an additional time study could be performed to determine the effect of the number of Newton sub-iterations on the solution, our experience [9-18] shows that 3 Newton sub-iterations is usually sufficient for accurate prediction of the unsteady flows about full-scale aircraft. All subsequent calculations are performed with a physical time step of $\Delta t = 0.0005$ seconds and 3 Newton sub-iterations.

9.4.2   Low Speed Medium to High Alpha Flight Conditions

There are four flight conditions with angles of attack greater than 10 degrees and subsonic Mach numbers. Three of the flight conditions are considered a medium angle of attack in the range 10 to 12 degrees (FC7, FC19, and FC46). The fourth condition, FC25, is considered a high angle of attack condition at 19.84 degrees. This section presents results for these four flight conditions.

9.4.2.1   Flight Condition 7

Flight Condition 7 (FC7) is at an angle of attack of 11.89 degrees, a Mach number of 0.304, and an altitude of 5,000 ft resulting in a Reynolds number of 44.4 million. This condition was used by the CAWAPI RTO Task

Group as an initial comparison case between the various research teams. Unfortunately, this particular case had no flight test data to use for comparison, although there were two flight conditions close enough to be considered comparable from Flight 44 with approximately the same angle of attack and Mach numbers of 0.37 and 0.42.

Figure 9-9 depicts the flowfield over the F-16XL at FC7. Iso-surfaces of vorticity magnitude of 250 1/sec colored by pressure are shown in the perspective view and surface C_p for the right wing are shown in the planform view. It is apparent that the dominant features of the flowfield are the leading edge vortex, the air dam vortex, the outer wing vortex, and a complicated set of vortices from the AIM-9 fins and fore-body. It can also be seen that the leading-edge vortex changes characteristic from a coherent structure to a complex structure with helical windings, similar to vortex breakdown, in the region of the actuator pod. It is also interesting to note that the helical vortex structure is above the vortex emanating from the air dam creating a very complex structure. Figure 9-10 shows a close up view of this region for an iso-surface of vorticity-magnitude level of 750 1/sec with labels for the dominant features. The approximate breakdown position of the leading-edge vortex is FS470.

(a)   (b)
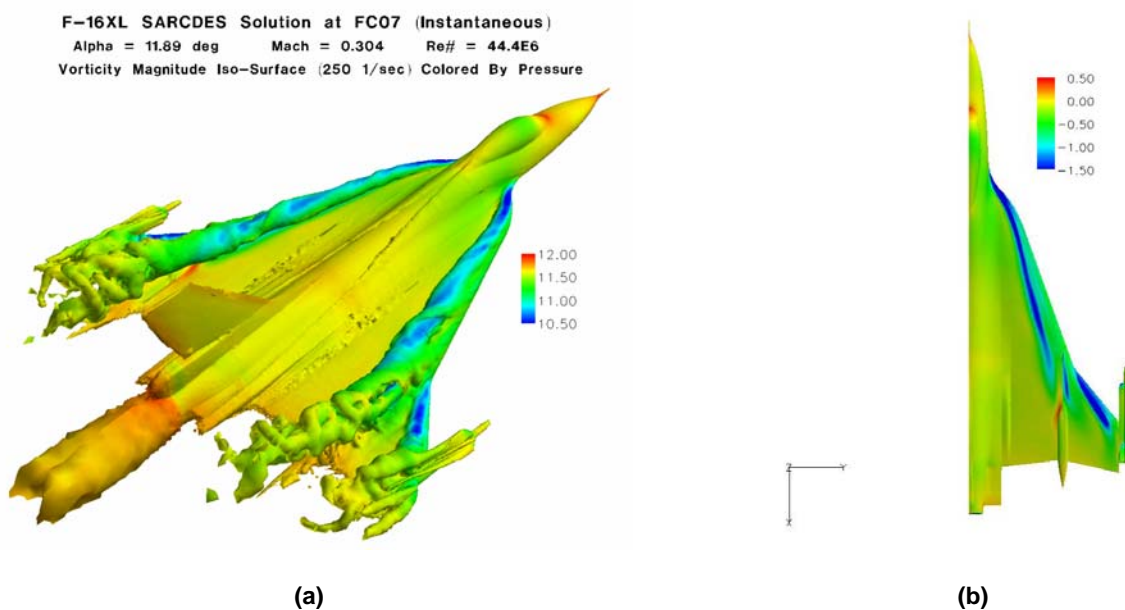
**Figure 9-9: Flight Condition 7: (a) Iso-Surfaces of Vorticity Magnitude Colored by Pressure
at an Instant in Time; (b) Time Averaged Surface Pressure Coefficient Distribution, C_p.**
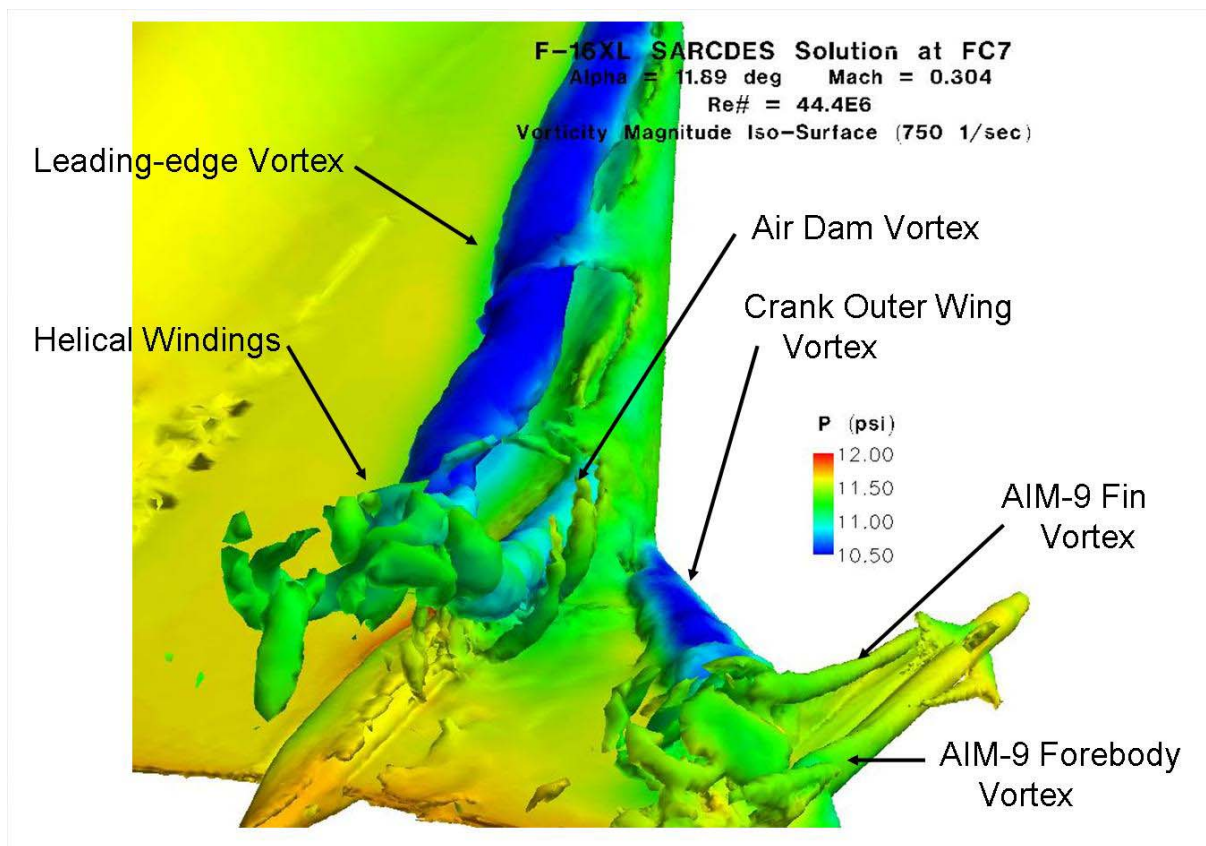
Figure 9-10: Close Up View of the Vortical Flowfield above the F-16XL-1 at Flight Condition 7; Iso-Surfaces of Vorticity Magnitude Colored by Pressure at an Instant in Time.

Determining the time-accurate characteristics of the flowfield is the central theme of this paper and so it becomes important to determine the relationship between the instantaneous solution, time-averaged solution, and a steady RANS solution. Figure 9-11 depicts iso-surfaces of vorticity magnitude and C_p at an instant in time on the lower half of the figure and a time average after 2000 time steps on the top half of the figure. The "pre-breakdown like" regions of each of the vortices seem comparable in position, size, and strength of both the vortices and their corresponding pressure "foot-prints" on the surface for the time averaged and instantaneous solutions. Aft of the breakdown-like region the helical windings are averaged out into a coherent structure. The time averaged solution is also very similar to the steady RANS solution using the SARC turbulence model (see Figure 9-12), although there are some differences aft of the breakdown-like region. Many of the standard turbulence models are unable to capture the post-breakdown windings as accurately as the SARC model [[9-5][9-6][9-8][9-9][9-10]].

(a)   (b)
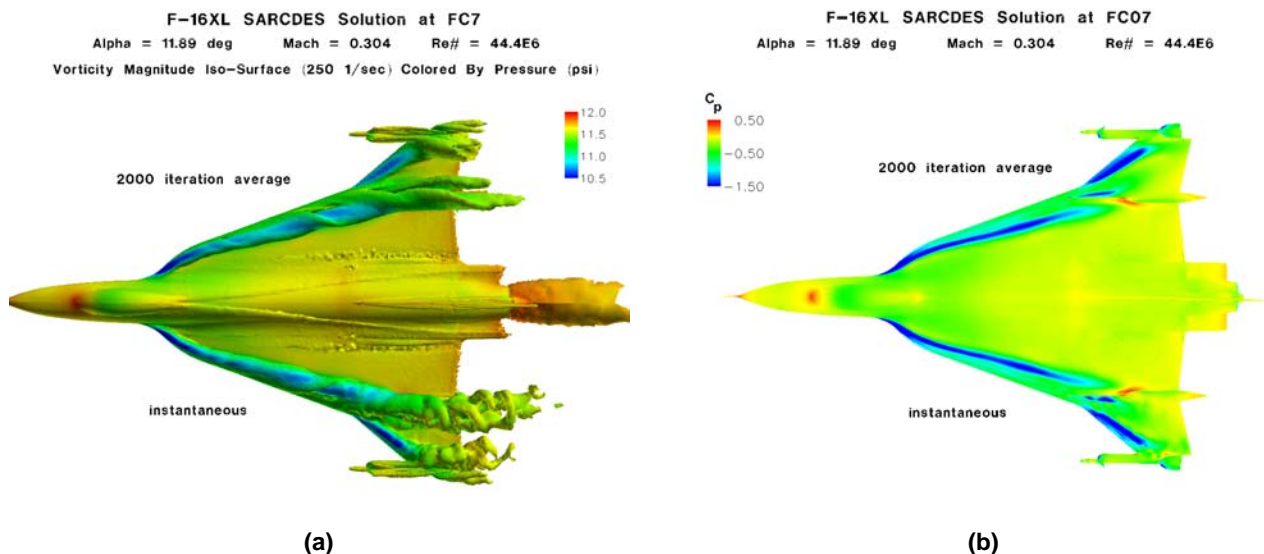
Figure 9-11: Comparison of an Instantaneous Solution to a Solution Time-Averaged after 2000 Time Steps: (a) Iso-Surfaces of Vorticity Magnitude Colored by Pressure; (b) Surface Pressure Coefficient Distribution, C_p.
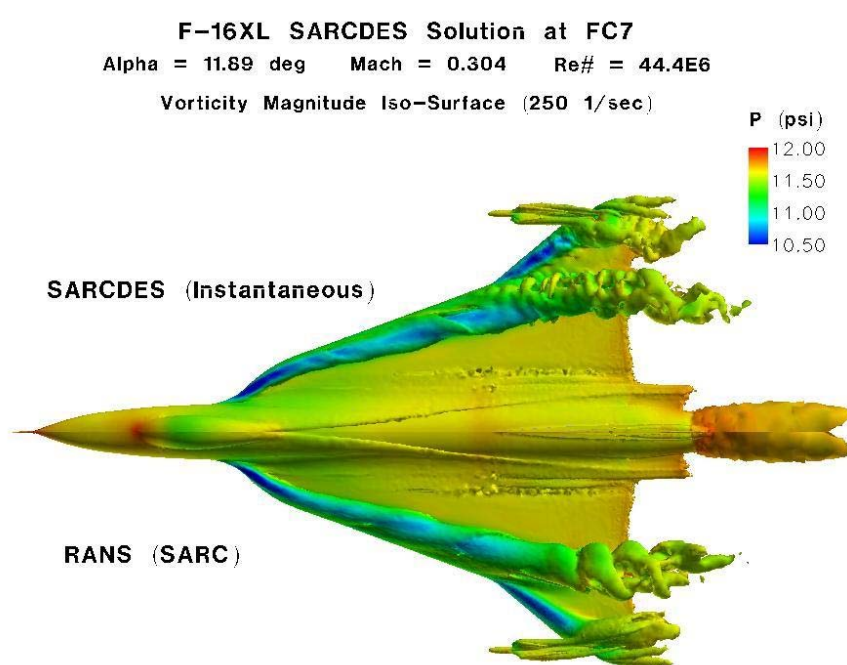
Figure 9-12: Comparison of an Instantaneous SARCDES Solution (upper half) to a SARC RANS Solution (lower half); Iso-Surfaces of Vorticity Magnitude Colored by Pressure.

Figure 9-13 depicts cross-planes of x-vorticity for various FS locations for both time averaged (left half of each pane) and instantaneous solutions (right half of each pane). At FS300 the shear layer emanating from the

wing leading-edge and the resulting vortex core can be seen in red and the secondary vortex can be seen below the primary vortex in blue. FS300 through FS375 all show similar vortical structures and very little difference between the time averaged and instantaneous solutions. At FS407.5 the air dam is just visible and the resulting vortex from the air dam has become apparent (in blue) as well as its effect on the secondary vortex previously seen. At FS450 the air dam vortex has lifted off the surface and begun to pair with the leading-edge vortex. The crank outer-wing vortex is also evident in red as well as the AIM-9 fin vortices (blue and red) at FS450. There are only minor differences in the time averaged versus instantaneous solutions evident in FS407.5 and FS450. At FS492.5 the same features exist but a large difference between the time averaged and instantaneous solutions can be observed due to the breakdown and resulting helical windings of the primary, outer crank, and AIM-9 fin vortices.
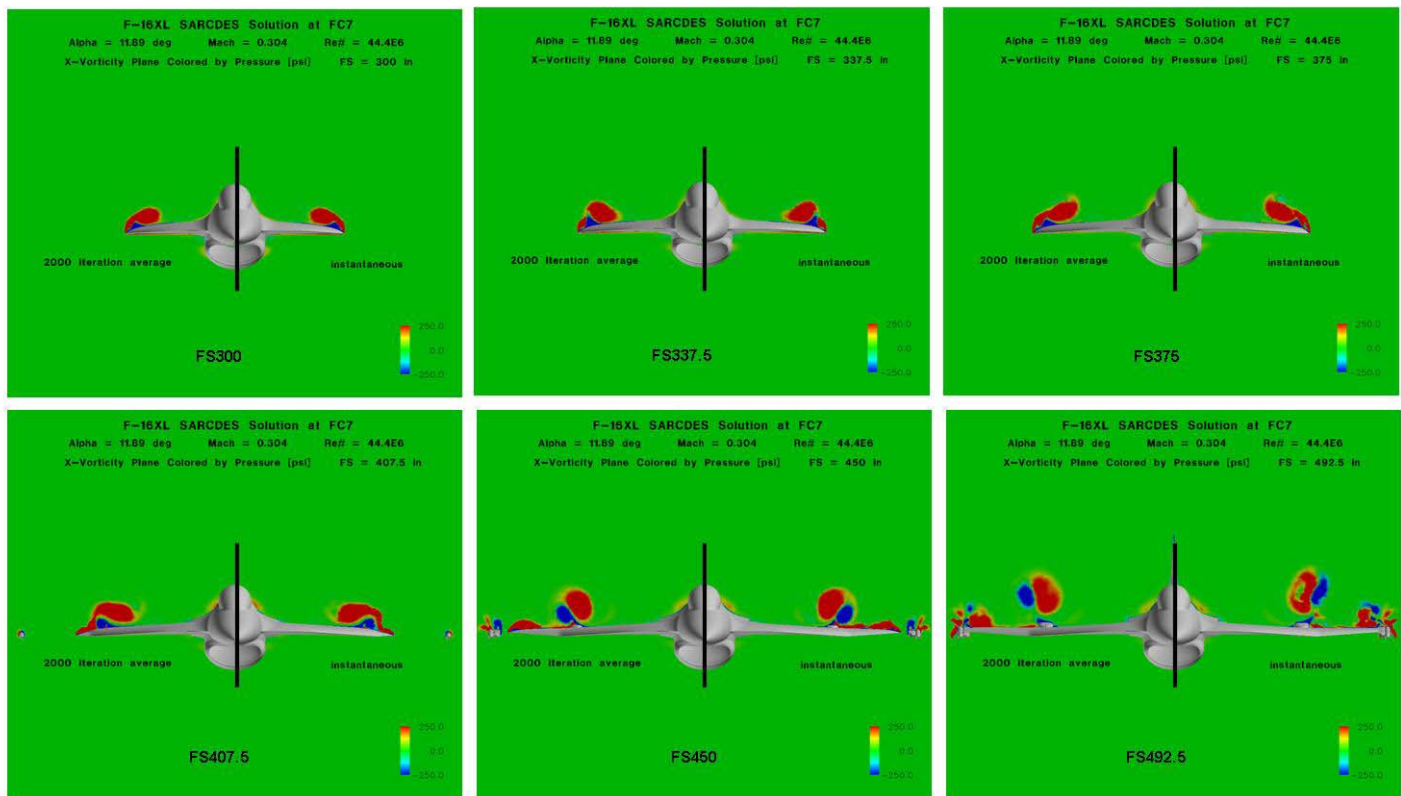
**Figure 9-13: Flight Condition 7; Cross-Planes of Vorticity in
the x-Coordinate Direction (Down the Fuselage Axis).**

Up to this point all of the data has been computational to show the complex flow features evident at this flight condition. Figure 9-14 depicts the flight test surface pressure coefficient, C_p, data compared to the computed time averaged C_p, computed min and max C_p at a given location, and the related RANS solution C_p for FC7 at various BL positions. As discussed earlier, the flight test data is at a slightly different condition but considered comparable. As is evident in the cross-planes of vorticity away from the air dam or crank, the BL40 through BL95 plots show that unsteady effects are minimal. BL55, BL70, BL80, and BL95 all show good agreement with the available flight test data with only minor discrepancies near the recovery from the strong suction peak. The suction peak C_p value and the position of the peak are in good agreement for all of these BL

locations. BL105 is located just inboard of the air dam/actuator pod and a small amount of unsteadiness is observed as evidenced by a widening of the min C_p, and max C_p curves from the mean C_p and RANS C_p curves. At BL127.5, BL153.5, and BL184.5 there are large differences in the min C_p and max C_p from the mean C_p curves, especially near the vortex induced suction peak, although the mean C_p curve compares well with the flight test data. At BL127.5 and BL184.5 we begin to see the difference between the mean C_p computed from a time accurate solution and the RANS C_p. This is especially evident at BL184.5 in the range of x/c from 0.1 to 0.4. In this region there is a large "hump" with the time-averaged C_p showing the best agreement with flight test. This discrepancy has been observed in other fighter aircraft simulations and is typically due to the inability of the RANS turbulence models to accurately capture the effect of the massive separation and strong unsteady vortices [[9-5][9-6][9-8][9-9][9-10]].

Figure 9-15 depicts similar data for various FS positions for FC7. As is true of all BL positions, all FS positions are in excellent agreement with the available flight test data. It is also evident at FS407.5, FS450, and FS492.5 that there is significant unsteadiness outboard of the air dam/actuator pod. This unsteadiness is due to the vortices from the air dam/actuator pod, crank outer wing, and AIM-9 tip missile and results in large variations in C_p in this region.
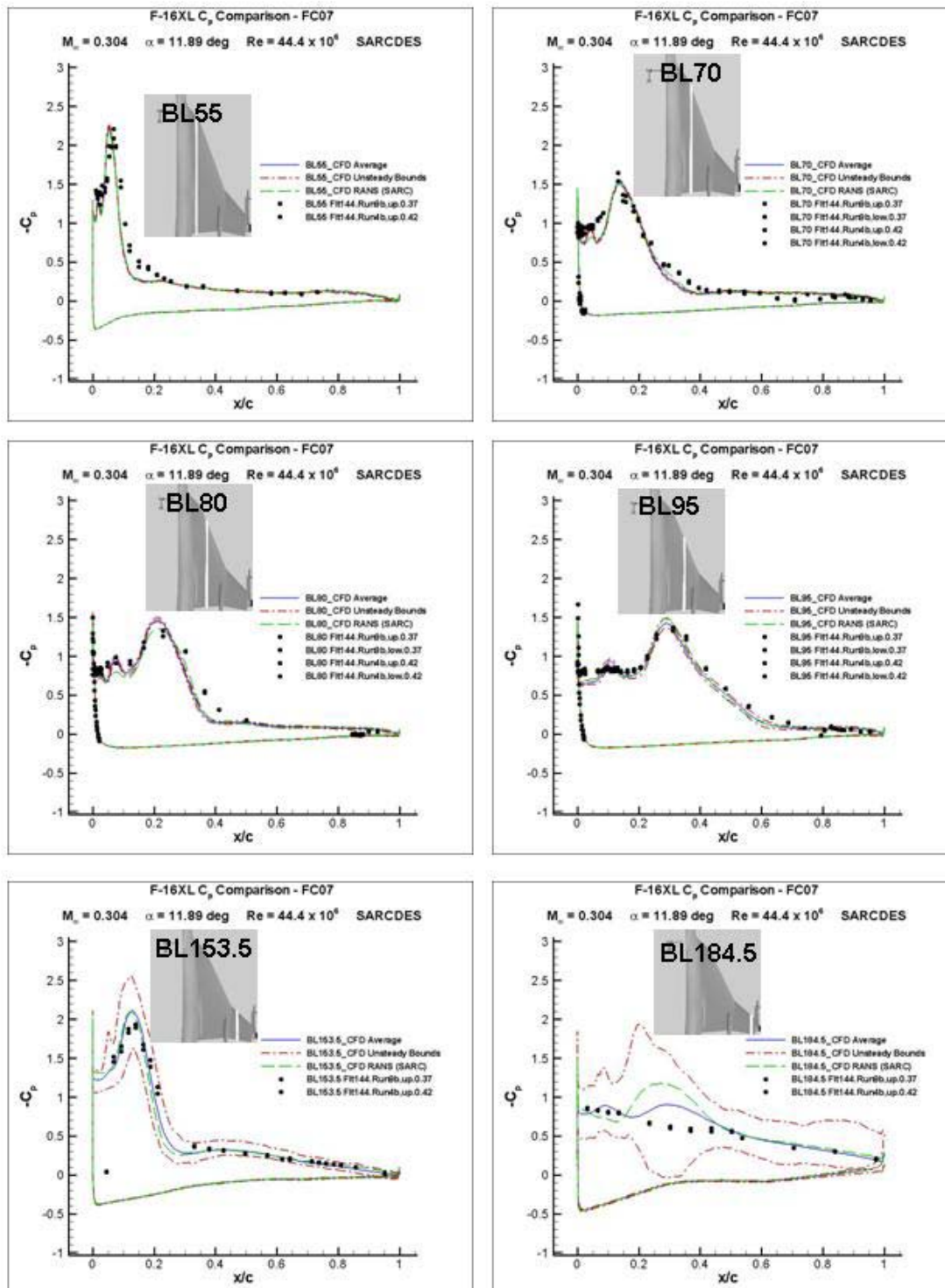
Figure 9-14: Flight Condition 7; Surface C$_p$ along Various F-16XL Butt Line Stations (BL) for Flight Test, Computed Mean, and Computed Max and Min Value for a Series of Time Accurate Solutions.
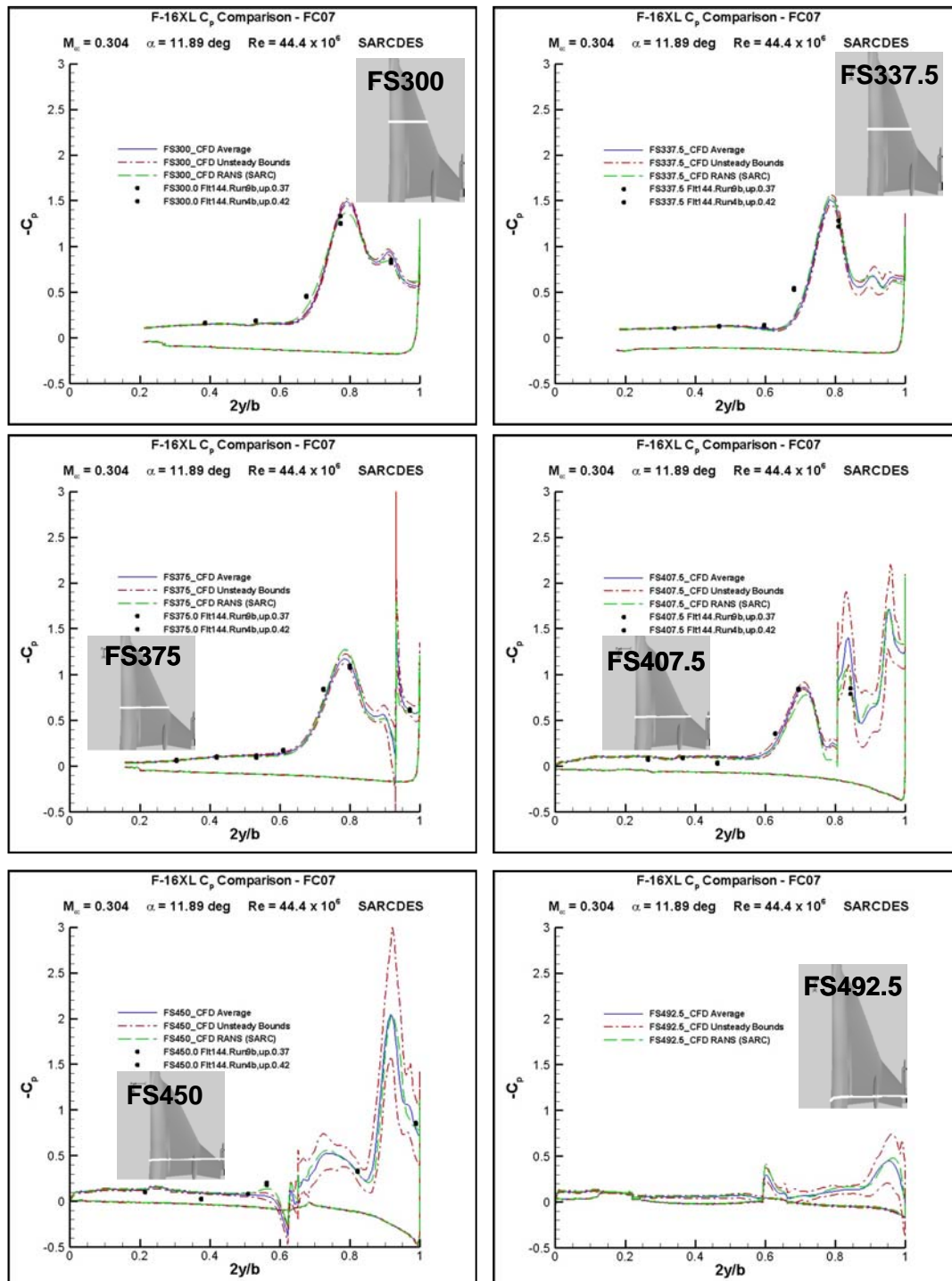
Figure 9-15: Flight Condition 7; Surface C_p along Various F-16XL Fuselage Stations (FS) for Flight Test, Computed Mean, and Computed Max and Min Values.

Figure 9-16 depicts the boundary layer rake comparisons between flight test and computed time average, min, and max scaled velocities at four locations in the neighborhood of FS300. The rakes are at locations along a line approximately perpendicular to the leading edge with Rake 3 most inboard and Rake 7 very near the leading edge and Rake 4 and Rake 5 in between. Rake 3 is well inboard of the leading edge vortex and shows the best agreement with fight test and essentially no unsteady effects of the vortex. Rake 4 is still in good agreement with the flight test data and we see unsteadiness as measured by the difference between min and max scaled velocity and the mean scaled velocity. In the Rake 5 data we see a large difference in the data near the "knee" in the curve and an increase in the unsteadiness of the data. Rake 7 shows the largest discrepancy from flight test including a velocity at the knee higher than the rake edge velocity which is not observed in the flight-test data. It should also be noted that this rake experiences a significant amount of unsteadiness. Rake 7 is located in the most challenging flow region due to the separation occurring somewhere near the leading edge and the transition of the model from RANS to LES. This particular data needs further study to determine the cause of the discrepancy.
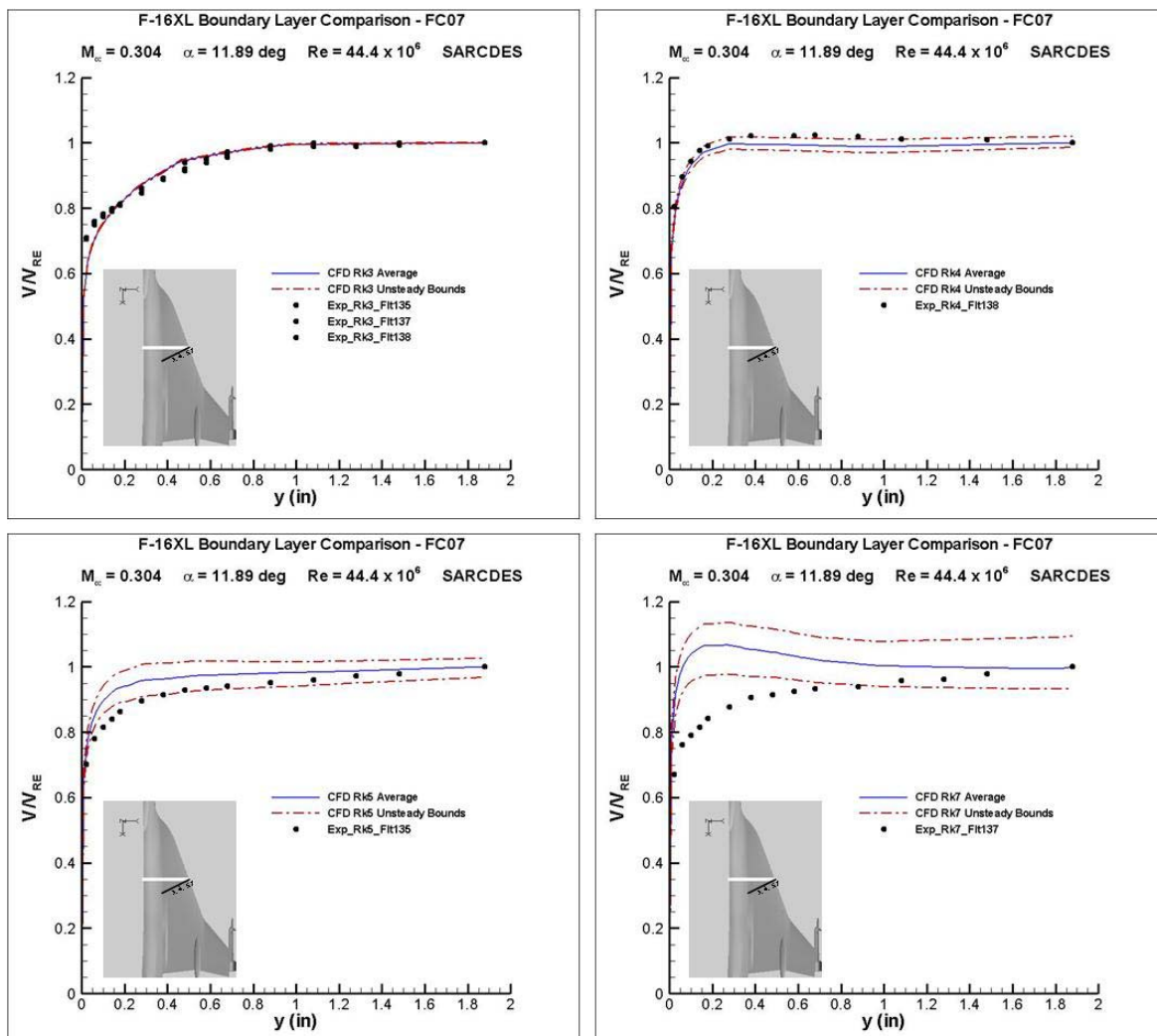
**Figure 9-16: Boundary Layer Rake Velocities Scaled by Rake-Edge
Velocity for Rakes 3, 4, 5, and 7 at Flight Condition 7.**

9.4.2.2   Flight Condition 19

Flight Condition 19 (FC19) is at an angle of attack of 11.85 degrees, a Mach number of 0.36, and an altitude of 10,000 ft resulting in a Reynolds number of 46.8 million. This condition was chosen for comparison due to the availability of skin friction data. Figure 9-17 depicts the flowfield over the F-16XL at FC19. As in FC7, iso-surfaces of vorticity magnitude of 250 1/sec colored by pressure are shown in the perspective view and surface C_p for the right wing are shown in the planform view. The dominant features of the flowfield are the same as in FC7 with only slight differences.

(a)   (b)
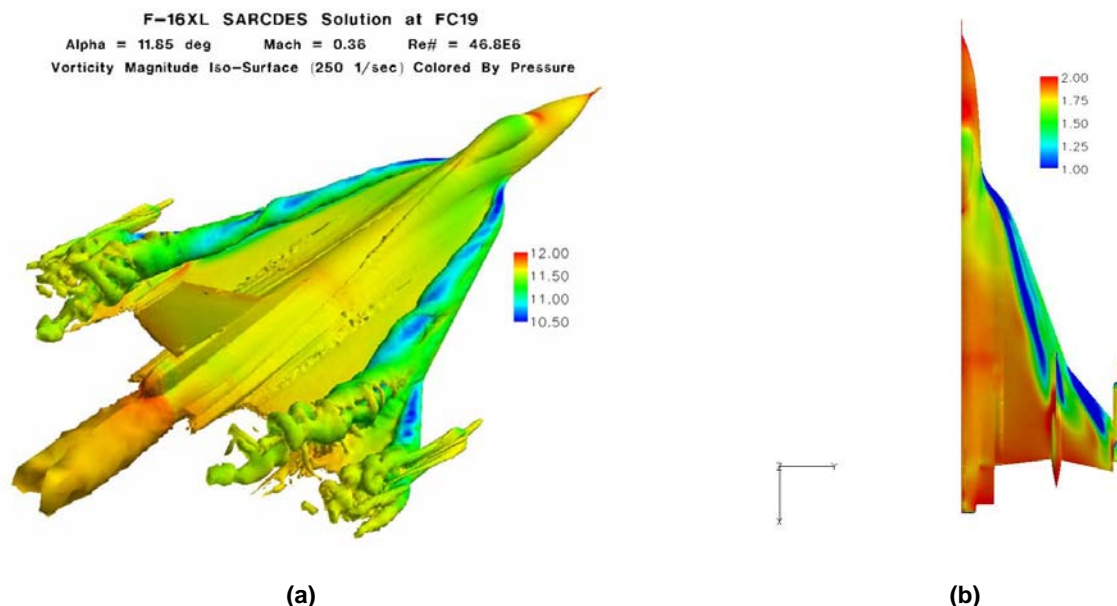
**Figure 9-17: Flight Condition 19: (a) Iso-Surfaces of Vorticity Magnitude
Colored by Pressure; (b) Surface Pressure Coefficient Distribution, C_p.**

Figure 9-18 depicts the local skin friction coefficient along FS330 for flight test and computed mean, min, and max. The flight test and computed data compare well qualitatively with the shape and position of the primary peak. However, quantitatively the magnitude of the skin friction coefficient primary peak is 22% different than the flight test data. It is well known that skin friction is one of the more challenging coefficients to match and may need additional grid resolution to improve the flight test data comparison. The secondary peak is well within the min and max values of the skin friction coefficient.
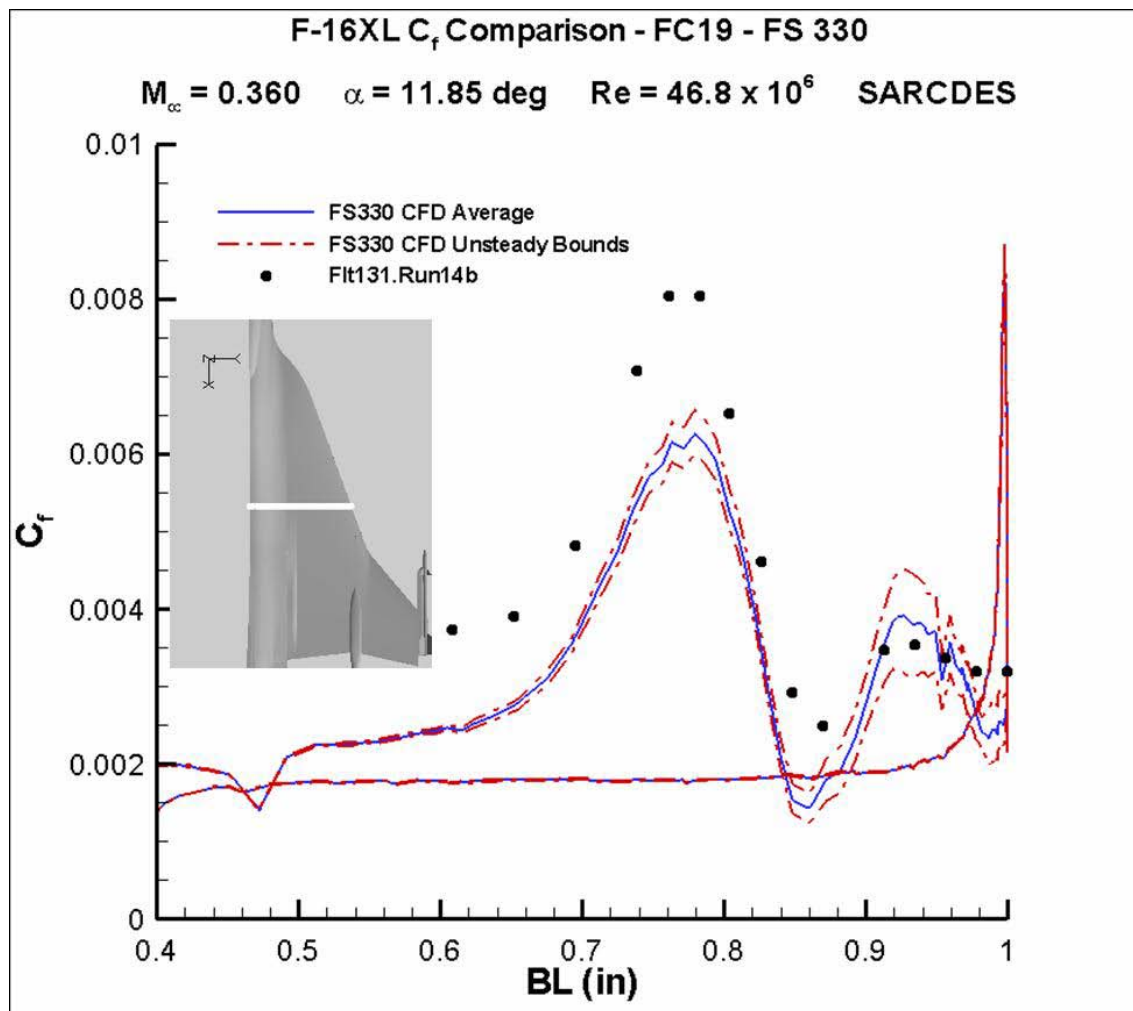
Figure 9-18: Local Skin Friction Coefficient along Fuselage Station 330.

9.4.2.3   Flight Condition 46

Flight Condition 46 (FC46) is at an angle of attack of 10.4 degrees, a Mach number of 0.527, and an altitude of 24,000 ft resulting in a Reynolds number of 46.9 million. This condition was chosen for comparison due to the availability of skin friction data. Figure 9-19 depicts the flowfield over the F-16XL at FC46. As in FC7, iso-surfaces of vorticity magnitude of 250 1/sec colored by pressure are shown in the perspective view and surface C_p for the right wing are shown in the planform view. The dominant features of the flowfield are the same as in FC7 with only slight differences.

(a)   (b)
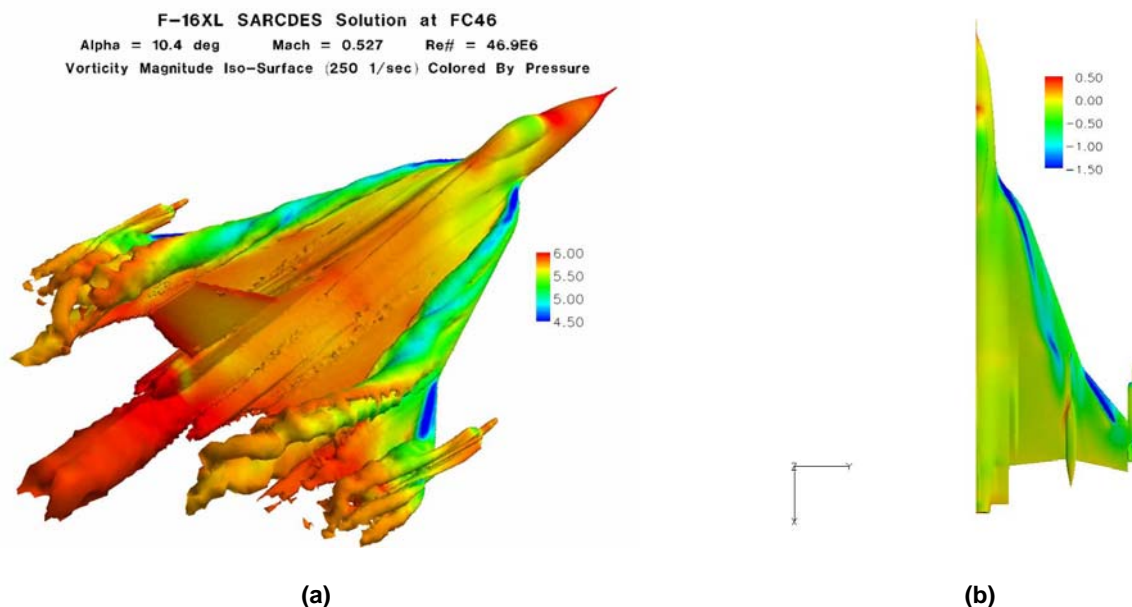
**Figure 9-19: Flight Condition 46: (a) Iso-Surfaces of Vorticity Magnitude
Colored by Pressure; (b) Surface Pressure Coefficient Distribution, C_p.**

Figure 9-20 depicts the flight test C_p data compared to the computed time averaged C_p, and computed min and max C_p at a given location for FC46 at various BL positions. As is the case with FC7, the BL40 through BL70 plots show that unsteady effects are minimal. However unlike FC7, FC46 shows unsteadiness in BL80 and BL95. The flight test comparison for BL55 is in excellent agreement in both shape and magnitude of surface C_p. Both BL70 and BL80 are in good agreement as well, with a slight shift outboard in the suction peak position and a slightly higher over all magnitude for the computational data. At BL95 the computations over predict the magnitude of both the primary and secondary vortex and predict a much sharper primary vortex. The BL153.5 computational data show an over prediction in suction peak magnitude and a shift outboard in the peak location. The BL184.5 computational data shows significant unsteadiness as in the FC7 case with the majority of the data within the min and max C_p bounds of the computational data. However, the computational data misses the inboard trend of a higher C_p. Overall this can be considered a fairly good comparison with flight test but due to the excellent agreement between flight test and computations for FC7, it is possible the actual flight test for FC46 may have been at a slightly different condition than simulated.
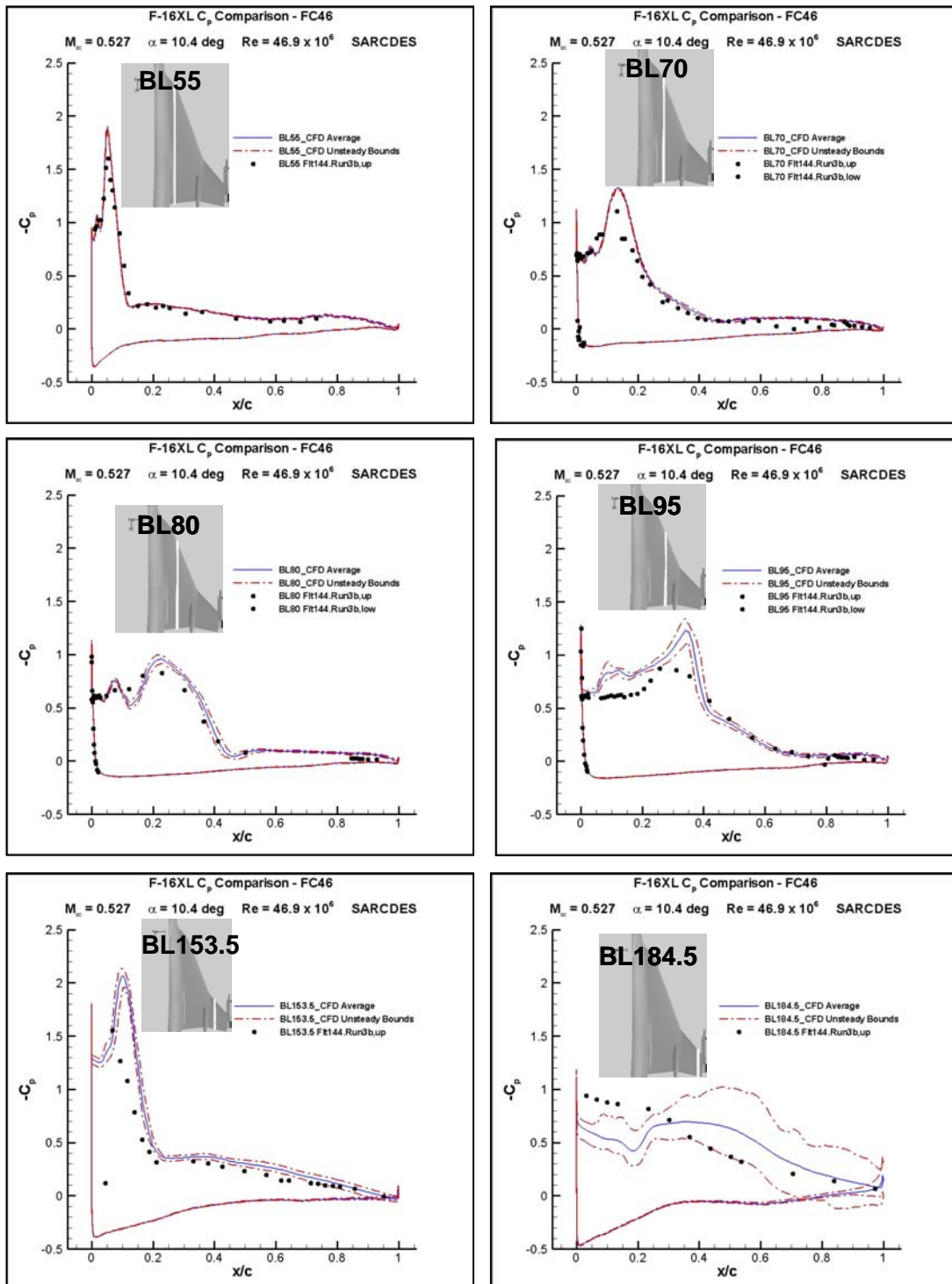
Figure 9-20: Flight Condition 46: Surface C_p along Various F-16XL Butt Line Stations (BL) for Flight Test, Computed Mean, and Computed Max and Min Value for a Series of Time Accurate Solutions.

9.4.2.4   Flight Condition 25

Flight Condition 25 (FC25) is at an angle of attack of 19.84 degrees, a Mach number of 0.242, and an altitude of 10,000 ft resulting in a Reynolds number of 32.2 million. This condition was added by the CAWAPI RTO Task Group to give a high angle of attack comparison case. Figure 9-21 depicts the flowfield over the F-16XL at FC25. Iso-surfaces of vorticity magnitude of 250 1/sec colored by pressure are shown in the perspective view and surface C_p for the right wing are shown in the planform view. As in the case of FC7, it is apparent that the dominant features of the flowfield are the leading-edge vortex, the air-dam vortex, the outer-wing vortex, and a complicated set of vortices from the AIM-9 fins and fore-body. However, the increased angle of attack has caused the breakdown of these vortices to occur earlier creating a more significantly unsteady flowfield. It is easier to label this classic vortex breakdown due to the fact that the breakdown position is well forward and inboard of the air dam/actuator pod. Figure 9-22 shows a close up view of this region for an iso-surface of vorticity-magnitude level of 900 1/sec with labels for the dominant features. The approximate breakdown position of the leading-edge vortex is FSXXX and the crank outer wing vortex is FSXXX.

(a)   (b)
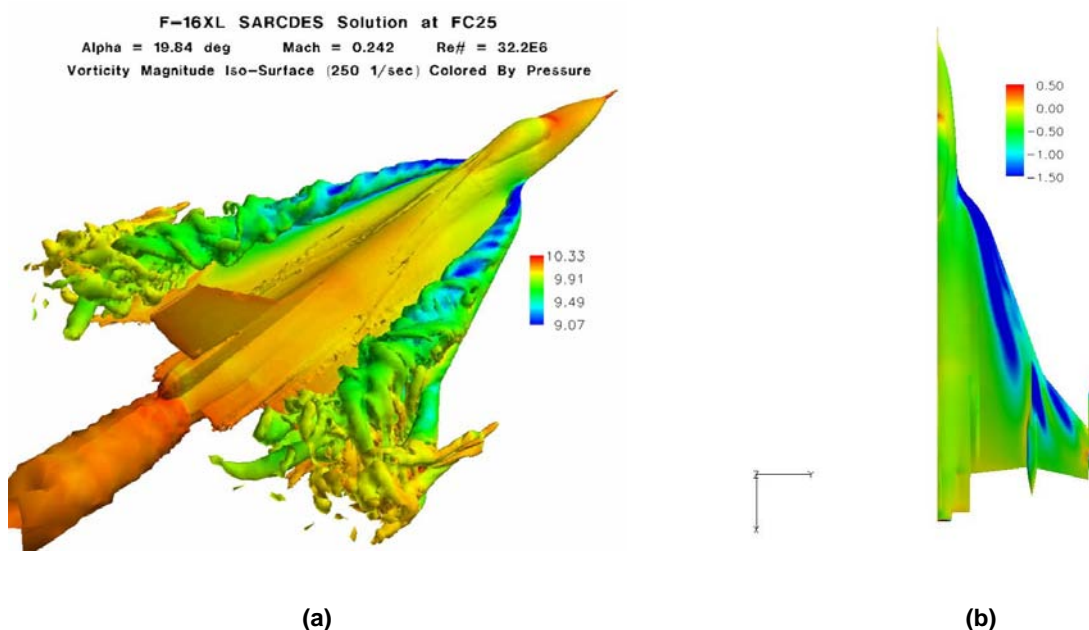
**Figure 9-21: Flight condition 25: (a) Iso-Surfaces of Vorticity Magnitude
Colored by Pressure; (b) Surface Pressure Coefficient Distribution, C_p.**
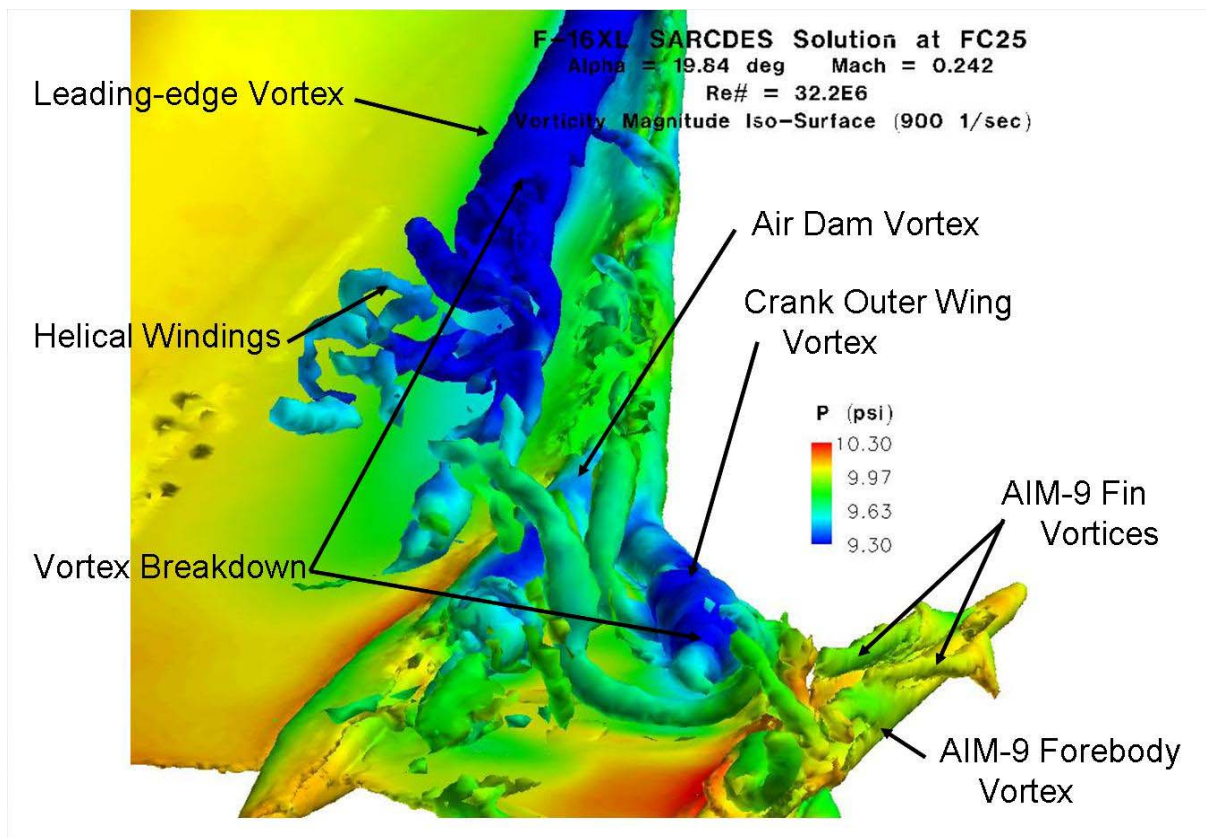
**Figure 9-22: Close Up View of the Vortical Flowfield above the F-16XL-1 at Flight
Condition 25; Iso-Surfaces of Vorticity Magnitude Colored by Pressure.**

Figure 9-23 depicts the flight test C_p data compared to the computed time averaged C_p, and computed min and max C_p at a given location for FC25 at various BL positions. The BL40 through BL70 plots show that unsteady effects are minimal. The BL80, BL95, and BL105 positions all show measurable unsteadiness. BL55, BL70, BL80, and BL95 all show excellent agreement with flight test data for this condition. The BL127.5, BL153.5, and BL184.5 positions all show significant unsteadiness in the surface C_p. All of the flight test data is within the bounds of the computed C_p min and max curves. Overall, there is excellent agreement with the flight test data for this flight condition and the comparison shows the utility of hybrid turbulence models and reliable CFD solvers to compute these complex unsteady fighter flowfields.

Figure 9-24 depicts similar data for various FS positions at FC25. As is true of all BL positions, all FS positions are in excellent agreement with the available flight test data. It is also evident that there is significant unsteadiness on the F-16XL wing at all FS positions aft of FS300 at this flight condition.
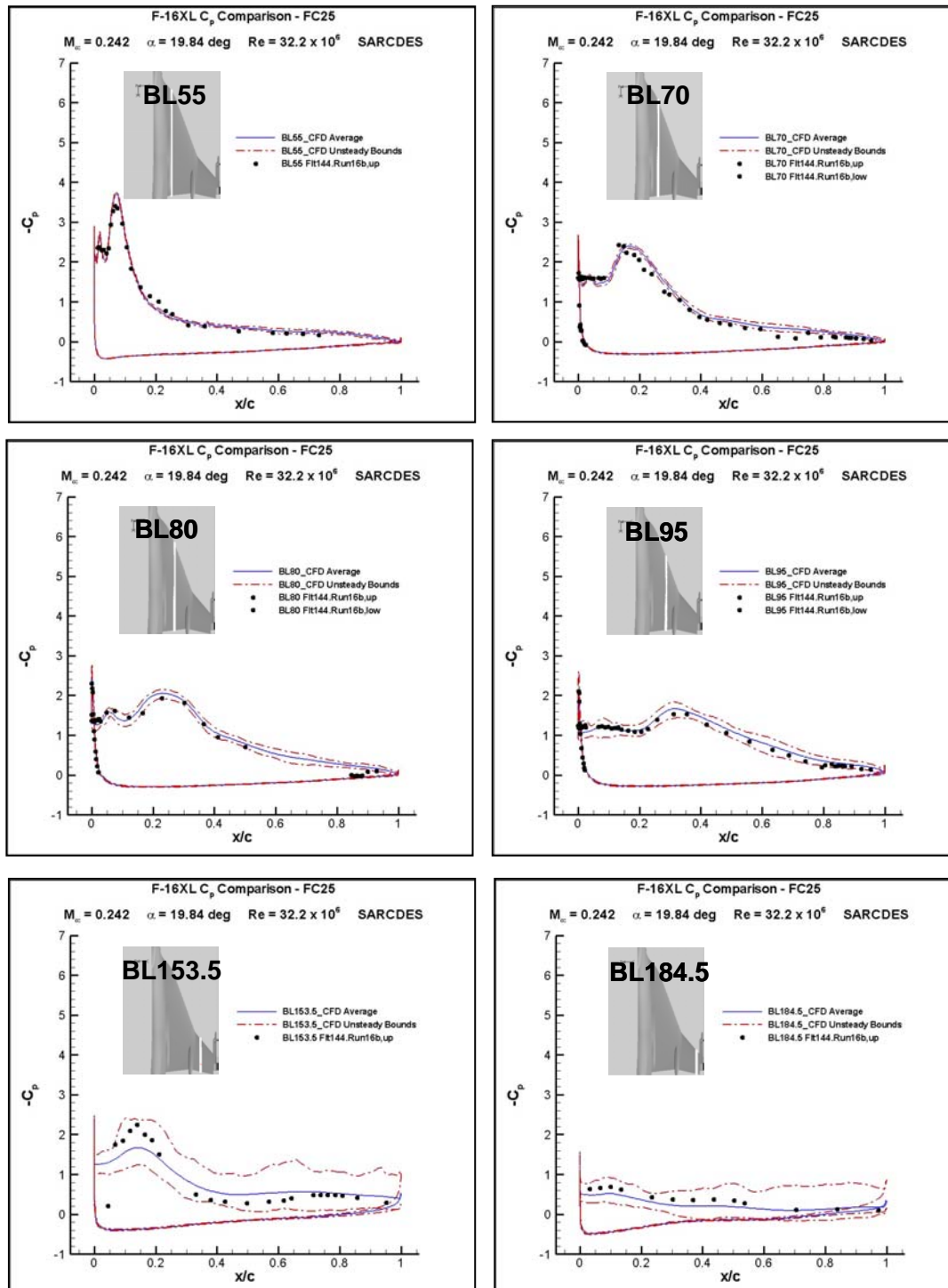
Figure 9-23: Flight Condition 25: Surface C_p along Various F-16XL Butt Line Stations (BL) for Flight Test, Computed Mean, and Computed Max and Min Value for a Series of Time Accurate Solutions.
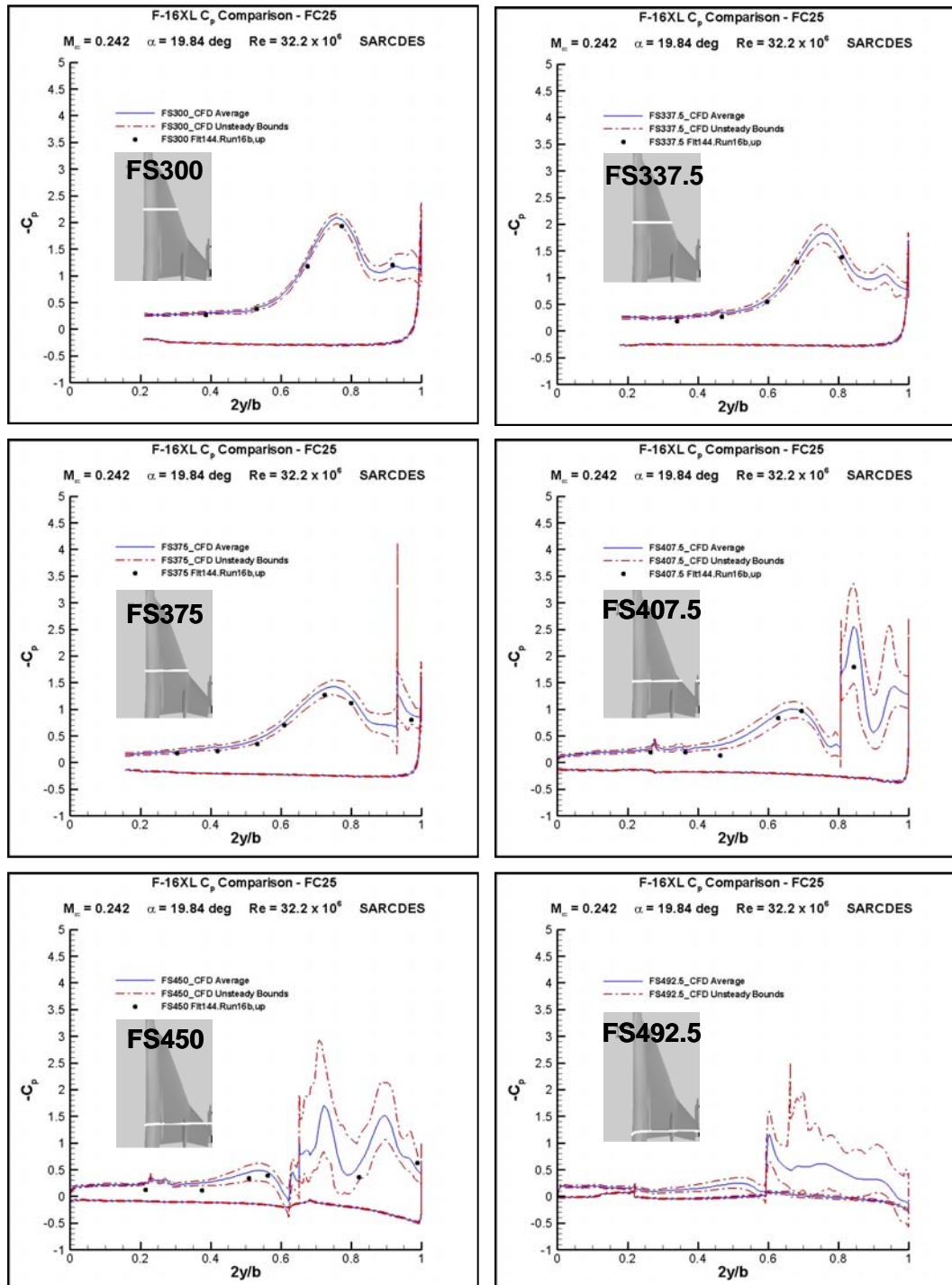
Figure 9-24: Flight Condition 25: Surface C_p along Various F-16XL Fuselage Stations (FS) for Flight Test, Computed Mean, and Computed Max and Min Values.

9.4.3 Transonic Flight Condition 70 (FC70)

The only transonic condition chosen by the CAWAPI RTO Task Group is Flight Condition 70. FC70 is at a Mach number of 0.97, an angle of attack of 4.37 degrees, and an altitude of 22,300 ft resulting in a Reynolds number of 88.8 million. Figure 9-25 depicts the flowfield over the F-16XL at FC70. Iso-surfaces of vorticity magnitude of 250 1/sec colored by pressure are shown in the perspective view and surface C_p for the right wing are shown in the planform view. The dominant features for this flowfield are no longer the same as the subsonic cases. There is a leading edge vortical structure that detaches from the leading edge and turns streamwise just after the s-curve portion of the leading edge. Also, the air dam/actuator pod and AIM-9 fin and forebody vortices exists but are minimal and close to the surface. Of course the more important features are the transonic shocks that are evident in the surface C_p distribution. The emphasis of this paper is the unsteady effects, which are essentially non-existent for this flowfield, so the data is provided for completeness but will not be discussed in great detail.

(a)　　　　　　　　　　　　　　　　　　(b)
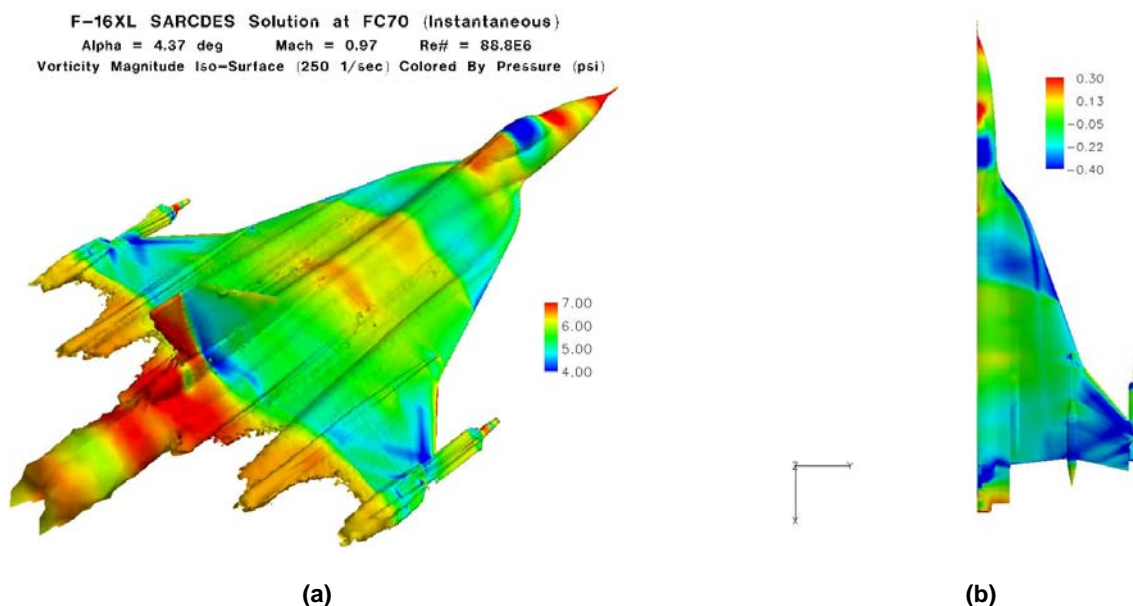
**Figure 9-25: Flight Condition 70: (a) Iso-Surfaces of Vorticity Magnitude
Colored by Pressure; (b) Surface Pressure Coefficient Distribution, C$_p$.**

Figure 9-26 depicts the flight test C_p data compared to the computed time averaged C_p, and computed min and max C_p at a given location for FC70 at various BL positions. The BL40 through BL184.5 plots show that unsteady effects are minimal. The BL55 and BL95 data are in good agreement with flight test data but the BL70, BL80, BL153.5, and BL184.5 data are in rather poor agreement with flight test data. This poor agreement may be due to the fact that a control surface in the outer portion of the wing was deflected in flight test but not in the grid. This discrepancy was discovered by the CAWAPI RTO Task Group too late in the study to make changes to the grid and therefore all participants have seen similar discrepancies.

Figure 9-27 shows very similar agreement between flight test and computations for all FS positions as the BL positions.
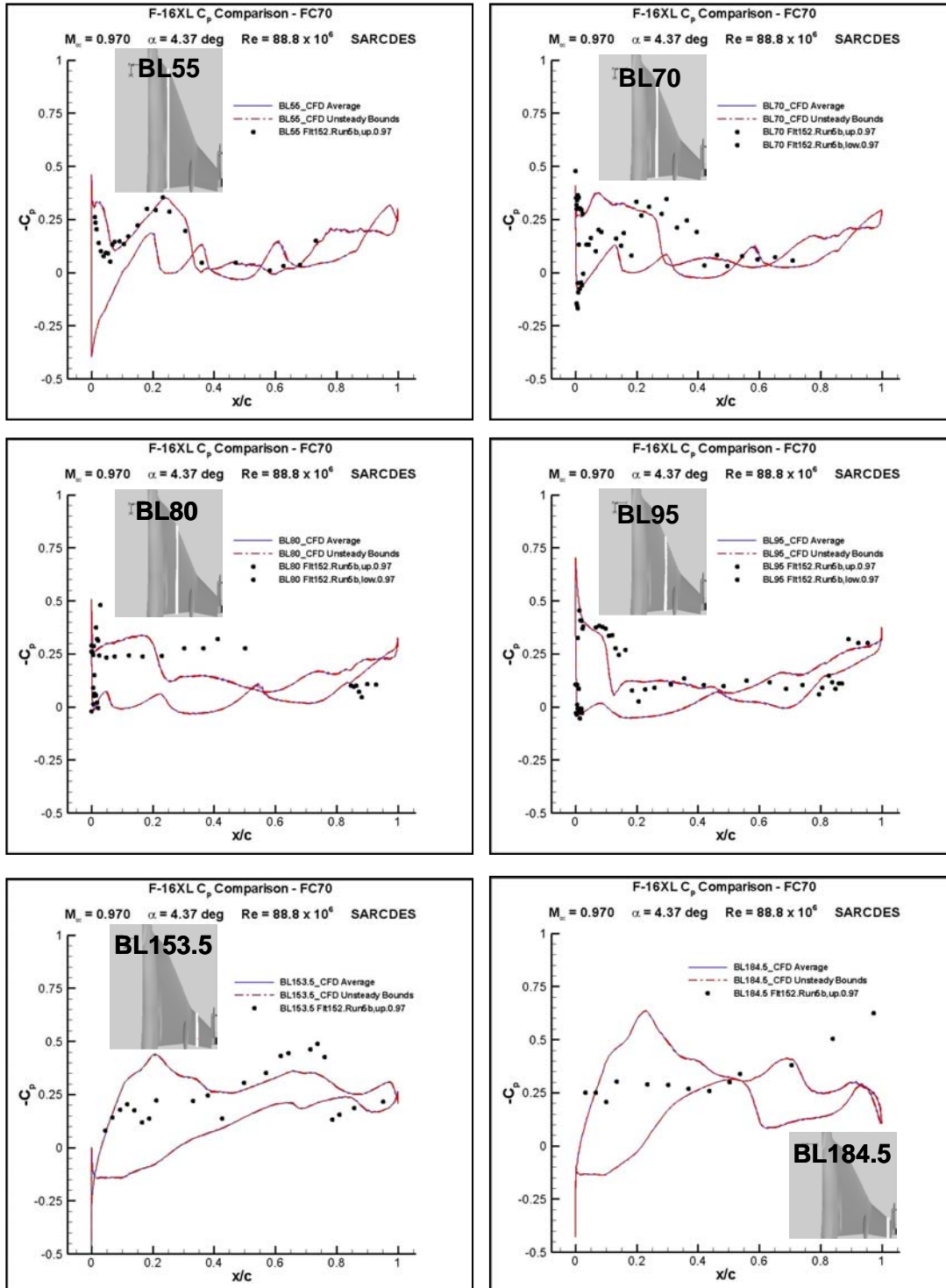
Figure 9-26: Flight Condition 70: Surface C_p along Various F-16XL Butt Line Stations (BL) for Flight Test, Computed Mean, and Computed Max and Min Value for a Series of Time Accurate Solutions.
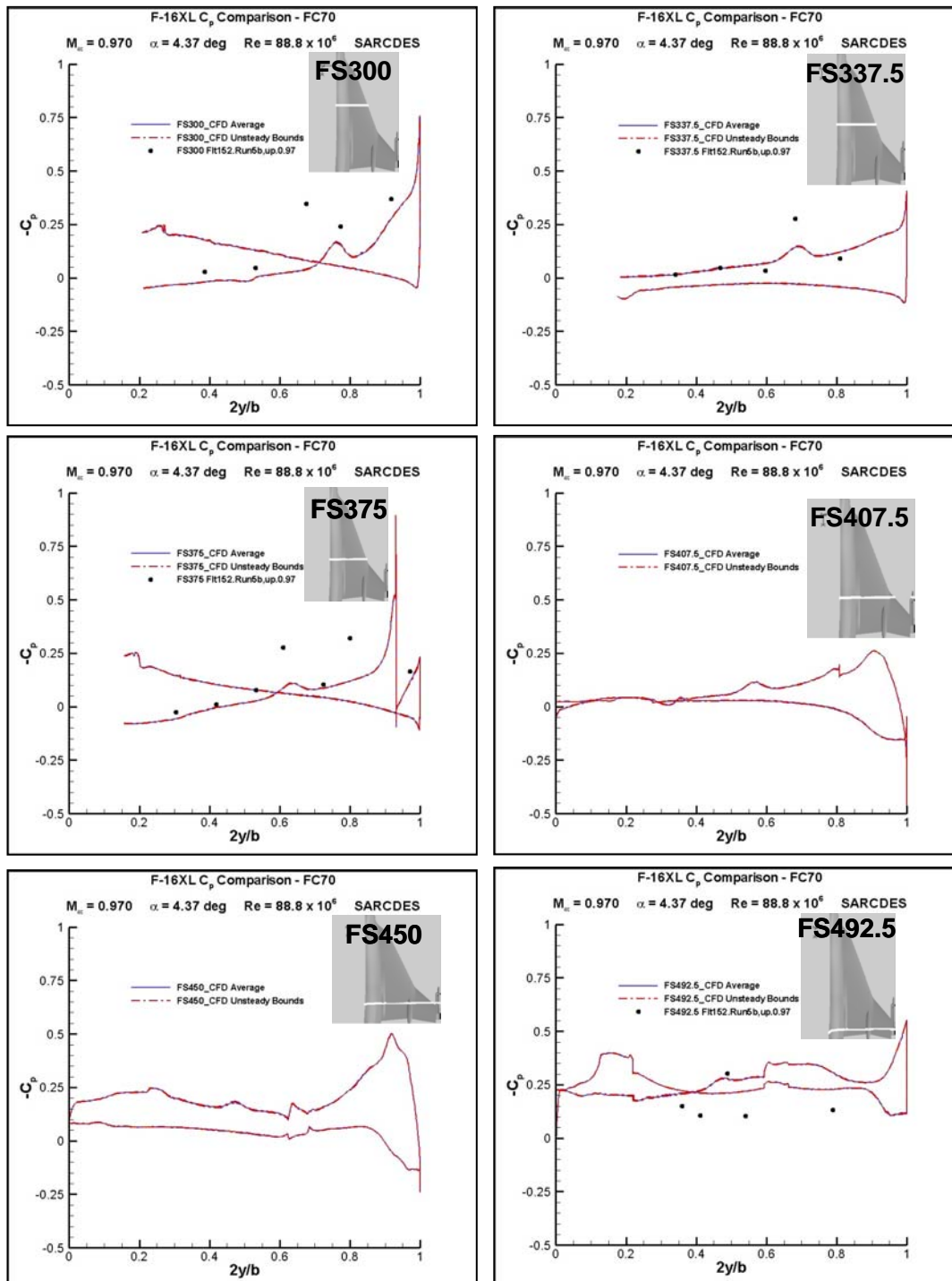
Figure 9-27: Flight Condition 70: Surface C$_p$ along Various F-16XL Fuselage Stations (FS) for Flight Test, Computed Mean, and Computed Max and Min Values.

9.4.4   Sideslip Flight Conditions

There are two flight conditions with non-zero sideslip angles, medium angles of attack, and subsonic Mach numbers. These two conditions have sideslip angles of +5.31 (FC50) and -4.58 (FC51). Solutions were computed for these two conditions with a mirrored full-span grid based on the original half-span grid used in all of the previously discussed computations. This section presents results for these two non-symmetric flight conditions.

9.4.4.1   Flight Condition 50

Flight Condition 50 (FC50) is at a sideslip angle of +5.31 degrees (wind in the right ear), an angle of attack of 13.56 degrees, a Mach number of 0.434, and an altitude of 24,000 ft resulting in a Reynolds number of 39.4 million. Figure 9-28 depicts the flowfield over the F-16XL at FC50. Iso-surfaces of vorticity magnitude of 250 1/sec colored by pressure are shown in the left view and surface C_p is shown in the right view. The dominant features of the left wing are similar to the FC7 baseline case but the right wing has additional vortical structures. The effect of a positive sideslip angle is an increase in the effective angle of attack and a reduction in the leading-edge sweep angle of the right wing. The increased effective angle of attack causes breakdown to occur sooner on the wing and the reduced sweep angle causes the double vortex observed by researchers performing studies of lower sweep delta wings [9-19]. The approximate breakdown position of the leading-edge vortex of the left wing is FSXXX and the right wing is FSXXX.

(a)   (b)
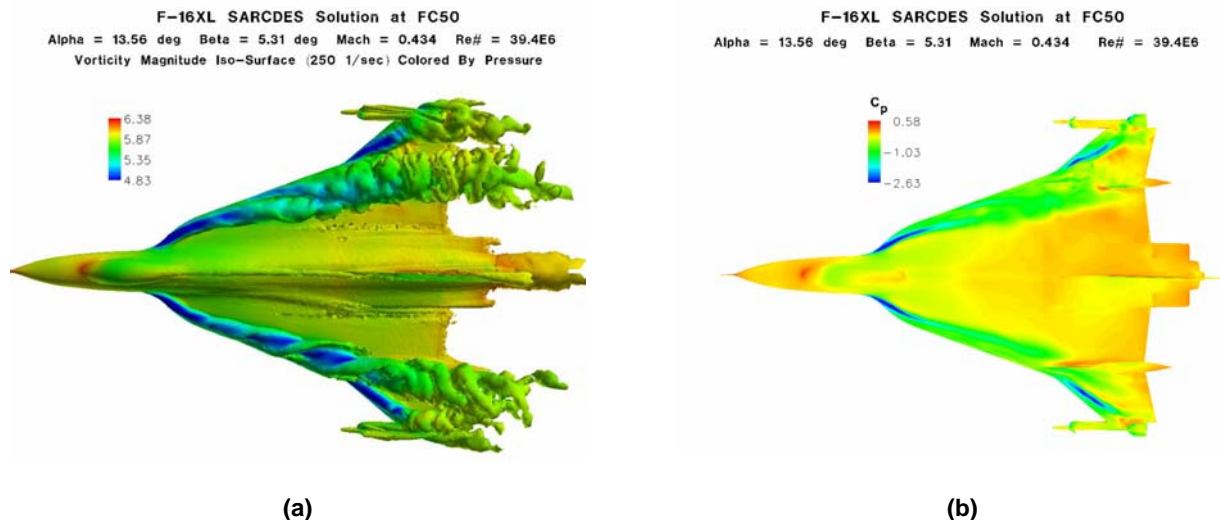
**Figure 9-28: Flight Condition 50: (a) Iso-Surfaces of Vorticity Magnitude
Colored by Pressure; (b) Surface Pressure Coefficient Distribution, C_p.**

Figure 9-29 depicts the right wing flight test C_p data compared to the computed time averaged C_p and computed min and max C_p at a given location for FC50 at various BL positions. It should be noted that for FC50 the comparison data is on the wing with the highest degree of unsteadiness due to the increased effective angle of attack and the reduced leading edge sweep. The BL40 and BL50 plots show that unsteady effects are minimal for these inboard stations and the flight test data matches fairly well for both BL40 and BL55. Unlike FC7, FC19, FC46, or even FC25, FC50 shows significant unsteadiness for BL70 through BL184.5 for the reasons discussed above. The BL70 through BL184.5 flight test data resides primarily inside

of the computed unsteady min and max C_p bounds. However, in BL95 there is a region near the leading edge that is over-predicted by the computations. Overall, these comparisons with flight test are considered good when considering the amount of unsteady massively separated flow on the right wing.

Figure 9-30 depicts similar data for various FS positions for FC50. As is true of all BL positions, all FS positions are in good agreement with the available flight test data and there is significant unsteadiness observed for FS300 through FS492.5 at this flight condition.
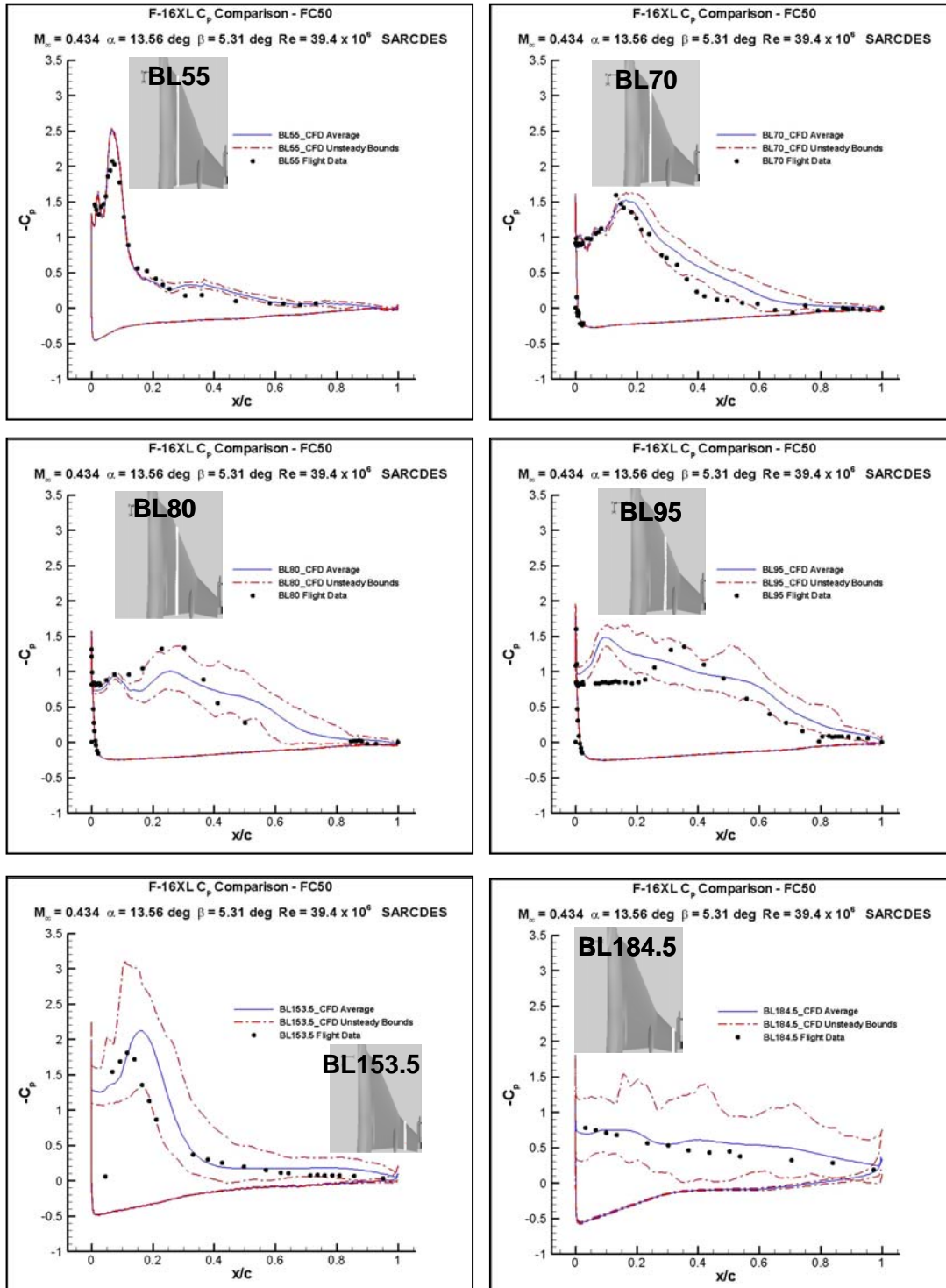
Figure 9-29: Flight Condition 50: Surface C_p along Various F-16XL Butt Line Stations (BL) for Flight Test, Computed Mean, and Computed Max and Min Value for a Series of Time Accurate Solutions.
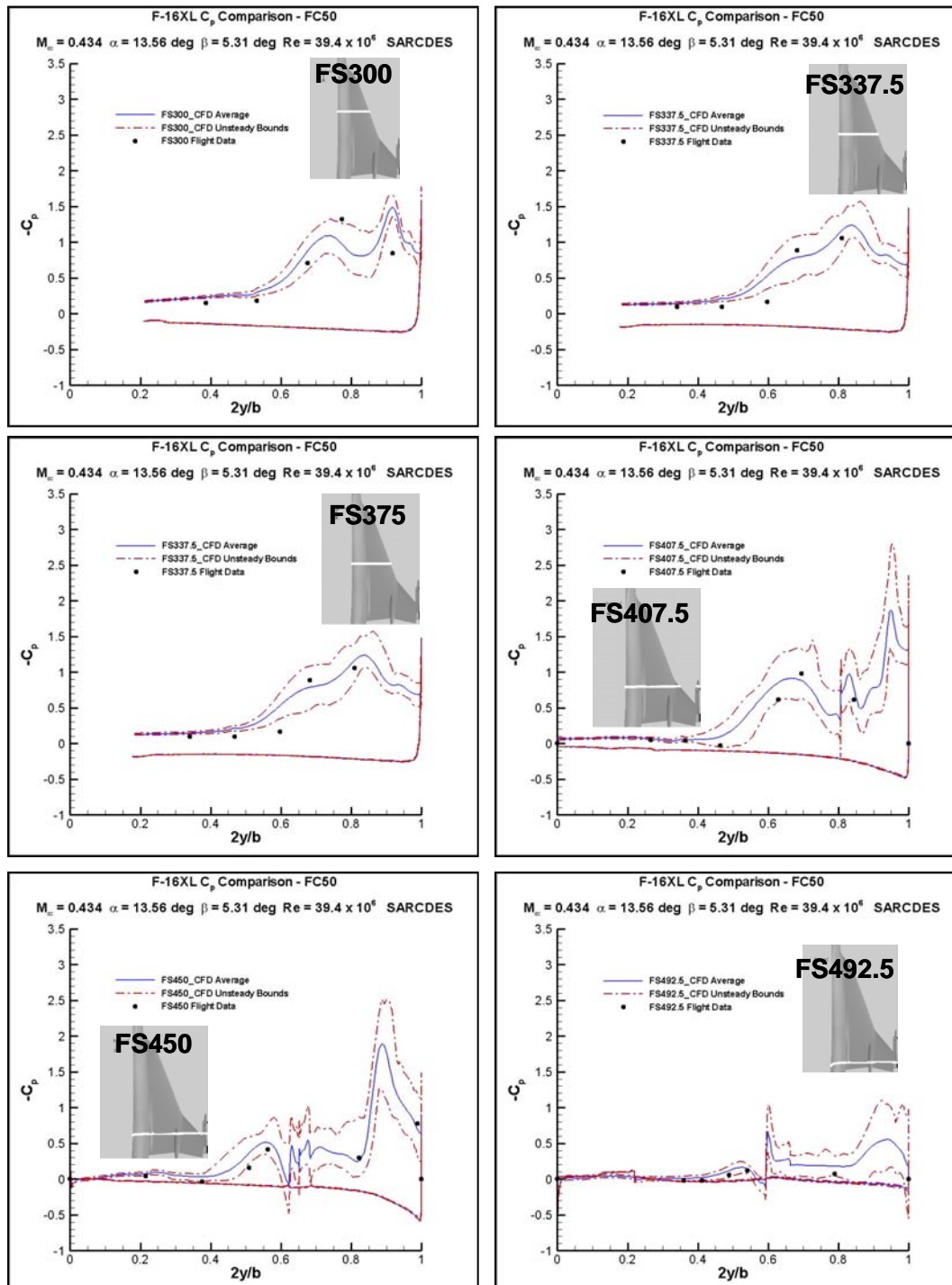
Figure 9-30: Flight Condition 50: Surface C_p along Various F-16XL Fuselage Stations (FS) for Flight Test, Computed Mean, and Computed Max and Min Values.

9.4.4.2   Flight Condition 51

Flight Condition 51 (FC51) is at a sideslip angle of -4.58 degrees (wind in the left ear), an angle of attack of 12.89 degrees, a Mach number of 0.441, and an altitude of 24,000 ft resulting in a Reynolds number of 39.0 million. Figure 9-31 depicts the flowfield over the F-16XL at FC51. Iso-surfaces of vorticity magnitude of 250 1/sec colored by pressure are shown in the left view and surface C_p is shown in the right view. Since the flight conditions of FC51 are nearly the same as FC50 but with an opposite sideslip, the discussions above hold for FC51 but for the opposite wing.

(a)   (b)
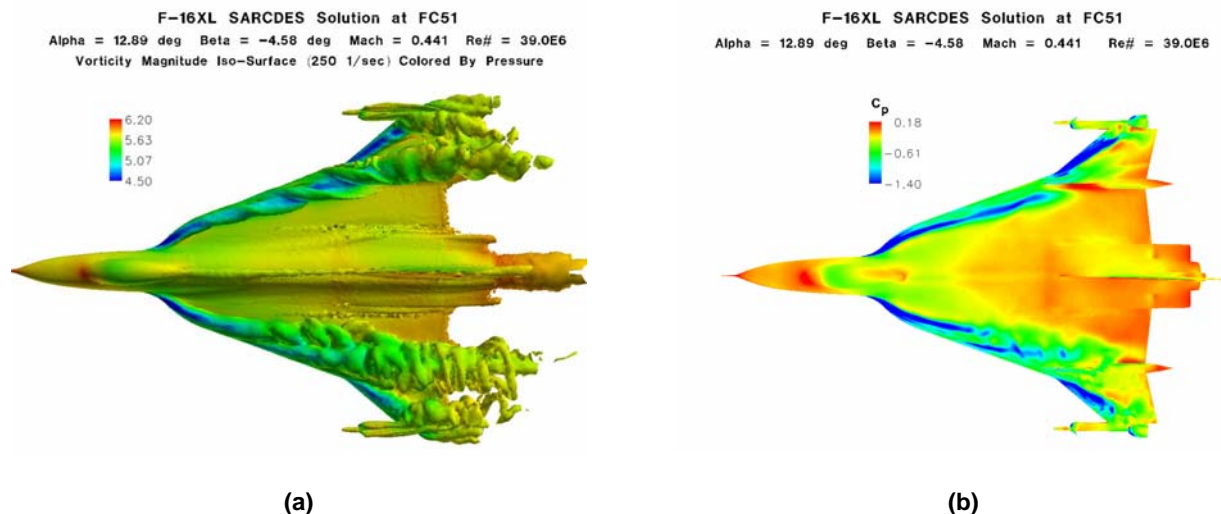
Figure 9-31: Flight Condition 51: (a) Iso-Surfaces of Vorticity Magnitude
Colored by Pressure; (b) Surface Pressure Coefficient Distribution, C_p.

Figure 9-32 depicts the right wing flight test C_p data compared to the computed time averaged C_p and computed min and max C_p at a given location for FC51 at various BL positions. It should be noted that for FC51 the comparison data is on the wing with the lowest degree of unsteadiness due to the decreased effective angle of attack and the increased leading edge sweep. The BL40 through BL105 plots show that unsteady effects are minimal and the flight test data matches very well for BL40 through BL105. The BL127.5 plot shows the largest discrepancy with an under-predicted peak located slightly inboard of the flight test data. The BL153.5 and BL184.5 plots show very good agreement with flight test data and a fairly large amount of unsteadiness for BL184.5.

Figure 9-33 depicts similar data for various FS positions for FC51. As is true of all BL positions, all FS positions are in good agreement with the available flight test data and there is very little unsteadiness observed for FS185 through FS492.5 at this flight condition.
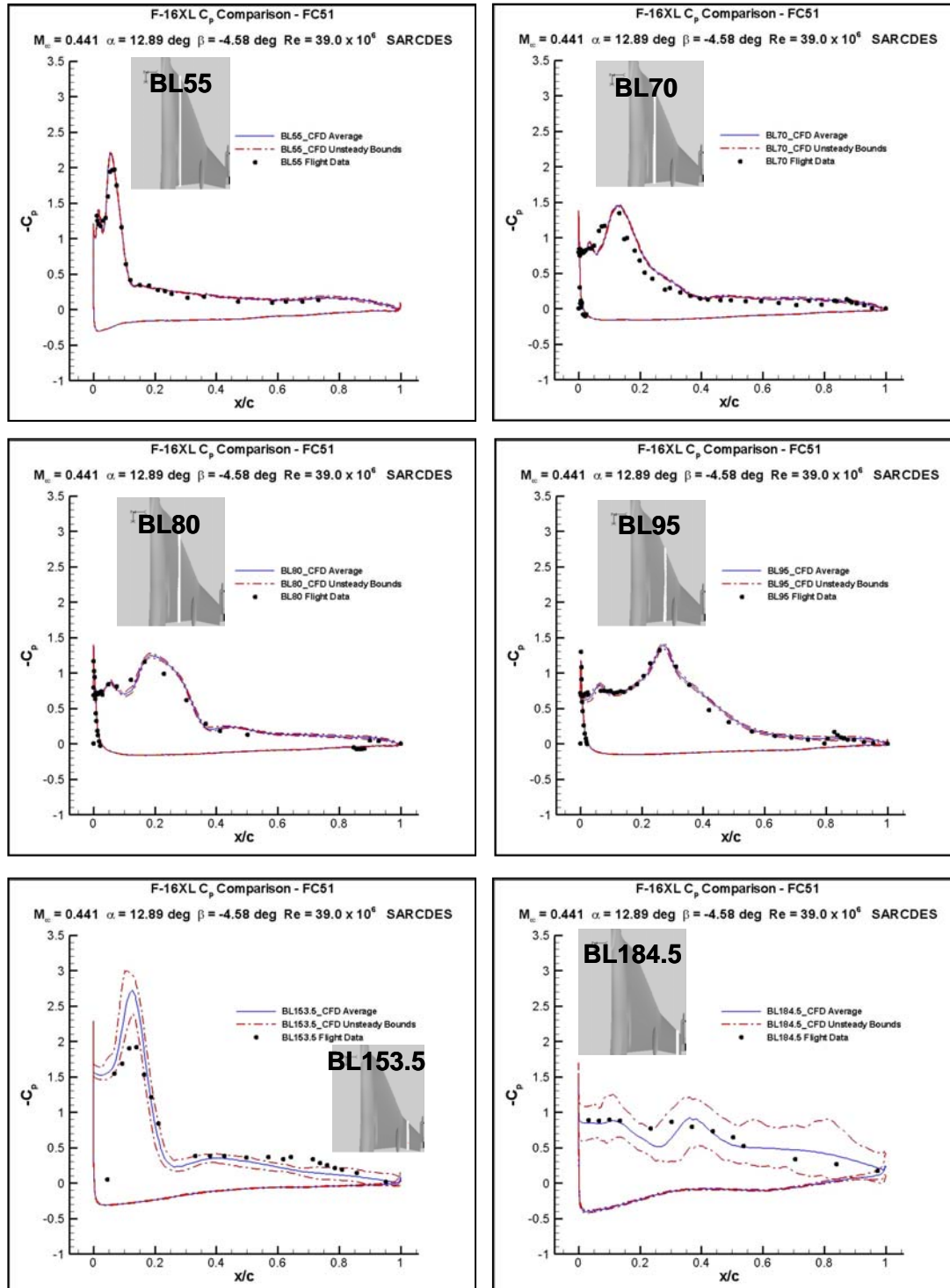
Figure 9-32: Flight Condition 51: Surface C_p along Various F-16XL Butt Line Stations (BL) for Flight Test, Computed Mean, and Computed Max and Min Value for a Series of Time Accurate Solutions.
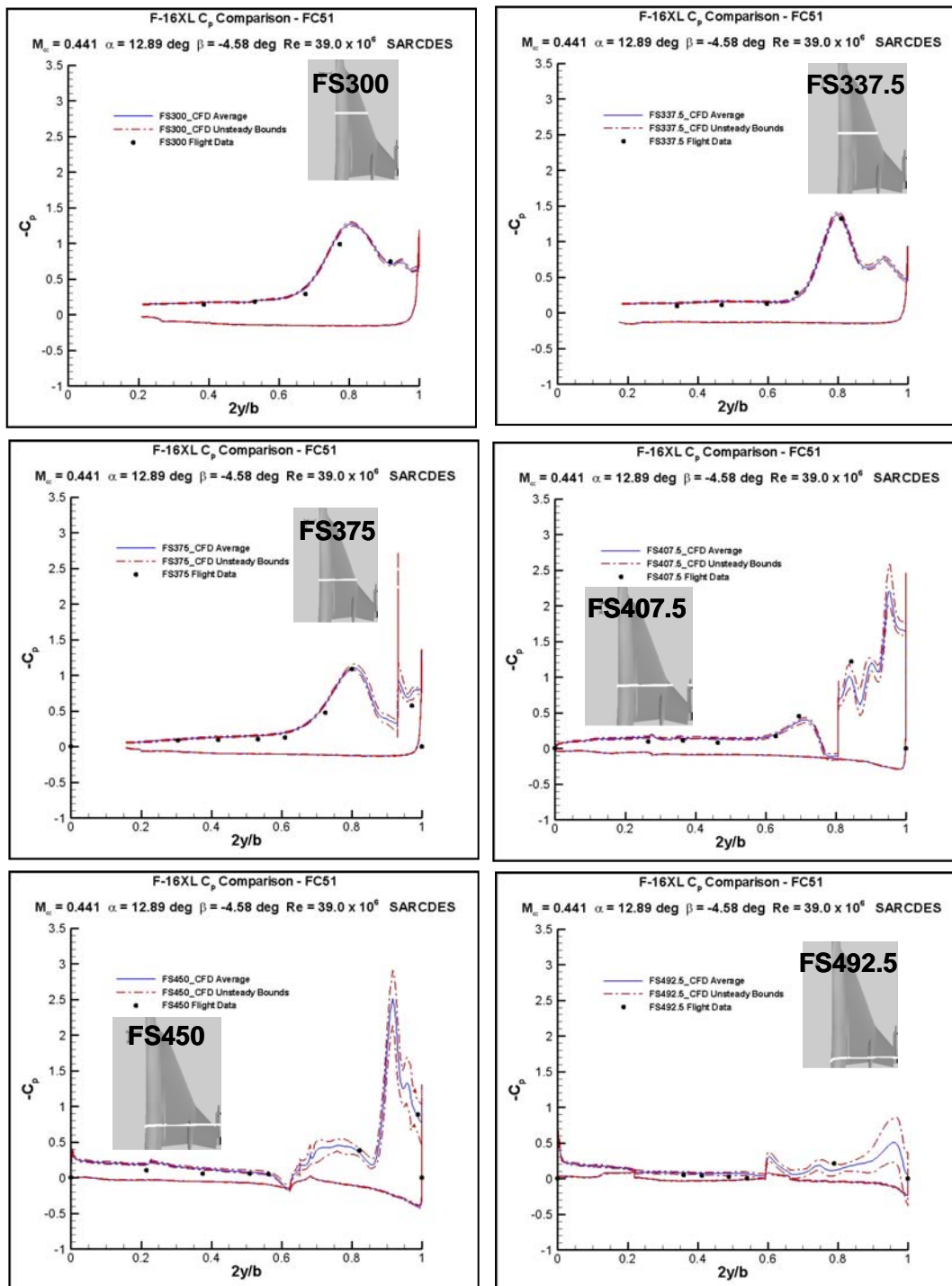
**Figure 9-33: Flight Condition 51: Surface C$_p$ along Various F-16XL Fuselage Stations
(FS) for Flight Test, Computed Mean, and Computed Max and Min Values.**

9.4.5   Improvements to the Baseline

This section describes modifications either to the flowfield conditions or the solver to account for differences between the computed data and the flight test data. The first improvement is to account for a non-zero sideslip in FC46 and the second is to incorporate recent improvements to the Detached-Eddy Simulation turbulence model.

9.4.5.1   Full Span FC46 Simulations
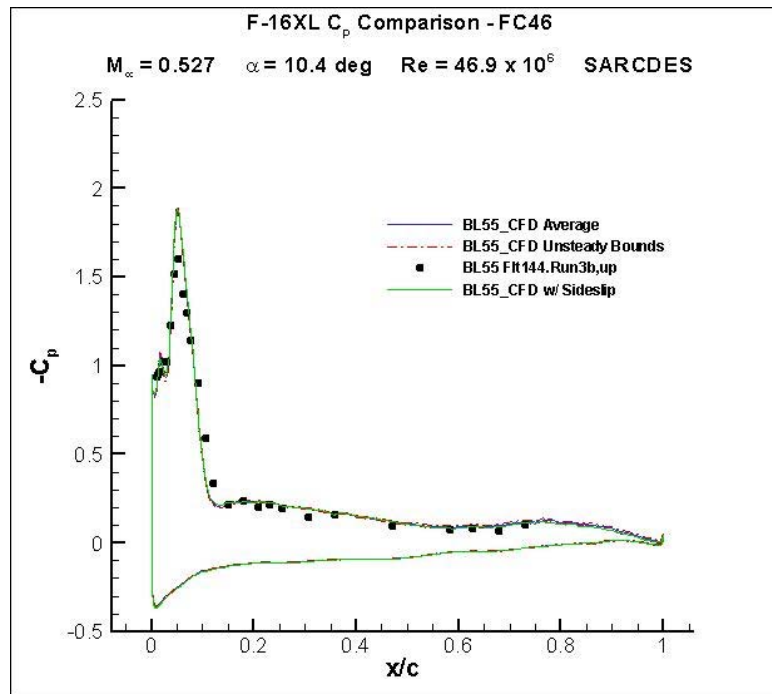
Figure 9-34: Flight Condition 46: F-16XL Surface C$_p$ for Butt Line Station (BL) 55. Comparison between Flight Test and CFD solutions for assumed symmetry and a slight side slip to exactly match flight test.
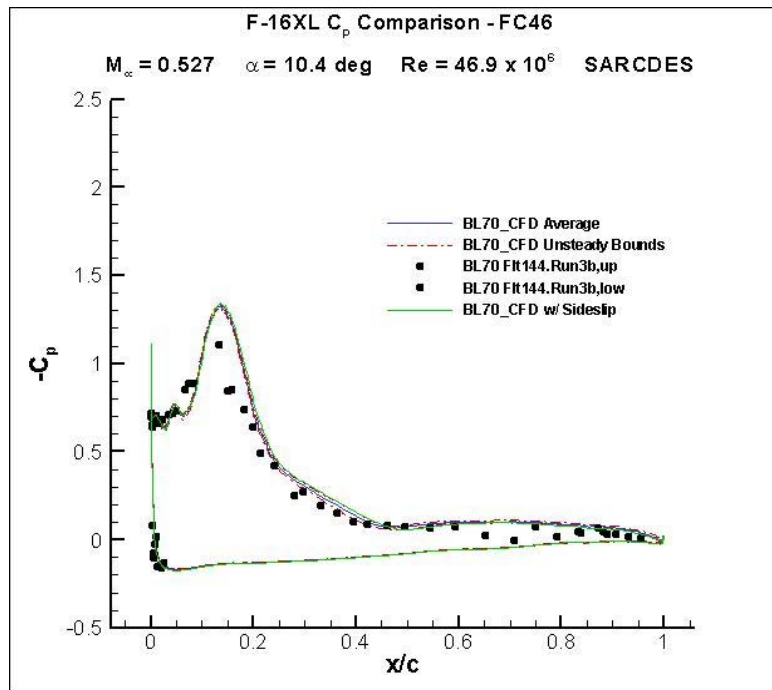
Figure 9-35: Flight Condition 46: F-16XL Surface C_p for Butt Line Station (BL) 70. Comparison between Flight Test and CFD solutions for assumed symmetry and a slight side slip to exactly match flight test.
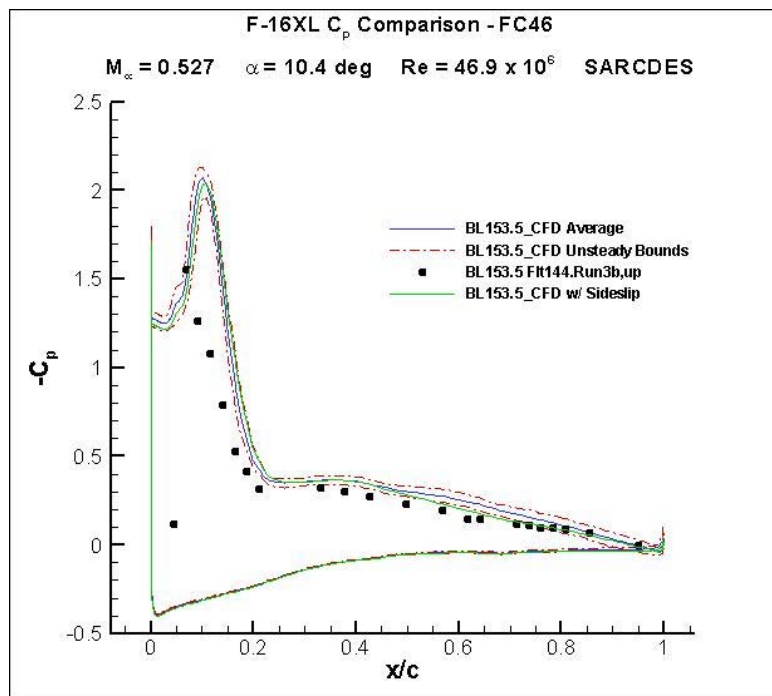
Figure 9-36: Flight Condition 46: F-16XL Surface C_p for Butt Line Station (BL) 153.5. Comparison between Flight Test and CFD solutions for assumed symmetry and a slight side slip to exactly match flight test.

9.4.5.2   Turbulence Model Improvements

Although the majority of comparisons were very good for the current unsteady solutions using the DES turbulence treatment, the boundary layer rake profiles of Rake 5 and 7 were disappointingly far from the flight test data. Since this mismatch was not evident in the C_p comparisons it was postulated that the differences may be due to the refined mesh near the leading edge creating an "embedded LES" region which is known to create incorrect boundary layer profiles [9-20]. This section presents solutions for an improved DES model called Delayed Detached Eddy Simulation (DDES) which delays the transition from RANS to LES to occur at the edge of the boundary layer. A complete discussion of the method is described in Reference [9-20].

Solutions were computed for Flight Condition 7 following the unsteady approach described in previous sections. Figure 9-37 depicts the comparison of C_p along BL 153.5 between DES and DDES turbulence treatments for both mean values and unsteady bounds of the simulation. It is clearly seen in the figure that the mean C_p values improved slightly to the flight test data for FC07. This improvement in C_p was consistent for all BL and FS data sets.
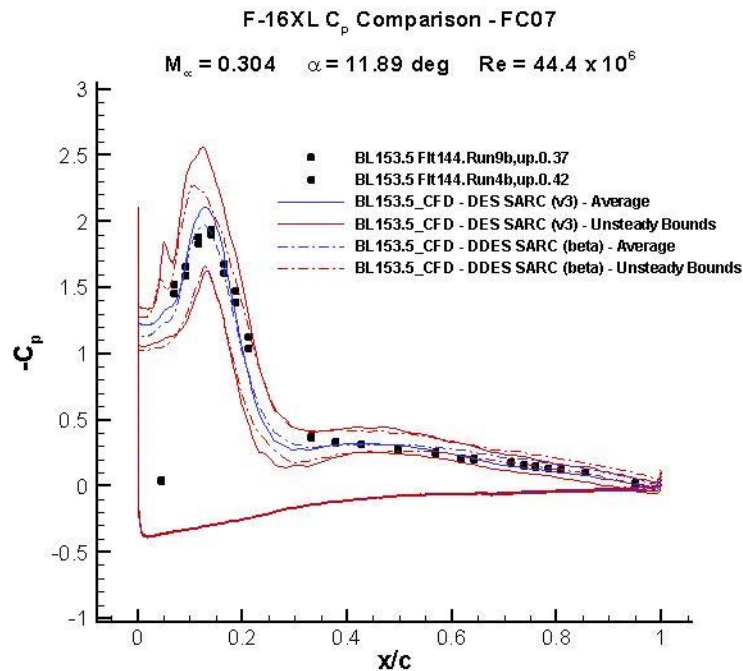
Figure 9-37: BL 153.5 C_p versus x/c for DES and DDES Turbulence Models and Flight Test.

The boundary layer rake profiles were also compared to determine if improvements were made with the DDES turbulence treatment. To review the issue, Rakes 3 and 4 compared well with experiments and CFD solutions from other CAWAPI participants. However, Rakes 5 and 7 significantly over predict the velocity ratio as a function rake height.
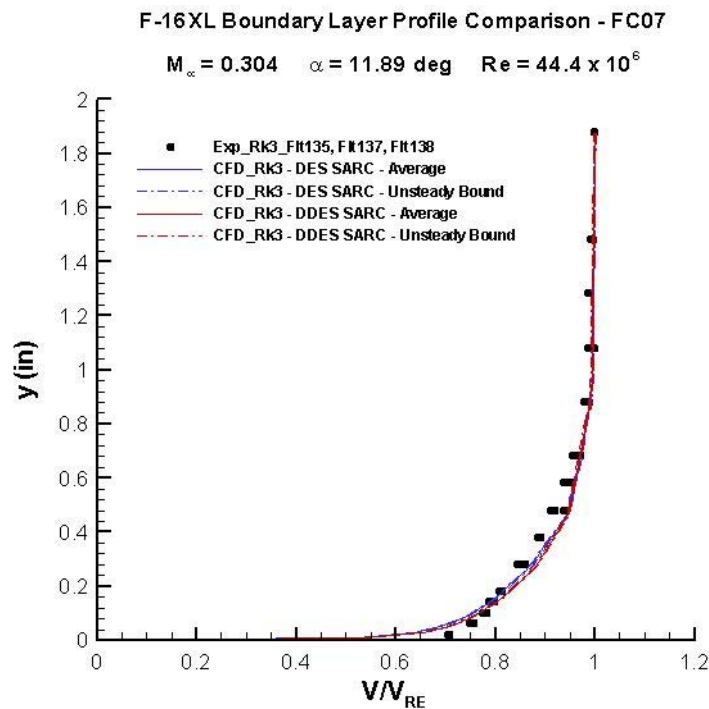
Figure 9-38: Rake 3 Boundary Layer Rake Velocity Scaled by Rake-Edge Velocity Profiles at Flight Condition 7. Mean and unsteady bounds for DES and DDES treatment solutions presented.
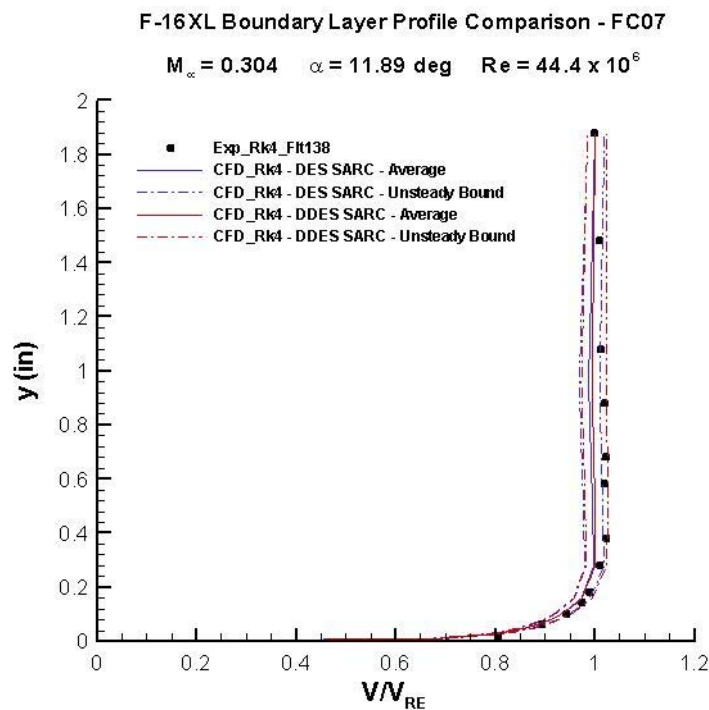
Figure 9-39: Rake 4 Boundary Layer Rake Velocity Scaled by Rake-Edge Velocity Profiles at Flight Condition 7. Mean and unsteady bounds for DES and DDES treatment solutions presented.
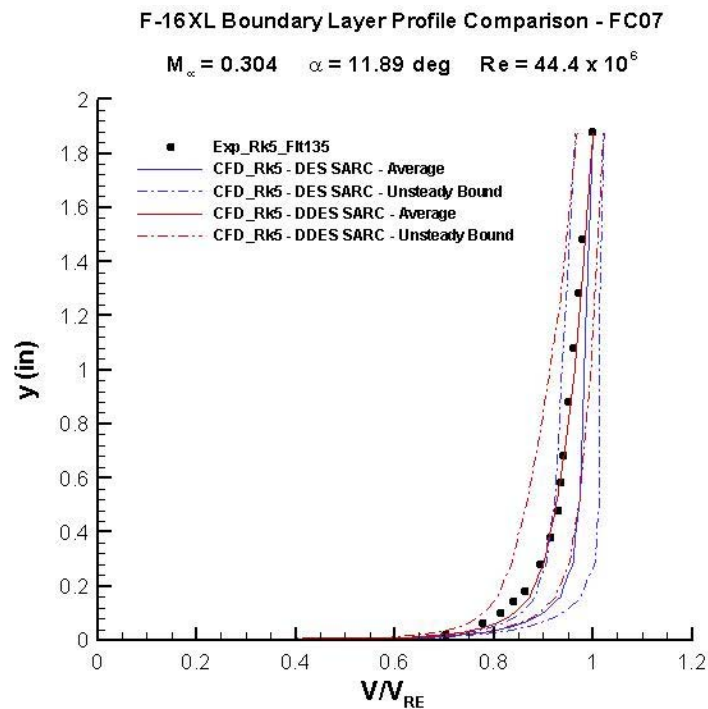
Figure 9-40: Rake 5 Boundary Layer Rake Velocity Scaled by Rake-Edge Velocity Profiles at Flight Condition 7. Mean and unsteady bounds for DES and DDES treatment solutions presented.
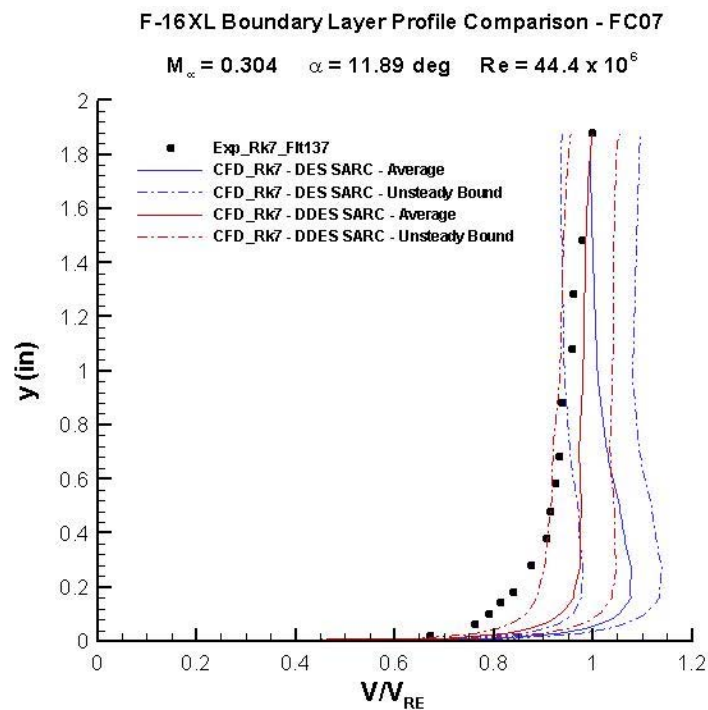
Figure 9-41: Rake 7 Boundary Layer Rake Velocity Scaled by Rake-Edge Velocity Profiles at Flight Condition 7. Mean and unsteady bounds for DES and DDES treatment solutions presented.

9.5 CONCLUDING REMARKS

Seven flight conditions of the F-16XL-1 aircraft were presented with comparisons to flight test data from the NASA CAWAP program. The ability of accurate CFD methods to compute and visualize these very complex vortical flowfields was evident and shown to be very useful for the aircraft industry. Very good agreement between surface C_p flight test data and computed data was seen in most subsonic cases. The unsteadiness of the simulations aft of vortex breakdown-like events were observed and quantified with min and max instantaneous C_p curves and compared to flight test, showing the utility of hybrid RANS-LES methods, such as DES, to compute these complex flowfields. The discrepancies for one of the rake boundary layer profiles and the surface skin friction data are subjects for further study and probably due to either miss-alignment of the velocity data in the case of the boundary layer velocity profile or grid refinement for both boundary layer and skin friction profiles.

9.6 REFERENCES

[9-1]   Lamar, J.E., Obara, C.J., Fisher, B.D. and Fisher, D.F.: *Flight, Wind-Tunnel, and Computational Fluid Dynamics Comparison for Cranked Arrow Wing (F-16XL-1) at Subsonic and Transonic Speeds*, NASA TP-2001-210629, 2001.

[9-2]   Lamar, J.E. and Obara, C.J.: *Review of Cranked-Arrow Wing Aerodynamics Project: Its International Aeronautical Community Role*, AIAA Paper 2007-0487, January 2007.

[9-3]   Spalart, P.R., Jou, W-H., Strelets, M. and Allmaras, S.R.: *Comments on the Feasibility of LES for Wings, and on a Hybrid RANS/LES Approach,* Advances in DNS/LES, 1st AFOSR Int. Conf. on DNS/LES, August 4-8, 1997, Greyden Press, Columbus OH.

[9-4]   Strang, W.Z., Tomaro, R.F. and Grismer, M.J.: *The Defining Methods of Cobalt: A Parallel, Implicit, Unstructured Euler/Navier-Stokes Flow Solver*, AIAA Paper 99-0786, January 1999.

[9-5]   Forsythe, J.R., Hoffmann, K.A., Cummings, R.M. and Squires, K.D.: *Detached-Eddy Simulation with Compressibility Corrections Applied to a Supersonic Axisymmetric Base*, Journal of Fluids Engineering, Vol. 124, No. 4, 2002, pp. 911-923.

[9-6]   Morton, S.A., Forsythe, J.R., Mitchell, A.M. and Hajek, D.: *Detached-Eddy Simulations and Reynolds-Averaged Navier-Stokes Simulations of Delta Wing Vortical Flowfields*, Journal of Fluids Engineering, Vol. 124, No. 4, 2002, pp. 924-932.

[9-7]   Mitchell, A.M., Morton, S.A., Forsythe, J.R. and Cummings, R.M.: *Analysis of Delta-Wing Vortical Substructures Using Detached-Eddy Simulation*, AIAA Journal, Vol. 44, No. 5, 2006, pp. 964-972.

[9-8]   Forsythe, J.R., Squires, K.D., Wurtzler, K.E. and Spalart, P.R.: *Detached-Eddy Simulation of Fighter Aircraft at High Alpha*, Journal of Aircraft, Vol. 41, No. 2, 2004, pp. 193-200.

[9-9]   Forsythe, J.R. and Woodson, S.H.: *Unsteady Computations of Abrupt Wing Stall Using Detached-Eddy Simulation,* Journal of Aircraft, Vol. 42, No. 3, 2005, pp. 606-616.

[9-10]   Morton, S.A., Cummings, R.M. and Kholodar, D.B.: *High Resolution Turbulence Treatment of F/A-18 Tail Buffet*, AIAA Paper 2004-1676, April 2004.

[9-11] Tomaro, R.F., Strang, W.Z. and Sankar, L.N.: *An Implicit Algorithm for Solving Time Dependent Flows on Unstructured Grids*, AIAA Paper 1997-0333, 1997.

[9-12] Grismer, M.J., Strang, W.Z., Tomaro, R.F. and Witzemman, F.C.: *Cobalt: A Parallel, Implicit, Unstructured Euler/Navier-Stokes Solver*, Adv. Eng. Software, Vol. 29, No. 3-6, pp. 365-373, 1998.

[9-13] Karypis, G., Schloegel, K. and Kumar, V.: *Parmetis: Parallel Graph Partitioning and Sparse Matrix Ordering Library*, Version 3.1, Technical Report, Dept. Computer Science, University of Minnesota, 2003.

[9-14] Samareh, S.: *GridTool: A Surface Modeling and Grid Generation Tool*, Proceedings of the Workshop on "Surface Modeling, Grid Generation, and Related Issues in CFD Solutions", NASA CP-3291, May 9-11, 1995.

[9-15] Pirzadeh, S.: *Progress Toward A User-Oriented Unstructured Viscous Grid Generator*, AIAA Paper 96-0031, 1996.

[9-16] *Cobalt Solutions*, Blacksmith User's Manual, Version 3.0, 2005.

[9-17] Gursul, I.: *Review of Unsteady Vortex Flows Over Delta Wings*, AIAA Paper 2003-3942, June 2003.

[9-18] Cummings, R.M., Morton, S.A. and Siegel, S.G.: *Computational Simulation and Experimental Measurements for a Delta Wing with Periodic Suction and Blowing*, Journal of Aircraft, Vol. 40, No. 5, 2003, pp. 923-931.

[9-19] Cummings, R.M., Morton, S.A., Siegel, S.G. and Bosscher, S.: *Numerical Prediction and Wind Tunnel Experiment for a Pitching Unmanned Combat Air Vehicle*, AIAA 41st Aerospace Sciences Meeting, Reno, NV, January 6-9, 2003. AIAA Paper 2003-0417.

[9-20] Travin, A.K., Shur, M.L., Spalart, P.R. and Strelets, M.: *Improvement of Delayed Detached-Eddy Simulation for LES with Wall Modeling*, European Conference on Computational Fluid Dynamics, 2006.

Chapter 10 – NUMERICAL SOLUTIONS FOR THE CAWAPI CONFIGURATION ON UNSTRUCTURED GRIDS AT KTH/FOI, SWEDEN – PART I

By

Stefan Görtz and Adam Jirásek

10.1 SUMMARY

Steady and unsteady viscous simulations of a full-scale, semi-span and full-span model of the F-16XL-1 aircraft at seven different flight Reynolds/Mach number combinations have been performed with an unstructured CFD code. The steady-state simulations are with several turbulence models of different complexity. Detached-Eddy Simulation (DES) has been used to compute the unsteady flow. The computed results are compared with public domain flight-test data. Very good agreement is demonstrated for surface pressure distribution, local skin friction and boundary velocity profiles. The different turbulence models performed almost equally well, except the Spalart-Allmaras model, which failed to predict the flow qualitatively and quantitatively. The Differential Reynolds Stress Model (DRSM) outperformed all other models when it comes to local span-wise skin friction. DES was superior over RANS modeling at the highest angle of attack, where the flow over the outer wing is separated and partly unsteady.

10.2 NOMENCLATURE

α	= angle of attack
β	= sideslip angle
b	= wing span
c	= cord length
c_f	= friction coefficient
c_P	= pressure coefficient
M_∞	= freestream Mach number
v	= velocity
BL	= butt line
CAWAPI	= Cranked Arrow Wing Aerodynamics Project International
FC	= Flight Condition
FS	= Fuselage station
RANS	= Reynold-Averaged Navier-Stokes

10.3 DENOTATION OF TURBULENCE MODELS

EARSM	= Explicit Algebraic Reynolds Stress Model based on standard k-ω model
EARSM + CC	= EARSM based on standard k-ω model with curvature corrections

Hellsten EARSM	= EARSM based on Hellsten k-ω model
Hellsten EARSM + CC	= EARSM based on Hellsten k-ω model with curvature corrections
DRSM	= Differential Reynolds Stress Model
DES	= Detached Eddy Simulation
S − A	= Spalart-Allmaras model

10.4   INTRODUCTION

Current requirements for military aircraft result in a need for a better understanding of aircraft characteristics before full-scale production. For this purpose new and existing computational fluid dynamics (CFD) codes have to be validated and their technology readiness level checked and/or increased for military aircraft - both manned and unmanned. The benefits resulting from validated CFD codes are a reduction of project risks, enhanced analysis of system performance prior to flight and the ability to analyze unexpected flight behavior.

Flight data for CFD code validation has been obtained on and off the surface of the F-16XL-1 aircraft at subsonic and transonic speeds as documented by Lamar [10.1]. This data is unique both in that it is for a high-performance fighter aircraft and it is publicly accessible on the internet [10.2]. Furthermore, the data is not subject to wind tunnel blockage-, scaling- or Reynolds-number effects. Comparison between numerical and experimental data can be done at flight Reynolds numbers as opposed to wind-tunnel Reynolds numbers, circumventing the problem of modeling transition.

Researchers from several countries, after learning of this high Reynolds number flight-test data set, expressed interest in validating their CFD codes against flight measurements of surface pressures and flow, boundary layer velocity profiles and skin friction obtained on this high-performance aircraft. As a result, they joined with American participants in one 'facet' of a NATO Research and Technology Organization (RTO) Applied Vehicle Technology (AVT) task group. This facet was named the "Cranked Arrow Wing Aerodynamics Project International" (CAWAPI). The aim was to develop and document the best practices for each code so as to raise its technology readiness level when applied to this class of aircraft. New CFD solutions were generated by the team members, among them KTH and FOI, and placed into a CAWAPI archiving system using common data standards to facilitate timely data access to other team members.

Previous computational investigations of the F-16XL-1 have been performed by Lamar [10.1, 10.3] and Lessard [10.4]. The former was a flight, wind-tunnel and CFD comparison at subsonic and transonic speeds using a structured flow solver (`CFL3D`) with wall functions, whereas the latter was a subsonic analysis of a 0.04-scale model using an unstructured Euler code.

The present paper documents the Swedish contributions to CAWAPI. We present wall-resolved viscous computations of the full-scale aircraft at flight Reynolds numbers using state-of-the-art numerical techniques and turbulence models. The goal is to improve the understanding and modeling of vortical flows and to identify weaknesses in the modeling process. The paper begins with a description of the aircraft and the associated flight test program, followed by a presentation of the numerical method and the grid used here. The main part discusses the computed results and compares them to flight-test data.

10.5   FLIGHT CONDITIONS

Seven of the 99 CAWAP flight conditions (FC) [10.1] were selected for computation in CAWAPI. They represent different Reynolds/Mach number combinations at subsonic and transonic speeds, with and without sideslip. All seven flight conditions are listed with their nominal and actual values in Table 10-1.

Flight conditions 7, 19, and 46 are medium angle-of-attack vortical flow conditions at various subsonic Mach

Table 10-1: Flight Conditions (FC) to be Examined (Nominal Altitude, actual Mach Number, actual Angle of Attack, actual Side-Slip Angle, actual Reynolds Number).

FC	alt. [ft]	M_∞	α [°]	β [°]	Re
Minimum Flight Conditions to be examined:					
FC07	5,000	0.304	11.89	-0.133	44.40×10^6
FC19	10,000	0.360	11.85	+0.612	46.80×10^6
FC46	24,000	0.527	10.40	+0.684	46.90×10^6
FC70	22,300	0.970	4.37	+0.310	88.77×10^6
Additional Flight Conditions to be examined:					
FC25	10,000	0.242	19.84	+0.725	32.22×10^6
FC50	24,000	0.434	13.56	+5.310	39.41×10^6
FC51	24,000	0.441	12.89	-4.580	38.96×10^6

numbers and altitudes, whereas FC70 is a low angle of attack attached flow condition at a transonic Mach number of 0.97. Flight conditions 50 and 51 are also medium angle-of attack vortical flow conditions, but at sideslip angles of +5.31 and -4.58, respectively, and a mirrored full-span grid created from the standard grid was used. Flight condition 25 is at a high incidence angle and most interesting in terms of unsteady modeling.

All seven flight conditions were computed by KTH/FOI. Note that all calculations were made assuming fully turbulent flow. Flight conditions 7, 19, 25, 46 and 70 have zero nominal side slip and were computed as symmetric using the semi-span standard unstructured grid although the actual side-slip angles ranged from +0.725 to -0.133. For the full-span model simulations at FC50 and FC51 the actual angle of side slip was specified. The angle of attack was set to the actual angle of attack for all flight conditions.

10.6   AIRCRAFT DESCRIPTION AND GEOMETRY

The F-16XL-1 is a single-seat fighter-type prototype aircraft built by the General Dynamics Corporation (now a part of the Lockheed-Martin Aeronautics Company). The aircraft has been developed from a full-scale development F-16A airframe by stretching the fuselage and adding a cranked-arrow wing, a modified fuel system and a modified flight-control system. It has scheduled leading-edge flaps, elevon, and ailerons on the wing for control. Details on the construction of the aircraft, its flight testing and its intended mission are given in Ref. [10.5–10.8].

The design of the cranked-arrow wing was a cooperative effort of the NASA Langley Research Center and the General Dynamics Corporation. The results of various wind-tunnel investigations are reported in Ref. [10.9–10.11]. The new wing was designed to provide the F-16 aircraft with improved supersonic performance, whilst maintaining transonic performance comparable with that provided by the current F-16 design, thus giving the aircraft a greater operational range. The resulting design has a leading-edge sweep angle of 70° inboard and 50° outboard of the crank. To alleviate a pitch instability that occurred at high angles of attack in wind-tunnel tests an "S-blend curve" was placed in the leading edge at the juncture of the wing with the fuselage. The aircraft was most recently used in the "Cranked-Arrow Wing Aerodynamics Project" (CAWAP) to test boundary layer pressures and distribution. The project began as a part of the high-lift element of the NASA High-Speed Research Program, developing technologies applicable to the High-Speed Civil Transport. This required modifications to the aircraft, which are described in detail in Ref. [10.1] and [10.3], notably strips of tubing along the leading edge to the trailing edge of the wing to sense static pressure on the wing and obtain pressure distribution data. The instrumented aircraft is shown in flight in Fig. 10-1. The starboard-side wing received data on pressure

distribution and the port-side wing had three types of instrumentation: modified Preston tubes to measure local skin friction, boundary layer rakes to measure boundary layer profiles and hot films to determine boundary layer transition locations. Surface tufts, surface oil flow and surface liquid crystal transducer responses were recorded using a special video installation. The pressure and surface-flow data were used for the purpose of establishing the effect of variations in Mach number on the local flow. The first flight of the CAWAP aircraft occurred on November 21, 1995, and the test program ended in April 1996. The CAWAP flight tests reported in Ref. [10.1] were with the air dams – upper-surface fences mounted near the wing leading-edge crank – and wingtip missiles installed. A detailed description of the CAWAP and CAWAPI projects can be found in Ref. [10.5].

Figure 10-1: F-16XL-1 Instrumentation Suite, Port Wing: Dummy Missiles with Built-in Video Cameras, Tufts, Flow-Visualization Paint Scheme, Video Targets; Starboard Wing: Pressure Belts (NASA Photo, 1996).

10.6.1 Geometry Simplifications

A geometry file of the F-16XL in `IGES` format, which is subject to International Traffic in Arms Regulations (ITAR), was provided to NASA and other CAWAPI team members by the Lockheed-Martin Aeronautics Company. Geometrical consistency between the real aircraft, including wing-tip mounted missiles, air dams and tail, and the CAD/CFD model was demonstrated in Ref. [10.1]. The `IGES` file was examined at EADS and multiple surfaces were found embedded in the description. A single set of surfaces was selected which includes some refinements in the leading-edge region for grid resolution. Later at NASA, certain features were adjusted for structured grid work, such as between the nozzle and the trailing-edge flap, the trailing edge of the missile rail fairing onto the wing, the engine inlet, a 'step' or 'plate' on the upper surface, and the smoothing out of a step in the longitudinal progression of the nose-boom outer diameter.

10.7 COMPUTATIONAL METHOD

10.7.1 Description of the Edge CFD Solver

KTH and FOI joined forces and used Edge [10.12] for contributing to CAWAPI. `Edge` is a flow solver for unstructured hybrid grids of arbitrary elements. The code is a proprietary code of the Swedish Defence Research Agency (FOI) where it is being developed. It is sheared with other users, among them KTH, based on a license agreement. User development of Edge is shared with FOI.

The parallel flow solver is based on an edge-based formulation and uses a node-centered finite volume scheme to solve the compressible Reynolds-Averaged Navier-Stokes (RANS) equations. For steady flows, the equations

are integrated toward steady state with an explicit multi-stage Runge-Kutta scheme. To accelerate convergence, implicit residual smoothing and a multi-grid technique can be employed. Low Mach-number preconditioning is also available. The spatial discretization is either second order central or second order upwind.

Time-accurate calculations are done either by Runge-Kutta time marching with a global time step or by implicit time marching with explicit sub-iterations, so-called "dual time stepping" [10.13].

The adaptive mesh refinement (AMR) module allows for local h-refinement of the hybrid grid by cell subdivision based on a sensor derived from the flow solution. In addition, there are three sensors for identifying vortices. They are based on the total pressure ratio, the production of entropy and an eigenvalue analysis of the velocity gradient tensor, respectively [10.14, 10.15].

10.7.2 Turbulence Modeling in Edge

The `Edge` code contains several eddy-viscosity turbulence models based on the Boussinesq hypothesis as well as a suite of Explicit Algebraic Reynolds Stress Models (EARSM). It also contains a Differential Reynolds Stress Model (DRSM), an algebraic hybrid RANS-LES (Large-Eddy Simulation) model [10.16, 10.17], and Detached Eddy Simulation (DES) capability.

10.7.2.1 Spalart-Allmaras Model of Turbulence (S-A)

The Spalart-Allmaras model [10.18] is a one-equation eddy viscosity model which models the Reynolds stress tensor as

$$\tau_{ij} = 2\mu_T S_{ij} \tag{1}$$

The Spalart-Allmaras model is one of the frequently used models in aerodynamic CFD calculations. The model is denoted S-A in this article.

10.7.2.2 Explicit Algebraic Reynolds Stress Model (EARSM)

The EARSM is an approximation of a Reynolds stress transport model in the weak-equilibrium limit. It behaves reasonably well for non-equilibrium flows. The Reynolds stress tensor is related to the anisotropy tensor a_{ij} through both the strain-rate tensor S_{ij} and the tensor of rotation Ω_{ij}. This model has been shown to give improved results but at a computational effort that is comparable to that of linear two-equation models. The implementation in Edge is done according to Wallin and Johansson [10.19]. The model has been used in combination with two types of k-ω models - the standard k-ω [10.20] model and the Hellsten k-ω model [10.21]. They are denoted EARSM and Hellsten EARSM, respectively, in this article.

10.7.2.3 Curvature Corrected Explicit Algebraic Reynolds Stress Model (EARSM + CC)

The weak-equilibrium limit can be too strong an assumption for flows with streamline curvature where the convective derivatives in the expression $\frac{Da_{ij}}{Dt}$ cannot be considered zero. The assumption of weak equilibrium can instead be defined in a curvilinear system. The tensor of rotation Ω_{ij} is corrected by adding the following term [10.22]

$$\Omega_{ij}^* = \Omega_{ij} - \frac{\tau}{A_0}\Omega^{(r)} \tag{2}$$

where A_0 is a constant. In general, the curvature correction has shown some improvements compared to the standard EARSM. However, it imposes some numerical problems and degenerates the convergence rate in some cases. In Edge, the correction was applied to both EARSM models, the one based on the standard k-ω model,

and the one based on the Hellsten k-ω model. They are denoted EARSM + CC and Hellsten EARSM + CC in this article.

10.7.2.4 Differential Reynolds Stress Model (DRSM)

This model does not model the Reynolds stress tensor in an algebraic formulation. It rather models additional correction terms in the Reynolds stress transport equation, for example

$$k\left(\frac{Da_{ij}}{Dt} - \mathcal{D}_{ij}^{(a)}\right) = \left(\mathcal{P}_{ij} - \frac{\overline{u_i u_j}}{k}\mathcal{P}\right) - \left(\epsilon_{ij} - \frac{\overline{u_i u_j}}{k}\epsilon\right) + \Pi_{ij} \tag{3}$$

$$a_{ij} = \frac{\overline{u_i u_j}}{k} - \frac{2}{3}\delta_{ij} \tag{4}$$

The model requires modeling of additional terms such as the pressure strain-tensor Π_{ij} and the dissipation rate ϵ_{ij}. The DRSM implementation in Edge has been done according to Hanjalic [10.23]. The model is denoted DRSM in this article.

10.7.2.5 Detached-Eddy Simulation (DES)

RANS methods have demonstrated an ability to predict attached flows very well at a relatively low computational cost. Large-Eddy Simulation (LES) methods, on the other hand, have proved to compute accurately separated flow fields. Although the computational costs of LES of turbulent flows is significantly less than that of direct numerical simulation (DNS), it is still too expensive for engineering applications involving thin boundary layers near surfaces, since the resolution needed to capture these layers results in exorbitant demands on CPU power and memory.

Spalart *et al* [10.24] proposed a hybrid LES/RANS turbulence model based on the one-equation Spalart-Allmaras eddy viscosity model as an alternative to the rather limited capabilities of inexpensive RANS models and improved features of computationally expensive LES. This hybrid approach, also called Detached-Eddy Simulation (DES), employs the S-A RANS turbulence model to overcome the near-wall resolution problem. This robust approach is aimed at high-Reynolds-number separated flows, where it smoothly switches from RANS mode in the boundary layer to LES in the separated region, improving results noticeably over purely RANS modeling. This model has shown promising performance in simulation of massively separated flows, for example, the flow over delta wings and delta-wing configurations at high angle of attack.

In the DES approach, the length scale d in the destruction term of the Spalart-Allmaras model,

$$\frac{D\tilde{\nu}}{Dt} = \underbrace{c_{b1}\tilde{S}\tilde{\nu}}_{\text{production}} + \underbrace{\frac{1}{\sigma}[\nabla \cdot ((\nu + \tilde{\nu})\nabla\tilde{\nu}) + c_{b2}(\nabla\tilde{\nu})^2]}_{\text{diffusion}} - \underbrace{c_{w1}f_w\left(\frac{\tilde{\nu}}{d}\right)^2}_{\text{destruction}} \tag{5}$$

$$\underbrace{\phantom{\frac{D\tilde{\nu}}{Dt}}}_{\text{convection}}$$

is modified so that the eddy viscosity crosses over from the usual Spalart-Allmaras RANS eddy viscosity near the wall to a proposed sub-grid scale (SGS) eddy viscosity, similar to that defined by Smagorinsky for SGS models, away from the wall. The Spalart-Allmaras wall destruction term, which reduces the turbulent viscosity in the laminar sub-layer, is proportional to $(\tilde{\nu}/d)^2$, where $\tilde{\nu}$ is the eddy viscosity and d the distance to the nearest wall. When this term is balanced with the production term, the eddy viscosity becomes proportional to $\hat{S}d^2$, where $\hat{S}$ is the local strain rate. The Smagorinski LES model, on the other hand, varies its sub-grid scale turbulent viscosity with the local strain rate and the grid spacing:

$$\nu \propto \hat{S}\Delta^2 \tag{6}$$

where $\Delta = \max(\Delta x, \Delta y, \Delta z)$. If d is replaced with Δ in the wall destruction term, the Spalart-Allmaras model will act similarly to the Smagorinski SGS model. Consequently, the DES formulation is obtained by replacing in the Spalart-Allmaras model the distance to the nearest wall, d, by $\tilde{d}$, where $\tilde{d}$ is defined as

$$\tilde{d} \equiv \min(d, C_{\text{DES}}\Delta) \tag{7}$$

Thus, the switch from RANS to LES depends on the spatial discretization. When the length scale d is smaller than the wall-parallel grid spacing Δ, which is typically the case for the highly stretched cells in the boundary layer, the model acts in RANS mode. When d is larger than Δ, the model acts in LES mode. This approach introduces only one additional model constant ($C_{\text{DES}} = 0.65$, calibrated from decaying isotropic turbulence) in the one-equation model of Spalart and Allmaras.

As `Edge` employs an edge-based formulation, where an edge connects two nodes, Δ is defined as the length of the largest edge of a cell,

$$\Delta = \max(\text{edge}_i) \tag{8}$$

or, on anisotropic grids, Δ can be based on the cell volume δV,

$$\Delta = (\delta V)^{1/3} \tag{9}$$

The DES implementation in `Edge` is described in more detail in Ref. [10.25, 10.26].

A powerful feature of DES is that it directly resolves turbulent eddies with increasing fidelity as the grid is refined [10.27]. Note that in RANS it is the mean flow that is computed – the role of grid refinement is to ensure convergence of the numerical solution and to minimize (or eliminate) the influence of the grid. In the fine-grid limit, the accuracy of RANS predictions are controlled by the turbulence model. In LES and DES, on the other hand, the role of grid refinement is resolution of additional physical features, i.e. a wider range of turbulent eddies are represented as grid spacings are decreased. Correspondingly, the contribution of the turbulence model to the solution decreases as the grid is refined. The fine-grid limit of DES (and LES) is a solution free of turbulence modeling errors, i.e. DNS. The model is denoted DES in the article.

10.7.3 Numerical Grid and Boundary Conditions

The standard unstructured grid used here was generated by NASA Langley Research Center using the grid generation packages `GridTool` [10.28] and `VGRIDns` [10.29]. It is described in detail elsewhere in this report. It is an all-tetrahedral viscous grid for the half-span, full-scale model of the F-16XL-1 (control surfaces not deflected) and is made up of 2,534,132 nodes, corresponding to 14,802,429 cells. The surface of the half-span model of the F-16XL was discretized with 160,266 triangular elements. The upper surface grid is shown in Fig. 10-2(a).

For the sake of completeness it must be pointed out that the grid generation approach followed by NASA is unconventional in that thin layers of right-angled tetrahedral cells are generated in the boundary layer region by the advancing-layers method (ALM). Unlike the conventional advancing-front method (AFM), which introduces cells in the field in a totally unstructured manner, the ALM generates layers of thin tetrahedral cells in a more orderly fashion while maintaining many advantageous features of the AFM. Outside the boundary layer a regular, nearly isotropic (inviscid) tetrahedral grid is generated by the AFM. The transition from thin layers to the regular grid is gradual and continuous because a common background grid is used to control both methods.

Note that for numerical reasons `Edge` requires the use of hybrid grids, where cell shapes that do not become skewed with stretching (e.g., hexahedral and prisms) are used in the viscous regions and tetrahedral cells away from viscous regions. To fulfill that requirement, the all-tetrahedral grid was converted into a hybrid
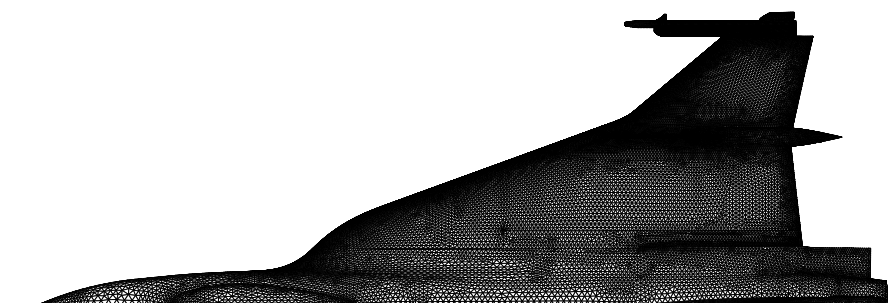
(a): **Unstructured surface grid for the F-16XL-1 half-span model (160,266 faces).**
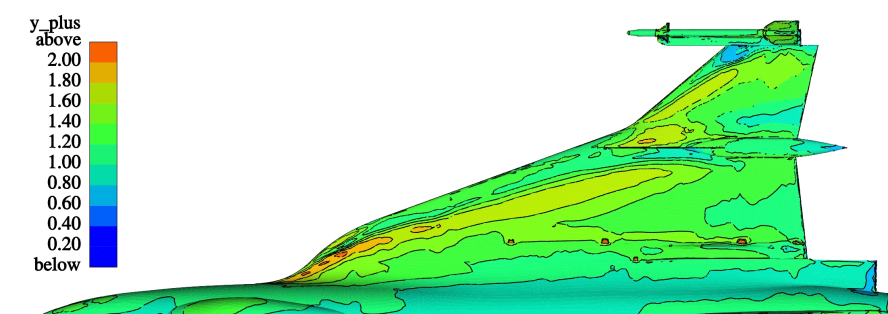
(b): **Levels of y^+ on the Upper Surface for FC19 (EARSM).**
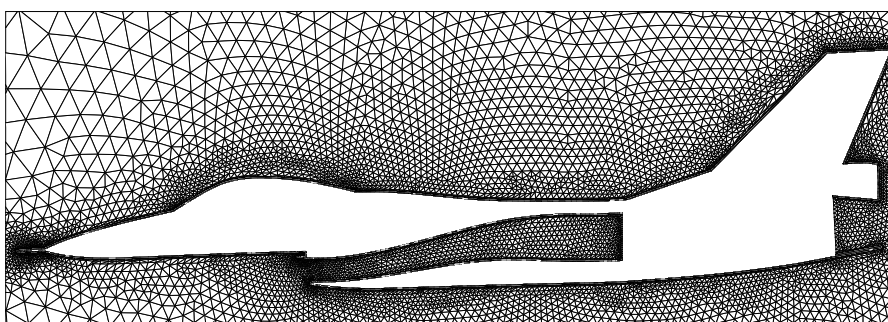
(c): **Symmetry plane of the hybrid grid showing the meshed inlet duct and nozzle.**

Figure 10-2: Computational Grid.

grid in `Cobalt` [10.30] format by combining the first nine layers of high-aspect-ratio, semi-structured tetrahedral cells off the aircraft surface into layers of prismatic cells using the commercial grid managements utility `Blacksmith` from Cobalt Solutions, LLC. This operation reduced the cell count to a total of 11,928,103, corresponding to 2,535,842 nodes. The program generated 9 layers of prismatic cells, corresponding to 1,442,394 prisms. The reason the grid has only 9 layers is that pyramids would be needed as "end caps" for layers that are not complete. Rather than adding another cell type it was decided to accepted 9 layers. It is important to note that the transition between the admittedly relatively few prismatic layers and the tetrahedral grid is very smooth, because there are a number of semi-structured ALM-generated viscous layers on top of the prismatic layers. The hybrid grid was used by the US Air Force Academy and KTH/FOI with `Cobalt` and `Edge`, respectively.

The resolution of the boundary layers requires the grid to be clustered in the direction normal to the surface with the spacing of the first grid point off the wall to be well within the laminar sublayer of the boundary layer. For turbulent flows, the first point off the wall should exhibit a y^+ value of less than 1.0. Here, the spacing of the first grid point normal to the solid wall is 5.0×10^{-6} m ($6.6 \times 10^{-7}c$). Away from the wall, the spacing increases by a ratio of 1.2. The resulting y^+ distribution over the upper surface of the aircraft model is shown for FC19 in Fig. (b). spacing normal to the numerical surface led to an average value of y^+ of less then one and a maximum y^+ of about two under the primary wing vortex, demonstrating that the grid is fine enough at the wall boundaries.

The engine duct is meshed all the way to the inlet duct exit plane. The nozzle is meshed from the engine mixing plane, see Fig. 10-2(c). The grid density off the aircraft surface is shown in Fig. 10-3, which depicts a wrinkly cutting plane through the grid at FS496 (fuselage station on airplane in inches, positive aft) , close to the trailing edge.
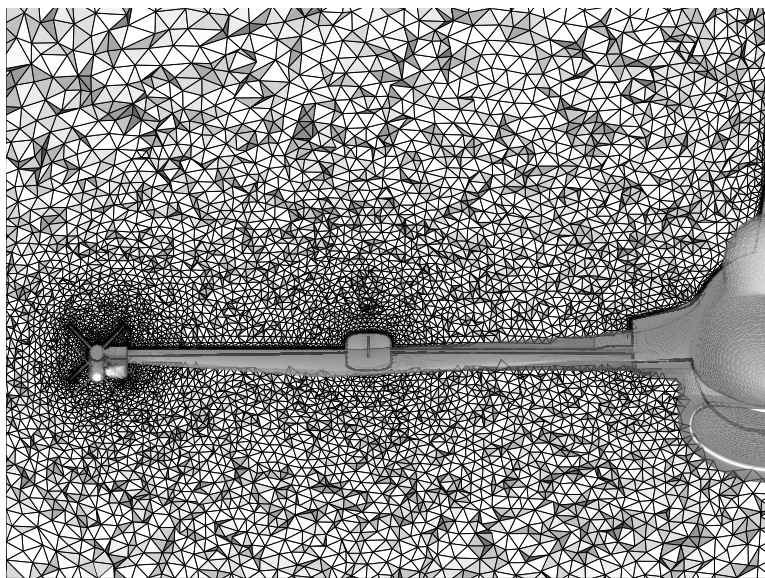
Figure 10-3: Wrinkly Cutting Plane at FS496 Showing the Grid Density off the Aircraft Surface close to the Trailing Edge.

Next, the hybrid grid was converted from Cobalt format to the "Flexible Format Architecture" (`FFA`) [10.31], the native `Edge` format. In this conversion step, all grid dimensions were converted from inches to meters. Finally, the `FFA`-format grid was converted to the CFD General Notation System (CGNS) [10.32], library version 2.3. The resulting `CGNS` file was uploaded onto the Virtual Laboratory (VL) [10.33] at the NASA Langley Research Center to be used by other researchers in the CAWAPI group. The tools for converting grids

Table 10-2: Propulsion Conditions as a Function of the Flight Condition (FC).

FC	Inlet duct exit conditions				Mixing plane cond.	
	T_{stat} [K]	p_{stat} [Pa]	u [m/s]	Mach	T_{tot} [K]	p_{tot} [Pa]
FC07	276.7	75,842	115.7	0.347	583.3	158,579
FC19	269.9	70,327	105.4	0.320	583.3	148,237
FC25	261.1	60,122	144.7	0.447	671.7	181,332
FC46	246.4	40,334	123.2	0.390	580.6	102,042
FC70	288.3	73,429	141.6	0.416	666.7	206,843
FC50	244.5	35,577	147.3	0.470	641.4	116,866
FC51	239.8	35,784	142.8	0.460	636.7	115,418

Figure 10-4: Convergence History of different RANS Turbulence Models for FC19: Density Residual versus Number of Iterations.

in `Cobalt` and `VGRIDns` format to `CGNS` format were also made available on the VL.

The boundary conditions are symmetry, adiabatic wall for the surface of the aircraft, and characteristic variable freestream conditions for the far-field boundaries, which are located about 10 aircraft length (24 root chord lengths) away from the aircraft. The boundary conditions on the inlet duct exit plane and the mixing plane are pressure outlet and total states inlet, respectively. The corresponding propulsion conditions are listed for the different flight conditions to be examined in Table 10-2. It should be noted that these conditions are generic engine conditions and do not correspond to any specific engine.

For the two flight conditions with non-zero sideslip the half-span grids were mirrored at the symmetry plane, resulting in a grid with 20,971,418 tetrahedra and 2,884,788 prisms. To investigate the influence of the number of prismatic layers on the accuracy of the results computed with the codes that require hybrid grids, a second unstructured hybrid grid with up to 20 prismatic layers was generated from the all-tetrahedral grid. This grid featured "chopped" prismatic layers with pyramids as end caps. It was used by KTH/FOI with `Edge`.

10.7.4 Convergence

A typical convergence plot is shown for FC19 in Fig. 10-4. As the convergence criterion we used residuals of

Table 10-3: Computed Cases: Turbulence Models Used for Computing the different Flight Conditions (FC).

FC	S-A	EARSM	Hellsten	EARSM + CC	Hellsten + CC	DRSM	DES	hybrid
FC07	×	×	×	×	×	-	×	×
FC19	×	×	×	×	×	×	-	-
FC46	×	×	×	×	×	×	×	-
FC25	×	×	×	×	×	-	×	-
FC50	×	×	×	-	×	-	-	-
FC51	×	×	×	-	×	-	-	-
FC70*	×[†]	×	×	×	×	-	-	-

* The wall resolution of the present grid is not sufficient for the higher Reynolds number at this flight condition.

[†] Calculation was performed but was unstable and no converged solution was obtained.

$\partial\rho/\partial t$ and lift coefficient history. Note that the residual dropped by more than three orders of magnitude for all turbulence models. Also note that the result for the Hellsten EARSM + CC were obtained with a newer version of the Edge code with improved convergence properties.

10.8   RESULTS AND DISCUSSION

This section contains comparisons between the CFD solutions and measured surface pressures, boundary-layer profiles and local skin friction. All mandatory and additional flight conditions have been investigated using six different turbulence closure models and DES. Table 10-3 lists the 37 different cases that have been computed. Note that the curvature corrected version of the EARSM have been considered here because the uncorrected model tends to overestimate the eddy viscosity in vortical flow. Curvature correction limits the maximum eddy viscosity in the vortex core. The steady-state solutions were computed using a second-order accurate central scheme for the mean flow equations and a second-order upwind discretization of the turbulent equations. The CFL number was set to 1.0. Convergence acceleration was achieved through local time stepping, residual smoothing and full multi-grid with three levels. Fully turbulent flow was assumed and the solutions were initialized with freestream conditions, which were computed from the flight conditions in Table 10-1 assuming the atmospheric properties of the 1976 Standard Atmosphere. The angle of attack α was set to the actual angle of attack, however, the side slip angle β was set to zero for a half-span model and to the actual angle of attack for the full-span models used for computing FC50 and FC51s.

For DES, assuming a local CFL number of one and a maximum velocity U_{max} in the LES (or focus) region equal to twice the freestream velocity, the guidelines for DES by Spalart [10.34] suggest a physical (outer) time step of $\Delta t = \Delta_0/U_{\mathrm{max}} \approx 2.5 \times 10^{-4}$ s, where the average cell size Δ_0 in the focus region was estimated to equal 0.05 m for the grid used here. This corresponds to a non-dimensional time step $\Delta t^* = \Delta t \cdot U_\infty/c$ of 0.0033. The inner loop CFL number was set to 1.0. The time-dependent simulations were initialized with the steady-state solution computed with the Spalart-Allmaras turbulence model. More than 10,000 outer time steps were run and time-averaged.

10.8.1   Surface Pressure Coefficient

Surface pressure coefficient data is available for all flight test conditions. Figure 10-5 shows positions of butt lines (BL) and fuselage stations (FS) where the pressure coefficient was measured.

Here we focus on three flight conditions, two at subsonic Mach numbers - one at a moderate angle of attack and one at a high angle of attack (FC46 and FC25, respectively) - and one at a transonic Mach number (FC70). All of those conditions were calculated with the Spalart-Allmaras model and two EARSM, with and without curvature corrections. In addition, DES was performed for both subsonic flight conditions. FC46 was also simulated with the DRSM.

The pressure distributions for the remaining flight conditions - FC07, FC50 and FC51 - are compared to flight-test data in the Appendix. Note that the experimental surface pressure data for FC07 (and FC19) were not available. The solutions for FC07 are therefore compared to flight test data for FC49, which is for the same nominal angle of attack and side slip angle.
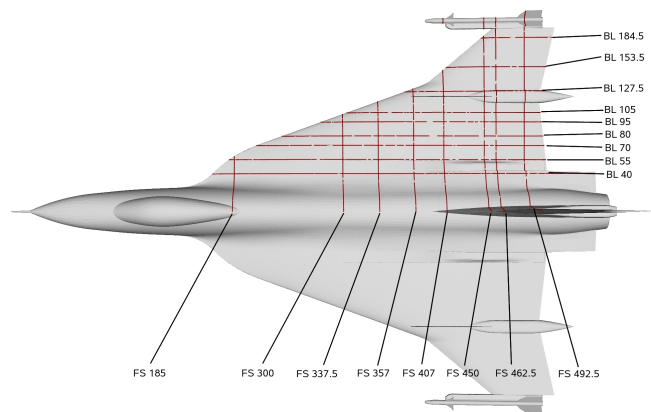
Figure 10-5: F-16XL-1 Geometry with Position of Butt Lines (BL) and Fuselage Stations (FS) where C_p Was Measured in Flight.

10.8.1.1 Flight Condition FC46

Flight condition FC46 is a condition at moderate angle of attack. The flow-field topology is shown in Fig. 10-6, which shows an iso-surface of helicity.

Figure 10-7 demonstrates that the the main C_p features, including suction peaks, are generally well predicted, both chordwise and spanwise, but not in all details. The primary suction peaks are slightly over-predicted, especially at BL 80, 95 and 105 (not shown here). The secondary suction peaks, on the other hand, are very well predicted. The chordwise location of the suction peak under the vortex outboard of the crank is predicted too far downstream/inboard (BL 153), only the DES results are somewhat closer to the leading edge. The height of the suction peak, however, is very well predicted by all models. The predictions close to the wingtip missile (BL 184.5) are rather poor, possibly due to local unsteady effects. The spread between the different turbulence models is rather significant for this BL. No firm conclusions

Figure 10-6: Iso-Surface of Helicity, FC46.

can be made regarding the predictive capability of the different turbulence models. The Spalart-Allmaras one-equation model, however, is generally seen to predict lower and wider suction peaks than the other models and the agreement with the measured data is rather poor. The DRSM is seen to predict the highest suction peaks, followed by DES. Almost no difference can be seen between the curvature corrected and the uncorrected EARSM, but all EARSM models show a stronger secondary vortex, which displaces the primary vortex. An interesting finding is that the increasing modeling complexity of DRSM and DES did not pay off in terms of the quality of the result.

(a): BL55

(b): BL70

(c): BL80

(d): BL95

(e): BL153

(f): BL184

Figure 10-7: Predicted and Measured C_p Distribution at FC46.

(g): FS337

(h): FS375

(i): FS407

(j): FS450

(k): FS492

Figure 10-7: Predicted and Measured C_p Distribution at FC46 (Cont.).

10.8.1.2   Flight Condition FC25

Flight condition 25 is for a higher angle of attack of 19.84°. The corresponding flow field is visualized by an iso-surface of helicity in Fig. 10-8. Comparison between flight test data and CFD is shown in Fig. 10-9. Trends which can be detected are: all model are good at predicting the primary suction peak at BL55 despite the fact that they over-predict the secondary suction peak. The S-A model departs quickly from the other models and over-predicts the primary suction peak throughout. From the family of EARSM models it is the Hellsten EARSM with curvature corrections that shows the best prediction of both primary and secondary suction peak. The only position where Hellsten EARSM + CC model shows different behavior in data compared to the flight test data is position BL 184.5. All models apart from the S-A model agree very well with the measured data at BL 153, which is outboard of the crank. None of them apart from DES predicts the C_p distribution qualitatively or quantitatively at BL 184.5, which is close to the wing tip. It turns out that the flow is separated and unsteady out there, and the higher modeling complexity of DES pays off here in predicting the correct trend in a time-averaged sense. This model is also superior over the other models when it comes to predicting the the secondary suction peak at BLs 70, 80 and 95. In addition, it is better at predicting the the span-wise position of the primary vortex, however, the magnitude of the suction peak is somewhat too low, which could be due to a displacement of the primary vortex away from the wing.
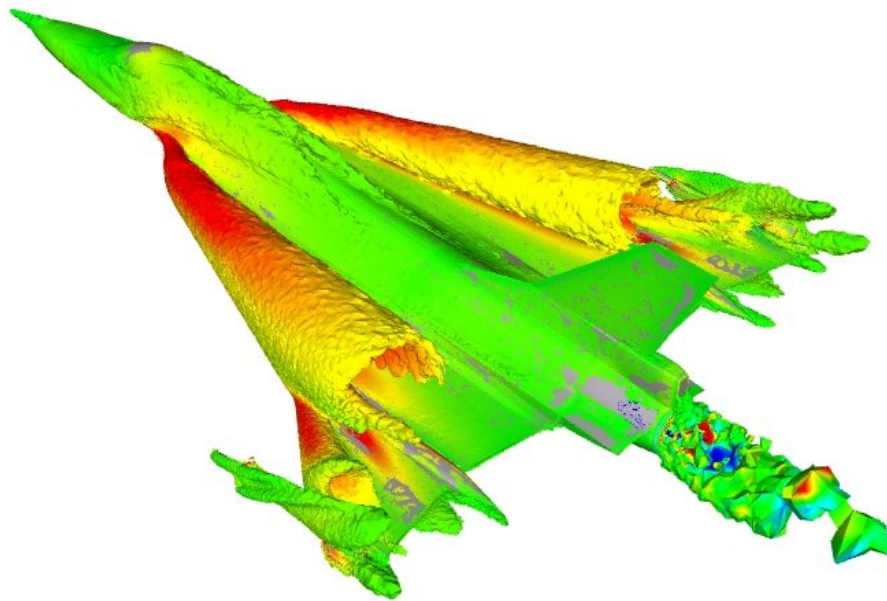
Figure 10-8: Iso-Surface of Helicity, FC25.

The unsteady nature of the vortex-dominated flow field is illustrated in Fig. 10-10, which shows a sequence of snapshots of instantaneous helicity iso-surfaces colored by C_p. The time interval between images is 5 ms and the entire sequence is over 90 ms long. Note that time increases from left to right, top to bottom. Figure 10-11 shows a time series of swirl iso-surfaces at the same intervals, which reveal that the unsteadiness is located over the rear of the wing, close to the wing tip. This explains why DES performed better than the other RANS models at BL 184.5.

(a): BL55

(b): BL70

(c): BL80

(d): BL95

(e): BL153

(f): BL184
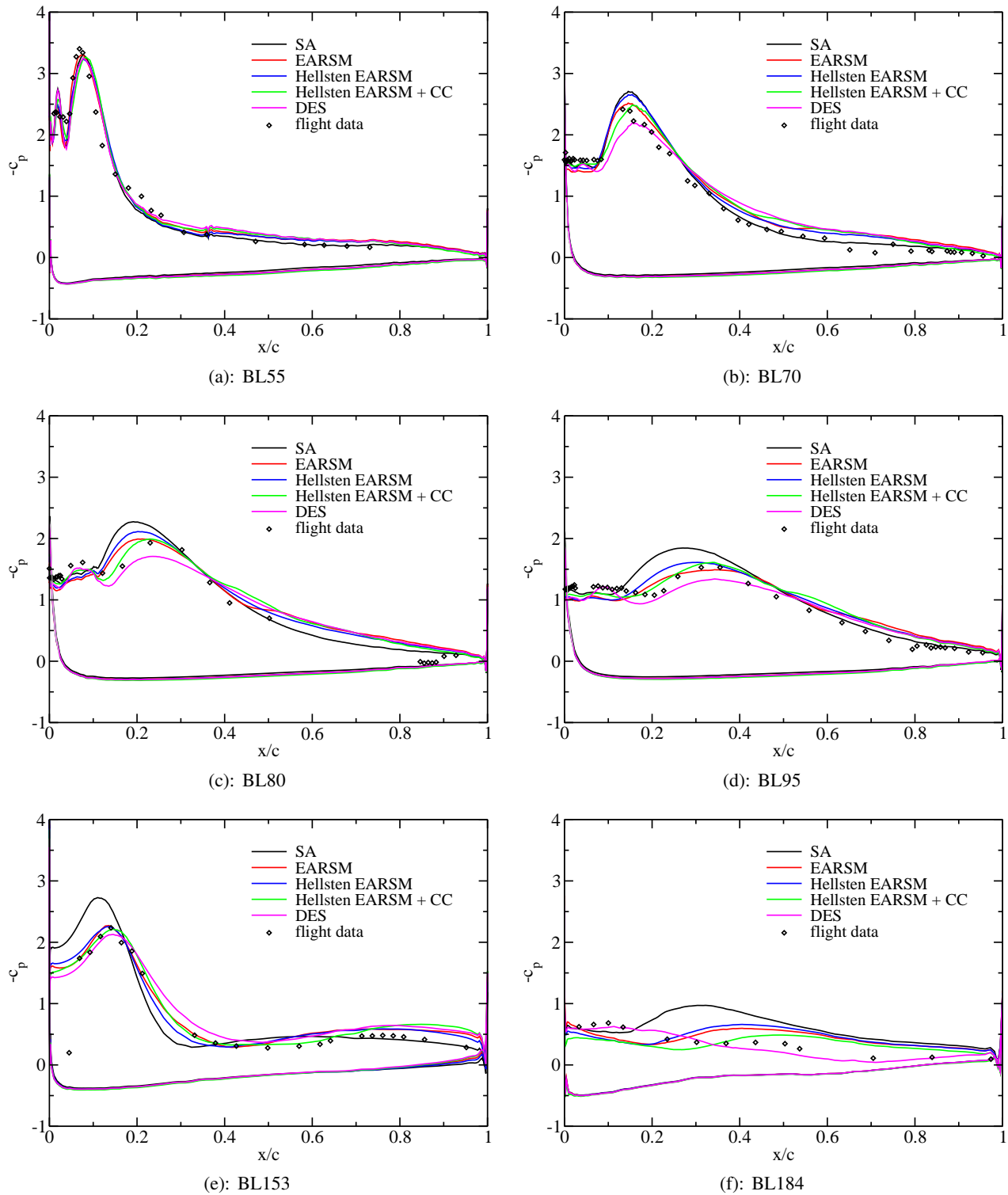
Figure 10-9: Predicted and Measured C_p Distribution at FC25.
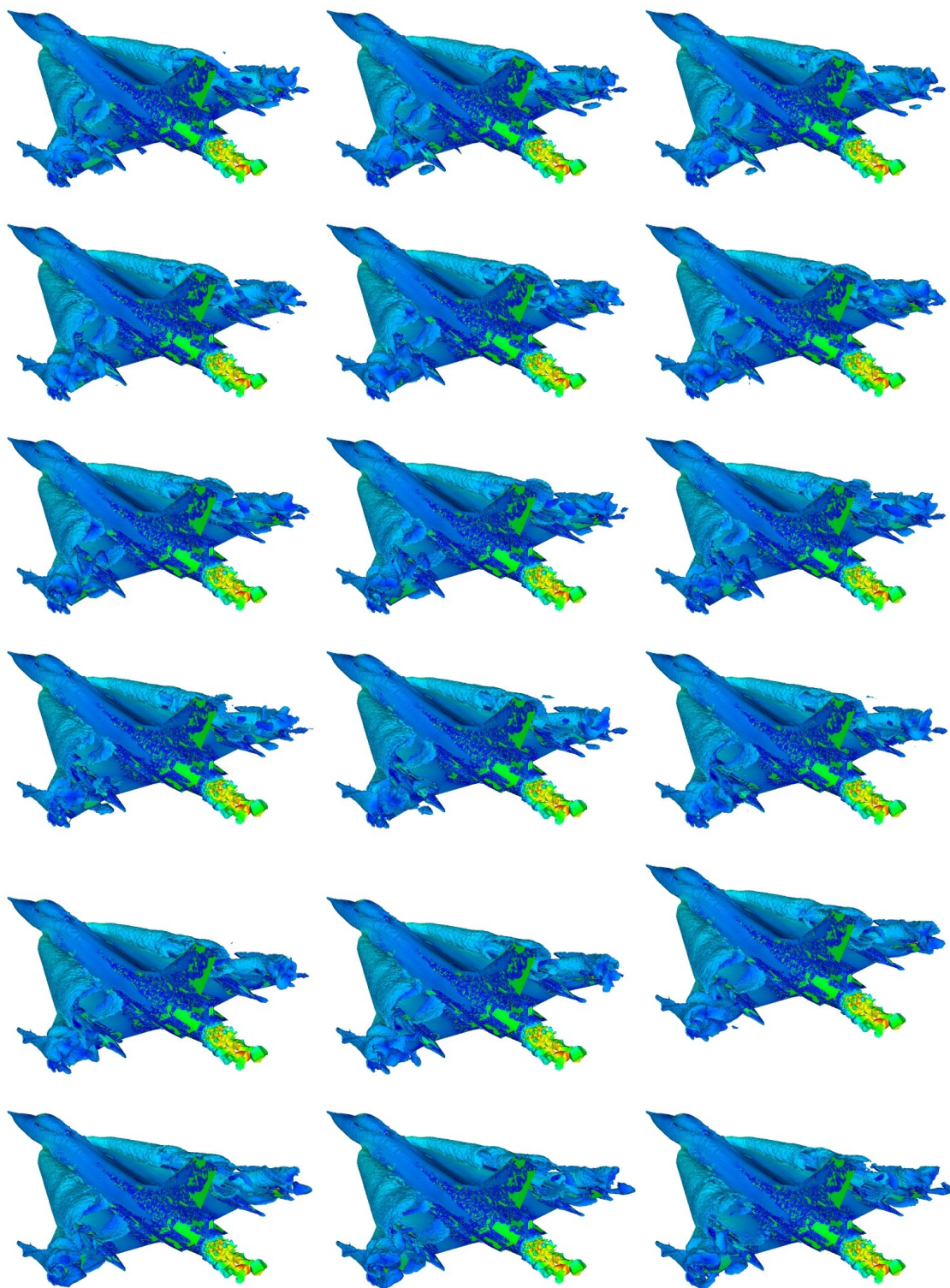
Figure 10-10: Iso-Surface of Helicity Colored by c_p**,** $t_1 = 0.416ms$**,** $\Delta t = 0.0001$**, FC25.**
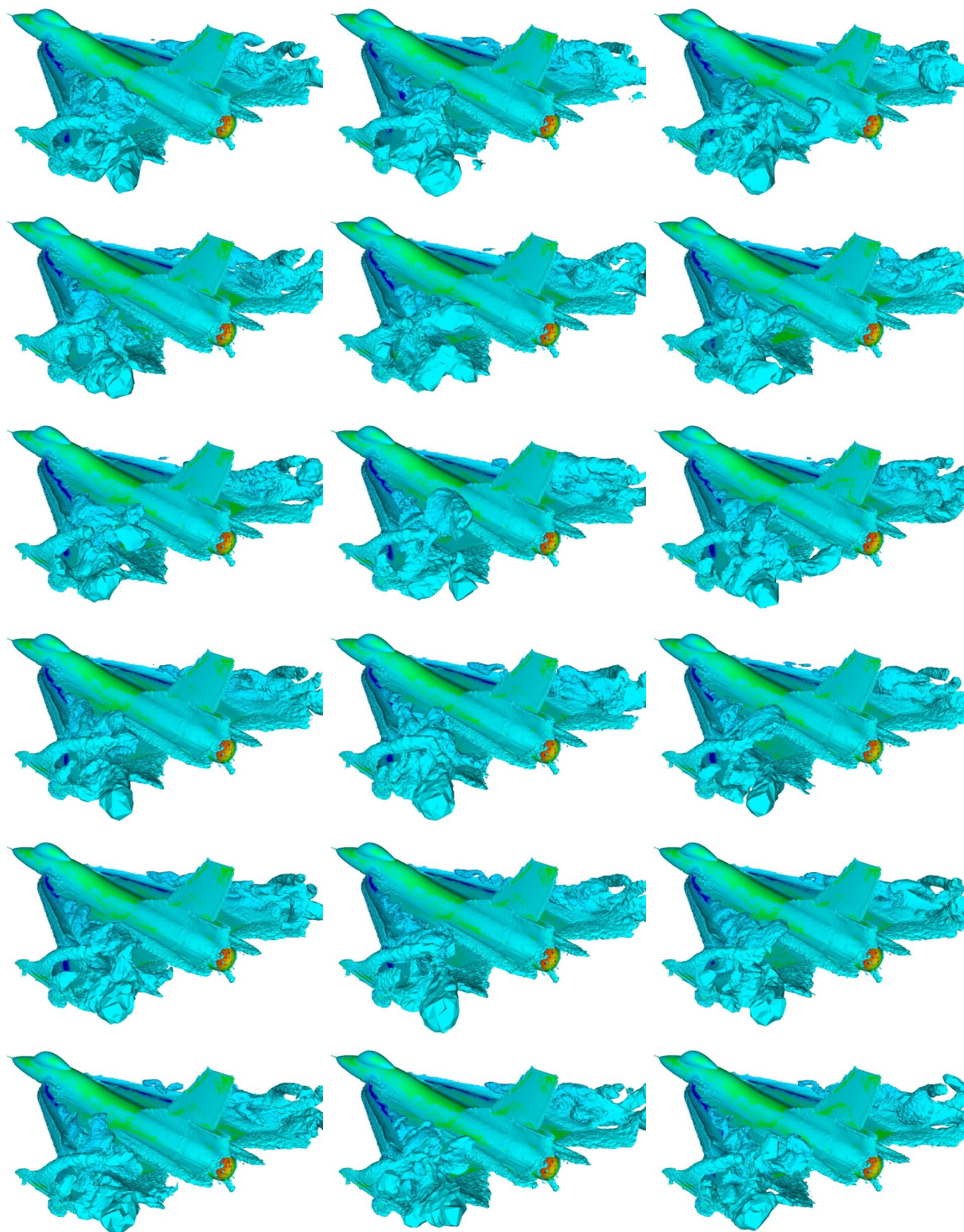
Figure 10-11: Iso-Surface of Swirl $t_1 = 0.416ms$, $\Delta t = 0.0001$, **FC25.**

10.8.1.3 Flight Condition FC70

Flight condition 70 corresponds to a transonic Mach number. The helicity iso-surface in Fig. 10-12(a) depicts the transonic flow field with multiple shocks. The comparison of the CFD results with flight test data is shown in Fig. 10-13.

<table>
<tr><td>(a): Iso-Surface of Helicity, FC70.</td><td>(b): Comparison of C_p Isolines from CFD and Flight Data (Lamar et al. [10.1]), FC70.</td></tr>
</table>
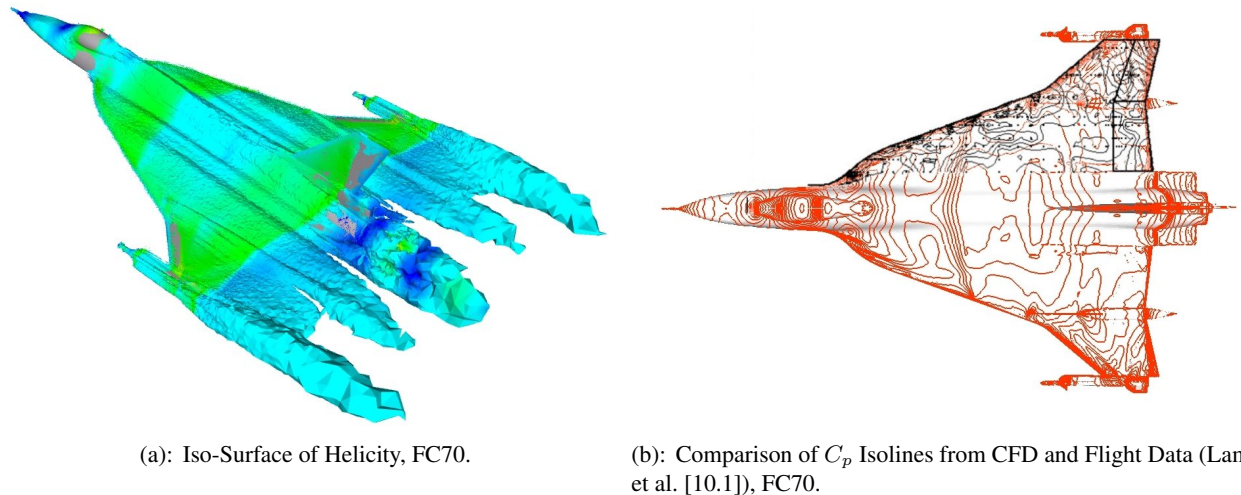
Figure 10-12: FC70.

Interestingly, it was not possible to obtain a converged solution using the S-A model. One possible explanation for this behavior is the production of kinetic energy in the vicinity of the shock wave for different models. While standard eddy-viscosity models have a dependency of the production of kinetic energy $k \approx S_{ij}^2$, EARSM builds this relation based on $k \approx S_{ij}$. As can be noticed, all four EARSM models gave identical results. All models have fairly good predictability in BL55, BL95 and BL105 and BL127 (last two positions not included in figure) and poor predictability at BL70 and BL80 and at outboard wing. CFD predicts shock wave on the lower side of wing early BL positions fairly well.

Figure 10-12(b) shows the superposition of isolines from the CFD solution with isolines generated from flight test data [10.1]. The shock predicted by CFD is almost normal to the main flow direction. The Flight data indicates that the shock persists up to BL70, from where the flow topology is different.

This can be also seen in the C_p distribution at FS 337 (Fig. 10-14(a)). CFD predicts a flat increase of pressure along the span up to 80% of span whilst the flight data shows a pressure distribution with large variations. Figure 10-14(a) shows two peaks of high suction around 60% and 80% of span. Again, the early positions on the span show fairly good agreement of CFD and flight data meanwhile mid section of the wing show completely deffierent behaviour of picture of pressure.

At outboard wing the prediction is poor. CFD predict higher suction in the frontal part of the wing meanwhile flight data show the flow acceleration up to a shock wave which is located possibly around the hingle line of the flap. Figure 10-12(b) shows also that the pressure coefficient in parts of outboard wing reaches values of $c_p < 0.5$ which is an indicator of possible buffeting. As pointed out in [10.1] the post-flight examination of the geometry determined the deflection of leading edge flaps, elevon and ailerons. Possibly this might be a cause of discrepancies. Figure 10-14(b) shows CFD and flight data comparison at fuselage station FS 492.5 which is a located mostly on the elevon and aileron. The question is wether the lower suction predicted by the flight test is an effect of the deflection of the control surfaces.
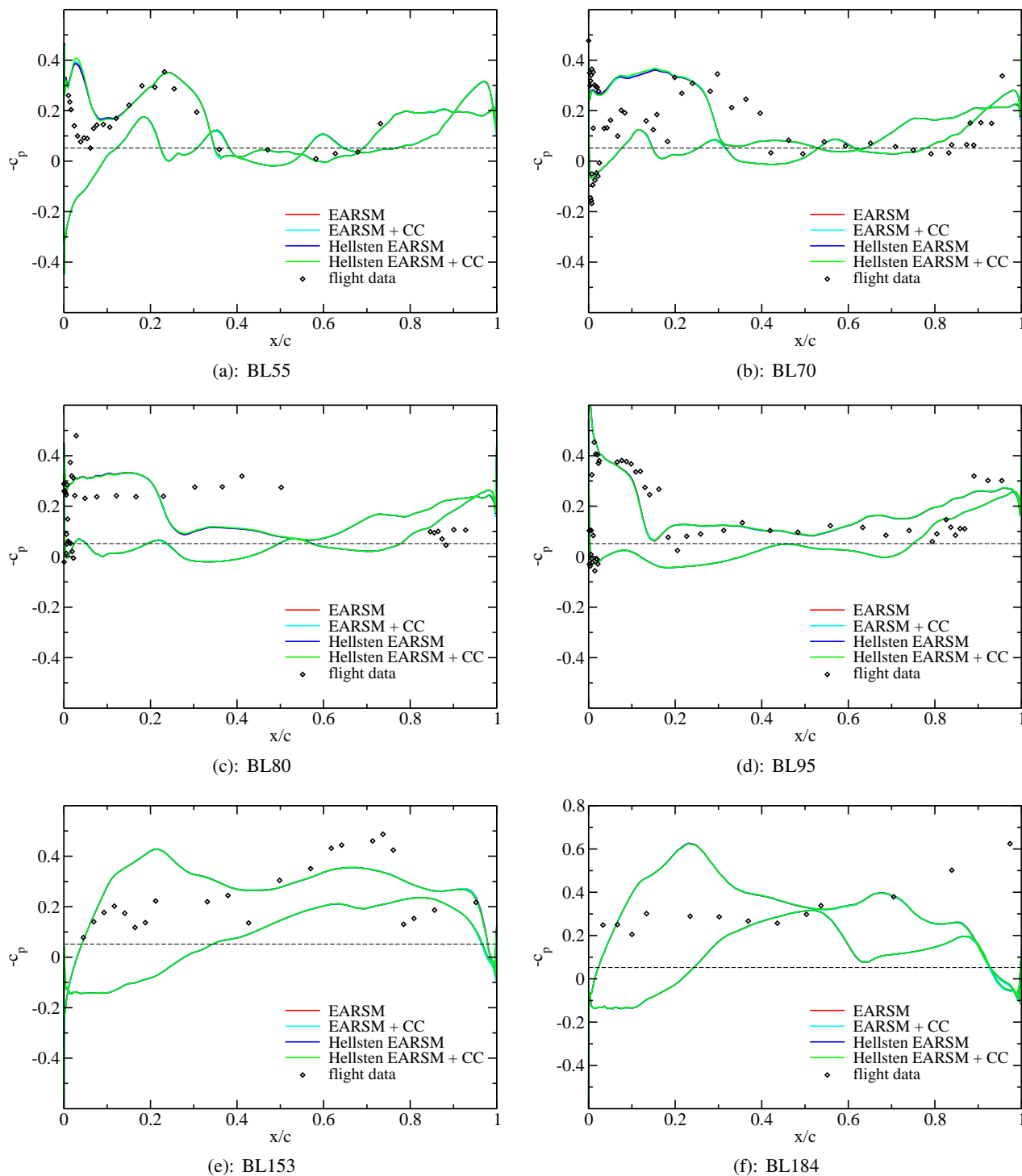
Figure 10-13: Predicted and Measured C_p Distribution for different Butt Line (BL) Stations at FC70.

(a): FS375.5

(b): FS492.5
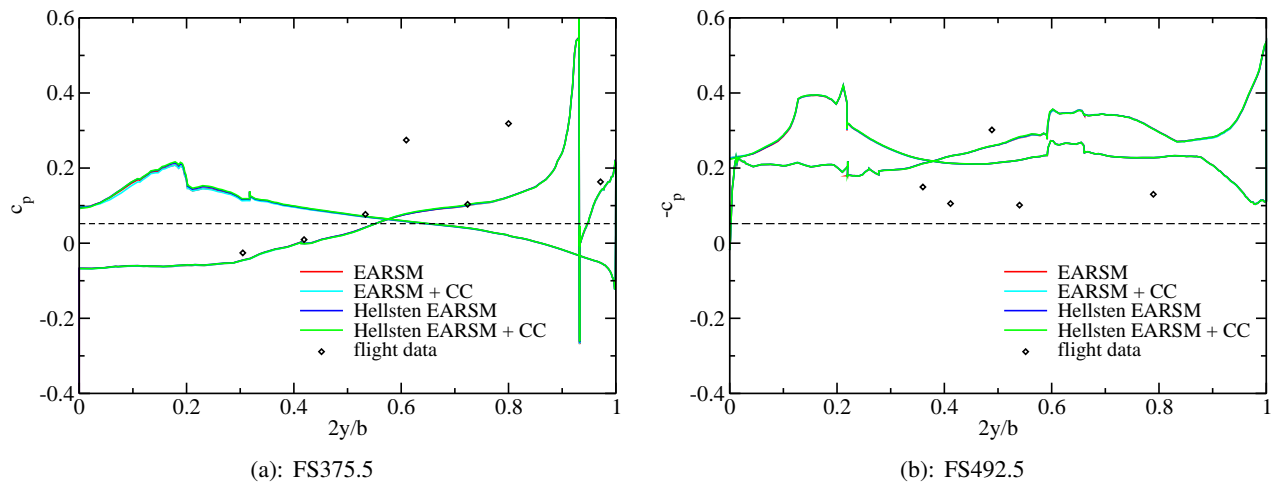
Figure 10-14: Predicted and Measured C_p Distribution for different Fuselage Stations (FS) at FC70.

The major cause of the differences between the CFD results for this transonic flight condition and the flight test data could be attributed to the grid density, which is not sufficient where the shock-vortex interaction takes place, as reported in the Lessons Learned chapter [10.35].

10.8.2 Skin Friction Coefficient at FC19

The local skin friction, c_f, across the left wing near FS 330 was determined with 16 modified Preston tubes in flight (the modification to each Preston tube was the integration of a static-pressure port with the total-pressure tub). The tubes were aligned with the local flow by using the same initial `CFL3D` solution at FC07 that was used to determine the rake orientations. The experimental c_f values were calculated from the pressure change between the total- and static-pressure tubes.

Figure 10-15 provides the measured and predicted c_f values at FS 330 for FC19. This figure can be used to locate and assess the impact of the vortex systems because they produce high velocities on the surface which are measured by the modified Preston tubes. Both data sets

Figure 10-15: Predicted and Measured Skin Friction Coefficient for FC19 as a Function of Span at FS 330.

feature two regions of high c_f, which is indicative of primary and secondary vortices. Excellent qualitative and quantitative agreement is observed for both the location and absolute value of c_f under the primary and secondary/tertiary vortices. Another c_f plateaus or peak is predicted between BL 50-65, inboard of the primary vortex. It is not clear at present what this peak is due to.

Significant differences are observed in terms of the predictive capability of the different turbulence models. The results obtained with the DRSM are in best agreement with the measured c_f values. The EARSM predicts a slightly lower peak value under the primary vortex. The Spalart-Allmaras model, however, fails to predict both the peak value under the primary vortex and the region of high skin friction under the secondary vortex. Observe that the curvature correction improved the predictive capability of the the EARSM underneath the primary vortex but worsened that of the Hellsten EARSM.

10.8.3   Boundary Layer Velocity Profiles at FC07

The boundary-layer measurements were made by using two rakes at a time at four different positions on the left wing with the most inboard one used as a control. Each rake used 16 active tubes, 15 total pressure and 1 static pressure, of the 23 available. The overall height of the rakes was 2 in (5.08 cm). When mounted on the airplane, each rake was oriented into the local flow at an average angle over its height based on initial CFD predictions from the `CFL3D` code. The flow conditions were for the complete airplane (half-airplane modeled with symmetry assumed) at $\alpha = 13°$, $M_\infty = 0.29$, and $Re = 46.1 \times 10^6$, that is, FC07. The four locations were chosen as follows: one well inboard of the shed vortex systems where the flow is nearly streamwise (rake #3), one underneath the primary wing vortex (rake #4), one underneath the secondary vortex (rake #5) and one at the secondary separation line (rake #7); all are at a nominal position of FS 295 along the predicted orientation which takes into account the flow at and slightly off the surface. The average of these local flow directions was used to establish the rake orientation angles. These angles were measured from the centerline with the rake pointing forward and inboard and have values of 7.5°, 45°, 27.5°, and 23.5°, for rakes #3, #4, #7, and #5, respectively.

The processing needed to determine the velocity magnitudes for comparison with the boundary-layer rake data was not straightforward, because the velocities needed to be established along a normal to the surface at the specified points in order to be comparable with the rake data. Nevertheless, the velocity profiles were extracted from the CFD solutions at exactly the locations where the flight test data were measured using the rake probes. The first step of the extraction procedure included identifying a grid cell on the surface containing the coordinates of a probe BL/FS location. The grid nodes of this cell on the surface were then used to calculate the corresponding surface normal vector. Since the distribution of the total pressure probes was known from the rake geometry, the physical coordinates were defined using the normal vector and rake geometry data. The velocity vectors were then interpolated in `Ensight` from the surrounding mesh nodes. At each point, the magnitude of velocity as well as the three components of the velocity vector were collected. The velocity profile used for comparison with the experimental data was computed by projecting the velocity vector in the rake direction using the rake orientation angles given above.

Figure 10-16 shows the comparison of measured and predicted boundary-layer profiles for rake locations #3, #4, #7, and #5, respectively, at FC07. Underneath the primary vortex (rake #4 location), Fig.10-16 (b) shows excellent qualitative and quantitative agreement between the measured and predicted results. Both the measurements and the CFD solutions indicate a "jet-type" flow to commence for $y > 0.25$. Both results also show regions of quasi-linear variation of the velocity with y, indicative of being outside the boundary layer and just in the influence of the primary vortex. The comparison at the secondary separation line (rake #7), shown in Fig.10-16 (d), is equally good, however, it appears that the measured velocity is not asymptotic at the rake extreme; this leads to the conclusion that the maximum velocity has not been achieved at this location. Under the secondary vortex (rake #5), Fig.10-16 (c), the numerical results predict a somewhat "fuller" velocity profile, whereas the measurements suggest a slightly more retarded profile. The measured profile for rake #5, underneath the estimated location of the secondary vortex, also only achieves edge velocity near the rake

(a): Rake #3

(b): Rake #4

(c): Rake #5

(d): Rake #7
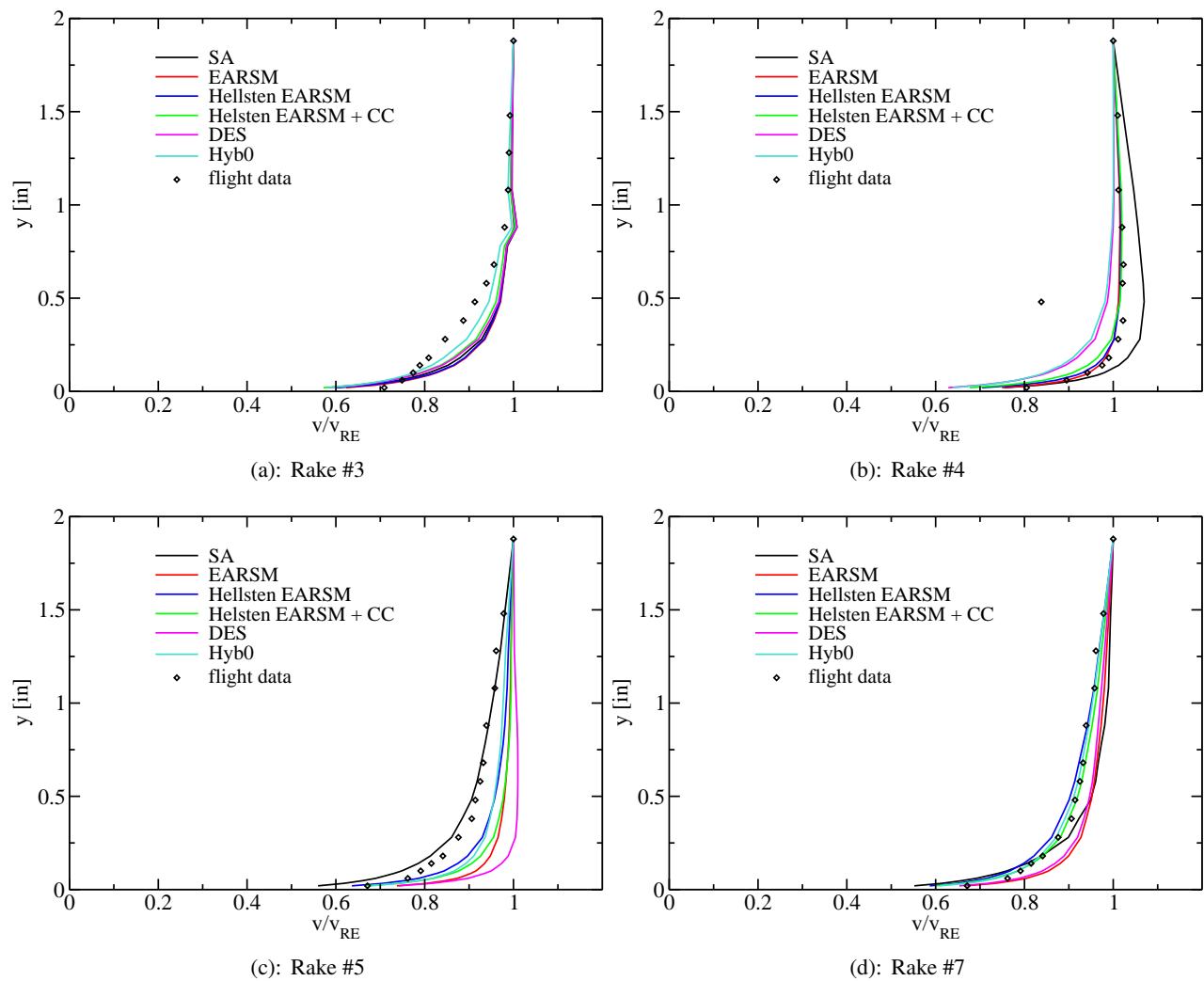
Figure 10-16: Predicted and Measured Velocity Profiles for Boundary Layer Rakes at FC07.

extreme. The quasi-linear growth of velocity for $y > 0.5$ for these profiles is associated with vortices around these boundary-layer rakes because the velocity field produced outside a representative vortex core varies as $1/r$.

Inboard of the shed vortex systems (rake #3), however, there is general disagreement between the measured and predicted values for $y < 0.8$ in, as shown in Fig. 10-16(a). The predicted values are significantly different. The numerical results predict a "fuller" velocity profile, whereas the measurements suggest a more turbulent profile. This comes somewhat as a surprise because rake #3 is located where the flow is streamwise and attached, which should be fairly easy to predict.

Generally, no major difference between the predictive capability of the different turbulence models is observed, apart from the results with the Spalart-Allmaras model, which predicts a stronger "jet-type" flow at rake location #4 and a more retarded flow at rake location #5. The EARSM + CC and the Hellsten EARSM + CC give the best overall results.

10.8.4 Adaptive Mesh Refinement at FC46

An important aspect in the simulation of vortical flows over delta-wing aircraft like the `F-16XL-1` is adaptive mesh refinement. Pirzadeh [10.36] presented a method based on a tetrahedral unstructured grid technology developed at NASA Langley Research Center with application to configurations with vortex dominated flow fields. In his method, the interior of entropy iso-surfaces are re-meshed to improve the grid resolution. The large improvement of the adapted solutions in capturing vortex flow structures over the conventional unadapted results was demonstrated by comparisons with wind tunnel data. Pirzadeh's method has been applied by Morton *et al* [10.37] to DES computations of a delta wing and an `F-18C` at high angle of attack.

A method similar to the one by Pirzadeh is applied here to refine the grid based on the solution computed for 46 with the curvature corrected EARSM, however, the mesh refinement technique used here is based on local h-refinement, or subdivision, rather than re-meshing. The refinement is edge-based and, depending on the number of edges marked for refinement, the tetrahedral cells are divided into two, four, or eight new cells. Here, a sensor for identifying vortices based on the ratio of total pressures [10.14, 10.15] was employed to refine the grid in the vortical flow region above the wing. To determine a suitable threshold value for p_0/p_{0_∞}, the solution for FC46 was visualized in a post-processing software. Several p_0/p_{0_∞} iso-surfaces were visualized and a value of $p_0/p_{0_\infty} = 0.9$ was found most suitable to delimit the region to be refined. A minimum cells size of 0.01 m was specified to avoid refining *ad infinitum*. New nodes were not projected to the surface. The refinement procedure resulted in 685,287 new tetrahedral cells being generated. The new, refined grid is made up of a total of 11,170,996 tetrahedral elements and 1,442,664 prismatic cells, corresponding to 2,652,135 nodes. The newly generated tetrahedral elements are shown in Fig. 10-17(a). The grid was refined in the vortical flow region, capturing the primary wing vortex, parts of the secondary wing vortex, the vortex originating at the air dam and a vortex over the outer part of the wing close to the wing tip.

The grid density before and after grid refinement is shown in Fig. 10-17(b), which depicts the grid in a wrinkly cutting plane close to the trailing edge (FS496). The refinement over the wing is clearly seen in the left side of the figure. Grid cells generated due to the primary wing vortex can be discerned from cells generated due to the air dam vortex. The surface pressure distribution computed on the refined grid is shown in Fig. 10-18 for five butt line (BL) stations and on fuselage (FL) station. The refinement is seen to have almost no influence on the inboard pressure distribution and a neglige influence on the outboard pressure distribution. Actually, over the outboard wing, the suction peak underneath the primary vortex is somewhat weaker on the refined grid than on the original grid. Further refinement steps may be necessary to come to conclusive results.

(a): **New tetrahedra (red) created by adaptive mesh refine-ment**

(b): **Wrinkly cutting plane at FS496 comparing the original grid (right) with the grid after adaptive mesh refinement (left)**
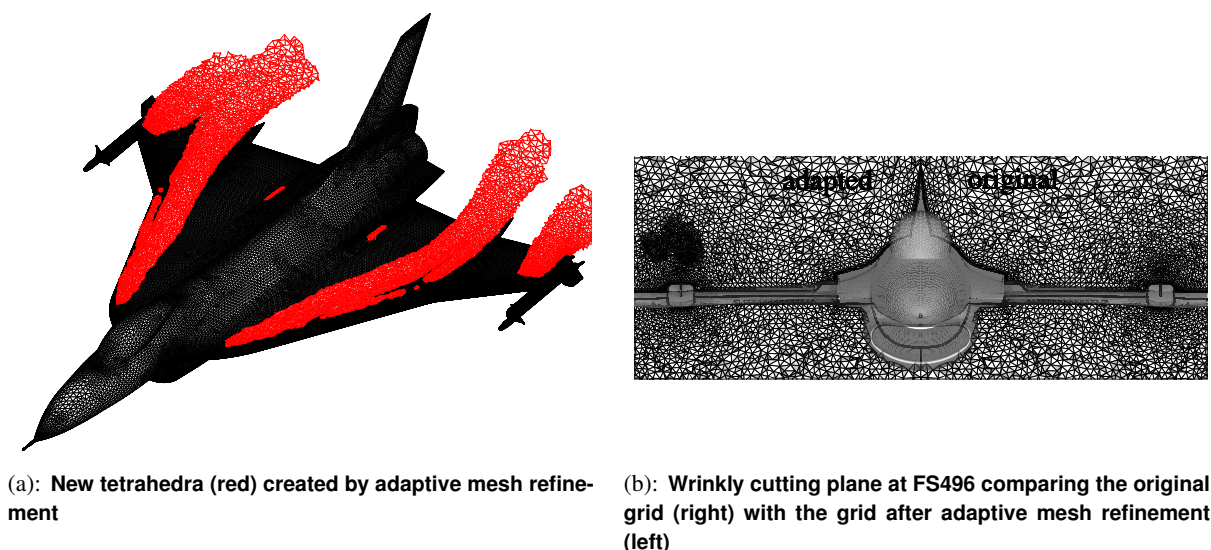
Figure 10-17: Solution-Adaptive Mesh Refinement at FC46.

10.9   BEST PRACTICES

The turbulent computations with the `Edge` code described above had to be sustained by changing several of the default numerical parameters, in particular the multi grid parameters.

When using the second-order accurate central scheme for the mean flow and three-level multi grid, the coarse grid dissipation coefficient, which adds 4th order dissipation on solid walls, was increased from 0.1 to 0.5. At the same time, the reduction factor for the CFL number on coarse grids was decreased from 0.8 to 0.5 and the multi-grid parameter for smoothing corrections was increased from 1.5 to 3.0. The implicit residual smoothing parameter was increased from 1.3 to 2.0 and the distance weighted residual smoothing by Mavripilis [10.38] was used instead of standard distance weighted residual smoothing.

In order to use three-level multi grid with the second-order upwind scheme for the mean flow (`minmod` limiter), the parameter for the multi-grid smoothing correction had to be increased from 1.5 to 2.0.

10.10   CONCLUSIONS

The vortical flow over a half-span, full-scale model of the `F-16XL-1` aircraft has been computed for six different flight conditions using up to six different turbulence closure models and Detached-Eddy Simulation. The CFD solutions have been compared to flight-test data for the surface pressures distribution, local skin friction and boundary layer velocity profiles.

For subsonic flight conditions the overall flow field was very well resolved. Primary, and secondary vortices inboard and outboard of the crank of the wing were captured, as well as air-dam and missile fin vortices. The only station where CFD consistently fail to predict the flight data, both quantitatively and qualitatively was the last butt line BL 184.5 where the flow is highly three-dimensional and possibly very chaotic due to proximity of AMRAAM missile.The only exception was DES which improved results at high angle of attack, however at moderate angle it does not bring any improvement. At transonic flight condition, CFD had a problem to reproduce results in the middle part of inboard wing and outboard wing. It is in contrast with rather good predictability of flight data at BL55, BL95 and BL105. At the time the cause of this is not known, it might be a

(a): BL 55

(b): BL 80

(c): BL 105

(d): BL 153.5

(e): BL 184.5

(f): FS 300
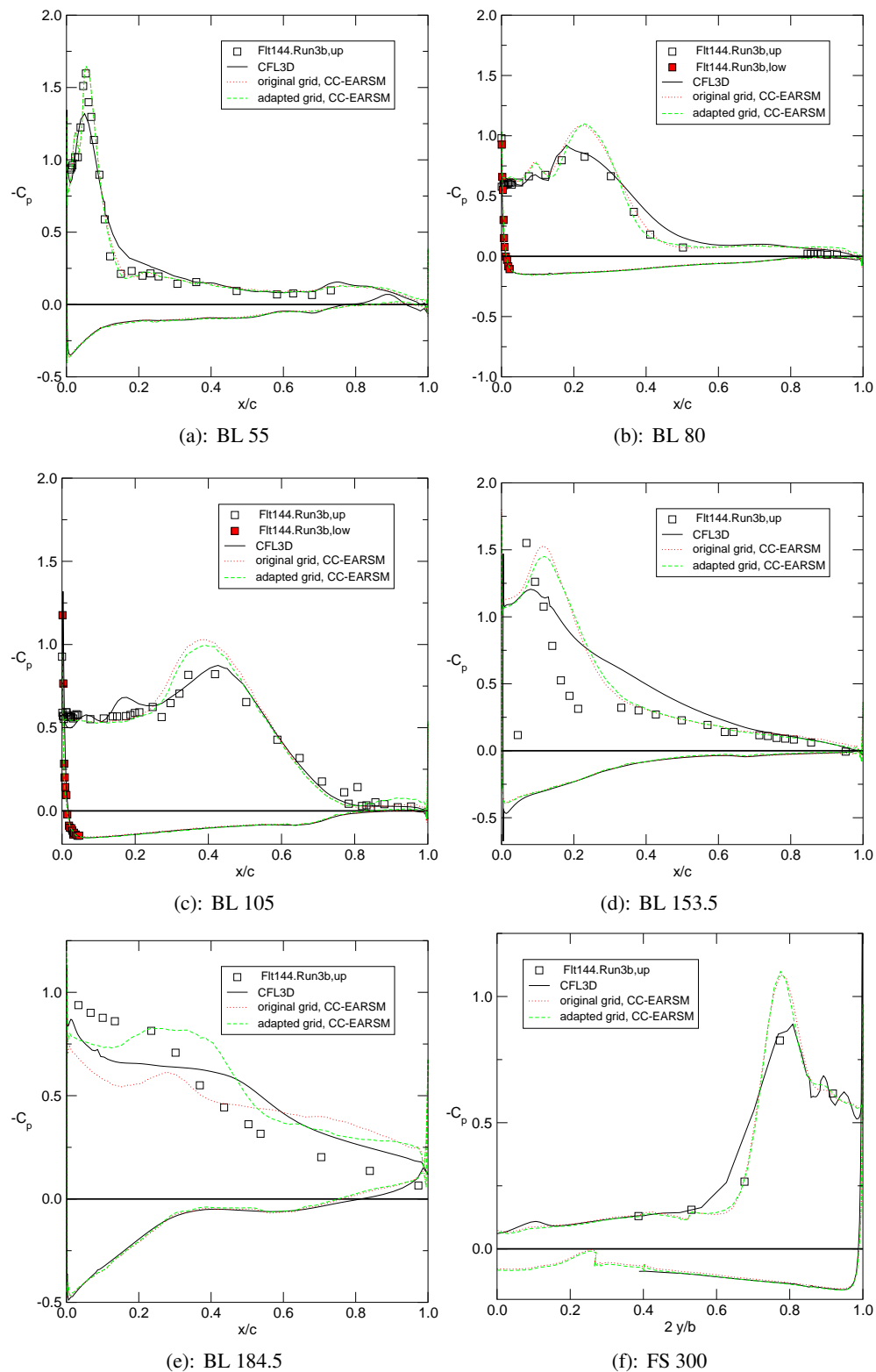
Figure 10-18: Pressure Distribution on Solution-Adapted Grid and on Original Grid Compared to Flight-Test Data at FC46.

geometrical changes such as flap, elevon and aileron deflections observed during a post-flight analysis. Evaluating results from different turbulence models point of view it can be concluded that the S-A model is the model which had the poorest performance. Its predictability of flight data is usually very good in stations close to the fuselage and then it becomes worst. Predictability of velocity profiles was fairly good. EARSM models have usually good predictability and have consistently fairly accurate predictions of the flight data in all stations Surprisingly, the curvature corrected versions of the explicit algebraic Reynolds stress model (EARSM) did not predict better results than the uncorrected model, which is known to overestimate the eddy viscosity in vortical flows. The Differential Reynolds Stress Model (DRSM) outperformed all other models when it comes to local skin friction. DES resolved more flow features than the steady-state simulations, however, at the additional time expense. The improvement was visible at FC25 which is high angle of attack case, at moderate angles the pressure distribution from eddy-viscosity models did not differ very much from the DES solution.

None of the models is the "very best". The use of a particular turbulence model would be perhaps motivated mostly by confidence of user with the particular model and consistency of its results at different flight conditions rather then its performance at one flight condition. From this point of view, the recommended turbulence model for these types of flow would be Hellsten EARSM for lower angle of attack and Hellsten EARSM + CC for higher angles of attack.

10.11   ACKNOWLEDGMENTS

10.12 REFERENCES

[10.1] Lamar, J. E., Obara, C. J., Fisher, B. D., and Fisher, D. F., "Flight, Wind-Tunnel, and Computational Fluid Dynamics Comparison for Cranked Arrow Wing (F-16XL-1) at Subsonic and Transonic Speeds," NASA/TP 2001-210629, NASA, February 2001.

[10.2] NASA Langley Research Center, "Homepage for the F-16XL Highlift Project CAWAP," http://cawap-prism.larc.nasa.gov, 2002, accessed 12/2004.

[10.3] Lamar, J. E., "Cranked Arrow Wing (F-16XL-1) Flight Flow Physics with CFD Predictions at Subsonic and Transonic Speeds," *NATO/RTO Applied Vehicle Technology Panel Symposium on Advanced Flow Management: Vortex Flow and High Angle of Attack*, RTO MP-69-P-44, Loen, Norway, May 7-10 2001.

[10.4] Lessard, W. B., "Subsonic Analysis of 0.04-Scale F-16XL Models Using an Unstructured Euler Code," NASA TP 3597, NASA, October 1996.

[10.5] Lamar, J. E. and Obara, C. J., "Review of Cranked-Arrow Wing Aerodynamics Project: Its International Aeronautical Community Role," AIAA Paper 2007-0487, Presented at 45th AIAA Aerospace Sciences Meeting and Exhibit Reno NV January 8-11 2007, 2007.

[10.6] Hillaker, H. J., "F-16XL Flight Test Program Overview," *AIAA Paper 83-2730*, 1983.

[10.7] Talty, P. K. and Caughlin, D. J., "F-16XL Demonstrates New Capabilities in Flight Test at Edwards Airforce Base," *Journal of Aircraft*, Vol. 25, No. 3, 1988, pp. 206–215.

[10.8] Brower, J. N. and Scott, S. R., "The F-16XL Flight Test Program," *Society of Flight Test Engineers 15th Annual Symposium*, August 1984, pp. 9–1–9–5.

[10.9] Hahne, D. E., "Low-Speed Aerodynamic Data for an 0.18-Scale Model of an F-16XL With Various Leading-Edge Modificiations," NASA/TM 1999-209703, NASA, 1999.

[10.10] Grafton, S. B. and Nguyen, L. T., "Wind-Tunnel Free-Flight Investigation of a Model of a Cranked Arrow-Wing Fighter Configuraton," NASA TP 2410, NASA, March 1985.

[10.11] Schoonover, Jr., W. E. and Finley, D. B., "Design and Wind-Tunnel Evaluation of Vortex Flaps for the F-16XL," NASA TP 3106, NASA, October 1991.

[10.12] Eliasson, P., "EDGE, a Navier-Stokes solver for unstructured grids," *Proc. To Finite Volumes for Complex Applications III*, 2002, pp. 527–534.

[10.13] Jamason, A., "Time dependent calculations using multigrid, with application to unsteady flows past airfoils and wings," *AIAA Paper 91-1596*, 1991.

[10.14] Le Moigne, Y., "Adaptive Mesh Refinement and Simulations of Unsteady Delta-Wing Aerodynamics," *European Congress on Computational Methods in Applied Sciences and Engineering (ECCOMAS 2004)*, 2004.

[10.15] Le Moigne, Y., *Adaptive Mesh Refinement and Unsteady CFD Simulations of Delta Wings*, Ph.D. thesis, Royal Institute of Technology (KTH), Department of Aeronautical and Vehicle Engineering, Stockholm, Sweden, 2004.

[10.16] Peng, S.-H., "Hybrid RANS-LES modeling based on zero- and one-equation models for turbulent flow simulation," *Proc. 4th International Symposium on Turbulence and Shear Flow Phenomena*, Vol.3, Williamsburg, VA, USA, 27-29 June 2005, pp. 1159–1164.

[10.17] Peng, S.-H., "Algebraic Hybrid RANS-LES Modelling Applied to Incompressible and Compressible Turbulent Flows," *AIAA Paper 2006-3910*, 2006.

[10.18] Spalart, P. R. and Allmaras, S. R., "A One-Equation Turbulence Model for Aerodynamic Flows," *AIAA Paper 92-0439*, 1992.

[10.19] Wallin, S. and Johansson, A., "A Complete Explicit Algebraic Reynolds Stress Model for Incompressible and Compressible Turbulent Flows," *Journal of Fluid Mechanics*, Vol. 403, 2000, pp. 89–132.

[10.20] Wilcox, D. C., "Reassessment of the scale-determining equation for advanced turbulence models," *AIAA Journal*, Vol. 26, No. 11, 1988, pp. 1299–1310.

[10.21] Hellsten, A. K., "New Advanced k-ω Turbulence Model for High-Lift Aerodynamics," *AIAA Journal*, Vol. 3, No. 9, 2005, pp. 1857–1869.

[10.22] Wallin, S. and Johansson, A. V., "Modelling streamline curvature effects in explicit algebraic Reynolds stress turbulence models," *Int. J. Heat and Fluid Flow*, Vol. 23, No. 5, 2002, pp. 721–730.

[10.23] Hanjalic, K., Jakirlic, S., and Hadzig, I., "Computation of oscillating turbulent flows at transitional Re-numbers," *Turbulent Shear Flows 9*, 1995, pp. 323–342, Springer Verlag.

[10.24] Spalart, P. R., Jou, W.-H., Strelets, M., and Allmaras, S. R., "Comments on the Feasibility of LES for Wings, and on a Hybrid RANS/LES Approach," *Advances in DNS/LES, 1st AFOSR Int. Conf. on DNS/LES*, August 1997.

[10.25] Peng, S.-H., "Detached eddy simulation for turbulent compressible flows using the EDGE solver," FOI Scientific report, to be published, 2006.

[10.26] Peng, S.-H., "Simulation of turbulent flows past a rectangular open cavity using DES and Unsteady RANS," AIAA Paper 2006-2827, 2006.

[10.27] Morton, S. A., Forsythe, J. R., Squires, K. D., and Wurtzler, K. E., "Assessment of Unstructured Grids for Detached-Eddy Simulation of High Reynolds Number Separated Flows," *Proceedings of the 8th International Conference on Grid Generation in Computational Field Simulations*, June 2002.

[10.28] Samareh, S., "GridTool: A Surface Modeling and Grid Generation Tool," *Proceedings of the Workshop on Surface Modeling, Grid Generation, and Related Issues in CFD Solutions*, NASA CP-3291, May 9-11 1995.

[10.29] Pirzadeh, S., "Progress Toward A User-Oriented Unstructured Viscous Grid Generator," *AIAA 96-0031*, 1996.

[10.30] Strang, W. Z., Tomaro, R. F., and Grismer, M. J., "The Defining Methods of Cobalt: A Parallel, Implicit, Unstructured Euler/Navier-Stokes Flow Solver," *AIAA Paper 99-0786*, 1999.

[10.31] Wallin, S., "Standardized Data Format," Tech. Rep. FFAP-A-950, The Aeronautical Research Institute of Sweden (FFA), Stockholm, Sweden, 1992.

[10.32] Poinot, M., Rumsey, C. L., and Mani, M., "Impact of CGNS on CFD Workflow," *AIAA Paper 2004-2142*, 2004.

[10.33] Lamar, J. E., Cronin, C. K., and Scott, L. E., "A review of steps taken to create an international virtual laboratory at NASA Langley for aerodynamic prediction and comparison," *Progress in Aerospace Sciences*, Vol. 40, No. 3, April 2004, pp. 163–172.

[10.34] Spalart, P. R., "Young-Person's Guide to Detached-Eddy Simulation Grids," CR 2001-211032, NASA, 2001.

[10.35] Rizzi, A., O.Boelens, Jirásek, A., Lamar, J., and Badcock, K., "What was learned from the numerical investigations on the CAWAPI configuration," *Understanding and Modeling Vortical Flows to Improve the Technology Readiness Level for Military Aircraft. Summary Report of Task Group AVT-113*, NATO RTO Report RTO-TR-AVT-113, 2008.

[10.36] Pirzadeh, S., "Vortical Flow Prediction Using an Adaptive Unstructured Grid Method," *NATO/RTO Applied Vehicle Technology Panel Symposium on Advanced Flow Management: Vortex Flow and High Angle of Attack*, RTO MP-069(I)-(SYA)-13, Loen, Norway, May 7-10 2001.

[10.37] Morton, S. A., Steenman, M. B., Cummings, R. M., and Forsythe, J. R., "DES Grid Resolution Issues for Vortical Flows on a Delta Wing and and an F-18C," *AIAA Paper 2003-1103*, 2003.

[10.38] Mavriplis, D., Jameson, A., and Martinelli, L., "Multigrid solution of the Navier-Stokes equations on triangular meshes," *AIAA Paper 89-0120*, 1989.
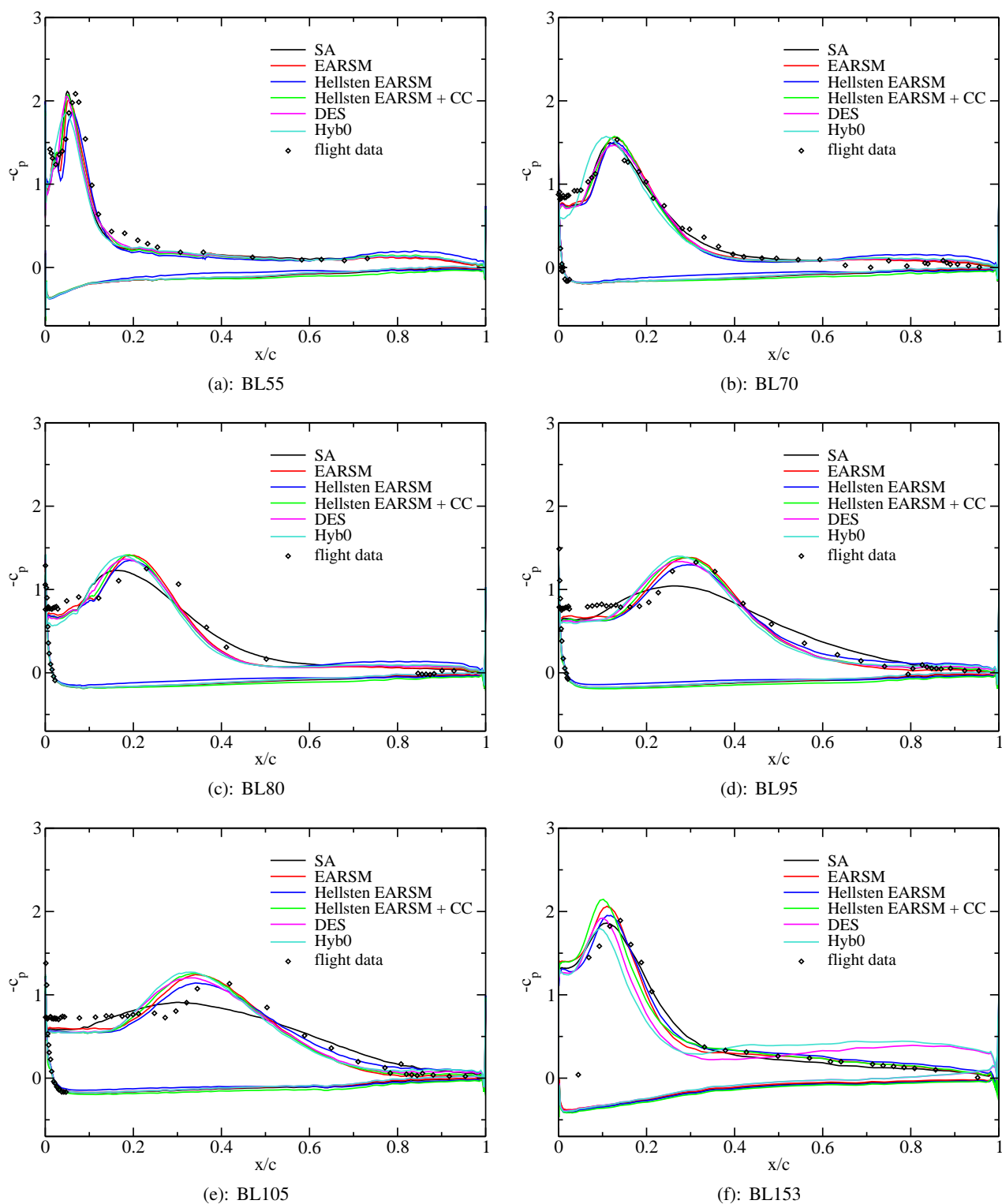
Figure 10-19: Predicted and Measured C_p Distribution at FC07.
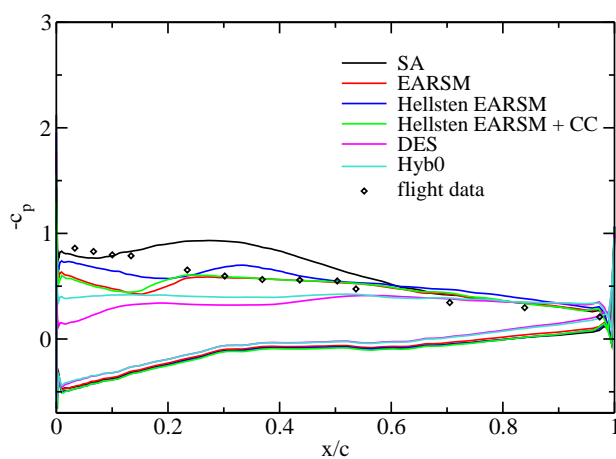
(g): BL184

Figure 10-19: Predicted and Measured C_p Distribution at FC07 (Cont.).
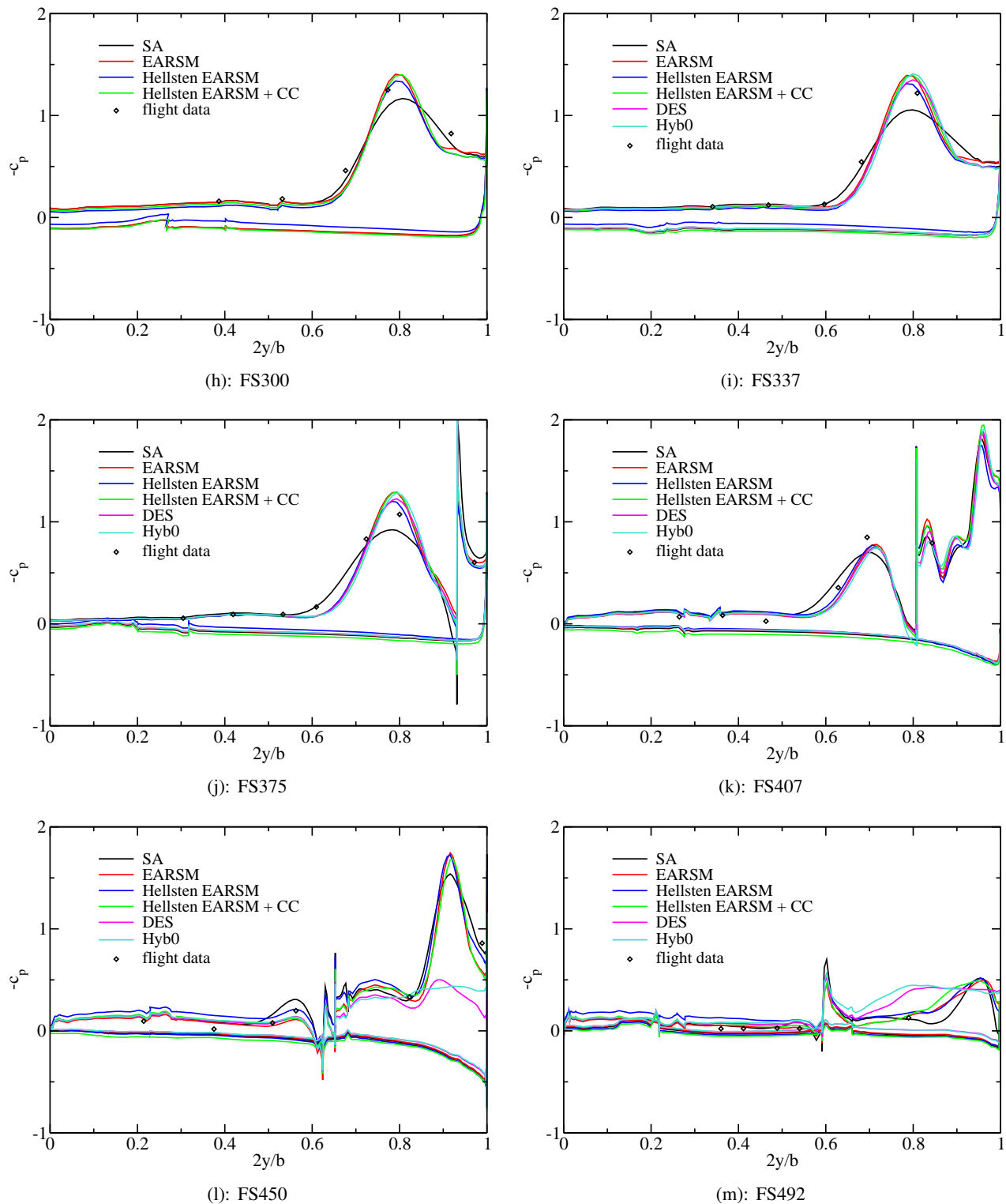
(h): FS300

(i): FS337

(j): FS375

(k): FS407

(l): FS450

(m): FS492

Figure 10-19: Predicted and Measured C_p Distribution at FC07 (Cont.).

Figure 10-20: Predicted and Measured C_p Distribution at FC50.
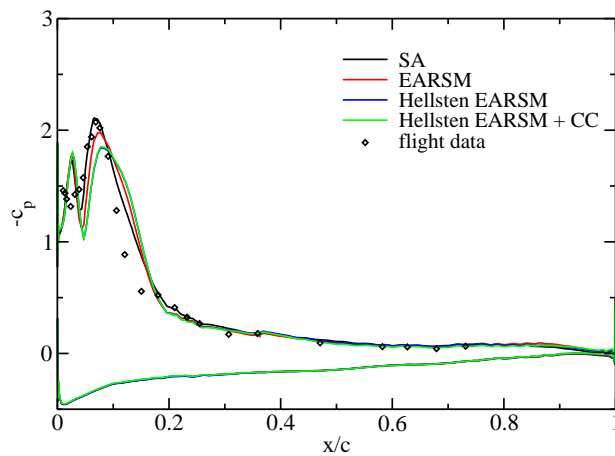
(a): BL55
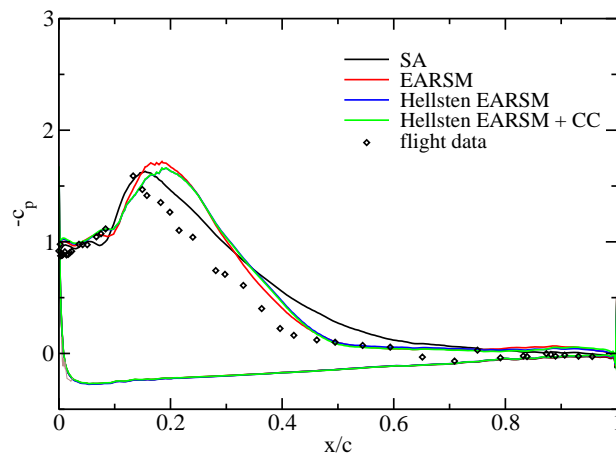
(b): BL70
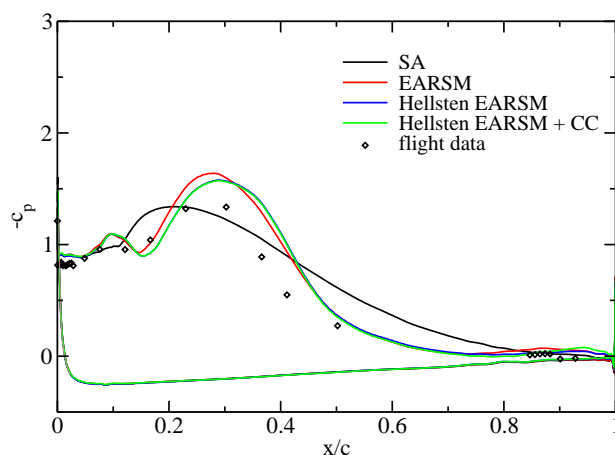
(c): BL80
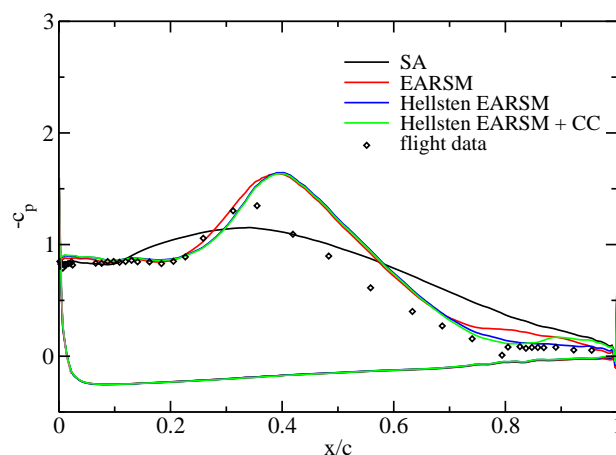
(d): BL95
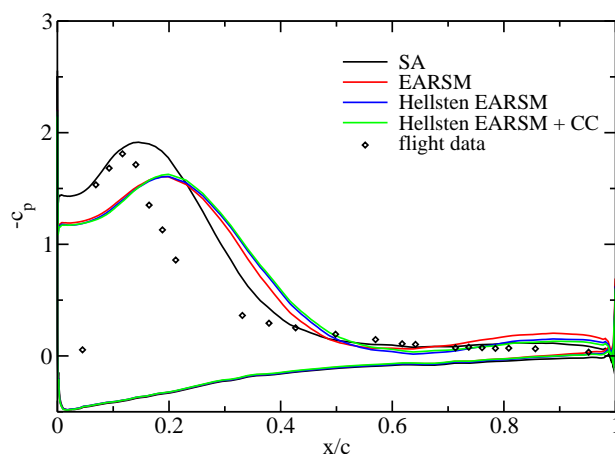
(e): BL153

(f): BL184.5
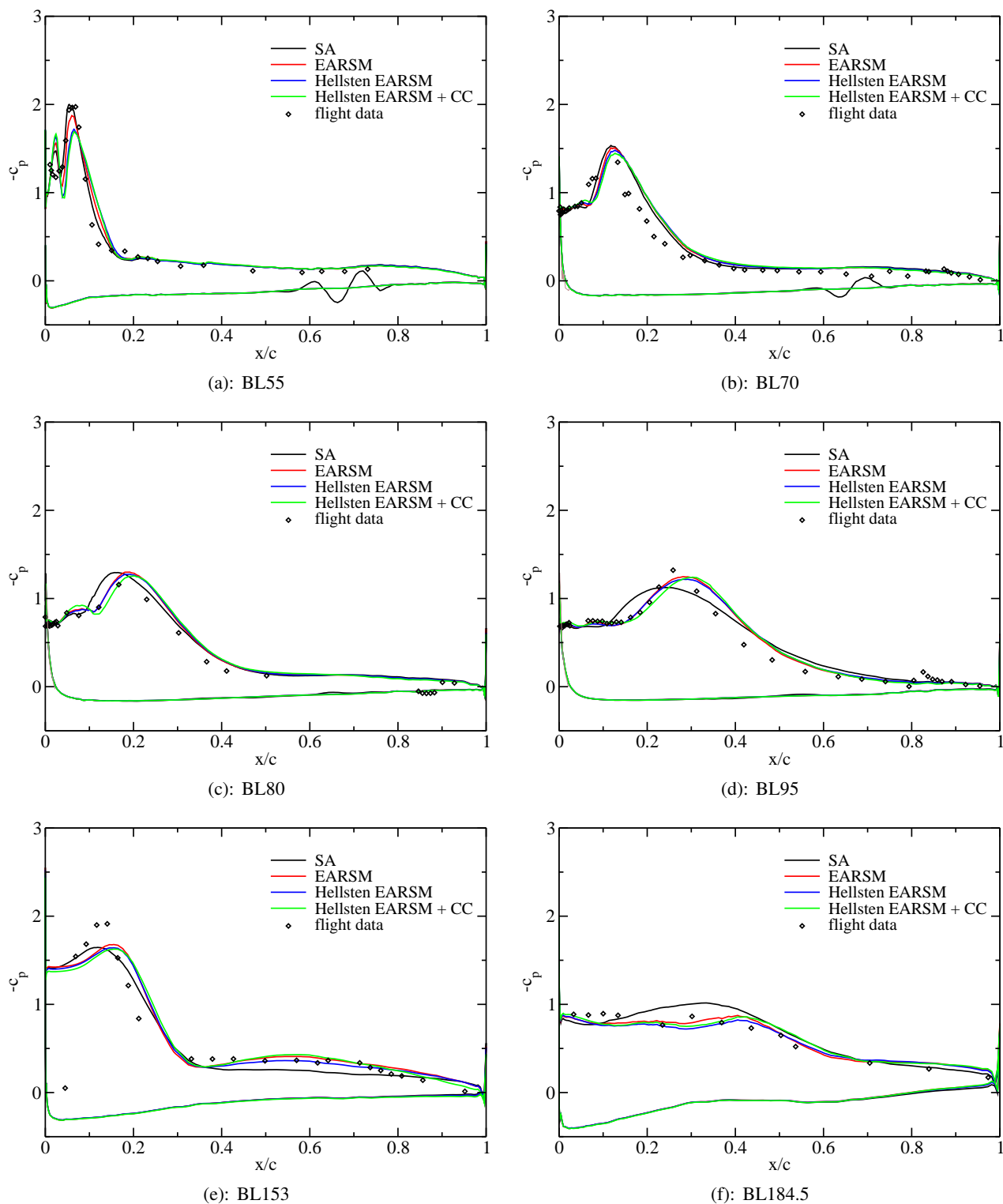
Figure 10-21: Predicted and Measured C_p Distribution at FC51.

Chapter 11 – NUMERICAL SOLUTIONS FOR THE CAWAPI CONFIGURATION ON UNSTRUCTURED GRIDS AT KTH/FOI, SWEDEN – PART II

by

Adam Jirásek[1] and Arthur Rizzi[2]

11.1   SUMMARY

This article represents a second contribution of the Swedish Defence Research Agency, FOI, and the Royal Institute of Technology, KTH, to the Cranked-Arrow Wing Aerodynamics Project International, CAWAPI. The main focus of this article is on evaluation of the effect of different formulation of boundary conditions on the engine mass flow and resulting wing upper surface pressures.

11.2   INTRODUCTION

This study is a part of CAWAPI international collaborative activities [11-1], [11-2] and complementary study to that of Goertz et al. [11-3] aiming at detailed testing of steady and non steady CFD analysis of an F-16XL fighter configuration. The detailed study of different turbulence models for steady and unsteady analysis of this configuration is in [11-3]. The study in this article focuses instead on formulation of boundary conditions in the inlet and engine exhaust face.

Figure 11-1 shows the CAWAPI configuration. It has two internal boundary conditions, one in the inlet and second at the mixing plane in the nozzle – see Figure 11-2.

Figure 11-1: CAWAPI F-16XL-1 Configuration at Higher Angle of Attack, NASA Photo, 1996.

---

[1] FOI R&D Engineer.

[2] Professor, Department of Aeronautics.
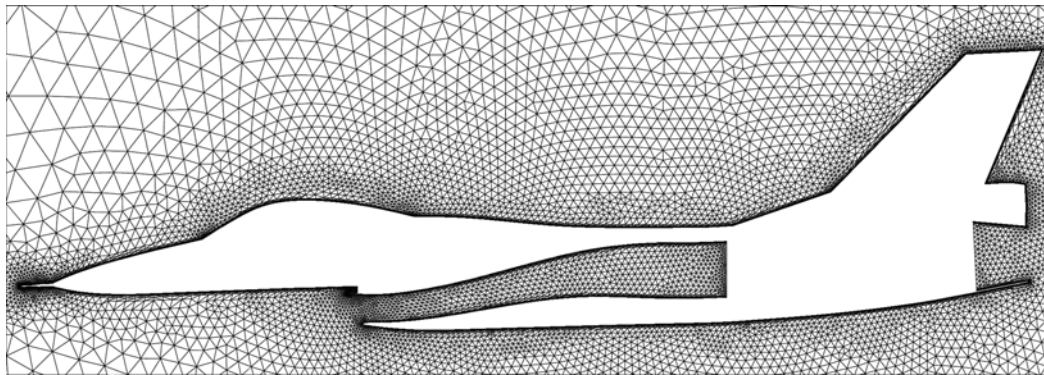
**Figure 11-2: CAWAPI F-16XL-1 Configuration, Symmetry Plane of
the Hybrid Grid Showing the Meshed Inlet Duct and Nozzle.**

The boundary conditions applied at these boundaries were static pressure at the outlet boundary in inlet and total states inflow boundary at the mixing plane. The values of static pressure in inlet and total states in the nozzle were estimated using generic engine model and are given in Lamar et al. [11-1] – see Table 11-1.

Table 11-1: Propulsion Conditions as a Function of Flight Conditions

	Inlet Duct Exit Conditions			Mixing Plane Conditions		
FC	T_{stat}[K]	P_{stat}[Pa]	u [m/s]	Mach number	T_0 [K]	P_0 [Pa]
FC07	276.7	75,842	115.7	0.347	583.3	158,579
FC19	269.9	70,327	105.4	0.320	583.3	148,237
FC25	261.1	60,122	144.7	0.447	671.7	181,332
FC46	246.4	40,334	123.2	0.390	580.6	102,042
FC70	288.3	73,429	141.6	0.416	666.7	206,843
FC50	244.5	35,577	147.3	0.470	641.4	116,866
FC51	239.8	35,784	142.8	0.460	636.7	115,418

The estimate does not take to account a balance of the mass flow. Despite that most participants use those conditions. The only organization which uses different type of boundary conditions is USAFA [11-4].

The inspection of the result with OMS boundary conditions shows large discrepancy between the values of the mass flow through inlet and through nozzle, where the value of mass flow leaving the engine through mixing plane was substantially larger then the amount of mass flow entering the engine through inlet. The effect of this discrepancy as well as the influence of substantially larger value of mass flow leaving the engine is unknown. This chapter focuses on study of the possible effect of the formulation of the boundary conditions in the inlet and nozzle on flow around delta wing of the CAWAPI configuration.

11.3   FLOW SOLVER

The CFD flow solver used for this study is the Edge [11-5], a finite volume Navier-Stokes solver for unstructured meshes. It employs local-time-stepping, local low-speed preconditioning, multigrid and dual-time-stepping for steady-state and time-dependent problems. The data structure of the code is edge-based so that the code is constructed as cell-vertex. It can be run in parallel on a number of processors to efficiently solve large flow cases. It is equipped with a number of turbulence models based both on the eddy-viscosity and an explicit algebraic Reynolds stress model EARSM combined with Hellsten k-ω model [11-6]. The solver is also equipped with several boundary conditions; one of them enables control of a mass flow through inflow and outflow boundary and Mach number at the outflow boundary [11-7].

11.4   CALCULATIONS WITH ENGINE BOUNDARY CONDITIONS

11.4.1   Methodology

Three formulations of boundary conditions were used:

- First, static pressure in the inlet and total states in the missing plane with values given in Lamar et al. [11-1]. This case is a benchmark case. Detailed description can be found in Goertz et al. [11-3]. This setup is called benchmark case.

- Value of static pressure from Lamar et al. [11-1],[11-2] was kept in inlet and resulting value of mass flow was used in boundary conditions in the nozzle. The value of mass flow is updated in every step of the international process. Total temperature in the nozzle was taken from Lamar et al. [11-1],[11-2]. This setup is called on-line shearing.

- Mass flow boundary conditions in both the inlet and nozzle were used. The value of mass flow is frozen for entire calculations and is taken from the benchmark calculations as the value of the mass flow through inlet. Total temperature in the nozzle was taken from Lamar et al. [11-1],[11-2]. This setup is called constant mass flow.

In some cases change of the boundary conditions worsened convergence of the computational process. In order to evaluate its effect on solution the following methodology was employed. The solution is not considered in terms of the average values and deviation. The computational process is run for sufficiently large number of steps so that it would be usually considered a converged solution. From that point the computational process was run for additional number of steps, usually 20% of entire length of international process. During this additional time the solution is sampled approx 20 times. Then the final solution is expressed in values of mean and deviation. As an example take a C_p coefficient in every mesh point:

$$C_p = C_{p_0} \mp \varDelta C_p$$

where mean is

$$C_{p_0} = \frac{1}{n} \sum C_p$$

and deviation

$$\varDelta C_p = \frac{1}{n} \sum \left(C_{p_0} - C_p \right)^2$$

The deviation of a particular variable should not be seen as an artefact of time-unsteadiness of solution, since the solution is calculated as a steady one using technique improving convergence such as multi-grid and local-time-stepping. It should be instead taken as an uncertainty due to sampling of the steady-state CFD solutions.

11.4.2   Results

Three flight conditions are investigated in depth – FC46, FC19 and FC7. Of particular interest are changes of the pressure distribution on the upper side of the wing and the value of total pressure in the mixing plane which is necessary to balance the value of mass flow through inlet.

11.4.2.1   Flight Condition FC46

At this flight conditions, the discrepancy between the value of mass flow through the inlet and nozzle in benchmark case is about $\dfrac{\dot{m}_{Nozzle}}{\dot{m}_{Inlet}} \approx 2$. Since the total temperature in the mixing plane is kept constant, it is expected that the value of total pressure would be substantially lower. Interesting is the effect of formulating boundary conditions on the pressure distribution on the upper side of wing. The constant mass flow setup had a minor effect on solution. The value of total pressure is as expected lower and there are noticeable differences of solution in vicinity of the nozzle but most of solution remains unaffected. Contrarily to this the on-line shearing setup worsened convergence of the computational process and changed pressure distribution on the upper side of wing. Figure 11-3 shows the distribution of absolute values of $C_{p_{Benchmark}} - C_{p_{sharedmassflow}}$
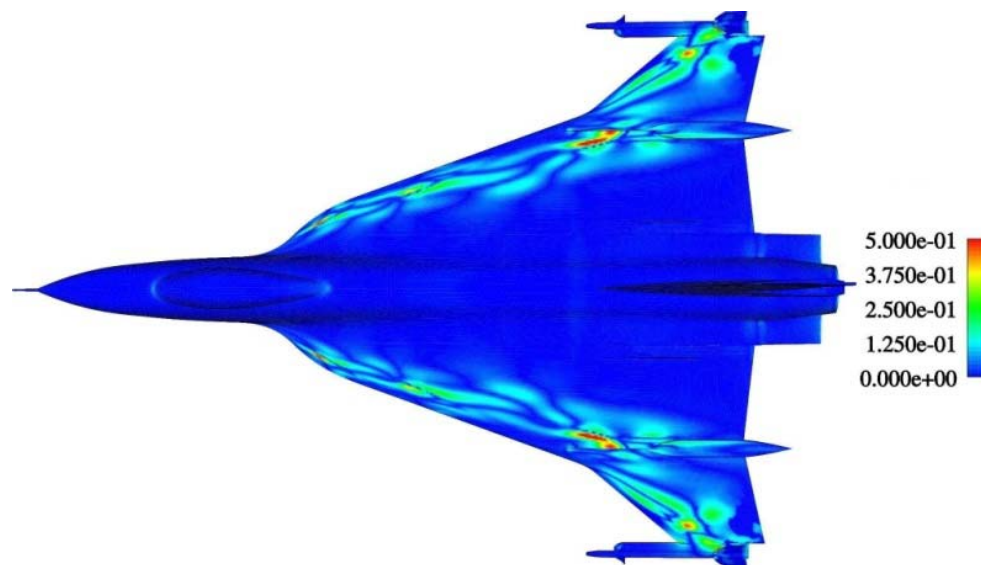
Figure 11-3: CAWAPI F-16XL-1, FC46, $C_{pBencmark} - C_{psharedmassflow}$.

The changes take place mostly along the leading edge and air dam, generally in areas where the pressure distribution is not flat but having large gradients and small change of solution is immediately visible. Figure 11-4 shows pressure distribution in butt lines for benchmark and on-line shearing setup calculations. Included is also a deviation of the pressure coefficient.
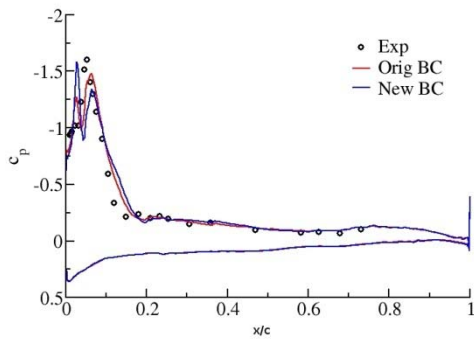
(a) BL55
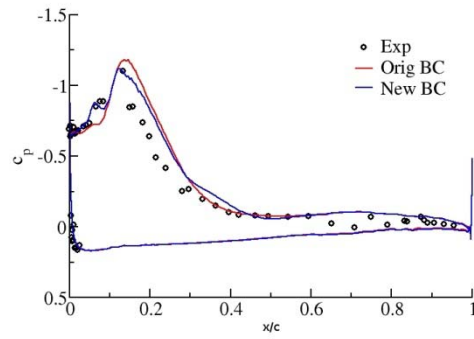
(b) BL70
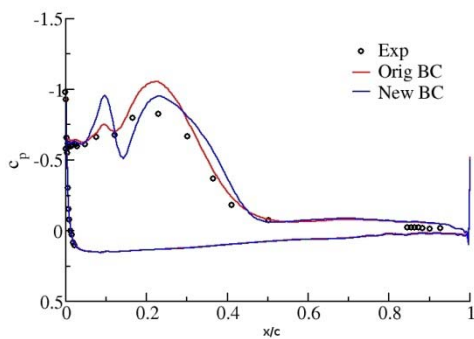
(c) BL80
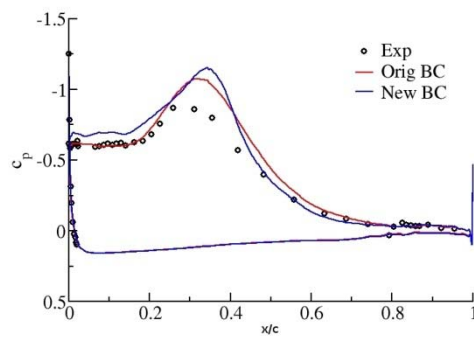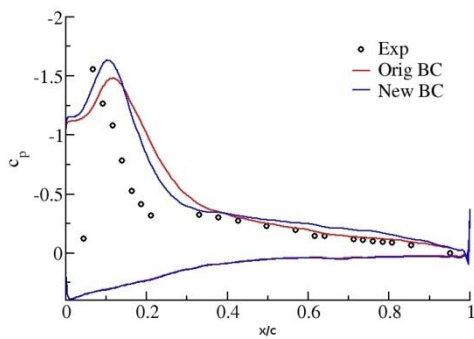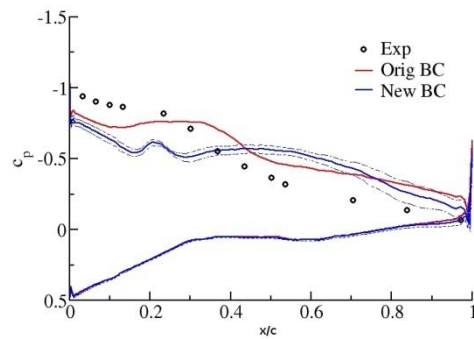
(d) BL95

(e) BL153.5

(f) BL184.5

Figure 11-4: FC46, Chordwise Comparison of Computed and Measured Surface Pressure Coefficient along Six Butt-Lines (BL) for Case FC46: (a) BL55; (b) BL70; (c) BL80; (d) BL95; (e) BL153.5; and (f) BL184.5.

It is difficult to say which result is better. Note the rather large scatter of C_p data at BL 185 from on-line shearing setup. The question is what causes this kind of behaviour. The examination of the flow-field of the

on-line shearing setup revealed rather localised but intense flow separation behind the lower inlet lip – see Figure 11-5.
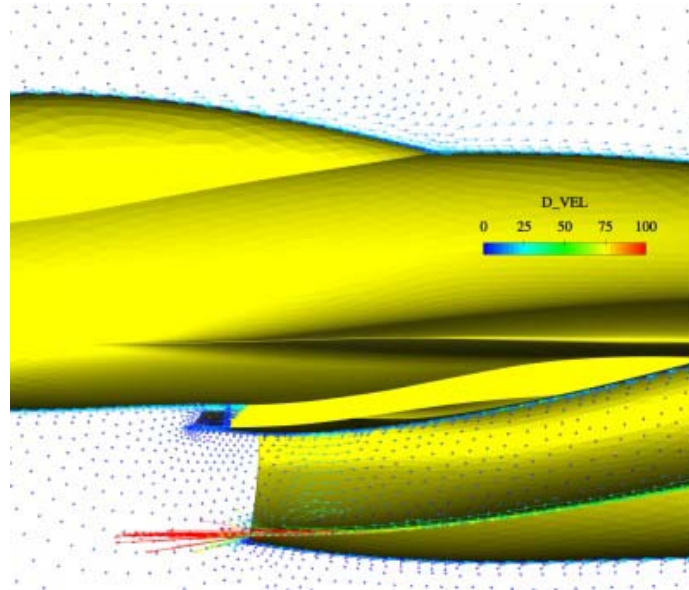
Figure 11-5: FC46, Velocity Vectors around Inlet Lips.

Apparently, this small but very intense spill-over makes the solution on the upper side change.

11.4.2.2   Flight Condition FC19

The analysis of flight conditions FC19 show similarity to previous flight conditions. The setup with online updated value of mass flow gave rise to flow separation behind the inlet lip with consequences to the pressure distribution on the upper side of the wing, as shown in Figure 11-6.
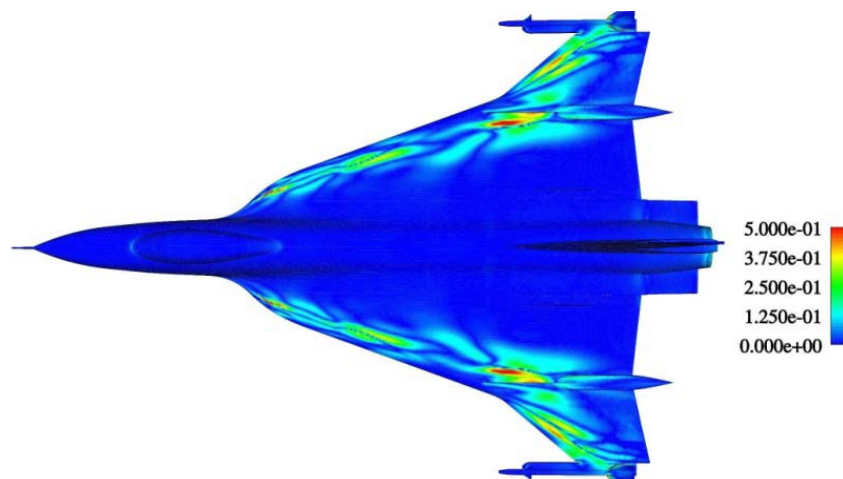
Figure 11-6: CAWAPI F-16XL-1, FC19, $C_{pBencmark} - C_{psharedmassflow}$.

Both C_p distribution and standard deviation of velocity show pretty much the same as in previous flight condition.

11.4.2.3   Flight Condition FC07

Unlike previous two cases, the flight condition FC07 does not show any dependency on different setup of boundary conditions. Detailed inspection of the figure revealed similar structure as in previous case – see Figure 11-7, however in order to visualize them the scale was updated. The largest difference in C_p between these two solutions is on the order of 0.05.
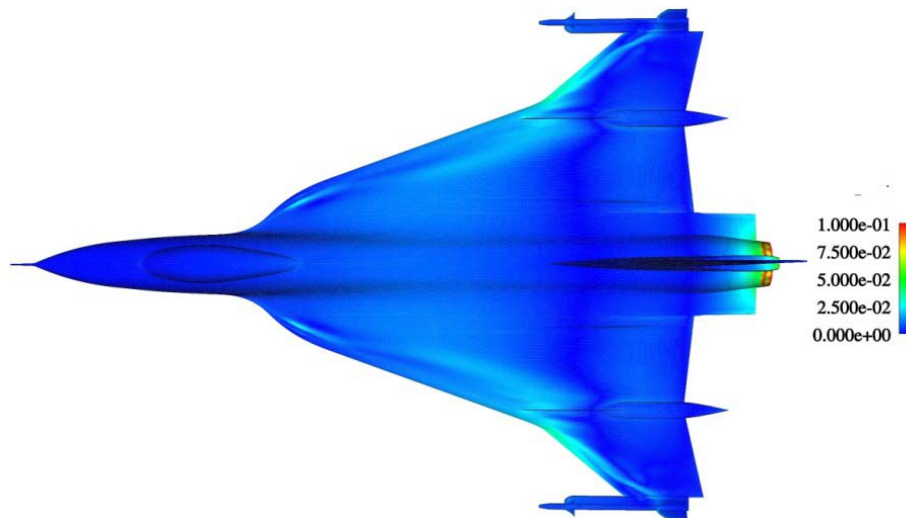
Figure 11-7: CAWAPI F-16XL-1, FC07, $C_{pBencmark} - C_{psharedmassflow}$.

11.4.3   Updated Values of Total Pressure in the Nozzle

Both on-line shearing setup and constant mass flow setup solutions were used to extract the value of total pressure at the mixing plane which is needed for balance of the mass flow through inlet and nozzle. The differences in values of the total pressure between these two setups are almost negligible. Table 11-2 shows these values.

Table 11-2: Values of Total Pressure in the Mixing Plane

FC	T_0 [K]	OMS P_0 [psia]	Corrected Value P_0 [psia]
FC07	583.3	23.0	14.17
FC19	583.3	21.5	11.39
FC46	580.6	14.8	8.86
FC25	671.7	21.5	12.99
FC70	666.7	21.5	9.48

As expected, the value of total pressure is substantially lower because the mass flow through the nozzle is lower. The inflow mass flow boundary condition which is used at the boundary in the mixing plane needs also the value of total temperature. This value is taken from Lamar et al. [11-1].

11.5   ADDITIONAL RESULTS

The inspection of the iso-surfaces of mean value and its deviation gives interesting figures. As an example, Figure 11-8 shows the iso-surface of the mean and its variance for entropy. Whilst the iso-surface of entropy in Figure 11-8 (a) shows several isolated vortices rising from the wing, the standard deviation of entropy shown in Figure 11-8 (b) shows more compact envelope of area including vortices.

(a) Entropy – **Mean Value**   (b) Entropy – **Deviation**
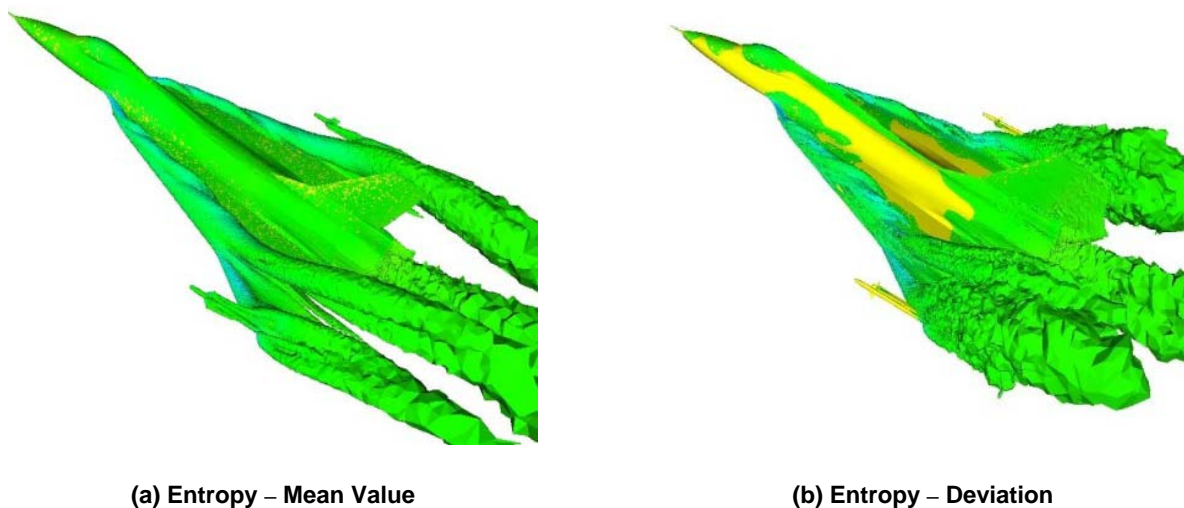
Figure 11-8: FC46, Iso-Surface of Entropy and its Standard Deviation.

Similar figures can be plotted for Mach number, total pressure or velocity – see Figure 11-9.

(a) Total Pressure P_0

(b) Mach Number
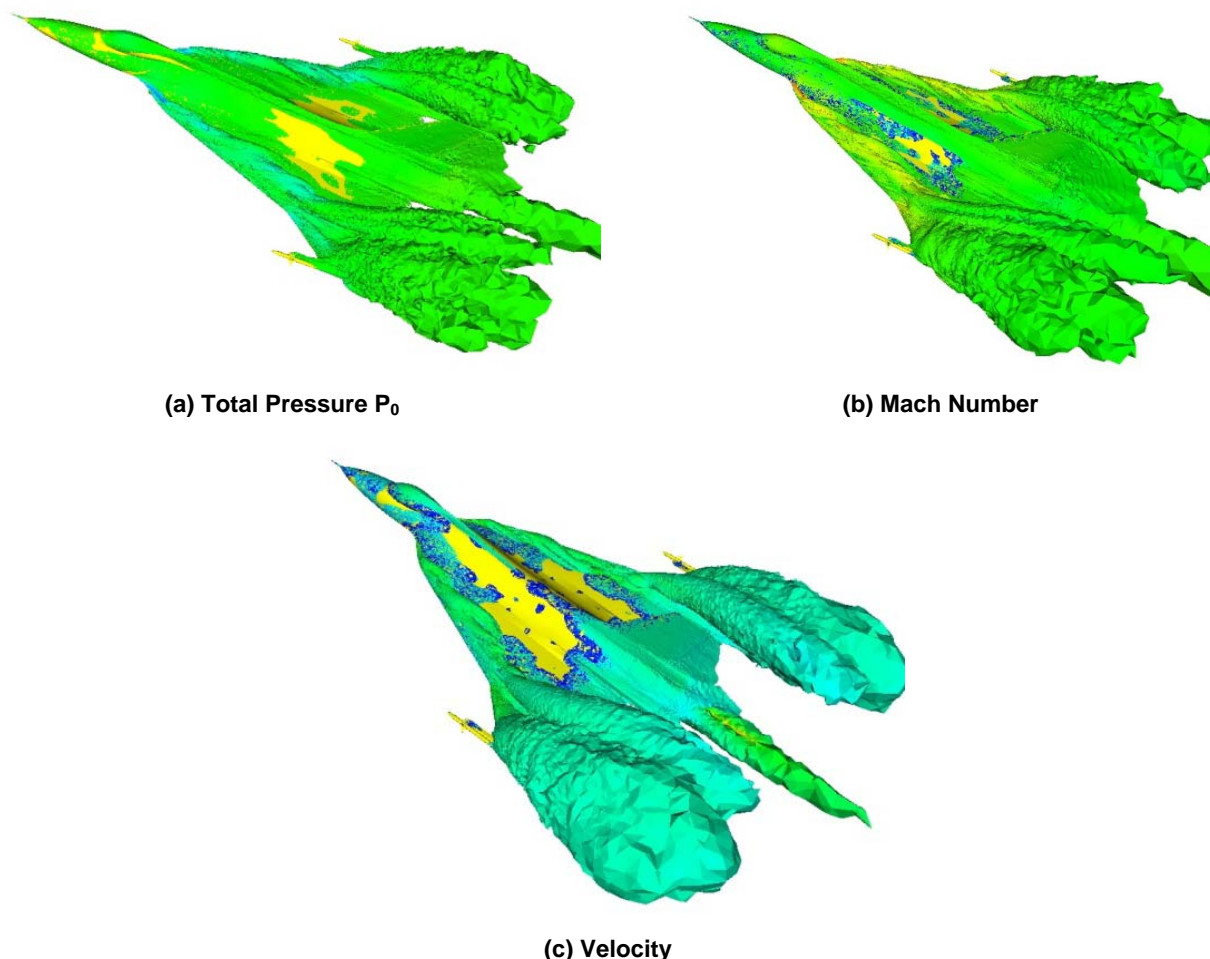
(c) Velocity

Figure 11-9: FC46, Iso-Surface for Standard Deviation of Total Pressure, Mach Number and Velocity.

What makes these figures interesting, particularly figures containing iso-surfaces of deviations is that they show very nicely vortical structure. It is also very easy to obtain such figures. It can be therefore expected that this approach can during mesh refinement for detecting areas where the flow structure may require improving of the computational mesh.

11.6   CONCLUSIONS

The standard boundary conditions at the inlet and the outflow from the nozzle used by all the CAWAPI participants were determined from a generic engine model. The exercise presented here focuses on the question of sensitivity of the formulation of these boundary conditions. Two approaches were chosen to determine alternative formulations to the standard one; the first is to keep the value of mass flow through the nozzle constant, and the second is to update the value of mass flow in the nozzle in every step of the computational process using the value of mass flow from the inlet. In both cases the total pressure in the nozzle are found to be substantially lower than that given by the formulation from the generic engine model. The first approach involves sharing the value of mass flow between the inlet and outlet boundaries and the mixing plane boundary in every step of the numerical process. It affects both solution and convergence of the numerical process at two

of the three flight conditions tested here. The most significant change in the solution takes place in the inlet where the flow is separated. This separation, whose extent is rather small, is intense and gives rise to changes of the flow around leading edge of the delta wing and consequently to the entire flow over the suction side of the wing. What cannot be answered is whether this observation is physically realistic or if it is just of a purely numerical nature.

The second approach, which simply corrects the value of mass flow through the inlet by prescribing its current-time value, had almost no effect on the flow around the wing. The only change occurred in the position of the shock on the outboard wing at the transonic flight condition. Rate of convergence of the computational process was the same as that of the benchmark case. In conclusion, although significant sensitivity was seen in one of the alternative formulations of the boundary conditions, there were not sufficient reasons to suggest that these conditions were better than the standard ones. Therefore the standard conditions have been used in CAWAPI.

11.7   ACKNOWLEDGEMENTS

11.8   REFERENCES

[11-1] Lamar, J.E., Obara, C.J., Fisher, B.D. and Fisher, D.F.: *Flight, Wind-Tunnel, and Computational Fluid Dynamics Comparison for Cranked Arrow Wing (F-16XL-1) at Subsonic and Transonic Speeds*, NASA/ TP 2001-210629, NASA, February 2001.

[11-2] Lamar, J.E. and Obara, C.J.: *Review of Cranked-Arrow Wing Aerodynamics Project: Its International Aeronautical Community Role*, AIAA Paper 2007-0487, Presented at 45th AIAA Aerospace Sciences Meeting and Exhibit, Reno, NV, January 8-11 2007.

[11-3] Görtz, S. and Jirásek, A.: *Chapter 10 – Numerical Solutions for the CAWAPI Configuration on Unstructured Grids at KTH/FOI – Part I*, RTO-TR-AVT-113, 2009.

[11-4] Morton, S.A., McDaniels, D.R. and Cummings, R.M.: *F-16XL Unsteady Simulations for the CAWAPI Facet of RTO Task Group AVT-113*, AIAA Paper 2007-0493, Presented at 45th AIAA Aerospace Sciences Meeting and Exhibit, Reno, NV, January 8-11 2007.

[11-5] Eliasson, P.: *EDGE, a Navier-Stokes Solver for Unstructured Grids*, Proc. to Finite Volumes for Complex Applications III, ISBN 1 9039 9634 1, 2002, pp. 527-534.

[11-6] Hellsten, A.: *New Advanced k-ω Turbulence Model for High Lift Aerodynamics*, AIAA Journal, Vol. 43, No. 9, 2005.

[11-7] Jirásek, A.: *Mass Flow Boundary Conditions for Subsonic Inflow and Outflow Boundary*, AIAA Journal, Vol. 44, No. 5, May 2006.

Chapter 12 – NUMERICAL SOLUTIONS FOR THE CAWAPI CONFIGURATION ON UNSTRUCTURED GRIDS AT BOEING-ST. LOUIS, UNITED STATES

by

Todd R. Michal, Matt Oser, Mortaza Mani and Frederick W. Roos

12.1 SUMMARY

Analyses performed with the Boeing Computational Fluid Dynamics code about the CAWAPI research aircraft at high angles of attack are presented. Results are compared with surface pressure and boundary layer measurements taken in flight. A sequence of investigations aimed at measuring the impact of grid resolution, grid topology, turbulence modelling and time accuracy on solution accuracy are described. Results from the studies are summarized in a collection of lessons learned to help guide future high angle of attack computations.

12.2 INTRODUCTION

Flight at high angle of attack is a critical part of the envelope for many of today's military aircraft and missile systems. Flight characteristics in this regime affect aircraft manoeuvrability, handling characteristics, stability and control, and safe store separation. High angle of attack flight is dominated by flow field features such as large areas of separation, complex vortical structures and unsteady flow. The ability to predict and understand the physics of these features enables them to be integrated into the vehicle design thereby improving performance.

Vehicle design in the high angle of attack regime has traditionally relied on empirical design methods and experience gained from previous designs. These methods provide a qualitative assessment of high-alpha characteristics but do not provide quantitative data on which to base a new vehicle design. Accurate data typically only becomes available late in the design process through wind-tunnel testing. Often this data becomes available too late to impact the vehicle design. In extreme circumstances, late discovery of adverse high-alpha interactions can lead to expensive program delays or program cancellation.

Computational Fluid Dynamic (CFD) simulation of high-alpha flows offers the possibility of providing quantitative data earlier in the design process. Unfortunately, the flow field features prevalent in high-alpha flight make accurate simulations in this environment challenging for today's CFD tools. Over the past several decades, steady progress has been made in modelling high alpha flows. Euler methods were shown to predict vortices on delta wings in the mid 1980's. The NASA High Angle of Attack Research Vehicle (HARV) program provided a wealth of test data for benchmarking CFD codes [12-1]. Several researchers compared structured CFD results against this data [12-2]. At Boeing, many programs have gained valuable data from CFD analysis of high angle of attack flows. Examples include assessment of tail buffet on the F/A-18C program and analysis of the booster separation aerodynamics for the Delta IV launch vehicle. For the most part these analyses were performed with structured grid methods and suffered from limited validation data upon which to verify the results. Structured grid CFD computations on complex vehicles can require several weeks or months to obtain, a time frame which severely limits their usefulness. Unstructured grid methods have demonstrated the ability to rapidly model and compute CFD data on complex configurations, but relatively little validation of unstructured grid methods has been performed for high-alpha flight.

A systematic study of CFD methods in the high-alpha flight regime is needed to quantify the accuracy, understand the best practices for modelling these flows, and increase the technology readiness of CFD for the next generation of fighter aircraft systems. This is particularly true for unstructured grid methods which have seen relatively little use in this flow field environment. In particular, a better understanding of the effect of unstructured grid discretization algorithms, turbulence modelling, and unstructured-grid topology and resolution requirements is needed.

In this chapter, data from the NASA Cranked Arrow Wing Aerodynamics Project is compared against the Boeing Computational Fluid Dynamics (BCFD) code. Results are presented from a series of computational studies. These studies were designed to investigate the impact of grid topology, grid resolution, solution algorithms and turbulence modelling. Comparisons with flight test data are used to assess the relative accuracy and formulate best practices for modelling high-alpha flow fields with the BCFD code.

12.3   CFD TOOLSET

The grids in this study were generated using the Boeing Modular Aerodynamic Computational Analysis Process (MADCAP). MADCAP was developed at Boeing as a modular framework to house grid generation capabilities from a variety of sources. MADCAP contains a fully automated surface mesh generation capability. In addition to the automated approach, the user can interactively control resolution and mesh element type through the selection of control nodes, edges and surfaces. Unstructured mesh algorithms can be selected from Boeing developed libraries and/or from the Advancing Front with Local Reconnection (AFLR) library [12-6]. Surface meshes can contain a combination of quadrilateral and triangular faces. The volume meshes used in this study were developed with the AFLR code using a combination of element types. Near the wall, advancing layers are used to place highly anisotropic prismatic elements across the boundary layer. Outside the boundary layer, isotropic tetrahedral elements are utilized. A smooth transition between the prismatic and tetrahedral elements is provided by growing each column of the boundary layer mesh until the element at the outside edge is nearly isotropic. The boundary layer resolution is controlled by specification of the initial spacing near the wall, an initial growth rate, a growth stretching and a maximum growth rate. In addition, the extent of the boundary layer thickness can be specified or an estimate of the boundary layer thickness for a turbulent flat plate can be used to extend the prismatic layers beyond the estimate. Control of the resolution of the tetrahedral portion of the mesh is provided by a linear interpolation from the surface mesh. Alternatively, the user can specify a geometry growth rate to control the stretching of resolution in the tetrahedral region. Sources in the form of individual nodes, curves or surfaces can be specified to control the off body resolution of the tetrahedral mesh.

The BCFD code is a general geometry and general purpose Euler and Navier-Stokes solver [12-7]. Any valid grid (structured, unstructured, and hybrid) can be utilized (tet, hex, prism, pyramid, and any mix of them) with the BCFD code. A mature second-order accurate zone coupling technique ensures continuity of the solution across zone boundaries. BCFD has an extensive library of boundary condition routines available on a point-by-point basis as well as various numerical algorithms such as Roe, HLLE, and Lax-Freidrichs/Rusanov. The default explicit spatial operator is a finite-volume second-order HLLE flux difference split scheme. Gradient reconstruction is performed at the cell centers and uses a total variation diminishing (TVD) limiter to improve robustness and convergence rate.

Turbulence models implemented in BCFD include the one-equation point-wise model of Goldberg, which does not require wall distance, and the one-equation Spalart-Allmaras (S-A) and two-equation Menter SST model, which utilize the wall distance. Also, the hybrid (RANS-LES) models SA/DES, SA/MDES, and SST/LESb , PRNS, and Detached-PRNS have been implemented.

BCFD incorporates a number of user-selectable (by zone) solution algorithms. The default time integration scheme is a first-order, implicit scheme where a point Gauss-Seidel with agglomeration multi-grid is used for unstructured grids. For steady-state flows, variable time steps based on local eigenvalues are used to speed convergence. For time-accurate calculation, BCFD offers a second-order Global Newton/dual-time algorithm which provides second-order accurate updates in the physical-time domain across all zones.

12.4   RESULTS

Studies were performed to investigate the impact of grid type, grid resolution and BCFD algorithmic options on solution accuracy about the F-16XL geometry. Flight Condition 7 was selected as the baseline condition for these studies because of the availability of both surface pressure and boundary layer data. All of the BCFD solutions presented in this chapter utilized the second-order accurate HLLE algorithm with TVD limiter.

Convergence of all BCFD solutions in this study was determined by monitoring the L2Norm of the residual of the solution variables and the overall integrated surface forces. A typical convergence history is shown in Figure 12-1. Because of the unsteady nature of the flow field, the surface forces did not converge to a steady value but rather they reached an oscillatory state about a mean value. It was found that reaching this oscillatory state was not an accurate prediction of convergence of the solution near the vortex core. To ensure full convergence, the surface pressure in the vicinity of the primary vortices was monitored as an additional gauge of solution convergence.
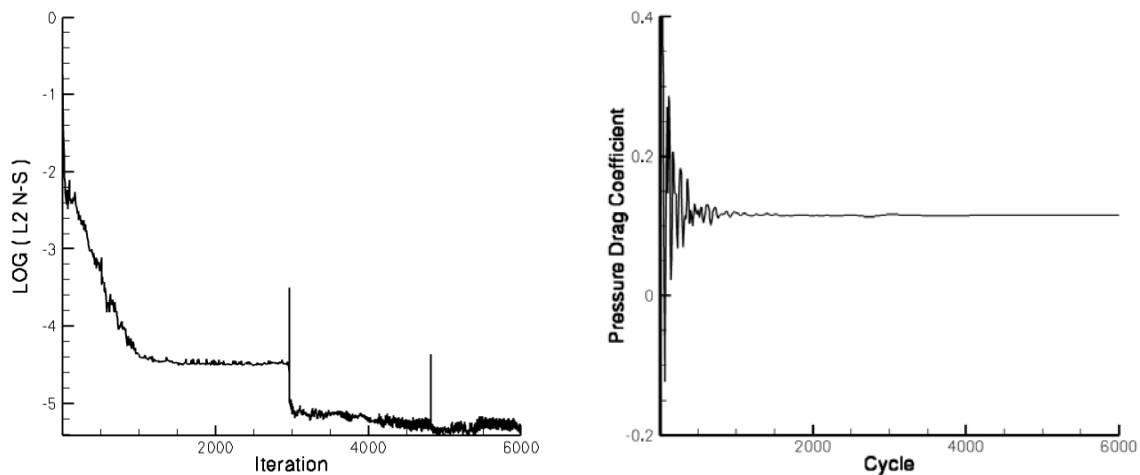
Figure 12-1: BCFD Convergence History from Sample AVT Solution.

The first study investigated the effect of grid resolution and cell topology on solution accuracy. A baseline solution was generated on the common unstructured grid supplied to the CAWAPI team members. This grid contains approximately 12 million volume elements. A complete description of the geometry and AVT common grid is provided in Reference [12-8]. The baseline BCFD solution was computed using the Spalart-Allmaras turbulence model and time integration to steady state was performed using 3 levels of multi-grid. Predicted contours of the surface pressure coefficient are shown in the left side of Figure 12-2. Cuts of the total pressure normalized by the free stream total pressure at several fuselage stations are shown in the right

side of Figure 12-3. The flow field is characterized by three primary vortices. The largest vortex forms at the root of the wing fuselage intersection and is fed by the flow around the 70 degree sweep inboard wing leading edge. About half way between the wing root and tip, the leading edge sweep suddenly changes to a sweep angle of 50 degrees. At this crank in the leading edge sweep, a second primary vortex is formed. Just inboard of the wing crank, there is a large vertical plate (fence) that limits communication between the inboard and outboard portions of the wing. A third primary vortex is generated at the leading edge of the fence and tracks on the outboard portion of the wing. Interactions between the inboard wing vortex and the fence play an important role in establishing the flow field.
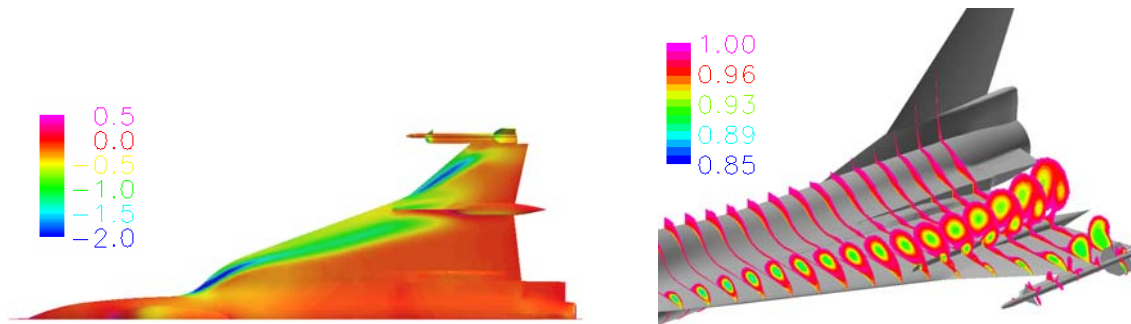
Figure 12-2: Surface Pressure Coefficient and Total Pressure Ratio
Contours Computed on the Common Grid at Flight Condition 7.

Cuts of the computed surface pressure from all of the BCFD study results at butt-line (BL) stations of 55, 70, 80, 95 153.5 and 184.5 inches are shown in Figure 12-3. The BL locations BL are illustrated by solid red lines overlaid on top of the wing plan form for each plot. BL stations 55, 70 and 80 are located inboard of the fence and stations 153.5 and 184.5 are outboard of the fence. The BCFD solution on the common grid is indicated by the dot dash red line. The results follow the general trends of the test data, but consistently under predict the strength of the suction peak centered along the inboard and outboard vortex cores. The computed location of the suction peak is slightly forward of the test data. A second smaller suction peak upstream of the primary vortex indicating the location of a secondary vortex is clearly evident in the test data. In the BCFD common grid solution this secondary vortex is absent or marginally visible. The lack of a secondary vortex may be partially responsible for the offset of the primary vortex location in the common grid CFD results.
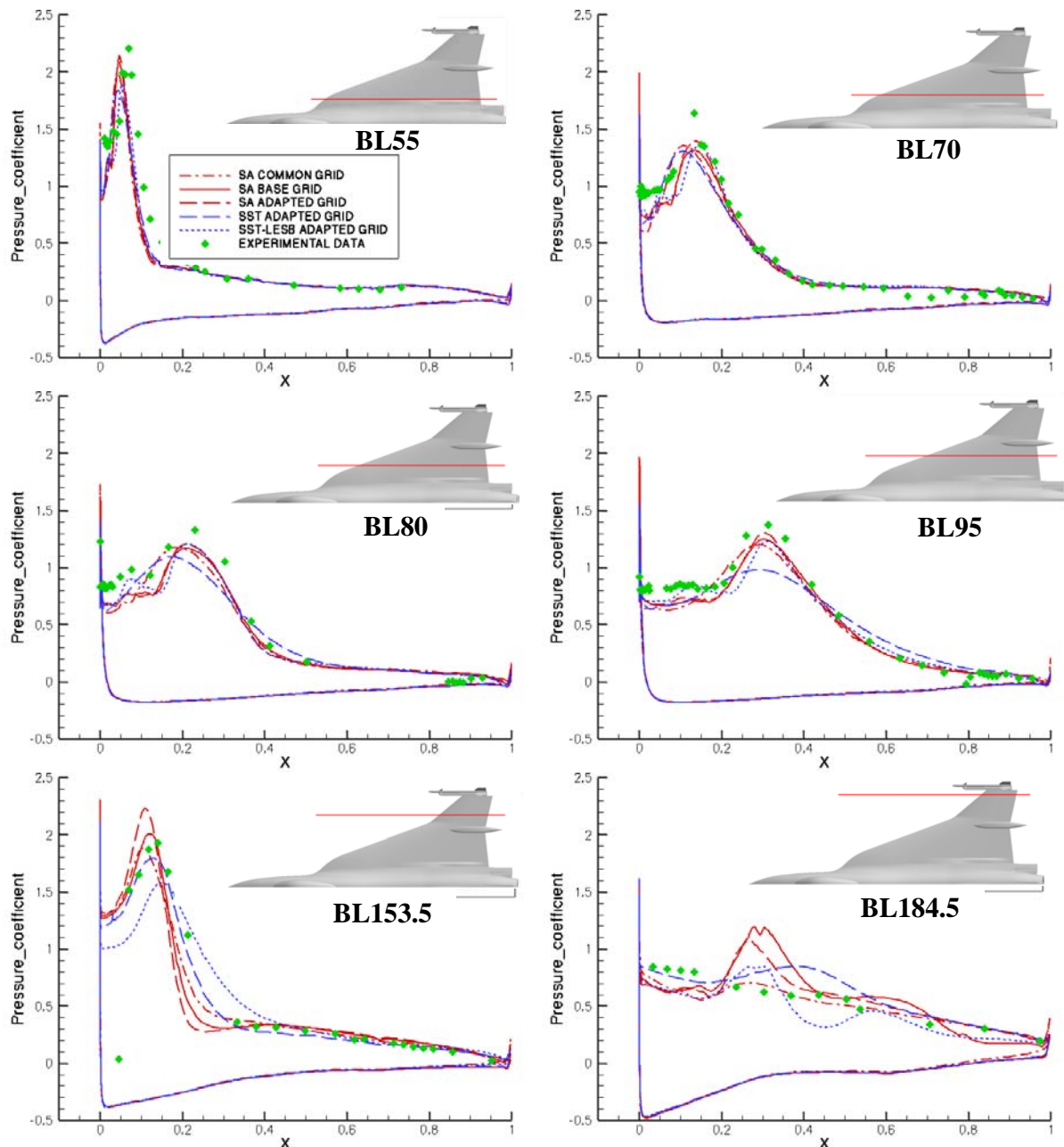
**Figure 12-3: Comparison of Computed Surface Pressure Coefficient
for Several Butt-Line Cuts at Flight Condition 7.**

Predicted velocity profiles across the boundary layer at 4 rake locations are shown in Figure 12-4. The locations of the rakes are illustrated by the red dots on the plan form view with each plot. BCFD results computed on the common grid are indicated by the dot-dash red line in Figure 12-4. The predicted profiles show a lower gradient in the near wall region compared to the test data. The predicted profile is particularly far from the test data at rake location 7.
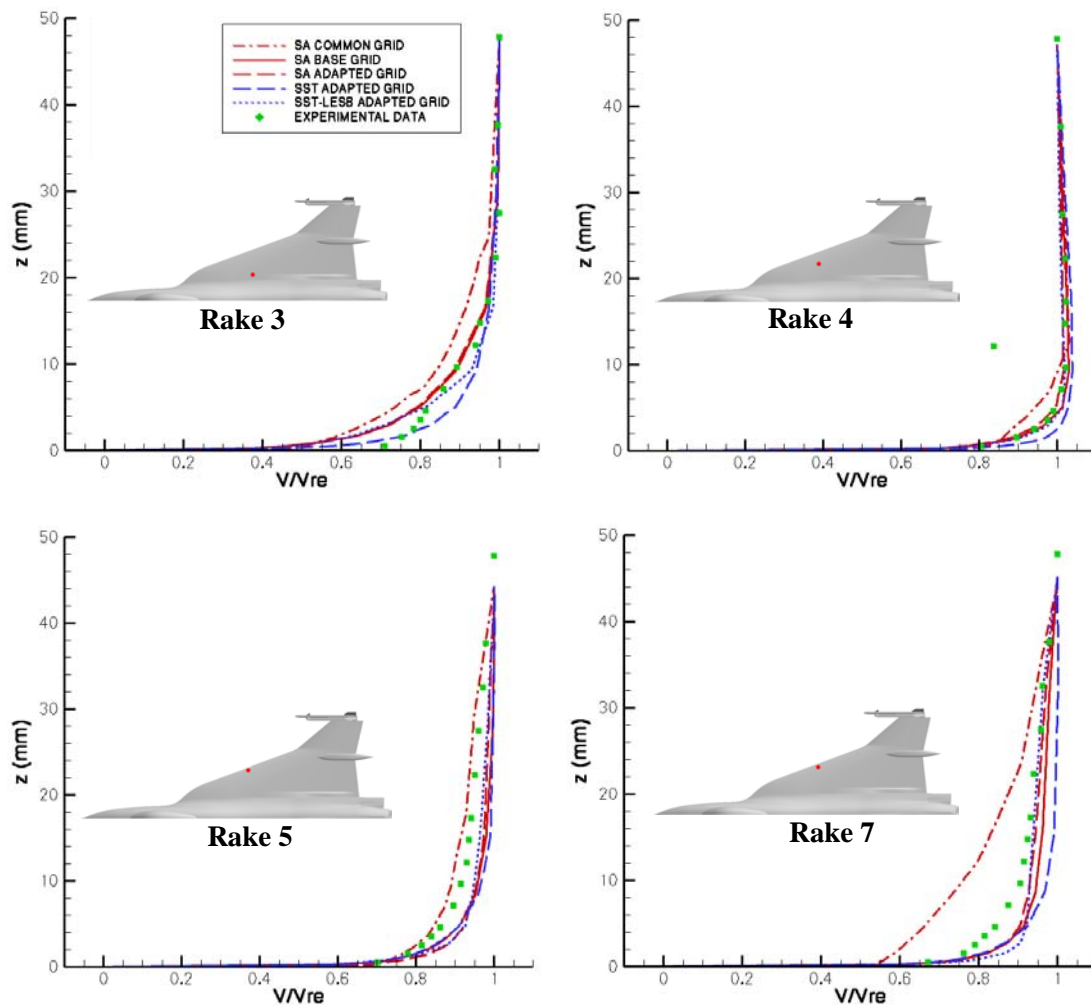
Figure 12-4: Comparison of Computed Velocity Profiles at Flight Condition 7.

One contributing factor to the lack of a secondary vortex in the CFD prediction may be the lack of adequate mesh resolution in the wing leading edge vortex region. The common mesh consists of an-isotropic triangular elements with an aspect ratio of about 10:1. The stream wise resolution at the leading edge is 0.228 inches resulting in about 10 faces circumferentially around the leading edge. The surface mesh near the wing leading edge is shown in Figure 12-5.

A mesh with higher-resolution was constructed in MADCAP to try and improve solution accuracy. In particular, the mesh was concentrated near the wing leading edge to try and improve the prediction near the secondary vortex. Mesh resolution was increased at the leading edge by introducing high aspect ratio quadrilateral elements into the surface mesh. The maximum aspect ratio of the quadrilateral faces is 25. The circumferential resolution at the leading edge is 0.05 inches inboard of the wing crank transitioning to 0.01 inch spacing near the wing tip. The quadrilateral elements were subdivided into triangles in the final mesh. A comparison of the Boeing and common meshes at the wing leading edge is shown in Figure 12-5. The resolution of the Boeing surface mesh is about double that of the common mesh in the immediate proximity of the wing vortices.
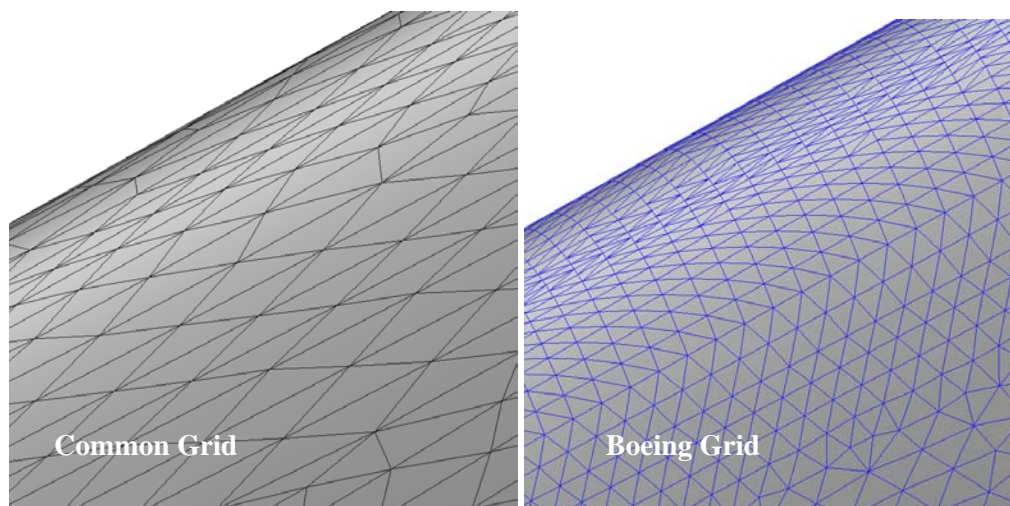
Figure 12-5: Comparison of Surface Meshes Near the Wing Leading Edge.

The volume portion of the Boeing mesh was generated in AFLR and consists of a semi-structured boundary layer extrusion connected to an isotropic tetrahedral grid. The extrusion used a 0.0003 inch initial spacing at the wall to yield a y+ of approximately 1 across the five flight conditions. The initial spacing grew geometrically with an initial growth ratio of 1.2 ending at a 1.8 maximum growth ratio. Extrusion terminated when the prisms achieved an aspect ratio near unity. The combination of the initial viscous spacing, growth rate parameters, and surface spacing produced approximately 15 prism layers. The resulting volume grid had 19.3 million cells. This mesh will be referred to as the Boeing baseline mesh.

A BCFD solution was generated on the Boeing baseline mesh at Flight Condition 7. Contours of the predicted surface pressure coefficient and normalized total pressure ratio at several fuselage station cuts are shown in Figure 12-6. The three primary vortices evident in the common grid solution are once again visible in the Boeing baseline mesh solution. Compared to the solutions on the common grid presented in Figure 12-3, the suction peak along the primary vortices is slightly more pronounced and the total pressure loss in the vortex core persists further downstream indicating less dissipation of the vortex.
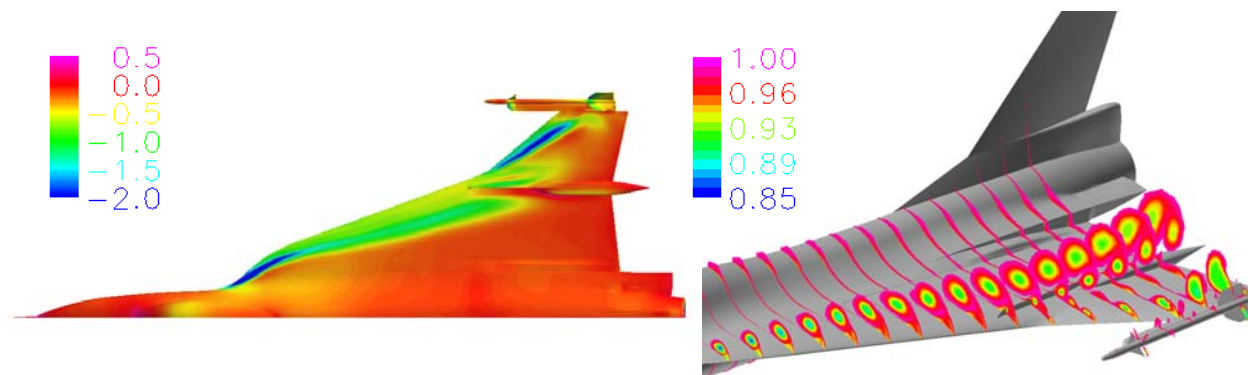
**Figure 12-6: Surface Pressure Coefficient and Total Pressure Ratio Contours
on Boeing Baseline Grid at Flight Condition 7 with the SA Turbulence Model.**

BCFD surface pressure predictions on the Boeing baseline mesh are indicated by the solid red line in Figure 12-3. Compared to the common mesh results, the surface pressure compares better with the test data near the wing leading edge. The most noticeable difference from the common grid results is the presence of a secondary vortex clearly visible at BL stations 70 through 95. Although there is not an appreciable change in the magnitude of the pressure peak compared with the common grid results, the location of the peak has moved aft and correlates better with the test data. The primary vortex outboard of the wing fence is much stronger in the Boeing mesh results. This is evident in the higher surface suction peak at BL station 153.5. The prediction deviates from the test data about the mid-chord location of BL 184.5. This BL is close to the tip missile. Examining the surface pressure contours in Figure 12-6 it appears that the track of the primary vortex is influenced by an interaction with the wing tip missile launcher. Predicted velocity profiles on the Boeing mesh at rake locations 4 through 7 are indicated by the solid red line in Figure 12-4. The improvement in the velocity profiles is most likely a result of the increased mesh resolution in the boundary layer and a better pressure prediction at the boundary layer edge.

Although the Boeing baseline mesh improved the location of the primary vortex over the common mesh, the magnitude of the suction peak is still under predicted. One possible explanation for this may be the off-body mesh resolution near the vortex core. As the primary vortex grows and convects downstream, it moves away from the surface and into the coarser tetrahedral portion of the volume mesh. This decrease in mesh resolution corresponds to an increase the numerical dissipation and may lead to a premature reduction in the predicted vortex strength and a smearing of the pressure suction peak on the surface.

To help assess the impact of the off body grid resolution, a new volume mesh was created with increased resolution along the vortex core path. The mesh was refined by placing grid resolution sources along traces of the three primary vortex cores predicted by the BCFD solution. This adapted grid utilized the same surface grid as the baseline Boeing grid, but the addition of sources increased the size of the volume grid to 23.3 million cells. The mesh resolution at BL cuts through the adapted and non-adapted volume meshes at BL 70 and BL 153.5 is shown in Figure 12-7 and Figure 12-8. The increase in off body resolution along the vortex path inboard of the wing fence is evident in Figure 12-7. Adaptation to the vortex core outboard of the fence had less impact on the mesh since the baseline volume mesh was already relatively dense in this area.
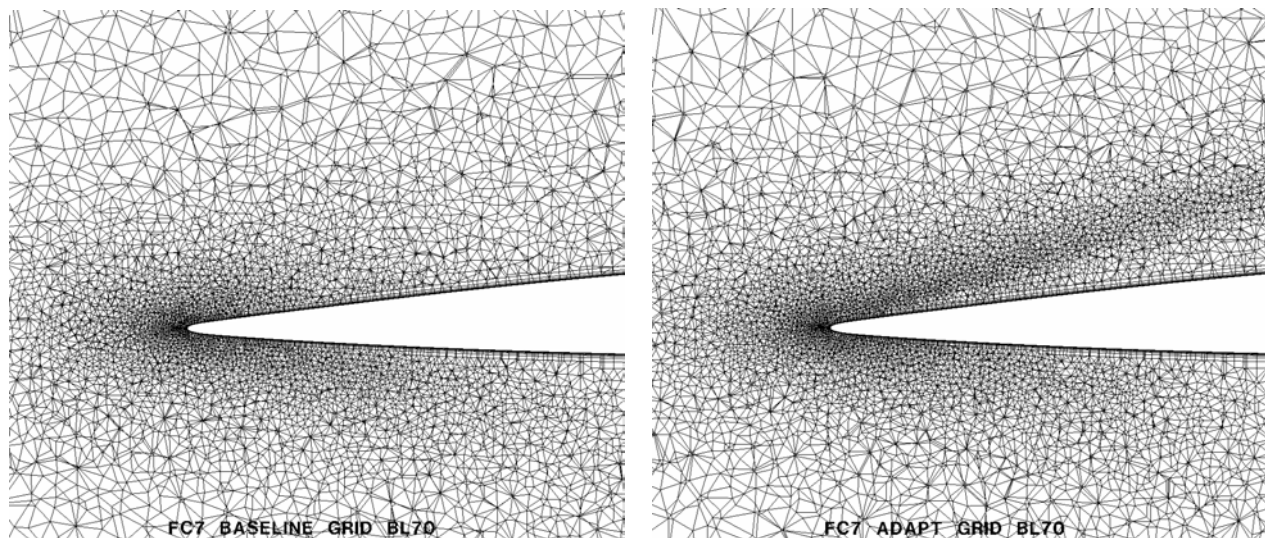
Figure 12-7: Cut Through Boeing Baseline and FC7 Adapted Grids at BL 70 Inches.
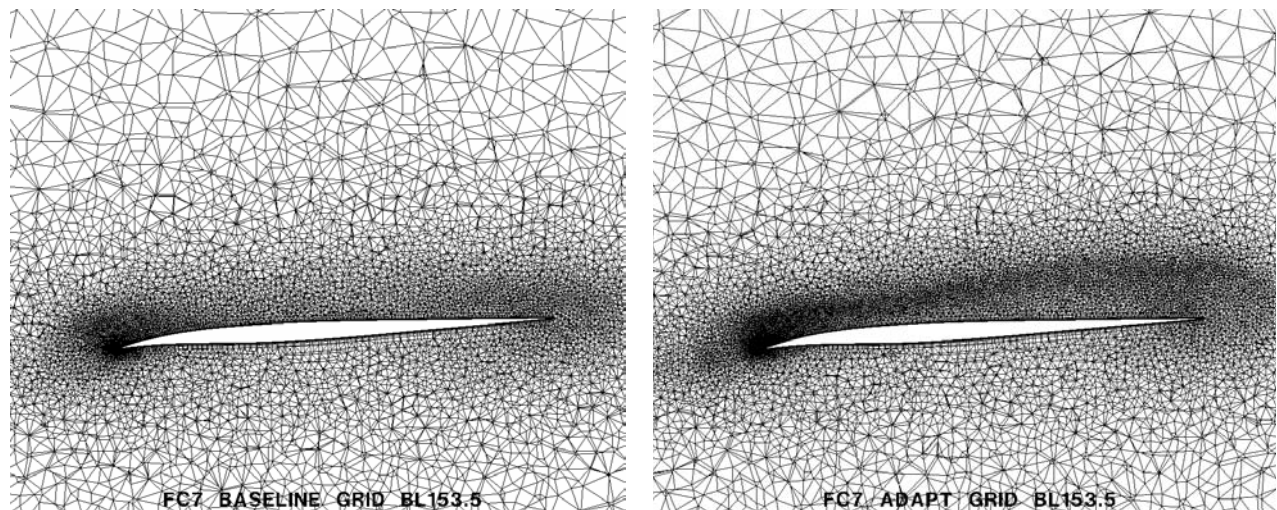
Figure 12-8: Cut Through Boeing Baseline and FC7 Adapted Grids at BL 153.5 Inches.

A BCFD solution was generated on the adapted mesh at Flight Condition 7. Contours of the predicted surface pressure coefficient and normalized total pressure ratio at several fuselage station cuts are shown in Figure 12-9. The contours inboard of the wing fence are similar to the non-adapted results shown in Figure 12-6. The primary vortex suction peak is slightly better defined in the surface pressure contours for the adapted grid solution. Outboard of the wing fence, the primary vortex in the adapted grid solution turns downstream earlier than the results on the non-adapted grid. The interaction with the tip missile launcher is slightly less pronounced.
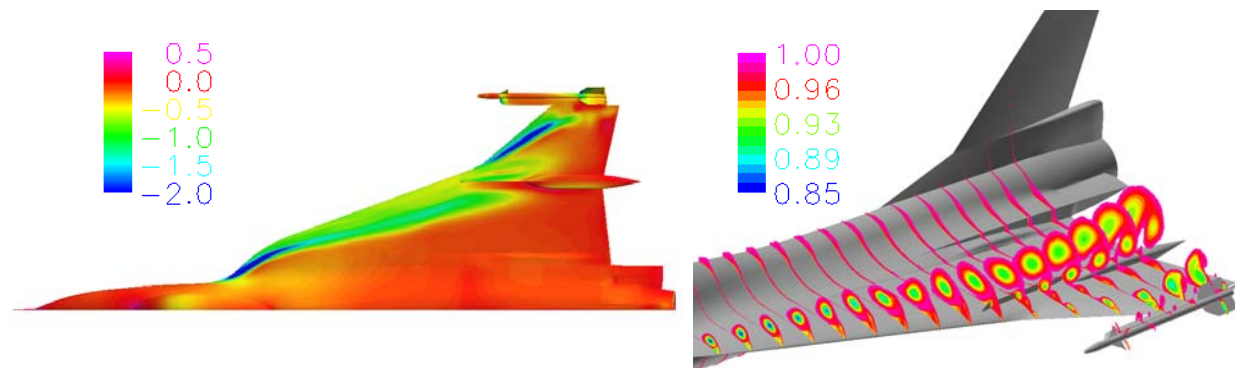
**Figure 12-9: Surface Pressure Coefficient and Total Pressure Ratio Contours on
Boeing Adapted Grid at Flight Condition 7 with the SA Turbulence Model.**

Surface pressure results on the Boeing adapted mesh are indicated by a dashed red line in Figure 12-3. Adaptation of the off body mesh near the vortex core resulted in a small but noticeable improvement in the surface pressure predictions at the inboard wing BL stations of 55 through 95. The primary change is a slight increase in the suction peak. The reduced interaction with the tip missile launcher changes the surface pressure at BL station 184.5 from the baseline grid, but the impact of the outboard vortex with the tip missile launcher still results in a pressure peak that is not evident in the test data. At this flight condition, the vortex remains relatively close to the surface for much of the track over the wing. The mesh resolution in this area is dominated by the surface mesh size thereby reducing the impact of the volume mesh adaptation. One lesson

learned from this study is that effective adaptation of the mesh for vortical flow computations, particularly when the vortices remain close to the surface, requires adaptation of the surface mesh in addition to the volume mesh.

Boundary layer velocity profiles predicted on the adapted mesh are represented by the dashed red line in Figure 12-4. The profiles from the adapted and non-adapted grid solutions are very similar with a slight improvement in the adapted mesh profiles at Rakes 4 and 7. Only the tetrahedral elements of the Boeing mesh were affected by the adaptation and the prismatic elements across the boundary layer are unchanged between the adapted and baseline meshes. The differences in the velocity profiles are therefore a result of the minor changes in the pressure distribution outside of the boundary layer at the four rake locations.

Turbulence plays an important role in the dissipation and entrainment of vortical flows. It is not surprising therefore that the choice of turbulence model can have a big impact on the quality of the CFD results. The BCFD solutions on the AVT common, Boeing baseline, and Boeing adapted grids were computed using the Spalart-Allmaras (SA) turbulence model. Previous computations have shown that the SA model over predicts the production of turbulence in the off body vortex core. A modification that reduces the turbulence production based on the local rotation of the flow helps to minimize this affect [12-9]. The rotational correction has also been shown to under predict the production of turbulence in the secondary vortex and was therefore not used in the BCFD computations.

To assess the impact of the choice of turbulence model, a BCFD solution was computed on the Boeing adapted mesh using the Menter SST two-equation turbulence model [12-10]. This model utilizes a combination of the k-ω formulation in the boundary layer and a k-ε formulation outside the wall bounded regions. The SST model has been shown to accurately predict off body flow-field features. Contours of the surface pressure coefficient and total pressure ratio at fuselage station cuts from the SST computation are shown in Figure 12-10. Compared to the SA turbulence model results on the same mesh, the strength of the vortex core is reduced with the SST turbulence model. This is evident from the reduction in the total pressure loss in the vortex core. BL station cuts of the surface pressure for the SST computations are indicated by blue dashed lines in Figure 12-3. Consistent with the reduced vortex strength indicated by the total pressure cuts, the surface pressure results show a reduced suction peak along the vortex core. This reduction in the vortex core strength with the SST model indicates an increase in dissipation of the vortex relative to the SA results. These results are contrary to what was anticipated and they are inconsistent with comparisons of these two models on other configurations using structured grids. As a result of this study, the implementation of the SST model on unstructured grids is being investigated.
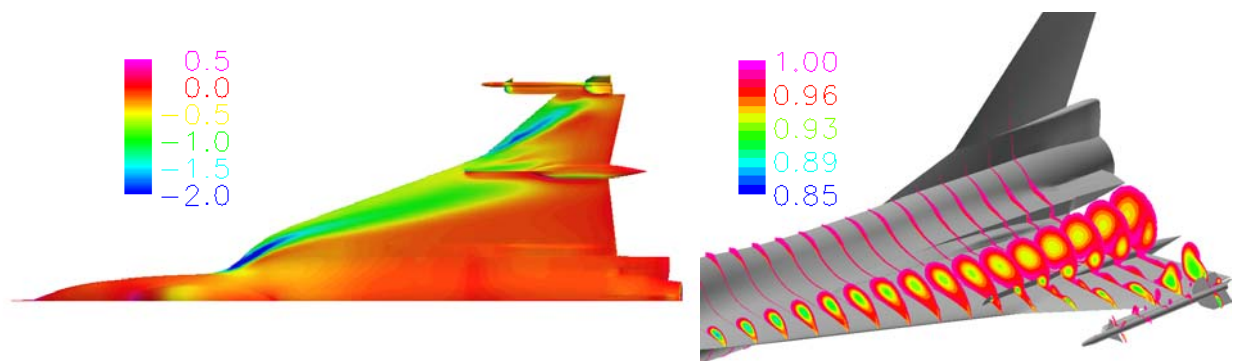
**Figure 12-10: Surface Pressure Coefficient and Total Pressure Ratio Contours
on Boeing Adapted Grid at Flight Condition 7 with SST Turbulence Model.**

Predicted velocity profiles from the SST results are shown by dashed blue lines in Figure 12-4. The profiles are similar to the SA results with the SST solution indicating a slight increase in the velocity gradient at the wall. Based on these results, the SA turbulence model provides better results for vortex dominated flows.

The sequence of BCFD solutions performed at Flight Condition 7 was repeated at Flight Condition 25. This consisted of solutions on the baseline Boeing mesh, an adapted Boeing mesh, and solutions with SA and SST turbulence models. The conditions at FC25, Mach 0.242, 19.84 degrees angle of attack and a Reynolds number of 32.22 million, are extremely challenging for CFD analysis. At this flight condition, the vortices are much stronger and the physical flow field is characterized by a larger degree of unsteadiness. Application of a steady state Reynolds Averaged Navier-Stokes (RANS) solution at these conditions may not be satisfactory. To measure the impact of time accuracy, an unsteady computation was also performed at this flight condition.

The computed surface pressure is compared with test results at several BL cuts in Figure 12-11. Predicted surface pressure and fuselage station cuts of the total pressure ratio are shown in Figure 12-15. The general trends observed at FC 7 are seen again at this flight condition. Overall, the CFD results agree well with the test data. There are details of the flow field, particularly near the vortices, were the CFD and test results differ. The predicted strength of the primary vortex compares favourably with the test results at most of the BL stations. However, the predicted suction peak is broader than the test data indicate. The steady-state CFD results show a very weak indication of a secondary vortex while the suction peak from the secondary vortex is very pronounced in the test data. These features are particularly noticeable just inboard of the fence at BL stations 80 and 95. Unlike the FC7 results, the SA and SST turbulence models provide very similar solutions at this flight condition. While the SA results in general are slightly closer to the test data, the spread between the two turbulence models is less pronounced than it was at FC7. This may be an indication that the vortex formation and tracking at high angle of attack is less influenced by turbulence effects and more dominated by convection. Because the SST results were comparable to the SA model, the solution on the adapted mesh was computed using the SST turbulence model. There is almost no difference between the adapted and non-adapted mesh solutions. As with the lack of turbulence model sensitivity, this may be an indication that the large strong vortices are primarily dominated by convection and that numerical dissipation plays a secondary role in the vortex prediction.
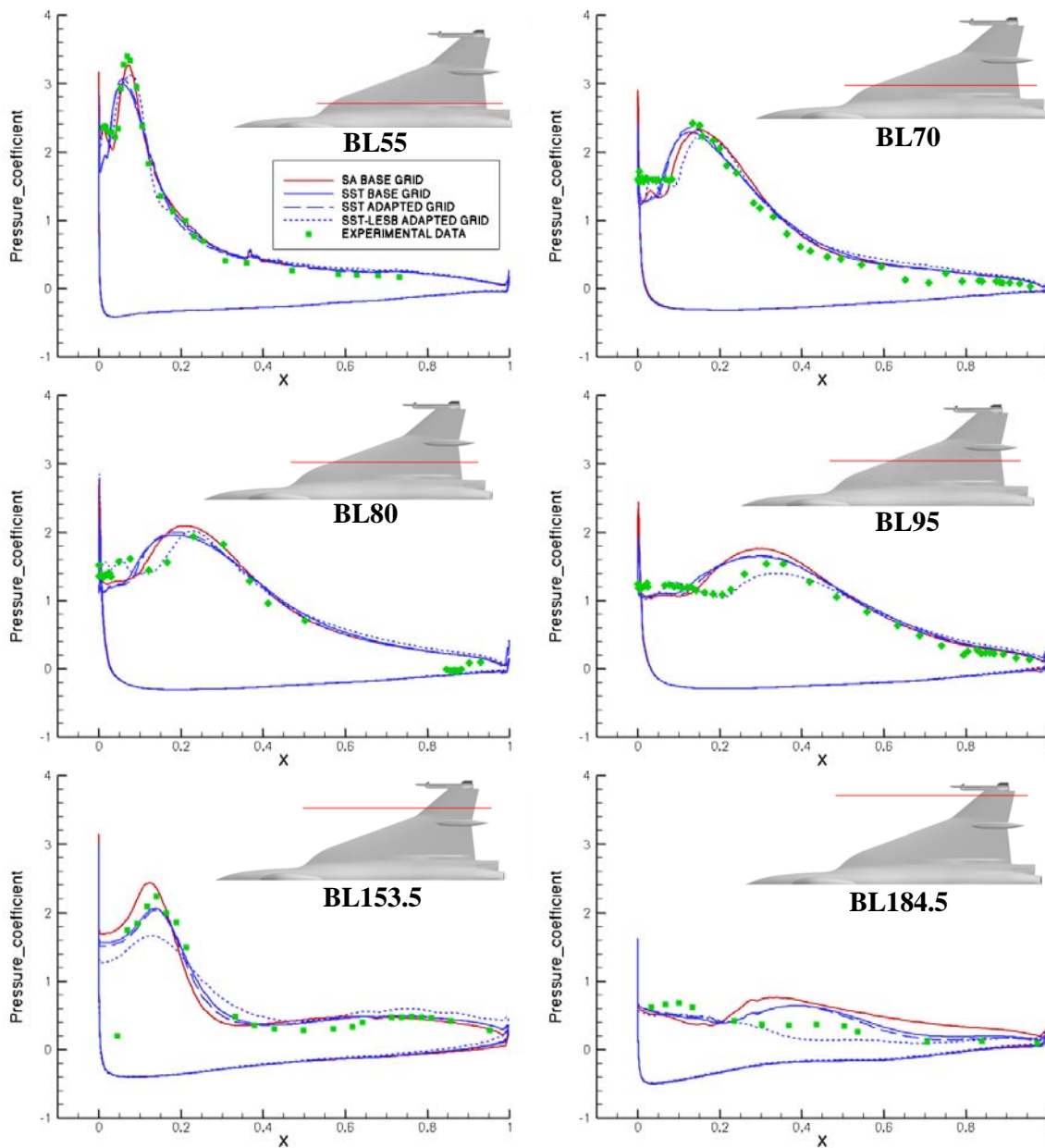
Figure 12-11: Comparison of Computed Surface Pressure Coefficient
for Several Butt-Line Cuts at Flight Condition 25.
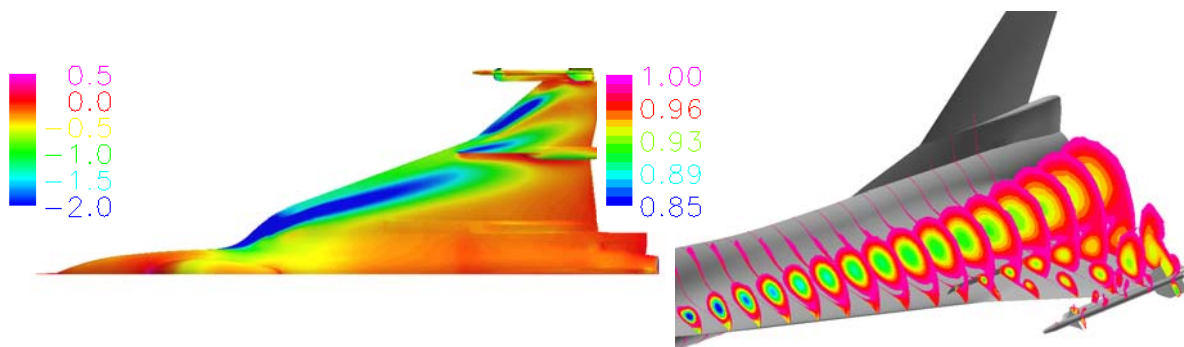
Figure 12-12: Surface Pressure Coefficient and Total Pressure Ratio Contours on Boeing Baseline Grid at Flight Condition 25 with the SA Turbulence Model.
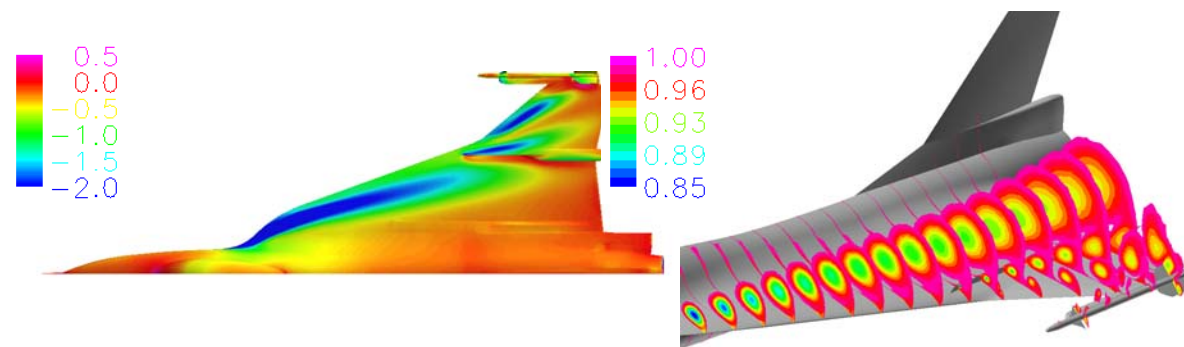
Figure 12-13: Surface Pressure Coefficient and Total Pressure Ratio Contours on Boeing Baseline Grid at Flight Condition 25 with the SST Turbulence Model.
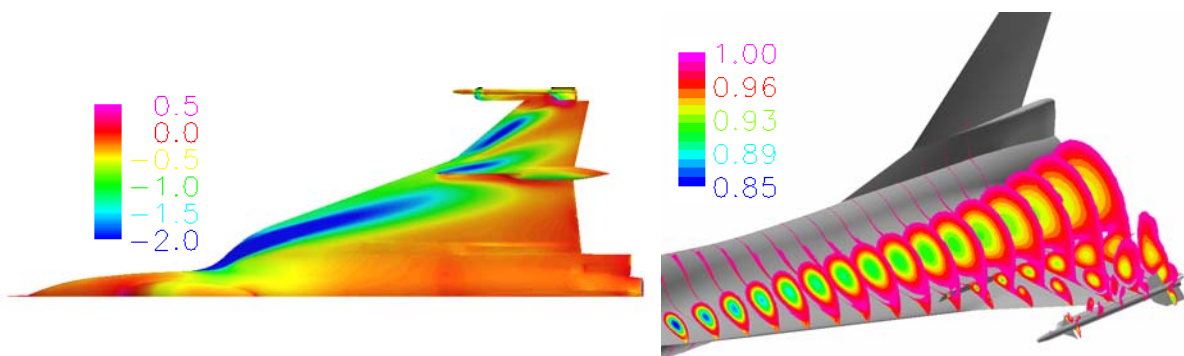
Figure 12-14: Surface Pressure Coefficient and Total Pressure Ratio Contours on Boeing Adapted Grid at Flight Condition 25 with the SST Turbulence Model.
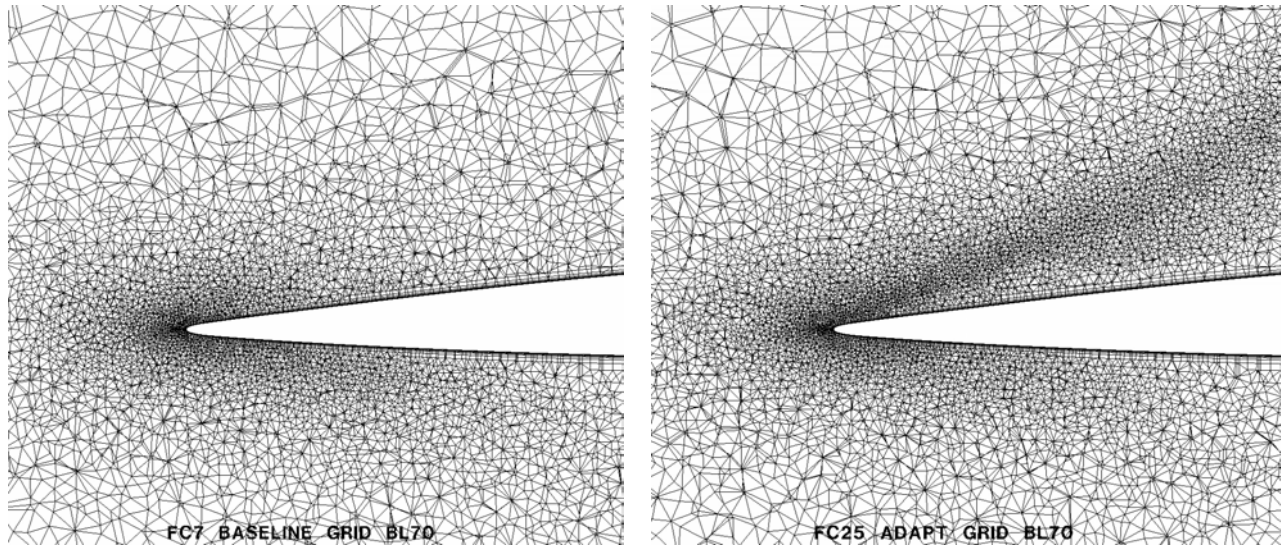
Figure 12-15: Cut Through Boeing Baseline and FC25 Adapted Grids at BL 70 Inches.
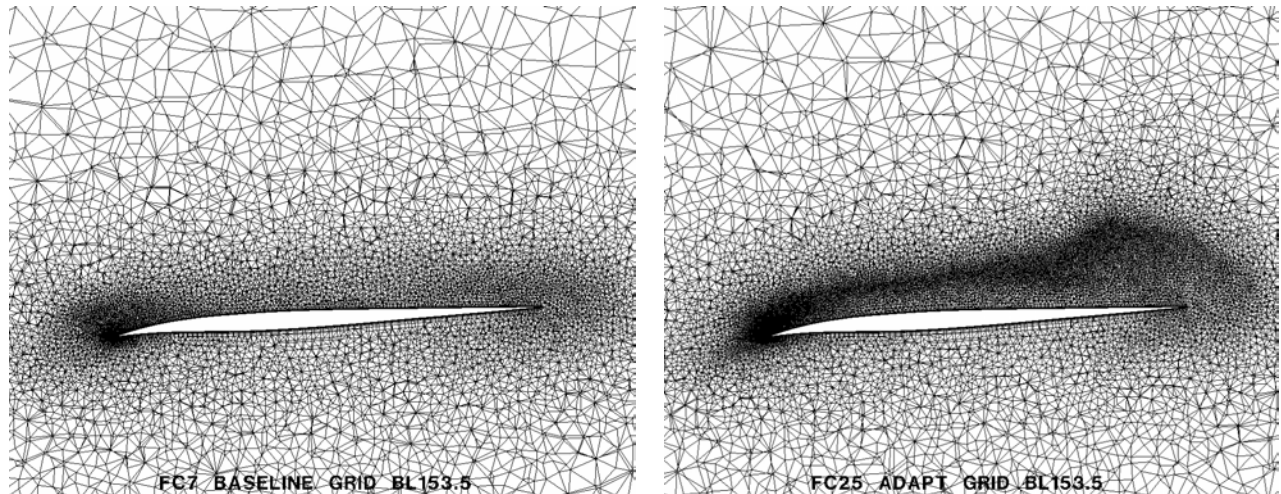
Figure 12-16: Cut Through Boeing Baseline and FC25 Adapted Grids at BL 153.5 Inches.

An assessment of the impact of time accurate computation was made by computing an unsteady BCFD computation using the hybrid SST/LESb turbulence model. The SST/LESb model was developed for unsteady massively separated flows [12-11]. The idea for the balanced Large Eddy Simulation (LESb) stems from the Detached Eddy Simulation of Spalart [12-12]. The distinction between various RANS turbulence models, and LES models, comes in the definition of the turbulent viscosity (μ_t). For RANS models the turbulent viscosity is related to a turbulent length scale and the turbulent kinetic energy per unit mass (k): $\mu_t = \bar{\rho} C_\mu l_\varepsilon \sqrt{k}$.

The key to the LESb model is a re-formulation of the turbulent viscosity based on the kinetic energy of the unresolved scales (k). $\mu_t = \bar{\rho} C_\mu C_B \Delta \sqrt{k}$.

Where C_μ is added for consistency with the two equation formulation and the coefficient C_B is added to allow refinement of the model.

LES formulations generally rest on a smooth transition between the modelled to unresolved scales of turbulence. Such a transition implies an isotropic resolution of the smallest resolved scales. This resolution requirement is generally the limiting factor of the scales and accuracy of the cases modelled and of the complexity of the flows that can be affordably computed. The LESb model will try to remove this restriction by allowing stretched grids to model high mean shear where the grid resolution required to capture the shear stress is greater than that required to capture the unsteadiness of interest. Of course, the stretched grids will not be able to resolve isotropic turbulence at these scales, so the model will rely on proven two-equation turbulence models as our best attempt to model the turbulence on this scale.

The two equation RANS models use k to represent all of the unsteady fluctuations, while the LES models use k to represent only the spatial average of the fluctuations within a filter width. For the balanced LES model (LESb), we define a new length scale l_B: $l_B = \min(l_\varepsilon, C_B \Delta)$ and the LESb model represents the turbulent viscosity as: $\mu_t = \overline{\rho} C_\mu l_B \sqrt{k}$.

For unresolved length scales ($\Delta \gg l_\varepsilon$) the model reverts to the standard two equation model. However, for resolved length scales ($\Delta \ll l_\varepsilon$) the model reverts to the LES model, and as the resolved length scale goes to zero (full resolution of all pertinent scales) the model approaches a Direct Numerical Simulation (DNS) of turbulence. To define Δ consistently with resolving the small eddies, for isotropic grids, we could easily set $\Delta = (Volume)^{1/3} = (1/J)^{1/3}$, where J is the Jacobian of the grid transformation. For stretched grids, we assume that the smallest resolved eddies should be roughly isotropic and so must be resolved in all three coordinate directions, and in time. Thus we set: $\Delta = \max(dx, dy, dz, u * dt, \sqrt{k} * dt)$.

The limiting length scales based on time step represent the scales based on convection velocity and SGS turbulence respectively. These scales are included to ensure that there is sufficient time resolution to resolve the captured physical phenomena. That is, if the time steps are too large, the unsteady phenomena cannot be resolved, and the RANS model should be used.

The BCFD unsteady solution was run with a Newton time stepping algorithm at a time step of 0.0005 seconds. The steady state RANS solution was used at the initial state and a total of 10,000 time steps were computed in the unsteady result. The solution over the last 2000 time steps was averaged for comparison with test data. The time average surface pressure is represented by the blue dotted line in Figure 12-11. Contours of surface pressure and total pressure ratio from the time averaged solution are shown in Figure 12-17. The total pressure loss in the vortex core is more pronounced and persists further down stream than for the RANS results. Also noticeable in the surface pressure and total pressure contours is the presence of a secondary vortex. The vortices on the outboard wing panel are reduced in strength from the steady state results. The comparison of the surface pressure with test data in Figure 12-11 is improved, particularly near the secondary vortex at BL stations 55 through 95. The location of the suction peak associated with the primary vortex core at these BL stations is also shifted aft and matches the test data better than for the steady state results.
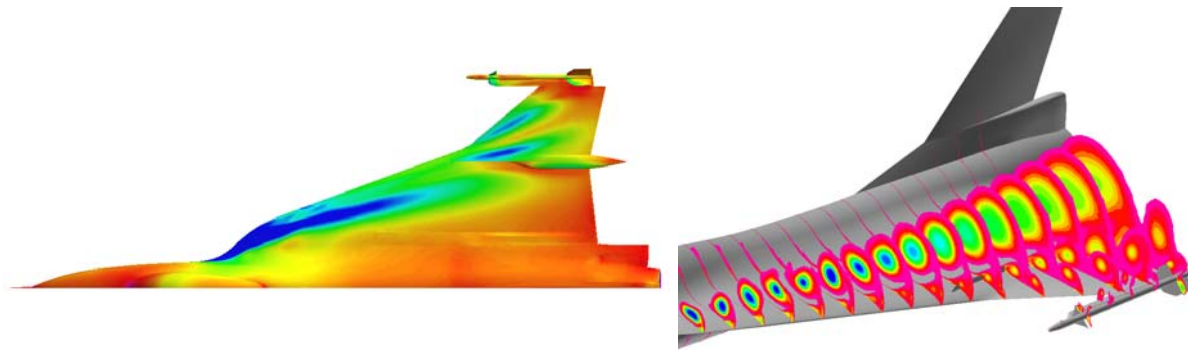
**Figure 12-17: Time Average Surface Pressure Coefficient and Total Pressure Ratio Contours
on Boeing Adapted Grid at Flight Condition 25 with the LESB Turbulence Model.**

12.5   SUMMARY AND CONCLUSIONS

BCFD computations were performed on the F-16 XL configuration at high angles of attack. Results were compared with surface pressure and boundary layer measurements taken in flight. Several studies were performed to assess the impact of grid resolution, turbulence model and time accuracy on the CFD results.

Given the complex nature of the flow field, the BCFD predictions match the test data very well. The BCFD computations accurately predict the formation and propagation of three primary vortices along the locations given by the test data. The resolution of the surface mesh around the leading edge and along the vortex core was found to be an important factor in the accurate prediction of the suction peak. Grid adaptation improved the prediction of vortex strength. The close proximity of the vortices to the surface reduced the effectiveness of the volume only adaptation procedure used in this study. Effective adaptation to wing vortices requires adaptation of the surface mesh in addition to the volume mesh. Of the two turbulence models used in this study, the Spalart-Allmaras turbulence model provided better results for a steady-state RANS solution. The steady-state RANS solutions tended to under predict the strength of the secondary vortex. Accuracy of the computations was improved by modelling the flow with and unsteady computation and a LESb turbulence model. Unsteady simulations using the SST-LESb turbulence model provided the best accuracy across all of the computed flight conditions.

12.6   REFERENCES

[12-1]   Del Frate, J.H., Fisher, D.F. and Zuniga, F.A.: *In-Flight Flow Visualization with Pressure Measurements at Low Speeds on the NASA F-18 High Alpha Research Vehicle*, NASA TM-101726, October 1990.

[12-2]   Meyn, L.A., Lanser, W.R. and James, K.D.: *Full-Scale High Angle-of-Attack Test of an F/A-18*, AIAA 92-2676.

[12-3]   Lamar, J.E., Obara, C.J., Fisher, B.D. and Fisher, D.F.: *Flight, Wind-Tunnel, and Computational Fluid Dynamics Comparison for Cranked Arrow Win (F-16XL-1) at Subsonic and Transonic Speeds*, NASA/TP-2001-210629, February 2001.

[12-4]   Lamar, J.E. and Obara, C.J.: *Review of Cranked-Arrow Wing Aerodynamics Project: Its International Aeronautical Community Role*, AIAA-2007-487, January 2007.

[12-5] Rizzi, A., Badcock, K.J., Jirásek, A. and Boelens, O.J.: *What was Learned from Numerical Simulations of F-16XL (CAWAPI) at Flight Conditions*, AIAA-2007-683, January 2007.

[12-6] Marcum, D.L.: *Advancing-Front/Local-Reconnection (AFLR) Unstructured Grid Generation*, Computational Fluid Dynamics Review, World Scientific – Singapore, 1998, p. 140.

[12-7] Mani, M., Cary, A. and Ramakrishnan, S.V.: *A Structured and Hybrid Unstructured Grid Euler and Navier-Stokes Solver for General Geometry*, AIAA-2004-524, January 2007.

[12-8] Boelens, O.J., Görtz, S., Morton, S. and Fritz, W.: *Description of the F16-XL Geometry and Computational Grids Used in CAWAPI*, AIAA-2007-488, January 2007.

[12-9] Spalart, P.R. and Shur, M.L.: *On the Sensitization of Turbulence Models to Rotation and Curvature*, Aerospace Science and Technology, No. 5, 1997, pp. 297-302.

[12-10] Menter, F.R.: *Improved Two-Equation K-ω Turbulence Models for Aerodynamic Flows*, NASA TM 103975, October 1992.

[12-11] Bush, R.H. and Mani, M.: *A Two-Equation Large Eddy Stress Model for High Sub-Grid Shear*, AIAA-2001-2561.

[12-12] Spalart, P.R., Jou, W.H., Strelets, M. and Allmaras, S.R.: *Comments on the Feasibility of LES for Wings, and on a Hybrid RANS/LES Approach*, 1st AFOSR Int. Conf. on DNS/LES, August 4-8, 1997, Ruston, LA.

Chapter 13 – NUMERICAL SOLUTIONS FOR THE CAWAPI CONFIGURATION ON UNSTRUCTURED GRIDS AT LOCKHEED MARTIN, UNITED STATES

by

M. Bruce Davis, Christopher L. Reed and Patrick J. Yagle

13.1 SUMMARY

As part of the Cranked Wing Aerodynamics Project International (CAWAPI), computational fluid dynamics (CFD) simulations were performed on the F-16XL geometry at high-lift and transonic flight conditions. This was part of a larger effort by several institutions and companies to try to characterize the relevant flow physics and to compare the results to flight test data. The work summarized in this report used the Lockheed Martin Aeronautics Company proprietary CFD flow solver Falcon v4, which is a general purpose Navier-Stokes flow solver which uses hybrid unstructured computational meshes. The computational mesh used in these studies consisted of prismatic and hexahedral cells near the solid surfaces, tetrahedral cells in the far field, and pyramidal cells transitioning between hexahedral and tetrahedral cells. This mesh was obtained from the UT SimCenter and was generated using Gridgen for the inviscid mesh and proprietary software to generate the viscous prismatic layers. The results on a set of test cases selected by the CAWAPI task group shows good agreement with the flight test data and consistency with the other computational results for the high-lift cases, with the exception of the leading edge suction peak. The key flow features of these types of configurations, including the primary vortex originating on the inboard leading edge of the wings, the secondary vortex on the aft portion of the wing next to the primary vortex, and the vortices shed from the wingtip missile fins are all adequately resolved. The transonic flight test case, which has caused some difficulty because of the nonlinear nature of the flow physics, did not match flight test data as well. The reason for the discrepancies are unknown at the present time, but the consistency of these discrepancies across a range of different flow solvers and grids suggests that there is a difference between the configuration and flow conditions in the test and those simulated in the CFD. A brief description of the simulations performed is presented below, a description of the Falcon v4 CFD solver is presented, and a summary of the results is presented and explained.

13.2 INTRODUCTION

The Cranked Arrow Wing Aerodynamics Project International (CAWAPI) was a combined flight test, wind tunnel test, and computational program which used the F-16XL aircraft to characterize and document the flow physics on the wing upper surface for aircraft configurations representative of the F-16XL, with emphasis on high-lift and transonic flight conditions [13-1],[13-2]. The CAWAPI program was also to provide a test data suite which could be used to compare and improve computational fluid dynamics (CFD) simulations for these configurations. The CFD solutions could also be used as an additional source of flow data to augment the flight and wind tunnel data.

The F-16XL was designed jointly by General Dynamics Corporation-Fort Worth (now Lockheed Martin Aeronautics Company (LM Aero)) and NASA Langley Research Center, and built by General Dynamics. The aircraft is based on the F-16 with the fuselage lengthened and a cranked-arrow wing replacing the existing wing. The wing has a leading edge sweep of 70 degrees inboard and 50 degrees outboard of the crank, and is

blended to the fuselage with an S-curve. Air dams are installed at the centerline of the actuator pod just inboard of the crank. The flight test configuration of the F-16XL is shown in Figure 13-1.

Figure 13-1: Flight Test Configuration of the F-16XL.

A variety of flight test data was taken, including surface static pressures, boundary layer rake pressures, hot-film, and surface visualization including tufts, oil, and liquid-crystals. The data most relevant to the present work is the surface pressure data collected by both flush ports and belts at certain Butt Line (BL) and Fuselage Station (FS) lines. CFD data are compared to the flight test data mainly by comparing pressures at these BL and FS cuts.

The computational effort for this particular program has focused on a set of seven flight configurations. A complete description of the flight conditions with relevant engine parameters is given in [13-2]. A summary of these conditions is shown in Table 13-1. There are five conditions with no appreciable sideslip, and two cases which include significant sideslip. All of the flight test cases are at low speed (Mach number less than .5) and high angle of attack (greater than ten degrees), with the exception of the single transonic case (M = 0.97), for which the angle of attack is 4.37 degrees. The flow Reynolds number based on the mean aerodynamic chord varies from 32 million to 89 million for the transonic case. Due to the time limitation, LM Aero concentrated on three different flight conditions, all of which are at zero nominal sideslip. The solutions are all run with a half-symmetry model. The flight conditions simulated at LM Aero (shown in red in Table 13-1) are FC7, FC19, and FC70. FC7 and FC19 are high-lift cases and FC70 is a transonic case.

Table 13-1: The CAWAPI Program Examined Seven Different Flight Conditions

Flight Condition	Actual Mach	Actual α	Actual β	Actual Re
FC7	0.304	11.89	-0.133	44.4×10^6
FC19	0.360	11.85	0.612	46.8×10^6
FC46	0.527	10.4	0.684	46.9×10^6
FC70	0.97	4.37	0.310	88.77×10^6
FC25	0.242	19.84	0.725	32.22×10^6
FC50	0.434	13.56	5.31	39.41×10^6
FC51	0.441	12.89	-4.58	38.95×10^6

LM Aero has developed and maintains a proprietary CFD solver called Falcon, and the latest version (v4) has added unstructured grid capability. Supported cell types include hexahedral, tetrahedral, pyramid, and prismatic cells. Falcon is a general purpose flow solver, having been used for external aerodynamics, nozzle and duct flows, low speed aircraft environment flows, and transonic and supersonic flows.

LM Aero, which designed and built the F-16XL, contributed the original computational geometry for the program. The company then contributed to the program in an observation and consultation capacity only, providing such data as engine parameters and flap settings. As a separate effort, LM Aero conducted a grid challenge in which several different grid vendors were asked to generate and submit a computational mesh for the F-16XL geometry appropriate for a simulation at one of the high-lift flight conditions. The submitted grids were evaluated by the LM Aero staff and an attempt was made to run the simulation on different CFD solvers used at LM Aero, including Falcon v4. Late in the CAWAPI effort, the CAWAPI suite was selected as a validation case for Falcon v4, which was nearing production release at the time. The results submitted here are the direct outgrowth of that validation effort.

13.3 FALCON V4

Falcon is a finite-volume computational fluid dynamics (CFD) system that has been developed and maintained by the Lockheed Martin Aeronautics (LM Aero) Aerodynamics and CFD Branch. Development of the code was initiated in the late 1980's and starting in the early 1990's the code became and continues to be routinely used on a number of aircraft programs and development projects at LM Aero, as well as several other Lockheed Martin Corporation, partner and government sites. In 2002 an effort was initiated to rewrite the code in a more modern form and allow multiple element types (hybrid grids). The desire was to expand the code's capability to use various grid types while retaining the accuracy and unique features of previous versions of Falcon. The rewrite also provided an opportunity to improve the code's user interface and maintainability. The improved code was designated version 4 (v4).

Falcon v4 is actually a system of codes that make use of a modular architecture that incorporates some object-oriented programming concepts. The software is designed to be modular to allow quick development of required aerodynamic analysis capabilities. Falcon v4 uses hybrid unstructured grids that may include a variety of cell (element) shapes. The majority of the code is written in a modern-style Fortran 90 that makes heavy use of

derived data types and modules. In order to implement this style, the code development process uses templates and code generated automatically by programs written in the Python programming language. This approach provides a much easier technology insertion capability, allows the solver to be used as an engine in other applications, and allows applications specific capabilities to be developed. All components of the Falcon v4 CFD system are compiled from the same source code to ensure consistency and to reduce maintenance requirements. Considerable effort has been taken in the design of the code to optimize it for efficient operation on commodity cache-based processors, while maintaining the ability to run efficiently on vector architectures as well.

The user interface to the Falcon v4 system has been greatly simplified from previous versions of Falcon. The interface starts with the Falcon v4 pre-processor which can be run in an interactive, interview-style mode or can be run in a batch mode. Queries and/or inputs to the system are intuitive and all inputs are stored for reuse and archival purposes. The Falcon v4 system also makes use of a unique perfect gas conditions calculator which assists in setting up consistent flow field conditions.

The governing equations in the Falcon v4 solver are the Reynolds averaged, compressible Navier-Stokes equations. A steady-state solution to the governing equations is obtained by using an implicit time marching scheme with upwind differenced fluxes for the inviscid terms and central differenced fluxes for the viscous terms. Inviscid fluxes are computed using Roe's approximate Riemann solver [13-3]. The primitive variables (ρ, u, v, w and T) are extrapolated to the face for higher order accuracy. Viscous fluxes are computed from gradient estimates at the cell faces. The face gradients are calculated as the distance weighted average of the gradients at the centroids of the two cells on either side of the face. The component normal to the interface is then replaced with the local information. The Falcon code includes the two-equation k-kl turbulence model by Smith [13-4] (with an algebraic stress model option) for accurate turbulence calculations. For unsteady calculations, an LES model can be used. A wall-layer model (or wall function) is generally used to reduce the number of points required for accurate boundary layer calculations.

A highly implicit numerical solver has been implemented using incomplete lower-upper (ILU) factorization. The implicit Jacobians are stored such that they do not need to be calculated at each time-step. This variable update of the Jacobians significantly reduces CPU time. All of the boundary conditions are applied/computed implicitly. The code also includes the capability to accurately solve very low speed and mixed speed flows using low speed preconditioning [13-5]. Currently, the code can be run with any of several different gas models. These include constant gamma, variable gamma as a function of temperature for air, variable gamma for a typical jet engine exhaust, or a four species flow model.

Although the code uses non-dimensional values internally, inputs to the code and outputs from the code can be in either English or SI units. The code can perform accurate unsteady (time-accurate) analyses using subiterations. Falcon v4 is set-up to efficiently perform on a parallel computer using the standard message passing interface (MPI), with domain decomposition produced by the METIS algorithm [13-6]. For restart files, grids and boundary condition specifications, the code uses an enhanced, self describing, platform independent file system to facilitate working on a heterogeneous computer network. A number of features of Falcon v4 have been developed/implemented to significantly reduce workload and provide a process that is completely consistent with LM Aero engineering processes and tools. Other code features include a variety of boundary condition types and a number of LM proprietary models that have been required for advanced development activities.

User oriented features include the capability to pick the flow output parameters from a menu of choices and then output that data to a file or files specified by the user. In this way an engineer can monitor the convergence of lift, drag, mass flow, thrust, pressure recovery, or any number of other integrated quantities.

13.4 F-16XL GEOMETRY AND COMPUTATIONAL GRID

The F-16XL was designed at LM Aero, and hence the geometry files were available in electronic format within the company. This geometry did require some preparation, however. All modifications to the geometry were made using Lockheed Martin's proprietary computer-aided design software. Existing gaps in the geometry were corrected to provide as water-tight a geometry definition as possible for CFD analysis. In order to simplify mesh generation, several aircraft features were simplified. The gap between the tip missile and the missile rail was filled. The gaps between the nozzle and the speed brakes on either side of the nozzle were filled. Lastly, the gap between the nozzle and the bottom of the vertical tail was filled. For all of the analyses, the aircraft control surfaces remain fixed and undeflected. All gaps related to the control surfaces are filled and were not modeled. All other aerodynamic features of the aircraft were modeled. The surface mesh on the top and bottom surfaces is shown in Figure 13-2. This shows the grid clustering near the leading edge, along the air dam and around the actuator pod, at the wing-fuselage junction, and a high grid density outboard of the crank and on the tip missile. Figure 13-3 shows the surface grid on the symmetry plane, with the obvious clustering near the aircraft surface transitioning to a much coarser mesh in the far field.
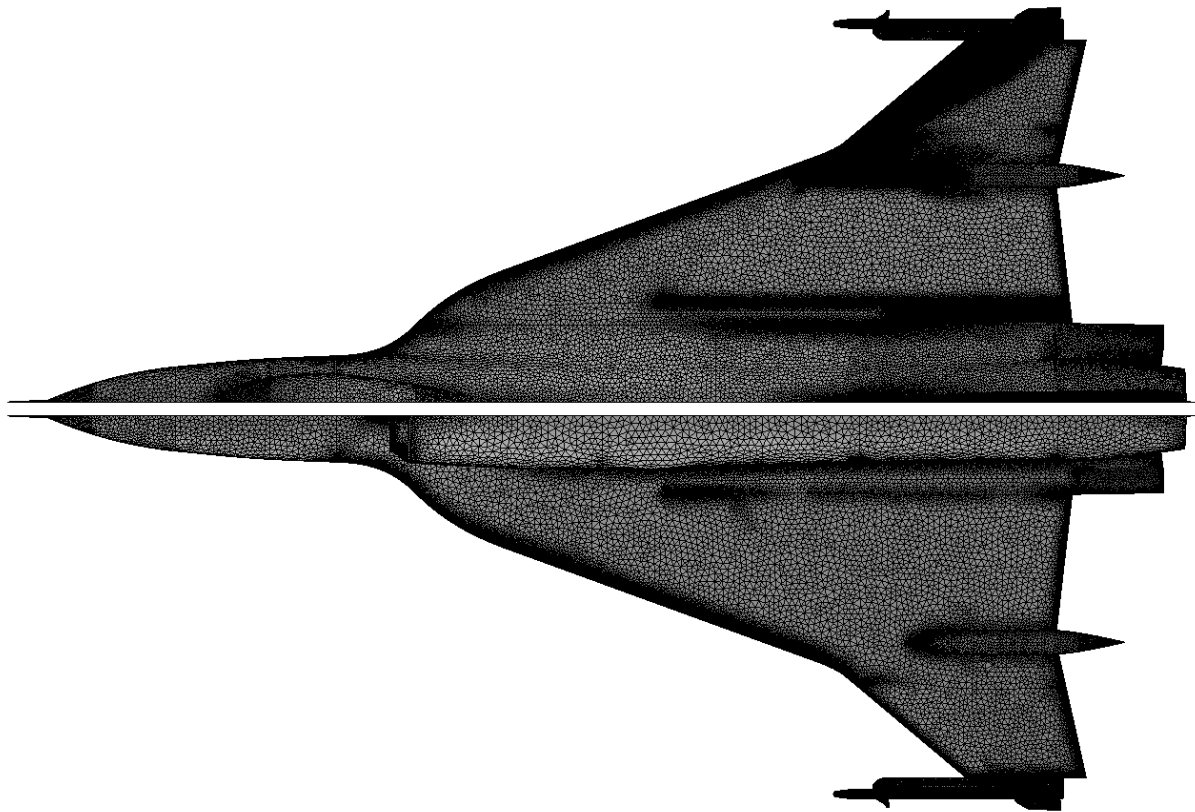
Figure 13-2: Top and Bottom Surface Grid of F-16XL Shows Clustering at Key Locations.
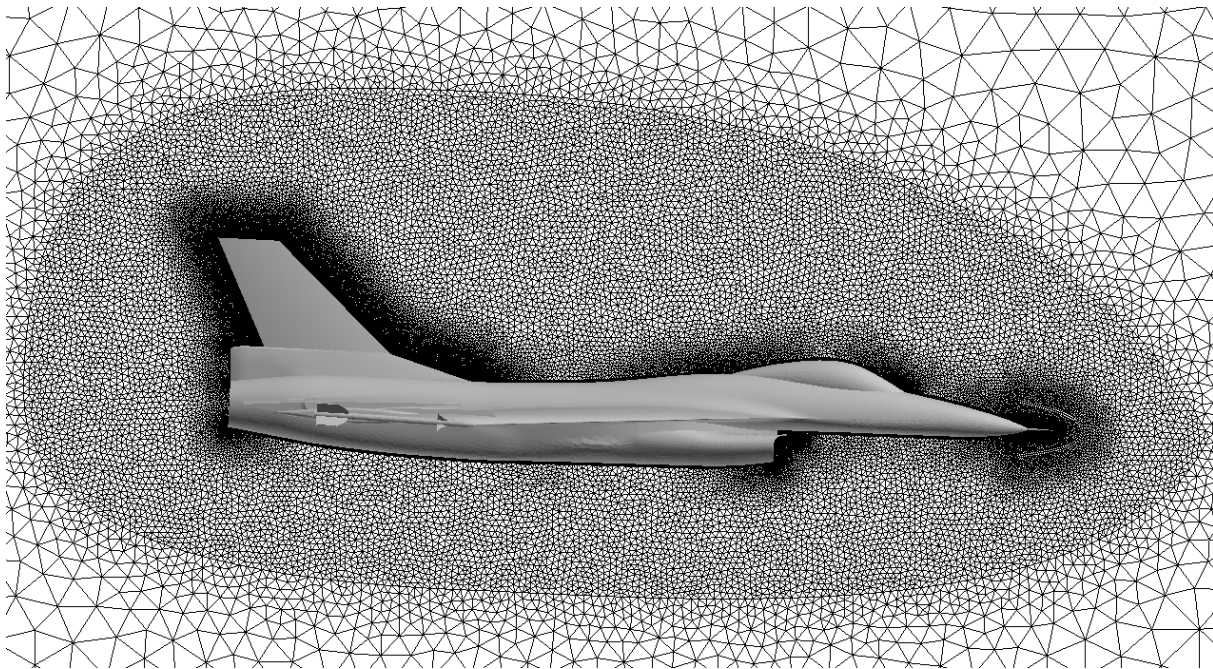
Figure 13-3: Surface Grid on the Symmetry Plane is Clustered Near the Aircraft.

The computational mesh for these analyses was provided to LM Aero by Dr. Steve Karman at the University of Tennessee SimCenter [13-7]. The grid was generated using two different mesh generation programs. The inviscid mesh was generated using the commercially available Gridgen software package. The surface mesh consists of triangular elements with proper resolution of the various features of the aircraft. Structured quadrilateral elements were used to mesh the leading and trailing edges of the wing. These quadrilaterals were then split into triangles in order to obtain anisotropic triangular mesh elements. Additionally, baffle surfaces were used to control mesh spacing in key areas of the inviscid volume mesh. A mesh generation program developed at the UT SimCenter was used to add viscous layers to the inviscid mesh already obtained [13-8]. The program adds viscous layers by pushing the existing mesh away from the aircraft surface, and then filling in with triangular prisms (see [13-8] for details of the algorithm). The number of prism layers varies locally based on the distance the inviscid mesh has been pushed away from the surface. A wall-normal spacing appropriate to the application of wall-function boundary conditions was chosen. The final mesh contains 32,415,471 tetrahedra, 9,612,208 triangular prisms, 212,408 hexahedra, and 188,175 pyramid mesh elements. A crinkle cut of the grid through the missile fins is shown in Figure 13-4. Note the thin prismatic cells near the surface transitioning to the tetrahedral further out. The large size of this problem necessitated simulation in a parallel environment. The final mesh was partitioned into 64 subdomains using the METIS partitioning software [13-6]. This decomposition is shown colored by process number in Figure 13-5. All results were generated on 64 processors.
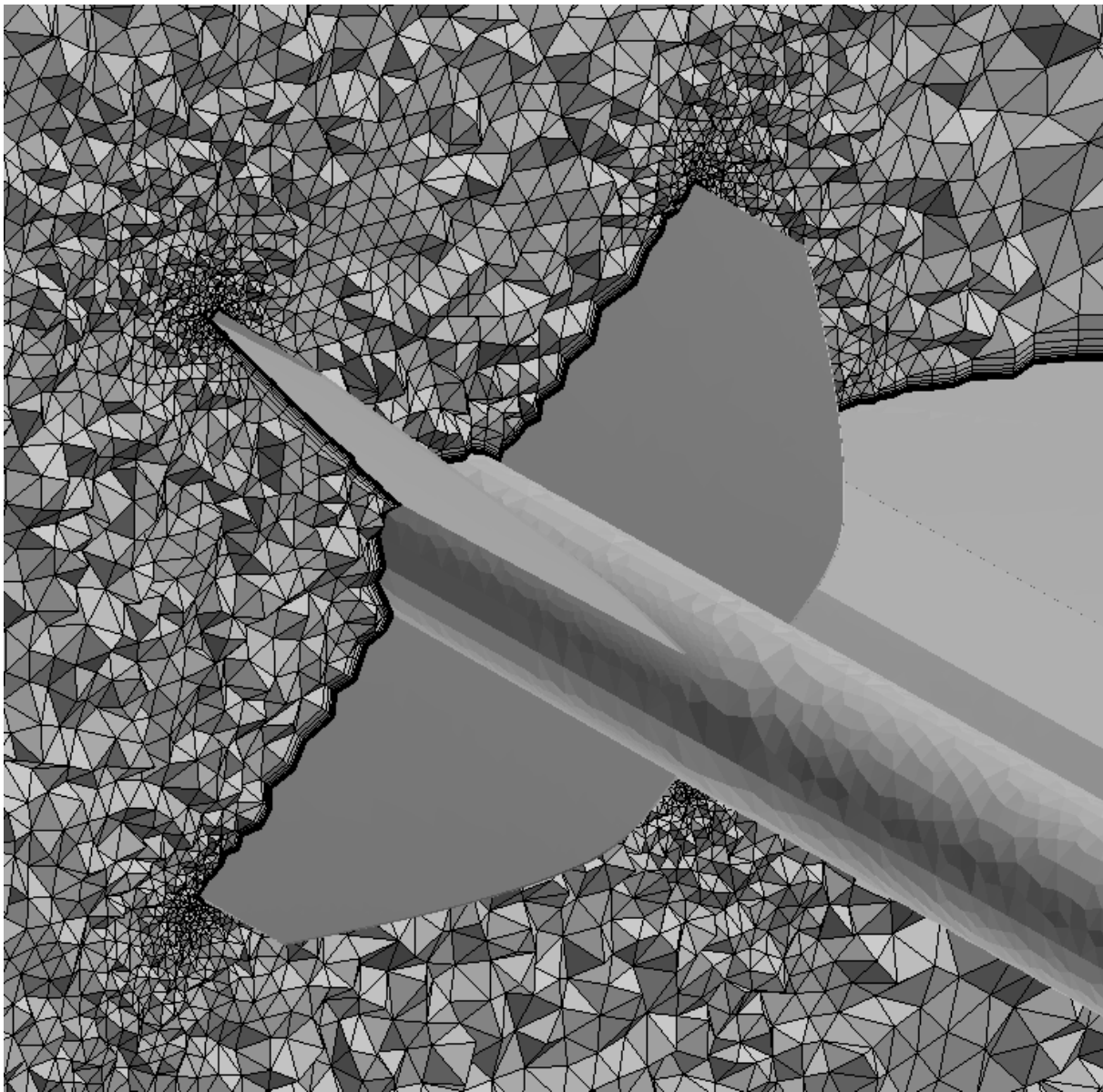
Figure 13-4: Crinkle Cut of Unstructured Mesh at Cut Through Tailfins of Wingtip Missile.
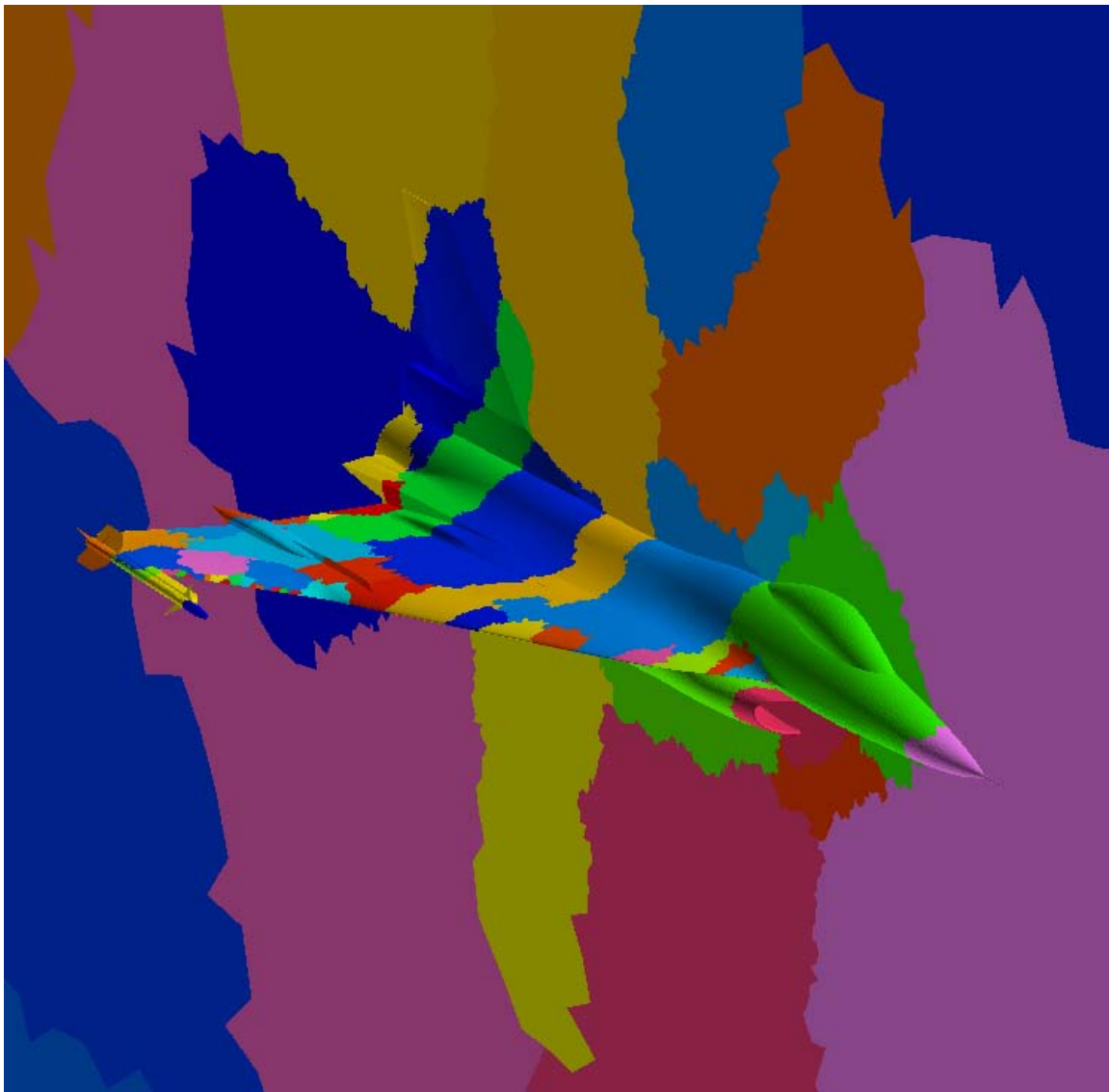
Figure 13-5: F-16XL Mesh was Partitioned to Run on 64 Processors.

13.5   RESULTS AND DISCUSSION

LM Aero produced CFD results for three of the seven cases shown in Table 13-1; FC7, FC19, and FC70. This gives two high-lift cases and one transonic case, yielding a representative cross-section of the relevant physics for this program. These cases are at zero nominal sideslip (although there is a small non-zero measured sideslip from the test), so all simulations are on half of the aircraft with symmetry conditions on the centerline plane. Although all of the sideslip angles are set to zero for symmetry, all other conditions are set to the exact value from the flight test.

13.5.1   Flight Condition 7

The first test case considered is FC7, which is one of the high-lift cases considered. The flight test data was taken at Mach number 0.304 at an altitude of 5000 feet, which gives a Reynolds number (based on mean aerodynamic chord) of 44.4 million. The angle of attack is 11.89 degrees. The pressure coefficient on the top surface of the wing is shown in Figure 13-6 for the full aircraft along with a detailed view of the outboard region of the wing. This clearly shows the strong suction peak on the leading edge near the wing root and outboard of the crank. The suction region follows the path of the vortices on the top surface and is evident on the inboard surface of the actuator pod. Figure 13-7 shows the path of the vortices using bounded cuts of total pressure. The primary vortex is clear, and the secondary vortex which forms next to the primary vortex is evident on close inspection. The vortex, which forms outboard of the crank, is also very clear. Also note the vortices being shed from the missile tailfins.
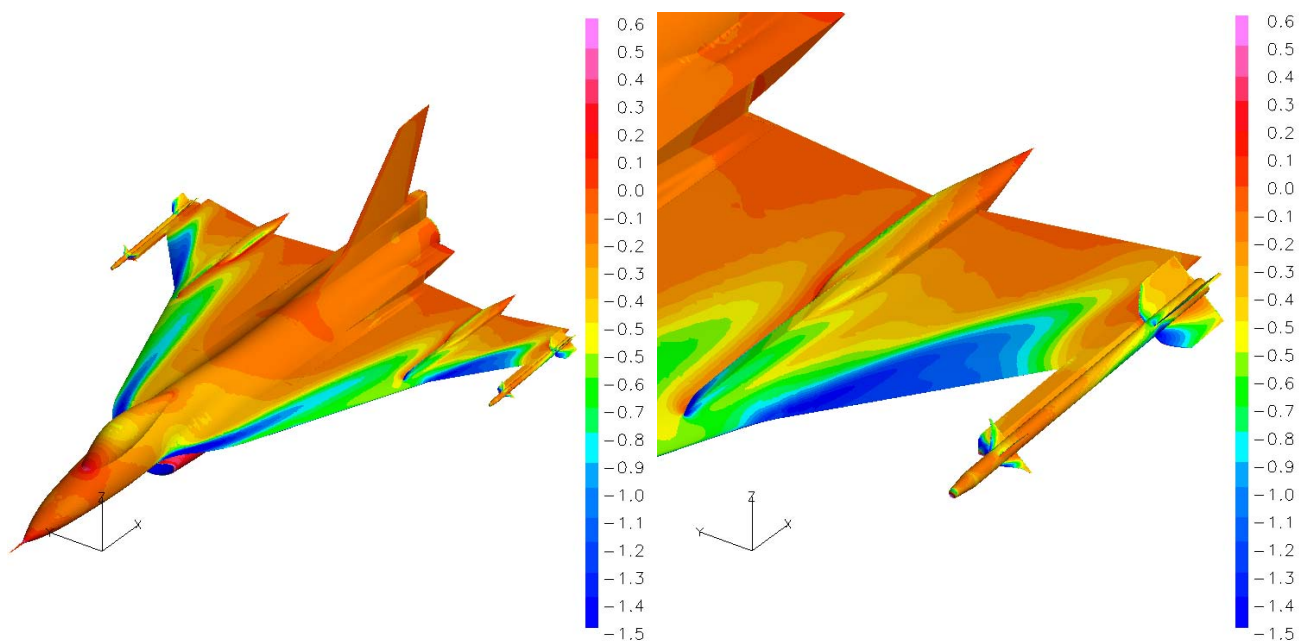
Figure 13-6: Surface C_p Distribution for FC7 on Upper Surface and Detail of Outboard Section of Wing.
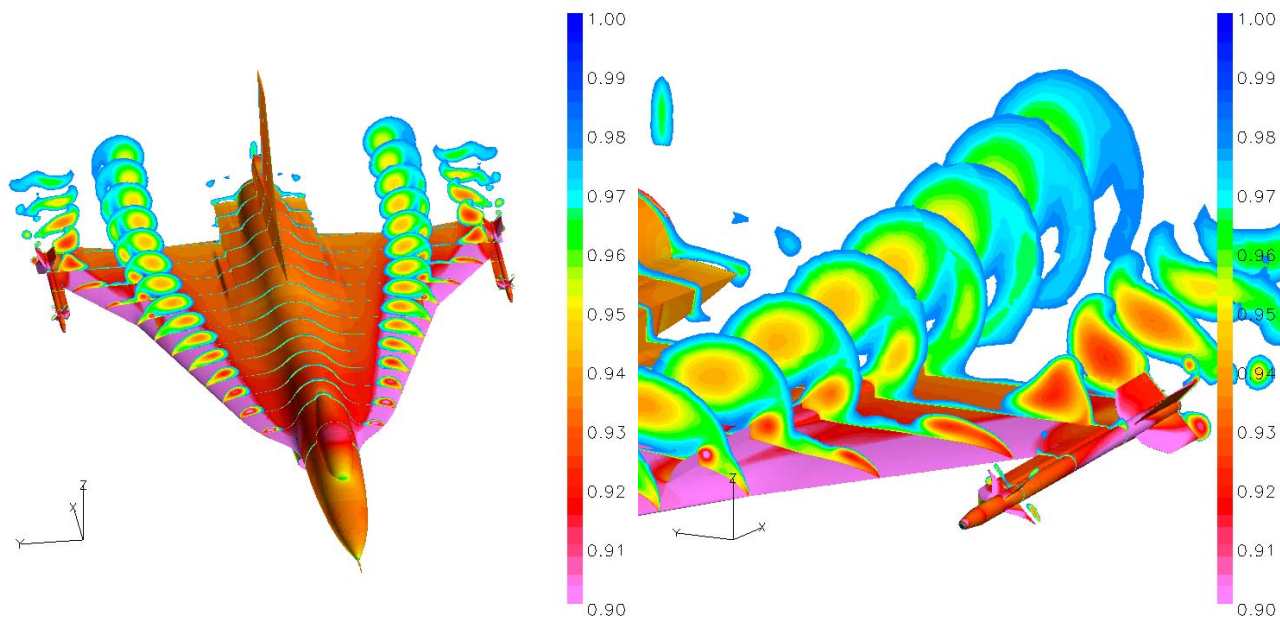
Figure 13-7: Bounded Total Pressure Cuts Colored by Total Pressure for FC7 Show Locations of Vortices.

The streamline pattern for this flow is shown with streamtubes colored by total pressure in Figure 13-8. The complexity of the flow pattern is evident from the streamlines. The primary vortex is plainly visible, as well as the secondary vortex, especially outboard of the air dam. The flow along the leading edge eventually wraps up into the third vortex outboard of the crank. Also evident is the total pressure loss in the center of the vortex cores.
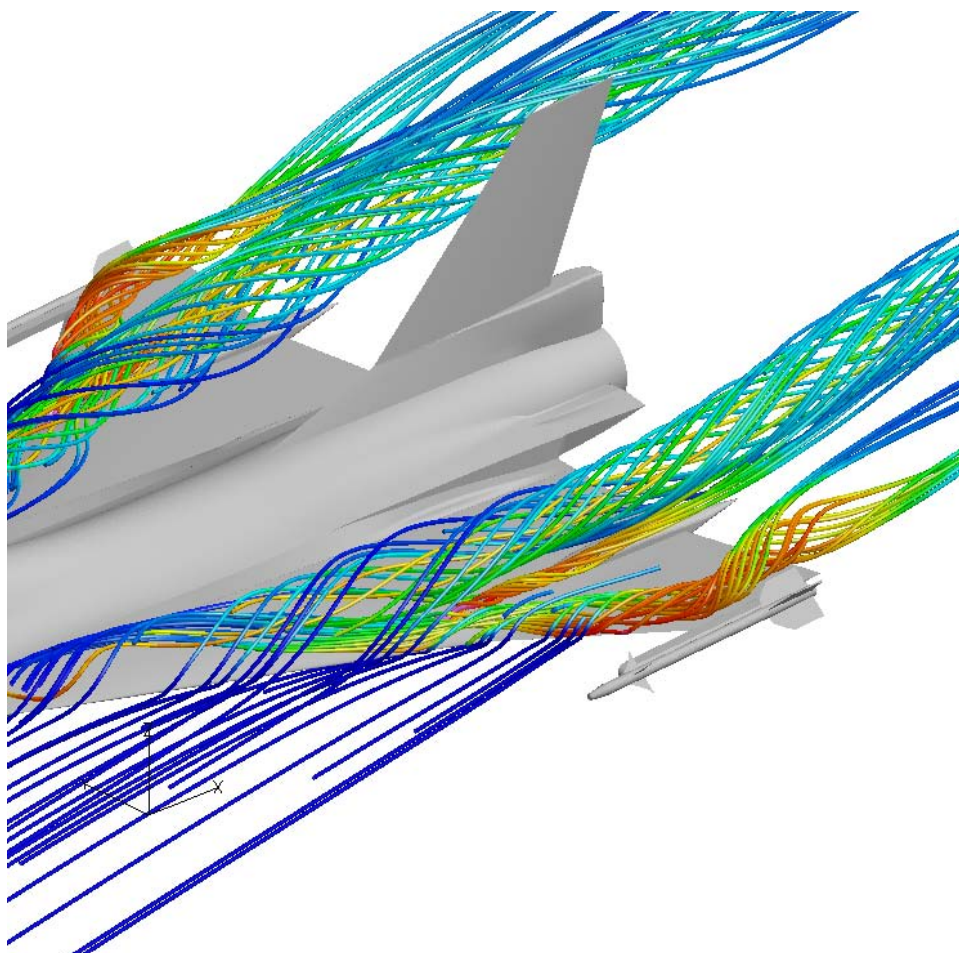
Figure 13-8: Streamtubes Colored by Total Pressure for FC7.

The pressure coefficient C_p was measured during the flight tests at specific buttlines (corresponding to the pressure belt placement) and fuselage stations. The CFD data was post-processed to compare to the C_p at these buttlines and fuselage stations. The buttline comparison for FC7 is shown in Figure 13-9. The CFD solver underpredicts the suction peak at each buttline except BL184.5, which does not have a suction peak. This may be the reason that the secondary vortex is not as evident as it should be. The C_p profile matches fairly well before and after the suction peak. This is important since the underprediction of the suction peak pressure does not seem to affect the solution elsewhere. The reason for the underprediction may be the flux limiter used. Previous experience with Falcon indicates that changing the parameters for the flux limiter may aid in prediction of the suction peak at high-lift conditions.
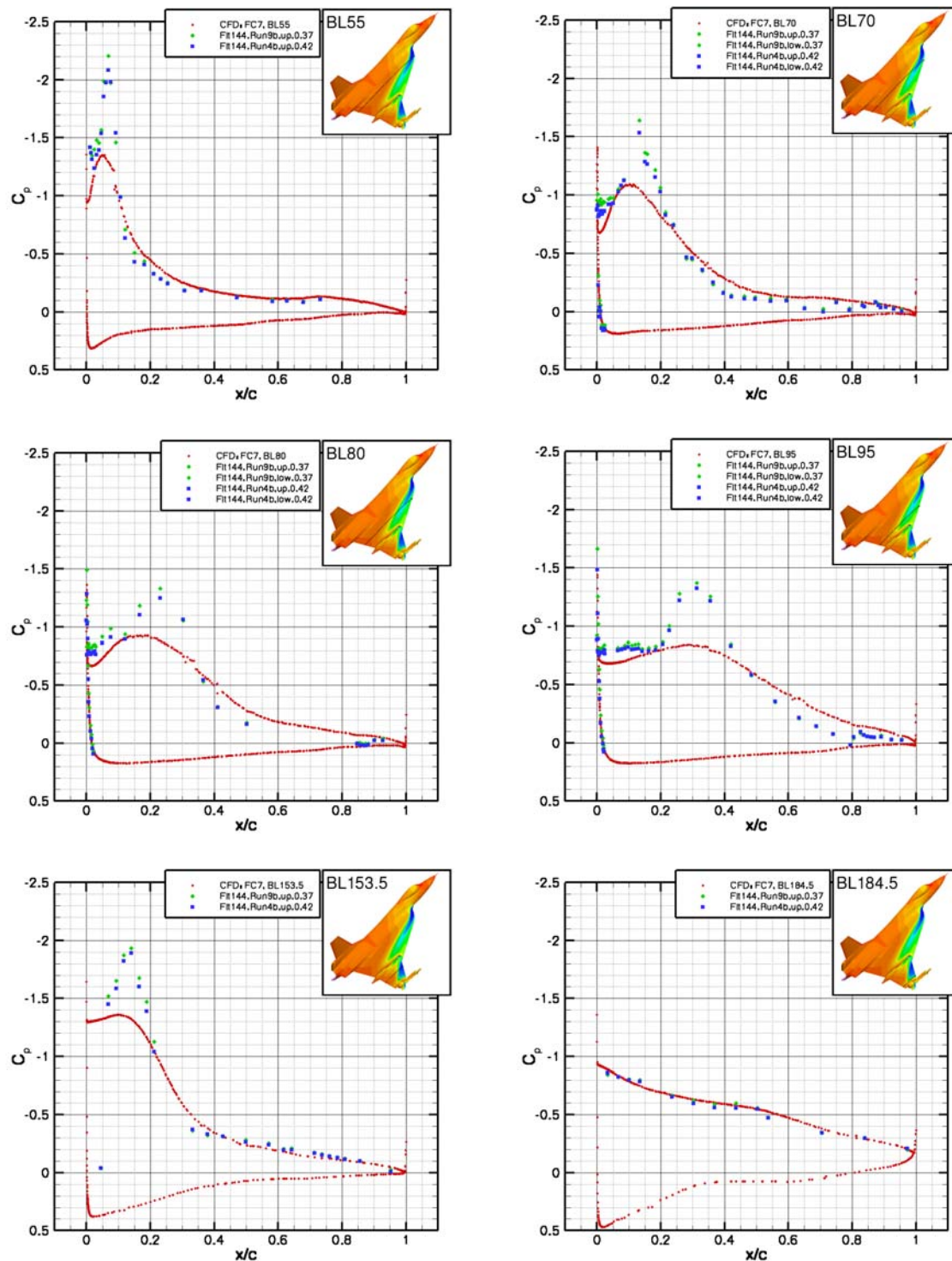
Figure 13-9: Comparison of C_p to Flight Test Data for FC7 at Various Buttlines.

The C_p distribution along the fuselage station cuts is shown in Figure 13-10. It is evident again at FS300 that the suction peak is underpredicted, but the rest of the comparisons are reasonable. At FS407.5 and FS450 the position of the air dam is evident by the discontinuous change in C_p at this location.
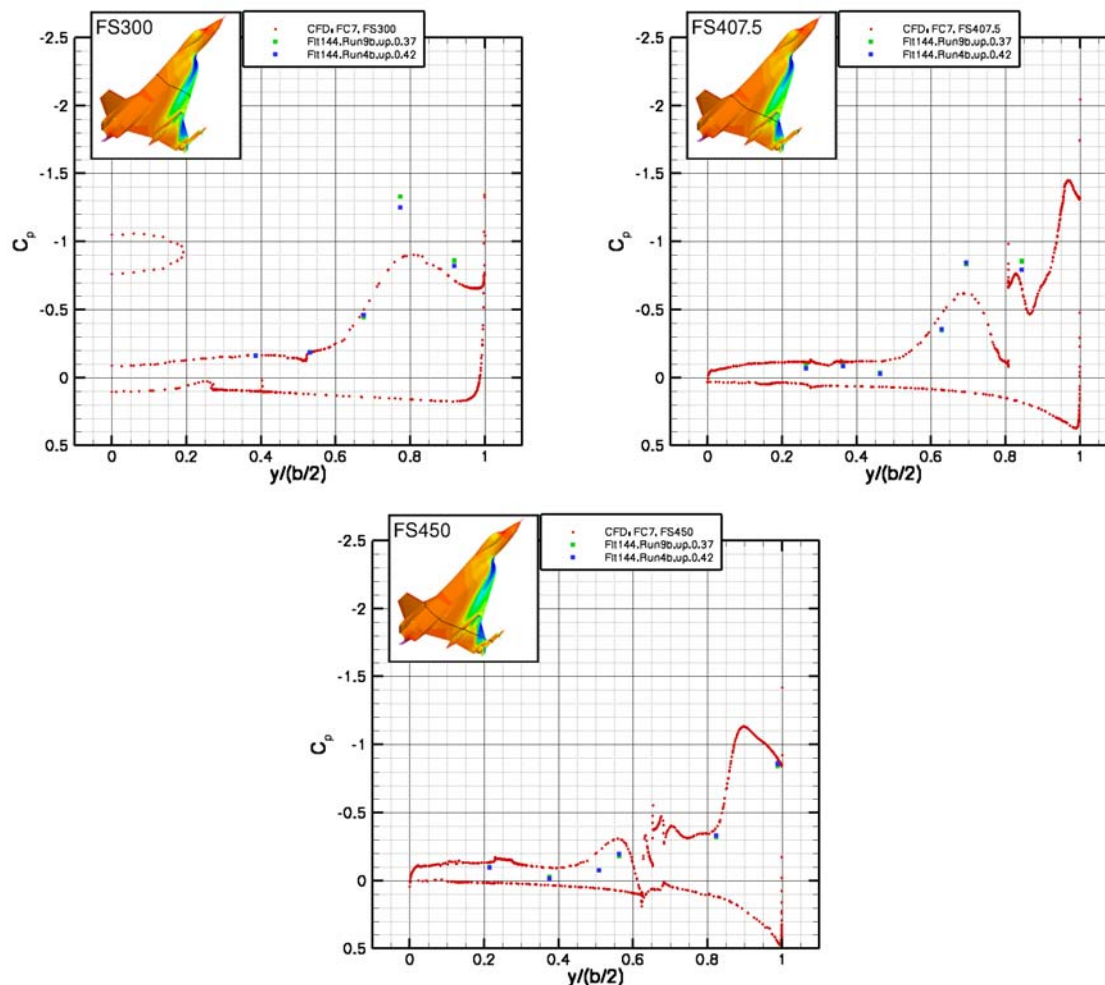
Figure 13-10: Pressure Comparison of C_p to Flight Test Data at Various Fuselage Stations for FC7.

The previous results show that the suction peak is missed consistently at each buttline and fuselage station location. A possible reason for this is excessive dissipation due to a low compression factor (1.0) in the flux limiter. Further simulations were performed at flight condition 7 using a compression factor of 1.4. The results at the same buttlines and fuselage stations are shown in Figure 13-11 and Figure 13-12 respectively. While increasing the compression factor does help increase the magnitude of the suction peak near the leading edge, it still does not raise it sufficiently to match the flight test data.
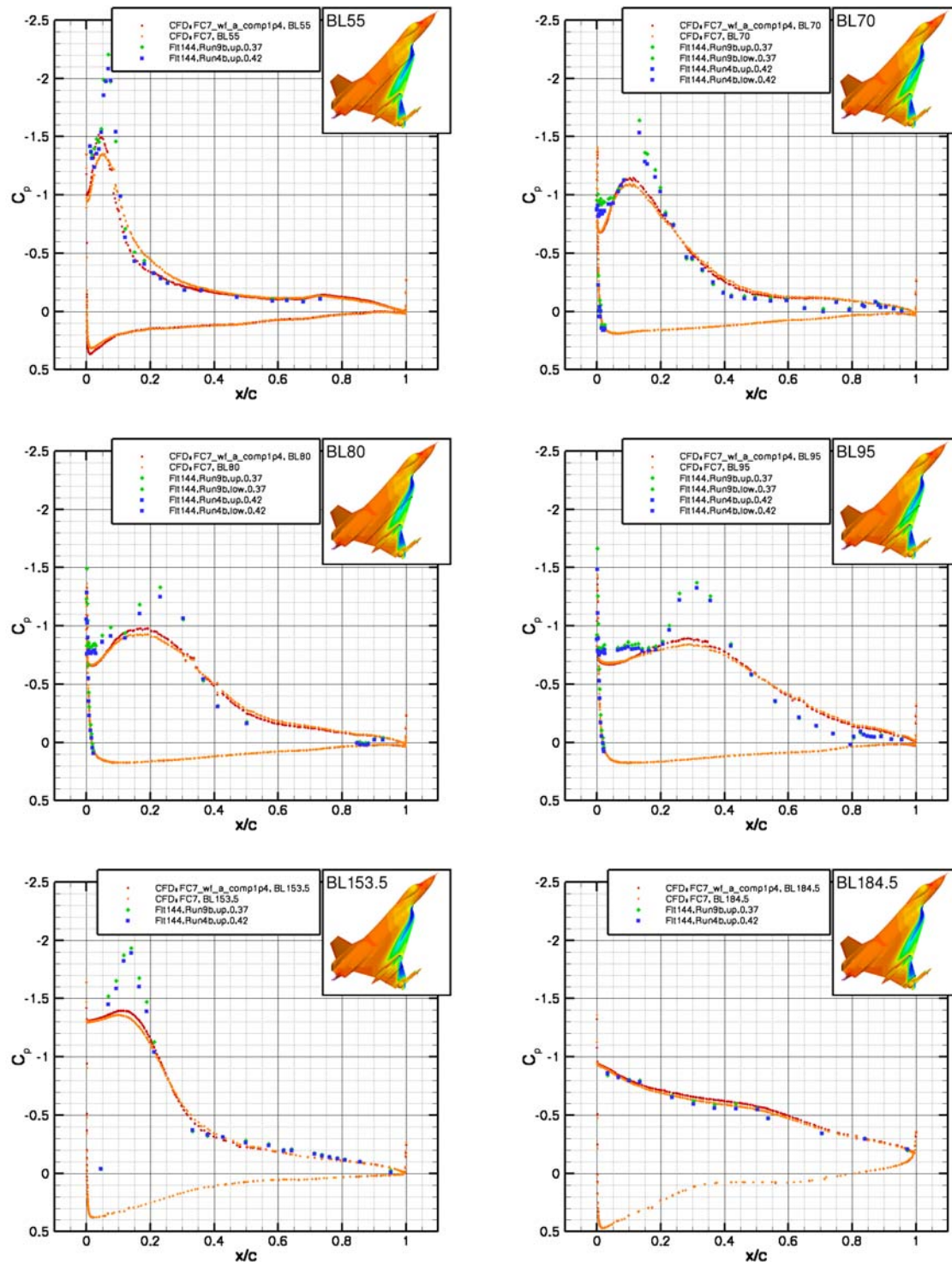
Figure 13-11: Pressure Coefficient Comparisons at Various Buttline
Locations, Flux Limiter Compression Factors 1.0 and 1.4, FC7.
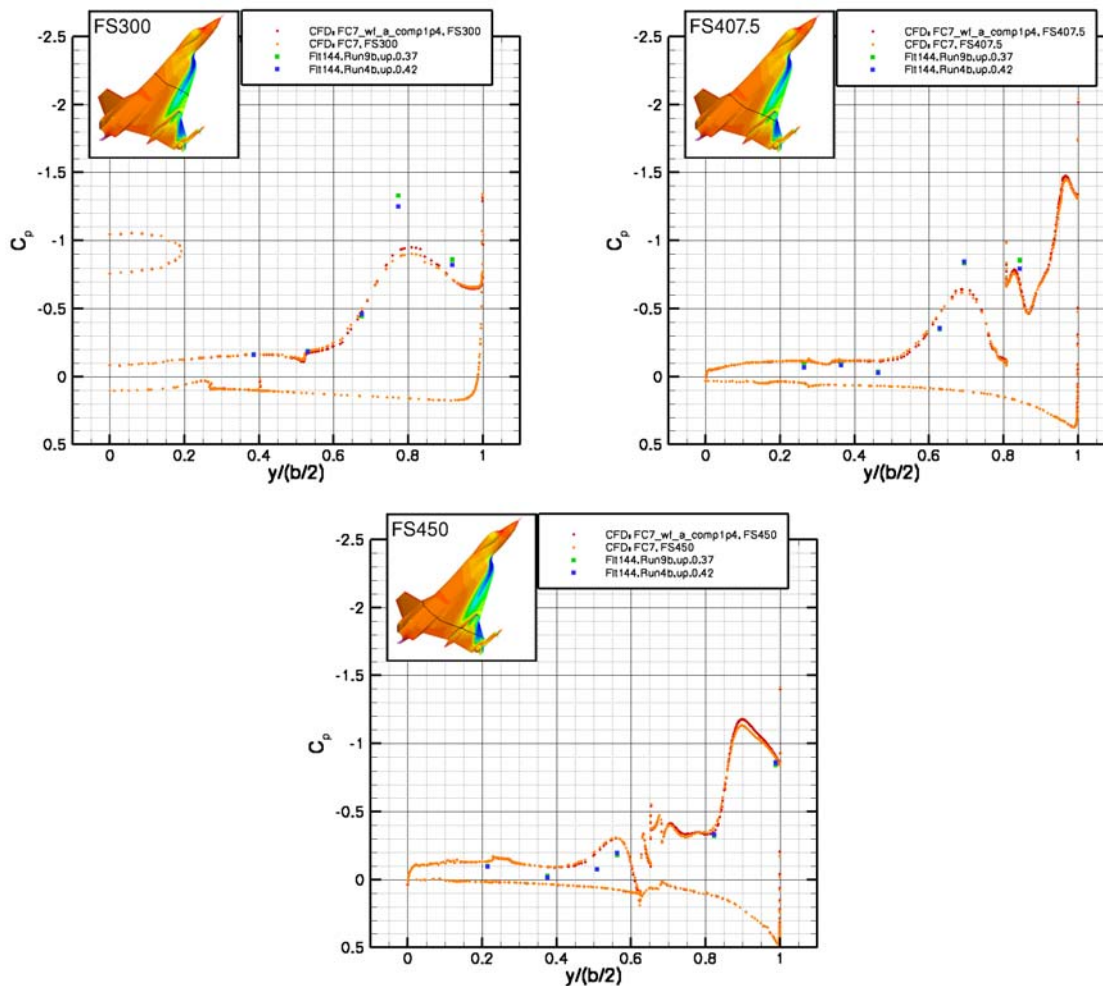
**Figure 13-12: Pressure Coefficient Comparison at Various Fuselage
Station Cuts, Flux Limiter Compression Factor of 1.0 and 1.4, FC7.**

13.5.2   Flight Condition 19

The flight condition FC19 is very similar to FC7 with the exception of altitude (10000 feet). The Mach number is 0.36, the Reynolds number is 46.8 million, and the angle of attack is 11.85 degrees. The C_p surface plots (Figure 13-13) are almost identical for the two cases, with the only discernable difference in and around the engine inlet, which is due to a difference in inlet conditions. The total pressure surfaces seem to show differences (Figure 13-14), but this is due to the fact that the magnitude of the total pressure loss is higher for FC19. The shape and placement of the primary, secondary, and outboard vortices is the same for the two cases. The streamline pattern is almost identical as well (Figure 13-15), again with the only difference the total pressure coloring the streamtubes. All of the C_p plots, both buttline and fuselage station, are identical.
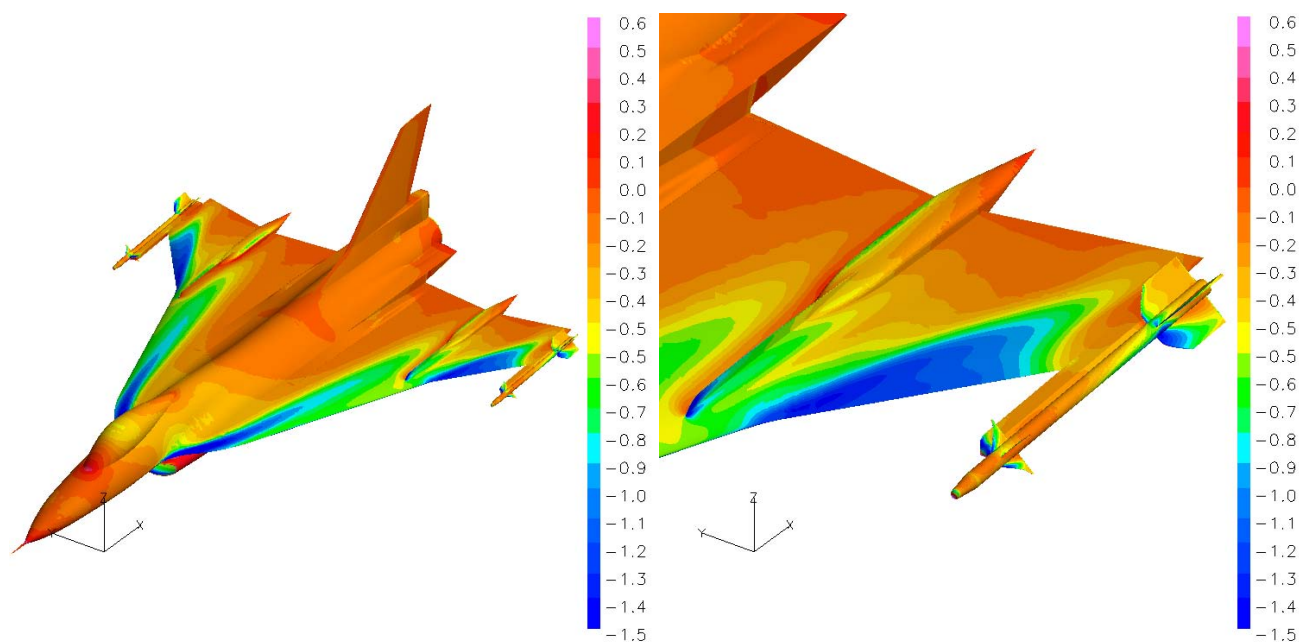
Figure 13-13: Surface C_p Distribution for FC19.
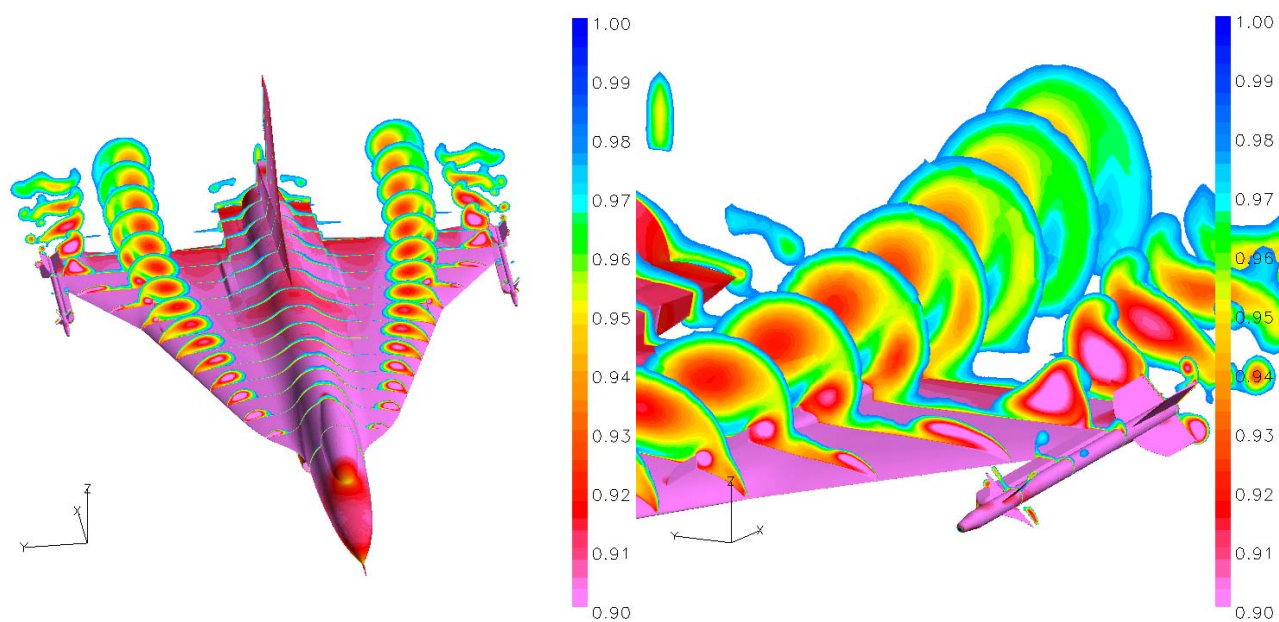
Figure 13-14: Bounded Total Pressure Cuts for FC19.
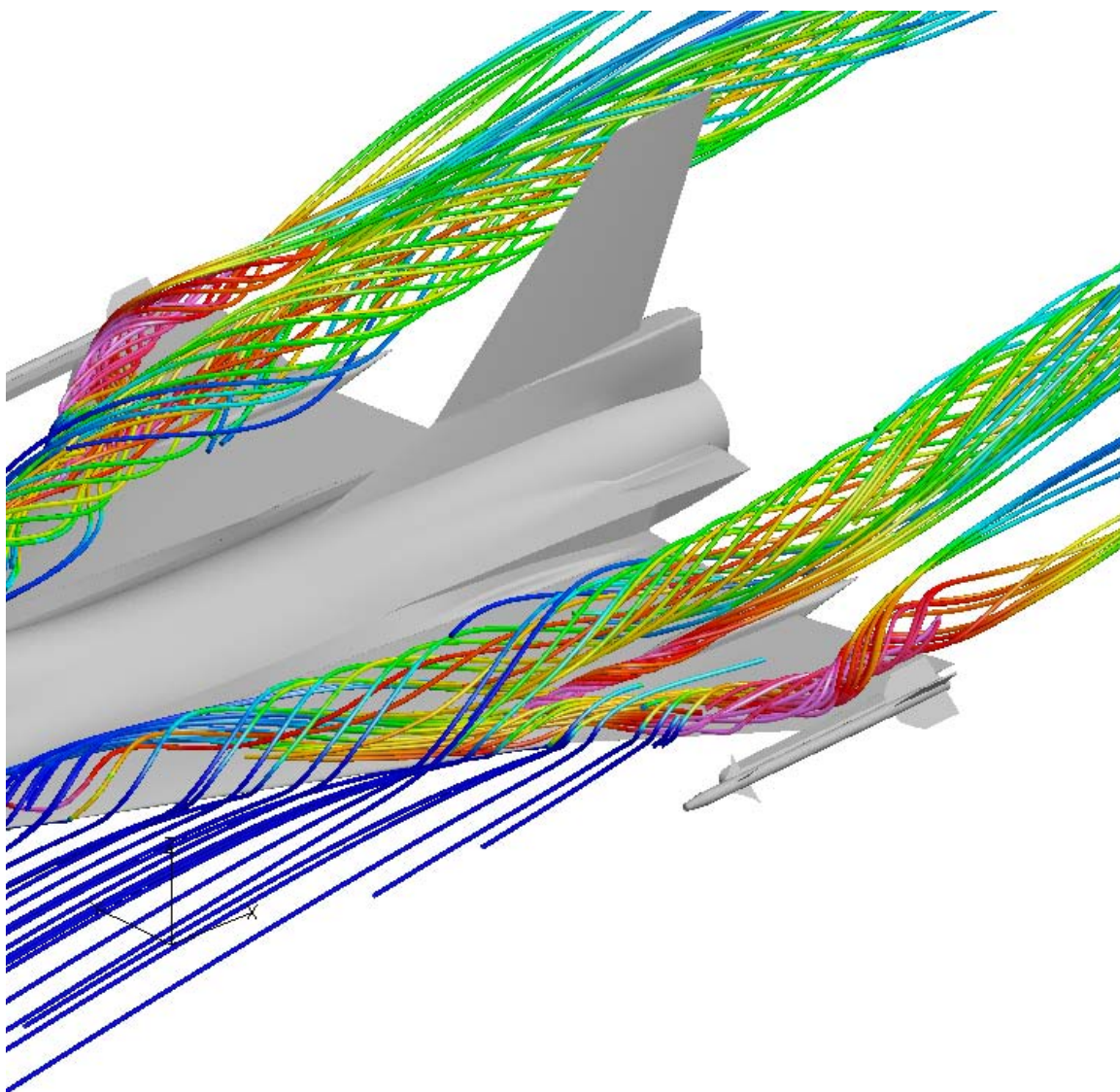
Figure 13-15: Streamtubes Colored by Total Pressure for FC19.
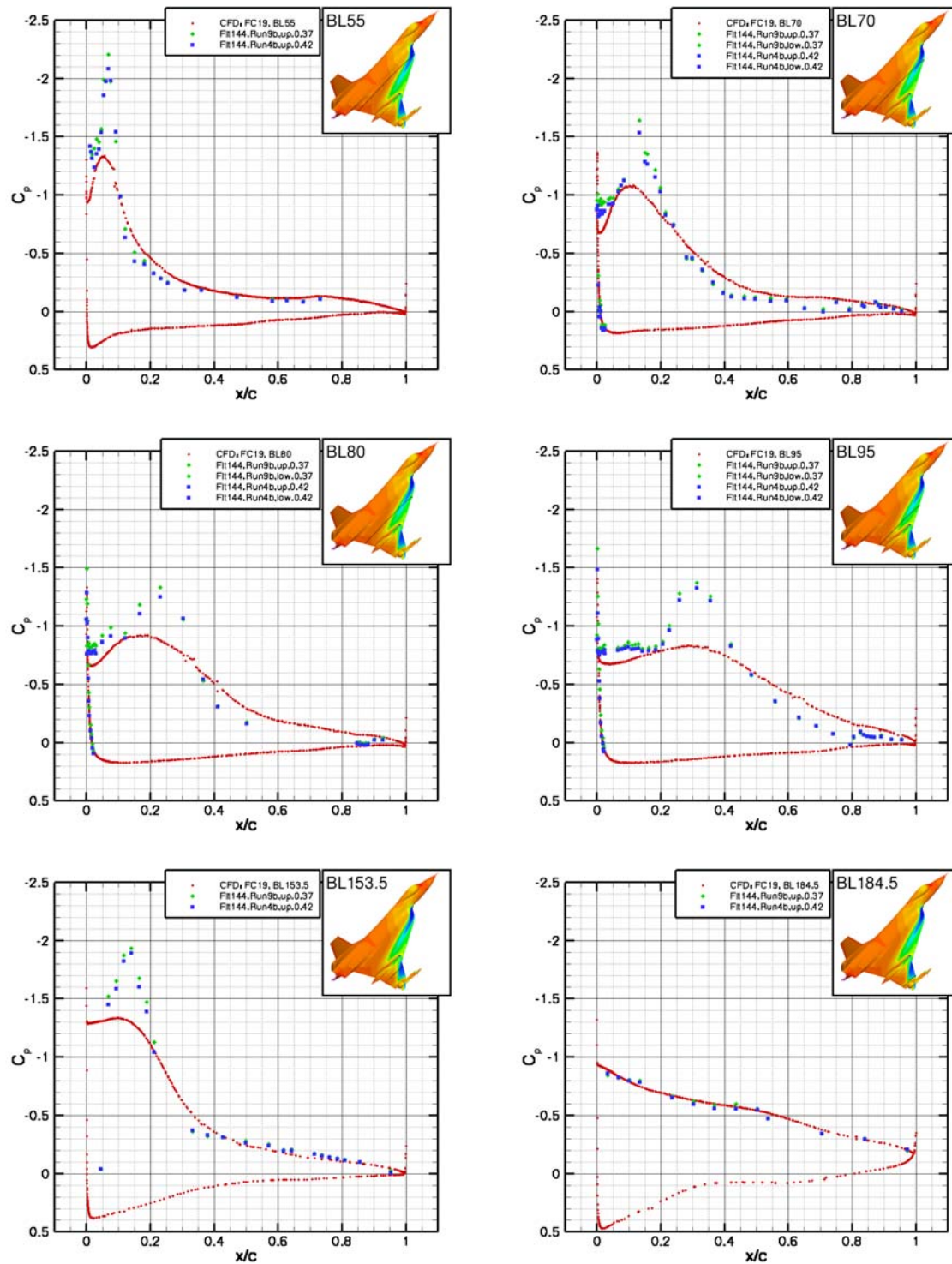
Figure 13-16: Comparison of C_p to Flight Test Data for FC19 at Various Buttlines.
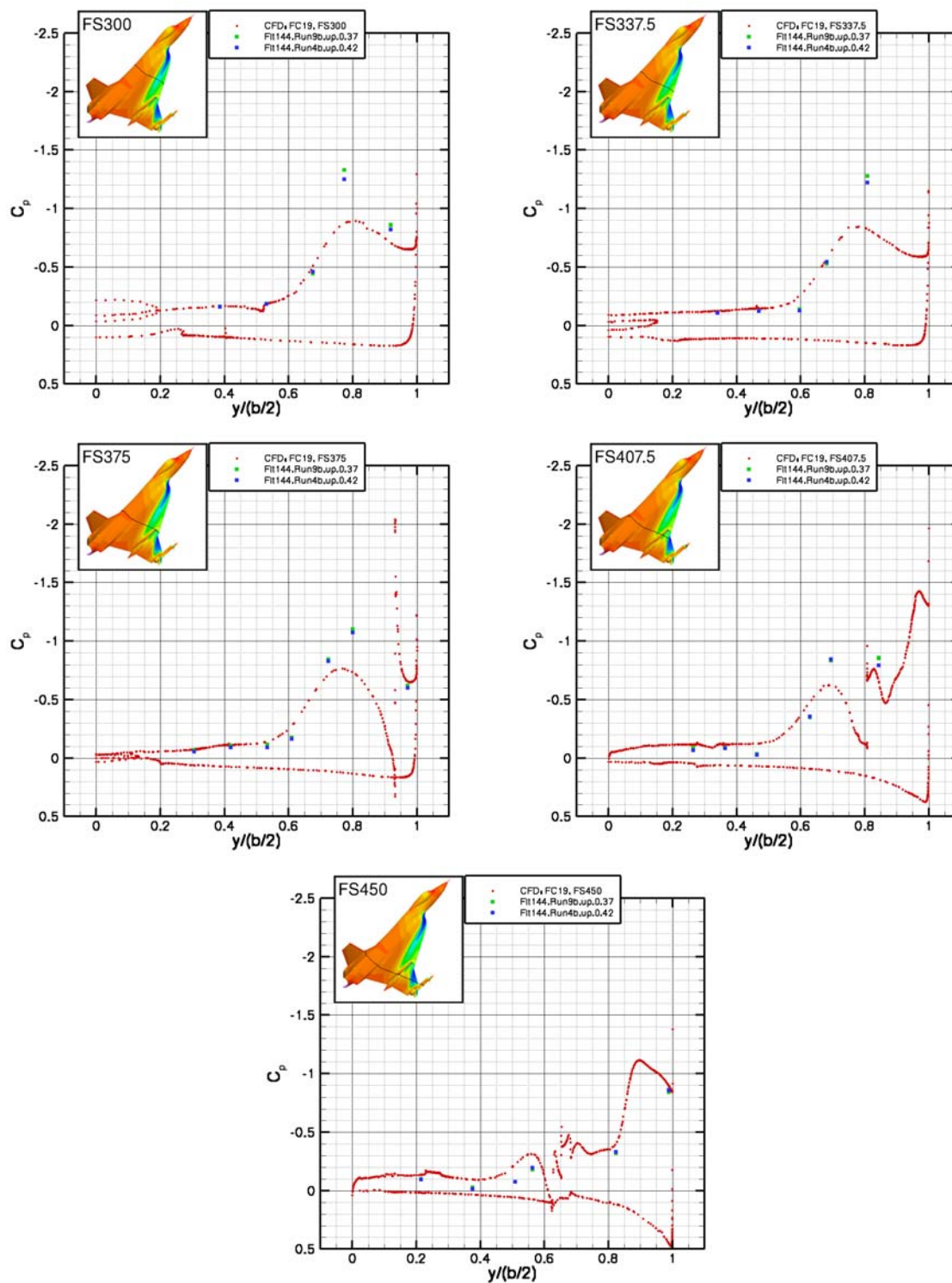
Figure 13-17: Comparison of C$_p$ to Flight Test Data for FC19 at Various Fuselage Stations.

13.5.3   Flight Condition 70

The only transonic case is FC70, which has a Mach number of 0.97. The angle of attack is low relative to the rest of the test suite (4.4 degrees), and hence the vortex structure is much less pronounced at this case. The flight test data was taken at an altitude of 22,300 feet, which yields a Reynolds number of 88.77 million. The shock structure is the dominant mechanism at these flight conditions. Iso-surfaces at Mach 1 are shown in Figure 13-19 (colored by total pressure), and these clarify the C_p surface plots shown in Figure 13-18. There are three large Mach surfaces which terminate in very weak shocks. The first starts and terminates on the canopy, the second starts very near the inboard leading edge and terminates at the middle of the inboard wing section, and the third starts roughly at the crank and terminates at the trailing edge. There is a region of smaller Mach surfaces that sit between the second and third large surfaces, which also seem to terminate in very weak shocks. Looking at the surface C_p distribution, the shock locations are evident from the pressure rise. Note also the Mach 1 surfaces at the missile nose, shoulder, and forward fins.
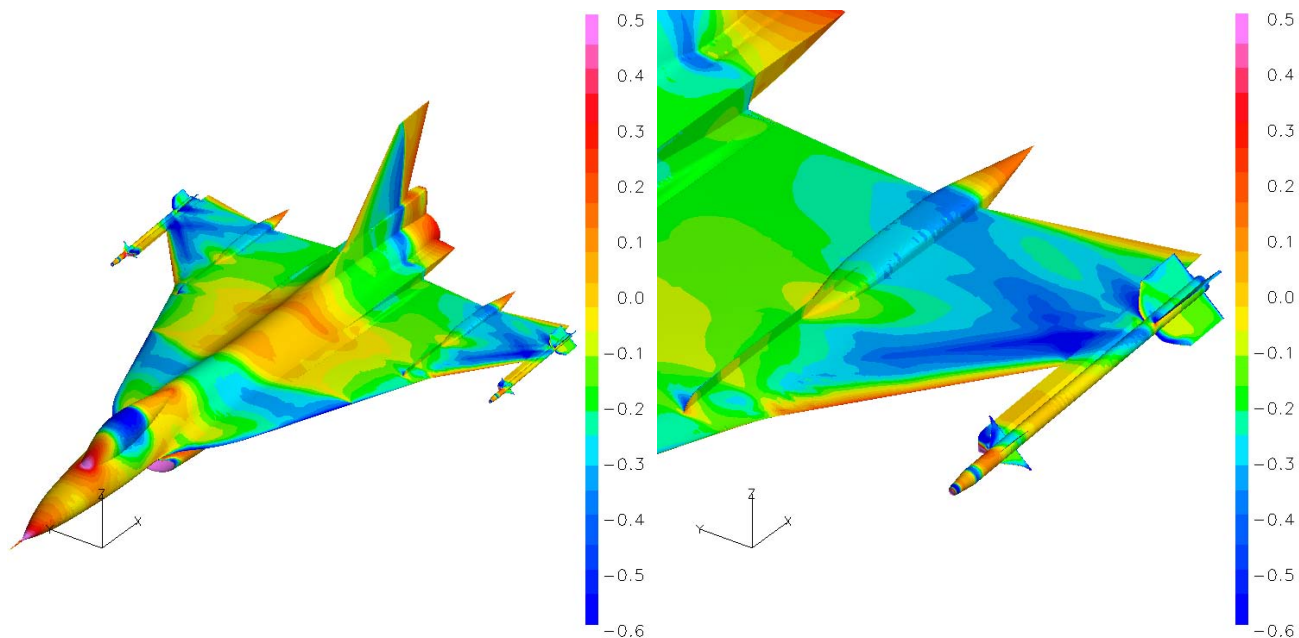
Figure 13-18: Surface C$_p$ Distribution for FC70.
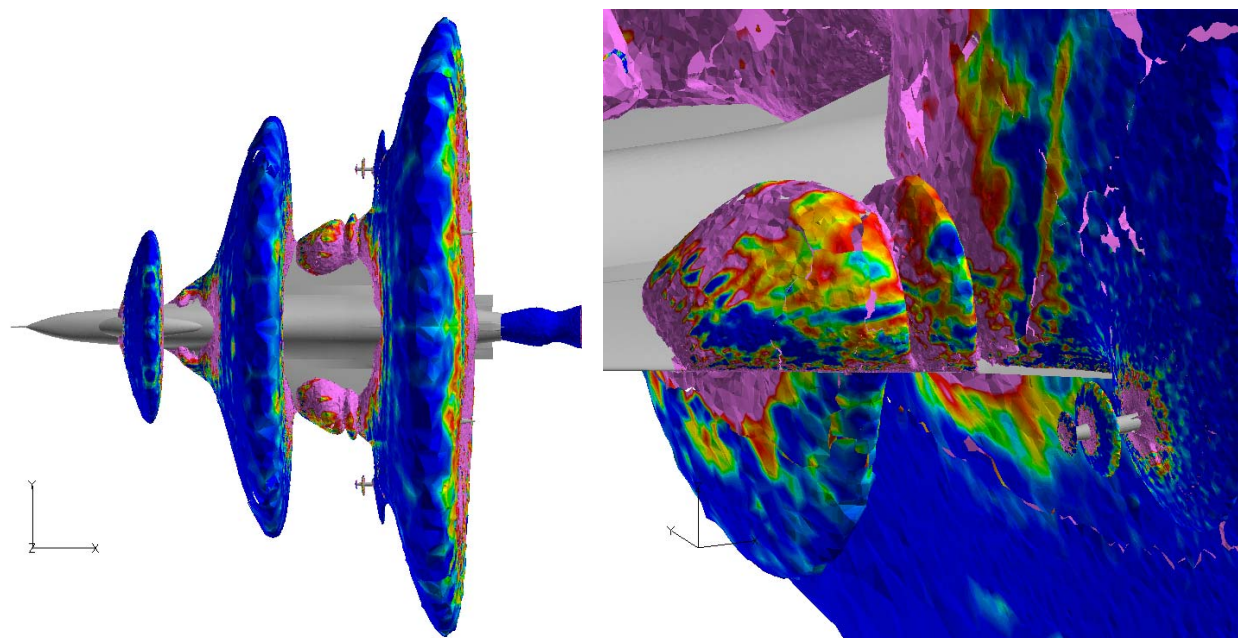
Figure 13-19: Mach 1.0 Iso-Surfaces Colored by Total Pressure for FC70.

The buttline C_p matches reasonably well with the flight test (Figure 13-20) at BL55 and BL95, but does not match very well at other buttlines. This disparity is also evident in the fuselage stations comparisons, with the exception of FS407.5. The reason for the gross differences at this flight condition are unknown at the present time, but the consistency of the differences across a range of different flow solvers and grids suggests that there is a difference between the configuration and flow conditions in the test and those simulated in the CFD.
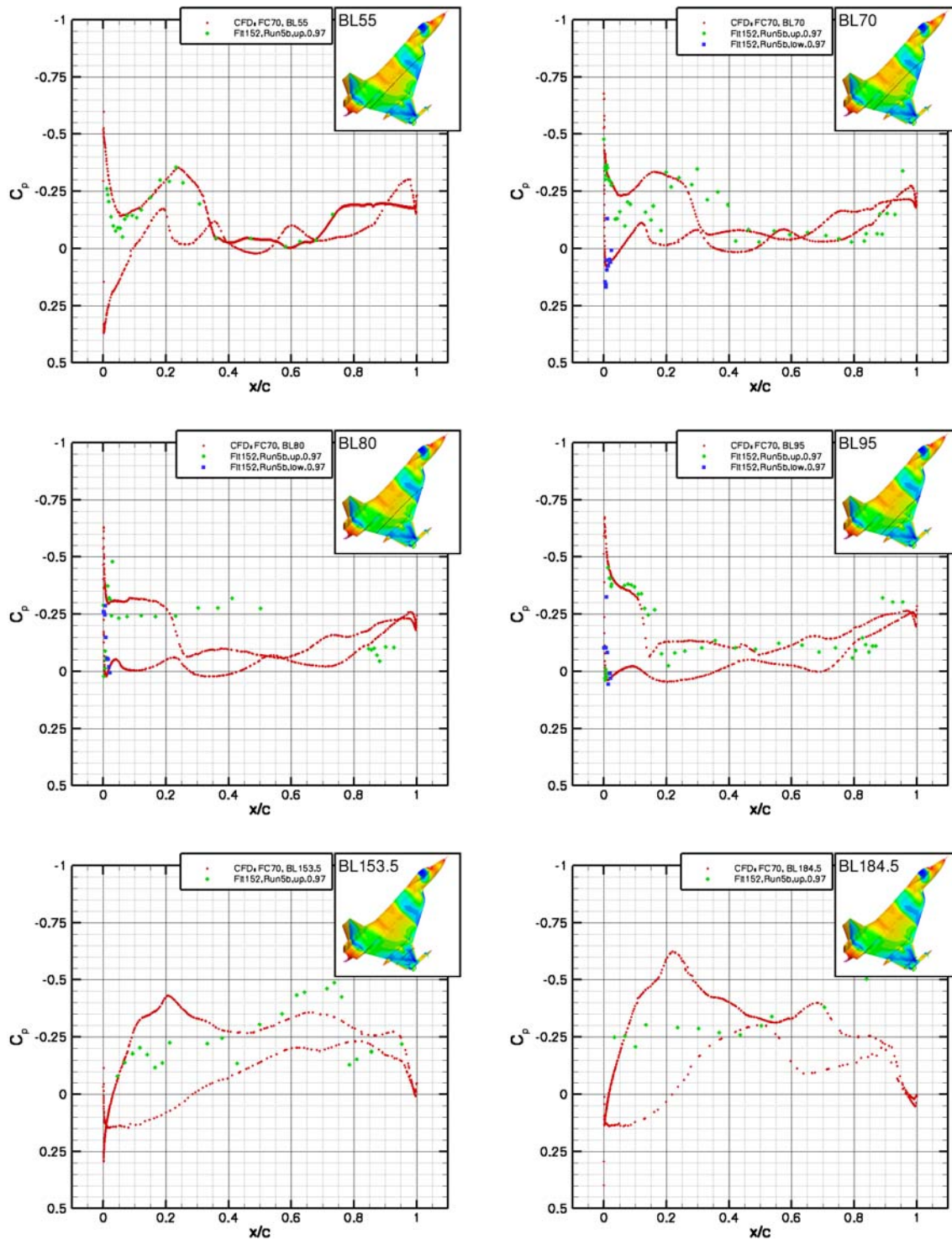
Figure 13-20: Comparison of C$_p$ to Flight Test Data for FC70 at Various Buttlines.
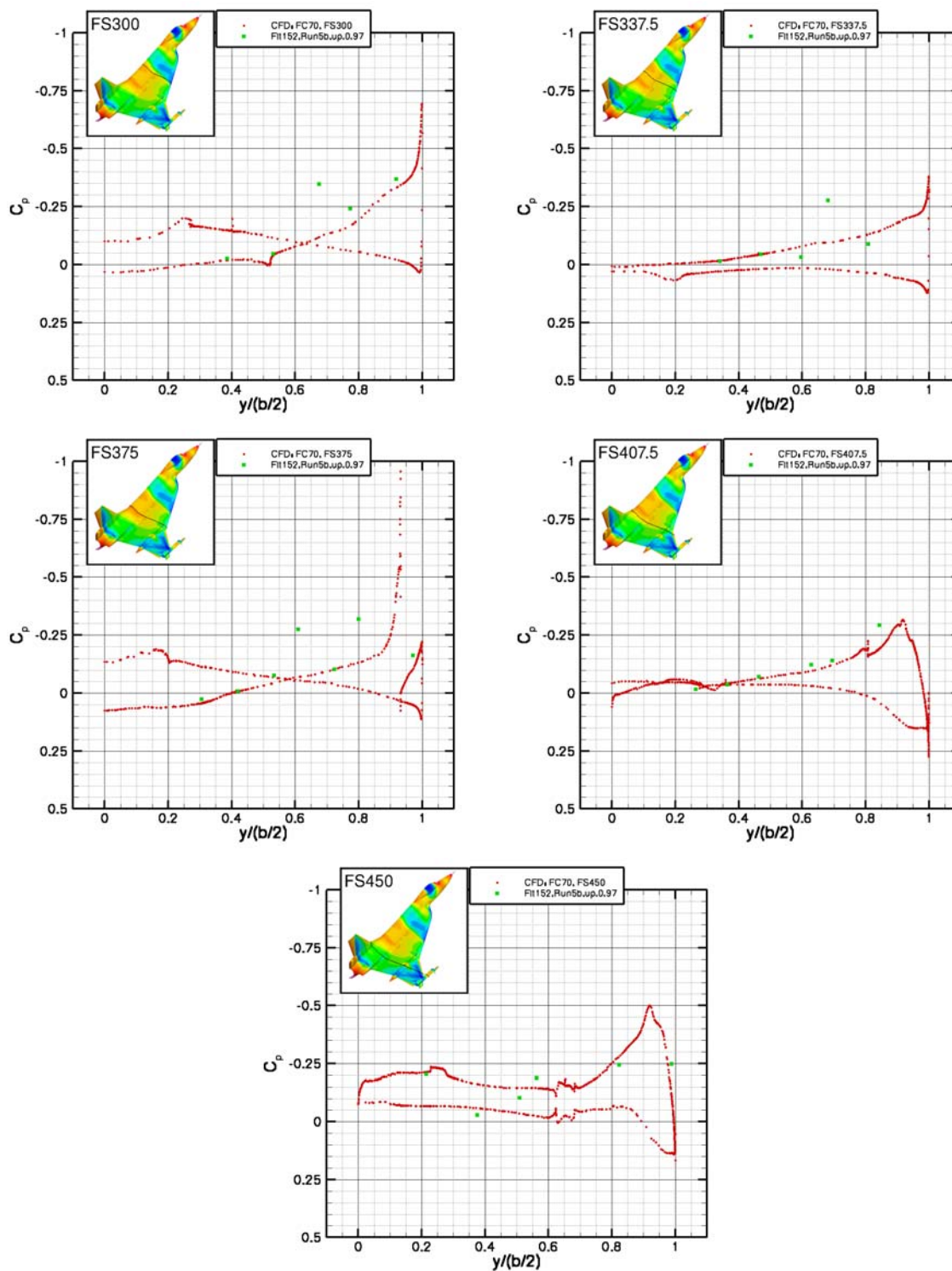
Figure 13-21: Comparison of C_p to Flight Test Data for FC70 at Various Fuselage Stations.

13.6   CONCLUSIONS

The LM Aero general purpose flow solver Falcon v4 was used to run simulations on the F-16XL geometry at high-lift and transonic flight conditions for which flight test data exists as part of the CAWAPI program. The hybrid computational mesh was produced by the UT SimCenter. The results were generally encouraging, with Falcon capturing the major flow features and placement. The suction peak at the leading edge of the wing was underpredicted, however, for all high-lift cases. This is partially due to the compression factor setting for the flux limiter. This does not totally account for the differences in the suction peak values, as an experiment raising the compression factor showed. The most likely reason for the discrepancy is that the simulations cited here used wall functions with a correspondingly coarser grid in the near wall region than one would use for a full viscous simulation. The use of wall functions seems to be inadequate for these types of problems. The C_p comparison to flight test at the transonic condition was poor at almost all buttlines and fuselage stations. There is good agreement, though, with the simulations performed by other flow solvers. The best explanation for this is that the geometric configuration or flow conditions simulated in the CFD are different from those used in the flight test.

13.7   REFERENCES

[13-1]   Lamar, J.E., Obara, C.J., Fisher, B.D. and Fisher, D.F.: *Flight, Wind-Tunnel, and Computational Fluid Dynamics Comparison for Cranked Arrow Wing (F-16XL-1) at Subsonic and Transonic Speeds*, NASA/ TP-2001-210629, February 2001.

[13-2]   Lamar, J.E. and Obara, C.J.: *Review of Cranked-Arrow Wing Aerodynamics Project: Its International Aeronautical Community Role*, AIAA Paper 2007-0487, Presented at 45th AIAA Aerospace Sciences Meeting and Exhibit, Reno, NV, January 2007.

[13-3]   Roe, P.L.: *Characteristic-Based Schemes for the Euler Equations*, Annual Review of Fluid Mechanics, Vol. 18, 1986, pp. 337-365.

[13-4]   Smith, B.R.: *The k-kl Turbulence Model and Wall Layer Model for Compressible Flows*, AIAA Paper 90-1483, June 1990.

[13-5]   Reed, C.L., Karman, S.L. and Anderson, D.A.: *Implementation of Low Speed Preconditioning in the Splitflow Code*, AIAA Paper 97-1867, June 1997.

[13-6]   Karypis, G. and Kumar, V.: *A Fast and High Quality Multilevel Scheme for Partitioning Irregular Graphs*, SIAM Journal on Scientific Computing, Vol. 20, No. 1, pp. 359-392, 1999.

[13-7]   Karman, S., Mitchell, B. and Sawyer, S.: *Unstructured Grid Solutions of CAWAPI F-16XL by UT SimCenter*, AIAA Paper 2007-0681, Presented at 45th AIAA Aerospace Sciences Meeting and Exhibit, Reno, NV, January 2007.

[13-8]   Karman, S.L. Jr.: *Unstructured Viscous Layer Insertion Using Linear-Elastic Smoothing*, AIAA-2006-0531, January 2006.

Chapter 14 – NUMERICAL SOLUTIONS FOR THE CAWAPI CONFIGURATION ON UNSTRUCTURED GRIDS AT UT-SIMCENTER, UNITED STATES

by

Steve L. Karman Jr., Brent Mitchell, Shane Sawyer, Justin Whitt

14.1   SUMMARY

Viscous solutions for a F-16XL configuration are computed using the CFD tools used by and developed at the University of Tennessee SimCenter at Chattanooga, Tennessee, USA. The study is performed in conjunction with a North Atlantic Treaty Organization Technical Team, AVT-113. Inviscid meshes are created using Gridgen. Viscous prismatic layers are added using a procedure that incorporates a Linear-Elastic smoothing scheme to perturb the existing mesh, creating room for the insertion of viscous layers. A vertex-centered, Reynolds averaged Navier-Stoke flow solver is used to compute seven test cases, defined by the NATO Technical Team AVT-113. Comparisons are made with available flight test data in the form of surface pressure coefficients.

14.2   INTRODUCTION

North Atlantic Treaty Organization (NATO) Technical Team AVT-113 was formed to investigate the state of the art in Computational Fluid Dynamics (CFD) solvers applied to viscous vortical flowfields. The goal of the study was to determine the accuracy and efficiency of modern CFD methods for analysis of highly vortical viscous flowfields typically encountered in modern fighter aircraft. The team is comprised of experimentalists and CFD researchers in the United States and Europe. The configuration chosen for the study is the F-16XL, originally built by General Dynamics. The only two existing F-16XL aircraft are owned by the National Air and Space Administration (NASA) in the United States and are used to conduct aerodynamic research. Data collected during flight tests includes surface pressures, boundary layer rakes and flow visualization [14-1]. This data can be used to validate the accuracy of CFD solvers. The NATO AVT-113 team selected a series of flight conditions to use in this CFD study. The flight conditions range from subsonic to transonic Mach numbers. The angle of attack range extends to near 19 degrees. These flight regimes generate multiple vortices that flow over the upper surface of the configuration and interact in numerous ways.

This chapter presents the results obtained at the University of Tennessee SimCenter at Chattanooga (UT SimCenter). The methods used by the UT SimCenter include some commercial CFD software packages, as well as some tools developed at the SimCenter. Brief descriptions of the procedures used in the analyses will be provided. The Navier-Stokes computations for seven cases are compared with data taken during the flight test.

14.3   UNSTRUCTURED MESH GENERATION

Two separate mesh generation programs were used to generate the viscous meshes for these analyses. The first program was a commercially available mesh generation package known as Gridgen [14-2]. Gridgen was used to create an inviscid unstructured mesh. The second mesh generation program was developed at the SimCenter and was used to insert viscous layers in the inviscid mesh. Brief descriptions of the tools are described below.

14.3.1   Geometry

The NATO Technical Team AVT-113 provided the F-16XL geometry in the form of an IGES file. Lockheed Martin Aeronautics Company produced the original IGES file. Some initial cleanup work was performed by NASA Langley Research Center to eliminate known gaps and overlaps in the defined surfaces. Additional cleanup work and geometry simplification was performed by EADS-M to prepare the geometry for mesh generation and analysis by all AVT-113 team members. Some of the simplifications included the elimination of duplicate geometry entities in regions such as the engine inlet lip and the elimination of the gap between the engine nozzle and the clamshell airbrake.

All major geometric features were defined in the final IGES file. The features included the air data probe at the nose, the cockpit canopy, the engine inlet and nozzle, the wing and vertical tail, the actuator pods and air dam on the wing and the wing tip rail and AIM-9 missile. The inlet duct was modeled all the way up to the compressor face. The nozzle duct was modeled from the turbine face aft. Also modeled was the boundary layer diverter located between the inlet and the fuselage.

14.3.2   Inviscid Mesh

Gridgen was used to create an unstructured inviscid mesh, comprised of mostly tetrahedra [14-2]. Surface meshes, consisting of triangular elements, were created on the geometry defined by the IGES file. Care was taken to ensure proper resolution of pertinent geometric features such as the leading and trailing edge of the wing. The high curvature of the leading and trailing edges needed fine resolution in the chord-wise direction to resolve the shape. The unstructured triangular surface meshing in Gridgen imposes nearly isometric triangular elements. In order to provide the desired resolution in the chord-wise direction and not have an excessive number of triangular elements in the span-wise direction a structured grid was used along sections of the leading and trailing edges of the wing. The aspect ratio of the quadrilateral elements was imposed to be no larger than 15. The resulting structured quadrilateral surface mesh was then converted to an unstructured triangular mesh by subdividing the quadrilateral elements into two triangles. Figure 14-1 shows a section of the leading edge where the converted structured mesh domain meets the unstructured mesh domains. A view of the mesh on the symmetry plane is shown in Figure 14-2.
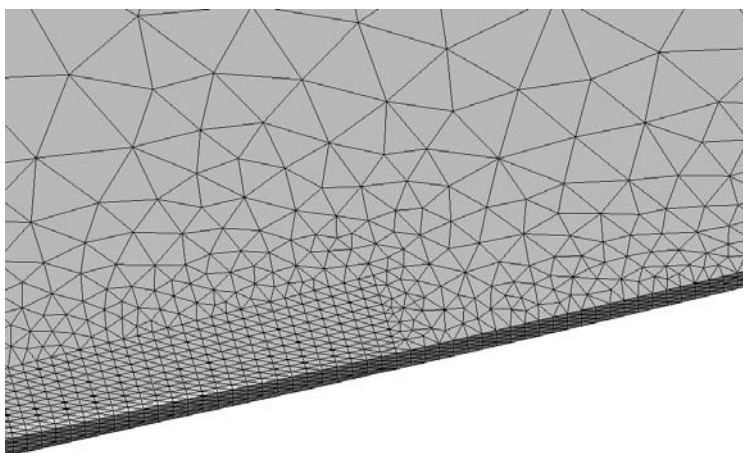
**Figure 14-1: Leading Edge Mesh Showing the Converted
Structured Domain Next to an Unstructured Domain.**
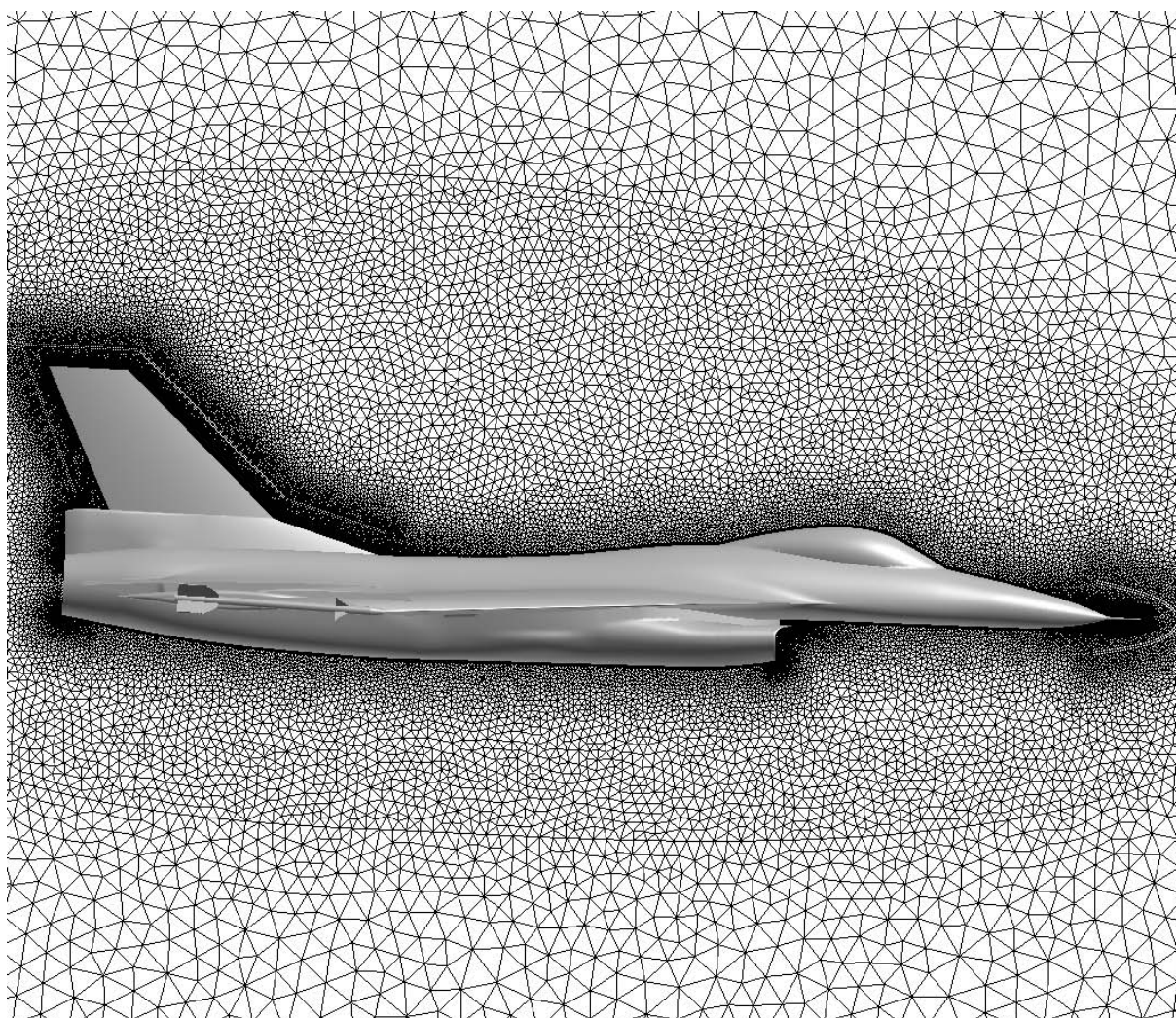
Figure 14-2: Symmetry Plane Mesh.

Baffle surfaces were used to control the spacing of the volume mesh, resulting in a hybrid unstructured inviscid mesh. The quadrilateral elements shown in the figure around the nose and tail are a result of these baffles. Additional baffles were created around the leading edge and trailing edge of the wing and at a near field boundary within a body length of the aircraft. The near field baffle boundaries can also be seen in Figure 14-2.

Views of the upper and lower surface mesh are shown in Figure 14-3. The total number of surface elements for the aircraft, minus the inlet face and nozzle face, is 599,676. The final inviscid mesh contained 4,858,525 nodes, 27,701,876 tetrahedra, 2186 pyramid and 195,044 prisms.
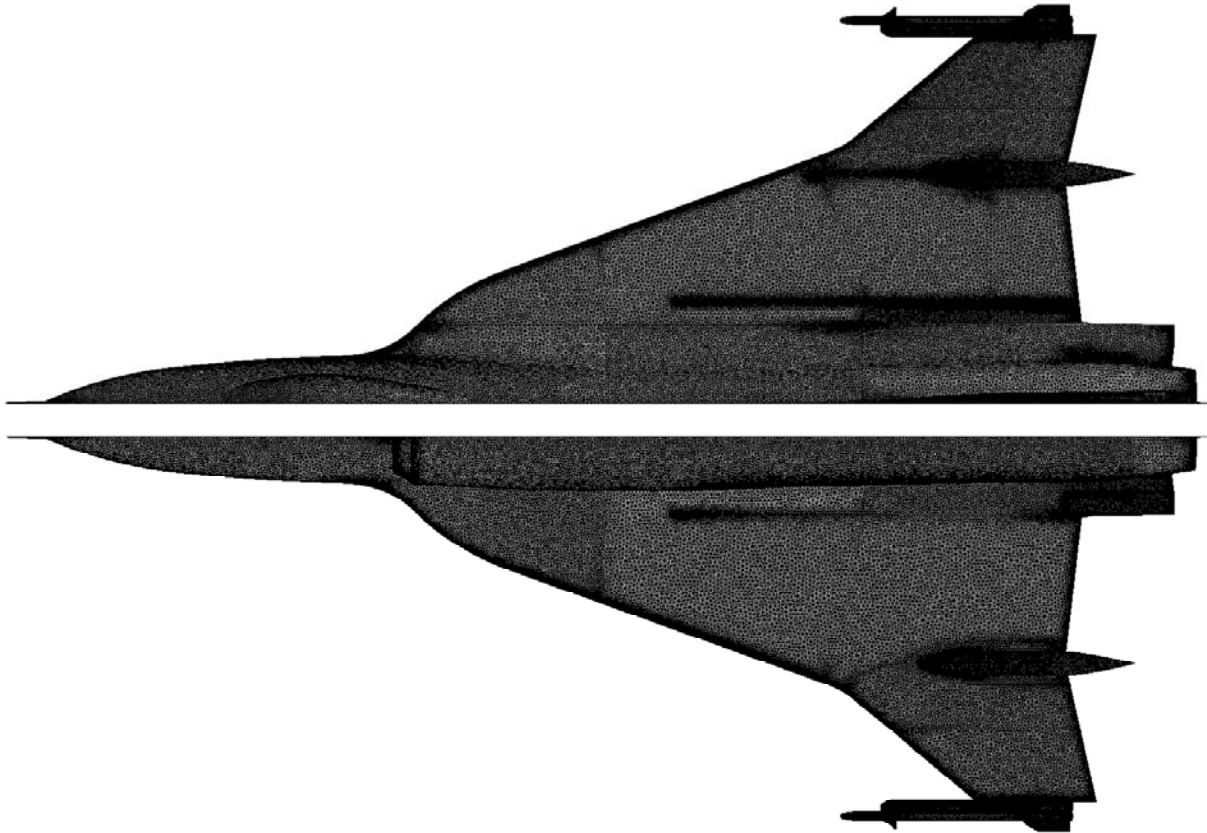
Figure 14-3: Top and Bottom Views of the Surface Mesh.

14.3.3   Viscous Mesh

A second mesh generation program was used to insert layers of triangular prismatic elements at the no-slip surfaces of the geometry [14-3]. This method uses a Linear-Elastic mesh-smoothing scheme to push the existing mesh away from the surface, making room for the viscous elements. The term normally used to define Young's Modulus in the linear-elastic relations is defined using a combination of element aspect ratio and corner angles to provide stiffness in regions of tight grid spacing. The Poisson's ratio term was set to a constant of 0.25. Only one layer of points is added at a time in reverse order; the top layer is added first and the final layer near the wall is added last. Points are only added where the local mesh spacing is larger than the desired spacing for the current layer. As a result, the number of triangular prismatic elements in a column varies over the surface. Figure 14-4 and Figure 14-5 show the varying number of elements per column for the mesh at the inlet. This capability allows the outer layer of prisms to match the spacing of the local tetrahedral elements without forcing each column to have unnecessary layers, which could result in kinking or buckling of the outer viscous layers.
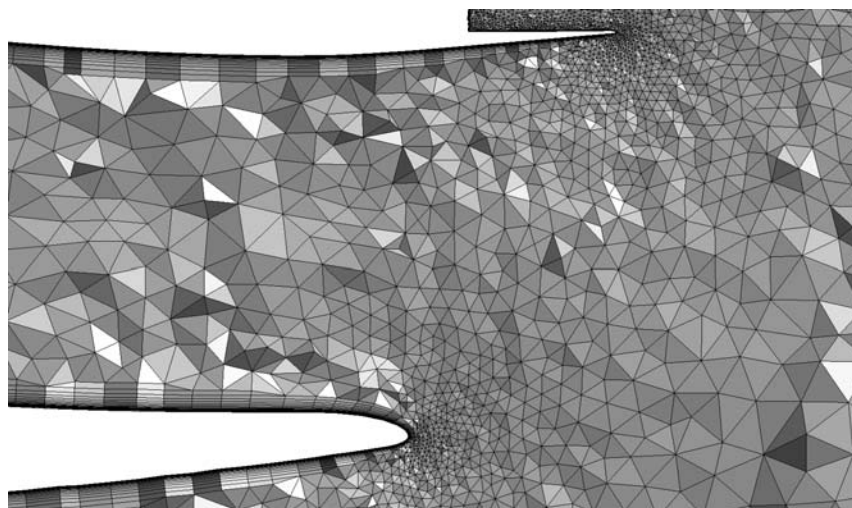
Figure 14-4: Crinkle Cut of Mesh Near the Symmetry Plane at the Inlet.
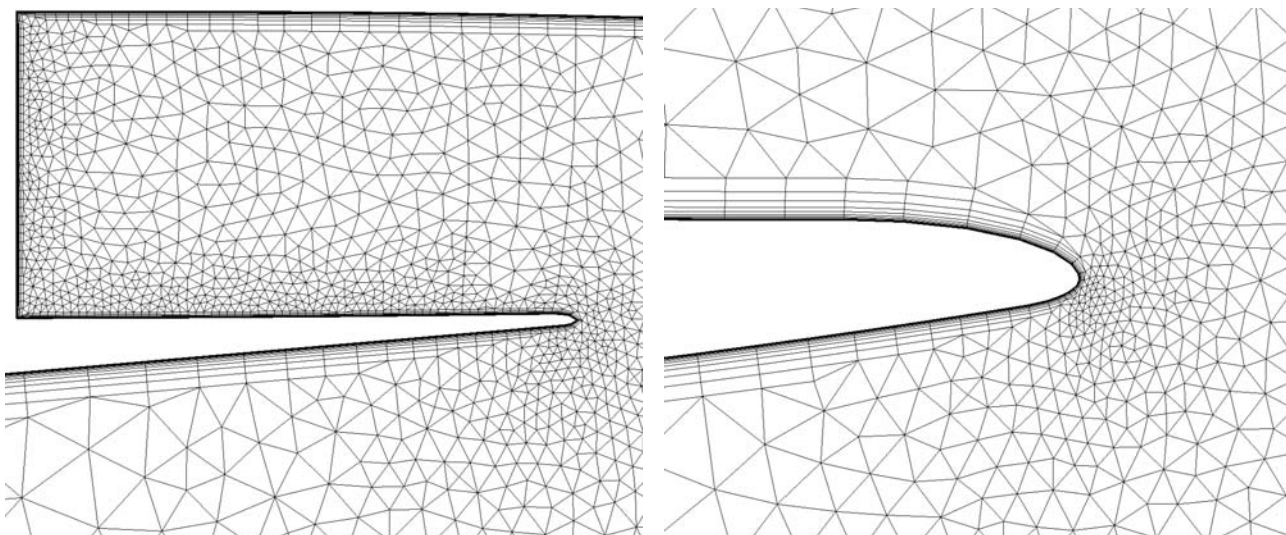
**Figure 14-5: Magnified Views of Symmetry Plane Mesh at
the Upper Inlet Lip (left) and the Lower Inlet Lip (right).**

A total of 25 layers were requested for the viscous region. The initial spacing was specified to correspond to an estimated Y+ value of 1. The height of the subsequent layers increases according to a geometric progression factor of 1.15 and a geometric growth rate of 1.02. A view of the viscous layers for the tip missile fins is shown in Figure 14-6. Finer resolution tetrahedra can be seen in the gap region between the fine and the missile rail. The layer insertion strategy matched the normal spacing of the layers with the existing local tetrahedral mesh. The half-model, viscous mesh contained 10,586,377 nodes, 28,092,773 tetrahedra, 982,975 pyramid and 10,822,176 prisms.
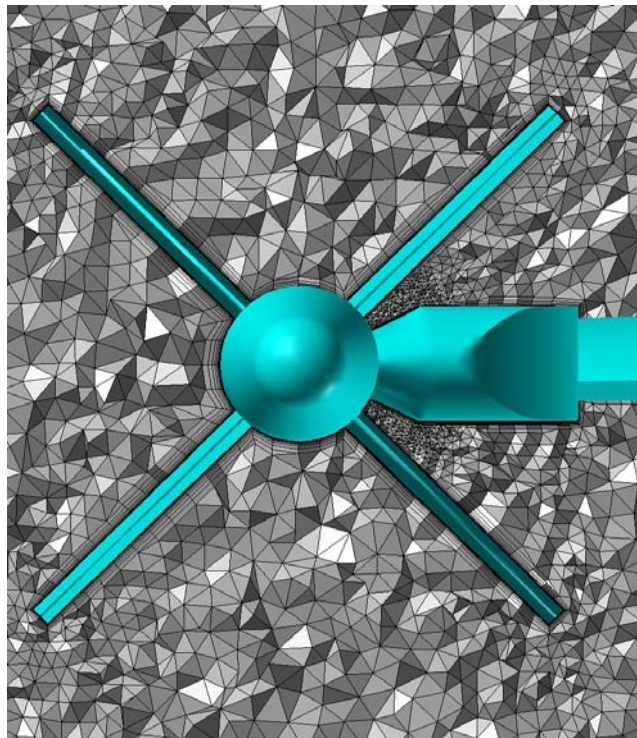
Figure 14-6: Magnified View of Axial Cut Through Tip Missile Fins and Wing.

14.4   UNSTRUCTURED FLOW SOLVER

The present flowfield solution algorithm used at the UT-SimCenter is related to several previous efforts and has evolved over more than 15 years of development. The approach is an evolution of the implicit flow solver and code of Anderson et al. [14-5] [14-6] [14-6]. The solver developed in this series of works demonstrated 3D, implicit, high Reynolds number solution capability. Aspects of the present approach are also related to the parallel multi-block structured grid solver of Pankajakshan [14-7]. The parallel version of the unstructured algorithm is detailed in Reference [14-8]. Brief descriptions of some of the aspects of the flow solver are described below.

14.4.1   Arbitrary Mach Algorithm

The staple of the structured and unstructured SimCenter flow solution code is an algorithm well suited for simulation of both high-speed and low-speed flows. This formulation was presented by Briley and is termed the arbitrary Mach number algorithm, which is a preconditioned Roe flux-difference formulation for non-dimensional primitive variables [14-9]. The unsteady three-dimensional compressible Reynolds-averaged Navier-Stokes equations are presented here in Cartesian coordinates and in conservative form:

$$\frac{\partial}{\partial t} \int_{\Omega} Q dV + \int_{\partial \Omega} \vec{F} \bullet \hat{n} dA = \frac{M_{\infty}}{Re} \int_{\partial \Omega} \vec{G} \bullet \hat{n} dA \tag{1}$$

The solution variables are expressed in their primitive form in the arbitrary Mach number algorithm:

$$Q = \left[\rho, u, v, w, P\right]^{T} \tag{2}$$

The arbitrary Mach algorithm depends on a simple, single-parameter diagonal matrix for conditioning of the system matrix eigenvalues:

$$\Gamma = \mathrm{diag}\begin{bmatrix} 1 & 1 & 1 & 1 & \beta \end{bmatrix} \tag{3}$$

where β is M_r^2 (reference Mach number) unless $M_r > 1$, in which case $\beta = 1$. This leads to a low-cost implementation of the algorithm that is an effective convergence accelerator that converges favorably regardless of the local flow speed. Thus, simulation domains that contain regions of high-speed and low-speed flow are particularly well treated by this algorithm. The algorithmic approach has been validated for a range of problems, from simple to complex geometries and from low ($M = 0.001$, incompressible) to high (supersonic) speed flows [14-9]. Above $M = 1$, this algorithm behaves exactly as a conservative compressible flow solver with solution variables in the primitive form. A flux limiter was employed to handle strong discontinuities and prevent overshoots in flow variables.

14.4.2   Iteration Hierarchy

The time evolution algorithm uses Newton iterations to remove time linearization error in the unsteady terms. The time evolution algorithm is implicit, such that a linear system of equations is solved at each Newton iteration. The solution of the linear system is obtained via a Symmetric Gauss Seidel algorithm (point relaxation) that has been used successfully and extensively [14-8].

14.4.3   Parallel Solver

The parallel solution procedure consists of a scalable solution algorithm implemented to run efficiently on grid sub-domains distributed across multiple processes and communicating through MPI. The algorithm has multiple nested kernels viz. time step, Newton iteration, LU/SGS iteration etc., and the sub-domain coupling is at the innermost level, i.e., in the solution of the linear system. A block-Jacobi type updating of the sub-domain boundaries ensures efficient parallelization with a small incremental cost incurred in terms of sub-iterations required to recover the convergence rate of the sequential algorithm. The solutions obtained in this study were partitioned over as few as 48 and as many as 200 processors. The full model solutions used 200 processors.

14.4.4   Turbulence Modeling

The current SimCenter flow solvers have a wide range of turbulence models including the one equation Spalart-Almaras and Menter-SAS models, the two equation q-ω and k-ε/k-ω models. The Spalart-Almaras turbulence model was initially used in this study. After a brief numerical study for the first test case comparing the results from using the various turbulence models, the two equations q-ω and k-ε/k-ω model was selected for use in the remaining cases in this study.

14.5   FLIGHT CONDITIONS AND ENGINE PARAMETERS

The details of the Flight Conditions (FC) of interest are given in Table 14-1 and the associated engine conditions are given in Table 14-2. These cover a range of Mach numbers from subsonic to transonic, angles of attack, α, up to ~20°, sideslips, β, ranging from ~-5° to ~5°, and Reynolds numbers up to ~89 million. For actual values of $\beta < 1°$, the computations were made at a $\beta_{nom} = 0°$. The first four FCs listed were those that all participants agreed to compute for comparison with the published results [14-1]. The other three were added to facilitate

comparisons either at a higher value of α or at the actual β value, nominally ±5°. Of course, solutions at these larger β values require full configuration modeling.

Table 14-1: Seven Flight Conditions Examined

Flight Condition	Actual Mach No.	Actual α	Actual β	Actual Reynolds No.
FC7	0.304	11.89	-0.133	44.4E+06
FC19	0.36	11.85	+0.612	46.8E+06
FC46	0.527	10.4	+0.684	46.9E+06
FC70	0.97	4.37	+0.310	88.77E+06
FC25	0.242	19.84	0.725	32.22E+06
FC50	0.434	13.56	+5.31	39.41E+06
FC51	0.441	12.89	-4.58	38.95E+06

Table 14-2: Associated Engine Parameters* for these Flight Conditions

Flight Condition	Free Stream Altitude, ft.	Free Stream Mach	Inlet Duct Exit Static Temp., degs. R	Inlet Duct Exit Static Press., psia	Inlet Duct Exit Velocity, ft/sec	Inlet Duct Exit Mach	Mixing Plane Total Temp., degs. R	Mixing Plane Total Press., psia
FC7	5000	0.304	498	11	379.6	0.347	1050	23
FC19	10000	0.36	485.8	10.2	345.8	0.32	1050	21.5
FC46	24000	0.527	443.6	5.85	404.3	0.39	1045	14.8
FC70	22300	0.97	519	10.65	464.7	0.416	1200	30
FC25	10000	0.242	470.1	8.72	474.8	0.447	1209	26.3
FC50	24000	0.434	440	5.16	483.3	0.47	1154	16.95
FC51	24000	0.441	431.8	5.19	468.6	0.46	1146	16.74

 * The numbers in this table do not represent any particular engine.

14.6   RESULTS

Solutions for the four required cases and three optional cases are presented in this section. The results are compared with surface pressure coefficient data, when available. All three-dimensional flowfield images in this paper were created using Fieldview [14-10]. All two-dimensional plots were created using Tecplot 360 [14-11].

14.6.1   Adapted Mesh

Solutions for many of the flight conditions were computed on the viscous mesh described in Section 14.3.3 Comparisons with the available flight test data were made with mostly very good results. However, in many of the cases the comparisons at the outboard span stations did not agree well with the data. The suction peaks were too close to the wing leading edge. Various turbulence models were used to determine if the physical modeling had an effect on the result. The pressure coefficient comparison for 4 different turbulence-modeling options is shown in Figure 14-7. The case labeled Turb 1 used the Spalart-Allmaras turbulence model. The case labeled Turb 2 used the one equation Menter SAS model. Turb 5 is a two-equation, q-ω, k-ε/k-ω model hybrid. And Turb 5 DES combines the two equation model with a Detached Eddy Simulation model, requiring unsteady flowfield analysis. No significant improvement was observed with any of the turbulence models. It appeared as though the vortex was traveling more outboard than the data showed, so the mesh resolution in the outboard region was examined.
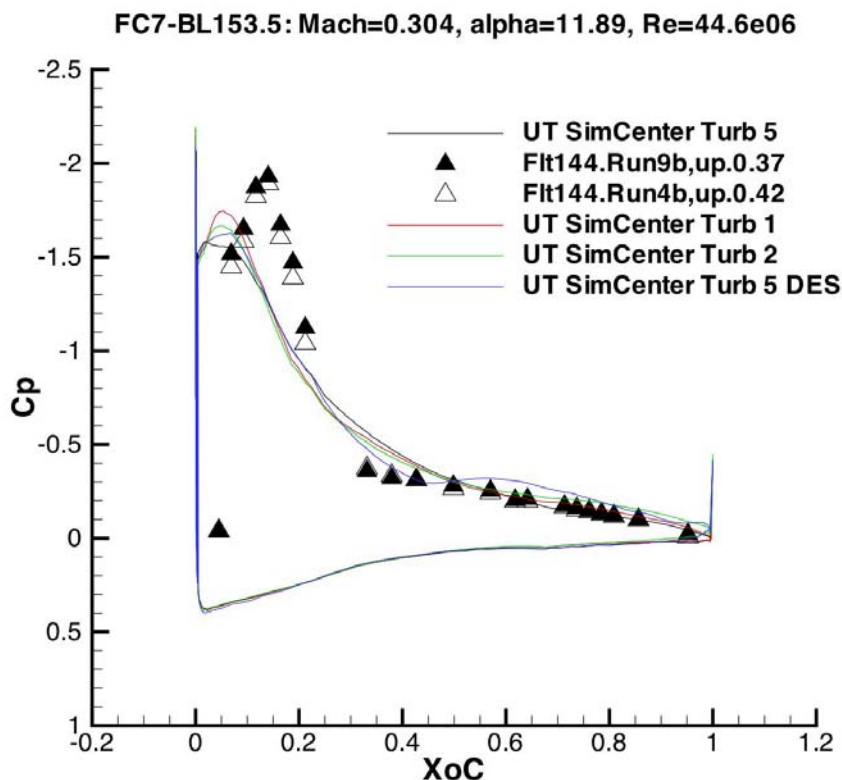
**Figure 14-7: Various Turbulence Modeling Options did not Significantly
Improve the Comparison at the Outboard Span Station.**

A new mesh was created that increased the resolution in the vicinity of the expected trajectory of the vortex. This mesh adaptation was performed manually within the described meshing process and did not involve any solution-based mesh refinement. The original mesh and new mesh for the top wing surface at the outboard stations can be seen in Figure 14-8 and Figure 14-9, respectively. The increased resolution is readily apparent in the image of the new mesh. This mesh was subsequently used with the two-equation turbulence model to re-compute all flight conditions. All results presented below used this enhanced mesh in the calculations. The new half-model, viscous mesh contained 13,906,708 points, 32,395,936 tetrahedra, 166,230 pyramid, 15,770,674 prisms and 352,656 hexahedra. One mesh was used for all cases analyzed in this study. Mirror-copying the half-model mesh about the symmetry plane created the mesh for the full configuration cases. Time and resource limitations prevented a grid convergence study.
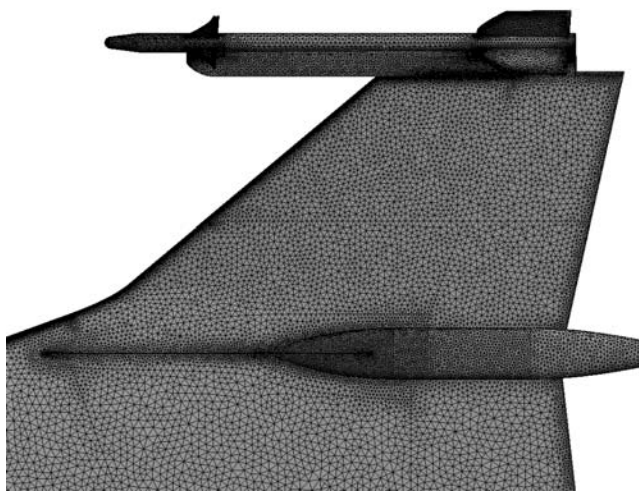
Figure 14-8: Top View of Original Surface Mesh at Outboard Wing Section.
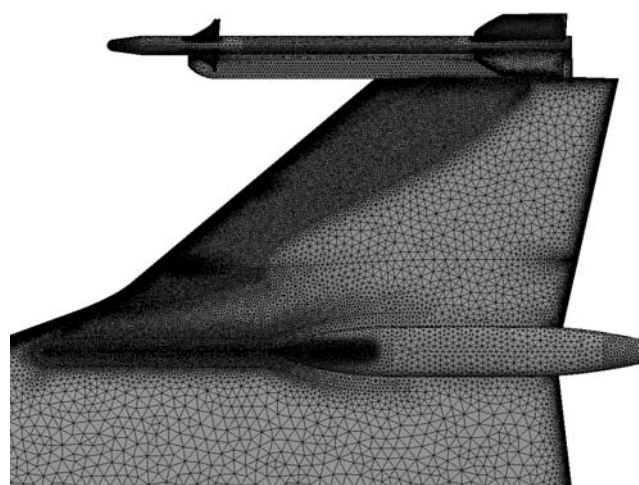
Figure 14-9: Top View of Adapted Surface Mesh at Outboard Wing Section.

14.6.2 Surface Pressure Coefficient Comparisons for All Flight Conditions

Surface pressure coefficient comparisons for span-wise stations and axial stations for all flight conditions are shown in Figure 14-10 through Figure 14-23. Each figure includes an image of the aircraft in the top of the figure to show the physical location of the various span stations or axial stations. The computed CFD solutions using the UT SimCenter solver are shown in solid lines. The flight test data is shown as filled and unfilled triangular symbols. The horizontal axes on the plots are normalized axial coordinate, X/C, from the leading edge for the span-wise station plots and normalized span-wise coordinate, Y/C, for the axial station plots. The vertical axes are the negative pressure coefficient. Some observations are provided in the following paragraphs.
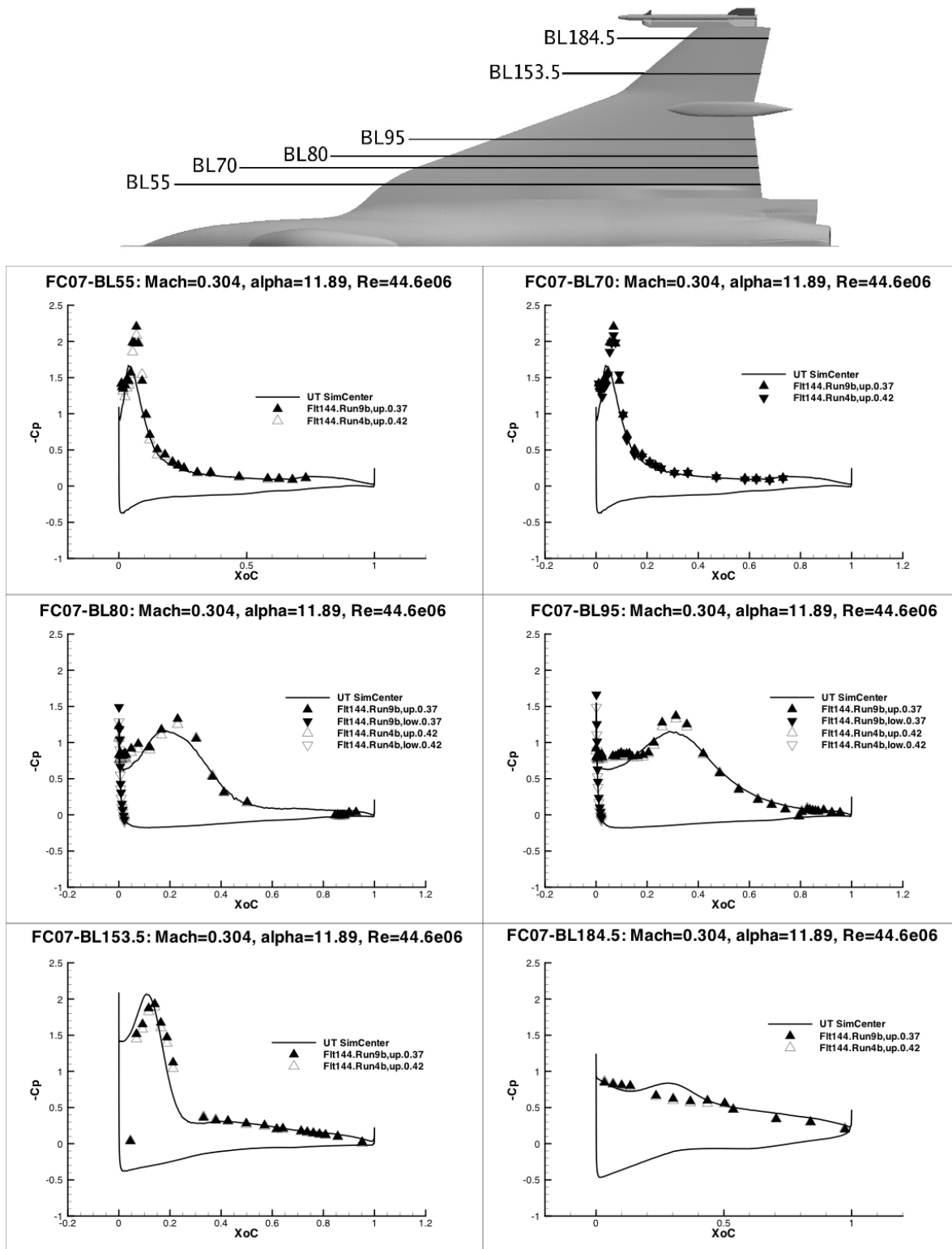
Figure 14-10: FC7 Surface Pressure Coefficient Comparisons for Span-Wise Stations.
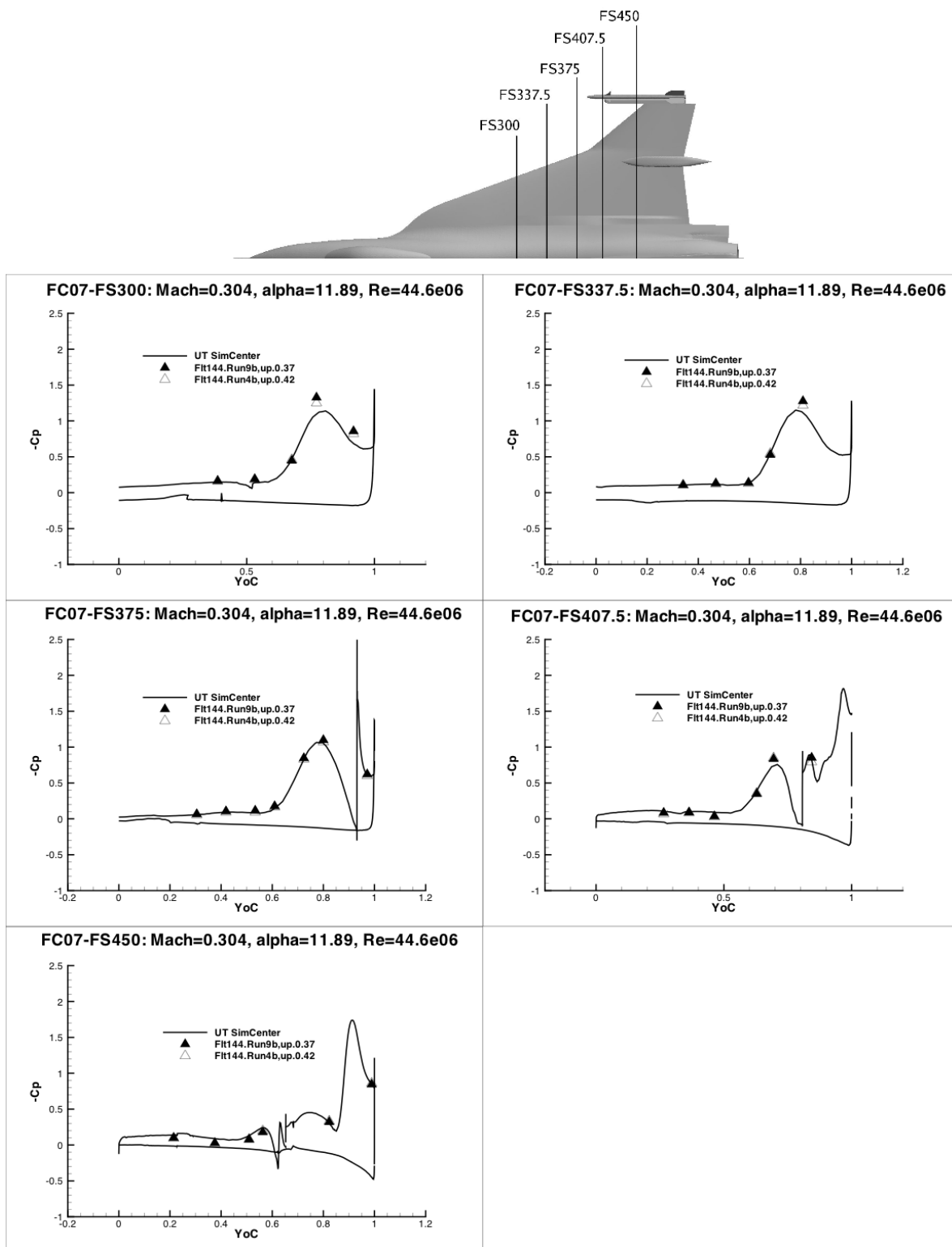
Figure 14-11: FC7 Surface Pressure Coefficient Comparisons for Axial Stations.

The comparisons for flight condition 7 (FC7) show good agreement with the flight test data. A couple of noticeable discrepancies occur at the suction peak of the two inboard stations, BL55 and BL70, and the suction peak at station BL153.5. The computed suction peaks are a little lower and positioned forward, slightly. Flight condition 19 (FC19) is compared to the same flight test data in Figure 14-12 and Figure 14-13. The freestream conditions are very close for these two cases; Mach 0.304 and alpha of 11.89 for FC7 and Mach 0.36 and alpha of 11.85 for FC19. The flight test data is reportedly at a Mach number of 0.37 and an angle of attack of 13 degrees. This could explain the slightly better agreement obtained with FC19.
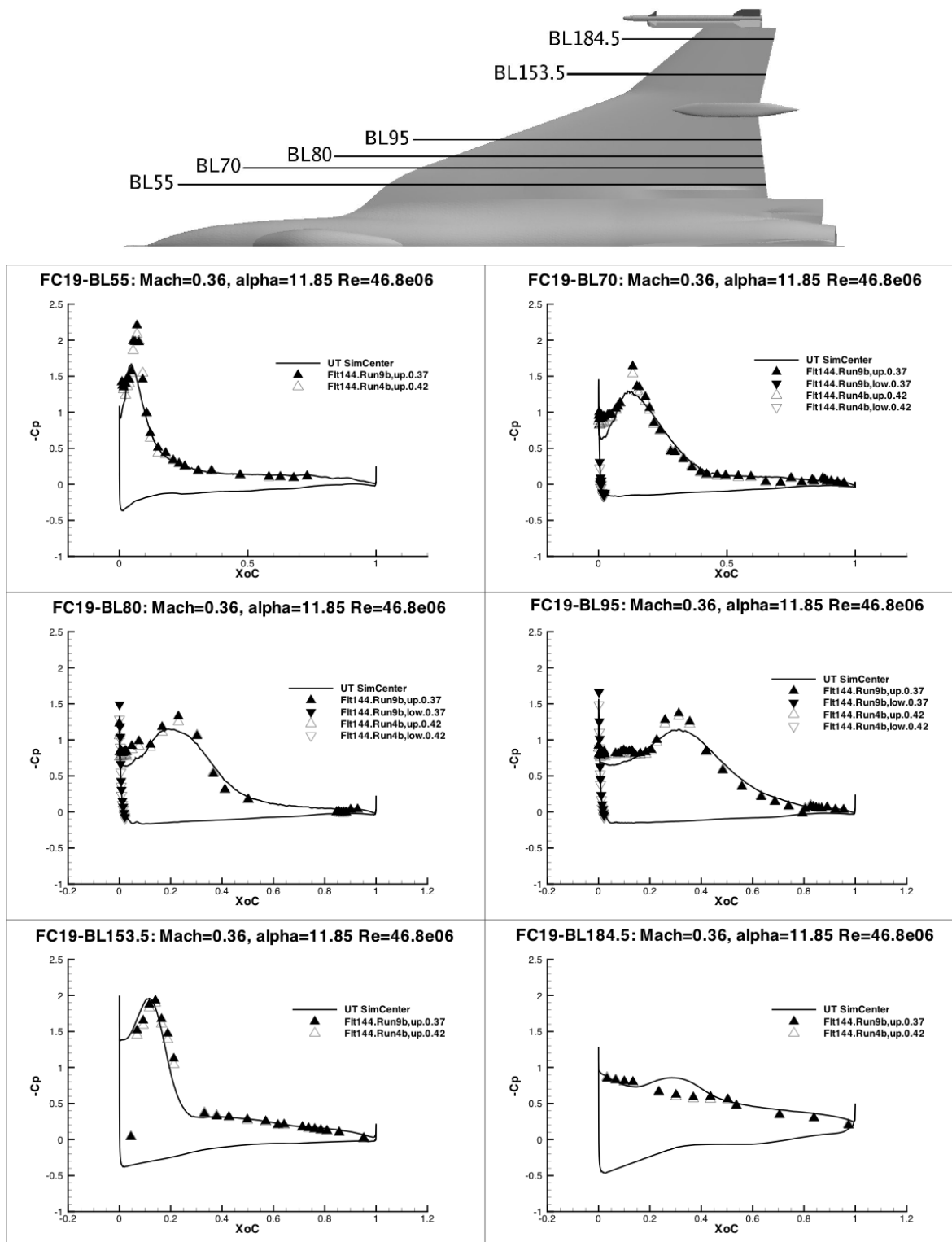
Figure 14-12: FC19 Surface Pressure Coefficient Comparisons for Span-Wise Stations.
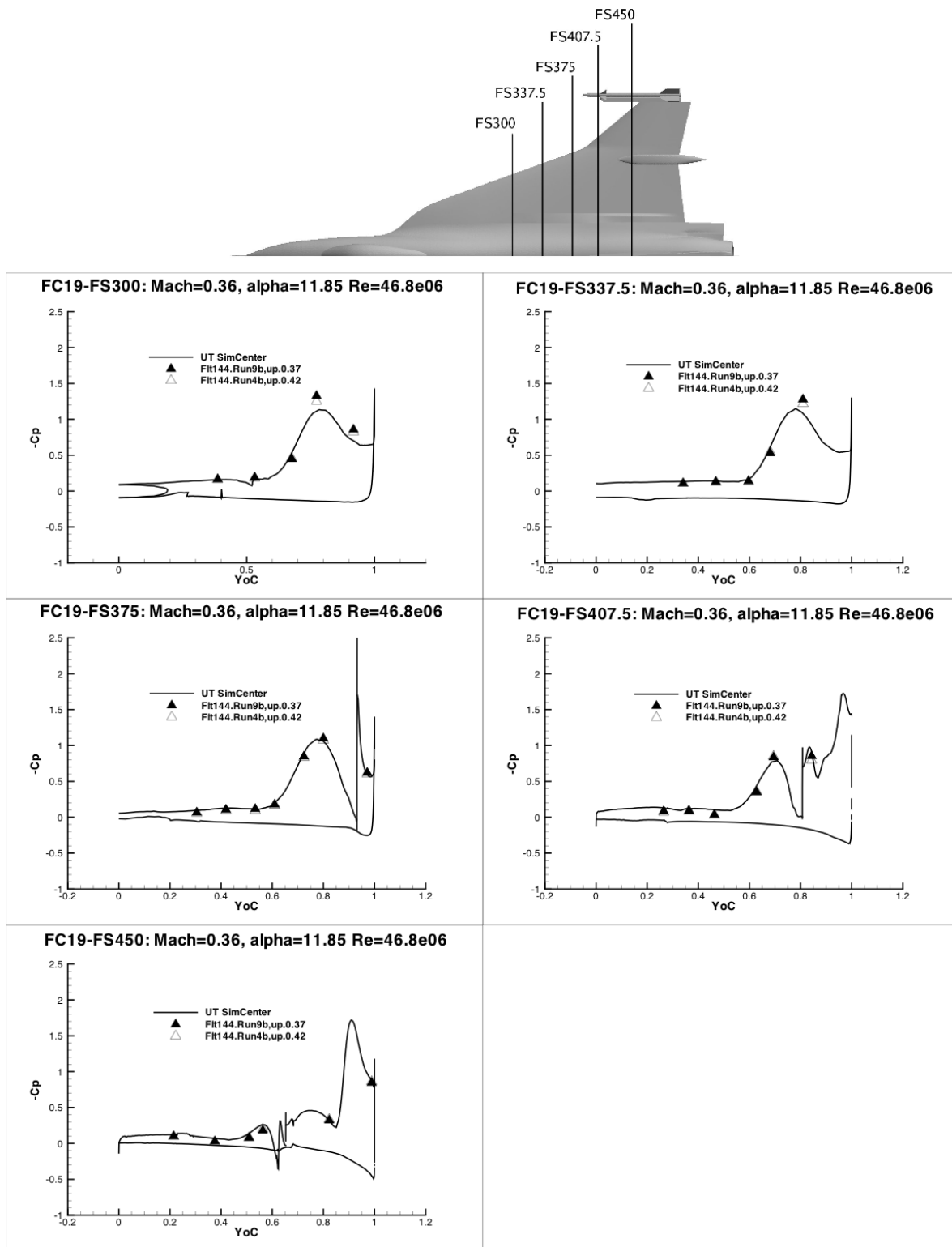
Figure 14-13: FC19 Surface Pressure Coefficient Comparisons for Axial Stations.

The comparisons for flight condition 46 (FC46), in Figure 14-14 and Figure 14-15 also show good agreement with the flight-test data; though span station 153.5 seems to show some differences between the computed solution and flight test results. The computed suction peak is slightly aft of the location in the flight-test data and is spread out more. The computed solution seems to show a larger (wider) vortex in this location. This is the first span station outboard of the air dam and was the focus of mesh adaptation mentioned in Section 14.6.1. It would seem from this plot that the adaptation caused the flow solver and turbulence model to over-compensate and spread the vortex out more. Although, this conjecture is not supported by the comparisons shown in the first two flight conditions or in other cases shown later.
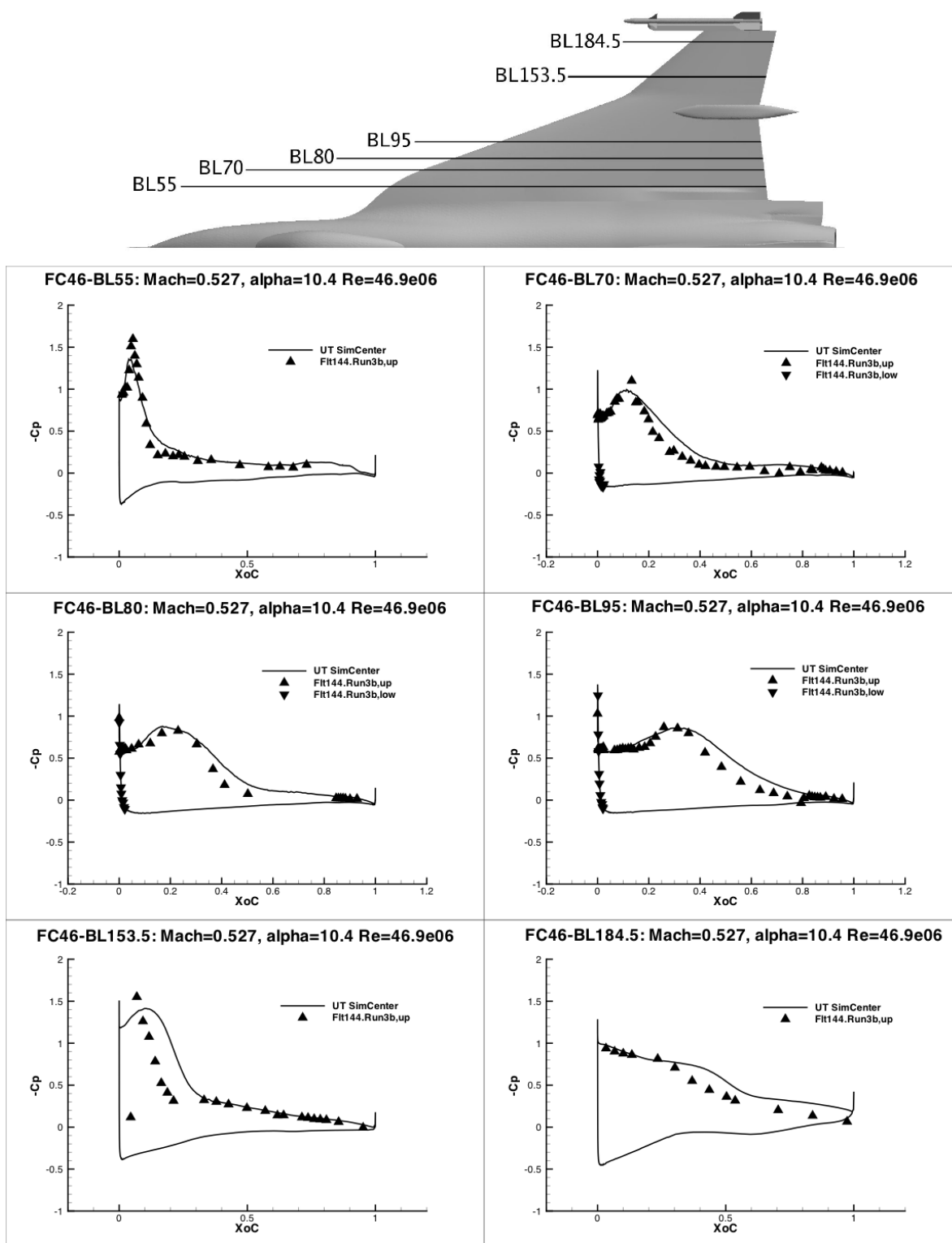
Figure 14-14: FC46 Surface Pressure Coefficient Comparisons for Span-Wise Stations.
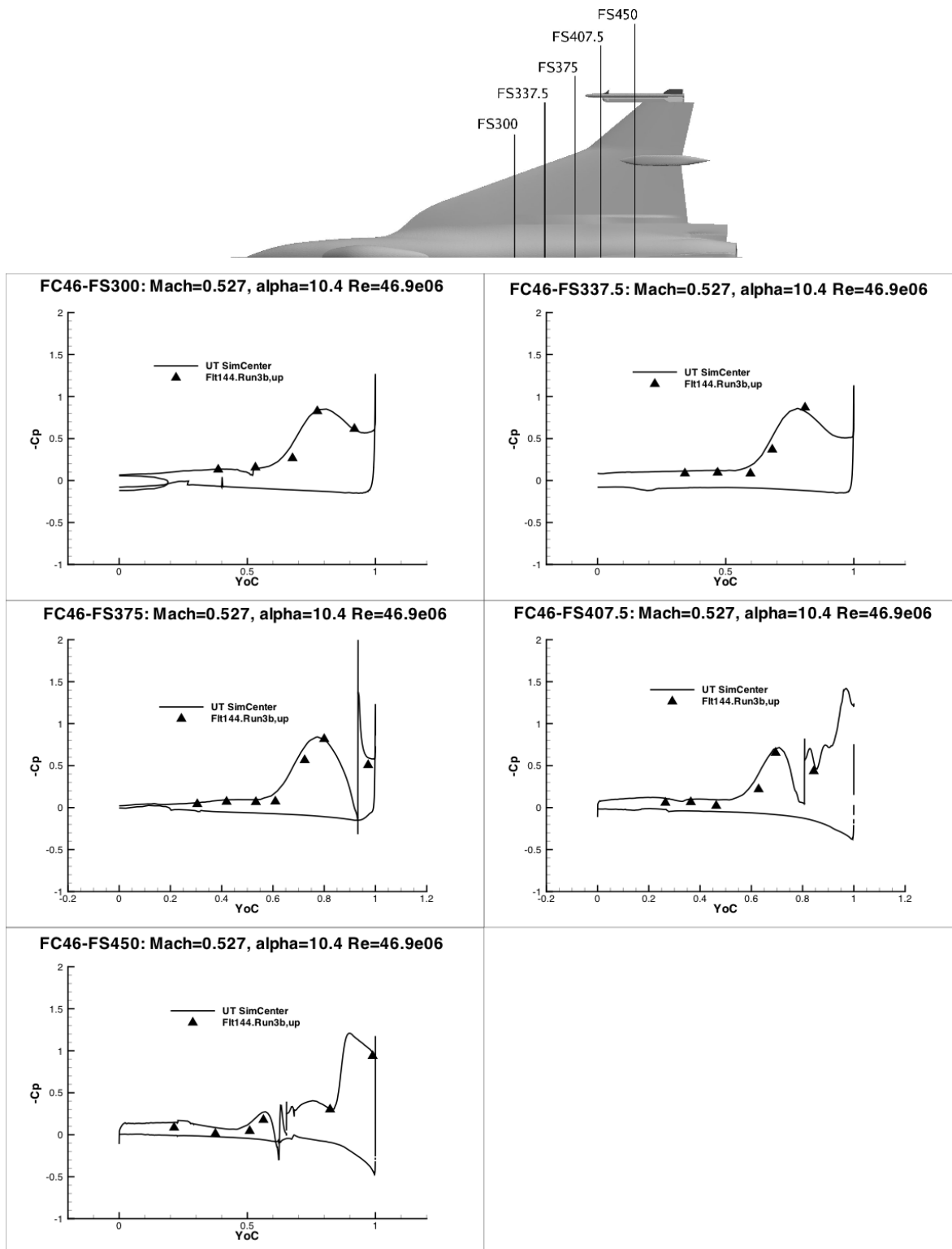
Figure 14-15: FC46 Surface Pressure Coefficient Comparisons for Axial Stations.

Comparisons for flight condition 70 (FC70), Figure 14-16 and Figure 14-17, show good agreement at span stations BL55 and BL95 and poor agreement elsewhere. After the case was computed, it was learned that the aircraft flight control system schedules the outboard leading edge flap between 5 and 9 degrees upward and the trailing edge flap about 2 degrees downward [14-1]. The geometry used to create the CFD model did not include leading or trailing edge flap deflections. The leading edge deflection could definitely impact the pressure distribution for the outboard stations. Lamar et al. in Reference [14-1] indicate that the small trailing edge deflection could also impact the pressure distribution and the shock location. So the differences at the two most outboard stations could be explained by neglecting to model the flap deflections. The differences at stations BL70 and BL80 cannot be explained by the flap deflections. From examining the flight test data between BL55 and BL95 it is hard to understand what physically takes place. These discrepancies also show up in the axial station plots for FS300, FS337.5 and FS375.
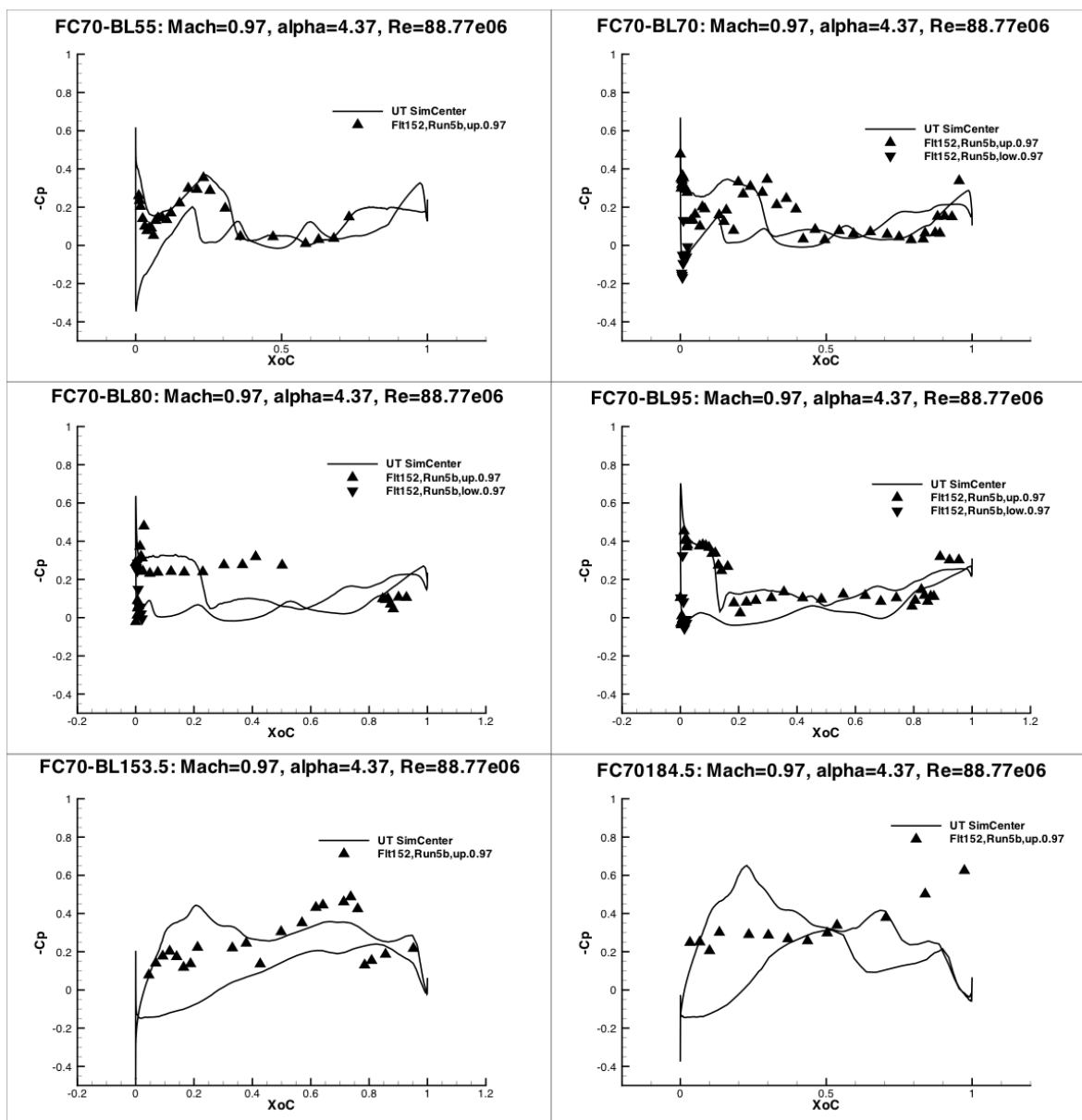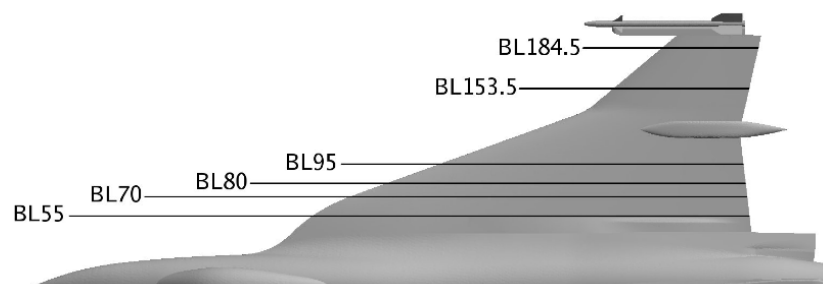
Figure 14-16: FC70 Surface Pressure Coefficient Comparisons for Span-Wise Stations.
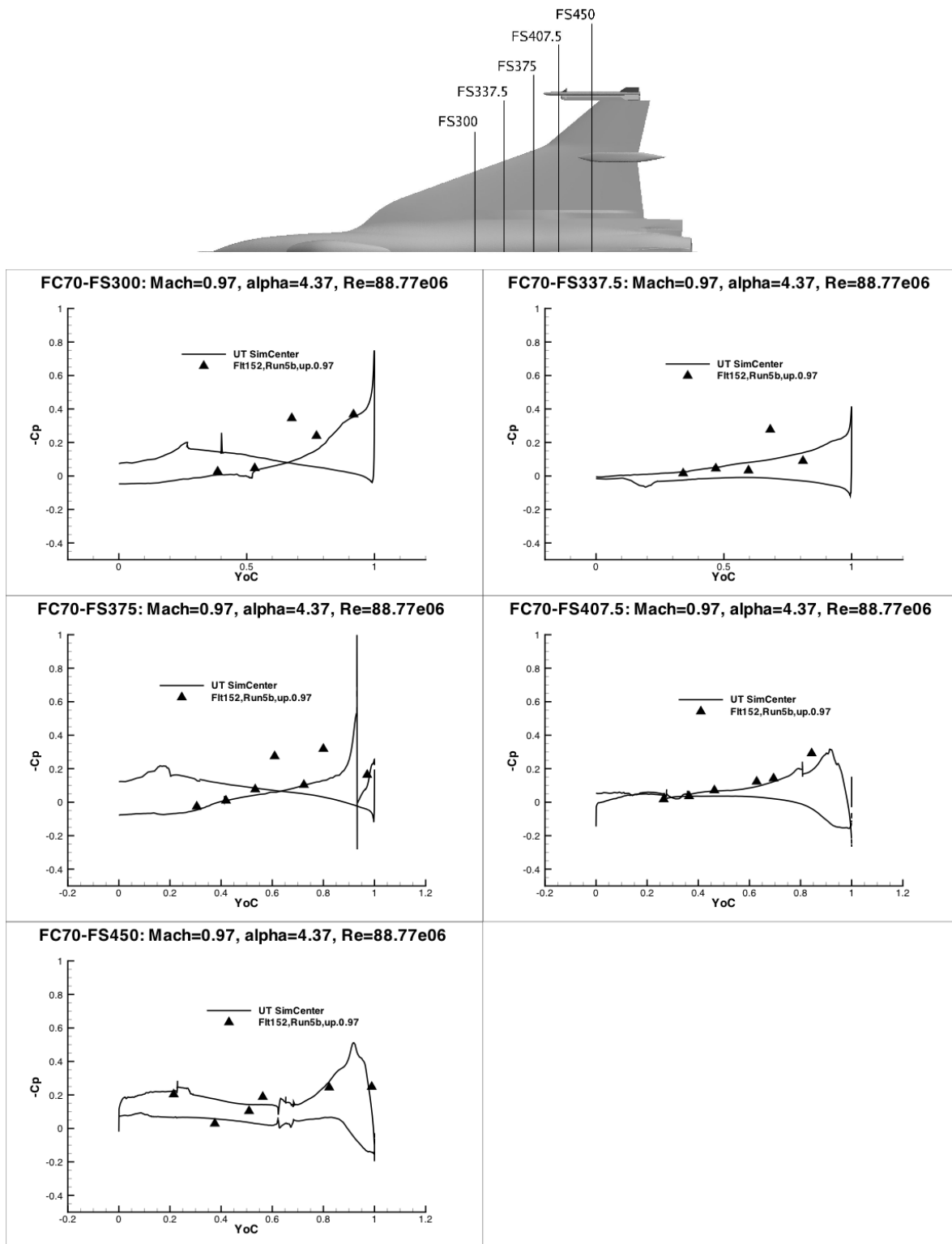
Figure 14-17: FC70 Surface Pressure Coefficient Comparisons for Axial Stations.

The first optional case is flight condition 25 (FC25), which is a subsonic Mach number at an angle of 19.84 degrees. The comparisons of the surface pressure coefficients are shown in Figure 14-18 and Figure 14-19. The computed solution agrees very well except at the last outboard *spa*n station. Since this is at a large angle of attack, it is reasonable to expect some unsteady flow. The last outboard station is close to the wing tip missile. Unsteady shedding of vortices from the missile is definitely possible. The integrated forces plotted versus iteration are shown in Figure 14-25. The X directed force seems to have leveled off, but the Y and Z directed forces are still oscillating after 8000 iterations. Unfortunately, the breakdown of forces on individual components of the aircraft was not computed, so it is hard to tell if the oscillations in the forces are emanating from the outboard location.
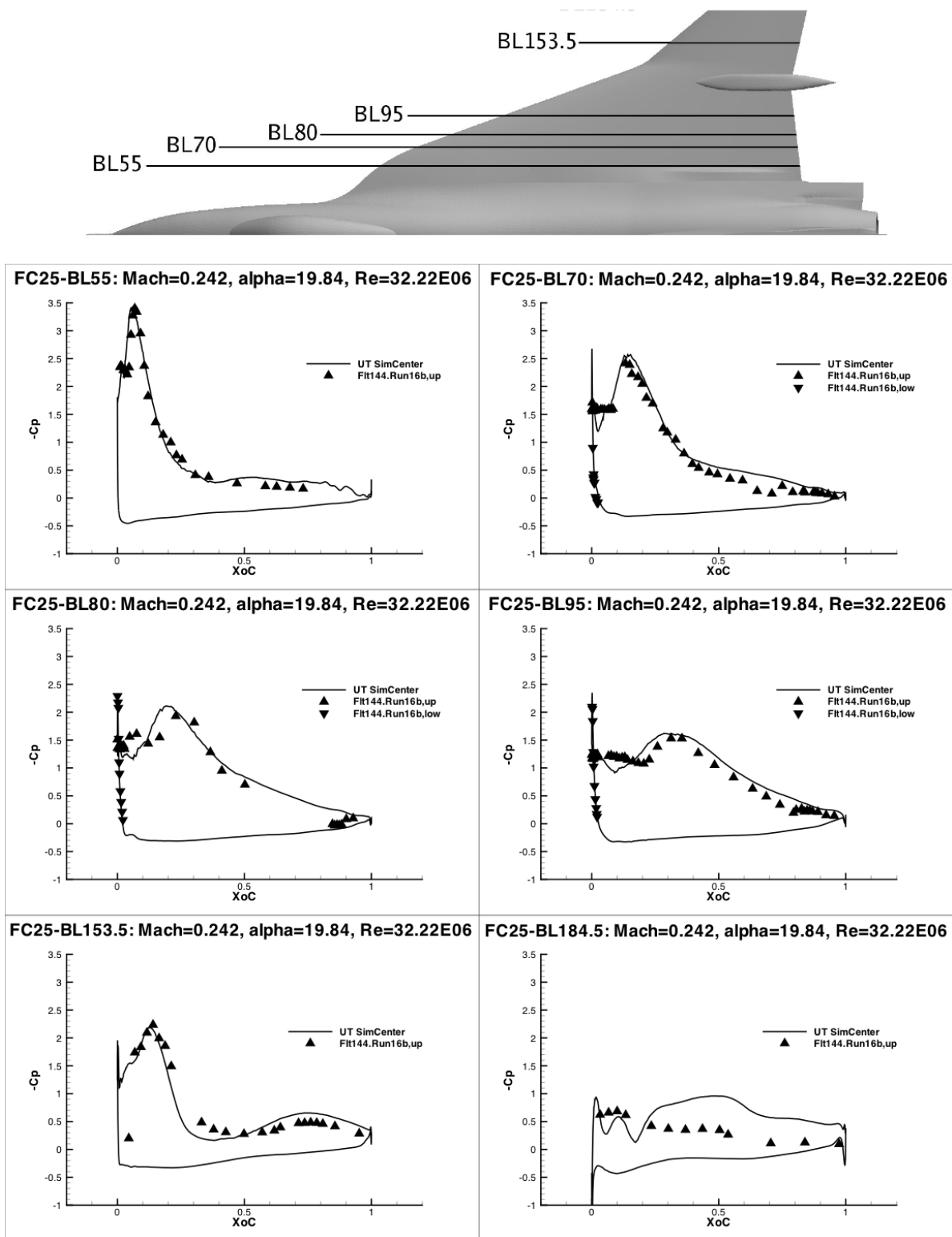
Figure 14-18: FC25 Surface Pressure Coefficient Comparisons for Span-Wise Stations.
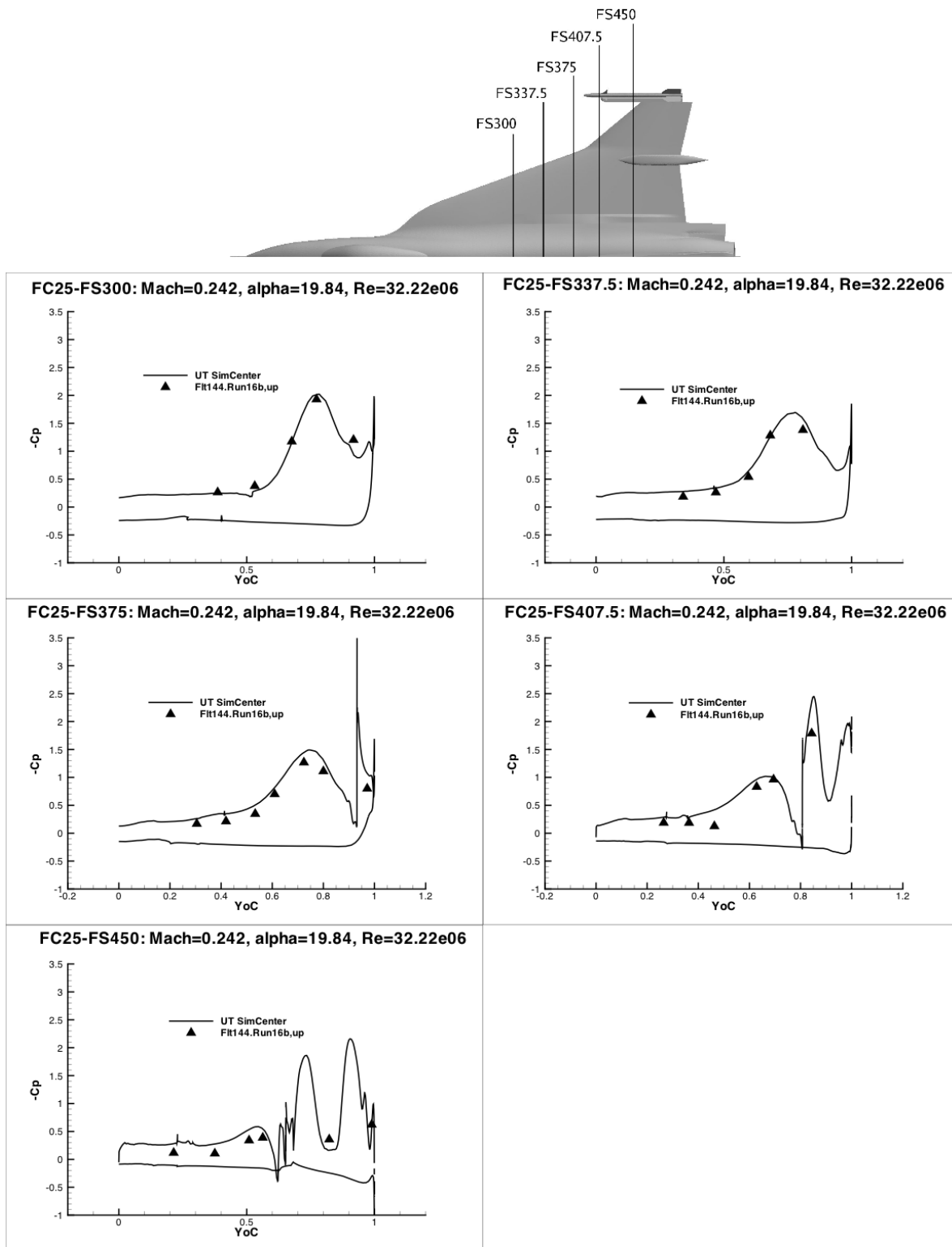
Figure 14-19: FC25 Surface Pressure Coefficient Comparisons for Axial Stations.

Flight condition 50 and 51 include positive and negative sideslip, respectively, so they require the use of a full span mesh. The half-span mesh used for all the previous cases was mirror-copied about the symmetry plane, creating a mesh with nearly 28 million points. These two cases were computed using 200 processors on a Linux cluster. Figure 14-20 and Figure 14-21 show the comparisons for flight condition 50, a positive sideslip of 5.31 degrees. The flight test data is listed as nominally +5 degrees. The computed results on the right side agree reasonably well with flight-test data. No flight test data was taken for the left side. Figure 14-22 and Figure 14-23 show the comparisons for flight condition 51, an input sideslip of -4.58 degrees.
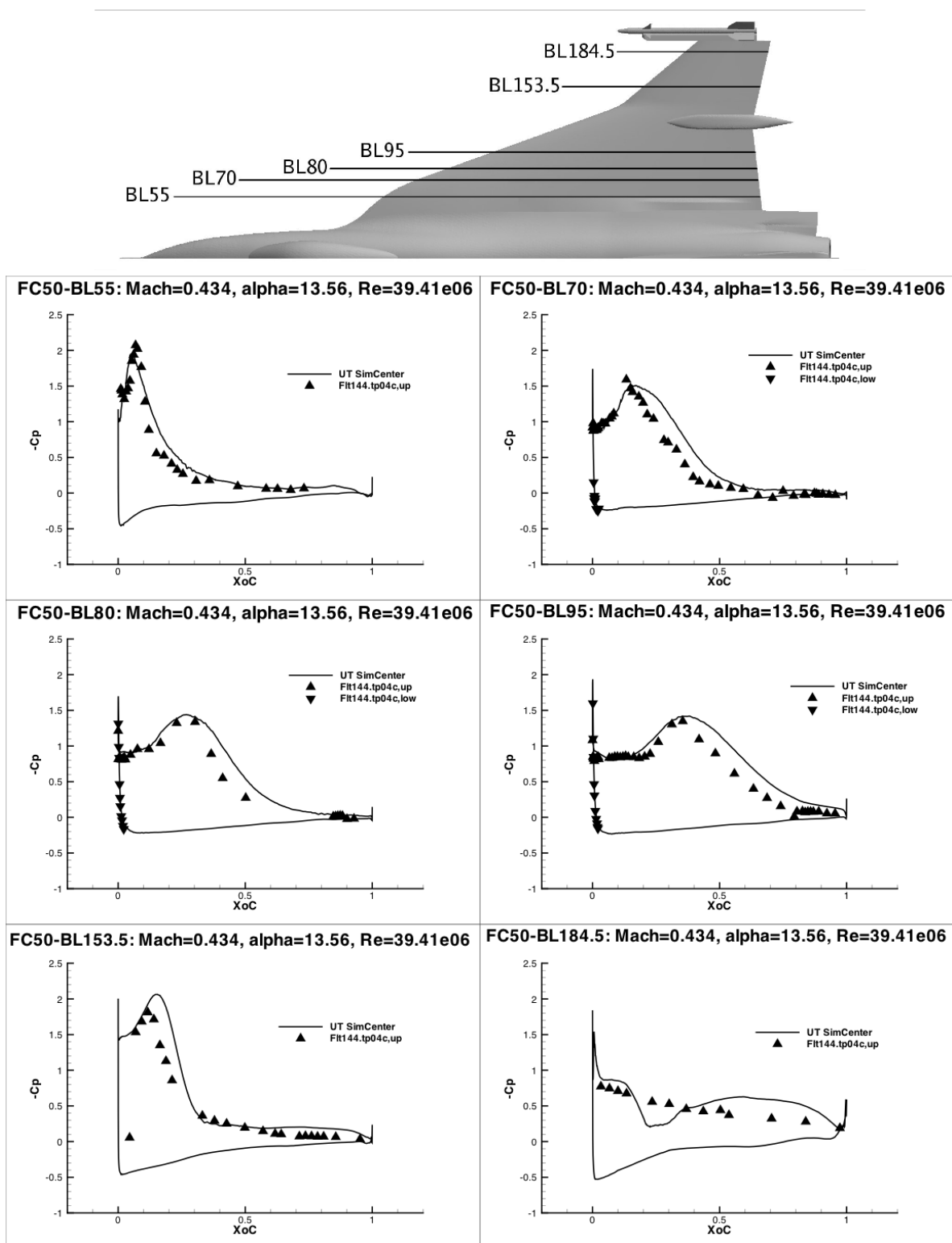
Figure 14-20: FC50 Surface Pressure Coefficient Comparisons for Span-Wise Stations.
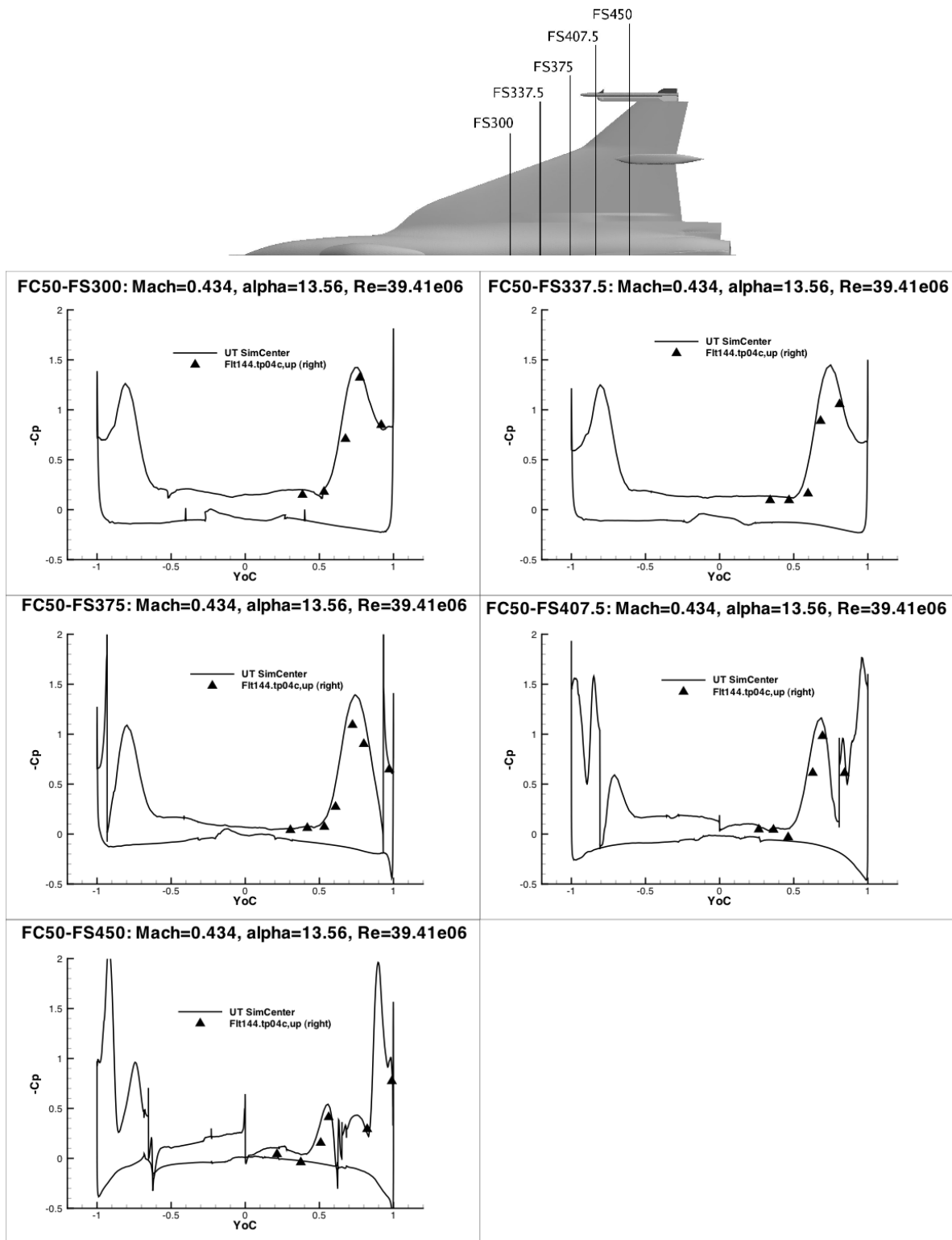
Figure 14-21: FC50 Surface Pressure Coefficient Comparisons for Axial Stations.
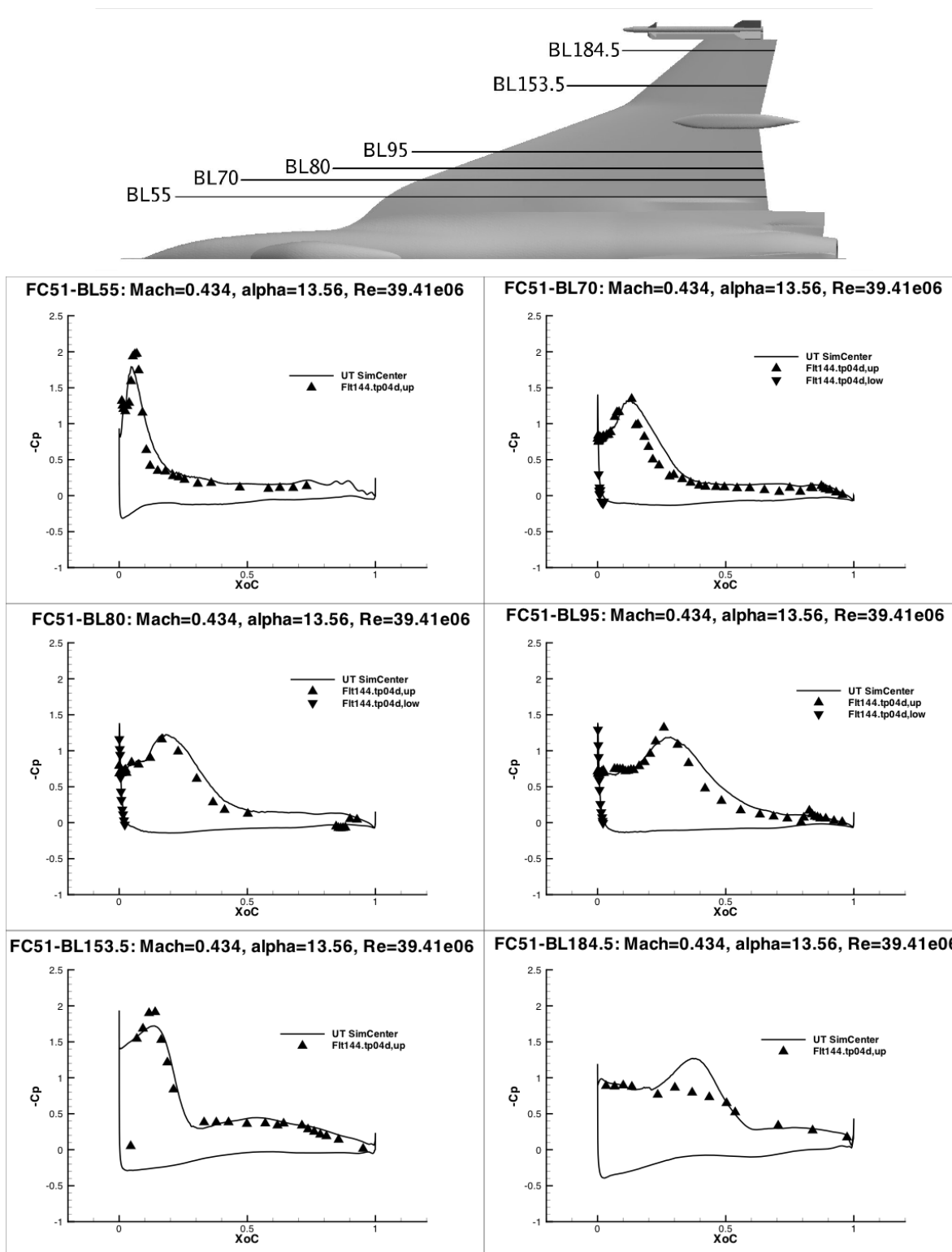
Figure 14-22: FC51 Surface Pressure Coefficient Comparisons for Span-Wise Stations.
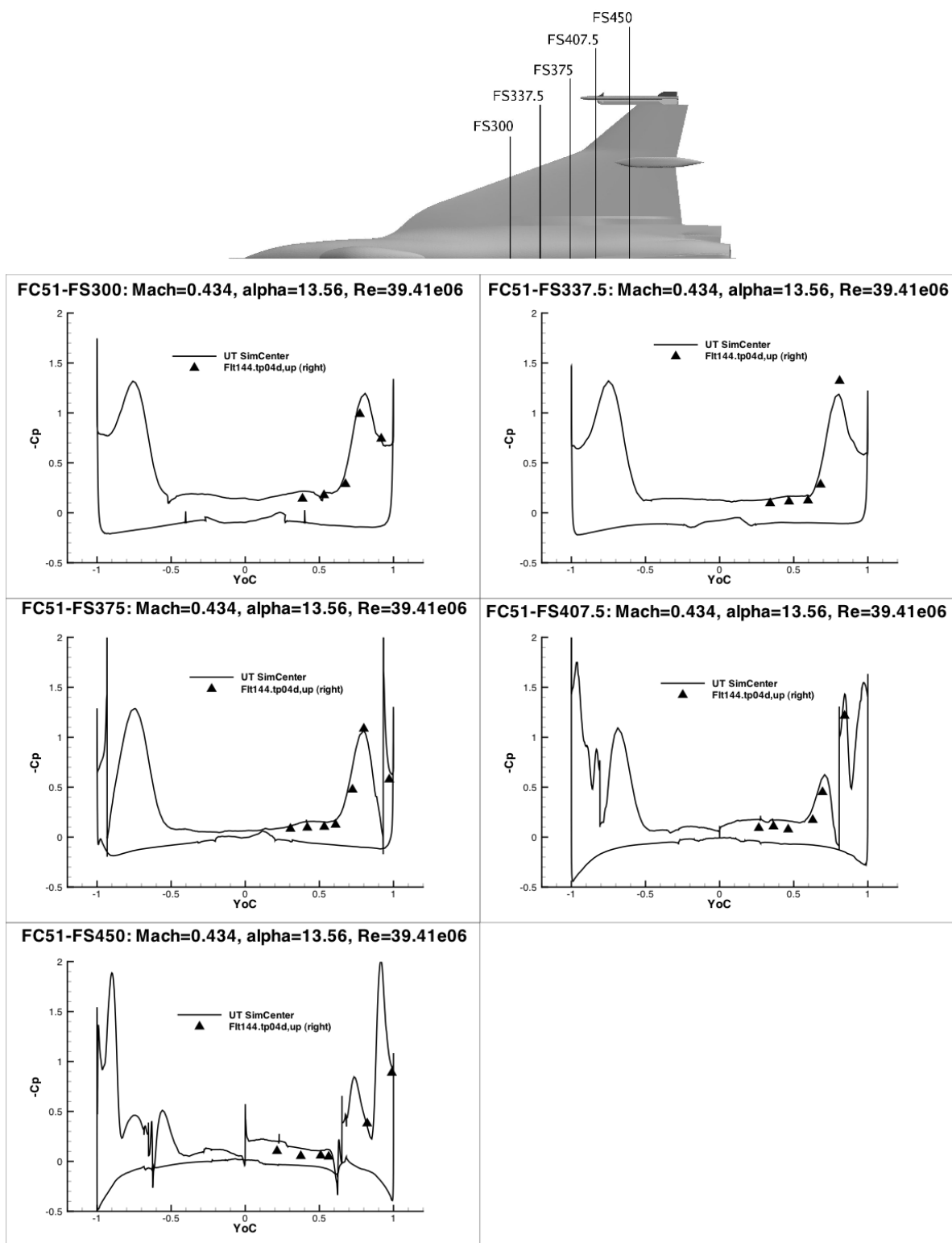
Figure 14-23: FC51 Surface Pressure Coefficient Comparisons for Axial Stations.

14.6.3   Selected Convergence Plots

Convergence histories for residual and integrated forces for selected cases are presented below. Only some of the cases are included to conserve space. The residual histories are shown to indicate the typical behavior seen with the use of the limiter. Figure 14-24 shows the residual history for case FC07. The flow solver was run with first order special accuracy for the first 2000 iterations. Then second order fluxes were used, but with a flux limiter. The residual exhibited an oscillatory behavior due to the flux limiter switching between first and second order accuracy. The main location where this switching took place was at the nozzle exit where the geometry was modeled with an aft facing base region. The flow attempts to accelerate around the sharp corner, but the limiter prevents overshoots and undershoots in flow variables by switching back to first order. The cell location where the switching takes place oscillates between mesh points. As a result of this oscillatory behavior, residual histories were not used to determine level of convergence of any of the cases.
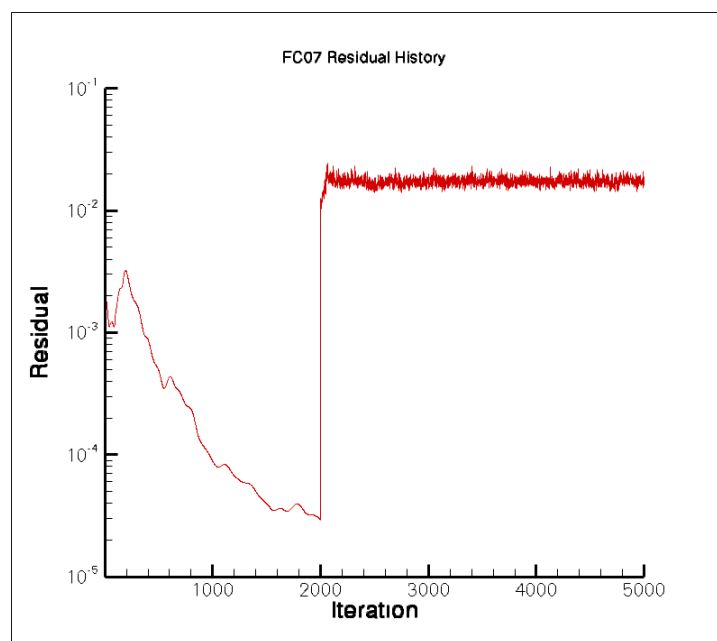
Figure 14-24: Residual History for Case FC07.

The force histories were used to track solution convergence. Most of the cases reached a steady state solution where all of the forces reached asymptotic values. Some cases exhibited an oscillatory behavior in one or more of the forces, indicating a tendency for unsteadiness in the solution. Figure 14-25 shows the oscillatory behavior in the Y & Z directed forces for case FC25, even after 8000 iterations. This is the high angle of attack case at subsonic speeds, so unsteadiness is reasonable. Judging from the pressure coefficient plots in Figure 14-18; the unsteadiness probably takes place at the outboard wing stations.
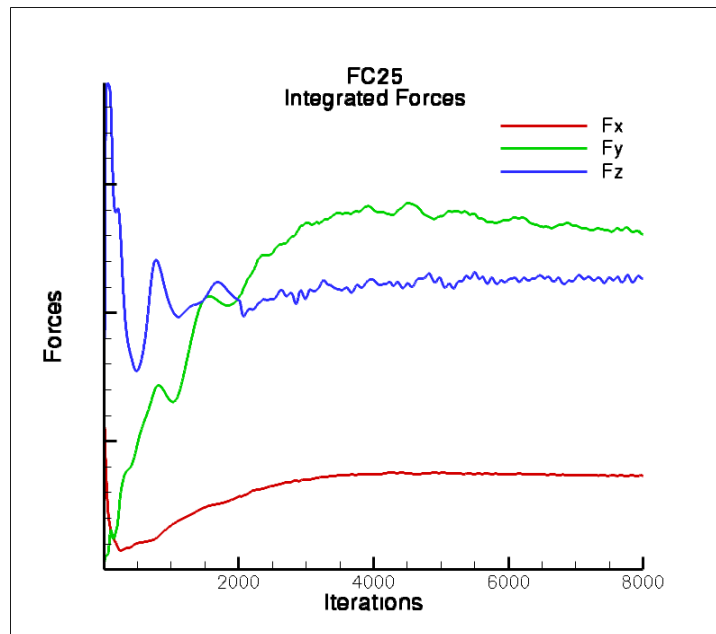
Figure 14-25: Integrated Forces Convergence History for Case FC25.

Other flight conditions did achieve a satisfactory level of convergence in the force histories. Figure 14-26 shows the convergence of the integrated forces for case FC51, a full configuration, sideslip case. The angle of attack is in the moderate range and the solution appears to be steady. All three forces show a steady behavior after 5000 iterations. Other flight conditions behaved in a similar manner.
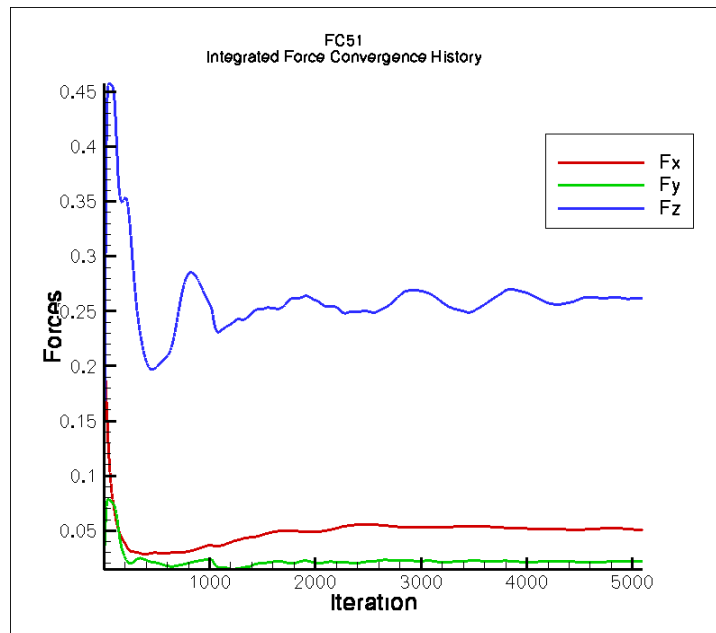
Figure 14-26: Integrated Forces Convergence History for Case FC51.

14.6.4   Field and Surface Color Contour Plots

Flowfield and surface color contours are shown in the next series of figures for selected flight conditions. Figure 14-27 shows color contours of pressure coefficient for flight condition FC07. This was a zero sideslip case that was computed using a half-span mesh. The solution was mirrored in the post-processing program, Fieldview, to make the plots [14-10]. Figure 14-28 shows color contours of vorticity magnitude for the same flight condition at various fuselage stations. Not all magnitudes of vorticity are shown; lower and higher values of vorticity magnitude are clipped from view.
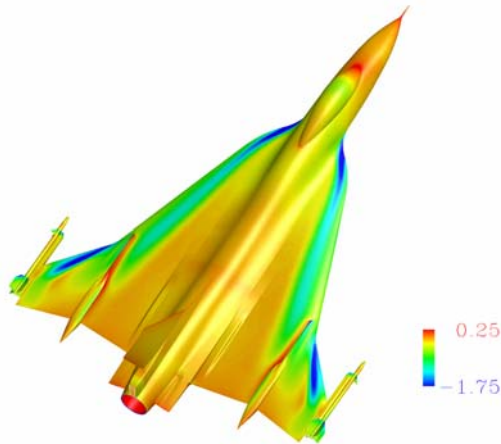
**Figure 14-27: Surface Pressure Coefficient
Color Contours for Case FC07.**
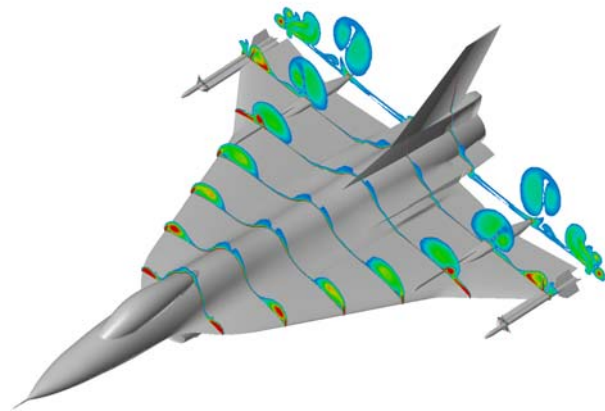
**Figure 14-28: Axial Station Cuts of Contours
of Vorticity Magnitude for Case FC07.**

The same plots are made for case FC25, the high angle of attack case, in Figure 14-29 and Figure 14-30. The color contour levels are the same as shown in the figures for case FC07. The stronger vortices are evident in the deeper blue surface C_p contours and the larger regions of red and green in the vorticity magnitude plots. Both cases exhibit a strong vortex emanating from the leading edge of the wing. The primary vortex in case FC07 stays closer to the surface as it passes the airdam. The two red regions outboard of the airdam near the leading edge are counter-rotating vortices, one originating at the airdam and rotating outward and the other originating at the wing leading edge and rotating inward.
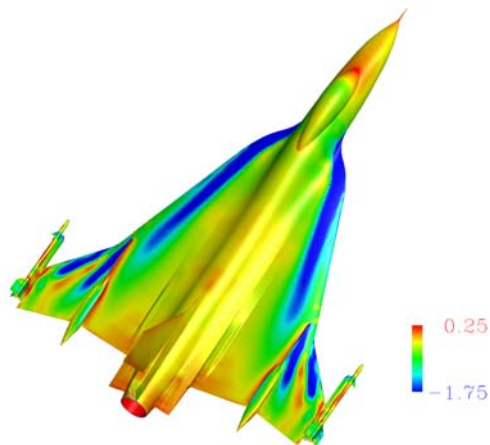
**Figure 14-29: Surface Pressure Coefficient
Color Contours for Case FC25.**
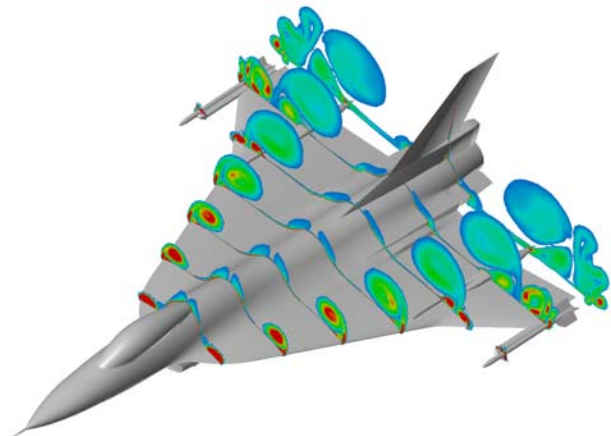
**Figure 14-30: Axial Station Cuts of Contours
of Vorticity Magnitude for Case FC25.**

Case FC70 is the transonic case at a small angle of attack. A plot of the sonic surface is shown in Figure 14-31. The region inside this surface is supersonic flow. This demonstrates the complicated system of shocks and acceleration as the air flows over the top surface of the aircraft. The shock diamond pattern emanating from the nozzle is also visible.
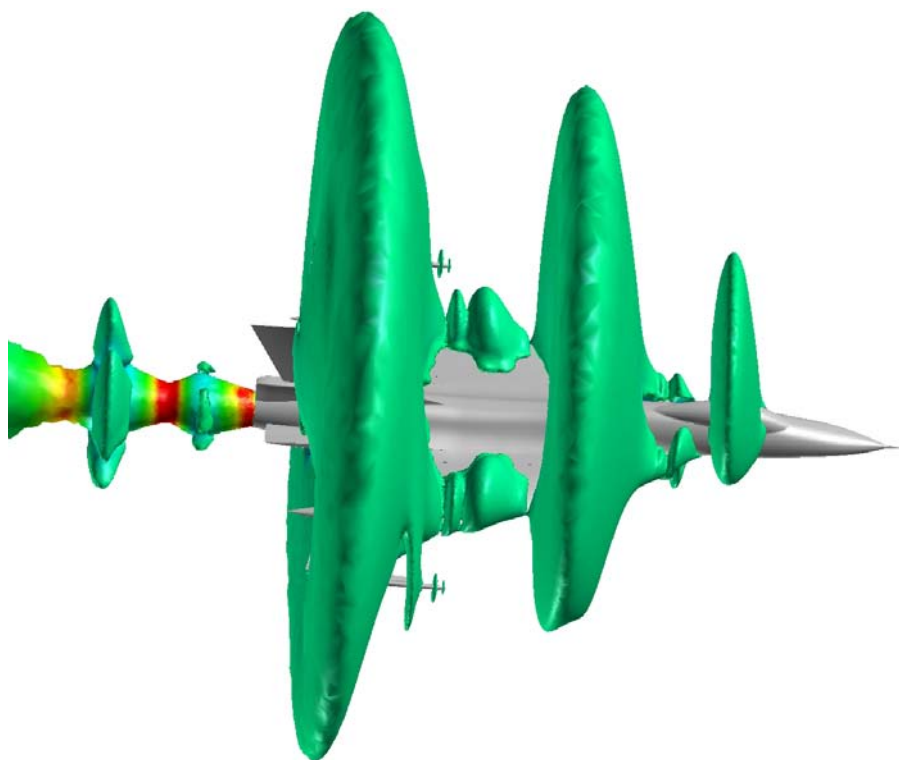
Figure 14-31: Case FC70 Sonic Surface Colored by Pressure.

Figure 14-32 shows the surface pressure coefficient color contours for cases FC50 and FC51. These are the two sideslip cases, so the full span mesh was used to compute the solutions. The color contour levels are the same for both images. FC50 had a positive sideslip angle of 5.31 degrees. The freestream vector impacts the aircraft from the right side. The paths of the leading edge vortices are shifted toward the left side of the aircraft, as shown in the top portion of the figure. FC51 had a negative sideslip angle of 4.58 degrees. The freestream vector impacts the left side of the aircraft, so the leading edges vortices are shifted toward the right side of the aircraft, shown in the bottom portion of the figure.
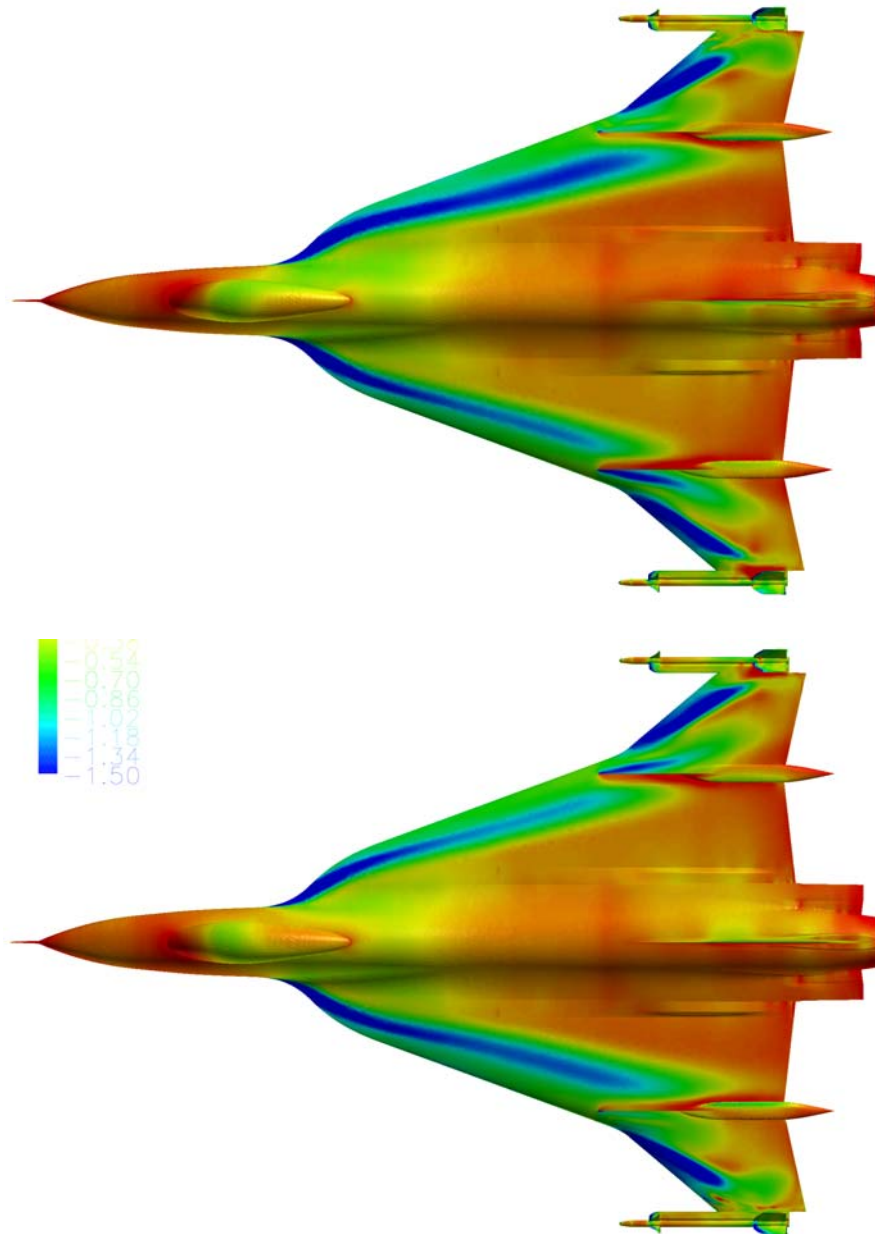
**Figure 14-32: Surface Pressure Coefficient Contours for FC50 (top)
and FC51 (bottom) with Color Range for C_p Values from -1.5 to 0.1.**

The path of the vortices is readily apparent in Figure 14-33. This plot shows color contours of vorticity at the axial stations where the experimental data was taken. These contours include the negative and positive magnitudes. From this view perspective negative values are counter-clockwise rotating vortices and positive values are clockwise rotating vortices. Also include in the plot are streamlines showing the paths of the vortices. These streamlines were generated in Fieldview by releasing particles at selected locations on the vorticity contours and allowed to flow forward and backward. The streamlines are colored by the local static pressure, blue being low pressure and read being high pressure. The sideslip angle is evident in the path the streamlines take approaching the leading edge of the wing and travel over the top side of the fuselage, as they cross from the right side of the aircraft to the left side.
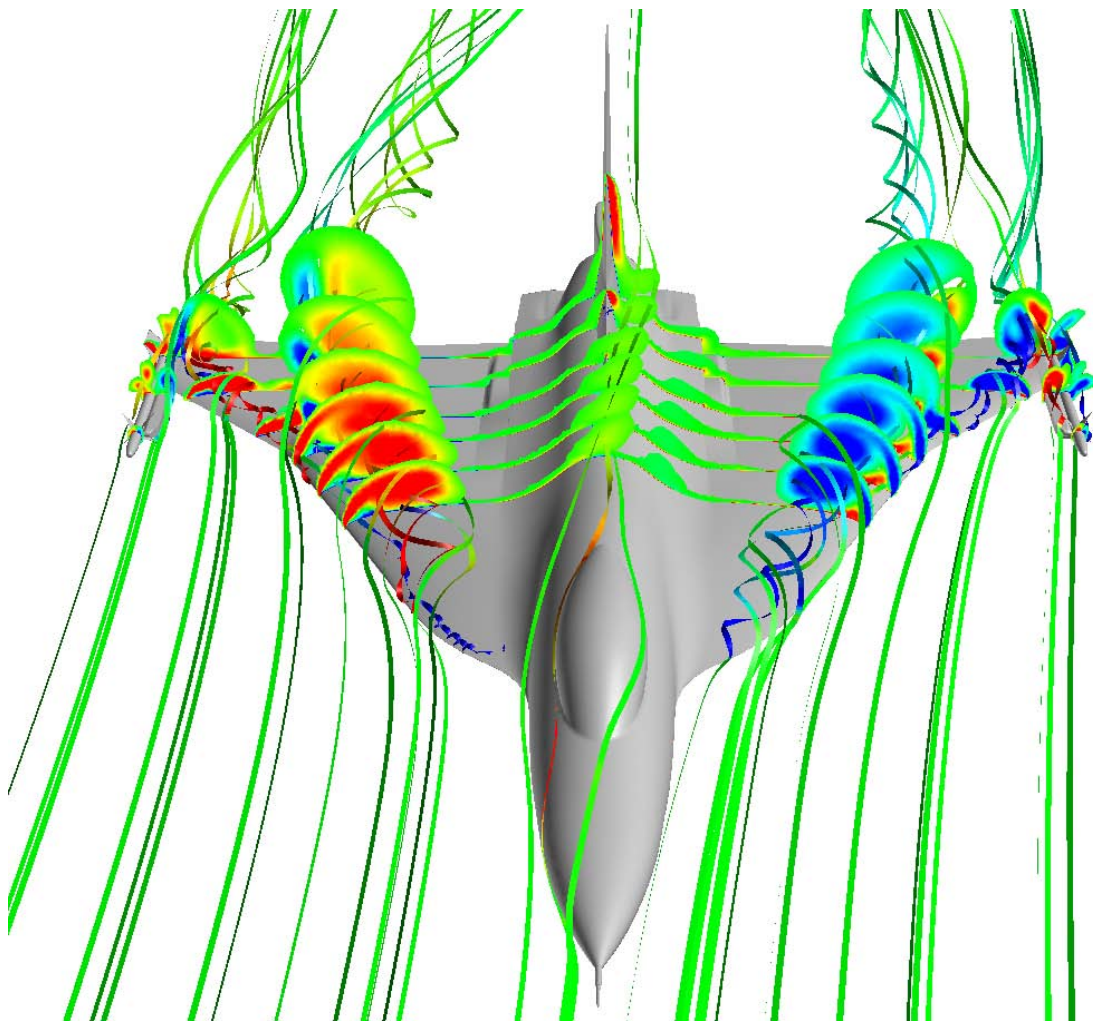
Figure 14-33: Axial Cuts of Vorticity Contours with Streamlines Tracking the Vortices for Case FC50.

14.7   CONCLUDING REMARKS

Seven viscous solutions for a F-16XL configuration were computed using the CFD tools at the UT SimCenter at Chattanooga as part of the NATO Technical Team AVT-113. The purpose of the NATO team was to determine

the readiness level for CFD solver to analyze highly vortical viscous flowfields. Viscous meshes for the analyzes were created using two different mesh generation packages. Inviscid meshes were generated using a commercial grid generation package call Gridgen. Viscous layers were added to this mesh using a mesh generation package developed at the SimCenter.

Initial solutions revealed grid resolution issues capturing the vortex path at the outboard span stations. A turbulence model study was performed to determine if the discrepancies were due to modeling issues. No improvement was observed based on turbulence modeling options. Finally, a manual refinement of the mesh was performed based on the known trajectory of the leading edge vortex at the outboard stations. The adapted mesh showed dramatic improvement in the solution accuracy at these span stations. All solutions were recomputed using the adapted mesh.

The computed solutions on the adapted mesh were compared to available flight test data, supplied to the team by NASA. Four of the computed cases were required of each team member. Three other cases were optional. Surface pressure plots showed reasonable agreement with the supplied flight test data for virtually all cases. Discrepancy between the computed surface pressure coefficients and the flight test data typically occurred near the wing tip; more so for the higher angle of attack than for the low to moderate angles of attack. The one transonic flight condition (FC70) showed the worst agreement with the flight test data. Comparisons at two of the six span stations for this case showed good agreement. One span station was near the wing root and the other was close to mid-span. One possible contributor to the discrepancy could be geometry modeling issues. The actual flight test for this case included significant leading and trailing edge flap deflections. No flap deflection was modeled in the CFD mesh. The computed vortex trajectories and strengths agreed well with the flight test data. The locations were generally accurate. The magnitudes of the suction peaks were slightly low in some cases and in agreement in other cases. Primary and secondary vortices were captured in the computed solutions.

Mesh resolution is critically important in accurately computing viscous vortical flowfields. The manual adaptation is evidence of that. A formal grid refinement study was not performed during this study, due to the required size of the full aircraft viscous mesh. This computer resource restriction is typical in cases of this size and complexity. An alternative to a formal grid refinement study might be to perform solution-based mesh adaptation. This can include mesh redistribution techniques as well as mesh refinement techniques.

14.8   REFERENCES

[14-1]   Lamar, J.E., Obara, C.J., Fisher, B.D. and Fisher, D.F.: *Flight, Wind-Tunnel, and Computational Fluid Dynamics Comparison for Cranked Arrow Wing (F-16XL) at Subsonic and Transonic Speeds*, NASA TP-2001-210629, NASA Langley Research Center, February 2001.

[14-2]   Pointwise, Inc., Gridgen User Manual, Version 15, http://www.pointwise.com/.

[14-3]   Karman, S.L. Jr.: *Unstructured Viscous Layer Insertion Using Linear-Elastic Smoothing*, AIAA Journal, Volume 45, No. 1, pp 168-190, January 2007.

[14-4]   Anderson, W.K.: *Grid Generation and Flow Solution Method for the Euler Equations on Unstructured Grids*, Tech. Rep. L-16986, NASA Langley Research Center, Hampton, VA 23665-5225, 1992.

[14-5]   Anderson, W.K. and Bonhaus, D.L.: *An Implicit Upwind Algorithm for Computing Turbulent Flows on Unstructured Grids*, Computers in Fluids, Vol. 23, No. 1, pp. 1-21, 1994.

[14-6]   Anderson, W.K., Rausch, R.D. and Bonhaus, D.L.: *Implicit/Multigrid Algorithms for Incompressible Turbulent Flows on Unstructured Grids*, AIAA Paper 95-1740, 1995.

[14-7]   Pankajakshan, R., Remotigue, M.G., Taylor, L.K., Jiang, M., Briley, W.R. and Whitfield, D.L.: *Validation of Control-Surface Induced Submarine Maneuvering Simulations Using UNCLE*, 24th Symposium on Naval Hydrodynamics, Fukuoka, Japan, 2002.

[14-8]   Hyams, D.G., Sreenivas, K., Sheng, C., Briley, W.R., Marcum, D.L. and Whitfield, D.L.: *An Investigation of Parallel Implicit Solution Algorithms for Incompressible Flows on Multielement Unstructured Topologies*, AIAA 2000-0271, 2000.

[14-9]   Briley, W.R., Taylor, L.K. and Whitfield, D.L.: *High Resolution Viscous Flow Simulations at Arbitrary Mach Number*, Journal of Computational Physics, pp. 79-105, 2003.

[14-10] Intelligent Light, Inc., URL: http://www.ilight.com/.

[14-11] Tecplot, Inc., URL:http://www.tecplot.com/.

Chapter 15 – NUMERICAL SOLUTIONS FOR THE CAWAPI CONFIGURATION ON UNSTRUCTURED GRIDS AT NASA LaRC, UNITED STATES

by

John E. Lamar *(Retired)* **and Khaled S. Abdol-Hamid**

15.1 SUMMARY

In support of the Cranked Arrow Wing Aerodynamic Project International (CAWAPI) with its goal of improving the Technology Readiness Level of flow solvers by comparing results with measured F-16XL-1 flight data, NASA Langley employed the TetrUSS unstructured grid solver, USM3D, to obtain solutions for all seven flight conditions of interest. A newly available solver version that incorporates a number of turbulence models, including the two-equation linear and non-linear k-ε, was used in this study. As a first test, a choice was made to utilize only a single grid resolution with the solver for the simulation of the different flight conditions. Comparisons are presented with three turbulence models in USM3D, flight data for surface pressure, boundary-layer profiles, and skin-friction distribution, as well as limited predictions from other solvers. A result of these comparisons is that the USM3D solver can be used in an engineering environment to predict vortex-flow physics on a complex configuration at flight Reynolds numbers with a two-equation linear k-ε turbulence model.

15.2 INTRODUCTION

Researchers at the NASA Langley Research Center (LaRC) performed a limited study with the flow solver portion of the NASA Tetrahedal Unstructured Software System [15-1] (TetrUSS), named USM3D, in order to predict the vortical flow physics on the F-16XL-1 airplane (See Figure 15-1). The Flight Conditions (FCs) (See Table 15-1 and Table 15-2) chosen for study were those of interest to the Cranked Arrow Wing Aerodynamics Project International (CAWAPI) facet [15-2] of the RTO/AVT-113 task group entitled "Understanding and Modeling Vortical Flows to Improve the Technology Readiness Level for Military Aircraft". This solver was chosen because it is a robust, accurate, well-validated Computational Fluid Dynamics (CFD) tool developed by resident in-house experts for use in a variety of flow physics and applied aerodynamics problems. Moreover, TetrUSS and/or the USM3D flow solver have won several awards, including: the competition in 1996 and 2004 for 'NASA Software of the Year'; recognition for its speed and accuracy of execution based on formulation at a 1989 NASA LaRC sponsored CFD unstructured grid solver workshop; and an 'Apple Design Award/Best OS X Scientific Computing Solution/Reno 2004'.
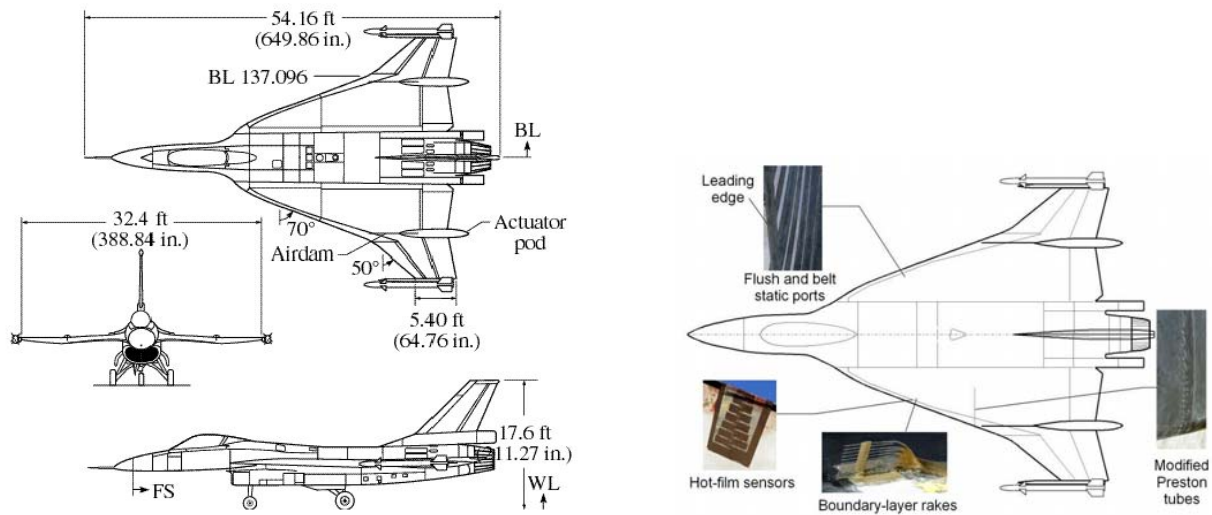
(a) Three-View Drawing; Linear Dimensions in ft. (in.)	(b) Pressure Instrumentation Layout

Figure 15-1: F-16XL-1 Airplane Drawing and Pressure Instrumentation Layout.

Table 15-1: Seven Flight Conditions to be Examined

Flight Condition	Actual Mach No.	Actual α, degs	Actual β, degs	Actual Reynolds No.
FC7	0.304	11.89	-0.133	44.4E+06
FC19	0.36	11.85	+0.612	46.8E+06
FC46	0.527	10.4	+0.684	46.9E+06
FC70	0.97	4.37	+0.310	88.77E+06
FC25	0.242	19.84	0.725	32.22E+06
FC50	0.434	13.56	+5.31	39.41E+06
FC51	0.441	12.89	-4.58	38.95E+06

Table 15-2: Associated Engine Parameters* for these Flight Conditions [15-2]

Flight Condition	Free Stream Altitude, ft	Free Stream Mach	Inlet Duct Exit Static Temp., degs R	Inlet Duct Exit Static Press., psia	Inlet Duct Exit Velocity, ft/sec	Inlet Duct Exit Mach	Mixing Plane Total Temp., degs R	Mixing Plane Total Press., psia
FC7	5000	0.304	498	11	379.6	0.347	1050	23
FC19	10000	0.36	485.8	10.2	345.8	0.32	1050	21.5
FC46	24000	0.527	443.6	5.85	404.3	0.39	1045	14.8
FC70	22300	0.97	519	10.65	464.7	0.416	1200	30
FC25	10000	0.242	470.1	8.72	474.8	0.447	1209	26.3
FC50	24000	0.434	440	5.16	483.3	0.47	1154	16.95
FC51	24000	0.441	431.8	5.19	468.6	0.46	1146	16.74

* The numbers in this table do not represent any particular engine.

A new version of USM3D [15-3] has recently become available with additional turbulence models beyond the standard Spalart-Allmaras (SA); these include the two-equation linear and non-linear (Algebraic Reynolds Stress Model) k-ε models. A series of classic flows such as; flat-plate, 2-D airfoil, 3-D wing-body, jet and other flows, have already been studied with this new version. The F-16XL-1, as a full airplane, provides an opportunity to extend and to understand the ability of this class of turbulence models to represent the flow physics around a complex configuration and this paper reports on the limited study, a first step.

The process employed here is to initially generate solutions for one vortical flow FC, i.e., FC46 ($M_\infty = 0.527$, $\alpha = 10.4°$, $R_n = 46.9 \times 10^6$) and one transonic flow FC, i.e., FC70 ($M_\infty = 0.97$, $\alpha = 4.37°$, $R_n = 88.77 \times 10^6$), using multiple turbulence models; then based on these comparisons with measured flight data [15-4] down-select to a turbulence model for the other five FCs, as resources would not permit obtaining solutions at all FCs with all turbulence models. This was not an exhaustive study and really represents an approach one would use in an engineering environment. To emphasize the last point, all solutions were also obtained on a common baseline, unstructured grid developed at LaRC specifically for FC19 ($M_\infty = 0.36$, $\alpha = 11.85°$, $R_n = 46.8 \times 10^6$) with a $y^+ \sim 1$. (See Ref. [15-5] for a description of the cooperative development of unstructured grids.) This choice was deliberate and was done, in part, to examine the limits of this robust solver with non-optimized grids at various FCs in which different flow physics dominate. For example, it is known [15-6] that grid adaptation in the flow-field can be very important for vortical flows, yet even the baseline grid, which was developed for a vortical flow FC, made no provision for such adaptation. Lastly, the paper provides a description of the solver; and comparisons with previous CFD solutions [15-4] and those of PAB3D [15-7], a structured grid flow solver at LaRC, for surface pressures, boundary-layer profiles and skin-friction distribution.

15.3 SOLVER DESCRIPTION AND APPLICATION TO CAWAPI

15.3.1 Description

The basic description of the USM3D flow solver used with emphasis on the CAWAPI application is as follows:

1) Domain discretization → unstructured tetrahedral, cell centered, finite volume;

2) Physical modeling → RANS, two-equation linear and non-linear k-ε models;

3) Space differencing (2nd order accuracy) → Roe's flux-difference splitting [FDS];

4) Boundary conditions used → engine inlet/outlet;

5) Steady state driver → Implicit scheme; and

6) Grid used → Tetrahedral grid 16,161,959 cells for symmetrical FCs on half-airplane with center-line plane of symmetry imposed, and 32,323,918 cells for full airplane at sideslip. See [15-1] for more details.

Regarding grids, the USM3D solver used a minimum of 16,161,959 cells. Solutions with it are compared with selected results from two LaRC structured solvers, PAB3D [15-7] using a linear version of the two-equation linear k-ε turbulence model and ~20 million cells and CFL3D [15-4]. The CFL3D solver used the Baldwin-Lomax with the Degani-Schiff turbulence model (in the *j-k* directions) on a multi-block, patched grid (1,372,096 cells) with the "wall function" option because the y^{+} ~82 [15-4]. [The figure captions refer to these results as CFL3D:BL-DS.] All codes compared in this paper are cell centered formulated and the wall function option was not used for any of the USM3D solutions reported here.

15.3.2 Engine Modeling, Flight Conditions, and Computers Used

The F-16XL-1 airplane engine was modelled in the code by using the specific boundary condition types, i.e., engine intake or exhaust, and the associated values of temperature, pressure (or a ratio of that to the free-stream value) along with Mach number at the inlet and exhaust/mixing-plane for each FC (See Table 15-2).

Most of the solutions reported here were obtained in 2006 on the Columbia high-speed cluster at NASA Ames using 128 processors, but a few solutions were obtained on the Langley PC/Linux cluster using 40 processors. Solution times ranged from 18 to 36 hours on the Columbia cluster, depending on whether the FC was for symmetrical or asymmetrical configuration, to 52 hours on the PC/Linux cluster for a symmetrical configuration.

15.3.3 Convergence Histories

The convergence history plots for the solutions reported here are shown in the appendix and labelled Figure 15-A1. These figures show that all solutions converged to a three-order reduction in the log residual-ratio for the mean-flow equations on this grid.

15.4 TURBULENCE MODEL STUDIES: RESULTS AND DISCUSSION

15.4.1 FC46 (M_∞ = 0.527, α = 10.4°, R_n = 46.9 x 10^{6}) [Flight at β < 1°, Modeled as β = 0°]

There is a pronounced effect of turbulence models on the vortical flow predictability at FC46, as seen in Figure 15-2. (A line on each included graphic shows the C_p dataset location.) Whereas, the effect of vortical

flows on the upper surface C_p is often better seen in the spanwise plots (Figure 15-2 (h) – (n)) than from the chordwise (Figure 15-2 (a) – (g)) ones, the presentation order of reference [15-4] is followed here which has the chordwise plots first. Figure 15-2 (o) – (q) show measured right-wing surface C_p, also mirrored about the center-line, with both the two-equation linear and non-linear k-ε model used in the USM3D solver.

(a) BL 55

(b) BL 70

(c) BL 80

(d) BL 95
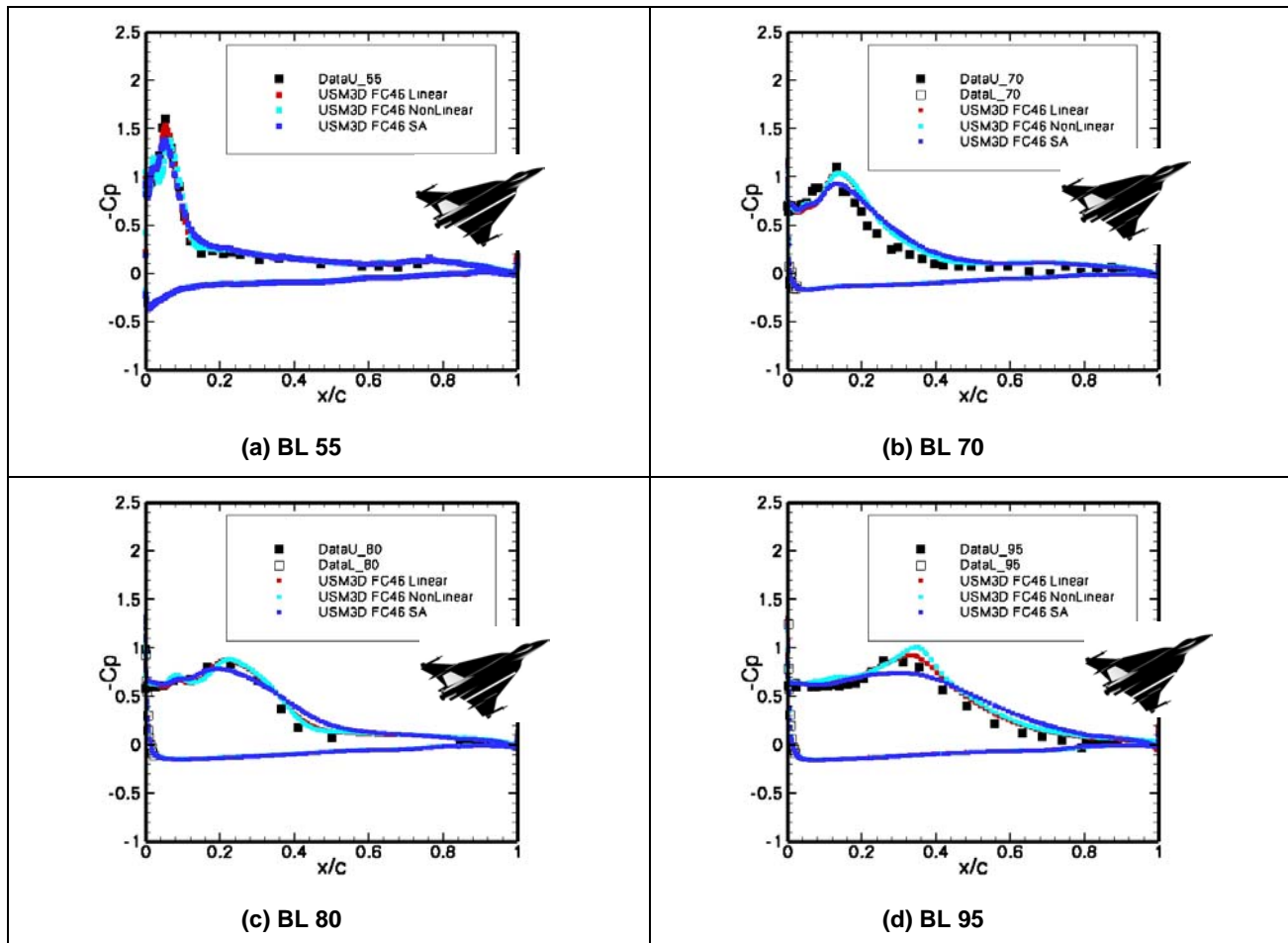
**Figure 15-2: Effect of Turbulence Modeling on C_p from USM3D at
FC46 (M_∞ = 0.527, α = 10.4°, R_n = 46.9 x 10^6); Data from Ref. [15-4].**

(e) BL 105

(f) BL 153.5

(g) BL 184.5

(h) FS 185

(i) FS 300

(j) FS 337.5

Figure 15-2: Continued.

(k) FS 375

(l) FS 407.5

(m) FS 450

(n) FS 492.5

Figure 15-2: Continued.

(o) Upper Surface C_p for the Turbulence Models with Flight Data
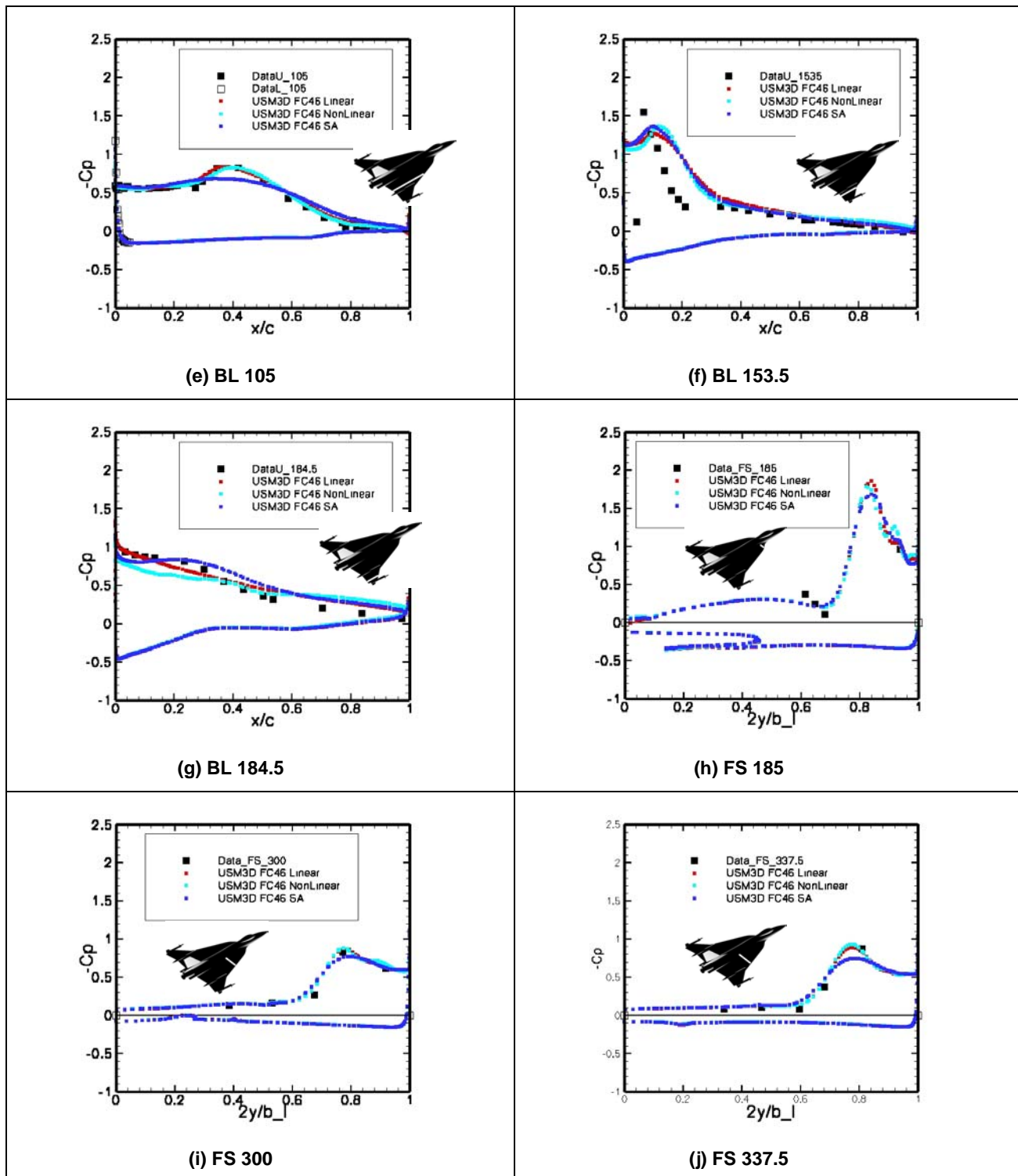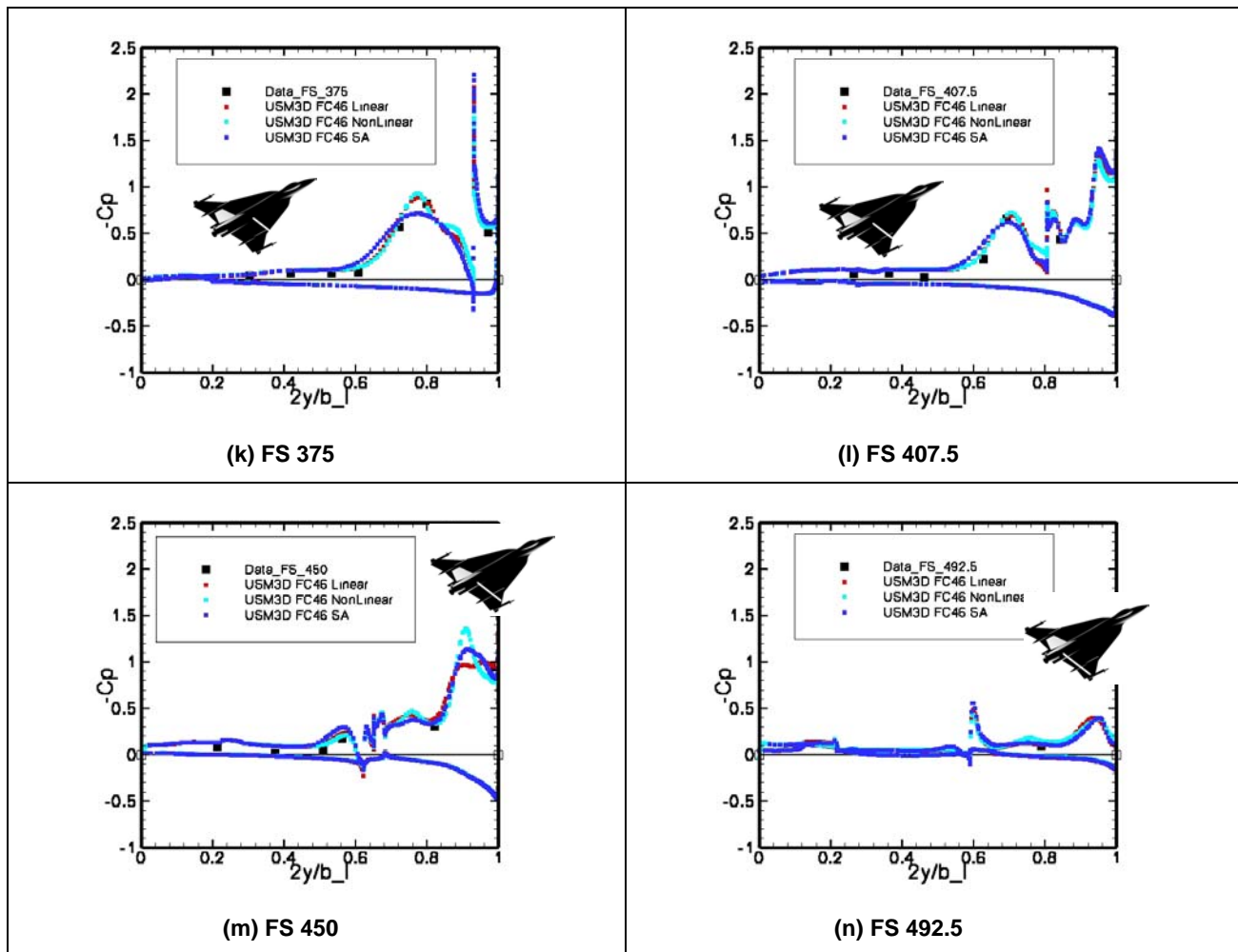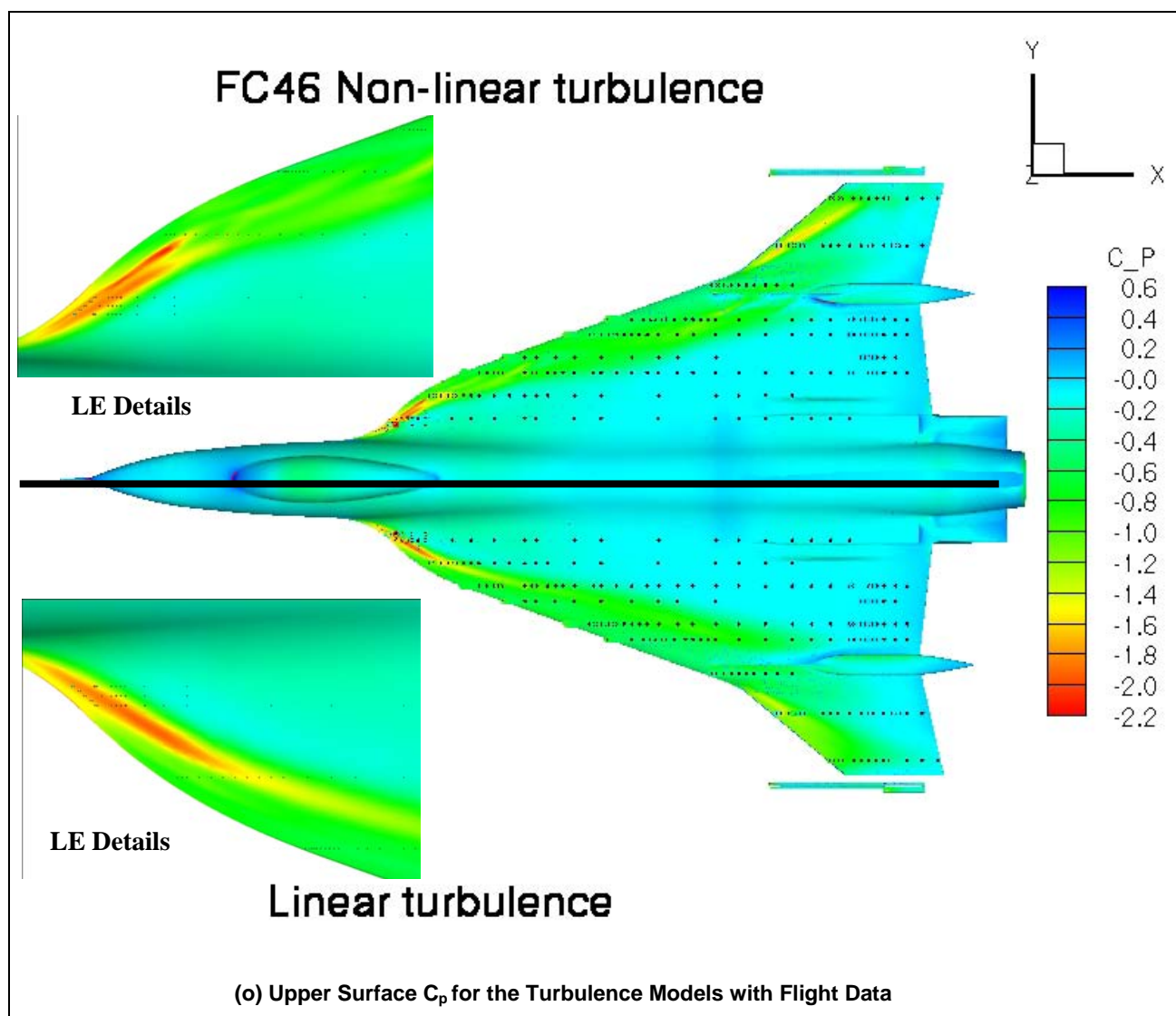
Figure 15-2: Continued.
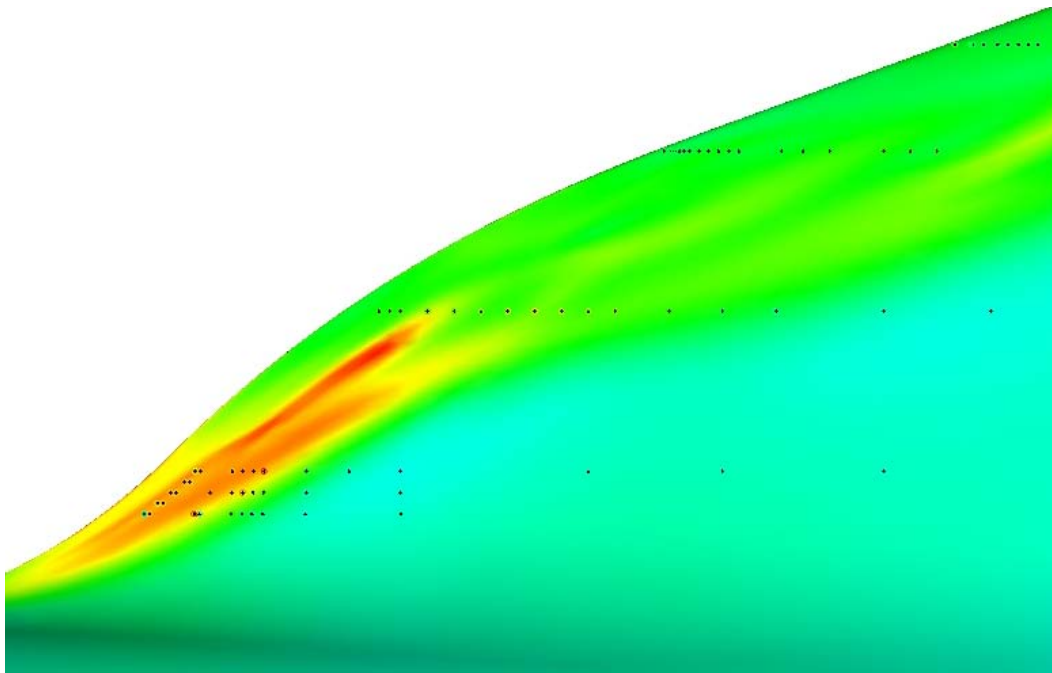
(p) Enlargement of LE Region for the Non-Linear k-ε Turbulence Model with Flight C_p Data
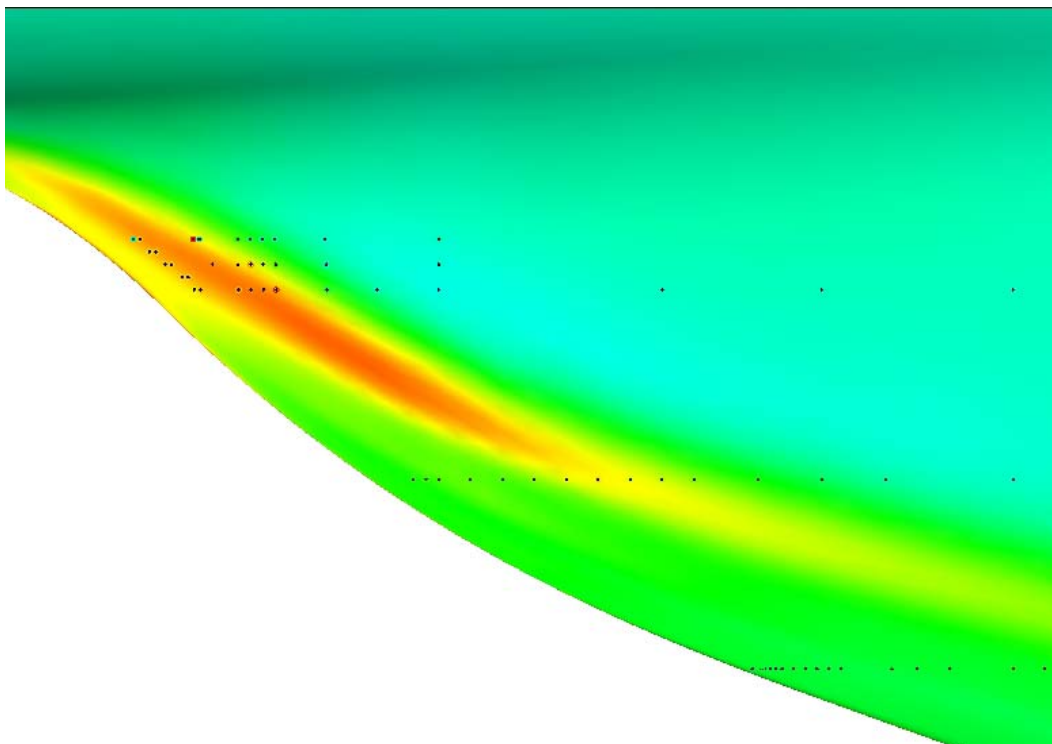
(q) Enlargement of LE Region for the Linear k-ε Turbulence Model with Flight C_p Data

Figure 15-2: Concluded.

The effects of turbulence modelling on the USM3D solutions for FC46, as determined from the various sub-parts of Figure 15-2, are summarized in the following statements:

1) The two-equation non-linear k-ε model is the best of the three based on comparison with the upper surface pressures, in spite of the grid not having refined viscous layers more consistent with the non-linear formulation (See Ref. [15-8]);

2) The two-equation linear k-ε model is slightly better than the SA model and almost as good as the non-linear one (See Ref. [15-8]); and

3) All models predict well the lower surface pressures.

Based on the inherent compatibility of this grid with the two-equation linear k-ε model, it was selected for use with those FCs that have vortical flow; though the non-linear model performed surprisingly well, as noted Figure 15-2 (b) – (c), where it predicted the suction peaks and the trailing compression better.

The black dots in Figure 15-2 (o) – (q) are the port locations – measurements were only made on the right wing – and the color of the circle around the dot has the same color graduation as for the USM3D surface pressures. Hence, if the colored circle is not visible then there is good agreement between the predicted and measured data at that location, which is the situation shown here. The inset figures and enlargements are provided to highlight the inboard LE region where there are many ports with much agreement, as emphasized by only the black dots being visible. (See similar inset comparison figures for FC46 in Ref. [15-4] for flight data and CFL3D:BL-DS.)

15.4.2 FC70 ($M_\infty = 0.97$, $\alpha = 4.37°$, $R_n = 88.77 \times 10^6$) [Flight at $\beta < 1°$, Modeled as $\beta = 0°$]

The effect of the three turbulence models on the USM3D solutions for this transonic flight condition (FC70) is shown in Figure 15-3 in a C_p comparison with measured data and results obtained a number of years ago with CFL3D:BL-DS [15-4] with an order of magnitude fewer cells.

(a) BL 55   (b) BL 70
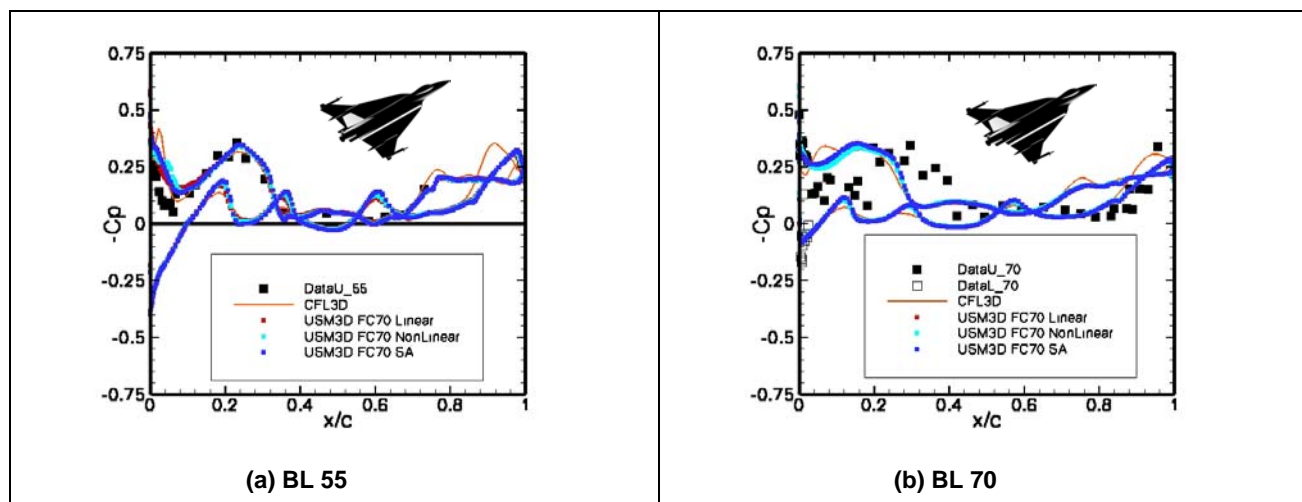
Figure 15-3: Effect of Turbulence Model on C_p from USM3D at FC70 ($M_\infty = 0.97$, $\alpha = 4.37°$, $R_n = 88.77 \times 10^6$); Data and CFL3D:BL-DS Results from Ref. [15-4].

(c) BL 80

(d) BL 95

(e) BL 105

(f) BL 153.5

(g) BL 184.5

(h) FS 185

Figure 15-3: Continued.

(i) FS 300

(j) FS 337.5

(k) FS 375

(l) FS 407.5

(m) FS 450

(n) FS 492.5

Figure 15-3: Continued.

(o) Upper Surface C$_p$ for the Turbulence Models with Flight Data
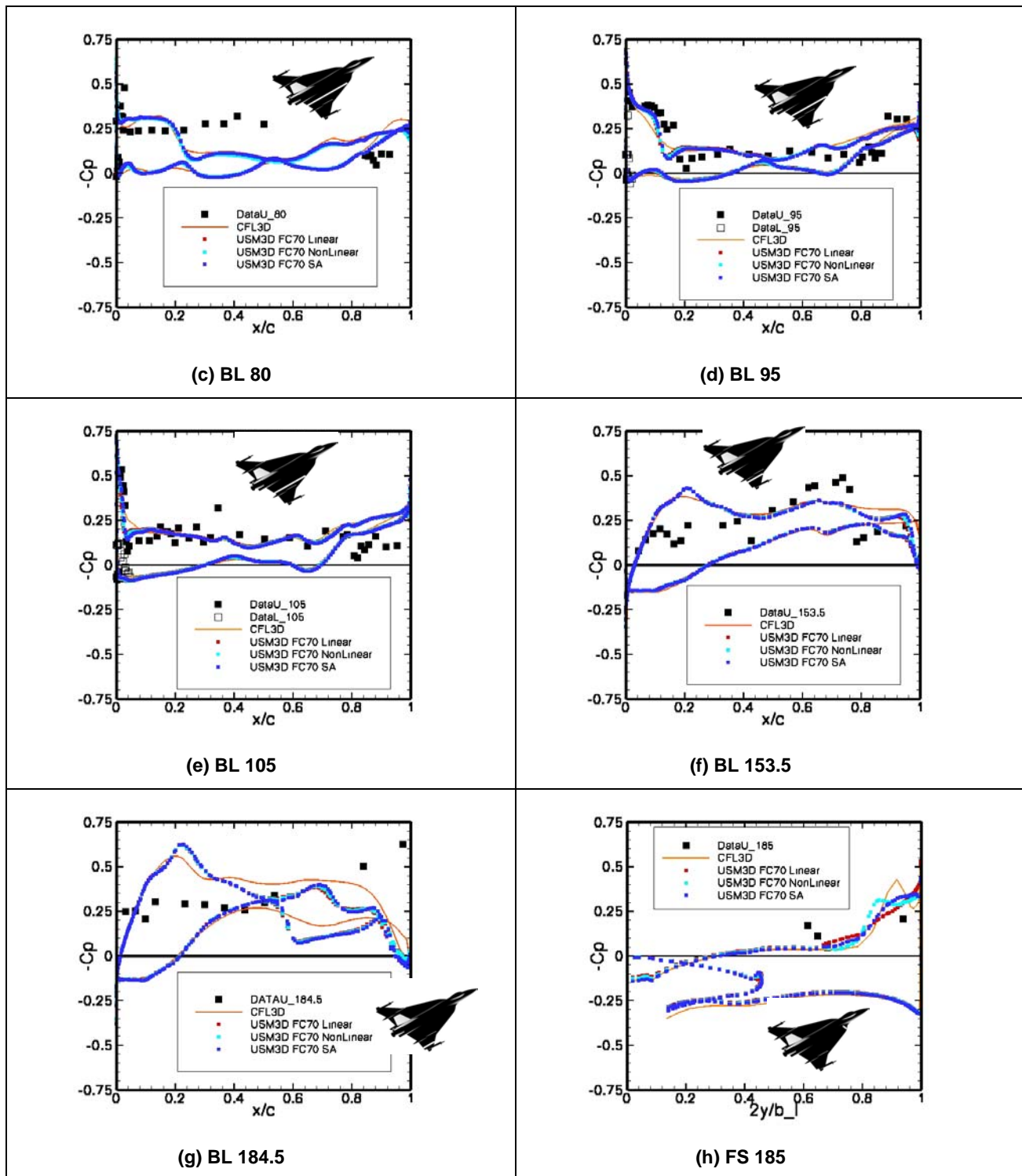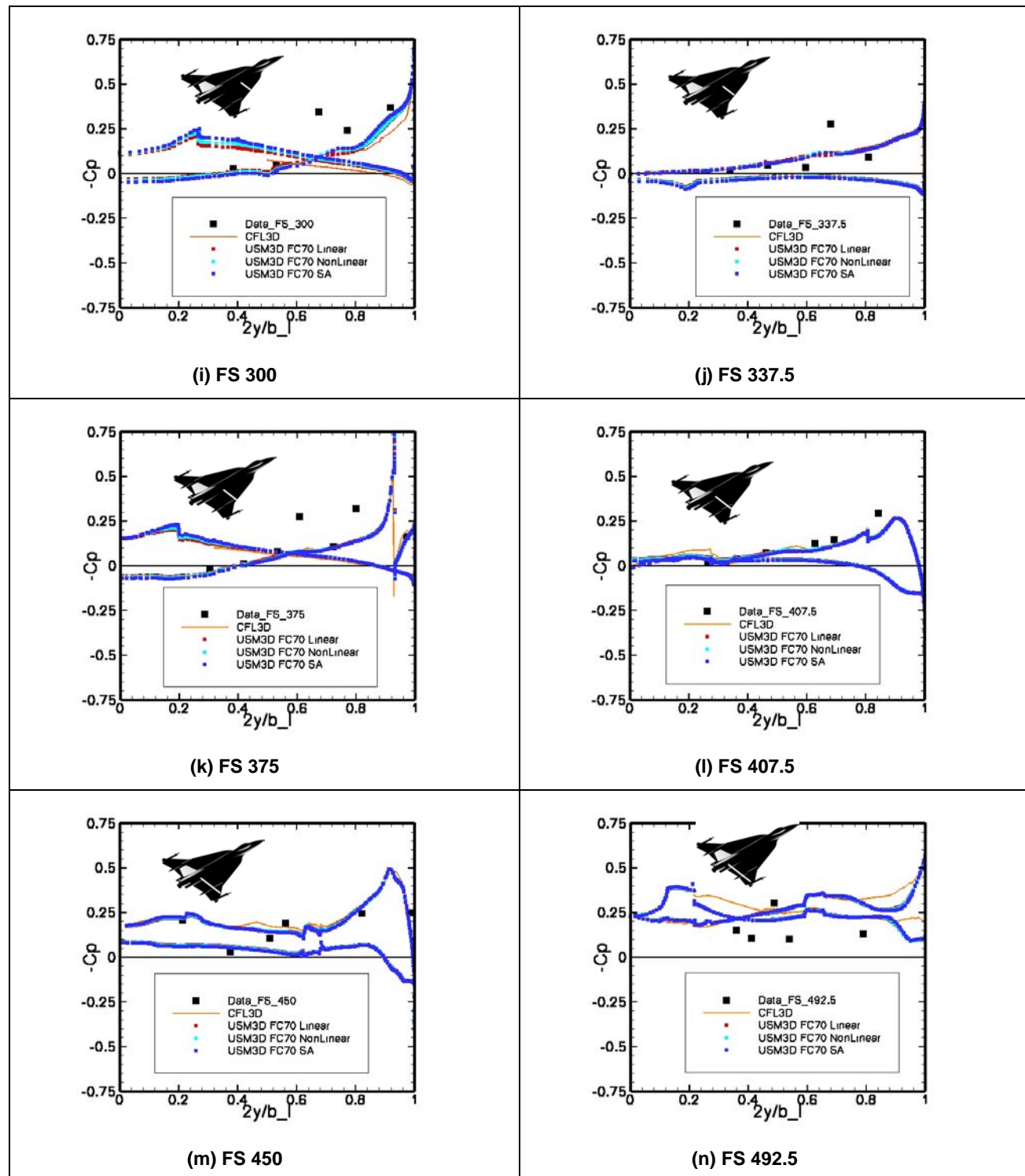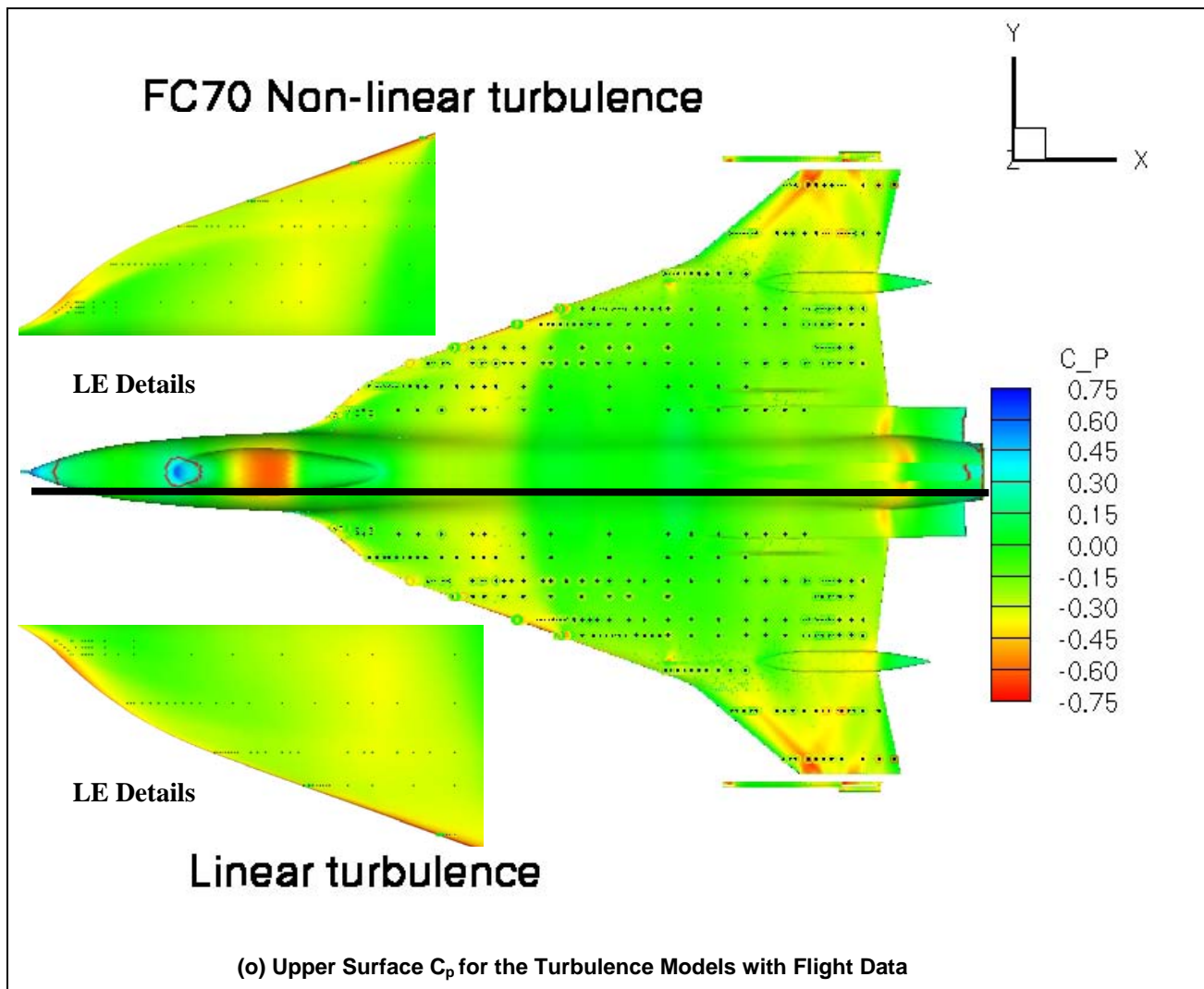
Figure 15-3: Continued.
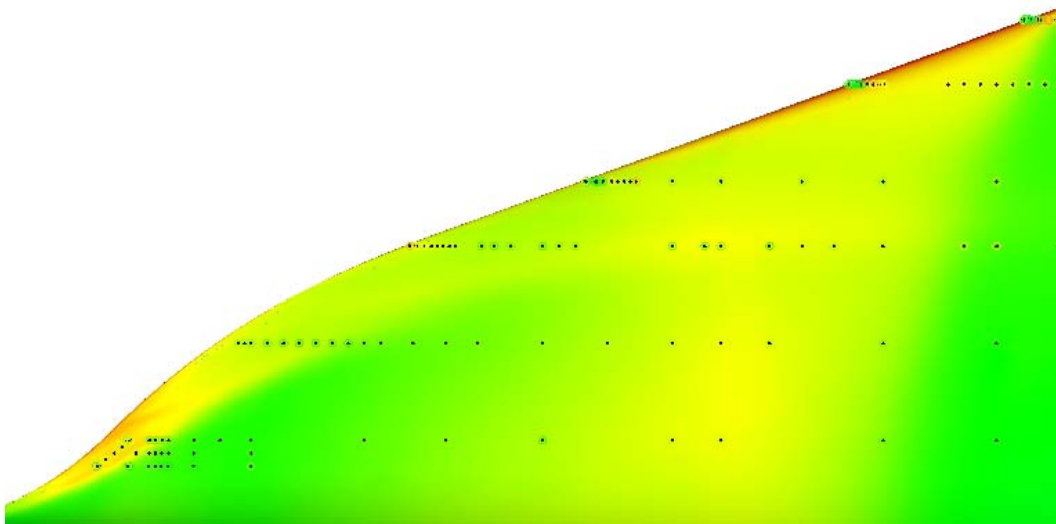
(p) Enlargement of LE Region for the Linear k-ε Turbulence Model with Flight C$_p$ Data
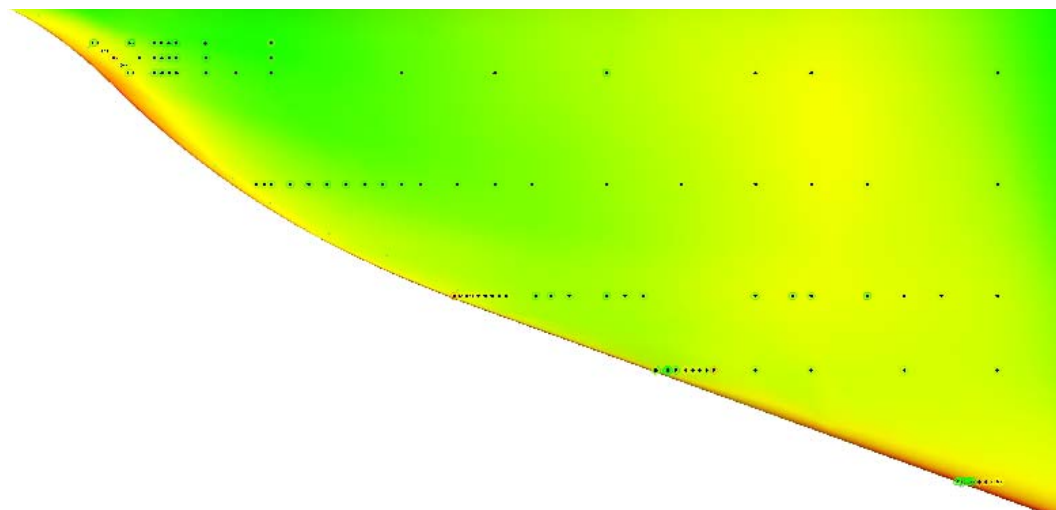
(q) Enlargement of LE Region for the Linear k-ε Turbulence Model with Flight C$_p$ Data

Figure 15-3: Concluded.

A summary of the turbulence model study for FC70 (Figure 15-3 (a) – (n)) is that there is very little effect of the model, except at FS 185, on the C$_p$ results and the agreement with measured data is mixed**.** In general, the USM3D predictions agree with measured data than those from CFL3D:BL-DS [15-4], but both solutions only fairly approximate the measurements. Similar trends are noted by others in the CAWAPI facet ([15-7] and [15-9] to [15-16]) of the AVT-113 task group. Moreover, from Figure 15-3 (a) – (n) the predictions of USM3D are seen to agree better with data on the inner wing than on the outer. There was a hope in the CAWAPI facet that other solvers with more grid cells and other turbulence models would produce better results than those published, in spite of two geometrical issues: unmodeled, upward-deflected leading edge (LE) flap (5° to ~9°)

[15-4] on the outer wing panel and any attendant aeroelastic effects in 1-g flight. This hope was not realized. Nevertheless, some improvements, in terms of generating the best USM3D solution possible for FC70 within the unmodeled constraints, would be expected with a **new grid** in which the boundary layer was refined consistent with the R_n for this transonic FC.

The USM3D C_p predictions differ only slightly from those of the structured grid solver CFL3D:BL-DS [15-4] – solution obtained on an order of magnitude fewer cells more than 5 years ago, and with the same unmodeled constraints – and have the most differences over the aft part of the wing and at FS 492.5. The differences noted are not necessarily in the direction of improved data agreement.

Lastly, Figure 15-3 (o) – (q) help to highlight the differences across the surface between the measured and predicted C_p results, especially at some locations along the LE. The inset figures and the enlargements of the inboard LE regions show the location of the ports for which there is agreement or disagreement between the predicted and measured data. As before, if the color of the circle surrounding the black dot (pressure port location) and representing the measured pressure value blends into that of the USM3D background color, the agreement is good; otherwise not. (See similar inset comparison figures for FC70 in Ref. [15-4] for flight data and CFL3D:BL-DS.)

15.5   OTHER SUBSONIC COMPARISONS

Now that the linear turbulence model has been chosen for use with the USM3D solver with this base unstructured grid, solutions are obtained with this combination at both symmetrical, $\beta = \sim 0°$, (FC7, FC19, FC25) and asymmetrical, $\beta \pm \sim 5°$, (FC50, FC51) flight conditions. Some of these are shown and all are discussed using the following figures. Solutions for FC7 and FC19 were primarily obtained in order to compare with data [15-4] for boundary layer (B.L.) rakes and skin friction, respectively.

15.5.1   Symmetric: FC25 ($M_\infty = 0.242$, $\alpha = 19.84°$, $R_n = 32.22 \times 10^6$) [Flight at $\beta < 1°$, Modeled as $\beta = 0°$]

Figure 15-4 for FC25 also has comparisons with the previous computational results [15-4].
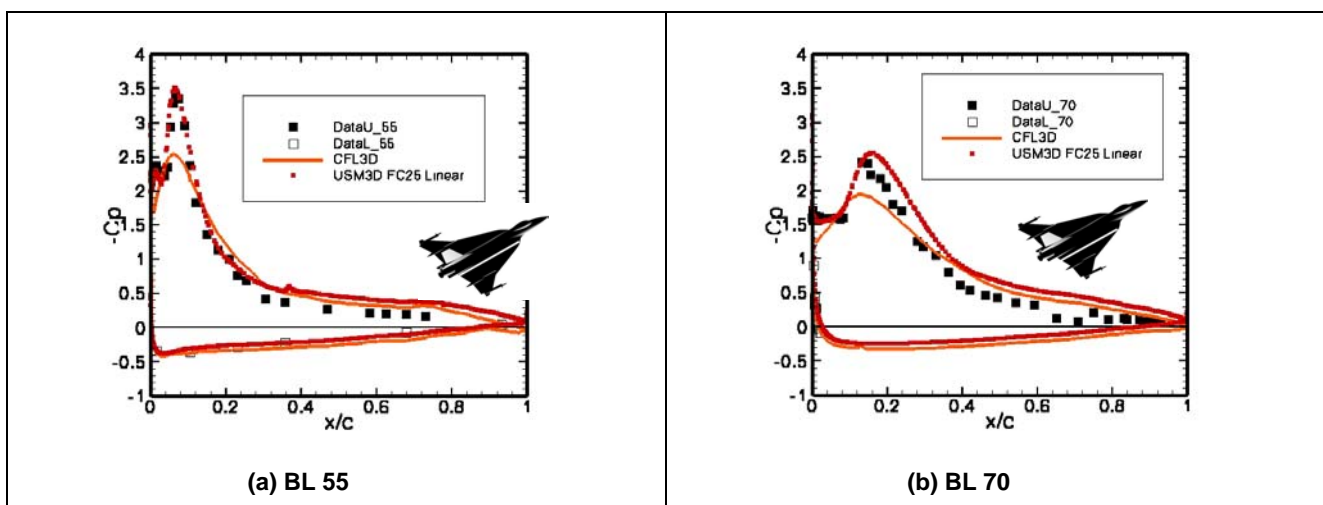
Figure 15-4: Prediction of C_p Flight Data from USM3D at FC25 ($M_\infty = 0.242$, $\alpha = 19.84°$, $R_n = 32.22 \times 10^6$); Data and CFL3D: BL-DS Results from Ref. [15-4].

(c) BL 80

(d) BL 95

(e) BL 105

(f) BL 153.5

(g) BL 184.5

(h) FS 185

Figure 15-4: Continued.

(i) FS 300

(j) FS 337.5

(k) FS 375

(l) FS 407.5

(m) FS 450

(n) FS 492.5

Figure 15-4: Continued.

(o) Upper Surface C_p
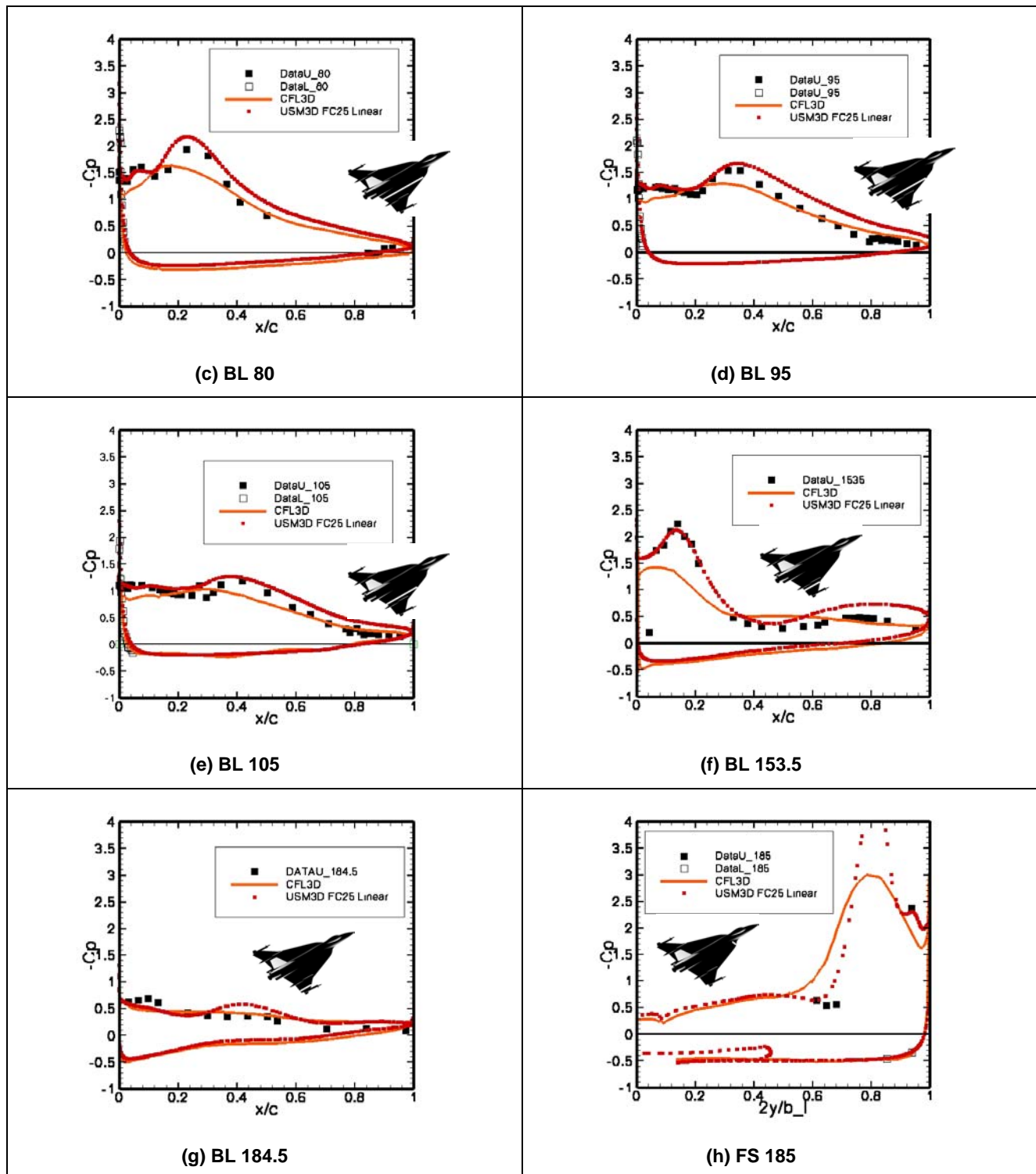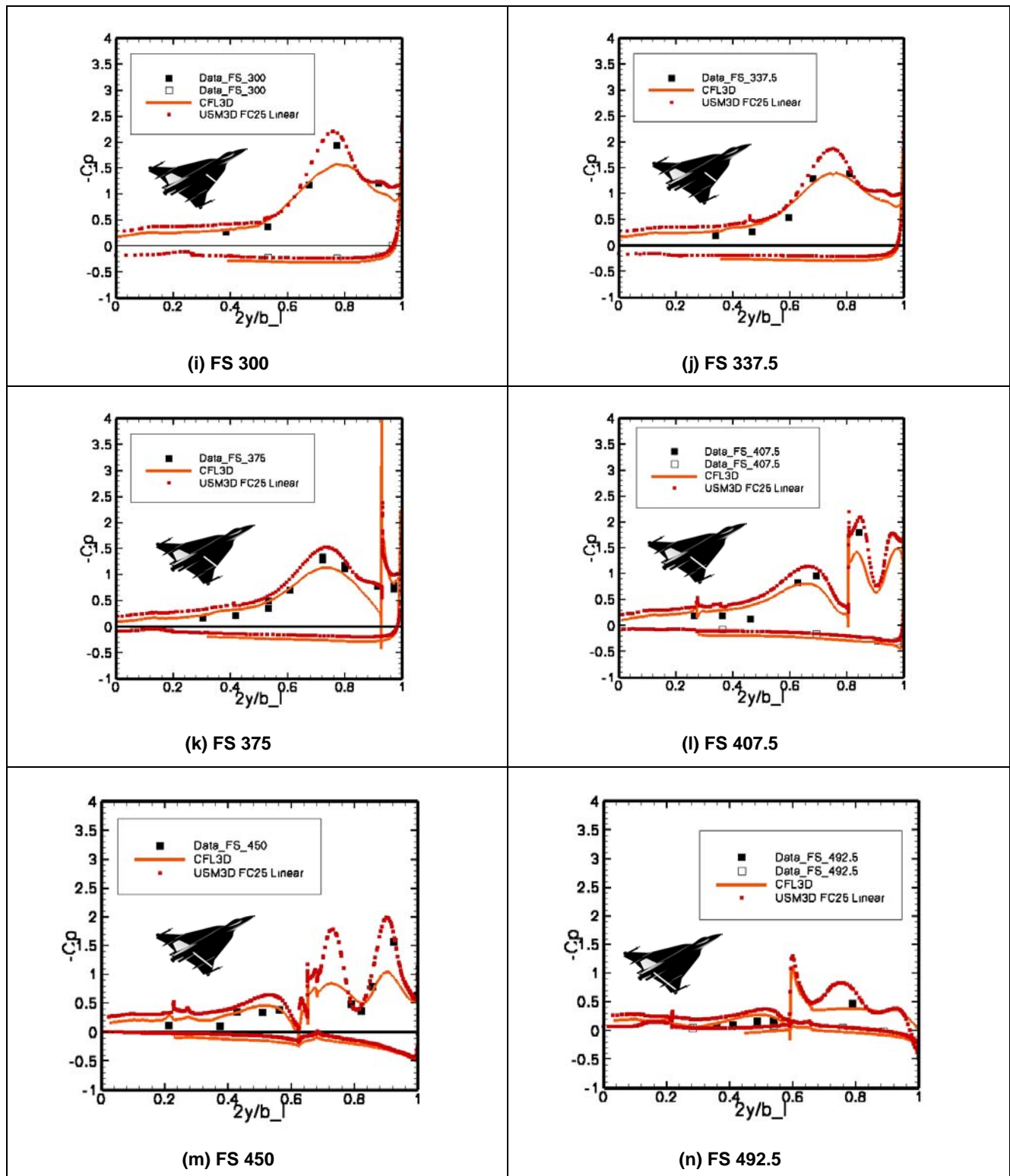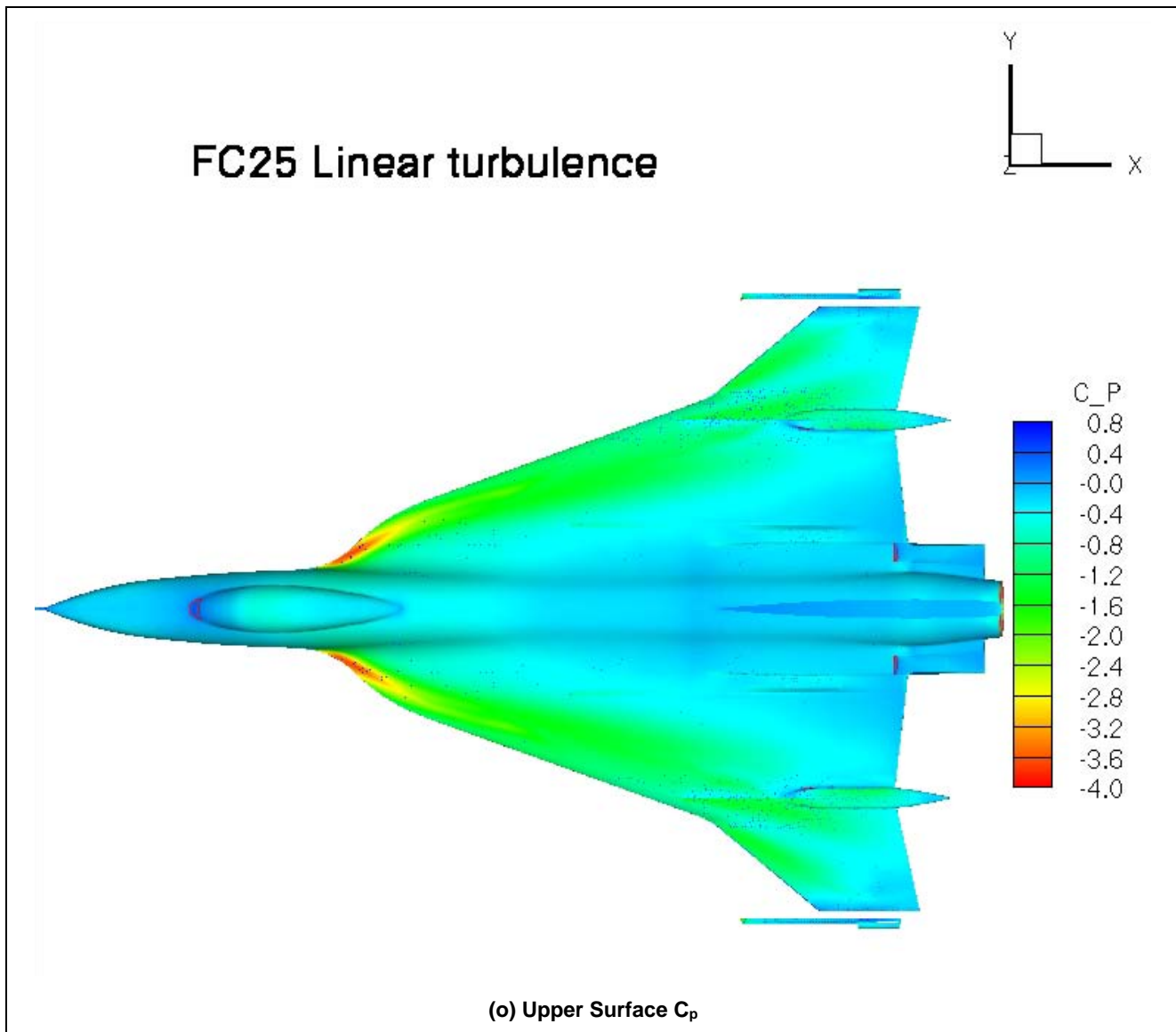
Figure 15-4: Concluded.

For FC25, the USM3D solution is in quite good agreement with measured data and offers some significant improvement over published CFL3D C_p results [15-4] – solution obtained on an order of magnitude fewer cells more than 5 years ago. An adaptive grid may offer additional improvement, but the results shown are remarkable, in that they predict all the suction peaks well and capture the overall surface C_p chordwise and spanwise distributions.

15.5.2   Asymmetric [Flight Parameter Value for $\beta \neq 0°$, Modeled]

As seen in Figure 15-5 and Figure 15-6, the USM3D solver generally predicts well the measured data for these two asymmetric flows at all BLs and FSs, including the peak values at BL55 but misses the ones at

BL153.5. This solver also captures the FS 185 measured data well. In general, the predictions at FC51 (β = -4.58°) are slightly better than those at FC50 (β = +5.31°). In particular, for FC51 at BL153.5 the measured C_p data aft of the peak is even well predicted, though the peak value is not. The situations where the peak is missed may be improved by using the non-linear turbulence model, as noted for FC46, or using an adaptive grid with the linear model.

15.5.2.1   FC50 (M_∞ = 0.434, α = 13.56°, β = +5.31°, R_n = 39.41 x 10^6)

Detail C_p figures are grouped as before and follow.

(a) BL 55

(b) BL 70

Internet (c) BL 80

(d) BL 95
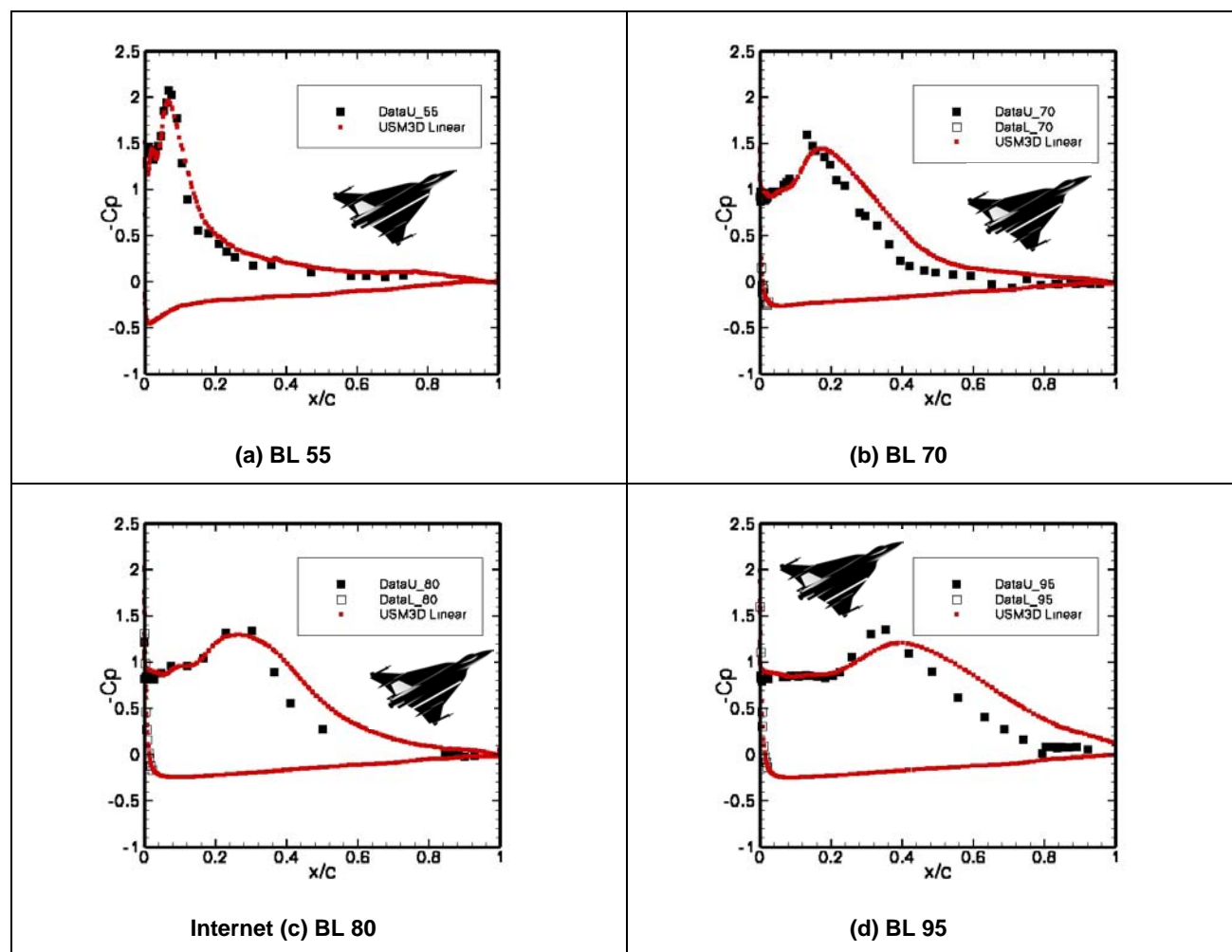
**Figure 15-5: Predicted and Measured C_p Data at FC50 (M_∞ = 0.434,
α = 13.56°, β = +5.31°, R_n = 39.41 x 10^6); Data from Ref. [15-17].**

(e) BL 105

(f) BL 153.5

(g) BL 184.5

(h) FS 185

(i) FS 300

(j) FS 337.5

Figure 15-5: Continued.

(k) FS 375

(l) FS 407.5

(m) FS 450

(n) FS 492.5

Figure 15-5: Continued.

(o) Upper Surface C_p.
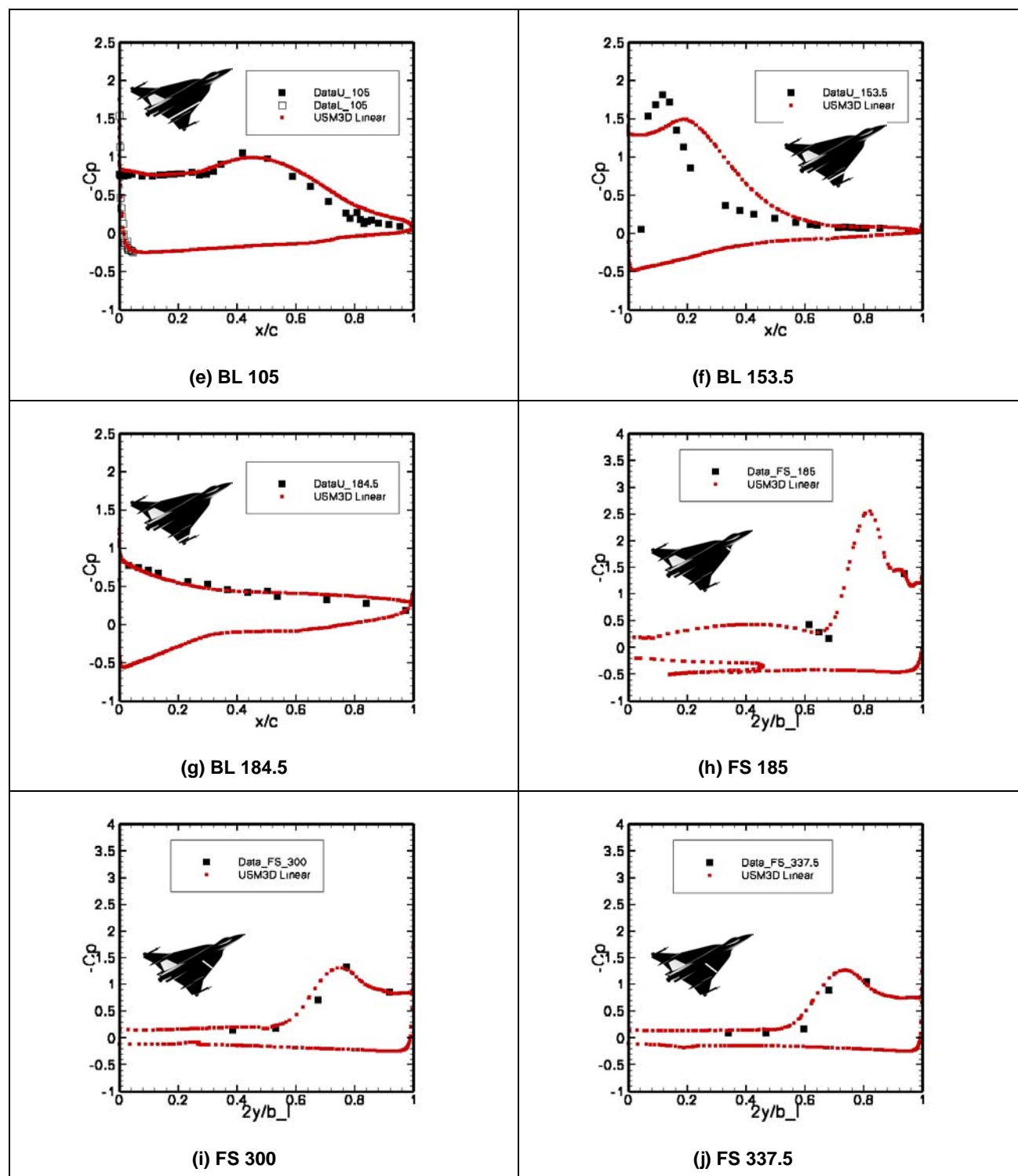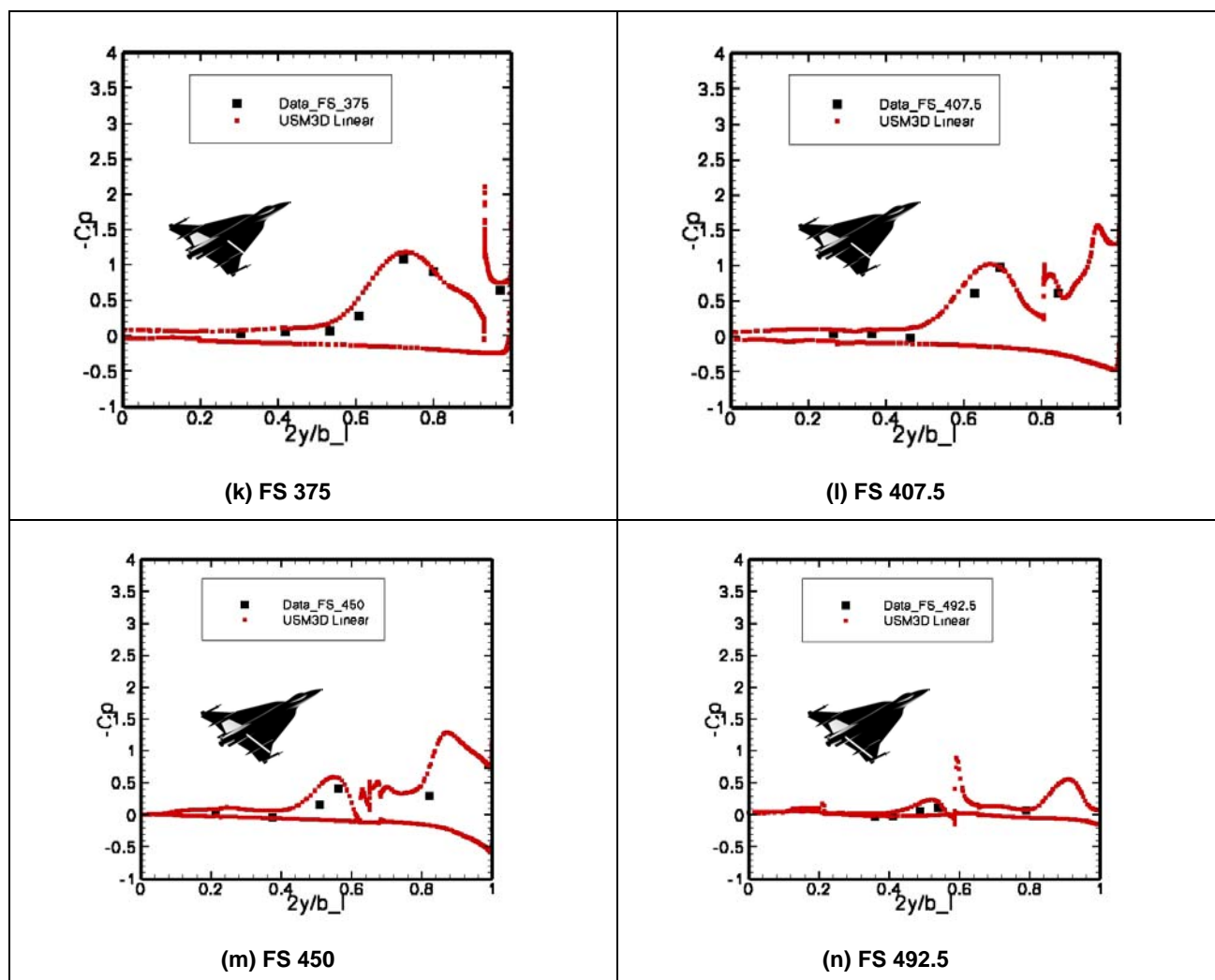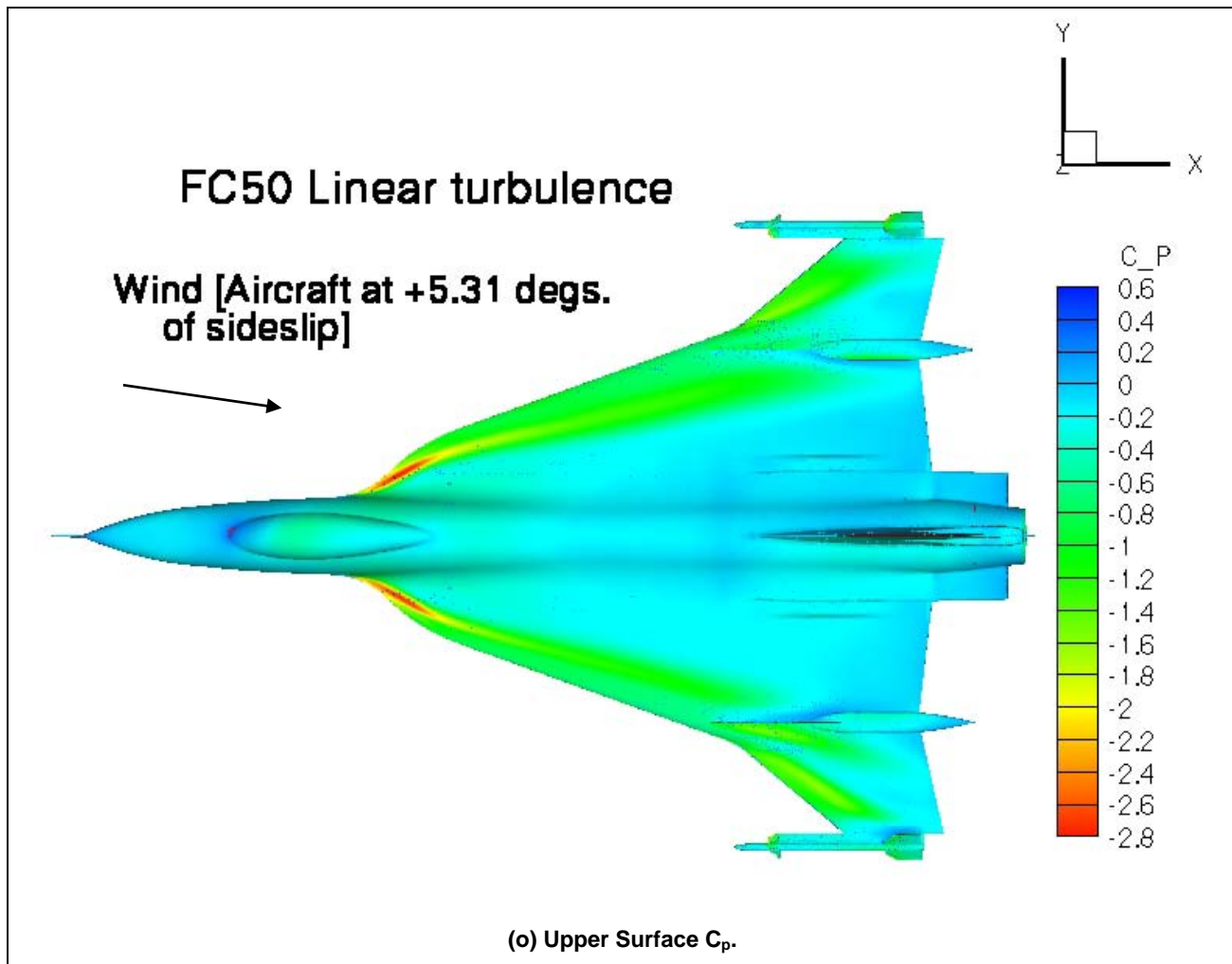
Figure 15-5: Concluded.

15.5.2.2 FC51 ($M_\infty = 0.441$, $\alpha = 12.89°$, $\beta = -4.58°$, $R_n = 38.95 \times 10^6$)

Detail C_p figures are grouped as before and follow.

(a) BL 55

(b) BL 70

(c) BL 80

(d) BL 95

(e) BL 105

(f) BL 153.5
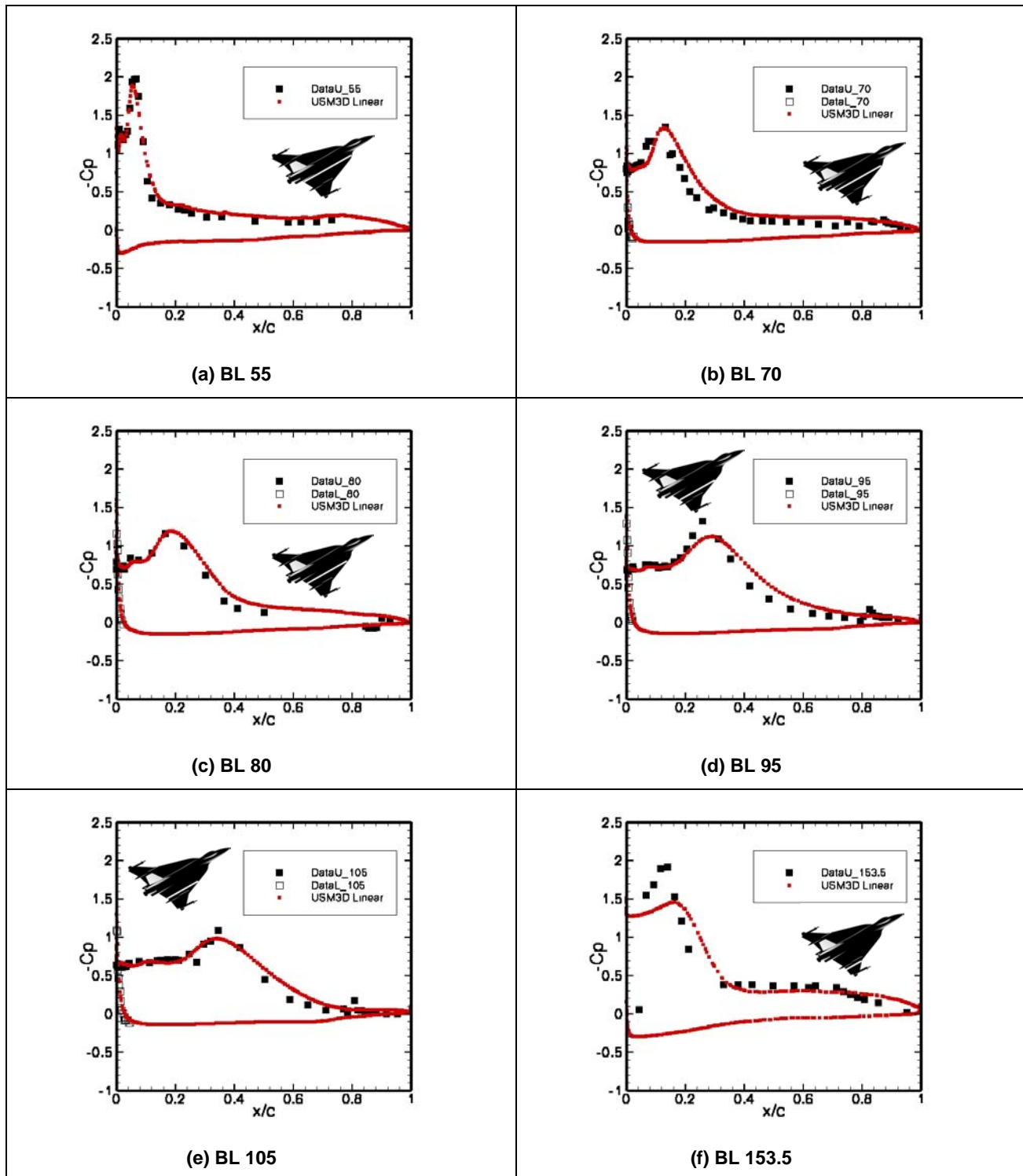
Figure 15-6: Predicted and Measured C_p Data at FC51 (M_∞ = 0.441, α = 12.89°, β = -4.58°, R_n = 38.95 x 10^6); Data from Ref. [15-17].

(g) BL 184.5

(h) FS 185

(i) FS 300

(j) FS 337.5

(k) FS 375

(l) FS 407.5

Figure 15-6: Continued.

(m) FS 450

(n) FS 492.5

(o) Upper Surface C_p
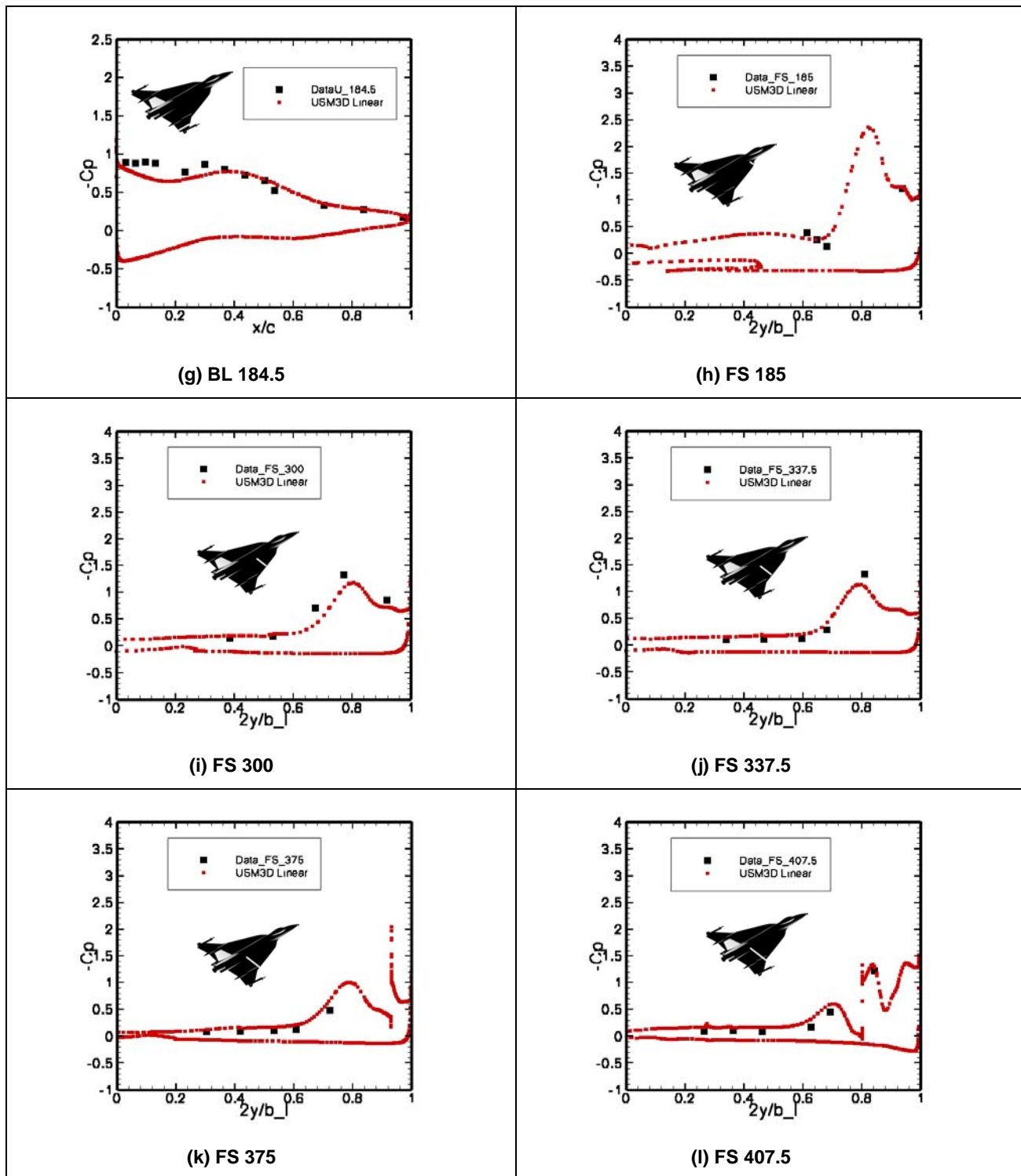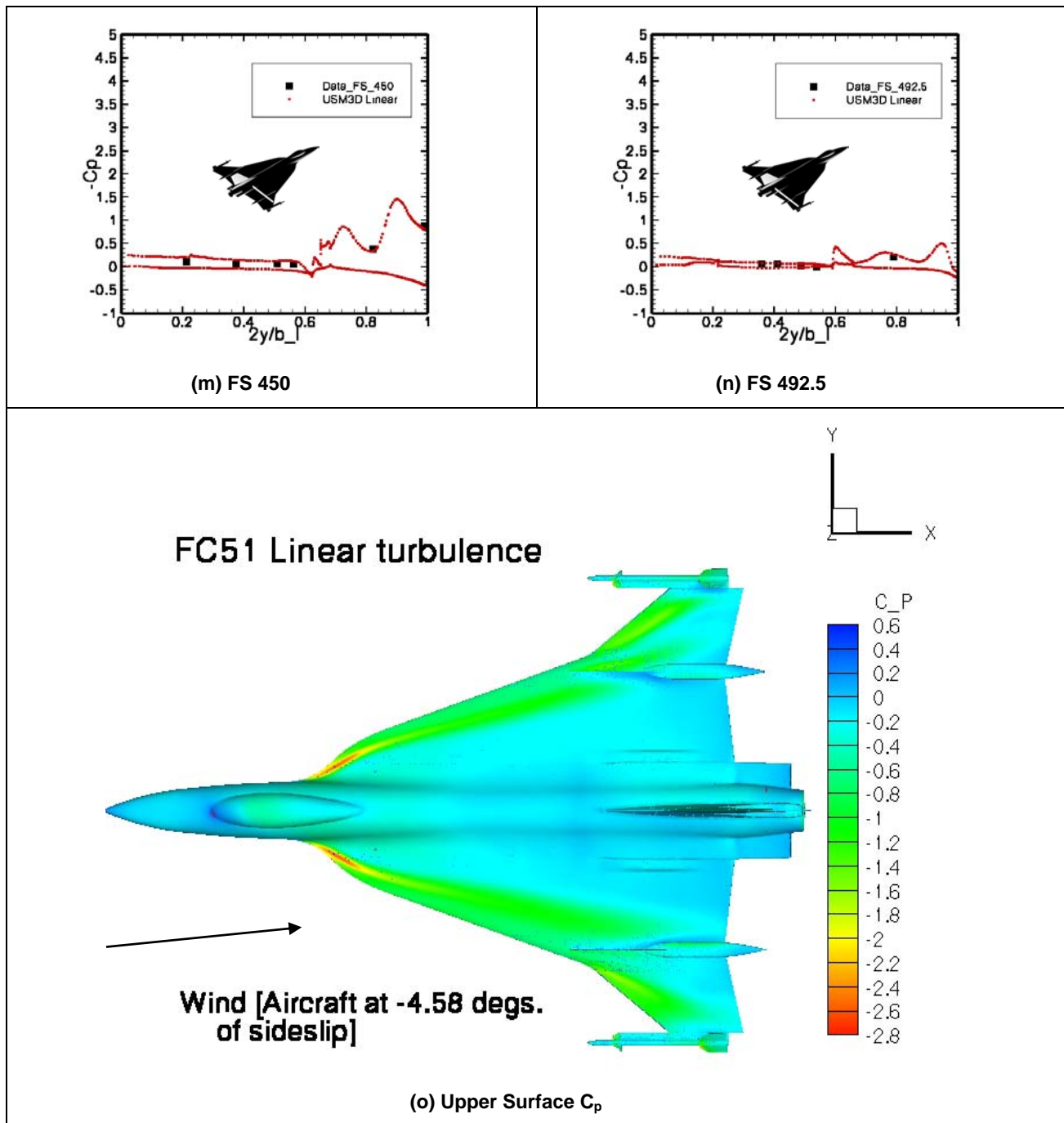
Figure 15-6: Concluded.

15.5.3   Boundary Layer Comparisons

Figure 15-7 presents comparisons of predicted and measured boundary-layer profiles at FC7. For each rake, the normalized profile is defined as the ratio of velocity magnitude at each rake total pressure tube to that at the top-most one, located 1.8 inches off the surface and normal to it. The B.L. rake positions were chosen [15-4]

so that #3 would be in basic free-stream flow, #4 underneath the primary vortex, #5 underneath the secondary vortex, and #7 on the secondary vortex separation line. Regarding the USM3D and PAB3D [15-7] solutions, both predict the entire profiles well for all four B.L. rakes, though USM3D is slightly better for rakes #3 and #7. For rake #7, both underestimate the profiles from 0.25 to 1.25 inches off the surface. Near the wall, both methods predict the profiles very well at all rake locations. With respect to the published results from CFL3D:BL-DS [15-4] – solution obtained on an order of magnitude fewer cells more than 5 years ago, USM3D shows the most significant prediction improvements for Rakes #5 and #7 – these are near the LE. Moreover, USM3D offers slight improvement near the wall for #3 over that of the PAB3D and CFL3D:BL-DS profiles.

Rake 3: FS 302.17, BL -52.93

Rake 4: FS 293.45, BL -76.22

Rake 5: FS 295.52, BL -94.33

Rake 7: FS 294.59, BL -96.06
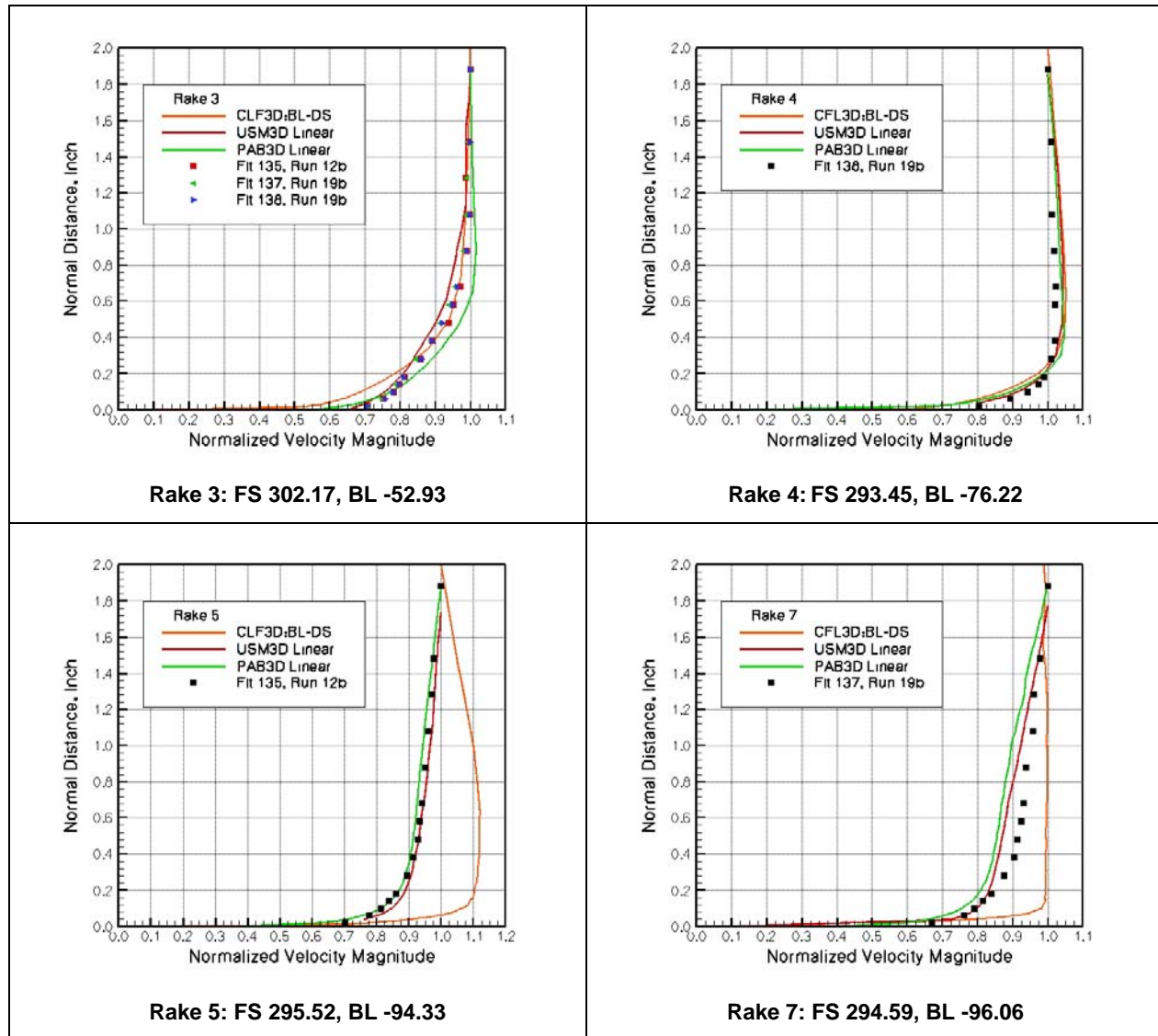
Figure 15-7: Velocity Profiles for Boundary Layer Rakes on F-16XL for FC7
(M_∞ = 0.304, α = 11.89°, R_n = 44.4 x 10^6); Data and CFL3D:BL-DS from Ref. [15-4].

In order to understand better this difference in boundary-layer profiles near the LE for the USM3D solution, Figure 15-8 – Figure 15-9 were prepared to look at the total pressure contours at FS 300 – the nominal value

where the B.L. rakes are located – and at FS 330 – the location where the skin-friction data were measured. The purpose of these figures was to ascertain whether there was significant off-surface vortical flow activity in the vicinity of the LE, where the secondary vortex would be expected to occur. These two figures illustrate two findings and they are:

1) Little change is noted between the two flow-fields, only 30 inches apart (See Figure 15-10 for relative locations — reconstructed from Ref. [15-4]); and

2) Little detailed activity is seen near the LE – even with increased magnification – indicating that the anticipated location of the secondary vortex is poorly captured with this grid/turbulence model combination at either FS.
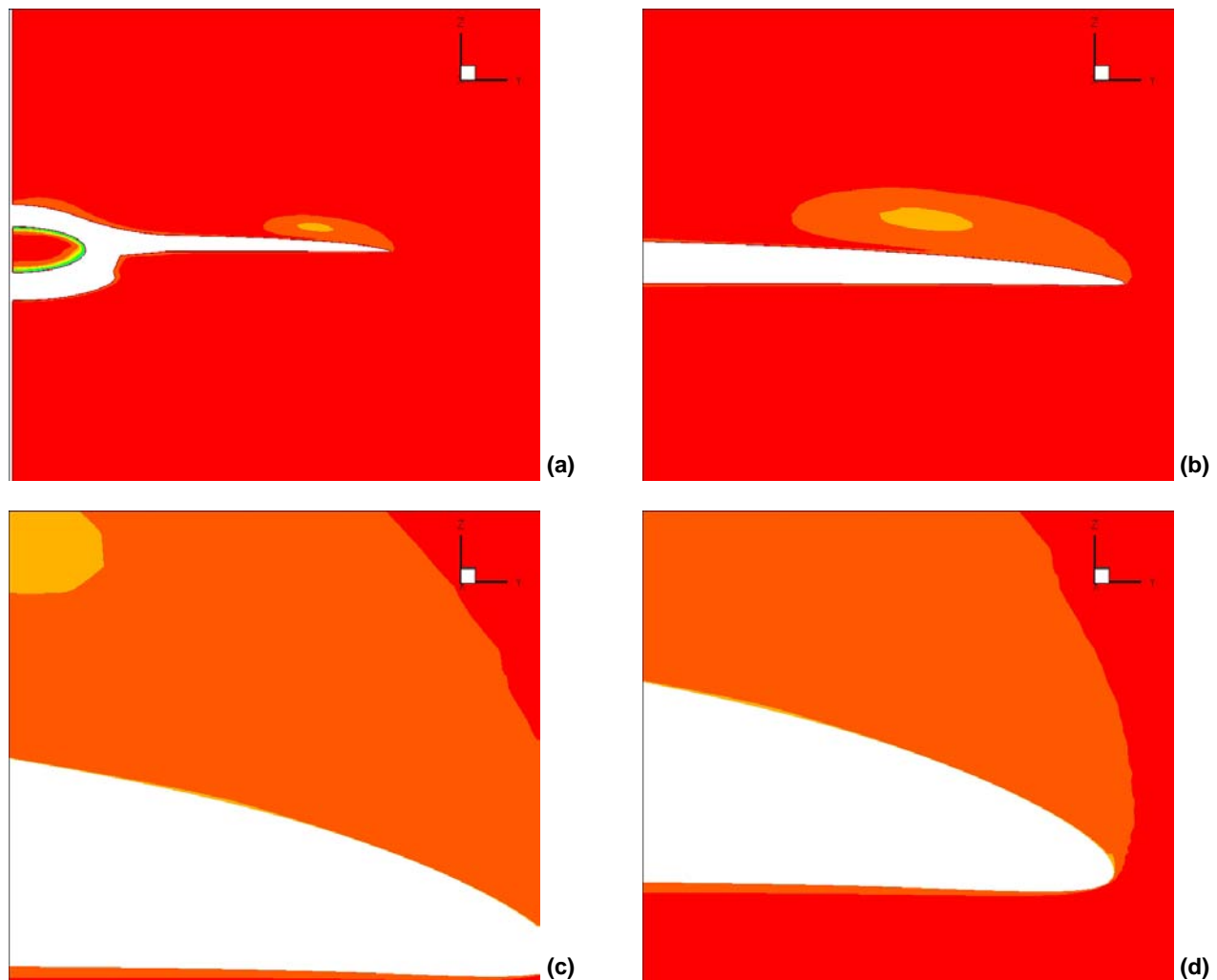
Figure 15-8: Four Increasing [(a) -> (d)] Magnification Levels of Total Pressure Contours at FS 300 Obtained from USM3D for FC7 using Linear k-ε Model (M_∞ = 0.304, α = 11.89°, R_n = 44.4 x 10^6).
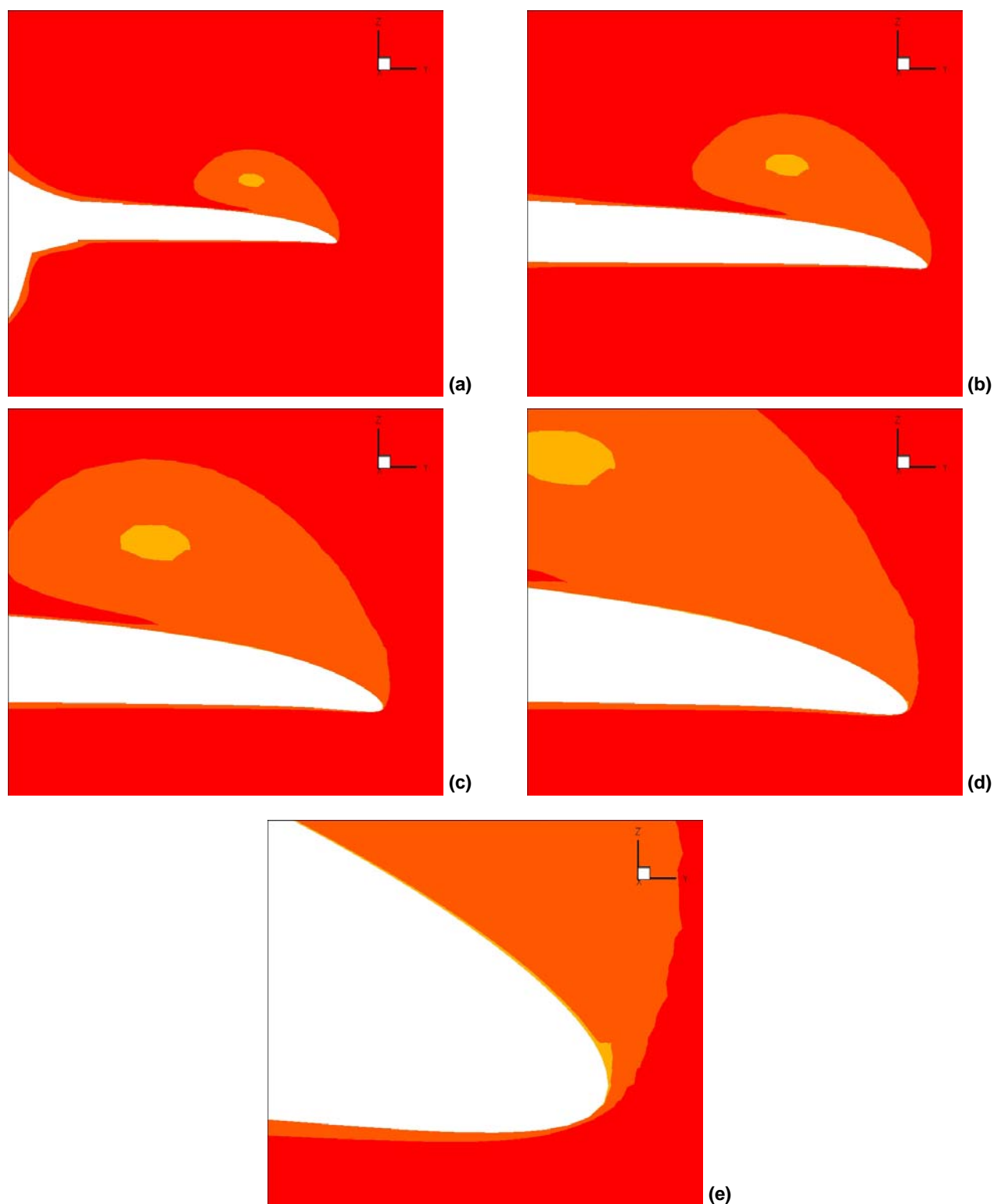
Figure 15-9: Five Increasing [(a) -> (e)] Magnification Levels of Total Pressure Contours at FS 330 Obtained from USM3D for FC7 using Linear k-ε Model (M$_\infty$ = 0.304, α = 11.89°, R$_n$ = 44.4 x 10^6).
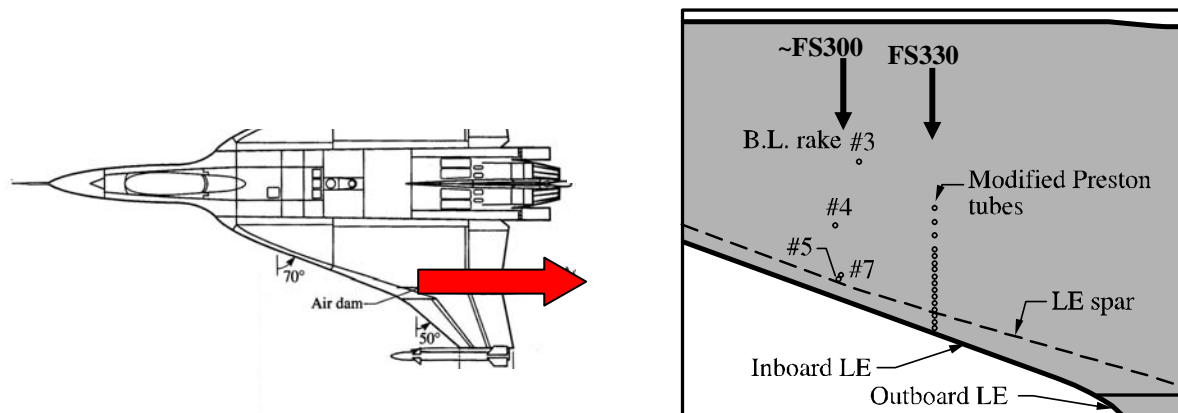
Figure 15-10: General Arrangement of Rake and Modified Preston Tube Relative Locations on F-16XL-1 Left Wing; Pressure Instruments Oriented for α = 13°; M_∞ = 0.29; and R_n = 46.1 x 10^6.

15.5.4 Skin Friction Comparisons

Figure 15-11 shows the c_f predictions and measured data for the USM3D and PAB3D [15-7] solvers using the linear turbulence model and CFL3D:BL-DS [15-4]. All solvers predict well the location of the skin-friction peak for the primary vortex but also have a smaller gradient on either side of the measured peak. The USM3D solution results are better than the other two in terms of being closer to the peak skin-friction value and its inboard gradient. Both the PAB3D and CFL3D:BL-DS predict the measured secondary vortex peak region and its value better than that of USM3D. Based on the preceding discussion, this was not a surprise. None of these solutions captures all the measured features for BL <-100.
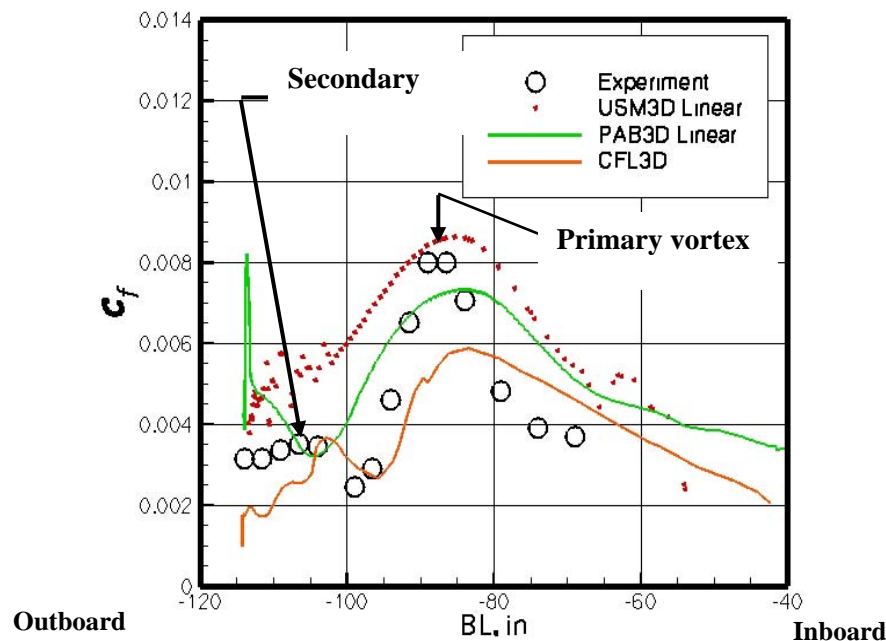
**Figure 15-11: Skin-Friction Distribution on F-16XL-1 Airplane at FS 330 for FC19
(M_∞ = 0.36, α = 11.85°, R_n = 46.8 x 10^6); Data and CFL3D:BL-DS from Ref. [15-4].**

15.6   CONCLUSIONS

Based on the studies and comparisons presented in this paper for the USM3D solver, the following conclusions are reached:

- The common grid used for all USM3D solutions presented yields converged results for each of the various turbulent models employed; namely, the two-equation linear and non-linear k-ε models and the SA. One pleasant surprise was that the non-linear version worked very well on this grid and the linear version worked almost as well in terms of C_p predictions for vortex dominated flows.

- The two-equation linear and non-linear k-ε models were better than the SA turbulence model in predicting the measured C_p data for vortex dominated flows. Some further improvement may be expected for these flows if an adaptive grid is used at the higher angles-of-attack, but the results to date have been very encouraging in this first test of the new code version on a complex airplane.

- The transonic predictions with either the two-equation linear or non-linear k-ε model show no appreciable improvement in terms of C_p predictions over those from the SA model or published results from the structured grid solver CFL3D:BL-DS (solution obtained on an order of magnitude fewer cells more than 5 years ago). This is one place where a finer grid in the boundary layer will likely prove to be beneficial. Further benefits could be expected by accounting for the unmodeled, upward deflection of the outboard leading-edge flap at this flight condition and any attendant aeroelastic effects in 1-g flight.

- Using the two-equation linear k-ε model produced the following results:

  - There was some improvement in the C_p predictions for two vortical flow flight conditions, FC25 and FC46, relative to published results from the structured grid solver CFL3D:BL-DS (solution obtained on an order of magnitude fewer cells more than 5 years ago);

  - The effects of sideslip are well predicted, though there is some room for improvement;

  - The boundary-layer profiles are generally well predicted, especially near the wall, compare favorably with the results from PAB3D, a structured solver with the same turbulence model and similar grid size, and are overall better than the CFL3D:BL-DS predictions on a coarser grid; and

  - The primary vortex skin-friction peak value and location are well predicted, but its nearby gradients and the secondary vortex features are not. These results differ from both those of PAB3D and CFL3D:BL-DS.

- A summary of the preceding is that the USM3D solver can be used in an engineering environment to predict vortex-flow physics on a complex configuration at flight Reynolds numbers with a two-equation linear k-ε turbulence model.

15.7   ACKNOWLEDGEMENTS

15.8   REFERENCES

[15-1]   Pandya, M.J., Parlette, E. and Frink, N.T.: *USM3D Users Manual Version 6.0 Prepared for: Configuration Aerodynamics Branch NASA Langley Research Center*, http://tetruss.larc.nasa.gov/usm3d/index.html Accessed on 07/09/08.

[15-2]   Lamar, J.E. and Obara, C.J.: *Review of Cranked-Arrow Wing Aerodynamics Project: Its International Aeronautical Community Role*, AIAA Paper 2007-0487, Presented at 45th AIAA Aerospace Sciences Meeting and Exhibit, Reno, NV, January 8-11, 2007.

[15-3]   Pandya, M.J., Abdol-Hamid, K.S., Campbell, R.L. and Frink, N.T.: *Implementation of Flow Tripping Capability in the USM3D Unstructured Flow Solver*, AIAA Paper No. 2006-0919, 2006.

[15-4]   Lamar, J.E., Obara, C.J., Fisher, B.D. and Fisher, D.F.: *Flight, Wind-Tunnel, and Computational Fluid Dynamics Comparison for Cranked Arrow Wing (F-16XL-1) at Subsonic and Transonic Speeds*, NASA/TP-2001-210629, February 2001.

[15-5]   Boelens, O.J., Görtz, S., Morton, S.A., Fritz, W. and Lamar, J.E.: *Description of the F-16XL Geometry and Computational Grids Used in CAWAPI*, AIAA Paper 2007-0488, Presented at 45th AIAA Aerospace Sciences Meeting and Exhibit, Reno, NV, January 8-11, 2007.

[15-6]   Pirzadeh, S.Z.: *Vortical Flow Prediction Using an Adaptive Unstructured Grid Method*, Presented at RTO AVT Symposium on "Advanced Flow Management; Part A – Vortex Flow and High Angle of Attack", Paper Number 13, in Loen, Norway, during May 7-11, 2001.

[15-7]   Elmiligue, A.A., Abdol-Hamid, K.S. and Massey, S.J.: *PAB3D Simulations for the CAWAPI F-16XL*, AIAA Paper 2007-0491, Presented at 45th AIAA Aerospace Sciences Meeting and Exhibit, Reno, NV, January 8-11, 2007.

[15-8]   Carlson, J.R.: *High Reynolds Number Analysis of Flat Plate and Separated Afterbody Flow Using Non-Linear Turbulence Models*, AIAA 96-2544, 32nd AIAA/ASME/SAE/ASEE Joint Propulsion Conference and Exhibit, Lake Buena Vista, Florida, July 1-3, 1996.

[15-9]   Boelens, O.J., Spekreijse, S.P., Sytsma, H.A. and de Cock, K.M.J.: *Comparison of Measured and Simulated Flow Features for the Full-Scale F-16XL Aircraft*, AIAA Paper 2007-0489, Presented at 45th AIAA Aerospace Sciences Meeting and Exhibit, Reno, NV, January 8-11, 2007.

[15-10] Badcock, K.J.: *Evaluation of Results from a Reynolds Averaged Multiblock Code Against F-16XL Flight Data*, AIAA Paper 2007-0490, Presented at 45th AIAA Aerospace Sciences Meeting and Exhibit, Reno, NV, January 8-11, 2007.

[15-11] Fritz, W.: *Hybrid Grid RANS Solutions for the CAWAPI F-16XL*, AIAA Paper 2007-0492, Presented at 45th AIAA Aerospace Sciences Meeting and Exhibit, Reno, NV, January 8-11, 2007.

[15-12] Morton., S.A., McDaniels, D.R. and Cummings, R.M.: *F-16XL Unsteady Simulations for the CAWAPI Facet of RTO Task Group AVT-113*, AIAA Paper 2007-0493, Presented at 45th AIAA Aerospace Sciences Meeting and Exhibit, Reno, NV, January 8-11, 2007.

[15-13] Görtz, S. and Jirásek, A.: *Unstructured Steady/Unsteady Solutions with Edge for CAWAPI F-16XL at KTH/FOI*, AIAA Paper 2007-0678, Presented at 45th AIAA Aerospace Sciences Meeting and Exhibit, Reno, NV, January 8-11, 2007.

[15-14] Michal, T., Oser, M., Mani, M. and Ross, F.: *BCFD Unstructured-Grid Predictions on the F-16XL (CAWAPI) Aircraft*, AIAA Paper 2007-0679, Presented at 45th AIAA Aerospace Sciences Meeting and Exhibit, Reno, NV, January 8-11, 2007.

[15-15] Davis, M.B., Reed, C. and Yagle, P.: *Hybrid Grid Solutions on the (CAWAPI) F-16XL Using Falcon v4*, AIAA Paper 2007-0680, Presented at 45th AIAA Aerospace Sciences Meeting and Exhibit, Reno, NV, January 8-11, 2007.

[15-16] Karman, S., Mitchell, B. and Sawyer, S.: *Unstructured Grid Solutions of CAWAPI F-16XL by UT SimCenter*, AIAA Paper 2007-0681, Presented at 45th AIAA Aerospace Sciences Meeting and Exhibit, Reno, NV, January 8-11, 2007.

[15-17] Lamar, J.E., Obara, C.J., Fisher, B.D., and Fisher, D.F.: *Flight, Wind-Tunnel, and Computational Fluid Dynamics Comparison for Cranked Arrow Wing (F-16XL-1) at Subsonic and Transonic Speeds*, NASA/ TP-2001-210629/Supplement, July 2008.

Appendix 15-1
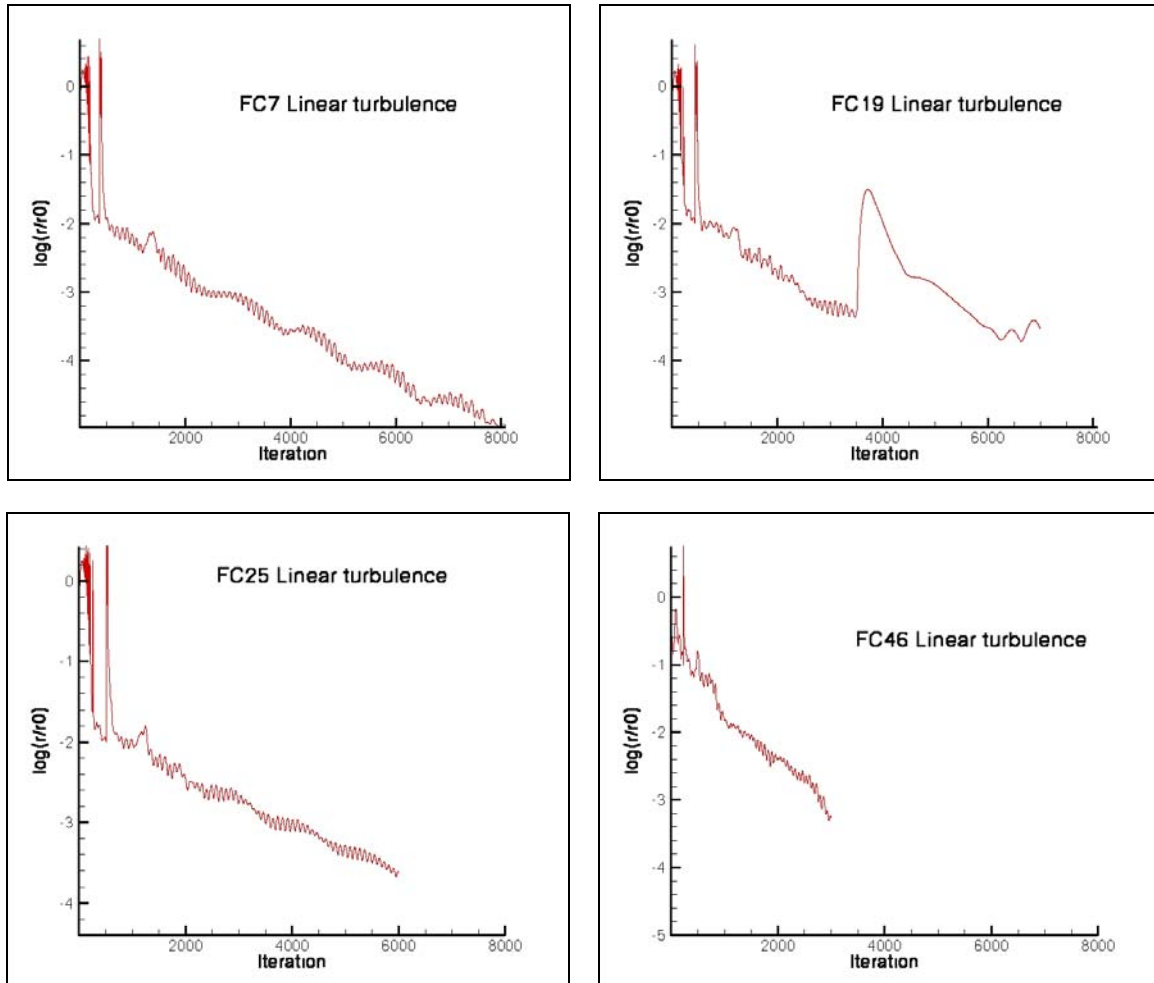
**Figure 15-A1: Convergence Histories of USM3D Solutions as Expressed in the Log Residual-Ratio
for the Mean-Flow Equations on this Grid for FC7, FC19, FC25, FC46, FC50, FC51 and FC70.**
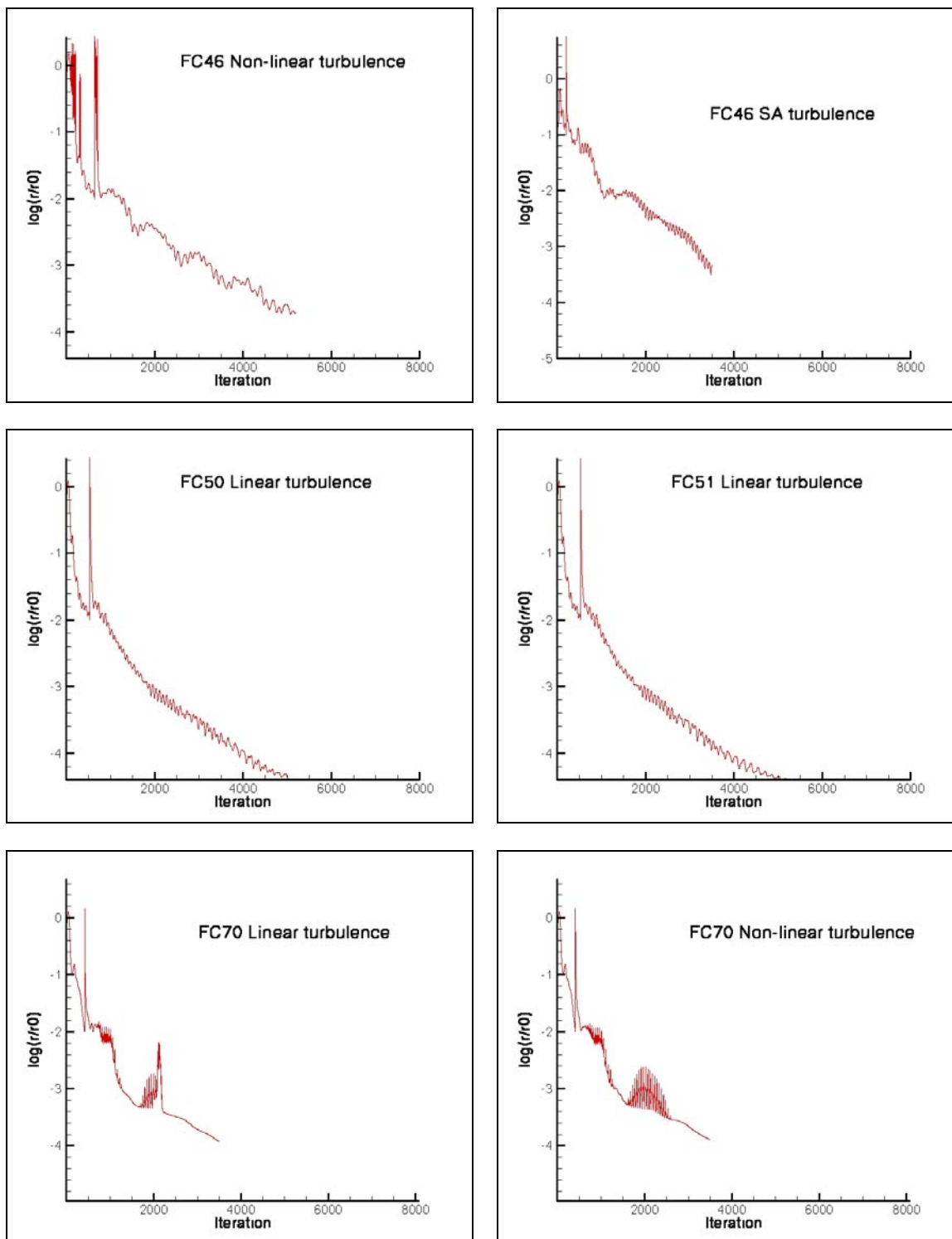
Figure 15-A1: Continued.
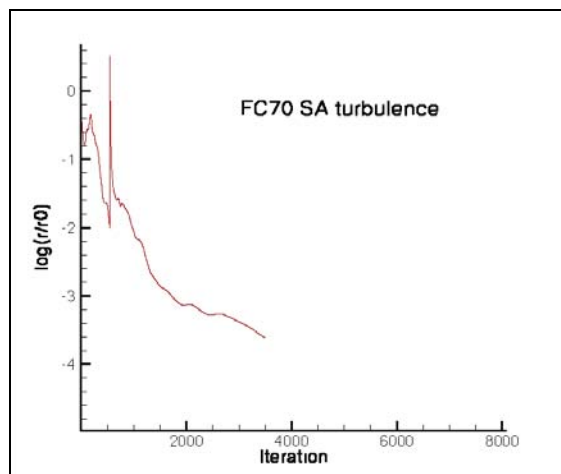
Figure 15-A1: Concluded.

Chapter 16 – WHAT WAS LEARNED FROM NUMERICAL SIMULATIONS OF F-16XL (CAWAPI) AT FLIGHT CONDITIONS

by

**Arthur Rizzi, Adam Jirásek, Ken J. Badcock, Okko J. Boelens,
John E. Lamar** *(Retired)* **and Simone Crippa**

16.1 SUMMARY

Nine groups participating in the CAWAPI project have contributed steady and unsteady viscous simulations of a full-scale, semi-span model of the F-16XL aircraft. Three different categories of flight Reynolds/Mach number combinations were computed and compared with flight-test measurements for the purpose of code validation and improved understanding of the flight physics. Steady-state simulations are done with several turbulence models of different complexity with no topology information required and which overcome Boussinesq-assumption problems in vortical flows. Detached-eddy simulation (DES) and its successor delayed detached-eddy simulation (DDES) have been used to compute the time accurate flow development. Common structured and unstructured grids as well as individually-adapted unstructured grids were used. Although discrepancies are observed in the comparisons, overall reasonable agreement is demonstrated for surface pressure distribution, local skin friction and boundary velocity profiles at subsonic speeds. The physical modeling, be it steady or unsteady flow, and the grid resolution both contribute to the discrepancies observed in the comparisons with flight data, but at this time it cannot be determined how much each part contributes to the whole. Overall it can be said that the technology readiness of CFD-simulation technology for the study of vehicle performance has matured since 2001 such that it can be used today with a reasonable level of confidence for complex configurations.

16.1.1 Nomenclature

C_p^*	=	static-pressure coefficient at critical condition
$k\,\hat{\sigma}$	=	estimate of population standard deviation
λ_2	=	second eigenvalue of S-Ω tensor
$\tilde{\mu}$	=	estimate of population mean

16.1.2 Organizations

Boeing	=	Boeing-Phantom Works-St.Louis, MO, USA
EADS-MAS	=	European Aeronautics and Defence Company – Military Aircraft Systems, Germany
FOI	=	Swedish Defence Research Agency, Sweden
KTH	=	Royal Institute of Technology, Sweden
LM Aero	=	Lockheed Martin Aeronautics Company, TX, USA
NASA	=	NASA Langley Research Center, Hampton, VA, USA
NLR	=	National Aerospace Laboratory, Netherlands
ULiv	=	University of Liverpool, UK
UTSimC	=	University of Tennessee at Chattanooga, TN, USA
USAFA	=	United States Air Force Academy, CO, USA

16.2   INTRODUCTION

The original NASA document [16-1] together with the preceding chapter [16-2] have introduced the problem that the AVT-113 task group studied, that of increasing the Technology Readiness Level (TRL) of the CFD solvers by establishing best practices with the solvers as applied to the F-16XL aircraft at a number of flight conditions. Another one of the preceding chapters [16-3] reported how the grids were established for each solver type (structured, unstructured common or tailored) or with a particular solver studied, and the remaining companion chapters [16-4] to [16-13] in this series presented analyses and representative results for each solver type. This chapter draws from the base papers, [16-4] to [16-13] presented at two Special Sessions of the AIAA ASM Conference in January 2007, along with new analysis and summaries, not previously available, to put into perspective what was accomplished by the Cranked Arrow Wing Aerodynamics Project International (CAWAPI) facet of the AVT-113 task group. Moreover, CFD comparisons are also offered with those reported in the basic document [16-1] which was used to launch this study.

This paper compares cumulatively all the computed results with the flight-test measurements, makes some overall observations about these comparisons, discusses some likely causes for discrepancies, and where possible draws tentative conclusions and tries to identify lessons learned in order to take a step forward towards establishing some best practices for this class of problem. Similar cumulative-comparison activities have been done before, notably among them, the series of AIAA Drag Prediction Workshops. What we do here differs in that it is a fighter configuration, a flying aircraft, and the comparisons are done against flight-test data not wind tunnel measurements, which makes it rather unique. Furthermore the objective is not the accurate prediction of say total drag counts, but instead is the prediction of complex vortical-flow phenomena that strongly impact the flying qualities of a fighter aircraft because the interaction of vortices over such an aircraft determines its stability and control characteristics.

The lessons learned in this five-year study are reported here by first reviewing the impact of the grid on the CFD solvers and the ensuing solutions, then the predictive capabilities themselves of the solvers for selected dominant vortical- and transonic-flow flight conditions, along with any deficiencies are noted. The flight condition (FC) at the highest angle of attack (FC25) is discussed using three sets of representative results. This case showed significant unsteady flow. For FC19, results are compared for the prediction of skin friction and for boundary-layer profiles in FC7. Next, a wide ranging effort to explain significant discrepancies between measurements and computations for the transonic flight condition (FC70) is described. A high-level overall assessment is then made by first comparing progress achieved since the NASA publication [16-1] from 2001, and secondly by quoting comments made by industry participants regarding the value of their participation in the study. Finally, conclusions are stated.

CFD solutions used in this study can be post-processed to predict not only surface flow physics but also the component force and moment coefficients for the aircraft. Appendix 16-1 provides a comparison of these coefficients from the different solvers along with a simple statistical analysis of the predicted data, and Appendix 16-2 details the means by which the statistical analysis was performed.

16.3   OVERVIEW OF CODES AND COMPARISONS

Table 16-1 lists the ten solvers utilized in CAWAPI along with a brief description of relevant information about each, including the models employed, whether steady or unsteady flow was computed and the grid type used. The flight conditions computed by each partner are also listed. The geometry used during this exercise is a detailed model of the F-16XL geometry. Details on both geometry and grids can be found in Lamar et al. [16-1], [16-2] and Boelens et al. [16-3]. More details on the solvers can be found in references [16-4] to [16-13].

Note that all turbulence models integrate to the wall with the exception of LM Aero, which used wall functions. The rows in the table are grouped by the grid type used. The first group used a common multi-block grid, the second group used a common unstructured grid. Finally, the third group used tailored grids, referred to in this paper as trimmed grids.

Table 16-1: Overview of Ten Solutions Generated by the Nine Participating Organizations

Contributor/Code	Grid type	Turbulence models	Numerics$^{\Upsilon}$	FC
NLR [16-4][16-14] *ENFLOW*	common structured	k-ω + vorticity corrections	CC, central	FC7, FC19, FC25, FC46, FC50, FC51, FC70
University of Liverpool [16-6] *PMB*	common structured	k-ω TNT + vorticity corrections	CC, Osher upwind, Roe flux-vector splitting	FC7, FC19, FC25, FC46, FC70
NASA-LaRC [16-7] *PAB3D*	common structured	k-ω SZL EARSM, Girimaji EARSM + vorticity corrections	CC, Roe flux-vector splitting, implicit 3 factor scheme, explicit - DTS	FC7, FC19, FC25, FC46, FC50, FC51, FC70
USAFA [16-12] *Cobalt*	common unstructured	SARC-DES$^{\Upsilon\Upsilon}$, SARC-DDES	CC, Godunov type with least square approximation, implicit with newtonian method	FC7*, FC19*, FC25*, FC46*, FC50*, FC51*, FC70*
KTH/FOI [16-8] *Edge*	common unstructured	SA, Hellsten EARSM k-$\omega^{\Upsilon\Upsilon}$, Hellsten EARSM k-$\omega$ + rotational corrections, DES, Hybrid RANS-LES	NC, central	FC7*, FC19, FC25*, FC46*, FC50, FC51, FC70 (Euler, RANS)
NASA-LaRC [16-11] *USM3D*	common unstructured	linear k-$\varepsilon^{\Upsilon\Upsilon}$, non-linear k-$\varepsilon$	CC, Roe FDS, implicit scheme	FC7, FC19, FC35, FC46, FC50, FC51, FC70
EADS-MAS [16-9] *TAU*	trimmed unstructured	SA	NC, AUSMDV, backward Euler implicit + LU-SGS	FC7, FC19, FC35, FC46, FC50, FC51, FC70
UT SimCenter [16-10] *TENASI*	trimmed unstructured	linear k-ω k-ε hybrid	NC, Roe flux-vector splitting, point implicit	FC7, FC19, FC35, FC46, FC50, FC51, FC70
Boeing [16-5] *BCFD*	trimmed unstructured	SA, Menter SST, SST-LESb	CC, HLLE, FDS	FC7*, FC19, FC25*, FC46, FC70

Contributor/Code	Grid type	Turbulence models	Numerics[ϒ]	FC
LM Aero [16-13] *Falcon v.4*	trimmed unstructured	k-kl	Roe approximate Riemann solver, implicit ILU	FC7, FC19, FC70

[ϒ]Numerical method Cell-centered (CC) or Node-centered (NC)

[ϒϒ]Turbulence model used in common comparisons

[*]Flight condition calculated as unsteady

The flight conditions are defined in detail in Lamar and Obara [16-2]. In this paper the conditions computed are split into two groups. The first (FC7, FC19, FC25, FC46, FC50 and FC51) are dominated by strong vortices and have low subsonic free-stream Mach numbers at moderate to high angles of attack. The second group (FC70) is at high subsonic free-stream Mach numbers and a relatively low angle of attack, and features shock waves and a weak vortex. The comparisons are made separately for these two groups of conditions.

16.4   LOW-SPEED FLOW CASES

16.4.1   Unsteady Flows at High Angle of Attack – FC25

16.4.1.1   Overview

The conditions for FC25 are $M_\infty = 0.242$, $\alpha = 19.8°$, $Re = 32.22 \times 10^6$. FC25 has the largest angle of attack and thus better defined vortical flow phenomena are expected over the upper surface, perhaps even vortex breakdown over the aft portion of the aircraft. Large-scale flow unsteadiness is also associated with such phenomena. For this flight condition surface pressure measurements are available.

16.4.1.2   Vortical Flow Features

Figure 16-1 presents sectional spanwise contours of iso-total-pressure, skin friction lines and flight tuft patterns.
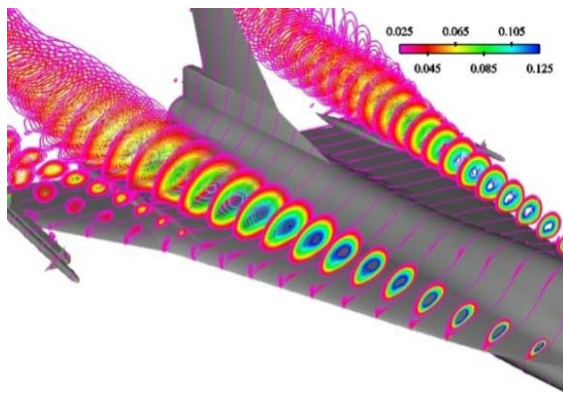
FC25: M_∞=0.242, α=19.84°, Re=32.22· 10

**(a) Sectional Spanwise Iso-Total-Pressure
Contours [16-4]**
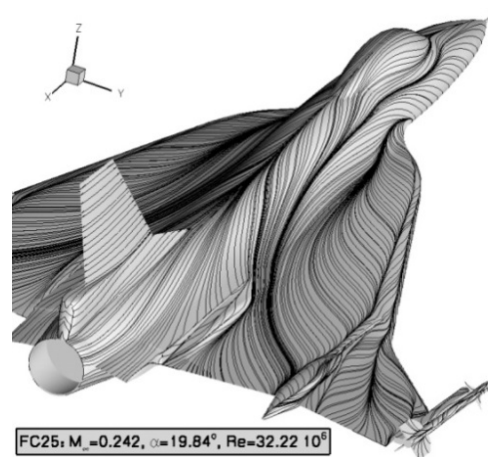
FC25: M_∞=0.242, α=19.84°, Re=32.22 10^6

(b) Skin Friction Lines [16-4]

**(c) Flight Tuft Photo from Vertical-Tail Top-Left Camera
Mirrored about the Vertical Axis of the Photo [16-1]**

Figure 16-1: Vortical-Flow Features over Upper Surface for FC25.

The contour plots indicate the presence and location of the inner wing primary and secondary vortices, the outer wing primary and secondary vortices. The convergence-divergence of skin friction lines indicates the occurrence and location of primary or secondary vortex separation-reattachment, respectively. Figure 16-1 (b) suggests that the separation layer on the fuselage is now drawn outboard towards the actuator pod where it may merge with the vortical flow around that structure. There are striking overall similarities with the in-flight photographs of the tufts shown in Figure 16-1 (c). Similar behavior is observed for the inward flow to the airdam on both the inner and outer wings and the marked flow division that occurs on the outer wing. Differences are seen for the inner wing spanwise flow extending toward the fuselage, especially near the trailing edge.

16.4.1.3 C_p Comparisons along Butt Line Sections

A down-select of the ten solutions makes the FC25 C_p comparison with flight data more tractable. One solution from each type of grid was selected, namely NLR for the standard structured grid, EADS for the tailored unstructured grid, and USAFA for the standard unstructured grid. Keep in mind that the first two results are steady-state RANS solutions whereas the third (USAFA) is a time-accurate DES solution [16-12]. These three results have been cross-plotted with the flight data and the previous CFL3D solutions [16-1] and their comparisons are now shown. The time-averaged value (mean) is plotted for the unsteady USAFA solution. In their chapters Görtz et al. [16-11] Morton et al. [16-12] report significant unsteadiness in their solutions located over the rear of the wing, close to the wing tip, especially at BL184.5.

Figure 16-2 shows comparisons of the computed and flight measured surface pressure coefficients C_p plotted along the butt lines, the first four along the inner wing and the last two along the outer wing where we expect strong interactions. The first four butt lines (BL55, BL70, BL80 and BL95) show that the pressures associated with inner wing primary and secondary vortices are being resolved. The leading edge vortex forms in the vicinity of BL55 and the measured values show a primary-vortex peak as well as a secondary-vortex peak, as do some, but not all, of the computed results. The fall off in primary suction peak from BL55 to BL95 is associated with the center of the vortex system moving farther from the surface the further the system travels downstream. This feature is caused by the system capturing more leading-edge shed vorticity, as it traverses the wing, yielding an enlarged cross-section. Morton et al. [16-12] present similar inner butt lines plots in which they plot the instantaneous values of minimum and maximum C_p that forms a band around the time-averaged mean values. Over the inner wing this band is very thin, indicating that the flow here is steady.

(a) BL55   **(b) BL70**
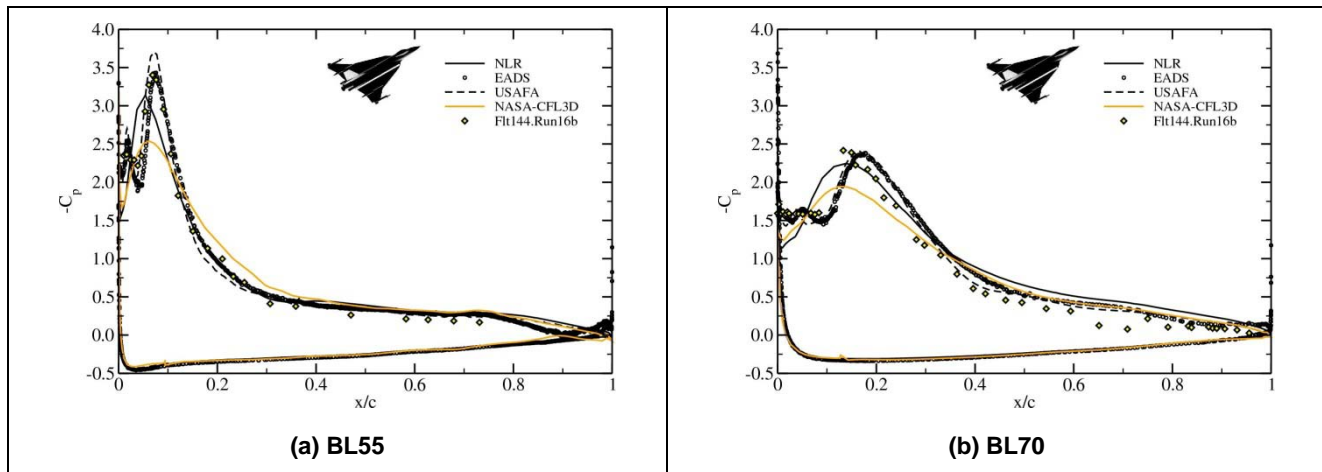
Figure 16-2: Chordwise Comparison for FC25 of Pressure Coefficient.
Solutions provided by respective, listed organization – see Table 16-1.
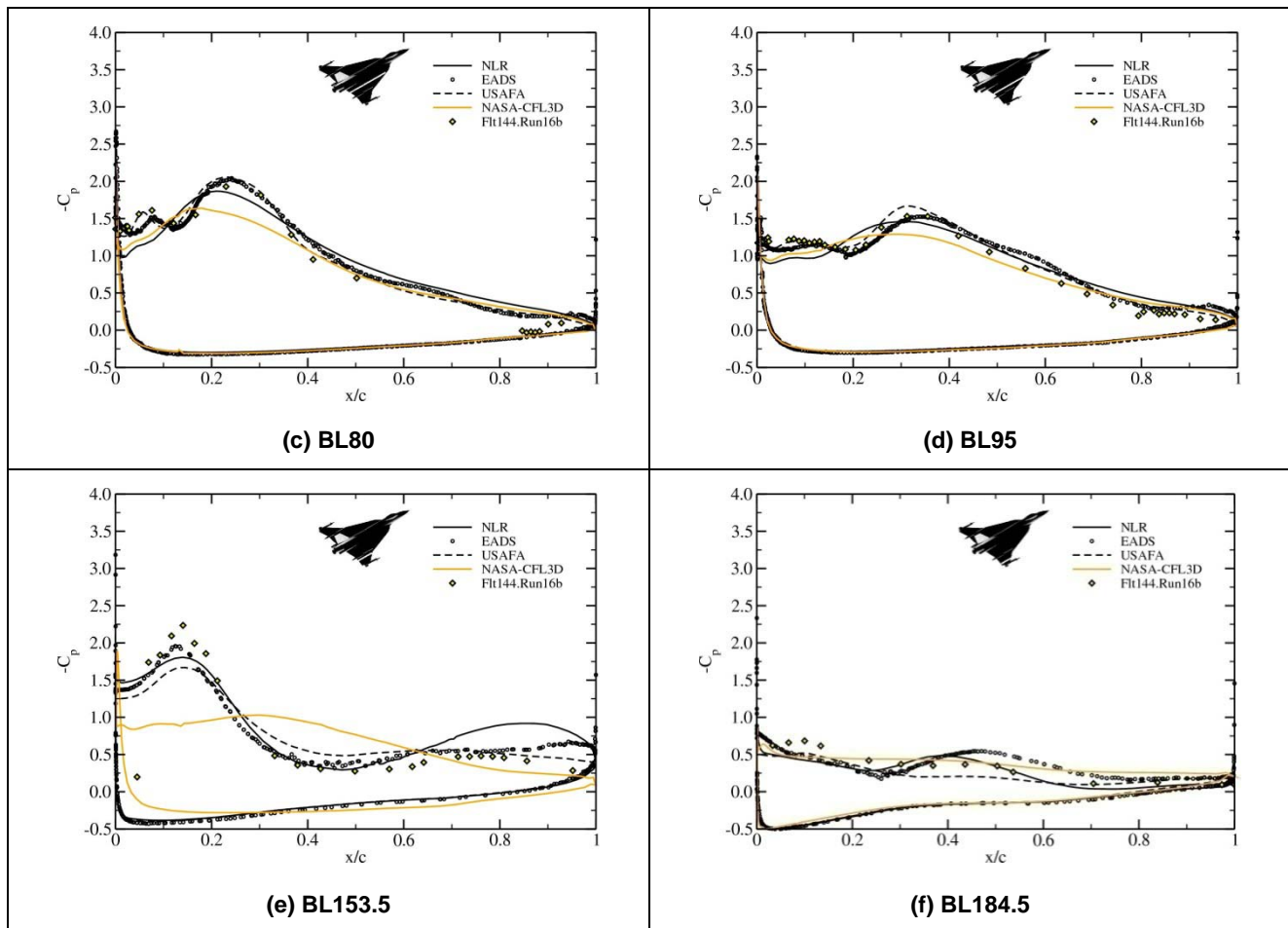
Figure 16-2: Concluded.

At BL153.5 and BL184.5 the predicted and measured pressures demonstrate that there are strong interactions between the vortices shed from the inner wing, actuator pod, airdam and crank. At BL153.5, just outboard of the juncture of these vortices, the computed and measured results show a suction peak for the outer wing primary vortex near 15% chord and a smaller peak near 75% chord from the combination of actuator pod/airdam/inner wing secondary vortices; however, the predictions for the second peak have something of a spread in the peak value and its location. At BL184.5 the measured peak value for the outer-wing primary vortex is much reduced and its location occurs closer the leading-edge, near 10% chord. A second, smaller peak is predicted to occur at this butt line near mid-chord and is primarily associated with the inner-wing secondary vortex (See Figure 16-1 (b)). Note that the flow in the vicinity of the wing tip is made even more complicated because of the vortex wake off of the missile fins, especially at this angle of attack. For these two butt line locations on the outer wing, the plot in Morton et al. [16-12] now shows bands between the minimum and maximum instantaneous C_p values that are very broad and encompass the measured data. This indicates that the flow over the outboard wing section has substantial unsteadiness. It also suggests that the USAFA mean value plotted in Figure 16-2 (e) and Figure 16-2 (f) is a more accurate estimate of the unsteady pressure distribution than the other Reynolds-averaged steady-state results.

From the comparisons presented, the solver used by the USAFA with the DES turbulence model produced the best overall agreement with the flight data, indicating that for this angle of attack, modeling the large-scale unsteadiness in a time accurate mode is a key to improved predictability. All of the new solvers showed superior agreement with data in comparison to that documented in Lamar et al. [16-1] for the CFL3D solver with an order of magnitude fewer grid points used and larger y^+ value.

16.4.2   Skin Friction Coefficient – FC19

16.4.2.1   Overview

The conditions for FC19 are $M_\infty = 0.36$, $\alpha = 11.85°$, Re = 46.8 x 10^6. FC19 is also a case of fully developed vortical flow over the upper surface. For this flight condition skin friction measurements are available.

16.4.2.2   Vortical Flow Features

Figure 16-3 shows sectional spanwise contours of iso-total-pressure and skin friction lines. The contour plots indicate the presence and location of the inner-wing primary and secondary vortices, the outer-wing primary and secondary vortices. Note the presence of small fuselage vortices that were not present for FC25 (see Figure 16-1).
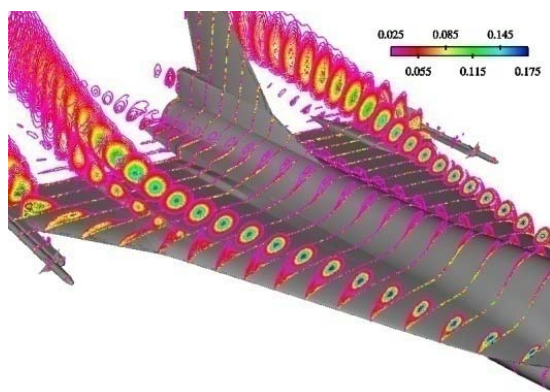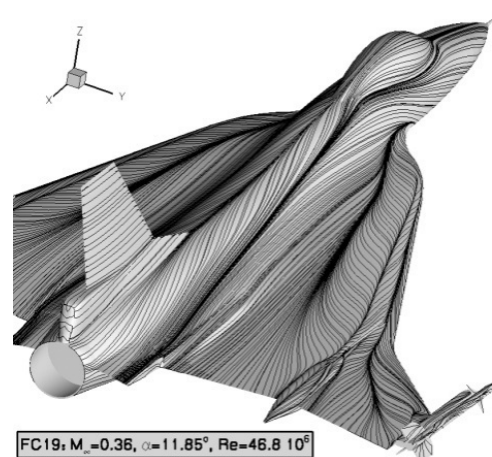
(a) Sectional Spanwise Contours Showing Vortical Flow Features over Upper Surface [16-4]	**(b) Skin-Friction Lines over Upper Surface [16-4]**

Figure 16-3: Vortical-Flow Features over Upper Surface for FC19.

16.4.2.3   Skin Friction Comparison

Figure 16-4 compares the computed and measured values of the skin friction coefficient c_f at fuselage station FS330. In general, the skin friction coefficient c_f is a vector quantity. The measurements were made with modified Preston tubes that pointed into the local flow direction – which varied across the FS330. The fact that the local skin friction can be correlated with the delta-p between the static and total pressure is the basis of these measurements, but these are a magnitude measurement. The comparison is made with the magnitude

of the computed vector quantity. The location FS330 is in the general vicinity of the boundary-layer rakes discussed below. The measured values show two peaks in c_f, the highest under the primary inner-wing vortex and the lower one under the secondary inner-wing vortex.

Color coding: **Black – Common structured mesh**
Blue – Common unstructured mesh
Red – Trimmed unstructured mesh
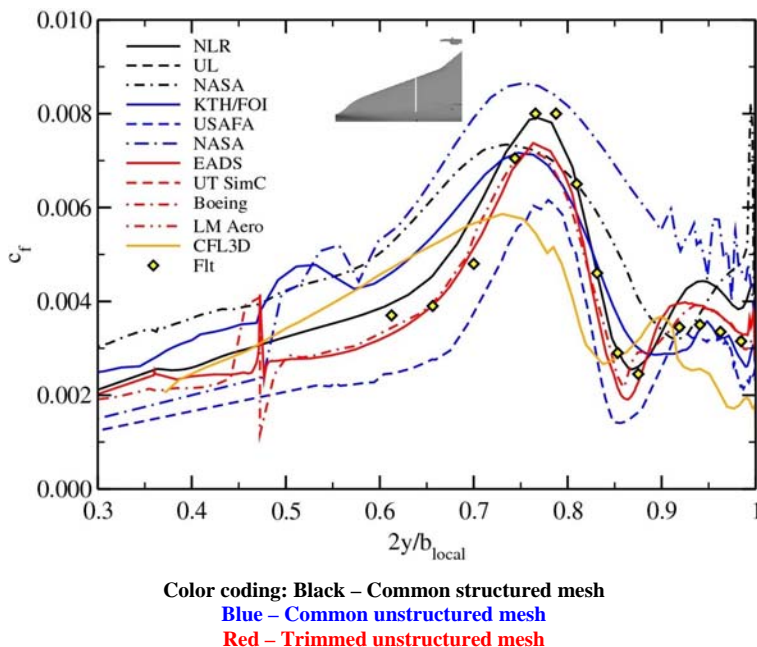
**Figure 16-4: Spanwise Comparison (FS 330) for FC19 of the Magnitude of the Skin Friction
Coefficient c_f. Solutions provided by respective, listed organization – see Table 16-1.**

The computed results of the KTH/FOI and the NASA unstructured solvers show three peaks, the inboard one occurs at a location where there are no measurements that could confirm it. USAFA results, which were obtained on the same mesh, do not show the third peak. It is clearly visible that unstructured trimmed mesh results (EADS and Boeing) give almost identical results.

16.4.3   Velocity Profiles – FC7

16.4.3.1   Overview

FC7 has conditions $M_\infty = 0.304$, $\alpha = 11.89°$, $Re = 44.4 \times 10^6$. These are similar to FC19, and the flow topology is also similar. For this case boundary layer measurements are available.

16.4.3.2   Velocity Comparisons

Figure 16-5 shows the comparison of measured and predicted boundary-layer profiles for rake locations #3, #4, #5 and #7 respectively, for all RANS solutions [16-4] to [16-11], [16-13], USAFA DDES [16-12] and CFL3D results [16-1]. The agreement with flight test data is very good for three of four positions #3, #4 and #5. In position #7 the spread of all results is rather large. Some of the results show "jet-type" flow (USAFA and NASA unstructured solvers). On the other side is EADS that predicts lower velocities. This rake is located underneath the separation line between primary and secondary vortex and so the flow is complicated in this

region. Inspection of the results shows that the structured meshes results have the smallest spread, especially in position #5 and #7 compared to other results. The largest spread is in the common unstructured results.
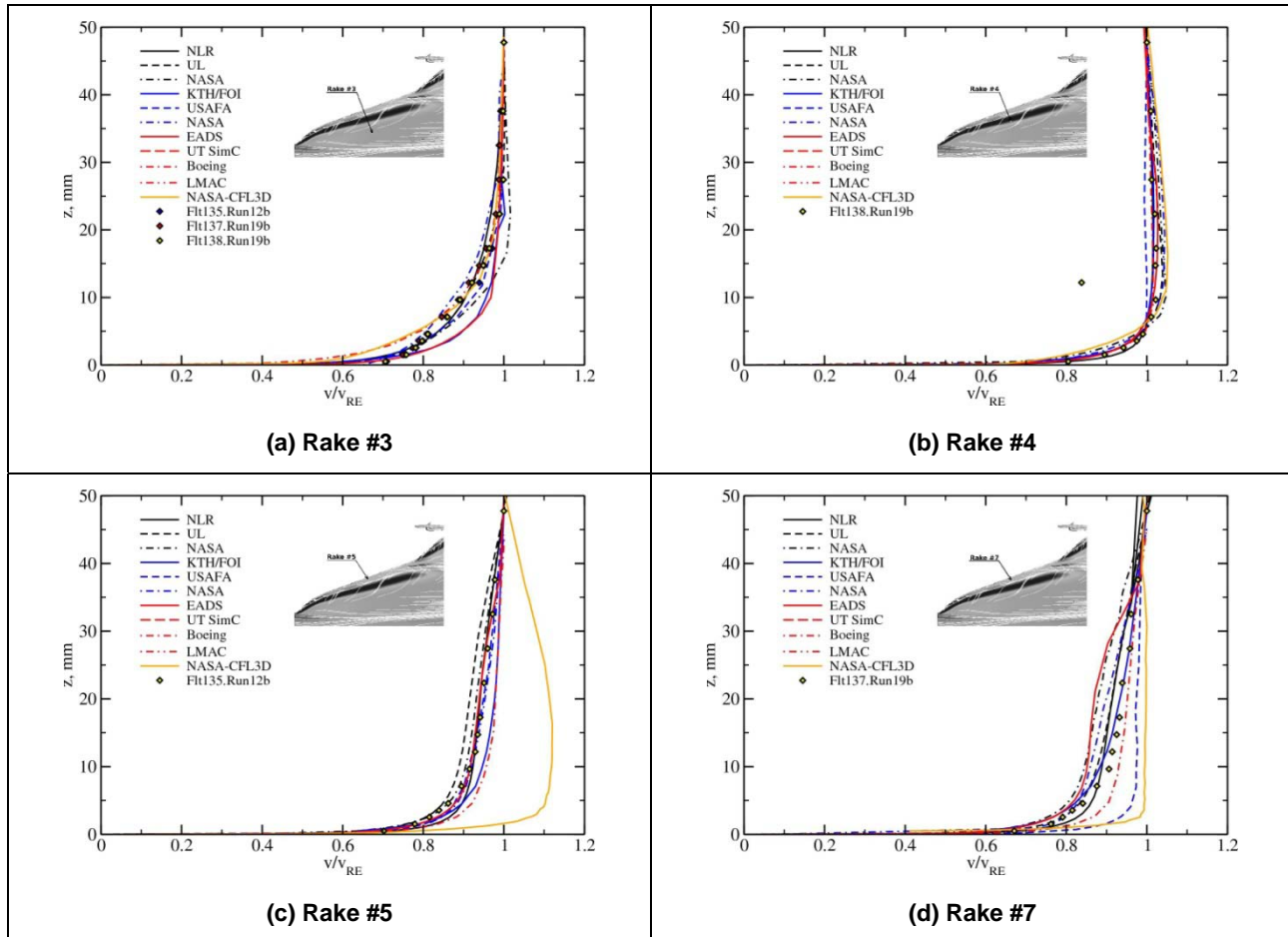
(a) Rake #3

(b) Rake #4

(c) Rake #5

(d) Rake #7

Color coding: Black – Common structured mesh
Blue – Common unstructured mesh
Red – Trimmed unstructured mesh

**Figure 16-5: FC07, Velocity Profiles Comparison. Solutions provided
by respective, listed organization – see Table 16-1.**

A comparison of steady versus unsteady results is also interesting. Figure 16-6 shows the envelope of velocity profiles for all RANS solutions in black with unsteady DES, DDES and Hybrid RANS-LES of USAFA and KTH/FOI [16-11] in two positions where comparisons are the most interesting – position #5 and #7. The scatter between RANS data at position #5 (Figure 16-6 (a)) is large which is also true for different unsteady methodologies. The KTH/FOI DES result shows the largest deviation to the average result whereas USAFA DES lie on the boundary of RANS models interval. USAFA-DDES and KTH/FOI Hybrid modeling moves velocity profiles closer to flight test data and into the cloud of RANS results. The results at rake #7 shown in Figure 16-6 (b) have large scatter. The KTH/FOI hybrid model shows good agreement with flight data. The DES model predicted velocity profile is on the boundary of the RANS results envelope. USAFA deviates from other results showing substantial improvement of the DDES over DES methodology.
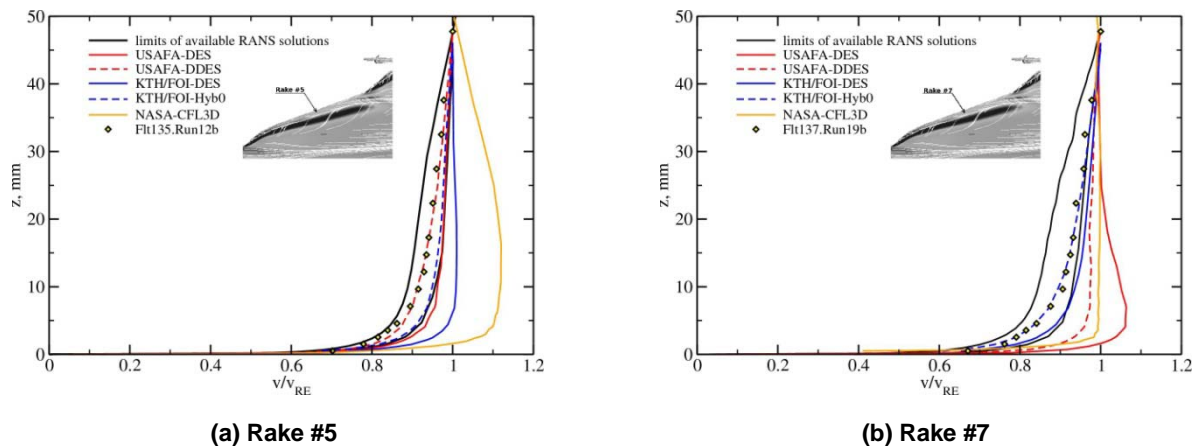
(a) Rake #5   **(b) Rake #7**

Color coding: Black – Common structured mesh
Blue – Common unstructured mesh
Red – Trimmed unstructured mesh

**Figure 16-6: FC07, Velocity Profiles Comparison; Effect of Turbulence Modeling and Time-Accuracy.
Solutions provided by respective, listed organization – see Table 16-1.**

The DES results have trouble in predicting velocity profiles in regions of highly stretched cells. One possible reason for this could be that the DES model does not use RANS in the boundary layer but switches to LES because the grid is so refined in the streamwise direction, resulting in a false log layer. Since the outer edge condition is used in the scaling for the comparisons, this can result in the jet like profile seen in the USAFA results. The DDES model forces the solver to stay RANS in the boundary layer even with refined grids in the boundary layer. These rakes are placed very close to the leading edge with a very refined grid to capture the leading edge suction peaks and therefore are susceptible to this problem. The overall pressure results are fairly insensitive to this but the boundary layer rake data and skin friction DES results seem to be suffering from the problem. The DDES model improves the situation for rake #5, but less so for rake #7.

16.4.4   Results at Sideslip Flight Conditions – FC50, FC51

Two additional flight conditions are side-slip conditions at angle of attack around $\alpha = 13°$ and subsonic Mach numbers around $M = 0.44$ and $Re = 39 \times 10^6$. These two conditions denoted FC50 and FC51 have the value of side-slip angle $\beta = 5.31°$ (FC50) and $\beta = 4.58°$ (FC51).

The effect of a sideslip angle is to decrease the effective leading edge sweep angle of the windward-side wing and to increase the leading edge sweep angle of the leeward-side wing. This effective decrease of sweep angle may cause vortex breakdown on the windward side to occur at a lower angle of attack than it would occur with no sideslip. In addition the reduced sweep angle may cause a double vortex structure [16-15].

These two flight conditions were not a main focus of the CAWAPI team. Two cases were however computed by some partners. Görtz et al. [16-11] Morton et al. [16-12] report on a study that outlines the effect of turbulence models and unsteadiness of the solution which seems to be significant for BL70 up to BL184.5.

16.5   TRANSONIC FLOW CASE

16.5.1   Overview

FC70 has conditions M_∞ = 0.97, α = 4.3°, Re = 88.8 x 10^6. This condition has the smallest angle of attack of all the test flights considered, and a high subsonic free-stream Mach number. Hence reduced-strength vortical-flow phenomena over the upper surface and strong transonic effects are expected. It must be pointed out that there is some degree of uncertainty in the flight-test data concerning whether, and how much, a flap was deflected during the measurements. Transonic effects are also very sensitive to flight conditions, and even weak interactions can lead to substantial changes in flow structure.

16.5.2   Overall Vortical Flow Features

Figure 16-7 presents sectional spanwise contours of iso-total-pressure and skin friction lines. The contour plots indicate that the fully developed and coherent vortex structures that have been observed in the previous flight conditions, namely primary and secondary vortices substantially above the inner and outer wings, are not present in this flight condition.

**(a) Sectional Spanwise Contours Showing Vortical
Flow Features over Upper Surface [16-4]**

**(b) Skin-Friction Lines over
Upper Surface [16-4]**
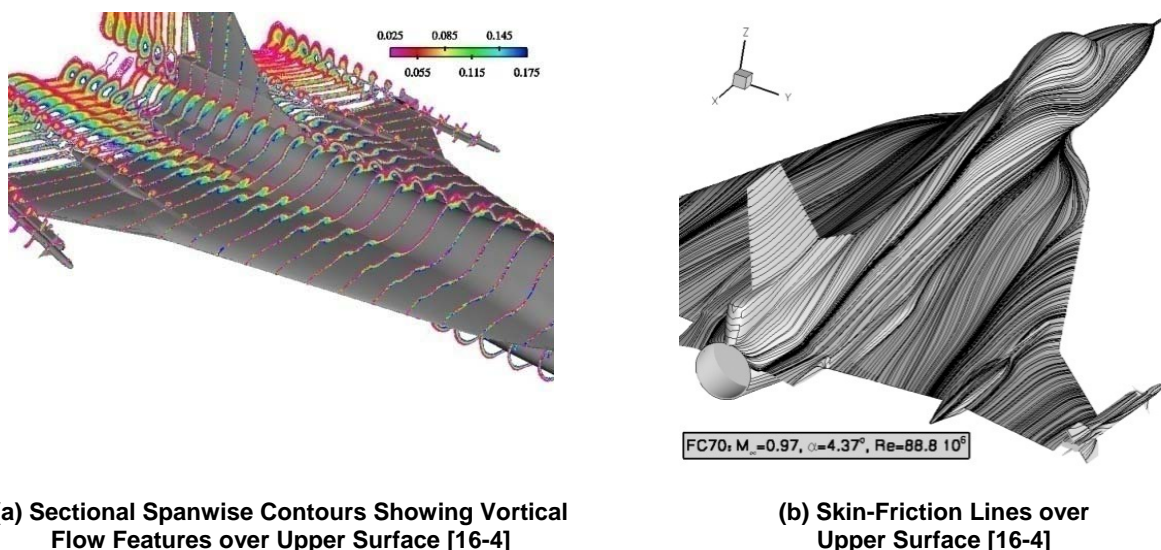
Figure 16-7: Low-Lying Vortices over Upper Surface for FC70.

The convergence-divergence of skin friction lines do show the confluence of vortical layers near the mid-span of the wing that likely separates and re-attaches inboard near the fuselage. Separation does seem to occur, but the lift-off appears to remain close to the upper surface, either just in, or just above the boundary layer. The flow does separate from the airdam/actuator-pod and a small vortex seems to develop. Notice, however, that no vortex is shed from the outer wing nor is there any sign of a secondary vortex over the inner wing, as found in the other cases.

As shown in Figure 16-8, at BL55 there is a shock wave at approximately 5% chord due to the decelerating effect of the low sweep of the inner-wing fairing. There is another shock wave at about 30% chord on the upper surface. In the computations there is also a shock at 20% chord of the lower wing surface. There are, however,

no measured values at this location to confirm it. Along BL70 and BL80 several computations agree with each other, but not with the measurements. The computed results show a shock on the upper surface located well upstream of the shock shown by flight data. The last two butt-lines, BL153.5 and BL184.5, are on the outer wing where the flow is influenced by the airdam, crank and missile. All computational results over-predict the suction peak near the leading edge; this could be due to the leading-edge flap on the outer wing that was reported to be deflected upward (from negative 5° to negative 9°) while the trailing-edge flap was deflected 2° downward in the flight test. Differences begin to grow in the computed results especially in the aft part of the chord. At BL153.5 the measurements might suggest a shock just before 80% chord, and just before 60% chord in BL184.5. This is in disagreement with the computations that could be due to the in-flight deflected trailing-edge flap, which is not modelled in the computations.
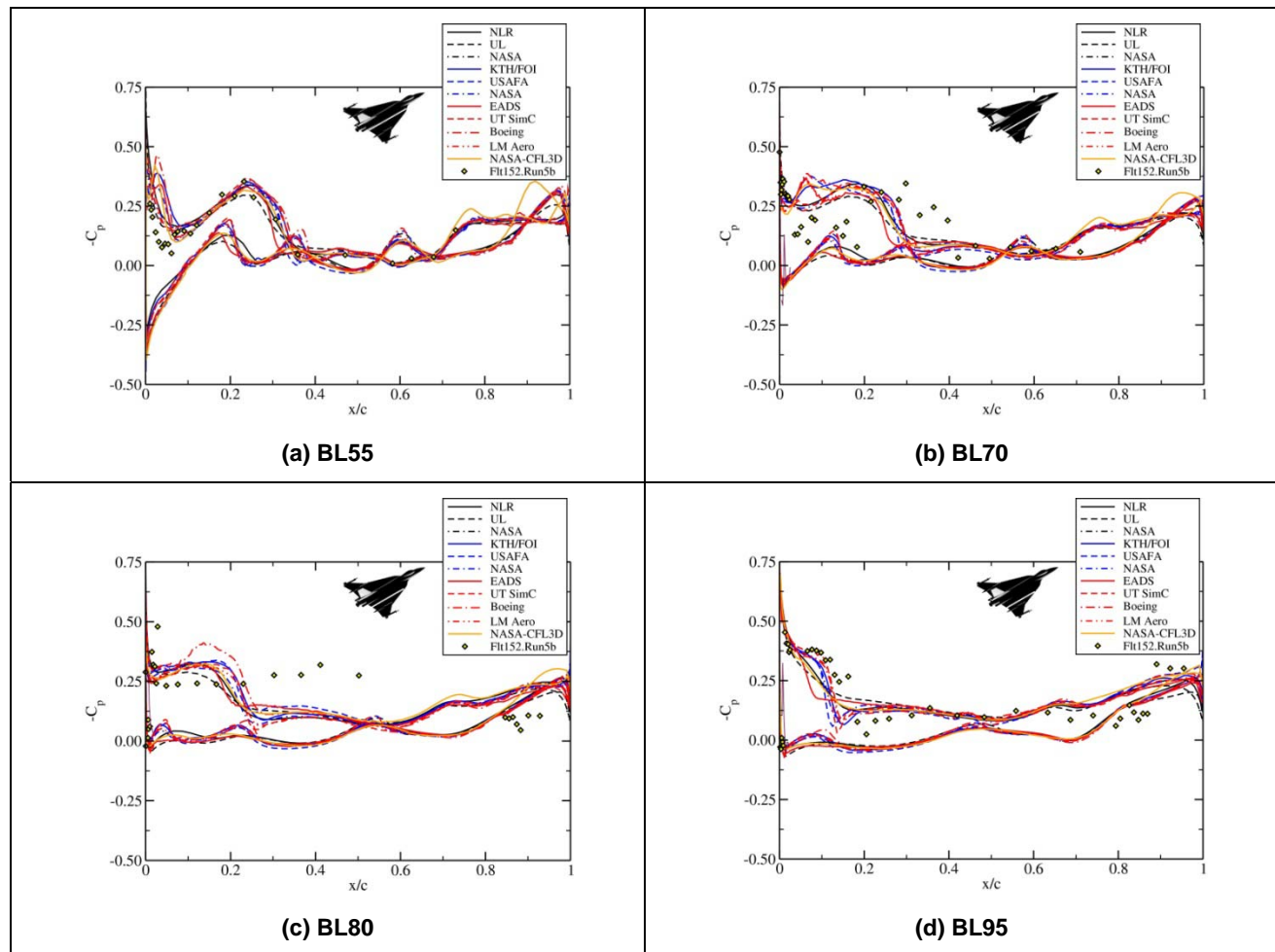
**Figure 16-8: Chordwise Comparison for FC70 of Pressure Coefficient.
Solutions provided by respective, listed organization – see Table 16-1.**

(e) BL153.5

(f) BL184.5
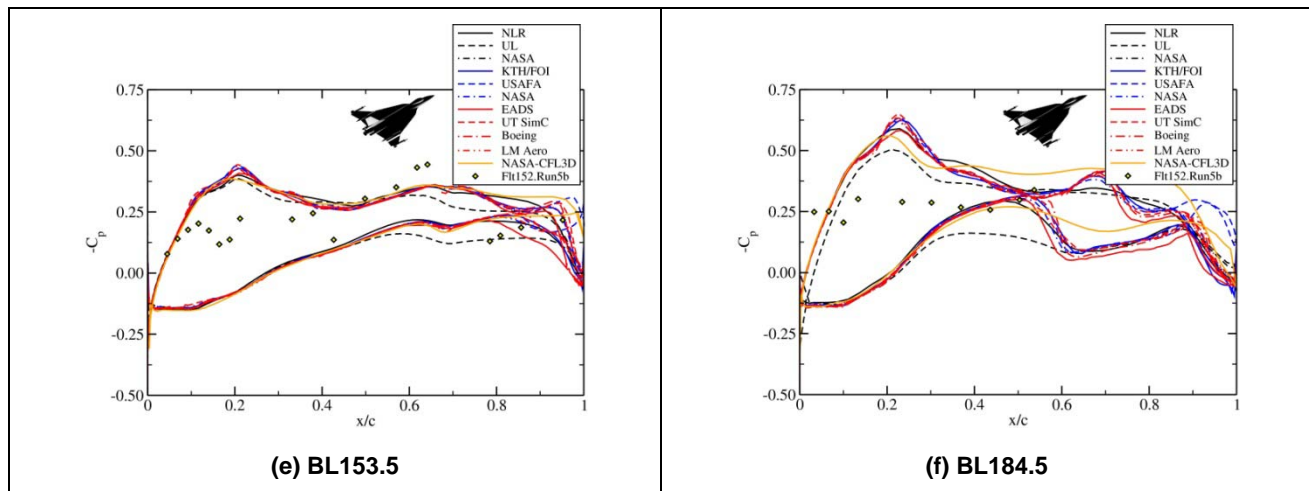
Color coding: Black – Common structured mesh
Blue – Common unstructured mesh
Red – Trimmed unstructured mesh

Figure 16-8: Concluded.

A general inspection of the butt-line C_p comparisons prompts the overall comment that the computed data agree very well among themselves but differ substantially from the measurements, except at BL55 and BL95 where all results are in fairly good agreement. If we accept the explanation of the negatively-deflected leading-edge flap to be the cause of the discrepancies at BL153 and BL184.5, then it is the discrepancies at BL70 and BL80 that beg for explanation. The work of CAWAPI members therefore focused on carrying out several additional activities to explain the cause of this discrepancy.

16.5.3   Investigating Possible Causes of Discrepancies

The investigations are divided into two categories: one, targeting possible computational reasons, and the other, targeting possible reasons that may have appeared during flight test.

16.5.3.1   Activities to Eliminate Possible Numerical Effects

The activities targeting possible numerical causes were: mesh dependency study, turbulence model effect study, physical model study, effect of unsteadiness and effect of different formulation of boundary conditions:

• **Mesh dependency study by mesh adaptation.** EADS [16-9] carried out a study investigating mesh dependency, particularly in and above the boundary layer. Manually adapted and solution-adapted grids were used. The finest grid solutions, both manually and solution-adapted, show a weak primary vortex over the inner part of the wing, whereas the coarser-mesh solutions show this vortex only in the most forward part of the wing. The vortical features obtained on the adapted grid are shown in Figure 16-7. However, the presence of this vortex does not change the overall character of the solution which may indicate that the mesh adaptation has not progressed far enough.

• **Reynolds-number effect – mesh y^+.** The grids which were used for all other FC calculations had the value of y^+ set by the requirement of subsonic flight where the Reynolds number is about half of the value of FC70. A mesh made at EADS that corrected this anomaly showed no difference in result.

- **Turbulence modeling effects.** KTH/FOI [16-8] and NASA [16-11] carried out an investigation aimed at testing different turbulence models and their possible effect on results. No major difference was observed.

- **Unsteady calculations.** USAFA [16-12] carried out unsteady calculations using SARC-DES. Their solution is very similar to the RANS solutions.

- **Effect of formulation of boundary conditions in inlet and nozzle.** KTH/FOI [16-16] carried out different tests with given values of static pressure at the inlet and total states in the nozzle as well as with mass-flow boundary conditions in the nozzle. No effect from the different boundary-condition formulations was observed.

16.5.3.2   Activities to Eliminate Possible Flight Test Reasons

The activities targeting possible flight test reasons for the discrepancies were: effect of angle of attack and side-slip angle, effect of change in aircraft geometry during flight test, effect of bending of the wing and a check on possible corruption of flight-test data:

- **Angle of attack and side-slip angle effect.** EADS and NLR carried out a study with a small value of angle of attack and side-slip angle. Despite changes in the solutions, the overall characteristics of the results do not indicate that any small change of angle of attack or angle of side-slip would explain the discrepancy between CFD and flight data.

- **Effect of change in aircraft geometry.** As pointed out in NASA/TP [16-1] post flight test analysis, the leading-edge flap was deployed $-9°$ during the test. UT SimCenter carried out tests with a deformed mesh to investigate the possible effect of the flap deflection. The result of this analysis shows that the airdam blocked any influence of the outboard flowfield on the inboard pressure field and thus the flap deflection does not explain the discrepancies between computational results and flight test.

- **Effect of wing bending.** The structures engineers designed the standard F-16 aircraft to sustain 9g maneuvers which means that the wing is stiff. At high loading it would be significant, but at a cruise condition the bending should be small. The computations agree well with the flight-test data at the first inboard span station (BL55) and the mid-span station (BL95). If bending occurred, it would certainly cause discrepancies also in these two stations. Furthermore, the bending effect would have to be visible at the high angle of attack flight conditions, which was not observed.

- **Check on flight-test data.** There is no indication in the flight-test reports that the flight data had been taken incorrectly or that the data has been corrupted. As a further check, KTH/FOI calculated the flowfield at FC68 and FC69 that are near transonic conditions. FC68 seems to be mostly subsonic and the results are in good agreement with flight data. At FC69, where the supersonic portion of the flow is much larger than that for FC68, but smaller than that for FC70, the differences between computations and flight data begin to grow substantially, but they are still less than at FC70.

The last item suggests a possible cause and effect. The conditions for FC68 are $M_\infty = 0.90$, $\alpha = 3.7°$; and for FC69 they are $M_\infty = 0.95$, $\alpha = 3.6°$. The only value that changes significantly between the three FC is the Mach number, from 0.90 to 0.97. When there is little supersonic flow (hence no shocks) the agreement is good, and when there is most supersonic flow and strongest shocks, the agreement is worst. We hypothesize that the accurate simulation of a shock wave-vortex interaction phenomena could be required to resolve the discrepancies.

16.5.4   Highly-Adapted Meshes to Resolve Interaction of Vortex with Shock

The KTH/FOI team undertook an extensive study of the FC70 flowfield by generating highly adapted meshes, as shown in Table 16-2. KTH/FOI began with the surface triangulation of the common unstructured mesh, and after some local refinement, arrived at 158 thousand surface triangles. Substantially more prism cells were added (6.12 million) in the boundary layer and fewer tetrahedral cells were included outside than in the common mesh. This became the KTH/FOI initial RANS grid. Running on this grid, the KTH/FOI unstructured code automatically adapted the mesh using a gradient sensor to produce the KTH/FOI singly-adapted grid with over 11 million cells in total. This is more than three times the number in the common grid. A second level of adaptation is not possible because the resulting mesh would go beyond what the KTH/FOI computing facilities can handle. However using the Euler solver, additional levels of adaptation could be handled because of the lighter computational load. Starting from the surface triangulation of the common grid, KTH/FOI created the initial Euler grid of 8.99 million nodes, and this grid was adapted three times. The first adaptation used the gradient sensor to mainly seek out shock waves, the second adaptation used the λ_2 sensor [16-17] that tracks vortex cores, and the third adaptation was again the gradient sensor. The result is the KTH/FOI triply-adapted grid of 902 thousand surface triangles and 16.2 million nodes.

Table 16-2: Computational Grid Sizes
(Pyramidal elements are included in the total volume cells counts)

Grid		Surface triangles $\times 10^3$	Prism cells $\times 10^6$	Tetra cells $\times 10^6$	Total volume cells $\times 10^6$/ nodes $\times 10^6$
RANS	common	160	1.44	10.49	11.94 / 2.54
	KTH/FOI initial	158	6.12	7.40	13.56 / 4.36
	KTH/FOI singly adapt.	433	16.81	14.65	31.52 / 11.03
Euler	KTH/FOI initial	158	–	8.99	8.99 / 1.53
	KTH/FOI triply adapt.	902	–	94.71	94.71 / 16.20

The wing of the F-16XL is swept and sharp enough that a vortex shed from the leading edge is expected even in an Euler simulation, although the location of where it is shed may not be correct in reality. And that is precisely what the Euler solution obtained on the triply-adapted mesh indicates. Figure 16-9 presents the surface meshes on the upper wing surface. The grid in the top-half of the figure is the Euler mesh adapted 3-fold yielding a total of 902 thousand triangles on the total surface (upper and lower), and the bottom half shows the unstructured common mesh with 160 thousand triangles on the total surface. The inset box is a zoom of the region where the leading-edge vortex intersects the shock wave. The adaptation procedure picks out the major flow features and these are clearly visible in the intensity of the triply-adapted grid clustering in the Euler mesh, compared with the rather uniform grid spacing in the common mesh. The dark, span-wise band is the result of two gradient-based adaptations to the shock wave. Of the three dark horizontal bands, the longest and middle one is the footprint of the primary vortex core as it shows three levels of adaptation,

two gradient based ones, and decisively, one vortex-tracking λ_2 -based adaptation. This dark band results from the vortex interacting with the shock wave, and persisting downstream of it. The shorter bands above and below this result from just the gradient-based adaptation.
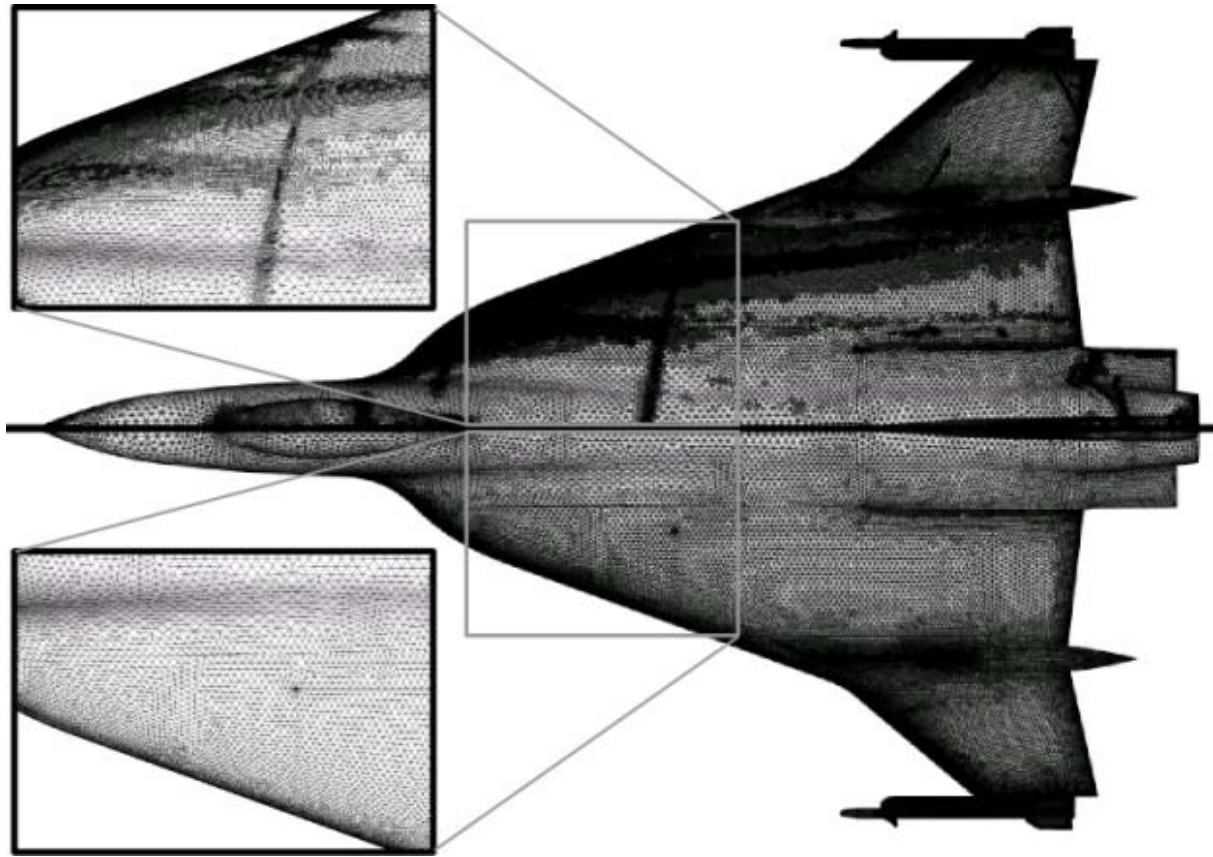
**Figure 16-9: Surface Grids on Upper Surface: Top Half: Triply-Adapted
Mesh for Euler; Lower Half: Common RANS Mesh.**

Figure 16-10 presents the Euler solution computed on the triply-adapted grid. Streamlines superimposed over iso-Mach contours on the upper surface of the inboard wing are shown in the top half, and isobars of C_p are shown in the bottom half. The impinging of supersonic streamlines in Figure 16-10 demonstrates that a vortex is shed from the fore section of the wing leading edge upstream of the shock wave. The diverging supersonic streamlines identify the location where the flow re-attaches after the vortex lift-off. The supersonic streamlines inboard of the re-attachment line decelerate to subsonic speed across the shock wave (blue region). The streamlines under the vortex however do not decelerate to subsonic speed but persist through the shock wave. Outboard of the primary separation line the supersonic streamlines again decelerate to subsonic speed across the shock. That a supersonic jet of vortical air issues through the shock, in effect annihilating the re-compression to subsonic flow, the usual shock-wave effect, is an important finding.
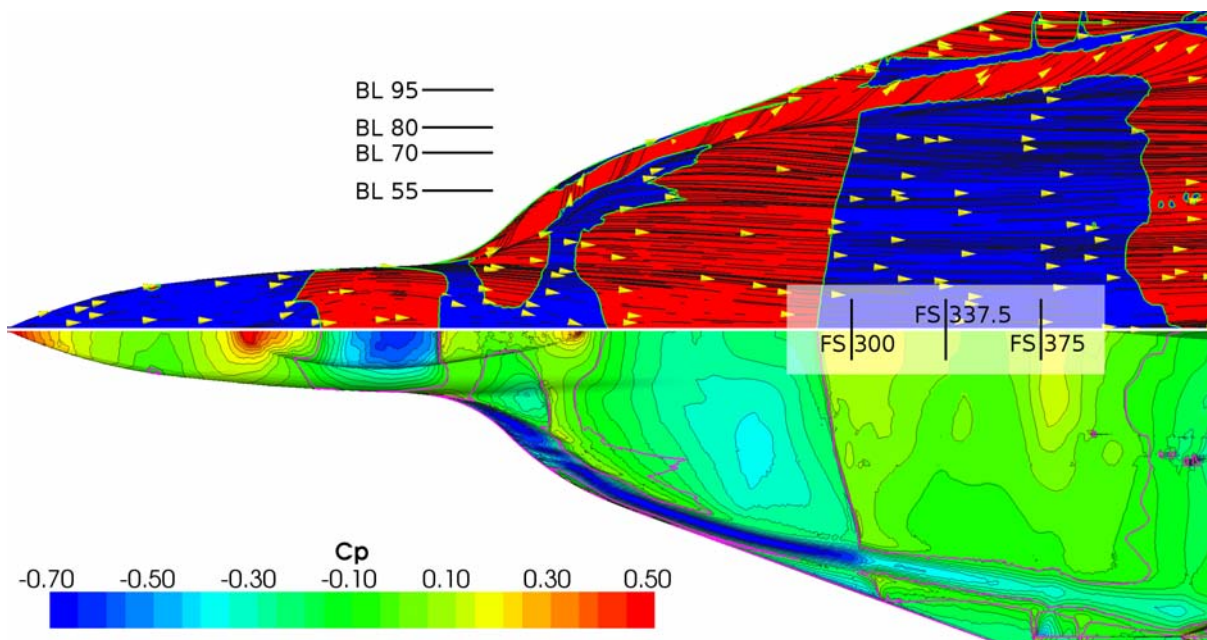
Figure 16-10: KTH/FOI Inviscid Solution on Upper Surface with Triply-Adapted Mesh:
Top Half: Streamlines Superimposed over Surface Mach Number (Blue: M < 1; green:
M = 1; red: M > 1); Bottom Half: Isobars of C_p (C_p = −0.052 magenta).

Figure 16-10 reveals further features of this shock wave-vortex interaction. Ahead of the shock wave the convergence of the surface streamlines that form the lift-off of the shear layer that feeds the vortex is almost entirely supersonic flow, as is the re-attachment of these streamlines. In the vortical jet downstream of the shock wave, this lift off and subsequent re-attachment occur in substantial regions of subsonic flow, i.e. the supersonic streamlines re-attach by decelerating to subsonic flow presumably through a shock wave. These features have not been seen in any of the previous RANS solutions, presumably because of insufficient grid resolution of both the shock and the vortex.

A RANS solution is needed to corroborate what was found in the Euler solution. Unfortunately the RANS solution computed on the singly-adapted KTH/FOI grid shows only the suggestion of the vortex shed from the leading edge, somewhat inboard of that shed in the Euler solution, interacts with the shock wave, but has insufficient strength to penetrate through it. Therefore we can only speculate that with still higher grid resolution, the RANS solution would proceed in the direction of the Euler solution.

16.5.5   Comparisons along Butt Line Sections

Figure 16-8 shows the largest C_p discrepancies to be at BL70 and BL80, and thus this region in the Euler and RANS solutions are of prime interest to investigate. Figure 16-11 presents a chordwise cut through three different unstructured grids in the BL80 section to illustrate the effects of mesh adaptation. The inset frame is a magnification of the first third of the wing chord that contains the region of the shock-vortex interaction. The dark bands of clustered cells in Figure 16-11 (a) and Figure 16-11 (b) visualize the location of the shock in section BL80 and the density of cells over the upper surface, features not seen in Figure 16-11 (c) of the common grid.

**(a) Euler Mesh Triply Adapted:
Twice for Shock, Once for Vortex**

**(b) RANS Mesh Singly Adapted,
Once for Shock**

(c) Common RANS Mesh, No Adaptation
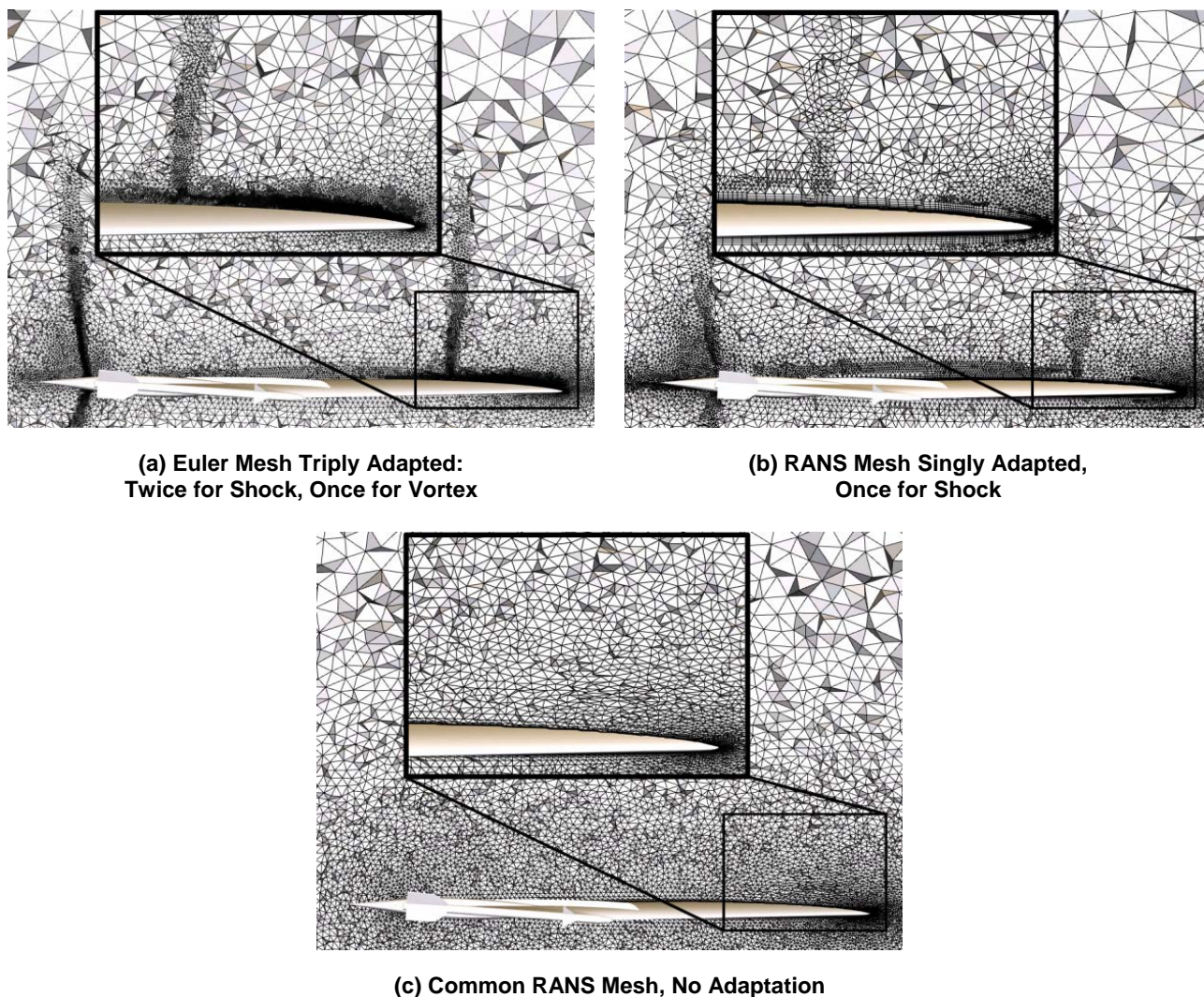
Figure 16-11: Chordwise Cut Through Three Unstructured Grids in BL80 Section.

Figure 16-12 compares the values of C_p computed on the triply-adapted Euler grid, the singly-adapted RANS grid and the common RANS grid with the values measured in the flight test for FC70. In BL55 all three computed values agree reasonably well with each other and with the flight-test results, although at the first 10% of the chord the computed results over predict the suction there. In the BL95 section the two RANS results agree with each other and with the measured data. The Euler results, however, differ from these. The flow does not compress through the shock to the subsonic values at about 15% chord as it does for the RANS result and the measurements. Instead it expands further out to about 20% chord and then gradually compresses (isentropically) to about 40% chord, i.e. there is no evidence that a shock is transversed. The following explanation is offered for this. If BL95 were to be marked in Figure 16-10 would pass through the region of interaction between the vortex and the shock wave. The footprint of the vortex is supersonic, hence no compression, which only comes further downstream where section BL95 passes outside of the vortex footprint. We can also conclude then that the position of the vortex in the Euler solution is not realistic. Again at BL80 the two RANS result agree with each

other and indicates the shock just past the 20% chord location. The Euler result displays a substantial suction peak at the nose and then a very sharp shock just past 20% chord that confirms the RANS computation, but all three results are in contradiction to the measurements which indicate supercritical flow to at least 50% and maybe further.

(a) BL55

(b) BL70

(c) BL80

(d) BL95
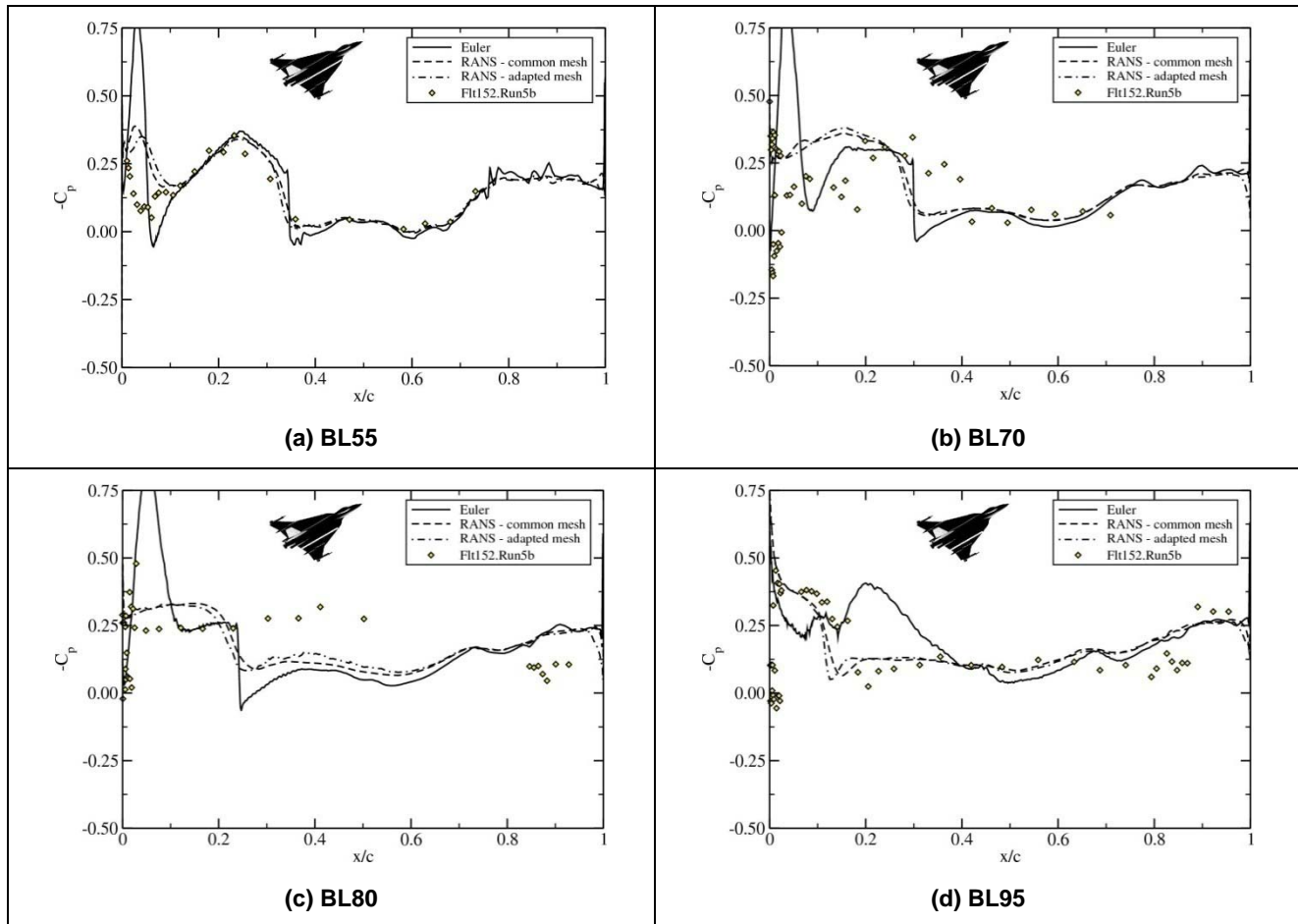
Figure 16-12: Chordwise Comparison of Computed and Measured Surface C_p for Case FC70.

What is found at BL95 and BL80 then suggests the following explanation. If we could compute RANS with sufficient resolution, the vortex footprint would remain supersonic through the shock, as we see in the Euler solution, but it would lie inboard of the location of the Euler result. We see in BL95 how the C_p values remained supercritical across the shock wave, but in RANS this would occur at approximately BL80. If this suggestion holds true, then the flight tests would confirm the passing of the supercritical vortex through the shock wave. Lastly in BL70 the two RANS values agree closely, and the sharp shock in the Euler results is in reasonable agreement with RANS, but the measurements show no evidence of the shock. The measurements rather show a continuous rise and fall in C_p reminiscent of the Euler computed values at BL95, in other words the BL70 line could also be cutting across the vortex footprint near the shock-vortex interaction zone.

16.5.6   Comparisons along Flight Stations

Let us further investigate the nature of the shock-vortex interaction and especially the character of the flow downstream of the shock wave. For this purpose it is useful to look in spanwise sections at constant chord position. Figure 16-13 shows the span-wise cut through the three different unstructured grids in the FS337.5 section to illustrate the effects of mesh adaptation on the vortex core just behind the shock wave. The upper inset frames of Figure 16-13 (a) and Figure 16-13 (b) present a magnification of the outer half of the cross-section. The lower inset frames present the same area as for the upper magnification inset, but here the total pressure loss iso-lines are plotted for the respective case. The left-half of Figure 16-13 (a) presents the Euler mesh with three levels of adaptation, and the right half presents the common unstructured mesh for RANS with no adaptation. The left-half of Figure 16-13 (b) presents the RANS mesh with one level of adaptation, and the right half presents the common unstructured mesh for RANS with no adaptation.

The large dark region of clustered cells in the centre of the left inset frame of Figure 16-13 (a) is the grid adaptation to the vortex core and gradients in the Euler solution and indicates the relative location of the vortex core along the span and above the wing. In comparison to the left inset it also indicates the increased grid resolution relative to the common grid. Compare this with the less dark region of clustered cells along the right edge of the left inset frame of Figure 16-13 (b) which is the corresponding grid adaptation to the vortex core in the singly-adapted RANS solution, less than that for triply-adapted Euler grid but more than that for the common grid. The total-pressure-loss iso-lines reveal the same picture as the analysis of the adapted mesh regions. The compact, circular iso-lines of the Euler solution in Figure 16-13 (a) reveal the location of the compact vortex. The superior resolution of the vortex in the Euler case is clear when comparing the iso-lines of total-pressure-loss to the common solution. By analyzing Figure 16-13 (b) it is possible to discern the effect of mesh adaptation on the resolution of the vortex for the RANS cases. The location of the vortex of the RANS cases does not change substantially, but the adapted RANS solution shows an improved vortex resolution with a discernible vortex core. This clearly indicates that the vortex core in the Euler solution is about the same distance above the wing but about 15%-span further outboard than the vortex core in the singly-adapted RANS solution. This finding supports our argument in the previous section that claimed the features seen in the Euler-computed C_p values in BL95 are comparable to the flight test values in BL80.

(a) Triply-Adapted Euler Grid on Left

(b) Singly-Adapted RANS Grid on Left
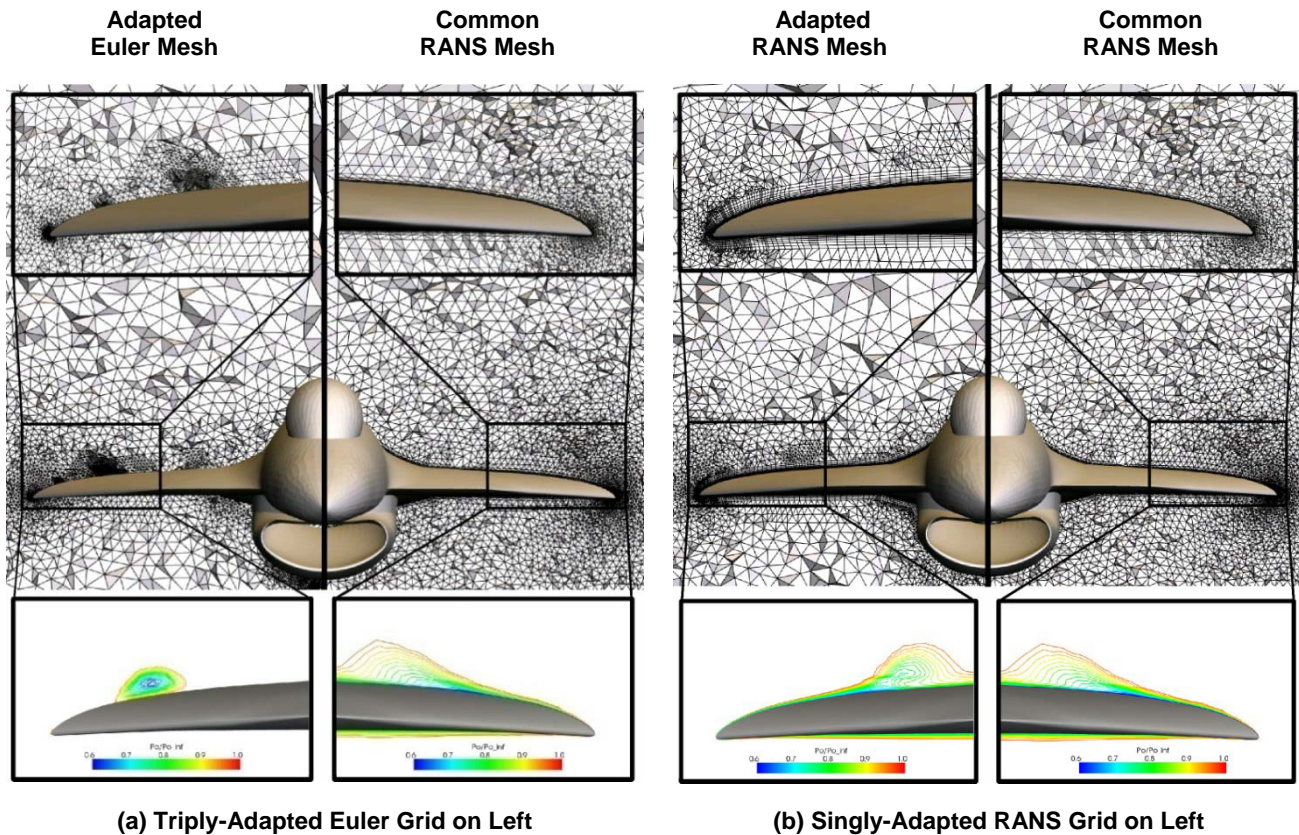
**Figure 16-13: Span-Wise Cuts at FS337.5 for Three Different Unstructured Solutions,
Euler Adapted Mesh, RANS Adapted Mesh, Common RANS Mesh;
Magnified Mesh and Total-Pressure-Loss Iso-Lines.**

In an exactly analogous manner Figure 16-14 shows the span-wise cut through the three different unstructured grids in the FS492.5 section to illustrate the effects of mesh adaptation to the vortex core just before the trailing edge of the wing. Now there are two dark regions of clustered cells in zoom frame of the Euler grid (left side of Figure 16-14 (a)). The inboard adaptation is a result of the very weak leading-edge vortex and the outboard region is due to the vortex shed from the airdam. Although the cell density is lower due to the lesser degree of adaptation, two regions in the zoom frame of the RANS grid (left side of Figure 16-14 (b)) have the identical interpretation, which in fact is consistent with the visualization of the two vortices at the trailing edge in Figure 16-7 (a). The total-pressure-loss iso-lines at the FS492.5 section reveal the location of either one or two vortices. The location of the air-dam induced vortex is fixed for all three cases. In the RANS solutions, this vortex is located above the actuator pod, whereas the main wing leading edge vortex is recognizable further inboard. For the RANS solutions, the further inboard located leading-edge vortex is so weak at this station that the total-pressure-loss iso-lines show no clear evidence of its location. In the Euler solution the further outboard located leading edge vortex merges with the air-dam vortex. This results in a markedly stronger and wider vortex above the actuator pod. Figure 16-15 compares the values of C_p computed on the triply-adapted Euler grid, the singly-adapted RANS grid and the common RANS grid with the values measured in the flight test for FC70 in the sections FS300, FS337.5, FS375 and FS492.5. At FS300, which is just in front of the shock, the Euler computed values show a suction peak at approximately 85% span. If we would place this at about 70% span to account for the vortex in the Euler solution being 15% further outboard, then this peak would be in fair agreement with the

suction peak in the flight test data at about 70% span. Notice also that there is a small peak in the singly-adapted RANS-grid solution at about this same position, which with further adaptation might increase to the level of the measurements. Station FS337.5 is downstream of the shock wave, and the three measured data values clearly indicate a supercritical suction peak. The Euler solution presents a peak, again about 15% further outboard, and the singly adapted RANS result shows the emergence of a small peak in the position that agrees with the measured one. Station FS375 is at the beginning of the airdam, and the flight data seems to suggest two suction peaks. The inboard one at about 60% span is the leading-edge vortex suction consistent with the smaller singly-adapted RANS one and the outboard peak in the Euler result. The second peak in the data measured at 80% span is due to the vortex shed from the airdam, consistent with the two vortices seen in Figure 16-7 (a). Lastly, the flight-test data in section FS492.5 is too sparse to distinguish the two vortices but the few points that exist are consistent with such an interpretation.

Adapted Euler Mesh   **Common RANS Mesh**   **Adapted RANS Mesh**   **Common RANS Mesh**

(a) Triply-Adapted Euler Grid on Left   **(b) Singly-Adapted RANS Grid on Left**
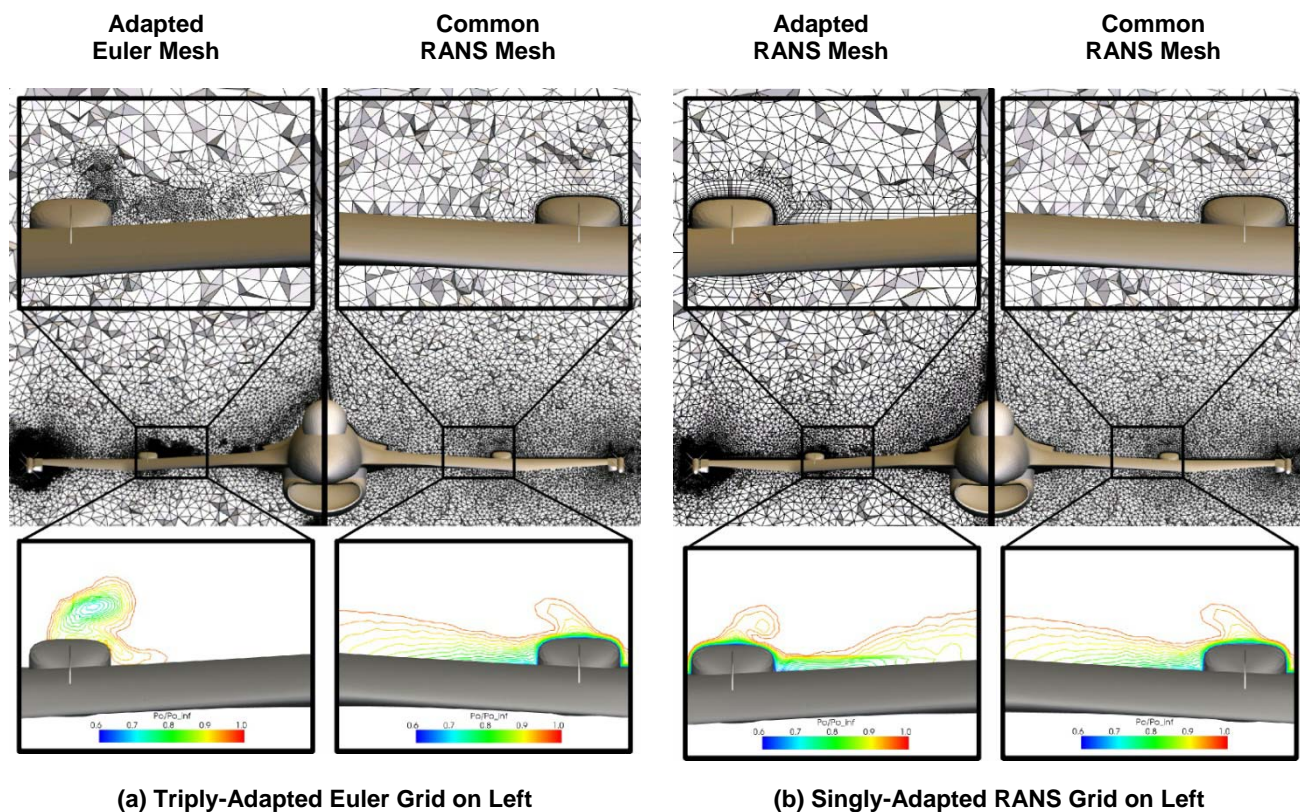
**Figure 16-14: Span-Wise Cuts at FS492.5 for Three Different Unstructured Solutions,
Euler Adapted Mesh, RANS Adapted Mesh, Common RANS Mesh;
Magnified Mesh and Total-Pressure-Loss Iso-Lines.**

(a) FS300

(b) FS337.5

(c) FS375

(d) FS492.5
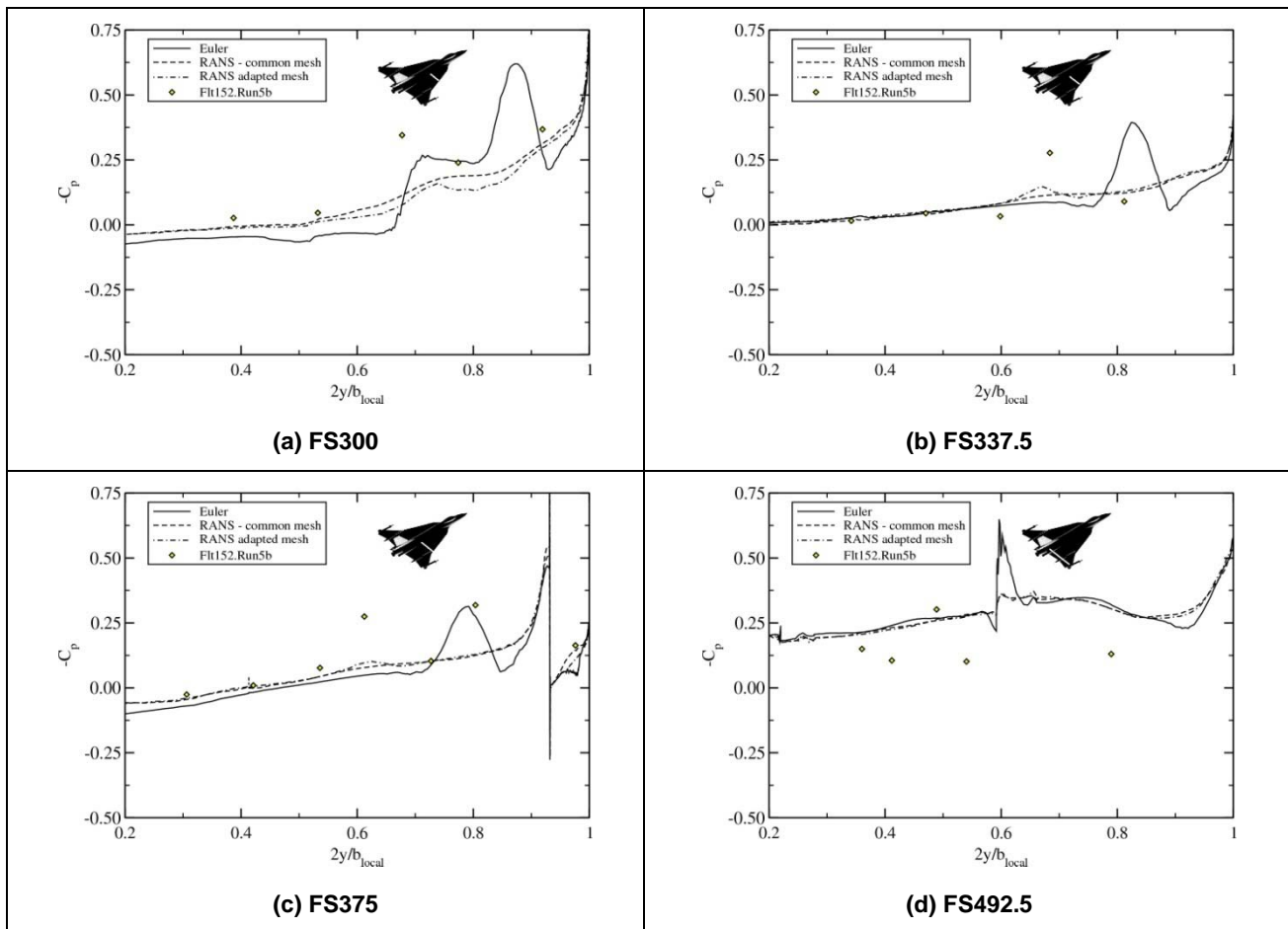
Figure 16-15: Spanwise Comparison of Computed and Measured Upper Surface C_p for Case FC70.

16.5.7 FC70 Concluding Remarks and Lessons Learned

Flight condition 70 is the highest Mach-number case examined by all participating organizations, also the highest Reynolds-number case and the lowest angle-of-attack case, so in a sense an extreme of the examined flow conditions. It is the only case examined with interacting supercritical vortex flow and shock waves. Before the CAWAPI team started work on FC70, the major focus was to determine the best practices needed to simulate accurately the vortical flow features and pressure distribution over the aircraft. The geometry used and the mesh generated was the same for all cases including the transonic one. Use of all the grids that lead to reasonable results for all the other test flights did not produce satisfactory results for this flight condition. It took a detailed Euler simulation with a highly adapted mesh to reveal the occurrence of a shock-vortex interaction that significantly changed the surface pressure distribution. One conclusion is if the mesh used offers sufficient resolution to resolve the shock-vortex interaction problem, one then observes a jet of supersonic flow blowing through the shock wave, delaying re-compression to further downstream that seems to be continuous, i.e. without a shock wave. If the goal is to resolve the detailed pressure distribution over the aircraft, then this feature must be resolved.

The lessons learned are:

- **At high Mach number, high Reynolds number and low angle of attack expect shock-vortex interaction.** This is difficult to resolve because the vortex does not lift very far off the surface and out above the boundary layer.

- **y^+ on the surface is not a conclusive indicator that one has a sufficient mesh.** The mesh must resolve the vortex lift-off and interaction across the entire boundary layer and beyond.

- **Adapt mesh for both shock and vortex.** The occurrence of the supercritical vortex core that persists across the shock wave requires resolving both the shock and the vortex. Adapting to just one of these will miss this combined effect. For example, the grids sufficient for all the other flight conditions, i.e. those that had just vortex phenomena missed the shock-vortex interaction in FC70. It could take well more than an order of magnitude increase in grid cells to resolve the associated interaction region and boundary layer.

- **Shock-vortex interaction may be unsteady.** This phenomena presumably has some unsteady components to it, but this aspect was not investigated here. We expect that these aspects would occur on a scale that would require high grid resolution of the interaction region to be captured.

There is no reason to expect that the difficulties (and features) encountered with FC70 are in any way specific to the F-16XL airframe. We are convinced that the same type of shock-vortex interaction will occur on other similar types of military aircraft at similar (routine) flight conditions.

16.6 PERSPECTIVES

16.6.1 Progress Since NASA-TP

In Lamar et al. [16-1] flight and wind tunnel test data are presented and are compared with CFD predictions. The code CFL3D was used, which was developed at NASA Langley and is widely used in the United States. A patched multiblock grid was generated on a simplified half configuration of the F-16XL, with the intention to focus grid points on the wing to resolve vortices and shocks. The wing tip missile and launcher, and the vertical fin were removed, although the air dam was retained. The final grid had 1.37 million cells, with the first cell spacing set for the wind tunnel Reynolds number. The flight Reynolds number was computed using a wall function. The turbulence model used was Baldwin-Lomax with the Degani-Schiff modification for vortical flow. The calculations were run on the Cray C-90 and each steady calculation required around 24 hours. The convergence was stopped after the residual had been driven down 2-3 orders, which is unlikely to be sufficient. Finally, the commercial package Fieldview was used to visualize the vortices.

For the vortical flight conditions considered in CAWAPI the C_p distributions generally show better agreement inboard. However, suction peaks are under-predicted. One contribution to this is the coarseness of the grid. There were also significant discrepancies between the skin friction and boundary layer predictions and measurements. For FC70 (transonic case), good agreement was again obtained inboard, with very poor comparison with flight measurements outboard of the crank. A possible cause of this was suggested to be the uncertain deployment of the leading edge flaps and the ailerons. It was also stated that the convergence of the transonic case was more difficult.

Computing Power: The computing power available to the participants in CAWAPI was one to three orders of magnitude larger than that available for the NASA-TP calculations. The codes used in AVT-113 all ran on distributed memory parallelism, with the exception of the NLR code that exploits a very high vector

performance. The cost of computing has fallen to such an extent that many participants used local resources, whereas Lamar et al. [16-1] relied on an allocation on a supercomputer.

Geometry Handling: Emphasis in the working group was placed on retaining as much of the detailed definition of the aircraft as possible. A number of minor simplifications were made [16-3] but to a very large degree this goal was achieved. A number of partners were able to use their own grid generation tools to generate a grid around the extremely complex shape. It seems likely that the geometry simplifications in Lamar et al. [16-1] were driven by the need to keep the number of grid points down.

Grid Generation: Several CAWAPI partners used their own tools to generate grids around the complex F-16XL shape. The most direct comparison with Lamar et al. [16-1] is with the structured grid generation of NLR. It is clear that the tools developed at NLR represent a major advance on what was available at the time of Lamar et al. [16-1]. A significant development is the ability to generate unstructured grids for viscous flows through the exploitation of grown layers in the boundary layer. A number of codes were able to generate grids in a reasonable time. Finally, EADS-MAS and KTH/FOI made effective use of automatic grid adaption, the use of which is not currently as widespread as might have been expected.

Turbulence: All participants in CAWAPI used turbulence treatments based on PDEs, in contrast to the algebraic model used in Lamar et al. [16-1]. The simplest turbulence treatment used was one or two-equation turbulence models. Rotation corrections to Boussinesq based models seemed to allow good solutions without too much difficulty, to the extent that they could be described as routine. Some partners used Reynolds stress models, but without significant obvious benefit. Finally, some partners used DES.

Unsteadiness: Some partners showed it is now possible to resolve unsteady effects, showing significant unsteadiness downstream of the crank. The origins of this need further study, but could originate from an interaction of the inner and outer wing vortices, or an interaction between the inner wing vortex and the air dam.

Solver: Discretization and solution schemes have advanced less since Lamar et al. [16-1]. The efficiency of the schemes was not really considered in CAWAPI, but interesting information about the performance on grids required for such a complex geometry could be obtained in the future. The spatial accuracy of the codes has not improved noticeably since the time of Lamar et al. [16-1].

Visualization: Possibly driven by improved computing, the visualization of solutions produced in CAWAPI far exceeded that shown in the NASA-TP. Visualization through iso-surfaces, surface streamlines and the automatic detection of vortex cores all effectively showed the behavior of the solutions, including unsteady effects.

16.6.2   Technology Readiness Level Improvements

The following statements were made by industry team members of CAWAPI regarding the benefits accrued by their participating organizations in CAWAPI. Obviously, it is this group that will be end users of any new technology developed and, in that role the concept of TRL improvement is not only academic but economic, since company growth or survival can be an outcome. (The statements are arranged in the order received.)

Mr. Willy Fritz of EADS-MAS, Munich Germany; Comments

Within the CAWAPI, EADS made essential experience with the solution based grid adaptation at complex configurations. We saw the benefit of the solution based grid adaptation, but we also learned that it is sometimes a laborious task. For the future application of the grid adaptation we got very useful guidelines. Our daily business is not only to calculate force and moment coefficients or pressure distributions, but also to find out the

physical causes for unexpected effects which were observed during flight test. Therefore we need a realistic computational model with correct slat-, flap- and rudder settings. So we have to use hybrid grids. These unexpected effects occur at the high angle of attack range or at special maneuvers. For these flow conditions, a carefully generated grid is an essential key towards a realistic numerical outcome. As grid-independent RANS solutions with globally refined hybrid grids are never possible in our production environment, the only possibility to minimize the grid dependency of the numerical outcome is again the use of solution adapted grids. Especially at vortical flow structures at high angles of attack even small vortices coming from slat corners, strakelets, etc., can become very important, as they can trigger or delay vortex breakdown at the big primary vortices. Even in apparent very fine grids such small vortices are represented too weak.

The solution based grid adaptation very often tracks such small vortices and we get considerable improvements of the numerical outcome. Since the CAWAPI, we know that the solution based grid adaptation at such complex configurations can be handled and we know how to handle it. By this, the experience of CAWAPI has improved the readiness level of the application of our CFD-tools. (Without this experience we never would have tried a solution based grid adaptation at a complex configuration). CAWAPI was also the first possibility to validate our CFD-tools at a full scale fighter-type aircraft with flight test pressure distributions. (Agreements of the force and moment coefficients can be accidental as disagreements in the pressure distributions can cancel out each other.)

Dr. Bruce Davis of Lockheed Martin Aeronautics, Ft. Worth, TX; Comments

Lockheed Martin Aeronautics Company (LM Aero) as a designer, developer, and manufacturer of advanced military aircraft is keenly aware of the importance of accurate CFD simulations. CFD is used in a variety of ways, from improving aerodynamic design to providing aerodynamic loads to improving the separation of stores from aircraft. The validation of CFD codes is of central importance since this increases the confidence in CFD results and can potentially save costly wind tunnel and flight test time.

LM Aero has recently been involved in updating Falcon, its general purpose Navier-Stokes flow solver. This effort, and specifically the validation of the flow solver, has coincided with the involvement in the CAWAPI program. This timely involvement has provided LM Aero with a challenging validation suite with high-quality flight test data. If for no other reason, the availability of this validation case has made the participation in CAWAPI a valuable experience for LM Aero, and the validation of our flow codes against this test database will not end with the CAWAPI program.

LM Aero did not generate the computational grids for this problem, but rather used grids supplied by the University of Tennessee Simulation Center (UTSimC). The grid used did not fully resolve the viscous sublayer of the turbulent boundary layer, but rather used wall functions. The LM Aero simulations underpredicted the suction peaks lying under the main vortices consistently. The suspicion is that the use of wall functions for this particular problem is not appropriate, and that simulations with the fully resolved viscous sublayer will bear this out. Even with the use of wall functions, the half-symmetry grid contained 42 million cells, which is the largest grid used to date for a Falcon v4. simulation. In this sense it allowed LM Aero to evaluate the code, as well as various utilities, for very large problems.

Dr. Todd Michal of Boeing Phantom Works, St. Louis, MO; Comments

Participation in the CAWAPI program has provided many tangible and intangible benefits to Boeing. The CAWAPI collaboration has provided an opportunity to establish contacts with leading researchers while working toward the common goal of expanding the envelope of CFD analysis. Perhaps the most beneficial aspect of this program has been the establishment of best-practices for CFD analysis for complex high angle

of attack, vortex dominated flow fields. Through our involvement, guidelines for grid properties, turbulence model, and algorithm option selection have been established that will directly benefit future Boeing programs. Another benefit of the CAWAPI effort has been the chance to compare and validate Boeing tools and processes with other industry, university and government codes. The comprehensive set of flight test results available for this effort enabled CFD to be validated in new parts of the flight envelope. This validation highlighted several areas where CFD tools do very well, and perhaps equally important, areas where current CFD methods fall short. It is our belief that identification of these short comings will guide future research efforts that will benefit Boeing as well as the greater CFD community.

In addition to benchmarking our current CFD capability, the CAWAPI program provided an excellent opportunity to investigate the use of new technologies to help solve complex problems. Capabilities such as grid adaptation, new turbulence models, and new numerical algorithms were all investigated. These studies provided a great deal of information that will help with the development and deployment of these new technologies.

16.7   CONCLUSIONS

Although differences were observed in the comparison of results from ten different CFD solvers with measurements, these solvers all functioned robustly on an actual aircraft at flight conditions with sufficient agreement among them to conclude that the overall objectives of the CAWAPI endeavour have been achieved. In particular, the status of CFD as a tool for understanding flight test observations has been confirmed. A number of specific points have arisen from CAWAPI:

- The "state-of-the-art" computations for FC70 showed a remarkable degree of agreement. However, the agreement with measurements was not close. After the assessment of several possible explanations it is suggested that this discrepancy is due to the poor prediction of a concentrated leading edge vortex and its interaction with a shock. This conclusion would not have been reached without performing a high-resolution inviscid analysis. These computations were only performed after the discrepancies between the "state-of-the-art" tools and measured data could not be explained. If this were an a-priori computational campaign, the conventional computations showing such a consistent agreement with each other, would have been interpreted differently. Then only a later flight test campaign would have recognized the discrepancy. This stands in clear contrast to the computations at FC25, where thanks to statistical tools the discrepancy between various computations would have triggered an alert. The "state-of-the-art" computations for FC70 would not have triggered such an alert. As shown at this condition, a necessary advance of the CFD tools is the reduction of discretization error, either from massive feature-driven grid adaption or higher order schemes.

- Time accurate simulations of the high angle of attack flight condition FC25 showed significant unsteadiness arising from the interactions of vortices downstream of the crank. This was unanticipated at the outset of the working group from a consideration of the flight test data. In this respect the CFD solutions have stimulated a reinterpretation of the measurements.

- Two considerations caused concern about the grid convergence of the CFD solutions. First, there is a large spread of the solutions for properties like vortex strength, as indicated by suction footprints on the wing surface. Secondly, grid adaption studies by some partners showed significant improvements in, for example, resolving secondary vortices. Given the large grids used (10-20 million points for half bodies), this emphasizes that advances in adaption and discretization scheme accuracy are important.

- The evaluation of predictions of boundary layer profiles showed the advantages of DDES over DES in this region.

- The generation of a block structured in similar times to those required to obtain quality unstructured grids showed what can be achieved with advanced grid generation tools generated by one of the CAWAPI partners.

The work of Lamar et al. [16-1] provides a suitable benchmark for identifying the advances since 2001. This reference described an application of CFD to the F-16XL using state of the art tools at the time. The ability in the current working group to use grids of much higher resolution has brought the predictions more in line with measurements. In addition, advances in block structured grid generation tools have allowed the retention of almost all of the geometrical features in structured grids. Turbulence treatments that overcome the limitations of the Boussinesq assumption for vortical flow were used routinely. Unsteady effects were simulated by some partners and were shown to be significant. The accuracy of the spatial discretization has not advanced since 2001 and this has been shown to be significant. To balance this, some advances have been shown in grid adaption for unstructured codes.

16.8   ACKNOWLEDGEMENTS

The authors gratefully acknowledge the support provided by Lockheed Martin Aeronautics Company – Fort Worth in providing a refined IGES geometry file and the parameter values of a generic engine that were subsequently used by facet members in their CFD studies, and the geometrical work performed by Mr. Edward B. Parlette of Vigyan, Inc. in generating a series of unstructured, tetrahedral grids from the IGES file, with the last one known as the base grid. Special thanks also to Todd Michal of Boeing, Stefan Görtz of DLR, Bruce Davis of Lockheed Martin, Willy Fritz of EADS, David McDaniels of USAFA and Steve Karman of UT Chattanooga for their valuable suggestions and kind assistance in the writing of the paper.

16.9   REFERENCES

[16-1] Lamar, J.E., Obara, C.J., Fisher, B.D. and Fisher, D.F.: *Flight, Wind-Tunnel, and Computational Fluid Dynamics Comparison for Cranked Arrow Wing (F-16XL-1) at Subsonic and Transonic Speeds*, NASA/TP 2001-210629, NASA, February 2001.

[16-2] Lamar, J.E. and Obara, C.J.: *The Cranked Arrow Wing Aerodynamics Project (CAWAP) and its Extension to the International Community as CAWAPI: Objectives and Overview*, NATO Research and Technology Organisation, RTO-TR-AVT-113, Chapter 3, 2009.

[16-3] Boelens, O.J., Görtz, S., Morton, S.A., Fritz, W. and Lamar, J.E.: *F-16XL Geometry and Grids*, NATO Research and Technology Organisation, RTO-TR-AVT-113, Chapter 4, 2009.

[16-4] Boelens, O.J., Spekreijse, S.P., Sytsma, H.A. and de Cock, K.M.J.: *Numerical Solutions for the CAWAPI Configuration on Structured Grids at NLR, The Netherlands*, NATO Research and Technology Organisation, RTO-TR-AVT-113, Chapter 5, 2009.

[16-5] Michal, T., Oser, M., Mani, M. and Ross, F.: *Numerical Solutions for the CAWAPI Configuration on Unstructured Grids at Boeing-St. Louis, United States*, NATO Research and Technology Organisation, RTO-TR-AVT-113, Chapter 12, 2009.

[16-6] Badcock, K.J.: *Numerical Solutions for the CAWAPI Configuration on Structured Grids at University of Glasgow/Liverpool University, United Kingdom*, NATO Research and Technology Organisation, RTO-TR-AVT-113, Chapter 6, 2009.

[16-7] Elmiligue, A.A., Abdol-Hamid, K.S. and Massey, S.J.: *Numerical Solutions for the CAWAPI Configuration on Structured Grids at NASA Langley Res. Cntr., United States*, NATO Research and Technology Organisation, RTO-TR-AVT-113, Chapter 7, 2009.

[16-8] Görtz, S. and Jirásek, A.: *Numerical Solutions for the CAWAPI Configuration on Unstructured Grids at KTH/FOI – Part I, Sweden*, NATO Research and Technology Organisation, RTO-TR-AVT-113, Chapter 10, 2009.

[16-9] Fritz, W.: *Numerical Solutions for the CAWAPI Configuration on Unstructured Grids at EADS-M, Germany*, NATO Research and Technology Organisation, RTO-TR-AVT-113, Chapter 8, 2009.

[16-10] Karman, S., Mitchell, B. and Sawyer, S.: *Numerical Solutions for the CAWAPI Configuration on Unstructured Grids at UT-SimCenter, United States*, NATO Research and Technology Organisation, RTO-TR-AVT-113, Chapter 14, 2009.

[16-11] Lamar, J.E. and Abdol-Hamid, K.S.: *Numerical Solutions for the CAWAPI Configuration on Unstructured Grids at NASA Langley Res. Cntr., United States*, NATO Research and Technology Organisation, RTO-TR-AVT-113, Chapter 15, 2009.

[16-12] Morton, S.A., McDaniels, D.R. and Cummings, R.M.: *Numerical Solutions for the CAWAPI Configuration on Unstructured Grids at USAFA, United States*, NATO Research and Technology Organisation, RTO-TR-AVT-113, Chapter 9, 2009.

[16-13] Davis, M.B., Reed, C. and Yagle, P.: *Numerical Solutions for the CAWAPI Configuration on Unstructured Grids at Lockheed-Martin, United States*, NATO Research and Technology Organisation, RTO-TR-AVT-113, Chapter 13, 2009.

[16-14] Boelens, O.J.: *Feature-Based Code Validation using F-16XL Flight Test and Wind Tunnel Data*, NATO Research and Technology Organisation, Athens, Greece, October 2007, RTO-MP-AVT-147, Chapter 56.

[16-15] Cummings, R.M., Morton, S.A., Siegel, S.A. and Bosscher, S.: *Numerical Prediction and Wind Tunnel Experiment for a Pitching Unmanned Combat Air Vehicle*, Proceedings of the 41st Aerospace Sciences Meeting & Exhibit, Reno, NV, January 2003, AIAA Paper 2003-0417.

[16-16] Jirásek, A. and Rizzi, A.: *Numerical Solution for the CAWAPI Configuration on Unstructured Grids at KTH/FOI – Part II, Sweden*, NATO Research and Technology Organisation, RTO-TR-AVT-113, Chapter 11, 2009.

[16-17] Le Moigne, Y.: *Adaptive Mesh Refinement and Simulations of Unsteady Delta-Wing Aerodynamics*, Ph.D. Thesis, KTH Farkost och flygteknik, 2004, ISBN 91-7283-770-3, TRITA-AVE 2004:17.

[16-18] Morrison, J.H. and Hemsch, M.J.: *Statistical Analysis of CFD Solutions from the Third AIAA Drag Prediction Workshop (Invited)*, Proceedings of the 45th AIAA Aerospace Sciences Meeting & Exhibit, Reno, NV, January 2007, AIAA Paper 2007-0254.

Appendix 16-1: Force and Moment Coefficient Comparisons

This appendix shows the force/moments data – lift C_L, drag C_D, friction drag C_{Df} and pitching moment C_M for several CFD solutions along with the statistical analysis for each flight tested flight condition – see Table 16-3 to Table 16-4. For sideslip flight conditions FC50 and FC51, the comparisons include the component values of side force C_Y, rolling moment coefficient C_X and yawing moment coefficient C_Z. The tables with statistical analysis list the population mean $\tilde{\mu}$ and the value $k\hat{\sigma}$ to add/subtract to reach the upper/lower limit that defines the population of "identical" solutions. It shows also the number of outliers – i.e. solutions which are located outside the interval of confidence. The definition of the population mean $\tilde{\mu}$ and the value $k\hat{\sigma}$ is in Appendix 16-2.

A1.1   Low-Speed Flow Cases

A1.1.1   FC25 – Force/Moments Comparison

**Table 16-3: Flight Condition FC25, Force/Moment Coefficients
(Values provided by respective, listed organization – see Table 16-1)**

Coefficient	NLR	KTH/FOI	USAFA	NASA - unstr	EADS[†]	UT SimC	Boeing
C_L	0.77328	0.79789	0.78402	0.80199	0.82795	0.76553	0.75560
C_D	0.45088	0.44800	0.40537	0.49923	0.44577	0.59244	0.52836
C_{D_f}	0.01270	0.01060	–	0.01989	–	0.01373	0.01030
C_M	0.02525	0.01061	0.01645	0.01653	−0.00492	0.00707	0.02228

[†] Data without inlet and nozzle surface

Table 16-4: Flight Condition FC25, Force/Moment Coefficients – Statistical Analysis

Coefficient	$\hat{\mu}$	$k\hat{\sigma}$	# identical solutions	# outliers
C_L	0.78402	0.04307	6	1
C_D	0.45088	0.12346	6	1
C_{D_f}	0.01270	0.00687	4	1
C_M	0.01645	0.01858	6	1

A1.1.2   FC19 – Force/Moments Comparison

Table 16-5: Flight Condition FC19, Force/Moment Coefficients
(Values provided by respective, listed organization – see Table 16-1)

Coefficient	NLR	KTH/FOI	USAFA	NASA - ustr	EADS[†]	UT SimC	LM Aero
C_L	0.43846	0.44693	0.37006	0.43851	0.46798	0.44190	0.44590
C_D	0.13289	0.13469	0.11084	0.15788	0.13648	0.16158	0.14265
C_{D_f}	0.00932	0.00772	-	0.01531	-	0.00919	-
C_M	0.00699	0.00124	0.00124	0.00112	-0.00590	-0.00021	-0.00390

[†] Data without inlet and nozzle surface

Table 16-6: Flight Condition FC19, Force/Moment Coefficients – Statistical Analysis

Coefficient	$\tilde{\mu}$	$k\hat{\sigma}$	# identical solutions	# outliers
C_L	0.44190	0.05434	6	1
C_D	0.13648	0.03000	7	0
C_{D_f}	0.00926	0.00625	4	0
C_M	0.00112	0.00744	7	0

A1.1.3   FC7 – Force/Moments Comparison

Table 16-7: Flight Condition FC7, Force/Moment Coefficients
(Values provided by respective, listed organization – see Table 16-1)

Coefficient	NLR	KTH/FOI	USAFA	NASA - ustr	EADS[†]	UT SimC	Boeing	LM Aero
C_L	0.43560	0.44258	0.43868	0.44076	0.45993	0.43996	0.44510	0.44430
C_D	0.13932	0.14571	0.13019	0.16942	0.08909	0.19609	0.14131	0.15135
C_{D_f}	0.01029	0.00850	-	0.01708	-	0.01104	0.00840	-
C_M	0.00772	0.00236	0.00300	0.00206	-0.00475	-0.00154	-0.00191	-0.00345

[†] Data without inlet and nozzle surface

Table 16-8: Flight Condition FC7, Force/Moment Coefficients – Statistical Analysis

Coefficient	$\tilde{\mu}$	$k\hat{\sigma}$	# identical solutions	# outliers
C_L	0.44036	0.01391	7	1
C_D	0.14351	0.05344	7	1
C_{D_f}	0.01029	0.00566	5	0
C_M	0.00026	0.00710	7	0

A1.1.4   FC50 – Force/Moments Comparison

Table 16-9: Flight Condition FC50, Force/Moment Coefficients
(Values provided by respective, listed organization – see Table 16-1)

Coefficient	NLR	KTH/FOI	USAFA	NASA - ustr	UT SimC
C_L	0.52908	0.53241	0.53569	0.52395	0.53485
C_D	0.15481	0.18115	0.12656	0.20383	0.18526
C_{D_f}	0.00907	0.00998	-	0.01447	0.00921
C_Y	-0.03941	-	-0.05068	-	-
C_M	0.00095	-0.00844	-0.00414	-0.00045	-0.0051
C_X	-0.02240	-0.01092	-0.01855	-0.01771	-
C_Z	0.01706	0.01450	0.01200	0.01167	-

Table 16-10: Flight Condition FC50, Force/Moment Coefficients – Statistical Analysis

Coefficient	$\tilde{\mu}$	$k\hat{\sigma}$	# identical solutions	# outliers
C_L	0.53241	0.00863	5	0
C_D	0.18115	0.05616	5	0
C_{D_f}	0.0096	0.00493	4	0
C_Y				
C_M	-0.00414	0.00664	5	0
C_X	-0.01813	0.00840	4	0
C_Z	0.01325	0.00449	4	0

A1.1.5   FC51 – Force/Moments Comparison

Table 16-11: Flight Condition FC50, Force/Moment Coefficients
(Values provided by respective, listed organization – see Table 16-1).

Coefficient	NLR	KTH/FOI	USAFA	NASA - ustr	UT SimC
C_L	0.49612	0.51564	0.50485	0.49180	0.48839
C_D	0.14019	0.16695	0.11232	0.18600	0.21902
C_{D_f}	0.00903	0.00967	-	0.01426	0.01035
C_Y	0.03508	-	0.04237	-	-
C_M	0.00155	-0.00817	-0.00485	-0.00068	-0.0027
C_X	0.01820	0.01058	0.01558	0.01436	-
C_Z	-0.01537	-0.01405	-0.00990	-0.00989	-

Table 16-12: Flight Condition FC50, Force/Moment Coefficients – Statistical Analysis

Coefficient	$\tilde{\mu}$	$k\hat{\sigma}$	# identical solutions	# outliers
C_L	0.49612	0.02004	5	0
C_D	0.16695	0.07128	5	0
C_{D_f}	0.01001	0.00439	4	0
C_Y				
C_M	-0.00270	0.00652	5	0
C_X	0.01497	0.00552	4	0
C_Z	-0.01198	0.00495	4	0

A1.2   Transonic Flow

A1.2.1   FC70 – Force/Moments Comparison

Table 16-13: Flight Condition FC70, Force/Moment Coefficients
(Values provided by respective, listed organization – see Table 16-1)

Coefficient	NLR	KTH/FOI	USAFA	NASA - ustr	EADS[†]	UT SimC	LM Aero
C_L	0.11682	0.12276	0.12044	0.12080	0.12641	0.12510	0.12412
C_D	0.04077	0.03901	0.04193	0.05179	0.01959	0.04661	0.04464
C_{D_f}	0.00674	0.00573	-	0.01018	-	0.00678	-
C_M	0.00219	-0.00103	-0.00153	-0.00129	-0.00452	-0.01385	-0.00289

[†] Data without inlet and nozzle surface

Table 16-14: Flight Condition FC70, Force/Moment Coefficients – Statistical Analysis

Coefficient	$\tilde{\mu}$	$k\hat{\sigma}$	# identical solutions	# outliers
C_L	0.12276	0.00571	6	1
C_D	0.04193	0.01782	6	1
C_{D_f}	0.00676	0.00357	4	0
C_M	-0.00153	0.00940	6	1

Appendix 16-2: Statistical Analysis

The forces and moments are statistically evaluated. The use of a statistical approach to analyze collective data is not new, having been used for the AIAA Drag Prediction Workshops, and the statistical formulas employed there [16-18] are used here. The basic idea is to analyze statistically the collective data to evaluate a mean and variance of the solution set and to identify those results which are statistically the same and those which are outliers, i.e. outside of the standard deviation. The population mean $\tilde{\mu}$ is estimated using the sample median $\tilde{x}$, which is given (for the sorted data) as:

$$\tilde{\mu} = \tilde{x}$$

$$\tilde{x} \equiv \begin{cases} x_{(n+1)/2} & \text{if } n \text{ is odd} \\ \dfrac{1}{2}\left(x_{n/2} + x_{n/2+1}\right) & \text{if } n \text{ is even} \end{cases}$$

The sample *standard deviation* $\hat{\sigma}$ is defined as:

$$\hat{\sigma} = \sqrt{\frac{1}{n-1}\sum(x_i - \tilde{x})^2}$$

The upper and lower limits for a particular integrated variable (e.g. lift coefficient) define the boundaries for the outliers, they are:

$$\text{upper limit} = \tilde{\mu} + k\hat{\sigma}$$
$$\text{lower limt} = \tilde{\mu} - k\hat{\sigma}$$
$$k = \sqrt{3}$$

Chapter 17 – THE INTERNATIONAL VORTEX FLOW EXPERIMENT 2 (VFE-2): OBJECTIVES AND OVERVIEW

by

Dietrich Hummel *(Retired)*

17.1 SUMMARY

In this chapter the objectives for the new International Vortex Flow Experiment (VFE-2) and its organization within the RTO Task Group AVT-113 are described. The available wind tunnel models and the applied experimental techniques, the program of work and its realization as well as the presentation of results within this Final Report and elsewhere are outlined.

17.2 INTRODUCTION

At the beginning of the 1980's the status of the Euler methods for the calculation of vortical flows had reached such a high standard that good experimental data were necessary to validate the codes. This lead to the First International Vortex Flow Experiment (VFE-1) [17-1], which has been carried out in 1984 – 1986: On a sharp edged cropped delta wing with a leading edge sweep of 65° combined with a fuselage, see Figure 17-1, force and pressure measurements as well as flow field studies have been carried out for a certain variety of flow conditions in various wind tunnels worldwide. The results have been summarized in [17-2], and later the state of the art has been reviewed in [[17-3] to [17-5]]. Even for sharp leading edges with fixed primary separation the Euler codes were not well suited to calculate the pressure distribution on a slender wing properly, see Figure 17-2, since the secondary separation is not modelled at all.
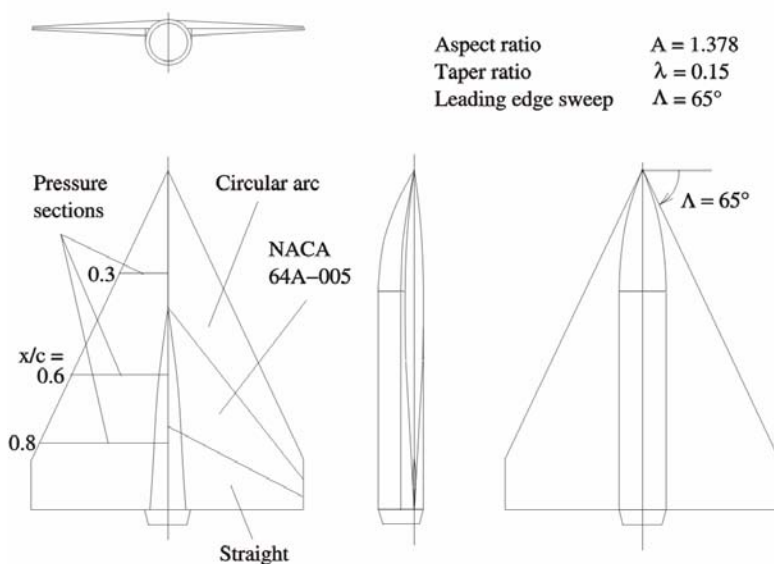
Figure 17-1: Configuration of the First International Vortex Flow Experiment (VFE-1).
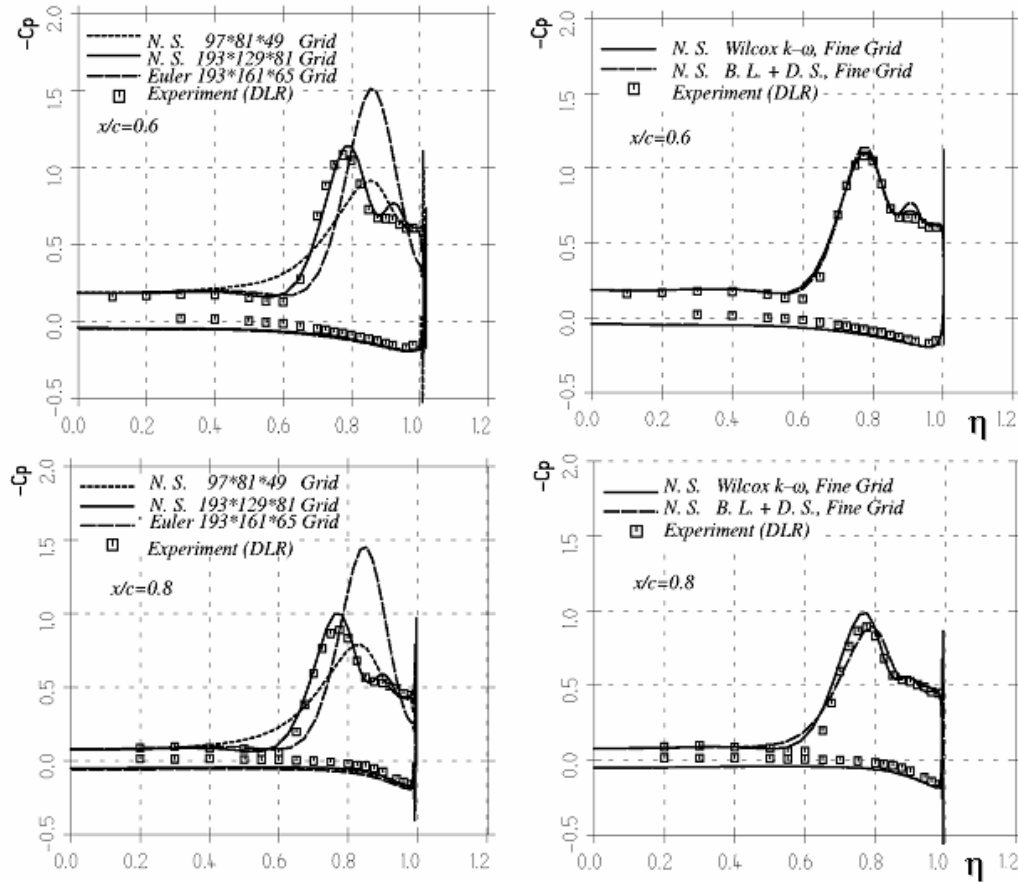
Figure 17-2: Surface Pressure Distributions on the Wing (Only) of the VFE-1 Configuration at M = 0.4, R_{mac} = 3.1 x 10^6, α = 9°. Comparison of solutions of the Euler and the RANS equations including effects of grid resolution and turbulence modelling. FLOWer code results according to W. Fritz, EADS Munich DEU.

In the last fifteen years considerable progress has been achieved in the numerical calculation of vortical flows by taking into account viscous effects through solutions of the RANS equations. This means that Reynolds number effects are now included and secondary vortices turn out. For turbulent flows in solutions of the RANS equations a turbulence model is necessary, which has to cover the attached boundary layers and the secondary vortex area properly. The calculated pressure distribution on the upper surface of the wing is very sensitive to correct modelling of the viscous regions of the flow field as shown in Figure 17-2. If the grid resolution is fine enough reasonable pressure distributions turn out, but according to Figure 17-3 considerable differences concerning the total pressure loss distribution are present in the flow field for different turbulence models.
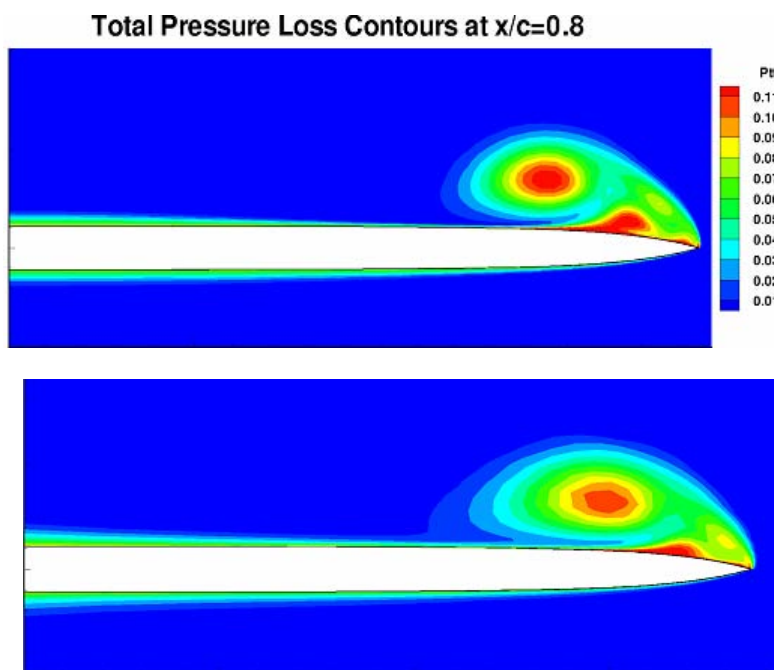
**Figure 17-3: Total Pressure Loss Contours in Section x/c = 0.8 on the VFE-1 Configuration
at M = 0.4, R_{mac} = 3.1 x 10^6, α = 9°. FLOWer code results using the Baldwin-Lomax (top)
and the k-ω (bottom) turbulence model according to W. Fritz, EADS Munich DEU.**

In order to validate the results of Navier-Stokes calculations new and more detailed experimental data are necessary, and therefore at the RTO AVT Symposium in Loen 2001 a Second International Vortex Flow Experiment (VFE-2) has been proposed [17-5], which will be described subsequently.

17.3   OBJECTIVES FOR NEW EXPERIMENTAL INVESTIGATIONS

17.3.1   Test Configuration

According to [17-5] the configuration for VFE-2 has been chosen in such a way that the flow regimes:

i)	Attached flow without vortex formation	$0° \leq \alpha \leq 4°$
ii)	Separated vortical flow without vortex breakdown	$4° \leq \alpha \leq 20°$
iii)	Separated vortical flow with vortex breakdown	$20° \leq \alpha \leq 40°$
iv)	Separated deadwater-type flow	$40° \leq \alpha \leq 90°$

are covered properly, and this lead to a delta wing with a leading edge sweep of 65°. Concerning the thickness distribution a flat plate inner portion in combination with interchangeable leading edges was desired, and these requirements were fulfilled by the NASA configuration [17-6], which is shown in Figure 17-4. Sets of one sharp and three rounded leading edges are available. The geometry of the wing as well as the shape of the sting are given by analytical expressions described in all details in [17-6]. Thus new wind tunnel models could be built quite easily.

$c_R = 25.734$ in

$b/2 = 12$ in.

$\Lambda = 65°$

$t = 0.875$ in.

Spanwise surface pressure stations
$x/c_R = 0.20, 0.40, 0.60, 0.80, 0.95$

$t/c_R = 0.0340$
$b/2c_R = 0.4663$
$d/b = 0.1375$

$d = 3.30$ in.

Streamwise leading-edge radii:
$r_{LE}/\bar{c} = 0, 0.0005, 0.0015, 0.0030$
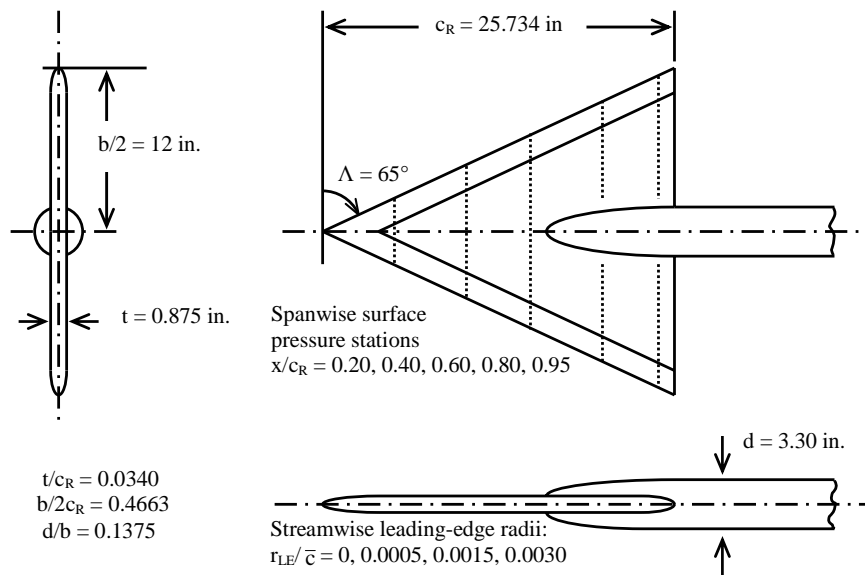
Figure 17-4: VFE-2 Configuration: NASA NTF Delta Wing A = 1.85, Λ = 65° [17-6].

For the NASA delta wing configuration comprehensive measurements of normal force and pitching moment as well as of pressure distributions in the sections according to Figure 17-4 and along the leading edges had already been carried out in the National Transonic Facility (NTF) at NASA, see Figure 17-5, for a large variety of Mach numbers and Reynolds numbers [17-6], and results of first numerical calculations have been made available at the Loen Conference [17-7].

Figure 17-5: NASA NTF Tests on the 65° Delta Wing [17-6].

17.3.2   Objectives for New Tests

For delta wings with sharp leading edges and fixed primary separation a large number of experimental investigations are available in the literature. Therefore it was decided to use the case of sharp leading edges within VFE-2 as reference only and to direct the main emphasis for new experiments towards studies of the vortex formation on the configuration with rounded leading edges. In the first place drag data should be added to the existing balance measurements in order to provide the full three-component data set. Since no investigations on the flow field around this configuration existed at all, the main general aim for VFE-2 was to provide flow field data for comparison with numerical results. The objectives for new experiments were:

- Investigations on the laminar/turbulent transition on delta wings.

- Detailed pressure distribution measurements, especially in the region of the onset of flow separations for configurations with rounded leading edges.

- Boundary layer measurements including distributions of the components of velocity and vorticity, of turbulent energy and eddy viscosity.

- Determination of the wall shear stress and detection of the secondary and tertiary separation lines.

- Flow field measurements in the primary and secondary vortices including the distributions of the components of velocity and vorticity, of turbulent energy and eddy viscosity.

- Investigations on the vortex breakdown flow field for delta wings with sharp and rounded leading edges including the surface pressure fluctuations caused by the spiral mode of vortex breakdown.

From the very beginning of VFE-2 the experimental investigations have been accompanied by CFD calculations for the relatively simple delta wing configuration including the sting. The objectives for these investigations were:

- Validation and improvement of the existing CFD codes by means of comparisons with new experimental results.

- Code to code comparisons through calculations on common unstructured and structured grids.

- Application of different turbulence models in RANS calculations and comparison with new experimental flow field data.

- Assistance related to the set up, the performance and the evaluation of the new wind tunnel experiments.

- Synergistic effects through the possibility for test runs on a simple configuration prior to expensive calculations for a complete aircraft, such as in the CAWAPI facet.

17.4   ORGANIZATION OF VFE-2

17.4.1   Formation of an RTO Task Group

At the RTO AVT-069 Symposium on "Vortex Flow and High Angle of Attack Aerodynamics" in Loen, Norway, 2001, the realization of the proposed [17-5] Second International Vortex Flow Experiment (VFE-2) has been discussed extensively by the audience. The NASA 65° delta wing configuration [17-6] had been put forward as an appropriate test configuration, and already prior to the Loen conference NASA informed the scientific community about the existence of a second smaller wind tunnel model at NASA Langley RC,

the dimensions of which were ¾ of those given in Figure 17-4 for the NTF wind tunnel model. Already at the early stage of the discussions in Loen, this second American wind tunnel model has been placed at disposal by NASA for use by the members of a forthcoming RTO Task Group in other wind tunnels worldwide. This offer was the starting point for the new VFE-2.

In the course of the RTO AVT meetings in Manchester 2001 and in Paris 2002 the establishment of a new AVT Task Group "Vortex Flow Experiment – 2" has been proposed. Another outcome of the conference in Loen 2001 was the idea to perform numerical calculations of the vortical flow around a complete military aircraft at full Reynolds numbers and to compare the results with already existing flight test data. Therefore at the same time another new AVT Task Group "F-16XL Numerical Simulations" has been discussed. Finally the RTO Applied Vehicles Technology Panel decided in Aalborg 2002 to combine the two proposals and to establish a new

> **Task Group AVT-113**: **"Understanding and Modeling Vortical Flows to Improve the Technology Readiness Level for Military Aircraft"**.

This new Task Group acted in two facets:

1) Cranked Arrow Wing Aerodynamics Project International (CAWAPI); and

2) Second International Vortex Flow Experiment – 2 (VFE-2).

Both facets worked closely together. The numerical calculations within CAWAPI for the complete aircraft F-16XL turned out to be extremely expensive both for grid size and CPU time. On the other hand the VFE-2 configuration was relatively simple and the amount for numerical investigations was comparatively small. From this contrast resulted considerable synergistic effects within AVT-113. Prior to future expensive calculations for the full aircraft geometry, the codes and the various turbulence models could be checked using the much simpler VFE-2 configuration. Some members were active in both facets of AVT-113, and the discussions within the Task Group during its semi-annual meetings on the experiences of the members supported the anticipated synergistic effects.

The inauguration of the AVT-113 Task Group took place at the AVT Panel spring meeting in Brussels 2003. Co-chairmen became Dr. John E. Lamar, NASA Langley Research Centre, USA, (CAWAPI), and Prof. Dr. Dietrich Hummel, Technische Universität Braunschweig, DEU, (VFE-2), and Prof. Charles Hirsch, Vrije Universiteit Brussel, BEL, acted as AVT Panel Representative for the Task Group. During the inaugural meeting experimental contributions to VFE-2 were announced by NASA Langley RC (USA), DLR Goettingen and TU Munich (DEU), University of Glasgow (GBR) and ONERA Lille (FRA), and numerical contributions were planned by EADS Munich (DEU), USAFA Colorado (USA) and University of Glasgow (GBR). In the course of the investigations within VFE-2 other groups of scientists joined, and all final members of the VFE-2 facet of the AVT-113 Task Group and their affiliations are listed in Appendix 1.

17.4.2   Selection of Flow Phenomena to be Studied within VFE-2

From the proposal for the Second International Vortex Flow Experiment [17-5] as well as from the list of objectives given in Section 17.3.2 a huge number of interesting flow cases for the 65° delta wing configuration can be deduced. From the very beginning the members of the Task Group realized that not all interesting flow phenomena could be treated successfully and that a concentration concerning the topics to be investigated was necessary.

Concerning the free stream flow conditions, i.e. Mach number and Reynolds number, from the available NASA matrix [17-6] the segment for the lower Reynolds numbers is shown in Figure 17-6. Only some of the

new measurements could be closely related to the test conditions of the National Transonic Facility (NTF) at NASA Langley RC [17-6], whereas most of the **new measurements** could only be carried out **for incompressible flows**. For this flow regime unpublished results of NASA investigations in the Low Turbulence Pressure Tunnel (LTPT) at Langley RC did already exist. The corresponding free stream flow conditions are included in Figure 17-6. These experiments have been carried out by means of the second smaller wind tunnel model, the dimensions of which were ¾ of those given in Figure 17-4 for the NTF wind tunnel model. The results of these measurements remained unpublished for a long time, and their evaluation and presentation within VFE-2 is part of the NASA contribution.
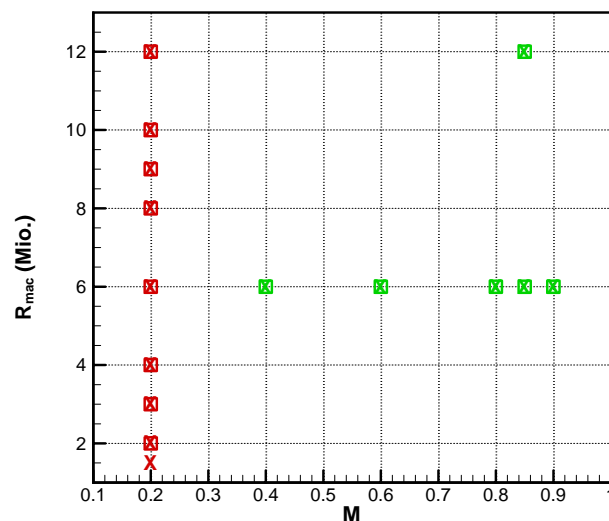
Figure 17-6: Available Test Conditions for the 65° Delta Wing Configuration at NASA Langley.

X sharp leading edges, Low Turbulence Pressure Tunnel (LTPT)
 medium radius leading edges, Low Turbulence Pressure Tunnel (LTPT)
X sharp leading edges, National Transonic Facility (NTF)
 medium radius leading edges, National Transonic Facility (NTF)

Since for delta wings with sharp leading edges and fixed primary separation a large number of experimental investigations are available in the literature, the Task Group decided on its meeting in Warsaw 2003 to use the case of sharp leading edges within VFE-2 as reference only and to direct the main emphasis for new experiments towards studies of the vortex formation on the configuration with **rounded leading edges**. The available NASA data [17-6] showed for the configurations with rounded leading edges spanwise pressure distributions with two separate suction peaks on the upper surface of the wing, see Figure 17-7, which have never been observed for sharp edged delta wings. Therefore the Task Group decided to study the onset of separated flow for rounded leading edges in more details, and for this purpose the medium radius leading edge configuration (= 0.0015) has been selected.

Sharp leading edge
$r_{LE} / \overline{c} = 0$ $r_{LE} / \overline{c} =$

Rounded leading edge
$r_{LE} / \overline{c} = 0.0015$

Spanwise distribution at $x/c_R = 0.6$
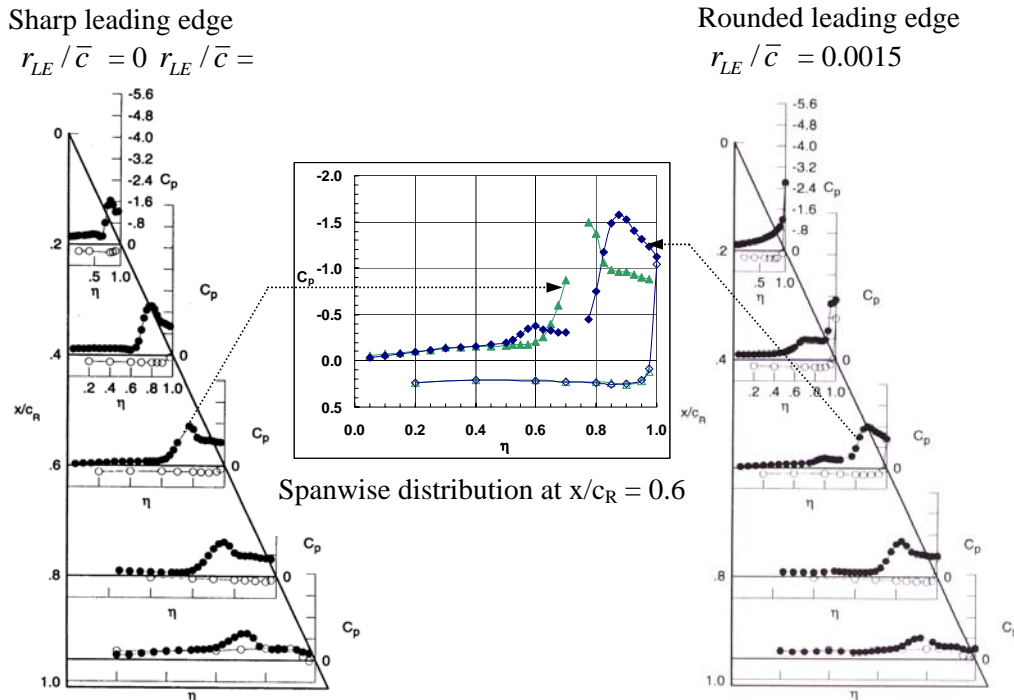
**Figure 17-7: Effect of Leading Edge Bluntness on the Pressure Distribution of the 65°
Delta Wing Configuration (A = 1.85) at M = 0.4, R_{mac} = 6 x 10^6, α = 13° [17-6].**

A huge matrix of possible investigations is given by the large variety of angles of attack, which lead to various flow regimes. The new measurements mainly concentrated on one rounded leading edge shape in comparison with the sharp leading edge configuration and according to the decision of the Task Group in Warsaw 2003 **three angles of attack**, corresponding to three different flow regimes, have been studied in detail. These are:

- Onset of vortical flow, α = 13°
  - Sharp leading edges: Separated flow
  - Medium radius leading edges: Partly attached, partly separated flow

- Separated flow without vortex breakdown, α = 18°
  - Sharp leading edges
  - Medium radius leading edges

- Separated flow with vortex breakdown, α = 23°
  - Sharp leading edges
  - Medium radius leading edges.

For the chosen flow conditions pressure distribution measurements as well as normal force and pitching moment data were already available from NASA for wide ranges of Mach number and Reynolds number [17-6]. The new experiments should complete these measurements by adding **drag data**.

However, the main emphasis for the new experiments was to obtain **flow field data**, mainly by PIV and hot-wire techniques (HWA).

On delta wings the formation of the boundary layers underneath the vortex system is very important for the vortex formation [17-8], [17-9], but the **status of the boundary layers** is poorly known. More detailed knowledge on this subject would be very useful either for the validation of related prediction methods or for the adaptation of the results of numerical calculations to the experimental status. Therefore attempts have been made to determine the laminar and the turbulent regions on the upper surface of the wing.

At large angles of attack **vortex breakdown** takes place in the primary vortices. Today it is common understanding that the flow past slender delta wings at large angles of attack becomes unsteady even for fixed wings. This means in other words that for large angles of attack and steady boundary conditions only unsteady solutions of the governing equations do exist. The spiral-type vortex breakdown is well predicted by numerical solutions of the Navier-Stokes equations [17-10], [17-11], see Figure 17-8. The instantaneous vortex axis spirals in space against the sense of rotation of the primary vortex and this spiral turns around with respect to time in the sense of rotation of the primary vortex, and in the center of the spiralling motion a region of reversed flow is present. Correspondingly all quantities of the flow field show oscillations. Therefore, in the new experiments **unsteady pressure distribution measurements** have been carried out in order to provide data on the oscillations including the governing frequencies for comparison with numerical results.
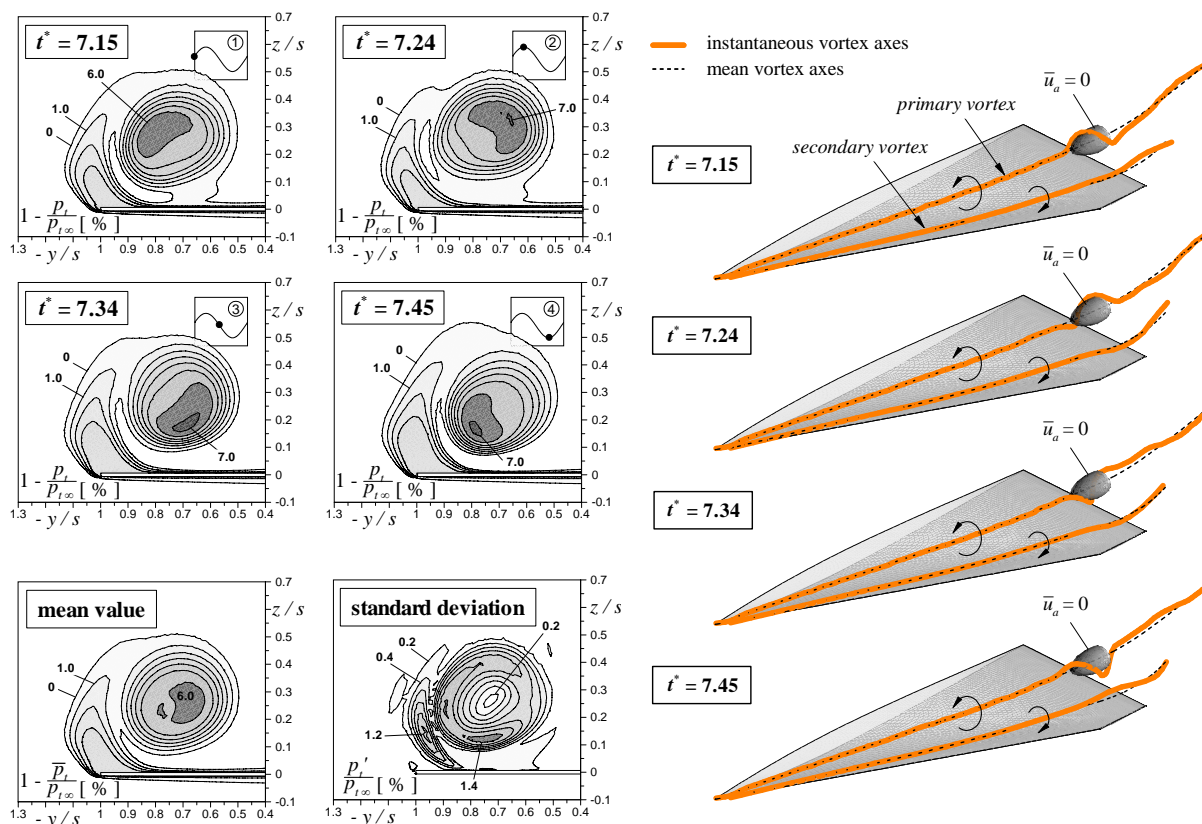
Figure 17-8: Numerical Simulation of Vortex Breakdown for the VFE-1 Configuration at M = 0.2, R = 1.55 x 10^6, α = 21°. Navier-Stokes solutions with k-ω turbulence model: Total pressure losses at x/c_R = 0.95 and vortex axes for different time steps [17-11].

17.4.3   Wind Tunnel Models

The wind tunnel models used within VFE-2 are listed in Table 17-1. As a reference the original NASA NTF wind tunnel model is included as Nr. 0. The smaller NASA LTPT wind tunnel model Nr. 1 has been made available by NASA Langley RC for use by the facet members. This model was shipped to Europe and tested by means of PSP and PIV at DLR (DEU) in the Transonic Wind Tunnel Goettingen (TWG of Deutsch-Niederlaendischer Windkanal, DNW) as well as by means of balance measurements and PIV at ONERA Lille (FRA). A new wind tunnel model Nr. 2 was built at TU Munich (DEU) in order to perform surface oil flow investigations, pressure distribution measurements as well as flow field surveys by means of the PIV and the hot-wire (HWA) techniques. The same wind tunnel model has also been tested by DLR in their Cryogenic Wind Tunnel KKK at Cologne (DEU). Additional PIV tests have been carried out there, and the TSP and infrared (IR) techniques have been applied for the detection of the laminar/turbulent transition. Another wind tunnel model Nr. 3 has been built and tested through unsteady balance, pressure distribution and flow field studies at University of Glasgow (GBR). Two other new wind tunnel models Nr. 4 and 5 have been built by ONERA Lille (FRA) in order to carry out balance measurements and flow visualization tests, and these two models were shipped to Turkey in order to perform balance measurements and to investigate the laminar/turbulent transition at TUBITAK-SAGE, Ankara (TUR).

Table 17-1: Wind Tunnel Models Used in VFE-2 [Notations for Leading Edge Shapes: (S) Sharp edged, (RS) Rounded: Small Radius, (RM) Rounded: Medium Radius, (RL) Rounded: Large Radius]

Model Nr.	Span [m]	Root Chord [m]	Leading Edge	Tested At	Owner
0	0.610	0.653	S, RS, RM, RL	NASA, NTF	NASA Langley RC
1	0.457	0.490	S, RS, RM, RL	NASA, LTPT DLR, TWG ONERA	NASA Langley RC
2	0.933	0.980	S, RM	TU Munich DLR, KKK	TU Munich
3	0.987	1.059	S, RM	Uni. Glasgow	Uni. Glasgow
4	0.457	0.490	S	ONERA TUBITAK-SAGE	ONERA Lille
5	0.457	0.490	RM	ONERA TUBITAK-SAGE	ONERA Lille

17.4.4   Numerical Investigations

At the very beginning of VFE-2 the results of numerical investigations at NASA Langley RC by means of an adapted unstructured grid were available [17-7].

New calculations within AVT-113 for the VFE-2 configuration have been carried out firstly on structured grids and secondly on unstructured grids. In the solutions of the RANS equations a large variety of existing

turbulence models has been applied. For (medium radius) rounded leading edges the flow field at lower angles of attack with two vortices on each side of the configuration has been considered for $\alpha = 13°$. The ordinary vortex formation with one vortex on each side of the configuration (accompanied by a secondary vortex) has also been studied numerically at $\alpha = 18°$ for sharp and rounded leading edges, and for very high angles of attack the unsteady behaviour of the vortical flow (vortex breakdown) has also been treated at $\alpha = 23°$.

Finally a semi empirical/numerical method to predict the onset of vortical flow over the upper surface of a delta wing with rounded leading edges with different radii has been developed.

17.4.5   Use of a Virtual Laboratory

Within the Task Group AVT-113 a Virtual Laboratory has been developed by NASA Langley RC, which enabled the members of the working group to upload and download computer programs, configuration geometries and grids as well as experimental and numerical results [[17-12], [17-13]]. This Virtual Laboratory enabled and facilitated collaborative research within the Task Group. It has been used in the first place by the F-16XL-1 related facet "Cranked Arrow Wing Aerodynamics International" (CAWAPI) of AVT-113. The corresponding communication among the members of the delta wing related facet "Vortex Flow Experiment 2" (VFE-2) has been developed after this, and therefore the communication within VFE-2 took place on a large extend on an individual basis.

17.4.6   Program of Work

At the inauguration of the Task Group AVT-113 in spring 2003 in Brussels, the facet VFE-2 has been formed and new experiments have been envisaged. The detailed program for these tests has been discussed at the autumn meeting 2003 in Warsaw, and the final Program of Work (POW) has been fixed at the spring meeting 2004 in Williamsburg. According to the original objectives for new tests (described in Section 17.3.2) and the selection of flow phenomena to be studied within VFE-2 (described in Section 17.4.2) the official POW contained:

- 3-component balance measurements.

- Surface pressure distribution measurements.

- 3D boundary layer investigations including the transition laminar/turbulent.

- Flow field measurements within the vortices.

- Investigations on the unsteady vortical flow at higher angles of attack (vortex breakdown) including surface pressure fluctuations.

- Numerical investigations on structured and unstructured grids and comparison with the new test results.

These new experiments and the related numerical investigations were aimed at the understanding of the vortex formation on the wing with rounded leading edges and the case with sharp leading edges would be used as reference only.

The realization of this program depended on the availability of wind tunnel testing time and CFD capacities. The steps to fulfil the POW will be described subsequently.

Progress in 2004. As the basis for VFE-2 the results of the NTF tests on the 65° delta wing with different leading edge shapes at various Reynolds- and Mach numbers, see [17-14] to [17-16], have been summarized by NASA Langley (USA) at the ICAS 2004 Congress in Yokohama [17-17].

The loan agreement between NASA (USA) and DLR (DEU) had already been signed in December 2003. The American wind tunnel model Nr. 1 was shipped to Europe in March 2004. DLR Goettingen performed PSP measurements in a first entry in the Transonic Windtunnel Goettingen (TWG) of Deutsch-Niederlaendischer Windkanal (DNW) in July and August 2004. Preliminary results have been discussed by the Task Group at their autumn meeting 2004 in Prague and presented in October 2004 at the RTO Symposium AVT-111 [17-9]. For the wing with rounded leading edges at an angle of attack of 13° two vortices on each side of the configuration were clearly indicated. At that time the inner vortex was regarded to represent the remains of a 3D bubble-type laminar/turbulent transition in the front part of the configuration. Concerning the forthcoming PIV investigations a tiny inner vortex resulting from a transitional boundary layer was expected.

Progress in 2005. Starting already in December 2004 first numerical calculations of the flow field have been carried out at EADS Munich (DEU) by means of the German FLOWer code on a structured grid, and pressure distributions with two suction peaks on each side of the configuration turned out in excellent agreement with the PSP measurements. Looking into the details of the numerical solution an inner vortex of about the size of the outer vortex turned out, but downstream of the onset of the outer vortex, the inner vortex decays, since it is no longer fed with vorticity. Using these numerical results the set-up for the forthcoming PIV investigations could be adjusted properly and the second entry of DLR in the TWG with stereo-PIV investigations took place in April 2005. Again the shape of the two vortices turned out as predicted in the calculations. Preliminary results of this cooperation between CFD and experiments have been discussed by the Task Group at their spring meeting 2005 in Budapest and presented at Cranfield University in September 2005 [17-15].

In 2005 further wind tunnel models came into operation: Model Nr. 2 at TU Munich (DEU) had been completed, and pressure distribution and flow visualization tests have been carried out there. Since the loan agreement between NASA (USA) and ONERA (FRA) was delayed, ONERA Lille built two new wind tunnel models Nr. 4 and 5 with sharp and rounded leading edges and performed balance and exploratory PIV tests. After the first successful calculations of the flow, a common structured grid was provided by EADS Munich (DEU) and a common unstructured grid by USAFA Colorado (USA). In addition also individual structured meshes were used by the participants, and calculations were underway at University of Glasgow (GBR), NLR Amsterdam (NLD) and EADS Munich (DEU). Calculations on unstructured grids have been started on individual meshes at KTH Stockholm (SWE) and DLR Braunschweig (DEU) as reported to the Task Group at the autumn meeting 2005 in Granada.

Progress in 2006. After full evaluation the PSP and PIV results from DLR Goettingen have been presented at various conferences, [17-19] to [17-23], and these results were mentioned as an outstanding experimental achievement for 2006 [17-24]. The NASA wind tunnel model Nr. 1 has been transferred from DLR Goettingen (DEU) to ONERA Lille (FRA), and new balance measurements have been carried out there. At TU Munich unsteady pressure distribution measurements have been performed on wind tunnel model Nr. 2 for angles of attack at which vortex breakdown takes place over the wing. Preliminary results were presented to the Task Group at the spring meeting 2006 in Amsterdam, and first results were published later this year [17-25], [17-26]. New experiments have been carried out in November/December 2006 on wind tunnel model Nr. 2 of TU Munich in the KKK cryogenic wind tunnel of DLR in Cologne (DEU) for additional PIV investigations and in order to investigate the laminar/turbulent transition by means of IR and TSP techniques. The two wind tunnel models Nr. 4 and 5 have been transferred from ONERA Lille (FRA) to TUBITAK-SAGE Ankara (TUR), and balance measurements as well as tests on transition laminar/turbulent have been carried out there.

New structured CFD solutions have been carried out by ONERA Lille (FRA), and at U. Glasgow (GBR) the formation of shock waves in the flow field has been studied in detail. Comparisons of the results of three

CFD-codes calculated on structured grids for the sharp-edged configuration provided by University of Glasgow (GBR), NLR Amsterdam (NDL) and EADS Munich (DEU) were presented at an AIAA conference [17-27]. Numerical calculations on unstructured grids were started at USAFA Colorado (USA), KTH Stockholm (SWE) and DLR Braunschweig (DEU). First results of such calculations within AVT-113 for the rounded leading edge case have been obtained at KTH Stockholm (SWE) and were presented at an AIAA Conference [17-28] and at the ICAS Congress 2006 [17-29] and comprehensive discussions within the Task Group took place at the autumn meeting 2006 in Vilnius. The semi-empirical method for the prediction of flow separations on the VFE-2 configuration with rounded leading edges developed by Nangia (GBR) as a consultant to AVT-113 has been reviewed in 2006.

Progress in 2007. The experiments at TU Munich (DEU) on their wind tunnel model Nr. 2 continued with PIV and HWA investigations, and further results have been published [17-30]. In autumn 2007 additional boundary layer HWA measurements have been carried out. At DLR the evaluations of the TSP and IR investigations in the KKK cryogenic wind tunnel have been started. The new PIV results led to an extension of the existing data base towards higher Reynolds numbers at low Mach numbers. The measurements on wind tunnel model Nr. 3 at Uni. Glasgow (GBR) have been carried out in the second half of 2007. The test results obtained for the two wind tunnel models Nr. 4 and 5 at ONERA Lille (FRA) and at TUBITAK-SAGE Ankara (TUR) have been evaluated and compared with those from NASA. Comprehensive discussions on this subject took place within the Task Group at the spring meeting 2007 in Florence and at the autumn meeting 2007 in Athens.

Towards the end of the working period of VFE-2 the activities on the numerical side increased very much. Based on the available experimental data a set of flow cases for comparisons of experiments and numerics has been proposed. Calculations have been carried out for $\alpha = 13°$, $18°$ and $23°$ on structured grids by EADS Munich (DEU), ONERA Lille (FRA) and TUSAS Ankara (TUR) and on unstructured grids by USAFA Colorado (USA), KTH Stockholm (SWE) [17-31] and DLR Braunschweig (DEU). The principal objective for these calculations was the comparison of the various results with the experimental data. Due to the lack of experimental information on the formation of the inner vortex in the apex region of the wing and on the interaction at the onset of the outer primary vortex, however, the numerical results from EADS Munich (DEU), KTH Stockholm (SWE), USAFA Colorado (USA) and DLR Braunschweig (DEU) have also been used to analyse the flow physics in these regions of the wing, and comprehensive discussions within the Task Group on this aspect took place at the autumn meeting 2007 in Athens. At Uni. Glasgow/Liverpool (GBR) the formation of shock waves in the flow field has been studied intensively on the basis of calculations on structured grids. This lead to a PhD-thesis [17-32], and later also results from calculations on unstructured grids have been taken into consideration in comparisons with experimental data [17-33], [17-34]. The semi-empirical method for the prediction of flow separations on the VFE-2 configuration with rounded leading edges developed by Nangia (GBR) has been settled and the final version has been accepted. At mid 2007 the status of VFE-2 has been summarized [17-35].

In addition to these detailed activities another objective for the VFE-2 facet of AVT-113 in 2007 was the preparation of 15 papers of VFE-2 members as well as an "Open Panel Discussion" to be presented in two special sessions at the 46th AIAA Aerospace Sciences Conference (Reno 2008), see [17-36] to [17-50].

17.5   PRESENTATION OF RESULTS

The Second International Vortex Flow Experiment (VFE-2) has been proposed in [17-5] and its basis were the already existing experimental investigations from the NTF at NASA Langley RC [17-6], which were later summarized in [17-14] to [17-17].

At the very beginning of VFE-2 in 2003 new experimental contributions were announced and later realized by NASA Langley RC USA (Chapter 18), DLR Goettingen DEU (Chapter 19), ONERA Lille FRA (Chapter 20), TU Munich DEU (Chapter 21), Univ. of Glasgow GBR (Chapter 22), and later also by TUBITAK-SAGE Ankara TUR (Chapter 23). The lessons learned from the new experiments will be discussed in a separate article (Chapter 24).

Within VFE-2 the first solution on a structured grid was provided by EADS Munich DEU (Chapter 25) and later other solutions on structured grids were added by ONERA Lille FRA (Chapter 26), NLR Amsterdam NLD (Chapter 27) and TUSAS Ankara TUR (Chapter 28), and studies on the vortex formation at transonic flow conditions have been initiated at the Universities of Glasgow and Liverpool GBR (Chapter 29).

A first numerical solution for the VFE-2 configuration on an unstructured grid was already available at the very beginning of VFE-2 by NASA Langley RC [17-7]. New solutions on unstructured grids for the VFE-2 configuration are due to KTH Stockholm SWE (Chapter 30), DLR Braunschweig DEU (Chapter 31) and USAFA Colorado USA (Chapter 32). In addition a semi-empirical prediction method for the vortex formation on delta wings with rounded leading edges is presented (Chapter 33). The experience from calculations on structured and unstructured grids is summarized in a separate article (Chapter 34), and the results of the whole VFE-2 are discussed in a concluding section (Chapter 35). All members of the VFE-2 facet of AVT-113 and their affiliations are listed in Appendix 17-1.

17.6   REFERENCES

[17-1] Drougge, G.: *The International Vortex Flow Experiment for Computer Code Validation*, ICAS-Proceedings Jerusalem 1988, Vol. 1, pp. XXXV-XLI.

[17-2] Elsenaar, A., Hjelmberg, L., Bütefisch, K.-A. and Bannink, W.J.: *The International Vortex Flow Experiment*, AGARD-CP-437 (1988), Vol.1, pp .9-1 to 9-23.

[17-3] Wagner, B., Hitzel, S., Schmatz, M.A., Schwarz, W., Hilgenstock, A. and Scherr, S.: *Status of CFD Validation on the Vortex Flow Experiment*, AGARD-CP-437 (1988), Vol. 1, pp. 10-1 to 10-10.

[17-4] Hoeijmakers, H.W.M.: *Modelling and Numerical Simulation of Vortex Flow in Aerodynamics*, AGARD-CP-494 (1991), pp. 1-1 to 1-46.

[17-5] Hummel, D. and Redeker, G.: *A New Vortex Flow Experiment for Computer Code Validation*, RTO AVT Symposium on "Vortex Flow and High Angle of Attack Aerodynamics", Loen, Norway, 7-11 May 2001, Meeting Proceedings RTO-MP-069 (I), SYA 8-1 to 8-31 (2003).

[17-6] Chu, J. and Luckring, J.M.: *Experimental Surface Pressure Data Obtained on 65° Delta Wing Across Reynolds Number and Mach Number Ranges*, NASA TM 4645 (1996).

[17-7] Pirzadeh, S.Z.: *Vortical Flow Prediction Using an Adaptive Unstructured Grid Method*, RTO AVT Symposium on "Vortex Flow and High Angle of Attack Aerodynamics", Loen, Norway, 7-11 May 2001, Meeting Proceedings RTO-MP-069 (I), SYA 13-1 to 13-36 (2003).

[17-8] Hummel, D.: *Experimentelle Untersuchung der Strömung auf der Saugseite eines schlanken Deltaflügels*, Z. Flugwiss. 13 (1965), 247-252.

[17-9] Hummel, D.: *Effects of Boundary Layer Formation on the Vortical Flow Above Slender Delta Wings*, RTO AVT Symposium on "Enhancement of NATO Military Flight Vehicle Performance by Management of Interacting Boundary Layer Transition and Separation", Prague, Czech Republic, 4-8 October 2004, Meeting Proceedings RTO-MP-AVT-111, 30-1 to 30-22, 2004.

[17-10] Visbal, M.R.: *Computed Unsteady Structure of Spiral Vortex Breakdown on Delta Wings*, AIAA Paper 96-2074 (1996).

[17-11] Müller, J. and Hummel, D.: *Numerical Analysis of the Unsteady Flow Above a Slender Delta Wing at Large Angles of Attack*, ICAS Proceedings 2000, Paper ICA0252 (2000).

[17-12] Lamar, J.E., Cronin, C.K. and Scott, L.E.: *A Review of Steps Taken to Create an International Virtual Laboratory at NASA Langley for Aerodynamic Prediction and Comparison*, Progress in Aerospace Sciences 40 (2004), 163-172.

[17-13] Lamar, J.E., Cronin, C.K. and Scott, L.E.: *Virtual Laboratory Enabling Collaborative Research in Applied Vehicle Technologies*, RTO AVT Symposium on "Flow Induced Unsteady Loads and the Impact on Military Applications", Budapest, Hungary, 25-28 April 2005, Meeting Proceedings RTO-MP-AVT-123, 2005.

[17-14] Luckring, J.M.: *Reynolds Number and Leading-Edge Bluntness Effects on a 65° Delta Wing*, AIAA Paper 2002-0419, 2002.

[17-15] Luckring, J.M.: *Transonic Reynolds Number and Leading-Edge Bluntness Effects on a 65° Delta Wing*, AIAA Paper 2003-0753, 2003.

[17-16] Luckring, J.M.: *Compressibility and Leading-Edge Bluntness Effects for a 65° Delta Wing*, AIAA Paper 2004-0765, 2004.

[17-17] Luckring, J.M.: *Reynolds Number, Compressibility, and Leading-Edge Bluntness Effects on Delta-Wing Aerodynamics*, ICAS Proceedings Yokohama 2004, Paper 4.1.4.

[17-18] Hummel, D.: *The Second International Vortex Flow Experiment (VFE-2): Objectives and First Results*, 2nd International Symposium on "Integrating CFD and Experiments in Aerodynamics", 5-6 September 2005, Cranfield University, UK, J. Aerospace Engineering, Vol. 220 (2006), Nr. 6: 559-568.

[17-19] Klein, C., Sachs, W., Henne, U., Wiedemann, A. and Konrath, R.: *Development of PSP Technique for Application on the VFE-2 65° Delta Wing Configuration in Sub- and Transonic Flow*, AIAA Paper 2006-0059 (2006).

[17-20] Konrath, R., Klein, C., Engler, R.H. and Otter, D.: *Analysis of PSP Results Obtained for the VFE-2 65° Delta Wing Configuration at Subsonic and Transonic Speed*, AIAA Paper 2006-0060 (2006).

[17-21] Schröder, A., Agocs, J., Frahnert, H., Otter, D., Mattner, H., Kompenhans, J. and Konrath, R.: *Application of Stereo-PIV to the VFE-2 65° Delta Wing Configuration at Sub- and Transonic Speeds*, AIAA Paper 2006-3486 (2006).

[17-22] Konrath, R., Schröder, A. and Kompenhans, J.: *Analysis of PIV Results Obtained for the VFE-2 65° Delta Wing Configuration at Sub- and Transonic Speeds*, AIAA Paper 2006-3003 (2006).

[17-23] Konrath, R., Klein, Ch., Schröder, A. and Kompenhans, J.: *Combined Application of Pressure Sensitive Paint and Particle Image Velocimetry to the Flow Above a Delta Wing*, 12th International Symposium on Flow Visualization, September 10-14, 2006, DLR Goettingen, Germany.

[17-24] Sheplak, M.: *The Year in Review: Aerodynamic Measurement Technology*, Aerospace America, December 2006: 22.

[17-25] Furman, A. and Breitsamter, Ch.: *Delta Wing Steady Pressure Investigations for Sharp and Rounded Leading Edges*, Notes on Numerical Fluid Mechanics and Multidisciplinary Design (NNFM), Vol. 92 (2006), 77 -84.

[17-26] Furman, A. and Breitsamter, Ch.: *Investigation of Flow Phenomena on Generic Delta Wing*, ICAS Proceedings 2006.

[17-27] Schiavetta, L.A., Boelens, O.J. and Fritz, W.: *Analysis of Transonic Flow on a Slender Delta Wing Using CFD*, AIAA Paper 2006-3171 (2006).

[17-28] Crippa, S. and Rizzi, A.: *Numerical Investigation of Reynolds Number Effects on a Blunt Leading-Edge Delta Wing*, AIAA Paper 2006-3001 (2006).

[17-29] Crippa, S. and Rizzi, A.: *Initial Steady/Unsteady CFD Analysis of Vortex Flow Over the VFE-2 Delta Wing*, ICAS Proceedings 2006.

[17-30] Furman, A. and Breitsamter, Ch.: *Stereo-PIV and Hot-Wire Investigations on Delta Wing*, Council of European Aerospace Societies (CEAS), 1st European Air and Space Conference, Berlin, 10-13 September 2007.

[17-31] Crippa, S. and Rizzi, A.: *Reynolds Number Effects on Blunt Leading Edge Delta Wings*, Council of European Aerospace Societies (CEAS), 1st European Air and Space Conference, Berlin, 10-13 September 2007.

[17-32] Schiavetta, L.: *Evaluation of URANS and DES Predictions of Vortical Flows Over Delta Wings*, PhD Thesis, Faculty of Engineering, Department of Aeronautical Engineering, University of Glasgow, 2007.

[17-33] Schiavetta, L.A., Badcock, K.J. and Cummings, R.M.: *Comparison of DES and URANS for Unsteady Vortical Flows Over Delta Wings*, AIAA Paper 2007-1085 (2007).

[17-34] Schiavetta, L.A., Boelens, O.J., Fritz, W. and Cummings, R.M.: *Sting Effects on Transonic Delta Wing Experiments*, 3rd International Symposium on Integrating CFD and Experiments in Aerodynamics, 20-21 June 2007, US Air Force Academy, CO, USA.

[17-35] Hummel, D.: *The Second International Vortex Flow Experiment (VFE-2): Objectives and Present Status*, AIAA Paper 2007-4446 (2007).

[17-36] Hummel, D.: *Review of the Second International Vortex Flow Experiment (VFE-2)*, AIAA Paper 2008-0377, 2008.

[17-37] Luckring, J.M.: *Initial Experiments and Analysis of Vortex Flow on Blunt Edged Delta Wings*, AIAA Paper 2008-0378, 2008.

[17-38] Konrath, R., Klein, Ch. and Schröder, A.: *PSP and PIV Investigations on the VFE-2 Configuration in Sub- and Transonic Flow*, AIAA Paper 2008-0379, 2008.

[17-39] Le Roy, J.F., Rodriguez, O. and Kurun, S.: *Experimental and CFD Contribution to Delta Wing Vortical Flow Understanding*, AIAA Paper 2008-0380, 2008.

[17-40] Furman, A. and Breitsamter, Ch.: *Turbulent and Unsteady Flow Characteristics of Delta Wing Vortex Systems*, AIAA Paper 2008-0381, 2008.

[17-41] Coton, F., Mat, S. and Galbraith, R.: *Low Speed Wind Tunnel Characterization of the VFE-2 Wing*, AIAA Paper 2008-0382, 2008.

[17-42] Luckring, J.M. and Hummel, D.: *What was Learned from the New VFE-2 Experiments*, AIAA Paper 2008-0383, 2008.

[17-43] Nangia, R.K.: *Semi-Empirical Prediction of Vortex Onset and Progression on 65° Delta Wings*, (RTO-AVT-113, VFE-2 facet), AIAA Paper 2008-0384, 2008.

[17-44] Fritz, W.: *Numerical Simulation of the Peculiar Subsonic Flow-Field about the VFE-2 Delta Wing with Rounded Leading Edge*, AIAA Paper 2008-0393, 2008.

[17-45] Gürdamar, E., Ortakaya, Y., Kaya, S. and Korkem, B.: *Some Factors Influencing the Vortical Flow Structures on Delta Wings*, AIAA Paper 2008-0394, 2008.

[17-46] Schiavetta, L.A., Boelens, O.J., Crippa, S., Cummings, R.M., Fritz, W. and Badcock, K.J.: *Shock Effects on Delta Wing Vortex Breakdown*, AIAA Paper 2008-0395, 2008.

[17-47] Cummings, R.M. and Schütte, A.: *Detached-Eddy Simulation of the Vortical Flowfield about the VFE-2 Delta Wing*, AIAA Paper 2008-0396, 2008.

[17-48] Crippa, S. and Rizzi, A.: *Steady, Subsonic CFD Analysis of the VFE-2 Configuration and Comparison to Wind Tunnel Data*, AIAA Paper 2008-0397, 2008.

[17-49] Schütte, A. and Lüdeke, H.: *Numerical Investigations on the VFE 2 65-degree Rounded Leading Edge Delta Wing Using the Unstructured DLR-TAU-Code*, AIAA Paper 2008-0398, 2008.

[17-50] Fritz, W. and Cummings, R.M.: *What was Learned from the Numerical Simulations for the VFE-2*, AIAA Paper 2008-0399, 2008.

Appendix 17-1: List of the Members of the VFE-2 Facet of AVT-113

Name and Full Postal Address	Email Address	Contribution to VFE-2	
		Numerical	**Experimental**
Lamar, Dr. John E. NASA Langley Research Center Mail Stop 499 Hampton, VA 23681-2199 USA	john.e.lamar@nasa.gov	Co-chairman	
Hummel, Prof. Dr.–Ing. Dietrich Institut für Strömungsmechanik TU Braunschweig Bienroder Weg 3 D-38106 Braunschweig Germany	d.hummel@tu-bs.de	Co-chairman	
Hirsch, Prof. Charles VrijeUniversiteit Brussel Pleinlaan, 2 1050 Brussels Belgium	charles.hirsch@numeca.be	Panel Mentor	
Arthur, Dr. Malcolm Terence Aerodynamics Integration Dept. QinetiQ, Cody, Ively Road Farnborough, Hampshire GU14 0LX United Kingdom	mtarthur@qinetiq.com	Structured Grid Transition	
Badcock, Prof. Dr. Ken J. Department of Engineering The University of Liverpool Brownlow Hill, Liverpool L69 3GH United Kingdom	k.j.badcock@liverpool.ac.uk	Structured Grid	
Bin Mat, Mr. Shabudin The University of Glasgow Dept. of Aerospace Engineering Glasgow G12 8QQ United Kingdom	smat@eng.gla.ac.uk		Model Nr. 3 Forces, Oilfl. Pressures by PSI, Kulites PIV
Boelens, Mr. Okko J. Aerospace Vehicles Division Dept. of Flight Physics and Loads National Aerosp. Laboratory NLR 2 Anthony Fokkerweg 1059 BM Amsterdam The Netherlands	boelens@nlr.nl	Structured Grid	

Name and Full Postal Address	Email Address	Contribution to VFE-2	
		Numerical	**Experimental**
Breitsamter, Dr.-Ing. Christian Lehrstuhl für Aerodynamik Technische Universität München Boltzmannstr. 15 D-85748 Garching Germany	christian.breitsamter@ aer.mw.tum.de		Model Nr. 2 Oilflow patt. Pressures by PSI, Kulites PIV, HWA
Coton, Prof. Frank N. The University of Glasgow Dept. of Aerospace Engineering Glasgow G12 8QQ United Kingdom	f.coton@aero.gla.ac.uk		Model Nr. 3 Forces, Oilflow Pressures by PSI, Kulites PIV
Crippa, Mr. Simone Royal Inst. of Technology (KTH) Aeron. and Vehicle Engineering Division of Aerodynamics Teknikringen 8 SE-10044 Stockholm Sweden	crippa@kth.se	Unstructured Grid	
Cummings, Prof. Russell M. US Air Force Academy Department of Aeronautics 2354 Fairchild Drive, Suite 6H27 Colorado Springs, CO 80840-6222 USA	russ.cummings@usafa.edu	Unstructured Grid	
Fritz, Mr. Willy Senior Development Engineer EADS – Military Air Systems Rechliner Straße D-85077 Manching Germany	willy.fritz@eads.com	Structured Grid	
Furman, Andrej Lehrstuhl für Aerodynamik Technische Universität München Boltzmannstr. 15 D-85748 Garching Germany	andrej.furman@ aer.mw.tum.de		Model Nr. 2 Oilflow patt. Pressures by PSI, Kulites PIV, HWA
Galbraith, Prof. Roderick The University of Glasgow Dept. of Aerospace Engineering Glasgow G12 8QQ United Kingdom	roddy@aero.gla.ac.uk		Model Nr. 3 Forces, Oilfl. Pressures by PSI, Kulites PIV

Name and Full Postal Address	Email Address	Contribution to VFE-2	
		Numerical	**Experimental**
Groot, Dr. Klaus de Institut für Aerodynamik und Strömungstechnik DLR Braunschweig Lilienthalplatz 7 D-38108 Braunschweig Germany	klaus.degroot@dlr.de		Model Nr. 2 IR (KKK)
Gürdamar, Emre Turkish Aircraft Industries TUSAS Ziyabey Cad.3 sok.No:16 06520 Balgat, Ankara Turkey	egurdamar@tai.com.tr	Structured Grid	
Kaya, Serpil Turkish Aircraft Industries TUSAS Ziyabey Cad.3 sok.No:16 06520 Balgat, Ankara Turkey	serkaya@tai.com.tr	Structured Grid	
Klein, Dr. Christian Institut für Aerodynamik und Strömungstechnik DLR Göttingen Bunsenstr. 10 D-37073 Göttingen Germany	christian.klein@dlr.de		Model Nr. 1 PSP (TWG) Model Nr. 2 TSP (KKK)
Konrath, Dr. Robert Institut für Aerodynamik und Strömungstechnik DLR Göttingen Bunsenstr. 10 D-37073 Göttingen Germany	robert.konrath@dlr.de		Model Nr. 1 PSI, PSP, PIV (TWG) Model Nr. 2 PIV, TSP, IR (KKK)
Korkem, Mr. Bulent Turkish Aircraft Industries TUSAS Ziyabey Cad.3 sok.No:16 06520 Balgat, Ankara Turkey	bkorkem@tai.com.tr	Structured Grid	
Kurun, Mr. Suleyman Aerodynamic Division TUBITAK-SAGE, P.K. 16 06261 Mamak, Ankara Turkey	skurun@sage.tubitak.gov.tr		Models Nr. 4 and 5 Forces, Transition

Name and Full Postal Address	Email Address	Contribution to VFE-2	
		Numerical	**Experimental**
Le Roy, Dr. Jean François ONERA – Centre de Lille 5, Boulevard Paul Painleve F-59045 Lille France	jean-francois.le_roy@onera.fr	Structured Grid	
Luckring, Dr. James M. NASA Langley Research Centre Mail Stop 499 Hampton, VA 23681-2199 USA	james.m.luckring@nasa.gov		Model Nr. 1 Balance Measurements Pressures PSI
Luedeke, Dr. Heinrich DLR Braunschweig Lilienthalplatz 7 D-38108 Braunschweig Germany	heinrich.luedeke@dlr.de	Unstructured Grid	
Nangia, Dr. Raj K. Nangia Aero Associates Maggs House 78 Queen's Road Clifton, Bristol BS8 1QX United Kingdom	nangia@blueyonder.co.uk	Invited Consultant	
		Prediction of vortex formation for blunt edged delta wings	
Ortakaya, Yüksel Turkish Aircraft Industries TUSAS Ziyabey Cad.3 sok.No:16 06520 Balgat, Ankara Turkey	yortakaya@tai.com.tr	Structured Grid	
Rizzi, Prof. Dr. Arthur Royal Inst. of Technology (KTH) Aeron. and Vehicle Engineering Division of Aerodynamics Teknikringen 8 SE-10044 Stockholm Sweden	rizzi@kth.se	Unstructured Grid	
Rodriguez, Dr. Ovide ONERA – Centre de Lille 5, Boulevard Painleve F-59045 Lille France	ovide.rodriguez@onera.fr		Models Nr.1, 4 and 5 Balance Pressures PSI PIV

Name and Full Postal Address	Email Address	Contribution to VFE-2	
		Numerical	**Experimental**
Schiavetta, Ms. Lucy The University of Glasgow Dept. of Aerospace Engineering Glasgow G12 8QQ United Kingdom	lschiave@aero.gla.ac.uk	Structured Grid	
Schröder, Dr. Andreas Institut für Aerodynamik und Strömungstechnik DLR Göttingen Bunsenstr. 10 D-37073 Göttingen Germany	andreas.schroeder@dlr.de		Model Nr. 1 PIV (TWG) Model Nr. 2 PIV (KKK)
Schütte, Dipl.-Ing. Andreas DLR Braunschweig Lilienthalplatz 7 D-38108 Braunschweig Germany	Andreas.Schuette@dlr.de	Unstructured Grid	

Chapter 18 – INITIAL EXPERIMENTS AND ANALYSIS OF BLUNT-EDGE VORTEX FLOWS

by

James M. Luckring[1]

18.1   SUMMARY

A review is presented of the initial experimental results and analysis that formed the basis the Vortex Flow Experiment 2 (VFE-2). The focus of this work was to distinguish the basic effects of Reynolds number, Mach number, angle of attack, and leading edge bluntness on separation-induced leading-edge vortex flows that are common to slender wings. Primary analysis is focused on detailed static surface pressure distributions, and the results demonstrate significant effects regarding the onset and progression of leading-edge vortex separation.

18.2   NOMENCLATURE

d	=	sting diameter
C_p^*	=	sonic pressure coefficient
LTPT	=	Low Turbulence Pressure Tunnel
mac	=	mean aerodynamic chord, (2/3) c_r
NTF	=	National Transonic Facility
r_{le}	=	streamwise leading-edge radius
t	=	wing thickness
VFE-2	=	Vortex Flow Experiment 2
x_v	=	longitudinal distance to vortex separation
β	=	Prandtl-Glauert compressibility factor, $[1-(M_\infty)^2]^{1/2}$
Λ	=	Leading-edge sweep, degrees

18.3   INTRODUCTION

In the early 1980's expanded planning was undertaken to develop models and test programs [[18-1], [18-2]] for the National Transonic Facility (NTF) at NASA Langley Research Center. The models spanned research distinctions from fundamental to configuration concepts. The test programs for the most part addressed combinations of Reynolds number effects and high Reynolds number aerodynamics for attached and separated flows at subsonic or transonic speeds.

One of these programs was focused on separation-induced leading-edge vortex flows from slender wings with blunt leading edges. Various aerodynamic and testing considerations led to the selection of a 65° swept delta wing for the basic geometry. The wing supported testing with different leading-edge components as a means to vary the leading-edge bluntness. Maneuvering aircraft develop these flows with blunt-edge separation, and thus it was felt that this program would extend the previous knowledge obtained with sharp-edged delta wings in a useful manner.

---

[1] Senior Research Engineer, NASA Langley Research Center, Hampton VA, USA, AIAA Associate Fellow.

This test program was executed in the early 1990's along with a companion experiment in the Low Turbulence Pressure Tunnel (LTPT), and first data analysis of the NTF data [[18-3]-[18-6]] was published [[18-2], [18-7]-[18-10]] in the early 2000's. The analyses not only demonstrated significant effects of the parameters investigated, but also indicated a new structure to the leading-edge vortex separation from the blunt edges that did not occur with sharp leading edges. Discussions and further analysis [18-11] led to the proposal [18-12] for an international research campaign that became known as Vortex Flow Experiment 2 (VFE-2).

In this paper a brief review is presented of the knowledge leading up to the beginning of VFE-2. Results are included from a number of the author's previous publications along with analysis of some new results.

18.4   BASIC CONSIDERATIONS FOR SLENDER-WING VORTEX FLOWS

Many overall characteristics of vortex flows for the sharp-edged and highly-swept delta wing have been established [18-13], [18-14]. For this case, the flow undergoes a primary separation at the wing leading edge and subsequently rolls up to form a stable, separation-induced leading-edge vortex over the wing. A sketch of this vortex, from Hummel [18-13], is shown in Figure 18-1. The primary vortex induces reattached flow over the wing, and the spanwise flow under the primary vortex subsequently separates a second time to form a counter-rotating secondary vortex outboard of the primary vortex. The flow under the vortices induces significant upper surface suction pressures that can result in large vortex-induced lift increments at moderate to high angles of attack. An example of these lift increments is also shown in Figure 18-1 along with theoretical estimates of the vortex lift due to Polhamus [18-14].
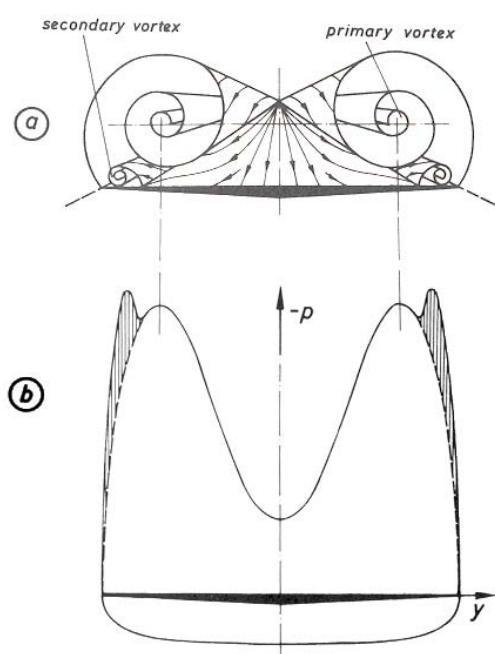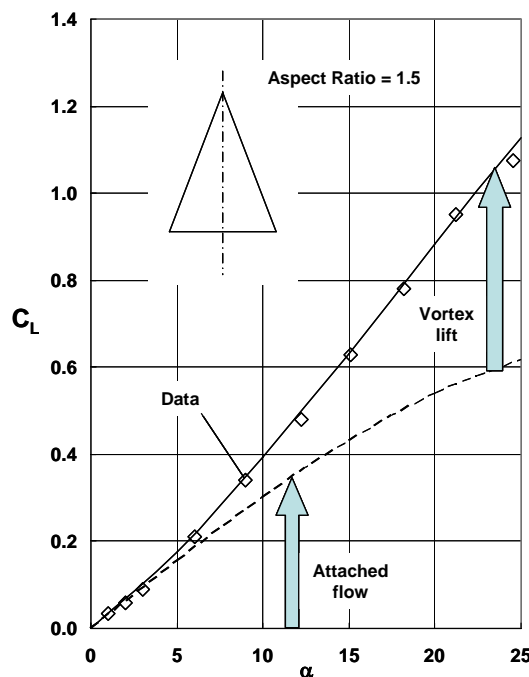
Hummel [18-13]   **Polhamus [18-14]**

**Figure 18-1: Basic Features of Separation-Induced Leading-Edge
Vortex Flows, Sharp-Edged Delta Wings.**

The blunt leading edge fundamentally alters this flow (Figure 18-2). The origin of the vortex will be displaced from the apex of the delta wing, and any leading-edge vortex separation will occur from a location near, but not necessarily at, the leading edge. Moreover, the onset and progression of the vortex separation will be a function of the flow conditions and wing geometry. For example, at low to moderate angles of attack the wing could exhibit fully attached flow. As angle of attack is increased, leading-edge separation will first occur at a location near the trailing edge for two reasons. First, delta wing leading-edge upwash distributions increase from the apex to the trailing edge, and thus the local angle of attack is higher near the trailing edge. Second, the crossflow bluntness (r_{le}/b_{loc}) tends to progress from blunter to sharper values as the trailing edge is approached. With further angle of attack increases the onset of this vortex separation will progress longitudinally up the leading edge. Thus, for some angle-of-attack range the wing will exhibit partial span leading-edge vortex separation with attached flow on the upstream portion of the wing and leading edge vortex separation on the downstream portion. Because the leading-edge vortex separation is now occurring from a smooth surface, the physics of this flow could be quite different from the sharp-edged case, and the strength, position, and the very existence of the vortex will be affected by leading-edge radius and will change with Mach number, Reynolds number, and angle of attack.
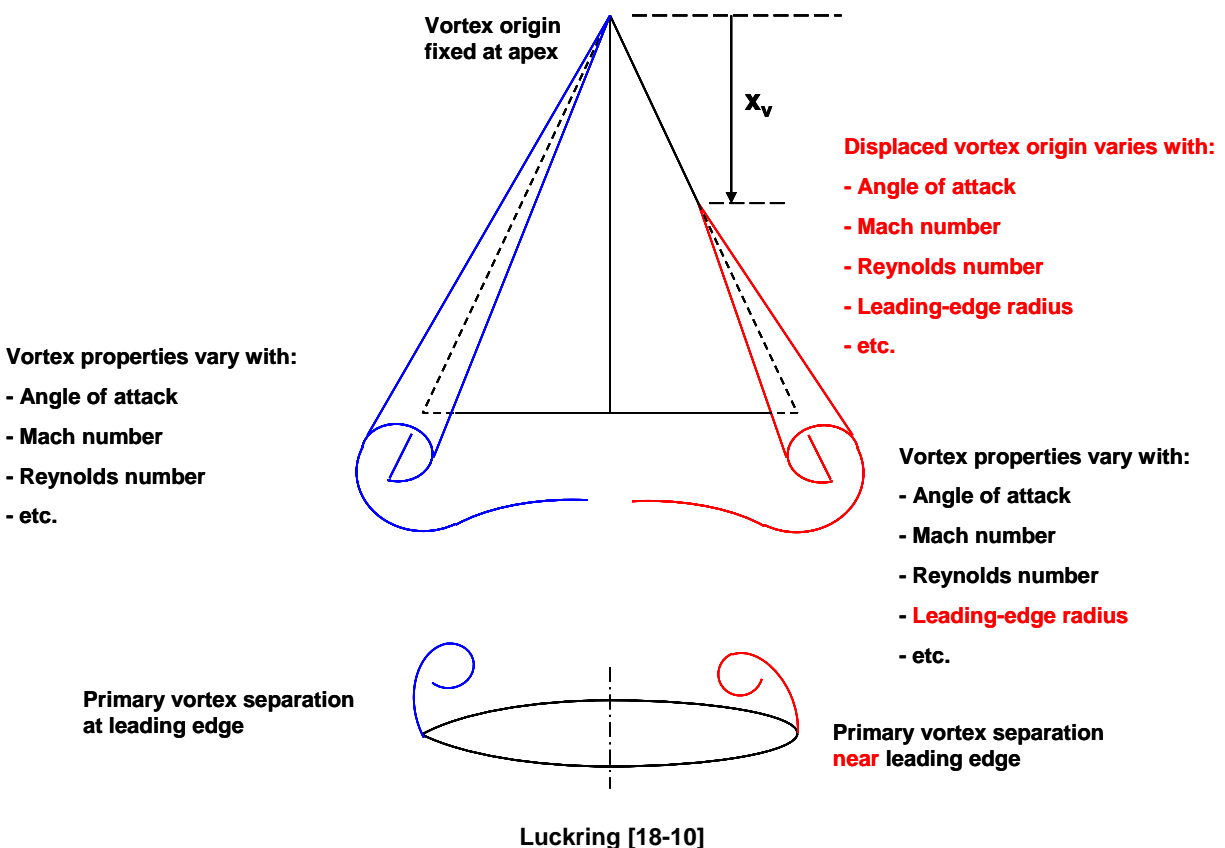
Figure 18-2: Leading-Edge Bluntness Consequences for the Primary Vortex Separation.

18.5   MODELS AND TESTS

The wind tunnel model and test programs were designed to quantify the independent effects of Mach number, Reynolds number, angle of attack, and leading edge bluntness on the onset and progression of leading edge vortex separation.

Some basic characteristics of the model are summarized in Figure 18-3. The 65° delta wing had no twist or camber and had interchangeable leading-edge segments that incorporated the various leading-edge radii. The central portion of the wing was flat. With this approach, the new blunt-edged delta wing data would relate to previous data bases developed with flat-plate sharp-edged delta wings. The wind tunnel model was designed to generate delta-wing aerodynamics with minimal wind-tunnel test interference effects.

$b/2 = 12$ in. (ref)

$t = 0.875$ in.

$c_r = 25.734$ in.

$\Lambda = 65°$

- Leading-edge surface pressure stations: $x/c_r =$ 0.10, 0.20, 0.30, 0.40, 0.50, 0.60, 0.70, 0.80, 0.90, 0.95

Spanwise surface pressure stations: $x/c_r =$ 0.20, 0.40, 0.60, 0.80, 0.95

t/c_r	0.0340
$b/2c_r$	0.4663
d/b	0.1375

$d = 3.30$ in.

Streamwise leading-edge radii:
$r_{le}/mac =$ 0., 0.0005, 0.0015, 0.0030
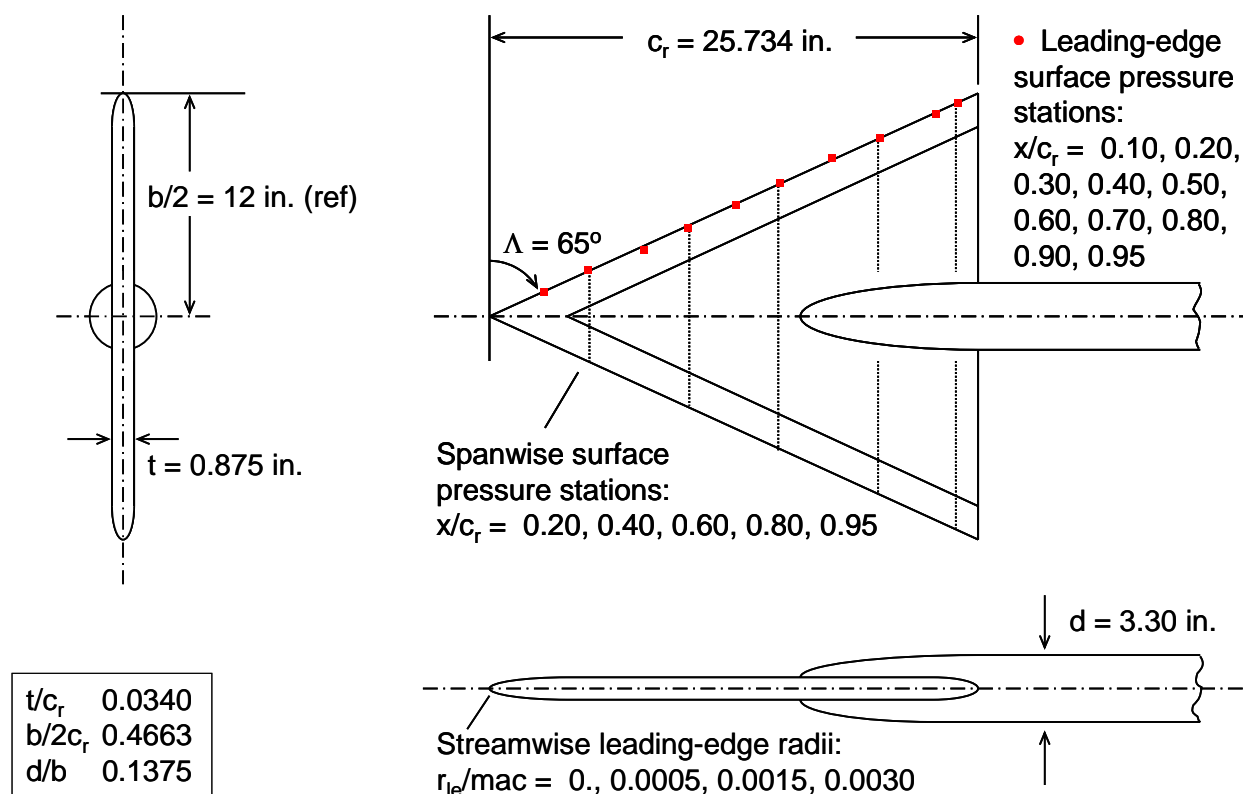
Figure 18-3: Delta Wing Configuration for Tests in NTF.

The leading-edge contours had a NACA-like polynomial form with a single parameter, the leading edge bluntness. See Figure 18-4. The contours matched the inner flat-plate portion of the wing with continuity through second derivative and, hence, curvature. This continuity is of course crucial to avoid unintended separation artificially induced by the model. The bluntness values were selected to be practical as regards values used for maneuvering aircraft and included a sharp leading edge ($r_{le} = 0$) within the same functional family.

Sharp
Small
Medium
Large

Contours not to scale

$z/z_m = a\ sqrt(\xi) + b\ \xi + c\ \xi^2 + d\ \xi^3\ ;\ \xi = x/x_m$

$r_{le}/mac = 0, 0.0005, 0.0015, 0.0030$

match
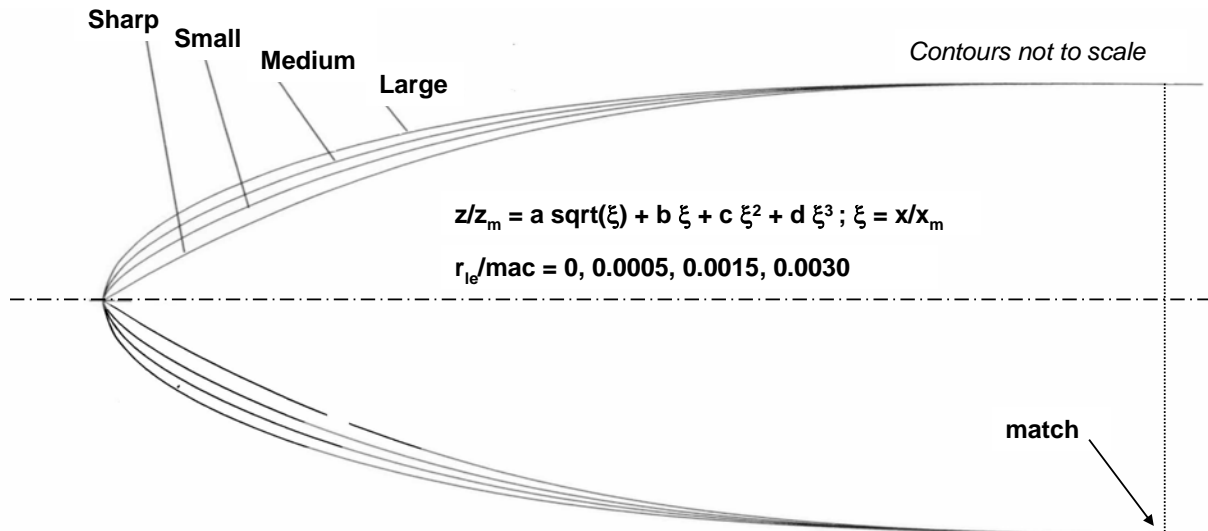
Figure 18-4: Leading-Edge Geometry.

The emphasis for the experiment was on static surface pressure measurements, and for most configurations there were approximately 183 pressure taps organized along constant percent local semispan locations at constant percent root-chord stations. Pressure taps were also situated directly on the leading edge (i.e., $\eta = 1$) to facilitate separation onset measurement. Because of the extensive pressure instrumentation, there was no room in the model for a conventional internal strain-gauge balance. However, the sting itself was gauged to provide measurement on normal force and pitching moment.

Primary experiments were performed in the National Transonic Facility [[18-15], [18-16] (NTF) at the NASA Langley Research Center. This tunnel allows for independent control of Mach number (0.1 to 1.2), total pressure (1.2 atm to 8.8 atm), and total temperature (-250 F to 120 F) through the injection of cryogenic nitrogen. The test section is slotted and 8.2 feet square.

Through the combination of pressure and cryogenic temperatures the NTF can test at very high Reynolds numbers. Because the tunnel has three degrees of freedom in operation conditions (speed, total pressure and total temperature), it can also be used to vary one free-stream parameter while holding two other free-stream parameters constant. For example, free-stream Reynolds number can be varied while holding Mach number (compressibility effects) and q_∞/E (aeroelastic effects, where E is Young's modulus) constant. This feature can be exploited for other means as well, say to vary Mach number while holding Reynolds number and q_∞/E constant. Thus, Reynolds number, Mach number, and aeroelastic effects can be isolated experimentally.

The facility operation envelope for the NTF delta wing along with the range of the delta wing experimental program is shown in Figure 18-5. The range of test conditions were chosen to be representative of operating conditions for a variety of aircraft incorporating slender-wing flows; transonic cruise conditions for a representative military transport (C17) and a conceptual High Speed Civil Transport (HSCT) are also shown for reference.
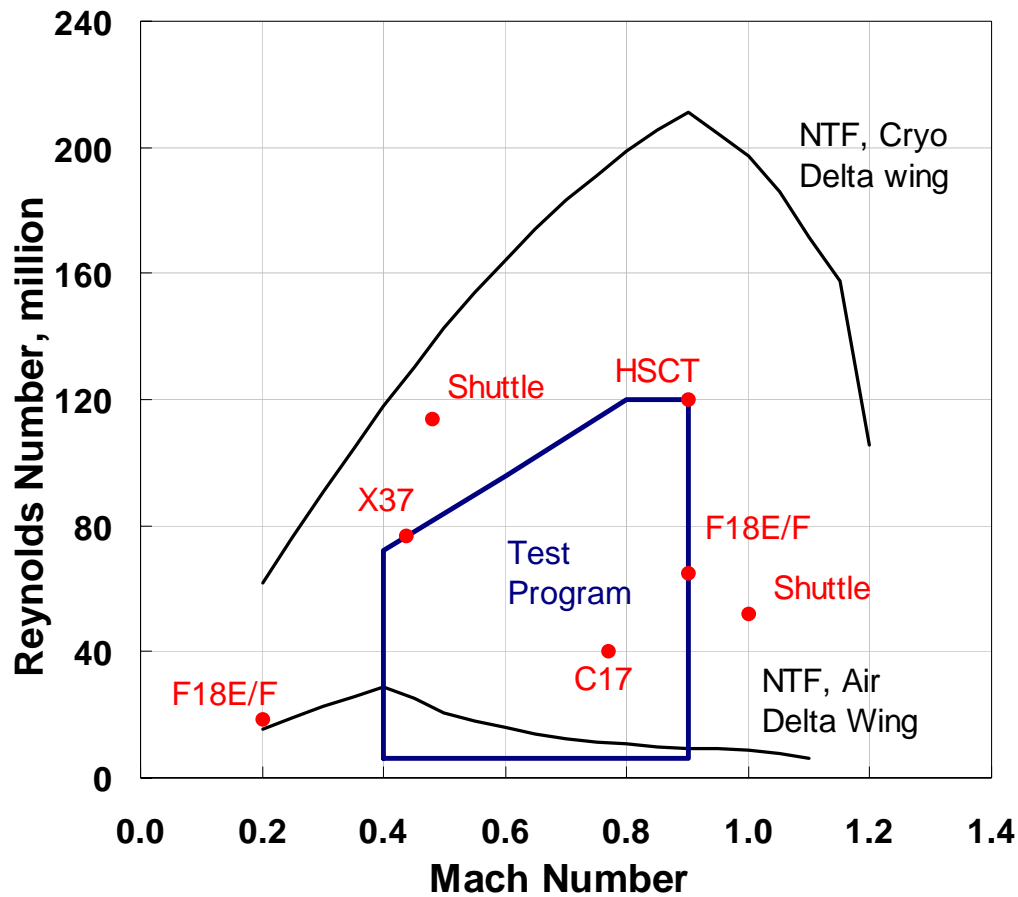
Figure 18-5: National Transonic Facility Test Program.

The tests were designed to minimize potential data contaminants including those often referred to as pseudo Reynolds number effects. The wing was hydraulically smooth (k^+<5) for the range of Reynolds numbers investigated. Wing design analysis indicated negligible aeroelastic effects. An offset sting kept the model on the tunnel centerline for the angle-of-attack range investigated. In addition, wind tunnel wall interference was believed to be negligible based on established best practices for the slotted-wall test section (e.g., the model span relative to the tunnel width, model area relative to the tunnel cross sectional area, model positioning).

The gauging requirements for the high loads encountered in the NTF test campaign precluded acceptable measurement accuracies at test conditions below a free-stream Mach number of 0.4. To obtain lower speed data, a second wing was designed for testing in the Low Turbulence Pressure Tunnel [18-17] (LTPT) located at the NASA Langley Research Center. The test conditions were focused at a free-stream Mach number of 0.2, and Reynolds numbers were varied between 2 x 10^6 and 12 x 10^6. The model was a ¾ scale version of the NTF delta wing model. This size was determined [[18-18], [18-19]] to provide correctable wall-interference effects. A comparison of the two models in their respective test sections is shown in Figure 18-6.

Figure 18-6: LTPT and NTF Delta Wings.

18.6 AERODYNAMICS OF BLUNT-EDGED VORTEX FLOWS

A contrast between sharp-edged and blunt-edged vortex flow results is presented first. These results are followed by a discussion of Reynolds number effects for the varying leading-edge bluntness values. Mach number effects are presented next followed by some discussion of the significance of isolating these effects.

18.6.1 Contrast of Sharp and Blunt Edge Flows

A comparison between the sharp and medium bluntness leading-edge configurations is presented in Figure 18-7 for the normal force and pitching moment coefficients at a free-stream Mach number of 0.4 and a free-stream Reynolds number of 6 million. The blunt leading edge separation weakens the vortex compared to the sharp leading edge case, and the normal force coefficient is reduced from the sharp-edged values for the angle of attack range investigated.
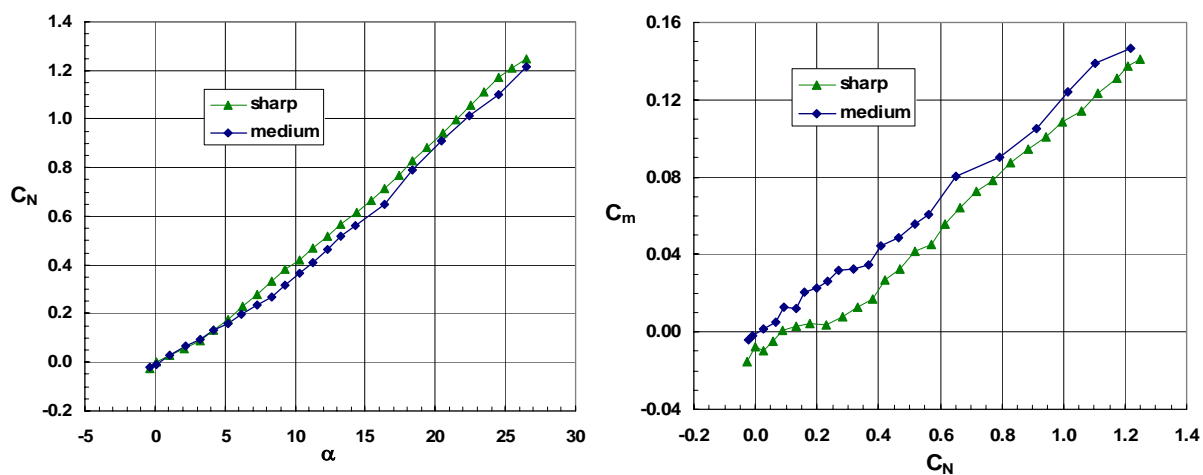
Figure 18-7: Effect of Leading-Edge Bluntness on Normal Force and Pitching Moment Coefficients.
Sharp and medium bluntness leading edges, M = 0.4, R_{mac} = 6 x 10^{6}; Data from NTF.

Pitching moment results show the blunt-edged wing to have a more forward (i.e., toward the wing apex) center of pressure than the sharp-edged case. Leading-edge vortex loadings tend to be situated further aft than attached flow loadings, and thus this forward shift in pitching moment is consistent with the reduced vortex strength from the blunt leading edge.

A comparison of the static surface pressure coefficients for the sharp-edged and medium bluntness delta wing is shown in Figure 18-8 for a nominal angle of attack of 13°. The sharp-edged wing exhibits typical separation-induced leading-edge vortex properties. The primary vortex suction peak is situated conically on the wing and diminishes in magnitude as the trailing edge is approached. At this moderate angle of attack vortex breakdown does not occur in the vicinity of the wing, and this drop in primary vortex suction is due to the trailing-edge Kutta condition in conjunction with longitudinal vortex curvature effects. Outboard of this suction peak turbulent secondary separation is also indicated.
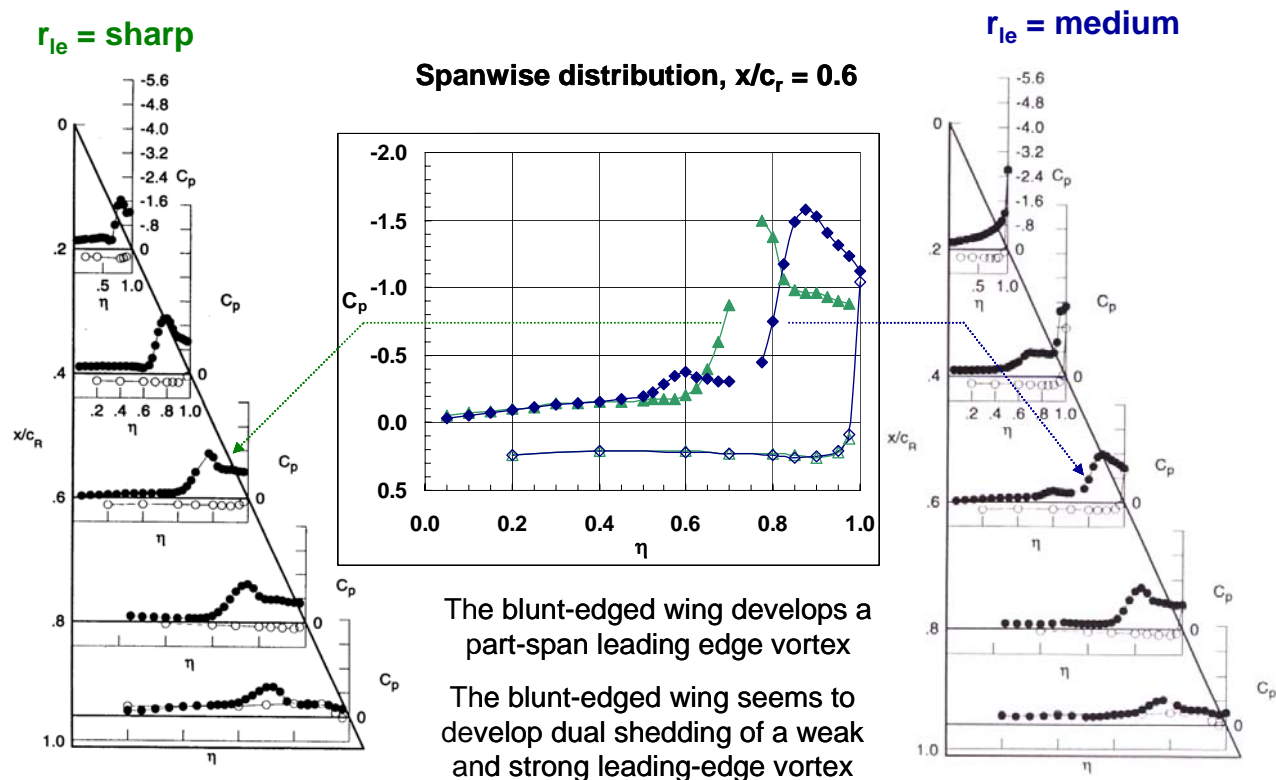
Figure 18-8: Static Surface Pressure Coefficients for Sharp and Medium Bluntness Delta Wings, α = 13°, M = 0.4, R_{mac} = 6 x 10^6; Data from NTF.

The blunt-edged delta wing surface pressure coefficients clearly demonstrate part span leading-edge vortex separation, Figure 18-8. Attached flow pressures are evident at 20% root chord while leading-edge vortex-like pressures are evident from 60% root chord aft. The origin of the blunt leading-edge vortex for this case is in the vicinity of 30% root chord. This class of leading-edge vortex separation does not exist for corresponding flat-plate sharp-edged wings. The direct comparison of the pressures in Figure 18-8 at 60% root chord demonstrates the outboard shift of the vortex footprint due to leading-edge bluntness.

The pressures at 60% root chord station also indicate a second suction peak near 60% local semispan. This is inboard of the primary suction peak and may indicate a second co-rotating primary vortex shed from the blunt leading edge. This was also a new feature for the blunt leading edge vortex separation as compared to the sharp edge case. Two sketches of this postulated flow structure of these vortices are presented below in Figure 18-9 from private discussions [18-11]. Co-rotating vortices can be sensitive to their relative strength and position, and small differences (flow, geometry, etc.) could result in the vortices either developing separate and roughly streamwise trajectories or developing a mutually intertwined trajectory. Such details are difficult to discern from the static surface pressures.
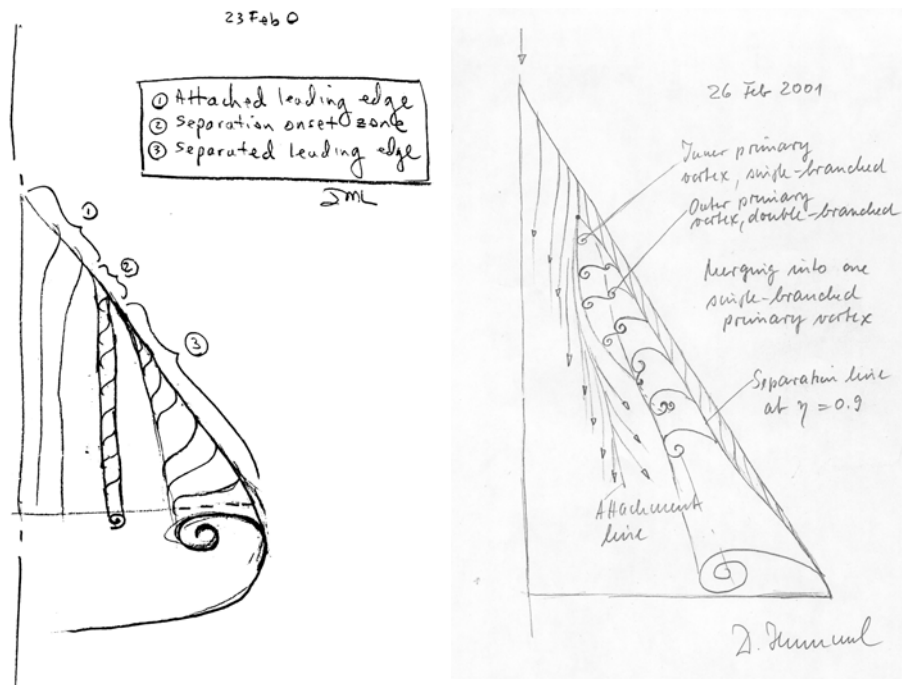
Figure 18-9: Sketches of Blunt Leading-Edge Dual Co-Rotating Leading-Edge Vortex Separation [18-11].

The details of the flow leading up to the primary vortex separation, with an inner and an outer co-rotation vortex also are curious. The pressures at 40% root chord in Figure 18-8 exhibit neither a customary attached flow nor a conventional vortex flow trend. It is unclear if the inner vortex separation is initiated upstream and then triggered by the outer primary separation or if the inner and outer vortex separation occurs in a more tightly coupled fashion.

18.6.2   Reynolds Number and Bluntness Effects

Reynolds number effects for a variety of constant Mach numbers were determined for all leading edges of the test program in both the NTF and the LTPT facilities. In this section Reynolds number effects on the static surface pressure coefficients and on the inferred onset and progression of leading-edge vortex separation will be reviewed.

The effect of Reynolds number on the blunt leading edge vortex flow is summarized in Figure 18-10. Results on the left portion of this figure are the same ones used in Figure 18-8 to compare with sharp-edged flow.

Comparison of these results at R_{mac} = 6 million (typical of wind-tunnel conditions) to those at 60 million (representative of flight conditions) show significant recovery of attached flow at the higher Reynolds number. The origin of the leading-edge vortex separation has shifted downstream in association with the higher Reynolds number.
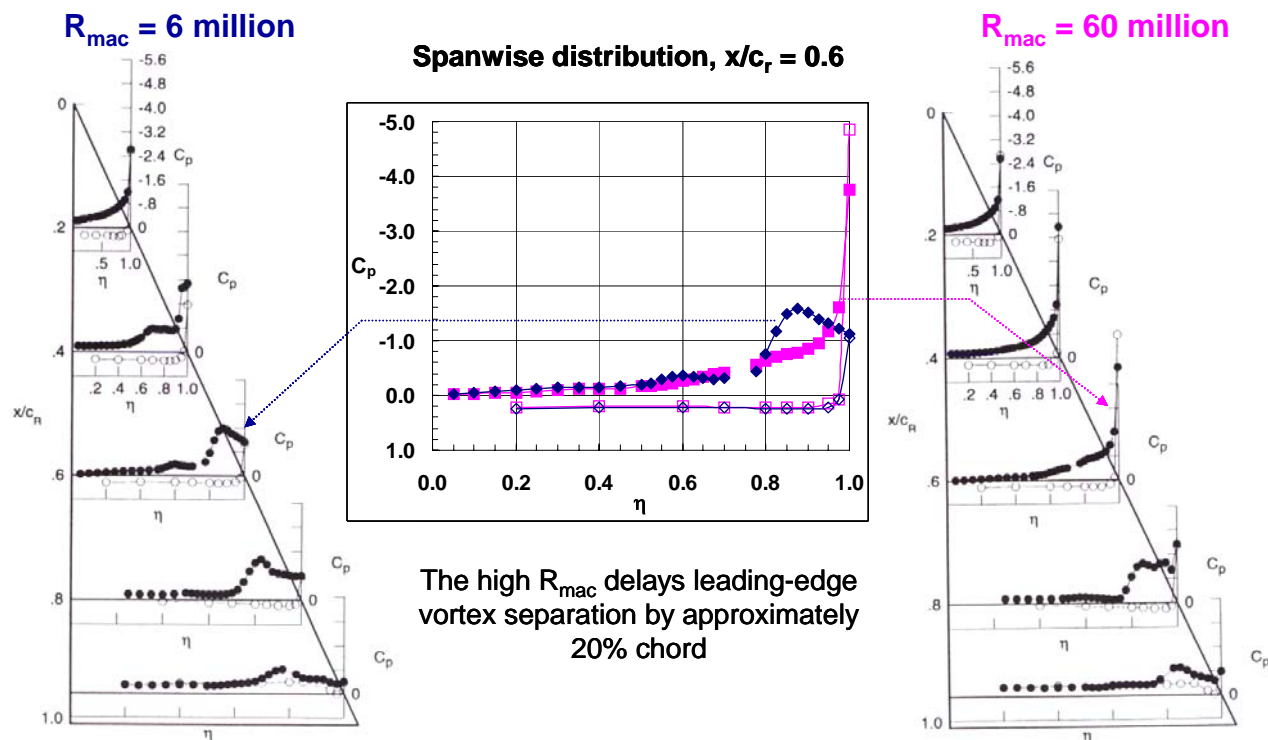
Figure 18-10: Effect of Reynolds Number on Static Surface Pressure Coefficients.
Medium bluntness, α = 13°, M = 0.4, R_{mac} = 6 x 10^6 and 60 x 10^6; Data from NTF.

Leading-edge pressures provide a useful means to identify the passage of leading-edge vortex separation onset (see Figure 18-11). At low angles of attack the leading-edge pressure will follow a trend that can be deduced from attached-flow slender wing theory as $C_{p,le} = C_0 - C_2 \sin^2\alpha$ where C_0 and C_2 are constants, obtained in this case from a fit to the data at low angles of attack. Analyses of the NTF data have demonstrated that this trend is sustained as angle of attack is increased and departure from this trend correlates with separation onset [18-7]-[18-9].
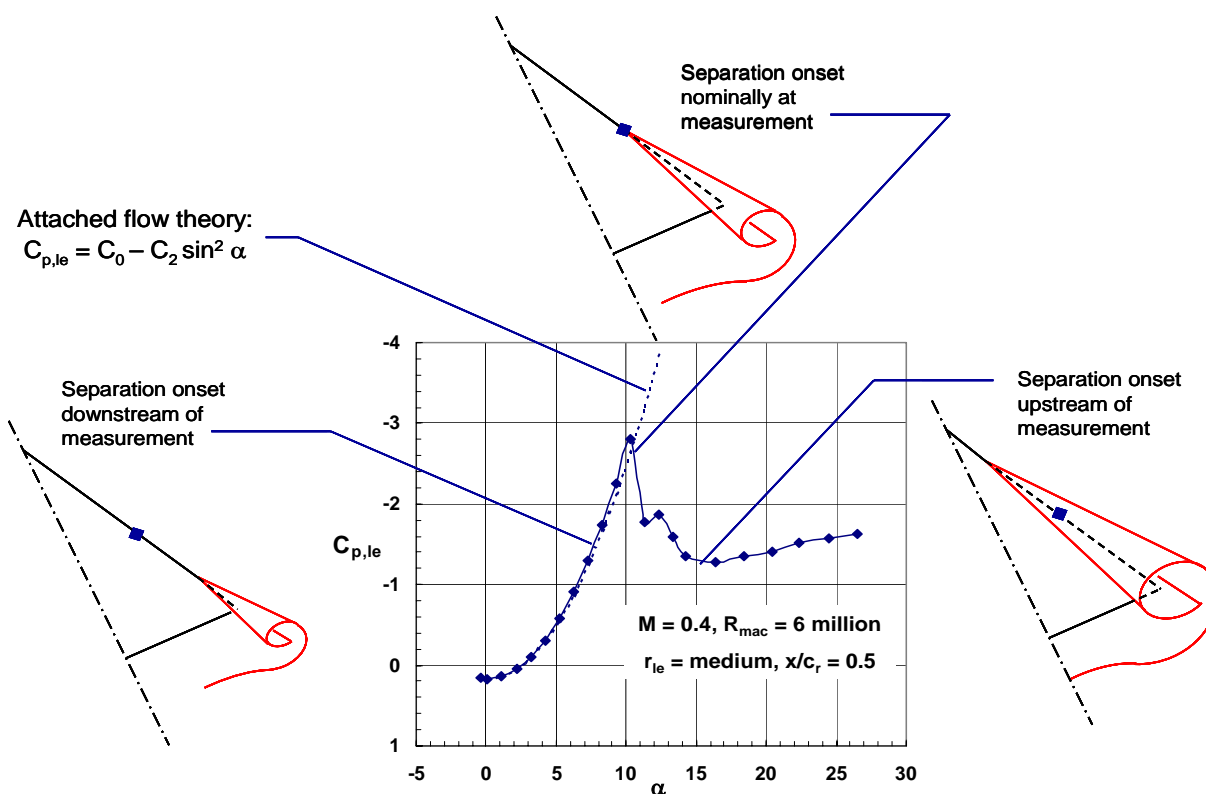
Figure 18-11: Correlation of Leading-Edge Pressure Coefficients with the Onset and Progression of Leading-Edge Vortex Separation. Medium bluntness, M = 0.4, R_{mac} = 6 x 10^6; Data from NTF.

The leading-edge pressures can be used to assess the effects of various parameters on leading-edge separation. An example is given in Figure 18-12. Here Reynolds number is shown to delay separation at three root chord stations. Reynolds number effects occur over a significant angle of attack range at values typical of maneuver conditions. The Reynolds number effects also persist over a greater angle of attack range on the forward portions of the wing.
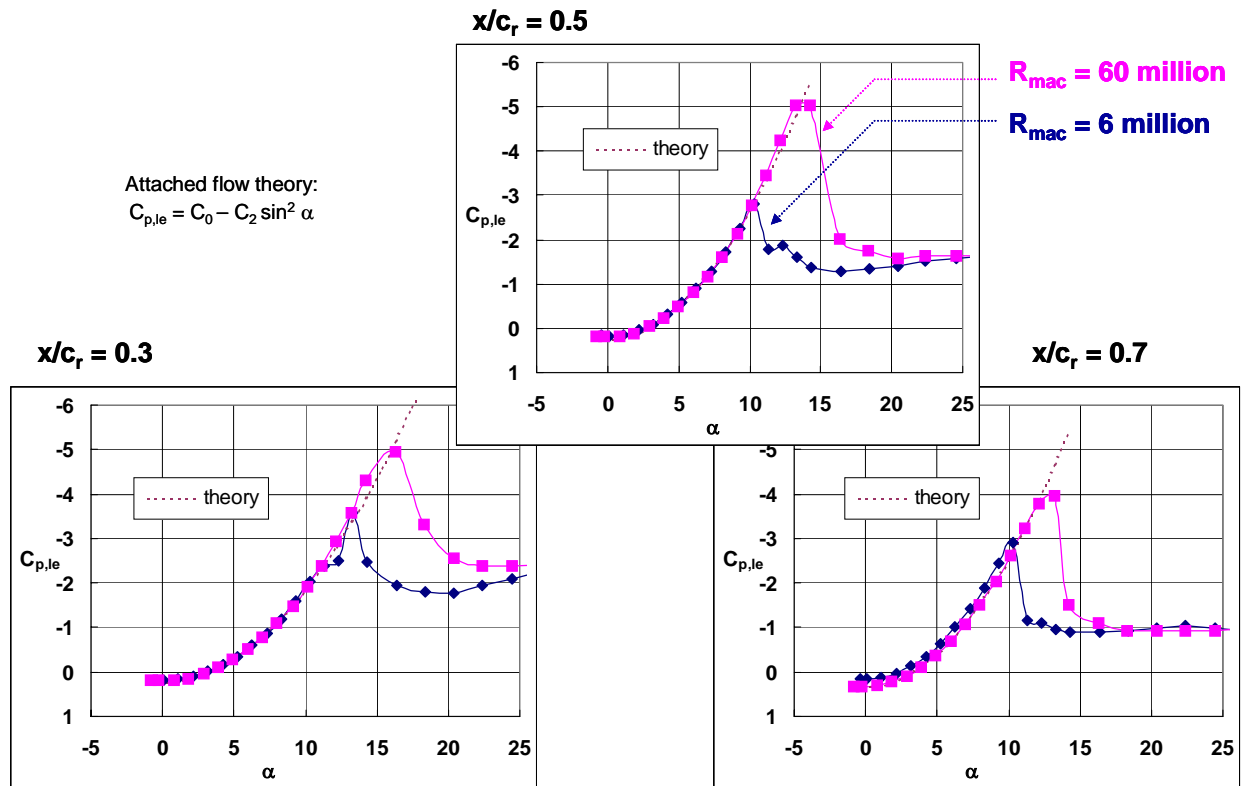
Figure 18-12: Reynolds Number Effect on Leading-Edge Pressures. Medium bluntness, M = 0.4.

A summary of leading-edge bluntness effects on the onset and progression of leading-edge separation at low and high Reynolds numbers is presented in Figure 18-13. At the low Reynolds number the smallest leading-edge bluntness delayed separation onset to approximately 6 degrees angle of attack. Both the medium and the large bluntness values further delayed separation onset. The largest bluntness showed a gradual progression of separation compared to the other two blunt leading edges. At high Reynolds number separation onset for the small and medium bluntness values has been delayed by about 2 degrees, and separation progression appears to be more gradual. Reynolds number had little effect on the bluntest leading edge. It must be noted that there is most likely some additional uncertainty associated with the results the results of Figure 18-13 because they are obtained by inference from the leading edge pressure distributions as opposed to being obtained by direct measurement (say, from surface flow visualization).

R$_{mac}$ = 6 million　　　　　　　　**R$_{mac}$ = 60 million**
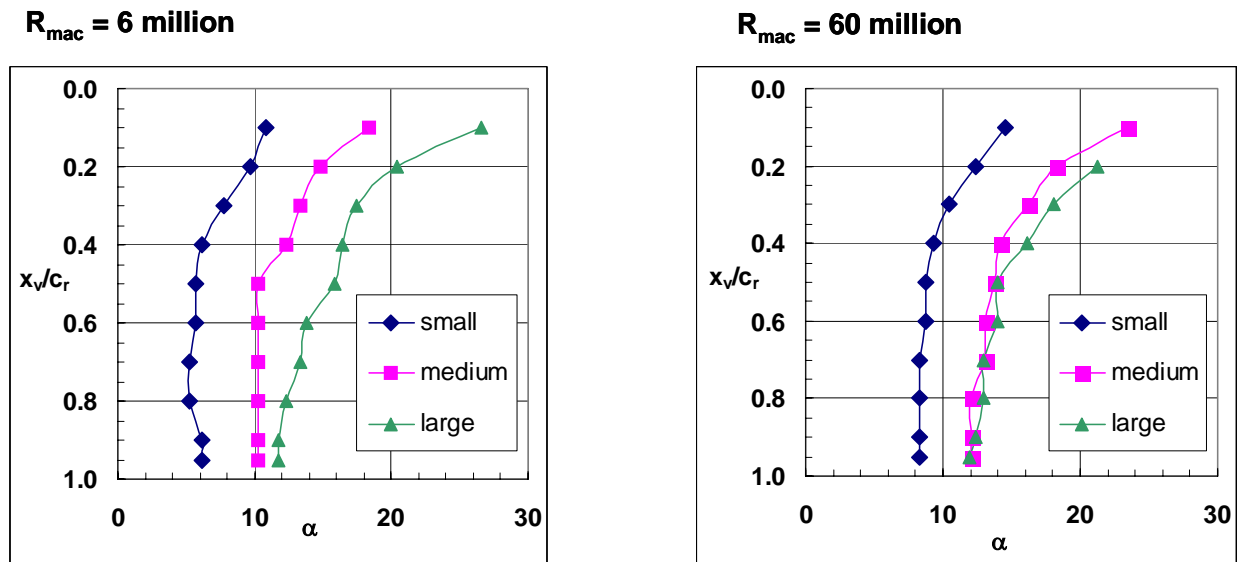
**Figure 18-13: Leading-Edge Bluntness and Reynolds Number Effects on
the Onset and Progression of Leading-Edge Vortex Separation, M = 0.4.**

18.6.3　Compressibility Effects

The effects of compressibility on the normal force coefficient are shown in Figure 18-14 for the medium bluntness configuration. Results are included from both the NTF and the LTPT experiments. Data from LTPT were not available at the identical Reynolds number as the data from NTF, but it is felt that any Reynolds number effect of this slight mismatch (6 million as compared to 8 million) should be small. For example, at these conditions the zero pressure gradient transition distance differs by only 1.4 percent root chord, and this transition would occur within the first 6 percent root chord from the apex.

Data	M_∞	R_{mac}
NTF	0.6	6×10^6
NTF	0.4	6×10^6
LTPT	0.2	8×10^6

Linear Prandtl-Glauert compressibility

$$\beta^2 = 1 - M_\infty^2$$
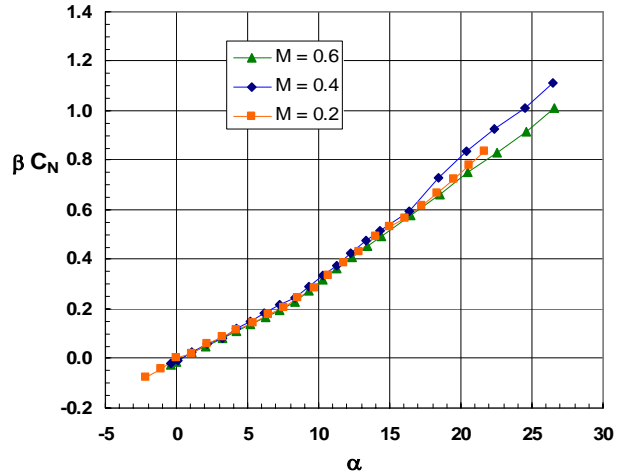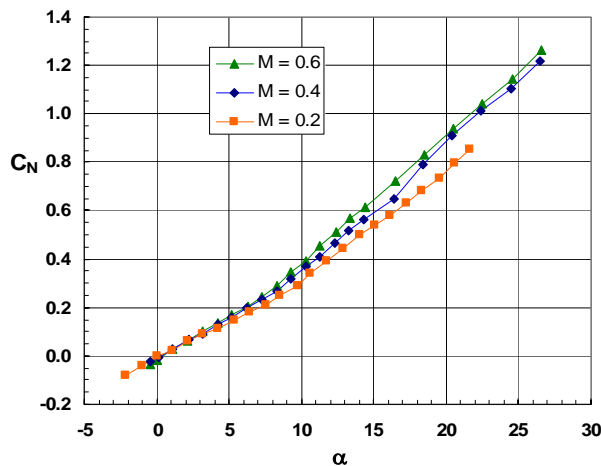
Figure 18-14: Effect of Compressibility on Normal Force Coefficients. Medium bluntness; Data from NTF, LTPT.

The primitive variable data (C_N) demonstrate expected compressibility trends, namely the increase of normal force slope as Mach number is increased. To more clearly assess this effect, similarity scaled results are also shown (βC_N) where the scaling is based upon linear Prandtl-Glauert theory. By this theory the data would be expected to collapse under conditions dominated by small perturbations and hence the linear Prandtl-Glauert governing equation. This would coincide with small angles of attack, and the collapse of the data is very good at low to moderate angles of attack. At the higher angles of attack the flow includes nonlinear effects in association with the leading-edge vortex, and this can also be seen in the scaled results of Figure 18-14.

To further assess the compressibility effects, a comparison among static surface pressure coefficients is presented in Figure 18-15 at a nominal angle of attack of 7° at one chordwise station for this same wing. At these conditions the flow is still attached, and the Prandtl-Glauert similarity scaling would be expected to hold under the same caveats just mentioned in association with Figure 18-14. Although not as compelling as the force data, the collapse of the pressure data is good over most of the station shown. The largest mismatch among the scaled results is near the leading edge for the highest Mach number of the comparisons for which the small perturbation assumption is expected to be less valid.

Data	M_∞	R_{mac}	α
NTF	0.6	6×10^6	7.3
NTF	0.4	6×10^6	7.3
LTPT	0.2	8×10^6	7.5

Linear Prandtl-Glauert compressibility

$$\beta^2 = 1 - M_\infty^2$$
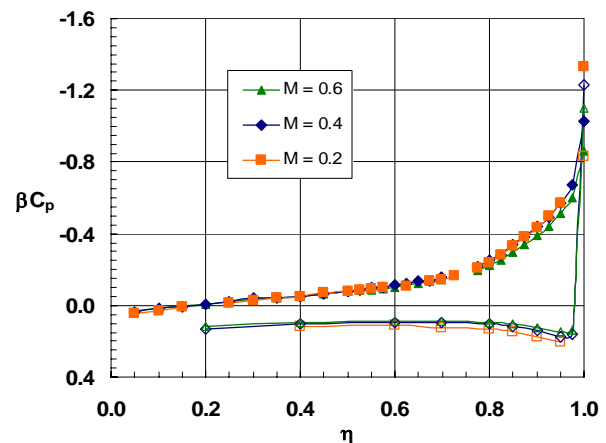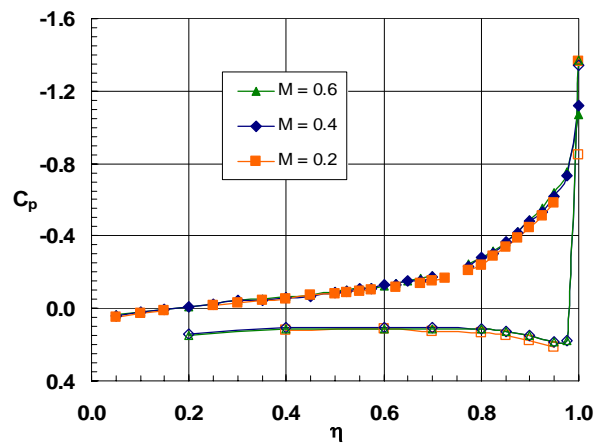
Figure 18-15: Effect of Compressibility on Static Surface Pressure Coefficients
(Medium Bluntness, $x/c_r = 0.6$, $\alpha = 7°$; Data from NTF, LTPT).

The leading-edge pressure coefficients were shown previously to be useful in inferring onset and progression of leading-edge vortex separation including assessment of Reynolds number and leading-edge bluntness effects. The effect of compressibility on the leading-edge pressure coefficient is shown in Figure 18-16 at the same mid-chord station as before and for a fixed Reynolds number of 6 million. Data are included from both the NTF and the LTPT experiments.
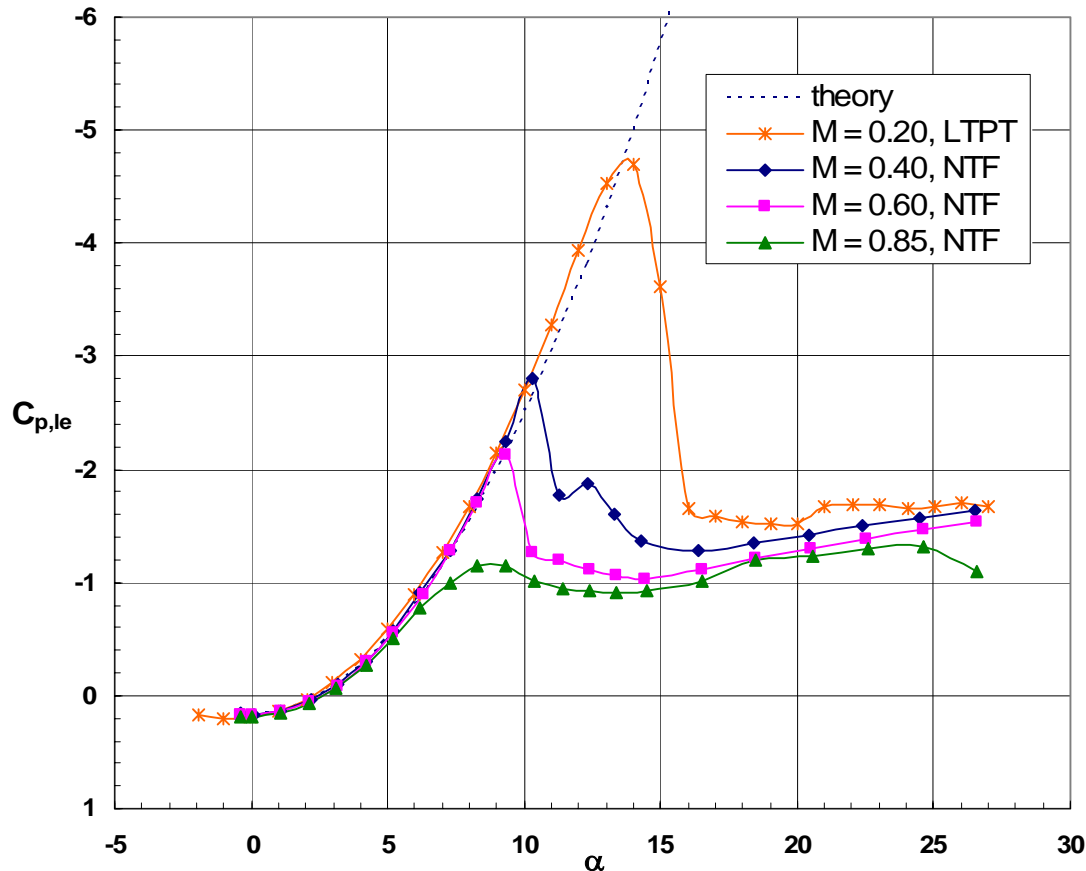
Figure 18-16: Compressibility Effect on Leading-Edge Pressures
(Medium Bluntness, $x/c_r = 0.5$, $R_{mac} = 6 \times 10^6$; Data from NTF, LTPT).

The data demonstrate that the trend with increasing Mach number is to promote departure of the data from attached flow theory and, hence, to promote leading-edge vortex separation. The leading edge flow includes nonlinear contributions since, in general, the perturbations will not be small in this region and, in particular, the onset and progression of leading-edge vortex separation is itself a nonlinear phenomenon. Thus, the correlation between the NTF and the LTPT measurements in terms of exhibiting consistent trends is very encouraging. Additional analysis of the LTPT results for the other leading edges configurations would be of interest.

The compressibility effects on overall static surface pressures are shown in Figure 18-17 for the medium wing at an angle of attack of 13° and a Reynolds number of 60 million. The increase of mach number from 0.4 to 0.6 has show a significant increase in the extent of leading-edge vortex flow over the wing. For example, at the 60% chord station the pressure coefficients exhibit an essentially attached-flow trend at M = 0.4 whereas these pressure coefficients show a well-defined leading-edge vortex distribution at M = 0.6. There is also evidence of incipient separation at the 40% chord station for the higher Mach number results. Similar trends were found at the lower Reynolds number case (6 million).
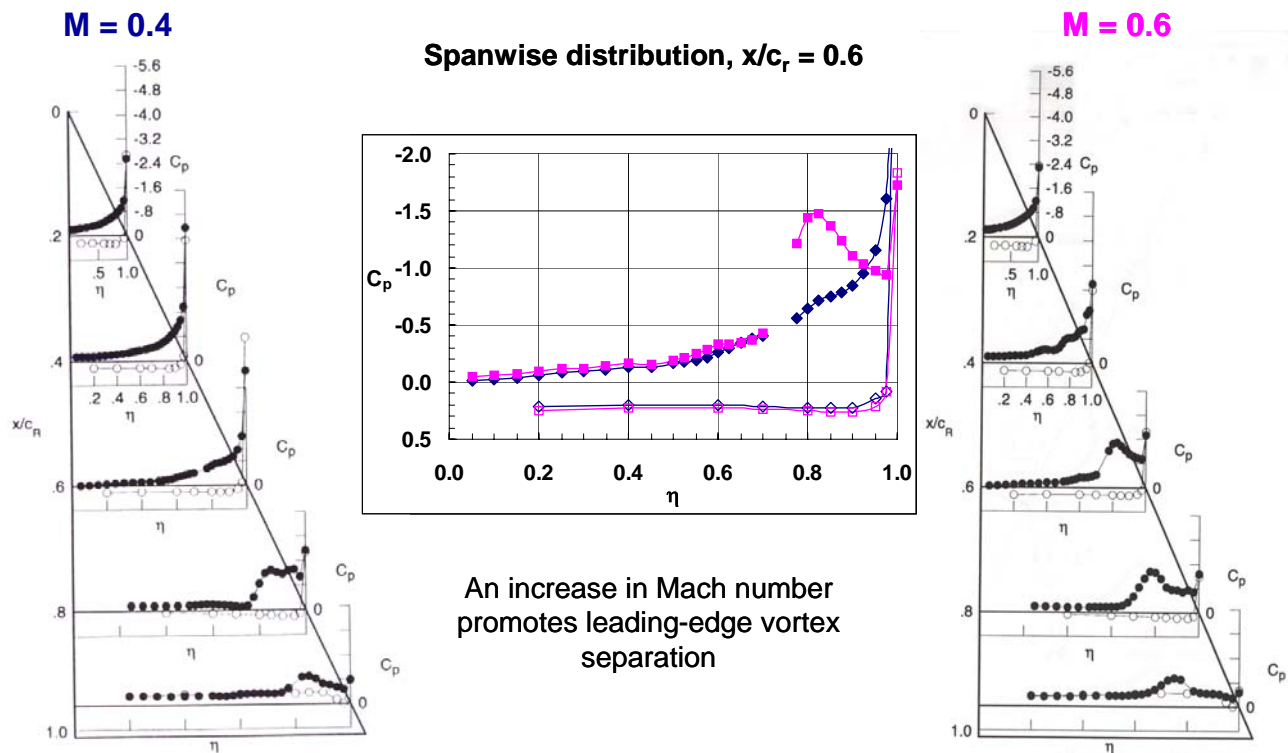
**Figure 18-17: Effect of Compressibility on Static Surface Pressure Coefficients
(Medium Bluntness, α = 13°, R_{mac} = 60 x 10^6; Data from NTF).**

18.6.4   Summary Effects

The following three figures present a summary of the combined effects of Mach number, Reynolds number, leading-edge bluntness, and angle of attack for the onset and progression of leading-edge vortex separation. For this analysis the leading-edge pressure coefficients are used.

The effects of compressibility and bluntness on the leading edge pressure coefficients are presented in Figure 18-18 at the mid-chord station for a Reynolds number of 6 million. Results are included only from the NTF experiments, and the medium bluntness leading edge results in this figure are the same as was shown in Figure 18-16. The smaller bluntness leading edge only shows minimal compressibility effects although the trend (increase of Mach number promoting leading-edge separation) is sustained. Onset of separation is confined to a narrow angle of attack between 4° and 5°.
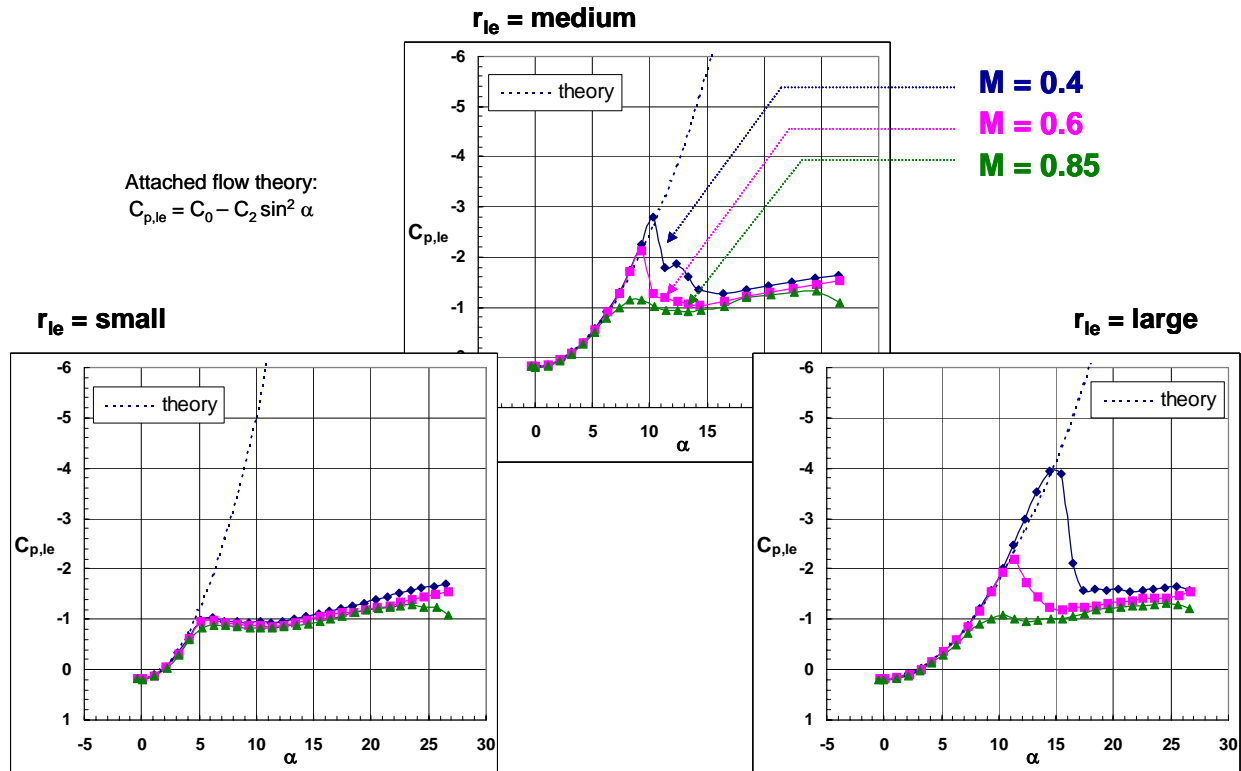
Figure 18-18: Compressibility and Bluntness Effects on Leading-Edge Pressures, $R_{mac} = 6 \times 10^6$, $x/c_r = 0.5$; Data from NTF.

Results with the bluntest leading edge show that separation onset occurs at a higher angle of attack than the medium bluntness configuration. For example, at a Mach number of 0.4 the departure from the attached flow trend line shifts from about 11° for the medium bluntness wing to about 15.5° for the large bluntness wing. Similar compressibility trends are sustained for the blunt leading edge.

The same organization of results is presented in Figure 18-19 but now for a Reynolds number of 60 million. At this Reynolds number, the small bluntness leading edge now exhibits significant compressibility effects consistent with the other data already discussed. Moreover, a comparison between Figure 18-18 and Figure 18-19 demonstrate the delay in separation onset and progression with an increase in Reynolds number. Using the same example from the discussion of Figure 18-18, the departure from the attached flow trend line for the medium bluntness leading edge at a mach number of 0.4 shifts from about 11° for the low Reynolds number case (Figure 18-18) to about 14° for the high Reynolds number case (Figure 18-19).

r$_{le}$ = medium

Attached flow theory:
$C_{p,le} = C_0 - C_2 \sin^2 \alpha$

M = 0.4
M = 0.6
M = 0.85

r$_{le}$ = small

r$_{le}$ = large
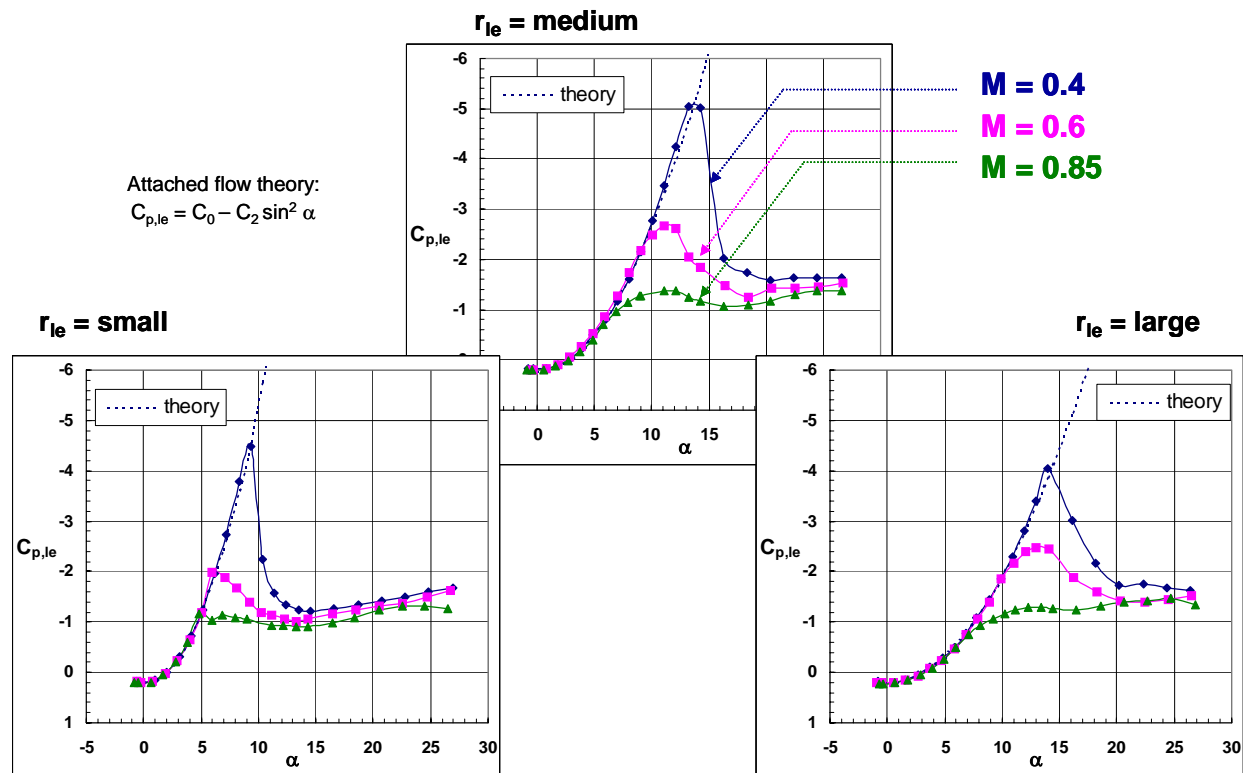
Figure 18-19: Compressibility and Bluntness Effects on Leading-Edge Pressures, R$_{mac}$ = 60 x 10^6, x/c$_r$ = 0.5; Data from NTF.

With the results shown in Figure 18-18 and Figure 18-19, as well as those from other wing stations or other free-stream flow conditions, the data from these experiments quantify the following trends:

i) An increase in Reynolds number delays the onset and progression of blunt-leading-edge vortex separation;

ii) An increase in Mach number promotes the onset and progression of blunt-leading-edge vortex separation;

iii) An increase in angle of attack promotes the onset and progression of blunt-leading-edge vortex separation; and

iv) An increase in leading-edge bluntness delays the onset and progression of blunt-leading-edge vortex separation.

One summary example is shown in Figure 18-20 for the medium bluntness leading edge. The results presented are the inferred location of vortex separation from the leading edge pressure coefficients as a function of angle of attack. The baseline case in this figure is at a Mach number of 0.4 and a Reynolds number of 6 million. The data demonstrate first that, at a fixed Mach number, an increase in Reynolds number delays the onset and progression of leading-edge vortex separation. These results also demonstrate that, at a fixed Reynolds number, and increase in Mach number delays the onset and progression of leading-edge vortex separation. It is also noteworthy that the Mach and Reynolds number effects are not only opposite in sign but of comparable magnitude. If Reynolds number and Mach number were varied simultaneously, as would be the case in conventional atmospheric wind
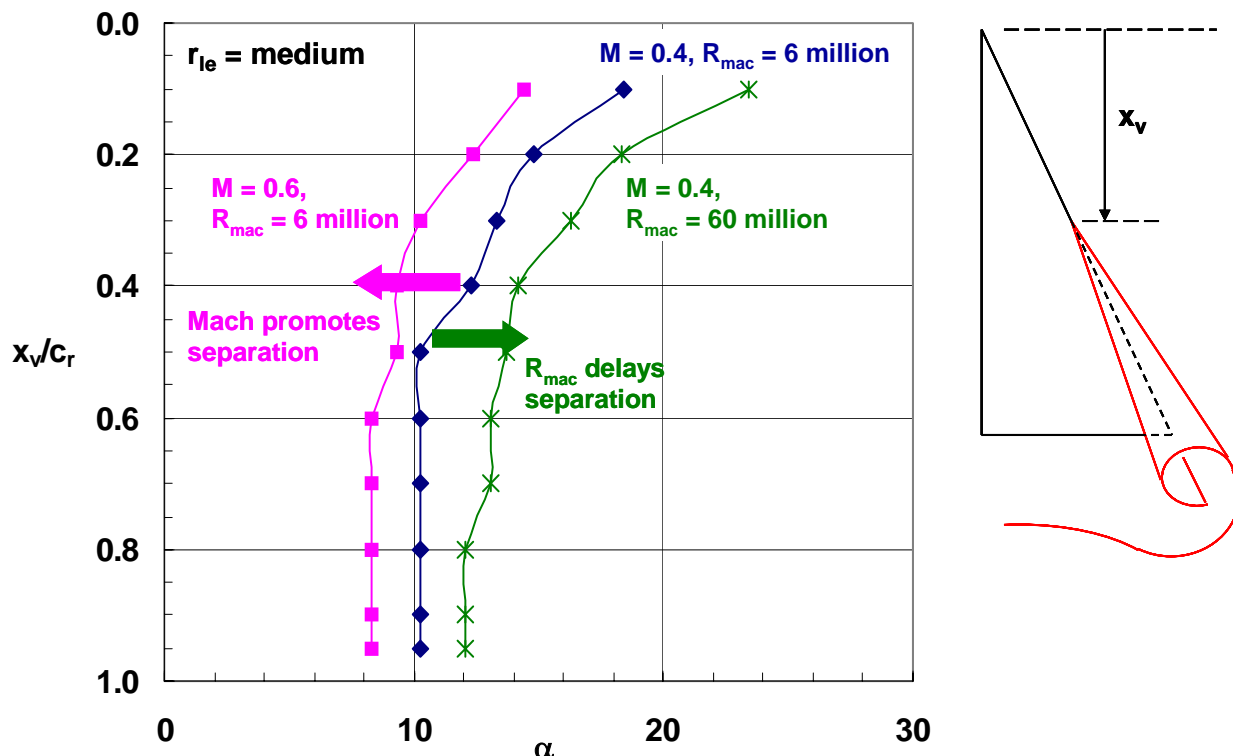
Mach and Reynolds number effects are _opposite in sign_ and can be _comparable in magnitude_ for the onset of leading-edge vortex separation

Figure 18-20: Compressibility and Reynolds Number Effects on Onset and Progression of Leading-Edge Vortex Separation. Medium bluntness; Data from NTF.

18.7 CONCLUDING REMARKS

A summary has been presented of some initial experiments and analysis for separation-induced leading-edge vortex separation for a 65° delta wing that lead to the initiation of an international collaborative research effort known as Vortex Flow Experiment 2. The baseline experimentation from NASA Langley showed significant effects of Mach number, Reynolds number, angle of attack, and leading-edge bluntness for the onset and progression of leading-edge vortex separation. The data primarily included detailed static surface pressure distributions for a wide range of Reynolds numbers and Mach numbers taken in a manner that allowed for the isolation effects associated with these free-stream parameters.

The physics of blunt-leading-edge vortex separation fundamentally differs from the sharp-edged case in at least two regards. First, for the blunt leading edge the origin of the leading edge vortex is displaced from the apex of the delta wing. The onset and progression of this separation will be a function of flow conditions as well as leading-edge bluntness. Second, the existence of an inner, co-rotating vortex was inferred from the

measurements. Neither of these phenomena occurs with the corresponding sharp leading edge. Both of these effects are quantified with the present data in terms as static surface pressure coefficients and limited force and moment coefficients.

However, it was clear that additional measurements would be required to better understand these effects. This need for new and more detailed data led to the VFE-2 experimental activities. The original experiments as well as the promise of new data sets also served as impetus for the computational program contained within VFE-2.

18.8   REFERENCES

[18-1]   Wahls, RA.: *The National Transonic Facility – A Research Retrospective*, AIAA Paper 01-0754, January 2001.

[18-2]   Luckring, J.M.: *An Overview of National Transonic Facility Investigations for High Performance Military Aerodynamics*, AIAA Paper 01-0906, January 2001.

[18-3]   Chu, J. and Luckring, J.M.: *Experimental Surface Pressure Data Obtained on 65° Delta Wing Across Reynolds Number and Mach Number Ranges, Volume 1 – Sharp Leading Edge*, NASA TM-4645, February 1996.

[18-4]   Chu, J. and Luckring, J.M.: *Experimental Surface Pressure Data Obtained on 65° Delta Wing Across Reynolds Number and Mach Number Ranges, Volume 2 – Small Leading Edge*, NASA TM-4645, February 1996.

[18-5]   Chu, J. and Luckring, J.M.: *Experimental Surface Pressure Data Obtained on 65° Delta Wing Across Reynolds Number and Mach Number Ranges, Volume 3 – Medium Leading Edge*, NASA TM-4645, February 1996.

[18-6]   Chu, J. and Luckring, J.M.: *Experimental Surface Pressure Data Obtained on 65° Delta Wing Across Reynolds Number and Mach Number Ranges, Volume 4 – Large Leading Edge*, NASA TM-4645, February 1996.

[18-7]   Luckring, J.M.: *Reynolds Number and Leading-Edge Bluntness Effects on a 65° Delta Wing*, AIAA Paper 2002-0419, January 2002.

[18-8]   Luckring, J.M.: *Transonic Reynolds Number and Leading-Edge Bluntness Effects on a 65° Delta Wing*, AIAA Paper 2003-0753, January 2003.

[18-9]   Luckring, J.M.: *Compressibility and Leading-Edge Bluntness Effects on a 65° Delta Wing*, AIAA Paper 2004-765, January 2004.

[18-10] Luckring, J.M.: *Reynolds Number, Compressibility, and Leading-Edge Bluntness Effects on Delta Wing Aerodynamics*, ICAS Paper ICAS04-414, September 2004.

[18-11] Hummel, D. and Luckring, J.M.: Private Discussions. 2001.

[18-12] Hummel, D. and Redeker, G.: *A New Vortex Flow Experiment for Computer Code Validation*, RTO-MP-069, Paper No. 9, March 2003.

[18-13] Hummel, D.: *On the Vortex Formation Over a Slender Wing at Large Incidence*, AGARD-CP-247, Paper No. 15, January 1979.

[18-14] Polhamus, E.C.: *A Concept of the Vortex Lift of Sharp-Edged Delta Wings Based on a Leading-Edge Suction Analogy*, NASA TN D-3767, 1966.

[18-15] Fuller, D.E.: *Guide for Users of the National Transonic Facility*, NASA TM-83124, 1981.

[18-16] Foster, J.M. and Adcock, J.B.: *Users Guide for the National Transonic Facility Research Data System*, NASA TM-110242, April 1996.

[18-17] McGhee, R.J., Beasley, W.D. and Foster, J.M.: *Recent Modifications and Calibration of the Langley Low-Turbulence Pressure Tunnel*, NASA TP-2328, July 1984.

[18-18] Frink, N.T.: *Computational Study of Wind-Tunnel Wall Effects on Flow Field Around Delta Wings*, AIAA Paper 87-2420, pp. 381-391 in Proceedings of the AIAA 5th Applied Aerodynamics Conference, 1987.

[18-19] Frink, N.T.: *Wind Tunnel Wall Effects on Delta Wings*, AIAA J. Aircraft, Vol. 26, No. 5, pp. 403-404, May 1989.

Chapter 19 – EXPERIMENTAL INVESTIGATIONS ON THE VFE-2 CONFIGURATION AT DLR, GERMANY

by

Robert Konrath, Christian Klein, Andreas Schröder, Klaus de Groot

19.1   SUMMARY

In the present chapter experimental investigations within the International Vortex Flow Experiment 2 (VFE-2) on a delta wing of 65° sweep angle with sharp as well as with rounded leading edges are described. High resolution surface pressure distributions are measured by means of the Pressure Sensitive Paint (PSP) technique at sub- and transonic speeds (M = 0.4 and 0.8). These tests were complemented by flow field measurements applying Stereo Particle Image Velocimetry (PIV) in different planes above the delta wing. Furthermore, under cryogenic conditions (M < 0.2) the Infrared (IR) and Temperature Sensitive Paint (TSP) techniques are used for the detection of laminar/turbulent transition in the boundary layer. The results were analysed with respect to the onset of the primary vortex on the delta wing with rounded leading edges, the occurrence of an inner vortex, the development of a vortex system consisting of an inner and outer primary vortex, and under transonic conditions to the sudden occurrence of vortex breakdown above the delta wing. Preliminary results of the transition measurements are available which will be discussed, too.

19.2   INTRODUCTION

The objectives of the International Vortex Flow Experiment 2 (VFE-2) are to provide experimental flow data by using modern measurement techniques for comparison with results from state-of-the-art CFD calculations, see Chapter 17. At the beginning of the 1980's the first VFE [19-3][19-5] was carried out on a cropped 65° delta wing-fuselage combination. Since in the last fifteen years considerable progress has been achieved in the numerical calculation of vortical flows [19-7][19-8][19-22] a new International Vortex Flow Experiment (VFE-2) has been proposed by Hummel and Redeker [19-9]. Since 2003 the VFE-2 is being carried out within the framework of the task group AVT-113 of NATO's Research and Technology Organization. Using NASA's definition of a 65° delta wing geometry [19-2] the investigations within VFE-2 now also consider delta wings with rounded leading edges (Figure 19-1). In the present investigations the sharp as well as the medium radius leading edge ($r / \overline{c} = 0.0015$) is considered.
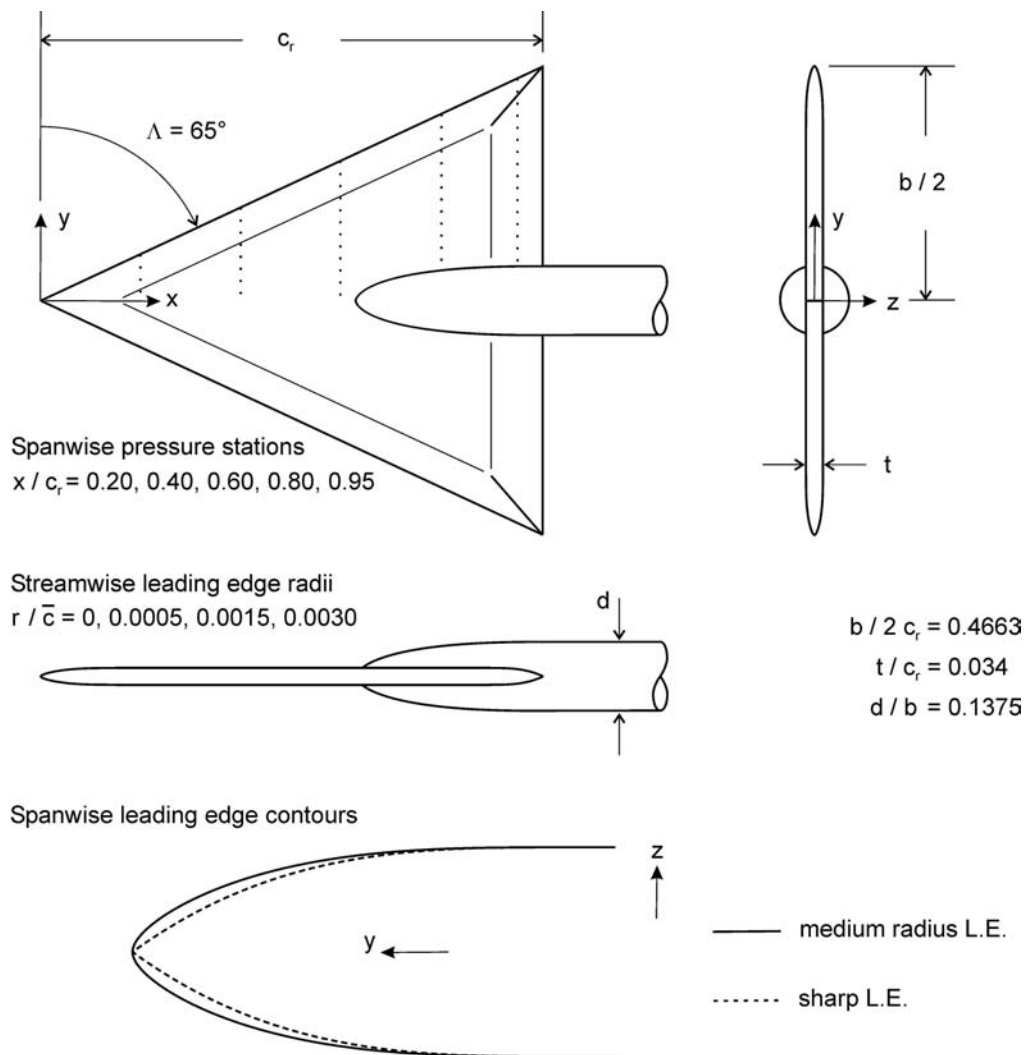
Figure 19-1: Geometry of VFE-2 Configuration (Details of contours are described in [19-2]).

The developments achieved so far at optical flow measurement techniques such as the Particle-Image Velocimetry (PIV), the Pressure Sensitive Paint (PSP), the Infrared (IR) or the Temperature Sensitive Paint under cryogenic conditions (TSP) techniques allow to cope with many technical problems arising especially in industrial wind tunnels. These techniques are able to capture a huge amount of experimental data during a wind tunnel test campaign. With PSP the pressure distribution on a whole surface can be determined giving much more insight in details of the flow topology than would be possible by discrete pressure taps. PIV provides instantaneous as well as time averaged flow velocity fields in different planes of the flow and enables the detection of large and small spatial flow structures. The Infrared and Temperature Sensitive Paint techniques provide high resolution information of transition for large areas on wings. The parallel application of these methods can help to save wind tunnel costs in order to get the necessary data for flow analysis or comparison with CFD results [19-15].

In the present study three measurement campaigns were performed by DLR in two different wind tunnels. The investigations started with PSP measurements in the transonic wind tunnel at Göttingen (DNW-TWG) of

the German-Dutch Wind tunnel association (DNW), which serve as "pathfinder" tests. For the tests in the TWG NASA provided its ¾ scale 65° delta wing model of $c_r = 0.49$ m (Model No. 1, see overview in Chapter 17 and Figure 19-1). The PSP results give first information of the flow topology over the delta-wing for a large range of angles of attack at sub- and transonic speeds. In a second test campaign Stereo-PIV measurements were performed. The used angles of attack and locations of the measurement planes for PIV were selected on the basis of the PSP results. The measured velocity fields provide details of the flow field. A last measurement campaign took place in the cryogenic wind tunnel in Cologne (DNW-KKK) using a delta wing model built by the Technical University of Munich (TUM) of $c_r = 0.98$ m (Model No. 2). The original objective of these tests was to investigate the effects of high Reynolds numbers at $M < 0.2$ on the flow. However, first CFD calculations show that the knowledge of transition on the delta wing is strongly needed in order to improve the numerical prediction of the flow. So, it was decided to apply IR and TSP in the KKK, too, although the construction of the TUM model was not particularly suitable for such tests. For all measurements the models were coated by different paints, which has to be taken into account when comparing the results with other data.

In the following Section 19.3 the test conditions and the results of the measurements in the transonic wind tunnel in Göttingen (DNW-TWG) are described. First the differences of flow separation at the leading edge for sharp and rounded edged delta wing are discussed. The onset of the primary vortex and chord positions of its origin is determined on the basis of the PSP results in dependency of angle of attack, Mach and Reynolds number. For the rounded leading edge at subsonic Mach numbers a flat inner vortical structure occurs close to the surface above the delta wing which is described using PSP and PIV. From this vortical structure an inner vortex develops after the onset of the primary vortex. The resulting vortex system is described in detail considering the effects of angle of attack and Reynolds number. The Q-criterion is applied to the PIV data to visualize vortices and to calculate the vortex circulation. At transonic speed ($M = 0.8$) results showing a sudden change of the pressure and velocity distributions at high angles of attack, which probably are related to the occurrence of vortex breakdown caused by an interaction between shock waves and the primary vortex, are discussed too. Further results form the TWG tests can be found in [19-16] and [19-17]. In Section 19.4 the measurements and preliminary results of the cryogenic wind tunnel in Cologne (DNW-KKK) are described. The transition on the delta wing is discussed, particularly, for the rounded leading edge case.

19.3   INVESTIGATIONS IN THE TRANSONIC WIND TUNNEL IN GÖTTINGEN

19.3.1   Test Conditions and Measurement Setups

19.3.1.1   Wind Tunnel Facility and Model Instrumentation

Two measurements campaigns were carried out in the Transonic Wind tunnel in Göttingen (DNW-TWG) which is a continuously running closed-circuit wind tunnel. The test section of 1 m x 1 m size is enclosed by a plenum chamber, within which the total pressure can be set in a range from 30 000 to 150 000 Pa, so that Reynolds and Mach number effects can be studied independently. Different test sections are available enabling sub-, trans- and supersonic flow conditions. The perforated test section is used here, because small observation windows can be installed in the upper and lower wall behind which the PSP cameras and light sources are positioned. The walls of the perforated test section incorporate 60 degree inclined holes of 10 mm diameter, giving a porosity of 5.6%. However, no suction was applied during the tests. For the perforated test section, the turbulence level was measured being between 1 and 1.4% depending on Mach number. The top and bottom wall of the test section are inclined, i.e. ±0.25° and ±0.563° for $M = 0.4$ and $M = 0.8$ respectively, such that the cross section size increases downstream in order to compensate the increasing boundary layer at

the walls. The lateral walls were equipped with 50 mm thick Schlieren windows of 450 mm x 950 mm in size getting optical access for PIV.

For the tests in the transonic wind tunnel (DNW-TWG) the ¾ scale model (c_r = 0.4902 m, b = 0.4572 m, $\overline{c}$ = 0.3268 m) was provided by NASA. It incorporates interchangeable leading edge segments. The sharp as well as one rounded leading edge with the medium radius ($r/\overline{c}$ = 0.0015) were used for the current investigations. The model is equipped with 183 pressure taps, mainly arranged at constant chord stations of x/c_r = 0.2, 0.4, 0.6, 0.8 and 0.95. Three PSI modules with each having 64 ports measure the static pressures at the tap locations. The quoted accuracy of the PSI modules is about ±50 Pa, e.g. 0.05% of the instrument maximum pressure. A 15°-bent sting was used to extend the positive angle of attack range. The model sting was equipped with strain gages configured for two moment bridges to measure the normal force and pitching moment in order to estimate the bending of the sting. The resulting effective angle of attack of the model could be determined with an accuracy of ±0.02°.

19.3.1.2   Application of Pressure Sensitive Paint

The first test campaign took place in 2004 and comprises surface pressure, which serve as "pathfinder" tests. By applying a pressure sensitive paint to a wind tunnel model surface pressure distributions can be determined by measuring the luminescence intensity of the molecule emission. Two different paints are applied for the current tests. Both are based on a two-color formulation with pyrene as the pressure sensitive luminophore and with Europium as reference dye. For the tests with rounded leading edges the DLR02 paint is used, which consists of a screen layer and an active layer giving a total thickness of about 60 µm. A further developed paint was applied for the tests with the sharp edged delta-wing model, which consists of a single layer only with a reduced paint thickness of 40 µm. Small windows in the top and bottom wall of the test section are used on the current PSP-setup (see [19-18] or [19-14] for details) for cameras and illumination (Figure 19-2). Only a small region close to the leading edge was not accessible optically because of the large angle between the viewing direction of the cameras and the surface normal. Therefore, the C_p data at spanwise locations larger than 99.2 % of the span width is blanked out in the results.
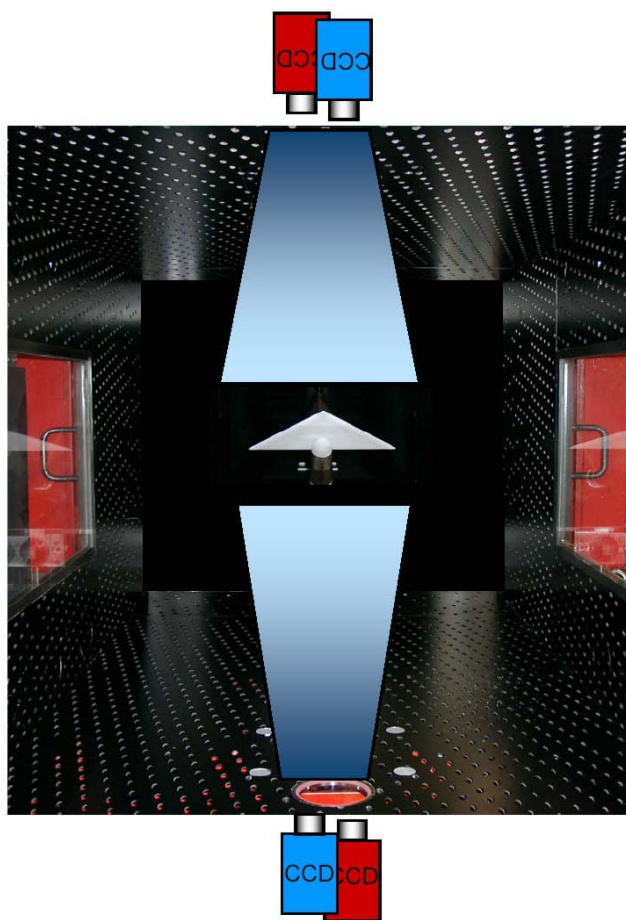
**Figure 19-2: Coated Delta-Wing Model in the Test Section
of the DNW-TWG and Arrangement of PSP Cameras.**

The comparison between the results of PSP and the PSI system of the wind tunnel at the pressure tap locations show a good agreement. The standard deviation is better than 1000 Pa. This includes a temperature dependency of the paint of 300 – 500 Pa/K [19-13]. Because of the higher temperature drop below the strong primary vortices, this leads to slightly underestimated suction peak heights in the PSP distributions as compared to the PSI results. For the PSP measurements the sharp as well as the medium radius leading edge, two Mach and two Reynolds numbers are used for a large range of angles of attack (Table 19-1).

Table 19-1: Test Cases for PSP Measurements in the TWG

Leading Edge	Sharp / Medium Radius
M	0.4 / 0.8
R_{mac}	$2 \times 10^6 / 3 \times 10^6$
α (nominal)	$10° – 25°$ in steps of $1°$

19.3.1.3   Application of Particle Image Velocimetry

In a second test campaign, which took place in 2005, Stereo-PIV was applied to the flow above the delta wing model. The velocity fields in different planes perpendicular to the model axis are determined. For the PIV tests the delta wing model was coated, too, with a specific black paint to avoid light flare on the surface coming from the impinging laser light sheet that allows PIV measurements down to the surface. The thickness of the paint is ca. 90 µm, which is slightly higher than that of the PSP paint. The PIV set-up is shown in Figure 19-3. The light-sheet and the cameras can be translated along the model axis during wind tunnel operation. The arrangement also incorporates rotary plates in order to adjust quickly the set-up for different angles of attack, see [19-18] or [19-26] for details.
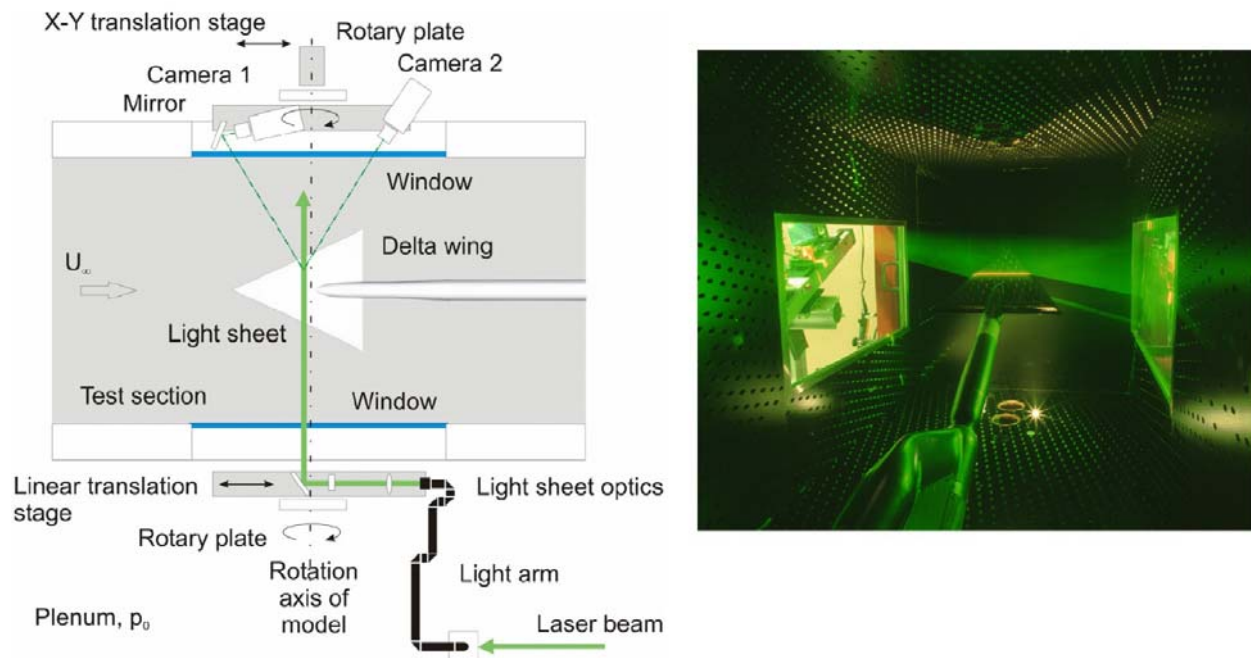
Figure 19-3: Stereoscopic PIV Arrangement at the TWG and Picture from Inside the Perforated Test Section Showing the Coated Delta-Wing, Light Sheet and the Two Lateral Schlieren Windows.

The uncertainty of the velocities after the stereoscopic reconstruction can be estimated for the current arrangement to be less than 3% for the u and w component and less than 2% for the v component with respect to the maximum velocity in the flow field. These values also include a maximum error of about 1% due to uncertainties in the determination of the camera positions. The spatial resolutions of the measurements are listed in the table below in dependency of field-of-view. The same test cases as chosen for PSP were taken with respect to leading edge shape, Mach and Reynolds number. Four different angles of attack and different chord locations were selected (Table 19-2).

Table 19-2: Test Cases for PIV Measurements in the TWG

Leading Edge	Sharp / Medium Radius	
M	0.4 / 0.8	
R_{mac}	2×10^6 / 3×10^6	
α (nominal)	10°, 13°, 20°, 25°	
Cross plane locations	$x/c_r = 0.35 - 0.9$ in steps of 0.05 / 0.1	
Field-of-view (*y,z*)	146 mm x 60 mm	for α = 10°, 13°, 20°
	219 mm x 108 mm	for α = 25°
Spatial resolution (*y,z*)	3.6 mm x 2 mm	for α = 10°, 13°, 20°
	5.3 mm x 3.6 mm	for α = 25°

19.3.1.4   Vortex Identification for Flow Field Analysis

In order to extract coherent vortical structures within complex flow fields different identification schemes can be used by evaluating the velocity gradient tensor $\nabla \vec{u}$ such as the λ_2-criterion. In the current case the Q-criterion is applied to the PIV data, whereas Q denotes the positive second invariant of $\nabla \vec{u}$ [19-1]:

$$Q = \frac{1}{2}\left[(\nabla \cdot \vec{u})^2 - tr\left(\nabla \vec{u}^2\right)\right].$$ (19-1)

For an incompressible flow Q is defined as:

$$Q = \frac{1}{2}\left[\|\Omega\|^2 - \|S\|^2\right],$$ (19-2)

whereas S and Ω are the tensors of rate of strain and vorticity respectively and correspond to the symmetric and anti-symmetric components of the velocity tensor:

$$\nabla \vec{u} = S + \Omega = \frac{1}{2}\left(\nabla \vec{u} + \nabla \vec{u}'\right) + \frac{1}{2}\left(\nabla \vec{u} - \nabla \vec{u}'\right).$$ (19-3)

Hence, Q constitutes a local indicator for the dominance of the rotation rate (Q > 0) compared to the strain rate. Since only planar velocity data is available the third derivatives are assumed to be negligible and the equation of *Q* reduces to:

$$Q = u_{1,1}u_{2,2} - u_{1,2}u_{2,1}.$$ (19-4)

The Q-criterion is used to define an area to calculate the circulation of a single vortex using the surface integral over the vorticity $\vec{\omega}$:

$$\Gamma = \int_{-\infty}^{\infty} \vec{\omega} \cdot \vec{n} \, dA \, . \tag{19-5}$$

To estimate the circulation of a single vortex the integration area is restricted using the criterion $Q > 0.1 \, Q_{max}$, whereas Q_{max} is the particular maximum Q-value close to the vortex center. In the current case the chosen threshold of 10% excludes the shear layer forming the primary vortex. This is demonstrated in Figure 19-4, which shows a slice of the velocity field through a primary vortex with the distributions of the out-of-plane vorticity ω_x and the Q-values. The black lines indicate the boundary of the integration area for calculating the circulation corresponding to the 10% drop of the Q-value within the vortex.
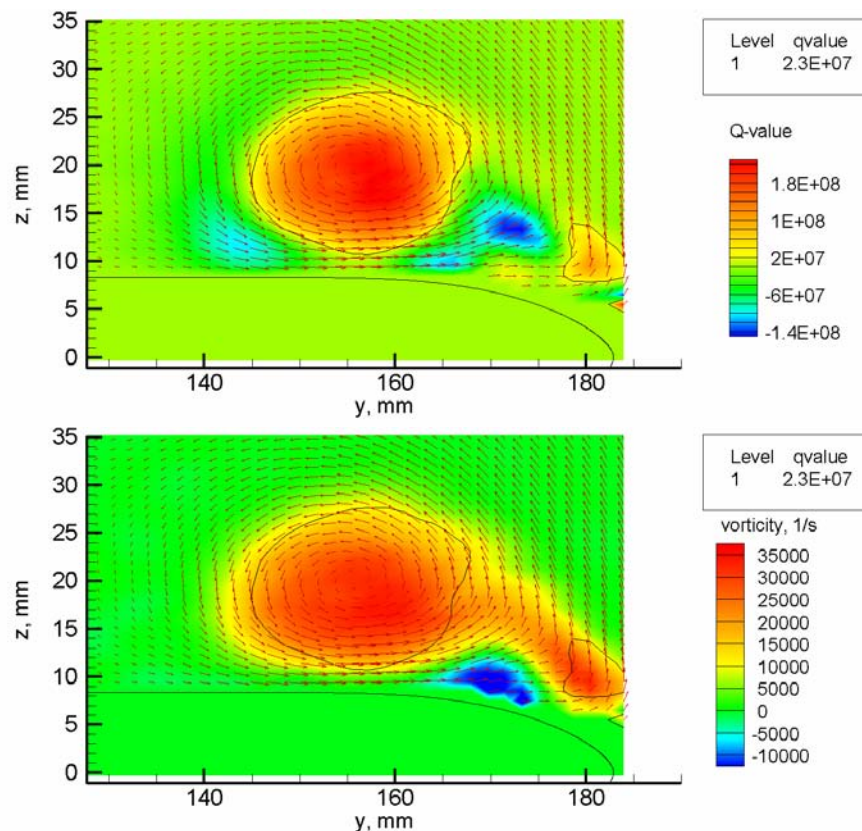
Figure 19-4: Velocity Vector Field of Primary Vortex for the Delta Wing with Medium Radius Leading Edges at x/c$_r$ = 0.8 for M = 0.4, R$_{mac}$ = 2 Million, α = 13.3° (top) Q-value and (bottom) Out-of-Plane Vorticity Distribution. The black line indicates the boundary of the integration area used for calculating the vortex circulation.

19.3.2   Results

19.3.2.1   Comparison of PSI Results Obtained in TWG by DLR and NTF by NASA

In the following the PSI data obtained at TWG is compared to the wind tunnel results of NASA obtained at the NTF [19-2] for the case: delta wing with medium leading edge, M = 0.85, R$_{mac}$ = 6 million. In the NTF the large

version of the delta-wing model of $c_r = 0.6536$ m was used. Figure 19-5 shows the PSI results for angles of attack of 13.4°, 20.6° and 24.8°. The last angle differs to the NTF result by 0.2°. In the results of the TWG the Mach numbers varies by about ±1% and the Reynolds number is at maximum 4% smaller than the set values.
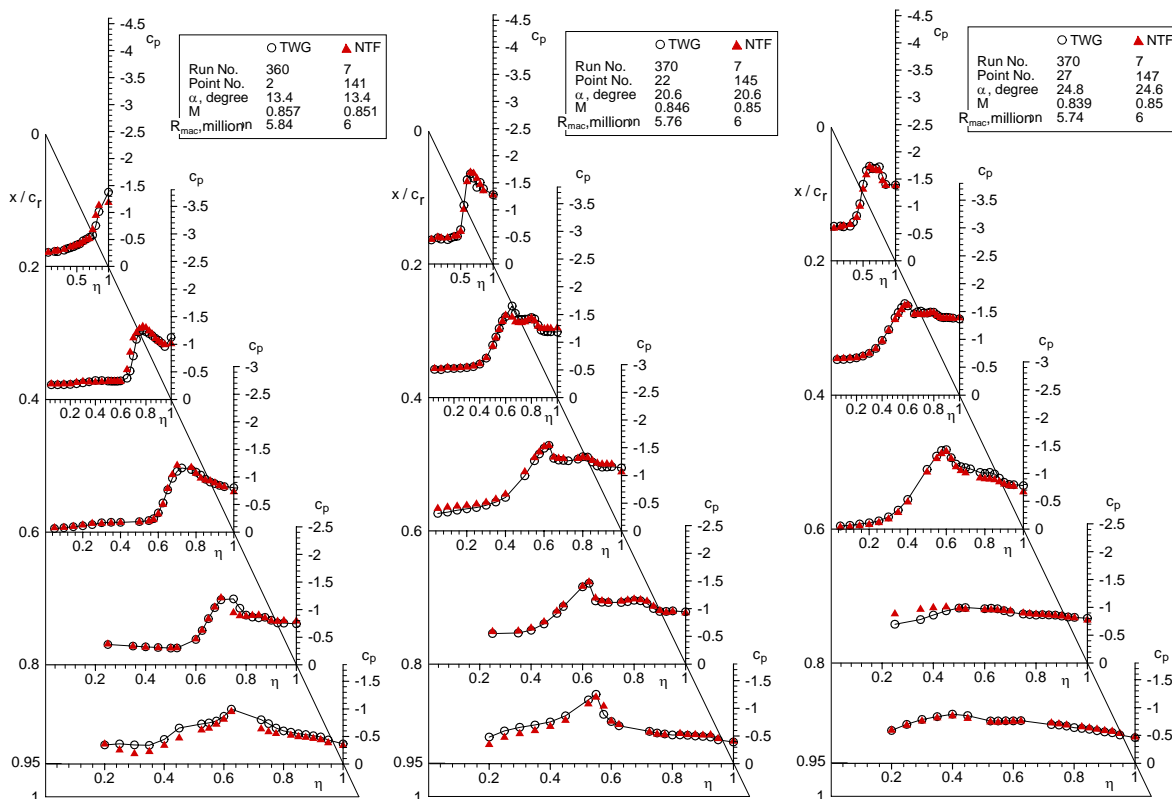
**Figure 19-5: Comparison of PSI Pressure Distributions Obtained in TWG and in NTF (NASA) [19-2]
of the Uncoated Delta Wing with Rounded Leading Edges at M = 0.85 and
R_{mac} = 6 Million for Three Different Angles of Attack.**

For all angles of attacks the results agree very well. Differences exists only in the foremost section of $\alpha = 13.4°$, where the onset of the leading edge separation seems to start a little earlier in the NTF and at $\alpha = 20.6°$ in the section $x/c_r = 0.4$, where the peak value of the primary vortex is slightly higher in the TWG. At $\alpha = 24.8°$ a breakdown of the primary vortex occurs downstream of $x/c_r = 0.6$, which is represented in both wind tunnels.

19.3.2.2   Effects of Model Coating

The approximate thickness of the DLR 02 PSP paint is 60 µm ± 5µm. That is about 12 percent of the radius of the rounded leading edge and should be taken into account at analysis of the data and comparison with numerical results. Differences in the pressure distributions can be found only in the case of the rounded leading edge for the small Mach number of 0.4 and at medium angles of attack. Figure 19-6 shows a comparison of PSI results obtained with the un-coated and the coated model with medium radius leading edges. At low angle of attack of $\alpha = 10.1°$ the results of the coated and the un-coated model agree very well. In both cases an attached flow exits

at the leading edge. At higher incidence of $\alpha = 13.2°$ larger deviations in the pressure plots can be seen. For this particular case, where an inner and outer suction peak occur (further described in Section 19.3.2.3), the flow is very sensitive to small changes of the model shape. The leading edge separation starts earlier in case of the un-coated model, which can be explained by the smaller leading edge radius. The pressure distributions differ at most after the onset of the leading edge separation, i.e. $x/c_r > 0.2$. At higher angles of attack the pressure distribution matches again as shown in Figure 19-6 for $\alpha = 20.5°$.
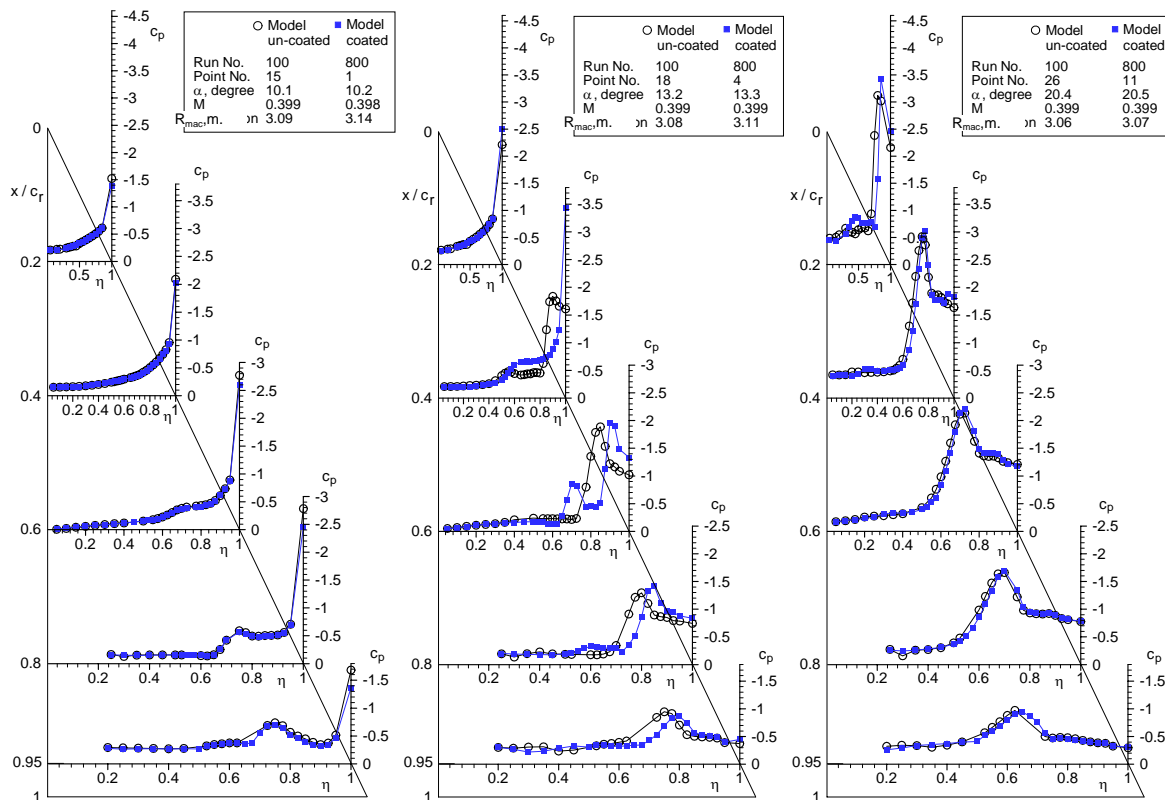
Figure 19-6: Comparison of PSI Pressure Distributions of the Un-Coated and the Coated Delta Wing with Rounded Leading Edges at M = 0.4 and R_{mac} = 3 Million for Three Different Angles of Attack.

19.3.2.3   Onset of Primary Vortex

For delta wings with sharp leading edges the flow separates at the leading edges already at small angles of attack. The shear layer rolls up and the flow re-attaches to the model surface. The primary vortices are formed starting at the apex of the delta wing. Depending on the angle of attack the attachment line is located at the center line of the delta wing or at a spanwise location between the primary vortex and the delta wing center line. Underneath the primary vortices an outboard directed flow establishes. After having passed the suction peak, the steep adverse pressure gradient towards the leading edge causes another flow separation and counter-rotating secondary vortices are formed.

In the case of rounded leading edges the flow separation is no longer fixed to the leading edges. The onset of the primary vortex becomes dependent on the leading edge radius, the angle of attack, the Reynolds and the

Mach number [19-20][19-21], see also Chapter 18. With increasing angle of attack the flow at the leading edge first separates at the rear part of the wing, where the ratio of the leading edge radius over the local wing span is small (VFE-2 configuration with constant leading edge radius). The onset of the primary vortex occurs at a specific incidence when the flow separates effectively. Its origin moves upstream with increasing angle of attack until it reaches the wing apex. In Figure 19-7 the PSP result for a delta wing with sharp as well as with medium radius leading edges are plotted. The suction peaks of the primary vortices are clearly visible, which starts for the sharp edged delta wing at the wing apex and in the rounded leading edge case at $x/c_r = 0.6$.
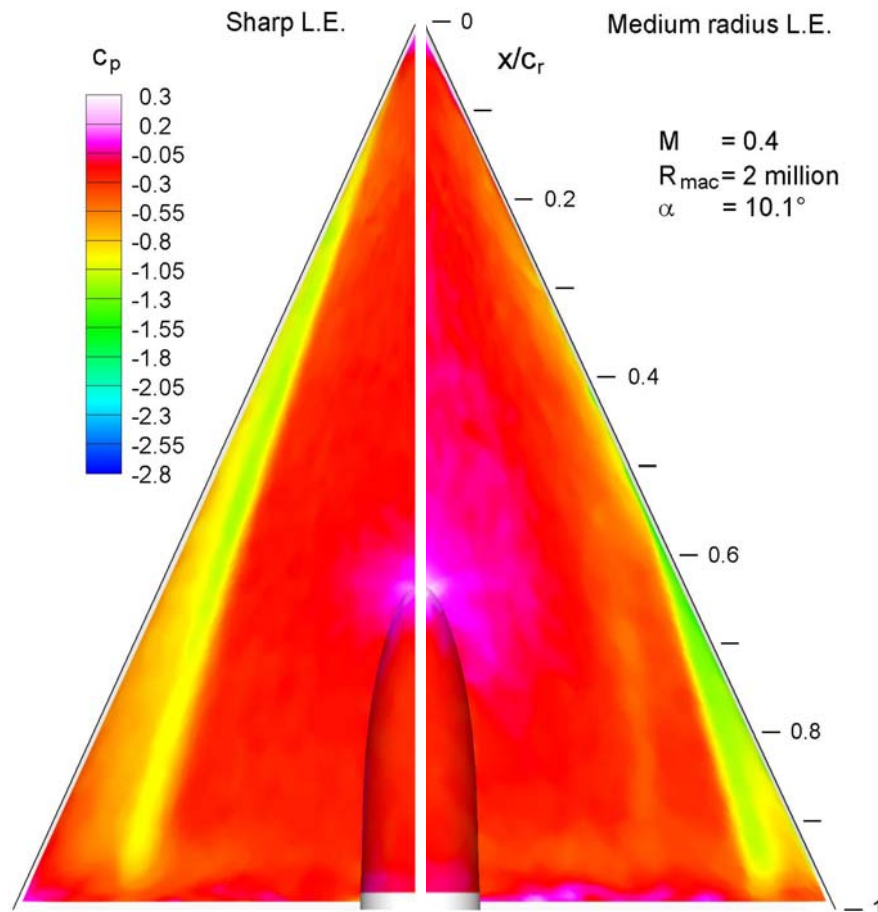
**Figure 19-7: Comparison of Surface Pressure Distributions Obtained with PSP at
Suction Side of Delta Wing with Sharp (left) and Medium Radius (right)
Leading Edge (M = 0.4, R_{mac} = 2 million, α = 10.1°).**

Using the PSP results, the chord locations of the primary vortex origins are determined at the starboard side of the wing. The results are plotted in Figure 19-8 against α in dependency of the Mach and Reynolds number. For M = 0.4 and R_{mac} = 3 million the onset of the primary vortex first takes place between α = 11.2° and 12.3°.
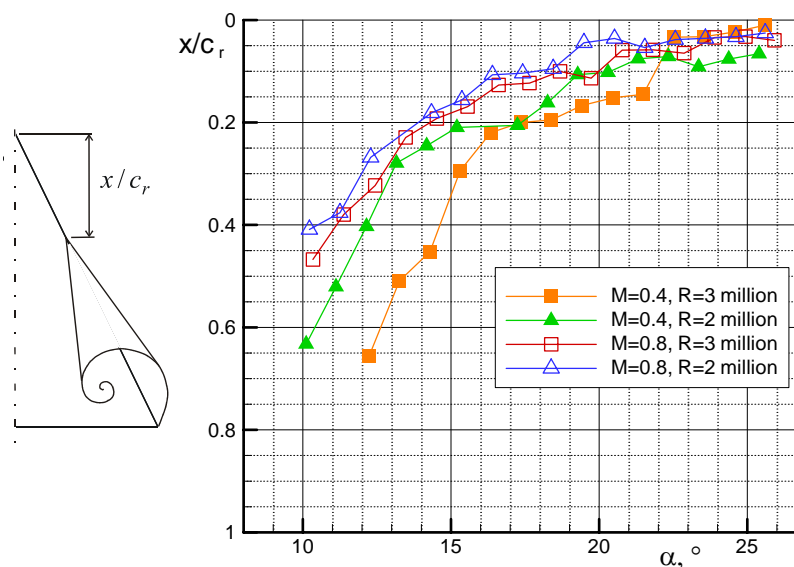
Figure 19-8: Origin Positions of Primary Vortex for α > 10° Obtained from PSP Results for the Delta Wing with Medium Radius Leading Edge for M = 0.4 and 0.8 and R_{mac} = 2 and 3 Million.

Its origin is located at about $x/c_r = 0.65$ for $\alpha = 12.3°$. After its onset, the vortex origin moves quickly towards the wing apex with increasing angle of attack until a chord position of about $x/c_r = 0.3$ is reached; i.e. $\alpha = 15.3°$. Passing this chord position the vortex origin moves more gradually upstream and asymptotically approaches a location close to the wing apex. The plot of $M = 0.4$ and $R_{mac} = 2$ million in Figure 19-4 has a similar slope, however, shifted to lower angles of attack by about 2°. This shows that the onset of the primary vortex is postponed for higher Reynolds numbers. The plots for the transonic cases show that the Mach number has an opposite effect on the vortex onset. Also, the differences between both curves of $R_{mac} = 2$ and 3 million are marginal for $M = 0.8$ in comparison to the subsonic case. The gradients of the curves, particularly for $M = 0.4$, show that the location of the primary vortex is very sensitive to small changes of angle-of-attack for chord positions smaller than $x/c_r = 0.3$.

19.3.2.4   Occurrence of Inner Vortical Structure

For the VFE-2 delta wing with rounded leading edges another vortex develops in the subsonic case inboard of the leading edge. Figure 19-9 shows the PSP results for $M = 0.4$, $R_{mac} = 3$ million and $\alpha = 10.2°$. In this case the onset of the primary vortex takes place first at an angle of attack between 11.2° and 12.2°. However, in the pressure distribution of Figure 19-8 a suction peak can be clearly seen, which is located inboard of the leading edge. In difference to the footprint of a primary vortex (s. Figure 19-6) this suction peak forms a line parallel to the leading edge with increasing peak height towards the trailing edge.
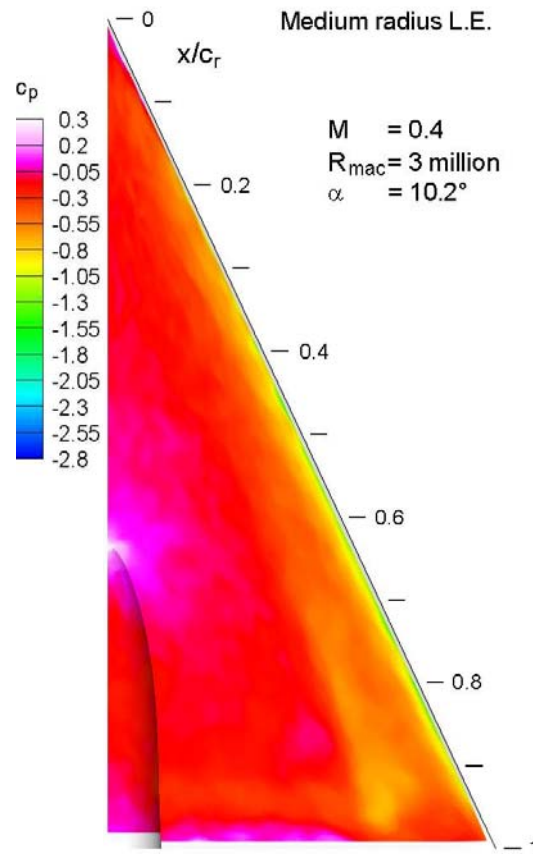
**Figure 19-9: Surface Pressure Distribution Obtained with PSP at the Suction Side of Delta
Wing with Medium Radius Leading Edge for M = 0.4, R_mac = 3 Million and α = 10.2°.**

In Figure 19-10 the PIV results are plotted from $x/c_r = 0.5$ to 0.9 together with the PSP result. It shows an inner vertical structure which increases downstream in size and circulation strength; see later blue dashed line in Figure 19-15. Details of the velocity field at a chord station of $x/c_r = 0.6$ are shown in Figure 19-11. Close to the model surface the time averaged flow field shows a flat vortical structure spreading in the spanwise direction with increasing vorticity towards the leading edge. The corresponding Q-value distribution reveals that this structure consists of several discrete vortices as indicated in Figure 19-11. Particularly, the outboard located vortices in this plot are fed with vorticity from the outer flow. Mainly these vortices produce the suction peak in the pressure distribution and increase in size and circulation strength further downstream.
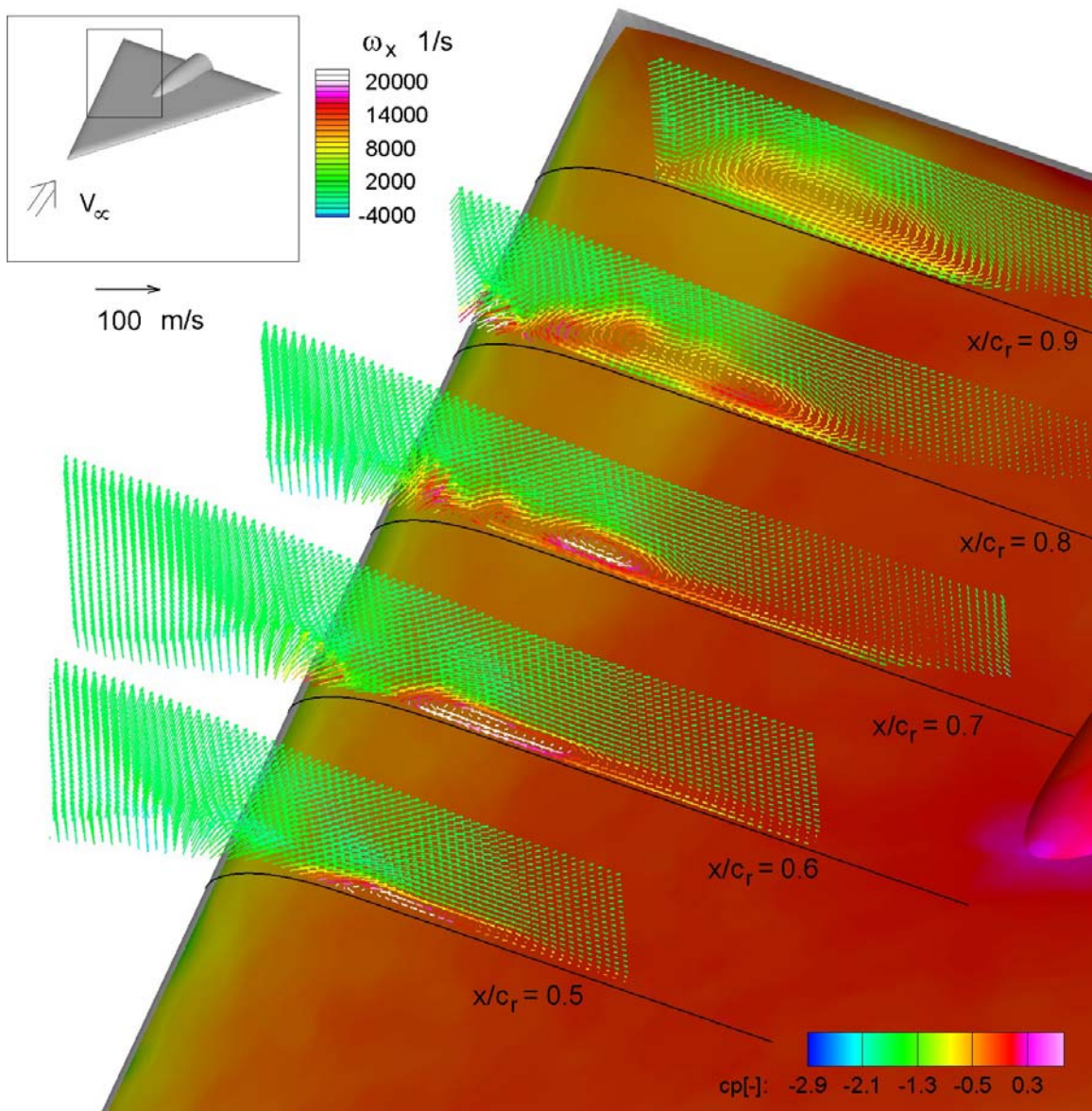
**Figure 19-10: Time Averaged Pressure, Velocity and Vorticity Distributions above the Delta Wing
with Rounded Leading Edges for α = 10.2°, M = 0.4 and R_{mac} = 3 Million. The in-plane velocity
vectors are plotted in different planes perpendicular to the delta wing axis. The color
of the vectors corresponds to the out-of-plane vorticity. The colors at the
surface are related to the local pressure coefficient.**
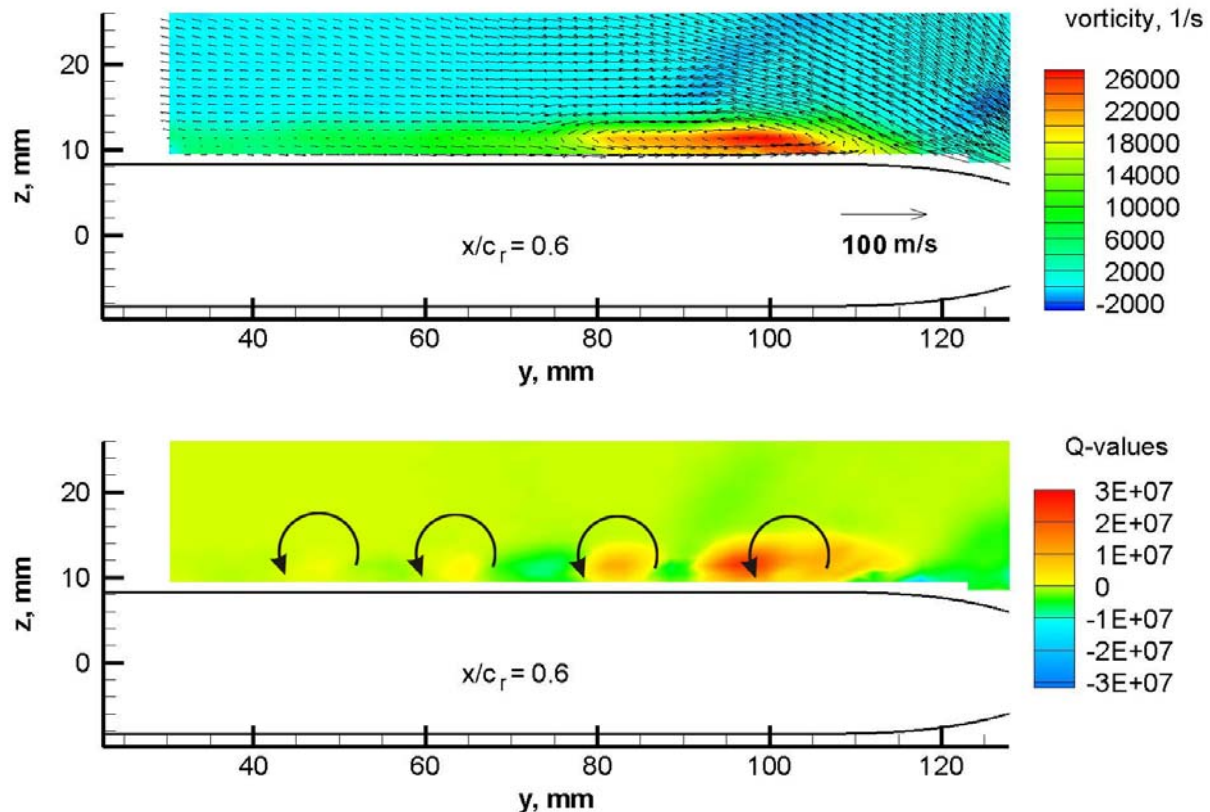
**Figure 19-11: Time Averaged PIV Result at x/c_r = 0.6 above the Delta Wing with Medium
Radius Leading Edges and M = 0.4, R_{mac} = 3 Million and α = 10.2° (top) Velocity
and Vorticity Distributions (bottom) Q-value Distribution.**

This inner vortical structure was not detectable for the delta wing with sharp leading edges that could be explained by the existence of the primary vortex starting at the apex just at small angles of attack which might inhibit the development of an inner vortical structure. However, inner vortices are also not detectable for the transonic cases (M = 0.8) regardless of the leading edge radius.

19.3.2.5   Formation of an Inner and Outer Primary Vortex

The flow topology above the delta wing with medium radius leading edges for M = 0.4 and R_{mac} = 3 million as discussed in the previous section changes at higher angles of attack, when the onset of the outer primary vortex takes place, see also Chapter 35. This is case at an angle of attack of α = 13.3° where the origin of the primary vortex is located at about x/c_r = 0.5 (Figure 19-12). Now, the footprint of the inner vortical structure in the pressure distributions has changed. Its maximum pressure peak height is reached just downstream of the origin of the outer primary vortex and drops down further downstream.
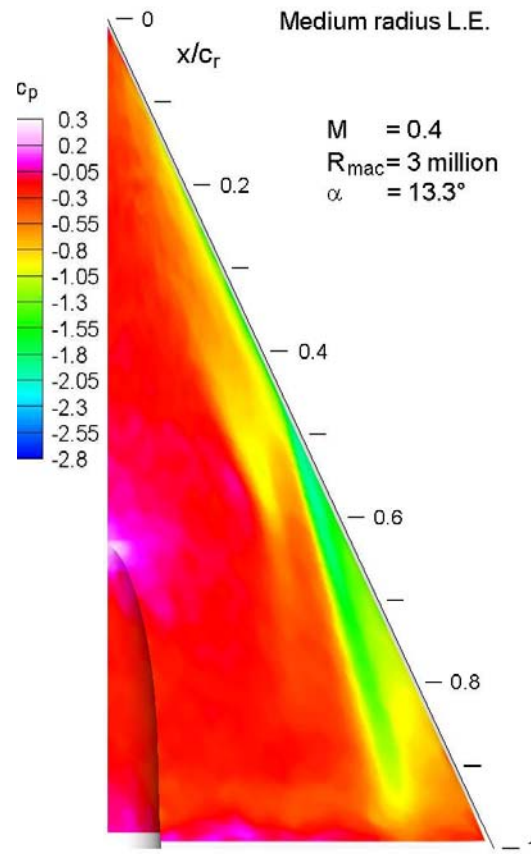
Figure 19-12: Surface Pressure Distribution Obtained with PSP at the Suction Side of Delta Wing with Medium Radius Leading Edge for M = 0.4, R_{mac} = 3 Million and α = 13.3°.

In Figure 19-13 the time averaged velocity and vorticity distributions are plotted of the delta wing in different planes. In the foremost shown chord station of $x/c_r = 0.4$, i.e. upstream the origin of the primary vortex, the inner vortical structure can be seen again as a flat vortex close to the surface similar to the case at α = 10.2° as described in the former section. At the leading edge an attached flow exists, whereas a local flow separation being embedded within the boundary layer may exist, which is not resolved by the used PIV and PSP setup.
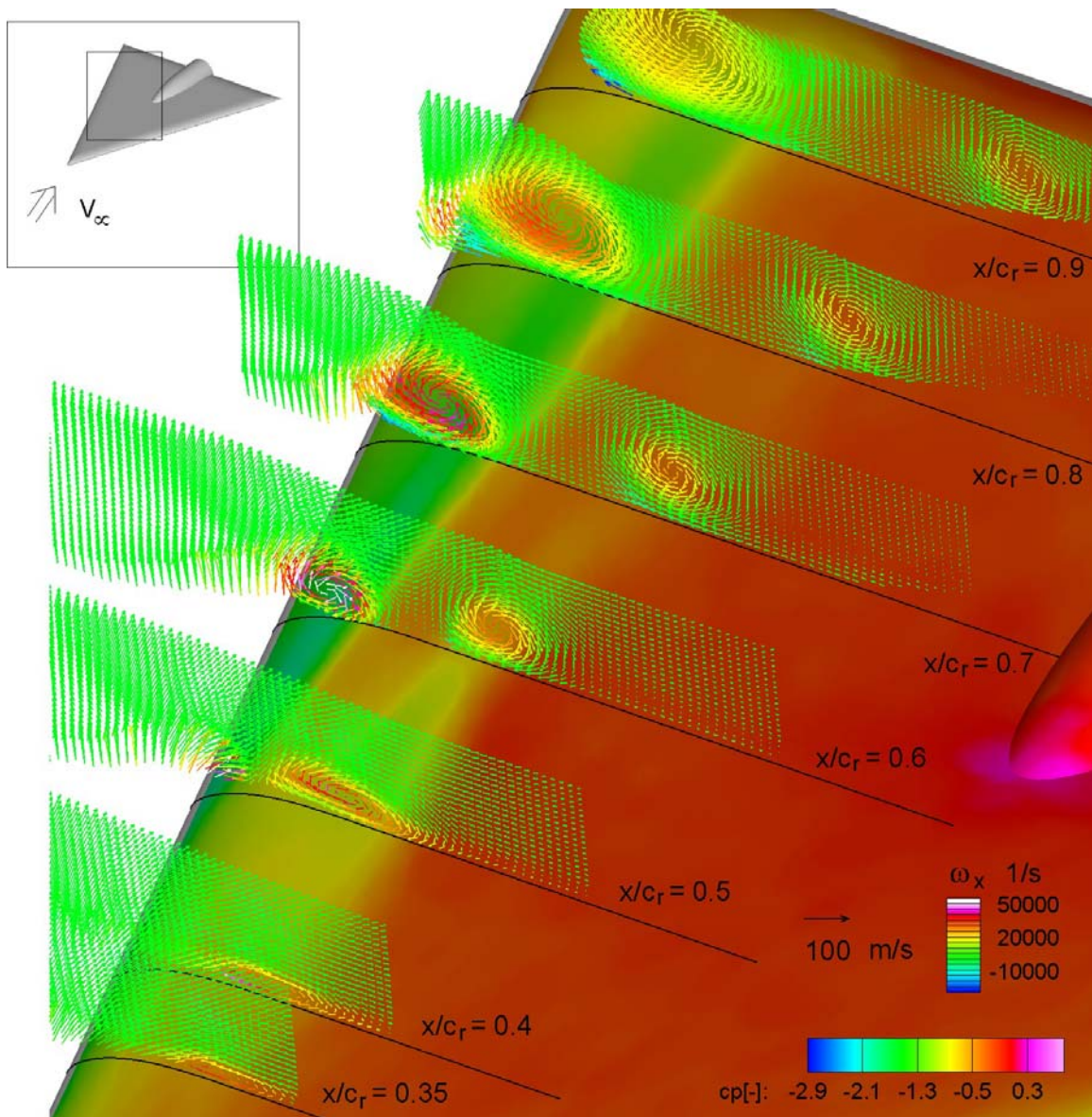
**Figure 19-13: Time Averaged Pressure, Velocity and Vorticity Distributions above the Delta Wing
with Rounded Leading Edges for α = 13.3°, M = 0.4 and R_{mac} = 3 Million. The in-plane velocity
vectors are plotted in different planes perpendicular to the delta wing axis. The color
of the vectors corresponds to the out-of-plane vorticity. The colors at the
surface are related to the local pressure coefficient.**

The velocity field at the chord station of $x/c_r = 0.5$ shows the primary vortex at an early state close the leading edge. Between the outer primary vortex and the inner vortical structure the flow reattaches to the surface and again separates. The inboard directed flow in the vicinity of the inner vortical structure now has changed with respect to the flow direction and velocity magnitude, so that the outer vortices of the inner vortical structure detach from the surface.

Therewith, the co-rotating vortices forming the inner flat vortical structure partly are able to merge and an inner circular vortex is formed, which can be seen in the velocity field at $x/c_r = 0.6$. Now, two co-rotating vortices of approximately the same size can be observed; i.e. an inner and outer vortex. Between both vortices a re-attachment and separation line exists at the surface. Further downstream the inner and outer vortices remain separated and do not merge (s. Figure 19-14, $x/c_r = 0.6$ to 0.8). With increasing size of the primary vortex a focus point is formed between the inner and outer vortex in the velocity field, so that at the surface an outboard directed flow establishes.
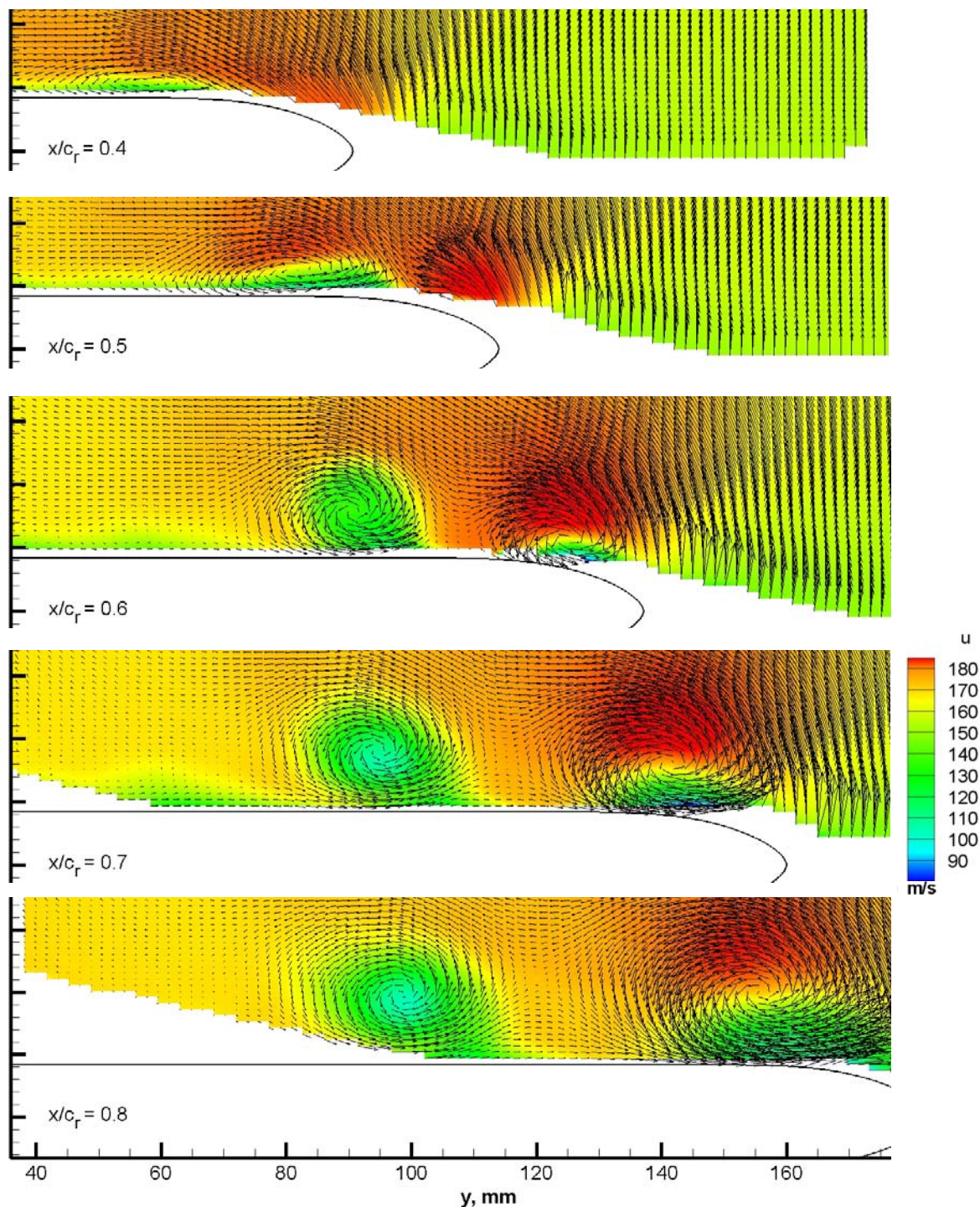
Figure 19-14: Time Averaged Velocity Fields at Different Chord Positions above the Delta Wing with Medium Radius Leading Edges for M = 0.4, R_{mac} = 3 Million and α = 13.3°. The color is related to the out-of-plane velocity u.

In Figure 19-15 the calculated circulations of the inner and outer vortices are plotted against the chord position for different Reynolds numbers and angles of attack. The dashed magenta line corresponds to the inner vortex for the current case. It shows that the circulation of the inner vertical structure first increases in a downstream direction until the primary vortex (solid magenta line) occurs. However, not all of the circulation contained in the inner vortical structure goes into the newly formed inner vortex, as the step in the dashed magenta line between $x/c_r = 0.5$ and 0.6 indicates. In the velocity field at $x/c_r = 0.7$ (Figure 19-14), obviously parts of the inner vortical structure can be detected inboard of the inner vortex.
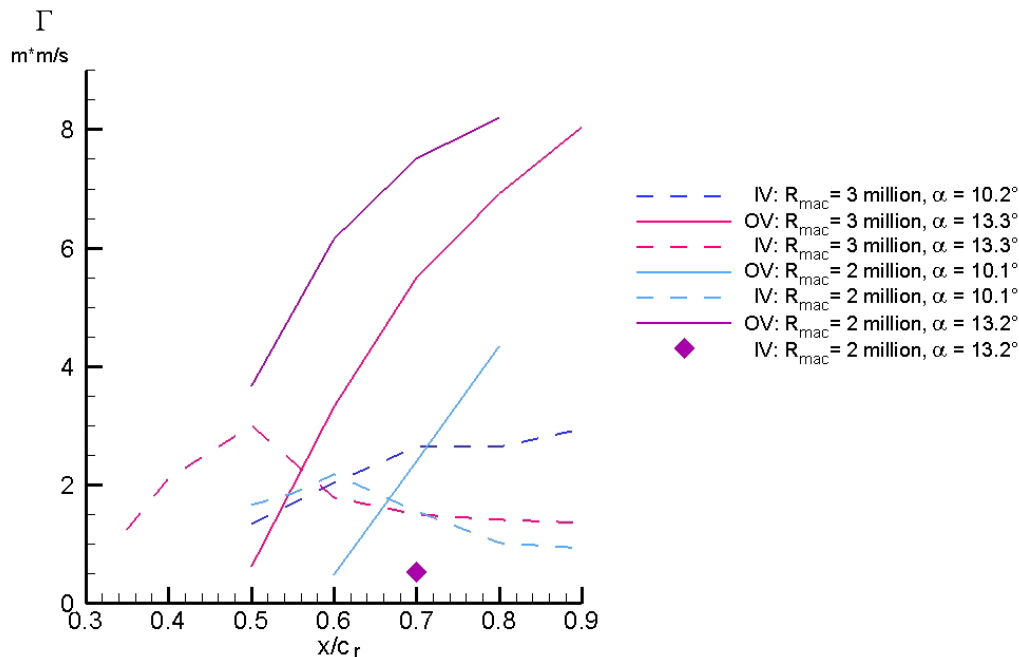
Figure 19-15: Calculated Circulations of the Inner Vortical Structure or the Inner Vortex
(IV, dotted lines) and the Outer Primary Vortex (OV, solid lines) against
Chord Position for the Medium Radius L.E. and M = 0.4.

Whereas the circulation of the primary vortex continuously increases in a downstream direction (solid magenta line in Figure 19-15), the circulation of the inner vortex decreases slightly. Therefore, after the flow separates effectively at the leading edge vorticity is fed mainly into the primary vortex and not into the inner vortex.

19.3.2.6   Effects of Angle-of-Attack on Vortex System Above Delta Wing with Rounded Leading Edges

In Figure 19-16 the surface pressure distributions are shown for $M = 0.4$, $R_{mac} = 3$ million and angles of attack from $10.2°$ to $25.6°$. The first PSP result for $\alpha = 11.2°$ shows an attached flow at the leading edge. In comparison with the result for $\alpha = 10.2°$ in Figure 19-8 the inboard suction peak is stronger, which indicates that the strength of the inner vertical structure increases with increasing angle of attack as long as the onset of a primary vortex has not taken place.
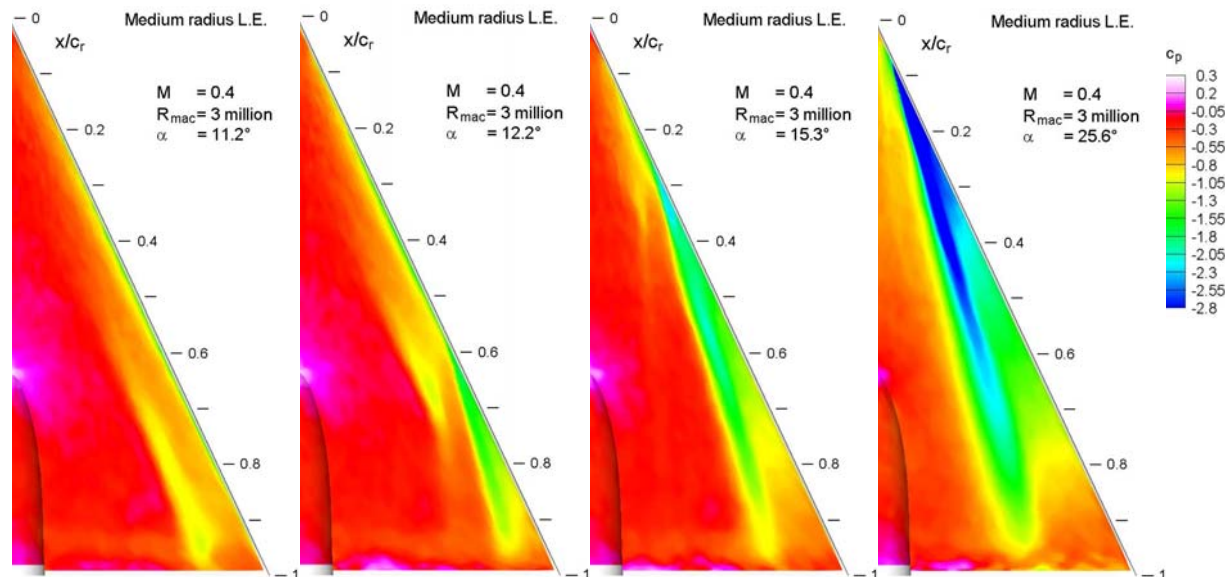
Figure 19-16: Surface Pressure Distributions Obtained with PSP at the Suction Side of the Delta Wing with Medium Radius Leading Edges for Different Angles of Attack (M = 0.4, R_{mac} = 3 million).

The onset of the primary vortex occurs at $\alpha = 12.2°$. With increasing angle of attack the origin of the primary vortex moves upstream, whereas the footprint of the inner peak is shifted upstream accordingly. Although the inner suction peak height increases with increasing angle of attack for a specific chord position upstream the onset of the primary vortex as stated above, the maximum peak height produced by the inner vortex weakens (s. Figure 19-16, $\alpha = 12.2°$ to $25.6°$). This effect can be explained by the quick upstream movement of the primary vortex, since vorticity is no longer fed into the inner vortical structure downstream the primary vortex origin. This can be quantified by comparing the resulting circulation values of the inner vortex in Figure 19-15 for R_{mac} = 2 million, i.e. $\Gamma = 0.5$ m^2/s for $\alpha = 13.2°$ (origin of the primary vortex: $x/c_r = 0.25$) and $\Gamma = 1$ m^2/s for $\alpha = 10.2°$ (origin of the primary vortex: $x/c_r = 0.6$).

19.3.2.7 Effects of Reynolds Number on Vortex System Above Delta Wing with Rounded Leading Edges

Figure 19-17 shows a corresponding series of pressure distributions as shown in Figure 19-16 (R_{mac} = 3 million), however, for a lower Reynolds number of R_{mac} = 2 million. Lowering the Reynolds number promotes the flow separation at the leading edge. Therefore, the onset of the primary vortex starts earlier and the origin of the outer primary vortex is shifted upstream by reducing the Reynolds number. As discussed formerly in Section 19.3.2.3 a more upstream located origin of the primary vortex leads to a lower circulation strength of the inner vortex, since after the occurrence of the primary vortex vorticity is fed mainly into the outer primary vortex and no longer into the inner vortical structure. This results in much lower peak values in the pressure distributions of the inner vortex in the low Reynolds number case. From Figure 19-14 it follows that the circulation is $\Gamma = 1.4$ m^2/s for R_{mac} = 3 million and $\alpha = 13.3°$ (origin of the primary vortex: $x/c_r = 0.5$), which is about three times higher than that for the case of R_{mac} = 2 million and $\alpha = 13.2°$. Figure 19-18 shows the flow topology above the delta wing for the lower Reynolds number and $\alpha = 13.2°$. Since the origin of the primary vortex is located more upstream the inner vortex is located more inboard in comparison to the corresponding case for R_{mac} = 3 million (Figure 19-13).
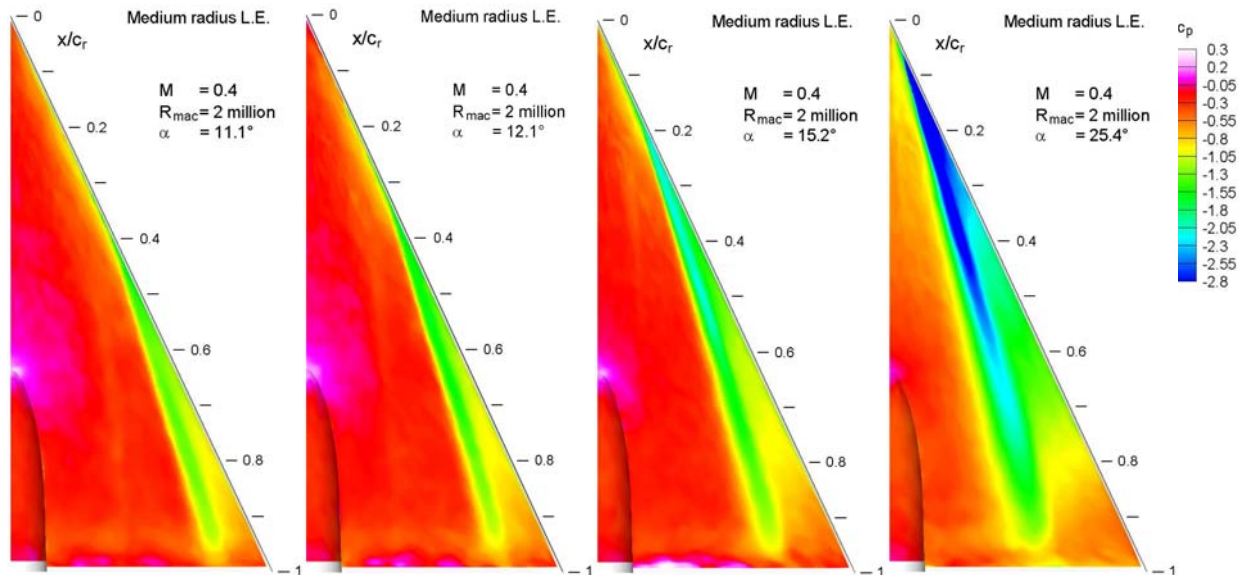
Figure 19-17: Surface Pressure Distributions Obtained with PSP at the Suction Side of the Delta Wing with Medium Radius Leading Edges for Different Angles of Attack (M = 0.4, R_{mac} = 2 million).
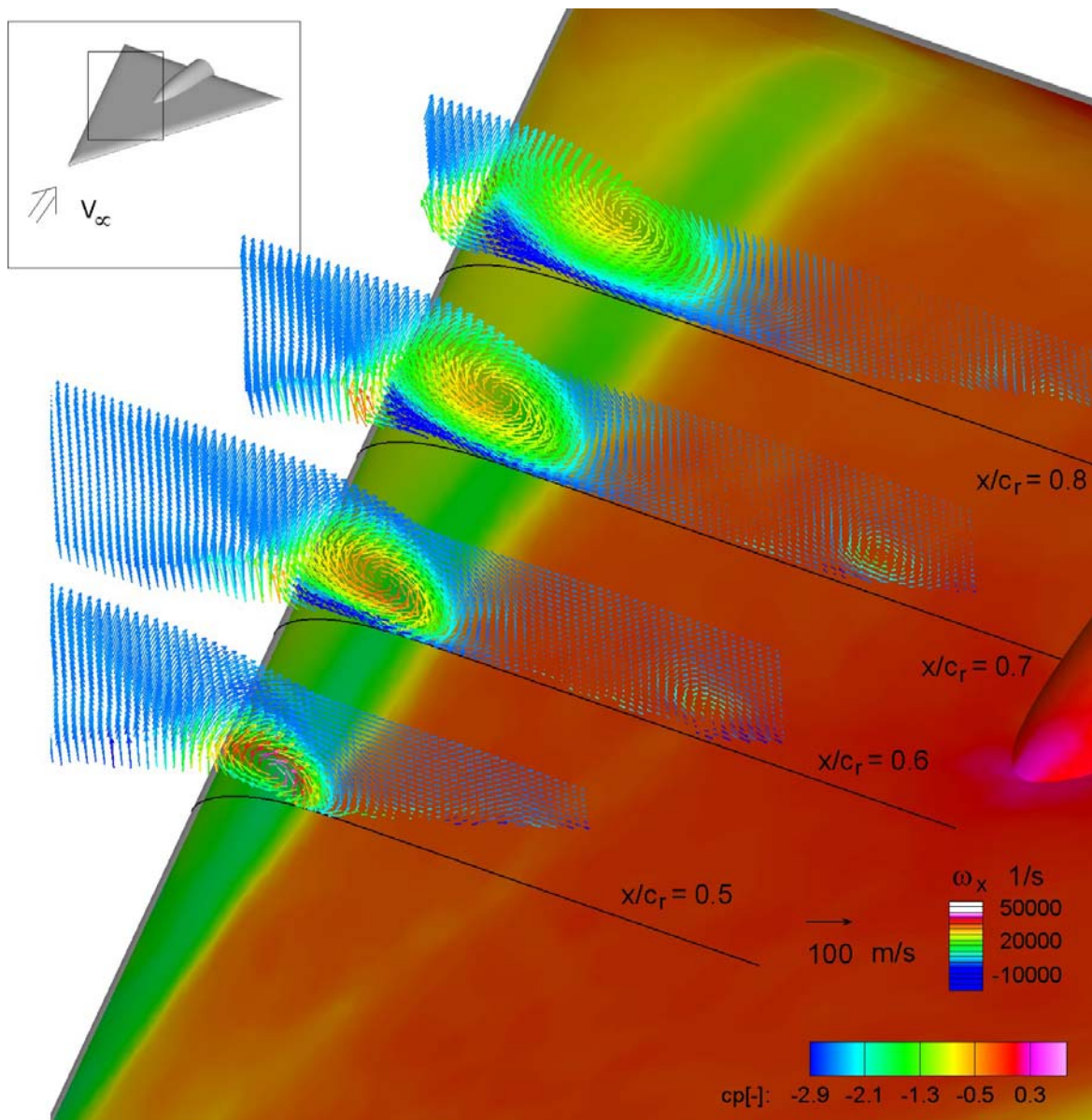
Figure 19-18: Time Averaged Pressure, Velocity and Vorticity Distributions above the Delta Wing with Rounded Leading Edges for α = 13.3°, M = 0.4 and R_{mac} = 2 Million. The in-plane velocity vectors are plotted in different planes perpendicular to the delta wing axis. The color of the vectors corresponds to the out-of-plane vorticity. The colors at the surface are related to the local pressure coefficient.

The circulation strength of the inner vortex formed downstream the origin of the primary vortex is mainly affected by the onset and streamwise position of the primary vortex. However, it is also important for which combination of angle of attack and Reynolds number a specific position of the primary vortex results. The amount of circulation fed into the inner vortical structure, i.e. upstream the primary vortex, depends also on the angles of attack, such that with increasing angle of attack the loss of circulation in the resulting inner vortex, i.e. downstream the primary vortex origin, caused by the according upstream movement of the primary

vortex is partly compensated. This is obviously not the case when the same upstream shift of the primary vortex is achieved by reducing the Reynolds number. The circulation plots in Figure 19-15 for the inner vortical structure of $R_{mac} = 2$ and 3 million and similar angles of attack, i.e. $\alpha = 10.1°$ and $10.2°$ respectively, are nearly identical which shows the strength of the inner vortical structure to be less sensitive to the Reynolds number upstream the primary vortex, i.e. $x/c_r \leq 0.6$. This explains the much weaker pressure peaks produced by the inner vortex for $R_{mac} = 2$ million in comparison to the cases of $R_{mac} = 3$ million.

19.3.2.8   Vortex Breakdown Above the Delta Wing in Transonic Flow

At the transonic speed of M = 0.8 the flow is much more complex, because the flow above the delta wing reaches supersonic speeds and shock waves occur [19-6], [19-25], see also Chapter 29. Figure 19-19 shows the pressure distributions for the sharp edged delta wing for different angles of attack. At $\alpha = 24.1°$ the footprints of the primary and secondary vortex originating from the wing apex are clearly visible. Plotted, are also constant lines of the sonic pressure coefficient c_p^*. This shows that the outboard directed flow underneath the primary vortex close to the surface is supersonic, so that probably in front of the secondary vortex a cross-flow shock wave is located.
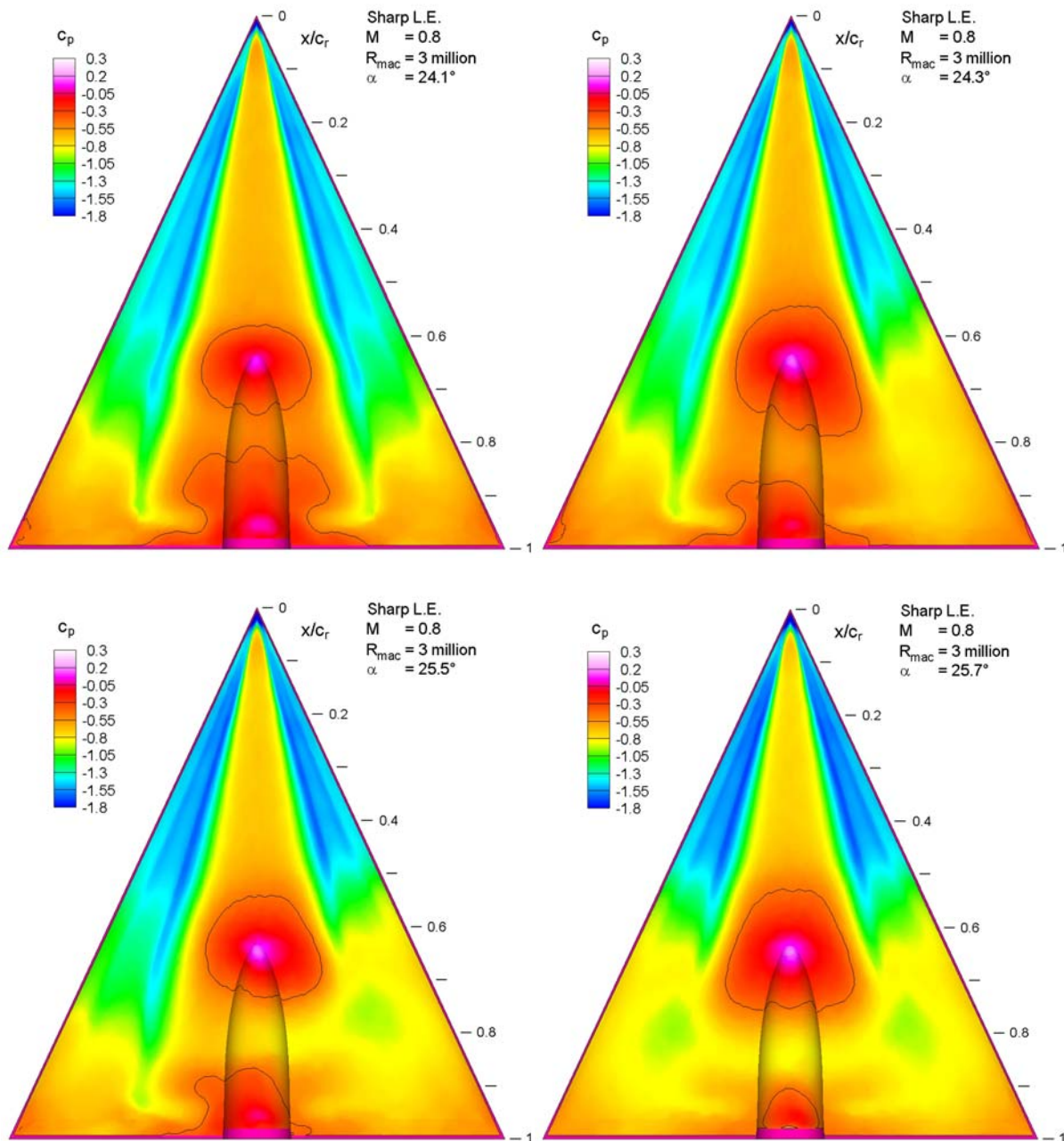
Figure 19-19: Surface Pressure Distributions Obtained with PSP at the Suction Side of the Delta Wing with Sharp Leading Edges in 0.2° Steps of Angles of Attack (M = 0.8, R_{mac} = 3 Million). The black contour lines indicate the sonic pressure coefficient C_p^* = -0.43.

In Figure 19-20 the velocity and vorticity distributions are plotted at x/c_r = 0.6 for an angle of attack of α = 25.7° showing the counter-rotating secondary vortex underneath the primary vortex. Also plotted are negative values of the divergence of the in-plane velocity vectors ($\nabla \cdot \vec{v}$) which gives an indication of the location and shape of a cross-flow shock wave.
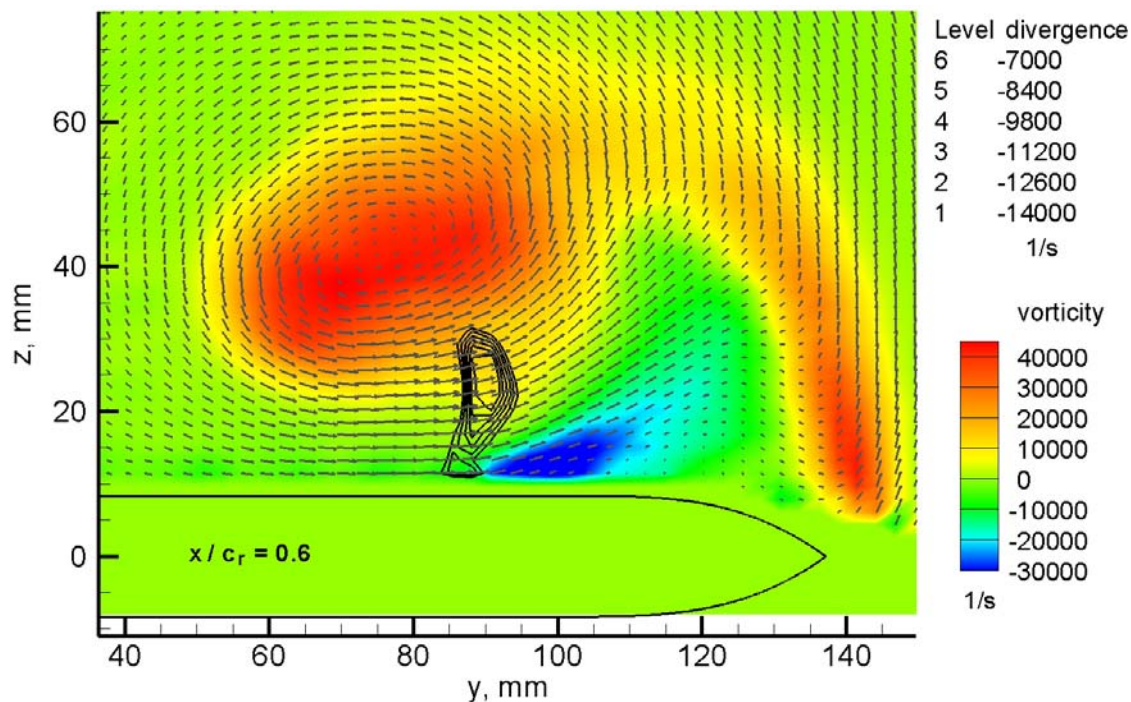
**Figure 19-20: Time Averaged Velocity and Vorticity Distributions for the Delta Wing with Sharp
Leading Edges at $x/c_r = 0.6$ (M = 0.8, R_{mac} = 3 Million, $\alpha = 25.7°$). The color of the vectors
corresponds to the out-of-plane vorticity. The block contour lines are
related to the divergence of the in-plane velocity vectors.**

The contour lines of the sonic pressure coefficient in the center of the delta wing give an indication of a terminating shock wave in front of the sting fairing, i.e. about $x/c_r = 0.55$, and a second one closer to the trailing edge downstream of $x/c_r = 0.8$. Increasing the angle of attack by only $0.2°$ the pressure distribution changes rapidly and becomes unsymmetric (s. Figure 19-19, $\alpha = 24.3°$). Following the suction peak of the primary vortex at the starboard side the peak enlarges suddenly downstream at a chord position of about $x/c_r = 0.7$ and the pressure increases. This gives reason to presume the occurrence of a vortex breakdown [19-27], which may the result from an interaction between the primary vortex and the terminating shock wave in front of the sting. This presumption is also proven by the fact that such an abrupt change of the pressure distribution does not occur in the subsonic cases as shown for example in Figure 19-16 for the delta wing with rounded leading edges and an angle of attack of $\alpha = 25.6°$. Please, notice also that this pressure change takes place by increasing the angle of attack by only $\alpha = 0.2°$. However, the assumed vortex breakdown first occurs only at the starboard side of the wing, which shows that this flow situation seems to be very sensitive to small misalignments of the model or minor imperfections of the model geometry. The pressure distributions become again symmetric at an angle of attack of $\alpha = 25.7°$. Again this takes place after an increase of angle of attack of only $0.2°$ (Figure 19-19). In Figure 19-21 the corresponding velocity distributions for $\alpha = 25.7°$ are plotted against the pressure distribution.The velocity field upstream the presumed vortex breakdown is shown for $x/c_r = 0.55$. The outward directed flow underneath the primary vortex separates at about $y = 135$ mm ($\eta = 0.85$) and a secondary vortex is formed. The flow field downstream the vortex breakdown at $x/c_r = 0.75$ shows a large region of reverse flow (up to $u = -60$ m/s), which is typically the case in the region of vortex breakdown.
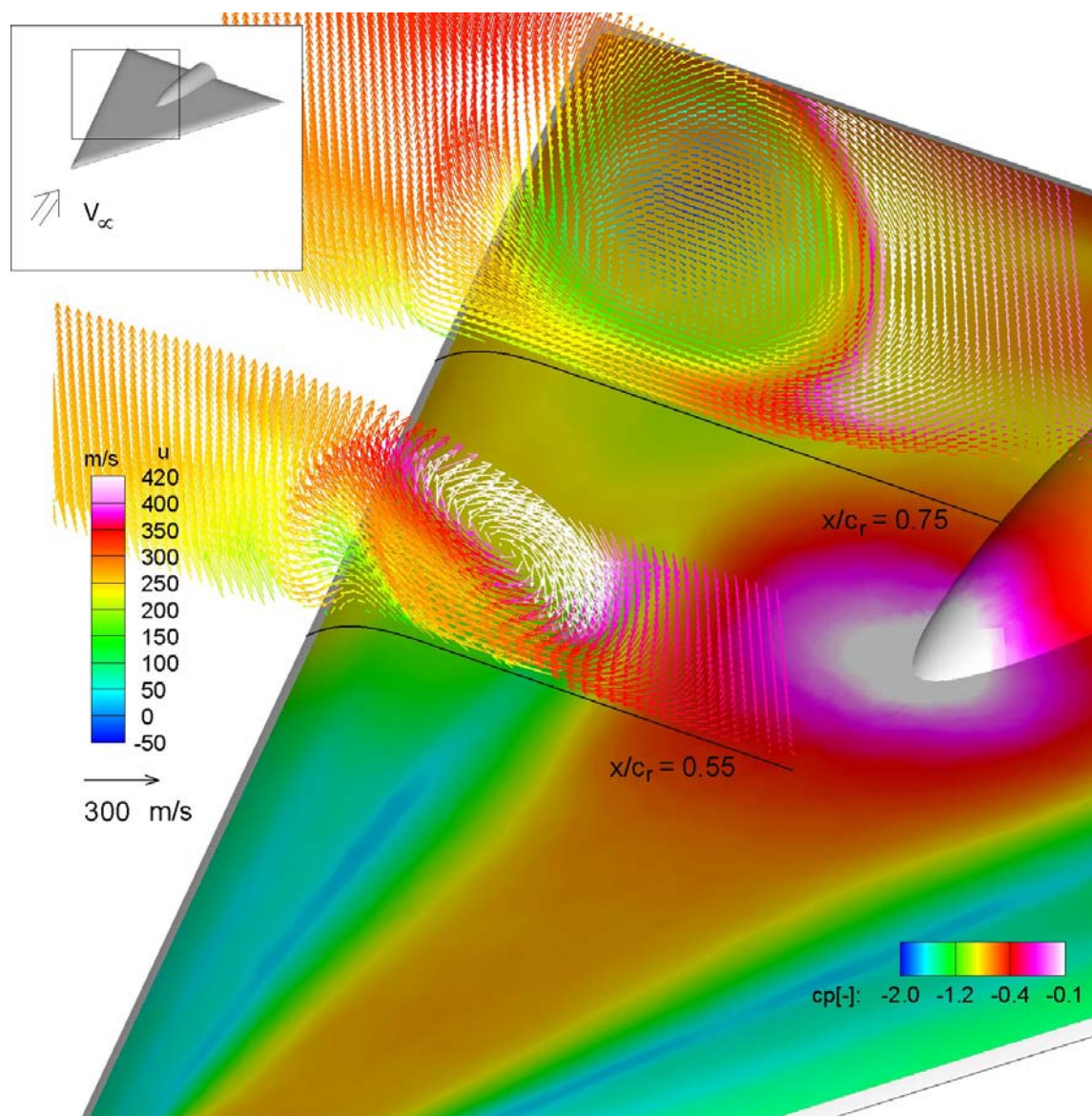
Figure 19-21: Time Averaged Pressure and Velocity Distributions above the Delta Wing with Sharp Leading Edges for M = 0.8, R$_{mac}$ = 3 Million and α = 25.7°. The in-plane velocity vectors are plotted in different planes perpendicular to the delta wing axis. The color of the vectors corresponds to the out-of-plane velocity. The colors at the surface are related to the local pressure.

19.4   INVESTIGATIONS IN THE CRYOGENIC WIND TUNNEL IN COLOGNE

19.4.1   Test Conditions and Measurement Setups

19.4.1.1   Wind Tunnel Facility and Model Instrumentation

The last measurement campaign was carried out in the Cryogenic Wind tunnel in Cologne (DNW-KKK). It is a closed-circuit low-speed (M ≤ 0.38) wind tunnel (Figure 19-22). To realise high Reynolds numbers the wind

tunnel can be operated with nitrogen gas. The flow temperature can be set within in the range of 100 K ≤ T ≤ 300 K by injecting liquid nitrogen. Beneath the test section a model conditioning room is located from which the model support can be lifted up to the test section and enables access to the model without warming up the complete wind tunnel.
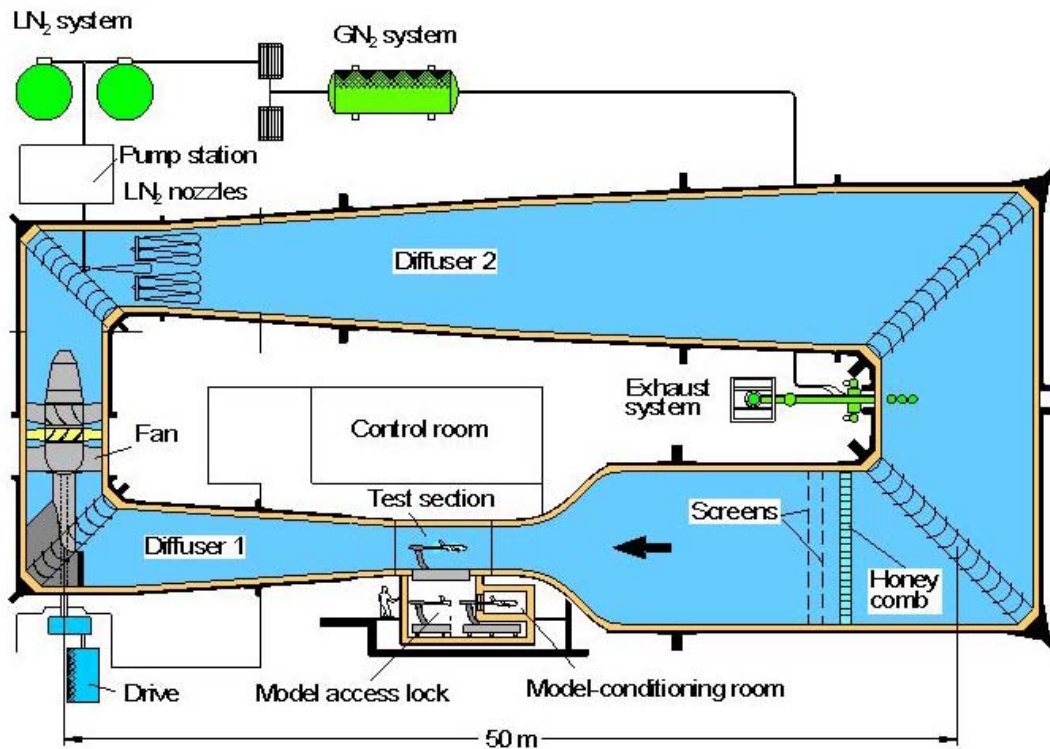
Figure 19-22: Sketch of Cryogenic Wind Tunnel in Cologne (DNW-KKK).

The delta-wing model of the TU-Munich was used for the tests, which is twice the size (c_r = 0.89 m) of NASA's ¾ scale 65° delta-wing model used in the DNW-TWG. The model is made of specific aluminium suitable for cryogenic temperatures and incorporates also interchangeable leading edge sections, so that the sharp as well as the medium radius ($r/\overline{c}$ = 0.0015) could be investigated. According to the geometry definitions a straight model sting was constructed by DLR which is connected to the 3d model support of the wind tunnel. The possible angle of attacks ranges from -15° to 30°. Similar to the model of NASA pressure taps are mainly arranged also at chord stations of 0.2, 0.4, 0.6, 0.8 and 0.95, whereas about 48 taps are equipped with pressure sensors to be able to measure instantaneous pressure fluctuations. However, these sensors are removed for the tests in the KKK resulting in a lower pressure tap resolution along the chord stations.

The model was applied with a Temperature Sensitive Paint (TSP) (Figure 19-23) which has a thickness of about 120 µm and is according to the scaling of the model twice the thickness of the PSP paint used for the measurements in the TWG. This coating was kept during the whole measurement campaign in the DNW-KKK.

**Figure 19-23: The 65° Delta Wing of TU-Munich Coated with TSP
in the Model Conditioning Room of the DNW-KKK.**

19.4.1.2   Application of the Temperature Sensitive Paint and Infrared Techniques

While the Infrared technique [19-15] works very well at temperatures higher than 200 K (low Reynolds numbers) the TSP technique for cryogenic wind tunnels [19-4] can be applied at temperatures lower than 240 K (high Reynolds numbers). In both cases, these non-intrusive observation techniques detect boundary layer transitions on a model by measuring the temperature difference generated between laminar and turbulent boundary layers due to the difference of their convective heat transfer coefficents. This means that a small temperature difference between model and the flow in necessary. However, the naturally generated temperature difference is usually too small to create a large enough temperature differences on a model made of aluminium. Therefore, one needs to apply artificial enhancement of the laminar-to-turbulent temperature difference for cryogenic testing. This was achieved by warming up the delta wing model before every measurement series in the model-conditioning room beneath the test section. Then the model was quickly lifted up to the test section which was kept at the test temperature (205 K and 240 K) and the tunnel started blowing immediately. After the tunnel reached the test condition, the images were obtained using the temperature difference between the model and the flow before the model temperature could adapt to the flow temperature.

A single component TSP for cryogenic wind tunnels (cryoTSP) which was developed by JAXA [19-12] was applied to the model. The paint consists of a Ruthenium complex: Di(tripyridyl)ruthenium(II) (denoted here by Ru(trpy)) as a temperature sensitive luminophore and urethane polymer as a binder. Before applying the TSP the model was coated with a white screen layer for thermal insulation. After curing of the paint, the surfaces were polished carefully at each step to get sufficiently high smoothness (Ra < 0.1 µm).

For TSP two observation views were realised (Figure 19-24). The suction side of the complete model was captured by a camera (PCO-Pixelfly qe, 12 bit, 1392 x 1024 pixel) using a window in the top side of the test

section. A second setup (PCO-4000, 14 bit, 4008 x 2672 pixel) uses a side window to capture the leading edge. The model is illuminated using high power blue LED lamps (excitation wavelength: 425 nm < λ < 525 nm). Each camera was equipped with optical filters to select the TSP emission wavelength (580 nm < λ < 680 nm).
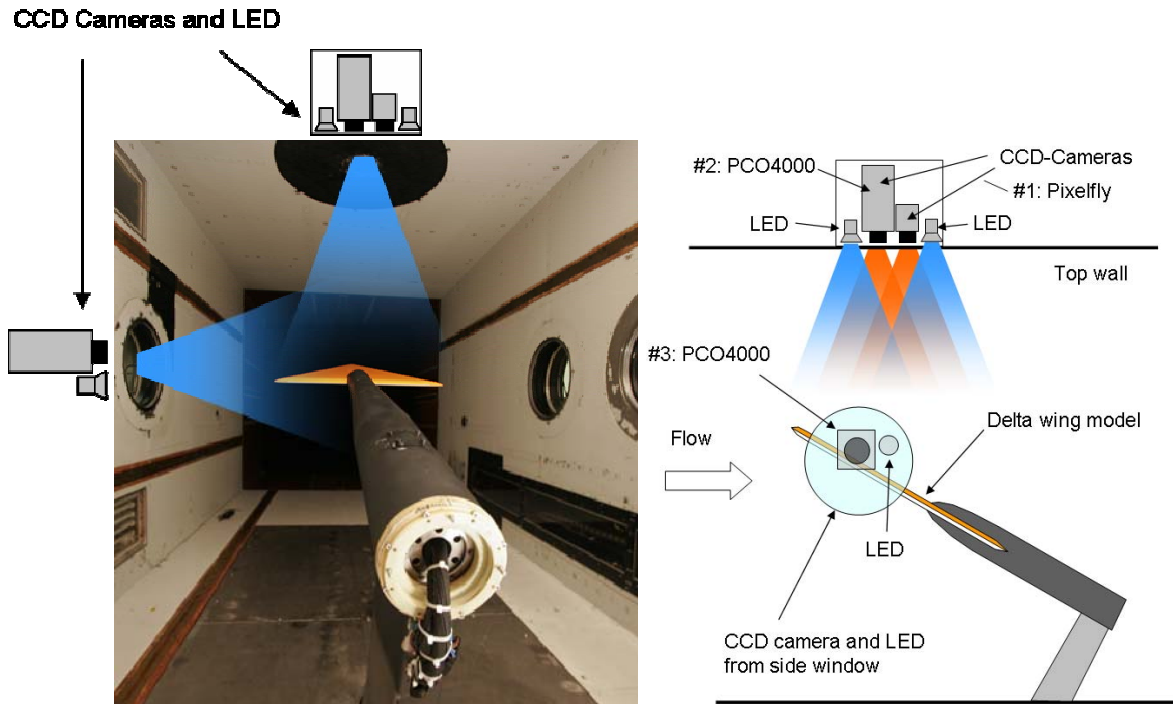
Figure 19-24: Delta Wing Model in the Test Section and Measurement Setups for TSP.

The Infrared measurements were performed separately. A single infrared camera (SC 3000 of FLIR Systems, 320 x 240 px, 50 fps, temperature resolution 20 mK) was placed behind the top window of the wind tunnel after removing the TSP arrangement. Also the glass window was changed by a special window made of Germanium which is transparent for infrared radiation in the wave length range of 10 µm. Since the spatial resolution of the infrared camera is much smaller that that of the TSP camera a infrared lens was chosen such that only about 40% of the model surface is captured within a single frame. Mainly the front part was recorded (Table 19-3), however, in some cases two camera adjustments were used to capture the front as well as the mid part of the model.

Table 19-3: Test Cases for IR Measurements in the DNW-KKK

Leading Edge	Sharp / Medium Radius
T	233 K / 258 K (sharp L.E.) 240 K (rounded L.E.)
M	0.113 / 0.147 (sharp L.E.) 0.051 / 0.077 / 0.103 / 0.154 (rounded L.E.)
R_{mac}	2 / 3 x 10^6 (sharp L.E.) 1/ 1.5 / 2 / 3 x 10^6 (rounded L.E.)
α (nominal)	α-sweeps from -5° to +28°

In the case of TSP an image post processing step is necessary to make the transition lines visible. A reference image taken at constant surface temperature distribution is divided by a run-image, which has the temperature difference between laminar and turbulent boundary layer superimposed and small temperature differences are amplified. For each test case (Table 19-4) a set of 12 run and reference images were taken from which an average is calculated for noise reduction. Also a dark image was subtracted from the averaged reference and run images to account for the camera dark current noise. Then, the ratio of the averaged reference and run images was taken. The obtained ratio images were further optimized to enhance the contrast in the images to make the flow phenomena on the delta model visible.

Table 19-4: Test Cases for TSP Measurements in the DNW-KKK

Leading Edge	Sharp / Medium Radius
T	205 K
M	0.042 / 0.063 / 0.083 / 0.125
R_{mac}	1 / 1.5 / 2 / 3 x 10^6
α (nominal)	5°, 10°, 13°, (18°, sharp L.E. only)

19.4.1.3   Application of Particle Image Velocimetry

To investigate the flow topology above the delta wing model with rounded leading edges at higher Reynolds numbers Stereo-PIV was also applied in the DNW-KKK under cryogenic conditions. A fixed measurement plane was used located at $x/c_r = 0.6$ and aligned perpendicular to the model axis for an angle of attack of 13°. The PIV laser (2 x 220 mJ) and the light sheet optics were attached to the side wall outside of the test section (Figure 19-25). One of the two available side windows is used to direct the light sheet to the model. The first PIV camera (PCO SensiCam QE, double-shutter, 1376 x 1060 px) is positioned within the test section using an thermal isolated and temperature controlled camera housing. The camera housing is mounted to the wind tunnel floor 4 m downstream the model such that the viewing angle to the light sheet is about 0°; i.e. 13° with respect to the wind tunnel axis. The second PIV camera is located outside the wind tunnel behind the second side wall window (s. Figure 19-25), which had a viewing angle of about 45° to the light sheet.
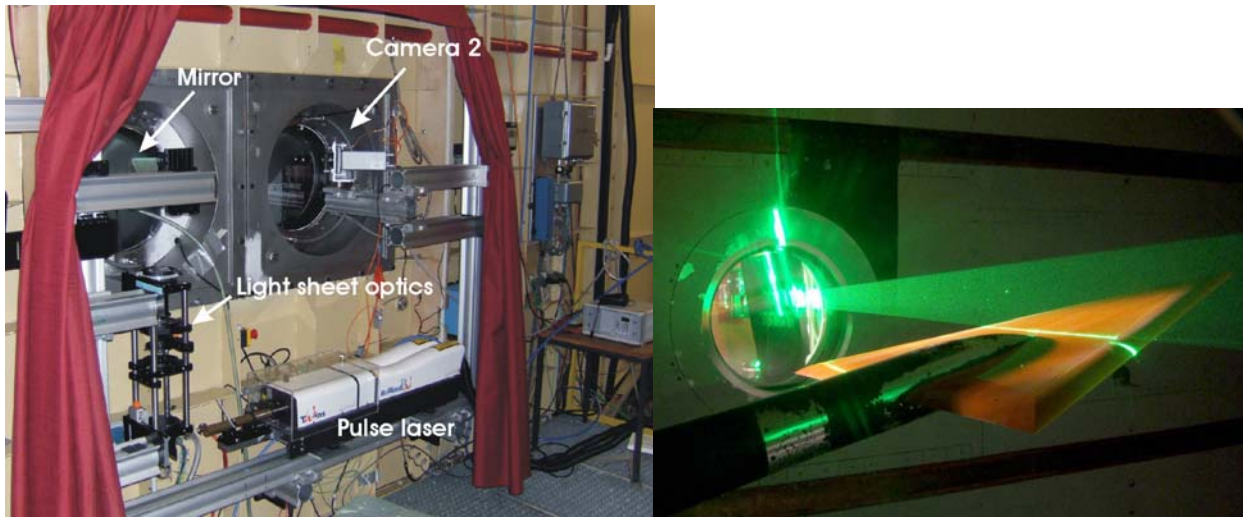
**Figure 19-25: Left: Stereoscopic PIV Arrangement at the DNW-KKK. Camera 1 is located
inside the wind tunnel 4 m downstream the model within a temperature
controlled camera housing. Right: Light sheet above delta wing.**

The test parameters were chosen according to the beforehand performed IR and TSP measurements (Table 19-5). Only the medium radius leading edge was investigated. Additional measurements were performed at very low temperatures of only 150 K to get data at higher Reynolds numbers of up to 6 million.

Table 19-5: Test Cases for PIV Measurements in the DNW-KKK

Leading Edge	Medium Radius
T	240 K / 205 K / 150 K
M	0.042 – 0175
R_{mac}	1 / 1.5 / 2 / 3 / 4 / 6 x 10^6
α (nominal)	5°, 10°, 13°, 16°, 18°, 20°, 23°, 25°, 28°

19.4.2   Preliminary Results from the DNW-KKK

The interpretation of the recorded TSP images as well as the IR images is not simple in the current case for two reasons. First, the model was not especially designed for transition detection measurements by means of comparing the different heat fluxes in a laminar and turbulent boundary layer. The model consists of different parts (exchangeable leading edge sections) and incorporates hollow spaces for instrumentation. This leads to non-uniform temperature distributions on the model surface which is reinforced by the fact that the model is made of aluminium of high heat conductivity and low thermal capacity. Second, also the strong vortices occurring above the delta wing produce a temperature signal at the surface, which is much higher than that of transition. Therefore, the measured temperature distributions are a superposition of the inhomogeneous cooling of the model, the temperature signal from the vortices and the laminar/turbulent transition. A separation of these signals is not always possible, so that the following analysis represents an incomplete description of the

transition lines above the delta wing. Future work on this topic will focus on the development of methods to separate the different signals.

In Figure 19-26 TSP results are shown of the delta wing with rounded leading edges for different Reynolds numbers and $\alpha = 5°$. The onset of the primary vortex has not taken place at this low angle of attack. The patterns in the TSP results in Figure 19-26 show two different effects leading to a transition from a laminar (bright areas) to a turbulent (dark areas) boundary layer. First, on the front part of the wing the transition line is located inboard of the leading edge; i.e. about 5 – 10% of the root chord length downstream the leading edge. The distance of the transition line from the leading edge slightly reduces downstream, which could be explained by an inboard movement of the free stream attachment line on the pressure side of the wing. Second, in the rear part of the wing a thin black line parallel to the leading edge can be observed. This indicates a closed flow separation caused by the high suction peaks at the rounded leading edge. Caused by this non-effective separation the boundary layer becomes turbulent; i.e. laminar separation and turbulent re-attachment. The TSP results show that the distance of the transition line to the leading edge reduces with increasing Reynolds number. Also the separation line in the rear part is shifted towards the leading edge. This can be also seen in Figure 19-27 showing results from the side view TSP camera.
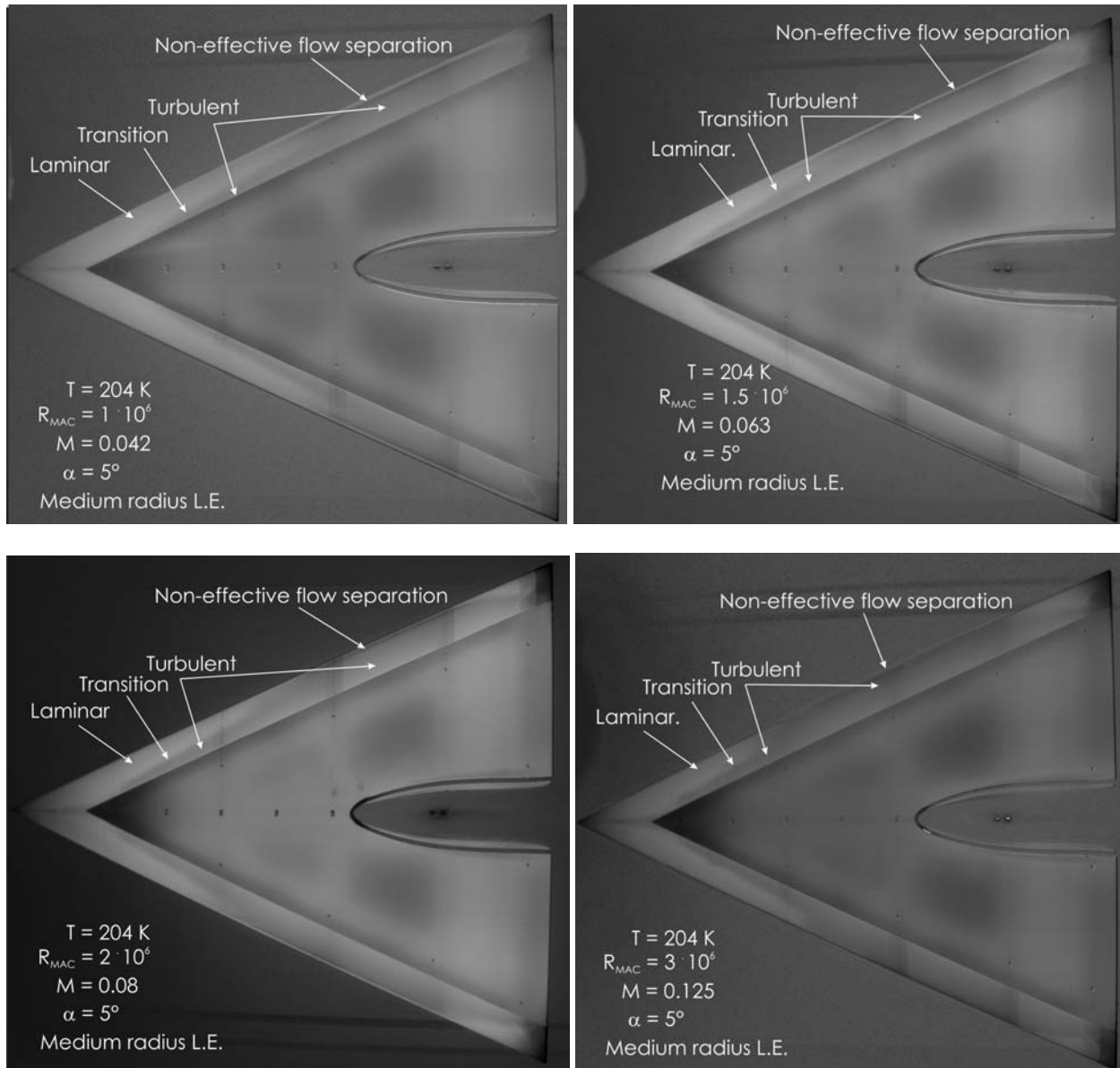
Figure 19-26: TSP Results of the Suction Side of the Delta Wing with Medium Radius Leading Edges at Low Angle of Attack of 5° for Different Reynolds Numbers.
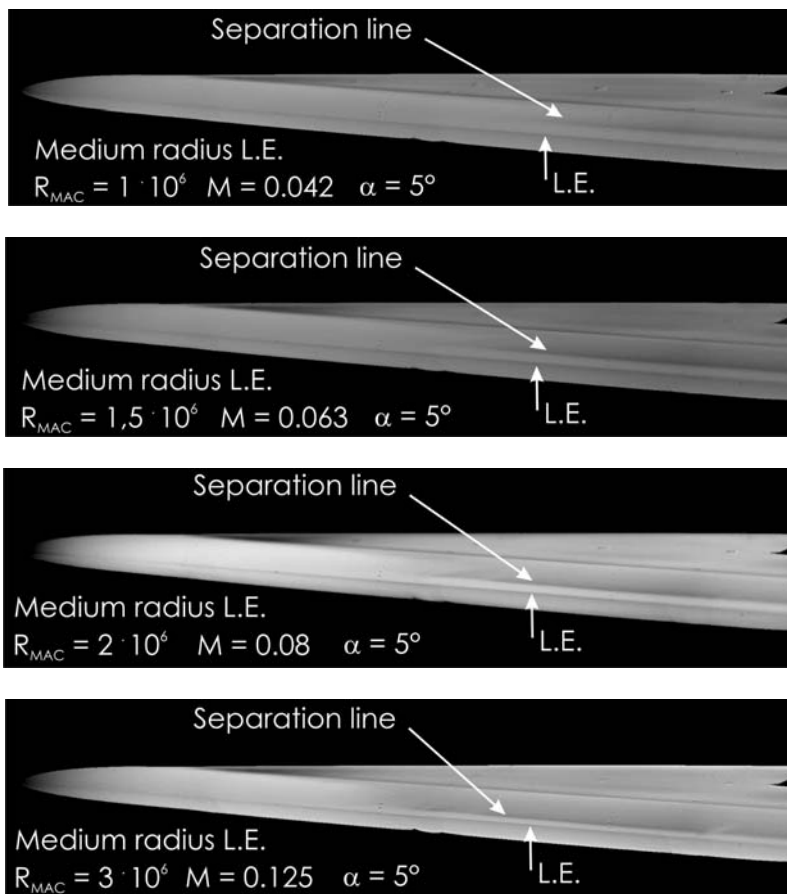
Figure 19-27: TSP Results from the Side View Camera Showing the Distribution along the L.E. of the Port Side of the Delta Wing at an Angle of Attack of 5° and Different Reynolds Numbers.

Because of the relatively low pixel resolution of the IR camera only a part of the wing was captured at one time. However, the camera's high sensitivity allowed for the recording of a complete alpha-sweep within a single run. Selected images of such an alpha sweep are shown in Figure 19-28 for a Reynolds number of $R_{mac} = 2$ million. The features as the development of the transition line on the front part of the delta wing, the non-effective flow separation at the leading edge and the occurrence of the primary vortex are indicated. At low angles of attack only the transition line can be seen which moves towards the leading edge and apex of the wing with increasing angle of attack. For $\alpha > 5°$ a thin black line gets visible in the temperature distribution close to the leading edge which is assumed to be a closed flow separation. The region of this non-effective flow separation moves towards the wing apex with increasing angle of attack accordingly to the increasing suction peaks at the leading edge.
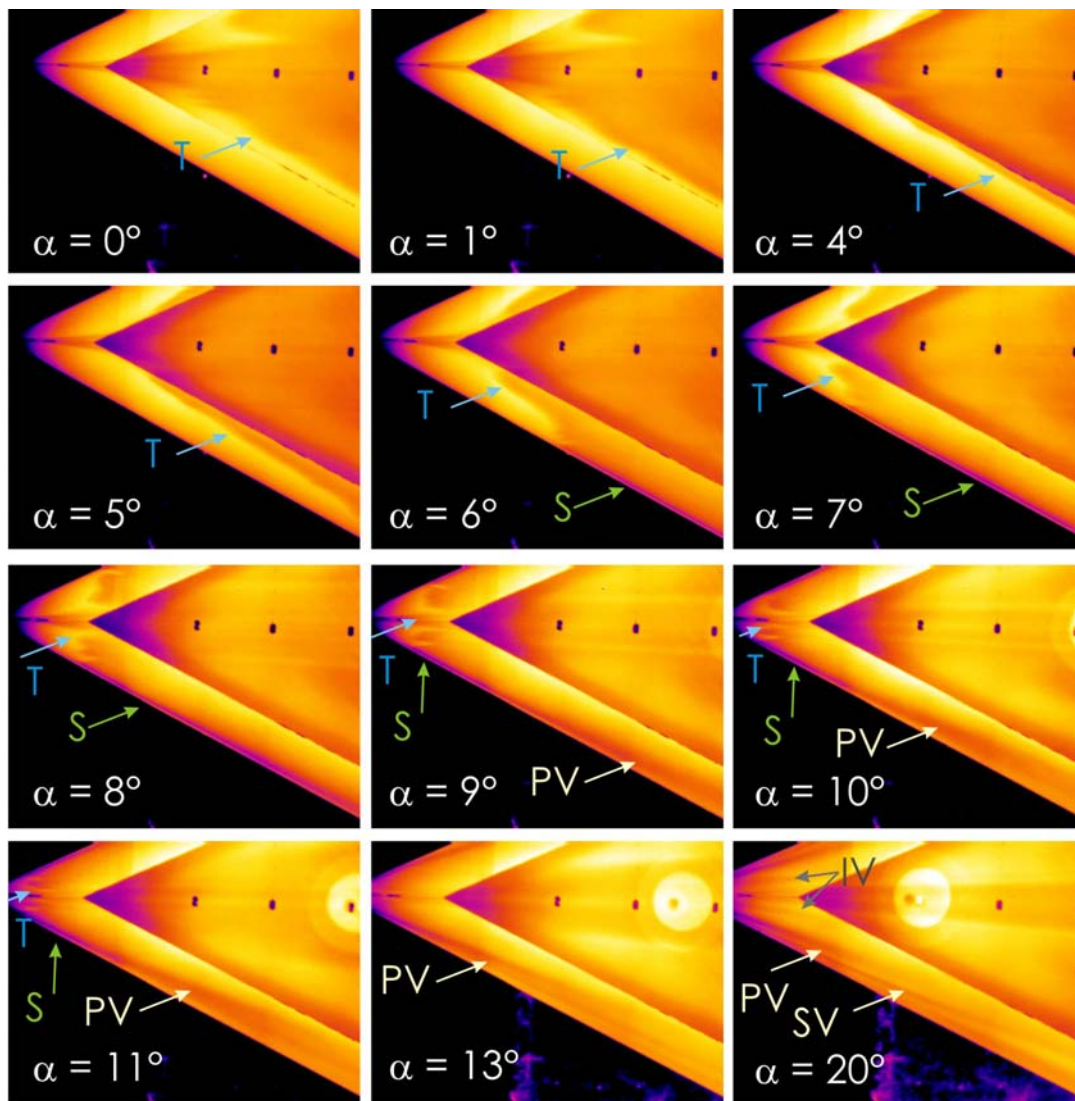
Figure 19-28: IR Results Showing the Temperature Distributions on the Suction Side of the Front Part of the Delta Wing with Rounded Leading Edges for R_{mac} = 2 Million, M = 0.103 (T = 240 K) for Different Angles of Attack. The three dot markers along the center line indicate the chord positions x/c_r = 0.2, 0.3 and 0.4 from left to right. (T) transition line (S) line of closed flow separation (PV) primary vortex (SV) secondary vortex (IV) inner vortex.

At an angle of attack of $\alpha = 9°$ the thin line in the temperature distribution broadens linearly downstream a point located at $x/c_r \cong 0.2$ which can be explained by the occurrence of the primary vortex. It seems that the primary vortex emerges from the closed flow separation; i.e. the non-effective flow separation changes into an effective flow separation forming the primary vortex. With the onset of the primary vortex a re-attachment line will occur inboard the vortex and beneath the vortex an outboard directed flow establishes. It was expected that a laminar boundary layer starts to develop at the re-attachment line and that a transition of the outboard directed flow occurs beneath the primary vortex probably after having passed the adverse pressure gradient [19-10]. Another transition line of the inboard directed flow should then be located somewhere inboard of the re-attachment line. However, no evidence for such a transition line can be seen within the TSP

and IR results. One reason for this could be the fact that the re-attachment line starts at the vortex origin which is located in the region where a closed flow separation occurs and transition takes place. Therefore, the boundary layer at the starting point of the re-attachment line can be assumed to be already turbulent or to be contaminated by turbulent structures. So, it is possible that a turbulent boundary layer develops along the complete re-attachment line of the primary vortex. Poll [19-23][19-24] investigated the transition on an inclined cylinder and observed transition on the attachment line when contaminated by turbulent structures.

Figure 19-29 shows the TSP results from the side view camera for $\alpha = 10°$ and $13°$ and $R_{mac} = 2$ million. The distribution at the leading edge for $\alpha = 13°$ has changed. First, downstream the origin of the primary vortex a dark area extends over the leading edge which indicates that the transition line is now located on the pressure side of the wing and the boundary layer is turbulent before the flow separates to form the primary vortex. Second, another structure can be observed at the apex upstream which is clearly separated from the signal of the primary vortex. This structure could be produced by another vortex, i.e. potentially by an inner vortex as observed in the results of the DNW-TWG measurements. A similar structure can be observed in the temperature distributions of the IR image at $\alpha = 20°$ close to the apex of the wing (Figure 19-28). However, the corresponding PIV results show no clear evidence for an existence of an inner vortex as described in Section 19.3.2. Only at a higher Reynolds number of $R_{mac} = 6$ million a weak inner vortex can be detected at $\alpha = 13°$ (Figure 19-30). Also the position of the primary vortex origin as detected by the PSP results for the TWG measurements (s. Figure 19-8, M = 0.4, $R_{mac} = 2$ million) differs from that as seen in the temperature distributions of the KKK measurements. The primary vortex starts more upstream in the case of the KKK; i.e. the primary vortex starts at $x/c_r \cong 0.15$ for $R_{mac} = 2$ million, M = 0.103 and $\alpha = 10°$ in the case of KKK (s. Figure 19-28) in comparison to an origin position of $x/c_r \cong 0.6$ for $R_{mac} = 2$ million, M = 0.4 and $\alpha = 10.1°$ in the case of TWG (s. Figure 19-7). This can be explained by the slightly different conditions in both wind tunnels, e.g. Mach number, or by small differences in the shape of the wind tunnel models. It was realized that the leading edge shape the TU-Munich deviates slightly from the given geometry resulting in a lower leading edge radius. This is in agreement with the observations mentioned above. The lower leading edge radius causes a more upstream located primary vortex and, therewith, a weaker inner vortical structure (s. Section 19.3.2).
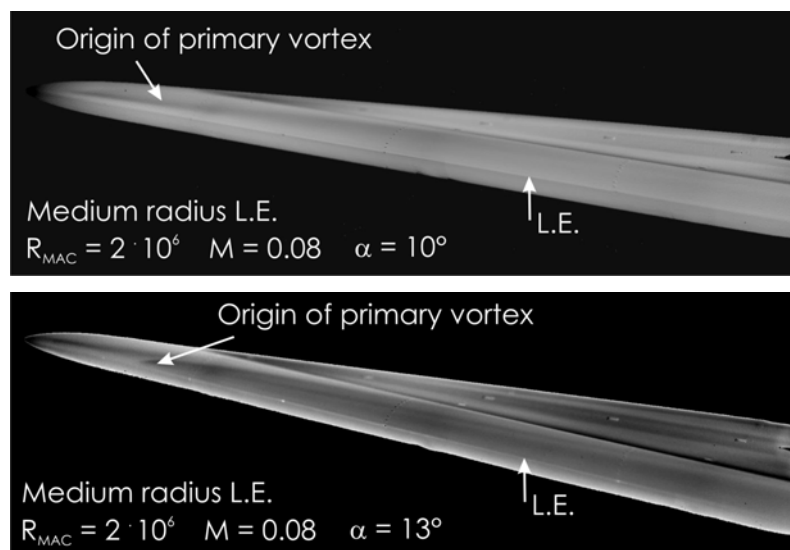
Figure 19-29: TSP Results from the Side View Camera Showing the Distribution along the L.E. of the Port Side of the Delta Wing at an Angle of Attack of 10° and 13°.
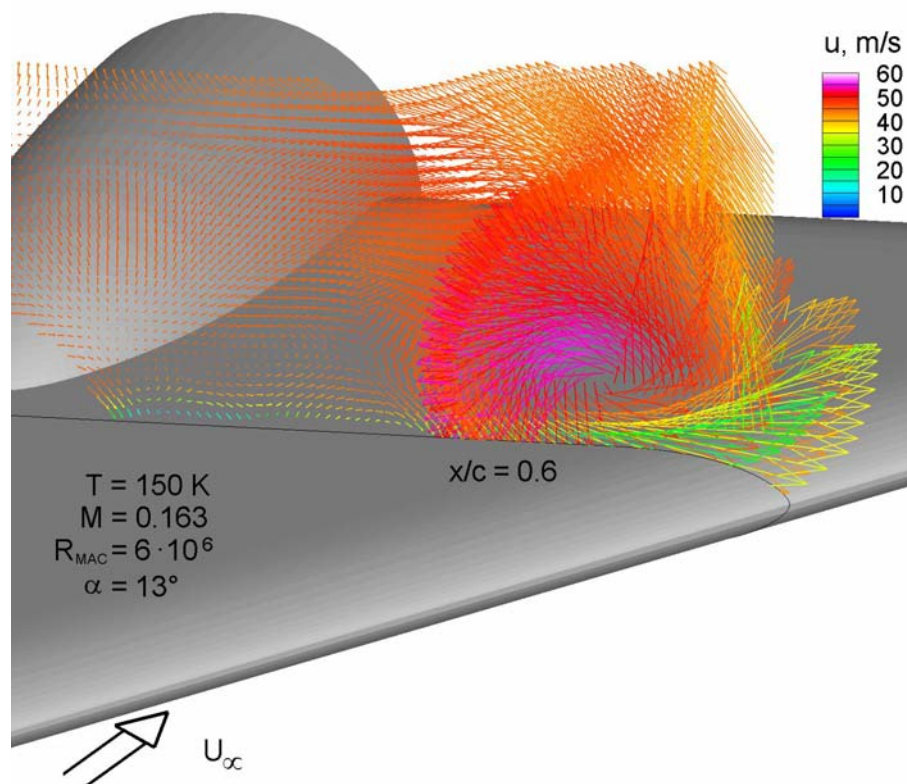
Figure 19-30: Time Averaged Velocity Field above the Delta Wing with Rounded Leading Edges for α = 13.3° and R_{mac} = 6 Million. The color of the vectors corresponds to the out-of-plane velocity.

19.5   CONCLUSIONS

Above the VFE-2 delta wing two different specific flow phenomena were observed in a transonic wind tunnel which could be investigated with the Pressure Sensitive Paint and Particle Image Velocimetry techniques. For the delta wing with rounded leading edges an inner vortical structure occurs above the delta wing at low angles of attack before a primary vortex develops; i.e. with an attached flow at the leading edge. This flat vortical structure develops close to the surface inboard of the leading edge and consists of several co-rotating vortices which increase in size downstream. The circulation strength of this structure increases with increasing angle of attack and seems to be in-sensitive to the Reynolds number as long as the onset of the outer primary vortex has not taken place. The flow at the rounded leading edge separates effectively at a specific angle of attack and a primary vortex is formed. The leading edge separation is promoted with reducing Reynolds number or increasing Mach number. Therewith, the origin of the primary vortex origin moves upstream. The occurrence of the primary vortex leads to a detachment of the outboard located vortices of the inner vortical structure. A new circular inner vortex is formed downstream the origin of the primary vortex. Both co-rotating vortices remain separated downstream. However, vorticity is fed only into the outer primary vortex so that the inner vortex keeps its size and decreases slightly in circulation strength downstream by viscous effects. At the beginning the flow re-attaches and again separates form the surface between both vortices. Further downstream a stagnation point can be observed in the cross flow fields such that an outboard directed flow exists at the surface underneath and between both vortices. Since vorticity is fed into the inner vortical structure only upstream the primary vortex the circulation strength of the inner vortex decreases with an upstream movement of the primary vortex; i.e. with

increasing angle of attack and decreasing Reynolds number. This probably is the reason why the inner vortex could not be observed for the delta wing with sharp leading edges where the flow separation is fixed at the leading edge and the primary vortex starts always close to the wing apex.

In the transonic case the flow field above the delta wing reaches supersonic speeds which lead to the formation of cross-flow and terminating shock waves. The results show at high angles of attack a sudden change of the surface pressure distributions within a range of increase of the angle of attack of only 0.2°. The velocity distributions show that a vortex breakdown occurs above the delta wing at about 65% of the root chord. This could be explained by an interaction between shock waves and the primary vortex. One terminating shock wave could be detected using the pressure distributions in front of the sting fairing; i.e. at about 55% of the root chord.

The activities within VFE-2 show also useful interactions between computational and experimental disciplines. After the first measurement campaign the PSP distributions clearly show the footprints of two separate suction peaks. However, the PSP results do not answer the question which flow produces the inner peak. On basis of the PSP result parameters for flow computation could be optimized (Fritz, EADS Munich) and the inner vortex came out. In turn the CFD result could be used for setting up parameters of the flow field investigation by means of PIV which verifies the CFD result. However, the CFD computations show a strong sensitivity against the location of transition. This leads to the performance of IR and TSP measurements for which first results are available.

19.6   ACKNOWLEDGEMENTS

19.7   REFERENCES

[19-1]   Carmer, C.F. von, Konrath, R., Schröder, A. and Monnier, J.-C.: *Identification of Vortex Pairs in Aircraft Wakes from Sectional Velocity Data*, Exp. Fluids 44: 367-380, 2008.

[19-2]   Chu, J. and Luckring, J.M.: *Experimental Surface Pressure Data Obtained on 65° Delta Wing Across Reynolds Number and Mach Number Ranges*, NASA TM 4645, 1996.

[19-3]   Drougge, G.: *The International Vortex Flow Experiment for Computer Code Validation*, ICAS-Proceedings 1988, Vol. 1, pp. XXXV-XLI, 1988.

[19-4]   Egami, Y., Fey, U., Klein, Chr., Sitzmann, M. and Wild, J.: *Transition Detection on High-Lift Devices in DNW-KKK by Means of Temperature Sensitive Paint*, Proc. of 12th International Symp. on "Flow Visualization", [CD-ROM], Göttingen, 2006.

[19-5]   Elsenaar, A., Hjelmberg, L., Bütefisch, K.-A. and Bannink, W.J.: *The International Vortex Flow Experiment*, AGARD-CP-437, Vol.1, pp. 9-1 to 9-23, 1988.

[19-6]   Elsenaar, A. and Bütefisch, K.-A.: *Experimental Study on Vortex and Shock Wave Development on a 65° Delta Wing*, Proc. IUTAM Symposium Transonicum III, Göttingen, 1988.

[19-7]   Görtz, S. and Rizzi, A.: *Computing the High-Alpha Aerodynamics of Delta Wings – Evaluation and Analysis*, AIAA Paper 01-0115, 2001.

[19-8]   Hilgenstock, A. and Vollmers, H.: *On the Simulation of Compressible Turbulent Flows Past Delta Wing, Delta Wing-Body and Delta Wing-Canard*, AGARD-CP-494, pp. 7-1 to 7-13, 1991.

[19-9]   Hummel, D. and Redeker, G.: *A New Vortex Flow Experiment for Computer Code Validation*, RTO AVT Symposium on "Vortex Flow and High Angle of Attack Aerodynamics", Loen, Norway, 7-11 May 2001, Meeting Proceedings RTO-MP-069 (I), SYA 8-1 to 8-31, 2003.

[19-10] Hummel, D.: *Effects of Boundary Layer Formation on the Vortical Flow Above Slender Delta Wings*, RTO Specialists' Meeting on "Enhancement of NATO Military Flight Vehicle Performance by Management of Interacting Boundary Layer Transition and Separation", Prague, Czech Republic, 4-7 October 2004, Meeting Proceedings RTO-MP-AVT-111, pp. 30-1 to 30-22, 2004.

[19-11] Hummel, D.: *The Second International Vortex Flow Experiment (VFE-2) – Objectives and First Results*, Proceedings of the 2nd International Symposium on "Integrating CFD and Experiments in Aerodynamics", Cranfield University (Shrivenham), UK, 5-6 September, pp. 1-12, 2005.

[19-12] Iijima, Y., Egami, Y., Nishizawa, A., Asai, K., Fey, U. and Engler, R.H.: *Optimization of Temperature-Sensitive Paint Formulation for Large-Scale Cryogenic Wind Tunnels*, Proc. of 20th International Congress on "Instrumentation in Aerospace Simulation Facilities (ICIASF)", Göttingen, Germany, pp. 70-76, 2003.

[19-13] Klein, C., Engler, R.H., Henne, U. and Sachs, W.: *Application of Pressure-Sensitive Paint for Determination of the Pressure Field and Calculation of the Forces and Moments of Models in a Wind Tunnel*, Exp. Fluids 39: 475-483, 2005.

[19-14] Klein, C., Sachs, W., Henne, U., Engler, R.H., Wiedemann, A. and Konrath, R.: *Development of PSP Technique for Application on the VFE-2 65° Delta Wing Configuration in Sub- and Transonic Flow*, AIAA-Paper 2006-0059, 2006.

[19-15] Kompenhans, J., Agocs, J., Egami, Y., Engler, R., Fey, U., Frahnert, H., de Groot, K., Henne, U., Kirmse, T., Klein, Ch., Klinge, F., Konrath, R., Mattner, H., Otter, D., Pallek, D., Sachs, W., Schröder, A. and Stasicki, B.: *Recent Developments of Image Based Measurement Methods for Application to Transonic Flows in Industrial Wind Tunnels*, ZHU, Zi-qiang [Ed.]: Chinese Journal of Aeronautics, EWHSFF2005, Vol. 19 (No. 2), AAAS, S. 115-125, ISBN CN 11-1732/V, ISSN 1000-9361, 2006.

[19-16] Konrath, R., Klein, C., Engler, R.H. and Otter, D.: *Analysis of PSP Results Obtained for the VFE-2 65° Delta Wing Configuration at Sub- and Transonic Speed*, AIAA-Paper 2006-0060, 2006.

[19-17] Konrath, R., Schröder, A. and Kompenhans, J.: *Analysis of PIV Results Obtained for the VFE-2 65° Delta Wing Configuration at Sub- and Transonic Speeds*, AIAA-Paper 2006-3003, 2006.

[19-18] Konrath, R., Klein, C., Schröder, A. and Kompenhans, J.: *Combined Application of Pressure Sensitive Paint and Particle Image Velocimetry to the Flow Above a Delta Wing*, Exp. Fluids 44: 357-366, 2008.

[19-19] Konrath, R., Klein, C. and Schröder, A.: *PSP and PIV Investigations on the VFE-2 Configuration in Sub- and Transonic Flow*, AIAA-Paper 2008-379, 2008.

[19-20] Luckring, J.M.: *Reynolds Number, Compressibility, and Leading-Edge Bluntness Effects on Delta-Wing Aerodynamics*, ICAS Proceedings, Paper 4.1.4, 2004.

[19-21] Luckring, J.M.: *Compressibility and Leading-Edge Bluntness Effects for a 65° Delta-Wing*, AIAA Paper 2004-0765, 2004.

[19-22] Morton, S.A., Forsythe, J.R., Mitchell, A.M. and Hajek, D.: *Detached-Eddy Simulations and Reynolds-Averaged Navier-Stokes Simulations of Delta Wing Vortical Flowfields*, AIAA Paper 2002-0587, 2002, and J. Fluids Eng. Vol. 124, No. 4, pp. 924-932, 2002.

[19-23] Poll, D.I.A.: *Some Observations of the Transition Process on the Windward Face of a Long Yawed Cylinder*, J Fluid Mech., Vol. 150, pp. 329-356. 1985.

[19-24] Poll, D.I.A.: *Transition in the Infinite Swept Attachment Line Boundary Layer*, The Aeronautical Quarterly, Vol. 30, Cranfield, pp. 607-629. 1979.

[19-25] Schiavetta, L., Boelens, O.J. and Fritz, W.: *Analysis of Transonic Flow on a Slender Delta Wing Using CFD*, AIAA-Paper 2006-3171, 2006.

[19-26] Schröder, A., Agocs, J., Frahnert, H., Otter, D., Mattner, H., Kompenhans, J. and Konrath, R.: *Application of Stereo PIV to the VFE-2 65° Delta Wing Configuration at Sub- and Transonic Speeds*, AIAA-Paper 2006-3486, 2006.

[19-27] Wedemeyer, E.: *Vortex Breakdown*, Proc. AGARD-LS-121, High Angle of Attack Aerodynamics, pp. 9-1 to 9-17, 1982.

Chapter 20 – EXPERIMENTAL INVESTIGATIONS ON THE VFE-2 CONFIGURATION AT ONERA, FRANCE

by

Ovide Rodriguez

20.1   NOTATIONS

U	velocity
u, v, w	components of U in (ξ,η,ζ) reference frame
U_∞	freestream velocity
U_1	velocity component in a plan parallel to the wing $(U_1^2 = u^2+v^2)$
ω_R	vorticity
ϕ	Euler angle in rotation around x-axis
C_Y	lateral force coefficient
C_N	yaw moment coefficient

20.2   INTRODUCTION

Although the flow topology over high sweep delta wing has been extensively studied and is now reasonably well understood [20-1], [20-2], [20-3], [20-4], a complete knowledge of the influence of the vortical flow on the obstacle generating it, and in particular of the local induced unsteady effects, is to be acquired for moderated and high incidences. Furthermore, the CFD solutions for rounded leading edges did not well predict the measured surface-pressures and some improvements are still needed on the prediction of unsteady effects. Therefore there is a significant need to establish complementary data bases allowing to focus mainly on the unsteady flow properties, both on the obstacle and in the flowfield for which available data are less documented. As a consequence CFD prediction of these flows should be improved.

Present works were carried out within the RTO AVT-113-VFE2 framework entitled 'Understanding and Modelling Vortical Flows to Improve the Technology Readiness Level for Military Aircraft' which aimed at a better understanding of the vortical flow physics, at completing existing data bases and improving their prediction by CFD. They are based on using a unique 65° symmetrical delta wing geometry common for all members of the task group. This delta wing model can be equipped with various leading edges ranging from sharp to rounded. It has already been tested in NTF and LTPT NASA wind tunnels over a wide range of Reynolds numbers, Mach numbers and angles of attack. Results are available in a pre-existent data set [20-5].

This chapter presents the ONERA experimental contribution to VFE-2, restricted to low speed tests ($Re_{mac} = 10^6$, M = 0.133) carried out at the Lille center, in the L1 ONERA wind tunnel:

- Steady pressure measurements on the obstacle with the model previously tested in LTPT and lent by NASA to ONERA, in order to validate the tests in L1.

- Aerodynamic forces and moments measurement by using a gauge balance, what had not been done up to now with the NASA model, especially for the drag.

- Characterisation of the velocity field by PIV when the vortex breakdown point is located on the obstacle approximately at mi-cord.

Experiments were conducted both for 'sharp' and 'medium' leading edges. The NASA model tested in LTPT is provided with numerous static pressure taps. Connections are made with nickel tubes which length and stiffness are not appropriate to a balance use under acceptable uncoupling conditions. So, two resin one-piece reproductions of the NASA models were manufactured at ONERA fitted out with a 'sharp' and a 'medium' leading edge respectively. Aerodynamic forces and moments and velocity fields by PIV were recorded with these models. Within the framework of the RTO AVT-113 Group these two models have been lent by ONERA to Tubitak-Sage (Turkey). Tests have been performed during three different campaigns. Tests using the NASA model were conducted in solid walls configuration so as to ensure boundary conditions as similar as possible to LTPT ones, and were restricted to the measurement of static pressure distributions on the obstacle. On the other hand tests using the ONERA models were performed for different boundary conditions, i.e. in solid walls and in open jet tunnel. In solid walls forces were measured and the velocity field was characterised by PIV whereas in open jet test section only polars were recorded. These data should bring some insight onto the effect of a modification of farfield boundary conditions. All the experimental results are provided into numerical data files in Appendix 3-4.

According to VFE-2 common notations NASA model is named Model 1, sharp and medium leading edge ONERA models are respectively named Model 4 and Model 5.

20.3 EXPERIMENTAL SET UP

20.3.1 L1 Wind Tunnel

The tests were conducted in ONERA Lille L1 wind tunnel. The facility is a closed circuit wind tunnel working in the incompressible domain. The test section is axisymmetrical 2.40 m in diameter and 2.40 m long. Walls are movable so that it is possible to operate in solid walls or in open jet tunnel. The maximum freestream velocity is 75 m/s in solid walls and 60m/s in open jet test section. The turbulence rate is 1.3%. No wall corrections were applied.

20.3.2 Model 1

The NASA model is a 65° swept symmetrical flat plate delta wing, $c_r = 0.49023$ m in root chord. It can be equipped with four interchangeable leading edges. Surfaces are represented by a fully analytical function. The different leading edges are named 'sharp', 'small', 'medium' and 'large' and are defined by their respective curvature radius $r/\bar{c} = 0, 0.05, 0.15$ and 0.30. As previously mentioned only 'sharp' and 'medium' leading edges are considered here. The model is provided with static pressure ports located on the lower surface and on the upper surface at $\xi = 0.2, 0.4, 0.6, 0.8$ and 0.95. In addition, orifices were located on both the port and the starboard 'medium' leading edges. A more detailed description of the model is given in [20-5] and [20-6]. A sketch of the model and a view in the test section are provided in Figure 20-1.
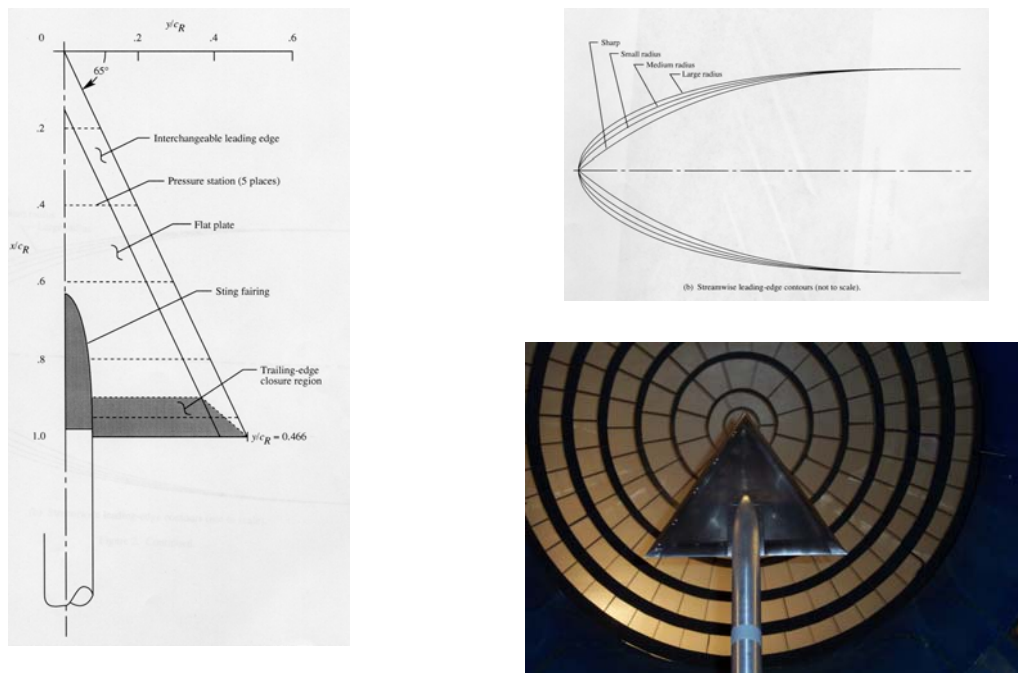
Figure 20-1: Sketches of Model 1 (from [20-5]) and View in Test Section.

20.3.3   Models 4 and 5

In order to perform forces and moments measurements under acceptable uncoupling conditions two resin one-piece copies of the 'sharp' and 'medium' NASA models were manufactured. The equipment of these models was reduced as far as possible. Every model was provided with 10 pressure taps located such that comparisons with LTPT data could be possible (Figure 20-2).Two accelerometers allowed the incidence measurements to be checked. A geometrical control of both shapes and pressure ports location has been made on NASA and ONERA models. Shapes were measured along three chord stations situated at $\Delta x = 98.23$ mm, 196.23 mm and 392.23 mm from the apex. Results have been compared to the analytical functions and are reported on Table 20-1. It can be observed that discrepancies are of same order when comparing Model 1 and Model 5 with the theoretical shapes. But Model 4 variations are twice Model 1 ones. These differences can be attributed to the fact that Model 4 and 5 are made out of resin. Their amplitudes however remain bounded within acceptable limits. Pressure ports locations are reported in Table 20-2. Discrepancy is higher for Model 4 and 5, but if the extreme cases are eliminated, differences are of same order than Model 1 ones.
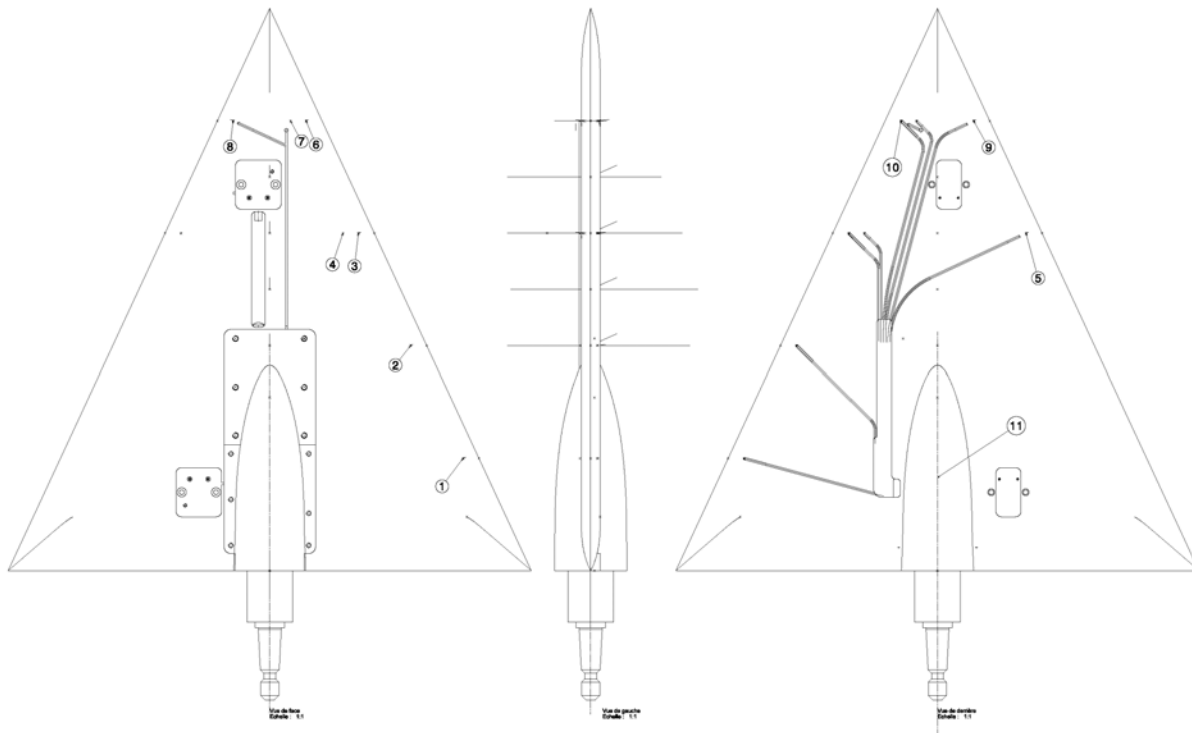
Figure 20-2: Sketch of Model 4 and 5 with Pressure Ports Locations.

**Table 20-1: Geometrical Discrepancy along Three Chord Sections between
Each Model and the Analytical Shape: Maximum Variations in mm**

Chord Section		Model 1 Sharp	Model 1 Medium	Model 4	Model 5
x = 98.23 mm	Δz max(+)	0.147	0.162	0.278	0.245
	Δz min(-)	0.147	0.123	0.234	0.235
x = 196.23 mm	Δz max(+)	0.181	0.234	0.278	0.143
	Δz min(-)	0.204	0.157	0.22	0.125
x = 392.23 mm	Δz max(+)	0.112	0.206	0.217	0.216
	Δz min(-)	0.096	0.186	0.181	0.142

**Table 20-2: Geometrical Discrepancy of Pressure Port Locations
Reduced by the Diameter d = 0.3 mm of the Orifice**

	Model 1 Sharp	Model 1 Medium	Model 4	Model 5
Theoretical Location (mm)	δl/d =	δl/d =	δl/d =	δl/d =
x = 98.04; y = 32.00 (lower s.)			1.7013	2.3393
x = 98.04; y = -32.00 (lower s.)	0.4028	0.7951	1.6826	3.1525
x = 98.04; y = -32.00			1.2257	1.1324
x = 98.04; y = 18.29	0.7923	1.1823	1.7754	0.8750
x = 98.04; y = 32.00	0.3887	0.9718	1.6275	0.7775
x =196.08; y = -77.72 (lower s.)			1.4380	1.8406
x = 196.08; y = 64.01	1.1035	1.7745	1.4896	0.5000
x = 196.08; y = 77.72	0.4123	0.7063	1.1557	0.3819
x = 294.13; y = 123.43	1.0022	1.3342	0.8800	0.3801
x = 392.17; y = 169.16	0.9672	1.1126	0.5831	6.4849

20.4   RESULTS

20.4.1   Model 1 in Solid Walls Configuration

20.4.1.1   Test Section Apparatus

The NASA sting supplied with the model was too long and too heavy to be easily fitted to the L1 structure. So the model in L1 was supported by a sting rigidly locked underneath the test section with a trolley moving along a hemi circular cradle. This set up provided two degrees of freedom in rotation, allowing imparting incidence and side-slip to the model. The displacement in incidence of the trolley being limited within ±15° it was not possible to cover the entire incidence range within the same run. So a metallic arm provided with a movable part held the sting line in position, so as to cover the incidence range within two runs, from -5° to 15°, and then from 13° to 40° after taking away the movable part. The accuracy was 0±0.15° in rolling and 0±0.1° in incidence and slide-slip. The fairing was geometrically similar to the NASA fairing (Figure 20-3).
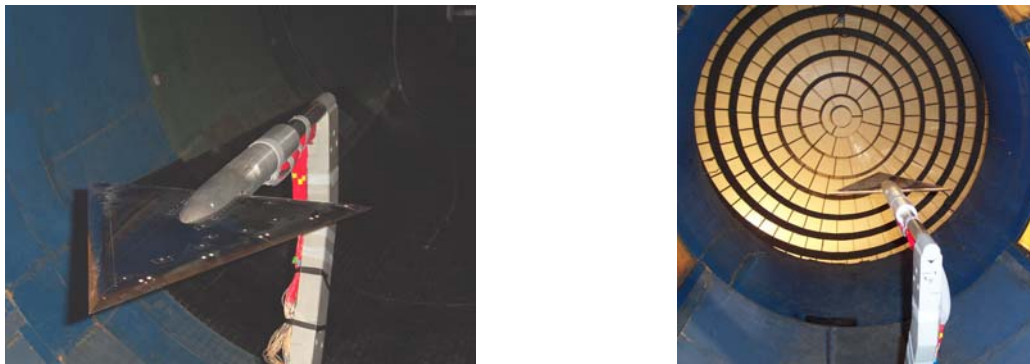
Figure 20-3: Views of the Model 1 in Test Section.

20.4.1.2   Tests

Static pressures were transmitted from the obstacle to PSI modules. A 25s time interval for propagation and 15s for stabilization had been estimated during calibration. A 60s time interval for stabilization was retained during tests. Signals were filtered at 2 Hz and averaged on 100 points before recording. The sampling rate was 10 Hz. Due to high number of pressure ports, it was not possible to record all the signals simultaneously. Therefore the different braids were successively connected to the sensors, and for a given configuration of connected pressure taps the whole incidence range was investigated before proceeding to the others braids. From three to four cablings were necessary to record all the pressures relative to each leading edge. Some blocked pressure taps were identified during the phase of numbering ports. They were kept off during the tests. Some others presenting an unusually long time for stabilization were identified but nevertheless taken into account for measurements. They deliver pressure levels very different from their neighbouring, are in that way easily recognizable and therefore have to be neglected.

20.4.1.3   Results

For each leading edge, pressure distributions at upper surface are presented in Figure 20-4 and Figure 20-5 for $5° \leq \alpha \leq 30°$ with a step of 5°, except for the 'sharp' for which LTPT data base is limited at $\alpha = 28°$. For the 'medium', surface-pressures at L1 from the inboard part of the wing at station $\xi = 0.60$ and over the entire span at station $\xi = 0.95$ exhibited a great shift when comparing with LTPT ones. These discrepancies were attributed to an offset effect and as a consequence are not reported on Figure 20-4 and Figure 20-5.
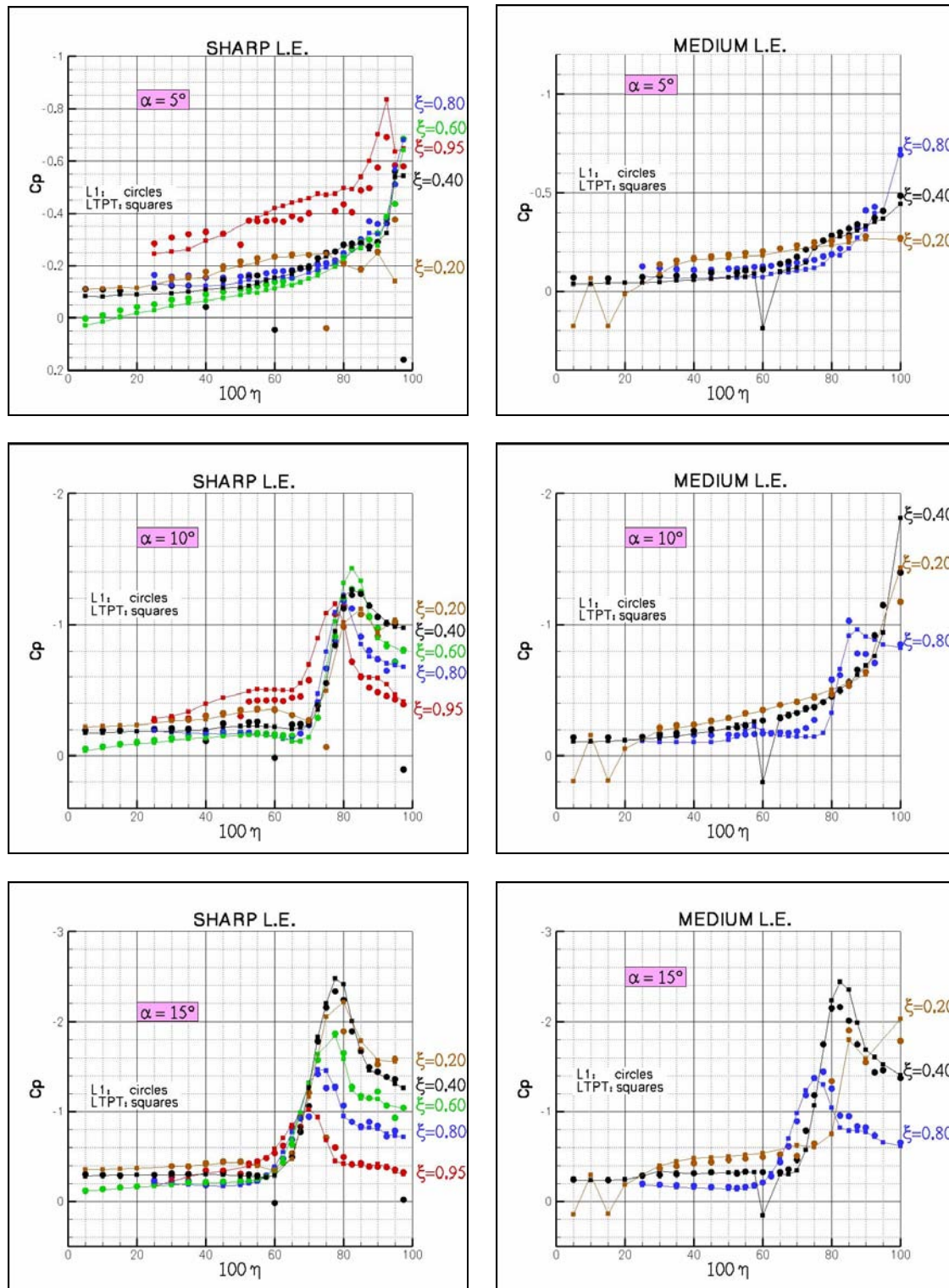
**Figure 20-4: Pressure Distributions on Model 1 Upper Surface – Solid Walls (Sharp: $Re_{mac} = 10^6$ at L1;
$Re_{mac} = 1.5 \times 10^6$ at LTPT – Medium: $Re_{mac} = 10^6$ at L1; $Re_{mac} = 2 \times 10^6$ at LTPT).**
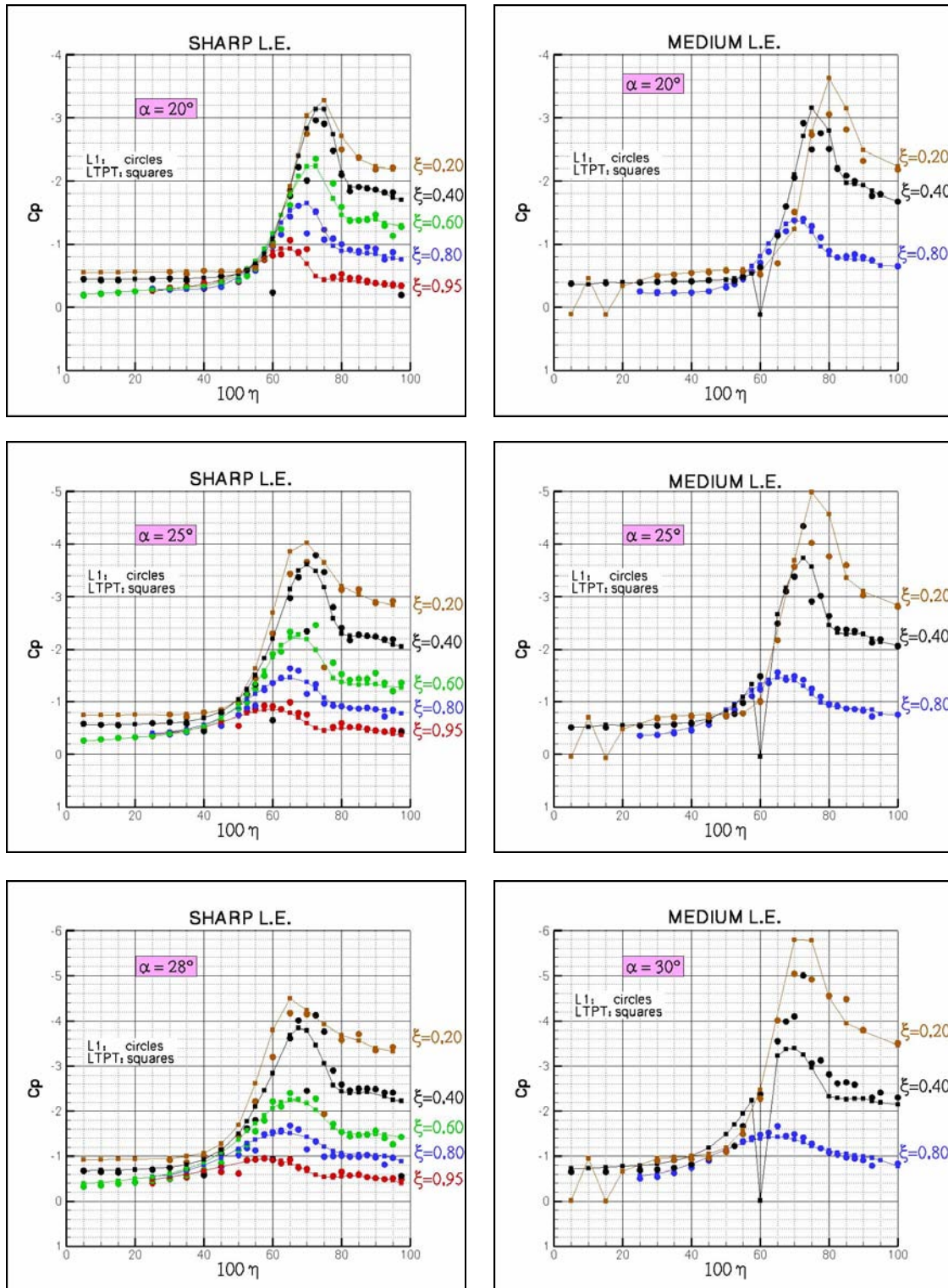
Figure 20-5: Pressure Distributions on Model 1 Upper Surface – Solid Walls (Sharp: $Re_{mac} = 10^6$ at L1; $Re_{mac} = 1.5 \times 10^6$ at LTPT – Medium: $Re_{mac} = 10^6$ at L1; $Re_{mac} = 2 \times 10^6$ at LTPT).

At α = 5° variations ΔC_p ~ 0.05 are observed for the 'sharp', the flow over nearly all the wing being at L1 slightly accelerated compared to LTPT. These differences remain small, of order 2% to 3% of the upstream velocity, except near the leading edge where they are somewhat higher. At the same incidence variations are slightly reduced for the 'medium'.

At α = 10° the' sharp' leading edge produces pressure distributions in rather good agreement with LTPT ones, except that the station ξ = 0.95 exhibits a $\Delta C_p \approx 0.1$ more or less constant. Pressure peaks induced by the primary vortex are relatively well reproduced. For the 'medium' the pressure distributions are also very similar to the LTPT ones except at ξ = 0.80 where variations $\Delta C_p \approx 0.1$ are recorded on the outer part of the wing corresponding to η>0.70. It can be observed that separation did not move upstream to the apex and that the primary vortex locates downstream the station ξ = 0.40 both at L1 and LTPT.

At α = 15° the' sharp' leading edge provides results relatively similar to LTPT ones, with a suction peak slightly underestimated at ξ = 0.20, which could be eventually attributed to a small lateral shift of the vortex axis on upper surface. For the 'medium' results relative to the pressure peak level of the primary vortex exhibit a maximum variation $\Delta C_p \approx 0.2$ observed at ξ = 0.40. It is clear that the differences in Reynolds numbers between the two experiments can play a role and partly explain these discrepancies.

At α = 20° L1 and LTPT pressure distributions are rather similar for both leading edges. Primary vortex is correctly captured in position and amplitude. As previously observed 'medium' distributions exhibit differences a little bit more pronounced in the vortex peak, at stations ξ = 0.20 and 0.40.

For $\alpha \geq 25$° the same trends are observed with variations for the 'medium' becoming more intense in the suction peak.

A good agreement is obtained between L1 and LTPT when comparing the lower surface pressure distributions. This is observed upon nearly all the wing except the station ξ = 0.95 where small variations decreasing with α are recorded between 5° and 25° (Figure 20-6). The gradual displacement of separation toward the apex can be deduced from an analysis of pressures transmitted from ports located along the leading edge [20-7]. Propagation of separation induces a pressure increase characterised by a bump in $C_p(\alpha)$ graph. Separation moves upstream to the apex when incidence increases (Figure 20-7). As a general rule peak pressure levels are lower at L1. Furthermore, while peaks at ξ = 0.40 and ξ = 0.60 are recorded for the same values of incidence in the two wind tunnels, a shift of about 1° incidence exists at ξ = 0.20, 0.80 and 0.95. Variations in these very high gradients zones could be attributed to a Reynolds number effect.
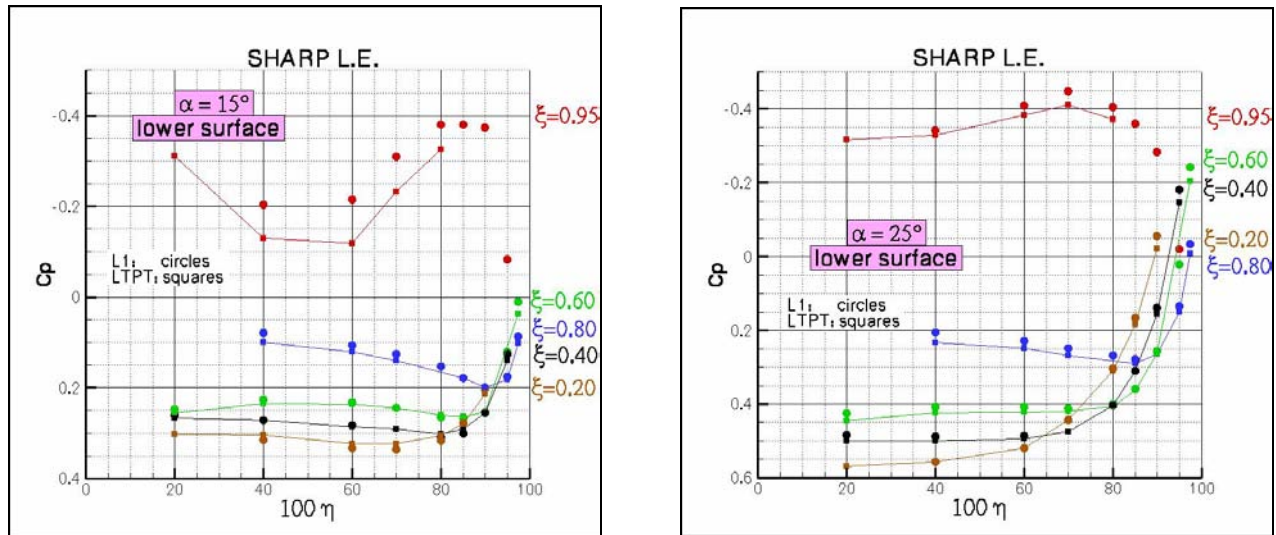
Figure 20-6: Pressure Distributions on Model 1 Lower Surface
(Sharp: $Re_{mac} = 10^6$ at L1; $Re_{mac} = 1.5 \times 10^6$ at LTPT).
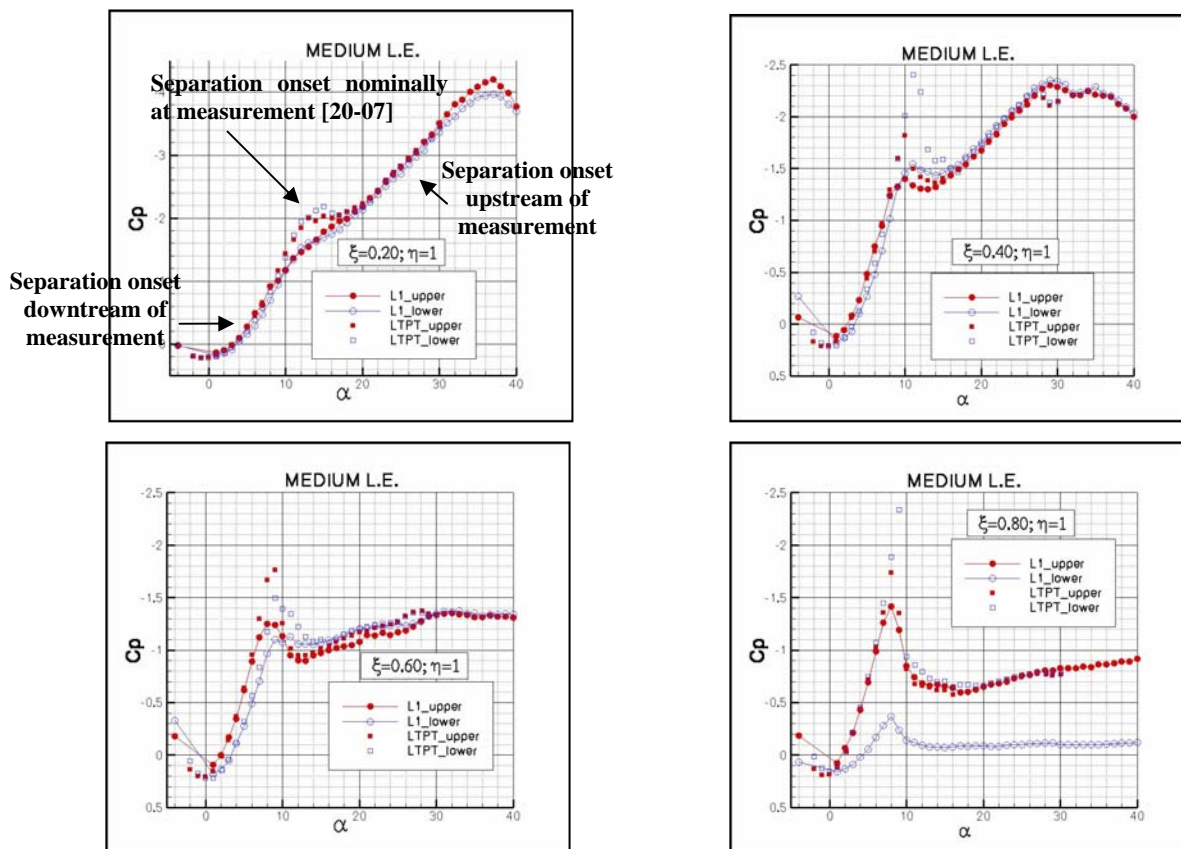
Figure 20-7: Pressure Distributions along the Model 1 Leading Edges. Correlation of separation onset with pressure distribution according to J.M. Luckring [20-7] (Medium: $Re_{mac} = 10^6$ at L1; $Re_{mac} = 2 \times 10^6$ at LTPT).

20.4.2   Forces Measurement in Open Jet Tunnel (Model 4 and 5)

These tests can be seen as an attempt to estimate the influence of variations of the boundary conditions. An analysis of that influence on torque is made in the following paragraph, where results are compared with those obtained in solid walls. Tests were carried out with Model 4 and 5. Models were held by a specific carbon sting (Figure 20-8). The Reynolds number was $Re_{mac} = 10^6$ and incidence range $0° \le \alpha \le 35°$. Polars were recorded while incidence was continuously increasing at $1°$/s, $2°$/s or $3°$/s. These measurements were then compared for validation to those recorded when the obstacle was held fixed in position, for some points between 0° and 30°.
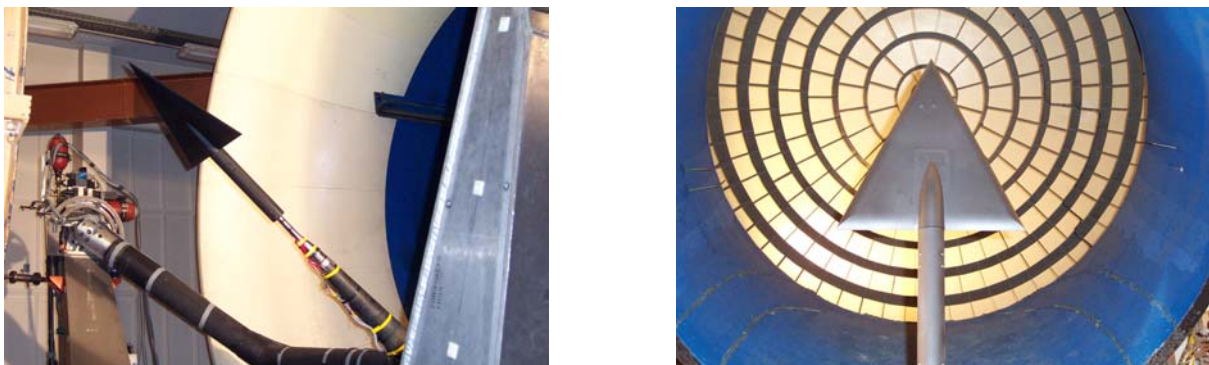
Figure 20-8: Views of Model 4 and 5 in the Open Jet Tunnel.

The wind tunnel upwash and sidewash were estimated by turning the model round the ξ-axis. In that way, two tests at $\phi = 0°$ and $\phi = 180°$ allowed to assess the upwash from lift analysis. Similar tests at $\phi = -90°$ and $\phi = +90°$ allowed to assess the sidewash. Figure 20-9 shows that there was no upwash. However a slight dissymmetry on the yaw moment increasing with incidence reveals the existence of a negative side-slip. When the wing is adjusted at $\phi = \pm90°$ a symmetrical lateral force is recorded with a positive lift if $\phi = +90°$, which corroborates the previous side-slip (Figure 20-10).Using the value $dC_L/d\alpha = 0.0425$ deduced from the lift curve of the 'sharp' leading edge for instance, and considering that amplitude of lift at $\phi = \pm90°$ is about 0.01 for $\alpha = 20°$, it can be estimated that the side-slip is about -0.2° at $\alpha = 20°$.
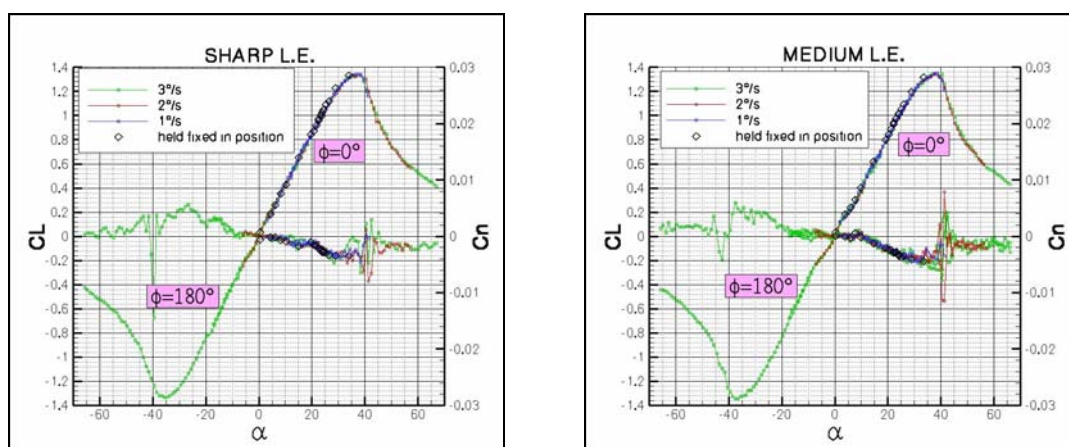
Figure 20-9: Lift and Yaw Moment Coefficients in Open Tunnel (Model 4 and 5).
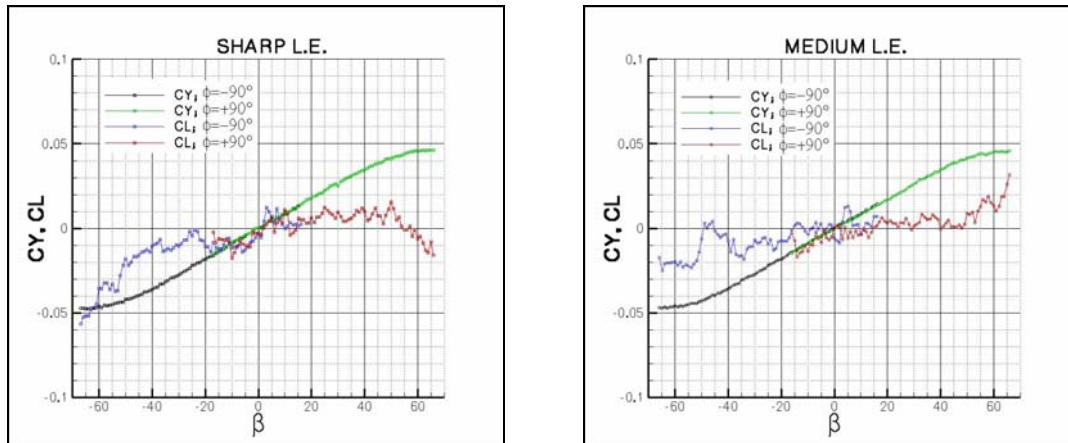
Figure 20-10: Lift and Lateral Force Coefficients in Open Jet Tunnel
when the Wing Undergoes $\phi = \pm90°$ Rotations (Model 4 and 5).

A good agreement is obtained between results relative to the different rates of incidence sweep on the one hand, and those recorded for fixed positions on the other hand (Figure 20-9 and Figure 20-11). Lift and drag curves are symmetric, at least up to stall. Lift is zero at $\alpha = 0°$ as expected and shows a good linearity on the range $0° \leq \alpha \leq 30°$ with $dC_L/d\alpha \approx 0.042$. $C_L$max is reached for $\alpha \approx 39°$ and is close to 1.35. Forces in the balance reference frame are commented in the next paragraph where they are compared with results obtained in solid walls.
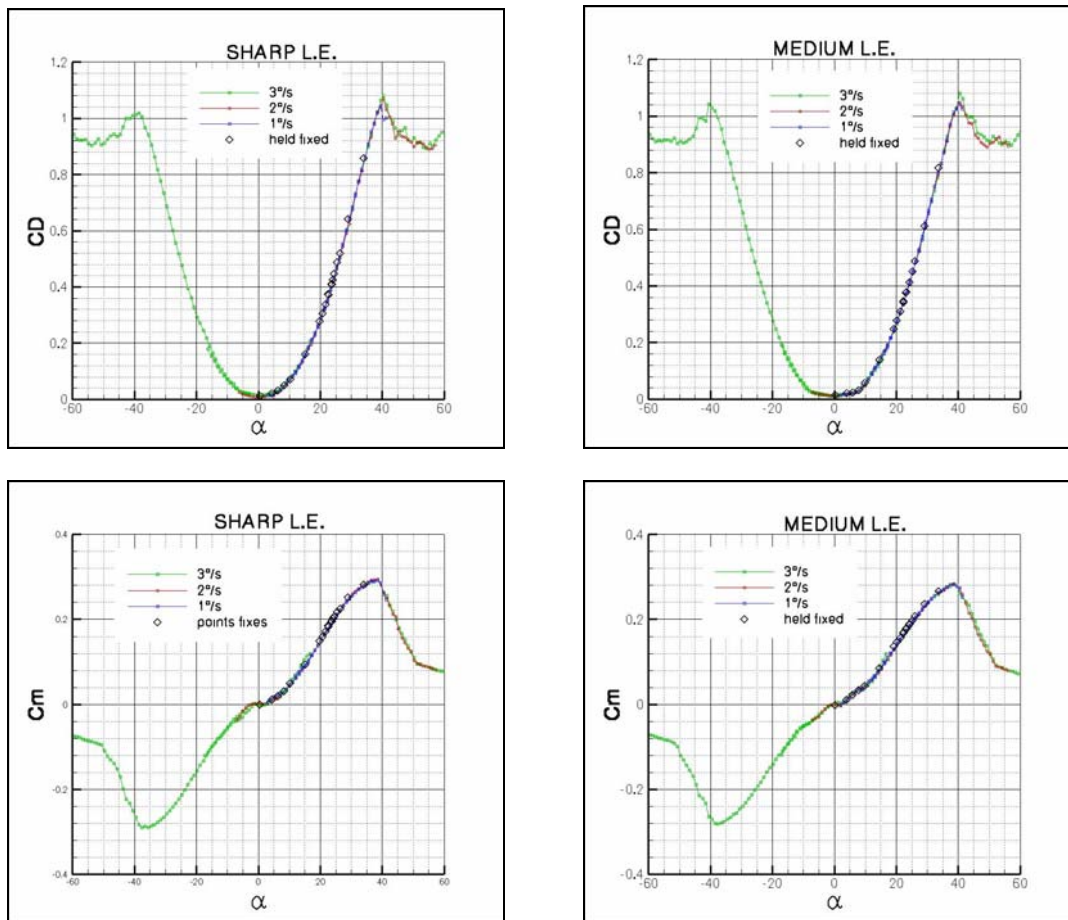
Figure 20-11: Drag and Pitching Moment Coefficients in Open Jet Tunnel (Model 4 and 5).

20.4.3   Forces Measurement and PIV Velocimetry in Solid Walls (Model 4 and 5)

20.4.3.1   Forces and Static Pressures

Normal force C_N, axial force C_A and pitching moment C_m coefficients measured at L1 are presented for each leading edge in Figure 20-12 and are compared with the values recorded in open jet test section. Differences between the two test sections are very weak for C_N and C_m. They become more intense on C_A when $\alpha>10°$. Apparently there is no explanation for that discrepancy on C_A. As expected, axial force amplitude is higher for the medium as suction effect from the leading edge is promoted.
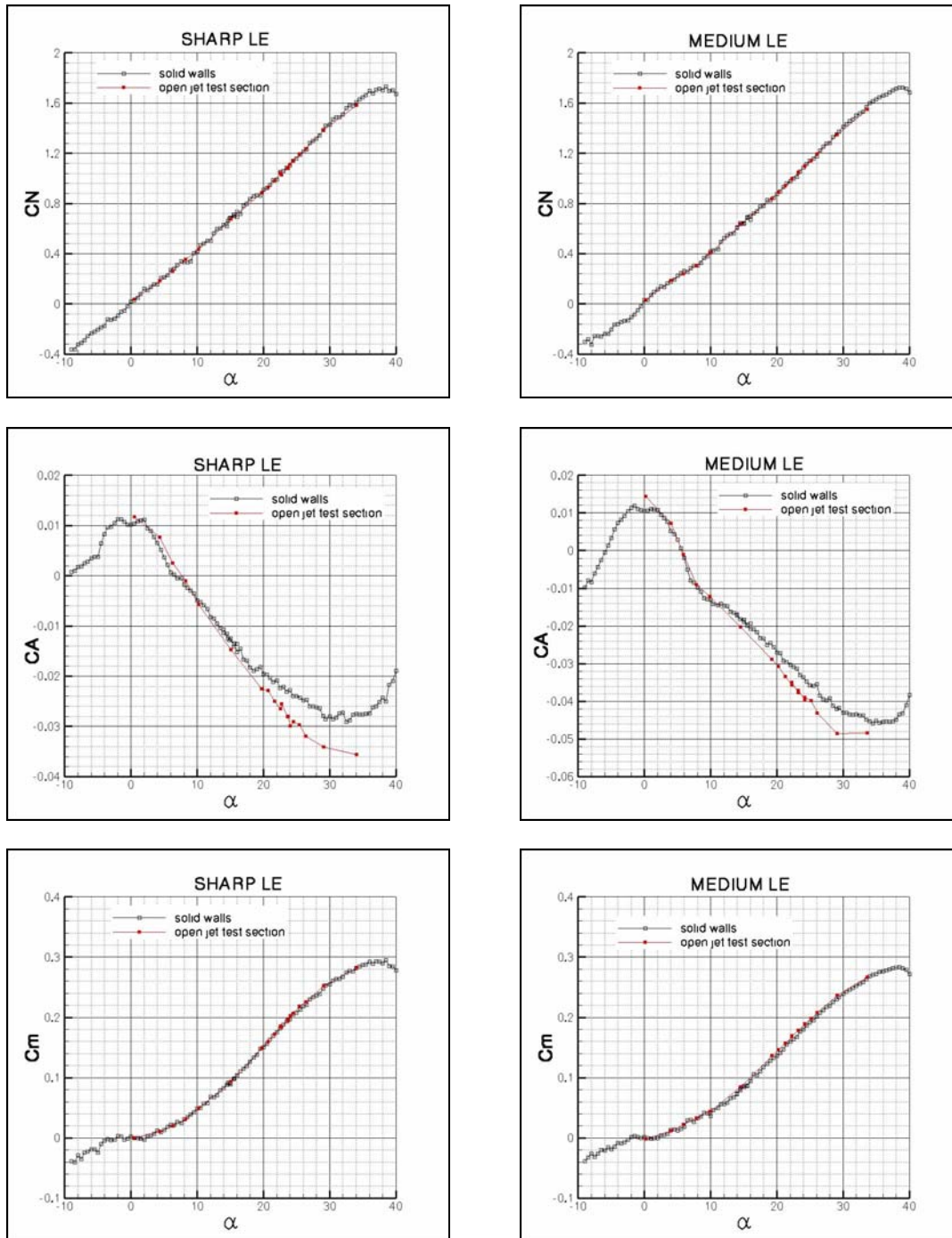
Figure 20-12: Normal Force, Axial Force and Pitching Moment Coefficients at L1 (Model 4 and 5).

Comparison of static pressures on the obstacle with LTPT distributions exhibits some differences (Figure 20-13). Variations are similar in amplitude to those recorded in open jet tunnel, although slightly smaller for the open jet tunnel. These pressure distributions are recapitulated in a more explicit form on Figure 20-14 and Figure 20-15

where it is possible to compare pressure distributions from the same model for both test section configurations at L1 (Model 4 and 5), pressure distributions in solid walls at L1 and LTPT from the same model (Model 1), pressure distributions in solid walls at L1 from different models (Model 1, 4 and 5).
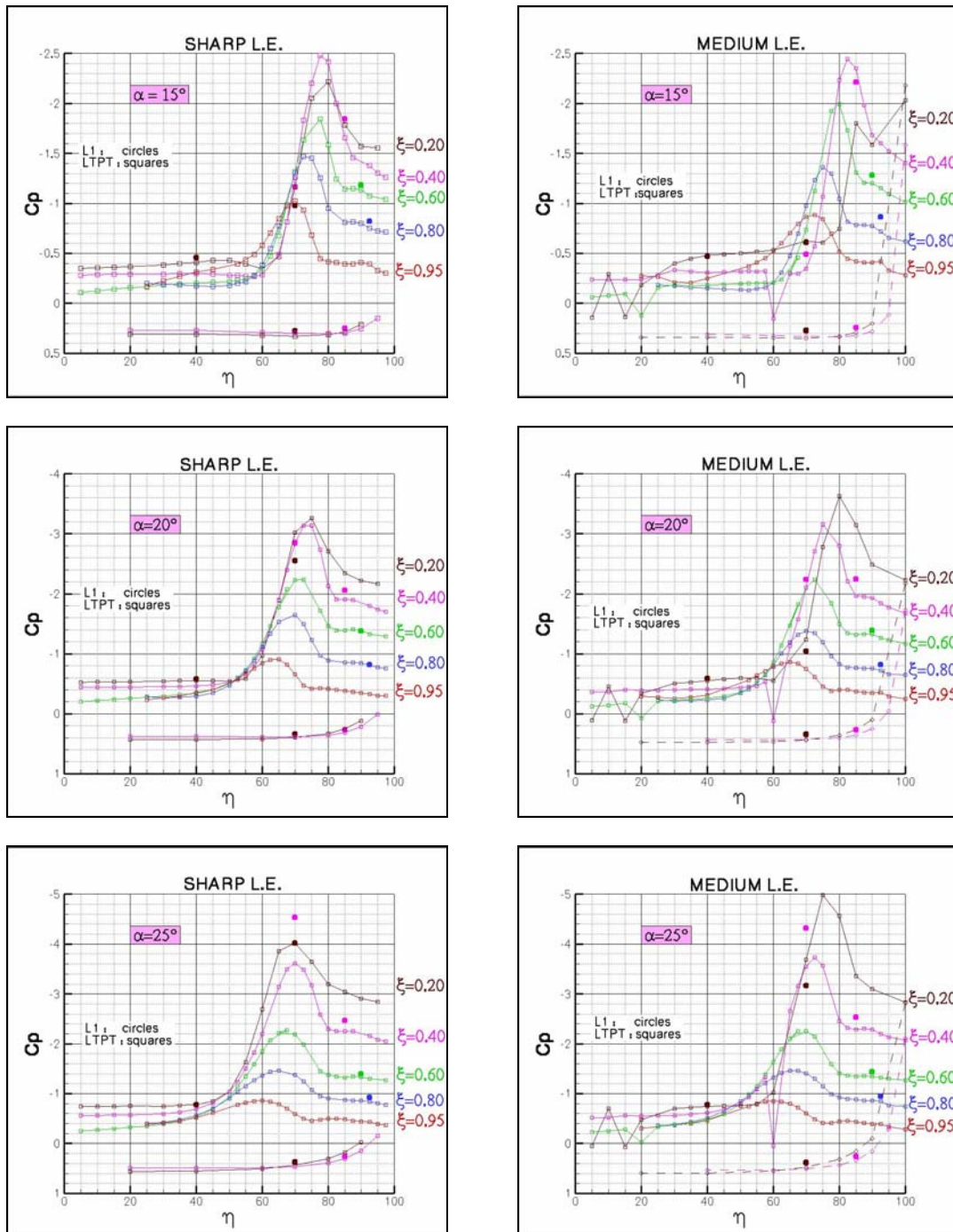
Figure 20-13: Pressure Distribution at L1 in Solid Walls (Model 4 and 5) and Comparison with LTPT
(Sharp: Re$_{mac}$ = 10^6 at L1; Re$_{mac}$ = 1.5 x 10^6 at LTPT – Medium: Re$_{mac}$ = 10^6 at L1; Re$_{mac}$ = 2 x 10^6 at LTPT).
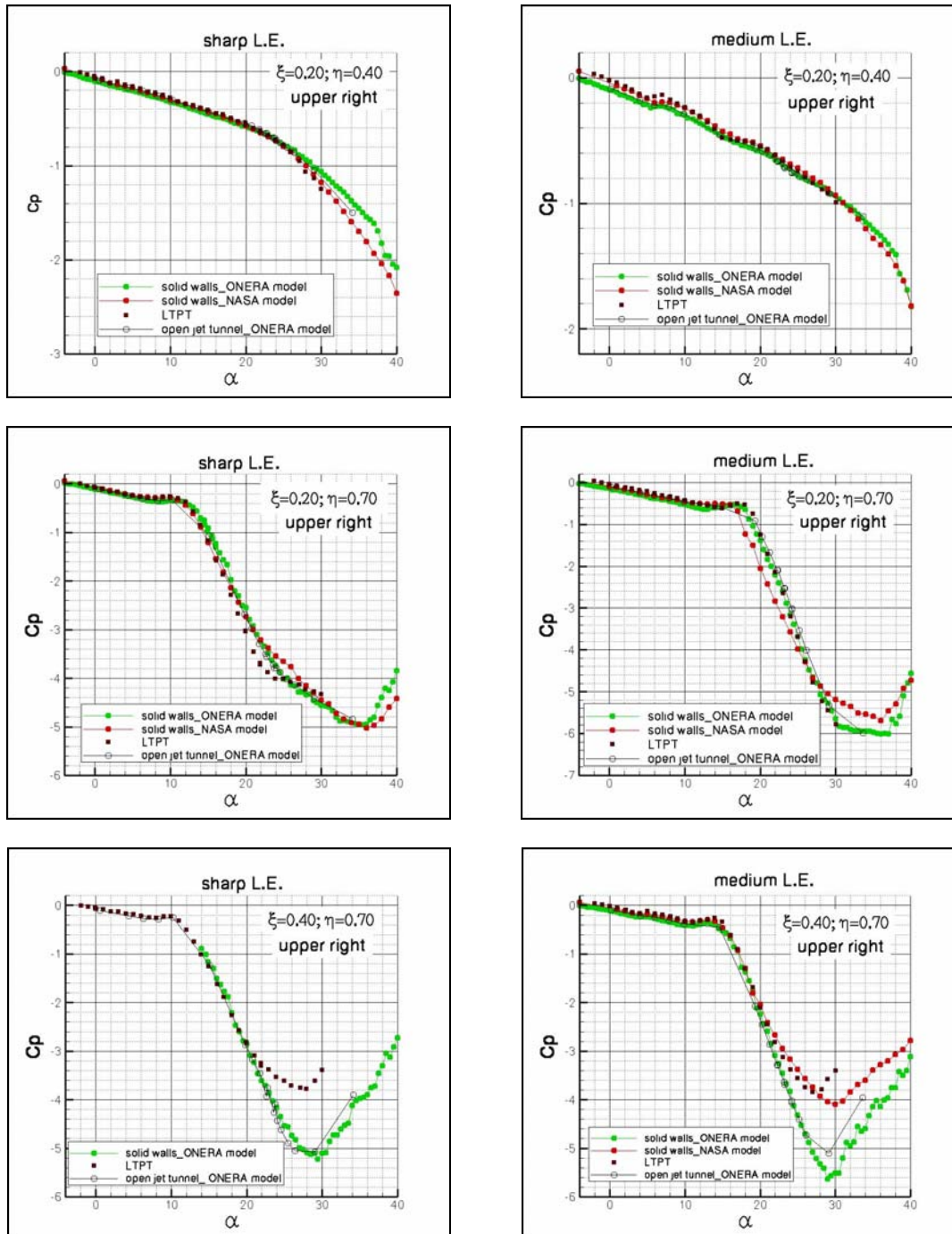
**Figure 20-14: Comparison of Pressure Coefficients Measured in
Solid Walls and in Open Jet Tunnel (Upper Surface, h ≤ 0.70).**
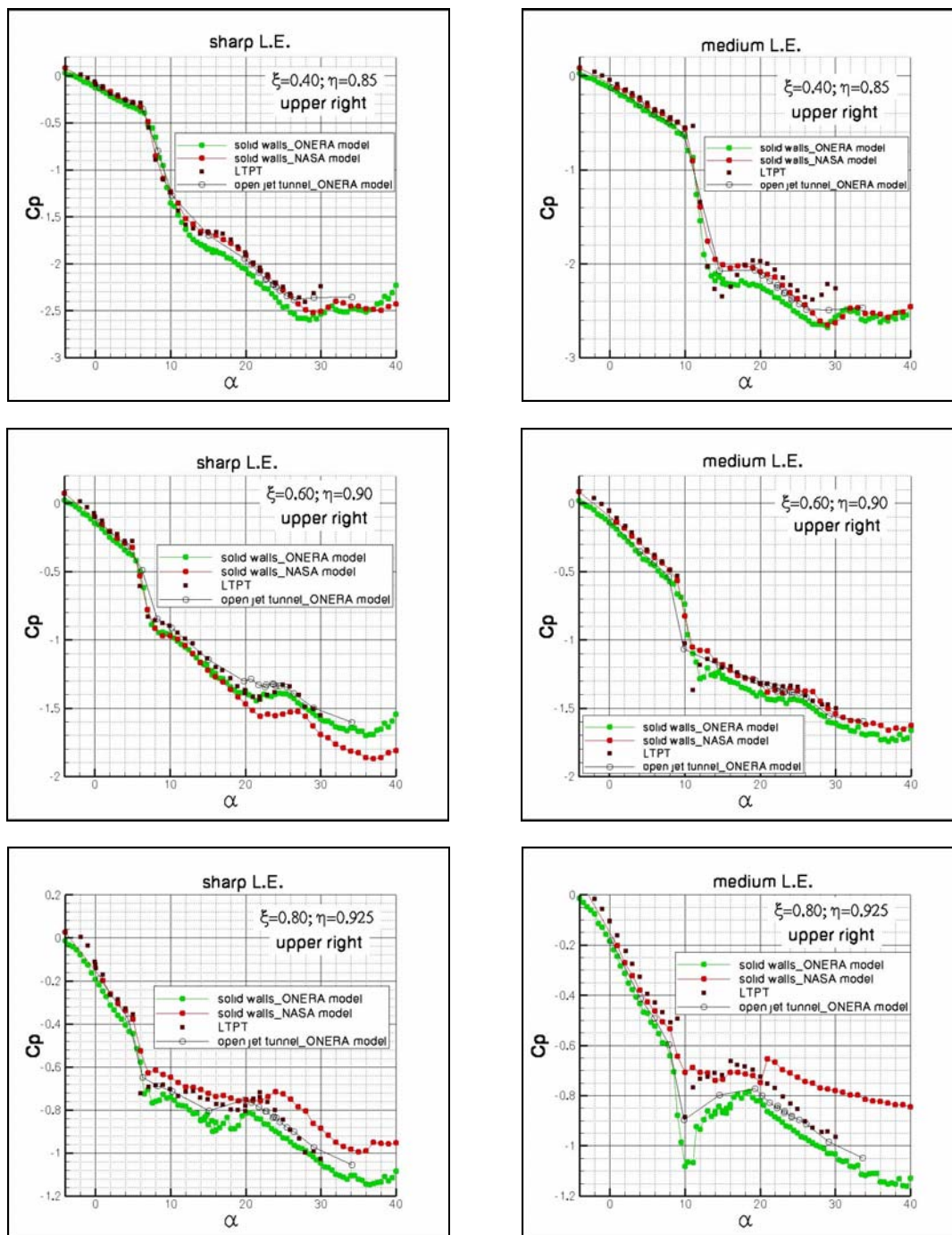
Figure 20-15: Comparison of Pressure Coefficients Measured in
Solid Walls and in Open Jet Tunnel (Upper Surface, h > 0.70).

Considering the differences in Reynolds numbers, the agreement between L1 and LTPT pressures at Model 1 upper surface can be estimated as acceptable over practically the whole incidence range if $\xi \leq 0.60$ (Figure 20-14,

Figure 20-15). At station $\xi = 0.80$ the variation increases when $\alpha > 20°$ and $\eta \geq 0.90$, corresponding to the area of the secondary vortex influence. Pressures at lower surface are similar (Figure 20-16).
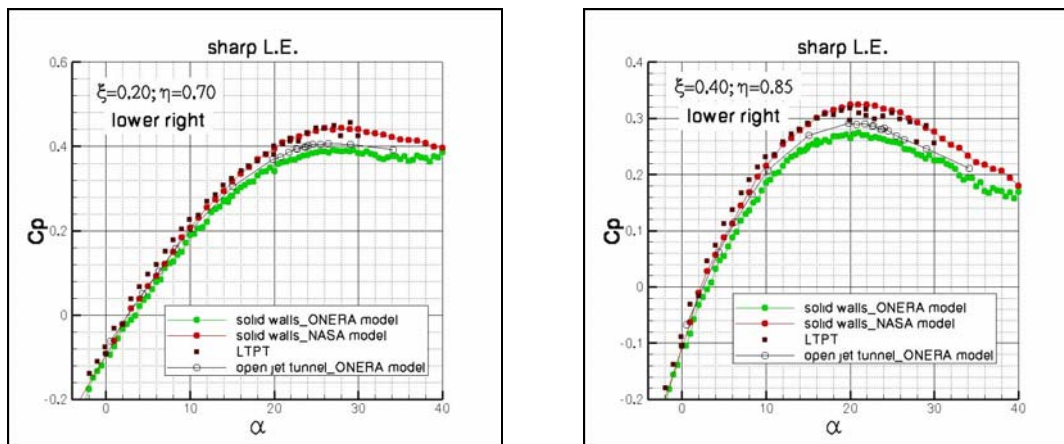
Figure 20-16: Comparison of Pressure Coefficients Measured
in Solid Walls and in Open Jet Tunnel (Lower Surface).

If only results relative to Model 4 and 5 in solid walls and in open jet tunnel are compared, agreement on upper surface is very good over the whole incidence range for the inboard part of the wing and for the region wetted by the primary vortex (more or less for $\eta < 0.80$). On the other hand, for the outboard part of the wing ($\eta > 0.80$) a small variation exists when $\alpha > 10°$ approximately, linked to the upstream motion of separation towards the apex and then to the secondary vortex development. The pressure is weaker in solid walls, which seems normal due to the confined aspect of the test section (Figure 20-14, Figure 20-15). Pressure distributions at lower surface are somewhat different (Figure 20-16). As a conclusion, the influence of test section configurations affects only the vicinity of the leading edge, where phenomena take place in connection with the upstream moving of separation towards the apex and then with the secondary vortex development if incidence increases more. Curiously results from the open jet tunnel test section are more similar to LTPT ones than results in solid walls are.

When the results obtained in solid walls at L1 with Model 1 and Model 4 and 5 are compared, no significant variations should be logically observed as models are identical according to the geometrical control (§20.2.3). However it appears that the pressure distributions from Model 1 at L1 are rather in better agreement with LTPT ones than those from Model 4 and 5 are (Figure 20-14, Figure 20-15). Over the inboard part of the wing flows are closely similar (Figure 20-14). On the other hand, at primary vortex location ($\xi = 0.40$, $\eta = 0.70$) the pressure peak amplitude is much more intense for Model 4 and 5. Furthermore, on the outer part of the wing, the pressure distributions from Model 4 and 5 are generally lower than those recorded in solid walls with the Model 1, which would indicate that the upstream moving of separation and then the development of the secondary vortex occur probably sooner with Model 4 and 5 (Figure 20-14, Figure 20-15). Only the small variations between the models geometries can explain these discrepancies.

20.4.3.2   Analysis of Axial Force Correlation with the Flow Structure

Figure 20-17 compares C_A evolutions in solid walls between 'sharp' and 'medium' leading edges. For $\alpha > 6°$ it can be observed that the suction effect induced at leading edge promotes an axial force which amplitude is more intense for the 'medium' than for the 'sharp'. Probably these differences can be related to the primary

vortex development which occurs differently according to the bluntness of the leading edge. For the 'medium' leading edge case the primary vortex development can be correlated to the gradual progression of separation towards the apex when α increases. Analysis of pressures transmitted from ports situated along the leading edge provides a means to locate the separation onset and its displacement when incidence is varying [20-7]. Figure 20-7 reproduces J.M. Luckring's analysis on LTPT data [20-7] and makes a comparison with measurements recorded at L1 with the same model. There are some differences between the results partly due to the fact that the Re_{mac} values are not strictly identical. Indeed an increase of the Reynolds number is known to delay separation on the leading edge [20-7]. In particular it can be observed on Figure 20-7 that separation is located at $\xi = 0.20$ when $12° < \alpha < 13°$ at L1, against $14° < \alpha < 15°$ at LTPT. The same result is obtained when analysing the primary vortex footprint on upper surface pressures (Figure 20-18). Now at L1 it is precisely for $\alpha \sim 12°$, that is to say when separation is moved upstream to the apex and when the origin of the primary vortex coincides with the apex, that the 'medium' $C_A(\alpha)$ curve slope changes indicating a decrease of the suction effect (Figure 20-17). A similar analysis can be conducted for the 'sharp' although this leading edge is not equipped with pressure ports. Indeed it can be seen that the primary vortex suction peak has moved upstream to the apex when $\alpha = 6°$ (Figure 20-19). Because of the existence of a geometrical discontinuity at the leading edge, it can be inferred that a reattachment occurs on the 'sharp' upper surface just downstream of the leading edge when $\alpha \leq 5°$. Now it is also for $\alpha \approx 6°$ that 'sharp' $C_A(\alpha)$ curve slope changes indicating a decrease of the suction rate (Figure 20-17). These phenomena show that the influence of the primary vortex on axial force is directly related to extension and location along the leading edge of the separation line that generated the vortex. Sketches in Figure 20-20 show the influence on suction of the flow structure at leading edge. As at low incidences the flow around 'sharp' and 'medium' can be considered as attached, the suction rate keeps the same value for the 2 leading edges when $\alpha < 6°$ is varying (Figure 20-17). For $\alpha > 6°$ the flow around the 'sharp' leading edge is entirely separated. Because it remains then fixed, the separation line sets limits to the suction effect at upper surface and that explains why the suction rate decreases when comparing with $\alpha < 6°$ case.
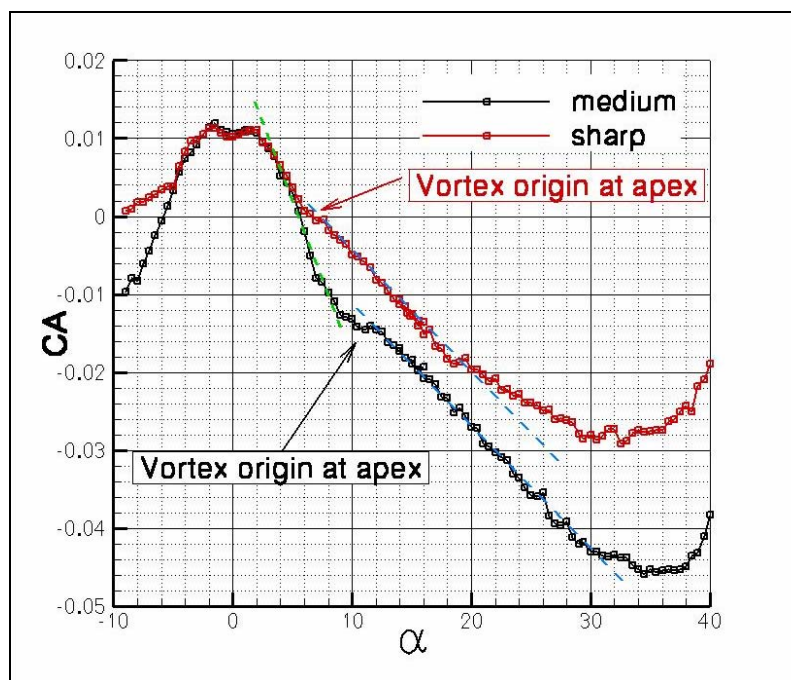
Figure 20-17: Axial Force Variations: L1, Solid Walls, $Re_{mac} = 10^6$.
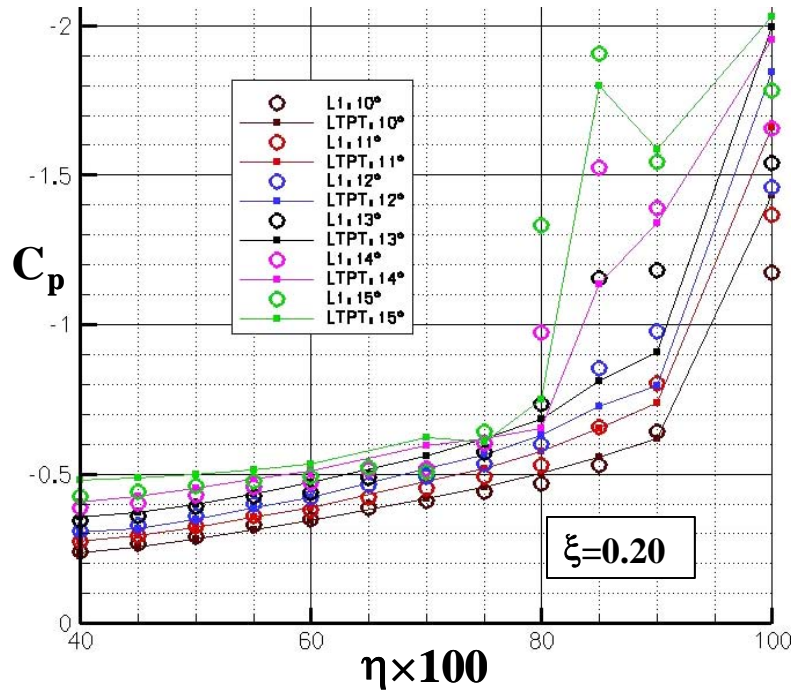
**Figure 20-18: Correlation of Primary Vortex Onset at ξ = 0.20 with Medium Leading Edge
Upper Surface Pressure Distribution – Model 1 – L1: Re_{mac} = 10^6; LTPT: Re_{mac} = 2 x 10^6.**
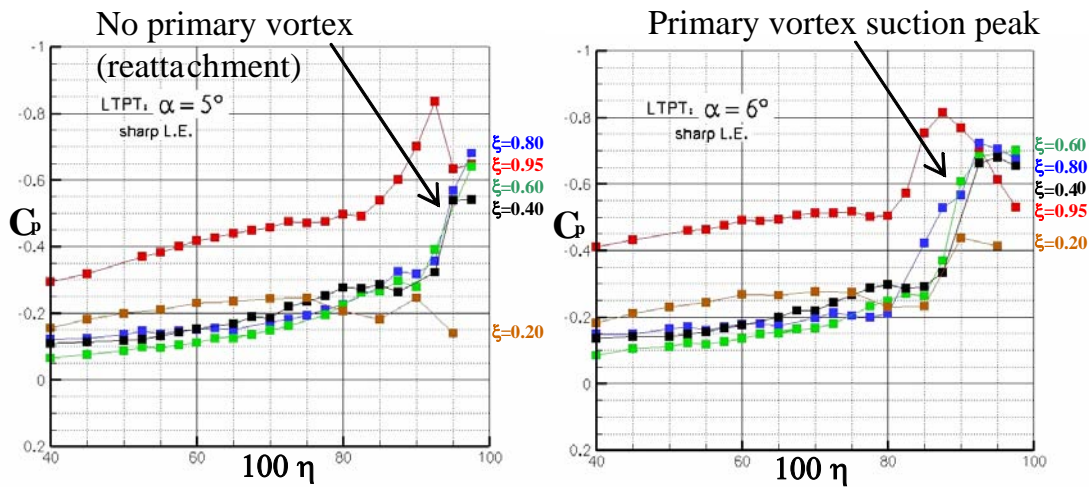
**Figure 20-19: Correlation of Primary Vortex Onset with Sharp Leading Edge Upper Surface
Pressure Distribution – Model 1 – LTPT: Re_{mac} = 1.5 x 10^6 (Chu and Luckring [20-5]).**

MEDIUM **SHARP**

Separation- reattachment

α_1
α_2
$\alpha < 6°$ $\alpha < 6°$

$\alpha > 12°$ $\alpha > 6°$ Primary
vortex at apex :
suction rate decrease
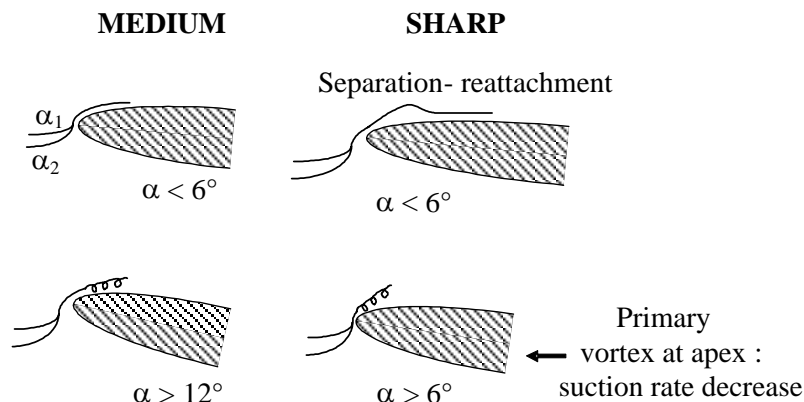
Figure 20-20: Influence of the Leading Edge Flow Structure on Suction Rate.

So, the suction effect for the 'sharp' is growing if $\alpha > 6°$ is increasing but the growing is then only due to suction variations at the lower surface. The same phenomenon can be observed for the 'medium' leading edge when $\alpha \geq 12°$, so it is not surprising that the suction rate is equal to the 'sharp' one over that range of incidence (Figure 20-17). But as the separation line is now located slightly downstream at the upper surface, the contribution of the upper surface to suction is stronger than for the 'sharp', leading to a shift between the two parallel lines characterising $C_A(\alpha)$ variations when vortex origin is at apex (Figure 20-17). That behaviour is observed at $Re_{mac} = 10^6$.

20.4.3.3   Flow Field Velocity Measurements by PIV

Velocity fields were measured by stereoscopic PIV across plans located at stations $\xi = 0.30, 0.40, 0.50, 0.60, 0.70$. The objective was to record velocity maps when the vortex breakdown point was located approximately at mid-chord. According to discussions within the AVT-113 task group this should correspond to $23° \leq \alpha \leq 25°$. So incidence of the test was fixed at $24.7°$. In addition to measurements in plans normal to the wing chord, velocity measurements were performed by 2C-PIV in a plan parallel to the obstacle and 4mm far from the wing (Figure 20-21, Figure 20-22). The laser sheet was 1 mm thick.
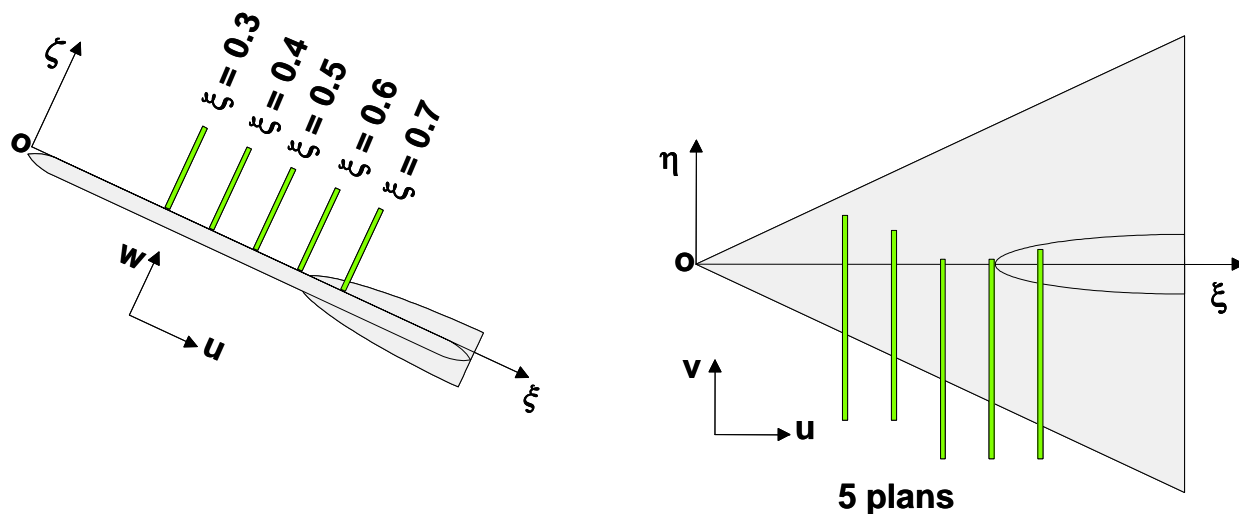
Figure 20-21: Localization of Stereoscopic PIV Plans.
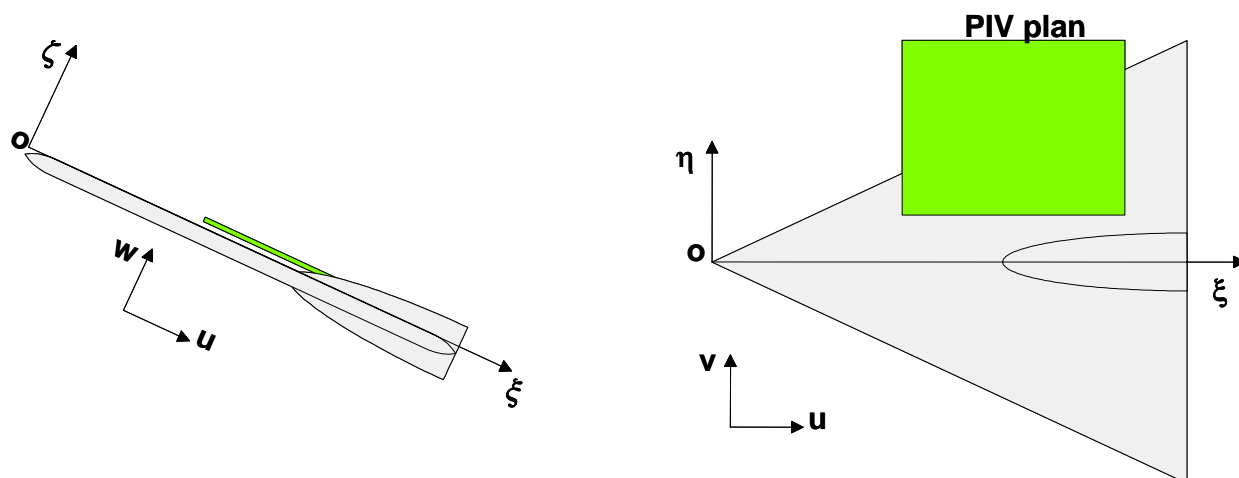
Figure 20-22: Localization of the PIV Plan Parallel to the Wing.

Figure 20-23 and Figure 20-24 provide some examples of vorticity and longitudinal velocity fields related to 'sharp' and 'medium' leading edges. Decreasing of the vortex intensity is clearly observed when moving downstream. Vortex intensity of the 'medium' leading edge is weaker than the 'sharp' one, but in both cases vortex breakdown occurs downstream the station $\xi = 0.70$, the longitudinal velocity at $\xi = 0.70$ being still highly positive. Such results were not expected a priori. In particular they do not seem in good agreement with University of Munich ones for which the vortex breakdown point is located, for open jet tunnel conditions and $Re_{mac} = 10^6$, at $\xi = 0.50$ when $\alpha = 23°$ [20-8].
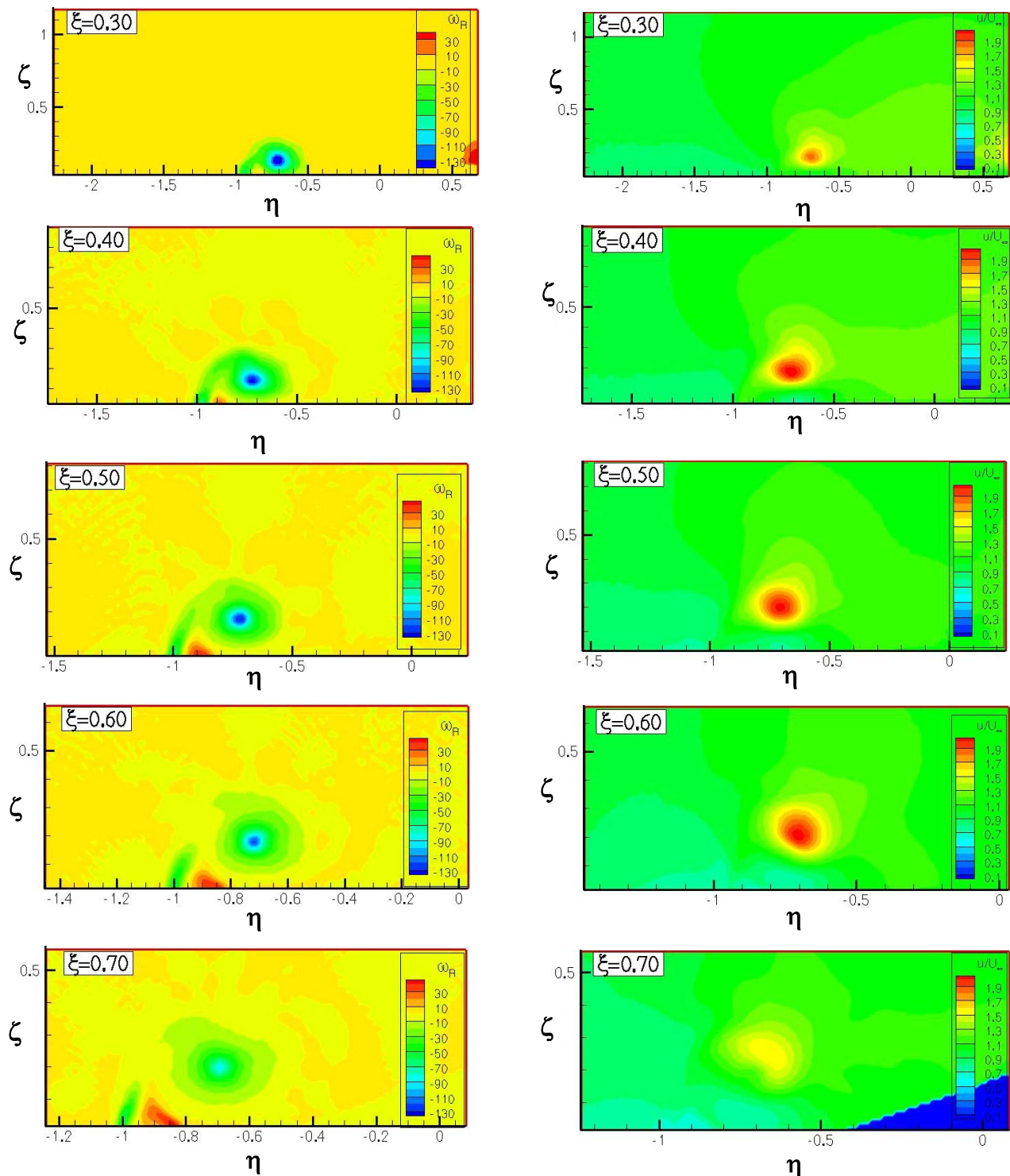
Figure 20-23: Vorticity and Longitudinal Velocity Fields – Model 4 – α = 24.7° – L1: Re$_{mac}$ = 10^6, M = 0.133.
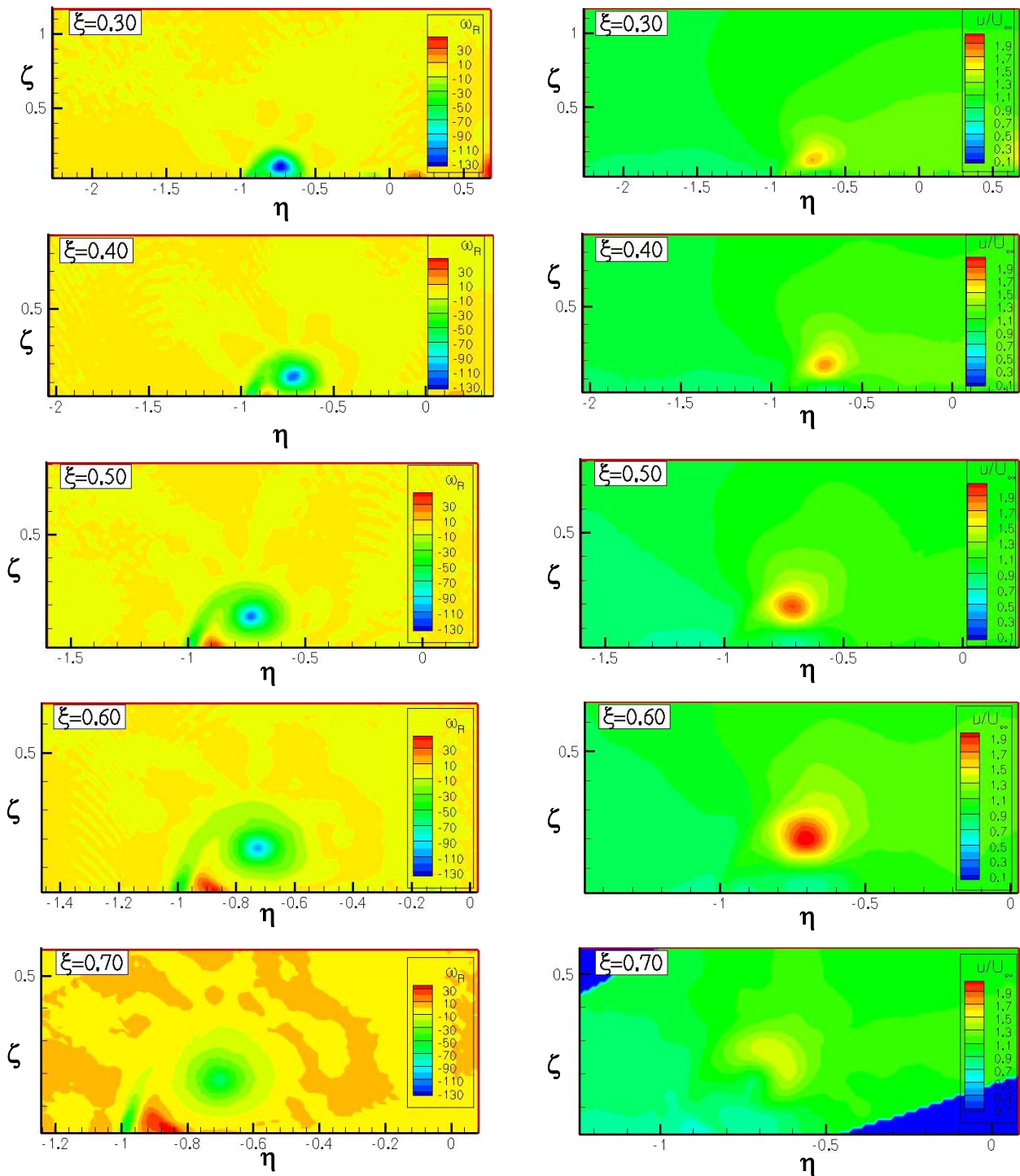
**Figure 20-24: Vorticity and Longitudinal Velocity Fields –
Model 5 – α = 24.7° – L1: Re$_{mac}$ = 10^6, M = 0.133.**

Figure 20-25 exhibits vorticity and velocity fields measured by PIV 2 components in a plan parallel to the wing. A comparison with Figure 20-23 and Figure 20-24 lead to primary and secondary vortex identification. For $\xi > 0.80$ a low speed area within the secondary vortex probably reveals the breakdown of that structure, while primary vortex obviously is not yet breakdown.
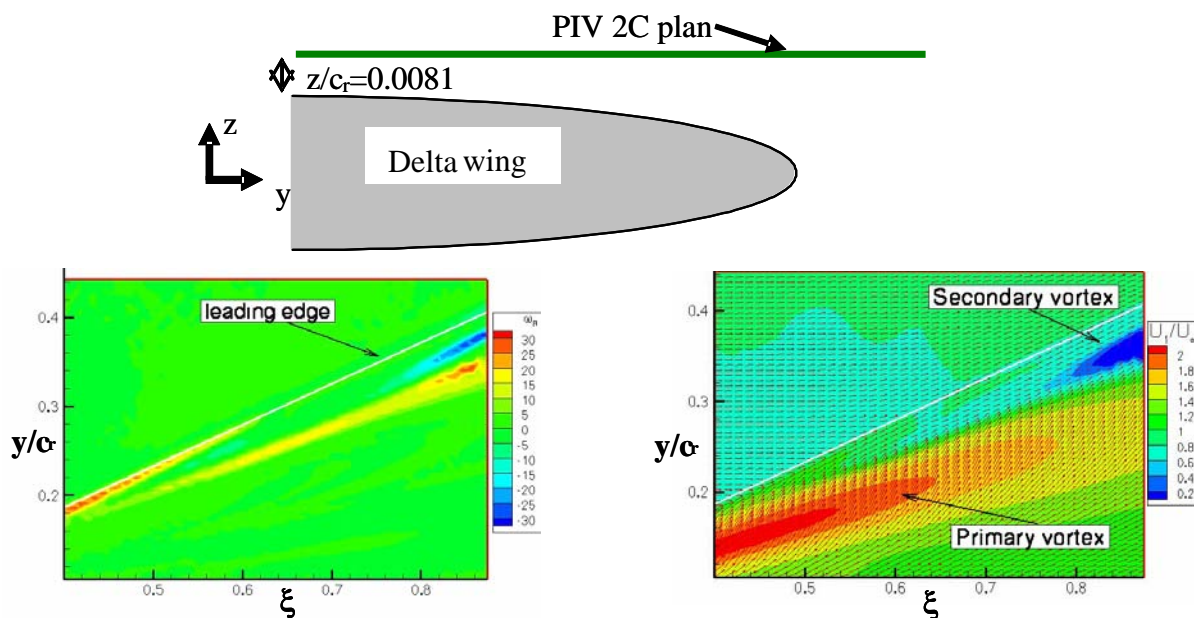
**Figure 20-25: PIV 2C Vorticity and Velocity Fields in a Plan Parallel to
Upper Surface – α = 24.7° – Model 5 – L1: Re$_{mac}$ = 10^6, M = 0.133.**

20.5   CONCLUSIONS

This work allowed to complete available data bases by measuring aerodynamic forces over a large range of incidence at low Reynolds and Mach numbers. Normal force and pitching moment are in good agreement with corresponding data from LTPT and NTF. The axial force depends on the suction effect and consequently on the flow structure at leading edge. So it appears to be directly correlated with the progressive upstream extension of separation along the leading edge when incidence is increasing. Surface pressures at L1 and LTPT are globally in good agreement but exhibit some variations partly due to differences in Reynolds numbers. Because the separation line is fixed at leading edge, 'sharp' is less affected by these variations. Especially at high incidence and in the vicinity of the leading edge, surface pressures seem somewhat affected by the models used as well as by the test section configuration. So impact of these parameters has not to be neglected. Velocity fields by PIV show that the vortex breakdown occurs at L1 for $\alpha > 25°$. That value is a little larger than initially expected.

20.6   REFERENCES

[20-1]   Hummel, D.: *On the Vortex Formation Over a Slender Wing at Large Incidence*, AGARD-CP-247, Paper N° 15, January 1979.

[20-2]   Rockwell, D.: *Three Dimensional Flow Structure on Delta Wings at High Angle-of-Attack: Experimental Concepts and Issues*, AIAA Paper 93-0050, January 1993.

[20-3]   Delery, J.: *Aspects of Vortex Breakdown*, Progress in Aerospace Sciences, Vol. 30, No. 1, 1994, pp. 1,59.

[20-4]   Visbal, M.R.: *Computational and Physical Aspects of Vortex Breakdown on Delta Wings*, AIAA Paper 95-0585, January 1995.

[20-5]   Chu, J. and Luckring, J.M.: *Experimental Surface Pressure Data Obtained on 65° Delta Wing Across Reynolds Number and Mach Number Ranges*, NASA Technical Memorandum 4645, Langley Research Center. Hampton, Virginia, February 1996.

[20-6]   Luckring, J.M.: *Understanding and Modeling Vortical Flows to Improve the Technology Readiness Level for Military Aircraft*, Chapter 18, RTO Report TR-AVT-113, 2009.

[20-7]   Luckring, J.M.: *Reynolds Number, Compressibility, and Leading Edge Bluntness Effects on Delta Wing Aerodynamic*, ICAS 2004 – 24th International Congress of the Aerodynamic Sciences.

[20-8]   Breitsamter, Ch.: *Understanding and Modeling Vortical Flows to Improve the Technology Readiness Level for Military Aircraft*, Chapter 21, RTO Report TR-AVT-113, 2009.

Chapter 21 – EXPERIMENTAL INVESTIGATIONS ON THE VFE-2 CONFIGURATION AT TU MUNICH, GERMANY

by

Andrej Furman[1] and Christian Breitsamter[2]

This report presents an overview of experimental investigations on a 65 deg swept delta wing as part of the International Vortex Flow Experiment 2 (VFE-2). Results obtained in low-speed wind tunnel facilities include oil flow and laser light sheet flow visualization, mean and unsteady surface pressure distributions as well as mean and turbulent velocity components of the flow field and close to the wing surface. Details of the delta wing vortex structure and breakdown phenomenon are discussed and analyzed. Special emphasis is on the occurrence of an inner vortex detected for the low Reynolds number and Mach number regime.

21.1   NOMENCLATURE

AR	aspect ratio
$\bar{c}_p$	mean pressure coefficient
$\hat{c}_p$	amplitude of pressure coefficient spectrum
c_{prms}	root mean square pressure coefficient
d_d	diameter of pressure probe
f	frequency
f_{dom}	dominant frequency
f_n	lens focal length number
k	reduced frequency, $f \cdot \bar{c} / U_\infty$
k_{dom}	dominant reduced frequency
l	length
p	static pressure
p_∞	free stream static pressure
q	dynamic pressure
s	wing semi span
S_{cp}	power spectrum of pressure coefficient fluctuations
S_{cp}^N	non-dimensional power spectrum of pressure coefficient fluctuations
S_p	power spectrum of pressure fluctuations
$S_{u_i'}$	power spectrum of velocity fluctuations

---

[1] Dipl.-Ing.

[2] PD Dr.-Ing. habil.

$S_{u_i'}^N$	non-dimensional power spectrum of velocity fluctuations
t	time
t_M	measurement time
Δt	pulse delay
T	temperature
u, v, w	axial, lateral and vertical velocities
$\overline{u}_i$	mean velocity components
u_i'	velocity fluctuations
$u_{i_{rms}}$	root mean square velocity components
$\overline{u_i' u_j'}$	turbulent shear stresses
U_∞	free stream velocity
X_p	Fourier transformed quantity of pressure fluctuation
$X_{u_i'}$	Fourier transformed quantity of velocity fluctuations
φ	leading-edge sweep
ρ	density

21.2   INTRODUCTION

Aerodynamic investigations of flow phenomena over generic and complex delta wing configurations have been performed for many years [[21-1]-[21-7], [21-15]-[21-19]]. The typical and well known delta wing flow physics is as follows: The flow separates already at low angles of attack at the highly swept leading-edges. The separated shear layer rolls up to form a large-scale vortex located over each half of the wing. Thus, two strong vortices influence the flow field of the wing upper side. Vortex formation along the leading-edge starts from the rear part to the apex. This primary vortex is fully developed when vorticity feeding exists over the entire leading-edge. The vortex cross flow area reveals a rotational core with an embedded subcore, the latter dominated mainly by viscous effects. The subcore is characterized by high axial velocities, low static pressures and enhanced velocity fluctuations due to the steep gradient in the cross flow components. The mean velocities on the wing upper surface are strongly increased by the leading-edge vortices resulting in high suction levels. The corresponding suction peaks in the spanwise pressure distribution indicate the track of the vortex axis on the wing surface. Therefore, leading-edge vortices in a fully developed, stable stage create additional lift and an increase in maximum angle of attack improving significantly maneuver capabilities of high-agility aircraft.

Sharp leading-edge configurations are often used in delta wing research work because primary separation is fixed and leading-edge vortex evolution is less sensitive to Reynolds number effects. Vortex aerodynamics becomes much more complicated for rounded or blunt leading-edge configurations as the position of primary separation varies to a certain extent depending on pressure gradient and boundary layer development. Thus, leading-edge radius, angle of attack and Reynolds number are the main parameters influencing the onset of vortex evolution as well as position and strength of the primary vortex whereas the angle of attack is the main parameter for the sharp leading-edge case only. There is a strong increase in the surface pressure when moving in spanwise direction from the station of the primary vortex suction peak to the leading-edge. This severe lateral pressure gradient provokes boundary layer separation in that region. The separated boundary layer rolls up by self induction and creates a small vortex, named secondary vortex, the rotation of which is opposite to that of the

leading-edge (primary) vortex. The formation of the secondary vortex depends strongly on the presence of a laminar or turbulent boundary layer [21-21]. Size and position of the secondary vortex affects the primary vortex location and, thus, the associated suction level.

Further, leading-edge vortices are subject to breakdown at high angles of attack. Vortex breakdown is caused by the stagnation of the low-energy axial core flow due to the increase of the adverse pressure gradient along the vortex axis with increasing angle of attack. This rise in the vortex core static pressure at the wing rear part is caused on the one hand by the diverging vortex subcore and on the other hand by the recompression in the trailing-edge area. Vortex breakdown is indicated by the rapid expansion of the vortex core accompanied by high velocity fluctuations. Downstream of breakdown, the fluctuation maxima are located in a limited radial range around the burst vortex core. In addition, the breakdown flow exhibits specific instability mechanisms leading to narrow-band unsteady aerodynamic forces [[21-1], [21-2], [21-15]]. The numerical simulation and analysis of the breakdown flow is still a challenging problem which needs the correct representation of the turbulent flow field and instability characteristics.

Euler methods were intensively developed in the 1980's, also aimed to calculate leading-edge vortex flows. Therefore, an experimental data base was needed for code validation and assessment established in frame of the International Vortex Flow Experiment 1 (VFE-1; 1984 – 1986). The tests included force and pressure measurements as well as flow field studies on a 65 deg swept cropped delta wing carried out in several wind tunnel facilities [21-10]. But Euler code results do not represent secondary vortices limiting the accuracy even for fixed primary vortices at sharp leading edges. The vortex induced surface pressure distribution is sensitive to viscous effects on the wing as well as in the rolled-up shear layers. Great efforts have been made in the last decade to develop and use high fidelity computational fluid dynamics methods. Unsteady Reynolds Averaged Navier-Stokes (URANS) Methods are available including a variety of turbulence models of algebraic type up to Reynolds stress transport equations. Further, methods of Detached Eddy Simulations (DES) are used as a combination of a Large Eddy Simulation (LES) to model separated flow dominated by large-scale structures in the outer domain and a turbulence model to calculate flow quantities in the wall-bounded domain. With such high fidelity methods available [[21-8], [21-9], [21-24]-[21-27]], there is again a strong need for an extended experimental data base. Consequently, a second International Vortex Flow Experiment (VFE-2) has been initiated. The VFE-2 activities are coordinated by the task group 113 of the Applied Vehicle Technology panel (AVT) of the NATO Research Technology Organization (RTO) named "Understanding and modeling of vortical flows to improve the technology readiness level for military aircraft" [21-20]. Latest test techniques are applied to gather high quality data. The research activities have been started in 2004 by partners of industry, research establishments and universities from Europe and the United States. The work is still on-going.

The Institute of Aerodynamics (AER) of the Technische Universität München (TUM) is part of the RTO AVT-113 task group focusing particularly on flow field turbulence and boundary layer quantities [11-14]. Both sharp and rounded leading edges are investigated. The tests are conducted on a new delta wing model which has been manufactured based on a NASA wing geometry served as reference configuration for VFE-2 [21-7]. The TUM-AER investigations have been performed in low-speed wind tunnel facilities using laser light sheet and oil flow visualization, steady and unsteady surface pressure measurements, stereo particle image velocimetry and hot-wire anemometry. The results are presented as distributions of mean, turbulent and spectral quantities, which give detailed information of the flow characteristics over the delta wing.

21.3 EXPERIMENTAL SET-UP

21.3.1 Facility

The measurements have been carried out in the low-speed wind tunnels A and B of the Institute of Aerodynamics at the Technische Universität München [21-11]. The wind tunnels are of closed-return type with an open test section. The free stream turbulence intensity is less than 0.4%. The uncertainty in the temporal and spatial mean velocity distribution is less than 0.6%. The uncertainty in free stream direction is below 0.2 deg and static pressure variations along the tunnel axis are below 0.4%.

21.3.2 Model

The present delta wing model [21-11] was designed to study leading-edge vortex flow features comparing sharp and rounded leading edges. The present model has a root chord length of $c_r = 0.980$ m, a wing span of $b = 0.914$ m, a leading edge sweep of $\varphi = 65°$, a wing area of $S = 0.448$ m^2 and an aspect ratio of AR = 1.86. The wing was designed using a CAD tool and then given to the manufacturer as digital three-dimensional model. The delta wing consists of an upper and a lower base plate, the trailing edge with a depth of $x_{TE}/c_r = 10\%$ and the pressure orifices being part of these plates. On the inside of these plates cut-outs are milled to house the tubes and wires from the pressure orifices and unsteady pressure transducers. The thickness is t = 0.033m, which is constant over the base plate. A sharp and a rounded leading edge ($r_{LE,rounded}, /\overline{c} = 0.0015$) are available, r_{LE} being the leading edge radius and $\overline{c}$ the mean aerodynamic chord. The leading edges are fitted on the left and right hand side of the lower base plate and have a depth of $x_{LE}/c_r = 15\%$. On each of the leading edge elements, five pockets for the pressure sensors have been milled, which are closed with separate lids. On the mounted wing a model sting is installed, which is attached to the three-axis model support via a model adapter. All parts are manufactured from aluminium "Certal" and, therefore, enabling measurements in cryogenic wind tunnels also. There are 177 pressure orifices with a diameter of d = 0.3 mm situated on the entire wing, 44 are equipped with unsteady pressure sensors. The pressure orifices are positioned in five chordwise positions ($x/c_r = 0.2, 0.4, 0.6, 0.8$ and 0.95).

21.3.3 Test Cases

The investigations have been carried out for three angles of attack, namely at:

- $\alpha = 13°$ for partly developed;
- $\alpha = 18°$ for fully developed; and
- $\alpha = 23°$ for burst leading-edge vortices.

The test Mach numbers (Table 21-1) for all cases are M = 0.07 and M = 0.14 and the corresponding Reynolds numbers based on the mean aerodynamic chord are $R_{mac} = 1 \times 10^6$ and $R_{mac} = 2 \times 10^6$, respectively. Except for the laser light sheet measurements, which have been obtained at Mach number M = 0.035 and a Reynolds number of $R_{mac} = 0.5 \times 10^6$.

Table 21-1: Test Cases of the TU München

Measurements	Sections x/c_r	Angle of Attack	Reynolds Number	Mach Number
PSI	0.2 / 0.4 / 0.6 / 0.8 / 0.95	0° – 30°	1×10^6 / 2×10^6	0.07 / 0.14
Unsteady Pressure	0.4 / 0.6 / 0.8 / 0.95	0° – 30°	1×10^6 / 2×10^6	0.07 / 0.14
Laser Light Sheet Visualisation	0.2 / 0.4 / 0.6 / 0.8 / 0.95 / 1.1	0° – 30°	0.5×10^6	0.035
	upper surface $z/c_r = 0.01$			
	upper surface $z/c_r = 0.041$			
Oil Visualisation	surface streamlines	13° / 18° / 23°	0.5×10^6 / 1×10^6 / 2×10^6	0.035 / 0.07 / 0.14
Stereo PIV	0.2 / 0.4 / 0.6 / 0.8 / 0.95	13° / 18° / 23°	1×10^6 / 2×10^6	0.07 / 0.14
Hot-Wire Anemometry	0.4 / 0.6 / 0.8	13° / 18° / 23°	1×10^6	0.07

21.3.4   Measurement Techniques

During the project several measurement techniques have been used:

Laser light sheet visualization [21-12] is used in order to survey the flow field in a plane, which is illuminated by a laser beam expanded by a cylindrical lens. The smoke particles in this plane are then recorded with a digital photo camera. The particle size is approximately 2 μm, in order to guarantee sufficient light reflection. For this investigation an air cooled class 3B Argon-Ion-laser has been used. This laser has a maximum power of 100 mW and the wave length of the light is between 457 ÷ 514 nm.

Oil flow visualization [21-12] illustrates the surface stream lines on the suction side of the wing. A black foil was stuck on the model surface to achieve good visual contrast between oil flow pigments and background color. A mixture of yellow paint pigments, petrol and paraffin was applied on the upper surface and exposed to the free stream flow briefly. The developed flow picture was then photographed.

Surface pressure measurements [[21-4], [21-11], [21-12]]. The **steady** pressures are measured on the upper and lower surface of the wing at five chord stations with 133 measuring tabs in total. The sampling rate of the measured values is f = 100 Hz with an averaging time of t = 10 s. The **unsteady** pressure measurements were accomplished in four chord stations on the suction side of the wing with 12 unsteady pressure sensors per chord station. A sampling rate of f = 2000 Hz and a sample time of t = 40 s is used. The frequency of the measurement system low-pass filter was set to 256 Hz.

Stereo Particle Image Velocimetry (Stereo-PIV) [[21-13], [21-14]] is performed with two cameras left and right of a laser light sheet. A pair of 135 mm, $f_n = 2.8$ objective lenses constitute the recording optics and are connected to the charge coupled device (CCD) camera with 1600 x 1186 pixel resolution. The light sheet was generated by a frequency doubled, double oscillator Nd-YAG laser with a maximum energy level of 200 mJ and a frequency of 10 Hz per pulse. The light sheet thickness was set at approximately 10 mm and the pulse delay was set to $\Delta t = 21$ μs.

Hot-Wire Anemometry (HWA) [[21-2], [21-13], [21-14]] is based on a dual-sensor probe of cross-wire type for measuring the fluctuating velocities. The probes were operated by a multi-channel constant-temperature anemometer system. By means of its signal conditioner modules, bridge output voltages were low-pass filtered at 1000 Hz before digitization and amplified for optimal signal level. The sampling time for each channel is 6.4 s, with the sampling rate set to 3000 Hz (Nyquist frequency of 1500 Hz), so that each sample block contains 19200 values. The use of cross-wires generally assumes some knowledge of the flow field, such as a known flow direction to which the probe must be aligned. To determine the three velocity components, the probe has to be rotated around its axis by 90 deg to adjust the wire plane once horizontal and once vertical against the main flow direction. Thus, two triggered traverse sweeps are necessary to obtain the streamwise u, lateral v and vertical w velocity components, respectively. Each digitized and temperature corrected voltage pair of the corresponding probe positions was converted to evaluate the time-dependent velocity vector. The numerical method used is based on look-up tables derived from the full velocity and flow angle calibration of the probe [21-2].

21.4   ANALYSIS OF RESULTS

The discussion and analysis of the measurement results address flow topology, mean and fluctuating surface pressures, mean and fluctuating flow field and boundary layer velocities and spectral quantities.

21.4.1   Flow Topology

21.4.1.1   Flow Field

Laser light sheet visualization can be used to determine the flow behaviour above and behind the wing as well as the size and position of the vortices [[21-2], [21-12], [21-22]]. The pictures taken from behind the wing for the stations x/c_r = 0.2, 0.4, 0.6, 0.8, 0.95, and 1.1 are shown on the right hand side of Figure 21-1. They illustrate cross sections of the vortex. Pictures from above, i.e. parallel to the wing upper surface, at z/c_r = 0.01 and 0.05 are shown on the left hand side of Figure 21-1. Based on such images, the position of the leading-edge vortex center (trajectories of vortex axis) and the breakdown location at high angles of attack can be determined, Figure 21-8.

(a) α = 13°

(b) α = 18°
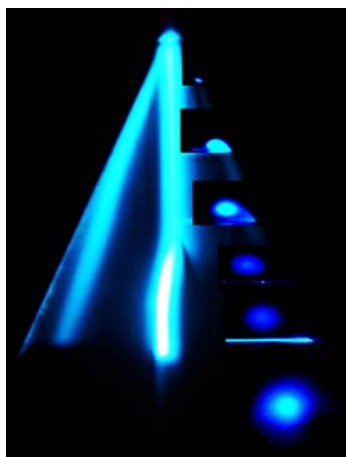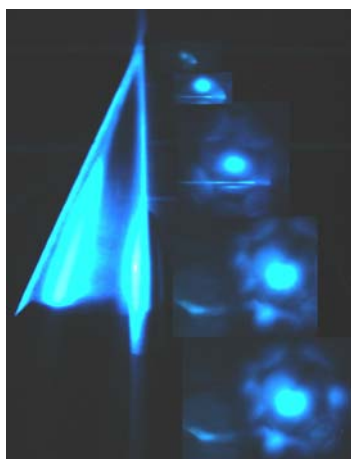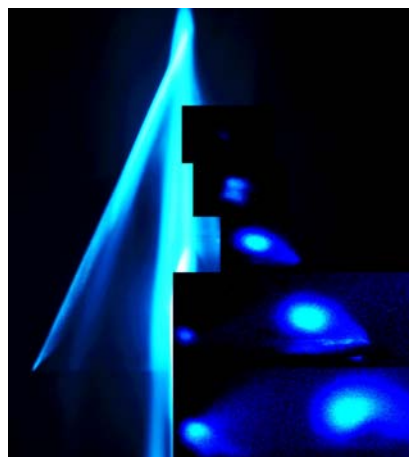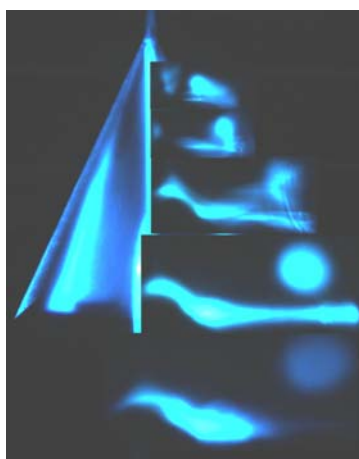
(c) α = 23°

**Figure 21-1: Laser Light Sheets of Vortex Structure above and behind the Wing at
R_{mac} = 5 x 10^5 and M = 0.035 for Sharp (left) and Rounded (right) Leading Edges.**

Regarding Figure 21-1 (a), the partly developed leading-edge vortex at $\alpha = 13°$ is depicted where the primary separation at the sharp leading-edge has not yet reached the apex. Also, the area of the secondary vortex can be detected underneath the primary vortex close to the leading-edge. The comparison between sharp and rounded leading-edge shows a delayed separation for the rounded leading-edge, which is also indicated by a smaller vortex core and a stronger trailing-edge effect. Figure 21-1 (b) illustrates the fully developed vortex for $\alpha = 18°$ where some coherent vortical structures can be observed in the primary vortex feeding shear layer for the case of sharp leading-edge (Figure 21-1 (b) left). Vortex breakdown takes place in the rearward portion of the wing at $\alpha = 23°$ highlighted by the expanded core area for both sharp and rounded leading-edge.

21.4.1.2   Surface Flow

Concentrating again on the flow behaviour for the rounded leading-edge case at $\alpha = 13°$, the corresponding surface streamlines are shown by oil flow visualization, Figure 21-2. A schematic representation depicts the flow topology derived from the laser light sheet and oil flow pictures, Figure 21-4. This schematic highlights the separation and attachment lines of the primary and secondary vortex as indicated by the surface streamlines. The leading-edge (primary) vortex starts from a turbulent separation at the wing rear part, with the turbulent shear layers of the wing upper and lower side rolling up along the leading-edge. The roll-up process does not reach the apex at this angle of attack but progresses up to the wing front part. There, a laminar boundary layer is present. Transition is indicated by an outboard shift of the separation line of the secondary vortex. Further, a laminar separation exists near the apex close to the symmetry plane. This three-dimensional separation bubble is caused by the pressure increase when the flow has turned around the leading-edge contour of the relatively thick wing. Downstream, the inboard separated flow forms a small inner vortex favoured by the positive lateral pressure gradient. The inboard vortex rotates in the same direction as the leading-edge (primary) vortex. Separation and attachment line of the inboard vortex are positioned closely together and can be clearly seen in the oil flow picture. The inboard vortex extends over the entire chord length to the wing rear edge. Further tests have shown that the trajectory and strength of the inboard vortex depends strongly on angle of attack (strength of primary vortex and adverse lateral pressure gradient) and Reynolds number (area of laminar flow). Therefore, this phenomenon is only visible at certain Reynolds numbers in the medium angle of attack range, Figure 21-2 and Figure 21-3.

(a) α = 13°

(b) α = 18°
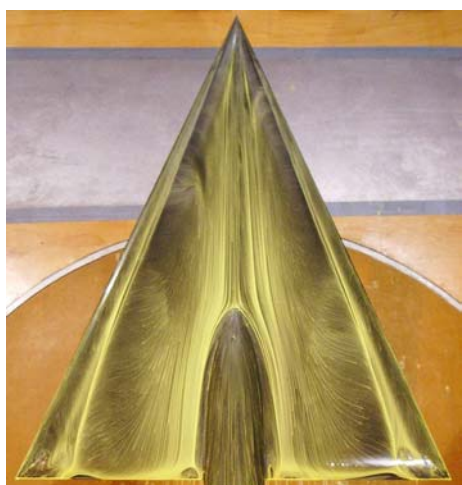
(c) α = 23°

**Figure 21-2: Surface Oil Flow Visualization at R_{mac} = 1 x 10^6 and
M = 0.07 for Sharp (left) and Rounded (right) Leading Edges.**

(a) α = 13°

(b) α = 18°
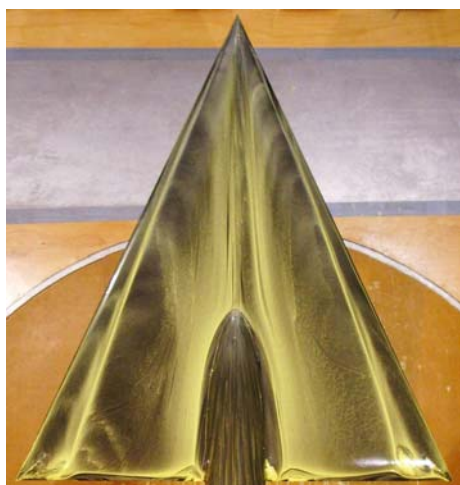
(c) α = 23°

Figure 21-3: Surface Oil Flow Visualization at R_{mac} = 2 x 10^6 and
M = 0.14 for Sharp (left) and Rounded (right) Leading Edges.
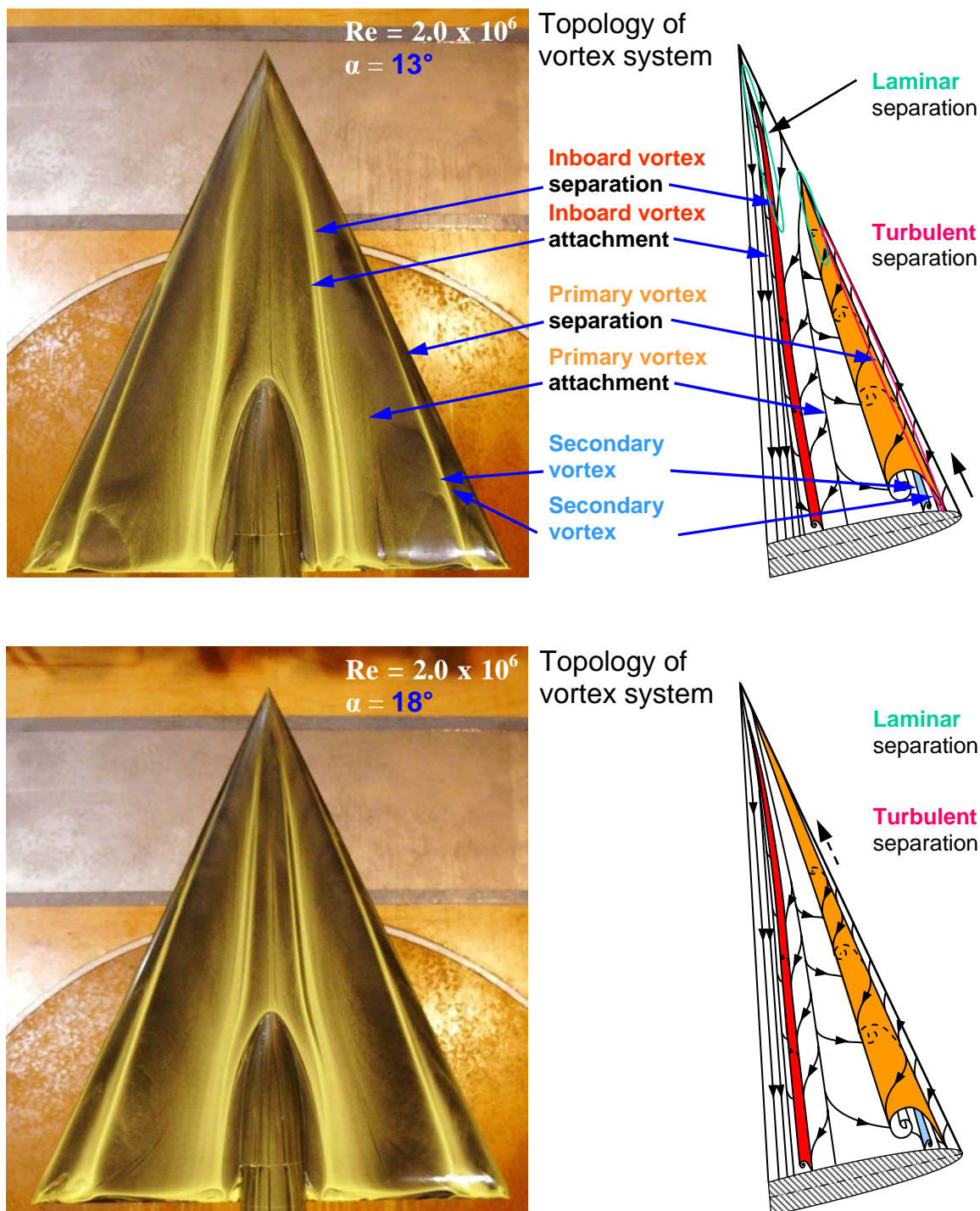
**Figure 21-4: Flow Topology Based on Laser Light Sheet and
Oil Flow Visualization for α = 13° and 18° at R_{mac} = 2 x 10^6.**

21.4.2   Mean Flow Field

21.4.2.1   Pressure Distribution

For the time-averaged pressure coefficients the surface pressures p(P,t) at the position P are converted in non dimensional values. The pressure coefficient is defined by

$$c_p(P,t) = \frac{p(P,t) - p_\infty}{q_\infty} \tag{1}$$

where p(P,t) is the static pressure, p_∞ the static free stream pressure and q_∞ the dynamic pressure. For each position P on the upper wing surface the time series of the non dimensional pressure coefficient $c_p(P,t)$ are then available at every test condition.

The average of the pressure coefficient $\overline{c}_p(P,t)$ is defined as

$$\overline{c}_p(P) = \frac{1}{t_M} \int_0^{t_M} c_p(P,t)dt \tag{2}$$

where t_M is the time of measurement or the length of the time series.

Three steady measurement results are shown for $\alpha = 13°$, $\alpha = 18°$ and $\alpha = 23°$ in Figure 21-5 and Figure 21-6. Each figure shows the development of the steady pressure distribution in several chordwise stations for the cases of sharp and rounded leading edge. Leading-edge separation occurring on a blunt or rounded leading-edge contour is a more complex phenomenon as the primary separation is no longer fixed to a geometric discontinuity as given by a sharp edge. Therefore, the onset of leading edge separation is determined by flow conditions and the particular wing geometry. For low to moderate angles of attack fully attached flow may be present. Leading-edge separation will first occur near the wing tip progressing then in direction to the apex with further increase in angle of attack. Consequently, the wing will exhibit partially developed leading-edge separation with attached flow on the upstream portion of the wing and leading-edge vortex formation on the downstream portion. The separation line of the primary vortex is free to move inboard or outboard depending on Reynolds number and Mach number conditions. This complexity in the flow physics can have considerable impact on the aerodynamic properties and maneuver performance of slender wing geometries. The correlation of separation onset for the present test conditions is summarized in Figure 21-10.

(a) α = 13°

(b) α = 18°

(c) α = 23°
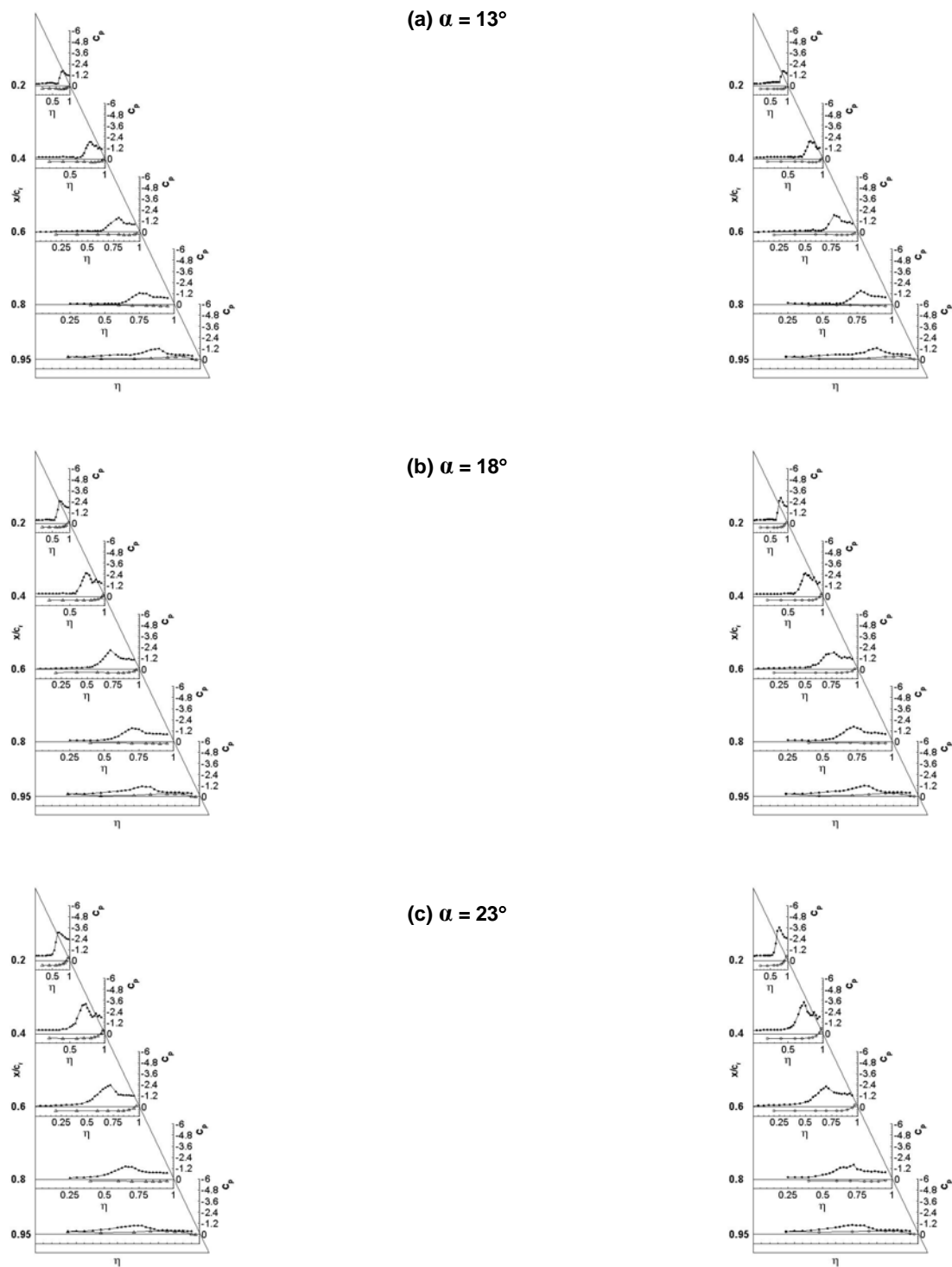
**Figure 21-5: Steady Pressure Distribution at $R_{mac} = 1 \times 10^6$ and
M = 0.07 for Sharp (left) and Rounded (right) Leading Edges.**

(a) α = 13°

(b) α = 18°

(c) α = 23°
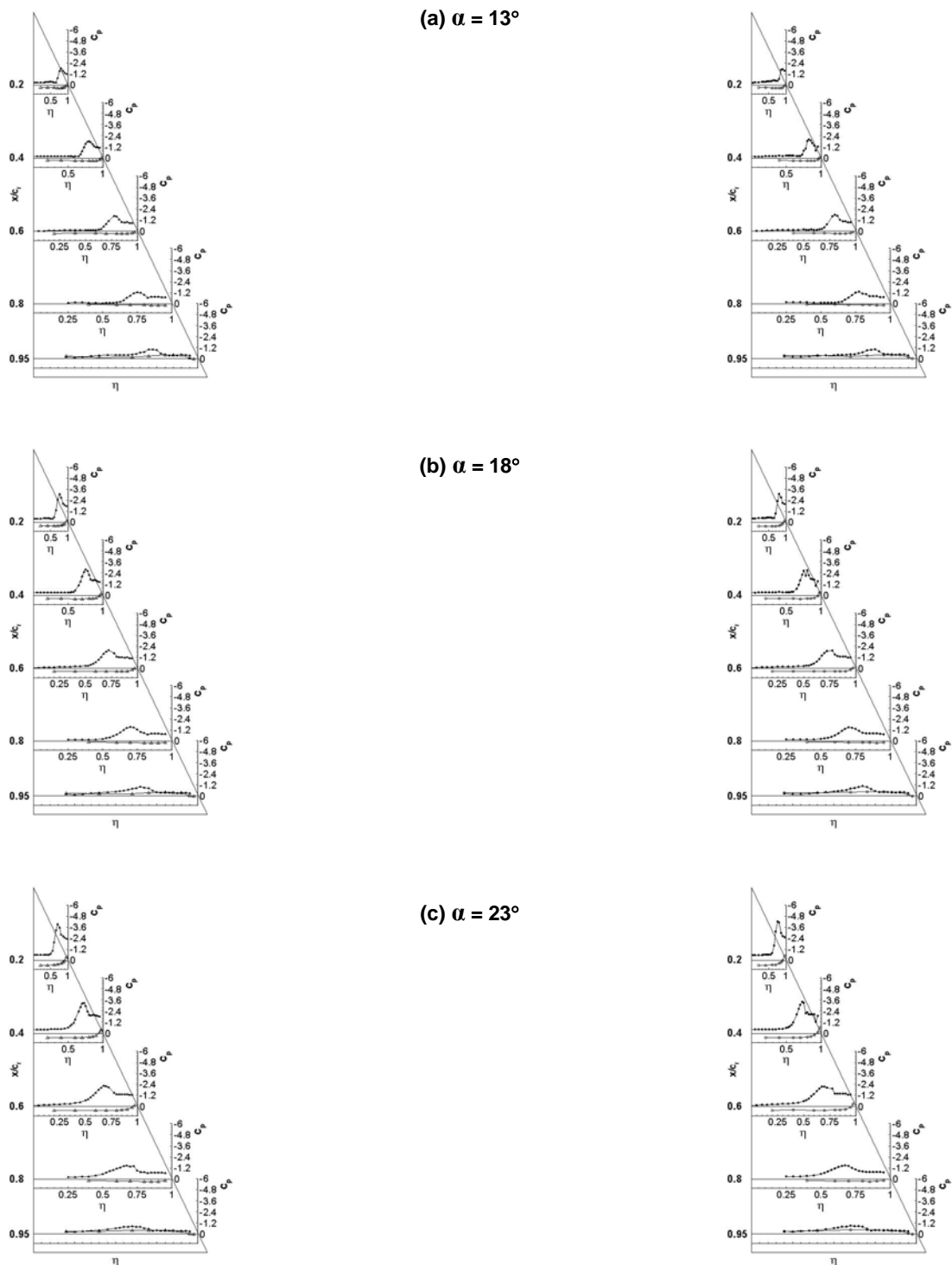
**Figure 21-6: Steady Pressure Distribution at $R_{mac} = 2 \times 10^6$ and
M = 0.14 for Sharp (left) and Rounded (right) Leading Edges.**

At $\alpha = 13°$ significant suction peaks are visible, marking the axis of the primary vortex, Figure 21-5 (a), Figure 21-6 (a). The suction peaks reduce with increasing chord station, except for the second station ($x/c_r = 0.4$), where the peak is slightly increased. This is due to the vortex not being fully developed at this angle of attack. The constant suction level over the inner wing area marks the region of reattachment. The secondary vortex is visible in all chord stations in form of a locally higher suction level outboard of the primary vortex, except for $x/c_r = 0.2$ for the rounded leading edge, where the secondary vortex is just forming. The suction peaks for the primary as well as for the secondary vortex also move inboard in the rear portion of the wing.

With increasing angle of attack, the suction peaks increase in all chord stations, Figure 21-5 (b), Figure 21-6 (b). The vortex diameter also increases, being evident in the suction peak broadening. The vortex axis moves inboard with increasing angle of attack and the reattachment lines are moved towards the wing center line.

Further increasing the angle of attack to $\alpha = 23°$, the suction peaks also increase in the chord stations $x/c_r = 0.2$, 0.4 and 0.6, Figure 21-5 (c), Figure 21-6 (c). Chord stations further downstream show decreased suction peaks. At $\alpha = 18°$ the suction peaks at $x/c_r = 0.8$ are $C_{p,sharp,18°} = -1.51$ and $C_{p,rounded,18°} = -1.44$. Increasing the angle of attack to $\alpha = 23°$ reduces the suction peak for the sharp leading-edge case and stay on the same level for rounded leading-edge $c_{p,sharp,23°} \approx c_{p,rounded,23°} = -1.45$. This is due to the vortex breakdown in this area [21-2]. Again, the primary vortex axes have been marked in Figure 21-10, also showing the position of vortex breakdown, which is slightly further upstream for the sharp leading edge. The position of primary vortex breakdown for the rounded leading edge was determined at $x/c_r \approx 0.8$ and for the sharp leading edge at $x/c_r \approx 0.75$.

The difference in the pressure distribution between the rounded and the sharp leading edge is most evident at $x/c_r = 0.2$ for all angles of attack illustrated here. This difference decreases with increasing chord station, Figure 21-7, disappearing completely at the aft station. The primary vortex for the rounded leading edge is located slightly further outboard than for the sharp leading edge. For an angle of attack of $\alpha = 23°$ the suction peak at $x/c_r = 0.2$ for the rounded leading edge is significantly higher than for the sharp leading edge. Increasing the angle of attack causes the pressure on the upper surface in the inboard area and also the pressure on the entire lower surface of the wing to slightly decrease. On the lower surface no significant difference between the sharp and the rounded leading edge is evident.
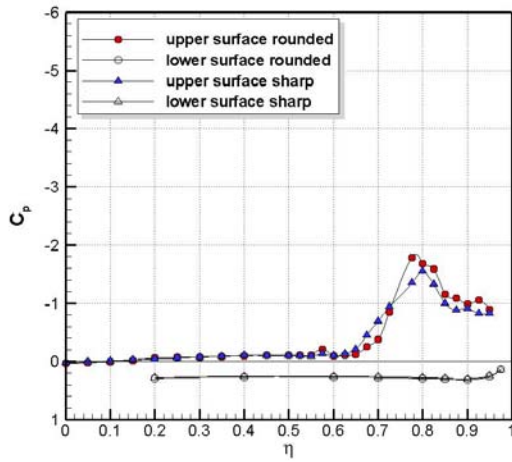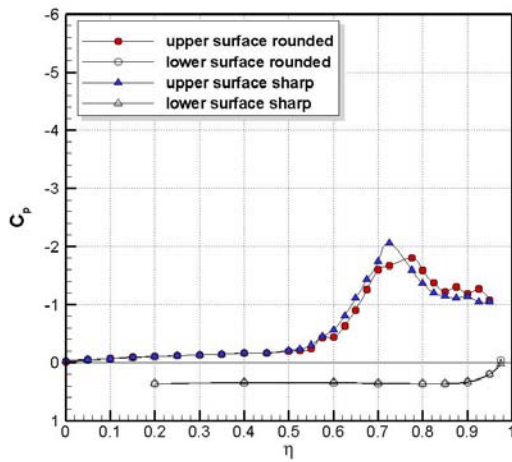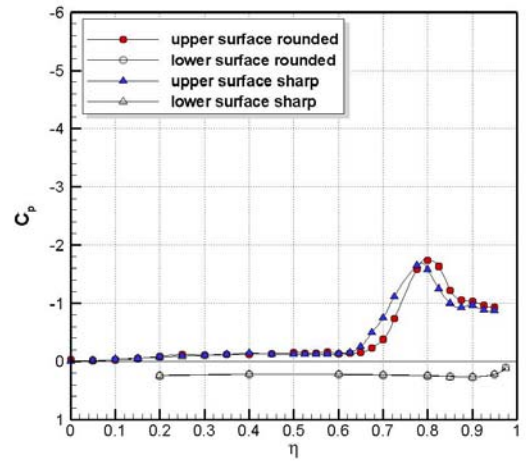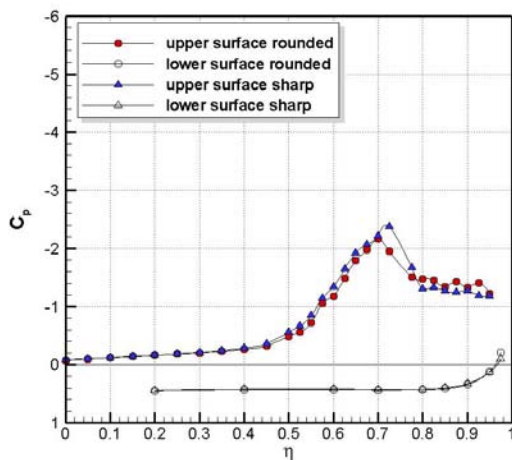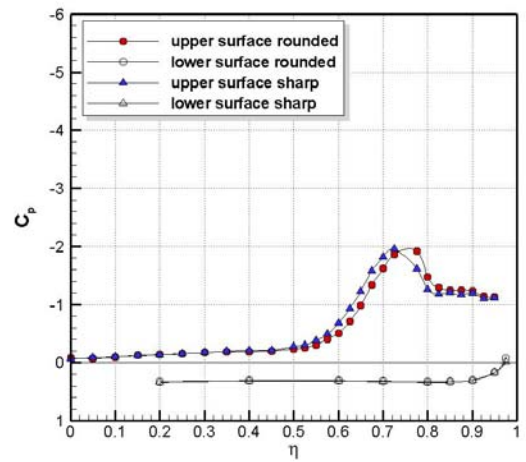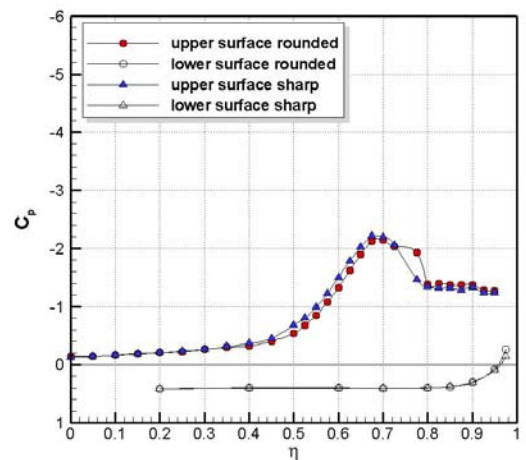
**Figure 21-7: Comparison of Steady Pressure Distribution between Sharp and Rounded
Leading Edge at $R_{mac} = 1 \times 10^6$ (left) and $R_{mac} = 2 \times 10^6$ (right) in Section $x/c_r = 0.6$.**

The quality of TUM-AER measurements have been judged by comparison with steady pressure measurements obtained by NASA for the delta wing reference configuration [[21-7], [21-23]]. Figure 21-8 contains the NASA results for R_{mac} = 2 x 10^6, M = 0.2 and the results obtained by TUM–AER for R_{mac} = 2 x 10^6, M = 0.14. The comparison shows a very good agreement between the steady pressure distributions, which clearly illustrates the comparability in terms of free stream, wind tunnel and model conditions.
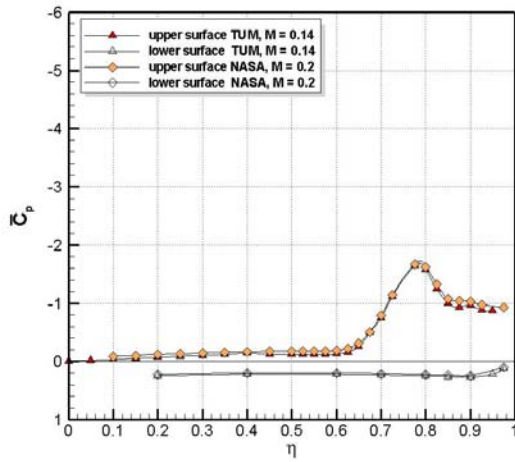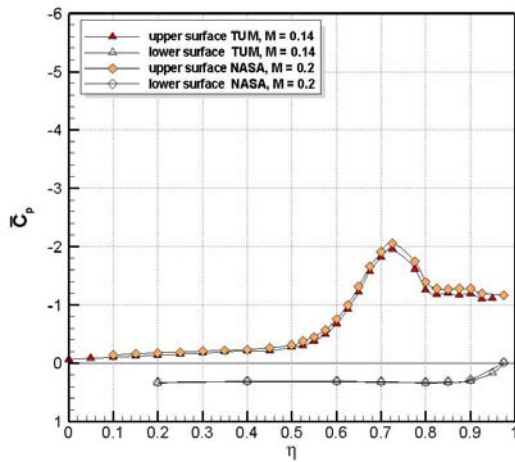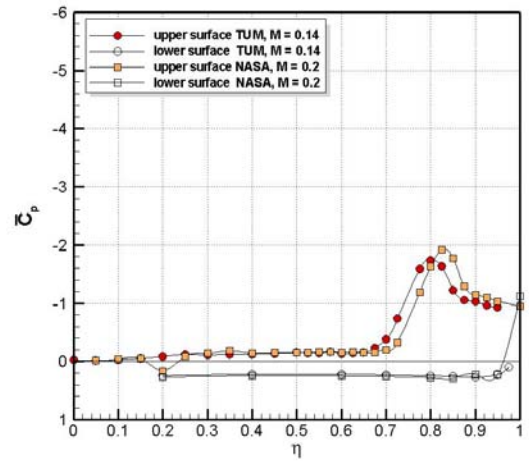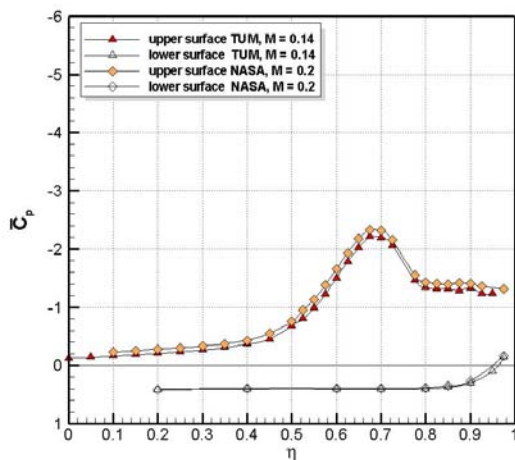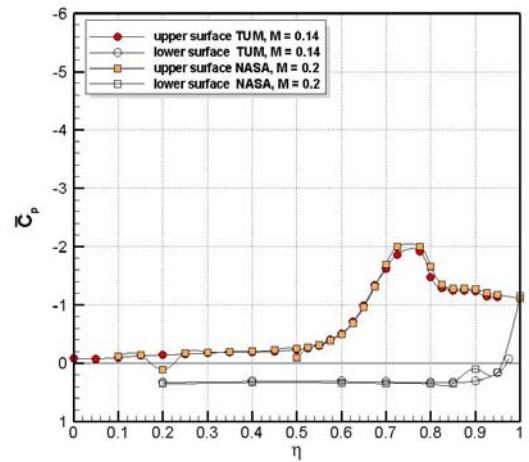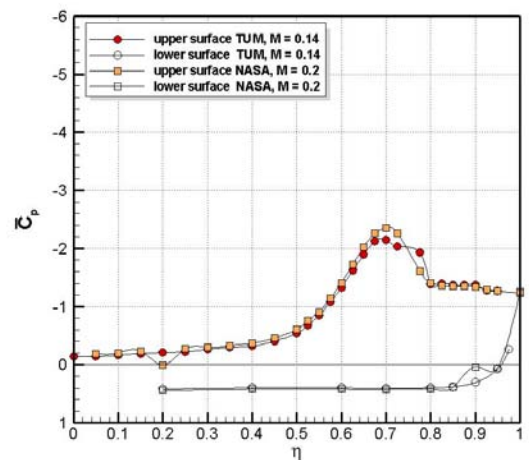
Figure 21-8: Comparison of Steady Pressure Distribution between NASA and TUM Measurements for Sharp (left) and Rounded (right) Leading Edge at $R_{mac} = 2 \times 10^6$ in Section $x/c_r = 0.6$.

(a) Lateral Position

(b) Vertical Position
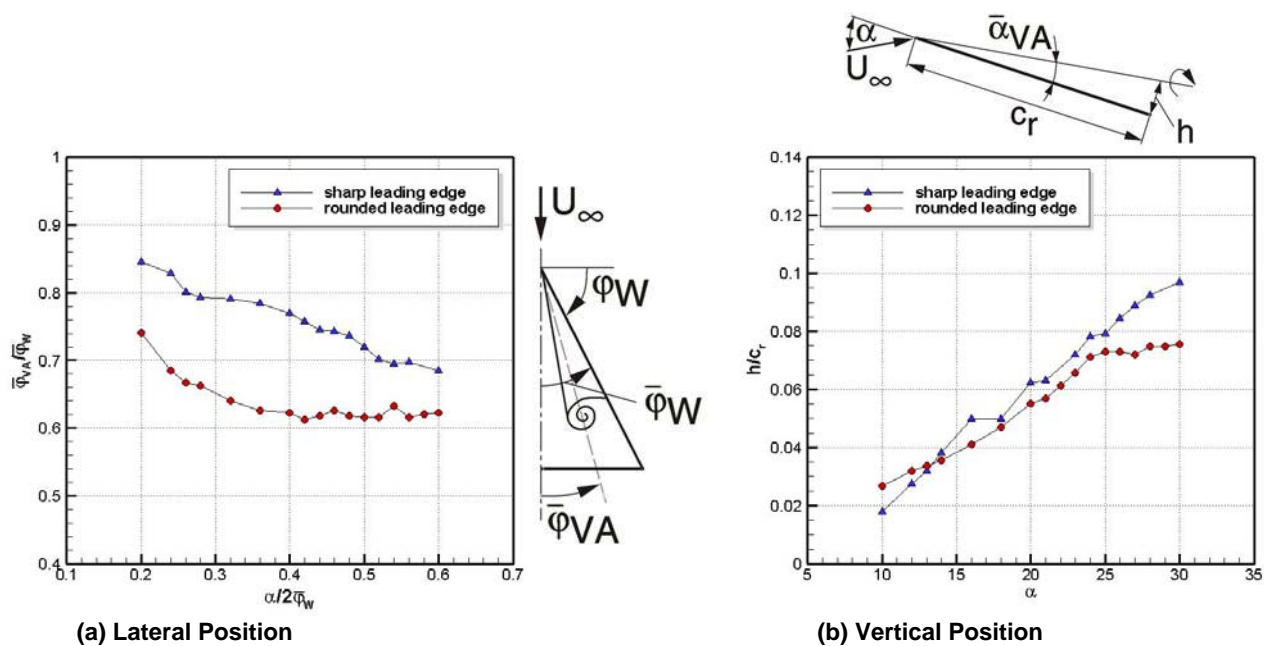
Figure 21-9: Position of the Primary Vortex Axis at R_{mac} = 5 x 10^5 and M = 0.035 (Values Taken at x/c_r = 0.95).

(a) Section x/c_r = 0.4

(b) Section x/c_r = 0.6
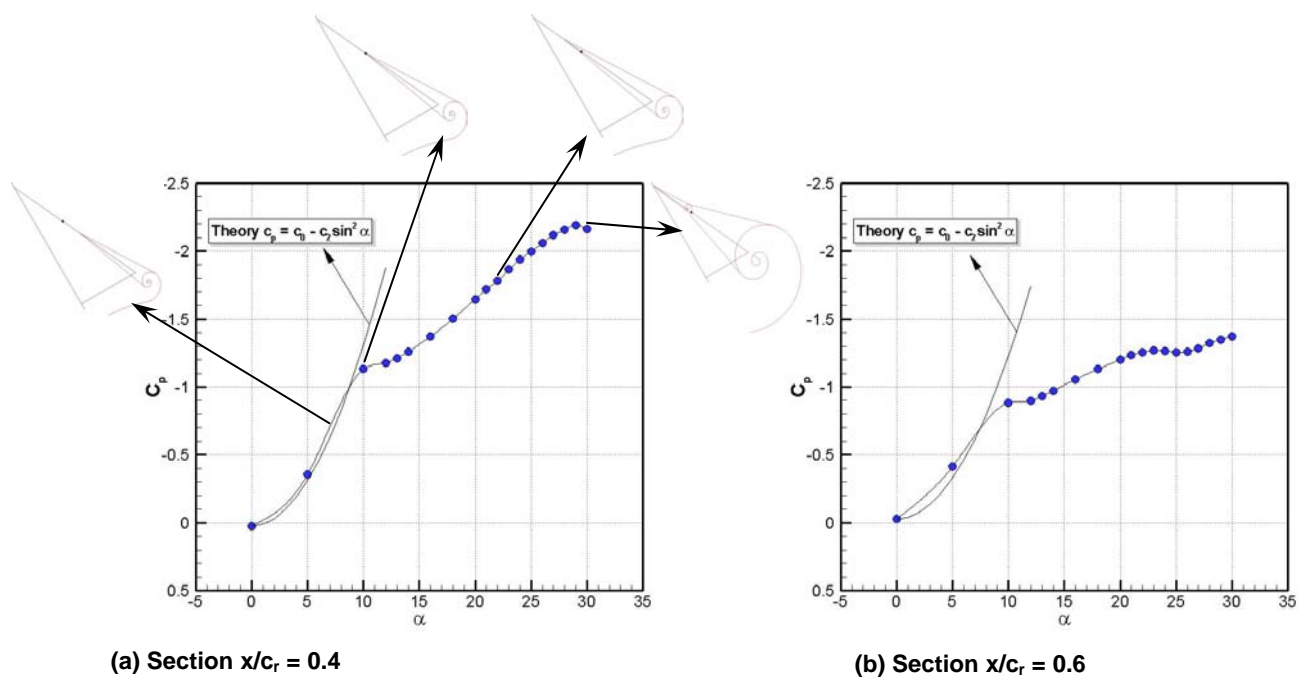
**Figure 21-10: Correlation of Separation Onset with Leading Edge Steady Pressure
Distribution for Sharp Leading Edge at R_{mac} = 2 x 10^6 in Position η = 0.95.**

21.4.2.2   Velocity Distribution

The time-averaged velocities obtained by Stereo-PIV at cross sections x/c_r = 0.2, 0.4, 0.6, 0.8 and 0.95 (R_{mac} = 1 x 10^6, M = 0.07) are shown for an angle of attack of α = 18° in Figure 21-11 and Figure 21-12. The velocity components in axial direction are displayed as contour plots and in lateral and vertical direction as vector plots. For both sharp and rounded leading edges, fully developed leading-edge vortices are present. The structure of primary and secondary vortex is depicted by the corresponding increased cross flow velocity vectors.

(a) α = 13°

(b) α = 18°

(c) α = 23°
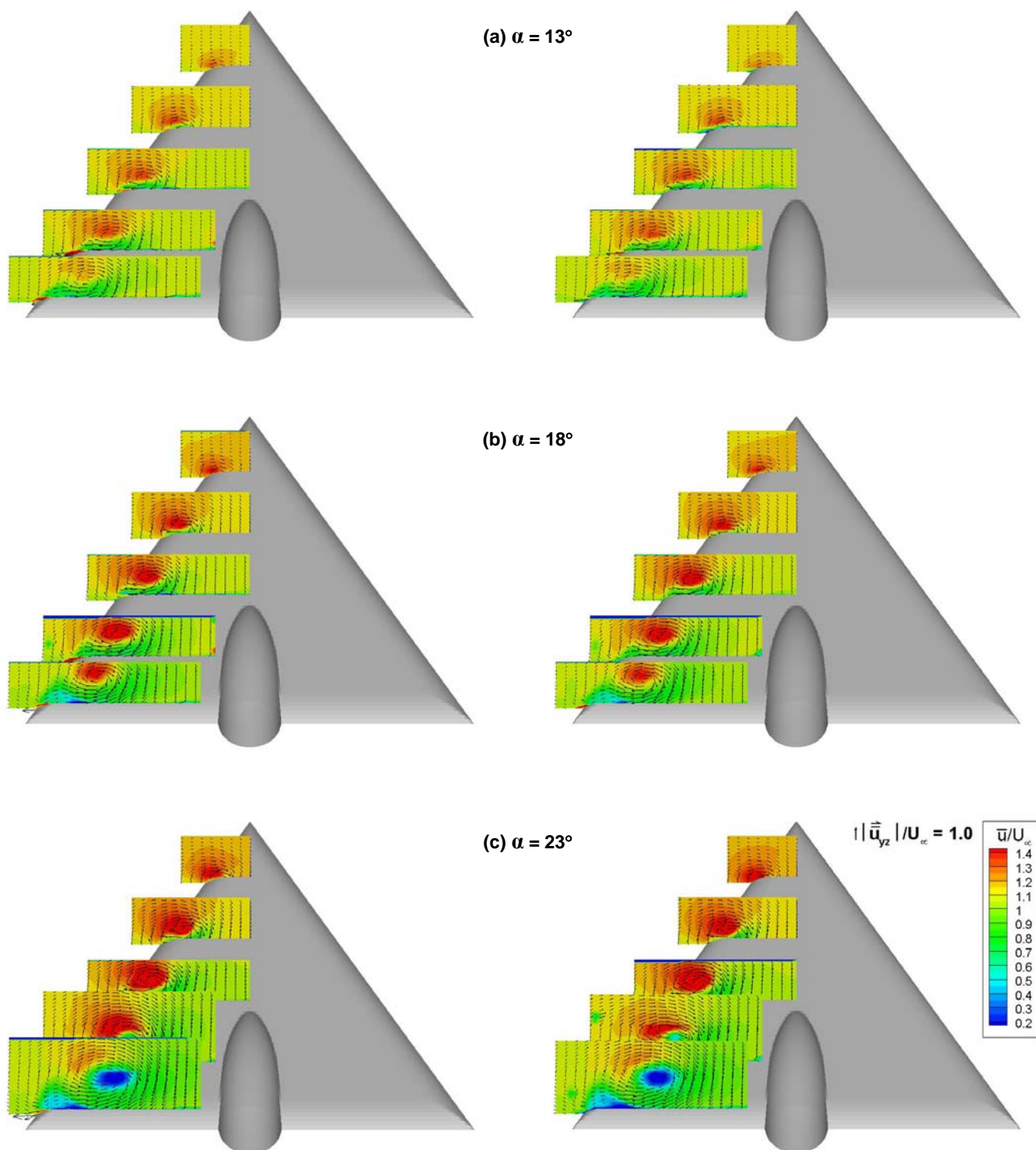
Figure 21-11: Mean Velocity Distribution at $R_{mac} = 1 \times 10^6$ and M = 0.07
for Sharp (left) and Rounded (right) Leading Edges.

(a) α = 13°

(b) α = 18°

(c) α = 23°
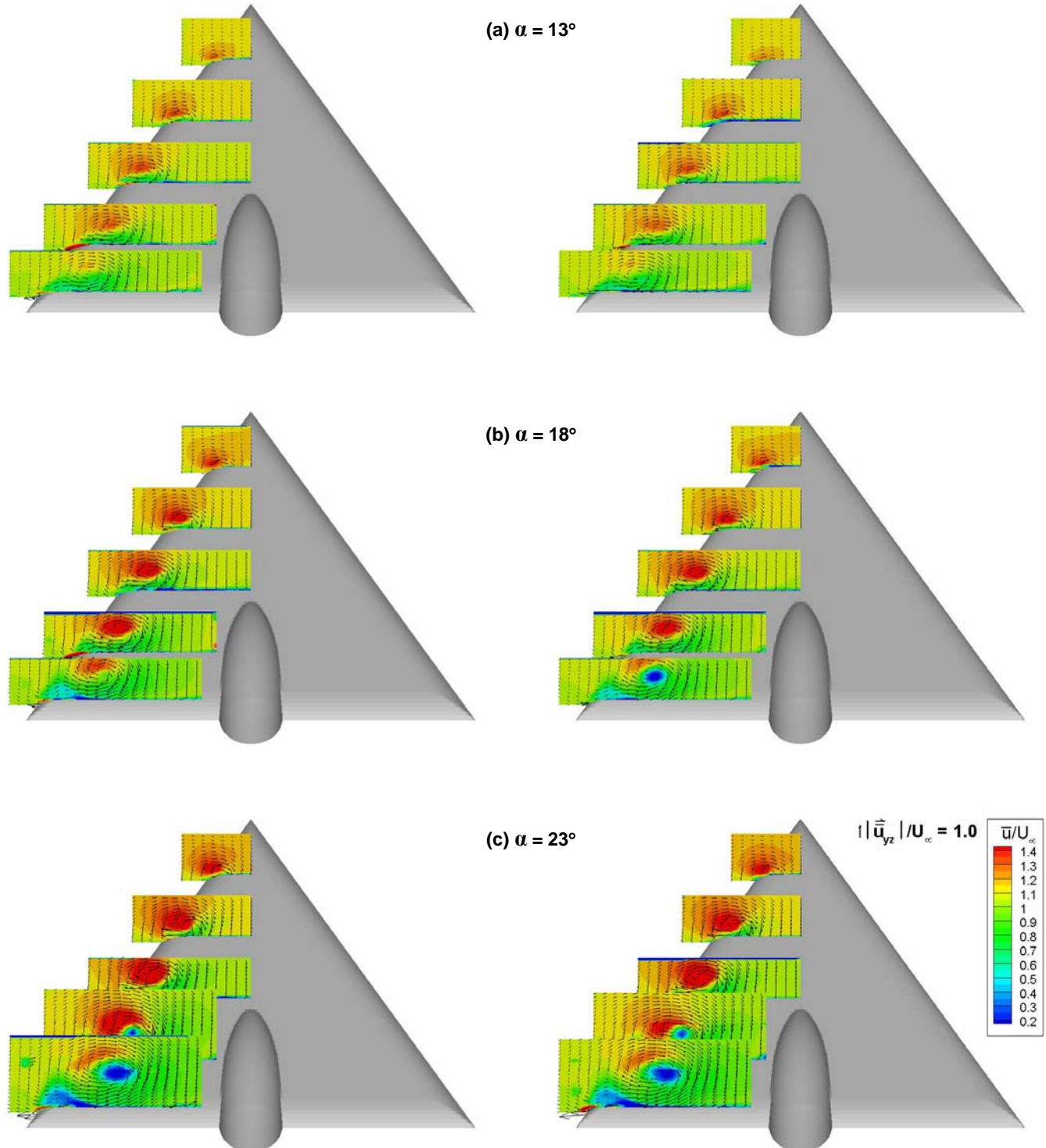
**Figure 21-12: Mean Velocity Distribution at $R_{mac} = 2 \times 10^6$ and
M = 0.35 for Sharp (left) and Rounded (right) Leading Edges.**

A comparison of the velocity fields obtained by Stereo-PIV and hot-wire anemometry for α = 18° and x/c$_r$ = 0.6 shows that the corresponding contour lines of all three velocity components, u, v, w, correspond very well, Figure 21-13. The primary vortex is associated with axial accelerated flow, with an axial peak velocity of $\overline{u}/U_\infty = 1.6$ for both sharp and rounded leading-edge [21-14]. The wing inboard region is characterized by attached flow while there is no clear indication for a small inboard vortex by this mean velocity field. The overall flowfield pattern does not show markable differences between the configurations of sharp and rounded leading-edge.

Figure 21-13: Comparison between Stereo-PIV and HWA Results for α = 18° at R_{mac} = 1 x 10^6 and M = 0.07 for Sharp (left) and Rounded (right) Leading Edge in Section x/c_r = 0.6.
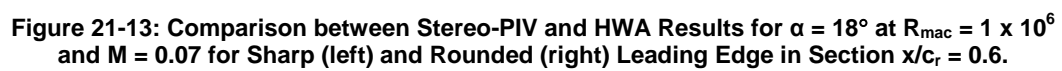
21.4.3   Turbulent Flow Field

21.4.3.1   Unsteady Surface Pressure Intensities

The fluctuation part of the pressure coefficient $c'_p(P,t)$ is described by:

$$c'_p(P,t) = c_p(P,t) - \overline{c}_p(P) \ . \tag{3}$$

The mean square value of the pressure coefficient $\overline{c'^2_p}(P)$ is therefore:

$$\overline{c'^2_p}(P) = \frac{1}{t_M} \int_0^{t_M} [c_p(P,t) - \overline{c}_p(P)]^2 \, dt \ . \tag{4}$$

The root mean square value is denoted rms-value $c_{p_{rms}}(P)$:

$$c_{p_{rms}}(P) = \sqrt{\overline{c'^2_p}(P)} \tag{5}$$

Referring again to angles of attack of $\alpha = 13°$, $\alpha = 18°$ and $\alpha = 23°$, the unsteady surface pressures are discussed based on root-mean-square (rms) values of the pressure coefficient and pressure amplitude spectra. The maximum peak of pressure fluctuation intensities C_{prms} in section $x/c_r = 0.6$ is observed in the area of the primary vortex outside of the suction peak near the attachment line of the secondary vortex (Figure 21-14 and Figure 21-15). The suction peak of the mean pressure $\overline{c}_p$ is broadened for the case of rounded leading-edge. It is located closer to the leading-edge due to retarded primary separation in comparison to the sharp leading-edge. The primary separation line, which is not geometrically fixed for the rounded leading-edge, is associated with increased pressure fluctuation intensities in the area of the leading edge $\eta = 0.8 \div 1$ in comparison to the sharp edge case.

(a) α = 13°

(b) α = 18°

(c) α = 23°
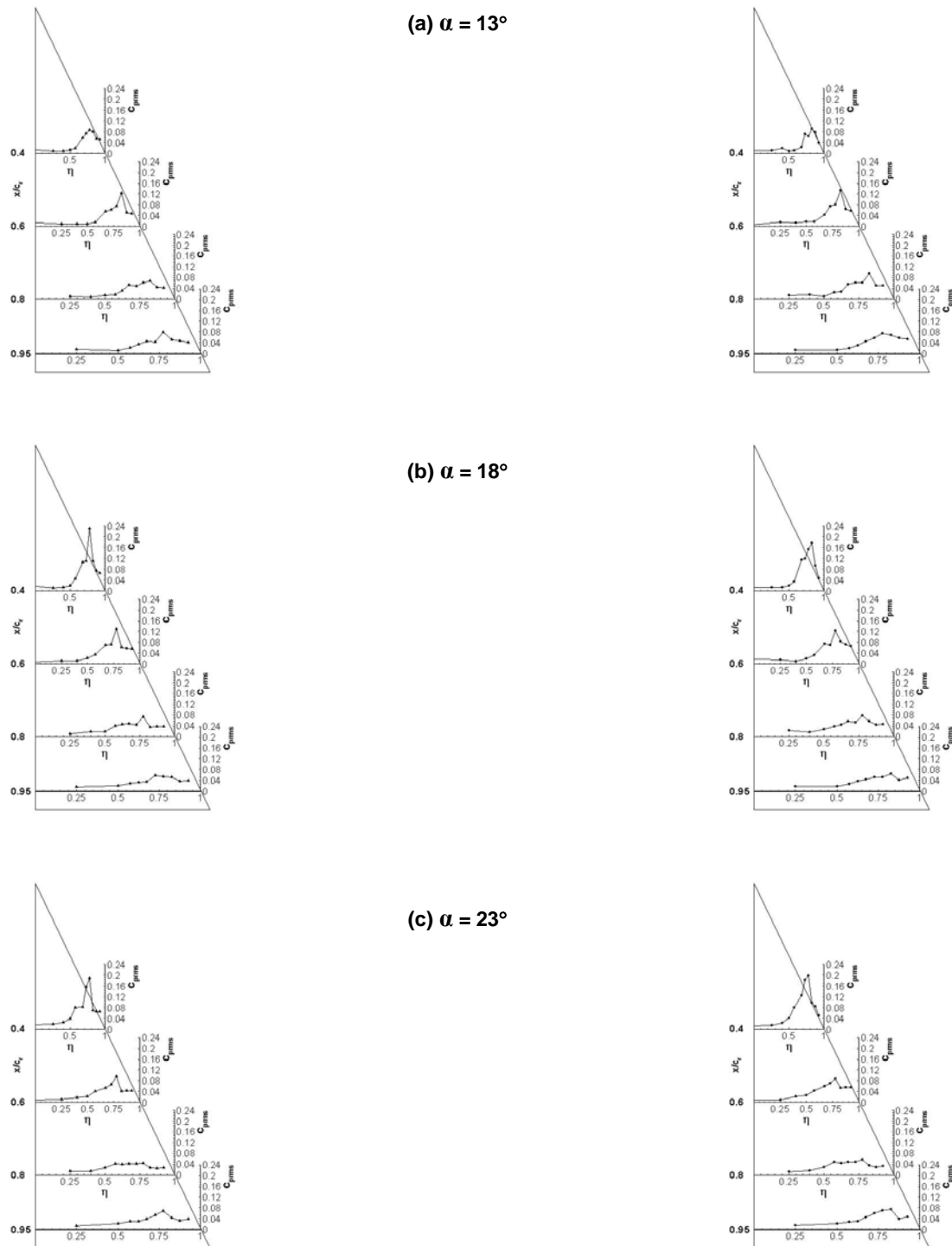
Figure 21-14: Pressure Fluctuation Intensity at $R_{mac} = 1 \times 10^6$ and
M = 0.07 for Sharp (left) and Rounded (right) Leading Edges.

(a) α = 13°

(b) α = 18°

(c) α = 23°
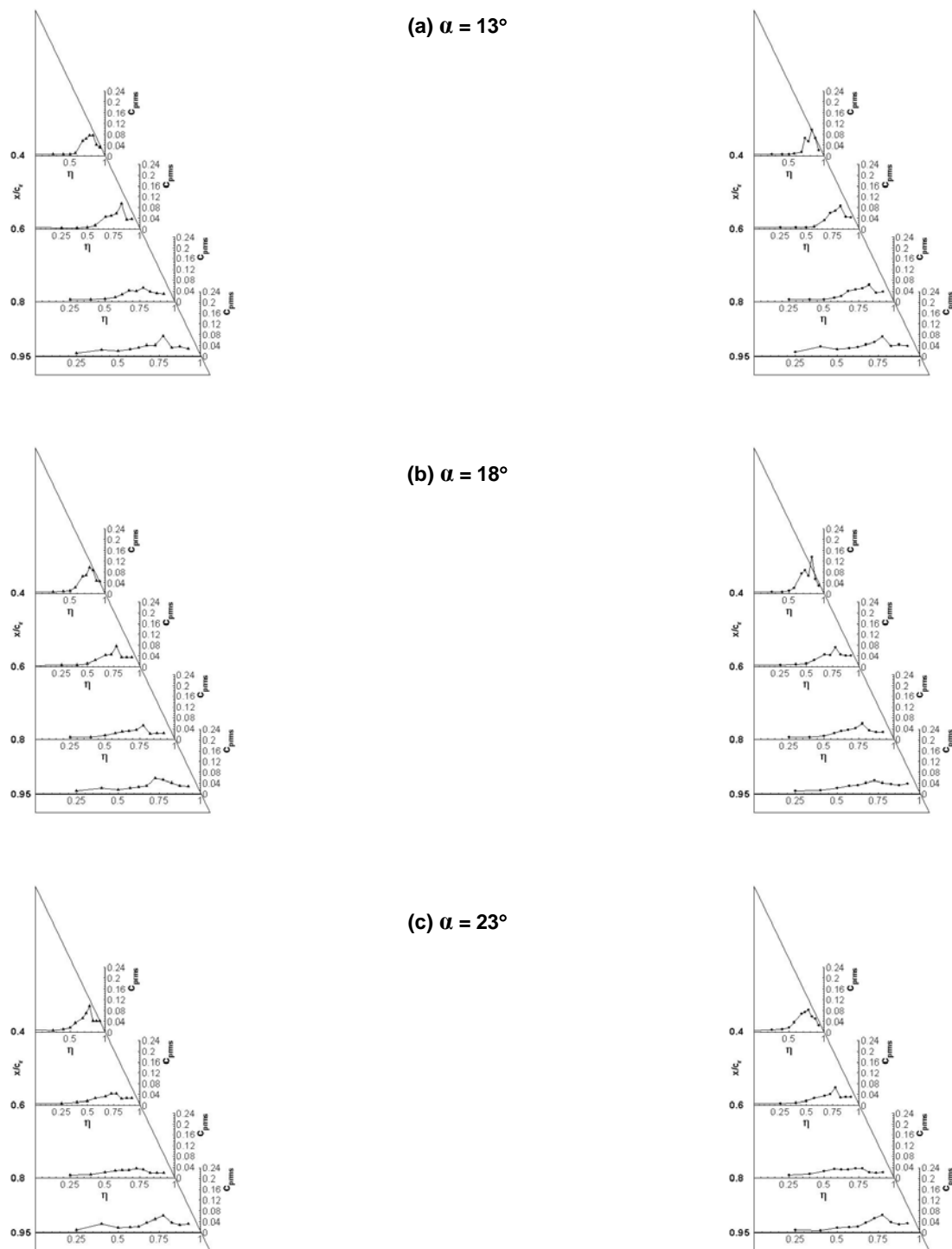
**Figure 21-15: Pressure Fluctuation Intensity at R_{mac} = 2 x 10^6 and
M = 0.14 for Sharp (left) and Rounded (right) Leading Edges.**

21.4.3.2   Unsteady Surface Pressure Spectra

The fluctuation part p'(P,t) of the discrete time function p(P,t), respectively is Fourier transformed based on the relation:

$$X_p(P,\omega) = \lim_{t_M \to \infty} \int_0^{t_M} p'(P,t)e^{-i\omega t} dt \; . \tag{6}$$

The multiplication of the Fourier transformed quantities $X_p(P,\omega)$ with its conjugated complex quantities $X_p^*(P,\omega)$ leads to the power spectral density function.

$$S_P(P,\omega) = \lim_{t_M \to \infty} \frac{2}{t_M} X_p^*(P,\omega) X_p^T(P,\omega) \tag{7}$$

Accordingly, the power spectral density for the fluctuating part $S_{cp}(P,\omega)$ can be derived. The power spectral density of the pressure coefficient fluctuations still has the dimension of time. Taking into account the definition of the reduced frequency (Eq. 9) leads to the non dimensional power spectral density of the pressure coefficient fluctuations:

$$S_{c_p}^N(P,k) = \frac{U_\infty}{l_\mu} S_{c_p}(P,k) \tag{8}$$

$$k = \frac{f \cdot \overline{c}}{U_\infty} \tag{9}$$

The non dimensional power spectral density of the pressure coefficient $S_{c_p}^N$(P,k) can be transformed to an amplitude spectrum of the pressure coefficient:

$$\hat{c}_p(P,k) = \sqrt{2 S_{c_p}^N(P,k) \Delta k} \tag{10}$$

The amplitude spectra of the fluctuating pressure coefficient $\hat{c}_p$ are plotted as function of reduced frequency k for each measured spanwise station η for α = 13°, 18°, and 23° in Figure 21-16, Figure 21-17, and Figure 21-18. At an angle of attack of α = 13°, the amplitude level of pressure spectra for the rounded leading edge is slightly higher as for the sharp leading edge, especially in the low frequency domain, Figure 21-16. By increasing the angle of attack to α = 18° no significant change is noticeable, except for the amplitude spectrum at x/c_r = 0.4 for the rounded leading edge, Figure 21-17. There, the level of the highest frequencies is clearly increased and reaches a maximum $\hat{c}_p$ = 0.012 in the range of k = 2 ÷ 3.1, which illustrates the separation of the secondary vortex. Raised amplitude values can be detected in direction to the leading-edge linked to fluctuations in the primary separation and secondary separation and attachment. The spectra reveal a broadband behavior and are typical for a fully developed leading-edge primary vortex [[21-1], [21-2], [21-11], [21-12]].
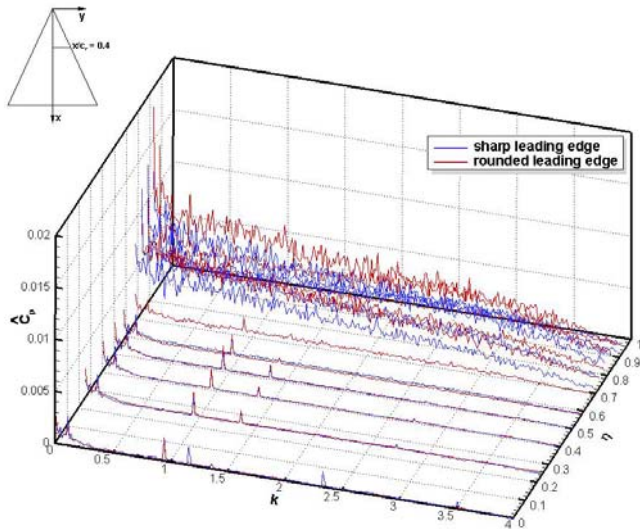
(a) $x/c_r = 0.4$
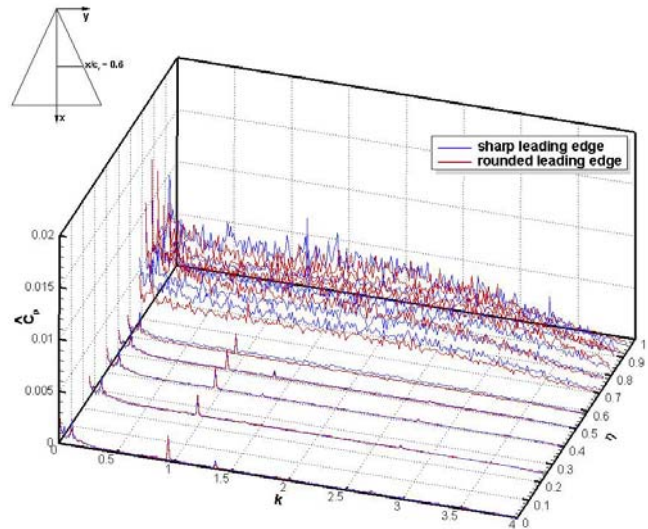
(b) $x/c_r = 0.6$
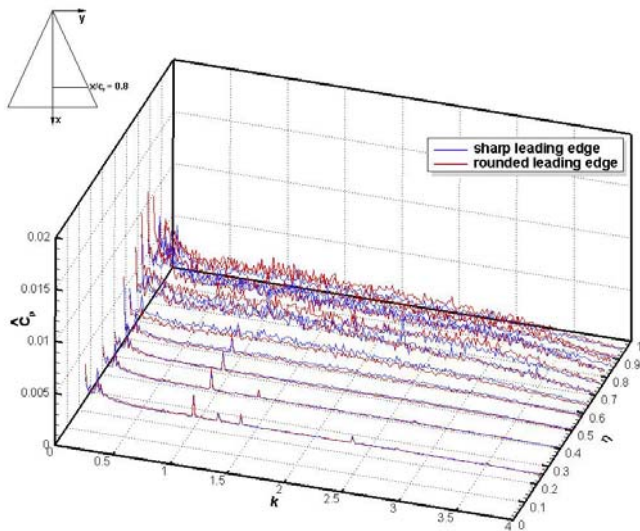
(c) $x/c_r = 0.8$
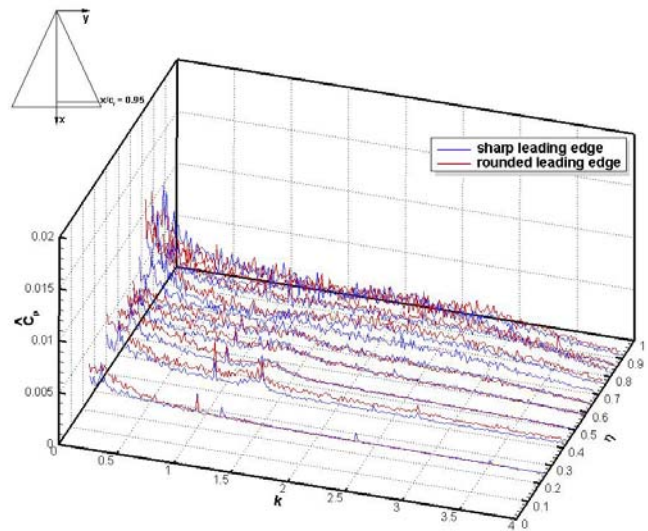
(d) $x/c_r = 0.95$

**Figure 21-16: Amplitude Spectra of Fluctuating Pressure Coefficient for
Sharp and Rounded Leading Edge at $\alpha = 13°$, $R_{mac} = 2 \times 10^6$ and M = 0.14.**
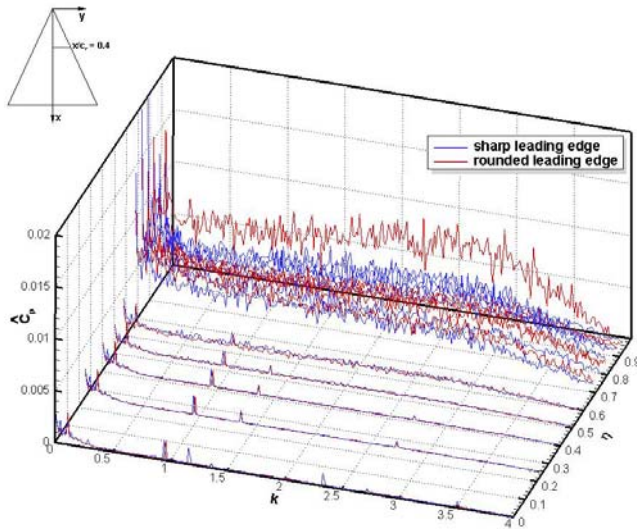
(a) x/c$_r$ = 0.4
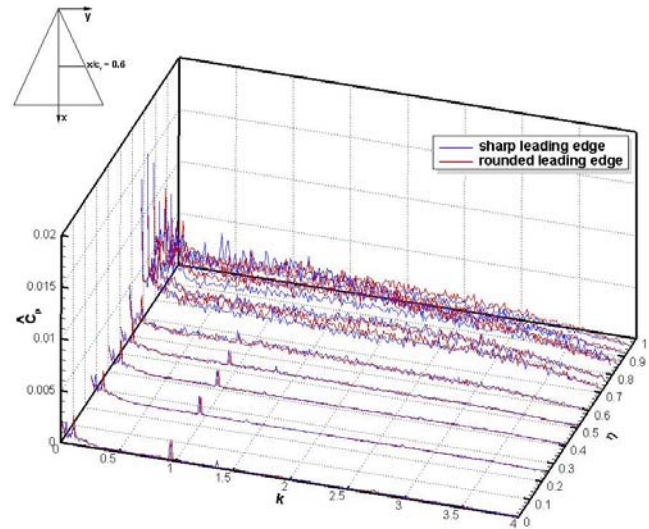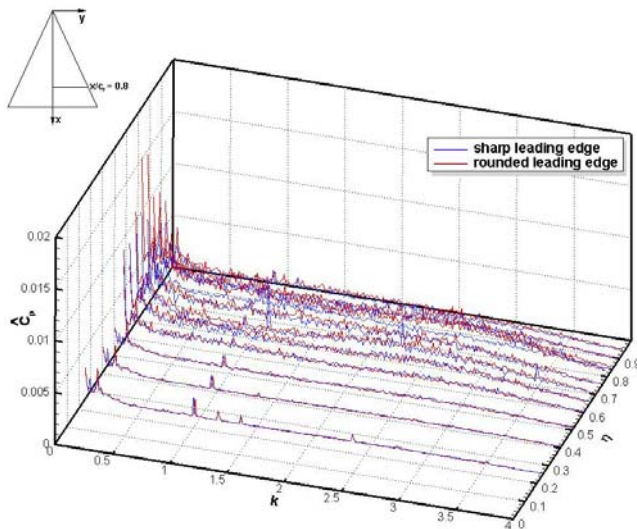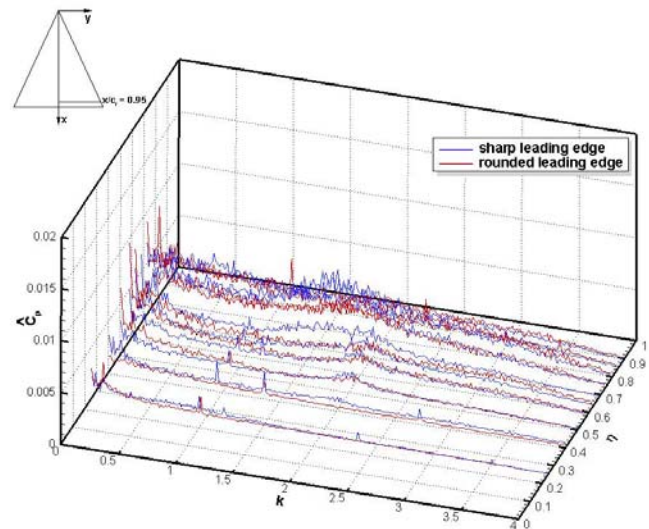
(b) x/c$_r$ = 0.6

(c) x/c$_r$ = 0.8

(d) x/c$_r$ = 0.95

Figure 21-17: Amplitude Spectra of Fluctuating Pressure Coefficient for
Sharp and Rounded Leading Edge at α = 18°, R$_{mac}$ = 2 x 10^6 and M = 0.14.
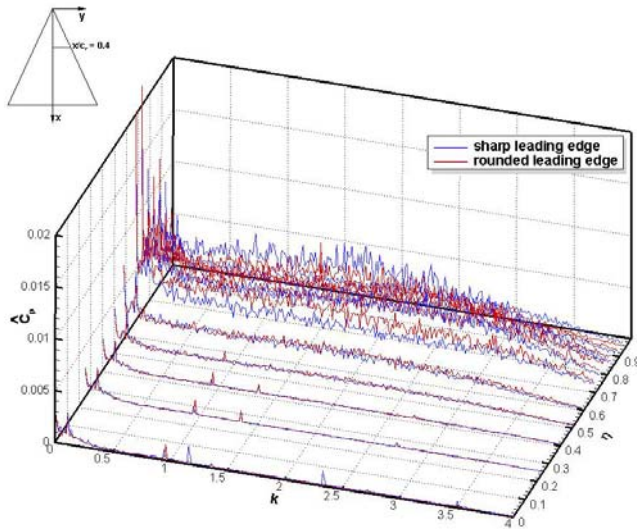
(a) $x/c_r = 0.4$
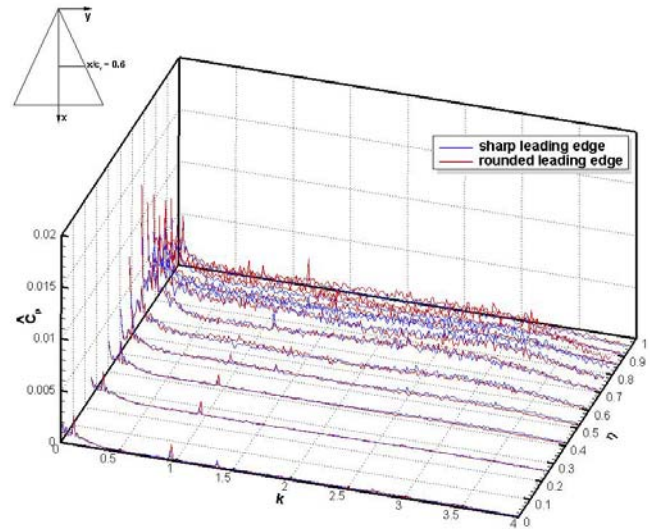
(b) $x/c_r = 0.6$
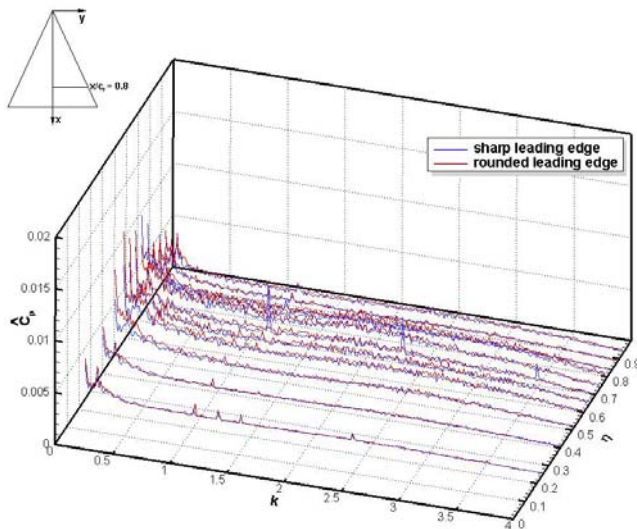
(c) $x/c_r = 0.8$
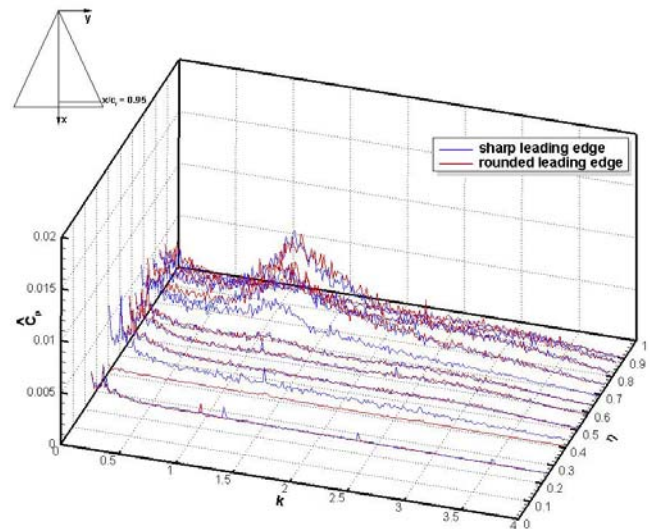
(d) $x/c_r = 0.95$

Figure 21-18: Amplitude Spectra of Fluctuating Pressure Coefficient for
Sharp and Rounded Leading Edge at α = 23°, R_{mac} = 2 x 10^6 and M = 0.14.

At an angle of attack of $\alpha = 23°$, the increase in amplitude for both leading-edge geometries is visible, whereby the increase in the chord station $x/c_r = 0.4$ for the sharp leading-edge is more significant, Figure 21-18. The increase in the chord station $x/c_r = 0.95$, especially the amplitude peaks $\hat{c}_p = 0.0095$ at k = 1.1 ÷ 1.4, indicate the breakdown of the primary vortex for both leading-edge geometries. This takes place for the rounded

leading at $\eta = 0.775$ and for the sharp leading edge at $\eta = 0.825$. An additional increase in the high frequency domain (k = 2.5 ÷ 3.0) to $\hat{c}_p = 0.005$ illustrates the separation at the trailing edge.

21.4.3.3   Velocity Fluctuation Intensities and Reynolds Stresses

For each flowfield position P the time series of the velocities $u_i(P,t)$ are available for every test condition.

The average of the velocity $\overline{u}_i(P,t)$ is defined as:

$$\overline{u}_i(P) = \frac{1}{t_M} \int_0^{t_M} u_i(P,t)dt \ , \tag{11}$$

with t_M as the measurement time or length of the time series. The fluctuation part of the velocity $u_i'(P,t)$ is described by:

$$u_i'(P,t) = u_i(P,t) - \overline{u}_i(P) \ . \tag{12}$$

The mean square value of the velocity fluctuations $\overline{u_i'^2}(P)$ is therefore:

$$\overline{u_i'^2}(P) = \frac{1}{t_M} \int_0^{t_M} [u_i(P,t) - \overline{u}_i(p)]^2 dt \ . \tag{13}$$

The root mean square value is denoted rms-value $u_{i_{rms}}(P)$ and is converted in non-dimensional values:

$$\frac{u_{i_{rms}}(P)}{U_\infty} = \frac{\sqrt{\overline{u_i'^2}(P)}}{U_\infty} \tag{14}$$

The fluctuating velocity field at station $x/c_r = 0.4$, $x/c_r = 0.6$ and $x/c_r = 0.8$ for $\alpha = 13°$, 18°, and, 23° is obtained by hot-wire measurements, the results of which are shown for sharp and rounded leading-edge in Figure 21-19 – Figure 21-23. In Figure 21-19, the rms values of the axial velocity fluctuations are plotted. The fluctuation intensities indicate high levels for the viscous core of the primary vortex and the region of the secondary vortex and moderate levels for the separating shear layer and primary vortex rotational core. The intensity of the lateral velocity fluctuations also displays high levels for the primary vortex subcore as well as for the shear layer, Figure 21-20. Considering the intensity of the vertical velocity fluctuations, increased values exist mainly in the primary vortex subcore, Figure 21-21. Moderate levels are found for the region of the secondary vortex because the vertical velocity fluctuations are the first to be damped approaching the wing surface. The shear stress $\overline{u'v'}/U_\infty{}^2$ shows high positive values in the vortex core and in the surface flow under the primary vortex, Figure 21-22. High negative values are visible in the region of the outboard shear layer and in the shear layer over the primary vortex subcore. Negative and positive values are determined by the direction of the lateral velocity when moving from outboard to inboard along the vorticity feeding shear layer. The shear stress distribution $\overline{u'w'}/U_\infty{}^2$ exhibit again increased levels for the regions of

vertical flow, Figure 21-23. Peak values are located in neighboured regions relative to the $\overline{u'v'}$-maxima and are of opposite sign. The direction of the vertical velocity determines the sign of this stress component.

(a) α = 13°

(b) α = 18°

(c) α = 23°
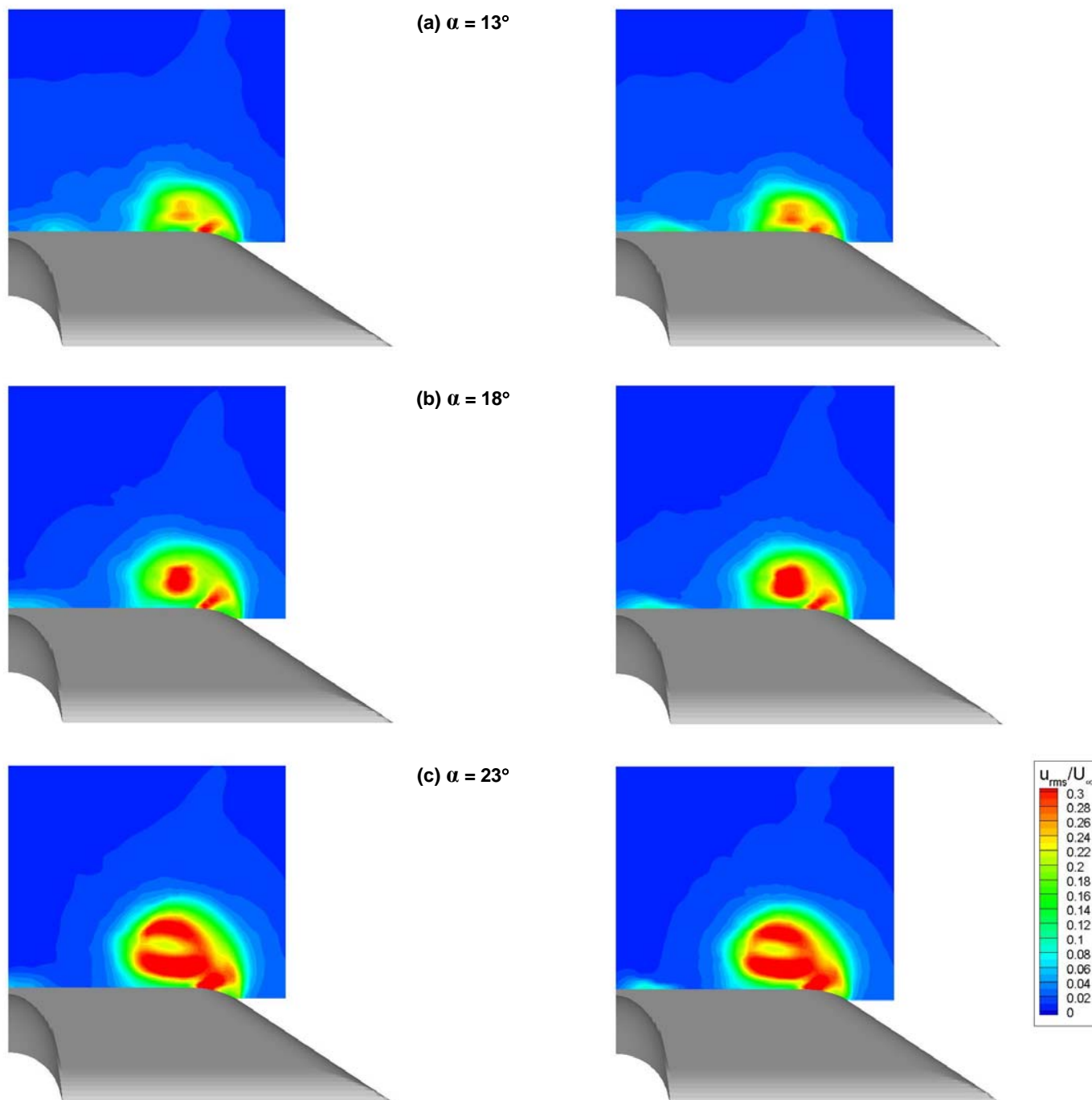
Figure 21-19: Turbulence Intensity Distribution of the Axial Velocity Fluctuations at R_{mac} = 1 x 10^6 and M = 0.07 for Sharp (left) and Rounded (right) Leading Edge in Section x/c_r = 0.6.

(a) α = 13°

(b) α = 18°

(c) α = 23°
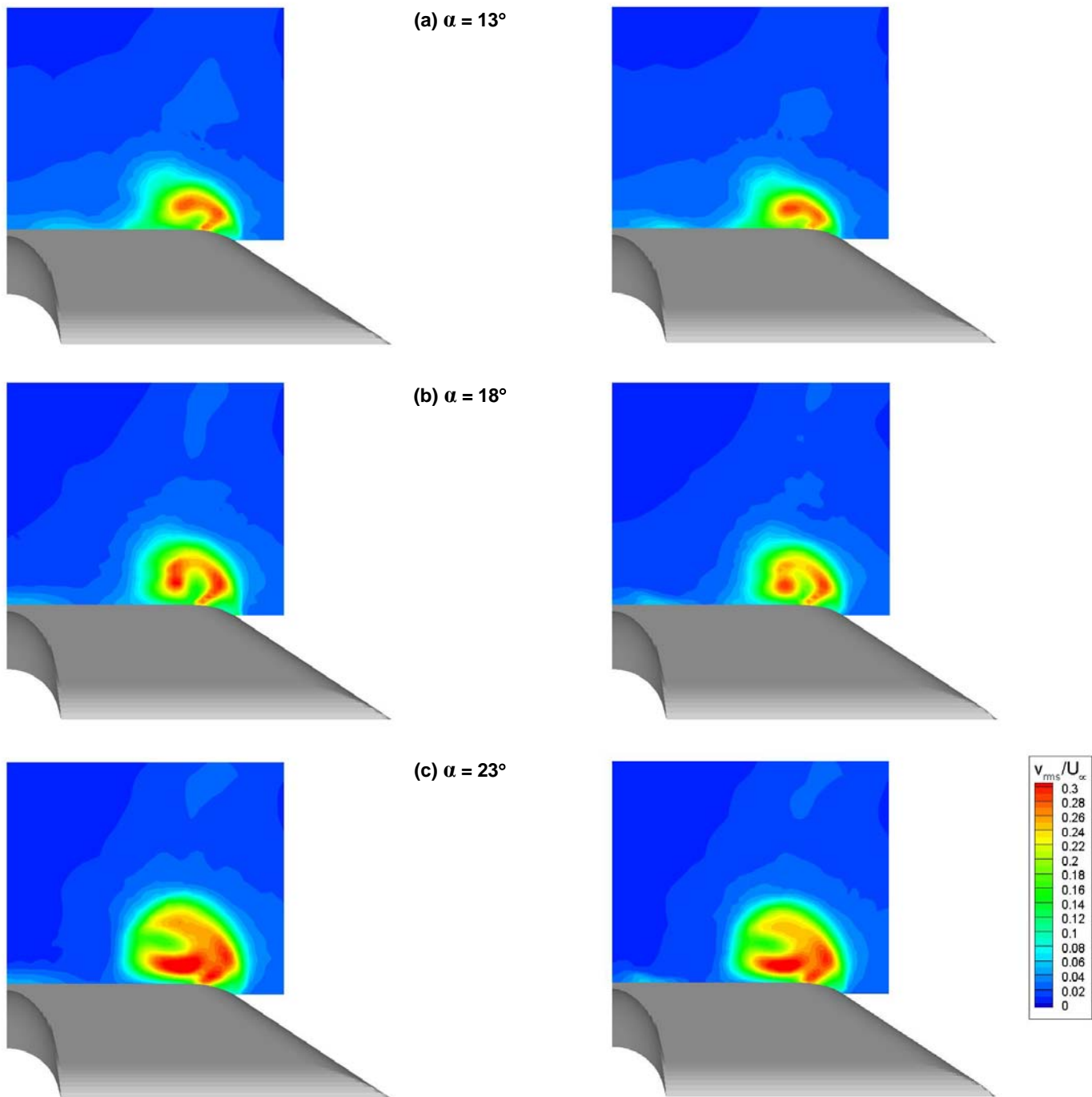
**Figure 21-20: Turbulence Intensity Distribution of the Lateral Velocity Fluctuations at R$_{mac}$ = 1 x 10^6
and M = 0.07 for Sharp (left) and Rounded (right) Leading Edge in Section x/c$_r$ = 0.6.**

(a) α = 13°

(b) α = 18°

(c) α = 23°
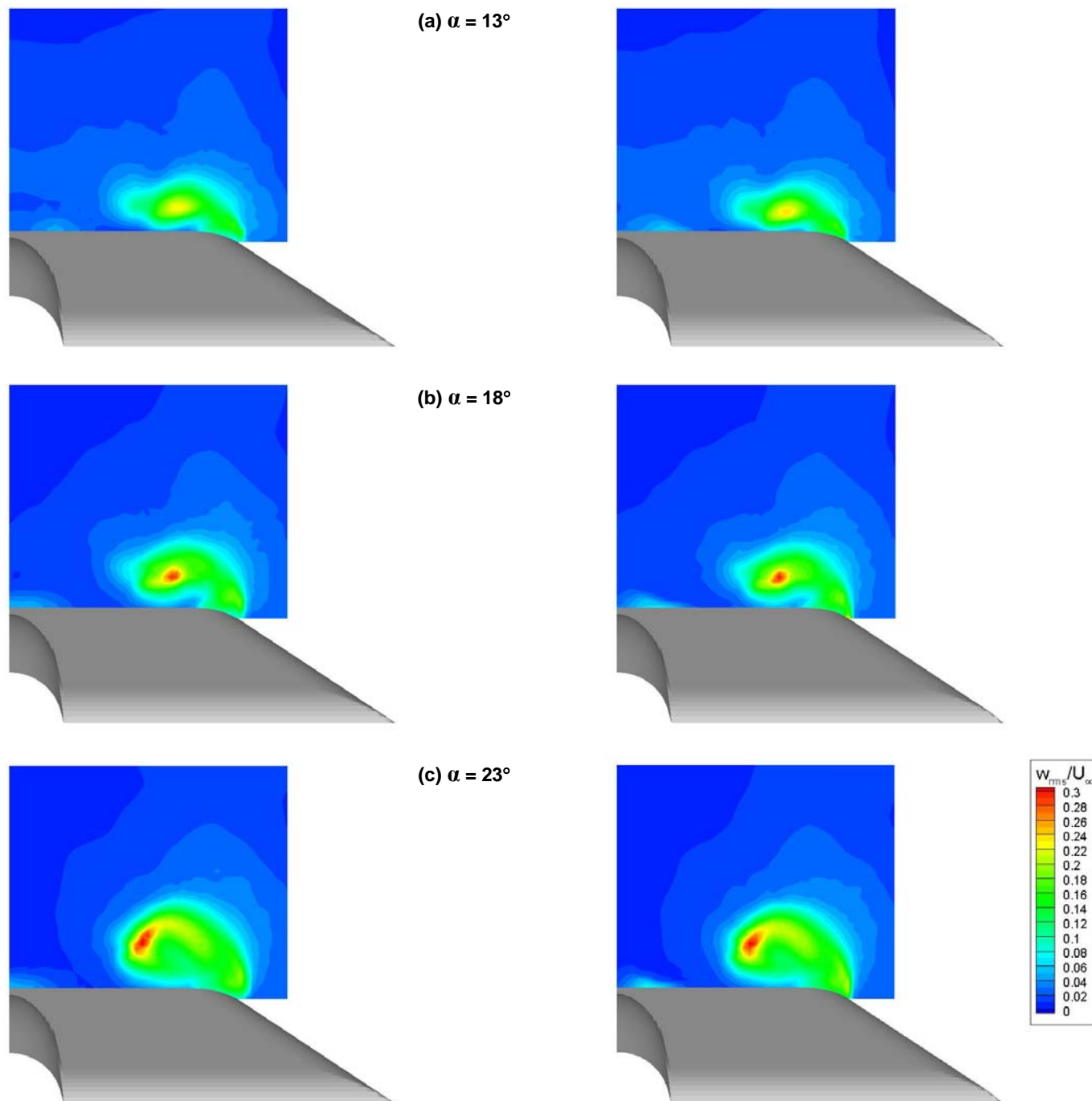
Figure 21-21: Turbulence Intensity Distribution of the Vertical Velocity Fluctuations at $R_{mac} = 1 \times 10^6$ and M = 0.07 for Sharp (left) and Rounded (right) Leading Edge in Section $x/c_r = 0.6$.
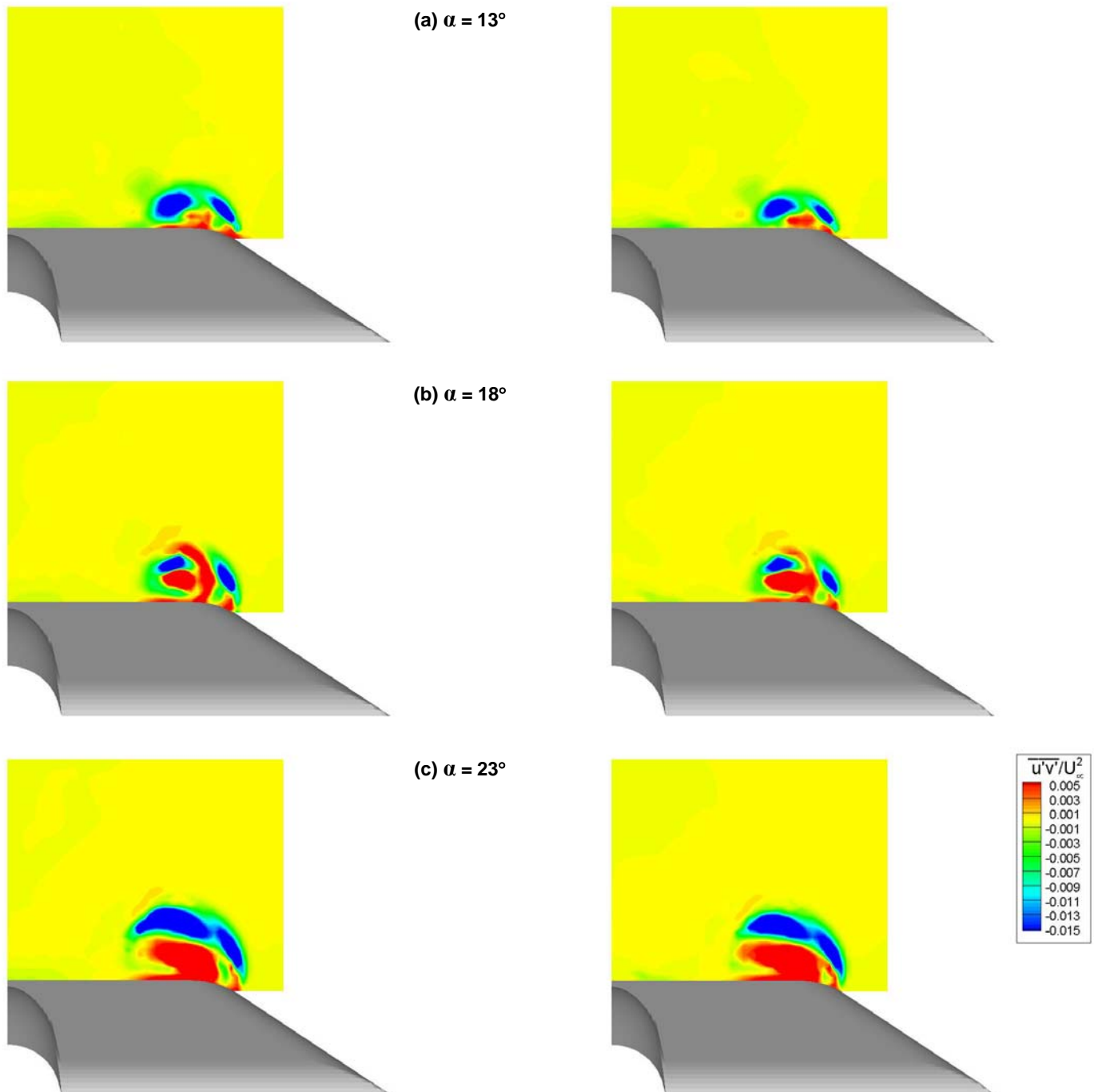
Figure 21-22: Shear Stress Distribution of the Axial and Lateral Velocity Fluctuations at $R_{mac} = 1 \times 10^6$ and $M = 0.07$ for Sharp (left) and Rounded (right) Leading Edge in Section $x/c_r = 0.6$.

(a) α = 13°

(b) α = 18°

(c) α = 23°
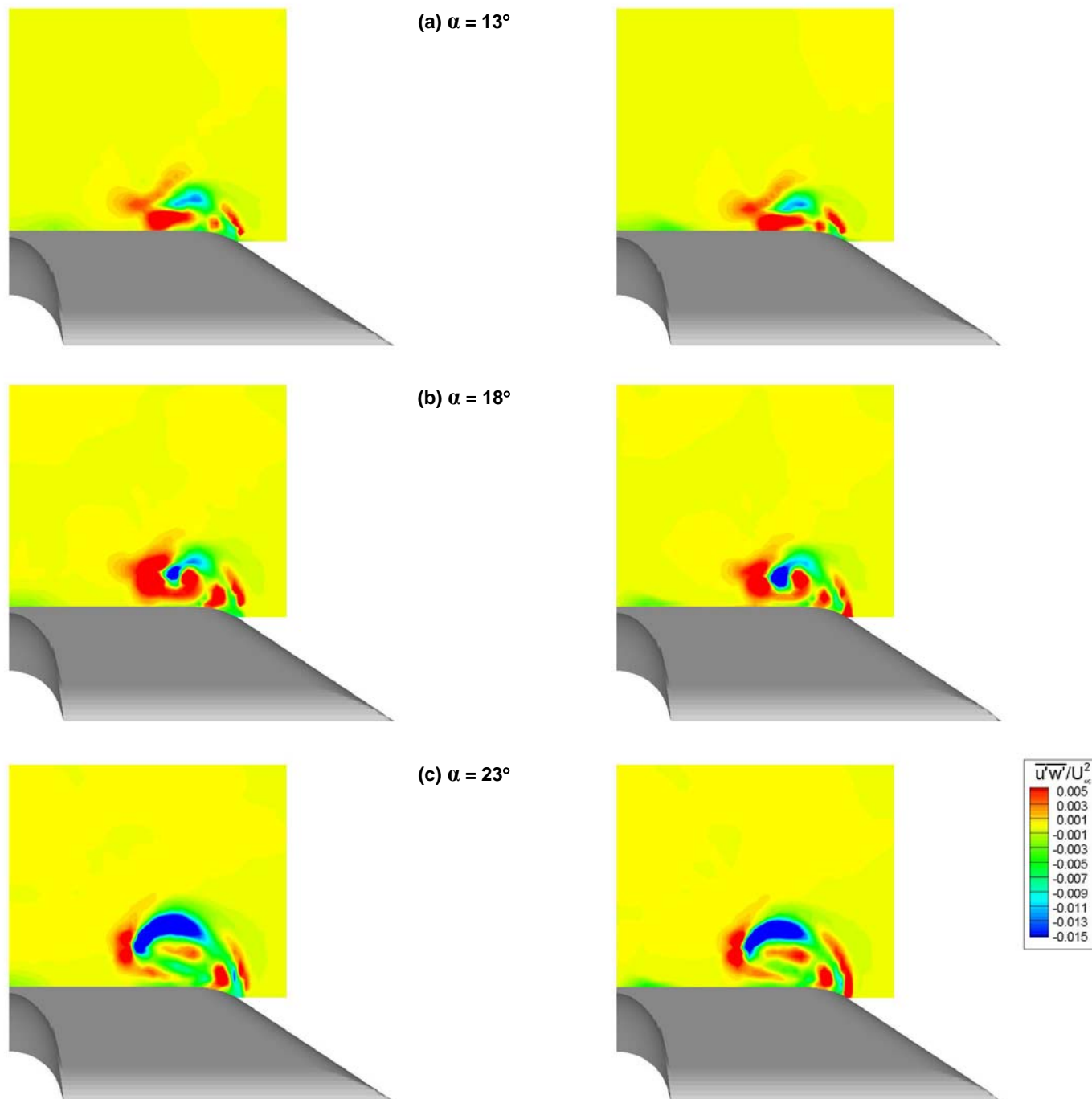
**Figure 21-23: Shear Stress Distribution of the Axial and Vertical Velocity Fluctuations at $R_{mac} = 1 \times 10^6$
and M = 0.07 for Sharp (left) and Rounded (right) Leading Edge in Section $x/c_r = 0.6$.**

A small region of slightly increased velocity fluctuations and turbulent shear stresses near the symmetry plane of the wing is due to the weak inboard vortex, the development of which was explained above.

21.4.3.4   Spectral Densities of Velocity Fluctuations

Spectral analysis is applied to the velocity time series to study the characteristics in the area of the highest velocity fluctuation intensity. The fluctuation part $u_i'(P,t)$ of the discrete time function $u_i(P,t)$ is Fourier transformed based on the relation:

$$X_{u_i'}(P,\omega) = \lim_{t_M \to \infty} \int_0^{t_M} u_i'(P,t) e^{-i\omega t} dt \ . \tag{15}$$

The multiplication of the Fourier transformed quantity $X_{u_i'}(P,\omega)$ with its conjugated complex quantity $X_{u_i'}^*(P,\omega)$ leads to the power spectral density function:

$$S_{u_i'}(P,\omega) = \lim_{t_M \to \infty} \frac{2}{t_M} X_{u_i'}^*(P,\omega) X_{u_i'}^T(P,\omega) \ . \tag{16}$$

The power spectral density of the velocity fluctuations has the dimension of the square of velocity and time. Taking into account the definition of the reduced frequency leads to the non dimensional power spectral density of the velocity fluctuations:

$$S_{u_i'}^N(P,k) = \frac{U_\infty}{\overline{c} u_i'^2} S_{u_i'}(P,k) \tag{17}$$

The power spectral density distributions of the axial velocity fluctuations are shown for a number of measurement points crossing laterally through the vortex core region and the separating shear layer. The angles of attack discussed include α = 18° and 23°. The measurement stations are depicted in Figure 21-24, Figure 21-25, Figure 21-26 and Figure 21-27 (left) for the three cross sections of interest, namely x/c_r = 0.4, 0.6 and 0.8, with respect to the contour lines of the turbulence intensity distributions of the axial velocity fluctuations. The corresponding power spectral density distributions are plotted in Figure 21-24 – Figure 21-27 (right).
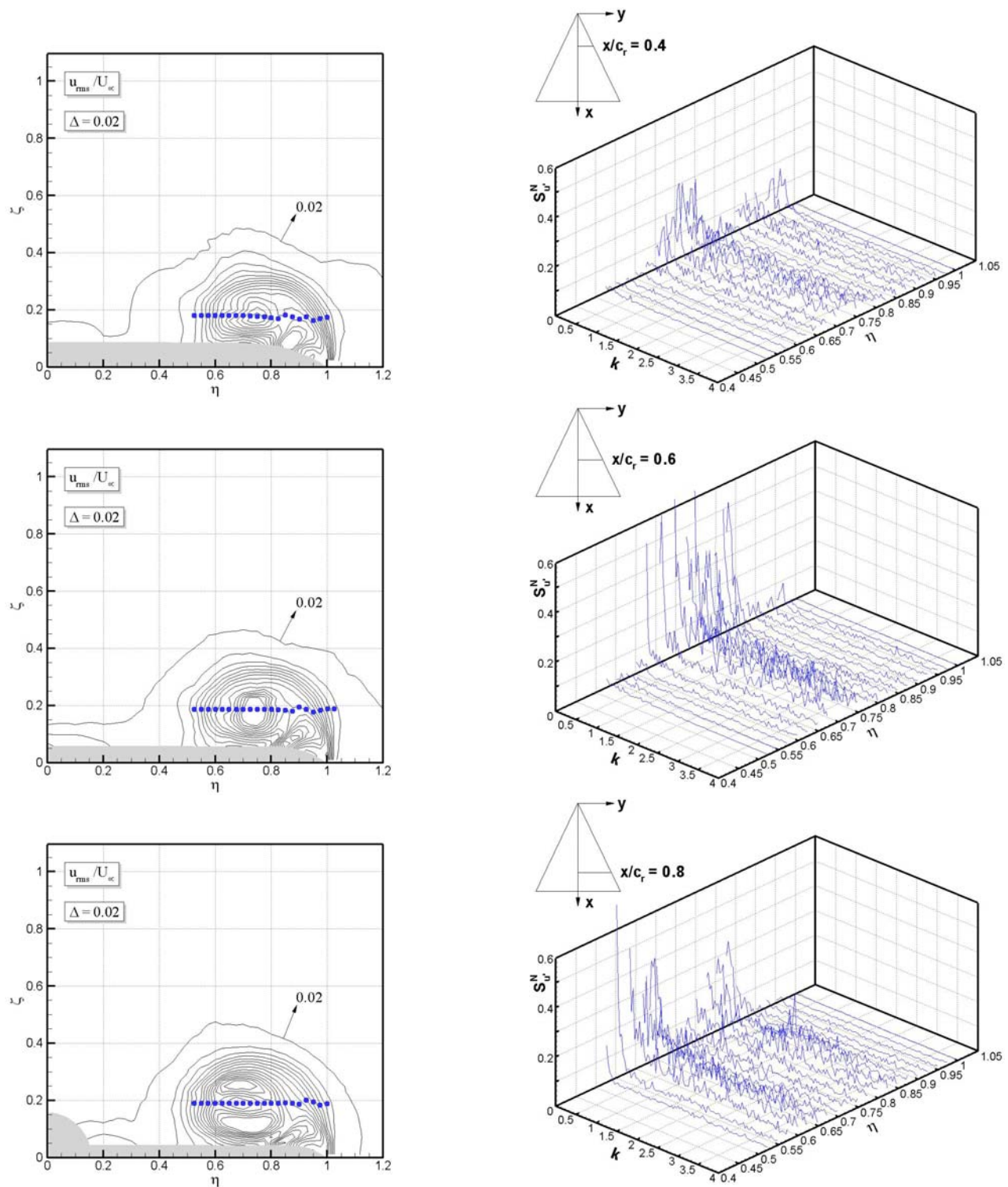
**Figure 21-24: Power Spectral Density Distributions of the Axial Velocity Fluctuations
at α = 18°, R_{mac} = 1 x 10^6 and M = 0.07 for Sharp Leading Edge.**
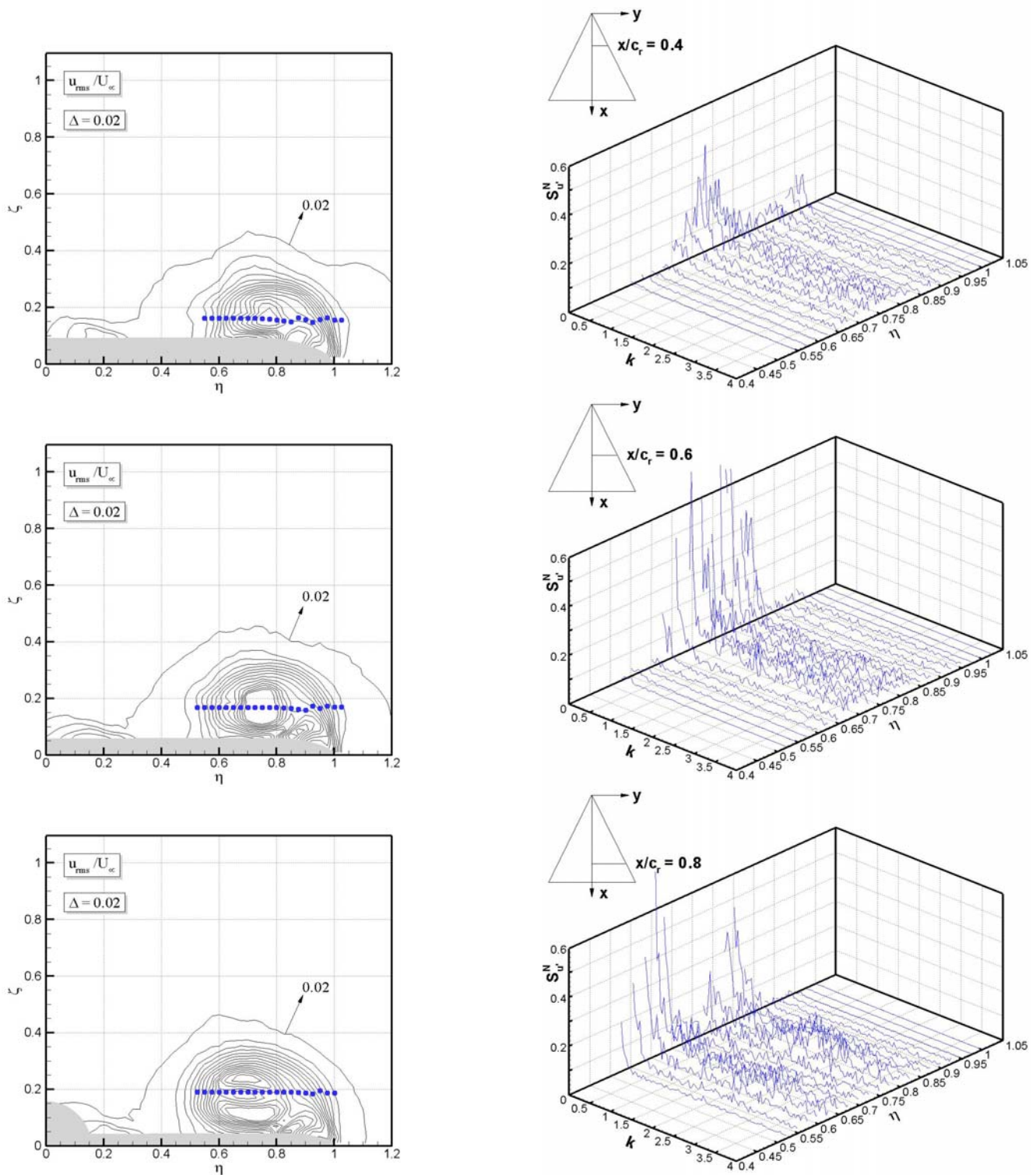
**Figure 21-25: Power Spectral Density Distributions of the Axial Velocity Fluctuations
at α = 18°, R_{mac} = 1 x 10^6 and M = 0.07 for Rounded Leading Edge.**
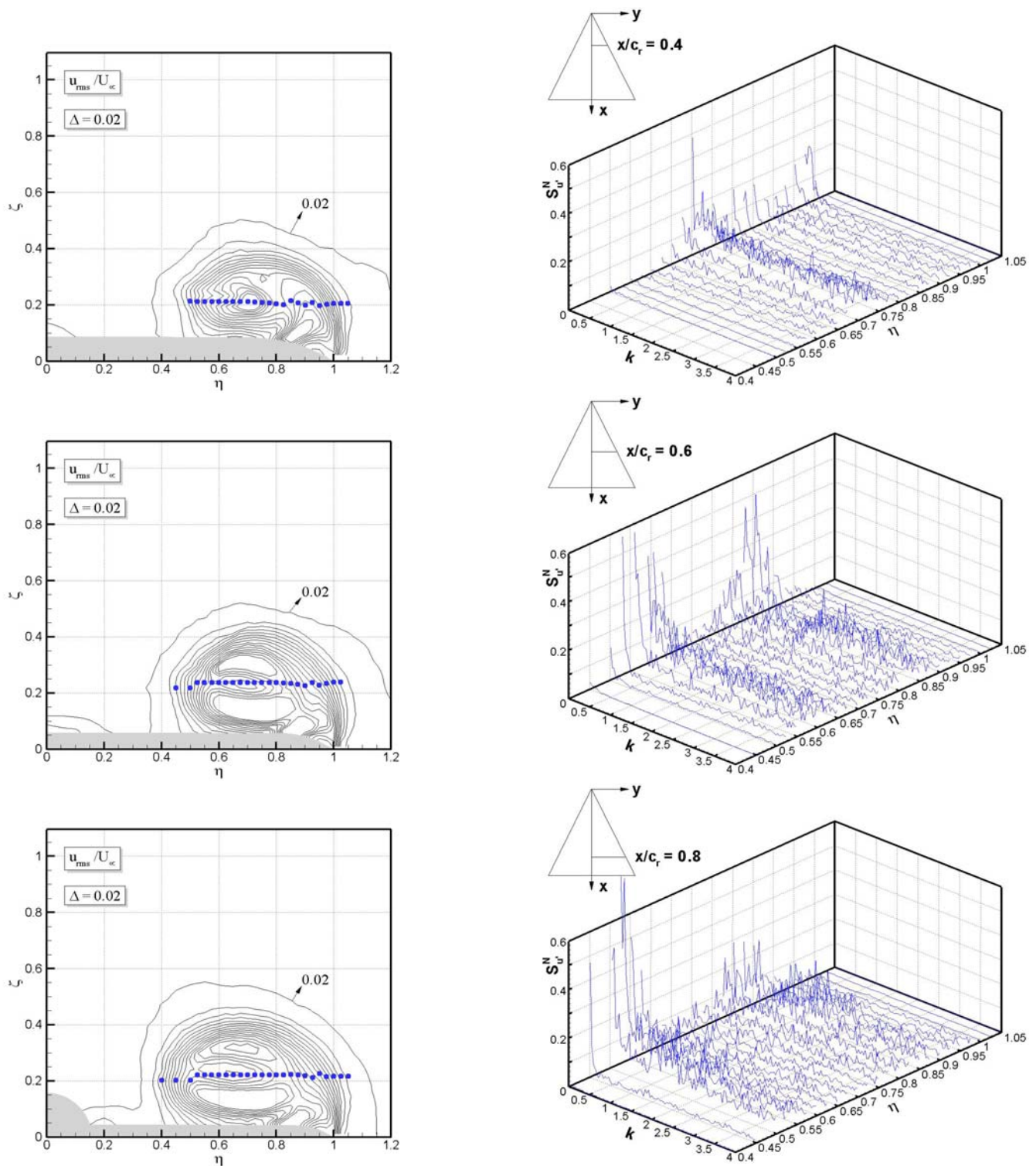
**Figure 21-26: Power Spectral Density Distributions of the Axial Velocity Fluctuations
at α = 23°, R_{mac} = 1 x 10^6 and M = 0.07 for Sharp Leading Edge.**
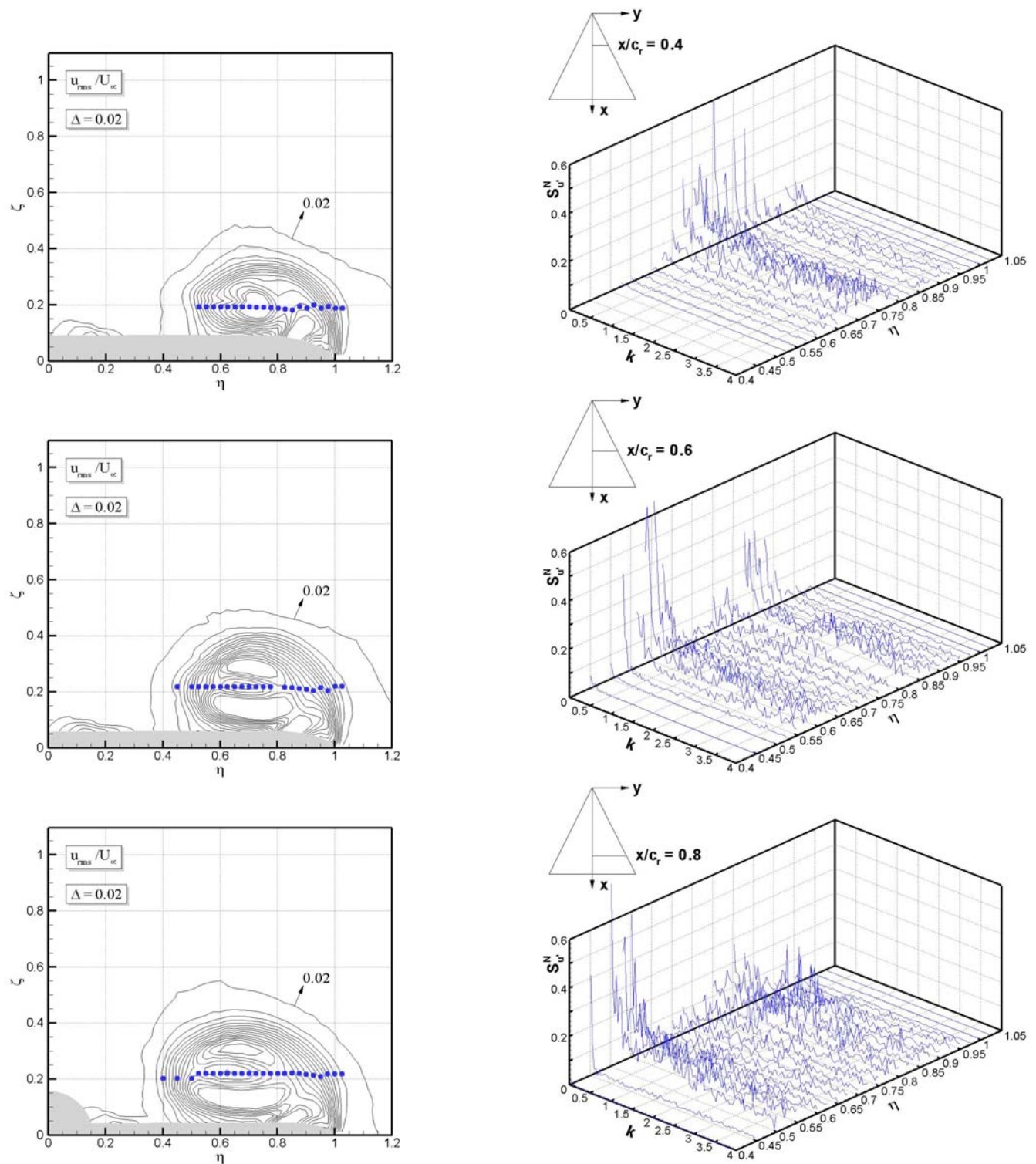
Figure 21-27: Power Spectral Density Distributions of the Axial Velocity Fluctuations
at α = 23°, R_{mac} = 1 x 10^6 and M = 0.07 for Rounded Leading Edge.

Considering the fully developed leading-edge vortex at $\alpha = 18°$ and $x/c_r = 0.4$, the power spectral densities exhibit increased values within the vortex core region and the rolled up shear layer, Figure 21-24 (a), Figure 21-25 (a). Some energy overshoots are present in the low frequency range. At $x/c_r = 0.6$, the power spectral densities of the core region increases revealing again some high peaks at lower frequencies, Figure 21-24 (b), Figure 21-25 (b). Downstream of vortex breakdown, $x/c_r = 0.8$, the power spectral densities exhibit increased levels in two laterally separated areas matching with the annular structure detected for the turbulence intensity distribution, Figure 21-24 (c), Figure 21-25 (c). Beside the spectral peaks in the low frequency range there is also a certain increase within a higher frequency range attributed to the helical mode instability of the breakdown flow. This instability results from the wake-type swirling flow in the breakdown region, Figure 21-26, Figure 21-27.

21.4.3.5   Vortex Bursting and Dominant Frequency

With increasing angle of attack vortex bursting occurs over the wing as shown by the turbulence intensity patterns and related spectral density distributions. Here, vortex breakdown takes place at $x/c_r = 0.75 \div 0.85$ for $\alpha = 23°$. The position of vortex breakdown can be determined by analyzing the surface pressure distribution [21-12]. If an increase in angle of attack does not cause an increase in the primary vortex suction peak comparing stations $x/c_r = const.$, then the leading-edge vortex may experience breakdown. This criterion fails, if the primary vortex detaches from the wing surface and thereby reduces its influence on the pressure distribution at the same time, as the breakdown location passes the trailing-edge upstream. The detachment of the vortex axis for strong leading-edge vortices, present at this delta wing planform, is only observed at angles of attack beyond the ones investigated here. Therefore, the described breakdown criterion is applicable. This criterion can also be discussed in context of the turbulence intensity distributions, shown for the axial velocity fluctuations at $x/c_r = 0.8$. The turbulence intensity distribution exhibits an annular concentration of local rms maxima, Figure 21-19 (c). This turbulence structure is a characteristic feature of spiral vortex breakdown which is related to Reynolds numbers above 10^4 [[21-1], [21-13]].

The velocity and surface pressure fluctuations show increased spectral levels in the near wall flow with some narrow-band concentration within $k = 1 \div 2$ [21-14], Figure 21-28 (top). That means vortex breakdown has started to influence the surface pressure fluctuations. The narrow-band concentration of turbulent kinetic energy at burst flow conditions reflects the helical mode instability of the vortex breakdown flow [[21-14], [21-15]]. This impact may result in strong excitation of structural modes of an aircraft. The energy peak of the velocity fluctuations or pressure fluctuations, respectively, is called "buffet peak" It can be further detected that the reduced frequencies associated with the buffet peak, i.e. the dominant frequencies, are shifted to lower values with increasing angle of attack. The burst vortex core expands with increasing angle of attack and, therefore, the wavelength λ of the instability mode becomes larger and the corresponding frequency smaller, $f_{dom} \sim 1/\lambda \sim 1/(b_{loc}/2)$. A universal frequency parameter k_{dom} can be derived using appropriate scaling quantities, Figure 21-28. Referring to velocity, the component normal to the leading-edge ($U_\infty \sin\alpha$) has to be considered. The characteristic length scale l_C must account for the vortex core expansion of the burst leading-edge vortex given approximately by the local half span ($\sim (b_{loc}/2) = x \cot \varphi_W$) and the shear layer distance ($\sim \sin^2\alpha$). Thus, the following scaling relationship for the dominant reduced frequency is applied,

$$k_{dom} = \frac{f_{dom} \cdot x \cdot \cot \varphi_w}{U_\infty} \sin \alpha \quad , \tag{18}$$

resulting in a characteristic frequency range of 0.28 ± 0.05, derived in Ref. 1 for other delta wing geometries.

Re = 2.0 x 10^6
α = **23°**

x/c$_r$ = 0.95

Re$_{l_\mu}$ = 2x10^6
η = 0.775
x/c$_r$ = 0.95
α = 23°

— sharp leading edge
— rounded leading edge

Dominant buffet peak

Vortex bursting

U_∞

$U_\infty \sin \alpha$

f_{dom}

α

$$k_{dom} = \frac{f_{dom} \cdot l_c}{U_c}$$
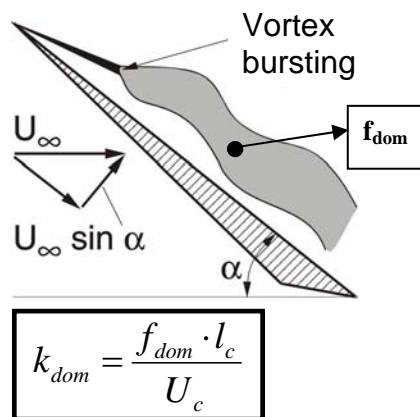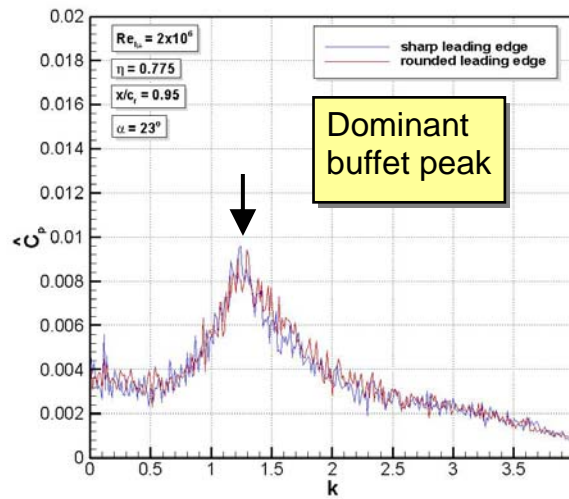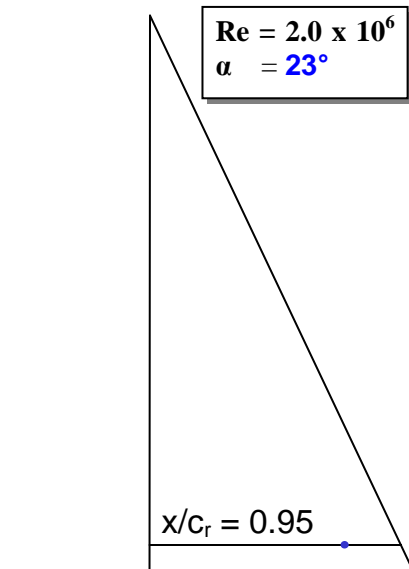
$$U_c = U_\infty \cdot \sin \alpha$$

$$l_c = x \cdot \cot \varphi_w \cdot \sin^2 \alpha$$

Frequency parameter:

$$k_{dom} \cdot \sin \alpha \cdot \cot \varphi_w \cong 0.28 \pm 0.05$$

Leading edge vortex breakdown flow

x

$s = c_r \cot \varphi_W$

U_∞

φ_W

l_c

c_r

~ x cot φ_W

~ $l_c \sin^2 \alpha$

$U_\infty \sin \alpha$

**65 deg
delta wing**

$\varphi_W = 50°$ $\varphi_W = 76°$

α [°]
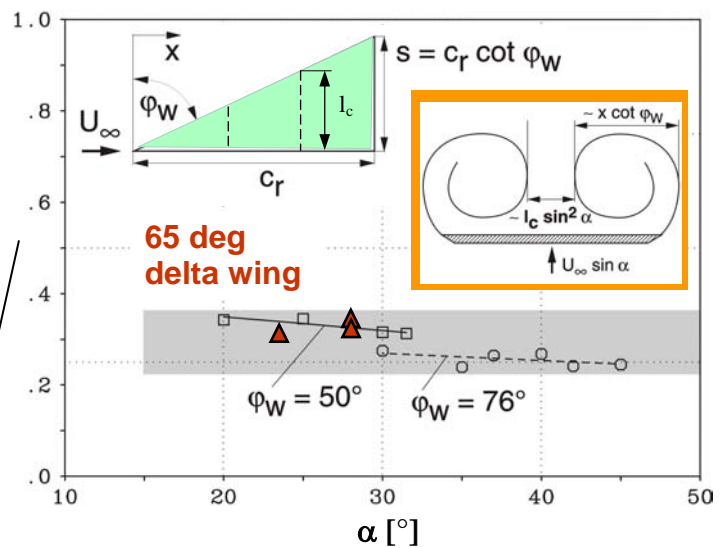
**Scaling of the dominant reduced frequency k$_{dom}$
with the local semi span (x cot φ_w) and sin α**

**Figure 21-28: Dominant Reduced Frequency Correlation Based on
Unsteady Surface Pressure (top) and Velocity Measurements [21-1].**

21.4.4   Boundary Layer

Boundary layer profiles of mean axial velocity and velocity fluctuation components are discussed, regarding again the cases of α = 13°, 18°, and 23° and rounded leading-edge. The measurement points located closest to the wall were placed 1 mm above the wing surface. Figure 21-29 – Figure 21-34 top and bottom left show results for chord stations x/c_r = 0.6 and lateral positions of η = 0.4 and η = 0.6. The x-axis in the diagram represents the vertical distance from wing surface based on the local wing semi span ς = $2z/b_{loc}$. The left y-axis refers to the range of the mean axial velocity based on free stream velocity and the right y-axis refers to the range of the non-dimensional velocity fluctuations. The middle picture of Figure 21-29 – Figure 21-34 shows the oil flow image, with the measurement positions marked by red dots. The corresponding sections of surface pressure fluctuation intensities are also included (cf. Figure 21-14 right). Regarding the two chordwise stations, the profiles of the mean axial velocity indicate a turbulent boundary layer. All three rms velocities show significantly increased levels in the boundary layer and a low constant level outside. The same trend holds for the turbulent shear stresses which are multiplied by a factor of -20 for appropriate representation in the diagram. These turbulent boundary layers are typical for the wing inboard region close to the primary vortex attachment line. Only low surface pressure fluctuations are evoked as the flow is accelerated in direction to the vortex axis.
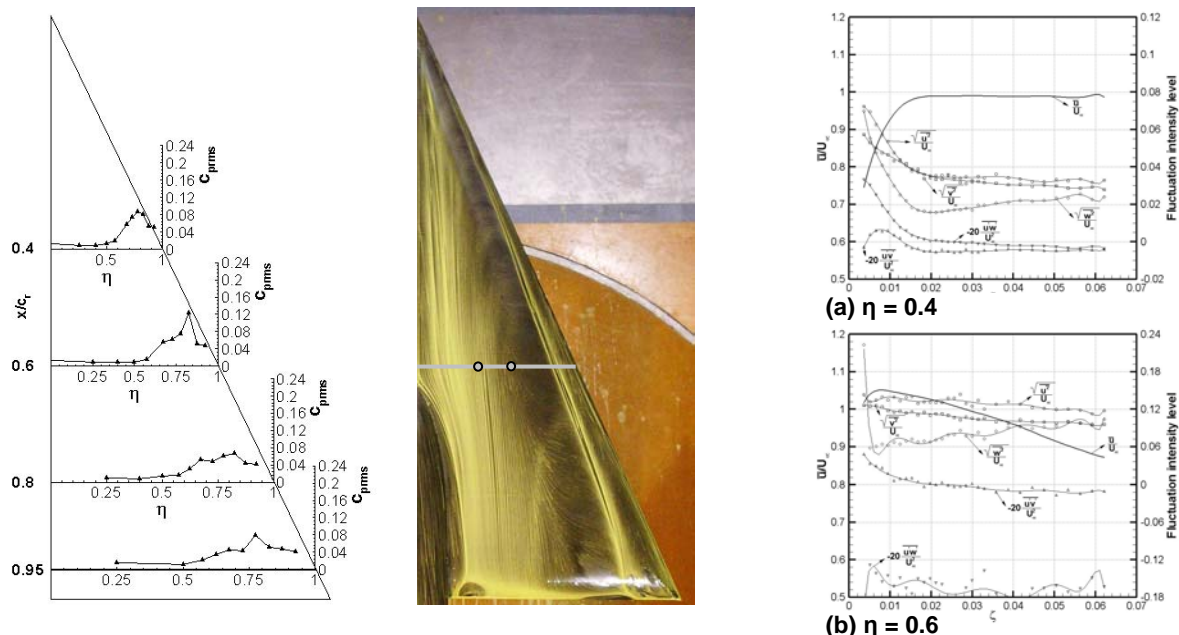
Figure 21-29: Surface Pressure Fluctuation Intensity (left), Surface Flow (middle) and Boundary Layer Profiles (right) for Sharp Leading Edge in Section x/c_r = 0.6 at α = 13°, R_{mac} = 1 x 10^6 and M = 0.07.
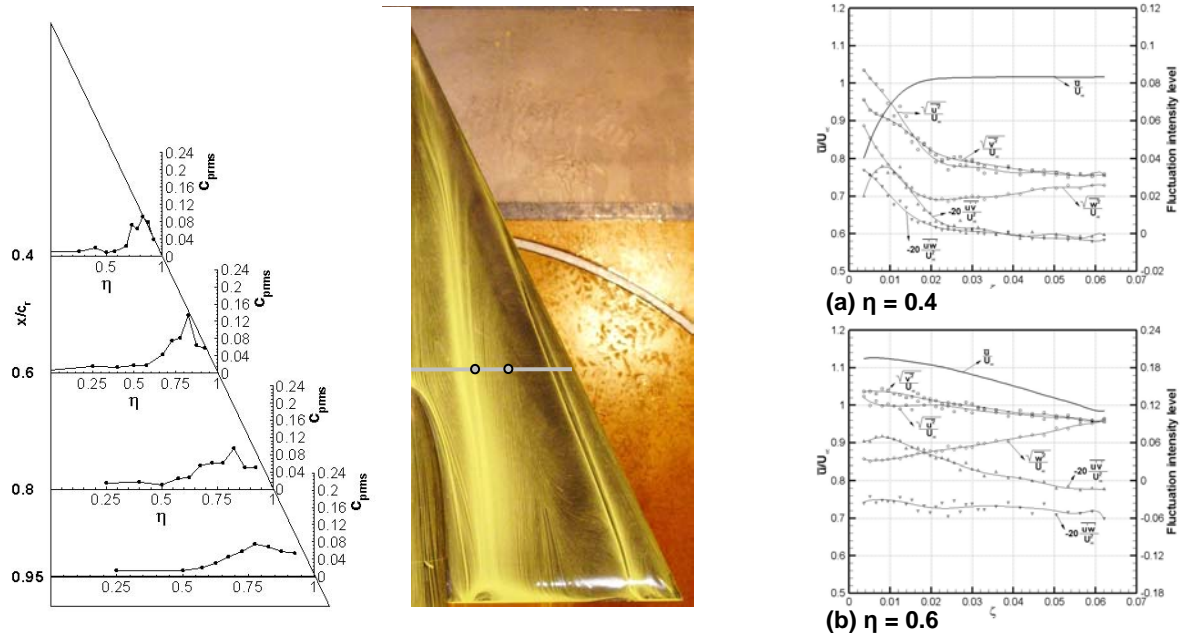
Figure 21-30: Surface Pressure Fluctuation Intensity (left), Surface Flow (middle) and Boundary Layer Profiles (right) for Rounded Leading Edge in Section x/c_r = 0.6 at α = 13°, R_{mac} = 1 x 10^6 and M = 0.07.
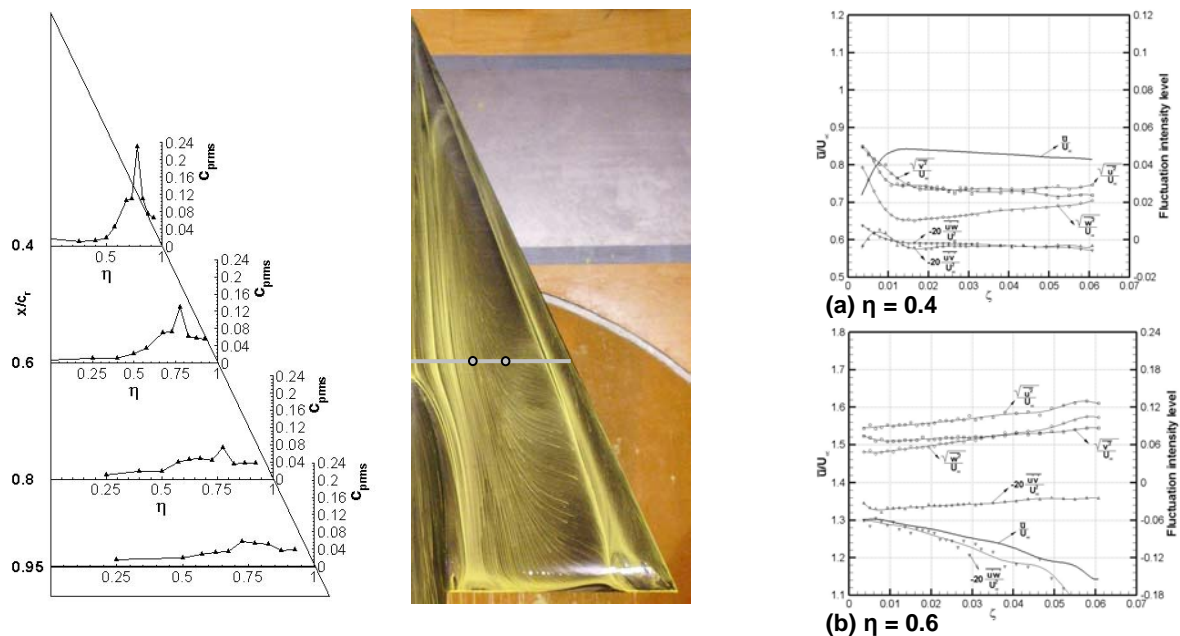
Figure 21-31: Surface Pressure Fluctuation Intensity (left), Surface Flow (middle) and Boundary Layer Profiles (right) for Sharp Leading Edge in Section x/c_r = 0.6 at α = 18°, R_{mac} = 1 x 10^6 and M = 0.07.
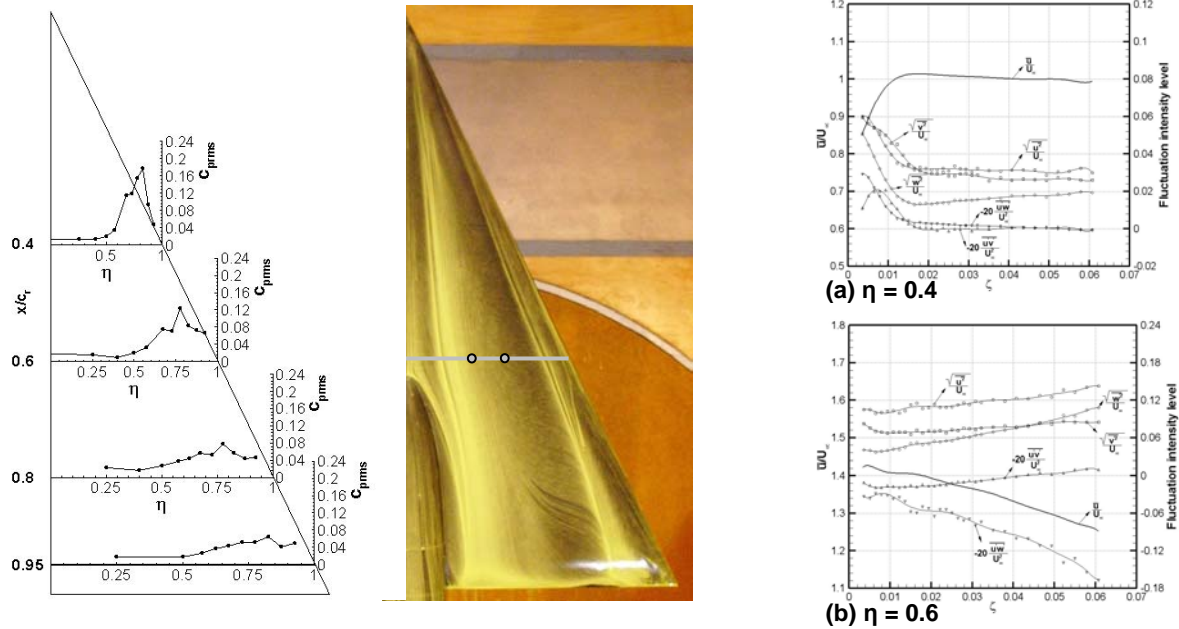
Figure 21-32: Surface Pressure Fluctuation Intensity (left), Surface Flow (middle) and Boundary Layer Profiles (right) for Rounded Leading Edge in Section x/c_r = 0.6 at α = 18°, R_{mac} = 1 x 10^6 and M = 0.07.
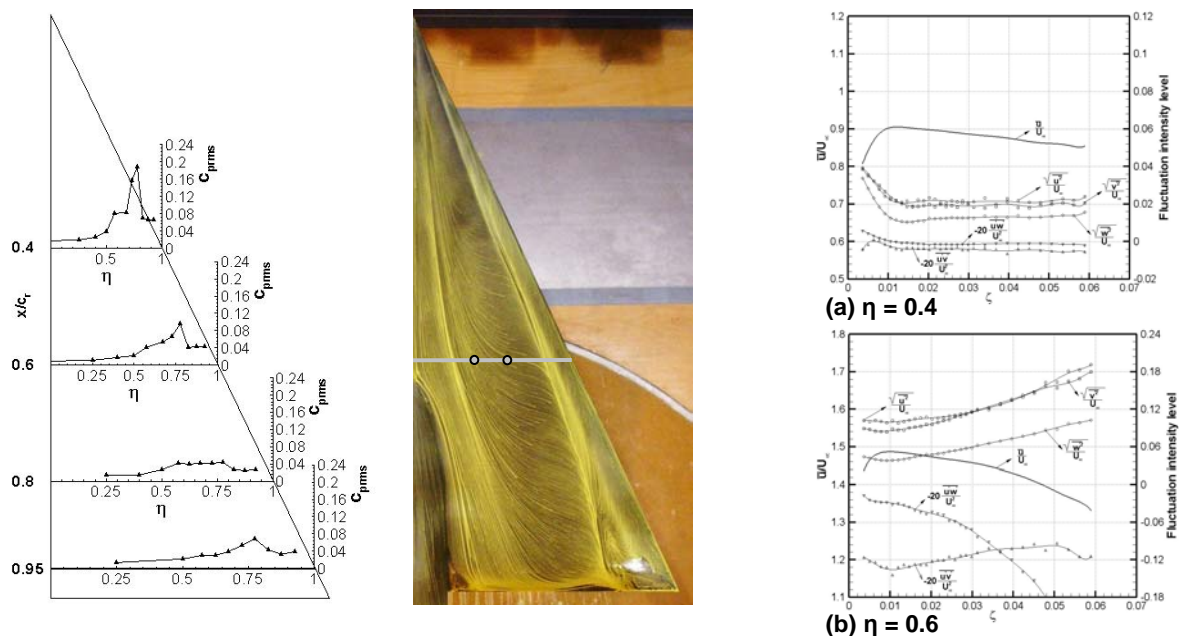
Figure 21-33: Surface Pressure Fluctuation Intensity (left), Surface Flow (middle) and Boundary Layer Profiles (right) for Sharp Leading Edge in Section x/c_r = 0.6 at α = 23°, R_{mac} = 1 x 10^6 and M = 0.07.
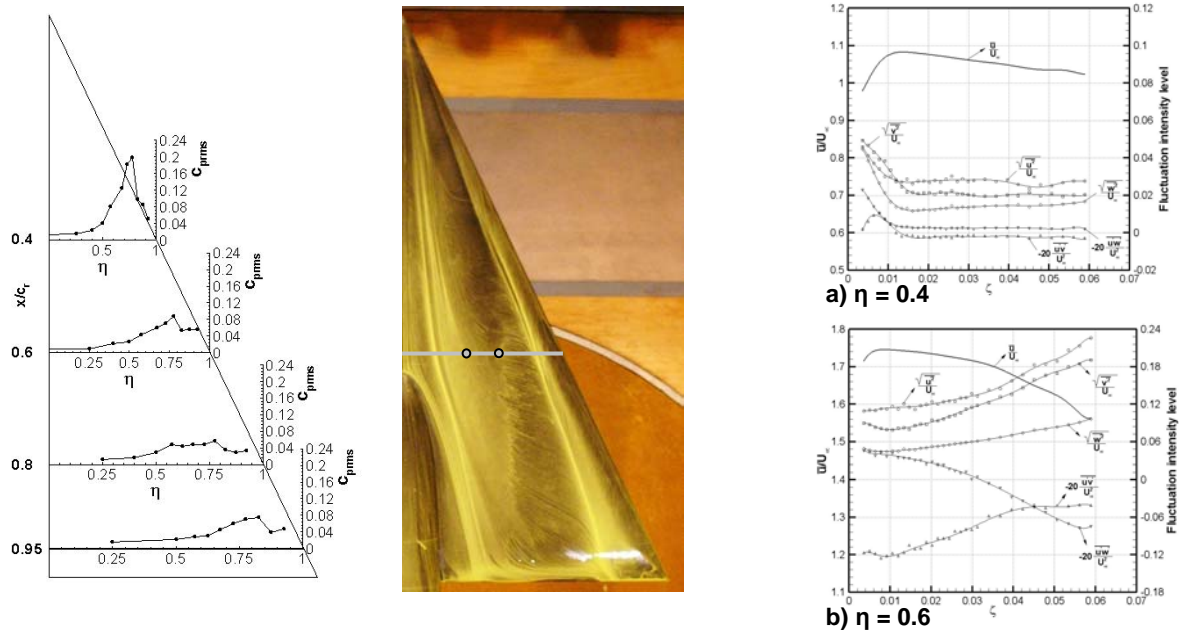
Figure 21-34: Surface Pressure Fluctuation Intensity (left), Surface Flow (middle) and Boundary Layer Profiles (right) for Rounded Leading Edge in Section x/c_r = 0.6 at α = 23°, R_{mac} = 1 x 10^6 and M = 0.07.

21.5   CONCLUSIONS AND OUTLOOK

Extensive experimental investigations on a delta wing model with a leading-edge sweep of 65 deg have been performed in the low-speed wind tunnel facilities A and B of the Institute of Aerodynamics at the Technische Universität München. The results contribute to the research work conducted within the International Vortex Flow Experiment 2 (VFE-2). The experiments performed contain different measurement techniques, like flow visualization using laser light sheet technique and oil flow technique, steady and unsteady surface pressure measurements, flow field velocity measurements using Stereo Particle Image Velocimetry and hot-wire anemometry, and boundary layer measurements based on hot-wire anemometry.

For the delta wing vortical flow structure some new and significant results are obtained, especially, when considering a rounded leading-edge:

• For medium angles of attack, a new flow phenomenon was found for delta wings with straight leading-edge depending strongly on Reynolds number. In addition to the classical primary vortex an inboard vortex occur close to the wing surface. This phenomenon appears stronger for the rounded than for the sharp leading-edge. While the primary vortex develops from the trailing-edge towards the apex with increasing angle of attack and therewith starts here from a turbulent separation, a laminar separation occurs at the wing surface in the region of the apex close to the symmetry plane. The flow is attached around the leading-edge, but the pressure increases towards the symmetry plane of the wing causing laminar separation in the inboard area. Downstream, the three-dimensional separation bubble transforms to a spatially small and weak vortex, which is situated close to the wing surface along the entire chord length.

- At high angle of attack, vortex breakdown dominates the wing flow associated with a characteristic annular region of local turbulence maxima surrounding the strongly expanded core of the burst primary vortex. Further, a narrow-band concentration of turbulent kinetic energy takes place. During the upstream movement of the breakdown location the turbulent flow field affects more and more the wing surface flow, thereby increasing the surface pressure fluctuations which also show coherent structures and significant concentrations in a certain frequency domain.

- Measurements of the boundary layer allow the quantification of the time averaged velocities as well as of the turbulent normal- and shear stresses close to the wing surface. For the Reynolds numbers investigated here and medium angles of attack, a turbulent boundary layer starts to develop at approximately 20% to 30% of the root chord for the attached flow in the inner part of the wing. Under the primary vortex the boundary layer becomes thinner by a factor of 2 to 5 due to the strong accelerated flow.

The comprehensive data base will be further evaluated and analyzed to improve the knowledge on the turbulent and unsteady flow quantities associated with the different stages of leading-edge vortex development.

21.6   ACKNOWLEDGEMENTS

21.7   REFERENCES

[21-1]   Breitsamter, C.: *Unsteady Flow Phenomena Associated with Leading-Edge Vortices*, Progress in Aerospace Sciences, Vol. 44, No. 1, January 2008, pp. 48-65.

[21-2]   Breitsamter, C.: *Turbulente Strömungsstrukturen an Flugzeugkonfigurationen mit Vorderkantenwirbeln*, Dissertation, Technische Universität München, Herbert Utz Verlag, ISBN 3-89675-201-4, 1997.

[21-3]   Breitsamter, C. and Laschka, B.: *Turbulent Flow Structure Associated with Vortex-Induced Fin Buffeting*, Journal of Aircraft, Vol. 31, No. 4, 1994, pp. 773-781.

[21-4]   Breitsamter, C.: *Experimentelle Untersuchung der instationären Feldgrößen und Oberflächendrücke bei wirbeldominierter abgelöster Strömung an einem Deltaflügel*, Jahrbuch der DGLR, Vol. I, DGLR-JT95-062, 1995, pp. 163-175.

[21-5]   Breitsamter, C. and Laschka, B.: *Fin Buffet Pressure Evaluation Based on Measured Flowfield Velocities*, Journal of Aircraft, Vol. 35, No. 5, 1998, pp. 806-815.

[21-6]   Breitsamter, C.: *Strake Effects on the Turbulent Fin Flowfield of a High-Performance Fighter Aircraft*, NNFM, Vol. 72, Vieweg Verlag, 1999, pp. 69-76.

[21-7]   Chu, J. and Luckring, J.M.: *Experimental Surface Pressure Data Obtained on 65° Delta Wing Across Reynolds Number and Mach Number Ranges*, NASA-TM-4645, 1996.

[21-8]   Crippa, S. and Rizzi, A.: *Numerical Investigation on Reynolds Number Effects on a Blunt Leading-Edge Delta Wing*, AIAA Paper 2006-3001, June 2006.

[21-9]   Crippa, S. and Rizzi, A.: *Initial Steady/Unsteady CFD Analysis of Vortex Flow Over the VFE-2 Delta Wing*, ICAS-2006-P2.18, 25th Congress of the International Council of the Aeronautical Sciences, Hamburg, Germany, 3-8 September 2006.

[21-10] Elsenaar, A., Hjelmberg, L., Bütefisch, K. and Bannink, W.J.: *The International Vortex Flow Experiment*, AGARD-CP-437, Validation of Computational Fluid Dynamics, Lisbon, Portugal, May 2-5, 1988, pp. 9-1-15-23.

[21-11] Furman, A. and Breitsamter, C.: *Delta Wing Steady Pressure Investigations for Sharp and Rounded Leading Edges*, New Results in Numerical and Experimental Fluid Mechanics V, NNFM Vol. 92, 2006, pp. 77-84.

[21-12] Furman, A. and Breitsamter, C.: *Investigations of Flow Phenomena on Generic Delta Wing*, ICAS-2006-3.1.2, 25th Congress of the Int. Council of the Aeronautical Sci., Hamburg, Germany, 3-8 September 2006.

[21-13] Furman, A. and Breitsamter, C.: *Stereo-PIV and Hot-Wire Investigations on Delta Wing with Sharp and Rounded Leading Edge*, CEAS-2007-430, 1st CEAS European Air and Space Conference, Berlin, Germany, 10-13 September 2007, pp. 1749-1761.

[21-14] Furman, A. and Breitsamter, C.: *Turbulent and Unsteady Flow Characteristics of Delta Wing Vortex Systems*, AIAA Paper 2008-381-736, January 2008.

[21-15] Gursul, I.: *Unsteady Flow Phenomena Over Delta Wings at High Angle of Attack*, AIAA Journal, Vol. 32, No. 2, 1994, pp. 225-231.

[21-16] Gursul, I. and Xie, W.: *Buffeting Flows Over Delta Wings*, AIAA Journal, Vol. 37, No. 1, 1999, pp. 58-65.

[21-17] Hoeijmakers, H.W.M.: *Modelling and Numerical Simulation of Vortex Flow in Aerodynamics*, AGARD-CP-494, 1991, pp. 1-1-1-46.

[21-18] Hummel, D.: *On the Vortex Formation Over a Slender Wing at Large Angles of Incidence*, AGARD-CP-247, High Angle of Attack Aerodynamics, Sandefjord, Norway, October 4-6, 1978, pp. 15-1-15-17.

[21-19] Hummel, D.: *Documentation of Separated Flows for Computational Fluid Dynamics Validation*, AGARD-CP-437, Validation of Computational Fluid Dynamics, Vol. 2, Lisbon, Portugal, May 2-5, 1988, pp. 18-1-18-24.

[21-20] Hummel, D. and Redeker, G.: *A New Vortex Flow Experiment for Computer Code Validation*, Vortex Flow and High Angles of Attack, Loen, Norway, May 7-11, 2001.

[21-21] Hummel, D.: *Effects of Boundary Layer Formation on the Vortical Flow Above Slender Delta Wing*, RTO-MP-AVT-111, Paper 30, Symposium on Enhancement of NATO Military Flight Vehicle Performance by Management of Interacting Boundary Layer Transition and Separation, Prague, Czech Republic, 4-7 October 2004.

[21-22] Hummel, D.: *The Second International Vortex Flow Experiment (VFE-2): Objectives and Present Status*, AIAA Paper 2007-4446, June 2007.

[21-23] Luckring, J.M.: *Reynolds Number, Compressibility, and Leading-Edge Bluntness Effects on Delta-Wing Aerodynamics*, ICAS-2004-4.1.4, 24th Congress of the International Council of the Aeronautical Sciences, Yokohama, Japan, 29 August – 3 September 2004.

[21-24] Mitchell, A.M., Molton, P., Barberis, D. and Delery, J.: *Characterization of Vortex Breakdown by Flow Field and Surface Measurements*, AIAA Paper 2000-0788, 2000.

[21-25] Müller, J. and Hummel, D.: *Time-Accurate CFD Analysis of the Unsteady Flow on a Fixed Delta Wing*, AIAA Paper 2000-0138, 2000.

[21-26] Rai, P., Finley, D.B. and Ghaffari, F.: *An Assessment of CFD Effectiveness for Vortex-Flow Simulation to Meet Preliminary Design Needs*, Vortex Flow and High Angles of Attack, Loen, Norway, May 7-11, 2001.

[21-27] Schiavietta, L.A., Badcock, K.J. and Cummings, R.M.: *Comparison of DES and URANS for Unsteady Vortical Flows Over Delta Wings*, AIAA Paper 2007-1085, January 2007.

Chapter 22 – EXPERIMENTAL INVESTIGATIONS ON THE VFE-2 CONFIGURATION AT GLASGOW UNIVERSITY, UNITED KINGDOM

by

Frank N. Coton, Shabudin Bin Mat, Roderick A.McD. Galbraith

22.1 INTRODUCTION

As part of the VFE-2 activities, Glasgow University constructed a replica of the Chu and Luckring [22-1] model for studies in the Glasgow University low speed wind tunnel. The model constructed at Glasgow is physically the largest model in VFE-2 team working project. The model has a root chord length of 1.059 m and a span of 0.987 m. It has an overall thickness of 36 mm. All four of the leading edge geometries were manufactured at Glasgow but, in accordance with the focus of the VFE-2 working group, only results for the sharp and medium radius leading edges will be presented here. In the wind tunnel experiments at Glasgow, a combination of force measurement and flow visualization were used to characterize the flow behavior.

22.2 EXPERIMENTAL SET UP AND WIND TUNNEL TESTING

22.2.1 Wind Tunnel Model

The VFE-2 model is a 65° delta wing with flat upper and lower surfaces (Figure 22-1). In the original paper of Chu and Luckring the entire geometry of the model is specified analytically and this is a major aid to accurate manufacture. The Glasgow University model has a chord length of 1.059 m, giving a wing area of 0.523 m^2. The model was machined from aluminum in five parts; upper surface, lower main body, two leading edges and trailing edge. In all, four sets of leading edges were manufactured ranging from sharp to highly rounded. In the current paper, only results for the sharp and medium radius leading edges sets are presented.
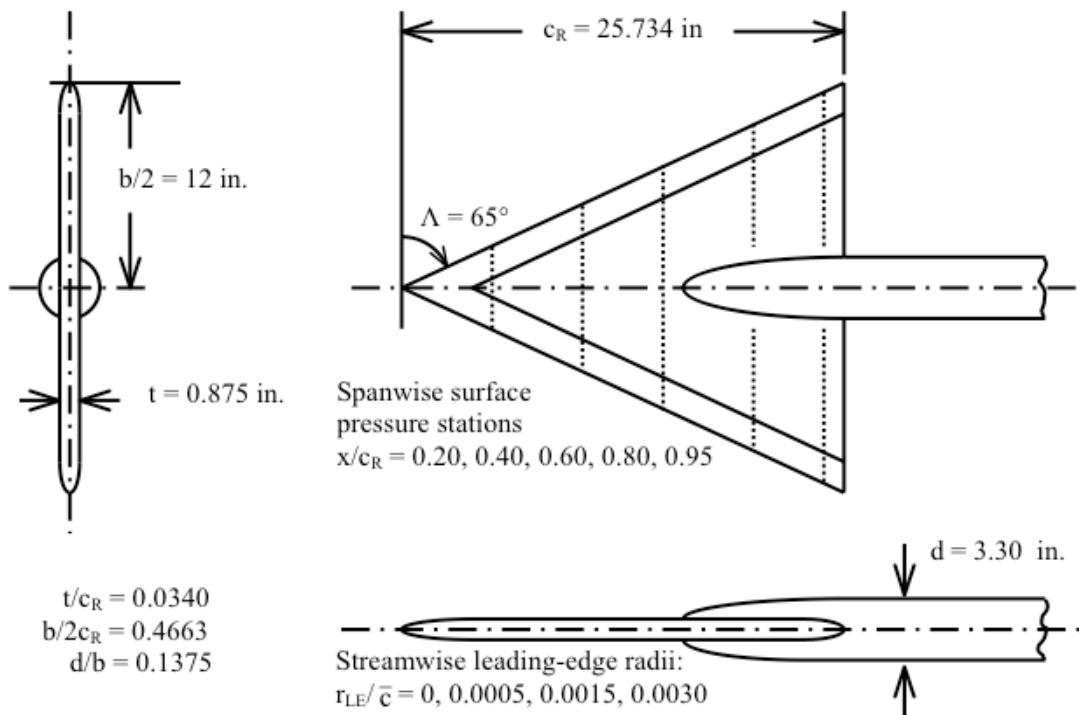
Figure 22-1: Model Geometry (Taken from Ref. [22-1]).

22.2.2 Test Set-up

The wind tunnel test set up involved the model being sting mounted from behind with the sting supported on a fabricated section located two chord lengths downstream of the model. The sting itself consisted of 3 main sub sting components; i.e. short sting, stub-sting and roller housing. The short sting, closest to the model, was set at an angle of 15 degrees to the straight line between the centre of rotation and the mounting point on the support section. This is, in turn, connected at its downstream end to the stub sting which was offset from the straight line between the mounting point and the centre of rotation by 17 degrees. The final part of the sting assembly was the roller housing which provided the interface between the sting and the support section. Its main function was to attach the sting to the support section whilst allowing the sting to move around the section. By moving the roller housing vertically on the support section, the model could be set at an angle of attack of between 0 and 30 degrees, rotating about its centre of rotation at the half root chord point. The general test set-up is shown in Figure 22-2.
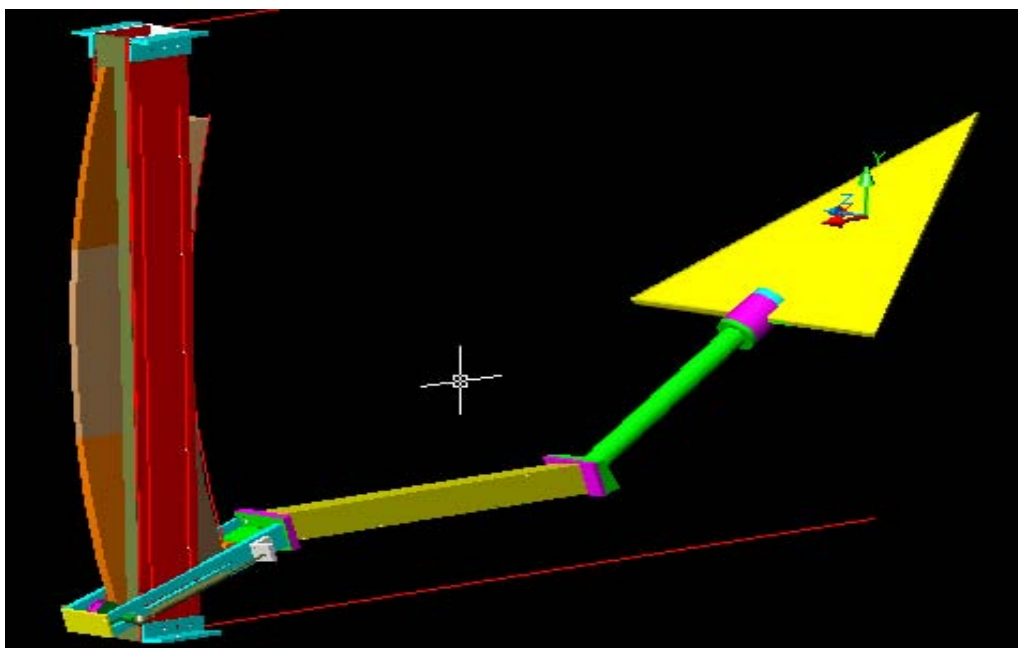
Figure 22-2 (a): Test Set Up.
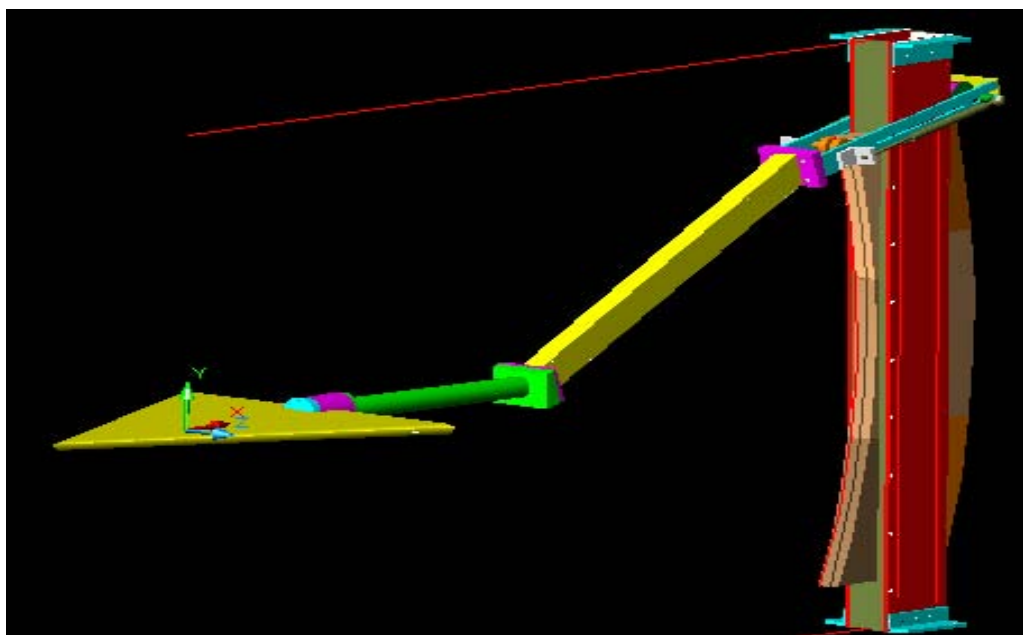
Figure 22-2 (b): Test Set Up (Alternative View).

Carbon fiber fairings for the short sting and wing interface were manufactured according to the analytic descriptions provided by Chu and Luckring to ensure that the entire model/sting geometry replicated the original NASA test. A factory modified six-component AMTI MC5-1250-6 loadcell was located between the

model and the short sting and was used measure the steady and unsteady forces acting on the wing. This loadcell is cylindrical and fitted neatly below the sting fairings and so care was taken to ensure that there was no transmission of load occurred through the fairings. Figure 22-3 shows load cell interface with the model with the short sting fairing covering the non-sensing section of the loadcell. Also shown in this figure is the location on the model of the inclinometer that was used to measure model angle of attack to within 0.05°.
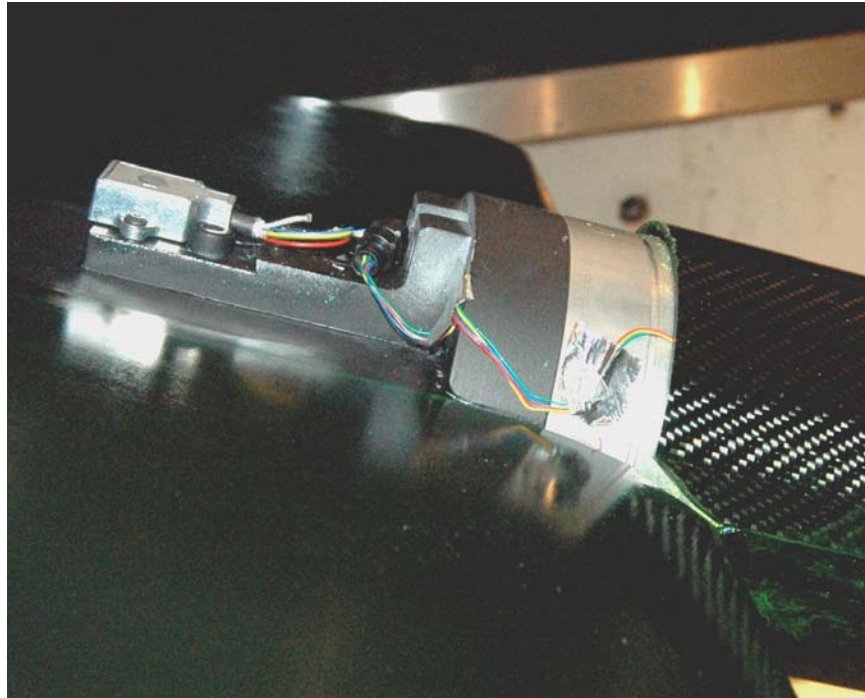
Figure 22-3: Balance and Inclinometer Attachment to the Delta Wing.

The final assembly is shown installed in the wind tunnel in Figure 22-4 where it may also be observed that additional stiffening of the sting assembly is provided by lateral and vertical bracing wires.

Figure 22-4: Model in the Glasgow University Argyll Wind Tunnel.

22.2.3   Wind Tunnel Testing

The experiments were carried out in the 2.65 x 2.04 meter, closed circuit, Argyll Wind Tunnel of the University of Glasgow. Tests were conducted at Reynolds numbers of 1×10^6 and 2×10^6 based on the mean aerodynamic chord and were conducted in two phases. In the first phase, force and moment data were recorded for the model at each angle of attack. In the second phase, oil flow visualization studies were conducted.

For the forces and moments, measurements were made at each angle of attack at sampling frequencies of 8 kHz and 100 Hz. Each test was repeated five times to determine repeatability. Time averaged values of the forces and moments were calculated from the measured data together with power spectra for each of the force components. In doing this, the natural frequency of the model and support structure was determined a priori and was removed from the spectra by digital filtering.

Oil flow visualization was carried out at 13.3°, 18.5° and 23° angles of attack for both 1 and 2 million Reynolds number. A mixture of Ondina oil thinned with paraffin was mixed with Dayglo powder and applied to the surface of the delta wing. The wind was then turned on and the flow pattern allowed to develop on the surface of the wing. After the flow pattern had stabilized, it was illuminated using ultraviolet light and photographed from above using a digital camera.

22.3   THE DELTA WING FLOWFIELD

22.3.1   Sharp Leading Edge

The flow on a slender delta wing at a certain speed and angle of attack can be described as a movement of the flow from the lower surface to the upper surface in a spiral type of motion. Flow separation will take place

at the leading edge and the resulting shear layer will roll up over the upper surface to form a primary vortex [22-2]. In effect, the primary vortices originate from a series of smaller vortices shed from the leading edge of the wing and contained within the shear layer. They rotate around each other to form the larger primary vortices as shown in Figure 22-5. As the angle of attack is increased the primary vortices grow both in strength and size. As they do so, the axial velocity in the core of the vortex can exceed three times the free stream speed [22-3].
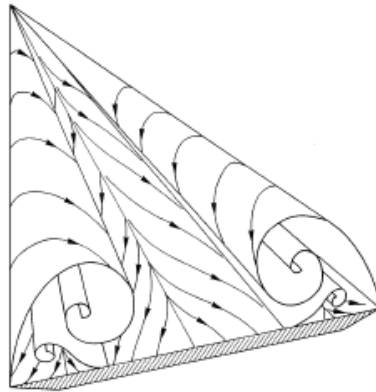
Figure 22-5: Delta Wing Flowfield (Taken from Ref. [22-4]).

Underneath each primary vortex, an attached flow is established on the upper surface of the wing with an attachment line located at a certain span-wise location. Due to the adverse pressure gradient, the attached flow will experience another flow separation which results in the formation of a secondary vortex. The secondary vortex is formed under the primary vortex [22-4]. It is located close to the leading edge but the exact position of the primary attachment and secondary separation lines depends on the angle of attack and Reynolds number. The status of the boundary layer on the wing has a very strong influence on the formation and size of the secondary vortex. The secondary vortex is bigger if the upper surface boundary layer is laminar. This is due to flow separation occurring earlier compared to a turbulent boundary layer. The larger secondary vortex causes a displacement of the primary vortex upwards and inwards [22-3].

At a certain point along the vortex axis, the structure of the primary vortex starts to break down. This happens as a result of the flow suddenly becoming stagnant and turning into an unsteady and unstructured flow. This situation is called vortex breakdown and its location depends on the wing sweep and angle of attack. At moderate angle of attack, vortex breakdown occurs at the trailing edge and moves upstream with increasing angle of attack. Experiments have shown that the breakdown position over a wing can be influenced by the geometry of the wing, tunnel wall interference, support interference, model deformation and Reynolds number [22-5].

22.3.2   Rounded Leading Edge

For a rounded leading edge, the flow separation location is no longer fixed to the leading edge. At a certain angle of attack and speed [[22-6], [22-7]] the primary separation line for the rounded leading edge is close to the upper surface near to the apex and progressively moves towards the lower surface with increasing distance from the apex. This situation increases the complexity of the aerodynamics of delta wing aircraft. Several flow phenomena may be observed moving downstream from the wing apex:

   1)   Laminar flow without flow separation;

2) Laminar flow followed by laminar separation;

3) A laminar separation line moving towards the leading edge followed by laminar flow separation at the leading edge; and

4) Laminar flow at a certain point followed by laminar/turbulent transition.

The complexity of the flow associated with a rounded leading edge has been discussed by Hummel [22-8], Luckring [[22-7], [22-9]] and Schröder et al. [22-10]. For such a case, the onset of the primary separation now depends on the angle of attack, the Reynolds number, the Mach number and the leading edge bluntness itself. The effect of angle of attack and Reynolds number will be addressed later on in this paper.

A particularly interesting feature of the rounded leading edge is the emergence, at moderate angles of attack, of a small suction peak lying inboard of the primary suction peak and originating near the half chord location. This feature has been discussed extensively by Hummel [22-8] and is indicative of an inner vortex with the same sign as the primary vortex. The occurrence of this inner vortex is related to separation near the apex where the relative thickness of the wing is high. Moving down the leading edge, the flow progressively experiences a relatively sharper leading edge and so separation moves back from the upper surface towards the leading edge itself. As it does so, the vorticity from this separation is channelled into a conventional primary vortex that originates further downstream than the inner vortex. With increasing angle of attack, more vorticity is fed into the primary vortex and the inner vortex becomes steadily weaker and finally disappears or merges with the primary vortex somewhere near the trailing edge.

22.4   RESULTS

It should be noted that the results presented in the following sections have not yet been corrected for wind tunnel wall interference effects. The main effect of such a correction would be to change the effective angle of attack of the wing.

22.4.1   Flow Visualization Results

Oil flow patterns on wing configurations develop with time. In the sections that follow, single oil flow images will be presented for each case to highlight the salient flow features. In fact, however, several images were recorded for each case as the oil flow pattern developed on the wing over time. This information can be important as the collection of oil at specific locations on the surface can, for sensitive flows, alter the flow state. A temporal series of images provides reassurance that this has not, in fact, happened.

As an example of the temporal development of the oil flow pattern on the VFE wing, two cases are presented. Figure 22-6 shows the flow development on the sharp-edged wing at a Reynolds number of 1×10^6 and angle of attack of 13.3°. Figure 22-7 shows the flow development for the medium radius wing at the same Reynolds number and angle of attack. In both cases, there are no changes in the apparent flow topology as regions of concentrated oil gather on the wing, suggesting that the flow behaviour is insensitive to the presence of the oil.
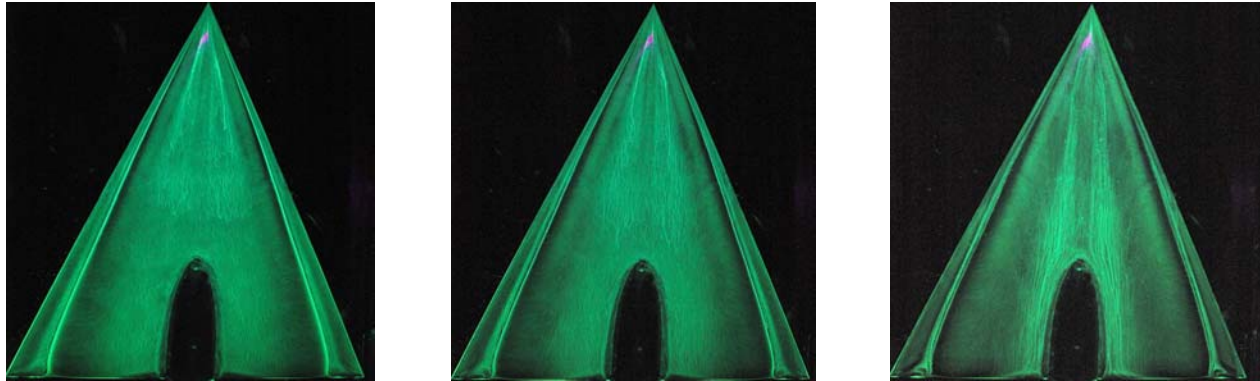
Figure 22-6: The Development of the Oil Flow for the Sharp-Edged Wing, R_{mac} = 1 x 10^6 and α = 13.3°.
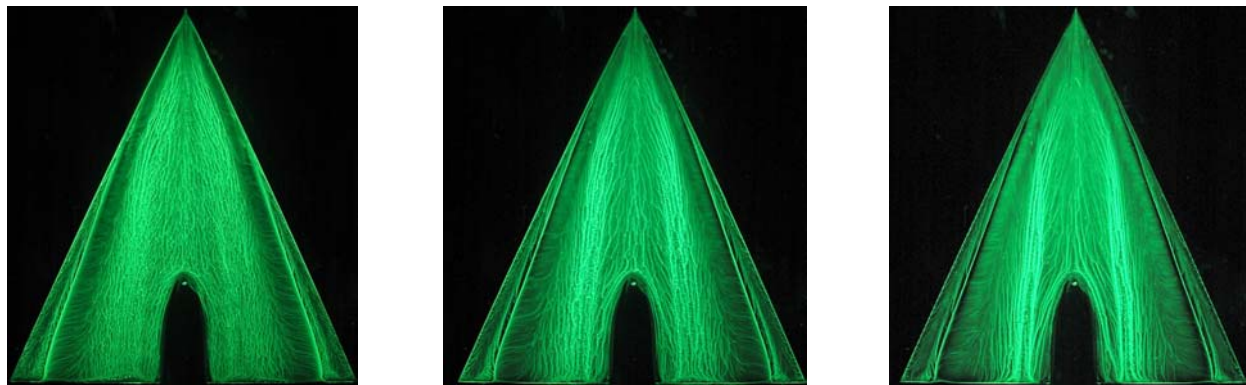
Figure 22-7: The Development of the Oil Flow for the Medium Radius Wing, R_{mac} = 1 x 10^6 and α = 13.3°.

22.4.1.1   Sharp Leading Edge Wing

Figure 22-8 shows the flow visualizations obtained at a Reynolds number of 2 x 10^6 and at three angles of attack, 13.3°, 18.5° and 23°. In all three cases, the flow patterns exhibit the footprint of a classical delta wing leading edge vortex system. Flow separation takes place at the leading edge and this separation creates the vortex system above the wing. It may be observed that at all three angles of attack the vortex system originates near the apex of the wing and persists to the trailing edge. In the images, the secondary separation line clearly delineates the primary and secondary vortex core locations. In the image corresponding to 23° angle of attack, there is evidence of a loss in coherence of the flow structures near the trailing edge. Presumably, this is indicative of the progression of vortex breakdown over the trailing edge.

(a)   (b)   (c)
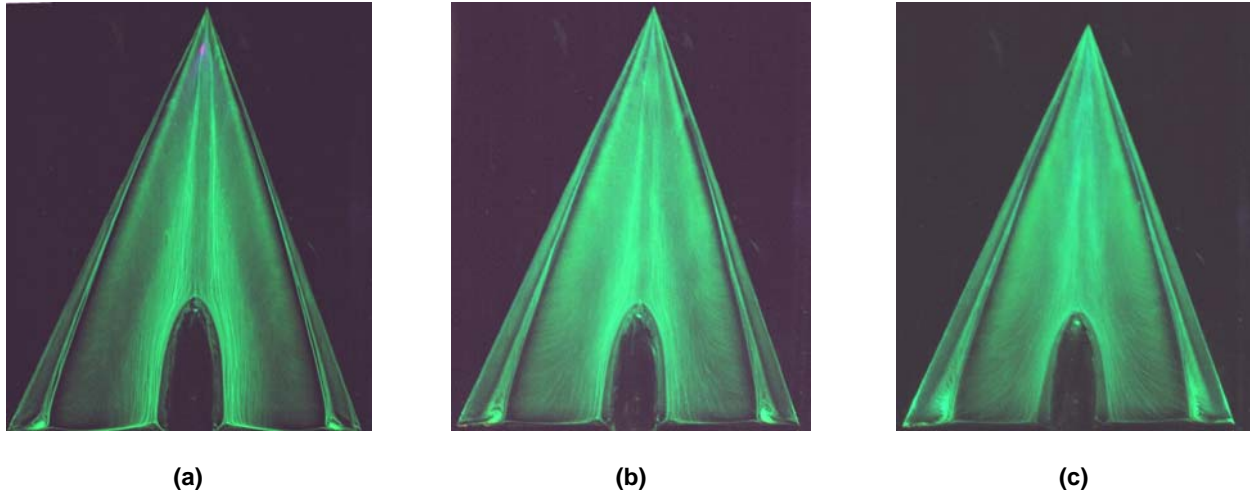
Figure 22-8: Flow Visualization Images for the Sharp Edge Configuration at
R_{mac} = 2 x 10^6 and Angles of Attack (a) 13.3°, (b) 18.5° and (c) 23°.

22.4.1.2   Medium Radius Leading Edge Wing

The most direct way to illustrate the effect of rounding the wing leading edges is to compare the flow visualization images from the sharp-edged cases with those obtained on the configuration with the medium radius edges. Figure 22-9 illustrates one such comparison for the 13.3° case at 2 x 10^6 Reynolds number. The first obvious feature of the figure is that the primary vortex structure on the round-edged wing no longer begins at the apex. In fact, it appears to have its origins at about 30% of the root chord down the leading edge. In addition, there is now clear evidence of an additional structure on the inboard sections of the wing. This structure appears to originate near the apex and is likely to be the inboard vortex suggested by Hummel. It has been suggested that this structure will progressively weaken in relation to the primary vortex as the angle of attack of the wing is increased. This is explored in Figure 10 where results are presented for 13.3°, 18.5° and 23°.

(a)   (b)
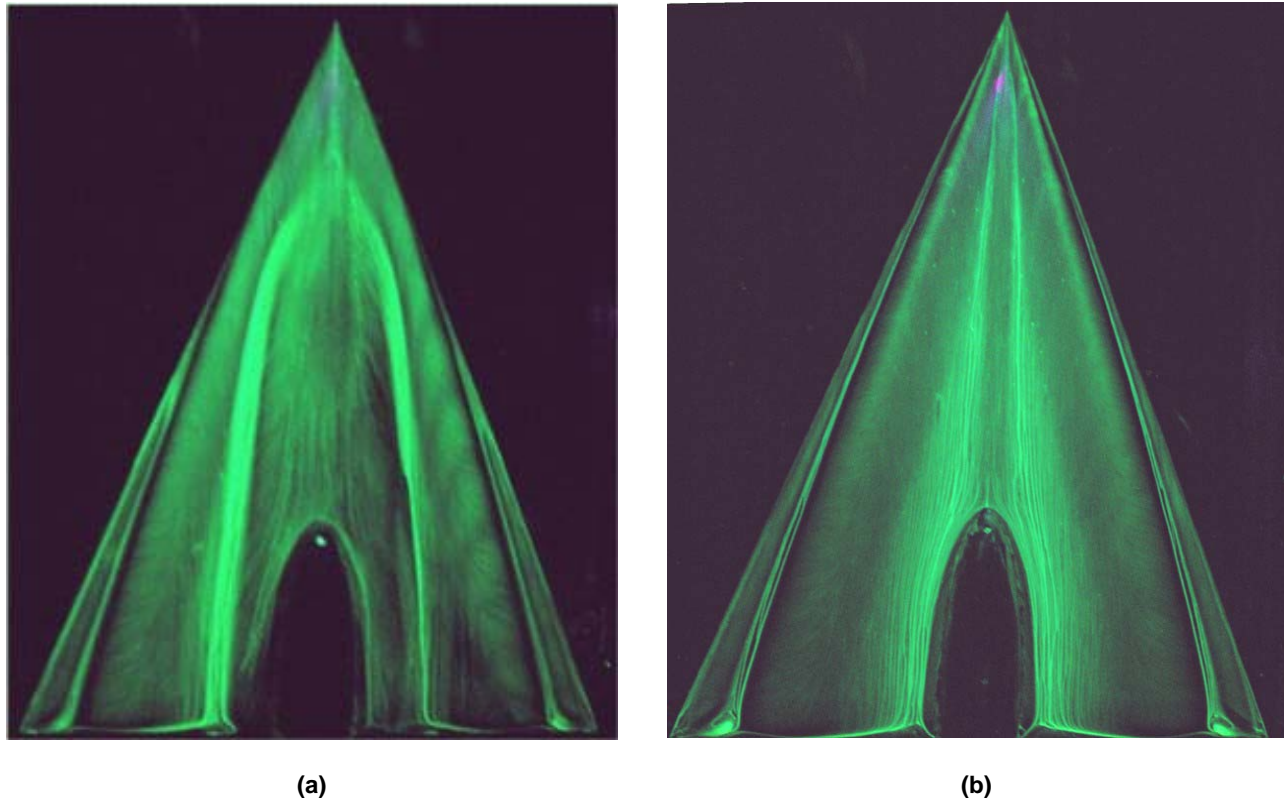
Figure 22-9: Comparison of Oil Flow Patterns for (a) Rounded and
(b) Sharp Leading Edge Configurations at $R_{mac} = 2 \times 10^6$, α = 13.3°.

An obvious feature of the results presented in Figure 22-10 is the progressive movement of the origin of the primary vortex from the 30% of root chord location towards the apex as the angle of attack increases from 13.3° up to 23°. At the same time, the inboard structure becomes less distinct and the images begin to resemble more closely those of the sharp leading edges. By 23° there is still a difference between the images for the sharp and medium radius edges suggesting that the flow on inboard sections of the wing differs in the two cases. This may be due to persistence of a weak inboard vortex structure but this cannot be confirmed without flowfield data.

(a)   (b)   (c)
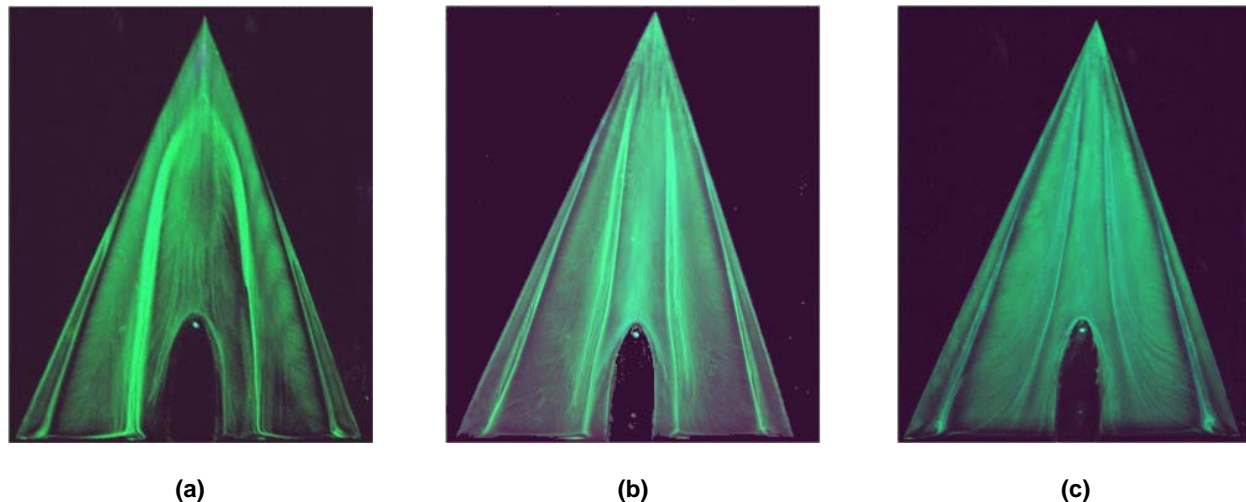
Figure 22-10: Flow Visualization Images for the Rounded Edge Configuration
at R_{mac} = 2 x 10^6 and Angles of Attack (a) 13.3°, (b) 18.5° and (c) 23°.

22.4.1.3   Influence of Reynolds Number on Rounded Leading Edge Flow

The sensitivity of the flow on a sharp edged delta wing to Reynolds number effects is restricted by the fact that separation is effectively forced at the sharp leading edges. For this reason, the Reynolds number has more of an influence on secondary separation rather than the primary separation and it principally alters the relative placement and size of the primary and secondary vortex systems. It has been shown to have almost no effect on the measured lift. On a wing with rounded leading edges, the boundary layer can persist beyond the leading edge before separating on the upper surface of the wing. This is particularly the case near the apex where the relative thickness of the wing is greater. The effect of this delay in separation has been discussed above in relation to the formation of the complex vortex system above the delta wing with the medium radius edges.

The influence of Reynolds number on this process can be observed in Figure 22-11. This figure shows surface oil flow visualizations for Reynolds numbers of 1 x 10^6 and 2 x 10^6 at an angle of attack of 13.3°. The characteristics of the flow pattern at Re = 2 x 10^6 have already been described and, although the flow pattern at 1 x 10^6 looks very similar, there are some important differences. At first glance it appears that the primary vortex structure may extend all the way to the apex for the Re = 1 x 10^6. Indeed the flow pattern in the vicinity of the leading edge looks very similar to that of the sharp-edged wing. The flow pattern further inboard, however, is very similar to that on the medium radius wing suggesting that the inner vortex structure still exists for this case. Closer examination of the leading edge region shows a distinct bend in the dark radial line associated with the primary vortex at about 20 – 30% of root chord. It is not clear that the continuation of this line towards the apex is part of the primary vortex. It is likely that laminar separation is initiated at the leading edge at this low Reynolds number right up to the apex. It may be that the shear layer then undergoes transition and reattaches close to the leading edge, leaving the footprint of a laminar separation bubble. The flow then subsequently behaves in a similar manner to the Re = 2 x 10^6 case.

(a)   (b)
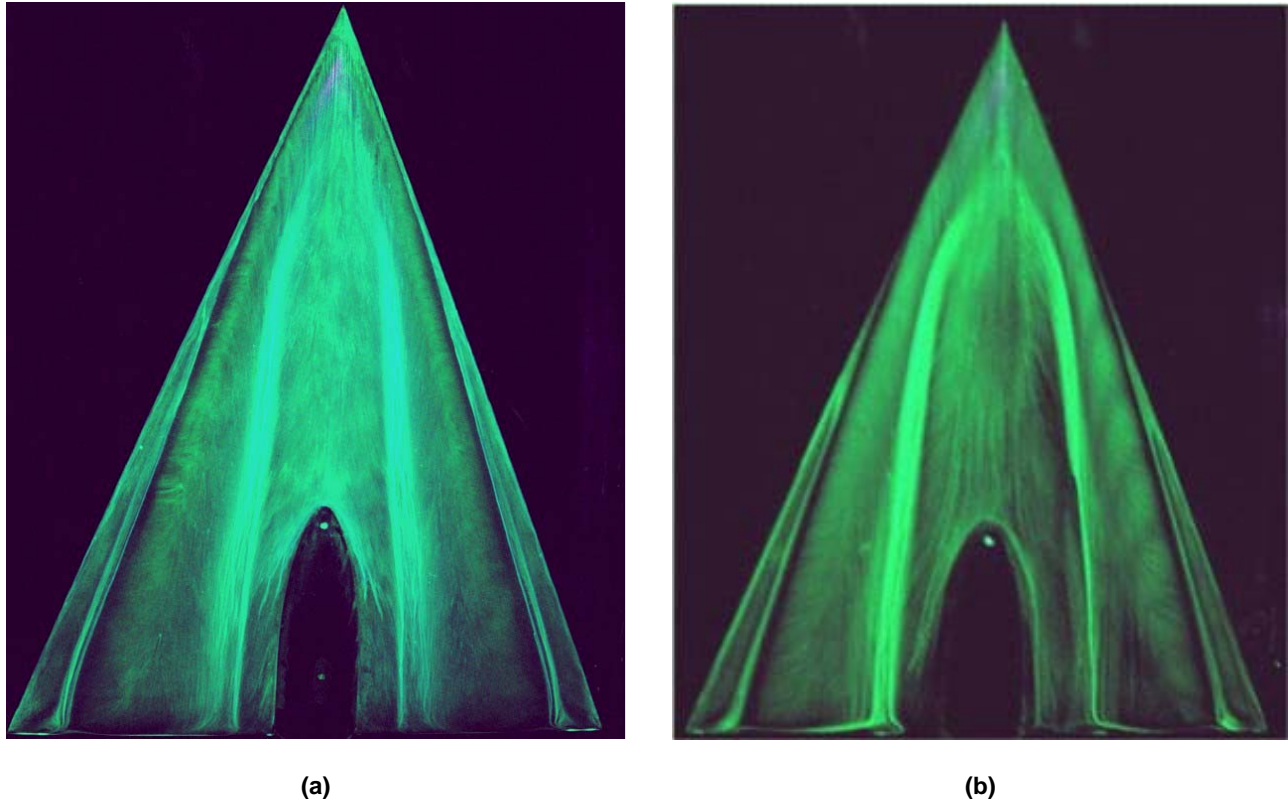
Figure 22-11: Comparison of Oil Flow Patterns for the Round Edged
Configuration at (a) Re = 1 x 10^6 and (b) R$_{mac}$ = 2 x 10^6, α = 13.3°.

At higher angles of attack, separation becomes restricted to the leading edge and the flow patterns at both Reynolds numbers become essentially identical.

22.4.1.4   Further Insight into Leading Edge Rounding

As mentioned previously, four sets of leading edges were manufactured at Glasgow to replicate the original leading edge geometries studied by Chu and Luckring. Although the work reported here focuses on the sharp and medium radius leading edge geometries, some insight into the effect of leading edge rounding can be gained by looking at results from the other cases. As an example, Figure 22-12 compares the flow over the sharp, medium and large radius wings at a Reynolds number of 2 x 10^6 and an angle of attack of 13.3°.
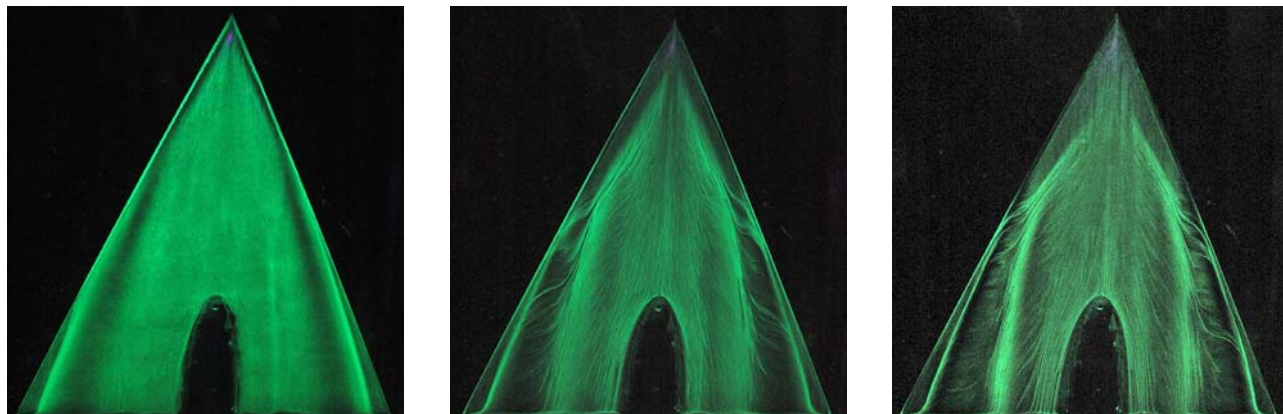
Figure 22-12: The Development of the Primary Vortex for the Large-Edged, R_{mac} = 2 x 10^6 and α = 13.3°.

In this figure, the leading edge vortex structure is clearly not present over the nose portion of the large radius wing. Instead, the flow appears to be initially attached in this region (with a possible leading edge separation bubble very close to the leading edge) and the oil moves in the freestream direction. There is then a separation front which starts some distance downstream of the apex and sweeps out towards the leading edge. The primary vortex system has its origins just upstream of where the separation front meets the leading edge. This case illustrates the fundamentally different flow structures that exist at the leading edge near the apex and further downstream. This is consistent with the observations made earlier in relation to flow structures on the medium radius wing.

22.4.2   Forces and Moments

22.4.2.1   Steady Forces and Moments

In this section data will be presented for all three cases discussed above, i.e. medium edges 1 x 10^6 and 2 x 10^6 and sharp edges 2 x 10^6. The normal force coefficient variations measured on the wing are presented in Figure 22-13. There is a clear Reynolds number effect at the lower angles of attack for the wing with the rounded edges. Initially, the normal force coefficient is higher at the lower Reynolds number. The reasons for this are not immediately obvious but are likely to be associated with the leading edge separation and the effect this has on the strength of the primary vortex system. This effect disappears at about 20° angle of attack in a manner consistent with the trend shown in the surface oil flow visualization, i.e. the flow patterns become identical at the higher angles of attack. Examination of the results for the sharp edged wing would tend to confirm this hypothesis since they have a very similar magnitude and gradient to the results at 1 x 10^6 for the round-edged wing.
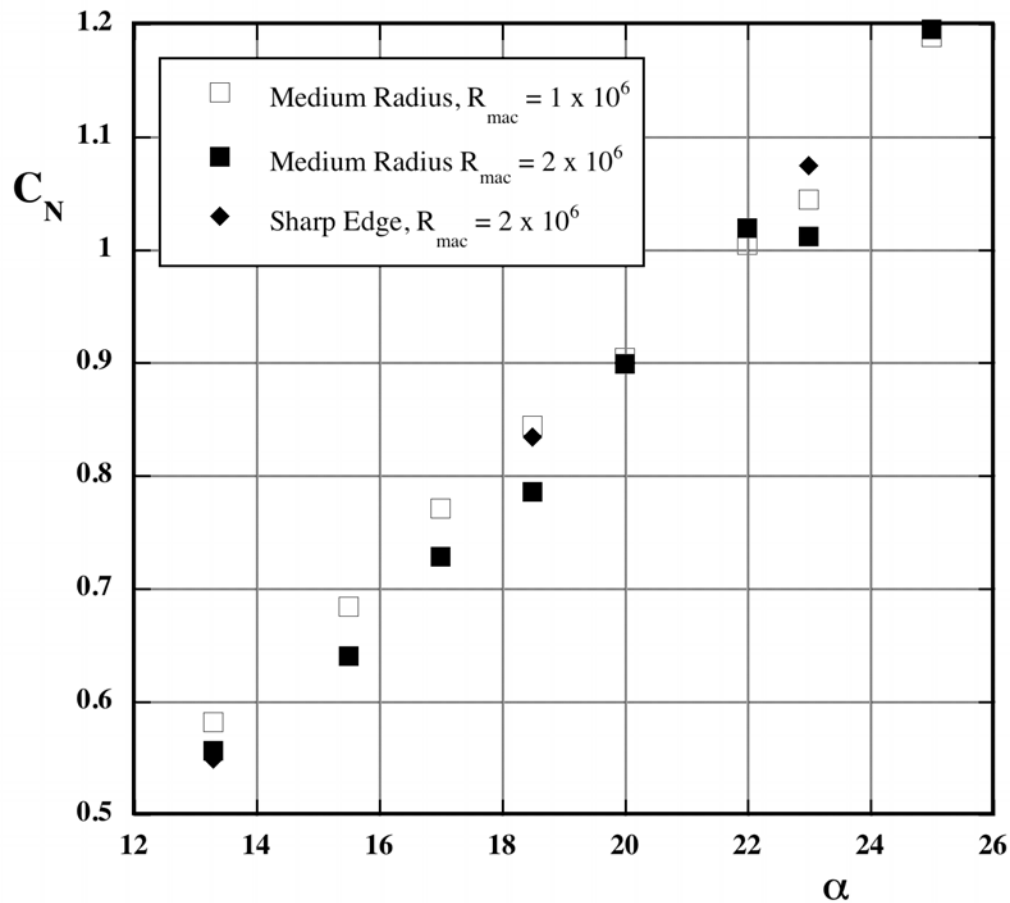
Figure 22-13: Comparison of Normal Force Coefficients for the Three Test Cases.

The measured axial force coefficients are presented in Figure 22-14. It is important to note there that the positive direction is defined as being in the direction of the airflow. The figure shows that although there are slight differences between the data sets for the two leading edge geometries at the same Reynolds number, the main effect visible in the data is the difference between two Reynolds numbers. The axial force coefficient is always higher for the $R_{mac} = 1 \times 10^6$ case and the curve with increasing incidence has a steeper gradient. This is consistent with a larger wake structure at lower Reynolds number that progressively increases as the angle of attack is increased.
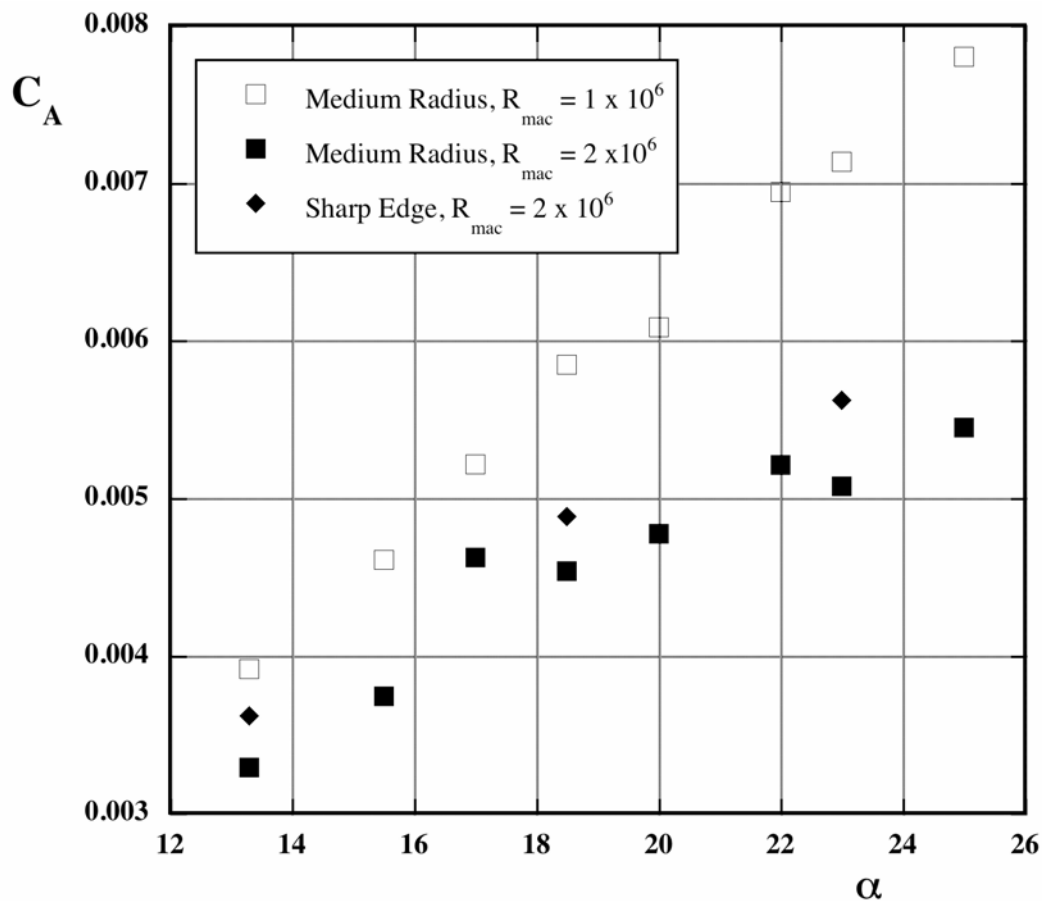
Figure 22-14: Comparison of Axial Force Coefficients for the Three Test Cases.

The final figure in this section, Figure 22-15, shows the pitching moment coefficient measured about the aerodynamic centre. At the lower incidence values, the rounded-edged wing exhibits lower nose down pitching moment values than the sharp-edged wing. In addition, the results for the round-edged wing appear to be relatively insensitive to Reynolds number below approximately 19°. At higher angles of attack, round-edged wing produces larger nose down pitching moments at the lower Reynolds number, achieving similar magnitudes to the sharp-edged wing at 2×10^6. The reason for this is not obvious at this stage.
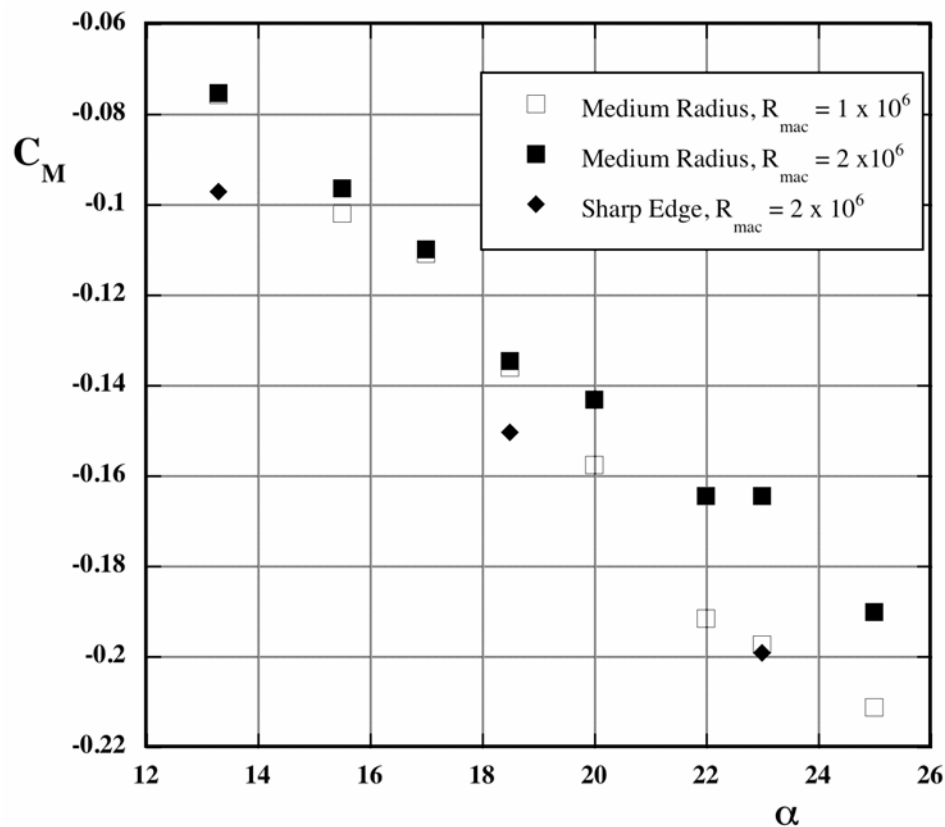
Figure 22-15: Comparison of Pitching Moment Coefficients for the Three Test Cases.

22.5 CONCLUSIONS

Flow visualization and load data have been presented for a 65° delta wing with rounded and sharp leading edges. The data have identified that, as may be expected, the flow topology and the resulting loads become sensitive to Reynolds number when the leading edges are rounded. At higher angles of attack, this sensitivity seems to diminish somewhat but the Reynolds number still influences the pitching moment and tangential force. Unsteady forces were measured but these have not yet been fully analysed. Sample datasets of time varying forces and moments are provided in Appendix 3.5.

Further testing is planned during 2008 to supplement the current measurements. This will include PIV measurement of the flowfield, unsteady surface pressure measurements and infra-red thermography studies of the boundary layer state.

Sample datasets from all the tests described in this chapter are provided in Appendix 3.5.

22.6 REFERENCES

[22-1] Chu, J. and Luckring, J.M.: *Experimental Surface Pressure Data Obtained on 65° Delta Wing Across Reynolds Number and Mach Number Ranges*, NASA TM 4645, 1996.

[22-2]   Gad-El-Hak, M. and Blackwelder, R.F.: *The Discrete Vortices from a Delta Wing*, AIAA Journal, Vol. 23, 1985, pp. 961-962.

[22-3]   Payne, F.M., Ng, T.T. and Nelson, R.C.: *Experimental Study of the Velocity on a Delta Wing*, 19th AIAA Fluid Dynamics, Plasma Dynamics and Lasers Conference, Honolulu, 1987.

[22-4]   Délery, J.M., Legendre, R. and Werlé, H.: *Toward the Elucidation of Three Dimensional Separation*, Annual Review of Fluid Mechanics, Vol. 33, 2001, pp. 129-154.

[22-5]   Gursul, I.: *Recent Developments in Delta Wing Aerodynamics*, The Aeronautical Journal, Vol. 108, No. 1087, 2004, pp. 437-452.

[22-6]   Renac, F., Barberis, D. and Molton, P.: *Control of Vortical Flow Over a Rounded Leading-Edge Delta Wing*, AIAA Journal, Vol. 43, No. 7, 2005, pp. 1409-1417.

[22-7]   Luckring, J.M.: *Reynolds Number and Leading-Edge Bluntness Effects on a 65° Delta Wing*, 40th AIAA Aerospace Sciences Meeting and Exhibit, Reno, 2002.

[22-8]   Hummel, D.: *The Second International Vortex Flow Experiment (VFE-2): Objectives and First Results*, Proceedings of IMechE Part G: Journal of Aerospace Engineering, Vol. 220, No. 6, 2006, pp. 559-568.

[22-9]   Luckring, J.M.: *Reynolds Number, Compressibility, and Leading Edge Bluntness Effects on Delta Wing Aerodynamics*, 24th International Congress of the Aeronautical Sciences, Yokohama, 2004.

[22-10] Schröder, A., Agocs, J., Frahnert, H., Otter, D., Mattner, H., Kompenhans, J. and Konrath, K.: *Application of Stereo PIV to the VFE-2 65° Delta Wing Configuration at Sub-and Transonic Speeds*, 24th AIAA Applied Aerodynamics Conference, San Francisco, 2006.

Chapter 23 – EXPERIMENTAL INVESTIGATIONS ON THE VFE-2 CONFIGURATION AT TUBITAK-SAGE, TURKEY

by

Suleyman Kurun

23.1   SUMMARY

In this chapter the experimental results of 65° delta wing configuration with sharp and rounded leading edges carried out at TUBITAK-SAGE Ankara Wind Tunnel in the Second International Vortex Flow Experiment (VFE-2) are presented. Test results include force measurements with six component internal balance and oil flow visualisation.

23.2   NOMENCLATURE

a	=	Speed of sound
$\bar{c}$	=	Mean aerodynamic chord, $= 2c_r / 3$
m	=	Meter
M	=	Mach number, $\equiv V / a$
R_{mac}	=	Reynolds number, $\equiv V_\infty \bar{c} / \nu_\infty$
s	=	Second
C_A	=	Axial Force Coefficient; $= A/q_\infty S$
C_D	=	Drag Force Coefficient; $= D/q_\infty S$
C_L	=	Lift Force Coefficient; $= L/q_\infty S$
LE	=	Leading Edge
V	=	Velocity (with x, y, z components of u, v, w)
α	=	Angle of attack, deg
μ	=	Viscosity
ν	=	Kinematic viscosity, $\equiv \mu / \rho$
ρ	=	Density
q	=	Dynamic pressure, $\equiv \rho V^2 / 2$
∞	=	Freestream conditions

23.3   INTRODUCTION

Experimental and Numerical Solutions have been carried out in NATO Research and Technology Organization (RTO) Applied Vehicle Technology 113 (AVT) Task Group named "Understanding and Modeling Vortical Flows to Improve the Technology Readiness Level for Military Aircraft" between 2003 and 2007. The task

group acted in two facets as CAWAPI and VFE-2. Both numerical and experimental solutions have been carried out in the Second International Vortex Flow Experiment (VFE-2) facet. TUBITAK-SAGE Ankara Wind Tunnel had the participation to the experimental part of the VFE-2 facet. In the vortex-flow research program, the NASA 65° delta wing configuration with sharp and rounded leading edges with different leading edge radius was chosen for new tests concerning additional drag and flow field data. The new experiments were aimed at an extension of the knowledge on the vortical flow around the configuration with sharp and rounded leading edges. The measurements were accompanied by numerical investigations to support the interpretation of the flow physics, and in the present paper only limited experimental details are used. The history of VFE-2 has been described by D. Hummel [23-8] and the authors of the experimental contributions to VFE-2 have presented their work in five separate papers from [23-9] to [23-13]. TUBITAK-SAGE and ONERA presented the work in a collective paper [23-11].

Before VFE-2 work started, experimental results from the National Transonic Facility (NTF) at NASA Langley Research Center on a 65° swept delta wing were already available [23-1]. For one sharp and three rounded leading edges normal force and pitching moment as well as pressure distribution measurements had been carried out for a large variety of Mach numbers and Reynolds numbers. The extensive pressure instrumentation used for experiments at NASA Langley prevented the use of an internal balance. Sting-gauging technique was employed to obtain normal force and pitching moment. Because NASA model was not appropriate for internal balance usage, ONERA models with model numbers 4 and 5 were used in Ankara Wind Tunnel tests. In the wind tunnel experiments at TUBITAK-SAGE, a combination of force measurement and flow visualization were used to characterize the flow behaviour.

23.4   EXPERIMENTAL SET UP AND WIND TUNNEL TESTING

23.4.1   Wind Tunnel

TUBITAK-SAGE Ankara Wind Tunnel (AWT) is a closed circuit horizontal type low subsonic wind tunnel having 10ft x 8ft x 20ft (width x height x length respectively) closed atmospheric test section. Maximum test speed is 90 m/s. Its sketch is given in Figure 23-1.
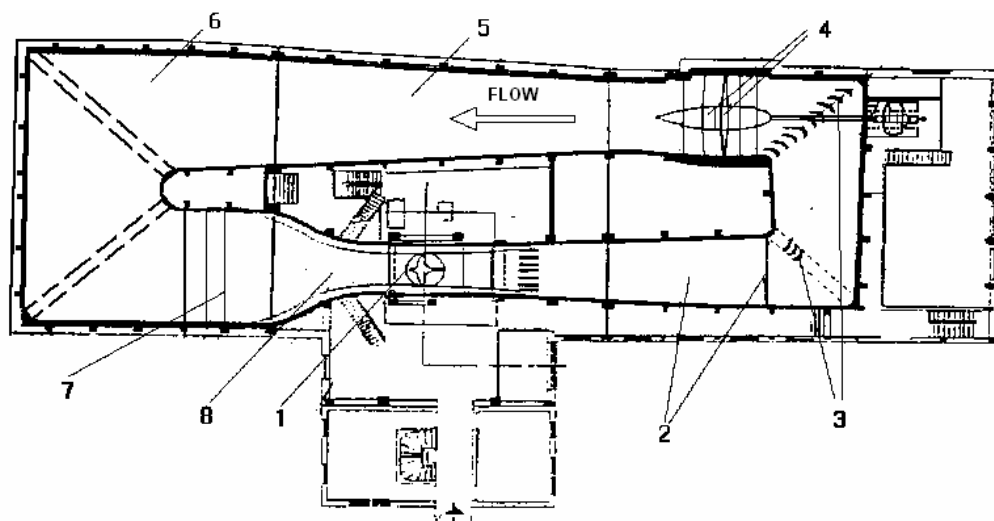
Figure 23-1: Ankara Wind Tunnel Sketch.

23.4.2   Wind Tunnel Model

In the task group 5 models with different sizes and properties according to different test needs were used at different wind tunnels. The model used at National Transonic Facility (NTF) before the task group was called as Model Nr. 0. The list of the models with sizes, owners and tested wind tunnels are given in Table 23-1.

Table 23-1: Wind Tunnel Models Used in VFE-2. [Notations for Leading Edge Shapes: (S) Sharp Edged, (RS) Rounded – Small Radius, (RM) Rounded – Medium Radius, (RL) Rounded – Large Radius]

Model Nr.	Span [m]	Root Chord [m]	Leading Edge	Tested At	Owner
0	0.610	0.653	S, RS, RM, RL	NASA, NTF	NASA Langley RC
1	0.457	0.490	S, RS, RM, RL	NASA, LTPT DLR, TWG ONERA	NASA Langley RC
2	0.933	0.980	S, RM	TU Munich DLR, KKK	TU Munich
3	0.987	1.059	S, RM	Uni. Glasgow	Uni. Glasgow
4	0.457	0.490	S	ONERA TUBITAK-SAGE	ONERA Lille
5	0.457	0.490	RM	ONERA TUBITAK-SAGE	ONERA Lille

ONERA models with model numbers 4 and 5 were used in Ankara Wind Tunnel tests. Two resin one-piece copies of the 'sharp' and 'medium' NASA models were manufactured by ONERA and shipped to Ankara Wind Tunnel. The VFE-2 model is a 65° delta wing with flat upper and lower surfaces. ONERA models tested in Ankara Wind Tunnel has the dimensions equal to NASA model and they are 65° swept symmetrical flat plate delta wings having a root chord length of 0.49023 m, giving a wing area of 0.11207 m^2. The model view is given in Figure 23-2.

Figure 23-2: Wind Tunnel Model.

Shapes were measured along three chord stations situated at $\Delta x = 98.23$ mm, 196.23 mm and 392.23 mm from the apex. Results have been compared to the analytical functions and are reported on Table 23-2. It can be observed that discrepancies are of same order when comparing NASA and ONERA 'medium' models with the theoretical shapes. But ONERA 'sharp' variations are twice NASA 'sharp' ones. These differences can be attributed to the fact that ONERA models are made out of resin. Their amplitudes however remain bounded within acceptable limits.

Table 23-2: Geometrical Discrepancy along Three Chord Sections between
Each Model and the Analytical Shape: Maximum Variations in mm

Chord Section		NASA Sharp	NASA Medium	ONERA Sharp	ONERA Medium
x = 98.23 mm	Δz max(+)	0.147	0.162	0.278	0.245
	Δz min(-)	0.147	0.123	0.234	0.235
x = 196.23 mm	Δz max(+)	0.181	0.234	0.278	0.143
	Δz min(-)	0.204	0.157	0.22	0.125
x = 392.23 mm	Δz max(+)	0.112	0.206	0.217	0.216
	Δz min(-)	0.096	0.186	0.181	0.142

Although the models had pressure ports for ONERA's needs, no surface pressure measurement has been done in AWT, only pressure measurements for base drag correction was taken and used.

23.4.3   Test Set-up

Considering the expected forces, it was decided to use the 35 mm sting type six component internal balance having 1000 N normal force, 375 N axial force and 150 N.m pitch moment maximum limits. Before tests some interface modifications of the internal balance with the model and sting have been done. Because the size and shape of AWT's balance was different than ONERA's, a new intermediate part was manufactured. The diameters of the AWT's sting and balance were different than ONERA's, and then a new aft body was manufactured with the same outer shape. Carbon fibre fairing of the sting and wing interface was manufactured according to the analytic descriptions provided by NASA and ONERA to be sure that the entire model/sting geometry replicated the original test. The six component internal balance was located between the model and the sting and was used measure the steady and unsteady forces acting on the wing. This balance is cylindrical and care was taken to ensure that there was no transmission of loads from the fairings. An inclinometer was used to measure model angle of attack to within 0.05°. These interfaces are shown on Figure 23-3.

Figure 23-3: Model-Internal Balance-Sting Interface.

Because existing Model Support System was designed for missile testing with less normal force, it couldn't overcome the high normal forces; therefore it became necessary to change the motor. Although new model support system has the capability to fix the model in the tunnel center, the existing system in test dates didn't have this capability. The test set-up views are given in Figure 23-4 and Figure 23-5.

Figure 23-4: Test Set-up 1.

Figure 23-5: Test Set-up 2.

23.4.4   Wind Tunnel Testing

The experiments were carried out in the 3.05 x 2.44 meter, closed circuit, Ankara Wind Tunnel of TUBITAK-SAGE. Tests were conducted at Reynolds numbers of 1.5 million based on the 326.82 mm mean aerodynamic chord. Tests have been done in two phases. In the first phase, force measurements have been done with two models from -4° to +30° with 1° increment. Force and moment data were recorded for the models at each angle of attack. In the second phase, china clay and oil flow visualization studies were conducted.

Investigations on the laminar/turbulent transition on delta wings had been tried to be made. China Clay method is based on shear stress variation. The china clay method of boundary layer flow visualization is a technique for discerning the area of transition from laminar to turbulent flow. The technique is based on the different evaporative qualities of flow in laminar, turbulent and transition regions. China clay, also known as Kaolin, is a ceramic raw material and also used in paper production and in many different industrial applications. A mixture of Kaolin and Kerosene is applied to the model immediately before testing equally and thinly. When the wind is turned on it causes the kerosene to evaporate, leaving streaks of clay powder in the form of the flow pattern. The fluid is dried earlier in a turbulent boundary layer region than a laminar boundary layer region and then, the transparent liquid changes back into white color of the powder in the turbulent boundary layer region. Transition point can be determined as the boundary between the dry region in turbulent region and wet region in laminar region on the surface of the model. Several attempts were made at assessing the transition characteristics of the delta wing but the experiments couldn't be readily implemented and didn't give sufficiently good resolution, because wind tunnel main drive characteristics had a negative effect in reaching the test velocities. The time needed to reach the test velocities was around 8 minutes (excluding the pre-operation time) which was too long to catch the flow phenomena sufficiently good. The china clay method was shelved and flow visualization by oil was made.

Oil flow visualization was carried out from 13° to 26° using different steps. A mixture of oil and pigment material was applied to the surface of the delta wing. After the preparation finished, the wind tunnel was

turned on and reached to test speeds. The flow pattern developed on the surface of the model and then the pictures and films were taken using ultraviolet light and cameras.

23.5 RESULTS

It should be noted that the results presented in the following sections have been corrected for wind tunnel wall interference effects and base drag effects. Although the balance is six component type balances, because of model symmetry only normal force, axial force and pitching moments have been taken into consideration.

23.5.1 Oil Flow Visualization Results

Oil flow visualizations with both models have been made. Only half portions of the models have been used in these tests. Flow visualization pictures are given in Figure 23-6 and Figure 23-7 for sharp and medium radius leading edges respectively.
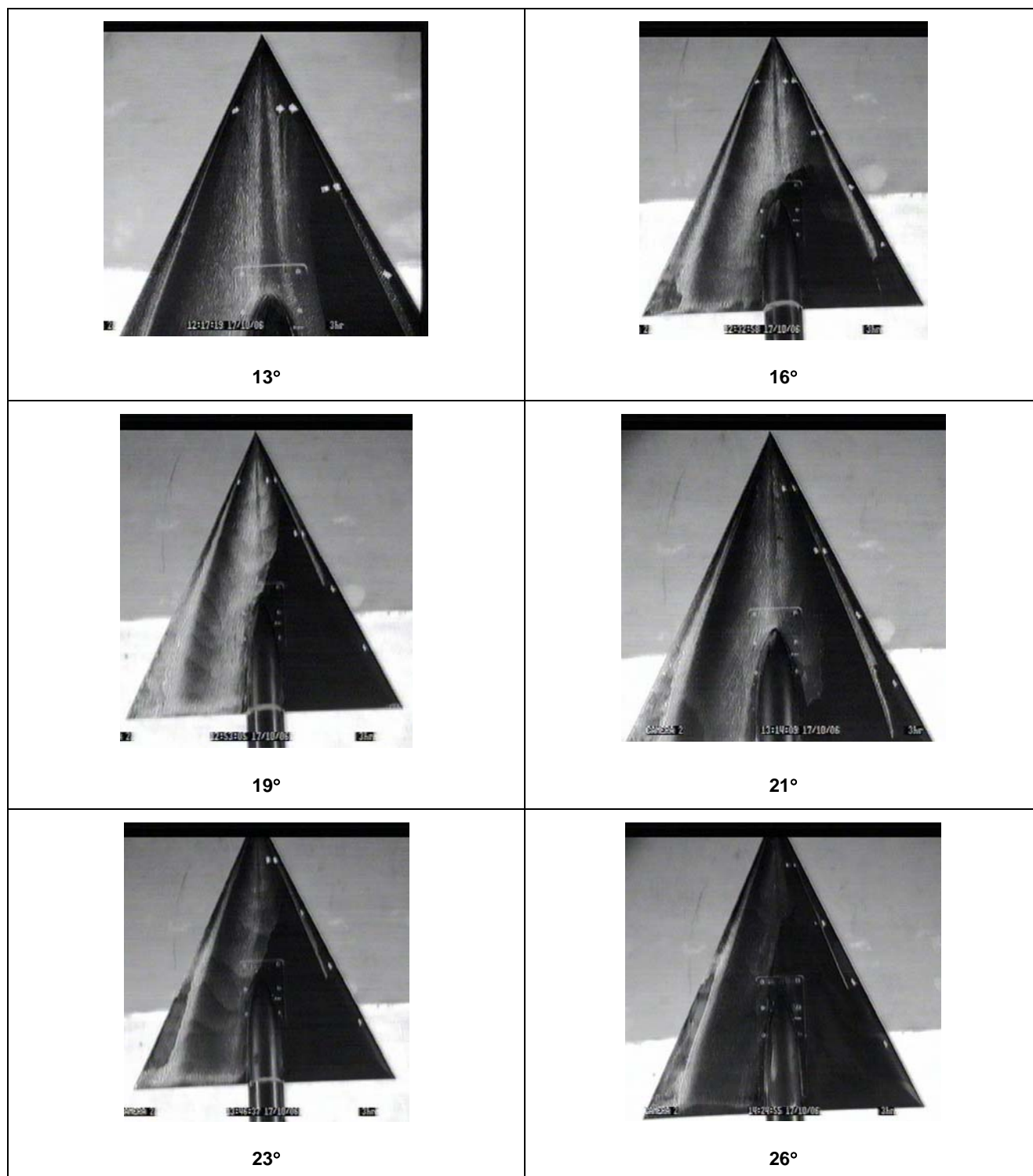
Figure 23-6: Sharp LE Oil Flow Visualization Pictures.
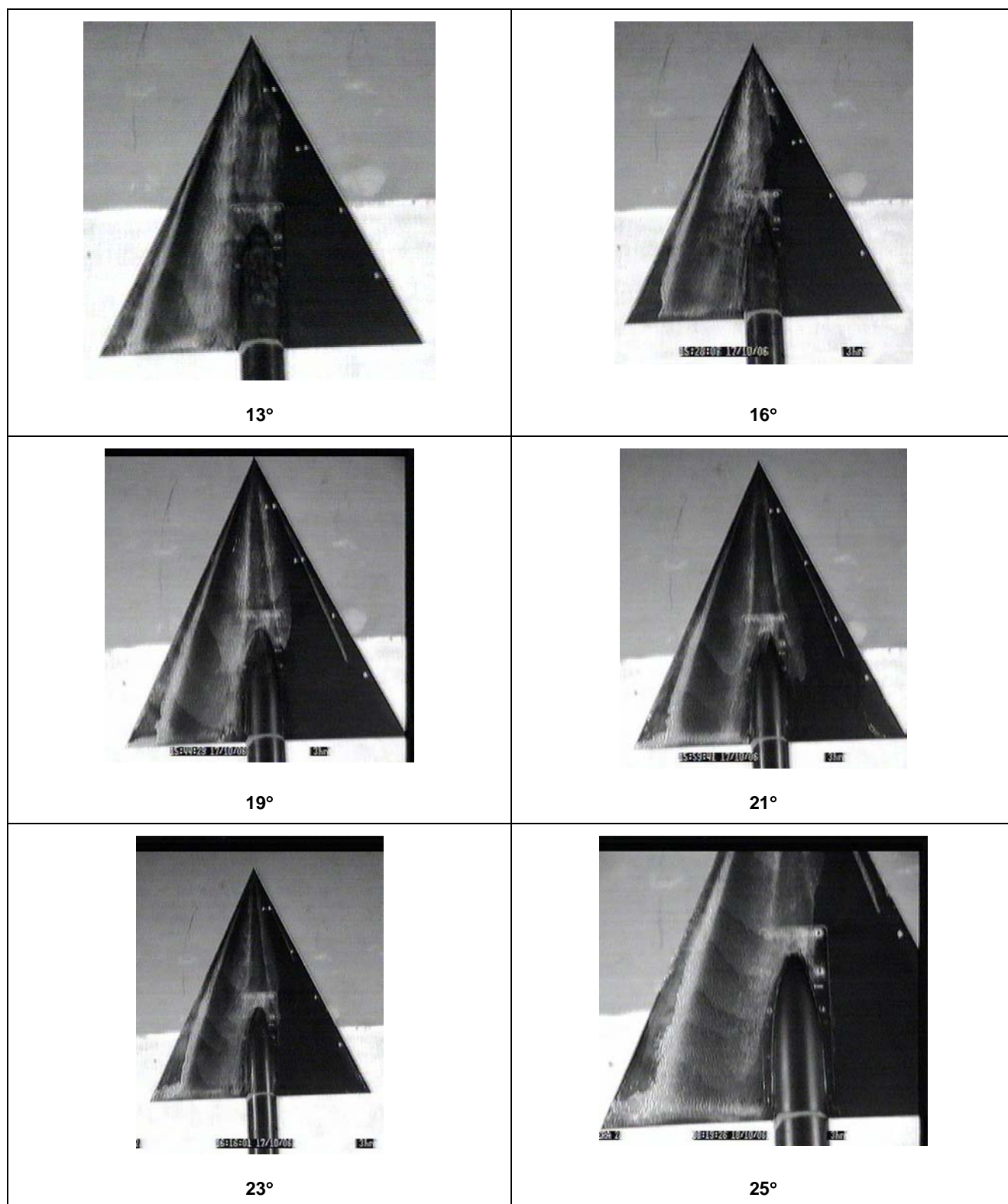
Figure 23-7: Medium Radius LE Oil Flow Visualization Pictures.

Sharp leading edge pictures show expected classical delta wing leading edge vortex system. Flow separation takes place at the leading edge and this separation creates the vortex system above the wing. It can be seen that the vortex system starts from the apex of the wing and goes to the trailing edge. Secondary separation line in many images makes clear the primary and secondary vortex core locations. It can't be observed clearly from the images that there is a vortex breakdown for the angle of attacks higher than 23° but there is evidence of a loss in coherence of the flow structures near the trailing edge. This behaviour may be caused by the progression of vortex breakdown. The first obvious difference between sharp LE and medium LE result is that the primary vortex structure on the rounded edged wing doesn't begin from the apex. Instead, it appears to have its origins at about 10 – 15% of the root chord down the leading edge. An additional structure on the inboard sections is sensed and this structure appears to start near the apex and may be the inboard vortex suggested by the committee. Flow field data is necessary to be sure about the vortex structure. Oil flow visualizations show the same behaviour with the other companies' tests in the task group. Flow visualization results have been compared with oil flow visualization results of the Munich TU and Glasgow University, PSP measurements of DLR and also many computational results and it is seen that there is a good agreement.

23.5.2   Force-Moment Measurement Results

In this section force-moment measurements are going to be given. Normal force, axial force and pitching moments have been taken into consideration and the results are also compared with ONERA results.

Force measurement results are given in Figure 23-8. Normal force and pitch moment results are not very different for two leading edges however the axial force coefficient starts to differ after 6° angle of attack. This may be caused by the flow phenomena described before.
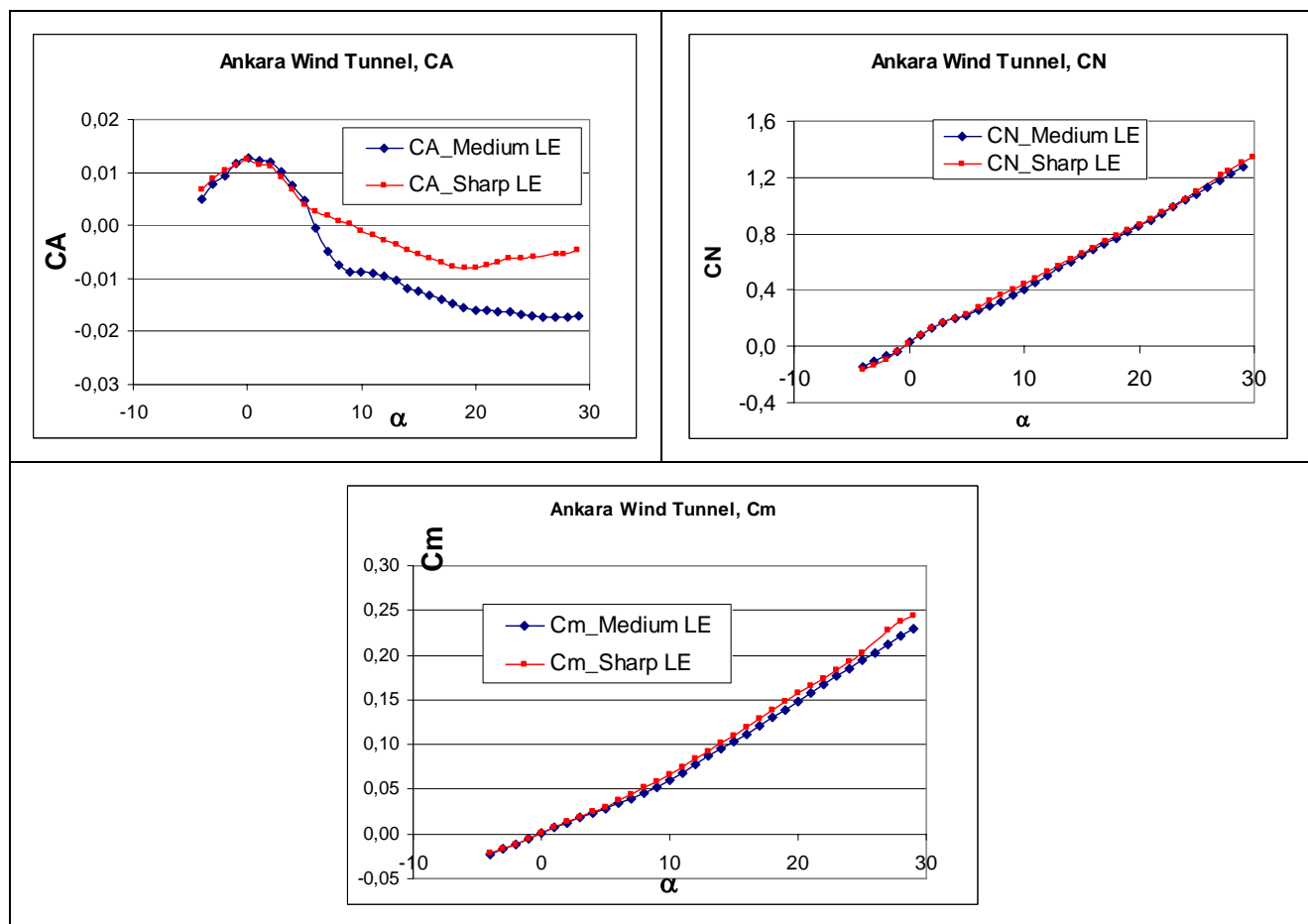
Figure 23-8: Ankara Wind Tunnel Force-Moment Results.

Comparisons have been made with the ONERA results in the following figures. Note that tests have been undertaken in two different wind tunnels at ONERA with open and closed test sections. Although the models are the same, the effects of different wind tunnels with different model support system, internal balance, data acquisition and other items can affect the results. It also has to be considered that ONERA tests were done 1 million Re number instead of 1.5 million.
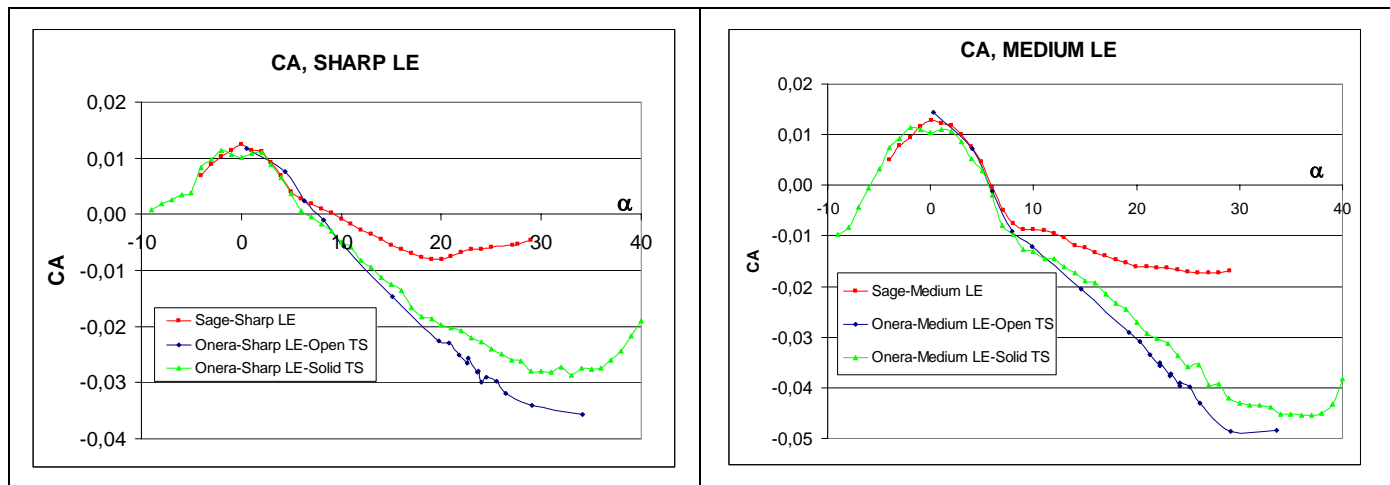
Figure 23-9: Axial Force Comparison.

As the angle of attack increases, the differences in the results increase for both type leading edges. Although it is not shown here, similar comparison has been made with University of Glasgow results and it was seen that the results don't coincide well.

As seen from the Figure 23-10, normal force results show a good agreement. The comparison with University of Glasgow results is also quite well.
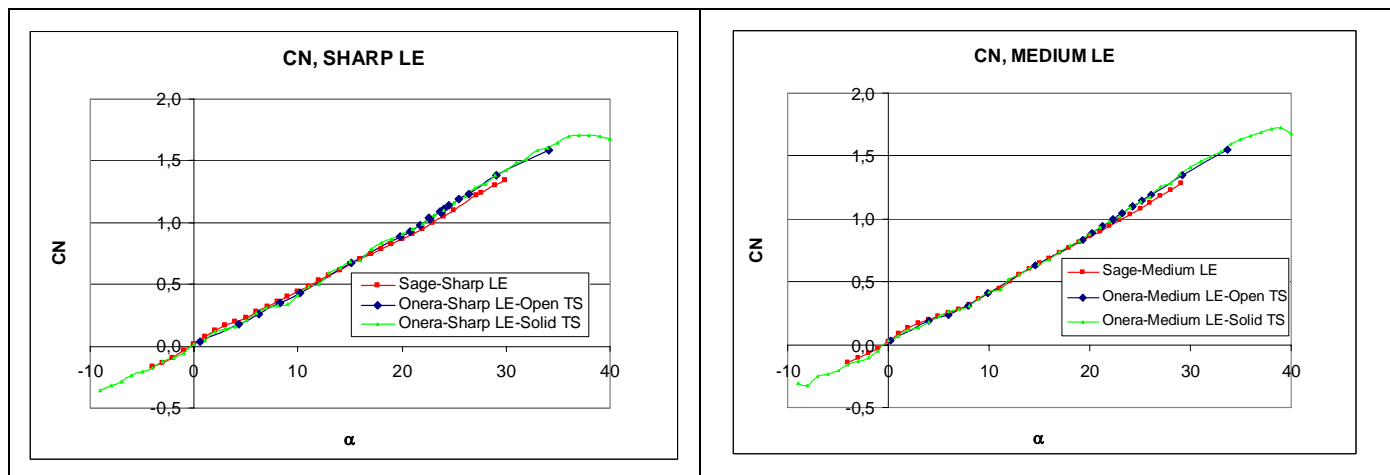
Figure 23-10: Normal Force Comparison.

As seen from the Figure 23-11, pitching moment results show a good agreement. The comparison with University of Glasgow results is also quite well.
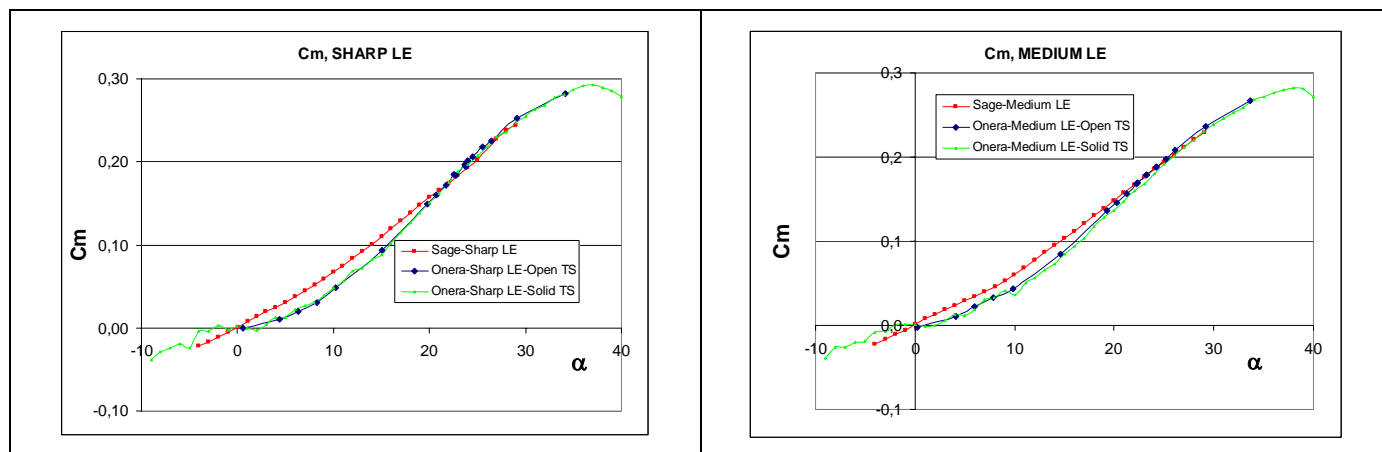
Figure 23-11: Pitching Moment Comparison.

As seen from the Figure 23-12 and Figure 23-13, drag force and lift force results show very good agreement.
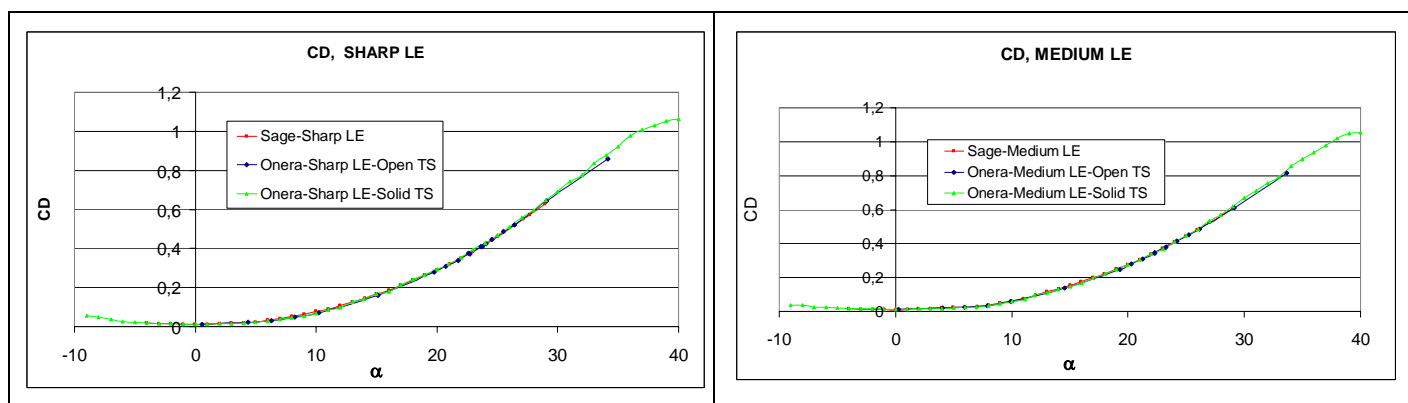
Figure 23-12: Drag Force Comparison.
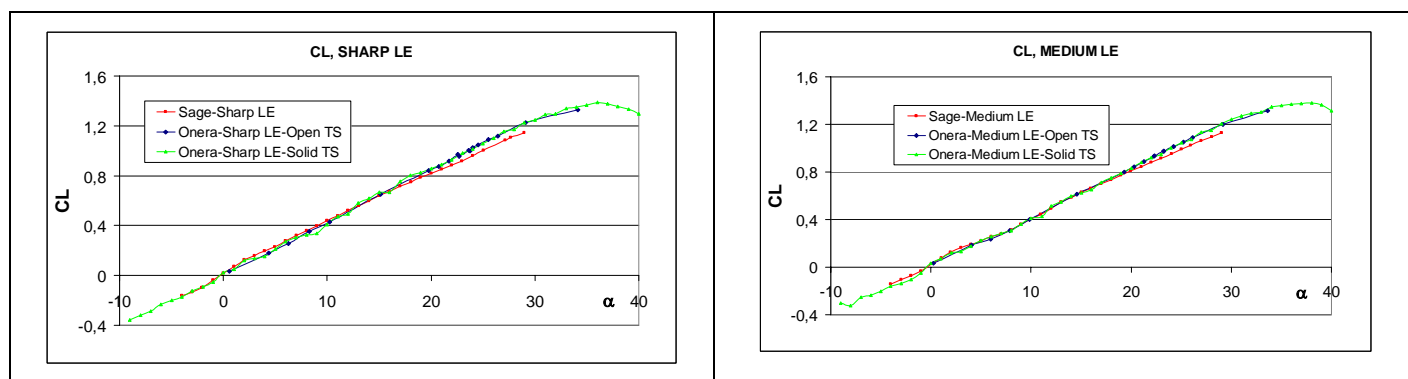
Figure 23-13: Lift Force Comparison.

Force and moment data for Sharp LE and Medium LE is given in Table 23-3 and Table 23-4 respectively.

Table 23-3: Force-Moment Data for Sharp LE

α	CA	CN	Cm	CD	CL
-4.00	4.0000	-0.1644	-0.0220	-0.1644	-0.0220
-3.01	3.0100	-0.1343	-0.0169	-0.1343	-0.0169
-2.01	2.0100	-0.0988	-0.0112	-0.0988	-0.0112
-0.99	0.9915	-0.0374	-0.0046	-0.0374	-0.0046
-0.01	0.0129	0.0176	0.0010	0.0176	0.0010
1.02	-1.0200	0.0760	0.0075	0.0760	0.0025
2.02	-2.0200	0.1288	0.0134	0.1288	0.0084
2.98	-2.9800	0.1660	0.0193	0.1660	0.0143
3.98	-3.9800	0.1954	0.0246	0.1954	0.0246
4.98	-4.9800	0.2298	0.0305	0.2298	0.0305
5.99	-5.9900	0.2772	0.0372	0.2772	0.0372
7.02	-7.0200	0.3229	0.0444	0.3229	0.0444
8.00	-8.0000	0.3631	0.0518	0.3631	0.0518
9.02	-9.0200	0.4041	0.0593	0.4041	0.0593
9.99	-9.9900	0.4459	0.0674	0.4459	0.0674
10.99	-10.9900	0.4846	0.0747	0.4846	0.0747
12.00	-12.0000	0.5316	0.0840	0.5316	0.0840
13.01	-13.0100	0.5714	0.0920	0.5714	0.0920
14.02	-14.0200	0.6166	0.1012	0.6166	0.1012
15.01	-15.0100	0.6591	0.1103	0.6591	0.1103
16.00	-16.0000	0.7009	0.1193	0.7009	0.1193
17.01	-17.0100	0.7452	0.1290	0.7452	0.1290
18.04	-18.0400	0.7866	0.1382	0.7866	0.1382
19.01	-19.0100	0.8298	0.1475	0.8298	0.1475
20.02	-20.0200	0.8694	0.1570	0.8694	0.1570
21.01	-21.0100	0.9080	0.1657	0.9080	0.1657
22.00	-22.0000	0.9492	0.1745	0.9492	0.1745
22.97	-22.9700	0.9961	0.1834	0.9961	0.1834
24.00	-24.0000	1.0461	0.1927	1.0461	0.1927
25.02	-25.0200	1.1029	0.2031	1.1029	0.2031
27.14	-27.1400	1.2171	0.2275	1.2171	0.2275
27.68	-27.6800	1.2452	0.2379	1.2452	0.2379
28.94	-28.9400	1.3047	0.2439	1.3047	0.2439

Table 23-4: Force-Moment Data for Medium LE

α	CA	CN	Cm	CD	CL
-4.02	0.0051	-0.1426	-0.0222	-0.1426	-0.0222
-3.00	0.0078	-0.1067	-0.0164	-0.1067	-0.0164
-1.97	0.0094	-0.0710	-0.0111	-0.0710	-0.0111
-0.99	0.0116	-0.0355	-0.0056	-0.0355	-0.0056
0.04	0.0128	0.0283	0.0009	0.0283	0.0009
1.04	0.0121	0.0839	0.0077	0.0839	0.0027
1.97	0.0119	0.1306	0.0128	0.1306	0.0078
2.98	0.0101	0.1682	0.0189	0.1682	0.0139
3.97	0.0076	0.1950	0.0240	0.1950	0.0240
4.97	0.0047	0.2216	0.0288	0.2216	0.0288
6.00	-0.0004	0.2565	0.0346	0.2565	0.0346
7.01	-0.0049	0.2828	0.0398	0.2828	0.0398
8.02	-0.0075	0.3139	0.0457	0.3139	0.0457
9.01	-0.0088	0.3624	0.0525	0.3624	0.0525
9.99	-0.0088	0.4088	0.0605	0.4088	0.0605
10.98	-0.0089	0.4485	0.0684	0.4485	0.0684
12.02	-0.0094	0.5026	0.0774	0.5026	0.0774
13.01	-0.0103	0.5578	0.0868	0.5578	0.0868
14.03	-0.0119	0.6028	0.0952	0.6028	0.0952
15.04	-0.0124	0.6484	0.1040	0.6484	0.1040
15.97	-0.0133	0.6856	0.1120	0.6856	0.1120
16.98	-0.0140	0.7288	0.1216	0.7288	0.1216
17.98	-0.0148	0.7688	0.1301	0.7688	0.1301
18.98	-0.0154	0.8113	0.1391	0.8113	0.1391
19.99	-0.0161	0.8560	0.1488	0.8560	0.1488
20.99	-0.0161	0.8980	0.1577	0.8980	0.1577
22.00	-0.0162	0.9425	0.1668	0.9425	0.1668
22.99	-0.0163	0.9893	0.1762	0.9893	0.1762
24.03	-0.0167	1.0387	0.1857	1.0387	0.1857
25.01	-0.0170	1.0846	0.1944	1.0846	0.1944
25.97	-0.0173	1.1306	0.2028	1.1306	0.2028
27.00	-0.0173	1.1821	0.2121	1.1821	0.2121
28.02	-0.0173	1.2322	0.2211	1.2322	0.2211
29.04	-0.0170	1.2798	0.2294	1.2798	0.2294

23.6   CONCLUSIONS

Very important results are found from the experiments and the knowledge on delta wing aerodynamics has increased very much. The effect of leading edge type was investigated. Good agreement with other wind tunnels and computational results has been seen in flow visualization and force measurement results.

23.7 ACKNOWLEDGEMENTS

23.8 REFERENCES

[23-1] Chu, J. and Luckring, J.M.: *Experimental Surface Pressure Data Obtained on 65° Delta Wing Across Reynolds Number and Mach Number Ranges*, NASA TM 4645 (1996).

[23-2] Luckring, J.M.: *Reynolds Number and Leading-Edge Bluntness Effects on a 65° Delta Wing*, 40th AIAA Aerospace Sciences Meeting and Exhibit, Reno, 2002.

[23-3] Luckring, J.M.: *Compressibility and Leading-Edge Bluntness Effects for a 65° Delta-Wing*, AIAA Paper 2004-0765, 2004.

[23-4] Luckring, J.M.: *Reynolds Number, Compressibility, and Leading Edge Bluntness Effects on Delta Wing Aerodynamics*, 24th International Congress of the Aeronautical Sciences, Yokohama, 2004.

[23-5] Hummel, D.: *Effects of Boundary Layer Formation on the Vortical Flow Above Slender Delta Wings*, RTO Specialists' Meeting on "Enhancement of NATO Military Flight Vehicle Performance by Management of Interacting Boundary Layer Transition and Separation", Prague, Czech Republic, 4-7 October 2004, Meeting Proceedings RTO-MP-AVT-111, pp. 30-1 to 30-22, 2004.

[23-6] Konrath, R., Klein, C., Engler, R.H. and Otter, D.: *Analysis of PSP Results Obtained for the VFE-2 65° Delta Wing Configuration at Sub- and Transonic Speed*, AIAA-Paper 2006-0060, 2006.

[23-7] Konrath, R., Schröder, A. and Kompenhans, J.: *Analysis of PIV Results Obtained for the VFE-2 65° Delta Wing Configuration at Sub- and Transonic Speeds*, AIAA-Paper 2006-3003, 2006.

[23-8] Hummel, D.: *Review of the Second International Vortex Flow Experiment (VFE-2)*, AIAA Paper 2008-0377, 2008.

[23-9] Luckring, J.M.: *Initial Experiments and Analysis of Vortex Flow on Blunt Edged Delta Wings*, AIAA Paper 2008-0378, 2008.

[23-10] Konrath, R., Klein, Ch. and Schröder, A.: *PSP and PIV Investigations on the VFE-2 Configuration in Sub- and Transonic Flow*, AIAA Paper 2008-0379, 2008.

[23-11] Le Roy, J.F., Rodriguez, O. and Kurun, S.: *Experimental and CFD Contribution to Delta Wing Vortical Flow Understanding*, AIAA Paper 2008-0380, 2008.

[23-12] Furman, A. and Breitsamter, Ch.: *Turbulent and Unsteady Flow Characteristics of Delta Wing Vortex Systems*, AIAA Paper 2008-0381, 2008.

[23-13] Coton, F., Mat, S. and Galbraith, R.: *Low Speed Wind Tunnel Characterization of the VFE-2 Wing*, AIAA Paper 2008-0382, 2008.

[23-14] Luckring, J.M. and Hummel, D.: *What was Learned from the New VFE-2 Experiments*, AIAA Paper 2008-0383, 2008.

[23-15] Nangia, R.K.: *Semi-Empirical Prediction of Vortex Onset and Progression on 65° Delta Wings*, (RTO-AVT-113, VFE-2 facet), AIAA Paper 2008-0384, 2008.

[23-16] Fritz, W.: *Numerical Simulation of the Peculiar Subsonic Flow-Field about the VFE-2 Delta Wing with Rounded Leading Edge*, AIAA Paper 2008-0393, 2008.

[23-17] Gürdamar, E., Ortakaya, Y., Kaya, S. and Korkem, B.: *Some Factors Influencing the Vortical Flow Structures on Delta Wings*, AIAA Paper 2008-0394, 2008.

[23-18] Schiavetta, L.A., Boelens, O.J., Crippa, S., Cummings, R.M., Fritz, W. and Badcock, K.J.: *Shock Effects on Delta Wing Vortex Breakdown*, AIAA Paper 2008-0395, 2008.

[23-19] Cummings, R.M. and Schütte, A.: *Detached-Eddy Simulation of the Vortical Flowfield about the VFE-2 Delta Wing*, AIAA Paper 2008-0396, 2008.

[23-20] Crippa, S. and Rizzi, A.: *Steady, Subsonic CFD Analysis of the VFE-2 Configuration and Comparison to Wind Tunnel Data*, AIAA Paper 2008-0397, 2008.

[23-21] Schütte, A. and Lüdeke, H.: *Numerical Investigations on the VFE 2 65-degree Rounded Leading Edge Delta Wing using the Unstructured DLR-TAU-Code*, AIAA Paper 2008-0398, 2008.

[23-22] Fritz, W. and Cummings, R.M.: *What was Learned from the Numerical Simulations for the VFE-2*, AIAA Paper 2008-0399, 2008.

[23-23] Settles, G.: *Modern Developments in Flow Visualization*, AIAA Journal, Volume 24, No 8, August 1996, pp. 1313-1323.

[23-24] Ura, H., Yokokawa, Y. and Ito, T.: *Experimental Study of Trailing Edge Noise in Low Speed Wind Tunnel*, AIAA Paper 2007-1038, 2007.

[23-25] Greenblatt, D., Paschal, K.B., Yao, C.-S., Harris, J., Schaeffler, N.W. and Washburn, A.E.: *Experimental Investigation of Separation Control Part 1: Baseline and Steady Suction*, AIAA Journal, Vol. 44, No. 12, December 2006, pp. 2820-2830.

Chapter 24 – WHAT WAS LEARNED FROM THE NEW VFE-2 EXPERIMENTS

by

James M. Luckring[1] and Dietrich Hummel *(Retired)*[2]

24.1   SUMMARY

In the present paper the main results of the new experiments from VFE-2 are summarized. These include some force and moment results, surface and off-body measurements, as well as steady and fluctuating quantities. Some critical remarks are added, and an outlook for future investigations is given.

24.2   NOMENCLATURE

A	=	aspect ratio of the wing
f	=	frequency
HWA	=	Hot Wire Anemometry
k	=	reduced frequency ($k = f\,\bar{c}\,/\,U_\infty$)
PIV	=	Particle Image Velocimetry
PSD	=	power spectrum density
PSP	=	Pressure Sensitive Paint
SD	=	Spectrum Density ($SD = PSD^{1/2}$)
U_∞	=	free stream velocity
u, v, w	=	components of the velocity vector
u', v', w'	=	fluctuations of the velocity components ($u = \bar{u} + u'$, etc.)
u_{rms}	=	root mean square of the fluctuations u'
Λ	=	leading edge sweep, deg
ω_x	=	x-component of vorticity

24.3   INTRODUCTION

At the very beginning of the Second International Vortex Flow Experiment (VFE-2), comprehensive experimental results from the National Transonic Facility (NTF) at NASA Langley Research Center on a 65° swept delta wing were already available [24-1]. For one sharp and three rounded leading edges normal force and pitching moment as well as pressure distribution measurements had been carried out for a large variety of Mach numbers and Reynolds numbers. The geometry of the wing and the positions of the pressure tubes according to [24-1] are given in Figure 24-1, and the corresponding arrangement of the wind tunnel model in the National Transonic Facility is shown in Figure 24-2. The results of these measurements have been analyzed and summarized in various papers [24-2]-[24-5].

---

[1] Senior Research Engineer, NASA Langley Research Center, Hampton VA, 23681 USA.

[2] Prof. Dr.-Ing. (retired), Technical University Braunschweig, Institute of Fluid Mechanics, Bienroder Weg 3, 38106 Braunschweig, Germany.

$c_R = 25.734$ in

$b/2 = 12$ in.

$\Lambda = 65°$

$t = 0.875$ in.

Spanwise surface
pressure stations
$x/c_R = 0.20, 0.40, 0.60, 0.80, 0.95$

$t/c_R = 0.0340$
$b/2c_R = 0.4663$
$d/b = 0.1375$

$d = 3.30$ in.

Streamwise leading-edge radii:
$r_{LE}/\overline{c} = 0, 0.0005, 0.0015, 0.0030$
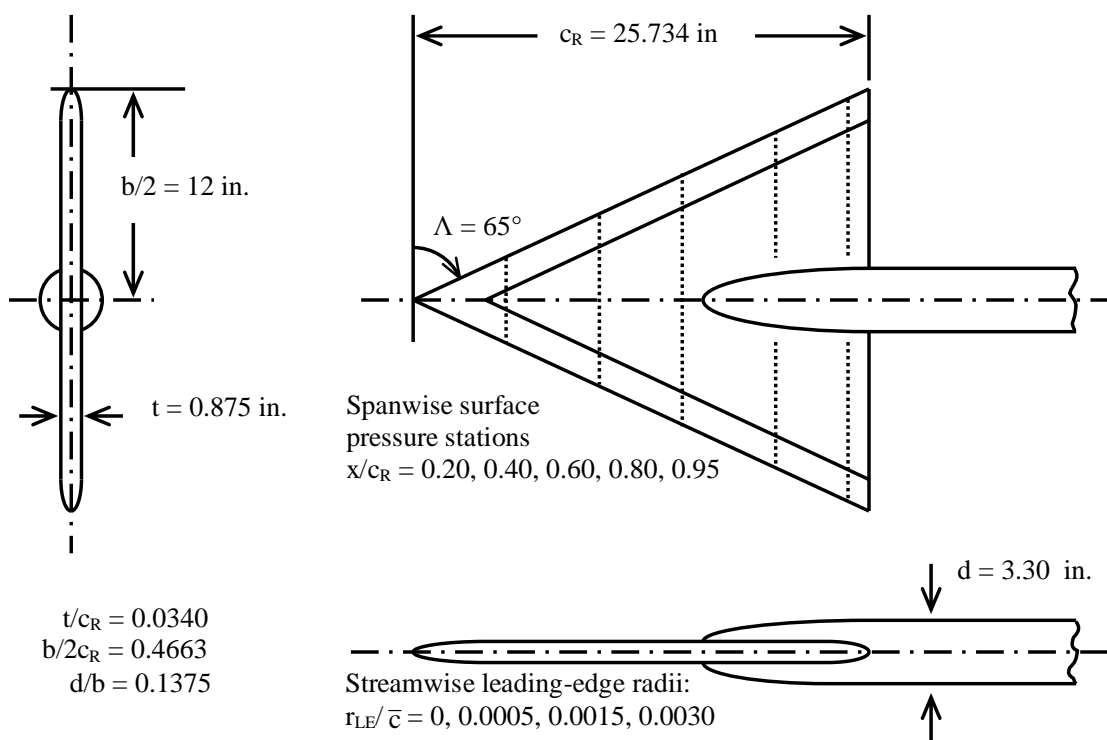
Figure 24-1: VFE-2 Configuration: NASA Delta Wing, Λ = 65°, A = 1.85 [24-1].

Figure 24-2: NASA NTF Tests on the 65° Delta Wing [24-1].

In the 2001 proposal [24-6] for a new vortex-flow research program, the NASA 65° delta wing configuration with sharp and rounded leading edges was chosen for new tests concerning additional drag and flow field data. This led to the Second International Vortex Flow Experiment (VFE-2), which was carried out within a Research and Technology Organization (RTO) Applied Vehicle Technology (AVT) Task Group 2003 – 2007. The new experiments were aimed at an extension of the knowledge on the vortical flow around the configuration with sharp and rounded leading edges. The measurements were accompanied by numerical investigations to support the interpretation of the flow physics, and in the present paper only limited numerical results are used in this capacity. The history of VFE-2 has been described by D. Hummel [24-7], and the authors [24-8]-[24-12] of the experimental contributions to VFE-2 have presented their work in separate papers. The main results of the new experiments within VFE-2 are summarized below.

24.4 NORMAL/AXIAL FORCES AND PITCHING MOMENT CHARACTERISTICS FOR SHARP AND ROUNDED LEADING EDGES

The extensive pressure instrumentation used for experiments at NASA Langley prevented the use of a conventional internal force and moment balance. However, a novel sting-gauging technique was employed to obtain normal force and pitching moment coefficient measurements over the full range of test conditions.

The effect of leading-edge bluntness on the normal force and pitching moment coefficients for the VFE-2 configuration is presented in Figure 24-3 from measurements taken in the NASA Langley NTF at a Mach number of 0.4 and a Reynolds number of 6 million. At low angles of attack both wings develop the same normal force. The blunt leading edge wing has attached flow at these conditions, and any leading-edge vortex separation effects for the sharp-edged wing are very small at these low angles of attack. Over the rest of the angle of attack range investigated the blunt leading edge wing develops less normal force than the sharp-edged wing. The blunt leading edge weakens the leading edge vortex [24-8] resulting in reduced vortex-induced normal force. Pitching moments show the blunt-edged wing has a more forward center of pressure, compared to the sharp-edged wing, over the range of conditions investigated. The vortex flow physics associated with these effects may be taken from the discussions in Section 24-5.
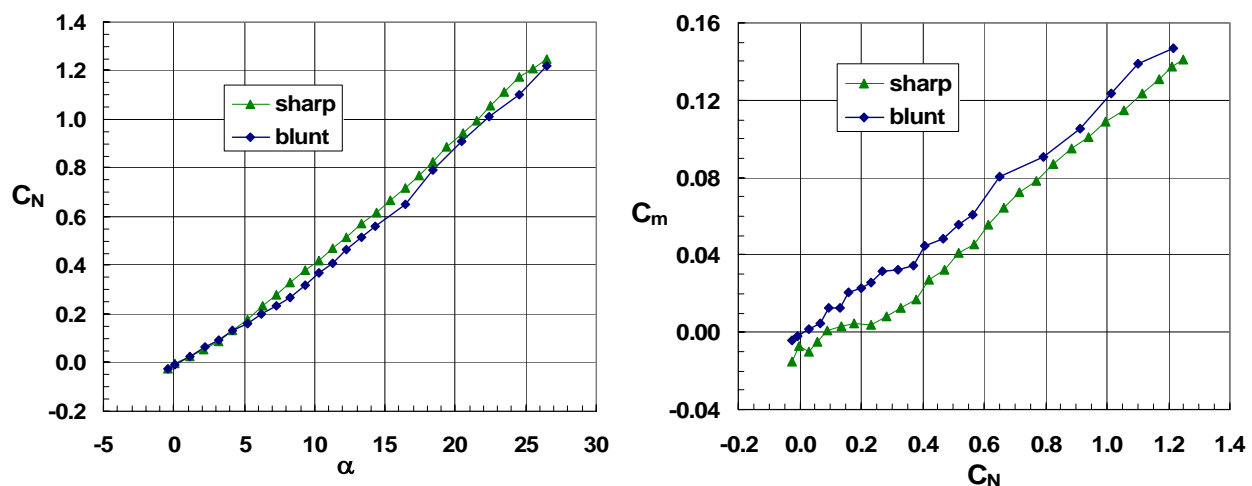
Figure 24-3: Effect of Bluntness on Experimental Normal Force and Pitching Moment Coefficients for the VFE-2 Configuration with Sharp and Medium Radius Rounded Leading Edges at M = 0.4, R_{mac} = 6 x 10^6. Results from NASA Langley NTF.

Low-speed compressibility effects on the normal-force coefficient are summarized in Figure 24-4 with measurements taken at NASA Langley in the NTF with the full-scale delta wing and in the Low Turbulence Pressure Tunnel (LTPT) with the ¾-scale delta wing. All results are for the medium-bluntness leading edge. Although the Reynolds numbers are not identical in this comparison, the differences due to Reynolds number are considered to be small. The left-hand side of the figure shows the variation of normal-force coefficient with angle of attack for Mach numbers ranging between 0.2 and 0.6. The right-hand side shows the same data, scaled by the linear Prandtl-Glauert similarity parameter, $\beta = [1-M^2]^{1/2}$. The Prandtl-Glauert scaled parameters will collapse under conditions largely governed by linear aerodynamics, and the correlation of the measurements over low to moderate angles of attack is quite good, especially considering that the results were obtained with different models in different facilities. Variations among the scaled measurements at high angles of attack are due to nonlinear aerodynamics, most probably due to leading-edge vortex separation. Similarity scaling of these effects requires more advanced methods than linear Prandtl-Glauert scaling.
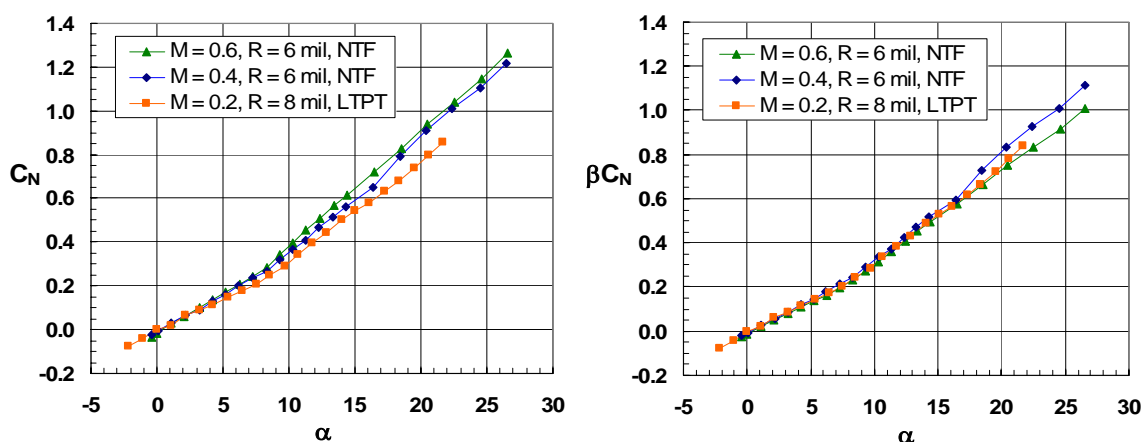
Figure 24-4: Effect of Mach Number on Experimental Normal Force Coefficients for the VFE-2 Configuration with Medium Radius Rounded Leading Edge at $R_{mac} = 6 \times 10^6$ or 8×10^6. Results from NASA Langley NTF and LTPT.

As mentioned earlier, the instrumentation used in the original NASA experiments did not allow for full force/ moment measurement, and in particular prevented the measurement of axial forces. It would be expected that the axial force coefficient should also show a significant effect of bluntness in association with the onset and progression of leading-edge separation.

The effect of bluntness on axial force coefficient from recent measurements [24-10] obtained in the ONERA L1 facility are shown in Figure 24-5 for a Mach number of 0.1 and a Reynolds number of 1 million. There is some scatter in the current measurements of normal force coefficient that prevent seeing the effect due to vortex separation shown in Figure 24-3. However, the effect of bluntness on axial force coefficient can clearly be seen in the right-hand portion of Figure 24-5. A theoretical estimate of attached flow trends is shown by fitting the data to the functional form $C_A = k_0 - k_1 \sin^2\alpha$ nominally in the 3 to 6 degree angle of attack range of the blunt-edge measurements. In this equation k_0 and k_1 are constants determined by the fit. Bluntness resulted in an extended range of attached-flow suction, compared to the sharp edge wing, and the reduction in axial force due to bluntness was manifested over the full range of measurements obtained at ONERA.
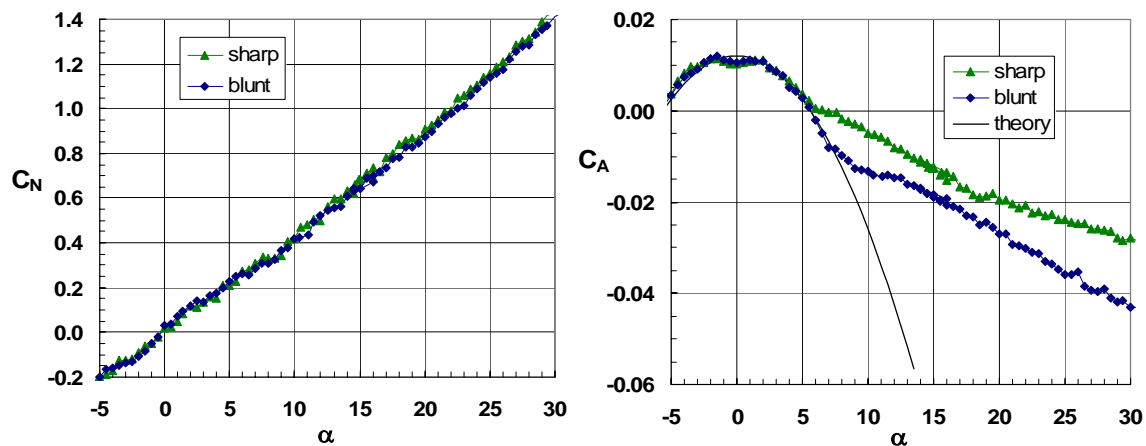
**Figure 24-5: Effect of Bluntness on Experimental Normal and Axial Force Coefficients
for the VFE-2 Configuration with Sharp and Medium Radius Rounded Leading
Edge at M = 0.1, $R_{mac} = 1 \times 10^6$. Results from ONERA L1.**

24.5 ONSET OF VORTICAL FLOW ON THE VFE-2 CONFIGURATION WITH ROUNDED LEADING EDGE

Since for delta wings with sharp leading edges and fixed primary separation many experimental investigations are available in the literature, the AVT Task Group decided in 2003 to use the case of sharp leading edges within VFE-2 as reference only and to direct the main emphasis for new experiments towards studies of the vortex formation on the configuration with *rounded leading edges*.

24.5.1 Principal Flow Structure at α = 13°

For the configurations with rounded leading edges the available NASA data [24-1] showed spanwise pressure distributions with two separate suction peaks on the upper surface of the wing, see Figure 24-6, which so far have never been observed for sharp edged delta wings. Therefore the AVT Task Group decided to study the onset of separated flow for rounded leading edges in more detail, and for this purpose the medium radius leading edge configuration with $r / \overline{c} = 0.0015$ has been selected.

Sharp leading edge
$r / \overline{c} = 0$

Rounded leading edge
$r / \overline{c} = 0.0015$

Spanwise distribution
at $x/c_R = 0.6$
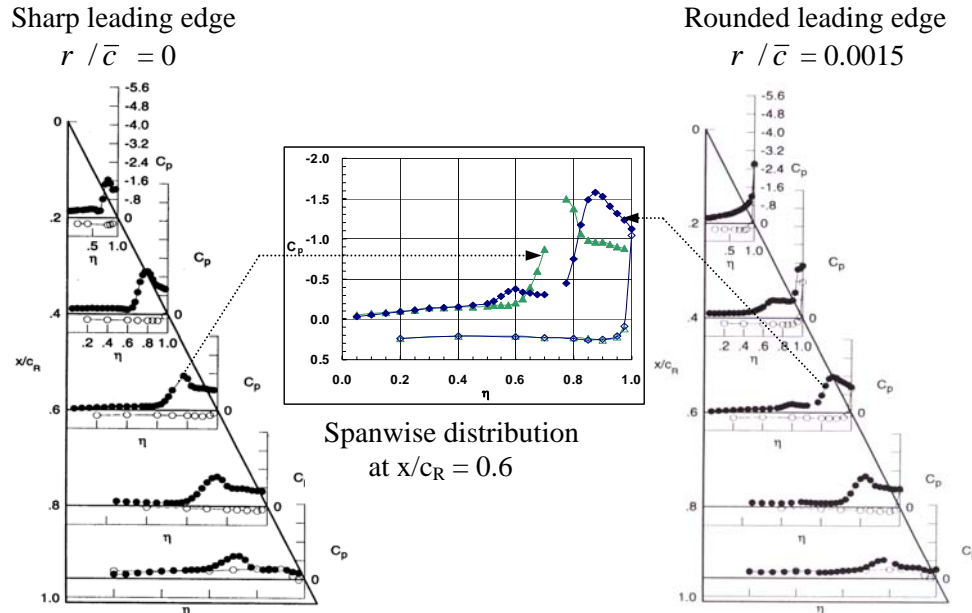
Figure 24-6: Effect of Leading Edge Bluntness on the Pressure Distribution [24-1]
of the VFE-2 Configuration at M = 0.4, R_{mac} = 6 x 10^6, α = 13°; NTF Data.

The experimental pressure distribution on the VFE-2 configuration with medium radius rounded leading edges at Mach number M = 0.4 and Reynolds number (based on the mean aerodynamic chord) R_{mac} = 3 million at an angle of attack α = 13° is shown in Figure 24-7 resulting from the measurements at DLR Goettingen [24-9], [24-13]. On the left-hand side the pressure distributions according to the static surface pressure (PSI) experiments for the model sections with pressure taps are shown. In general, these measurements show very similar results as the earlier NTF tests [24-1] although precise correlation would not be expected due to the difference in Reynolds number. In the region of attached flow near the apex of the wing high suction occurs at the leading edge. Further downstream an inner suction peak develops followed by an even higher outer suction peak, which replaces the original leading edge suction. Towards the trailing edge of the wing the outer suction peak is still maintained, whereas the inner suction peak reduces more and more and finally disappears. The PSP results on the right-hand side show these features in the same way. The full view of the pressure distribution on the configuration is given in the colored figure in the centre of Figure 24-7. It shows on both sides the onset of the strong outer suction peak to be located at about $x/c_R = 0.45$ and undoubtedly this suction peak is related to the primary vortex of the separated flow. The inner suction peak, however, could not be understood so easily. It starts earlier than the outer suction peak and the shape of its initial pressure distributions resembled that of a separation bubble related to the transition from laminar to turbulent flow [24-13]. After the formation of the primary vortex the inner suction peak reduces more and more in the downstream direction [24-14],[24-15].

PSI results   **PSP results**   **PSP results**
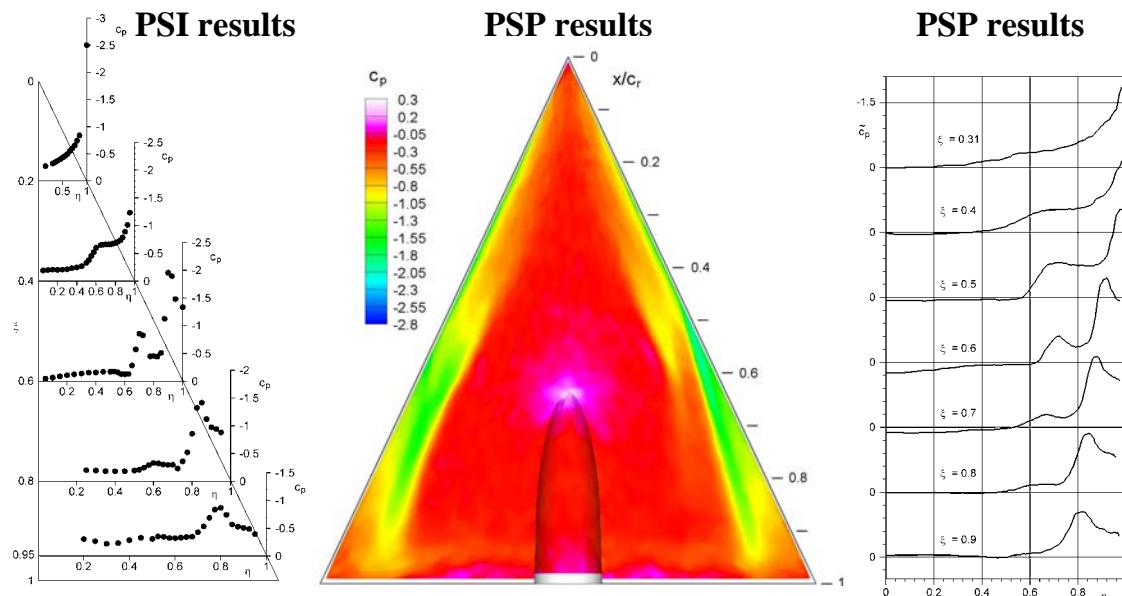
Figure 24-7: Experimental Pressure Distribution on the VFE-2 Configuration with Medium Radius Rounded Leading Edges for M = 0.4, R_{mac} = 3 x 10^6, α = 13°; Results from DLR Goettingen.

On the right-hand side of the colored central plot in Figure 24-7 the inner suction region remains separate from the primary vortex, but on the left-hand side it merges into the suction area of the primary vortex. The inner and outer vortices are co-rotating, and their interaction can be sensitive to small asymmetries that arise from a variety of sources (e.g., flow angularity, model orientation, surface geometry, etc). According to detailed investigations of the model shape carried out at DLR Goettingen these asymmetries are most likely the result of imperfections of the model geometry. At this stage of the investigations the inner suction peak in the pressure distribution was thought to be the outcome of boundary layer effects resulting from a 3D bubble-type laminar/turbulent transition at about $x/c_R = 0.3$, and these effects could be sensitive to disturbances and to model imperfections. At about $x/c_R = 0.5$ a small inner vortex might have been formed, whose path downstream could be either separate or merged with the main primary vortex.

After some substantial support by numerical investigations [24-16] within VFE-2 concerning the technical equipment [24-7], 3D PIV investigations [24-17],[24-18] have been carried out at DLR Goettingen. Figure 24-8 shows the result for the flow field in various cross-sectional planes for the same free stream conditions as in Figure 24-7 and in comparison with the numerical result [24-16]. The surface pressure distribution from the PSP investigations, see Figure 24-7, is displayed in colors for the right half of the wing on the left side of Figure 24-8. The outer suction peak underneath the primary vortex is marked by the green area and the one underneath the inner vortex can be identified by a yellow band. Due to the position of the light source in the wind tunnel there exists a certain region in the vicinity of the leading edge, which was not illuminated, and therefore no velocity measurements are available for this region. Two vortices with the same sense of rotation are clearly indicated in the rear part of the wing. Around $x/c_r = 0.7$ the size of both vortices is about the same as predicted by the CFD results. Further downstream the outer vortex becomes the stronger one, whereas the inner vortex decays. These experimental results are in excellent qualitative agreement with the numerical findings [24-16] as shown in the right-hand figure. The results of the two campaigns in the Transonic Wind Tunnel at Goettingen in 2004 and 2005 have been summarized [24-19] and they were also a subject of the 2006 AIAA achievements review [24-20] as well as to some VFE-2 status reports [24-21],[24-22].
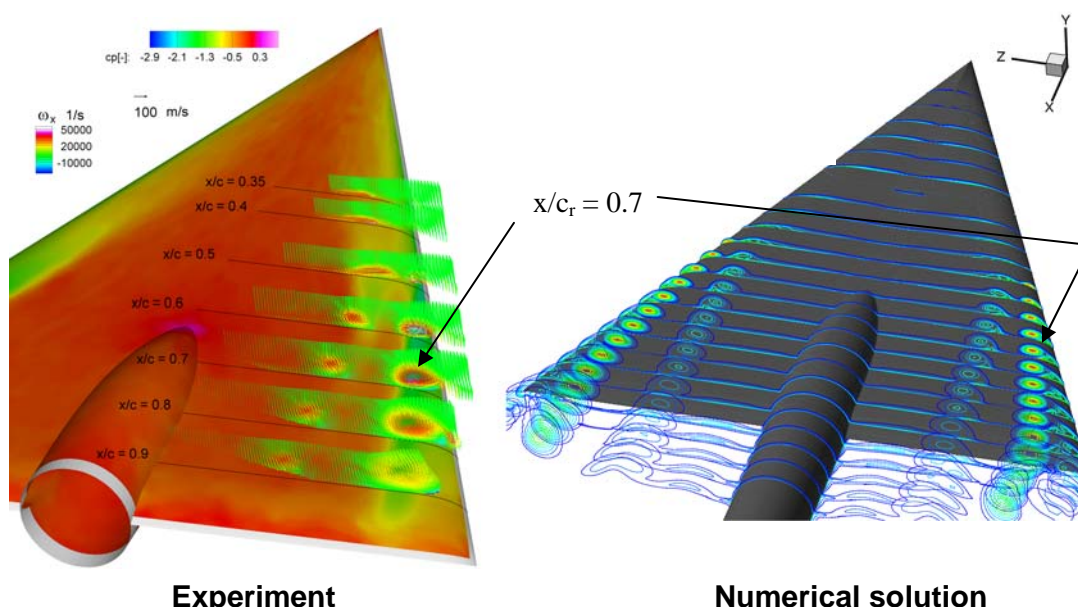
Figure 24-8: Pressure (Surface Color), Velocity (Vectors) and Vorticity (Vector Color) Distributions above the VFE-2 Configuration with Rounded Leading Edges (Medium Radius) for M = 0.4, R_{mac} = 3 x 10^6, α = 13°. Comparison of the PSP and PIV measurements [24-19] at DLR Goettingen (left) with the numerical solution [24-16] of EADS Munich (right).

The understanding of the onset of the vortical flow on the present delta wing with rounded leading edge can be summarized as follows: On the medium radius rounded leading edge VFE-2 configuration at α = 13° the first flow separation takes place in the front one-third of the wing, where the wing is relatively thick. At its very beginning the separated flow region is located close to the wing surface, but further downstream a concentrated inner primary vortex is formed quite rapidly. Along the blunt leading edge the curvature radius of the leading edge remains constant, whereas the local half span increases downstream. This means that the leading edge becomes relatively sharper (r/b_{loc}) towards the trailing edge of the wing. Correspondingly the suction at the leading edge increases downstream, and finally new flow separations take place in the outer portion of the rear part of the wing, forming an outer primary vortex there. In the region of the onset of this outer primary vortex, strong interference with the already existing inner primary vortex takes place. The dominant part of vorticity, shed from the leading edge, is now fed into the outer primary vortex, whereas the feeding of the inner vortex with vorticity is reduced. Therefore the inner primary vortex decays downstream due to dominating viscous effects. Unfortunately within VFE-2 not all details of the onset of vortical flow in the front part of the configuration could be investigated experimentally because of geometric constraints of the PIV setup in the wind tunnel, but due to the encouraging agreement between the experimental and the calculated results, further study of these details can be guided with analysis of numerical solutions.

24.5.2   Variation of the Angle of Attack

The flow pattern described so far depends on the angle of attack. From previous studies [24-2]-[24-5] the progression of leading-edge flow separation of the outer primary vortex with angle of attack was established as:

1)   A low angle-of-attack range where the flow was attached;

2) An intermediate angle-of-attack range where the primary separation progressed up the leading edge, from trailing edge to apex, with increasing angle of attack; and

3) A high angle-of-attack range where essentially the entire leading edge exhibited primary vortex separation.

A series of pressure distributions for M = 0.4 and R_{mac} = 3 million and for various angles of attack from the PSP measurements [24-15],[24-19] at DLR Goettingen is shown in Figure 24-9. Up to α = 11.2° only the inner primary vortex exists, and the corresponding suction on the wing surface reaches considerable values near the trailing edge. With further increasing angle of attack the outer primary vortex is formed in the rear part of the configuration, and already at α = 12.2° its onset has reached a position at x/c_R = 0.6. The strength of the inner primary vortex increases up to the region of the onset of the outer primary vortex, but then decreases suddenly downstream towards the trailing edge. This is due to the fact that the vorticity shed from the leading edge is now fed into the outer primary vortex, and this leads to the considerable reduction of the strength of the inner primary vortex. Another effect can also be recognized from Figure 24-9. In that region where an outer primary vortex already exists, the weakened inner primary vortex moves inboard. For further increasing angles of attack the onset of the outer primary vortex moves upstream, see α = 13.3° and α = 15.3°. At α = 20.5° the outer primary vortex covers almost the whole leading edge, but some weak remnants of an inner primary vortex can still be detected.
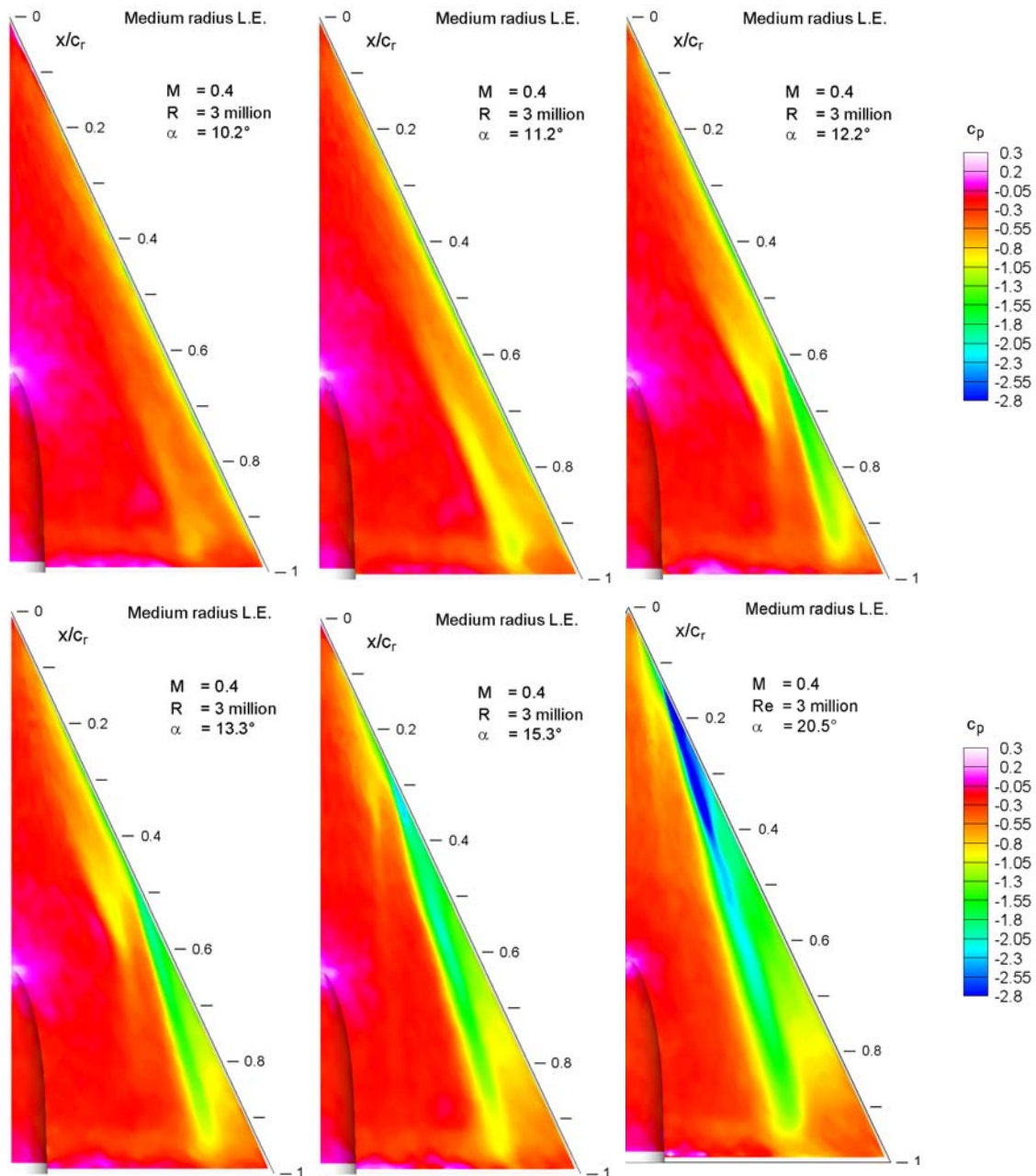
Figure 24-9: Pressure Distributions on the VFE-2 Configuration with Rounded Leading Edges (Medium Radius) for M = 0.4, R_{mac} = 3 x 10^6 at Various Angles of Attack from the PSP Experiments at DLR Goettingen [24-15],[24-19].

24.5.3   Variation of Reynolds Number

The vortex formation strongly depends on the Reynolds number as shown in Figure 24-10 and Figure 24-11. With decreasing Reynolds number the onset of the outer primary vortex moves upstream and its strength increases, whereas the inner primary vortex is weakened and its position moves distinctly inboard.
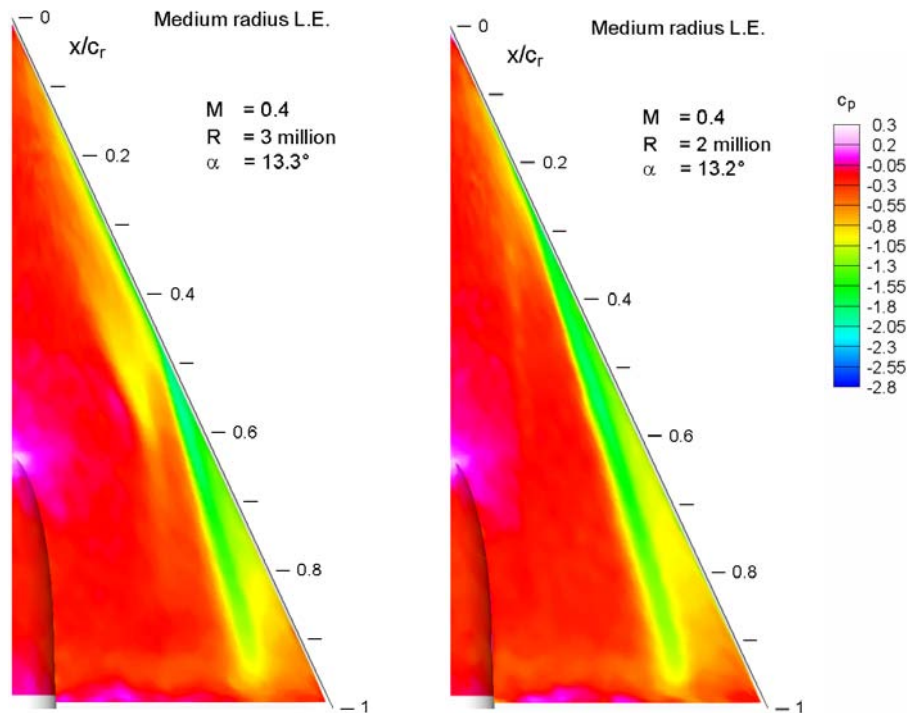
Figure 24-10: Pressure Distributions on the VFE-2 Configuration with Rounded Leading Edges (Medium Radius) for M = 0.4, α = 13° at Different Reynolds Numbers from the PSP Experiments at DLR Goettingen [24-19].

$R_{mac} = 3 \times 10^6$ $R_{mac} = 2 \times 10^6$
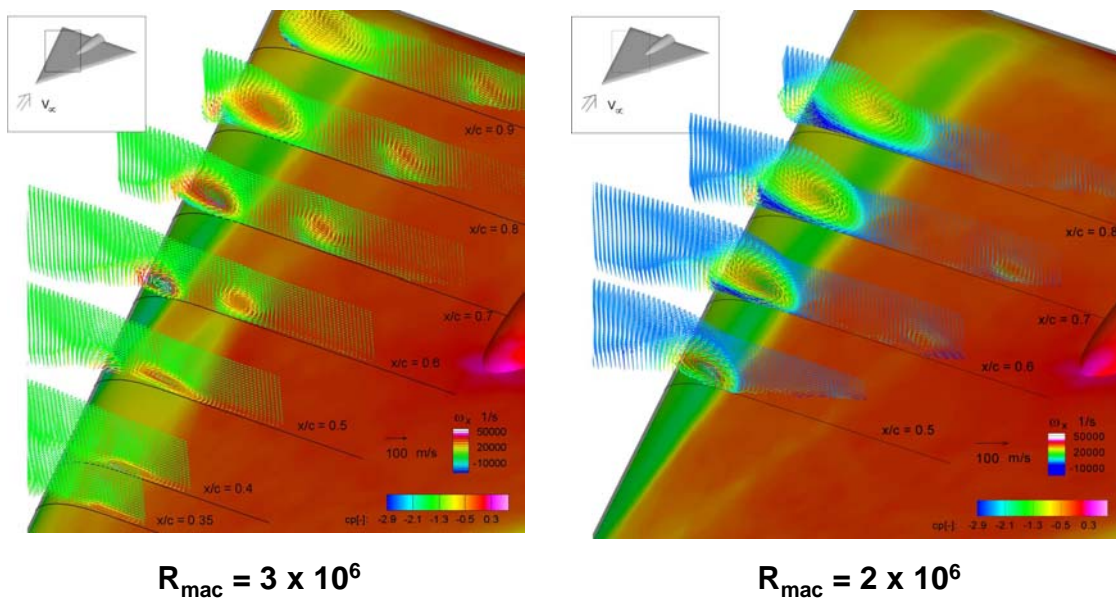
Figure 24-11: Pressure Distributions and Flow Fields on the VFE-2 Configuration with Rounded Leading Edges (Medium Radius) for M = 0.4, α = 13° at Different Reynolds Numbers from the PSP and PIV Experiments at DLR Goettingen [24-19].

A reduction in Reynolds number has an analogous effect as an increase of the angle of attack according to Figure 24-9, but nevertheless the reasons for this upstream movement of the onset of the outer primary vortex are different for both cases. With increasing angle of attack the adverse pressure gradients on the upper surface of the wing increase as well, and this leads to the upstream movement of the onset of the outer primary vortex. If the angle of attack is unchanged, however, the adverse pressure gradients remain at the same level, but with decreasing Reynolds number the viscous flow is no longer able to stay attached, and this leads again to an upstream movement of the onset of the outer primary vortex.

This effect of Reynolds number has also been demonstrated with surface oilflow patterns. Figure 24-12 shows this effect for results obtained in the Argyll wind tunnel at Glasgow University [24-12] for Reynolds numbers of 2 million and 1 million at low speeds (M = 0.12, 0.06). At these relatively low Reynolds numbers it can certainly be postulated that laminar separation and transitional flow physics are affecting the flow in the vicinity of the wing apex with subsequent downstream consequences.
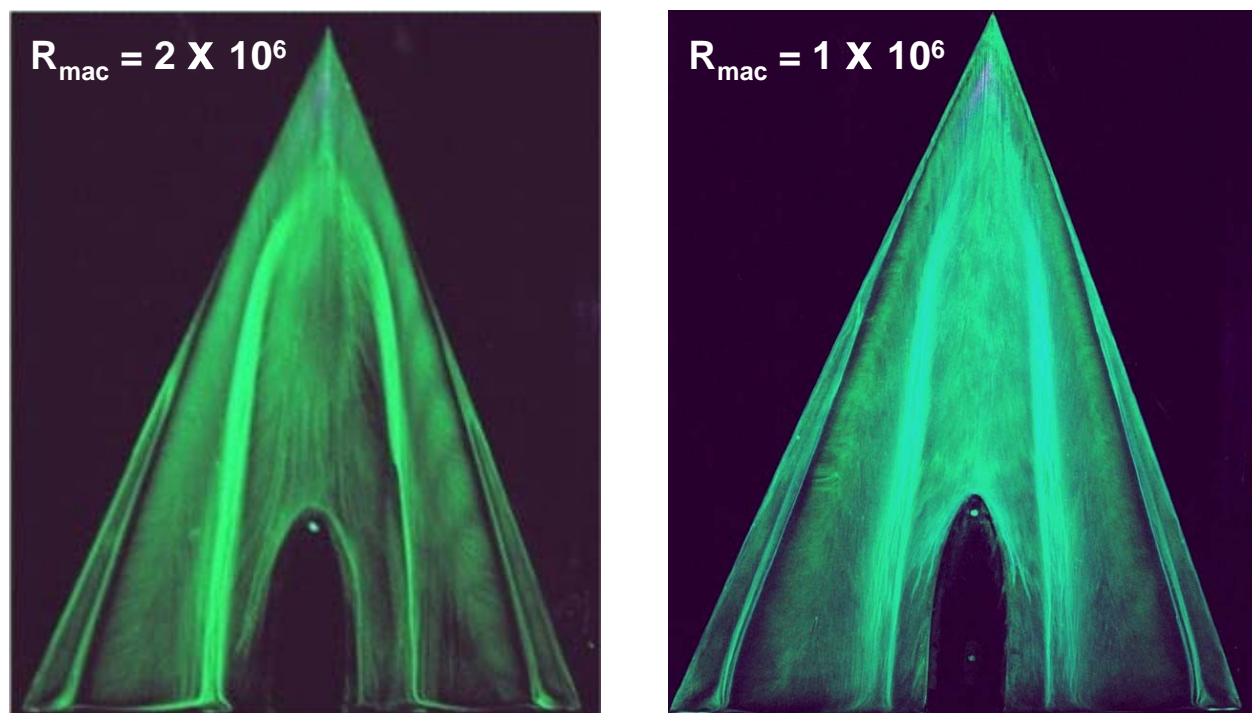
Figure 24-12: Comparison of Oil Flow Patterns for the Round Edged Configuration at α = 13.3° from the Low-Speed Measurements at Glasgow University [24-12].

The topology of the flow field can also be assessed by means of surface oilflow patterns. Figure 24-13 shows surface streamlines for $\alpha = 13°$ and $R_{mac} = 2 \times 10^6$ from TU Munich [24-23],[24-24]. The two primary vortices are clearly indicated and their positions coincide nicely with the result according to Figure 24-10. For low Reynolds numbers the inner primary vortex is found in a more inboard position as compared with higher Reynolds numbers. There is an excellent agreement between the oilflow patterns at $R_{mac} = 2 \times 10^6$ from TU Munich (Figure 24-13) and Glasgow University (Figure 24-12).
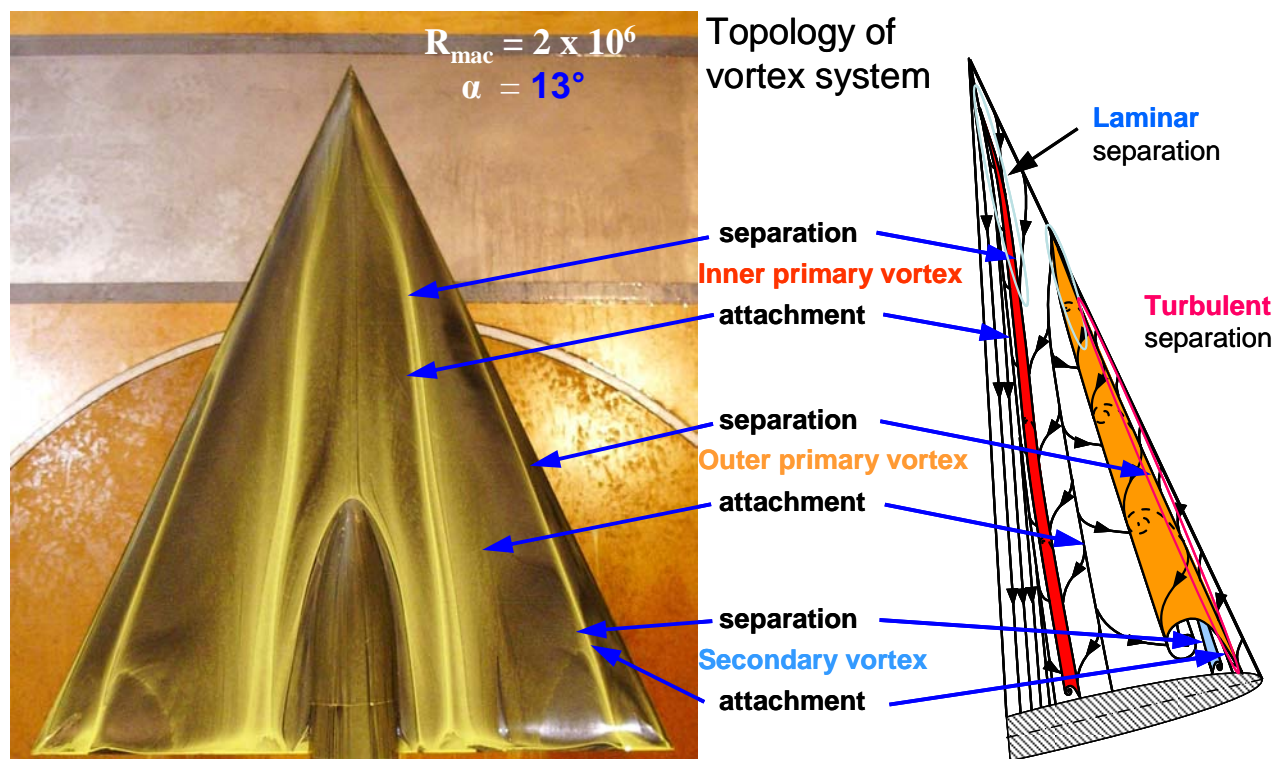
Figure 24-13: Surface Oilflow Patterns and Flow Topology for the VFE-2 Configuration with Rounded Leading Edges (Medium Radius) for M = 0.14, R_{mac} = 2 x 10^6, α = 13° from the Measurements at TU Munich [24-23],[24-24].

24.5.4 Variation of Mach Number

In contrasting a subsonic and a transonic Mach number condition, the principal vortex topology remains unchanged, but some compressibility effects can be recognized. In transonic flow the formation of the outer primary vortex starts earlier [24-15]. Figure 24-14 shows the pressure distributions at α = 13° and R_{mac} = 2 x 10^6 for two different Mach numbers. At the higher Mach number the onset of the outer primary vortex has moved slightly upstream and its axis is distinctly shifted inboard. For M = 0.8 an inner primary vortex was no longer found. If it exists at all in transonic flow, this vortex must be very weak. The corresponding effect of Mach number on the flow field is further illustrated in Figure 24-15. The outer primary vortex is shifted inboard and its flow field is enlarged.
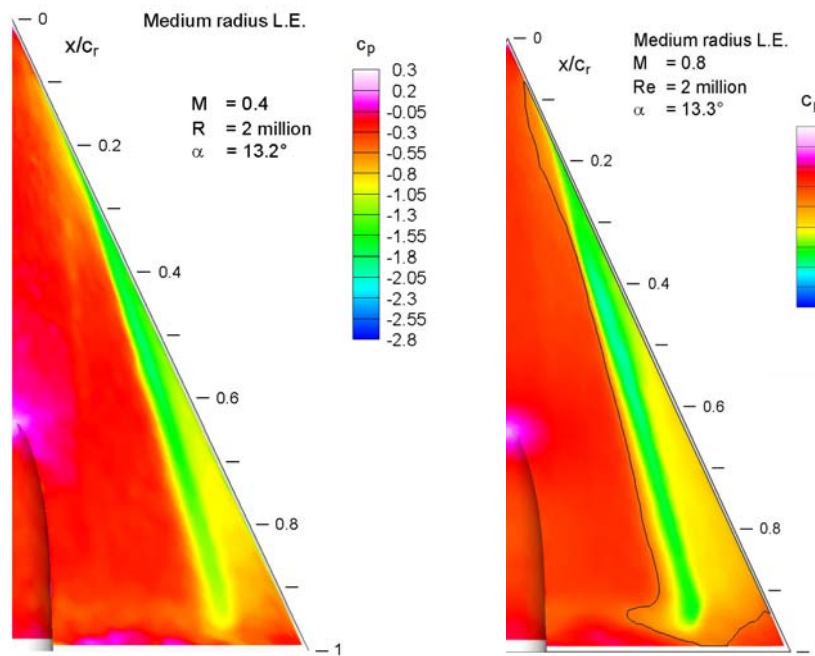
Figure 24-14: Pressure Distributions on the VFE-2 Configuration with Rounded Leading Edges (Medium Radius) at $R_{mac} = 2 \times 10^6$ and $\alpha = 13°$ for Different Mach Numbers from the PSP Experiments at DLR Goettingen [24-15]. The black line indicates the sonic pressure coefficient.
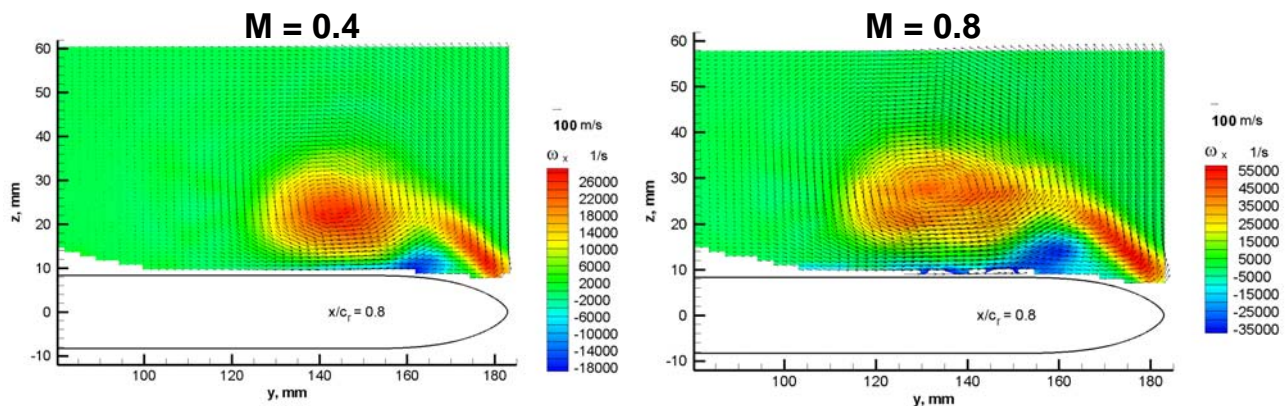
Figure 24-15: Flow Field on the VFE-2 Configuration with Rounded Leading Edges (Medium Radius) at $R_{mac} = 2 \times 10^6$ and $\alpha = 13°$ for Different Mach Numbers from the PIV Experiments at DLR Goettingen [24-18]. Velocity vectors and axial vorticity in the cross section at x/c = 0.8.

24.5.5   Status of the Boundary Layers at $\alpha = 13°$

The 3D vortical flow field has been analyzed by means of hot-wire measurements, in which large portions of the boundary layers were covered. A typical result for incompressible free stream conditions (M = 0.07, $R_{mac} = 1 \times 10^6$) is shown in Figure 24-16. The inner measurement station at $\eta = 2y/b_{loc} = 0.4$ is located inboard

of the outer primary vortex attachment line according to Figure 24-13 and it is thus related to the inner primary vortex.
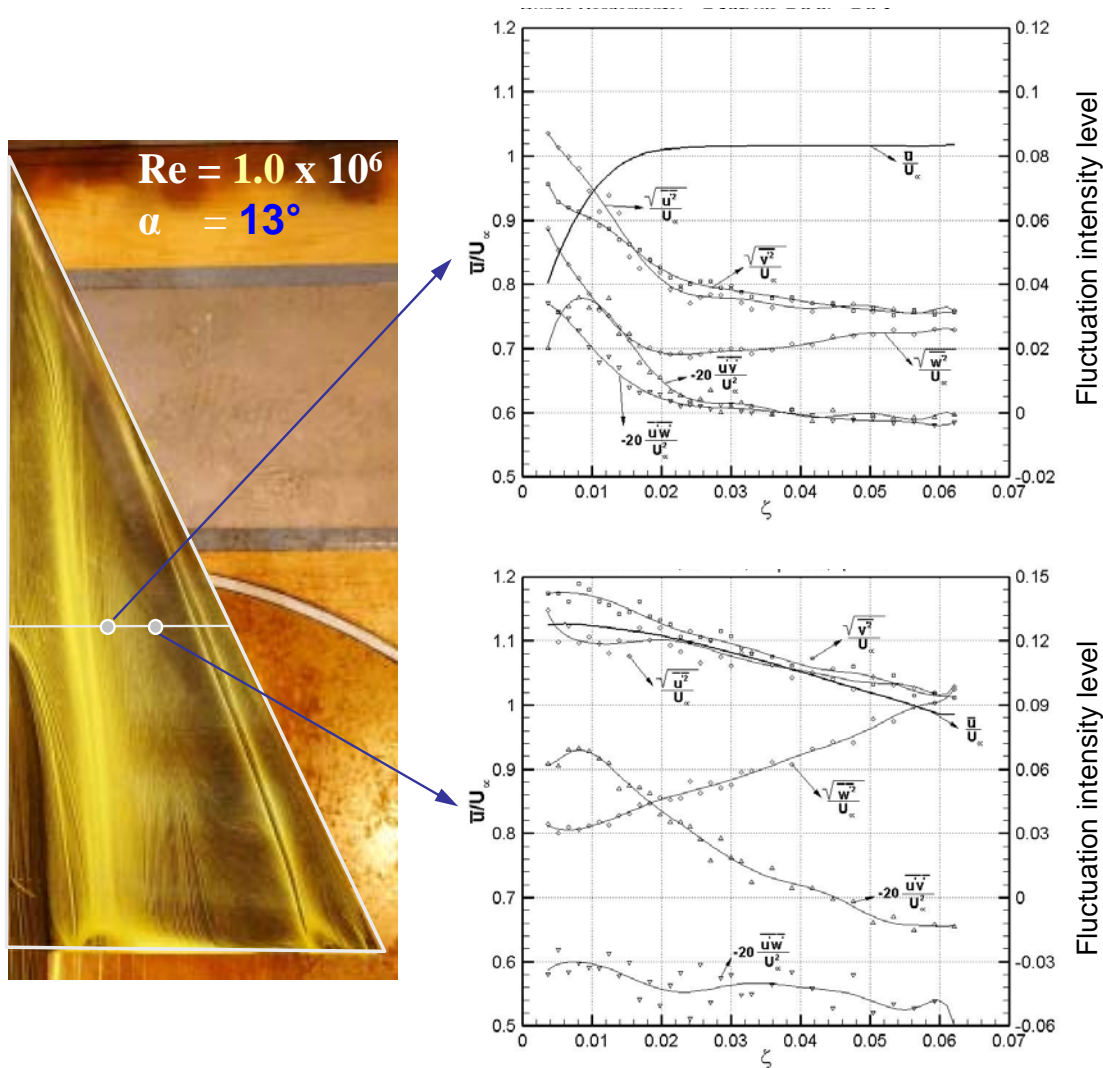
Figure 24-16: Results of Boundary Layer Measurements on the VFE-2 Configuration with Rounded Leading Edges (Medium Radius) for M = 0.07, R_{mac} = 1 x 10^6 and α = 13° at Two Stations (top η = 0.4, bottom η = 0.6) in the Section x/c_r = 0.6 from the Hot-Wire Anemometry at TU Munich [24-11].

At this station the boundary layer is very thick ($\zeta = 2z/b_{loc} = 0.025$) as indicated by the time-averaged longitudinal velocity component $\overline{u}/U_\infty$. Outside of the boundary layer the fluctuations of almost all velocity components increase towards the wing surface with the only exception of a slight decrease in $\sqrt{(w')^2}/U_\infty$, and within the boundary layer all fluctuations increase rapidly towards the wall.

The same applies for the outer measurement station at $\eta = 2y/b_{loc} = 0.6$, but the boundary layer is much thinner there ($\zeta = 2z/b_{loc} = 0.008$). The outer measurement station is located outboard of the outer primary vortex

attachment line. Thus an accelerated outboard flow underneath the outer primary vortex is present, which leads to the strong decrease of the boundary layer thickness. Simultaneously measured pressure fluctuations on the wing surface according to Figure 24-17 indicate, that the flow in the region of the outer primary vortex is distinctly turbulent. At the inner measurement station, however, the boundary layer status remains unclear: At the wall almost no pressure fluctuations were found (Figure 24-17), whereas in the boundary layer some fluctuations are present.
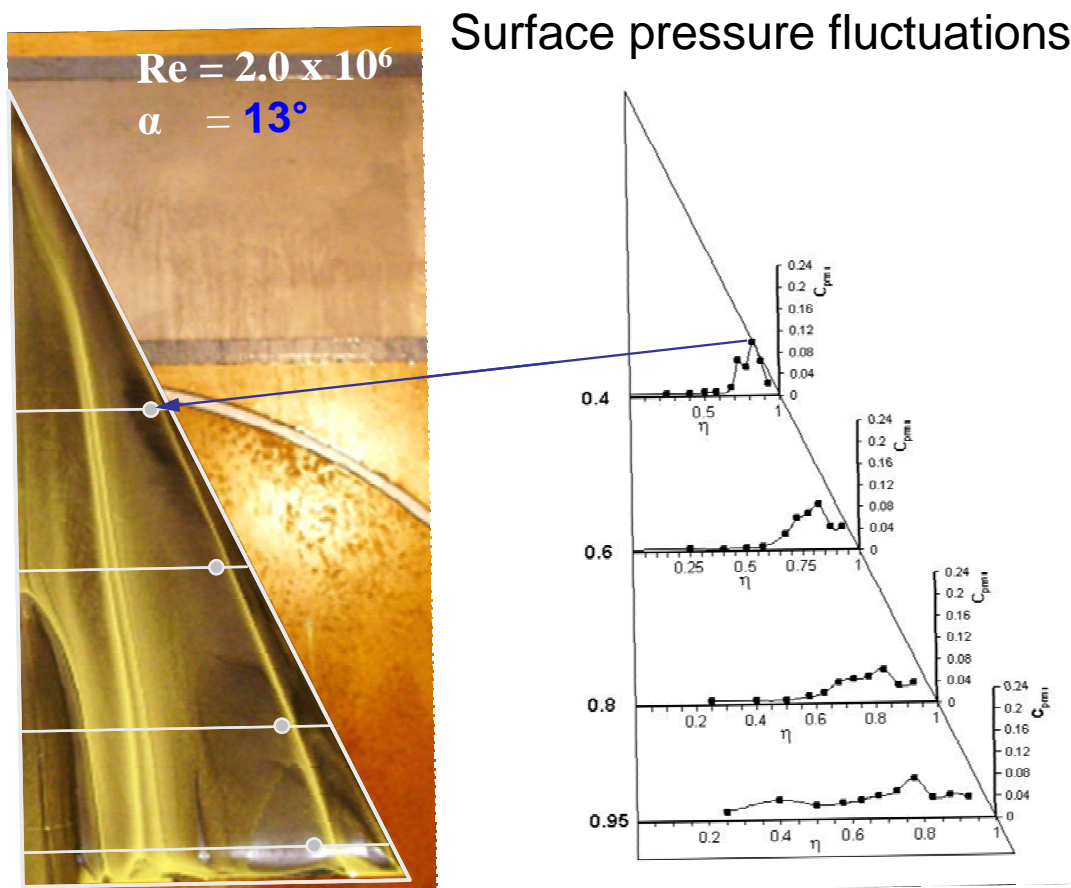
Figure 24-17: Pressure Fluctuations on the VFE-2 Configuration with Rounded Leading Edges (Medium Radius) for M = 0.14, R_{mac} = 2 x 10^6 and α = 13° in Four Sections from the Measurements at TU Munich [24-11].

24.6 FULLY DEVELOPED VORTICAL FLOW WITHOUT VORTEX BREAKDOWN

For the sharp edged configuration a single primary vortex occurs along the whole leading edge from moderate to high angles of attack. For the blunt edged configuration (medium radius) an inner and an outer primary vortex are formed in the same angle of attack range as described in Section 24-5. With increasing angle of attack the outer primary vortex becomes more and more dominant along the whole leading edge, whereas the inner primary vortex is weakened.

At α = 18° in both cases a fully developed vortical flow with a single primary vortex is present according to Figure 24-18. For the rounded leading edge configuration only very weak remnants of an inner primary vortex can be detected for the low Mach number case. The pressure distributions for both Mach numbers indicate that the primary vortex on the configuration with blunt leading edge is located slightly more outboard than for the configuration with sharp leading edge, and some differences concerning the suction magnitude can also be recognized, but the overall behavior of the flow is very similar. Although difficult to see, this is also demonstrated in Figure 24-19 for the two flow fields through PIV results for the time-averaged velocities in various cross sections.
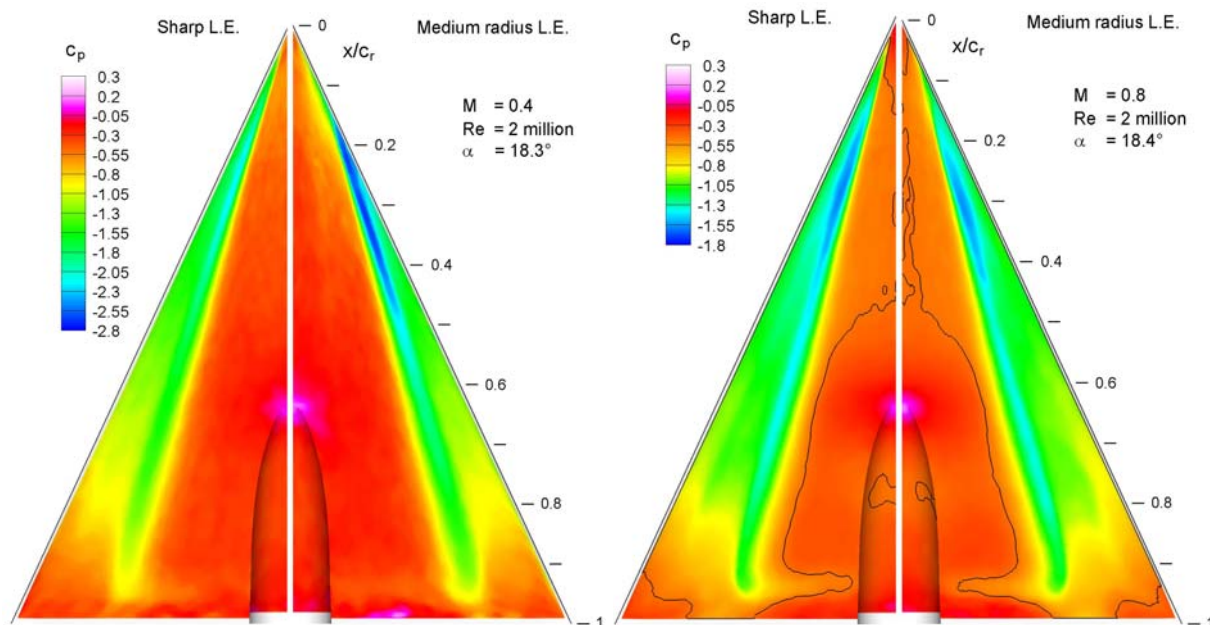
Figure 24-18: Pressure Distributions on the VFE-2 Configuration with Sharp and Rounded Leading Edges (Medium Radius) at R_{mac} = 2 x 10^6 and α = 18° for Two Mach Numbers According to the PSP Experiments at DLR Goettingen [24-15]. The black line indicates the sonic pressure coefficient.

Within VFE-2 the case α = 18° with a well developed single primary vortex will be used to check the various turbulence models for their proper description of vortical flow. For this purpose hot-wire anemometry (HWA) has also been applied at TU Munich. Concerning the time averaged velocity components $\overline{u}, \overline{v}, \overline{w}$ the results according to Figure 24-19 have been confirmed with these measurements. In addition, however, the complete field of the velocity fluctuations u', v', w' is now available. As examples Figure 24-20 shows the measured fluctuations of the velocity component u_{rms}/U_∞ as well as $\overline{u'w'}/U_\infty^2$ in the cross section plane at x/c = 0.6. Again there are only minor differences between the measurements for sharp and for medium radius rounded leading edges, but from the full field of the fluctuations u', v', w' the distributions of the turbulent kinetic energy and the eddy viscosity can be determined. Corresponding evaluations of the experiments are presently under way, and the results will be used for comparisons with numerical simulations of the vortical flow field by means of various turbulence models.

Sharp Leading Edge **Round Leading Edge**
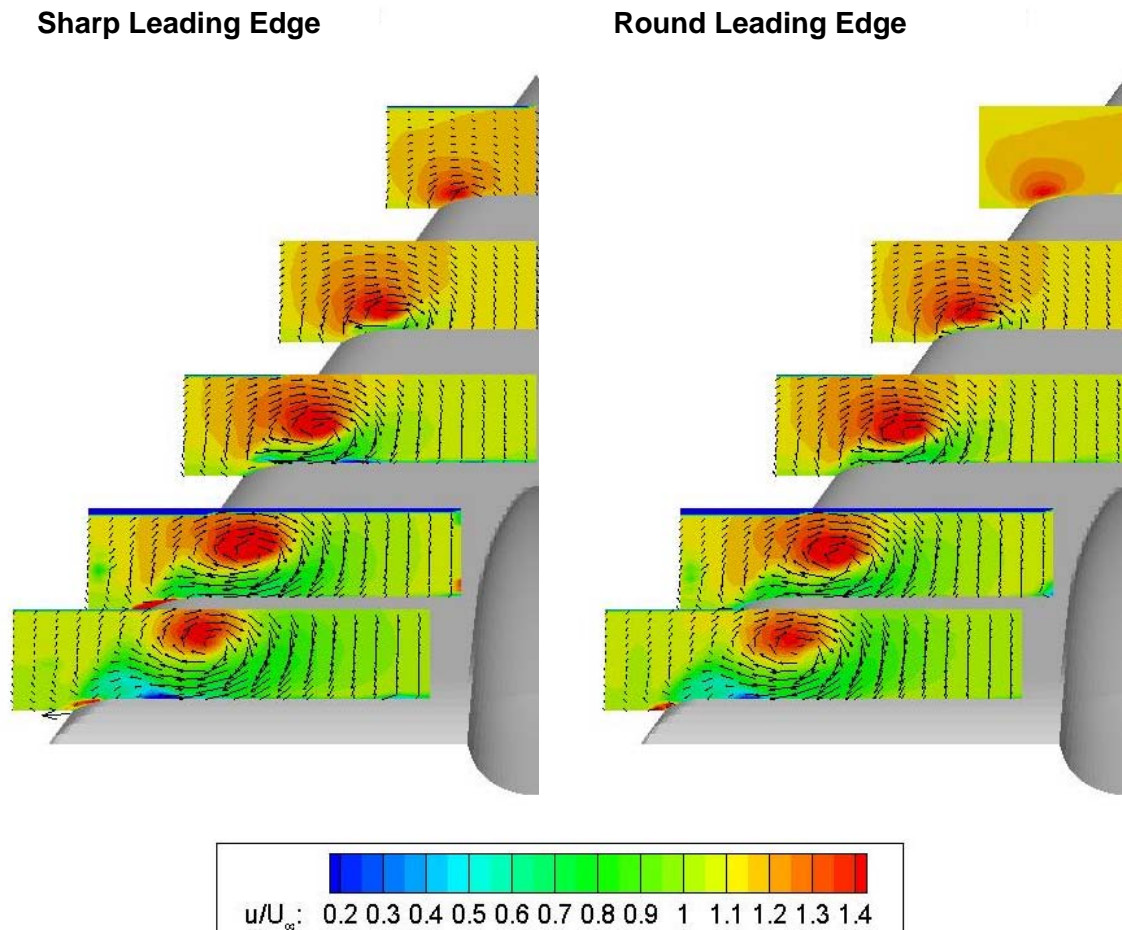
Figure 24-19: Flow Field around the VFE-2 Configuration with Sharp and Rounded Leading Edges (Medium Radius) at M ≈ 0.1, R_{mac} = 1 x 10^6, α = 18° − PIV Results from TU Munich [24-25] for the Time-Averaged Velocity in Various Cross Sections: x/c_r = 0.2, 0.4, 0.6, 0.8, 0.95.
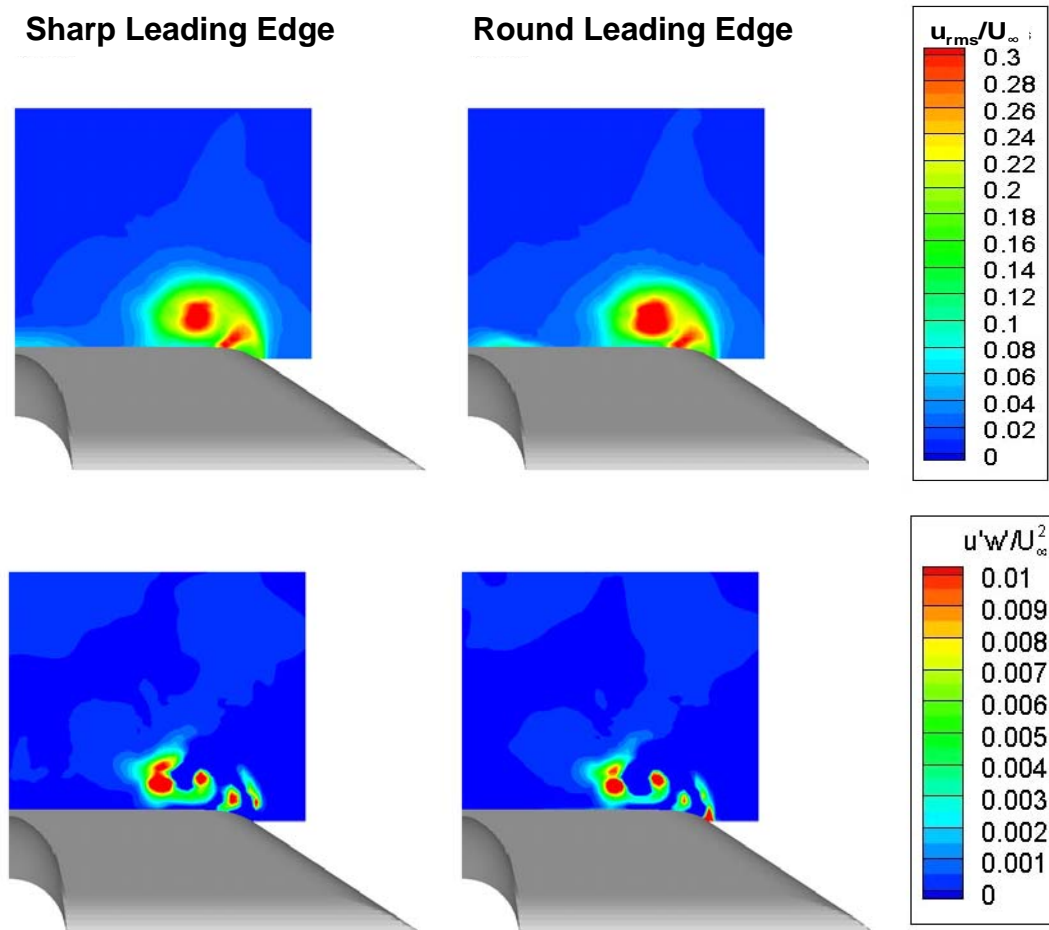
Figure 24-20: Flow Field around the VFE-2 Configuration with Sharp and Rounded Leading Edges (Medium Radius) at M ≈ 0.1, R_{mac} = 1 x 10^6, α = 18° – HWA Results from TU Munich [24-25] for the Velocity Fluctuations u_{rms}/U_∞ (top) and $\overline{u'w'}/U_\infty^2$ (bottom) in the Plane at x/c = 0.6.

The unsteadiness of the flow can also be evaluated from these experiments by determining the power spectrum density distribution of any fluctuating flow quantity as function of the frequency at any measured position of the flow field. An example of this kind is shown in Figure 24-21 for the sharp leading edge configuration. In the left-hand graph the distribution of the fluctuations of the u-component of the velocity u_{rms}/U_∞ shown in Figure 24-20 (upper left) is given. On the right side of Figure 24-21 the power spectrum density distribution for the velocity component u/U_∞ is shown at a location near the vortex core (indicated by the large dot on the left side of Figure 24-21). In this turbulent flow near the vortex centre a large variety of frequencies is present with distinctly high values at low frequencies.
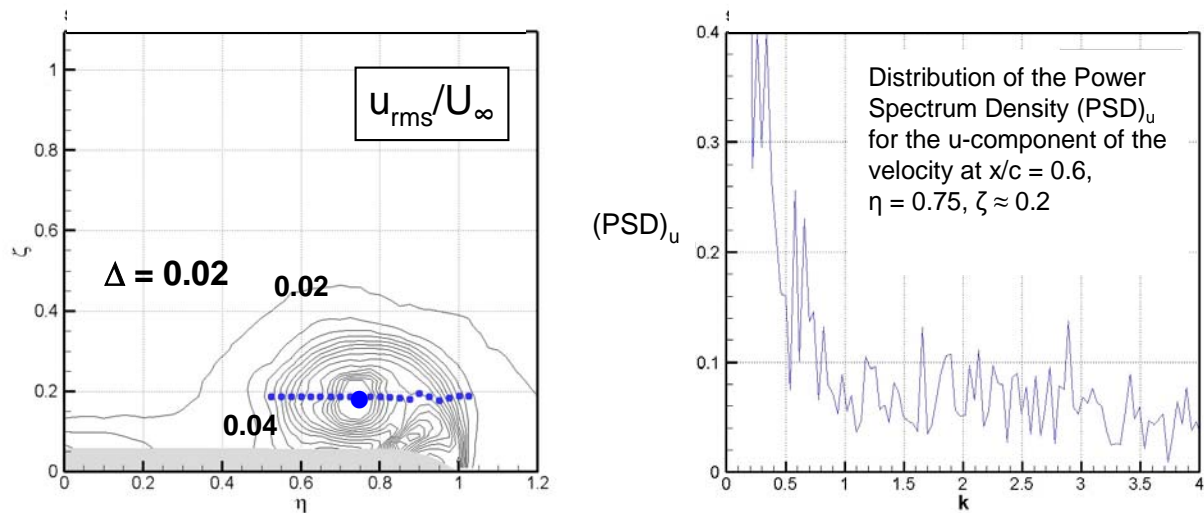
Figure 24-21: Flow Field around the VFE-2 Configuration (65° Delta Wing) with Sharp Leading Edges at M ≈ 0.1, R_{mac} = 1 x 10^6, α = 18°. Power spectrum density (PSD)$_u$ for the u-component of the velocity as function of the reduced frequency k at x/c = 0.6, η = 0.75, ζ ≈ 0.2 according to HWA at TU Munich [24-25]. Δ denotes contour interval.

Flow unsteadiness has also been assessed in terms of normal force with recent measurements from Glasgow University [24-12]. Although the results must still be considered preliminary, an example from these measurements is shown in Figure 24-22 for both the sharp and blunt edge wings at a Reynolds number of 2 million at an angle of attack of 18.5°. At this condition there is very little effect of bluntness in terms of the overall normal force coefficient spectra. For both geometries at this angle of attack, the leading-edge vortices are fully developed over the wing, and it is not anticipated that vortex breakdown has yet occurred over the wing. According to Mabey [24-26], a modified reduced frequency, $k^* = (f\ c_R\ /\ U_\infty) \sin \alpha$, would be constant for these two wings as regards the dominant frequency in their power spectra. For a 65° delta wing, this parameter would have a value of approximately 0.58. This value corresponds almost exactly to the dominant frequency from the Glasgow measurements shown in Figure 24-22.
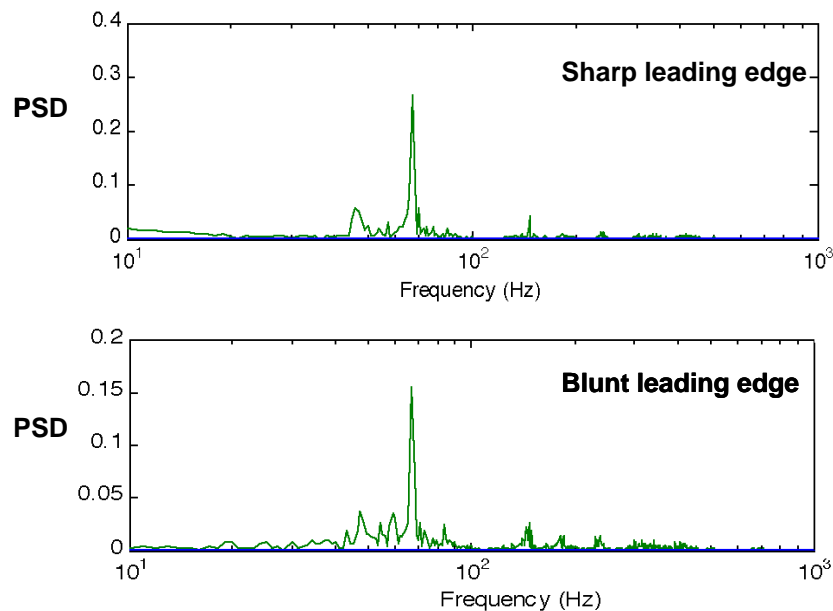
Figure 24-22: Normal Force Power Spectrum for Sharp and Blunt Edged Wings,
$R_{mac} = 2 \times 10^6$, α = 18.5° from the Low-Speed Measurements at Glasgow University [24-12].

24.7   FULLY DEVELOPED VORTICAL FLOW WITH VORTEX BREAKDOWN

At large angles of attack vortex breakdown takes place in the primary vortices. Today it is common understanding that the flow past slender delta wings at large angles of attack becomes unsteady even for a fixed wing. This means that for large angles of attack and steady boundary conditions only unsteady solutions of the governing equations do exist. The spiral-type vortex breakdown is well predicted by numerical solutions of the Navier-Stokes equations [24-27],[24-28]. The instantaneous vortex axis spirals in space against the sense of rotation of the primary vortex and this spiral rotates in the sense of the primary vortex, and in the center of the spiraling motion a region of reversed flow is present. Correspondingly all quantities of the flow field show oscillations and on the surface of the wing an unsteady pressure distribution is present.

The unsteadiness due to vortex breakdown starts in a region with steep pressure gradients in streamwise direction, and this region is usually located in the vicinity of the trailing edge of the wing. As angle of attack is increased the extent of unsteady vortical flow increases in size and the vortex breakdown onset point moves upstream. In the rear part of the wing, which is directly influenced by the unsteadiness of the flow in the primary vortices, the time-averaged pressure distributions generally show distinct reductions of suction, and this leads to a certain loss of lift.

For the VFE-2 configuration vortex breakdown in the primary vortex has already progressed over the wing at α = 23° for sharp and for medium radius rounded leading edges. For both configurations the unsteady vortical flow field has been measured at TU Munich by means of unsteady surface pressure measurements and by PIV and HWA investigations. For the configuration with medium radius rounded leading edges Figure 24-23 shows the surface pressure fluctuations $(C_p)_{rms}$ at four cross sections of the wing, and for a certain station in each of these distributions the amplitude spectrum density $(SD)_{cp}$ of the pressure fluctuations is given. The high values of the fluctuations around the reduced frequency k ≈ 1.3 in the last section are caused by the spiral motion of vortex breakdown.
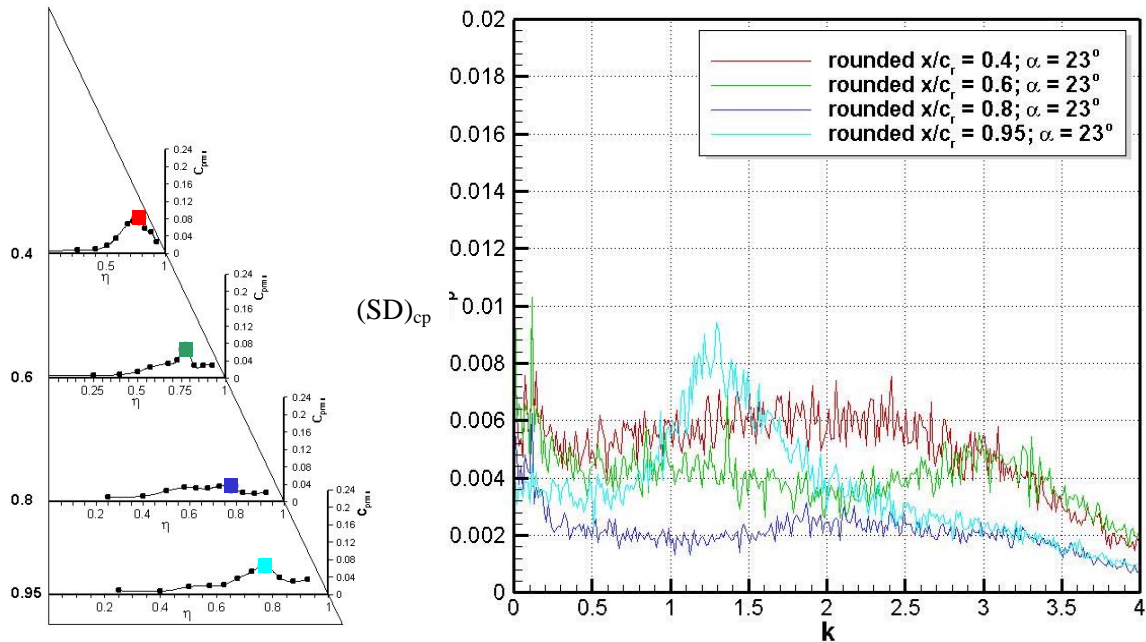
Figure 24-23: Flow Field around the VFE-2 Configuration with Medium Radius Rounded Leading Edges at M = 0.14, R_{mac} = 2 x 10^6, α = 23°. Surface pressure fluctuations (C$_p$)$_{rms}$ and spectrum density (SD)$_{cp}$ for certain stations in four cross sections according to measurements at TU Munich [24-25].

In these cross sections the time-averaged flow field has been measured at TU Munich by means of PIV investigations and the complete unsteady flow field has been determined using the HWA technique. For the configuration with medium radius rounded leading edge Figure 24-24 shows the unsteadiness of the flow field with vortex breakdown in the cross section at x/c = 0.8. The annular form of the area with high fluctuations is typical for the spiral mode of vortex breakdown. Further analysis according to Figure 24-23 and Figure 24-24 will lead to experimental data for the frequency of the spiral mode of vortex breakdown. Evaluations of this kind are presently under way and comparisons with numerical results are prepared.
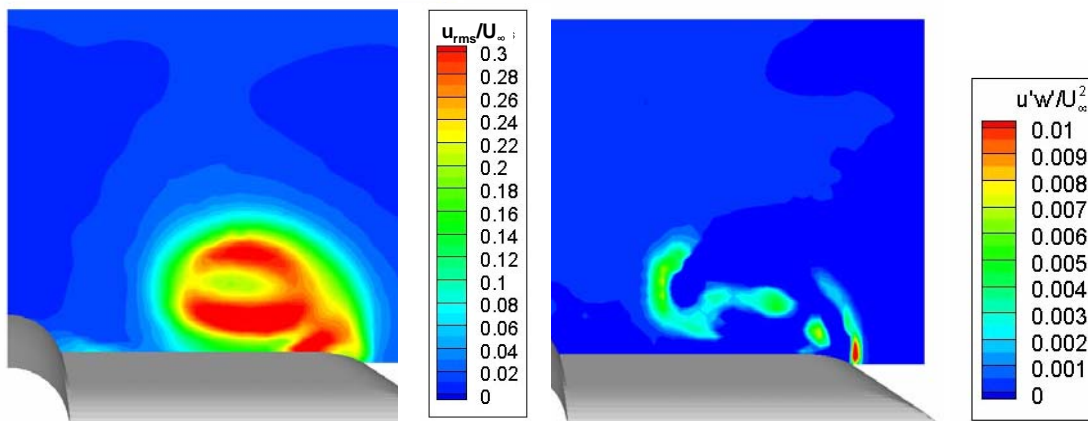
Figure 24-24: Flow Field around the VFE-2 Configuration with Medium Radius Rounded Leading Edges at M ≈ 0.1, R_{mac} = 1 x 10^6, α = 23°. HWA results from TU Munich [24-25] for the velocity fluctuations u_{rms}/U_∞ and $\overline{u'w'}/U_\infty^2$ in the cross section at x/c = 0.8.

Figure 24-25 shows PSP measured pressure distributions for sharp and (medium radius) rounded leading edges at α = 25° and R_{mac} = 2 x 10^6. For both Mach numbers there exist moderate differences between the results for sharp and blunt leading edges. At the lower Mach number M = 0.4 (left-hand part) no supersonic zones and no shock waves exist for an angle of attack of α = 25°. At this angle of attack vortex breakdown would certainly be ahead of x/c = 0.8, given the results just discussed with Figure 24-23 and Figure 24-24, although the precise breakdown location is in general difficult to discern from subcritical surface pressure information.
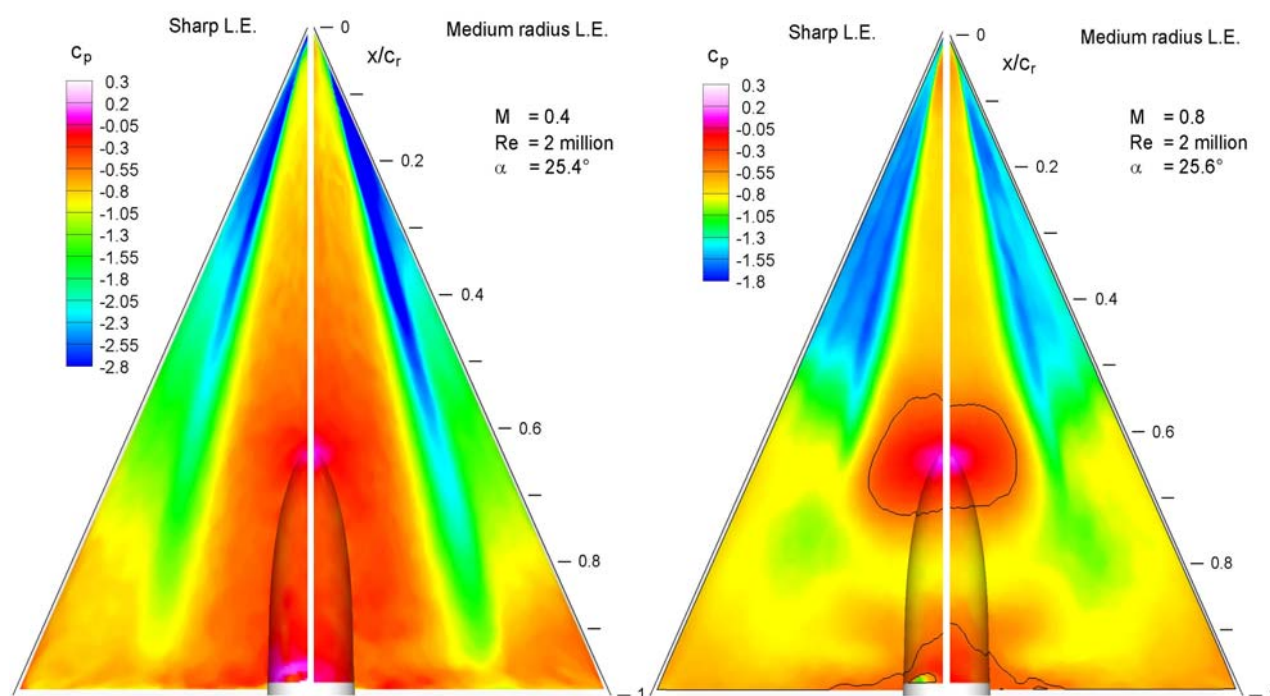
Figure 24-25: Pressure Distributions on the VFE-2 Configuration with Sharp and Rounded Leading Edges (Medium Radius) at $R_{mac} = 2 \times 10^6$ and $\alpha = 25°$ for Different Mach Numbers According to the PSP Experiments at DLR Goettingen [24-15]. The black line indicates the sonic pressure coefficient.

At constant angle of attack and with the increase to a transonic Mach number, however, a distinct change of the pressure distribution on the wing can be taken from the results for M = 0.8 (right-hand part). At this transonic Mach number a local supersonic zone with a terminating shock wave is formed in the vicinity of the sting mount. The adverse pressure jump in the shock wave causes additional unsteadiness in the vortical flow field, and most likely shifts vortex breakdown upstream.

24.8   CONCLUDING REMARKS

At the onset of Vortex Flow Experiment 2 an initial data base had been established by NASA to examine the effects of Mach number, Reynolds number, angle of attack, and leading-edge bluntness on separation-induced leading-edge vortex flows common to slender wings. The data spanned a wide range of Mach and Reynolds numbers in such a way to isolate Mach and Reynolds number effects for four different leading-edge bluntness values. Measurements were limited to fairly detailed static surface pressure coefficients as well as to the normal force and pitching moment coefficients. These experiments demonstrated significant effects of the parameters studied and also indicated a multiple-vortex characteristic of the leading-edge vortex separation from the blunt leading edge different from that observed with sharp leading edges.

As a result of VFE-2 significant details of this flow have now been measured. This was accomplished through 15 new wind tunnel experiments coordinated among four countries. A focus was established on two of the leading edges (sharp and medium bluntness) from the NASA experiments, and four new wind tunnel models were fabricated to support the new testing. Surface and off-body measurements, for both steady and fluctuating

quantities, have been accumulated using a wide variety of test techniques as well as six-component forces and moments.

The experimental campaigns confirm the multiple-vortex structure of blunt leading edge vortex separation and considerably more detail of this flow is now available through the use of pressure sensitive paints. Detailed flow field measurements provide new insight into this vortical structure, and surface and off-body fluctuating measurements show the turbulent structure of these flows. Surface transition measurements have been very difficult to accomplish, and to date the evaluation of these measurements is not finished. The state of transition still needs to be documented for these flows. The data from VFE 2 present a significant opportunity for further experimental analysis as well as comparison with computational fluid dynamics.

24.9 ACKNOWLEDGEMENTS

24.10 REFERENCES

[24-1] Chu, J. and Luckring, J.M.: *Experimental Surface Pressure Data Obtained on 65° Delta Wing Across Reynolds Number and Mach Number Ranges*, NASA TM 4645, 1996.

[24-2] Luckring, J.M.: *Reynolds Number and Leading-Edge Bluntness Effects on a 65° Delta Wing*, AIAA Paper 2002-0419, 2002.

[24-3] Luckring, J.M.: *Transonic Reynolds Number and Leading-Edge Bluntness Effects on a 65° Delta Wing*, AIAA Paper 2003-0753, 2003.

[24-4] Luckring, J.M.: *Compressibility and Leading-Edge Bluntness Effects for a 65° Delta Wing*, AIAA Paper 2004-0765, 2004.

[24-5] Luckring, J.M.: *Reynolds Number, Compressibility, and Leading-Edge Bluntness Effects on Delta-Wing Aerodynamics*, ICAS Proceedings Yokohama 2004, Paper 4.1.4, 2004.

[24-6] Hummel, D. and Redeker, G.: *A New Vortex Flow Experiment for Computer Code Validation*, RTO AVT Symposium on "Vortex Flow and High Angle of Attack Aerodynamics", Loen, Norway, 7-11 May 2001, Meeting Proceedings RTO-MP-069 (I), SYA 8-1 to 8-31, 2003.

[24-7] Hummel, D.: *Review of the Second International Vortex Flow Experiment (VFE-2)*, AIAA Paper 2008-0377, 2008.

[24-8] Luckring, J.M.: *Initial Experiments and Analysis of Vortex Flow on Blunt Edged Delta Wings*, AIAA Paper 2008-0378, 2008.

[24-9]   Konrath, R., Klein, Ch. and Schröder, A.: *PSP and PIV Investigations on the VFE-2 Configuration in Sub- and Transonic Flow*, AIAA Paper 2008-0379, 2008.

[24-10] Le Roy, J.F., Rodriguez, O. and Kurun, S.: *Experimental and CFD Contribution to Delta Wing Vortical Flow Understanding*, AIAA Paper 2008-0380, 2008.

[24-11] Furman, A. and Breitsamter, Ch.: *Turbulent and Unsteady Flow Characteristics of Delta Wing Vortex Systems*, AIAA Paper 2008-0381, 2008.

[24-12] Coton, F., Mat, S. and Galbraith, R.: *Low Speed Wind Tunnel Characterization of the VFE-2 Wing*, AIAA Paper 2008-0382, 2008.

[24-13] Hummel, D.: *Effects of Boundary Layer Formation on the Vortical Flow Above Slender Delta Wings*, RTO AVT Symposium on "Enhancement of NATO Military Flight Vehicle Performance by Management of Interacting Boundary Layer Transition and Separation", Prague, Czech Republic, 4-8 October 2004, Meeting Proceedings RTO-MP-AVT-111, 30-1 to 30-22, 2004.

[24-14] Klein, C., Sachs, W., Henne, U., Engler, R.H., Wiedemann, A. and Konrath, R.: *Development of PSP Technique for Application on the VFE-2 65° Delta Wing Configuration in Sub- and Transonic Flow*, AIAA Paper 2006-0059, 2006.

[24-15] Konrath, R., Klein, C., Engler, R.H. and Otter, D.: *Analysis of PSP Results Obtained for the VFE-2 65° Delta Wing Configuration at Subsonic and Transonic Speed*, AIAA Paper 2006-0060, 2006.

[24-16] Fritz, W.: *Numerical Simulation of the Peculiar Subsonic Flow Field about the VFE-2 Delta Wing with Rounded Leading Edge*, AIAA Paper 2008-0393, 2008.

[24-17] Schröder, A., Agocs, J., Frahnert, H., Otter, D., Mattner, H., Kompenhans, J. and Konrath, R.: *Application of Stereo-PIV to the VFE-2 65° Delta Wing Configuration at Sub- and Transonic Speeds*, AIAA Paper 2006-3486, 2006.

[24-18] Konrath, R., Schröder, A. and Kompenhans, J.: *Analysis of PIV Results Obtained for the VFE-2 65° Delta Wing Configuration at Sub- and Transonic Speeds*, AIAA Paper 2006-3003, 2006.

[24-19] Konrath, R., Klein, Ch., Schröder, A. and Kompenhans, J.: *Combined Application of Pressure Sensitive Paint and Particle Image Velocimetry to the Flow Above a Delta Wing*, 12th International Symposium on "Flow Visualization", September 10-14, 2006, DLR Goettingen, Germany, In Grant, I. [Ed.]: CD Rom Proceedings (ISFV12-67.2), Optimage Ltd., Edinburgh, UK, pp. 1-14.

[24-20] Sheplak, M.: *The Year in Review: Aerodynamic Measurement Technology*, Aerospace America, December 2006, p. 22.

[24-21] Hummel, D.: *The Second International Vortex Flow Experiment (VFE-2): Objectives and First Results*, 2nd International Symposium on "Integrating CFD and Experiments in Aerodynamics", 5-6 September 2005, Cranfield University, UK, J. Aerospace Engineering, Vol. 220, 2006, No. 6, pp. 559-568.

[24-22] Hummel, D.: *The Second International Vortex Flow Experiment (VFE-2) – Objectives and Present Status*, AIAA Paper 2007-4446,2007.

[24-23] Furman, A. and Breitsamter, Ch.: *Delta Wing Steady Pressure Investigations for Sharp and Rounded Leading Edges*, In: Rath, H.-J., Holze, C., Heinemann, H.-J., Henke, R. and Hönlinger, H. (Eds), "New Results in Numerical and Experimental Fluid Mechanics V", 2004, Vol. 92 of "Notes on Numerical Fluid Mechanics and Multidisciplinary Design", pp. 77-84.

[24-24] Furman, A. and Breitsamter, Ch.: *Investigations of Flow Phenomena on Generic Delta Wing*, ICAS Proceedings Hamburg 2006, Paper 3.1.2 (2006).

[24-25] Furman, A. and Breitsamter, Ch.: *Stereo-PIV and Hot-Wire Investigations on Delta Wing with Sharp and Rounded Leading Edge*, 1st CEAS Conference Berlin 2007, Paper 2007-430, 2007.

[24-26] Mabey, D.G.: *Unsteady Vortex Flow Phenomena on Delta Wings at High Angles of Attack*, ICAS Proceedings Sorrento 1996, pp. 1167-1176.

[24-27] Visbal, M.R.: *Computed Unsteady Structure of Spiral Vortex Breakdown on Delta Wings*, AIAA Paper 96-2074, 1996.

[24-28] Müller, J. and Hummel, D.: *Numerical Analysis of the Unsteady Flow Above a Slender Delta Wing at Large Angles of Attack*, ICAS Proceedings Harrogate 2000, Paper ICA0252, 2000.

Chapter 25 – NUMERICAL SOLUTIONS FOR THE VFE-2 CONFIGURATION ON STRUCTURED GRIDS AT EADS-MAS, GERMANY

by

Willy Fritz

The Second International Vortex Flow Experiment provided a variety of experimental data for a 65-degree swept delta wing sharp and blunt leading edges. Flow details including forces and moments, surface pressures, Pressure Sensitive Paint measurements, and off-surface flow variables from Particle Image Velocimetry were made available for comparisons with computational simulations. This chapter concentrates on some typical problems of delta wings with rounded leading edges at subsonic speed: the prediction of the main leading edge separation, the generation of the second inner vortex, the effect of transition, and Reynolds number effects.

25.1   NOMENCLATURE

b	=	wing span
CFD	=	Computational Fluid Dynamics
c_r	=	root chord (also c)
d	=	sting diameter
M	=	Mach number, $\equiv V / a$
MRLE	=	Medium Range Leading Edge Radius
p	=	pressure
PSP	=	Pressure Sensitive Paint
Re	=	Reynolds number based on mean aerodynamic chord, $\equiv V_\infty c_{mac} / \upsilon$
r_{le}	=	leading edge radius
S	=	wing plan form area
t	=	wing maximum thickness
x	=	longitudinal dimension ($x = 0$ at apex of wing)
x_v	=	position of vortex origin
α	=	angle of attack, deg
η	=	normalized local half span of the wing $\equiv 2y/b$
∞	=	free stream condition

25.2   ORGANIZATIONS

DLR	=	German Aerospace Center / Germany
EADS	=	European Aeronautic Defence and Space Company / Germany
NASA	=	National Aeronautics and Space Administration / United States
TUM	=	Technical University of Munich /Germany

25.3   INTRODUCTION

The First International Vortex Flow Experiment [25-1] (VFE-1) has focused on a 65° swept delta wing with a sharp leading edge. This configuration generates the "classical" vortical flow field consisting of a dominating primary vortex, a weaker secondary vortex, and sometimes even of a tertiary separation. Since the mid 1980s delta wing flow fields are simulated using Reynolds-Averaged Navier-Stokes (RANS) methods, first with algebraic turbulence models, later with 1- and 2-equation turbulence models (see Ref. [25-2] for example). In recent time hybrid turbulence models have also been applied to the flow around delta wings with good success [25-3]. Together with carefully generated grids, RANS methods are able to predict the flow features over a wide range very well. Two problem areas are however remaining: vortex break down, and the region of the secondary vortex. Vortex break down is predicted very often at earlier angels of attack as in the experiment, and in the region of the secondary vortex there are often problems in predicting the correct strength and location of this secondary vortex. Both problems are commonly related to still existing defects of the actual turbulence models. But such defects are only concluded from the disagreement of the surface pressure data. Detailed volume data like velocity vectors, and velocity fluctuations in special cross sections, which would allow a better assessment of the turbulence model, are still rarely.

To provide the computational community with such field data was one important motivation for the Second Vortex FLOW Experiment (VFE-2), as it was suggested by Hummel [25-4] 2001 in Loen. Another motivation was to provide improved experimental data also for delta wings with rounded leading edges. With this background, the VFE-2 was embedded into the RTO task group AVT-113 under the facet VFE-2.

Before the beginning of VFE-2 experimental results from the NASA Langley Research Center on a 65° swept delta wing were already available (Ref. [25-6] and Chapter 18).. For one sharp and three rounded leading edges normal force and pitching moment as well as pressure distribution measurements had been carried out for a large variety of Mach numbers and Reynolds numbers. The results of these measurements have been analyzed and summarized in Refs. [25-7] through [25-10]. This data base has been used at EADS for an assessment of different turbulence models in a very early phase of the VFE-2, as new experimental results were not yet available. Especially the effect of the Reynolds number (Re = 6 Mio and Re = 60 Mio) on a delta wing with a more realistic round leading edge was of interest. At the end of these validation calculations first results of new VFE-2 measurements were available ([25-5] and Chapter 19). The PSP measurements at DLR have shown very clearly the footprint of a second primary vortex for the round leading edge test case 11. The origin of this second primary vortex was not clear from the PSP results, but in [25-12] there is already given a first numerical visualization of this second vortex by Chiba and Obayashi.

So at EADS the simulation of this second primary vortex was also considered as a special assessment of the quality of the CFD tools, and some additional work towards the simulation of this peculiar flow field was done. These investigations have been concentrated on the test cases listed in Table 25-1.

Table 25-1: CFD Test Cases Used in the Present Calculations

Case No.	Leading Edge	Mach No., M_∞	Angle of Attack, α (deg)	Reynolds Number, Re
4.5	MRLE	0.4	13	3×10^6
5	MRLE	0.4	13	6×10^6
14	MRLE	0.4	18	6×10^6

A complete listing of all 28 CFD test cases of VFE-2 is given in Ref. [25-25] and in Chapter 34. Test case 5 was used for a study of the effects of small and large variations of the Reynolds number, and of the effect of transition. The test cases 4.5 and 14 were used for a numerical analysis of the peculiar flow field of the delta wing with rounded leading edge.

25.4   GEOMETRY AND COMPUTATIONAL GRIDS

The geometry for the VFE-2 is a 65° swept delta wing with a flat plate inner portion and interchangeable leading edges. It has been initially tested at the NASA Langley Research Center (see Ref. [25-6] and Chapter 18). Three different leading edge configurations were chosen: a sharp leading edge and three rounded leading edges of varying radii [25-6]. Because of the analytical geometry definition and because of its general availability it was also chosen as test case for the new experimental investigations (see Refs. [25-13], [25-15], [25-16]-[25-18] and Chapters 19 – 23. Figure 25-1 shows this geometry.
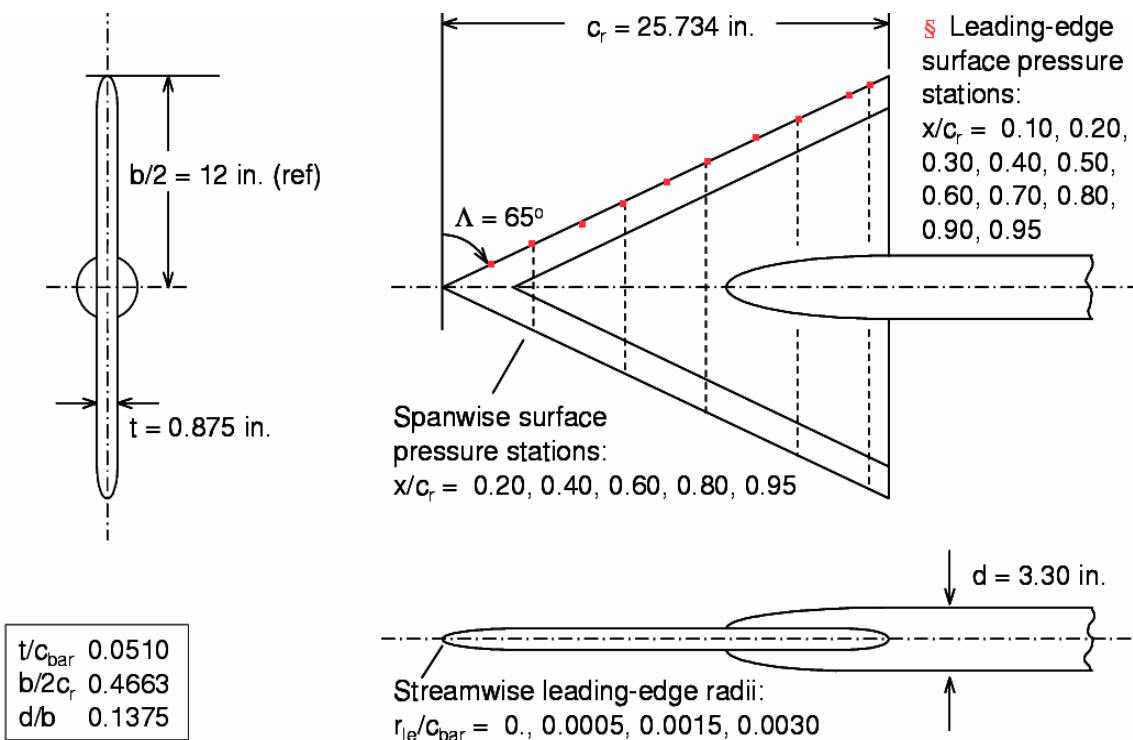
Figure 25-1: Geometry of VFE-2 Delta Wing; (Ref. [25-6] and Chapter 18).

Because of the very simple geometry, a structured approach was used for the numerical simulations at EADS. This allows the generation of well tailored, rather orthogonal grids which minimize the numerical discretization error. The grids have been generated by an in-house developed hyperbolic grid generator which runs automatically and allows the generation of grids with 10 million grid points within several minutes. The grid structure is shown in Figure 25-2.
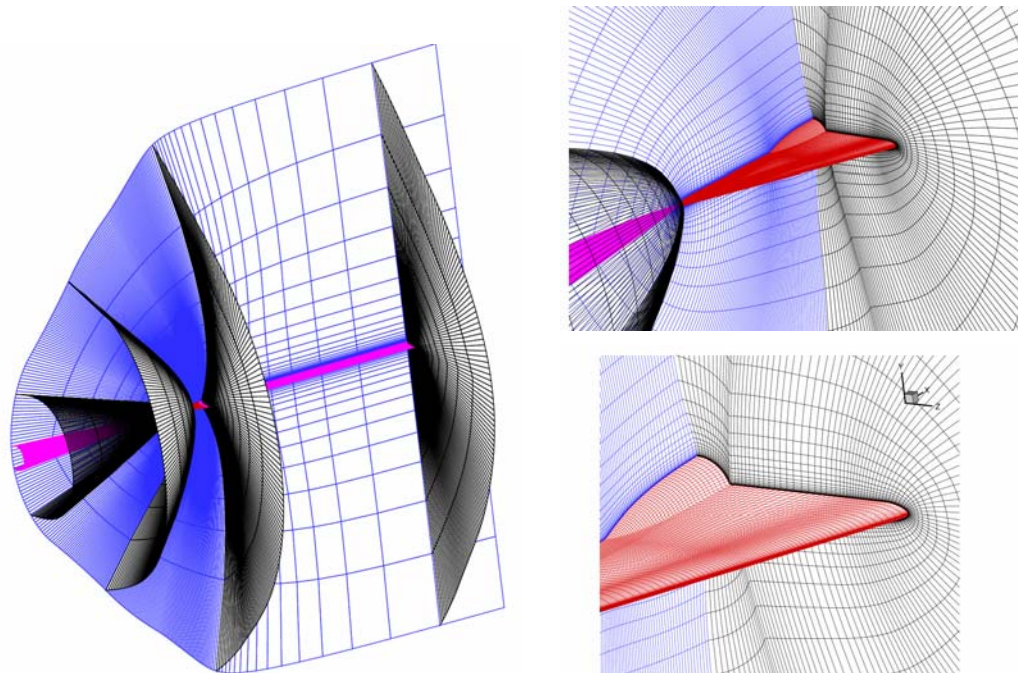
Figure 25-2: 3-D Grid Structure (only each second line in each direction is shown).

The configuration of Figure 25-1 was used with sharp and medium range rounded leading edge (which is generally referred as round leading edge within VFE-2) for all new experiments and also for the numerical calculations) within VFE-2 (Refs. [25-19] – [25-23] and Chapters 26 – 33).

The grid is a so called conical C-O type mesh. This grid type has proven to be very suitable for vortical flow in numerous calculations. It has a singular line from the wing apex to the upstream far field boundary. The sting is kept with constant diameter until to the downstream far field boundary. Close to the surface and around the round leading edge, the grid lines are nearly orthogonal. The grid is build up by 321 points in stream wise direction (starting from the wing apex, and 257 point aligned with the wing surface), 257 points in circumferential direction, and 129 points normal to the wing surface. This results in a total number of 10^6 million grid points. The grid is subdivided into 24 blocks for use of the flow solver in parallel mode.

25.5   FLOW SOLVER

The DLR flow solver FLOWer [25-24] has been used for the RANS calculations at EADS. The FLOWer code is designed for application on multi-block grids and has been operated in a Jameson-type mode as a cell-vertex explicit multi-grid scheme using a finite volume approach and a Runge-Kutta type scheme with central differences in space for the time integration. The numerical dissipation model is the anisotropic dissipation model of Jameson, where the dissipation terms are scaled with the relations of the convective eigenvalues in each direction of the control volume. Additionally the dissipative flux vector is optimized by a relaxation between old and new values within the Runge-Kutta scheme.

Convergence acceleration has been achieved by local time stepping, implicit residual smoothing and by use of the full multi-grid strategy (3-level W-cycle). For further reduction of computing time, FLOWer was run on

24 processors on a Linux cluster. Depending on the flow features, 2000 – 4000 multi-grid cycles were necessary for a converged solution.

In the RANS mode, FLOWer offers a variety of different one- and two equation turbulence models and also several Reynolds Stress models. The calculations have been performed using the SAE-model, the Wilcox k-ω model, and the RSM model, but all the following results were obtained with the Wilcox k-ω model.

For all the different turbulence models, FLOWer has the option to specify transition. This option was used in some calculations by specifying transition along a conical line along the upper side of the wing. Upstream of the transition line, laminar flow is simulated by zero production in the turbulent transport equations.

25.6   RESULTS AND DISCUSSION

25.6.1   Effect of Leading Edge Bluntness

The experimental results of the NASA Langley Research Center [25-6] offer a data base for three different round leading edges. So before starting the investigation for a delta wing with a realistic round leading edge, some general investigations at the delta wings with different leading edges have been performed at EADS. A typical result is presented in Figure 25-3.

| (a) Sharp L. E. | (b) Small Range | (c) Medium Range | (d) Large Range |
| L. E. Radius | L. E. Radius | L. E. Radius | L. E. Radius |
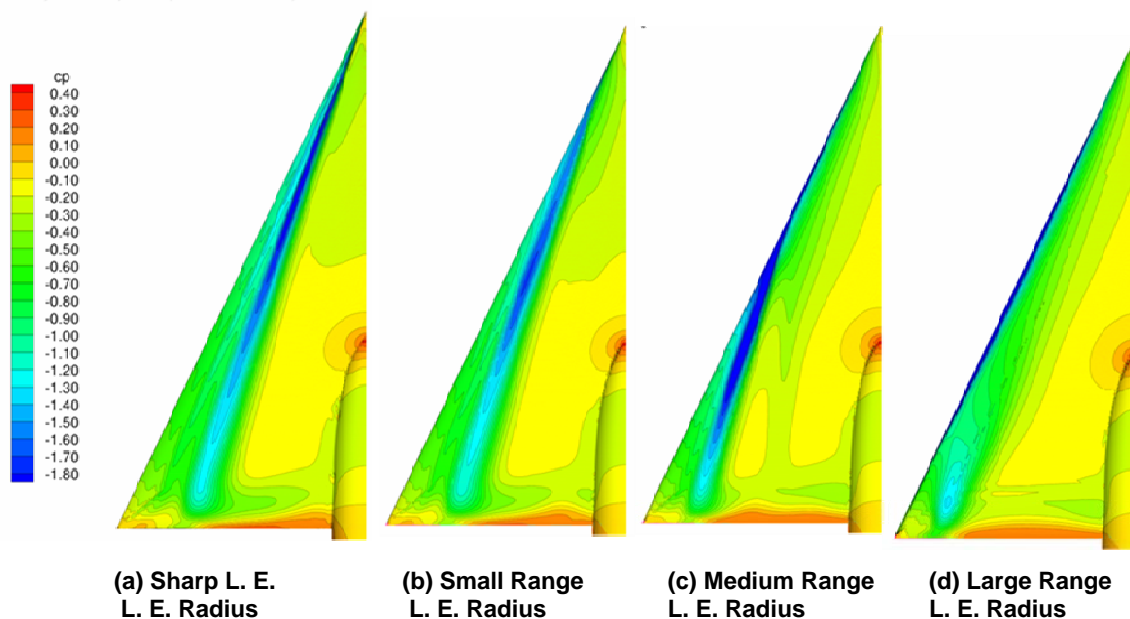
Figure 25-3: Effect of Leading Edge Bluntness, M = 0.4, Re = 6 x 10^6, α = 13°.

This figure shows surface pressure contours for the VFE-2 delta wing with different leading edges. The sharp leading edge (Figure 25-3 (a)) shows the typical leading edge vortex beginning at the wing apex. The wing with the small range leading edge (Figure 25-3 (b)) shows a very similar flow pattern, the leading edge separation begins very close to the wing apex. With the large range leading edge radius (Figure 25-3 (d)) there is no leading separation; the leading edge is too blunt. The medium range leading edge radius (Figure 25-3 (c)) generates a

combination of the latter two cases. In the forward part of the wing, the flow passes the round leading edge (as the absolute leading edge radius is constant, the leading edge is relative blunt in this part of the wing). By the increasing half span of the wing and the constant leading edge radius, the wing gets relatively sharper in stream wise direction. So at a certain distance of the wing apex, the flow separates and the leading edge vortex develops. This transition of the relative leading edge sharpness is very important for the understanding of the flow field about this wing. There is also the footprint of a second, inner vortex in the surface pressure contours of the wing with the medium range leading edge radius. This vortex, which makes the flow field peculiar, will be discussed in more details within this chapter.

25.6.2   Effect of Reynolds Number and Transition

The simulation of Reynolds number effect can be a very important application of the numerical simulation, as it would help very much to scale wind tunnel test data to real flight conditions. As the NASA experiments [25-6] offer test data for a variation of the Reynolds number from 6 million to 60 million, they have been used for first test calculations within EADS. The results are discussed in this section.

Figure 25-4 shows very clearly, that the higher Reynolds number delays the leading edge separation. At the lower Reynolds number (Figure 25-4 (a)) the development of the primary vortex begins at $x/c_r \approx 0.2$, whereas at the high Reynolds number it begins somewhere between $x/c_r = 0.6$ and $x/c_r = 0.8$.

(a) Re = 6 Mio   (b) Re = 60 Mio
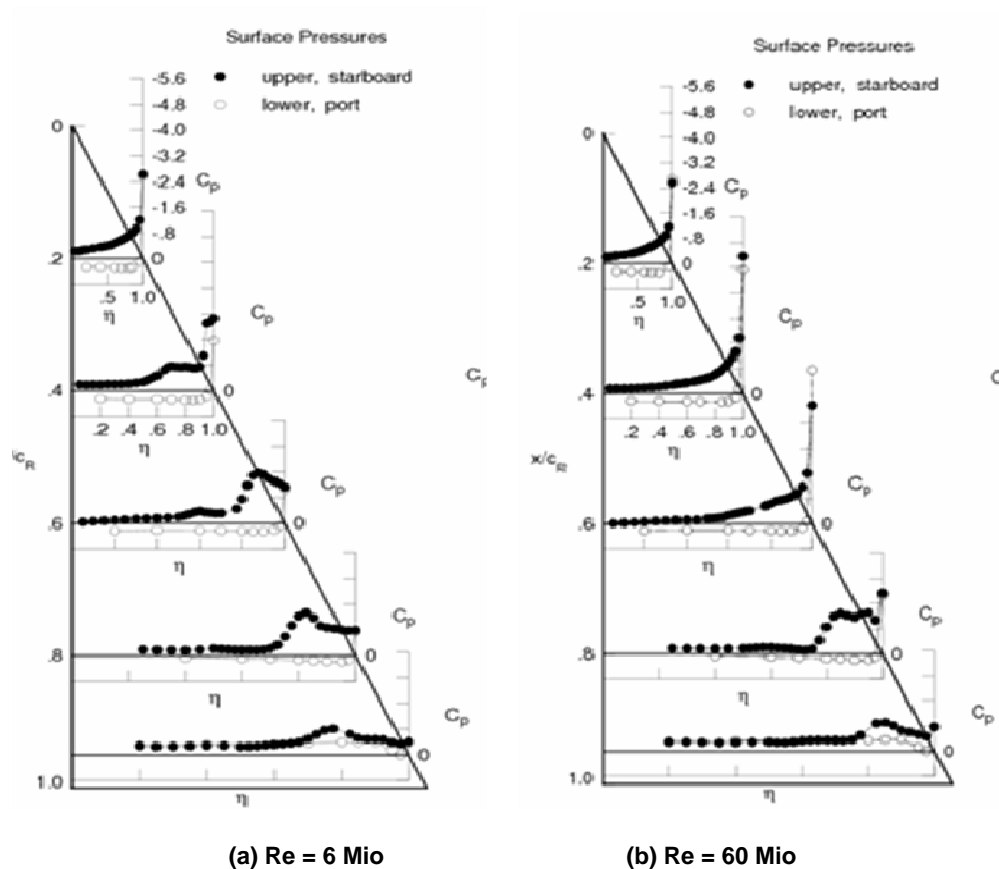
Figure 25-4: Effect of Large Reynolds Number Variation in the Experiments, M = 0.4, α = 13°; Ref. [25-6].

In Figure 25-5 the effect of the different Reynolds numbers is shown for two different numerical calculations. The left hand side of the figure shows the results for calculations without setting transition (fully turbulent, which is by default used in RANS calculation). On the right hand side there are the results for calculations with prescribed transition along a conical line. The distance of the transition line from the leading edge is *0.003* of the local (full) wing span (0.3%). The impact of the transition setting is quite considerable. Without transition the leading edge separation at the low Re is delayed too much, and at the high Re it is promoted too much (left hand side of Figure 25-5). With transition however, the effect of the Reynolds number is matched very well and also the position of the separation points are very close to the experimental separation points. This effect of the transition setting was also observed at other turbulence models (SAE, RSM): only by prescribing transition, reasonable results were obtained at Re = 60 Mio, and at Re = 6 Mio, without transition all three turbulence models delayed the primary separation too much.

(a) No Transition   (b) Transition at $2z_{tr}/b = 0.03$
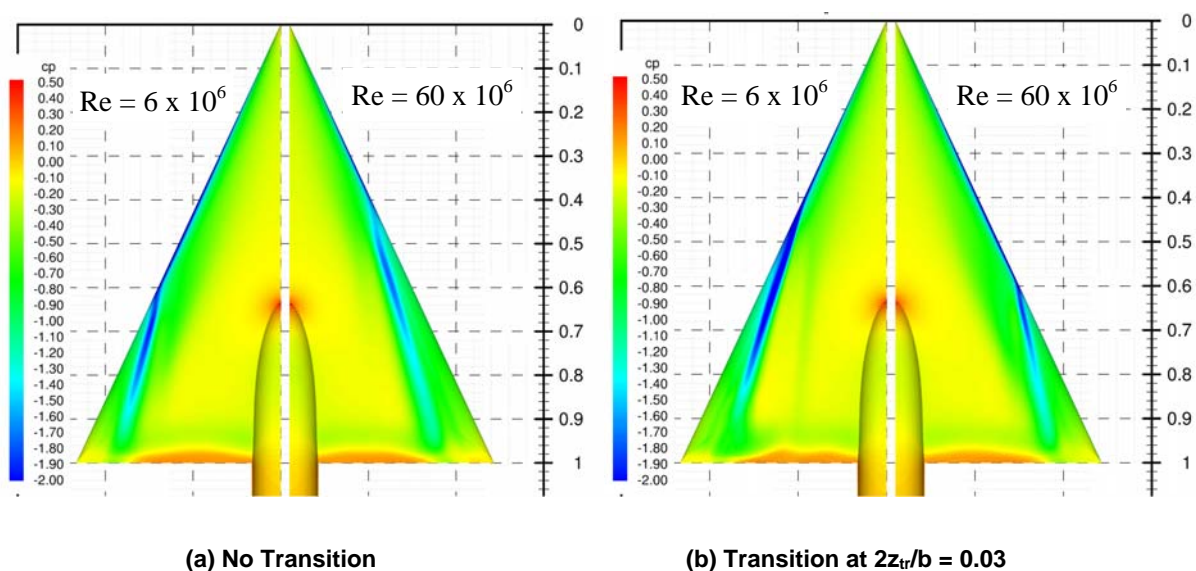
**Figure 25-5: Effect of Large Reynolds Number Variation
in the Calculations (RANS, Wilcox k-ω, M = 0.4, α = 13°).**

It is not quite clear, whether this is a real physical effect or only a numerical effect of the turbulence model (possibly the turbulence model produces too much eddy viscosity around the leading edge, which then is corrected by forcing laminar flow in this region). As long as no experimental data about transition locations or effects of different transition locations are available, the transition setting at 0.3% is arbitrary, but it shows, how sensitive to small variations this primary separation is. The position of this separation point has of course great impact on the local surface pressure distribution as Figure 25-6 illustrates.
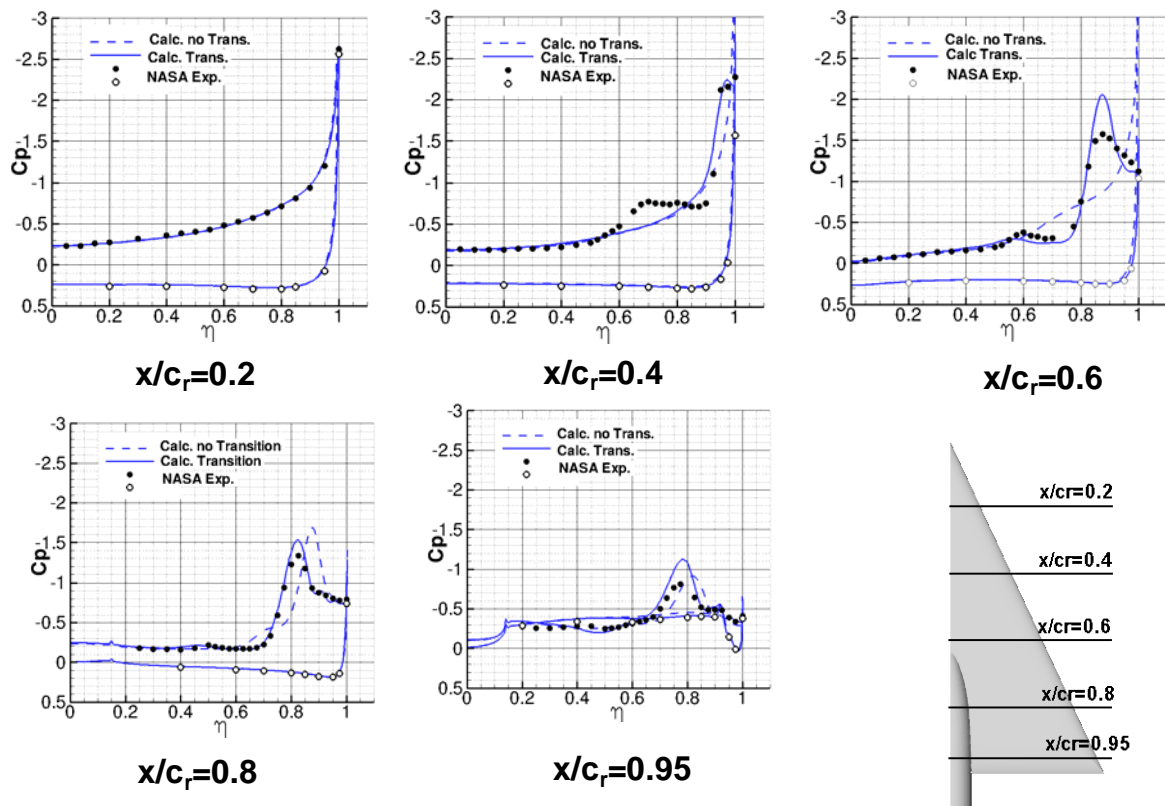
Figure 25-6: Comparisons of Surface Pressure with Experiments (Ref [25-6])
for M = 0.4, Re = 6 Mio, α = 13° With and Without Transition.

With the specified transition, the experimental data are fitted quite well, whereas the calculation without transition shows a too much delayed leading edge separation. This investigation shows very clearly, that the correct prediction of the primary separation for a round leading edge is a very difficult task and very sensitive to small variations of the eddy viscosity (and by this of course also to numerical viscosity). At very high Reynolds numbers this sensitivity seems to be much stronger. As the setting of the transition at 0.03% local half span is rather arbitrary (this value was found after some trials to fit best the experiments), and as long as there are no physical reasons to do this, the transition setting has only been used for this investigation in order to demonstrate the impact of it. All further calculations have been done without transition.

At least for small variations of the Reynolds number the fully turbulent RANS solution shows the correct effect of the Re variation as it can be seen in Figure 25-7. The leading edge separation is now delayed by the increasing Reynolds number, but compared with the experiments too much (see Figure 25-6). So it can be concluded that the effects of Reynolds number variations which are of interest within this chapter (Re = 1 Mio, Re = 2 Mio, Re = 3 Mio, Re = 6 Mio) are prescribed qualitatively correct by fully turbulent RANS simulations.
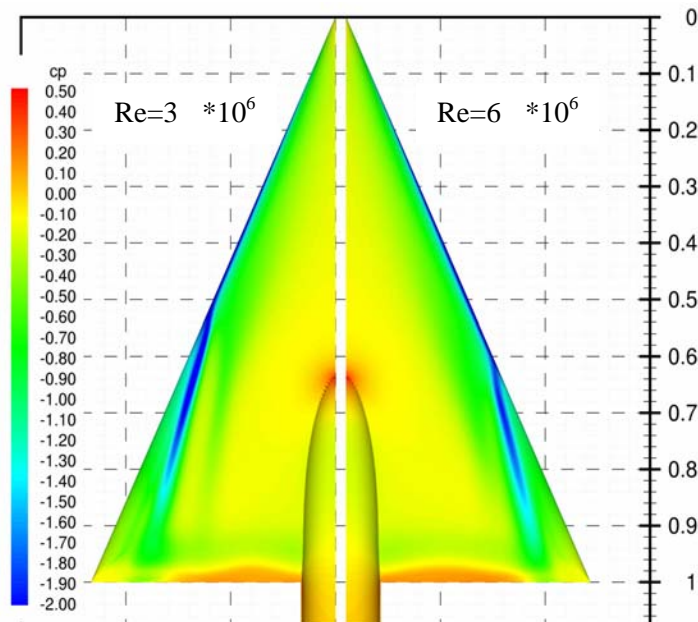
**Figure 25-7: Effect of a Small Reynolds Number Variation
in the Calculation (RANS, Wilcox k-ω, M = 0.4, α = 13°).**

The surface pressure contours of the numerical solution for Re = 3 Mio are very similar to the corresponding surface pressure contours of the DLR PSP experiments (Ref. [25-15] and Chapter 19), as it is shown in Figure 25-8. This case is the famous test case 4.5 within the VFE-2 and will be investigated in more details in the next section.

(a) Calculation   **(b) DLR PSP Experiment
Ref. [25-15] and Chapter 19**
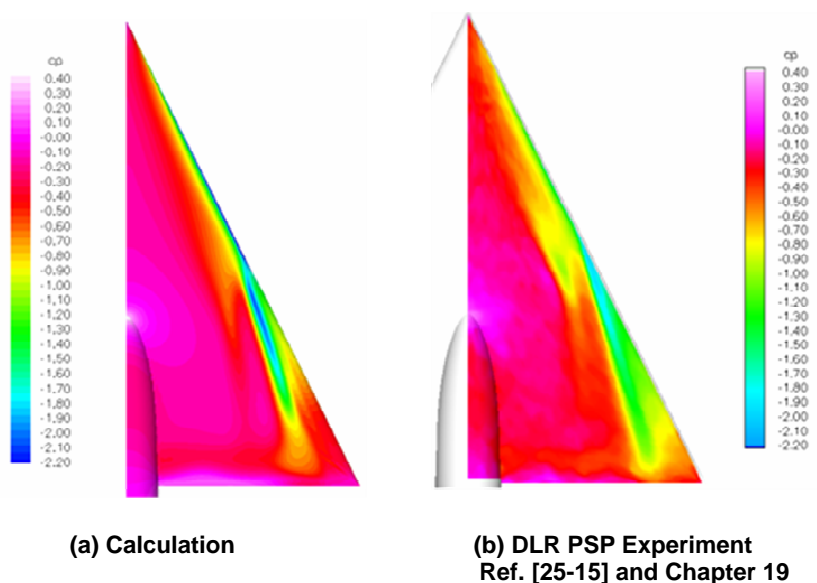
**Figure 25-8: Comparison of Numerical and Experimental Surface
Pressure Contours for Case 4.5 (M = 0.4, Re = 3 x 10^6, α = 13°).**

25.6.3 Test Case 4.5, M = 0.4, Re = 3 x 10⁶, α = 13°

Figure 25-9 shows the comparison of the surface pressure contours from the numerical solution and from the DLR PSP experiment ([25-15] and Chapter 19). Obviously the separation point of the primary vortex is very close to the experimental separation point for this test case. Both surface pressure contours show very clearly the footprint of this second inner vortex. There is a rather compact suction peak at the beginning of this secondary vortex in the experiment. In the numerical result this suction peak is not present, the pressure contours are smoother, but besides this, both pressure contours are rather similar.

$x/c_r=0.2$ $x/c_r=0.4$ $x/c_r=0.6$

$x/c_r=0.8$ $x/c_r=0.95$
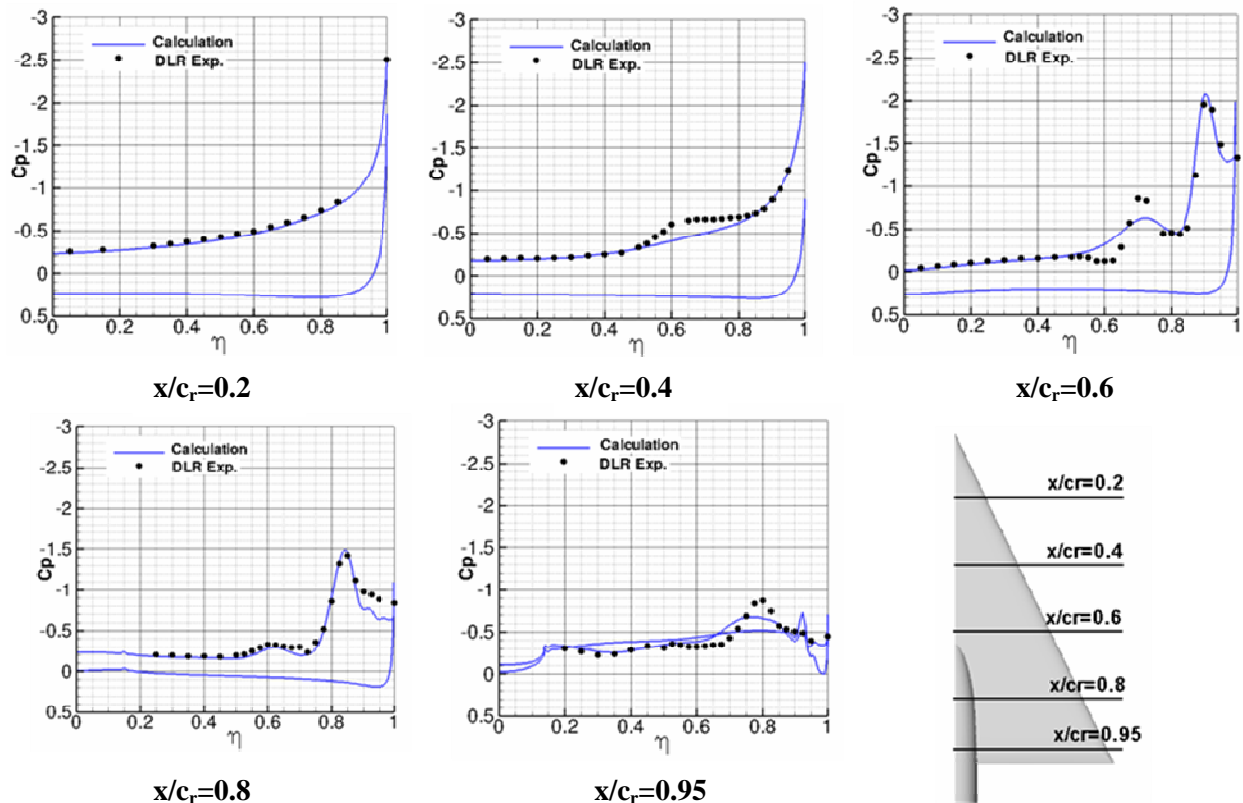
Figure 25-9: Comparison of Numerical and Experimental (Ref. [25-15] and Chapter 19)
Surface Pressure Distributions for Case 4.5 (M = 0.4, Re = 3 x 10⁶, α = 13°).

The main flow features for this test case are really well predicted by the RANS solution as Figure 25-9 underlines. The second vortex is at the correct position, but compared to the experiment it is too weak. The primary vortex is matched very well. At the cross section $x/c_r = 0.8$ there can be seen the typical problem of RANS: deficits in the pressure prediction in the region of the secondary vortex. Te experimental data are not fitted exactly, but due to the good agreement of the overall flow features, the CFD data can be used for an analysis about the origin of this second vortex.

Figure 25-10 gives a first impression about the origin of this inner vortex. The iso-surface of 5% total pressure loss indicates an already separated, thick boundary layer in the apex region of the wing. Possibly by the leading edge suction this thick and rotating boundary is sucked towards the leading edge. Thus it gets thicker

and then finally rolls up to this inner vortex. As soon as the main leading edge separation sets on, all separated flow material is fed into this primary vortex, which consequently grows up in stream wise direction.
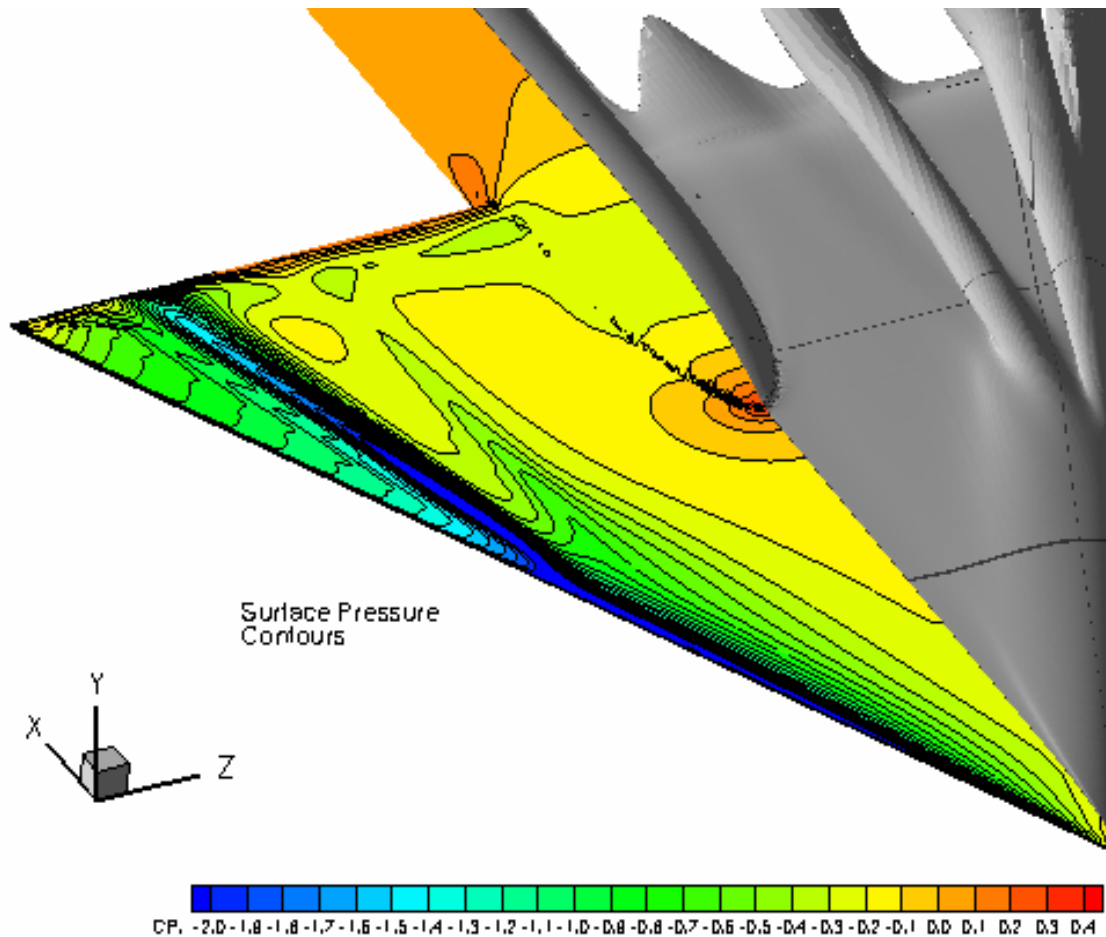
**Figure 25-10: Surface Pressure Contours and Iso-Surface of 5%
Total Pressure Loss for Case 4.5 (M = 0.4, Re = 3 x 10^6, α = 13°).**

The total pressure loss contours in different cross sections, which are shown in Figure 25-11, give an impression about the dimension of this inner vortex. It is nearly as big as the main primary vortex, but much weaker. It is not fed by the leading edge therefore it gets weaker in downstream direction. At the very beginning this inner vortex also induces a secondary vortex. Figure 25-11 also shows that the leading edge vortex follows the leading edge, whereas the inner vortex is more parallel to the main flow direction.
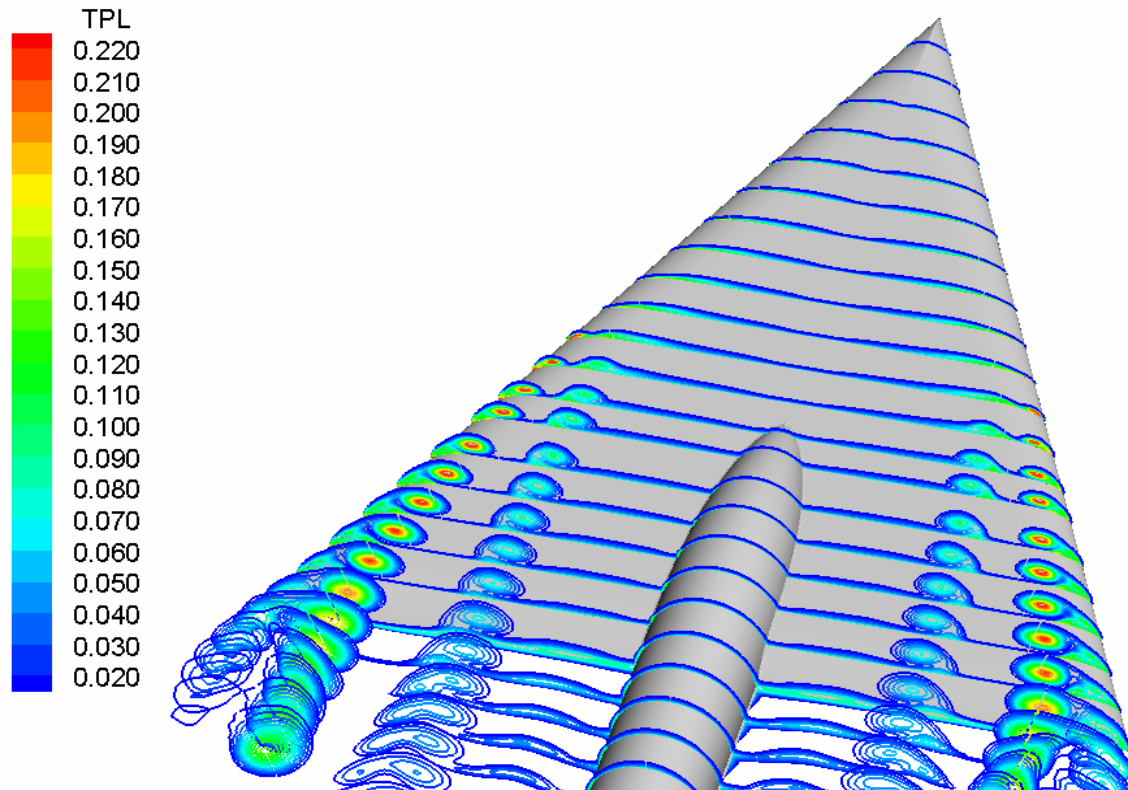
Figure 25-11: Total Pressure Loss Contours in Different Cross Sections for Case 4.5 (M = 0.4, Re = 3 x 10^6, α = 13°).

The velocity vectors in Figure 25-12 show that already in the very forward region of the wing (x/c_r = 0.2) there is a thin separated region. The total pressure loss contours (the range from 2% blue, to 24% red) indicate, that this separated region becomes thicker and stronger in stream wise direction. (The close-up range and the length scale of the velocity vectors is not identical in both pictures, is has been chosen such that details can be seen, and not all vectors are shown).
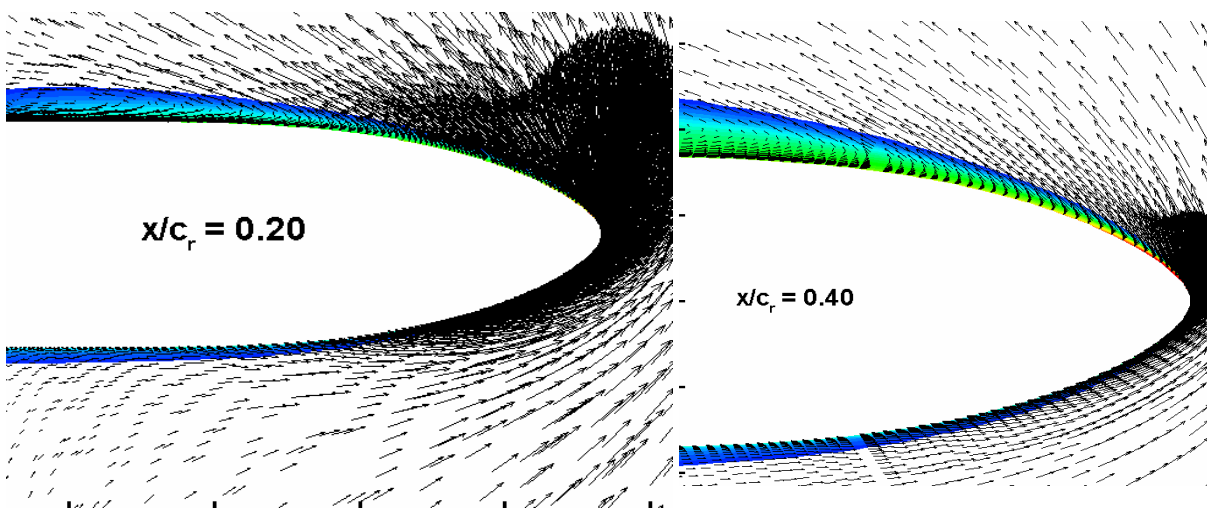
Figure 25-12: Velocity Vectors and Total Pressure Loss Contours in Two Cross Sections
for Case 4.5 (M = 0.4, Re = 3 x 10^6, α = 13°) – x/c$_r$ = 0.20 and x/c$_r$ = 0.40.

At x/c$_r$ = 0.5 (left hand side of Figure 25-13) the separated region is already very thick, but it is still growing continuously from the leading edge towards the inner part of the wing. At x/c$_r$ = 0.55, the leading edge separation sets on and the separated region now grows much faster close to the leading edge. More inboard, the thick boundary layer gradually forms a flat vortex.
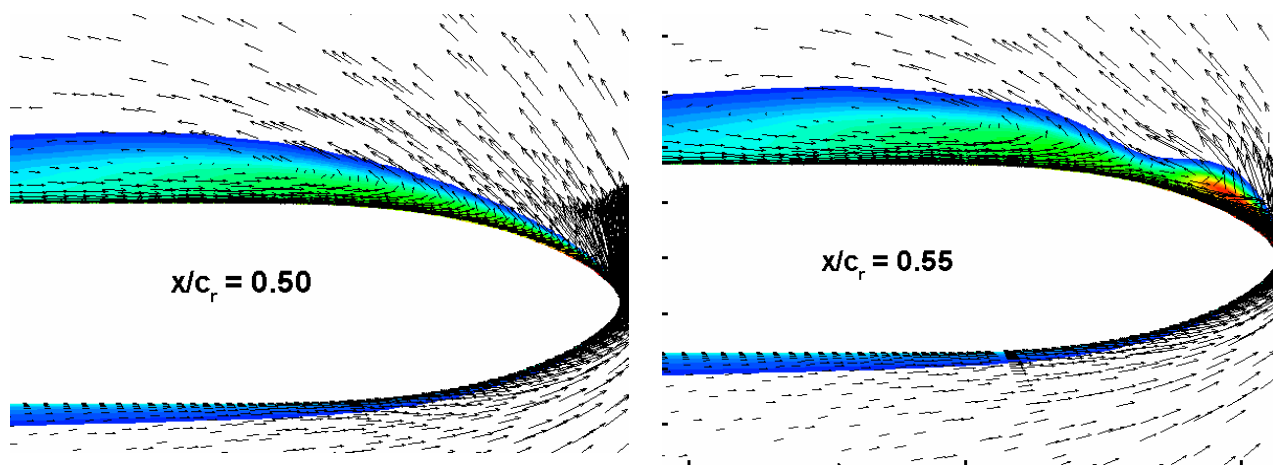
Figure 25-13: Velocity Vectors and Total Pressure Loss Contours in Two Cross Sections
for Case 4.5 (M = 0.4, Re = 3 x 10^6, α = 13°) – x/c$_r$ = 0.50 and x/c$_r$ = 0.55.

The situation at the cross section x/c$_r$ = 0.60 and x/c$_r$ = 0.65 is shown in Figure 25-14. At x/c$_r$ = 0.6 there is a double branched vortex and at x/c$_r$ = 0.6 there are finally two separate vortices. The inner vortex is much weaker than the outer one, but has the same dimension. From this position (x/c$_r$ = 0.6), the inner vortex has no longer a connection to the leading edge and thus it is no longer fed. The outer vortex is fed by the leading edge and thus further growing.
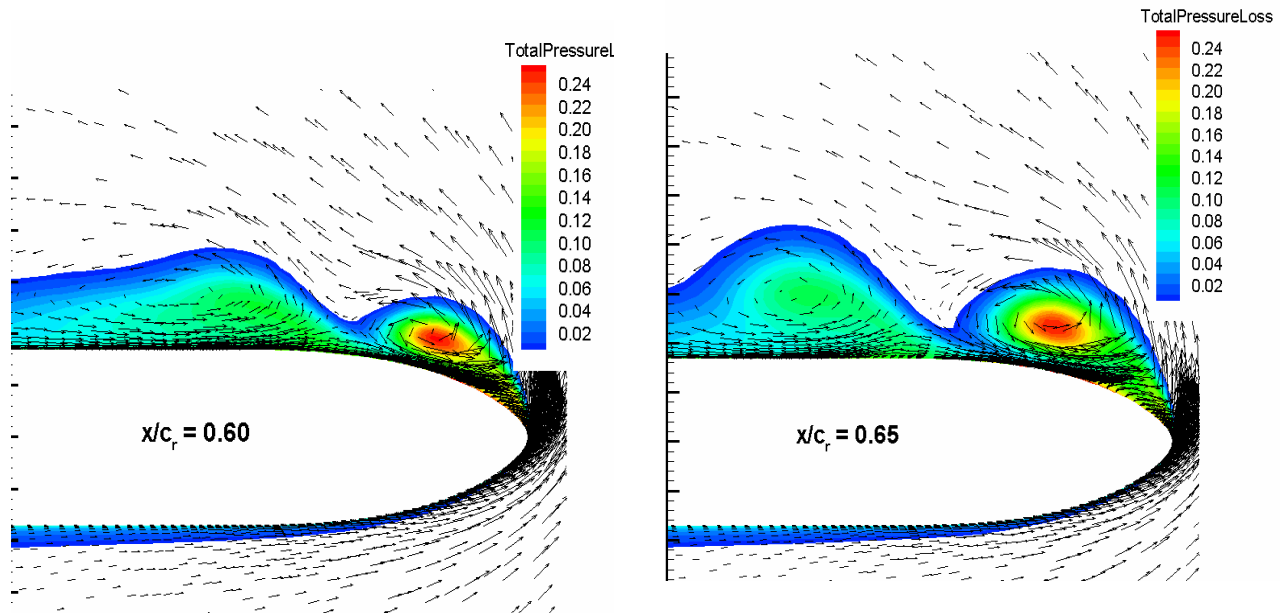
Figure 25-14: Velocity Vectors and Total Loss Contours in Two
Cross Sections for Case 4.5 (M = 0.4, Re = 3 x 10^6, α = 13°).

The spatial development of the two vortices is shown in Figure 25-15 by 3-D stream traces. The volume ribbons are colored by the local C_p values. The volume ribbons are generated by placing rakes into the vortex cores and in the boundary layer region at the wing apex, then tracing the ribbons in upstream and downstream direction. By their twist the ribbons also indicate the local vorticity. At the foremost part of the wing, the flow passes the leading edge with little vorticity and then runs along the inner wing surface towards the trailing edge (left hand side of Figure 25-15). More downstream along the leading edge the vorticity in the boundary layer increases and the flow particles are bound to the inner vortex. The close up at the right hand side of Figure 25-15 shows the onset of the main primary vortex. There is a region, where the primary separation already exists, but the inner vortex still gets flow material from the outer flow. As soon as the primary vortex gets certain strength, the inner vortex no longer gets material from the outer flow.
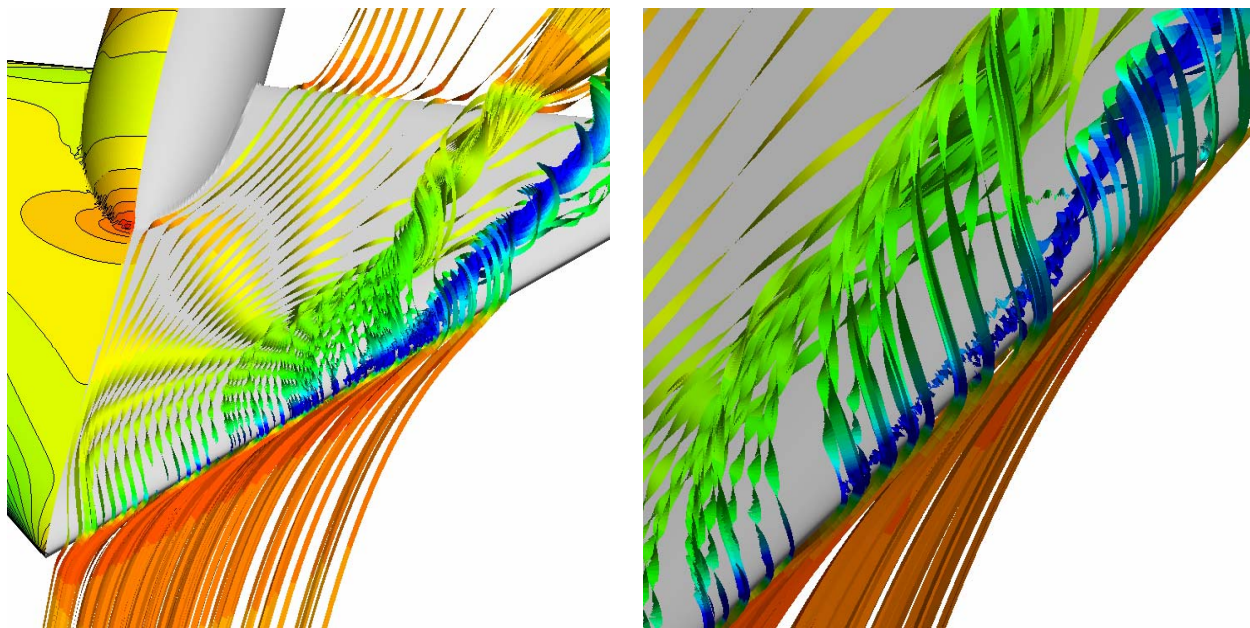
**Figure 25-15: 3-D Flow Features (Stream Traces by 3-Volume
Ribbons) for Case 4.5 (M = 0.4, Re = 3 x 10^6, α = 13°).**

During the VFE-2 experiments at TUM (Ref. [25-17] and Chapter 21), it was seen, that this inner vortex varies considerably with a decrease of the Reynolds number. Surface visualizations by oil flow pattern at Re = 1 Mio have shown a much more inboard position and an earlier onset of the inner vortex as shown in Figure 25-8. For a better understanding of this effect, the variation of the Reynolds number was also investigated numerically.

Figure 25-16 shows the effect of the decreasing Reynolds number in the surface pressure contours. (The Mach number was kept constant, only the Reynolds number was changed in the calculations). As the figure indicates, the smaller the Reynolds number gets, the more upstream moves the primary separation and in turn the earlier begins the inner vortex and the weaker it gets.

(a) Re = 1 Mio   **(b) Re = 2 Mio**   **(c) Re = 3 Mio**
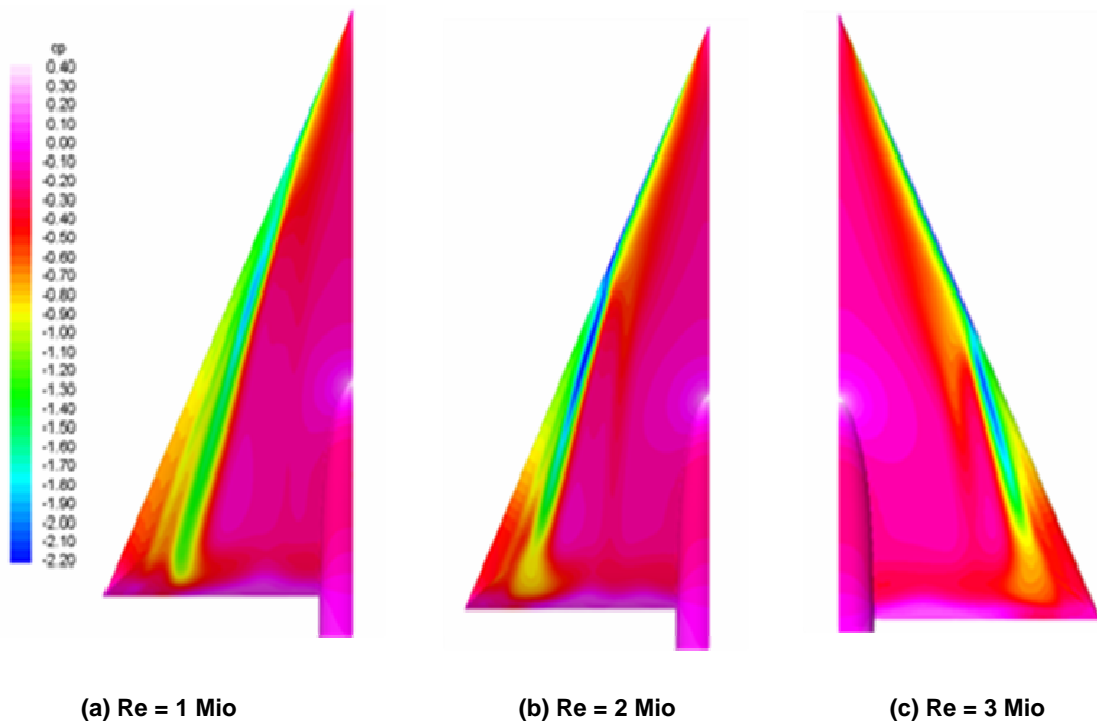
Figure 25-16: Effect of Decreasing Reynolds Number on Surface
Pressure Contours for Case 4.5 (M = 0.4, Re = 3 x 10^6, α = 13°).

In the 3-D flow structure, which is shown in Figure 25-17 by means of total pressure loss contours, the impact of the decreasing Reynolds number can be seen very clearly. With the upstream moving primary separation the origin of the inner vortex also moves upstream and its axis moves more inboard. Between Re = 2 Mio and Re = 3 Mio there are only small differences, but at Re = 1 Mio, there is a considerable inboard shift of the inner vortex.

(a) Re = 1 Mio   **(b) Re = 2 Mio**   **(c) Re = 3 Mio**
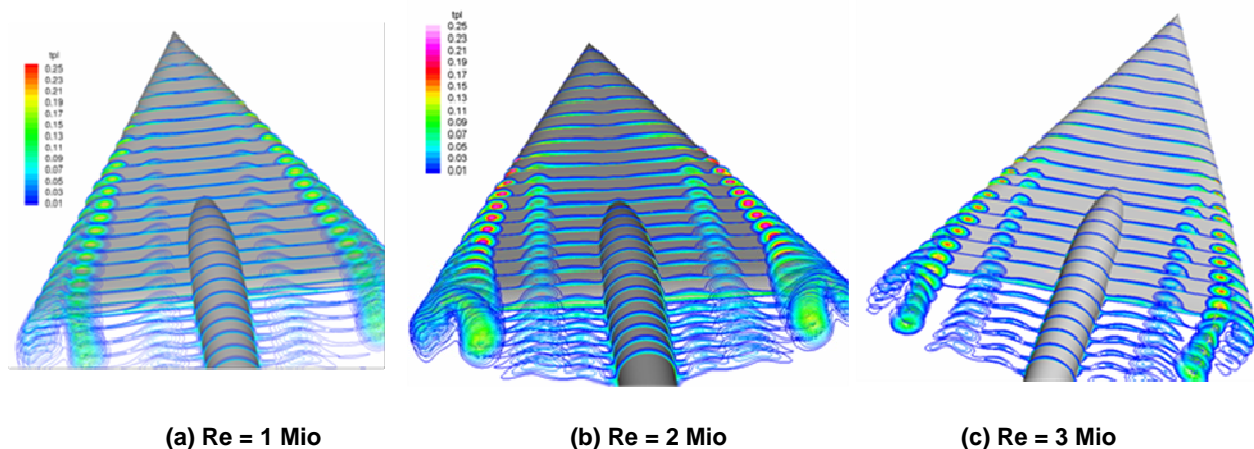
Figure 25-17: Effect of Decreasing Reynolds Number for Case 4.5 (M = 0.4, Re = 3 x 10^6,
α = 13°). Total pressure loss contours at different cross sections.

25.6.4 Test Case 14, M = 0.4, Re = 6 x 10^6, α = 18°

This test case is again the round leading edge geometry, but at a higher angle of attack. The leading edge separation now moves close to the wing apex and the inner vortex has no considerable effect. A fully developed primary vortex without vortex break down should be expected for this case. The vortical flow structure is shown in Figure 25-18.
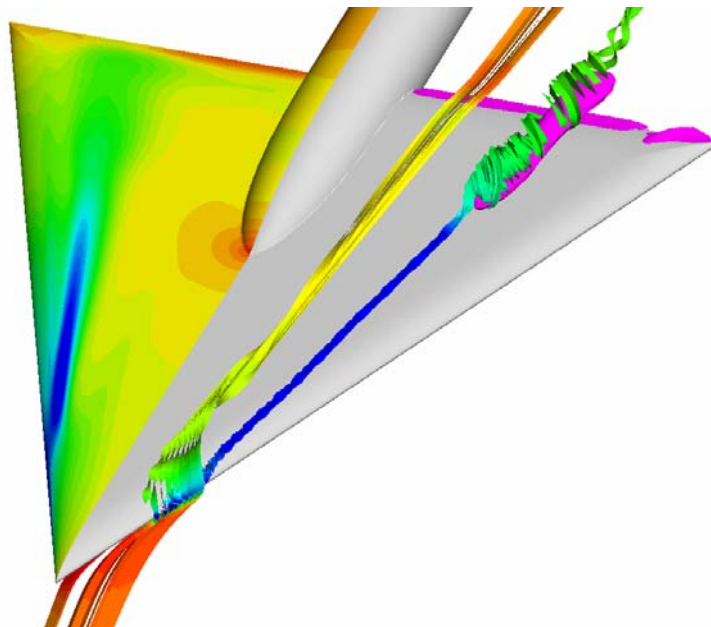
Figure 25-18: 3-D Flow Features (Stream Traces by 3-Volume Ribbons) for Case 14 (M = 0.4, Re = 6 x 10^6, α = 18°).

In Figure 25-18 the vortical flow structure is visualized again by 3-D volume ribbons. There is a separation at the apex region of the wing which rolls up into a small inner vortex. But this inner vortex only has a small impact on the pressure distribution in the apex region. The leading edge separation now begins very close to the wing apex. The core of the leading edge vortex remains very compact until $x/c_r = 0.8$. At this position the core forms a small bubble until to the rear end of the wing where the core becomes compact again. The pink colored bubble in the figure is an iso-surface of zero axial velocity. Inside the bubble the axial velocity is negative and outside it is positive. Negative axial velocity in the vortex core is a criterion for vortex breakdown, which means that the calculation shows a very weak vortex breakdown. In general for a 65° swept delta wing, vortex breakdown is expected at α = 21°, but the geometry has a highly curved trailing edge region, which induces an additional increase in pressure. This may lead to an earlier vortex breakdown at the very rear end of the wing. Another reason may be an under-prediction of the axial velocity in the numerical calculation due to still existing defects for vortical flow in the actual turbulence model. This earlier vortex break down was also observed in some other numerical solutions [25-25].

Figure 25-19 shows the surface pressure contours compared with the NASA LTPT experiments from Ref. [25-6]. The leading edge separation has now moved upstream, very close to the wing apex and thus there is less boundary layer material which can form the inner vortex. The inner vortex is consequently very weak in the calculation (Figure 25-19 (a)). In the experimental pressure distributions (Figure 25-19 (b)) there is a

rather compact suction peak up to $x/c_r = 0.8$. At $x/c_r = 0.95$, there is still a vortical flow structure, but the suction peak is smeared out. This may indicate a very weak vortex breakdown at the rear end of the wing (due to the high curvature of the trailing edge).

(a) Calculation

(b) NASA LTPT Experiments
Ref. [25-6] and Chapter 18
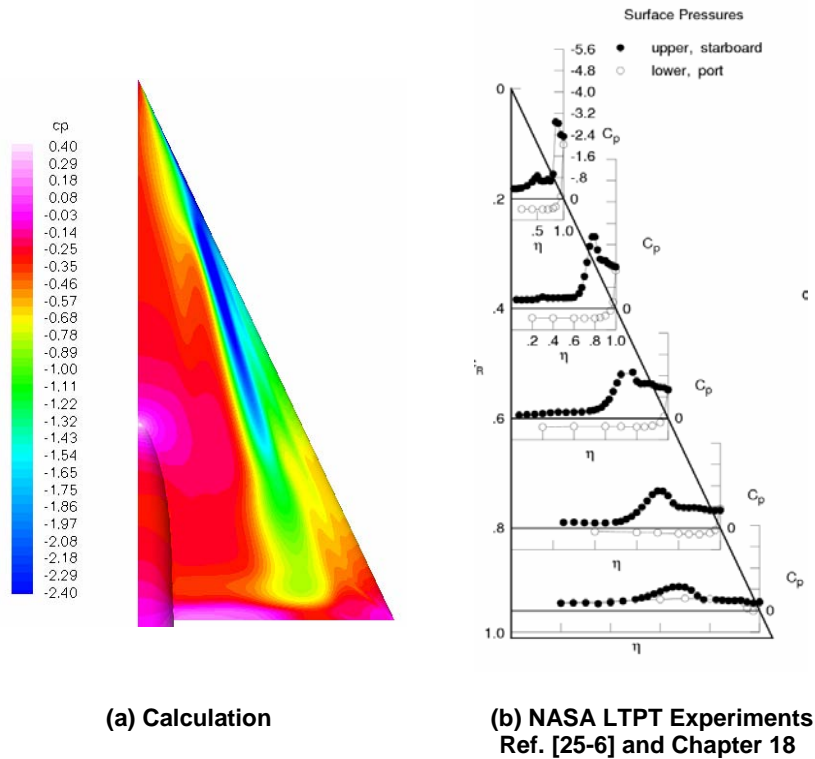
**Figure 25-19: Comparison of Numerical Surface Pressure Contours
with Experimental Data for Case 18 (M = 0.4, Re = 6 x 10^6, α = 18°).**

A detailed comparison of the surface pressure distribution with the NASA LTPT experiments [25-6] is given in (Figure 25-20). Essential differences are at $x/c_r = 0.2$. The numerical solution does not yet show a primary vortex, whereas the experiment shows already a primary vortex and also an inner vortex in this cross section. Again, the numerical solution predicts the primary separation slightly more downstream as it is in the experiment.

x/c_r = 0.2

x/c_r = 0.4

x/c_r = 0.6

x/c_r = 0.8

x/c_r = 0.95
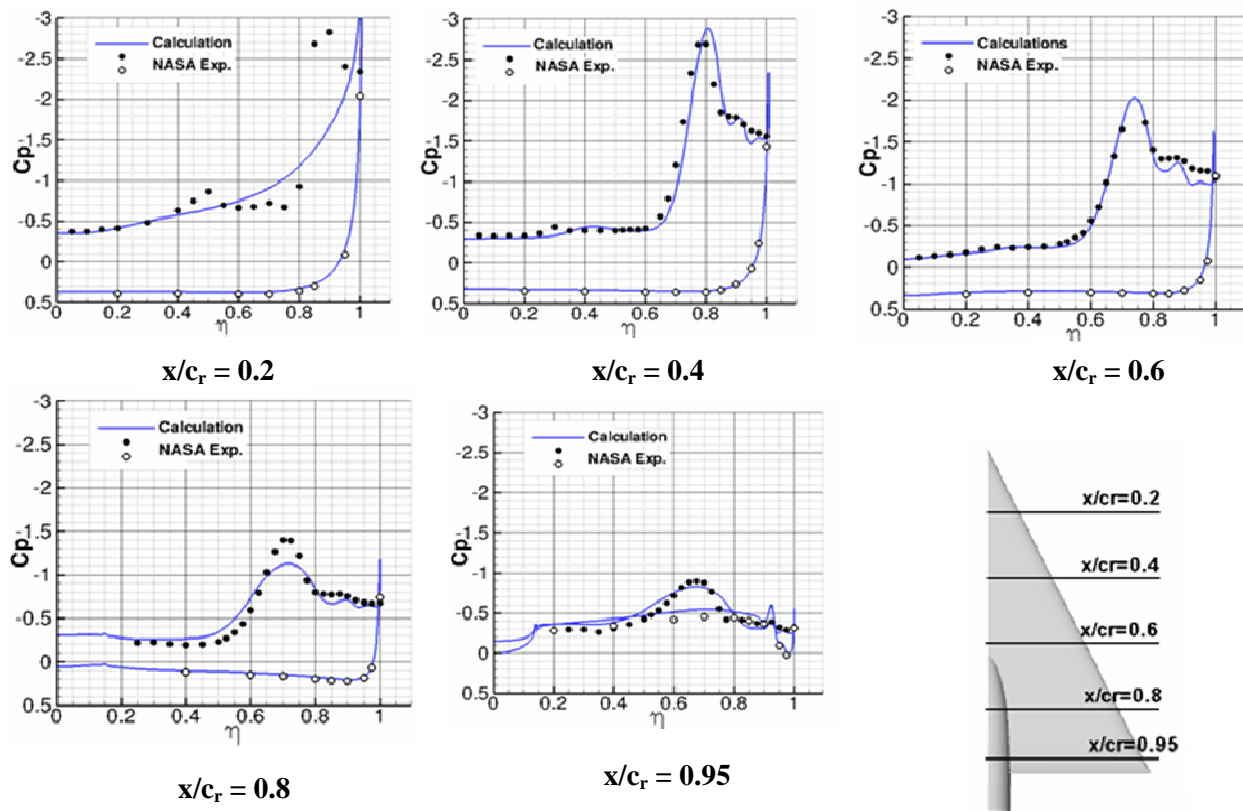
**Figure 25-20: Comparison of Numerical and NASA LTPT (Ref. [25-6]) Surface
Pressure Distributions for Case 14 (M = 0.4, Re = 6 x 10^6, α = 18°).**

At $x/c_r = 0.4$ and $x/c_r = 0.6$ the numerical solution shows the correct flow features. There is a dominating primary vortex and the effect of a secondary vortex (between the leading edge and suction peak). Differences between calculation and experiments occur again in the region of the secondary vortex and are typical for RANS solutions. At $x/c_r = 0.8$ the numerical solutions is under-predicting the main suction peak and smearing it out. The reason, therefore, may be the above mentioned spread of the vortex core. At the cross section $x/c_r = 0.95$ the calculation with its weak vortex breakdown matches quite well to the experimental data. This indicates that the above mentioned weak vortex breakdown due to the high curvature of the rear end of the wing is also present in the experiment.

25.7 CONCLUSIONS

For a delta wing with a rounded leading edge, the prediction of the onset of the primary leading edge separation is the most essential problem. The position of this separation point can be predicted too much upstream or too much downstream or (by accident?) at the correct position. Depending on this, the agreement between numerical and experimental results can be very good or less good. One uncertainty parameter which was found for these test cases is the unknown transition, which can have a strong effect on the solution. So transition modeling should be further promoted. Another difficulty is the effect of the Reynolds number at delta wings with round leading edges. This effect also can be under- or over-predicted.

At higher incidence, the correct prediction of vortex break down is also a very difficult task. In the numerical solution, vortex break down occurred at earlier angles of attack compared to the experiment. This may be due to an under-prediction of the axial velocity in the vortex core. Either there is still a deficit of the existing turbulence models for a proper treatment of vortical flow, or RANS methods are overstrained and DES methods are required for the correct prediction of vortex break down.

Summarizing it can be stated, that not for all presented test cases the experimental results could be predicted in detail correctly, but anyhow detailed numerical flow analysis gave an essential insight into the complex flow structure of the double vortex system at round LE and the numerical calculations helped to design the PIV experiments.

25.8   ACKNOWLEDGEMENTS

25.9   REFERENCES

[25-1]   Drougge, G.: *The International Vortex Flow Experiment for Computer Code Validation*, ICAS Proceedings, 1988, Vol. 1, pp. 35-41.

[25-2]   Ekaterinaris, J.A. and Schiff, L.B.: *Numerical Simulation of Incidence and Sweep Effects on Delta Wing Vortex Breakdown*, Journal of Aircraft, Vol. 31, No. 5, 1994, pp. 1043-1049.

[25-3]   Mitchell, A.M., Morton, S.A., Forsythe, J.R. and Cummings, R.M.: *Analysis of Delta-Wing Vortical Substructures Using Detached-Eddy Simulation*, AIAA Journal, Vol. 44, No. 5, 2006, pp. 964-972.

[25-4]   Hummel, D. and Redeker, G.: *A New Vortex Flow Experiment for Computer Code Validation*, RTO AVT Symposium on "Vortex Flow and High Angle of Attack Aerodynamics", Loen, Norway, 7-11 May 2001, Meeting Proceedings RTO-MP-06(I), SYA 8-1 to 8-31, 2003.

[25-5]   Hummel, D.: *The Second International Vortex Flow Experiment (VFE-2): Objective and First Results*, 2nd International Symposium on "Integrating CFD and Experiments in Aerodynamics", Cranfield University, 2005.

[25-6]   Chu, J. and Luckring, J.M.: *Experimental Surface Pressure Data Obtained on 65° Delta Wing Across Reynolds Number and Mach Number Ranges*, NASA TM 4645, 1996.

[25-7]   Luckring, J.M.: *Reynolds Number and Leading-Edge Bluntness Effects on a 65° Delta Wing*, AIAA Paper 2002-0419, 2002.

[25-8]   Luckring, J.M.: *Transonic Reynolds Number and Leading-Edge Bluntness Effects on a 65° Delta Wing*, AIAA Paper 2003-0753, 2003.

[25-9]   Luckring, J.M.: *Compressibility and Leading-Edge Bluntness Effects for a 65° Delta Wing*, AIAA Paper 2004-0765, 2004.

[25-10] Luckring, J.M.: *Reynolds Number, Compressibility, and Leading-Edge Bluntness Effects on Delta-Wing Aerodynamics*, ICAS Proceedings Yokohama 2004, Paper 4.1.4, 2004.

[25-11] Konrath, R., Klein. C., Engler, R.H. and Otter, D.: *Analysis of PSP Results Obtained for the VFE-2 65° Delta Wing Configuration at Subsonic and Transonic Speed*, AIAA Paper 2006-0060, 2006.

[25-12] Chiba, K. and Obayashi, S.: *CFD Visualization of Second Primary Vortex Structure on a 65-Degree Delta Wing*, AIAA Paper 2004-1231, January 2004.

[25-13] Hummel, D.: *Review of the Second International Vortex Flow Experiment (VFE-2)*, AIAA Paper 2008-0377, January 2008.

[25-14] Luckring, J.M.: *Initial Experiments and Analysis of Vortex Flow on Blunt Edge Delta Wings*, AIAA Paper 2008-378, January 2008.

[25-15] Konrath, R., Klein, C. and Schröder, A.: *PSP and PIV Investigations on the VFE-2 Configuration in Sub- and Transonic Flow*, AIAA Paper 2008-0379, January 2008.

[25-16] Le Roy, J. and Rodriguez, O.: *Experimental and CFD Contribution to Understanding Delta Wing Vortical Flow*, AIAA Paper 2008-0380, January 2008.

[25-17] Furman, A. and Breitsamter, C.: *Turbulent and Unsteady Flow Characteristics of Delta Wing Vortex Systems*, AIAA Paper 2008-0381, January 2008.

[25-18] Coton, F., Mat, S., and Galbraith, R.: *Low Speed Wind Tunnel Characterization of the VFE-2 Wing*, AIAA Paper 2008-0382, January 2008.

[25-19] Gürdamar, E.: *Influence of Grid Resolution on the Accuracy of High Angle of Attack Delta Wing Simulations*, AIAA Paper 2008-0394, January 2008.

[25-20] Schiavetta, L., Boelens, O.J., Crippa, S., Cummings, R.M., Fritz, W. and Badcock, K.J.: *Shock Effects on Delta Wing Vortex Breakdown*, AIAA Paper 2008-0395, January 2008.

[25-21] Cummings, R.M. and Schütte, A.: *Detached-Eddy Simulation of the Vortical Flowfield about the VFE-2 Delta Wing*, AIAA Paper 2008-0396, January 2008.

[25-22] Crippa, S.: *Steady, Subsonic CFD Analysis of the VFE-2 Configuration and Comparison to Wind Tunnel Data*, AIAA Paper 2008-0397, January 2008.

[25-23] Schütte, A. and Lüdeke, H.: *Numerical Investigations on the VFE-2 Rounded Leading Edge Configuration Using the Unstructured DLR TAU Code*, AIAA Paper 2008-0398, January 2008.

[25-24] Kroll, N., Aumann, P., Bartelheimer, W., Bleecke, H., Eisfeld, B., Lieser, J., Heinrich, R., Kuntz, M., Monsen, E., Raddatz, J., Reisch, U. and Roll, B.: *FLOWer Installation and User Handbook*, DLR Doc. No. MEGAFLOW-1001, 1998.

[25-25] Fritz, W. and Cummings, R.M.: *What was Learned from the Numerical Simulations for the VFE-2*, AIAA Paper 2008-0399, January 2008.

Chapter 26 – NUMERICAL SOLUTIONS FOR THE VFE-2 CONFIGURATION ON STRUCTURED GRIDS AT ONERA, FRANCE

by

Jean-François Le Roy and Jacques Riou

26.1 INTRODUCTION

The flow over delta wings is the place of numerous vortical phenomena. The flow separates at leading edge for lower incidence in the case of a sharp leading edge than for a rounded leading edge. Separation generates a mixing layer leading to a primary vortex on the upper side of the wing. According to the value of the angle of attack and the wing shape, a secondary vortex or even a tertiary one can be observed. These vortices contribute for a large part to the lift (vortical lift). At high angle of attack the primary vortex breakdown occurs, what strongly alters the flow. This phenomenon is characterised by a sudden expansion of the vortical core and a rapid drop of the axial velocity. This leads to large variations of lift, drag and roll coefficients because the vortices become unstable, yielding to asymmetric oscillations [[26-1], [26-2]]. The lift coefficient is then highly correlated to the longitudinal location of the vortex breakdown. The breakdown negative effects appear not only through the average performance, but also because the essential unsteady nature of the flow generates buffet and loss of control. Accurate CFD simulations of these types of flow will help the designer and will also allow assessing efficient control means of large scale vortical structures.

In the following sections, steady and unsteady approaches are presented. General description of the methods, meshes, turbulence models and boundary conditions are described. The results of the simulations are compared with experimental data to validate the numerical approach. Finally, a conclusion is given to exhibit the ability of CFD methods to predict such flows.

26.2 NOMENCLATURE

U_0, U_∞	freestream velocity, m/s
u, v, w	velocity components, m/s
Ωx	x vorticity component, $= (dw/dy - dv/dz)$
St_c	Strouhal number, based on the root chord
$\dfrac{f.G(f)}{\sigma^2}$	Power Spectral Density

26.3 STEADY APPROACH

All the steady simulations have been done with the ONERA elsA software (standing for Ensemble Logiciel pour la Simulation en Aérodynamique). The elsA software solves the compressible, three-dimensional Reynolds average Navier-Stokes equations in a cell centered finite-volume formulation from low subsonic to high supersonic velocities [[26-3], [26-4]].

26.3.1   Computational Grids

The configurations considered in this study are the NASA 65 degrees delta wing with a sharp and a medium leading edges. The recommended computational domain sets the outer boundary at 10 Root Chord (c_r) upstream from wing apex, 20 c_r downstream from wing apex, 20 c_r above wing apex, 20 c_r under wing apex and 10 c_r spanwise from wing center-line.

In a first step, our own grids have been built around the two geometries with the ICEM Hexa meshing tool. These structured grids have an H-H topology to fit between the model at zero incidence and the far field and a O topology around the sting, Figure 26-1 (a). The wing is described by 165 points along the x direction and 93 points in the spanwise direction. Preliminaries computations allowed to set a local refinement in the upper blocks in order to better resolve the separated region, Figure 26-1 (b). The wing is then described by 281 points in the upper block and 165 points in the lower block along the x direction and 97 points in the spanwise direction.

(a) Original Grid   **(b) Patched Grid**
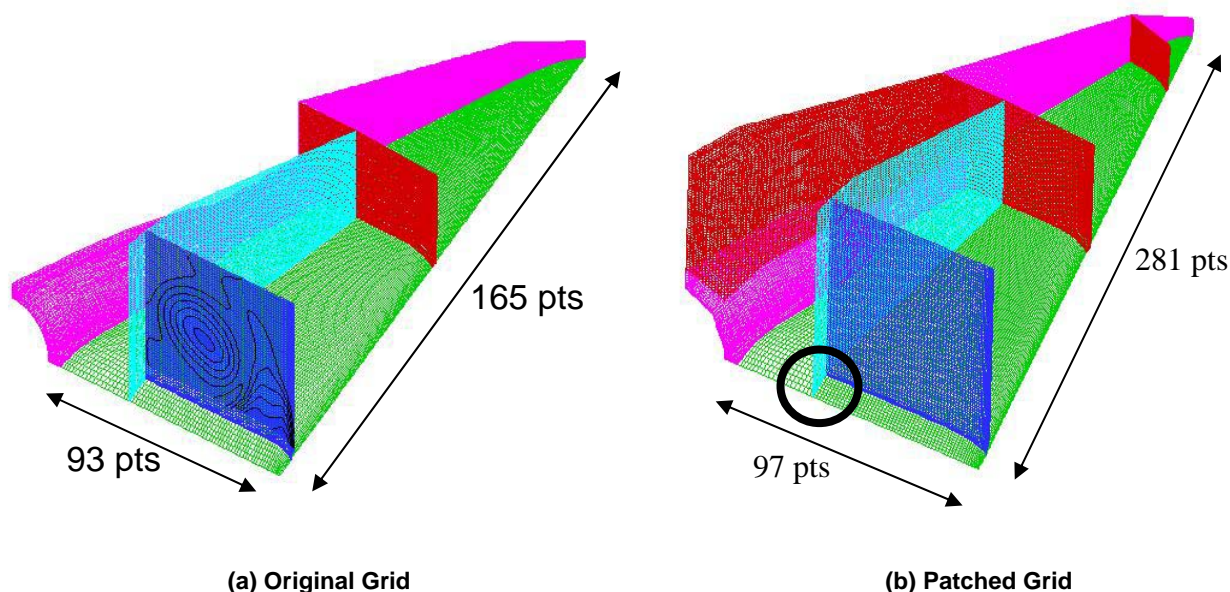
Figure 26-1: Structured Grids.

In a second step, common grids generated by W. Fritz from EADS-M Germany have been used to complete the comparisons [26-5]. These two kinds of grid are noted PG for patched grid and CG for common grid.

26.3.2   Computational Method

The set of ordinary differential equations in time is solved by means of the implicit backward Euler scheme. The resolution of the turbulence equations are not coupled to the others and the Harten's parameter is set equal to a small value (0.05) in order to achieve the needed accuracy. The 2nd order scheme of Jameson is used to compute the convective fluxes. The combination of the latest with the backward Euler resolution ensures a sufficient robustness. Due to the fact that only the steady state is of interest the different equations are solved by a local time stepping approach based on the maximum allowable time step for each cell in the current

investigations (CFL = 5.0). Since the convergence speed-up is an important issue, a multi-grid technique has been used to improve the convergence rates: 2 levels with a V cycle and two sub-iterations on the coarse grid.

Different turbulence models have been used. At low angle of attack when the flow is attached the Wilcox k-ω turbulence model is preferred. At higher incidence when the flow is massively separated the Spalart-Allmaras turbulence model with rotational correction (SARC) is better adapted.

26.3.3   Aerodynamic Conditions

Computations have been performed as closely as possible to experimental conditions. The Mach numbers range from 0.2 to 0.4. As a result, the associated Reynolds numbers based on the root chord of the model are in the order of 2 to 6 millions.

Three interesting incidences have been selected for the computations: α = 13, 19 and 23°. While at an incidence of 13° the flow remains attached for the 'medium' leading edge, it is separated for the 'sharp' leading edge. At 19° of incidence, the vortex breakdown appears close to the trailing edge and at 23°, the vortex breakdown should be located in the vicinity of the mid chord.

Initial conditions are those of the uniform flow.

A single processor NEC SX-8R (2.2 GHz) has been used for the RANS simulations. The 'patched grid' associated with the SARC model requires a memory of 3900 Mo and the 'common grid' associated with the same model requires 8100 Mo.

26.3.4   Sharp Leading Edge Results

The flow behaviour is analysed from the streamlines and the pressure distributions on the wing surface, the axial vorticity or total pressure losses in some planes and 3D visualizations. Comparisons between our simulations and Luckring's database [26-6] are mainly performed on the pressure distributions.

At an incidence of 13° the surface pressure distribution shown in Figure 26-2 (a) illustrates the separation of the flow along the leading edge. The fluctuations of pressure between the primary vortex and the leading edge indicate that a secondary vortex takes place around the mid chord. This phenomenon is only simulated with the Patched Grid, showing that the grid refinement is important.
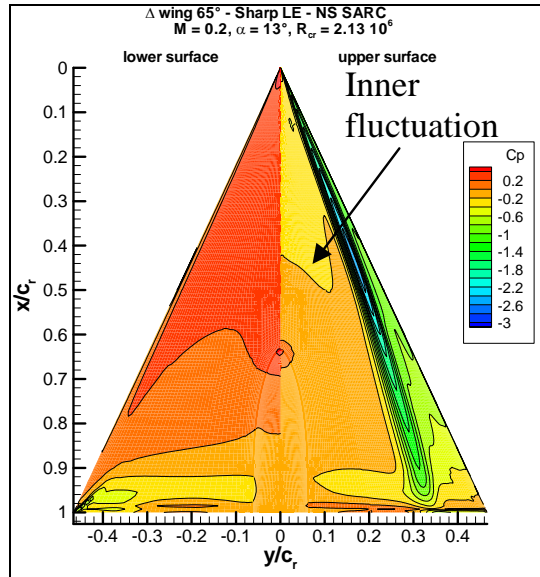
(a) Surface Pressure Distribution for PG
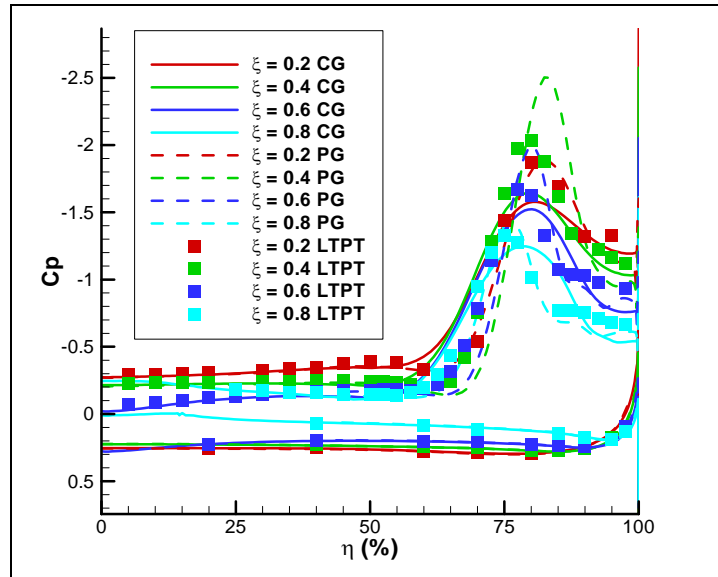
(b) Comparison CFD Results and LTPT Data

Figure 26-2: Sharp Leading Edge Results – α = 13°.

A comparison between the results obtained with the different grids at the same aerodynamic conditions and LTPT data is plotted in Figure 26-2 (b). The common grid (CG) provides an expanded weak primary vortex. The patched grid (PG) pressure distribution seems to be in a better accordance with the experimental values. Nevertheless at the second station ($\xi = 0.4$) the suction peak is over estimated. The flow along the vortex axis accelerates up to the second station but it is not so intense in the experiments. A very small variation of pressure, noted as 'inner fluctuation' is visible on surface pressure distribution. This fluctuation is also observed in the inner part at the first station. This vanished phenomenon is inherent to the type of leading edge and it will be shown in the following that the same phenomenon can be observed for the 'medium' leading edge with an amplified intensity, emerging then as an additional inner vortical structure.

At 19° of incidence, Figure 26-3 (a) indicates that the primary vortex becomes stronger. The axial vorticity increases with the incidence along the leading edge and in the vortex core. The fluctuations of pressure observed between the primary vortex and the leading edge indicate the presence of a secondary vortex. The secondary vortex is developed all along the primary vortex. The phenomenon is clearly visible for all results at each station. The pressure distributions obtained with the different grids are in better accordance in this configuration. The secondary vortex onset moves upstream towards the apex as incidence increases. An analysis of velocity field shows that the vortex breakdown is located close to the trailing edge at $x/c_r = 0.89$.

(a) Surface Pressure Distribution for CG

(b) Comparison CFD Results / LTPT Data
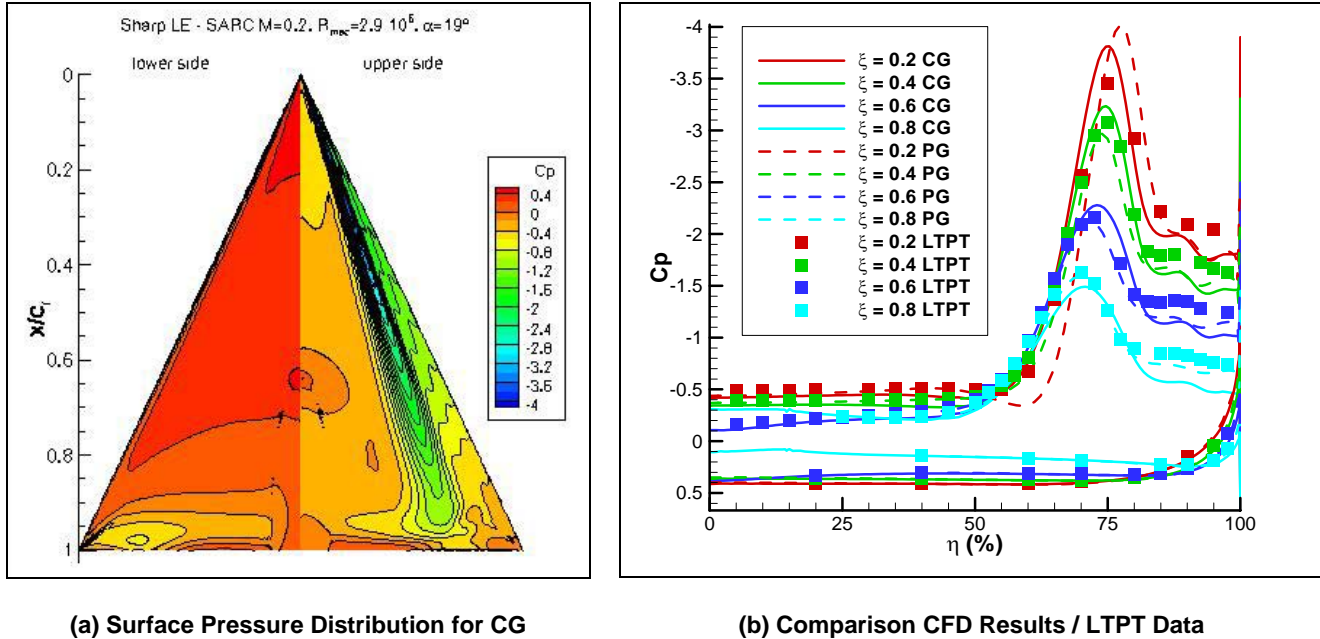
Figure 26-3: Sharp Leading Edge Results – α = 19°.

For a higher incidence (23°), the intensity of the suction peak keeps on rising up (Figure 26-4 (a)). The analysis of the velocity field shows that the vortex breakdown is located at $x/c_r = 0.82$ for the common grid and 0.75 for the patched grid, Figure 26-4 (b). The location of the primary vortex breakdown moves upstream as the incidence increases. Figure 26-5 (a) shows the axial velocity distribution in a plane parallel to the wing at $\Delta z/c_r = 0.0034$. The primary vortex is not visible in this plane but it is marked by a dashed line. The secondary vortex core is not very intense before the emergence of a negative velocity area. The secondary vortex breakdowns in the rear part of the wing ($x/c_r = 0.9$). The streamlines are plotted in Figure 26-5 (b). The secondary vortex breakdown pointed out in the previous figure generates a reverse flow above the rear part of the wing between the attachment and the separation lines.
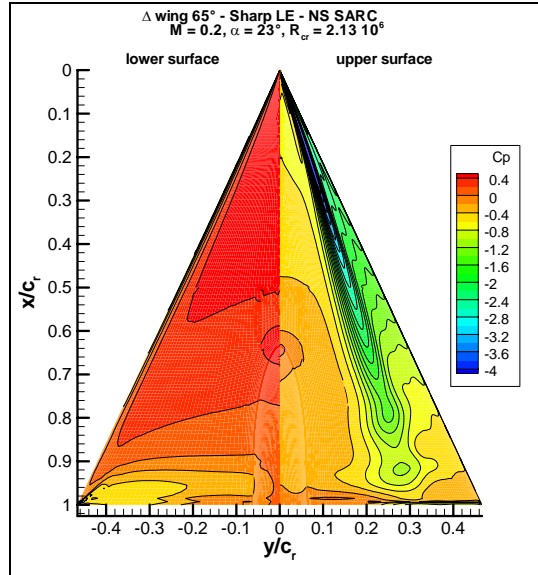
(a) Surface Pressure Distribution
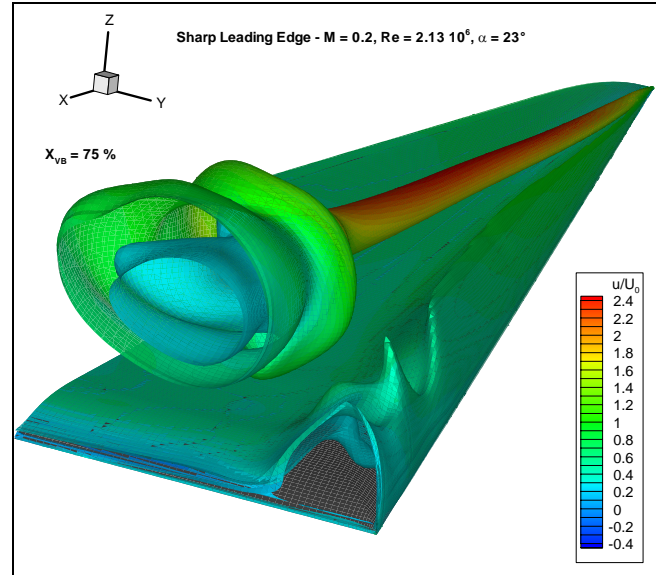
(b) Visualization of the Vortex Breakdown

Figure 26-4: Sharp Leading Edge Results for PG – α = 23°.
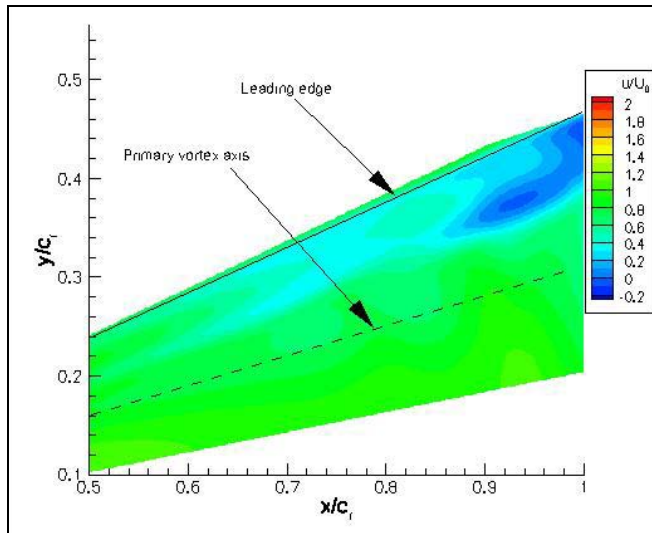
(a) Parallel Plane Δz/c_r = 0.0035
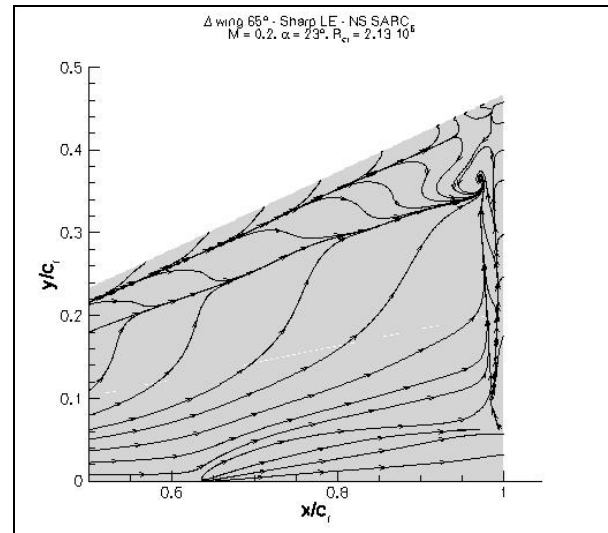
(b) Streamlines

Figure 26-5: Velocity Distribution and Streamlines – Sharp Leading – α = 23° – PG.

The comparison of the results relative to the two grids is presented in Figure 26-6. At this incidence, the pressure distributions are quite similar in space and intensity.
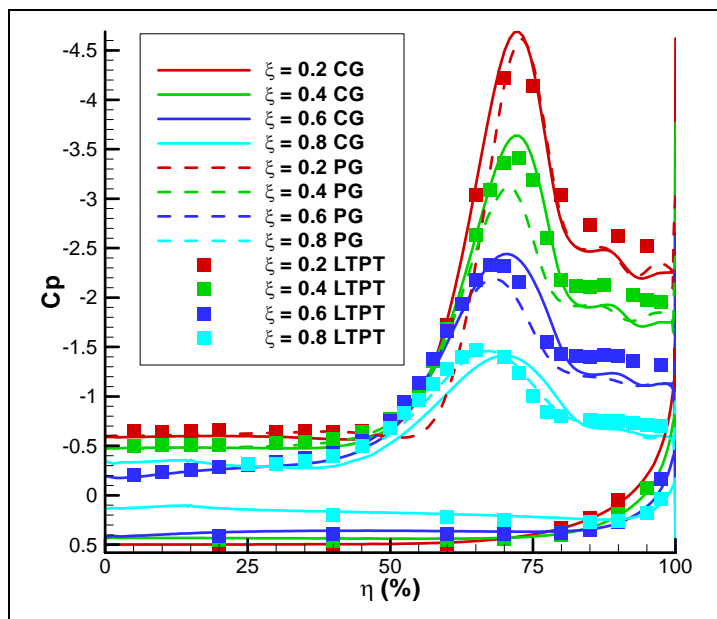
Figure 26-6: Comparison CFD Results / LTPT Data.

A higher incidence has been computed in order to observe the behaviour of the vortex breakdown since its axial displacement is not quite important between 19 and 23°. Figure 26-7 shows the surface pressure distributions at $\alpha = 28°$. The analysis of the velocity field indicates that the position x/c_r of the vortex breakdown is now lower than 0.5. In these conditions, it is very difficult to predict an accurate position of vortex breakdown when this phenomenon moves in the order of 30 % for a range of 5°. From the experiments conducted in open and closed sections, it has been observed that the sensitivity to the far field conditions must be important for this feature.
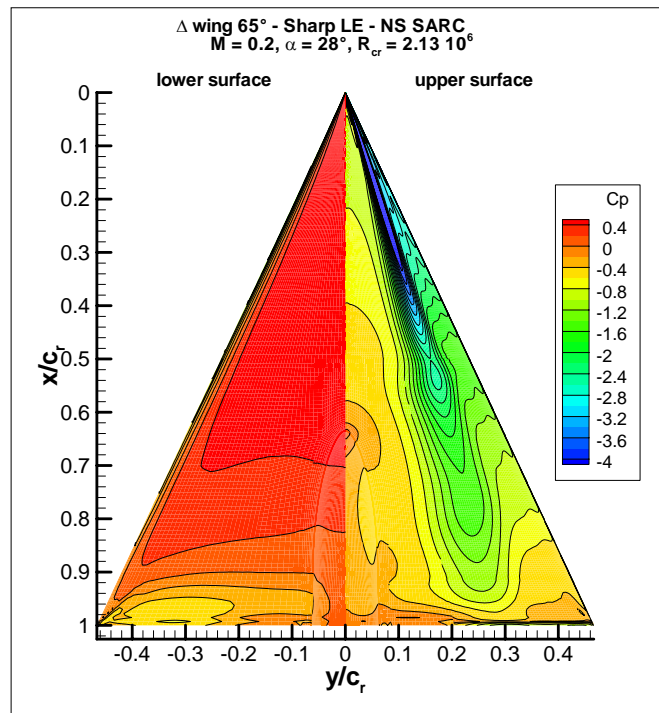
Figure 26-7: Surface Pressure Distribution for the Sharp Leading Edge – PG – α = 28°.

Additional simulations have been carried out at low incidence in order to get further insight to the primary vortex generation mechanism. Most significant results are presented for α = 8°. Figure 26-8 highlights the streamlines in the apex area. As mentioned before, even at very low incidence the flow separates along the leading edge. Although the axial vorticity magnitude is higher in the fore part than in the rear part of the wing, the shear layer is pulled down on the upper surface and generates a unique vortex. Reattachment is observed very close to the leading edge (Figure 26-9 (a)). On and after the second station, the shear layer goes up and supply the primary vortex located further inboard (Figure 26-9 (b), (c) and (d)).
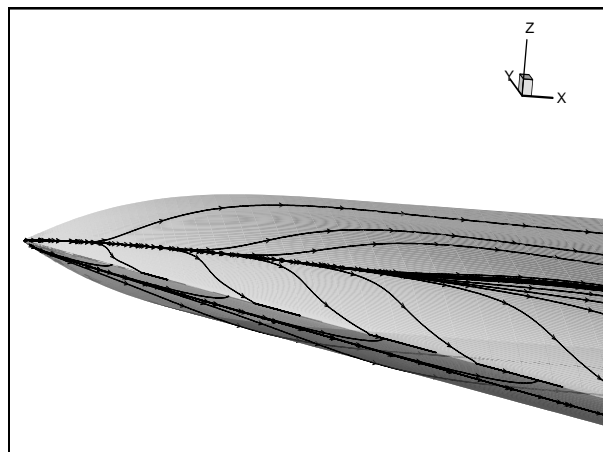
Figure 26-8: Streamline at the Apex of the Sharp Leading Edge – α = 8° – CG.

(a) ξ = 0.2

(b) ξ = 0.4

(c) ξ = 0.6

(d) ξ = 0.8
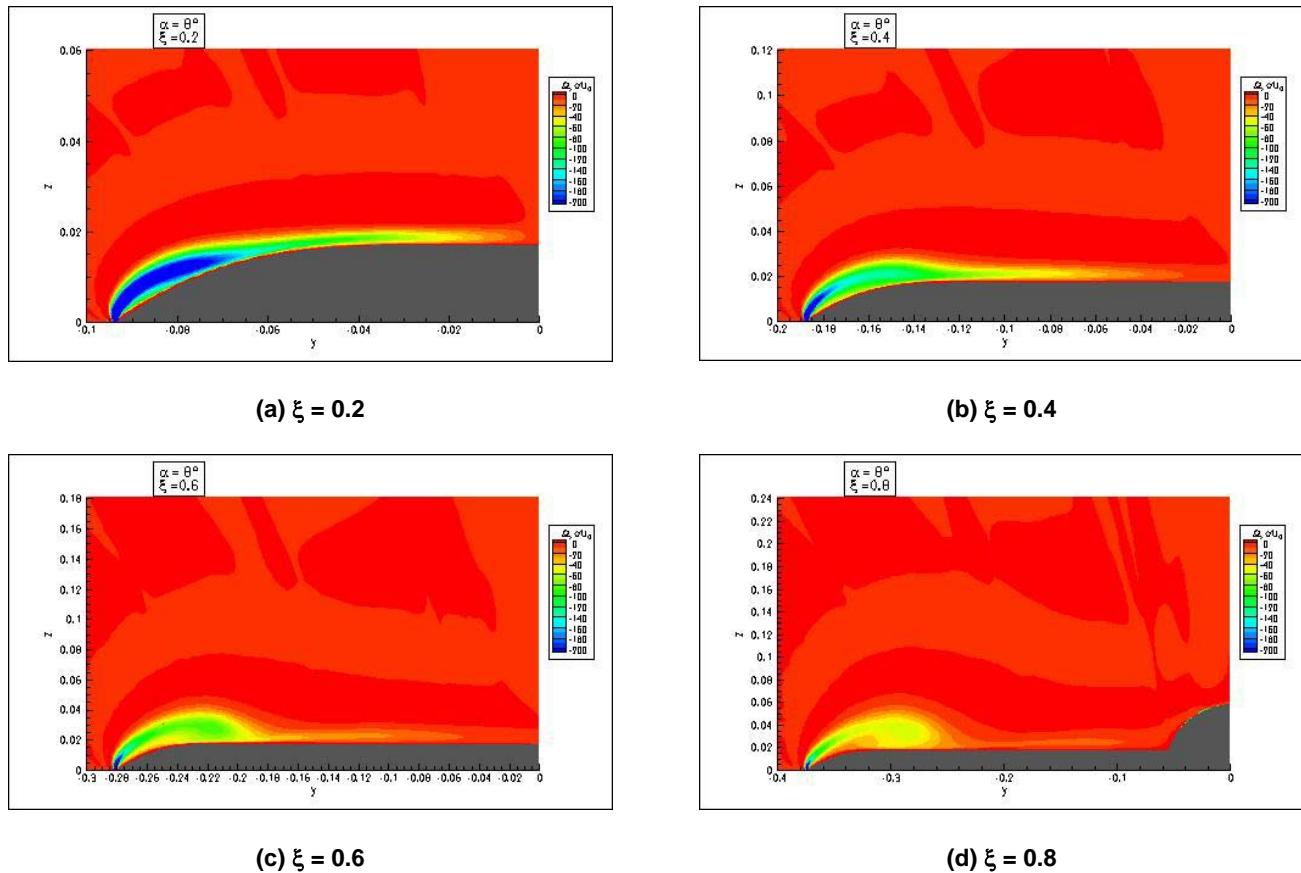
Figure 26-9: Axial Vorticity around the Sharp Leading Edge – CG – α = 8°.

26.3.5   Medium Leading Edge Results

For the 'medium' configuration, the computations are restricted to α = 13, 19 and 23°. As computations carried out with the common grid are relative to higher Mach and Reynolds numbers, no comparison is made between the different grids.

The effect of the turbulence model (SARC and Wilcox k-ω) has been studied in the case of α = 13°. The Figure 26-10 (a) shows the surface pressure distribution. The separation onset takes place at $x/c_r = 0.3$. A comparison of pressure distributions is plotted in Figure 26-10 (b). For this configuration, the SARC model generates a weaker primary vortex than with the k-ω model. The pressure fluctuations located between the primary vortex and the leading edge indicate that a secondary vortex is present at the third and fourth station with the k-ω turbulence model. So, the two equations model is better adapted when the flow is attached on an important part of the wing.
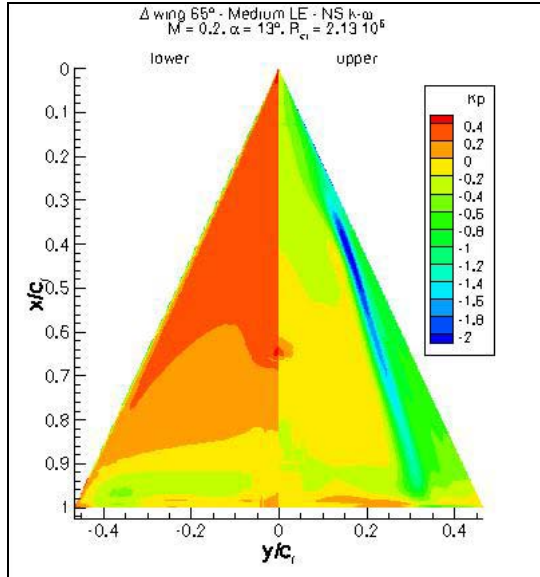
(a) Surface Pressure Distribution
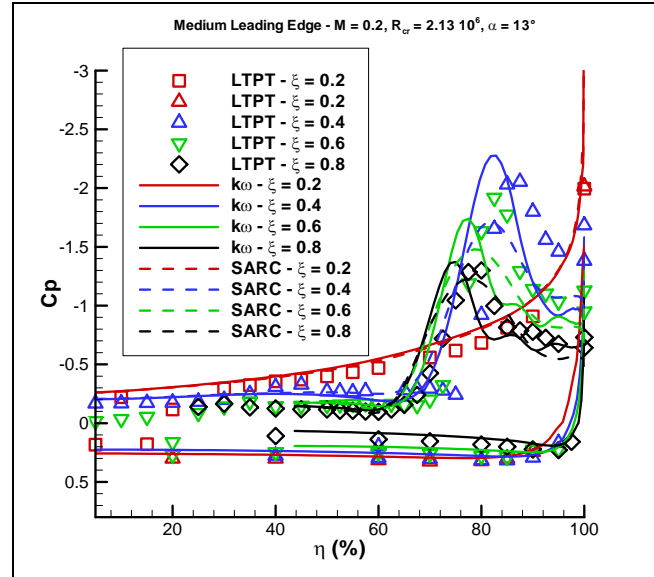
(b) Comparison CFD Results / LTPT Data

Figure 26-10: Effect of Turbulence Model for the Medium Leading Edge – α = 13° – PG.

Within this study, another aerodynamic condition is considered (M = 0.4, R_{cr} = 4 x 10^6) for the same incidence. The surface pressure distributions obtained with the Wilcox k-ω turbulence model fit quite well with Konrath's experiments [26-8] (Figure 26-11 (a) and (b)). This configuration is very interesting for mainly two reasons: the primary vortex appears at mid chord and an inner vortex is observed. As the Mach number increases the flow remains attached on a more important part of the wing. The separation appears at x/c_r = 0.5 at M = 0.4 (Figure 26-11 (b)) against x/c_r = 0.3 at M = 0.2 (Figure 26-10 (a)). A variation of pressure is observed in the central part of the wing for the two configurations. It is more important at M = 0.4 because the inner vortex is confined between the fairing and the primary vortex.

(a) Konrath's Experiment – PSP Measurement   **(b) CFD Result – CG**
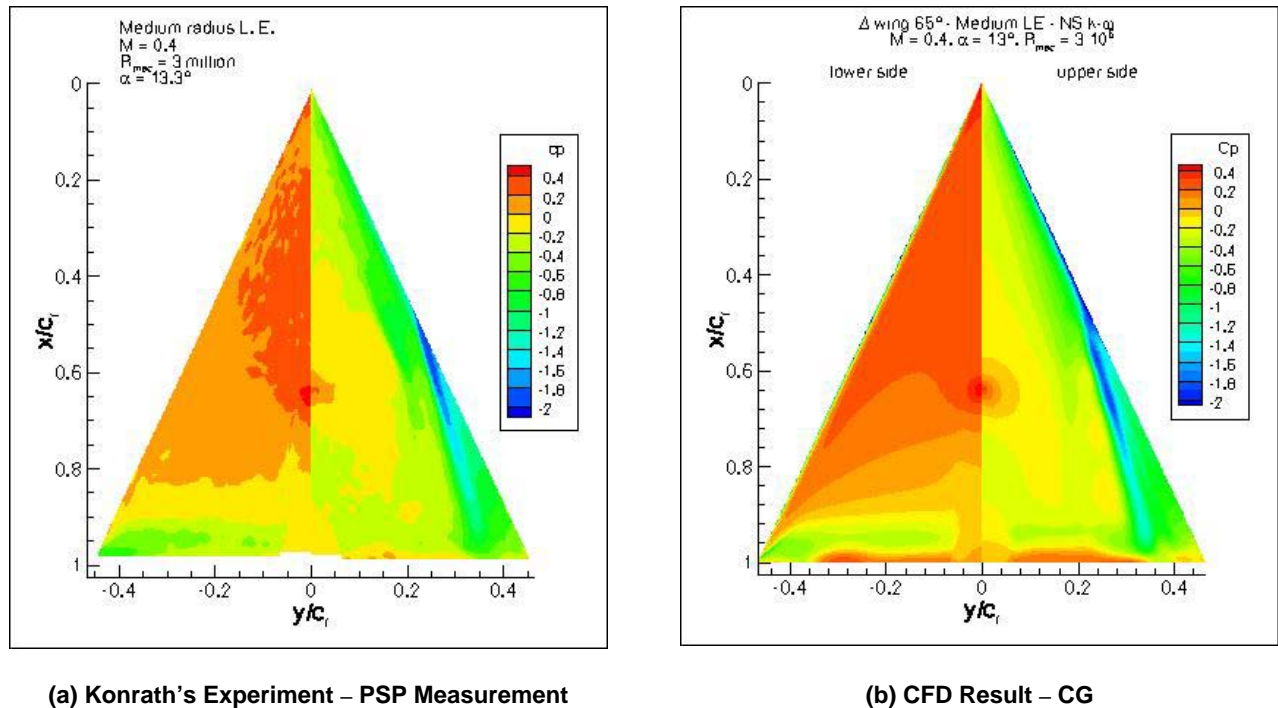
Figure 26-11: Medium Leading Edge Results – M = 0.4, R_{mac} = 3 x 10^6, α = 13°.

A detailed comparison of pressure distributions is plotted in Figure 26-12. The inner vortex appears earlier in experiment than in computation and the computed inner vortex exhibits a lower intensity. The spatial extensions of the primary vortex are similar but not exactly located at the same place. The difference indicates that the primary vortex appears earlier in the computation.
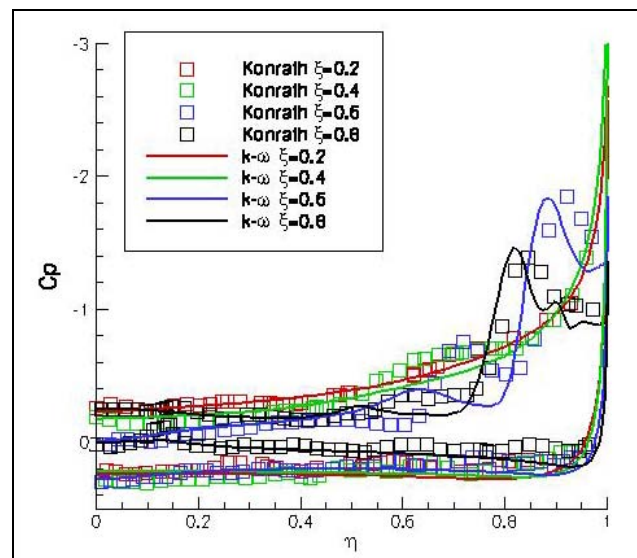
Figure 26-12: Comparison Pressure Distributions – Medium Leading Edge – M = 0.4, R_{mac} = 3 x 10^6, α = 13° – CG.

The Figure 26-13 reveals the topology of the flow by plotting the total pressure loss in different planes above the upper surface. The inner vortex is not very strong but its size is quite large and expands towards the trailing edge. The strong primary vortex starts in the vicinity of mid chord and induces a secondary vortex further downstream.
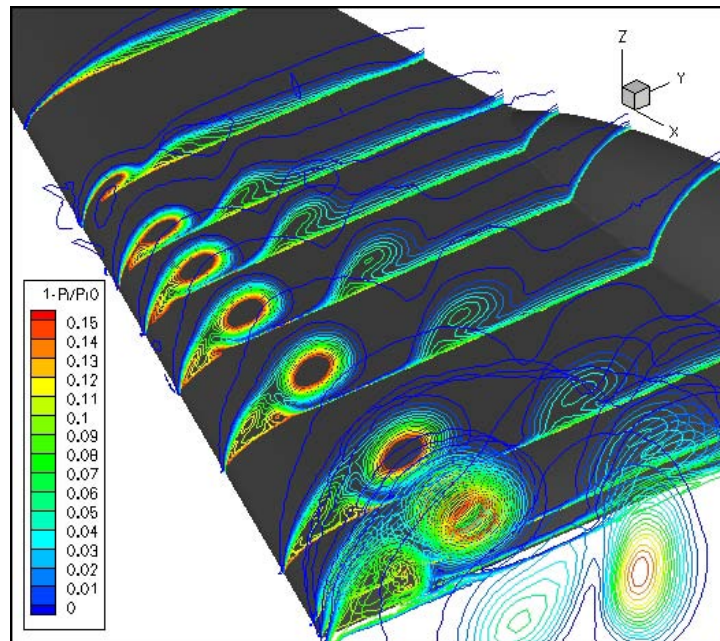
Figure 26-13: Medium Leading Edge Results – M = 0.4, R_{mac} = 3 x 10^6, α = 13° – CG.

For the incidences of 19 and 23°, the SARC turbulence model has been used to compute the solutions since the flow is massively separated. Figure 26-14 shows the surface pressure distribution for the two incidences. The medium leading edge results are quite similar to the sharp leading edge results, excepted in the fore part. Small variations of pressure are observable in the area close to the apex. Figure 26-15 shows the axial vorticity close to the apex for these two incidences. The flow remains attached for x/c_r less than 0.1. The separation moves towards the apex as the incidence increases. The core of the primary vortex is clearly defined and is characterised by high velocity ratio greater than 2. At an incidence of 23° the analysis of the velocity field shows that the primary vortex breakdown appears approximately at the same place for the two leading edges : x/c_r = 0.76 for the medium leading edge against x/c_r = 0.75 for the sharp leading edge. Since the location of the primary vortex is very sensitive to the Mach and Reynolds numbers, the comparison of results when far field conditions are not exactly identical can be misleading.

(a) α = 19°
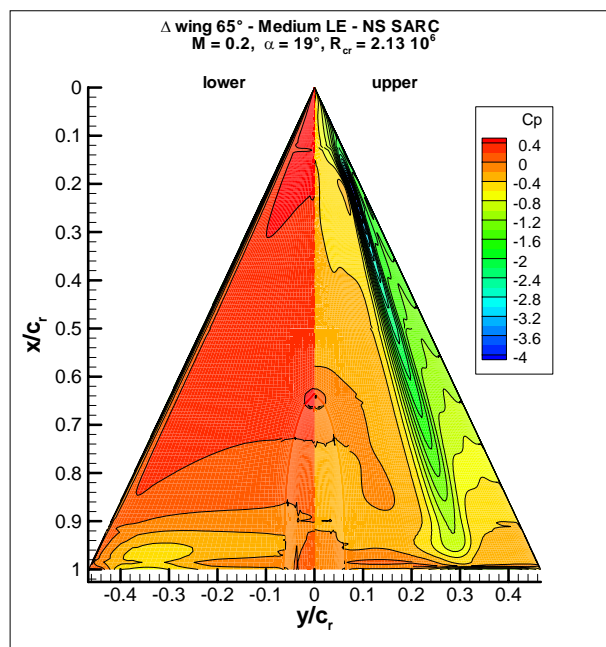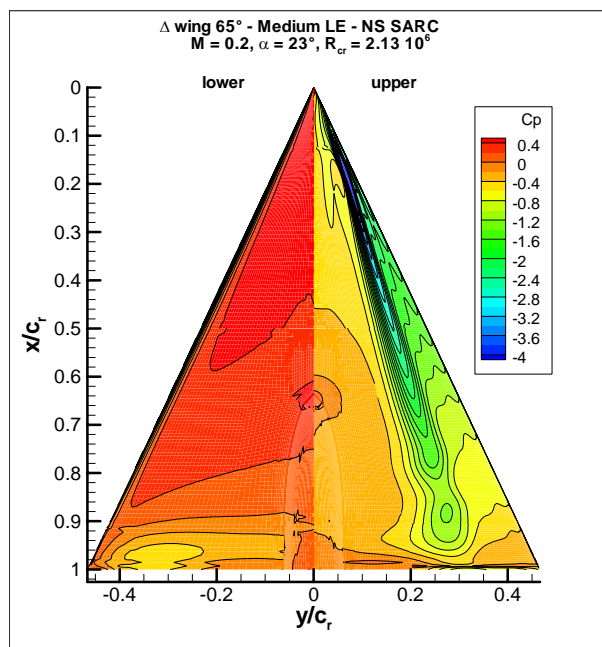
(b) α = 23°

Figure 26-14: Medium Leading Edge – Surface Pressure Distributions – PG.

(a) α = 19°
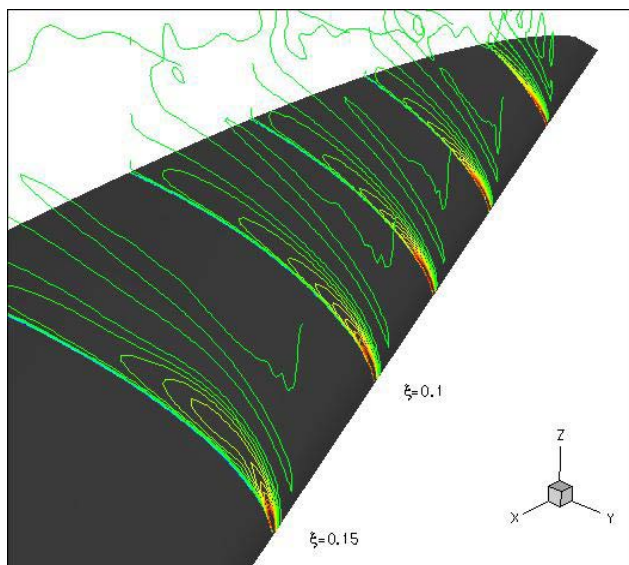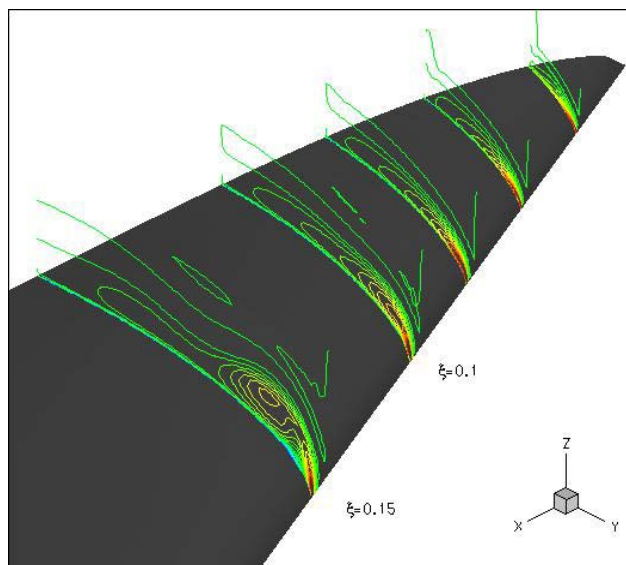
(b) α = 23°

Figure 26-15: Medium Leading Edge Results – Axial Vorticity – PG.

26.4 UNSTEADY APPROACH

In the way to capture the unsteady phenomena present in the rotational flow over slender delta wings, two unsteady computations have been carried out. These computations concern the sharp leading-edge configuration for two different Mach numbers: M = 0.4 and M = 0.8. The Reynolds number based on the mean aerodynamic chord is $R_{mac} = 2 \times 10^6$ and the angle of attack is $\alpha = 25.5°$ for the two computations.

All the computations presented in this section have been performed using the FLU3M solver [26-9], developed by ONERA. This code solves the compressible Navier-Stokes equations on multiblock structured grids. The accuracy of the solver for DNS, LES and hybrid RANS/LES has been assessed in various applications including flows around a two-dimensional airfoil in near stall conditions [26-10], after-body flows [[26-11] – [26-13]], cavity flows [26-14] and synthetic jets in a cross flow [[26-15] – [26-16]].

26.4.1 Computational Method

The second order AUSM scheme [26-17] is used for the discretization of the Euler fluxes. The set of equations is advanced in time using the second-order accurate backward implicit scheme of Gear [26-18]. Moreover, 4 sub-iterations are used in the sub-iterative Newton process and the time step is set equal to 5.0×10^{-7} s.

Hybrid RANS/LES approaches [26-19] represent a credible alternative to RANS and LES computations to improve the description of the rotational flow over slender delta wings at a reasonable cost by taking into account most of the flow unsteadiness. The main idea of these methods is to model the turbulent structures in the attached region of the flow and to solve the large scale structures elsewhere. The global hybrid method used in the current investigation is the EDDES method [26-20], based on the Spalart-Allmaras equation [26-21], which is an evolution of the DDES method [26-22].

The structured grid used in the current study has been generated with the ICEM Hexa meshing tool. The topology is O-H and the number of points is 21×10^6. Moreover, as it is depicted in Figure 26-16, the mesh is locally refined in the region of the rotational flow on the upper surface of the VFE-2 wing.
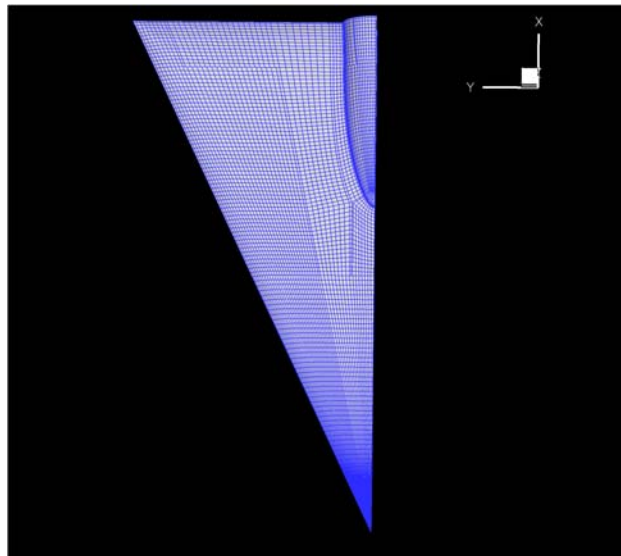
Figure 26-16: Mesh for Unsteady CFD on the Suction Side of the VFE-2 Delta Wing (Only 1 Point Every 4).

26.4.2 Study of the Instantaneous Flow

The aim of this section is to present the instantaneous flow developing over the sharp leading edge configuration for the two Mach numbers. The turbulent structures can be educed by plotting an iso-surface of the Q criterion defined as follows [26-23]:

$$Q = -\frac{1}{2}(S_{ij}S_{ij} - \Omega_{ij}\Omega_{ij})$$

where S and Ω denote respectively the strain and rotation tensors.

This is a useful quantity to highlight the flow regions where the turbulence is resolved. Thus, an iso-surface of $Q = 1000 \times \frac{c}{U_\infty}$ flooded by the non-dimensional longitudinal velocity $\frac{u}{U_\infty}$ is shown in Figure 26-17 for the two considered Mach numbers.
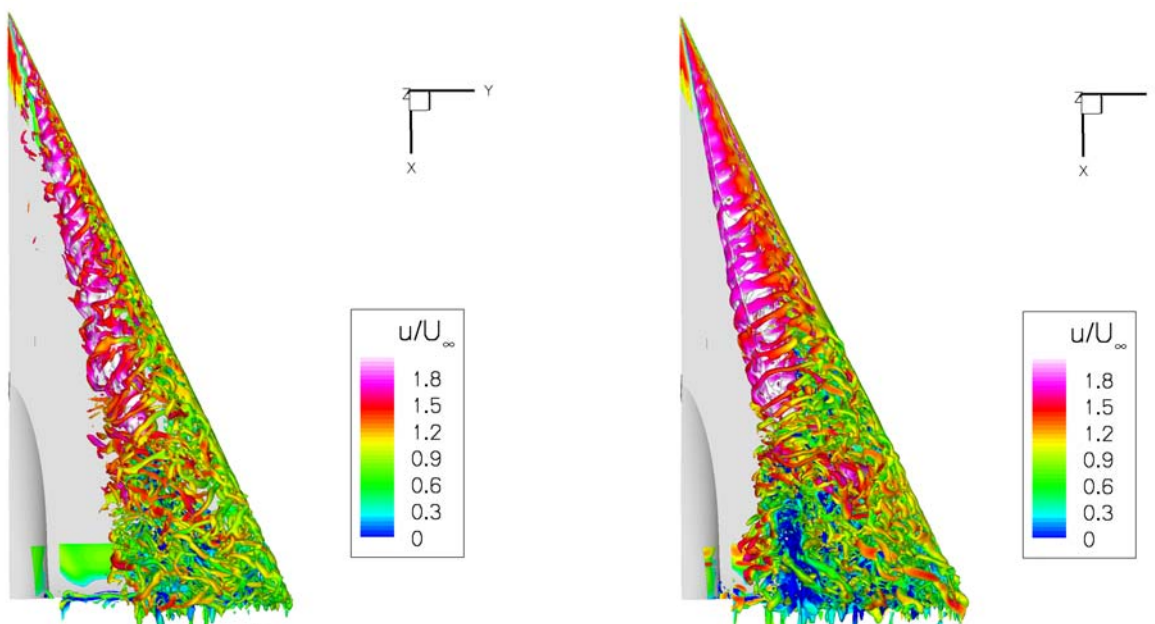
Figure 26-17: Representation of the Flow Unsteadiness (Left: M = 0.4; Right: M = 0.8).

Similarities in the two flows clearly appear in this figure. One can observe the formation of the leading-edge vortex, denoted by the intense acceleration of the longitudinal flow. This vortex undergoes an abrupt disorganisation, known as vortex breakdown and which is identified by a sudden appearance of a stagnation flow (appearing in blue in this figure). Moreover, small-scale structures (in comparison with the length-scale of the leading-edge vortex) are visible in the shear layer emanating from the leading-edge all around the vortex. These structures are identified as being the Kelvin-Helmholtz structures.

Both flows exhibit some differences. The first one is the shape of the leading-edge vortex, which is flatter and more extended in the M = 0.8 case than in the other case. Moreover, the reverse flow, consequence of the vortex breakdown is more extended and inboard in the transonic case than in the subsonic one. These observations will be pursued in the study of the time-averaged flow.

26.4.3   Study of the Time-Averaged Flow

The two computations have been time-averaged on a period of 5 T_c, where T_c is the time-scale defined by $T_c = \dfrac{c}{U_\infty}$. It represents a duration equals to 9.8 ms for the transonic case and 19.6 ms for the subsonic one.

The distributions of the pressure coefficient C_p on the suction side of the VFE-2 delta wing for the two computational cases are represented in Figure 26-18 and are compared to the experimental data.
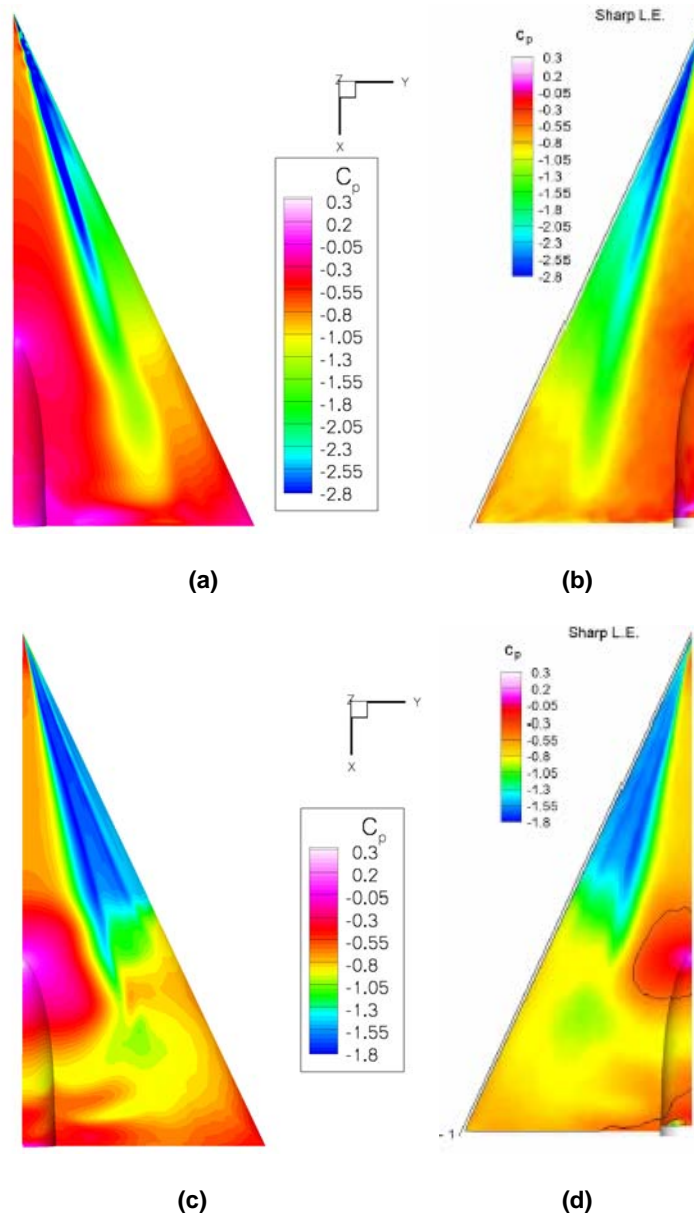
Figure 26-18: Distribution of C_p on the Suction Side for the M = 0.4 Case
((a): Numerical; (b): Exp.) and M = 0.8 Case ((c): Numerical; (d): Exp.).

As depicted in this figure, a very good agreement with the experimental PSP data of Konrath et al [26-8] is obtained for the two computations. Note that the color map is not quite identical between the experimental and numerical representations but the levels of C_p are quite identical. For the subsonic case, a large low-pressure area is predicted on the suction side, this region being the foot print of the leading-edge vortex. The distribution of C_p is somewhat different for the transonic case. In fact, the first observation which can be made is that the low-pressure peak is much weaker in this case than in the previous one. Moreover, the foot print of the leading-edge vortex is more inboard and a second low-pressure peak is observed between the one associated to the primary vortex and the leading-edge. Furthermore, an increase of the Mach number leads to a shortening of the depression. In fact, only a small region of low C_p is present in the last half part of the delta wing.

In order to understand these observations, Figure 26-19 shows contours of $\dfrac{u}{U_\infty}$ in several planes perpendicular to the surface of the VFE-2 delta wing.

x/c_r = 0.6

x/c_r = 0.7

x/c_r = 0.75
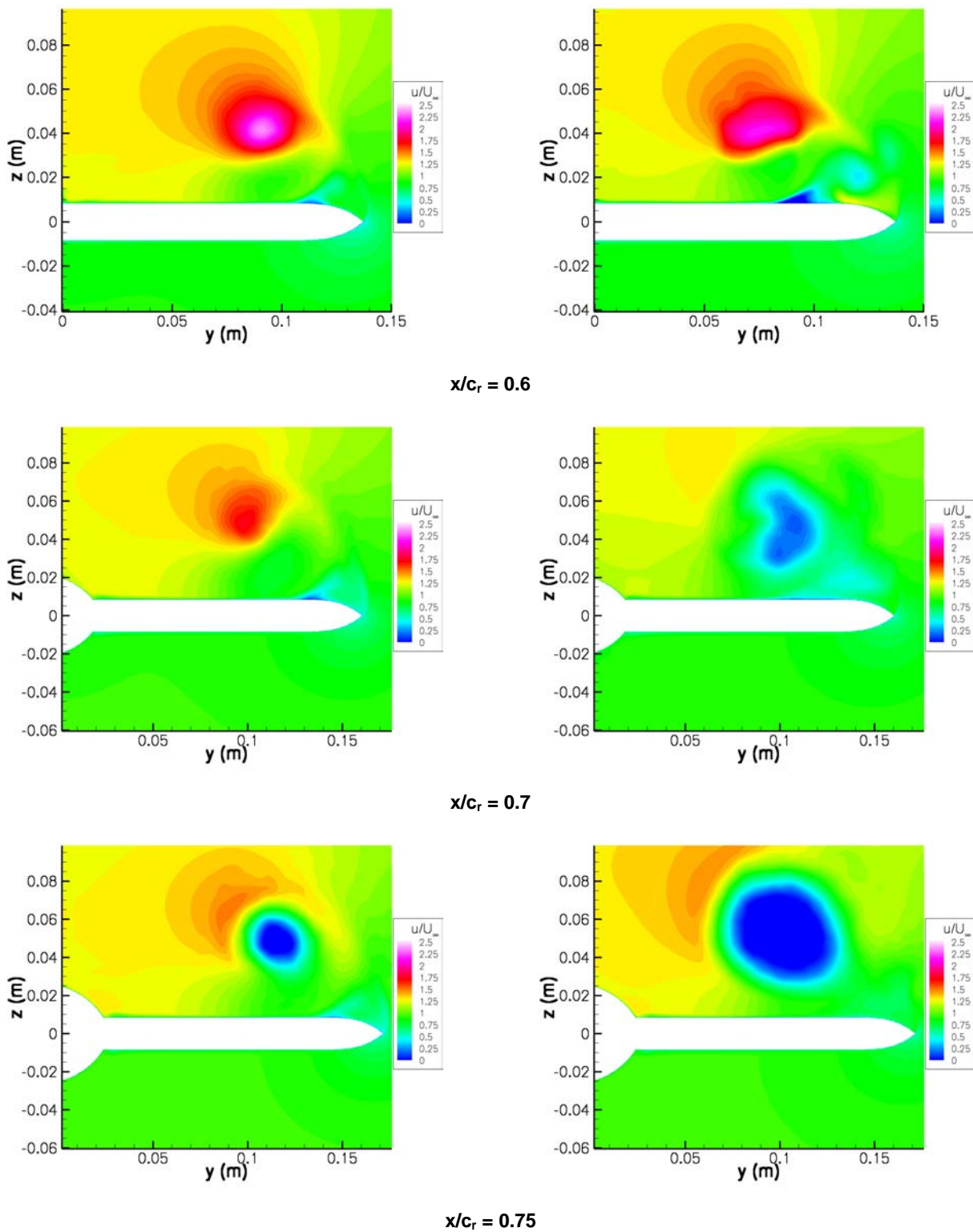
**Figure 26-19: Evolution of the Longitudinal Velocity in Several Planes
Perpendicular to the Surface of the Wing (Left: M = 0.4; Right: M = 0.8).**

The observation of the longitudinal velocity at $x/c_r = 0.6$ confirms that an increase of the Mach number leads to a modification of the shape of the leading-edge vortex. In the transonic case, the vortex is flatter and nearer to the surface of the wing than in the subsonic case. These observations are in agreement with experimental results of Squire [26-24] and Erickson [26-25]. Moreover, the acceleration of the longitudinal flow in the vortex core is more important in the subsonic case ($\frac{u}{U_\infty}$ reaches 2.5) than in the transonic one, where the maximum of the non-dimensional velocity equals to 2.2 (resulting in a local Mach number equals to 1.96). Another important feature of the flow in the M = 0.8 case at $x/c_r = 0.6$ is the intense second separation just outboard of the primary vortex. This is caused by the embedded cross-shock waves which occur between the primary vortex and the surface of the delta wing [26-26]. This second separation is the cause of the second low-pressure peak observed in the previous figure. Moreover, it appears that the vortex breakdown occurs earlier in the transonic case as it is illustrated by the reverse flow at $x/c_r = 0.7$. Note that this time-averaged position is in a good agreement with stereo-PIV observations of Schröder et al [26-27]. Parallel to this observation, a strong leading-edge vortex is still present at this position for M = 0.4. The vortex breakdown occurs further downstream, as it is illustrated by the reverse flow at $x/c_r = 0.75$. Furthermore, one can observe at this position the acceleration of the flow between the sting and the region of reverse flow. In fact, the non-dimensional velocity reaches 1.5 in the two cases, resulting in a supersonic flow (M = 1.1) in the M = 0.8 case.

The transonic flow over delta wing is the place of several shocks waves. The interactions between the shock waves and the primary vortex could explain the difference in the time-averaged vortex-breakdown localization. The acceleration of the flow and the variation of the section beneath the primary vortex induce the formation of shocks (see Figure 26-20), the previously evocated cross-flow shocks waves. But some shock waves are also observed in the region of the trailing edge, the rear/terminating shock waves.
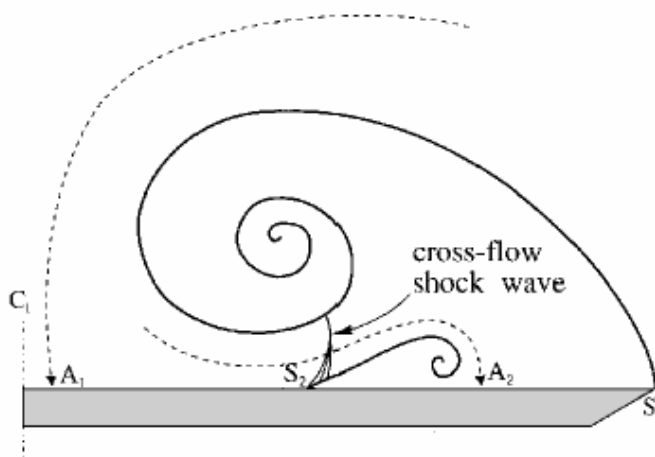
Figure 26-20: Representation of the Cross-Flow Shock Waves (from [26-26]).

The Figure 26-21 presents an isosurface of $Q = 400 \times \frac{c}{U_\infty}$ in the time-averaged flow flooded by C_p and numerical schlieren-like visualization (isocontours of $\|grad(\rho)\|$) in the symmetry plane.
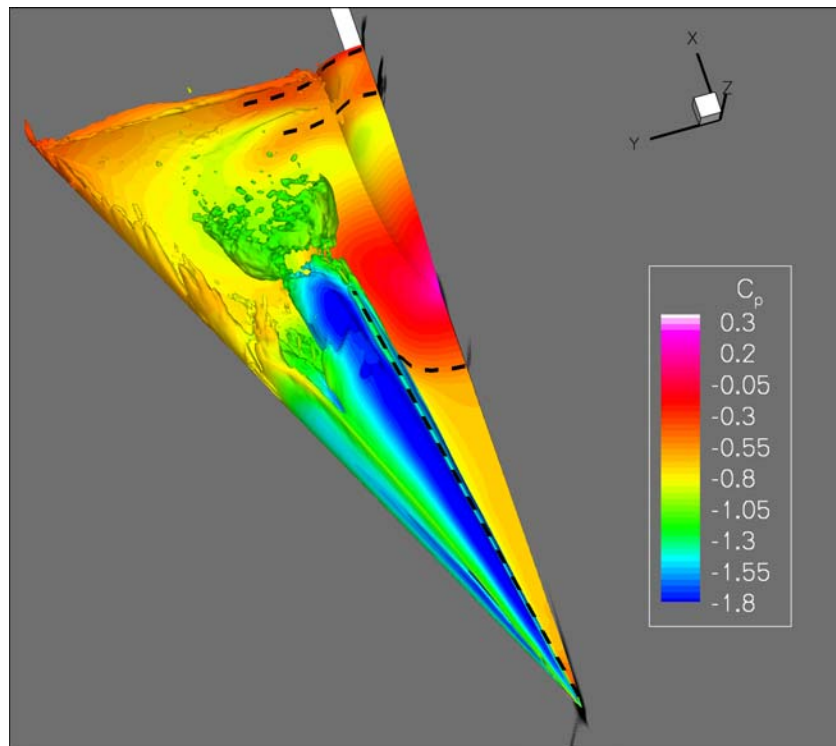
Figure 26-21: Representation of Time-Averaged Flow in the
M = 0.8 Case (the dashed-lines represent the shocks).

This figure highlights the existence of three shocks in the symmetry plane. The first one is located just upstream of the sting ($x/c_r = 0.54$) and is curved in the longitudinal direction (see the shape of the black dashed-line). The occurrence of this shock is imputable to the slowing down of the flow induced by the presence of the sting. Two other shocks are visible, just upstream of the trailing-edge of the delta wing. The one located at $x/c_r = 0.98$ ensures the natural balance of the upper and lower surface pressures. The presence of the shock at $x/c_r = 0.92$ may be caused by the progressive slowing down of the supersonic flow between the sting and the reverse flow downstream from the time-averaged position of the vortex breakdown. The presence of two rear shocks had been underlined in experimental investigations of the transonic flow over delta wings of Elsenaar and Hoeijmakers [26-28] and Houtman and Bannink [26-29].

The interaction of these shocks with the leading-edge vortex can cause a premature vortex-breakdown, in comparison with the subsonic case, as suggested by experimental observations by Donohoe et al [26-26] and Kandil et al [26-30]).

26.4.4 Spectral Analysis

One interest of hybrid RANS/LES methods in comparison with classical RANS computations is the access to the unsteadiness of the flow, as it was suggested in the presentation of the instantaneous flow.

To accomplish this spectral analysis, the temporal evolution of the longitudinal velocity is analysed at two different positions: the first one (probe P_1) in the leading-edge vortex core and the second one (probe P_2) in the reverse flow downstream from the mean vortex-breakdown location (see Figure 26-22).
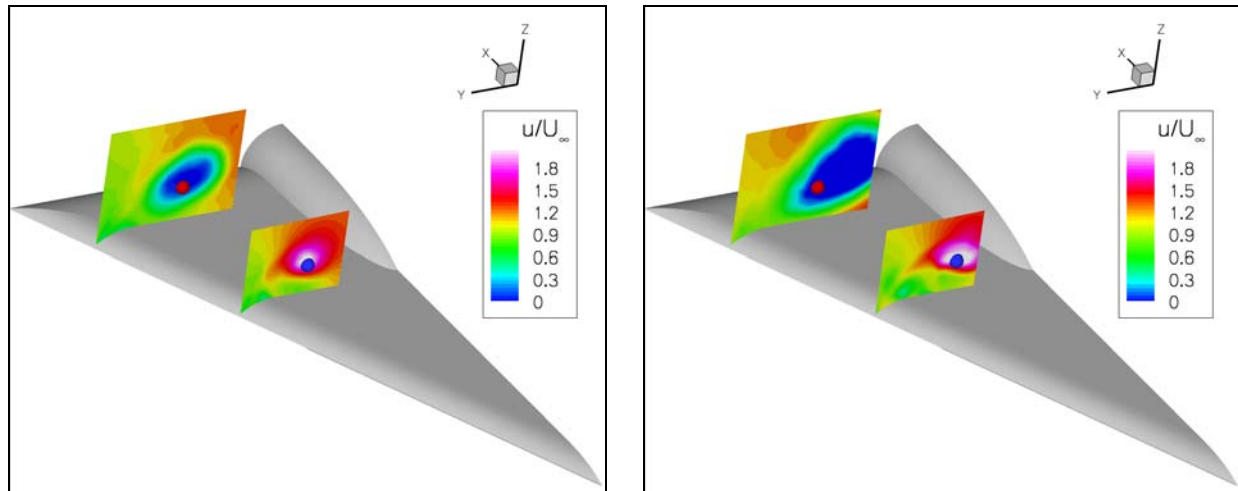
**Figure 26-22: Positions of the Two Probes P₁ and P₂ Relatively
to the Time-Averaged Flow (Left: M = 0.4; Right: M = 0.8).**

The spectral analysis of these signals has been performed using the method of Burg [26-31] and the Power Spectral Density (PSD) is represented in Figure 26-23.
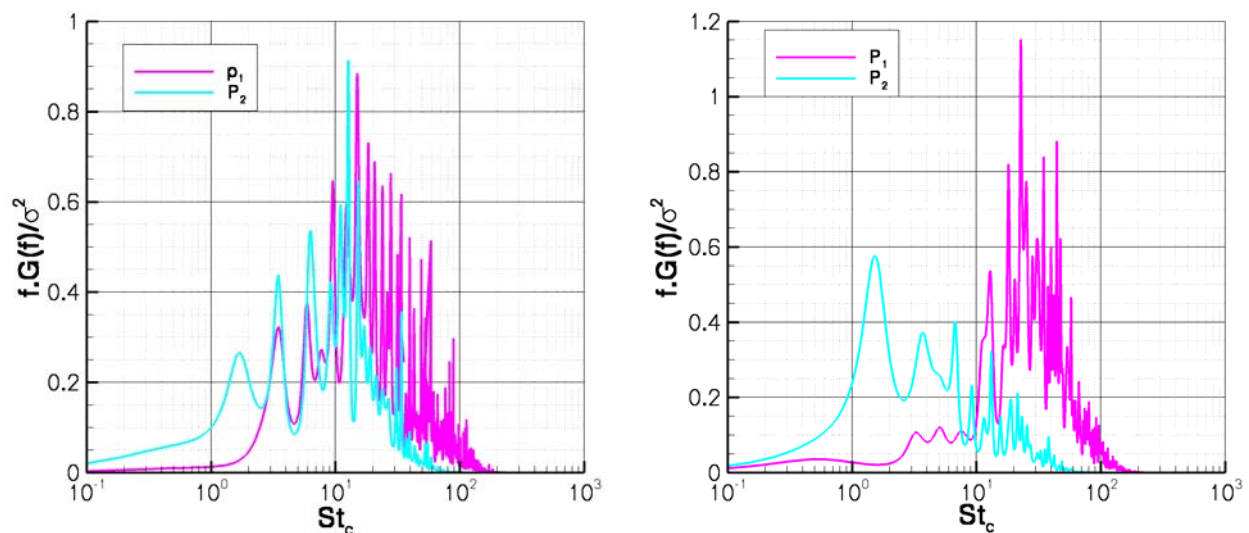
**Figure 26-23: PSD of the Non-Dimensional Longitudinal
Velocity at P₁ and P₂ (Left: M = 0.4; Right: M = 0.8).**

The first observation which can be made is that the two signals exhibit a dominant frequency at the first probe location P_1. This frequency corresponds to $St_c = 16$ in the M = 0.4 case and $St_c = 22$ in the transonic case. Moreover, two peaks at $St_c = 3$ and $St_c = 5$ are also present at this position. These frequencies are usually observed in experimental [[26-32] – [26-33]] and numerical [26-34] investigations and are associated to the Kelvin-Helmholtz instability in the shear layer emanating from the leading-edge.

The PSD at the probe P_2 is somewhat different of the previous one. In fact, a dominant frequency at Stc ≈ 10 is still present in the subsonic case but high-frequency is no more discernable in the transonic case. In spite of this, the two PSD present some similarities. An increase of the amplitude of the peaks at $St_c = 3$ and $St_c = 5$ is observed. Moreover, a new peak appears in the two signals at the non-dimensional frequency Stc = 1.6. Once again, this non-dimensional frequency is experimentally [[26-35] – [26-36]] and numerically [26-37] observed downstream from the vortex breakdown location and is associated with the helical mode instability.

26.5   CONCLUSIONS

The flow over a delta wing equipped with a sharp leading edge at high angle of attack is exceedingly complex, including separated flow, high streamwise curvature and large pressure gradient. Viscosity promotes a secondary vortex and influences the location of the vortex breakdown which is difficult to calculate. In the case of the rounded leading edge the flow can remain attached on an important part of the wing and the separation line is not fixed by the leading edge.

The phenomenon of vortex breakdown observed at high angle of attack can be merely predicted by Euler simulations. The introduction of viscosity is needed to simulate the secondary vortex and its interaction with the primary one. The choice of an adapted turbulence model is important to capture some aspect of the flow especially when the flow remains attached on the fore part of the wing. Since the results of simulations are in relatively good agreement with experimental data for these aerodynamic conditions (low Mach and Reynolds number) steady RANS approach with sufficiently refined grids is sufficient to predict the main features of the flow and determine the general tendency of Reynolds and Mach number effects.

However, this approach reveals several discrepancies with respect to experimental results: location of the vortex breakdown at high incidence due to an under-prediction of longitudinal and streamwise velocity in the vortex core and the secondary vortex is under-estimated. For the case with rounded leading edge, the onset of the primary leading edge separation is shifted upstream in comparison with the experimental data.

The EDDES computations allow the study of the effect of the compressibility on the vortical flow over the sharp leading-edge wing. As it has been presented, the flow over the VFE-2 delta wing in the M = 0.4 and M = 0.8 (α = 25.5°) cases exhibits some common characteristics. In fact, the formation of the primary vortex and the occurrence of its breakdown are observed in the two computations. Moreover, the spectral analysis reveals the existence of the Kelvin-Helmholtz instability in the region of the vortex core and the existence of the helical instability downstream from the time-averaged location of the vortex breakdown in the two computations. In spite of these similarities, these two computations highlight the effect of an increase of the Mach number on the vortical flow which develops over delta wings. In fact, several shocks occur in the M = 0.8 case. Cross-flow shocks lead to the separation of the boundary layer beneath the leading-edge vortex and then induce the second vortex. The presence of three shocks perpendicular to the surface of the VFE-2 delta wing and to the longitudinal direction may cause the premature vortex-breakdown in comparison with the subsonic case.

26.6   REFERENCES

[26-1]   Rediniotis, O.K., Stapountzis, H. and Telionis, D.P.: *Periodic Vortex Shedding over Delta Wing*, AIAA Journal, Vol. 31, No. 9, September 1993, pp. 1555-1561.

[26-2]   Menke, M., Yang, H. and Gursul, I.: *Experiments on the Unsteady Nature of Vortex Breakdown Over Delta Wings*, Exp. Fluids, Vol. 27, No. 3, 1999, pp. 262-272.

[26-3]   Cambier, L. and Gazaix, M.: *elsA: An efficient Object-Oriented Solution to CFD Complexity*, 40th AIAA Aerospace Science Meeting and Exhibit, Reno (USA), January 14-17, 2002.

[26-4]   Cambier, L. and Veuillot, J.: *Status of elsA Software for Flow Simulation and Multidisciplinary Applications*, 46th AIAA Aerospace Science Meeting and Exhibit, Reno (USA), January 7-11, 2008.

[26-5]   Fritz, W.: *VFE-2 Delta Wing Structured Grids*, EADS-M Technical Note.

[26-6]   Chu, J. and Luckring, J.M.: *Experimental Surface Pressure Data Obtained on 65° Delta Wing Across Reynolds Number and Mach Number Ranges*, NASA Technical Memorandum 4645, Langley Research Center, Hampton, Virginia, February 1996.

[26-7]   Le Roy, J.-F., Rodriguez, O. and Kurun, S.: *Experimental and CFD Contribution to Delta Wing Vertical Flow Understanding*, 46th AIAA Aerospace Science Meeting and Exhibit, Reno (USA), January 7-11, 2008.

[26-8]   Konrath, R., Klein, C., Engler, R. and Otter, D.: *Analysis of PSP Results Obtained for the VFE-2 65° Delta Wing Configuration at Sub- and Transonic Speeds*, 44th AIAA Aerospace Science Meeting and Exhibit. Reno (USA), January 9-12, 2006.

[26-9]   Pechier, M.: *Prévisions numériques de l'effet Magnus pour des configurations de munition*, PhD Thesis, 1999.

[26-10] Mary, I. and Sagaut, P.: *Large Eddy Simulation of the Flow around an Airfoil Near Stall*, AIAA Journal, Vol. 40, No. 6, pp. 1139-1146, 2002.

[26-11] Deck, S., Garnier, E. and Guillen, P.: *Turbulence Modelling Applied to Space Launcher Configurations,* Journal of Turbulence, Vol. 3, No. 1, 2002.

[26-12] Deck, S. and Thorigny, P.: U*nsteadiness of an Axisymmetric Separating-Reattaching Flow: Numerical Investigation*, Physics of Fluids, Vol. 19, 2007.

[26-13] Simon, F., Deck, S., Guillen, P., Sagaut, P. and Merlen, A.: *Numerical Simulation of the Compressible Mixing Layer Past an Axisymmetric Trailing Edge*, Journal of Fluid Mechanics, Vol. 591, pp. 215-253, 2007.

[26-14] Larchevêque, L., Labbé, O., Mary, I. and Sagaut, P.: *LES of a Compressible Flow Past a Deep Cavity*, Physics of Fluids, Vol. 14, 2003.

[26-15] Dandois, J., Garnier, E. and Sagaut, P.: *Unsteady Simulation of Synthetic Jet in a Crossflow*, AIAA Journal, Vol. 44, No. 2, pp. 225-238, 2006.

[26-16] Dandois, J., Garnier, E. and Sagaut, P.: *DNS/LES of Active Separation Control*, Journal of Fluid Mechanics, Vol. 574, pp. 25-58, 2007.

[26-17] Mary, I.: *Méthode de Newton approchée pour le calcul d'écoulements instationnaires comportant des zones à très faible nombre de Mach*, PhD Thesis, 1999.

[26-18] Gear, C.W.: *Algorithm 407-DIFSUB for the Solution of Ordinary Differential Equations*, Commun. ACM, Vol. 14, No. 3, pp. 185-190, 1971.

[26-19] Sagaut, P., Deck, S. and Terracol, M.: *Multiscale and Multiresolution Approaches in Turbulence*, Imperial College Press, 2006.

[26-20] Riou, J., Garnier, E., Deck, S. and Basdevant, C.: *An Extension of DDES Applied to the Computation of a Generic Missile Fin in Transonic Regime*, ERCOFTAC-ETMM7, N95, 2008.

[26-21] Spalart, P.R. and Allmaras, S.R.: *A One-Equation Turbulence Model for Aerodynamic Flows*, AIAA Paper 1992-04339, 1992.

[26-22] Spalart, P.R., Jou, W.H., Strelets, M. and Allmaras, S.R.: *Comments on the Feasibility of LES for Wings, and on a Hybrid RANS/LES Approach*, In Proceedings pp. 137-147, 1st AFSOR Int. Conf. on DNS/LES Ruston, 1998.

[26-23] Jeong, J. and Hussain, F.: *On the Identification of a Vortex,* Journal of Fluid Mechanics, Vol. 285, pp. 69-94, 1995.

[26-24] Squire, L.C.: *Leading-Edge Separations and Cross-Flow Shocks on Delta Wings*, AIAA Journal, Vol. 23, No. 3, pp. 312-325, 1985.

[26-25] Erickson, G.E.: *Experimental Study of the Vortex Flow Behaviour on a Generic Fighter Wing at Subsonic and Transonic Speeds*, AIAA Paper 87-1262, 1987.

[26-26] Donohoe, S.R. and Bannink, W.J.: *Surface Reflective Visualisations of Shock-Wave/Vortex Interactions Above a Delta Wing*, AIAA Journal, Vol. 35, No. 10, pp. 1568-1573, 1997.

[26-27] Schröder, A., Agocs, J., Frahnert, H., Otter, D., Mattner, H., Kompenhans, J. and Konrath, R.: *Application of Stereo PIV to the VFE-2 65° Delta Wing Configuration at Sub- and Transonic Speeds*, AIAA Paper 2006-3486, 2006.

[26-28] Elsenaar, A. and Hoeijmakers, H.W.M.: *An Experimental Study of the Flow over a Sharp-Edged Delta Wing at Subsonic and Transonic Speeds*, AGARD Conference Proceedings Vortex Flow Aerodynamics, pp. 15.1-15.19, AGARD-CP-494, 1991.

[26-29] Houtman, E.M and Bannink, B.J.: *Experimental and Numerical Investigation of the Vortex Flow over a Delta Wing at Transonic Speed*, AGARD Conference Proceedings Vortex Flow Aerodynamics, pp. 5.1-5.11, AGARD-CP-494, 1991.

[26-30] Kandil, O.A., Kandil, H.A. and Liu, C.H.: *Shock-Vortex Interaction Over a 65-degree Delta Wing in Transonic Flow*, AIAA Paper 93-2973, 1993.

[26-31] Burg, J.P.: *Maximum Entropy Spectral Analysis*, Modern Spectrum Analysis, D.G. Childers, pp. 34-41, IEEE Press, 1978.

[26-32] Gad-El-Hak, M. and Blackwelder, R.F.: *The Discrete Vortices from a Delta Wing*, AIAA Journal, Vol. 23, No. 6, pp. 961-962, 1985.

[26-33] Lowson, M.V.: *The Three Dimensional Vortex Sheet Structures on Delta Wings*, In Fluid Dynamics of Three Dimensional Turbulent Shear Flows and Transition, pp. 11.1-11.16, AGARD-CP-438, 1988.

[26-34] Gordnier, R.E. and Visbal, M.: *Compact Difference Scheme Applied to the Simulation of a Low Sweep Delta Wing Flow*, AIAA Journal, Vol. 43, No. 8, pp. 1744-1752, 2005.

[26-35] Furman, A. and Breitsamter, C.: *Investigation of Flow Phenomena on Generic Delta Wing*, ICAS, 2006.

[26-36] Lambert, C. and Gursul, I.: *Insensitivity of Unsteady Vortex Interactions to Reynolds Number*, AIAA Journal, Vol. 38, No. 5, pp. 937-939, 2000.

[26-37] Görtz, S.: *Time Accurate Euler Simulations of a Full Span Delta Wing at High Incidence*, AIAA Paper 2003-4304, 2003.

Chapter 27 – NUMERICAL SOLUTIONS FOR THE VFE-2 CONFIGURATION ON STRUCTURED GRIDS AT NLR, THE NETHERLANDS

by

Okko J. Boelens

27.1   INTRODUCTION

The analysis of vortex-dominated flows is of great importance for the assessment of the aerodynamics, the stability and control characteristics, the aero-elastics and the structural dynamics of fighter aircraft. The importance of vortical flow to fighter aircraft manifests itself for example as follows:

- *Aerodynamics:* Manoeuvring capabilities depend critically on vortex-induced lift; maximum vortex-induced lift is affected by vortex stability.

- *Stability and control characteristics:* The roll stability of complete fighter aircraft can heavily depend on asymmetric vortex breakdown.

- *Aero-elastics:* Unsteady vortex flow can affect the flutter speed and the level of limit cycle oscillations.

- *Structural dynamics:* Fatigue life of tail surfaces and ventral fins depends significantly on the unsteady aerodynamic energy input to the vibrations of these surfaces; this energy input can be due to vortices.

These observations motivate the investigation of the ability of CFD codes to capture the details of vortical flows around generic configurations such as delta wings.

In the late 1990s, the Netherlands National Aerospace Laboratory NLR performed an assessment of its ENFLOW flow simulation system using the data available from experiments carried out by Chu and Luckring in the National Transonic Facility (NTF) at NASA Langley ([27-1]-[27-4]). These experiments considered a 65° delta wing with four leading edge profiles (one sharp and three rounded with small, medium and large radii) for a wide range of conditions both subsonic and transonic and for both test and flight Reynolds numbers, and were used again during the second International Vortex Flow Experiment (VFE-2) ([27-5] and [27-6]), a facet of the NATO RTO AVT-113 Task Group, which was set up to consider the flow behaviour both experimentally and computationally over the 65° delta wing geometry.

Results of this investigation by NLR, more specifically results obtained for the sharp leading edge delta wing and the large radius leading edge delta wing, were presented during the bi-annual meetings of the NATO RTO AVT-113 Task Group, and are the subject of this chapter. Based on the geometry description of both delta wings ([27-1] and [27-4]), structured (multi-block) grids were generated at NLR. The grids used in simulations will be discussed in Section 27.2. Section 27.3 will discuss the important features of the flow solver ENSOLV, which is part of NLR's flow simulation system ENFLOW. Section 27.4 will discuss some of the results obtained at NLR. A section with concluding remarks (Section 27.5) completes the chapter.

27.2   GRID

At NLR the following structured (multi-block) grids have been generated using the grid generation algorithms, which are part of NLR's ENFLOW flow simulation system [27-7]:

- A baseline grid around the sharp leading edge delta wing consisting of 12 blocks, 2,048,000 grid cells and 2,169,180 grid points (see Figure 27-1 (a)).

- A baseline grid around the large radius leading edge delta wing consisting of 12 blocks, 2,048,000 grid cells and 2,169,180 grid points.

- For each flow condition considered, an adapted grid around the large radius leading edge delta wing consisting of 12 blocks, 2,048,000 grid cells and 2,169,180 grid points (see Figure 27-1 (b) for $M_\infty = 0.85$, $\alpha = 10.2°$, $Re_{mac} = 60 \times 10^6$). The baseline grid around the large radius leading edge delta wing is adapted to a computed flow solution, such that after re-computation on the adapted grid, a flow solution with higher numerical accuracy is obtained. The topological structure of the multi-block grid is maintained. The number of grid points in each block and also the geometry of the block faces are kept fixed. In each block the grid points are re-distributed based on the modified anisotropic diffusion equations developed at NLR. Corrections are used at block interfaces in order to obtain a continuous grid across block boundaries. Details can be found in [27-8]. For the large radius leading edge delta wing only results obtained on these grids are presented.

(a)   (b)
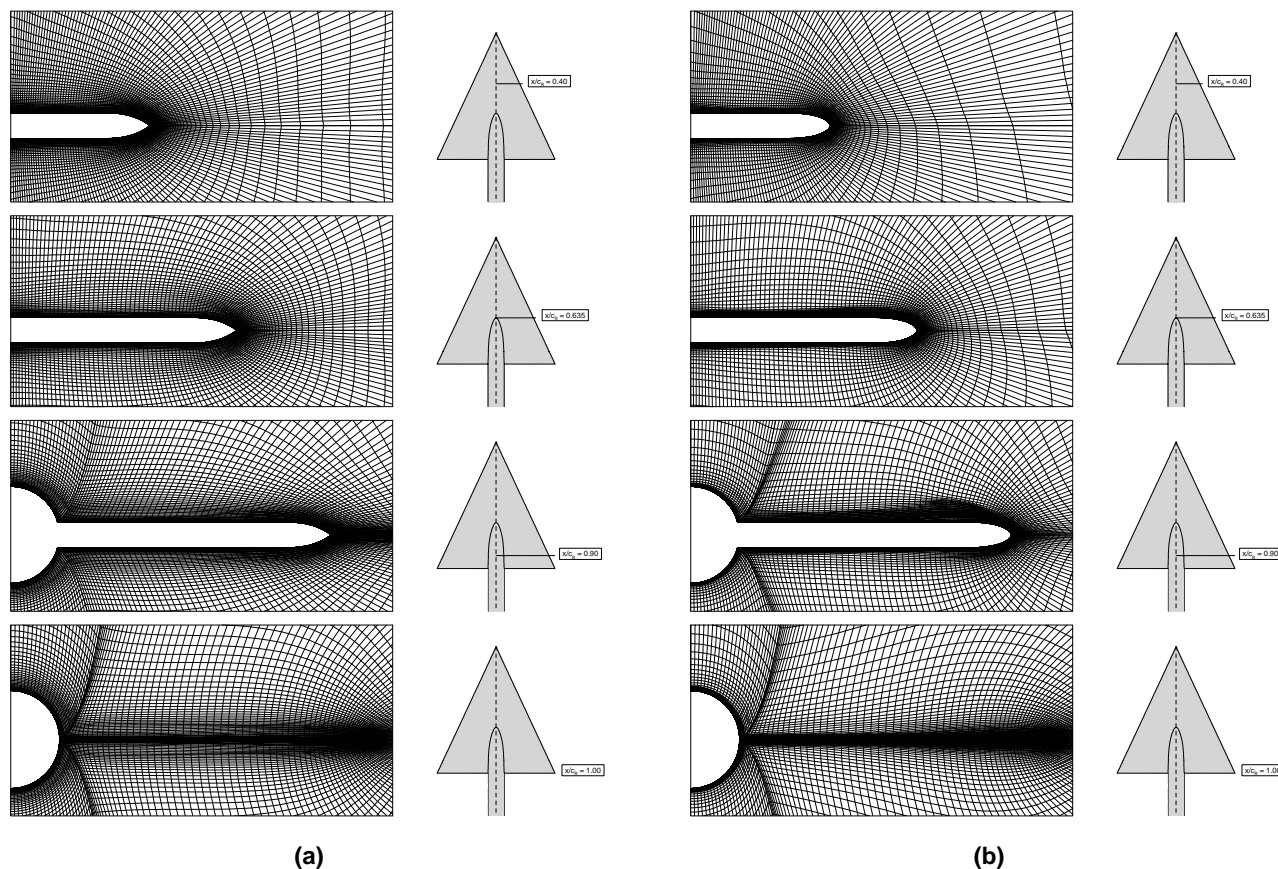
Figure 27-1: Computational Grid in Four Cross-Flow Planes: (a) Grid for the Sharp Leading Edge Wing;
(b) Adapted Grid for the Large Radius Leading Edge Configuration at $M_\infty = 0.85$, $\alpha = 10.2°$, $Re_{mac} = 60 \times 10^6$.

27.3   FLOW SOLVER

The flow solver ENSOLV (version 3.23 has been used for the present study), which is part of NLR's flow simulation system ENFLOW [27-7], is capable of solving the Euler and Navier-Stokes equations on multi-block structured grids for arbitrary configurations. The configuration can be either fixed or moving relative to an inertial reference frame, and can be either rigid or flexible.

The flow equations are cast into a full conservation form employing the density ρ, the components of the momentum vector $\rho\mathbf{u}$ and the total energy per unit volume ρE as dependent variables. The equations are non-dimensionalized using the free-stream static pressure, the free-stream density, the free-stream temperature and a reference length (for example the reference wing chord).

The equations in full conservation form are discretized in space by a second-order accurate, cell-centred, finite-volume method, using multi-block structured grids, central differences, and matrix artificial diffusion. The artificial diffusion consists of a blending of second-order and fourth-order differences with a Jameson-type shock sensor for the basic flow equations and a TVD discontinuity sensor for the turbulence model equations.

For steady flow simulations, the discretized time-dependent system of equations is integrated toward the steady-state solution using a five-stage explicit Runge-Kutta scheme. Local-time stepping, implicit residual averaging and multi-grid acceleration techniques are applied.

For all computations in the present study, the original Wilcox k-ω turbulence model with cross diffusion is employed.

For more details on the flow solver ENSOLV, see also Chapter 5.

27.4   RESULTS

27.4.1   Sharp Leading Edge Delta Wing

Results obtained for the sharp leading edge delta wing are shown in Appendix 27-1. Simulations were performed for the following conditions: $M_\infty = 0.85$, $\alpha = 10.4$ or $14.5°$ and $Re = 6$ or 36×10^6.

27.4.2   Large Radius Leading Edge Delta Wing

Results obtained for the large radius leading edge delta wing are shown in Appendix 27-2. Simulations were performed for the following conditions: $M_\infty = 0.85$, $(\alpha, Re_{mac}) = (10.4°, 6 \times 10^6)$, $(10.2°, 36 \times 10^6)$, $(10.2$ or $14.4°$, $60 \times 10^6)$ or $(10.4°, 120 \times 10^6)$.

27.5   CONCLUDING REMARKS

Results of an investigation on the sharp leading edge delta wing and the large radius leading edge delta wing performed by NLR have been presented. It has been shown that agreement between computations and experiments for the sharp leading edge delta wing is good. For the large radius leading edge delta wing the agreement is much poorer. This is mainly caused by the difference in the experimental and computed location where the primary separation occurs along the round leading edge and the subsequent differences in the vortical flow structure on the upper part of the wing.

The results shown are representative for the capabilities of the flow solver during the late 1990s. Since then much progress has been made in the turbulence models used for such simulations (see [27-9] and [27-10]). Recently obtained results can be found in Chapter 5, 16 and 29.

27.6   REFERENCES

[27-1]   Chu, J. and Luckring, J.M.: *Experimental Surface Pressure Data Obtained on a 65° Delta Wing Across Reynolds Number and Mach Number Ranges: Volume 1 – Sharp Leading Edge*, NASA Technical Memorandum 4645, NASA Langley Research Centre, February 1996.

[27-2]   Chu, J. and Luckring, J.M.: *Experimental Surface Pressure Data Obtained on a 65° Delta Wing Across Reynolds Number and Mach Number Ranges: Volume 2 – Small Radius Leading Edge*, NASA Technical Memorandum 4645, NASA Langley Research Centre, February 1996.

[27-3]   Chu, J. and Luckring, J.M.: *Experimental Surface Pressure Data Obtained on a 65° Delta Wing Across Reynolds Number and Mach Number Ranges: Volume 3 – Medium Radius Leading Edge*, NASA Technical Memorandum 4645, NASA Langley Research Centre, February 1996.

[27-4]   Chu, J. and Luckring, J.M.: *Experimental Surface Pressure Data Obtained on a 65° Delta Wing Across Reynolds Number and Mach Number Ranges: Volume 4 – Large Radius Leading Edge*, NASA Technical Memorandum 4645, NASA Langley Research Centre, February 1996.

[27-5]   Hummel, D. and Redeker, G.: *A New Vortex Flow Experiment for Computer Code Validation*, In Proceedings of the RTO-AVT Symposium on "Advanced Flow Management: Part A – Vortex Flows and High Angle of Attack for Military Vehicles" – RTO-MP-069(I), Pages 8.1-8.32. NATO RTO, 2001.

[27-6]   Hummel, D.: *The Second International Vortex Flow Experiment (VFE-2): Objectives and First Results*, 2nd International Symposium on "Integrating CFD and Experiments in Aerodynamics", 5-6 September 2005, Cranfield University, UK. J. Aerospace Engineering, Vol. 220 (2006), No. 6: 559-568.

[27-7]   *ENFLOW: A Computer Code System for Accurate Simulation of Three-Dimensional Flows*, URL: http://www.nlr.nl/documents/flyers/f222-01.pdf [cited July 2008].

[27-8]   Hagmeijer, R.: *Grid Adaption Based on Modified Anisotropic Diffusion Equations Formulated in the Parametric Domain*, Journal of Computational Physics, Vol. 115, pp. 169-183, 1994.

[27-9]   Kok, J.C.: *Resolving the Dependence on Free-Stream Values for the k-ω Turbulence Model*, NLR-TP-99295. 1999.

[27-10] Brandsma, F.J., Kok, J.C., Dol, H.S. and Elsenaar, A.: *Leading Edge Vortex Flow Computations and Comparison with DNW-HST Wind Tunnel Data*, NLR-TP-2001-238, 2001.

Appendix 27-1: Sharp Leading Edge Delta Wing

Figure 27-2 shows a comparison of the computed upper surface pressure distributions. In addition, the projections of the vortex core trajectory obtained by the experiment and the computations are compared. These vortex core trajectories were detected from the upper surface minimum pressure. The agreement between the computed and experimental vortex core trajectories is good.

(a)   (b)
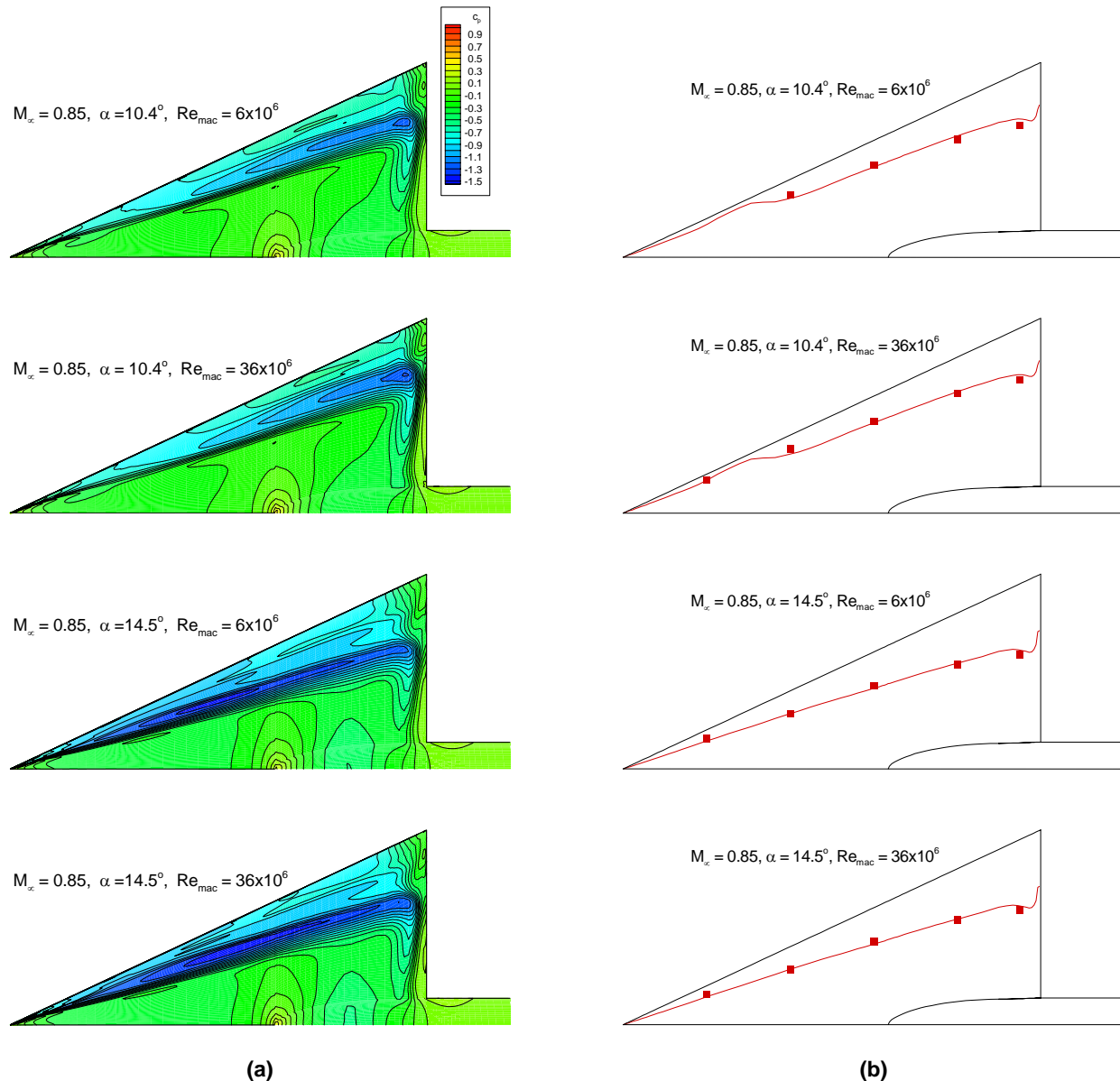
Figure 27-2: Comparison of Computed Distributions for the Sharp Leading Edge Delta Wing (M_∞ = 0.85, α = 10.4° or 14.5°, Re_{mac} = 6 or 36 x 10^6): (a) Upper Surface Pressure Distributions; (b) Projections of the Vortex Core Trajectory as Detected from Upper Surface Minimum Pressure (lines: simulation, symbols: experiment).

In Figure 27-3, a comparison of the computed and experimental upper surface peak pressure along the vortex trajectories (see also Figure 27-2) is presented. For both angles of attack the agreement is fair.
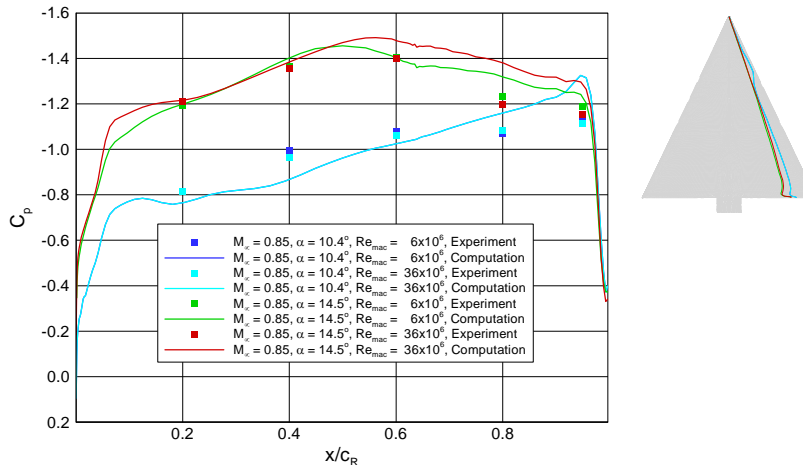
Figure 27-3: Comparison of Computed and Experimental Upper Surface Peak Pressures along Vortex Trajectory for the Sharp Leading Edge Delta Wing (M_∞ = 0.85, α = 10.4° or 14.5°, Re_{mac} = 6 or 36 x 10^6) (lines: simulation, symbols: experiment).

Figure 27-4 and Figure 27-5 show a comparison of the computed and experimental spanwise pressure distribution at x/c_r = 0.60 and x/c_r = 0.80, respectively. At both chordwise stations good agreement between the experiment and the computations is shown. The observed Reynolds number effects are small.

(a)

(b)
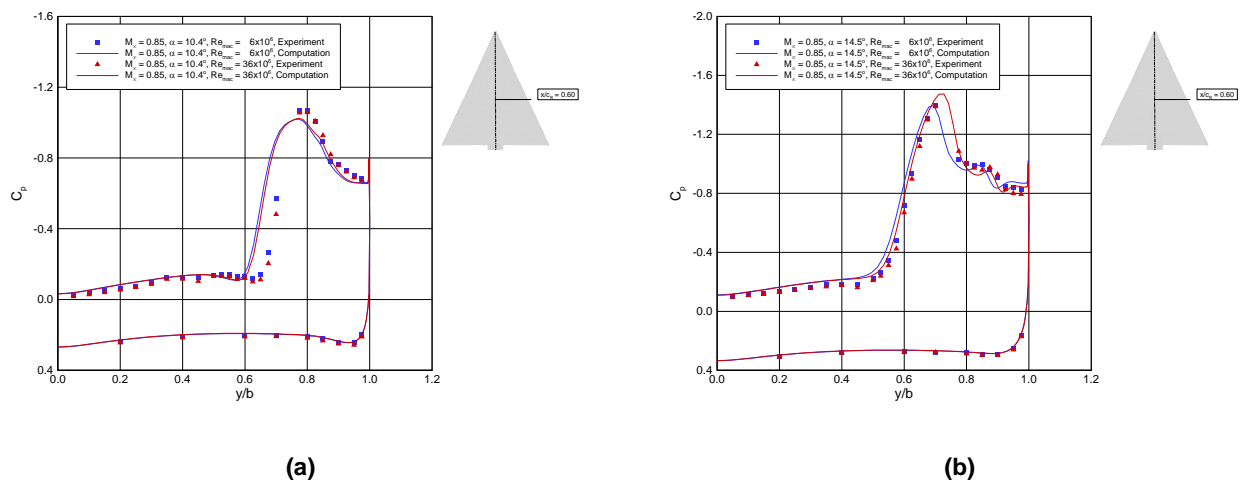
Figure 27-4: Comparison of Computed and Experimental Spanwise Pressure Distributions for the Sharp Leading Edge Wing at x/c_r = 0.60: (a) M_∞ = 0.85, α = 10.4°, Re_{mac} = 6 or 36 x 10^6; (b) M_∞ = 0.85, α = 14.5°, Re_{mac} = 6 or 36 x 10^6.

	(a)	(b)
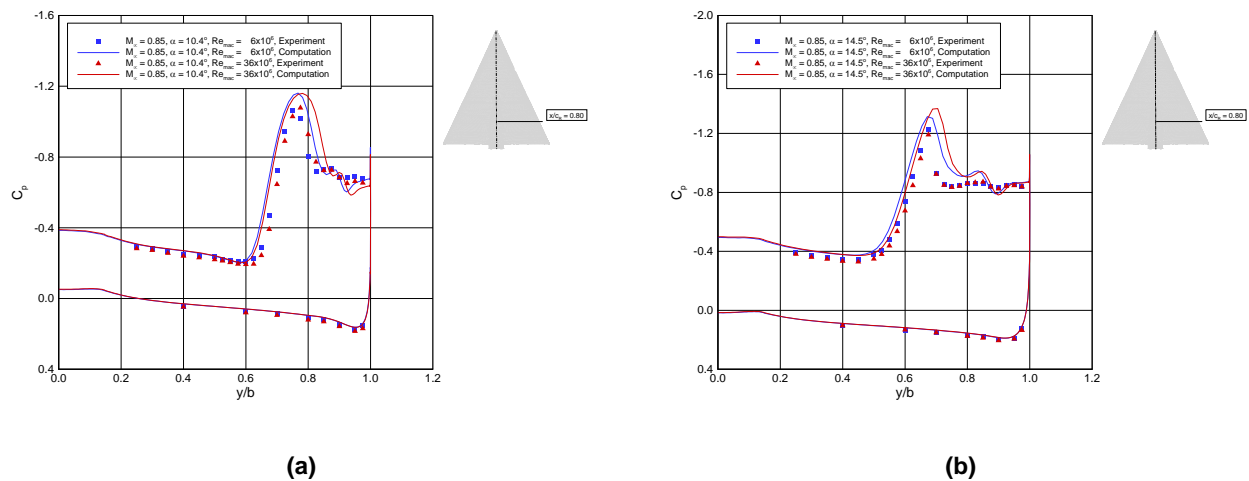
**Figure 27-5: Comparison of Computed and Experimental Spanwise Pressure Distributions for the
Sharp Leading Edge Wing at x/c$_r$ = 0.80: (a) M$_\infty$ = 0.85, α = 10.4°, Re$_{mac}$ = 6 or 36 x 10^6;
(b) M$_\infty$ = 0.85, α = 14.5°, Re$_{mac}$ = 6 or 36 x 10^6.**

Figure 27-6 shows the computed separation and re-attachment patterns on the upper surface for the following conditions: M$_\infty$ = 0.85, α = 10.4° and Re = 6 x 10^6 and M$_\infty$ = 0.85, α = 14.5° and Re = 36 x 10^6. In addition, Figure 27-7 shows the influence of the Reynolds number on the position of the upper surface separation and re-attachment lines for all simulated conditions. From these figures, it can be seen that the secondary separation starts halfway at the wing for α = 10.4°, whereas for α = 14.5° it starts right at the apex. In addition, the extent of the trailing edge separation region is increased in the spanwise direction going from α = 10.4° to α = 14.5°. Furthermore, the observed Reynolds numbers effects are small.

(a)   (b)
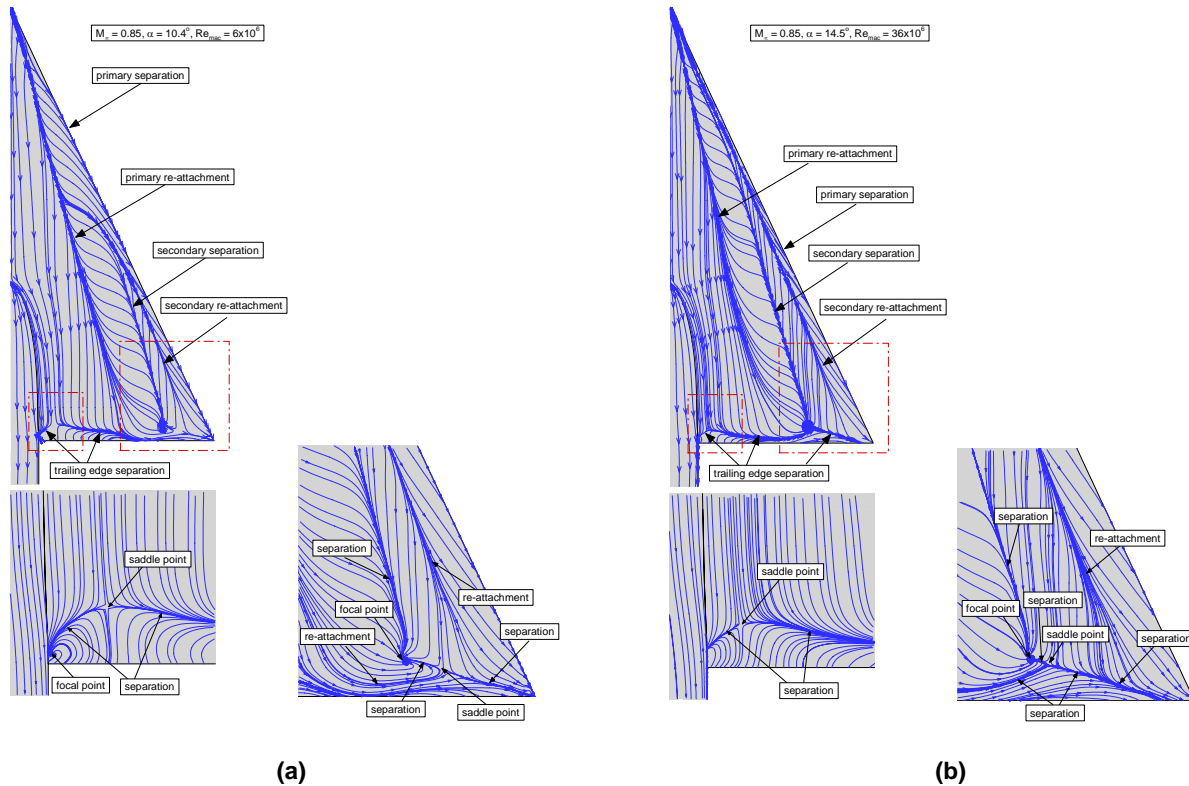
Figure 27-6: Topology of Computed Separation and Re-attachment Patterns on the Upper Surface of the Sharp Leading Edge Delta Wing: (a) $M_\infty = 0.85$, $\alpha = 10.4°$, $Re_{mac} = 6 \times 10^6$; (b) $M_\infty = 0.85$, $\alpha = 14.5°$, $Re_{mac} = 36 \times 10^6$.

(a)

(b)
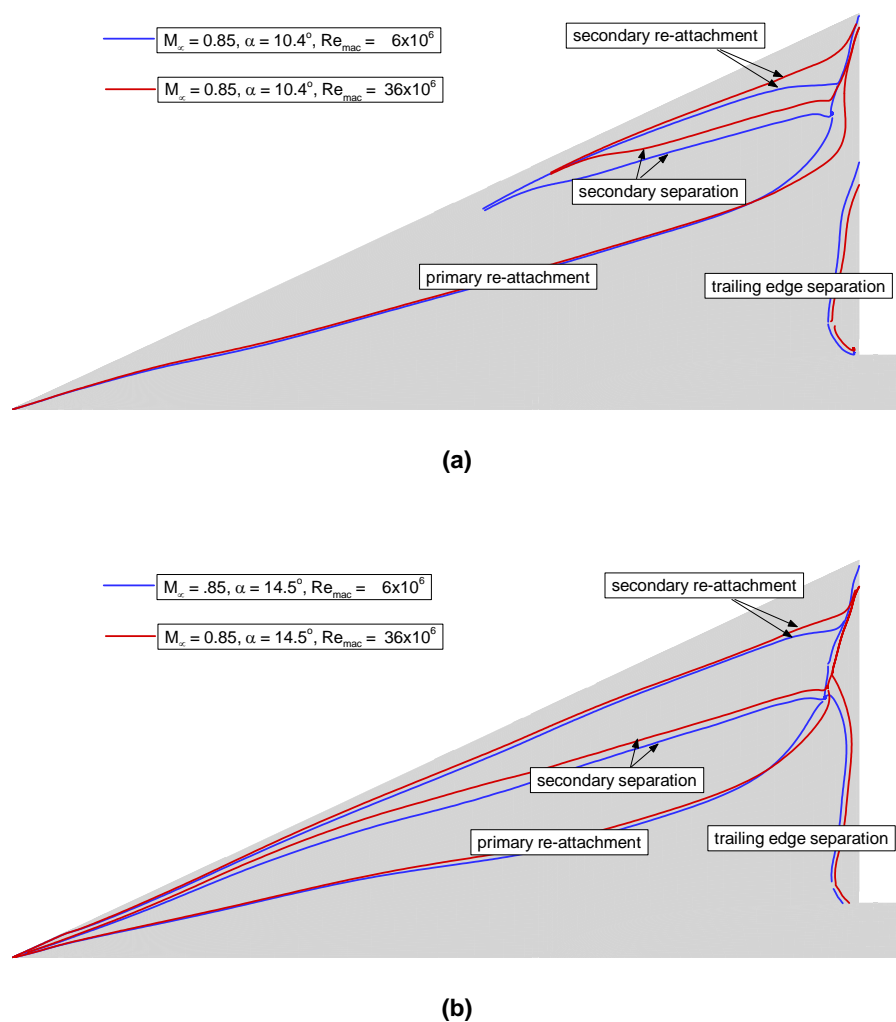
Figure 27-7: Influence of Reynolds Number on the Position of the Upper Surface Separation and Re-attachment Lines for the Sharp Leading Edge Delta Wing: (a) M_∞ = 0.85, α = 10.4°, Re_{mac} = 6 or 36 x 10^6; (b) M_∞ = 0.85, α = 14.5°, Re_{mac} = 6 or 36 x 10^6.

Finally, Figure 27-8 presents a comparison of the computed and experimental normal force and pitch moment coefficient as function of the angle of attack. The normal force coefficient shows excellent agreement. For the pitch moment coefficient, however, a constant positive shift ($\Delta C_m = C_{m\ computation} - C_{m\ experiment} \sim 0.025$) is observed.
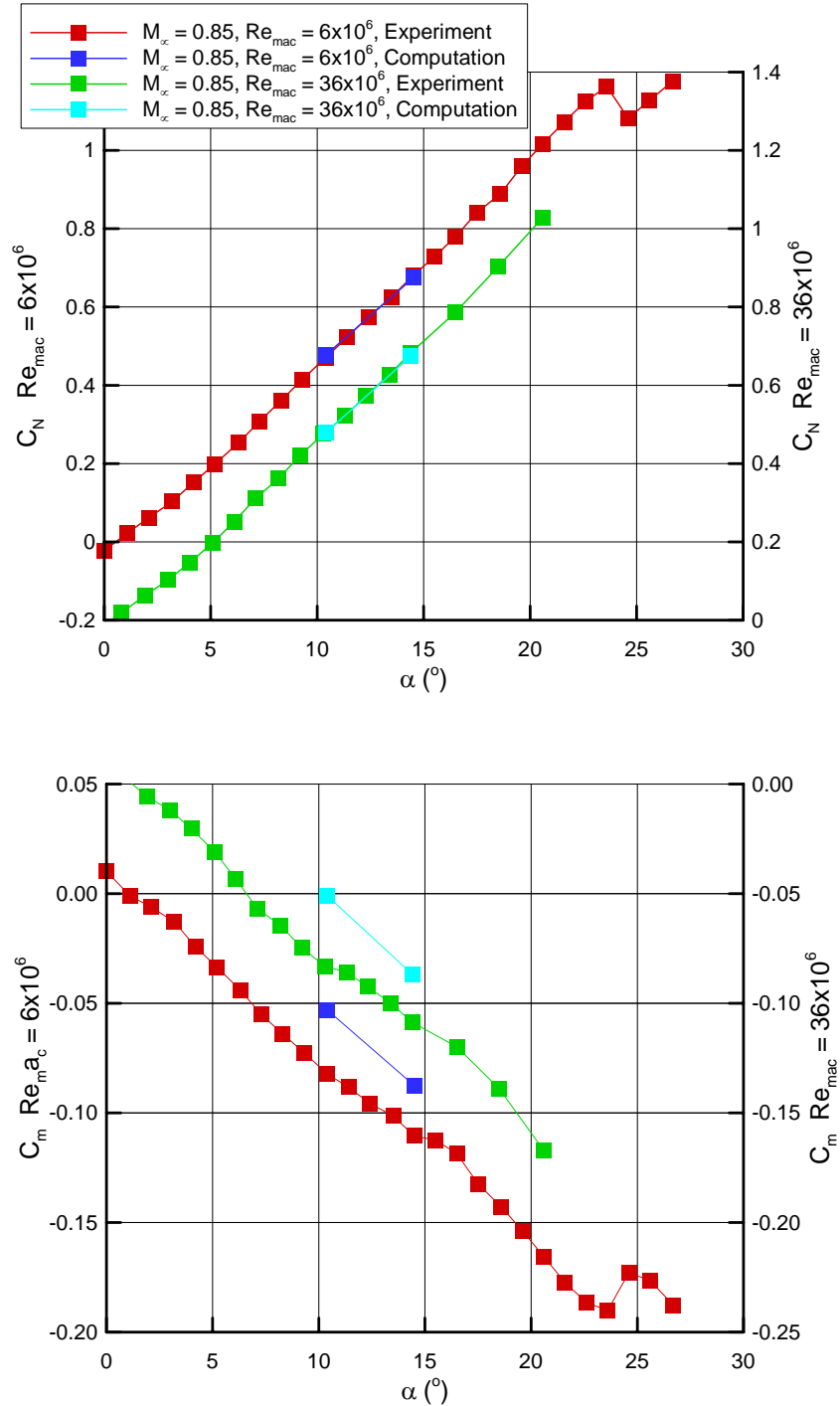
**Figure 27-8: Comparison of Computed and Experimental Normal Force and Pitch Moment
Coefficient as a Function of Angle of Attack for the Sharp Leading Edge Delta Wing.**

Appendix 27-2: Large Radius Leading Edge Delta Wing

Figure 27-9 shows a comparison of the computed upper surface pressure distributions. In addition, the projections of the vortex core trajectory obtained by the experiment and the computations are compared. These vortex core trajectories were detected from the upper surface minimum pressure. The vortices seem to originate more aft on the delta wing in the computations than during the experiment. Whereas in the experiment already a vortex core trajectory is found at $x/c_r = 0.60$, in the simulations the vortex core trajectory can only be determined after approximately $x/c_r = 0.75$.

(a)   **(b)**
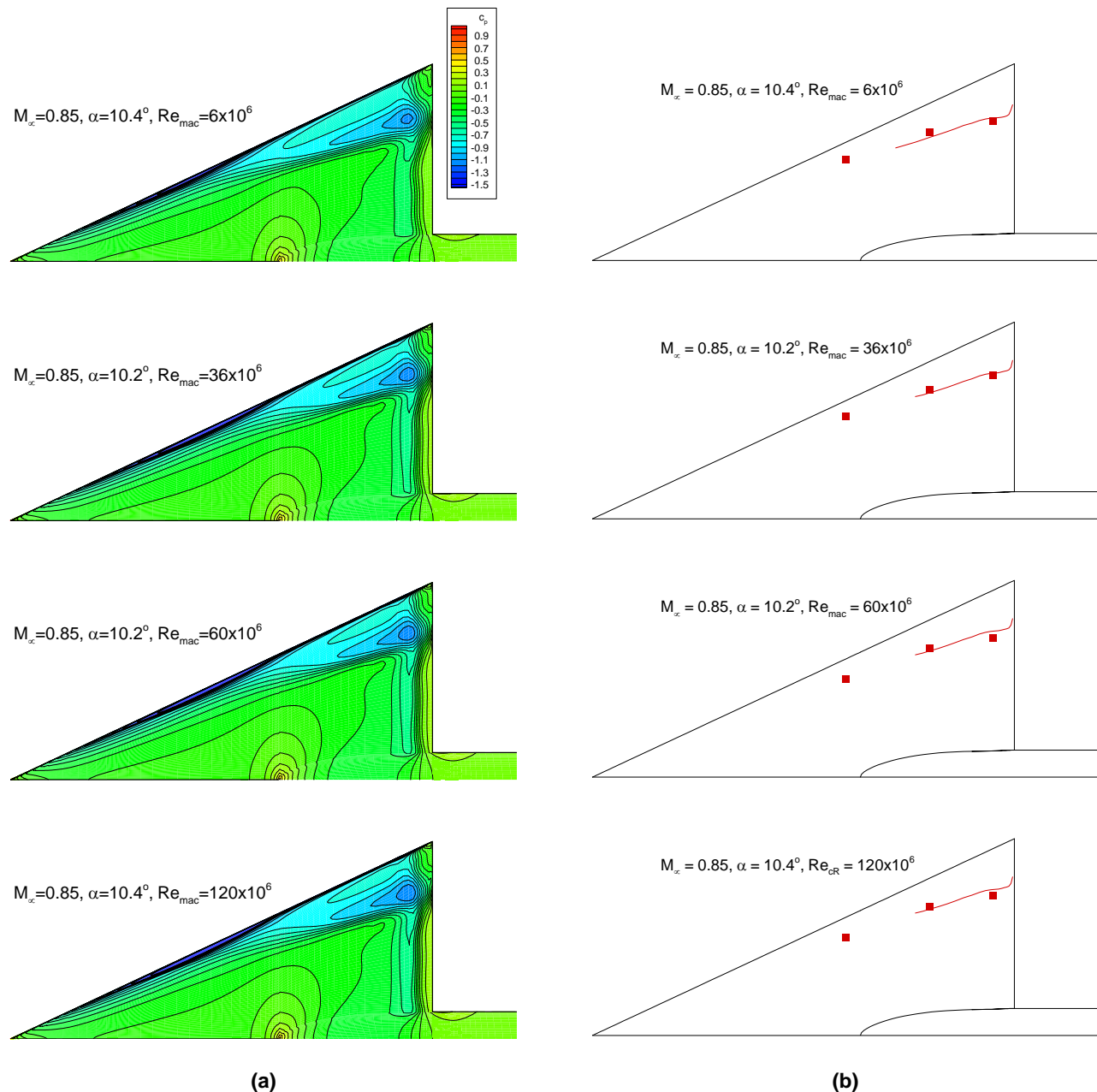
**Figure 27-9: Comparison of Computed Distributions for the Large Radius Leading Edge Delta Wing
($M_\infty = 0.85$, (α,Re_{mac}) = (10.4°, 6 x 10⁶), (10.2°, 36 x 10⁶), (10.2°, 60 x 10⁶) or (10.4°, 120 x 10⁶)): (a) Upper
Surface Pressure Distributions; (b) Projections of the Vortex Core Trajectory as Detected
from Upper Surface Minimum Pressure (lines: simulation, symbols: experiment).**

In Figure 27-10, a comparison of the computed and experimental upper surface peak pressure along the vortex trajectories (see also Figure 27-9) is presented. The agreement found is poor. This is mainly caused by the difference in the experimental and computed location where the primary separation occurs along the round leading edge and the subsequent differences in the vortical structure on the upper part of the wing.
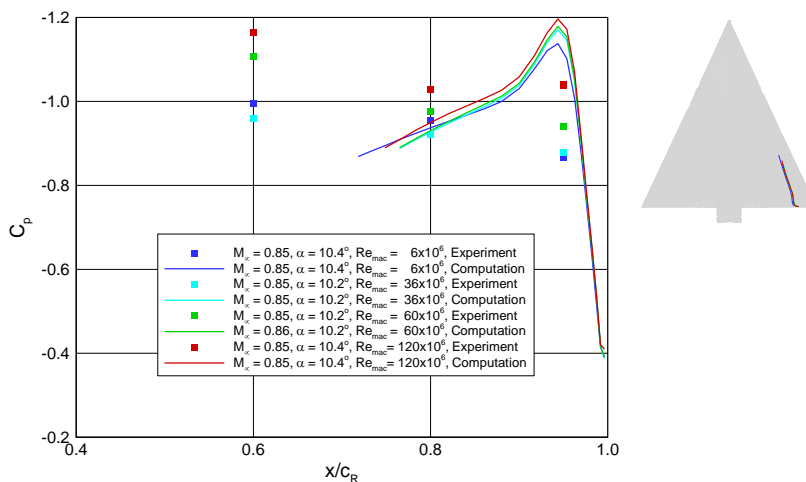
**Figure 27-10: Comparison of Computed and Experimental Upper Surface Peak Pressures along Vortex Trajectory
for the Large Radius Leading Edge Delta Wing (M_∞ = 0.85, (α,Re_{mac}) = (10.4°, 6 x 10^6), (10.2°, 36 x 10^6),
(10.2°, 60 x 10^6) or (10.4°, 120 x 10^6)) (lines: simulation, symbols: experiment).**

Figure 27-11 and Figure 27-12 show a comparison of the computed and experimental spanwise pressure
distribution at x/c_r = 0.60 and x/c_r = 0.80, respectively. At x/c_r = 0.60 the agreement between the computations
and the experiment is poor for all Reynolds numbers at α = 10.2 resp. 10.4°. Again, this is mainly caused by
the difference in the experimental and computed location where the primary separation occurs along the
round leading edge and the subsequent differences in the vortical structure on the upper part of the wing.
However, at x/c_r = 0.80 the agreement is good. At α = 14.4° good agreement is obtained at x/c_r = 0.60. However,
at x/c_r = 0.80 the pressure peak is over predicted in the simulations.

(a)

(b)
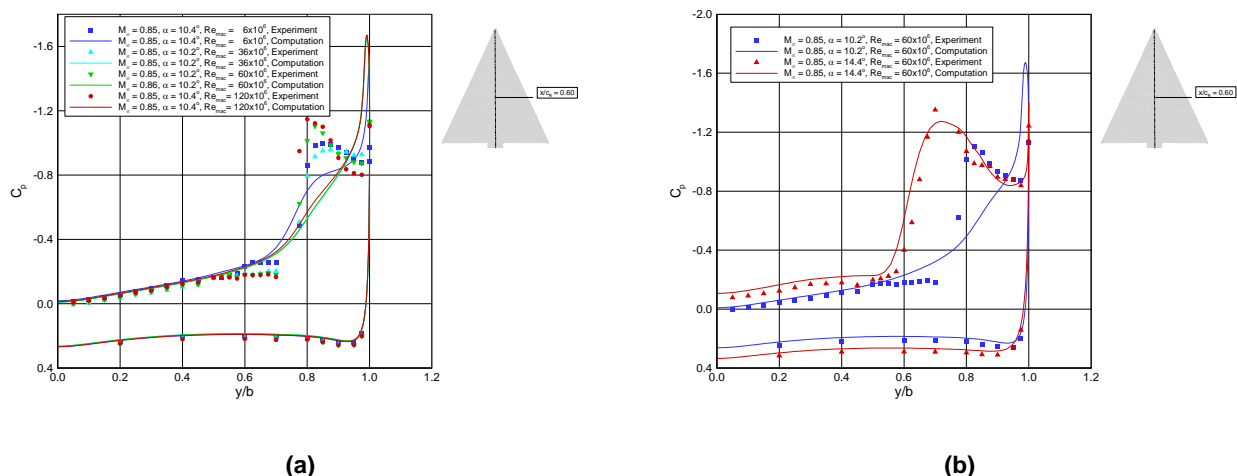
**Figure 27-11: Comparison of Computed and Experimental Spanwise Pressure Distributions for the Large
Radius Leading Edge Wing at x/c_r = 0.60: (a) M_∞ = 0.85, (α,Re_{mac}) = (10.4°, 6 x 10^6), (10.2°, 36 x 10^6),
(10.2°, 60 x 10^6) or (10.4°, 120 x 10^6); (b) M_∞ = 0.85, α = 10.2 or 14.4°, Re_{mac} = 60 x 10^6.**

(a)   **(b)**

Figure 27-12: Comparison of Computed and Experimental Spanwise Pressure Distributions for the Large Radius Leading Edge Wing at x/c_r = 0.80: (a) M_∞ = 0.85, (α,Re_mac) = (10.4°, 6 x 10^6), (10.2°, 36 x 10^6), (10.2°, 60 x 10^6) or (10.4°, 120 x 10^6); (b) M_∞ = 0.85, α = 10.2° or 14.4°, Re_mac = 60 x 10^6.

Figure 27-13 shows the computed separation and re-attachment patterns on the upper surface for the following conditions: $M_\infty = 0.85$, $\alpha = 10.4°$ and Re = 6 x 10^6. To see the effect of the leading edge geometry on the flow topology, this figure should be compared with Figure 27-6 (a). Figure 27-14 shows the influence of the Reynolds number on the position of the upper surface separation and re-attachment lines for all simulated conditions at $\alpha = 10.2°$ resp. 10.4°. Going from $Re_{mac} = 6$ x 10^6 to 36 x 10^6 both the primary re-attachment line and the trailing edge separation move aft on the wing upper surface. For Reynolds numbers larger than 36 x 10^6 the observed Reynolds numbers effects are, however, small.
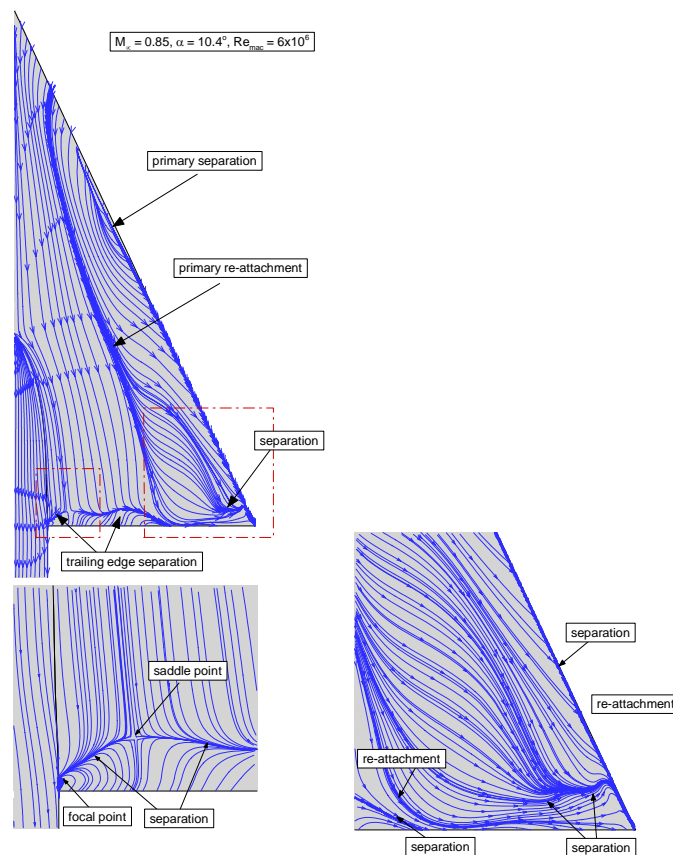
Figure 27-13: Topology of Computed Separation and Re-attachment Patterns on the Upper Surface of the Large Radius Leading Edge Delta Wing ($M_\infty = 0.85$, $\alpha = 10.4°$, $Re_{mac} = 6 \times 10^6$).
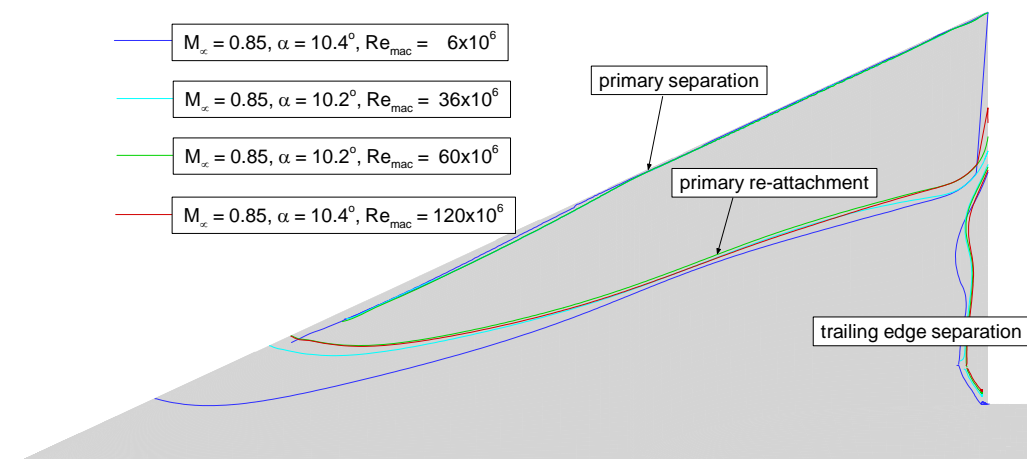
Figure 27-14: Influence of Reynolds Number on the Position of the Upper Surface Separation and Re-attachment Lines for the Large Radius Leading Edge Delta Wing ($M_\infty = 0.85$, $(\alpha, Re_{mac}) = (10.4°, 6 \times 10^6)$, $(10.2°, 36 \times 10^6)$, $(10.2°, 60 \times 10^6)$ or $(10.4°, 120 \times 10^6)$).

Chapter 28 – NUMERICAL SOLUTIONS FOR THE VFE-2 CONFIGURATION ON STRUCTURED GRIDS

by

Emre Gurdamar, Yüksel Ortakaya,
Serpil Kaya, Bulent Korkem

To understand and model vortical flows, experimental investigations and flow simulations were carried out within the task group of NATO RTO AVT-113 International Vortex Flow Experiment. As being a member of the task group, TAI performed flow simulations on structured grids with an in-house, three dimensional Navier-Stokes solver, xFLOWg. Aim is to understand the physical characteristics of the vortical flow on delta wing configurations and to realize the ability of the flow solver for complex flow simulations.

TAI has studied a number of subsonic and transonic test cases in VFE-2 facet of AVT-113 RTO Applied Vehicles Technology panel. These test cases were medium radius and sharp leading edge delta wing configurations. In the early stages of the study, TAI carried out computations for 20 test cases (Table 28-1) to identify distinct flow characteristics. Another idea behind choosing such a test matrix was to provide detailed information about the capabilities of the numerical approaches and the flow solver used.

Reynolds-Averaged Navier-Stokes simulations were performed for the chosen 20 test cases. The simulations were carried out with algebraic Baldwin-Lomax turbulence model. Based on the first results, it is seen that essential features of the flows were not resolved accurately. Pressure peaks, representing the vortical region, did not match well with the experimental data. Since turbulence plays an important role for vortex dominated flows, it is decided to add a new turbulence model to xFLOWg. Based on this fact, one-equation Spalart-Allmaras turbulence model which is widely known and used especially for external aerodynamics, has been implemented for better vortical flow resolution. In addition to 4 cases selected from the first 20 cases studied, two cases at higher angle of attack were chosen to compare the turbulence models and see the effects on the flow field. They were listed in Table 28-5. It was assumed that flow is fully turbulent. Noteworthy improvement in the results has been achieved. Once accurate results were obtained, test matrix was limited to nine cases to concentrate on the physics of the flow for the identified flow regimes (Table 28-2, Table 28-3, Table 28-4).

Experiments showed that distinct flow regimes can be classified with respect to angle of attack. Special attention was paid on the separated vortical flow without vortex breakdown at angles of attack smaller than 20 degrees. Flow is attached and vortex formation is not observed at angles smaller than 4 degrees, therefore there was no interest to low angles of attack cases. Larger than 20 degrees, vortex breakdown phenomenon is present in the flow field. For transonic cases, another challenge was to resolve the shock-vortex interaction accurately. Implementation of Spalart-Allmaras turbulence model provided better simulation capability such that those distinct regions could be captured.

The common structured grid provided by EADS-M was used for all the simulations. Results showed that besides the turbulence model, grid must also be investigated to resolve some of the characteristics of the flow field. The suction peaks on the upper surface of the wing were poorly matched with the experimental data. Some computations were performed regarding this issue but more consideration is necessary, and therefore, they are not presented here. One outlook might be to make a grid dependency study, another would be to make solution based mesh adaptation study and see the effects on the results.

To analyse the flow simulation results, detailed pressure distribution at a variety of chord wise locations were compared with the measurements. These plots were useful to clarify onset of separation for blunt leading edge configuration. For better understanding of the flow features and comparison, vorticity lines were also drawn. Special interest was given to the cases (Table 28-2, Table 28-3, Table 28-4) in order to show the influence of compressibility, angle of attack and leading edge bluntness on the flow field.

In conclusion, numerical simulations provided clear pictures for the flow field. Even though the geometry is simple, governed flow phenomena is quite complex and it is shown that the complex flow features can be simulated with a suitable Navier-Stokes solver and turbulence model. This flow simulation capability is crucial for understanding the details of flow field and effective wind tunnel testing.

28.1   COMPUTATIONAL DETAILS

28.1.1   Flow Solver

xFLOWg is a parallel, three dimensional, structured, multi-block, finite-volume, Reynolds-Averaged Navier-Stokes solver developed at TAI [[28-1], [28-2], [28-3], [28-4]]. Steady or unsteady flows can be simulated with xFLOWg. Fifth order accurate WENO and first, second and third order accurate Roe scheme with MUSCL have been implemented for inviscid flux calculations. For viscous flux calculations, second order accurate central difference scheme has been used. Multi-stage Runge-Kutta or LU-SGS scheme can be used for time integration. It contains Baldwin-Lomax, Spalart Allmaras turbulence models. Additionally, standard k-omega, and SST k-omega turbulence models have been implemented.

In the studies, steady calculations were performed. For spatial discretization, the Roe scheme with 3rd order MUSCL and local time stepping with LU-SGS scheme were used. Calculations were carried out using both Baldwin-Lomax and Spalart-Allmaras turbulence models. No transition model has been utilized and flow has been considered as fully turbulent during the flow simulations for VFE-2. Different solutions are discussed in detail in the following sections.

28.1.2   Numerical Grid and Boundary Conditions

Single block grid which is provided by EADS-M was used for the flow simulations within this study and grid is illustrated in Figure 28-1. This grid is a C-Mesh around the apex of the wing and at the cross sections it is of O-type. The single block grid has been decomposed into 8 sub domains with point matching interfaces and used in parallel computations. It has dimensions of 128 x 160 x 96 in span wise, stream wise and boundary layer directions, respectively with a 2,092,872 number of total nodes. Multi-blocks were obtained by dividing the single block mesh in the axial direction. First three blocks enclose wall boundaries, only for the delta wing. The following blocks, numbered 4, 5 and 6, include wall boundaries for both wing and sting and the rest of the blocks include the sting. The multi-block structure is shown in Figure 28-2. All sub domains consist of almost similar dimensions for the sake of balancing the load on each processor. This results in increased efficiency of parallel simulation. The first cell height was chosen so that it has a y+ value between 0.2 and 3.7, an average of 1.5.
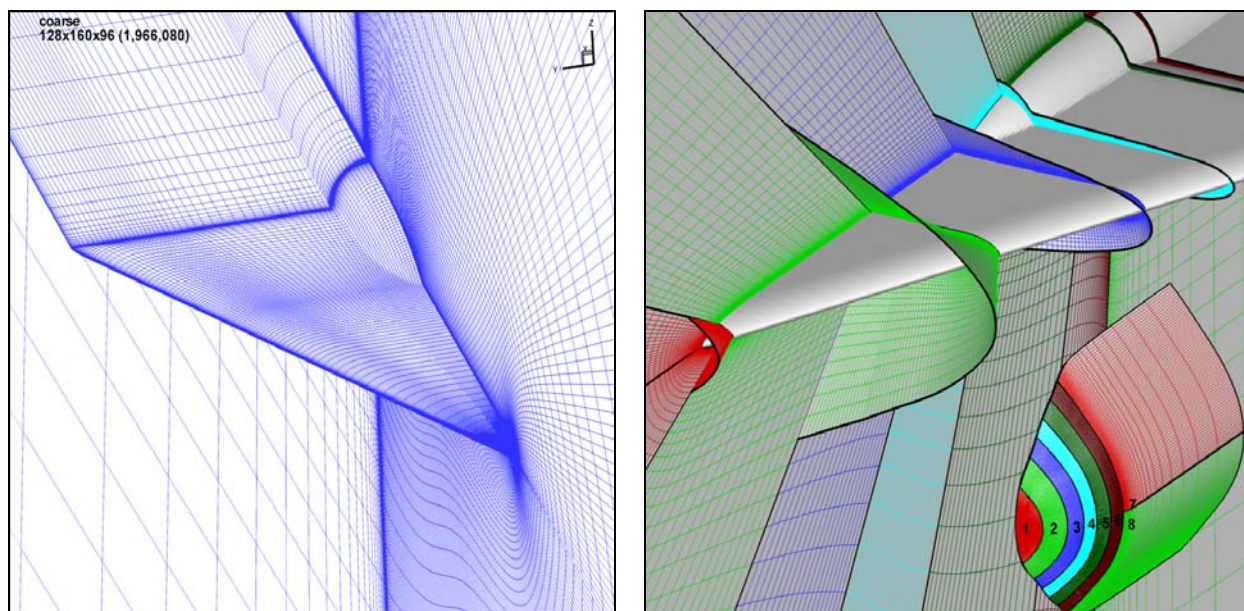
Figure 28-1: Computational Grid, Multi-Block Mesh Structure.
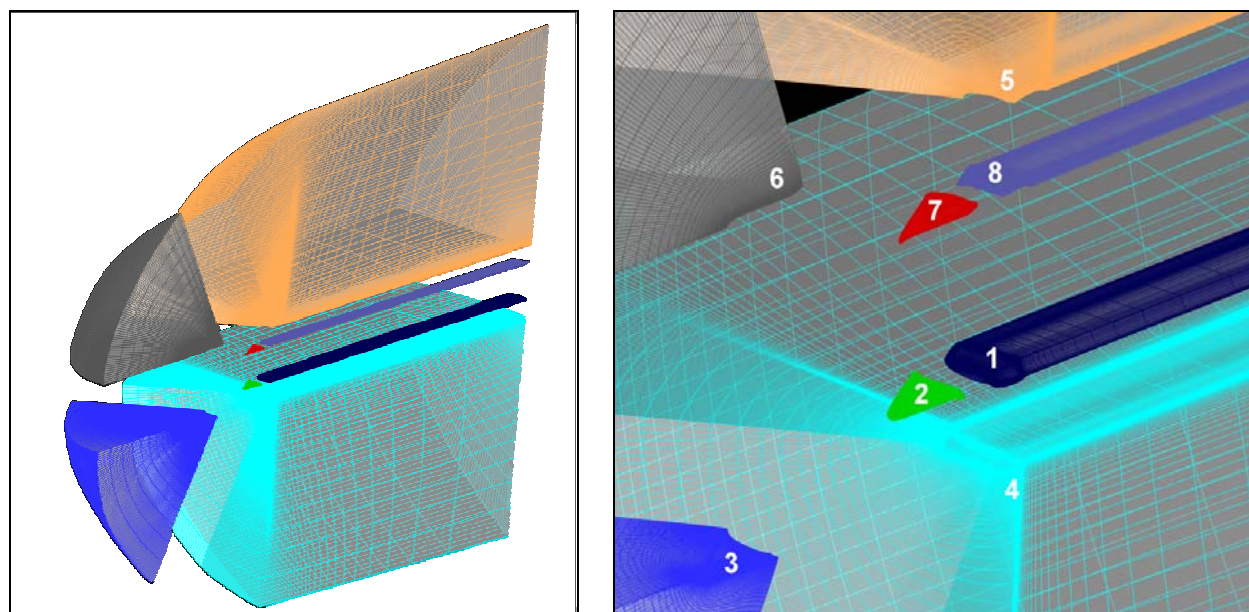
Figure 28-2: Close View of Sub Domains.

Half of the delta wing was modelled with a symmetry boundary condition. The boundary condition for the solid walls is adiabatic, no-slip type. Outer boundary was located nearly 7 chord lengths from the surface of the wing and 4 chord lengths away in the wingspan direction. At the outer boundary, far field boundary condition was applied.

28.2   TEST CASES

Table 28-1 shows the test matrix for the first computations, carried out by TAI. These calculations were performed with Baldwin Lomax turbulence model and they were used to evaluate the solver, xFLOWg. The wind tunnel test measurements of these cases were provided by Langley National Transonic Facility at NASA [[28-5], [28-6], [28-7], [28-8]]. For a constant Reynolds number of 6 million, subsonic and transonic cases were chosen. Angle of attack variation from 13.3 to 22.6 degree was also investigated for both medium radius and sharp leading edge types. Even though results for all cases were not mentioned, they were listed here for the sake of completeness.

Table 28-1: Test Cases, Analysed with Baldwin-Lomax Turbulence Model

Case	Geometry	Mach	AoA (deg.)	Reynolds (Mil.)
1	SHARP	0.851	13.5	6.0
2	SHARP	0.850	17.5	6.0
3	SHARP	0.851	18.6	6.0
4	SHARP	0.850	20.6	6.0
5	SHARP	0.850	22.6	6.0
6	SHARP	0.400	13.3	6.0
7	SHARP	0.401	17.4	6.0
8	SHARP	0.400	18.4	6.0
9	SHARP	0.401	20.5	6.0
10	SHARP	0.401	22.5	6.0
11	MEDIUM RAD.	0.400	13.3	6.0
12	MEDIUM RAD.	0.400	16.4	6.0
13	MEDIUM RAD.	0.400	18.4	6.0
14	MEDIUM RAD.	0.400	20.4	6.0
15	MEDIUM RAD.	0.400	22.4	6.0
16	MEDIUM RAD.	0.851	13.4	6.0
17	MEDIUM RAD.	0.849	16.5	6.0
18	MEDIUM RAD.	0.849	18.5	6.0
19	MEDIUM RAD.	0.850	20.6	6.0
20	MEDIUM RAD.	0.850	22.6	6.0

In the next stage, instead of Baldwin-Lomax, Spalart-Allmaras turbulence model was used. In order to evaluate the performance of these two turbulence models, 6 cases were studied which were listed in Table 28-5. Selected 6 cases were all at transonic speeds, 4 of them were from the cases listed in Table 1 and other two cases are at

higher angle of attack. The aim of calculations for these additional two cases was to evaluate the flow solver at high angle of attack cases since modelling the phenomenon at high angles of attack is challenging. Finally, focus was identification of the different flow regimes and confirmation of validity of the solver. It is aimed to see the compressibility effects, effect of the leading edge bluntness and angle of attack variation. The test cases studied were listed in the following tables (Table 28-2, Table 28-3, Table 28-4) and for convenience the VFE-2 test matrix nomenclature has been kept.

Table 28-2: Leading Edge Bluntness Effect

Case	Geometry	AoA(deg.)	Mach	Reynolds (Mil.)
11	SLE	18.5	0.2	2
12	RLE	18.5	0.2	2
26	SLE	23.0	0.85	6
27	RLE	23.0	0.85	6

Table 28-3: Angle of Attack Effect, RLE, Re = 6E+6

Case	AoA(deg.)	Mach
5	13.3	0.4
14	18.5	0.4
23	23.0	0.4

Table 28-4: Mach Number Effect, RLE, Re = 6E+6

Case	AoA(deg.)	Mach
23	23	0.4
26	23	0.85

28.3   RESULTS AND DISCUSSION

In this section, only representative cases were chosen to discuss the results of the study. Algebraic Baldwin-Lomax and one equation Spalart-Allmaras turbulence models were compared. Once the numerical concerns were fixed, physical phenomena became the focus of the study. For that goal, Mach number, angle of attack, and leading edge bluntness effects on the flow field were described in detail.

28.3.1   Flow Solver (xFLOWg) Evaluation

The first computations were carried out with algebraic Baldwin-Lomax turbulence model. This model is comparably straightforward, but it did not give acceptable results. Results of only Case 1 from the 20 test cases listed in Table 28-1, were explained here to draw conclusion. Computations for all other cases show similar behavior as Case 1.

As can be seen in Figure 28-3, pressure coefficient (C_p) distribution on the surface of the wing was shown for the sharp leading edge configuration. Mach number is 0.851 with an angle of attack 13.4 degree. Pressure coefficient variation at 5 chord wise locations were plotted and compared with the experimental data. Close to the leading edge, only average values were obtained. At $x/c_r = 0.2$ and 0.4 locations, suction peaks could not be resolved. This also resulted in inaccurate predictions at further downstream locations.
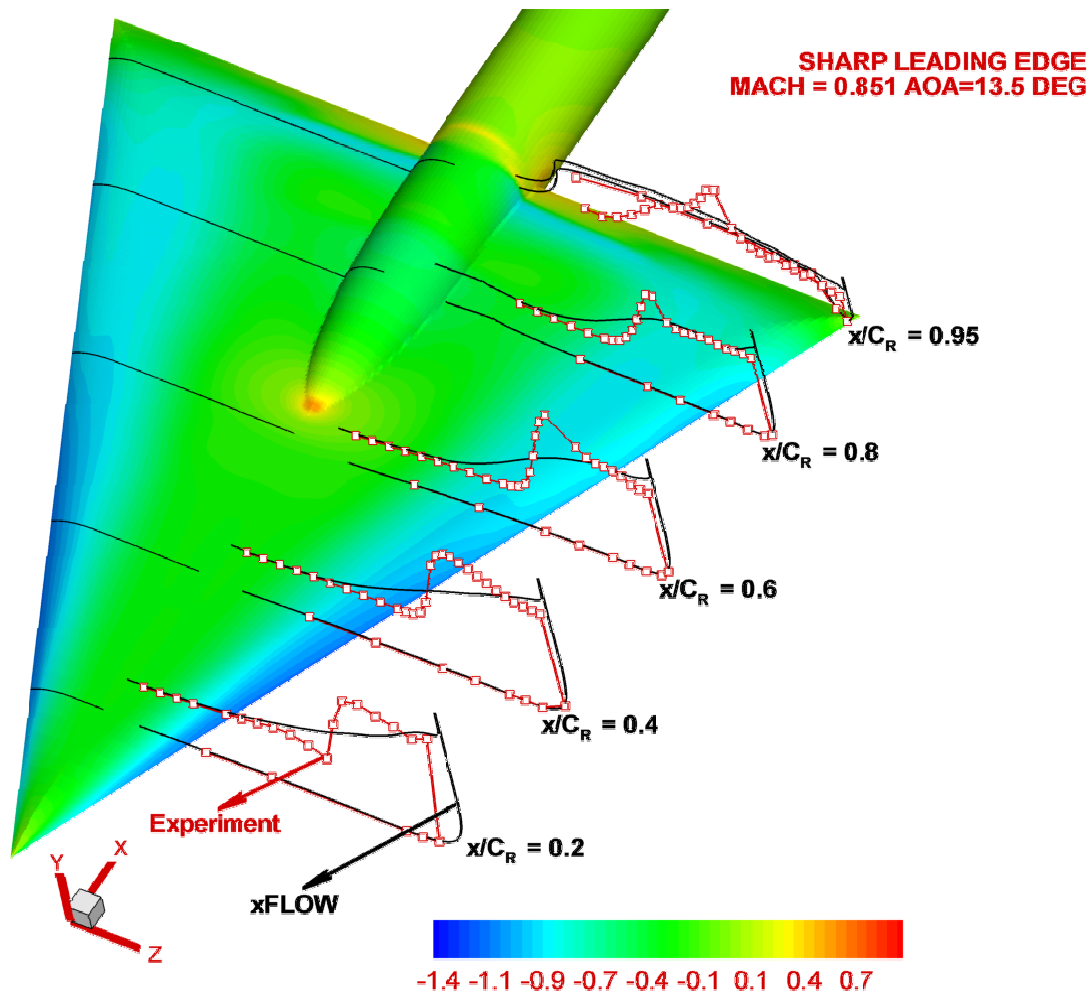
Figure 28-3: C_p Comparisons at x/c_r = 0.2, 0.4, 0.6, 0.8, 0.95 Chord Wise Locations and Surface C_p Plot (Case 1, Table 28-1).

Even though C_p is not totally in agreement with the experimental data, some of the characteristics of the vortical flow structure can be seen. To illustrate the flow patterns clearly, vorticity magnitude lines at different locations and stream lines are shown in Figure 28-4. Streamlines just from the apex rolls into the aft of the wing and forms the longitudinal vortex and flow separates at the leading edge of the wing.
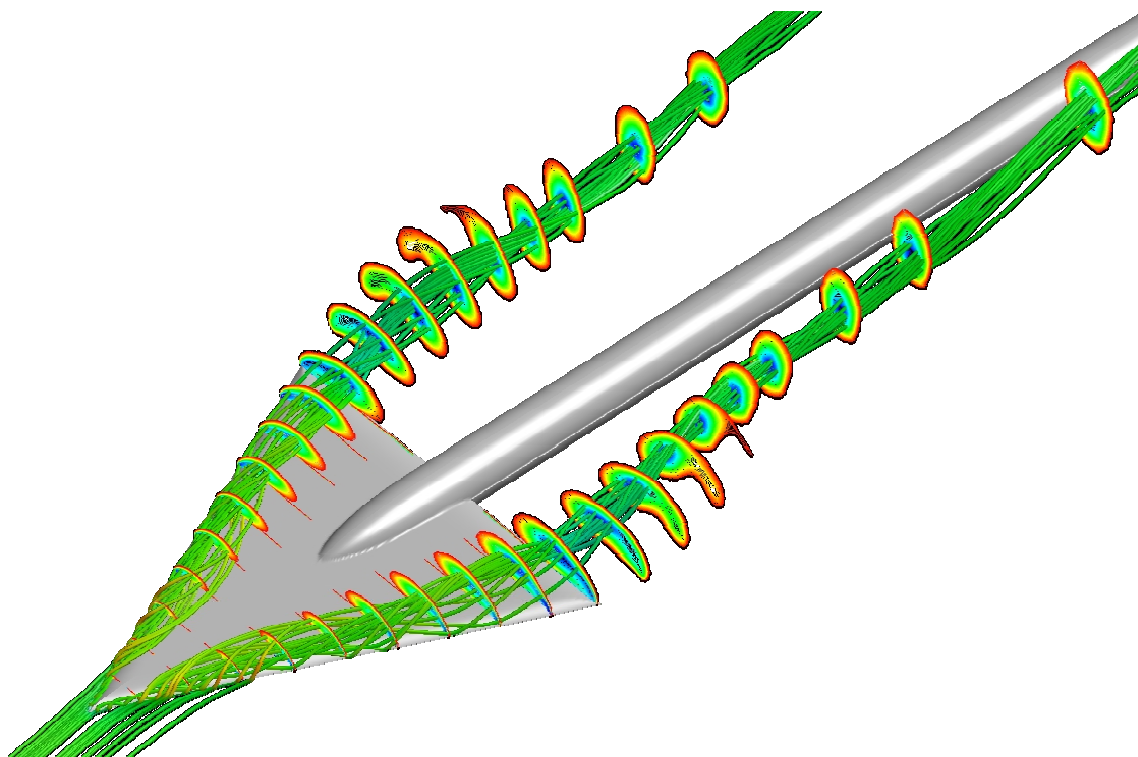
Figure 28-4: Vorticity Magnitude Contours and Stream Lines (Case 1, Table 28-1).

Also, normal force coefficients were calculated for comparison with the measurements. Figure 28-5 shows the normal force coefficient variation versus angle of attack for sharp leading edge configuration at both subsonic and transonic regimes. As can be seen, surprisingly normal force coefficients seem to be in better agreement. The reason for this situation can be understood by referring back to the Figure 28-3. It can be seen that close to apex region, at chord wise locations of 0.2 and 0.4 C_p distribution obtained is correct in the average sense. Since force is obtained by integrating the pressure, results are close to the measurements.
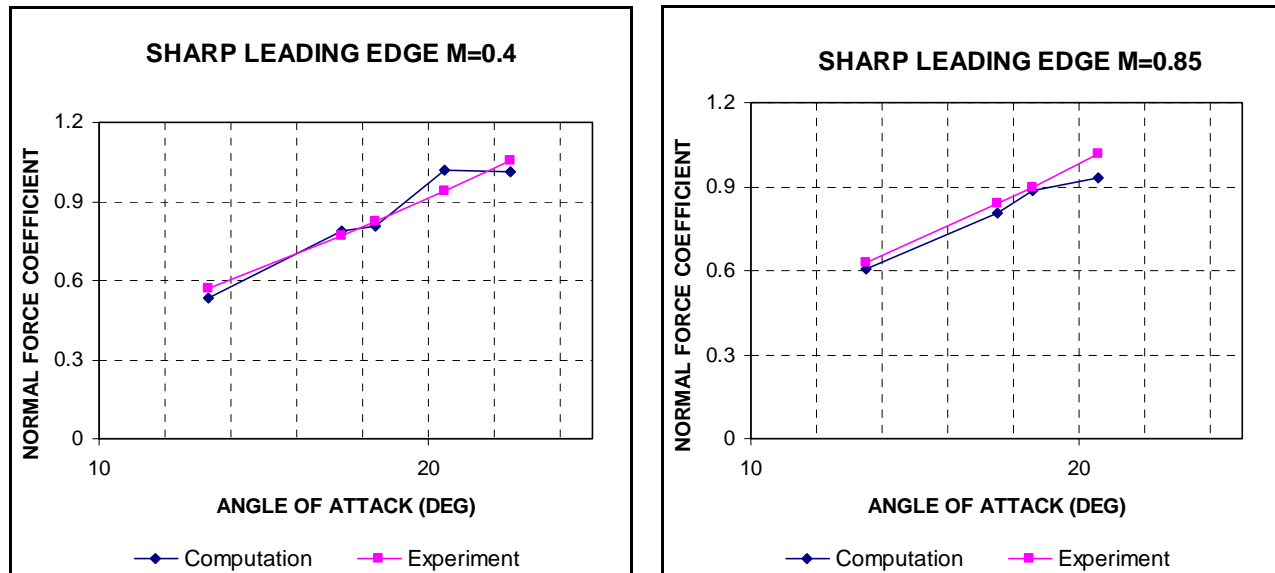
Figure 28-5: Comparison of Normal Force Coefficients for Sharp
Leading Edge Configuration for 0.4 and 0.85 Mach Numbers.

For this specific case and for other cases, inaccurate C_p distribution is mainly due to miss prediction of the onset of separation, inaccurate resolution of vortex shock interaction and vortex breakdown or coupling of these depending on the case. It is difficult to draw reliable physical conclusions from such simulations. It seems that Baldwin-Lomax model does not simulate essential characteristics of this complex vortical flow field.

One of the drawbacks of Baldwin-Lomax turbulence model is that it yielded average values at the vortical regions. Suction peaks representative of the vortical regions could not be obtained properly. Turbulence model is important for resolving this type of vortex dominated flows. In the following sections of this study, instead of Baldwin-Lomax, Spalart-Allmaras turbulence model was used. Special attention was paid for 6 transonic test cases which are listed in Table 28-5. With these test cases, focus is on resolving shock-vortex interaction which turned out to be another challenge for the numerical simulations. Also, high angle of attack cases were chosen to capture vortex breakdown.

Table 28-5: Test Cases for Turbulence Model Study [28-5], [28-8]

Run No	Leading Edge	Point No	AoA (deg.)	Mach	Re (Mil.)
7	MRLE	141	13.4	0.851	6.0
7	MRLE	144	18.5	0.849	6.0
7	MRLE	147	24.6	0.850	6.0
88	SLE	1945	13.5	0.851	6.0
88	SLE	1950	18.6	0.851	6.0
88	SLE	1956	24.6	0.851	6.0

Presence of the longitudinal vortex can be observed with Spalart-Allmaras turbulence model compared to Baldwin-Lomax turbulence model [Figure 28-6]. Streamlines above the surface separate in the front region and rolls into a vortex as can be seen in Figure 28-7. The suction peaks on the upper surface of the wing were captured for "Run No 7" at an angle of attack 18.5 degrees. However, especially close to the apex the strength of the so called primary vortex could not be predicted fairly and the second peaks observed in the experiments were not resolved in the calculations. The presence of those secondary inner vortices is highly dependent on the correct prediction of the strength and location of the primary vortex [28-9]. Beside turbulence model concern, relatively coarse grid might be one reason for not resolving this inner vortex.
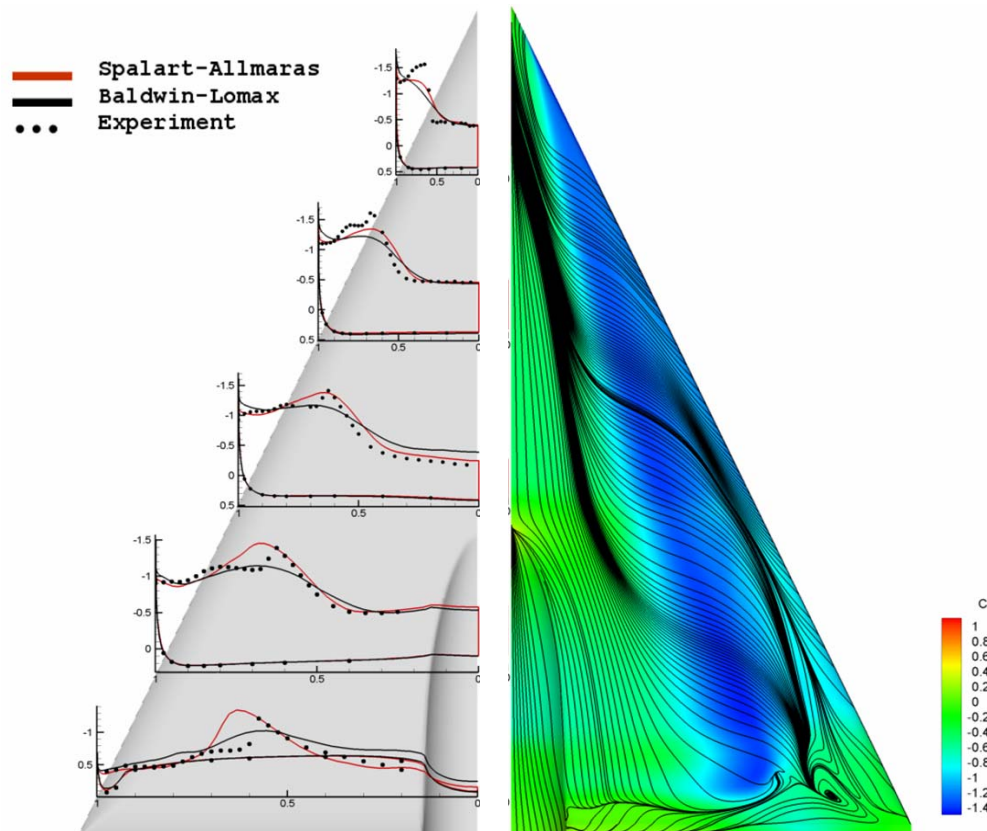
Figure 28-6: C$_p$ Comparisons at x/c$_r$ = 0.2, 0.4, 0.6, 0.8, 0.95 Chord Wise Locations (Point No 144, Table 28-5).

Figure 28-7: Streamlines Close to the Surface on the Suction Side of the Wing (Point No 144, Table 28-5).

At higher angle of attack, 24.6 degree experiment shows the vortex breakdown phenomenon at the rear part of the wing whereas this feature was not captured in the calculations. However, close to the apex separated flow without vortex breakdown was captured successfully (Figure 28-8).
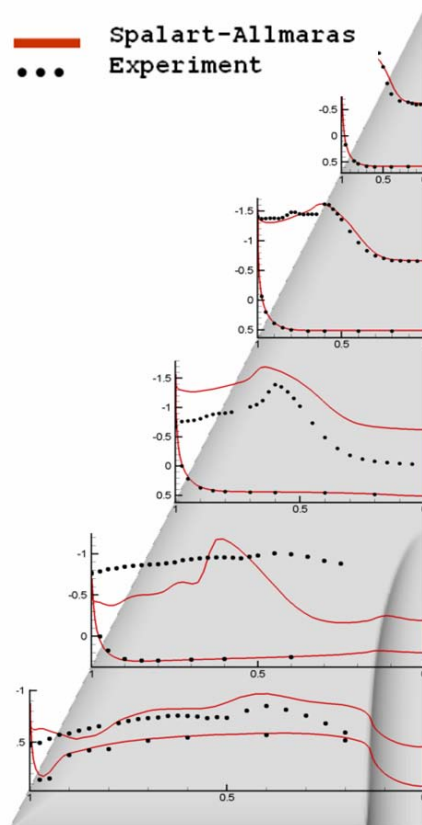
Figure 28-8: C_p Comparisons at x/c_r = 0.2, 0.4, 0.6, 0.8, 0.95 Chord Wise Locations (Point No 147, Table 28-5).
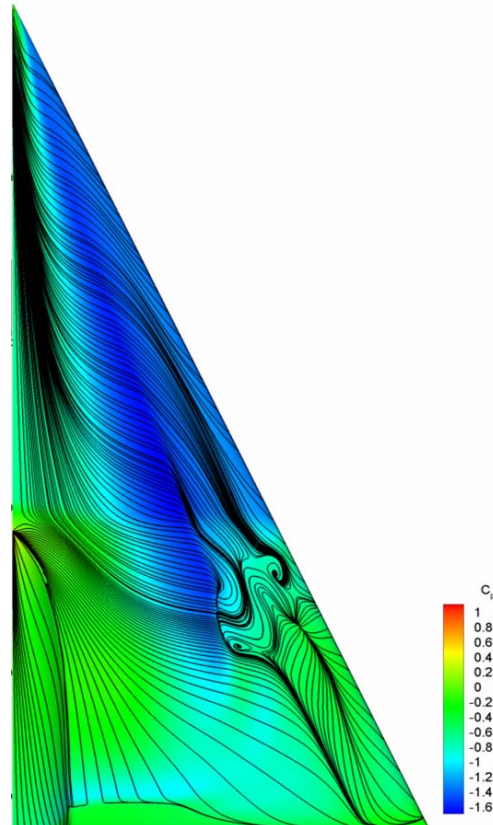
Figure 28-9: Streamlines Close to the Surface on the Suction Side of the Wing (Point No 147, Table 28-5).

There is also some discrepancy with the experimental data as plotted in Figure 28-10, for the sharp leading edge configuration. Vortical flow in the front part of the wing could not be predicted reasonably. On the other hand, Spalart-Allmaras turbulence model produces proper results compared to Baldwin Lomax turbulence model. Especially close to the trailing edge, vortex strength and location predictions are in better agreement with the measurements.

Point No 1945   **Point No 1950**
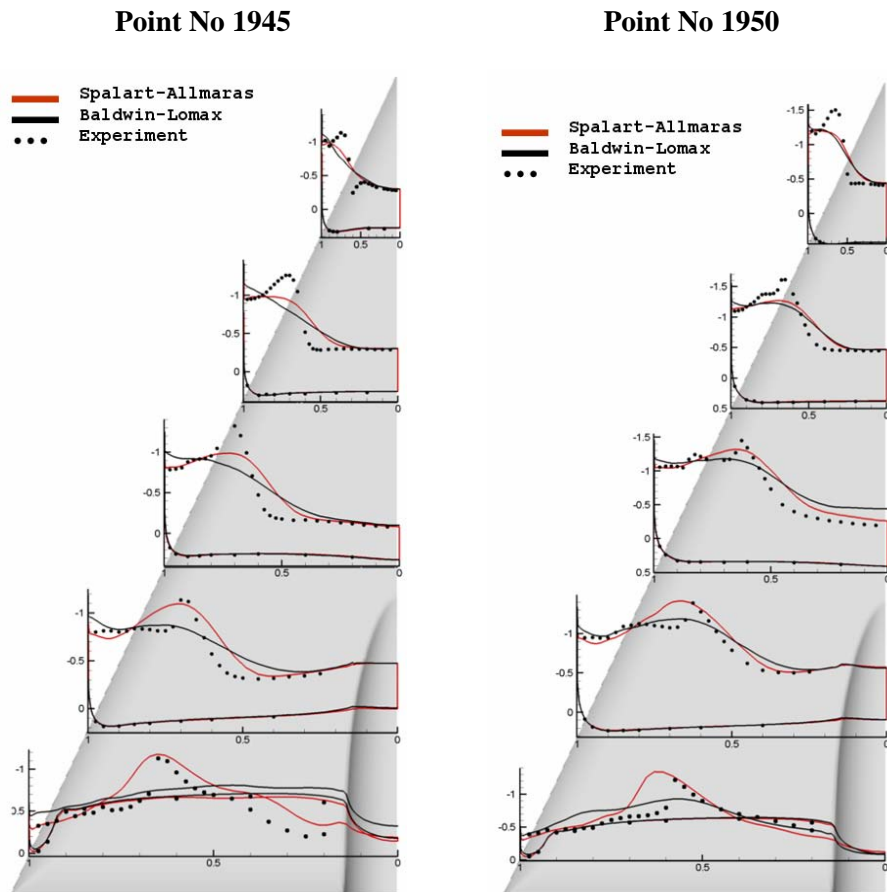
Figure 28-10: C_p Comparisons at x/c_r = 0.2, 0.4, 0.6, 0.8, 0.95
Chord Wise Locations (Point No 1945, 1950, Table 28-5).

The above figures (Figure 28-6, Figure 28-8, Figure 28-10) show that prediction capability of the solver was significantly improved with implemented Spalart-Allmaras turbulence model. In the rest of the study, focus is on the detailed description of the flow field. Angle of attack, compressibility and leading edge bluntness effects on the flow field characteristics were presented. As will be clear in the following section, flow characteristics are strongly dependent on the above stated items, and clear distinction can be made on the governed flow physics. First emphasis is on the validation of the test cases before explaining the physics behind.

28.3.2   Comparison with Experimental Results

Following figures show the pressure coefficient comparison between the experimental and computational results of the cases studied. The solid lines correspond to numerical results and the dots represent the measured values. Numerical results mostly match well with the experimental data at subsonic and transonic speeds for sharp and round leading edge configurations. As shown in Figure 28-11 and Figure 28-19, the suction peaks and their locations were predicted well at chord wise and span wise locations. There is a discrepancy between numerical and experimental values close to apex for Case 11 and 12 as can be seen in Figure 28-11. The suction peak corresponding to strength of primary vortex was under predicted. However, further downstream flow development was correctly simulated and solutions matched with the experimental data satisfactorily.

Case 11 RLE   **Case 12 SLE**
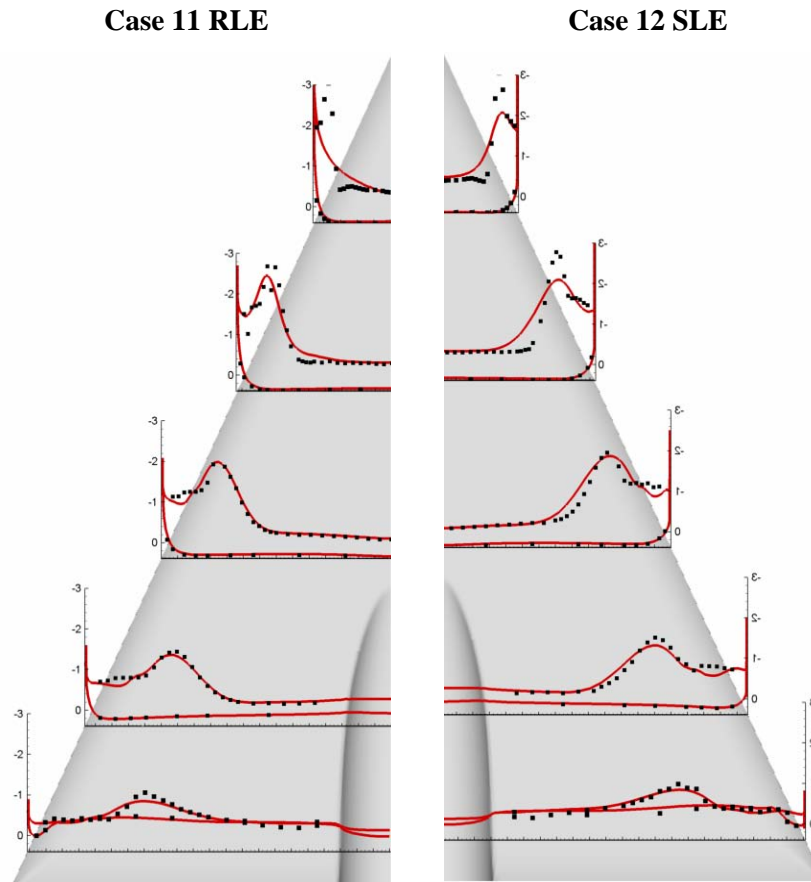
Figure 28-11: C$_p$ Comparisons at x/c$_r$ = 0.2, 0.4, 0.6, 0.8, 0.95
Chord Wise Locations (Case 11-12, Table 28-2).

Vortical flow structure was resolved well for Case 26 and 27 even at the upstream locations compared to Case 11 and 12. In fact, flows in Case 11 and 12 are incompressible. Since xFLOWg is a compressible solver, there is a need of a prediction method for incompressible flows. Though, satisfactory results for compressible cases confirm the validity of the solver.

Case 26 RLE   **Case 27 SLE**
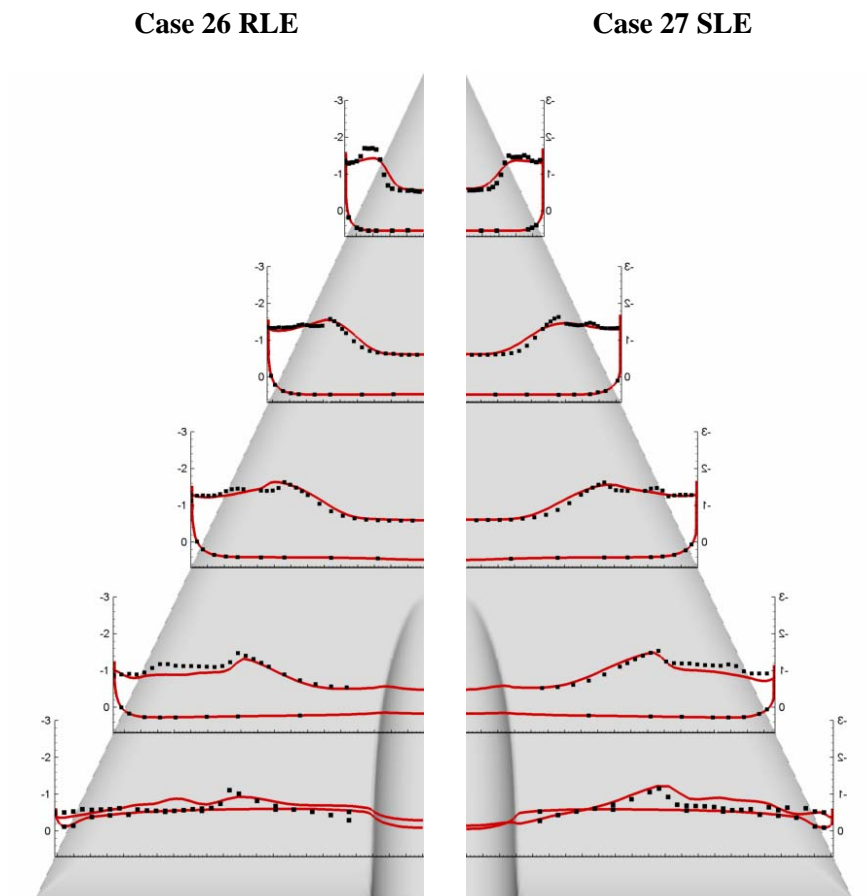
**Figure 28-12: C$_p$ Comparisons at x/c$_r$ = 0.2, 0.4, 0.6, 0.8, 0.95
Chord Wise Locations, (Case 26-27, Table 28-2).**

Figure 28-13 shows that there is a slight disagreement at the highest angle of attack, but again topology of the vortical flow field was resolved well. At high angles of attack, unsteadiness of flow dominates the problem. In this study all the calculations were done at steady state conditions. As a result, solution for this case might be improved by taking unsteadiness into account. Also, better resolution of the grid or solution based grid adaptation might yield better results.

Case 5   **Case 14**   **Case 23**
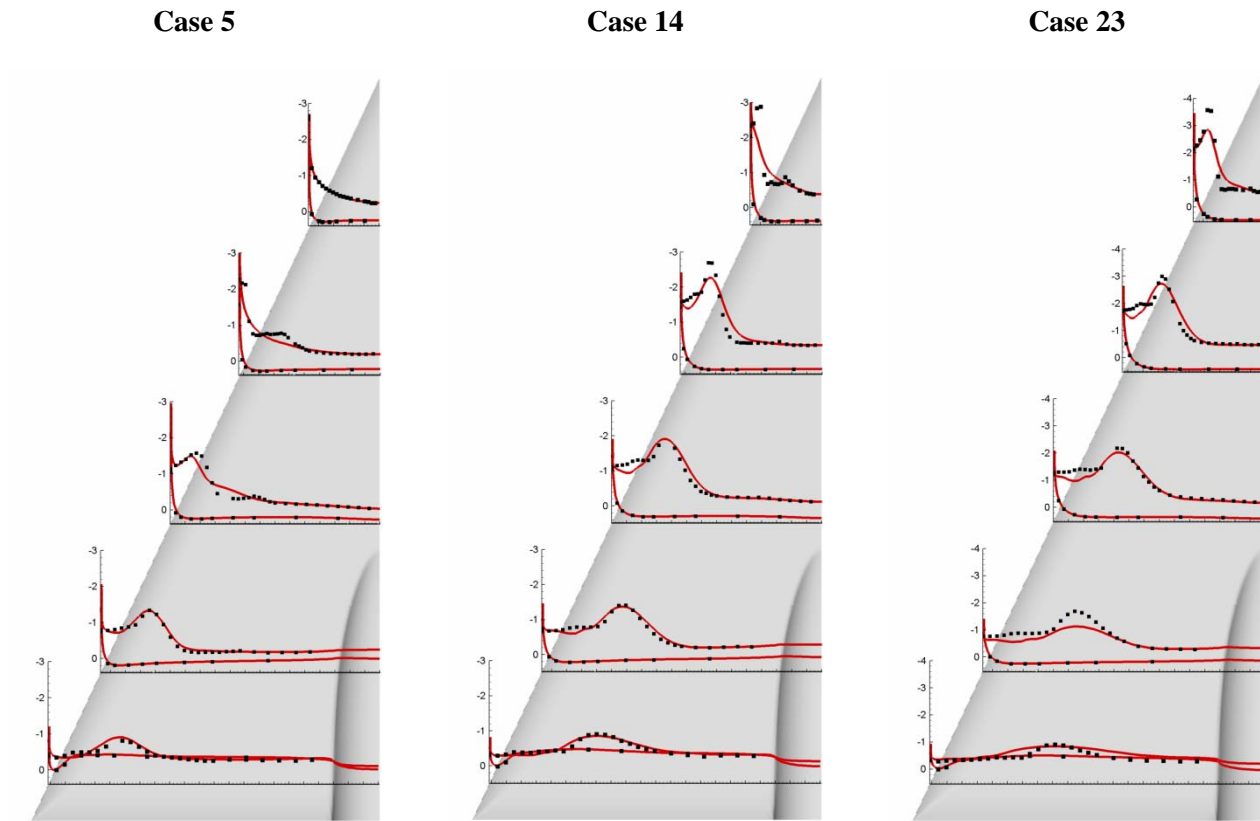
Figure 28-13: C$_p$ Comparisons at x/c$_r$ = 0.2, 0.4, 0.6, 0.8, 0.95
Chord Wise Locations (Case 5 ,14, 23, Table 28-3).

28.3.3   Some Factors Influencing the Vortical Flow Field

Following sections were dedicated for better understanding of the physical aspects of the flow field for a range of Mach number, and angles of attack. It is seen that features of flow is highly dependent on these parameters. Also, depending on the shape of the leading edge different flow features were observed.

28.3.3.1   Influence of Mach Number

Case 23 and 26 with Mach number of 0.4 and 0.85 for medium radius leading edge configuration were selected to investigate the compressibility effect on the flow field. Angle of attack is 23 degree, and vortex breakdown phenomenon is also present. As illustrated in Figure 28-14, Figure 28-15, Figure 28-16, Figure 28-17, increase in Mach number results in:

- Movement of primary vortex to the inboard;

- Increase in vortex strength;

- Stronger secondary vortex formed close to leading edge;

- Decrease in suction peak in the surface pressure distribution; and

- Onset of separation closer to the apex.

Case 23 Mach = 0.4   **Case 26 Mach = 0.85**
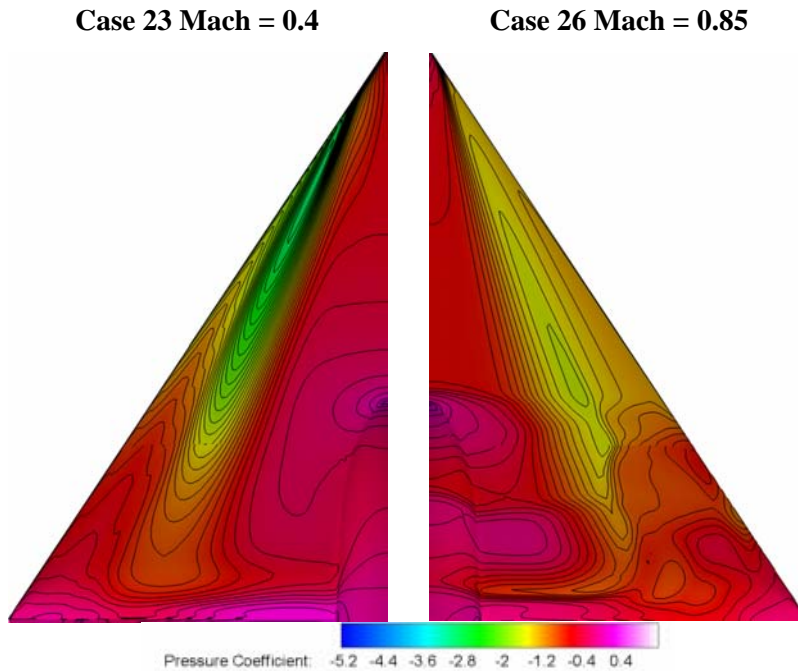
Figure 28-14: Surface Pressure Contours (Case 23 and 26, Table 28-4).

Case 23 Mach = 0.4   **Case 26 Mach = 0.85**
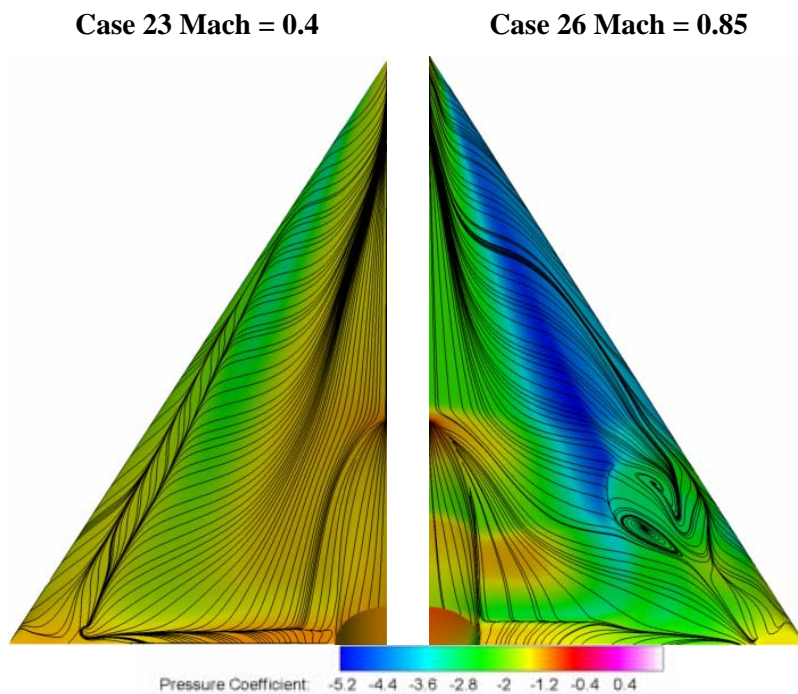
Figure 28-15: Streamlines Close to the Surface (Case 23 and 26, Table 28-4).

Case 23 Mach = 0.4   **Case 26 Mach = 0.85**
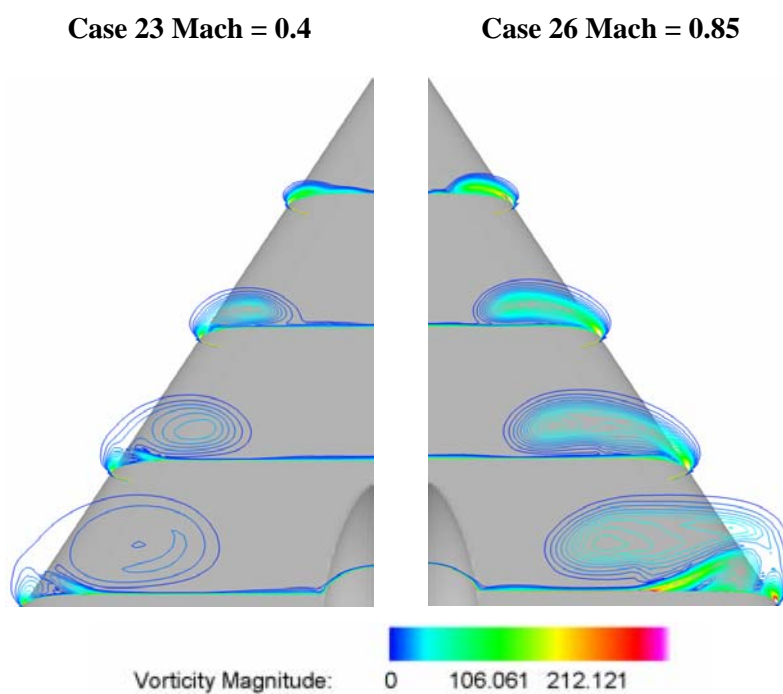
**Figure 28-16: Vorticity Magnitude Isolines at Various
Chord Wise Locations (Case 23 and 26, Table 28-4).**
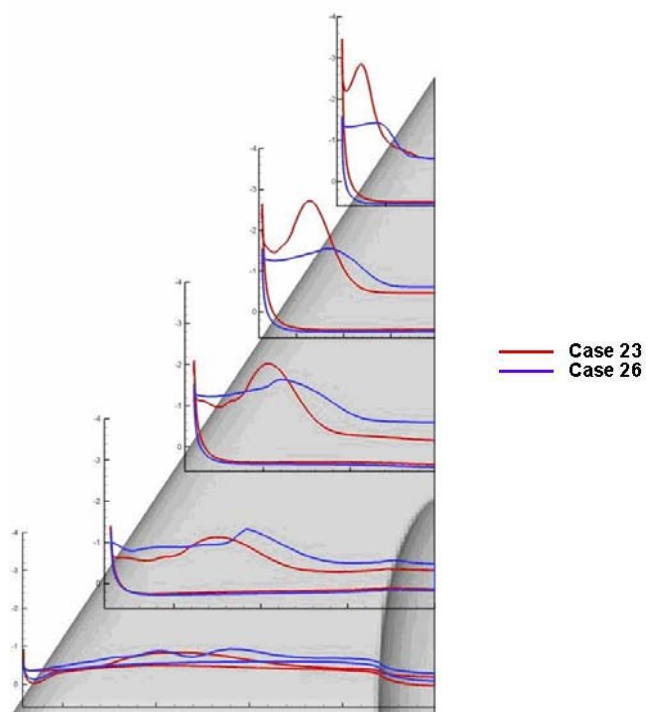
Figure 28-17: C_p Lines at x/c_r = 0.2, 0.4, 0.6, 0.8, 0.95 Chord Wise Locations (Case 23 and 26, Table 28-4).

A shock is observed for Case 26, on the delta wing close to the nose of the sting, and two other cross shocks were also seen close to the rear part of the wing as shown in the Figure 28-15. This case was challenging since interaction between vortex and the shocks were not easy to describe. Resolving this feature resulted in accurate C_p distribution on the surface of the wing.

28.3.3.2   Influence of Leading Edge Bluntness

Rounded leading edge (RLE) and sharp leading edge (SLE) configurations have similar basic flow patterns. The difference for RLE is that, primary separation line is no longer at leading edge. The leading edge curvature is one of the parameters influencing the onset of flow separation. Flow separates just from the apex of the leading edge for SLE while for RLE there is a larger area of attached flow around the apex at low angle of attack as shown in the Figure 28-19. Comparing the Case 11 and 12, with a Mach number of 0.2 and 18.5 degree angle of attack, the main difference is at the fore part of the wing. For high angle of attack and high speed flow condition, vortical core moves slightly toward inboard for the sharp leading edge (Case 26 and 27). The two cases show that bluntness has a significant influence on the flow field at low angle of attacks and low Mach numbers but when the flow conditions are vigorous, flow features over delta wing is less affected by leading edge type.
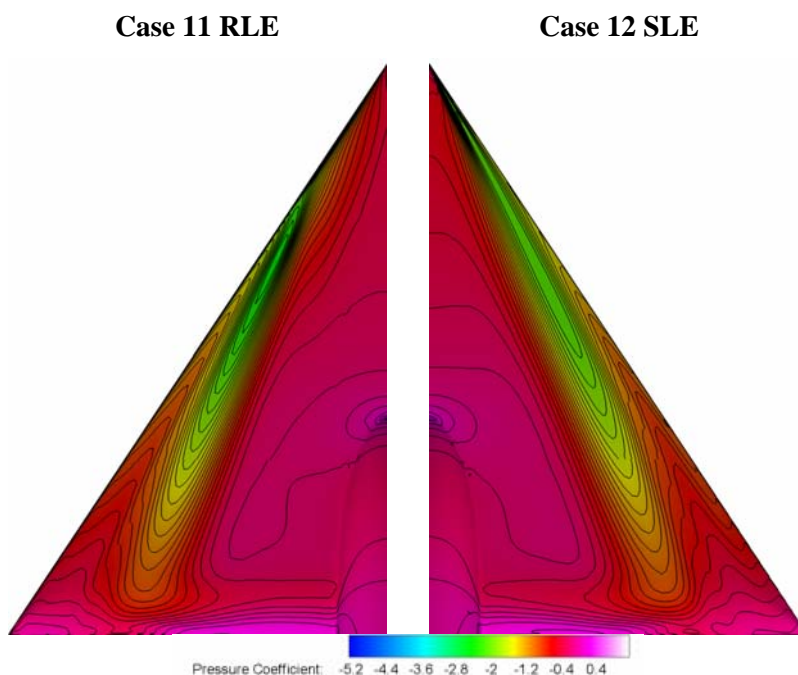
Figure 28-18: Surface Pressure Contours (Case 11 and 12, Table 28-2).

Case 11 RLE   **Case 12 SLE**
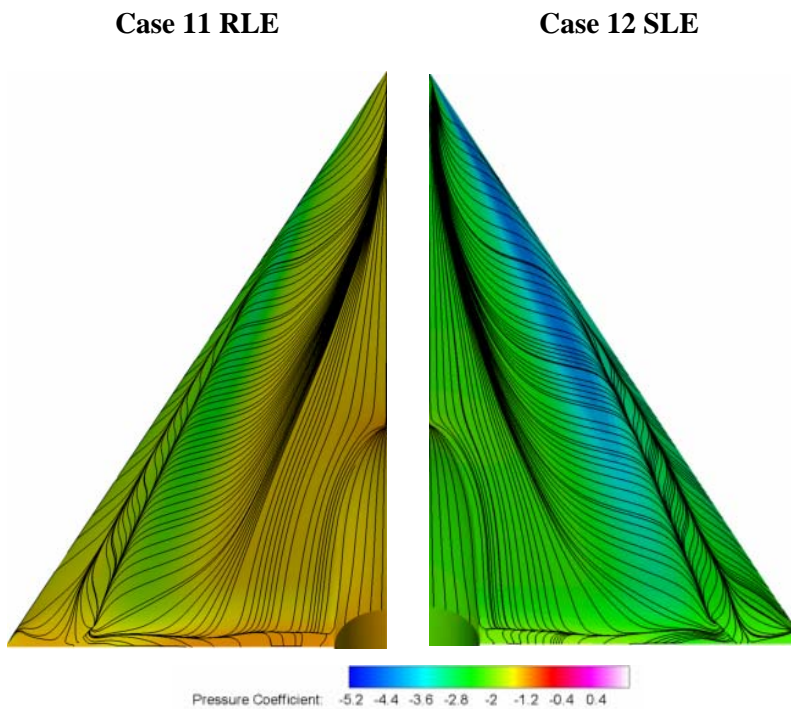
Figure 28-19: Streamlines Close to the Surface (Case 11 and 12, Table 28-2).

Case 11 RLE   **Case 12 SLE**
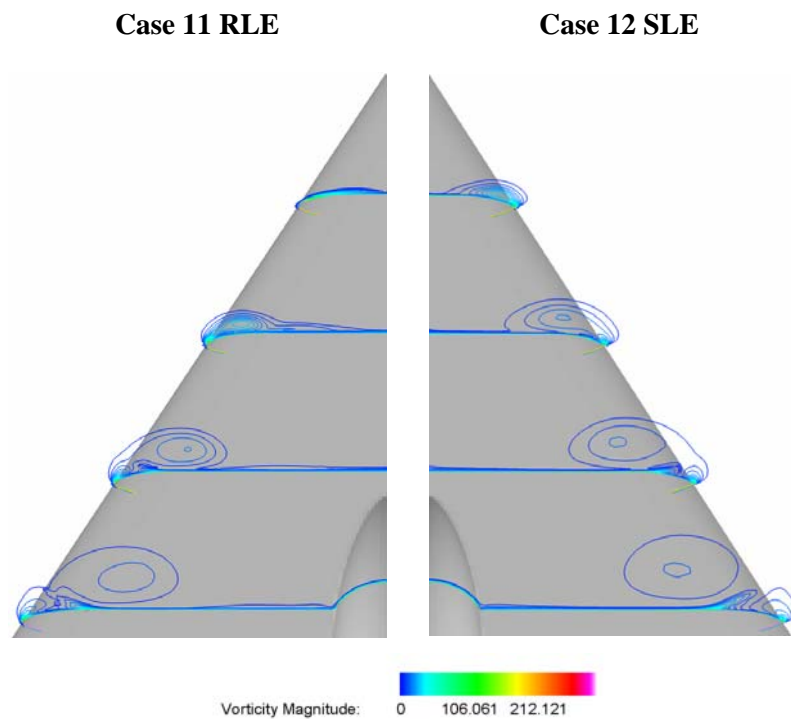
Figure 28-20: Vorticity Magnitude Isolines at Various Chord Wise Locations (Case 11 and 12, Table 28-2).
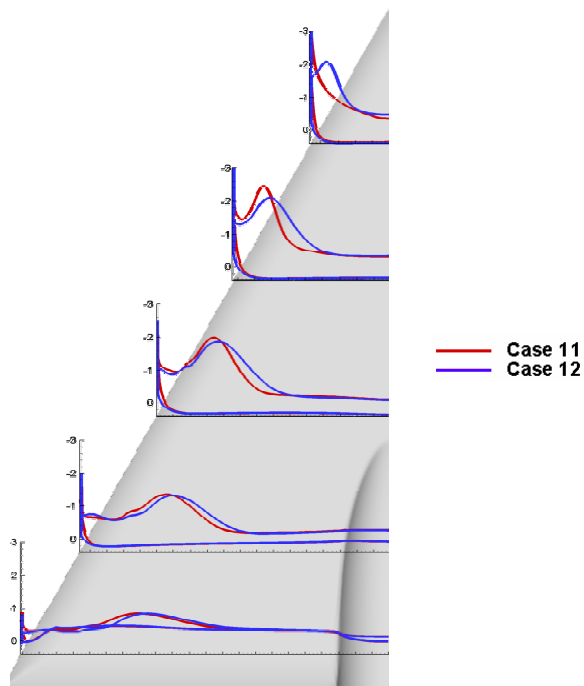
Figure 28-21: C$_p$ Lines at x/c$_r$ = 0.2, 0.4, 0.6, 0.8, 0.95 Chord Wise Locations (Case 11 and 12, Table 28-2).

Case 26 RLE   Case 27 SLE
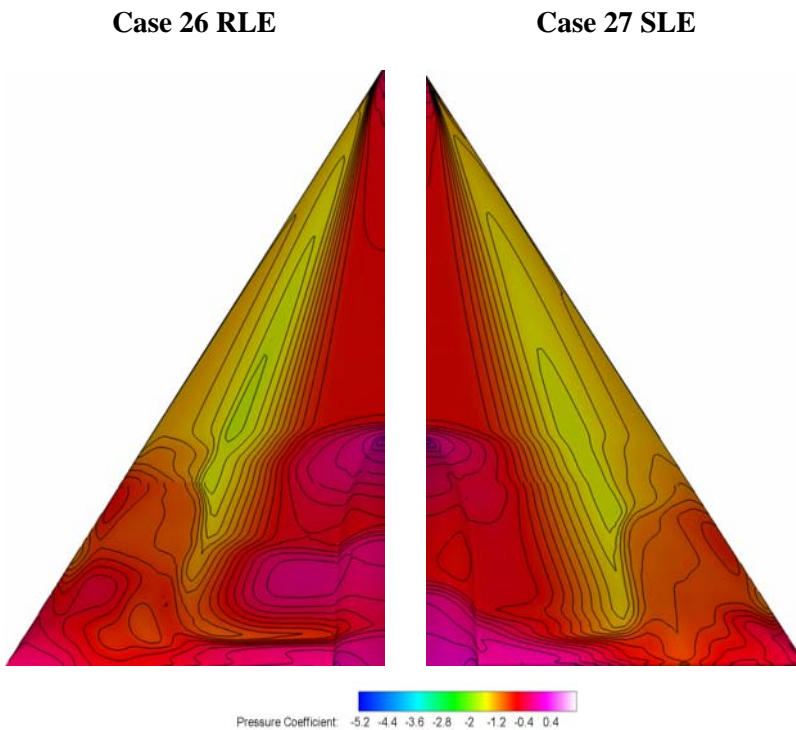
Figure 28-22: Surface Pressure Contours (Case 26 and 27, Table 28-2).

Case 26 RLE   **Case 27 SLE**
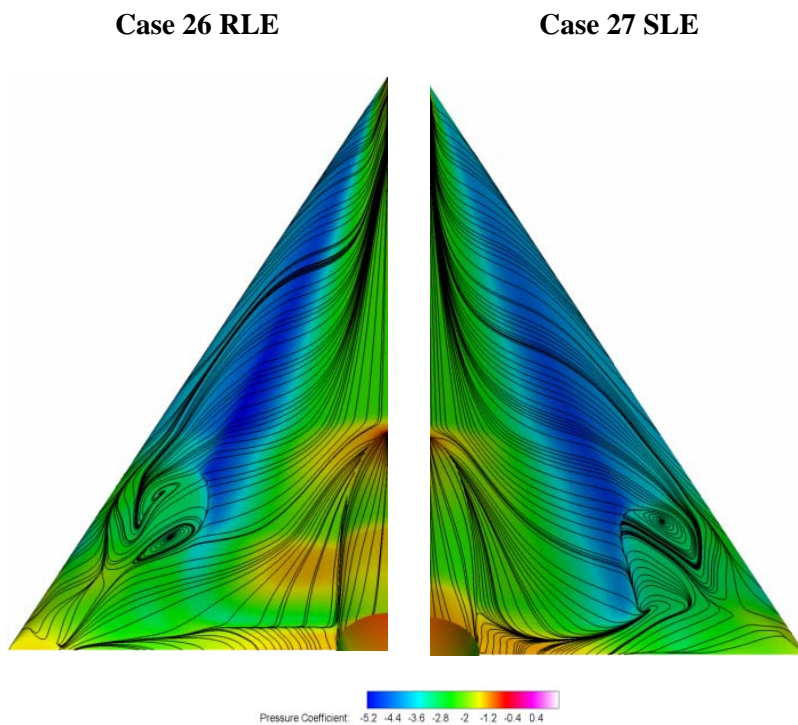
Figure 28-23: Streamlines Close to the Surface (Case 26 and 27, Table 28-2).

Case 26 RLE   **Case 27 SLE**
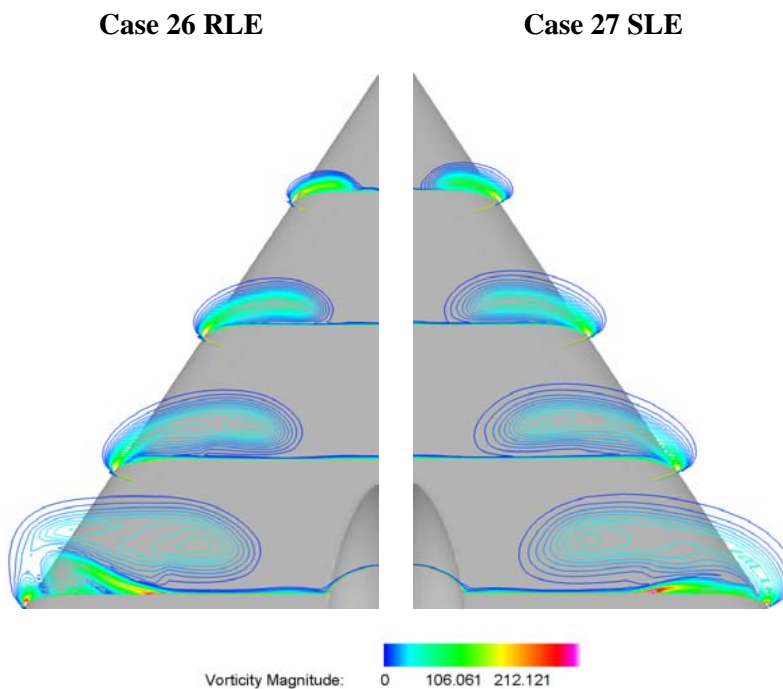
Figure 28-24: Vorticity Magnitude Isolines at Various Chord Wise Locations (Case 26 and 27, Table 28-2).
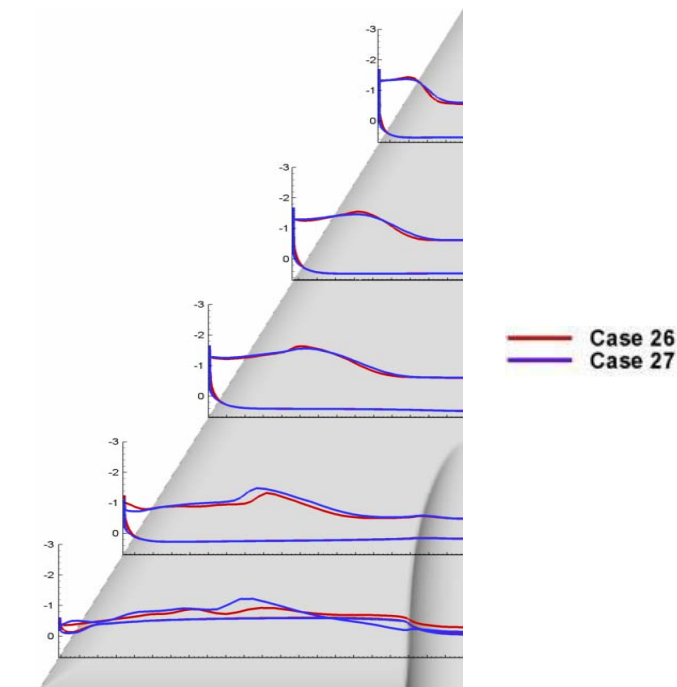
**Figure 28-25: C$_p$ Lines at x/c$_r$ = 0.2, 0.4, 0.6, 0.8, 0.95
Chord Wise Locations (Case 26 and 27, Table 28-2).**

28.3.3.3   Influence of Angle of Attack

To investigate the angle of attack effect, Case 5, Case 14 and Case 23 were compared. All cases are for rounded leading edge configuration with a Mach number of 0.85 and Reynolds number of 6 million. Figure 28-26 and Figure 28-27 show the C$_p$ distribution on the upper surface of the wing. Streamlines and vorticity magnitude lines at three different angles of attack were drawn in the following figures.

Case 5, AoA = 5 deg   **Case 14, AoA = 18.5 deg**   **Case 23, AoA = 23.0 deg**

Pressure Coefficient: -5.2   -4.4   -3.6   -2.8   -2   -1.2   -0.4   0.4
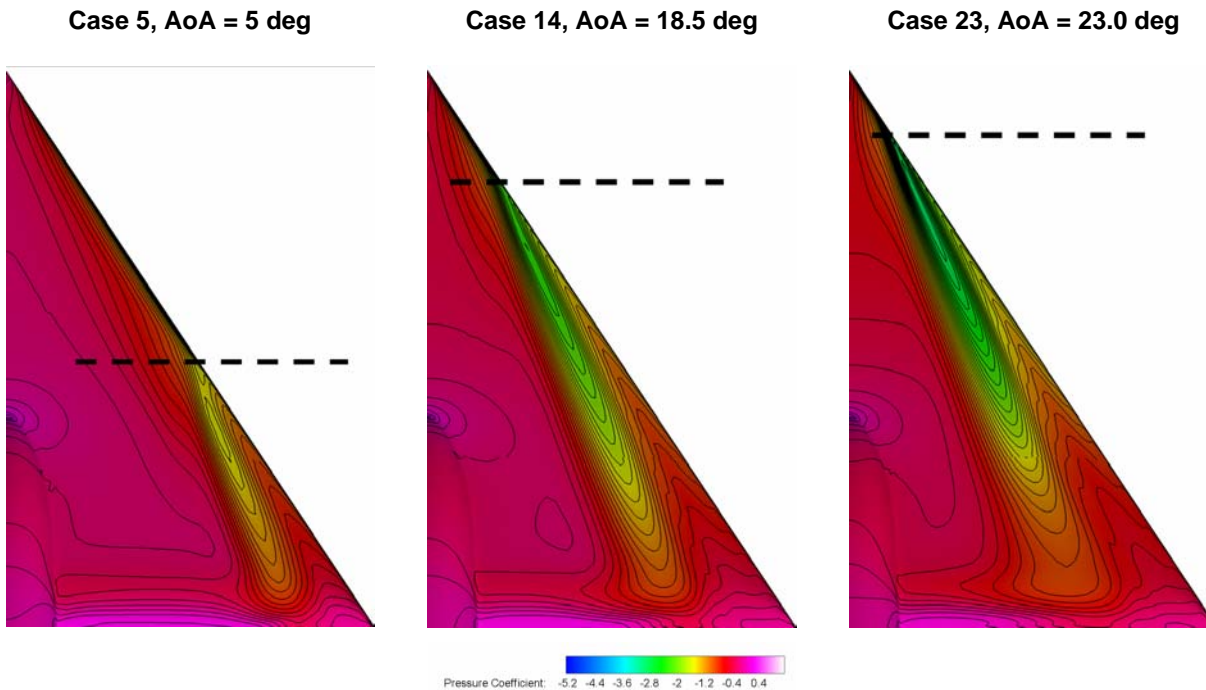
Figure 28-26: Surface Pressure Contours (Case 5, 14 and 23, Table 28-3).
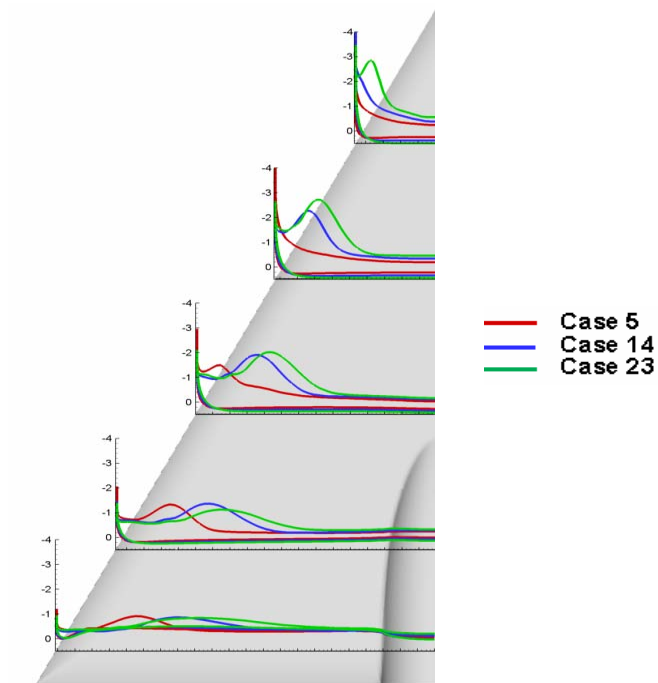
Figure 28-27: C$_p$ Lines at x/c$_r$ = 0.2, 0.4, 0.6, 0.8, 0.95 Chord Wise Locations (Case 5, 14 and 23, Table 28-3).

For case 5, it is clearly seen that flow is mostly attached on the surface as can be seen from the Figure 28-26 and Figure 28-28. The onset of the leading edge vortex is close to $x/c_r = 0.5$ location as shown in Figure 28-26. Case 14 is again for the round leading edge configuration at higher angle of attack, the leading edge separation moves towards to the apex as shown in Figure 28-26. As shown in Figure 28-29, Figure 28-31, and Figure 28-33, vortex strength increases with the angle of attack, attachment and separation lines are also obvious in Figure 28-28, Figure 28-30, Figure 28-32 for the three angles of attack.
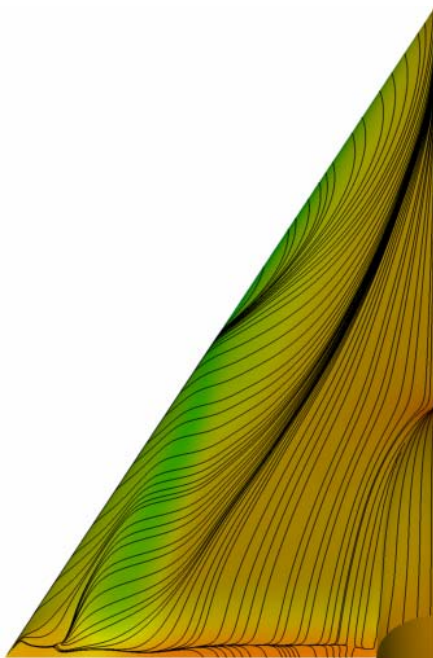
Figure 28-28: Streamlines Close to the Surface (Case 5, Table 28-3).
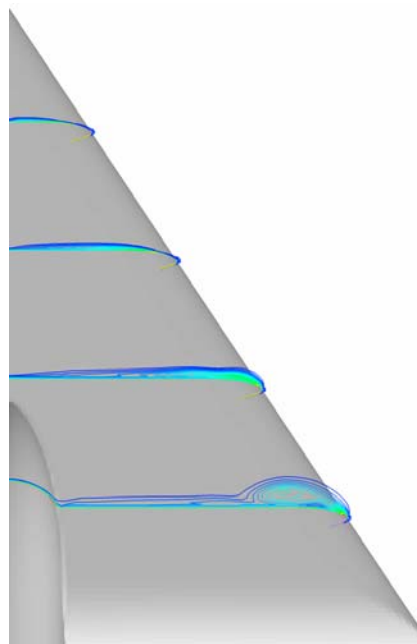
Figure 28-29: Vorticity Magnitude Isolines at Various Chord Wise Locations (Case 5, Table 28-2).
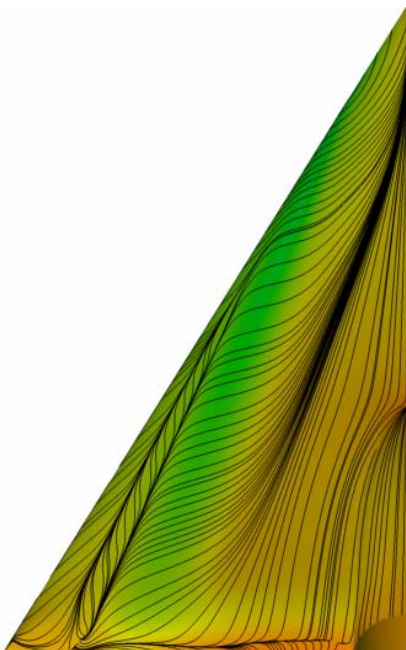
**Figure 28-30: Streamlines Close to
the Surface (Case 14, Table 28-3).**
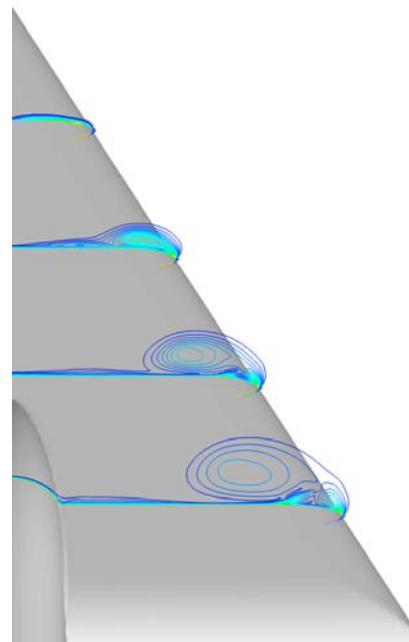
**Figure 28-31: Vorticity Magnitude Isolines at Various
Chord Wise Locations (Case 14, Table 28-2).**
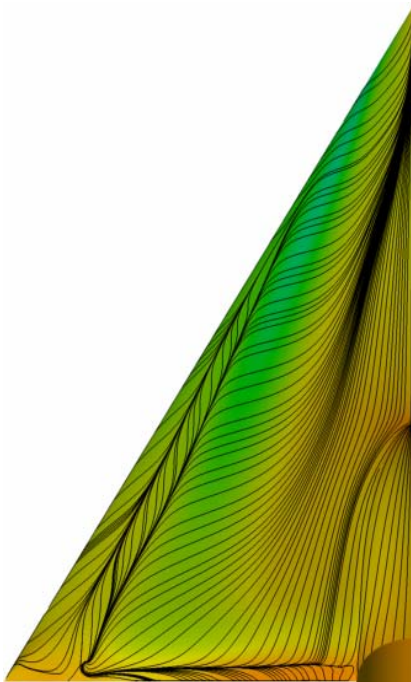
**Figure 28-32: Streamlines Close to
the Surface (Case 23, Table 28-3).**
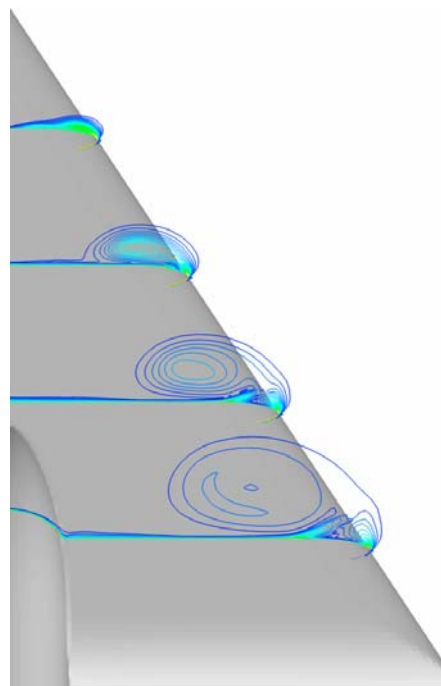
**Figure 28-33: Vorticity Magnitude Isolines at Various
Chord Wise Locations (Case 23, Table 28-2).**

In summary, increase in angle of attack results in:

- Onset of separation point movement toward the upstream;

- Higher vortex strength; and

- Vortex moving away from the leading edge towards to the center of the wing.

28.4 CONCLUSIONS

Within the framework of VFE-2 AVT-113 task group, TAI performed numerical calculations to investigate the vortical flow field characteristics on delta wing configuration. In-house developed structured, 3D Navier-Stokes solver has been used. Both subsonic and transonic cases with sharp and rounded leading edge configurations were numerically simulated. A range of angle of attack was chosen to investigate its effect on the flow field.

Two different turbulence models were used. Compared to Baldwin-Lomax, Spalart-Allmaras turbulence model resolved the vortical structure more properly. Significant improvement has been achieved on the predictions just by this turbulence model concern. It is concluded that the in-house developed solver yields reasonable results especially for the compressible flows. Discrepancies with the experimental data in incompressible regime were present. Therefore, to improve the solver capability for incompressible flows is under consideration. Another concern is that at high angle of attacks flow becomes unsteady. Since steady calculations result in some discrepancy with the experimental data, it is better to perform unsteady calculations for high angle of attack cases. In addition to these concerns, grid resolution is another important parameter on the results. Solution based grid adaptation will yield better results to resolve vortical and shock dominated flows.

Computations shed light on the physics of the flow field. From the physical point of view, effect of Mach number, leading edge bluntness, and angle of attack on the flow features of delta wings were investigated. Regarding the factor of leading edge bluntness, it is shown that as flow becomes vigorous, which means at high angles of attack and high speeds, leading edge type has less influence on the flow structure. Different flow phenomena govern the flow field depending on the angle of attack and classification can be done accordingly. Compressibility has also big importance on the vortical flow topology.

Both numerical and experimental studies gave better insight on the flow physics of delta wings. The studies made within this work group have led the evaluation of the CFD solvers of various participants. Comparison with both experiments and with other codes turned out to be beneficial for understanding and simulation of complex flow problems. Considerable improvement concerning the mentioned aspects has been achieved through the VFE-2 International Vortex Flow Experiment.

28.5 REFERENCES

[28-1] Gürdamar, E., Tarhan, E., Ortakaya, Y. and Korkem, B.: *Parallel Navier-Stokes Solutions of NASA 65°
Delta Wing,* International Conference on Parallel Computational Fluid Dynamics, 21-24.05.2007
Antalya, Turkey.

[28-2] Tarhan, E., Ortakaya, Y., Gürdamar, E. and Korkem, B.: *Parallel Navier-Stokes Solutions of a Wing-
Flap Configuration on Structured Multiblock Oversetting Grids*, International Conference on Parallel
Computational Fluid Dynamics, 21-24.05.2007 Antalya, Turkey.

[28-3]   Şahin, P., Gürdamar, E., Tarhan, E., Ortakaya, Y. and Korkem, B.: *Parallel Turbulent Navier-Stokes Solutions of Wing Alone Geometries Used in the Drag Prediction Workshop III*, International Conference on Parallel Computational Fluid Dynamics, 21-24.05.2007 Antalya, Turkey.

[28-4]   Güzel, G., Ortakaya, Y. and Korkem, B.: *An Implementation and Validation Study on the Actuator Disk Model*, International Forum on Rotorcraft Multidisciplinary Technology, October 15-17, 2007 Seoul, Korea.

[28-5]   Chu, J. and Luckring, J.M.: *Experimental Surface Pressure Data Obtained on 65° Delta Wing Across Reynolds Number and Mach Number Ranges, Volume 1 – Sharp Leading Edge, Appendix C*, NASA Technical Memorandum 4645, February 1996.

[28-6]   Chu, J. and Luckring, J.M.: *Experimental Surface Pressure Data Obtained on 65° Delta Wing Across Reynolds Number and Mach Number Ranges, Volume 1 – Sharp Leading Edge, Appendix D*, NASA Technical Memorandum 4645, February 1996.

[28-7]   Chu, J. and Luckring, J.M.: *Experimental Surface Pressure Data Obtained on 65° Delta Wing Across Reynolds Number and Mach Number Ranges, Volume 3 – Medium Radius Leading Edge, Appendix C*, NASA Technical Memorandum 4645, February 1996.

[28-8]   Chu, J. and Luckring, J.M.: *Experimental Surface Pressure Data Obtained on 65° Delta Wing Across Reynolds Number and Mach Number Ranges, Volume 3 – Medium Radius Leading Edge, Appendix E*, NASA Technical Memorandum 4645, February 1996.

[28-9]   Fritz, W. and Cummings, R.M.: *What was Learned from the Numerical Simulations for the VFE-2*, AIAA 2008-389, 46th AIAA Aerospace Sciences Meeting and Exhibit, 7-10 January 2008, Reno, Nevada.

Chapter 29 – SHOCK EFFECTS ON DELTA WING VORTEX BREAKDOWN

by

**Lucy A. Schiavetta, Okko J. Boelens, Simone Crippa,
Russell M. Cummings, Willy Fritz, Ken J. Badcock**

ABSTRACT

It has been observed that delta wings placed in a transonic freestream can experience a sudden movement of the vortex breakdown location as the angle of incidence is increased. The chapter reports on the use Computational Fluid Dynamics (CFD) to examine this behaviour in detail. The study shows that a shock-vortex interaction is responsible. The balance of the vortex strength and axial flow, and the shock strength, is examined to provide an explanation of the sensitivity of the breakdown location. Limited experimental data is available to supplement the CFD results in certain key respects, and the ideal synergy between CFD and experiments for this problem is considered.

29.1 INTRODUCTION

The occurrence of shocks on delta wings introduces complex shock/vortex interactions, particularly at moderate to high angles of incidence. These interactions can make a significant difference to the vortex breakdown behaviour. For subsonic flows the motion of the location of onset of breakdown towards the apex is relatively gradual with increasing incidence [29-1]. The strengthening of the shock which stands off the sting as the incidence is increased can lead to a shock/vortex interaction triggering breakdown. The location of breakdown can shift upstream by as much as 30% of the chord in a single one degree incidence interval [[29-2], [29-3]] due to this interaction.

From the study of the interaction between longitudinal vortices and normal shocks in supersonic flow [29-4] it has been found that it is possible for a vortex to pass through a normal shock without being weakened sufficiently to cause breakdown. The flow over slender delta wings is potentially more complex as the shock is not necessarily normal to the freestream in the vortex core region [29-5]. Investigation is needed to consider the behaviour and onset of vortex breakdown, particularly with respect to shock/vortex interactions.

To consider this behaviour, the flow over a sharp leading edged, slender delta wing was considered under subsonic and transonic conditions. This investigation was undertaken as part of the 2nd International Vortex Flow Experiment (VFE-2), a facet of the NATO RTO AVT-113 Task Group, which was set up to consider the flow behaviour both experimentally and computationally over a specified 65° delta wing geometry. The work of VFE-2 built on the first International Vortex Flow Experiment (VFE-1) [29-6] carried out in the late eighties, which was used to validate the inviscid CFD codes of the time. Progress has been made in both experimental and computational aerodynamics, particularly in turbulence models since the conclusion of the VFE-1. Therefore, it was proposed by Hummel and Redecker [29-7] that a second experiment should be undertaken to provide a new, comprehensive database of results for various test conditions and flow regimes, to further the understanding of vortical flows. The test conditions considered under the VFE-2 framework include both subsonic and transonic Mach numbers for low, medium and high angles of incidence at a range of Reynolds numbers [29-8].

The measured data at transonic conditions showed a sudden jump of the breakdown location towards the wing apex when a critical angle of incidence was reached. The current study uses CFD to investigate this effect towards an explanation of the detailed factors contributing to this behaviour. The paper continues with a description of the test case and observed experimental behaviour. A summary of a wide ranging CFD study is then presented. Finally, the combined results are considered to produce an assessment of the mechanisms driving the flow behaviour.

29.2   EXPERIMENTS

The geometry used for the VFE-2 was originally tested in experiments carried out by Chu and Luckring [[29-9], [29-10], [29-11], [29-12]] in the National Transonic Facility (NTF) at NASA Langley. These experiments considered a 65° delta wing with four leading edge profiles (one sharp and three rounded with small, medium and large radii) for a wide range of conditions both subsonic and transonic and for both test and flight Reynolds numbers. This data has been compiled into a comprehensive experimental database and formed the basis for the investigations of the VFE-2. The geometry is analytically defined for all leading edge profiles. Both the medium radius and sharp leading edge profiles are considered within VFE-2, however, for this investigation, only the sharp leading edge profile is considered. Figure 29-1 shows the wing situated in the NTF wind tunnel along with the information on the geometry.
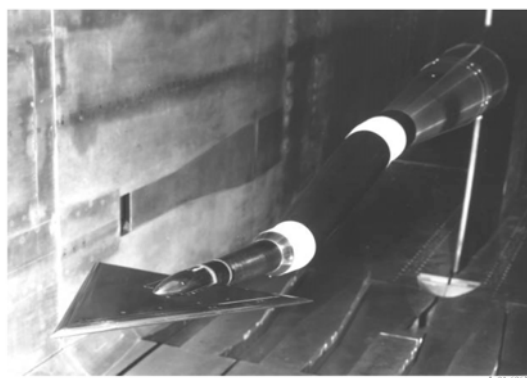
| (a) Wing in NTF Facility at NASA Langley | (b) Definition of the Wing Geometry |
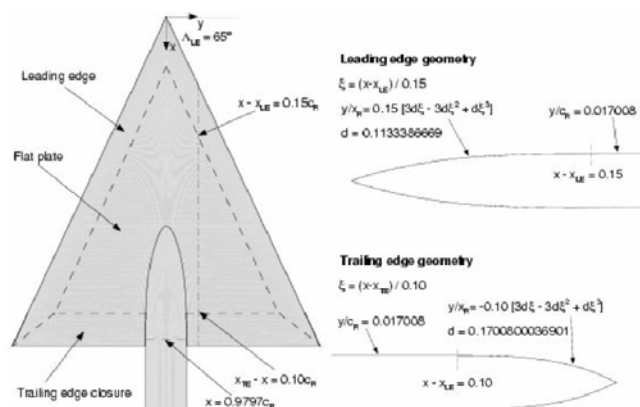
Figure 29-1: VFE-2 65° Delta Wing Geometry Used in Investigation [29-9].

The location of vortex breakdown for a freestream Mach number of 0.85 with incidence measured in the NTF [29-9] and in subsequent tests at DLR [29-13] experiments is plotted in Figure 29-2. The CFD data also plotted in this figure is discussed later in this paper. For the experimental data, the exact location of vortex breakdown is not known, however from the surface pressure coefficient distributions the approximate locations could be determined. The behaviour of vortex breakdown is clear, with a sudden movement of the breakdown location towards the apex when a critical angle is reached. It is however difficult to see why this happens from the measured data. At least a larger density of pressure measurements is needed. In fact it is seen from the CFD study that flowfield data is also needed to reveal details of the state of the vortex.
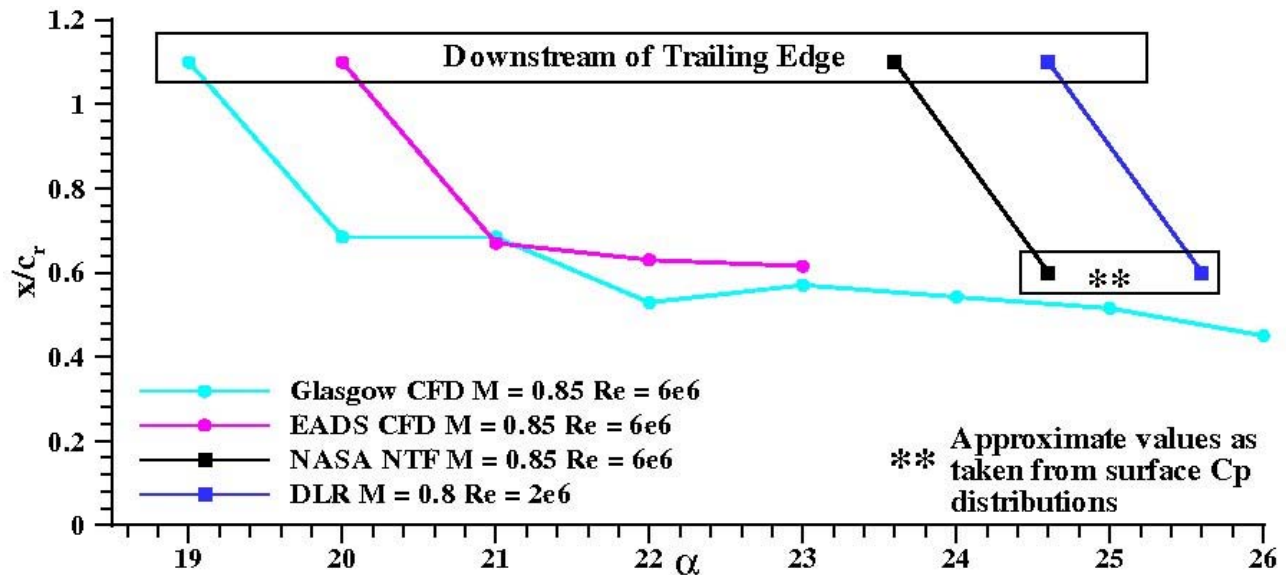
Figure 29-2: Vortex Breakdown Location for Both Computational and Experimental Results.

The objective of this paper is to use CFD to investigate the cause of the sudden motion of breakdown location towards the apex.

29.3   CFD STUDY

A CFD study was undertaken using several codes, grids and modelling options. The purpose of this study was to see if the behaviour observed in the measurements (i.e. the sudden jump in breakdown towards the apex) could be predicted, and if so with what sensitivity to the details of the simulation. A summary of the codes and grids is given in Table 29-1.

Table 29-1: Summary of Grids and Turbulence Models Used for VFE-2 Structured Grid Comparisons (Coarse grid dimensions are given in parentheses for the Glasgow code)

Institution	Topology	Size x 10^6	No. of Grid Points on Wing			Turbulence Model
			Spanwise	Streamwise	Normal	
EADS [29-14]	C-O	10.6	129	257	129	Wilcox k-ω and Reynolds Stress Model
NLR [[29-15],[29-16]]	C-O	4	192	112	96	TNT k-ω with P_ω Enhancer
Glasgow [29-17]	H-H with O-grid	7	170 (117)	228 (171)	81 (49)	Wilcox k-ω with P_ω Enhancer and NLEVM
USAFA [29-18]	unstr	7.9	–	–	–	SA-DES $\Delta t = 0.0047$, 20000 time steps
KTH	unstr	10.8	–	–	–	SA-DES $\Delta t = 0.0048$, 10760 time steps

29.3.1   Subsonic Results

First, a case at a freestream Mach number of 0.4 was computed. This case has no shock waves present. Two angles of incidence were calculated (at 18.5 degrees where no breakdown is present over the wing and at 23 degrees where it is) and compared with the NTF measurements. Sample results are shown in Figure 29-3 which compares the predictions of the Glasgow, NLR and EADS simulations, with excellent agreement between all predictions and the measurements. This is typical of the expected performance of CFD codes for the prediction of pressures on a sharp edged delta wing in subsonic flow, even if breakdown is present.
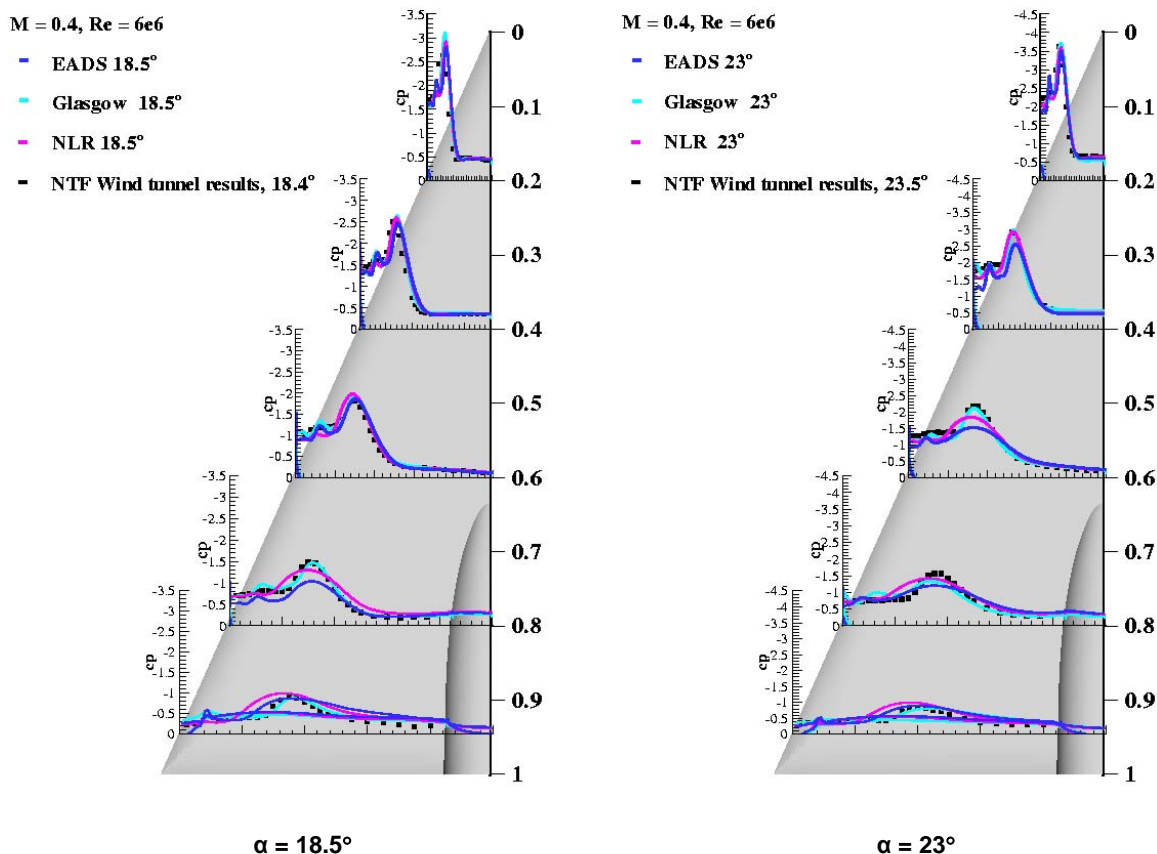
**Figure 29-3: Comparison of Computational Results
and Experimental Data, M = 0.4 and Re = 6 x 10^6.**

29.3.2 Transonic Results

Next, cases with a freestream Mach number of 0.85 were considered, when shock waves are expected to be present. The same angles of incidence were computed, with 18 degrees again giving no breakdown over the wing and 23 degrees resulting in breakdown. The comparisons are shown in Figure 29-4. The case before breakdown shows similar levels of agreement with the measurements. However, the case after breakdown shows significant discrepancies arising from the premature prediction of vortex breakdown. In fact the sudden movement of breakdown is predicted about 3 degrees earlier for the CFD when compared with the measurements.

α = 18.5° α = 23°
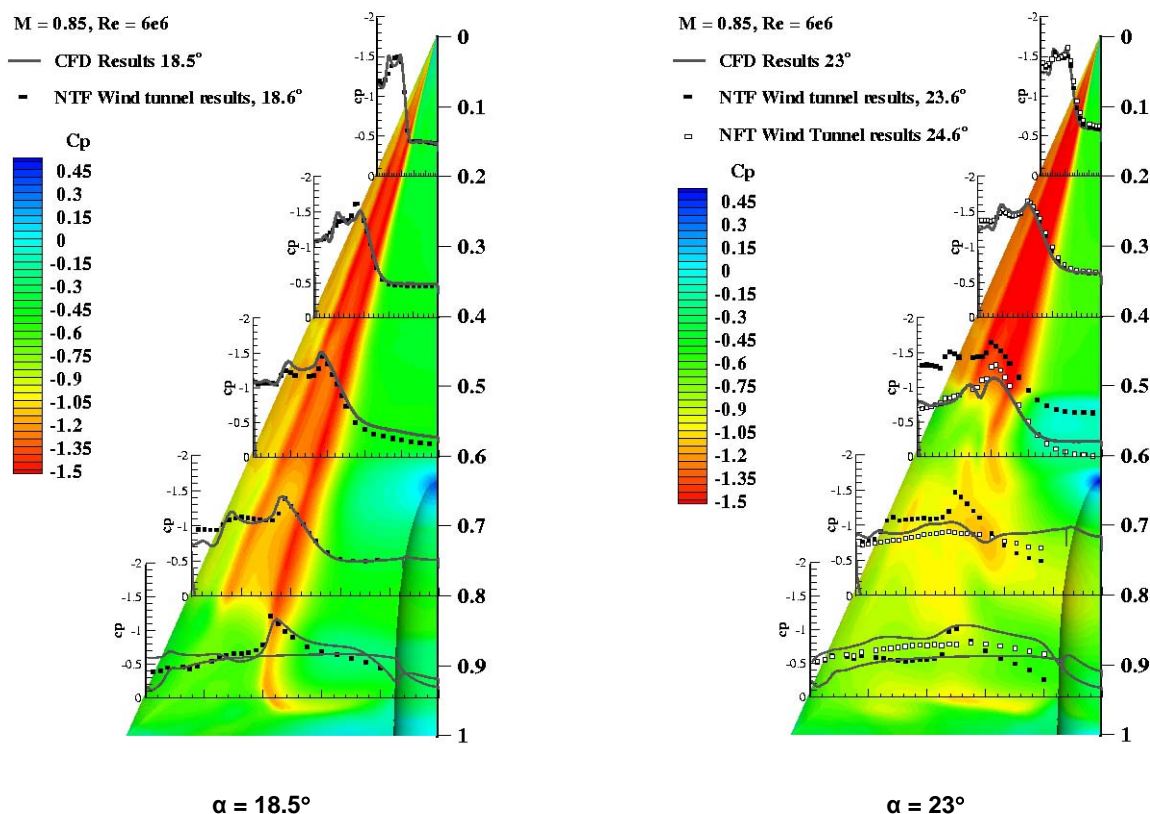
Figure 29-4: Comparison of Computational Results (Glasgow) and Experimental Data (NTF), M = 0.85 and Re = 6 x 10^6.

29.3.3 Location of Shock Waves in Glasgow Solution

Normal and crossflow shocks were found to occur in this flow. The main focus here is on the normal shocks, which can be identified by plotting the pressure coefficient along the symmetry plane as shown in Figure 29-5 for both angles of incidence. For the 18.5° case, it is clear that two normal shocks occur at the symmetry plane. The first occurs upstream of the sting tip at approximately $x/c_r = 0.6$. Further downstream at approximately $x/c_r = 0.85$ a second shock is found. This second shock is likely to correspond to the rear/terminating shock as described in the literature [[29-2], [29-5], [29-19]] for similar conditions. A third compression region is also found close to the trailing edge, and a third shock is found from the surface pressure contours at this location outboard of the symmetry plane on the wing surface. A shock occurring at this location is likely to be caused by the high curvature of the wing geometry and the necessity of the flow to return to freestream conditions at the trailing edge.
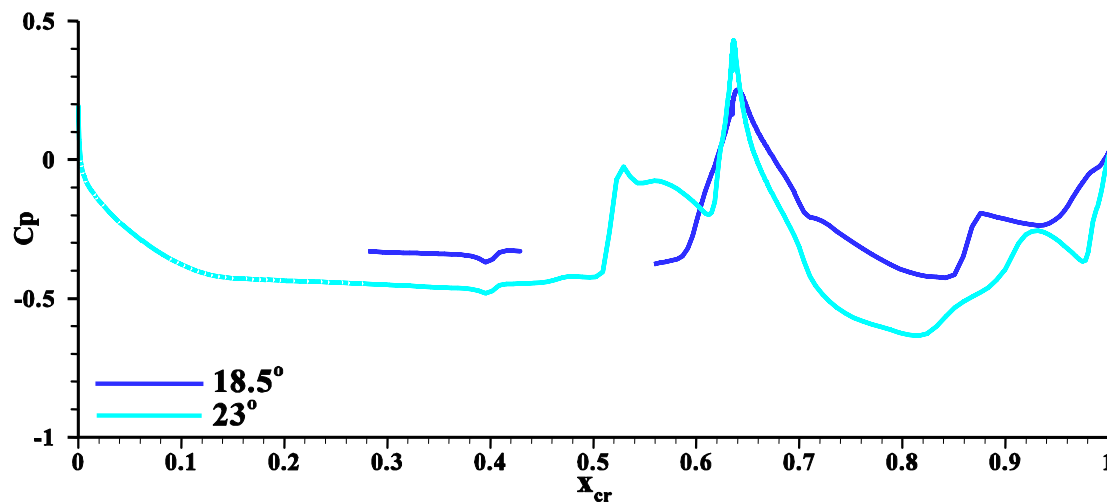
**Figure 29-5: Pressure Coefficient Distribution from Glasgow Code at
the Symmetry Plane on the Wing for Both Angles of Incidence.**

As the incidence is increased and vortex breakdown occurs on the wing, the behaviour at the symmetry plane, again, shows the shock at the sting tip at approximately $x/c_r = 0.6$. However, another shock is also found in the flow slightly upstream of this location at about $x/c_r = 0.52$. Downstream of the sting tip, it is evident that the rear/terminating shock described for the $\alpha = 18.5°$ case is no longer present. From the behaviour described in the investigations of Elsenaar and Hoeijmakers [29-2] under similar conditions, it is possible that the new shock upstream of the sting tip is the rear/terminating shock having undergone an upstream shift with the increase of incidence. As before, it is found that three normal shocks occur at the symmetry plane and close to the trailing edge, as also found in the experiments, a second normal shock is observed.

Considering the three-dimensional behaviour of the normal shocks, it is found that the shock occurring upstream of the sting tip curves downstream and intersects the rolled up shear layer of the vortex as shown in Figure 29-6 and highlighted by the dashed lines. This is also in agreement with the observations of Donohoe and Bannink [29-5]. Also highlighted are the locations of the other normal shocks described above. The rear/terminating shock in the 18.5° solution is found to be normal to the freestream and wing surface and does not appear to curve downstream outboard of the symmetry plane. This lack of curvature may be due to the influence of the sting, as previous investigations have considered a flat wing without sting support [29-5].
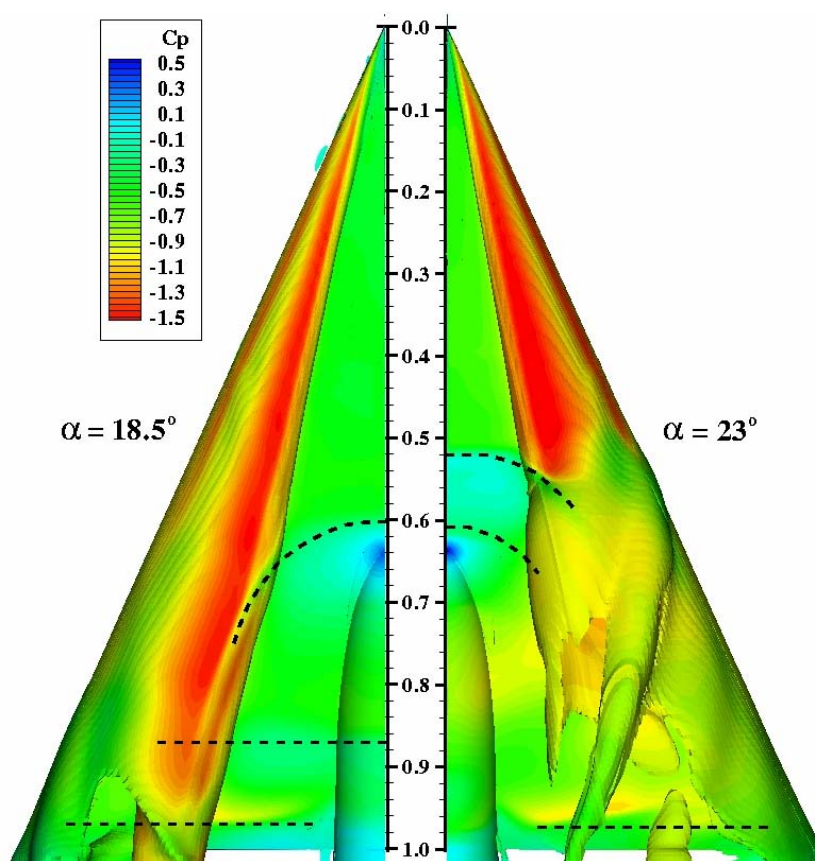
Figure 29-6: Isosurface of x Vorticity Coloured by Pressure Coefficient Showing Primary Vortex Shear Layer and Normal Shock Shape for Both Angles of Incidence (from the Glasgow Code).

29.3.4 Sensitivity Study

A sensitivity study was carried out to assess the CFD predictions of the sudden motion of the breakdown location. A large number of calculations are summarised here. The conclusion in all cases is that the sudden motion of the breakdown location was present no matter what the details of the calculation used, and that the critical angle is predicted to be lower in the computations than in the measurements.

29.3.4.1 Effect of Grid Refinement

The effect of grid refinement was considered for both pre- and post-breakdown flow for the transonic conditions using the Glasgow results. Comparisons of the surface pressure coefficient distributions for both angles of incidence with the relevant experimental data are shown in Figure 29-7. There are some differences in detail between the two solutions. However, the behaviour and location of vortex breakdown are not greatly affected by the grid refinement carried out. It is also the case that the critical angle for vortex breakdown onset is independent of the grid refinement used, with vortex breakdown predicted to occur at lower angles of incidence on both grids.

α = 18.5°   **α = 23°**
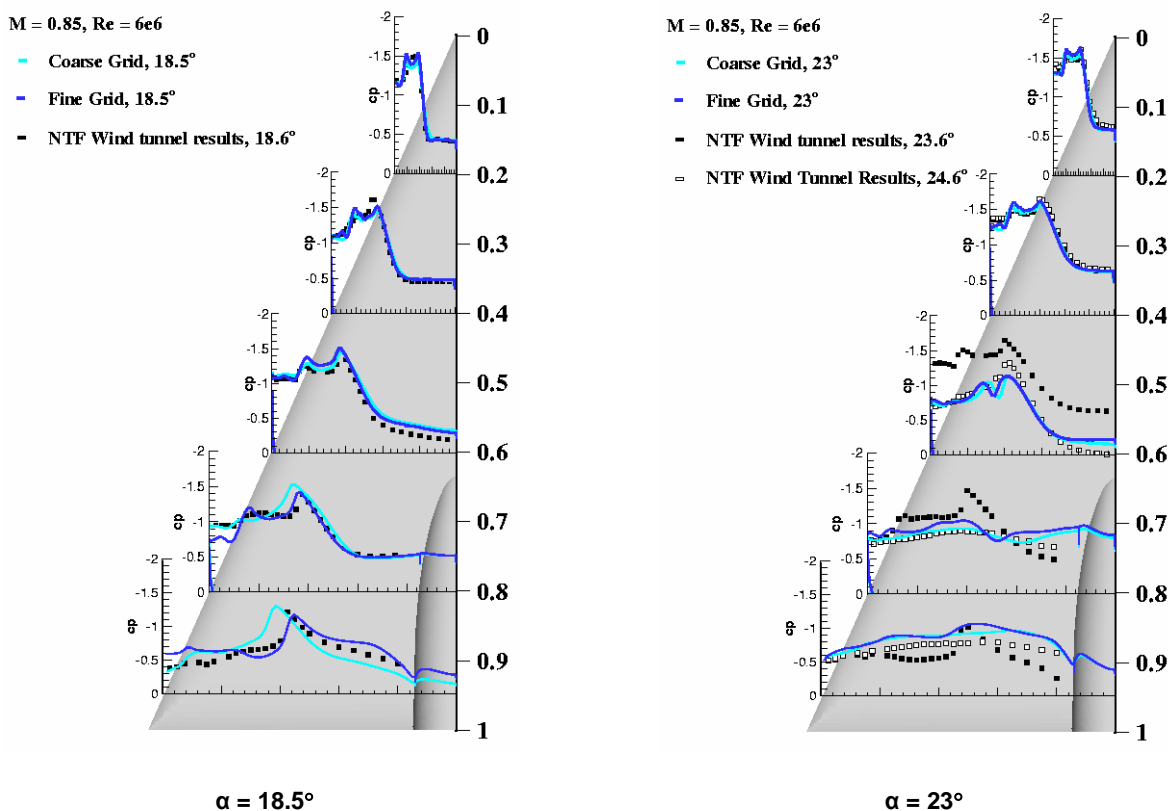
**Figure 29-7: Comparison of Glasgow Results between the H-H Grids for
Transonic Conditions at α = 18.5° and 23° (from the Glasgow Code).**

29.3.4.2   Effect of Turbulence Model

The effect of the turbulence model on the flow behaviour was considered by comparing results calculated using the k-ω with $P_ω$ Enhancer model and the Non-Linear Eddy Viscosity model in the Glasgow code, and the standard Wilcox k-ω and a Reynolds Stress model (RSM) by EADS. The surface pressure coefficients are shown in Figure 29-8. Each model predicts breakdown to occur on the wing at an incidence which is lower than that witnessed in the experiment. Some differences in the breakdown location are present due to the different vortex strengths predicted. However, the behaviour of a rapid motion forward of the breakdown location is the same in each case.
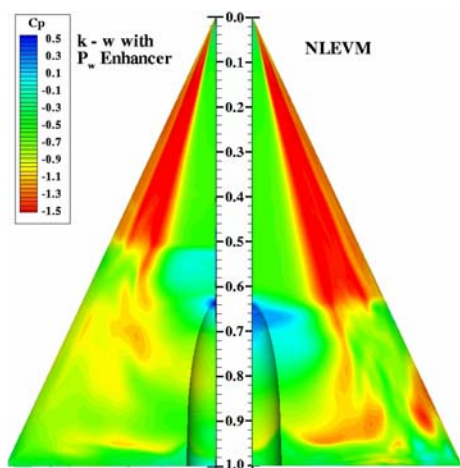
(a) Comparison between NLEVM and k-ω with
P_ω Enhancer Model (Current Results)
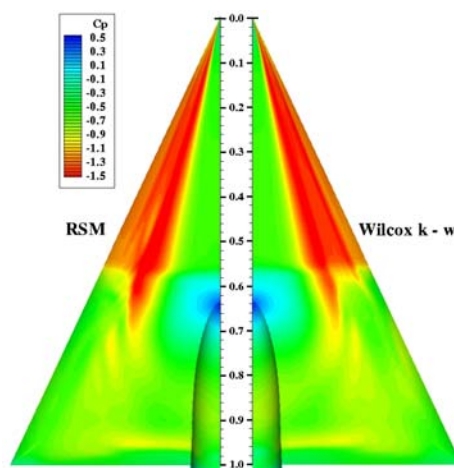
(b) Comparison between RSM and Wilcox
k-ω Model (EADS-MAS Results)

**Figure 29-8: Contours of Surface Pressure Coefficient Showing Effect of Turbulence Model
on Flow Solution with Comparison to Experiment for α = 23°, M = 0.85 and Re = 6 x 10^6.**

29.3.4.3   Comparison of Structured Grid Results

Comparison of the structured solutions obtained at Glasgow, NLR and EADS was made. The locations of the normal shocks in the flow solutions, and the vortex breakdown locations, are slightly different for each solution, as shown in Figure 29-9. These are likely to be due to the slightly different turbulence treatments and grids. However, the motion of the breakdown location is very similar in each case.
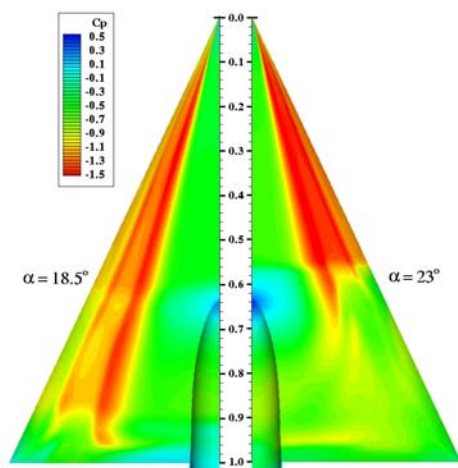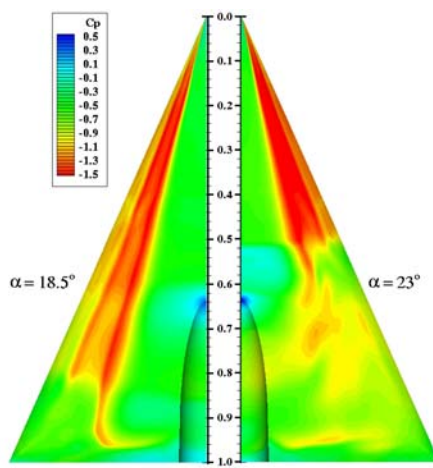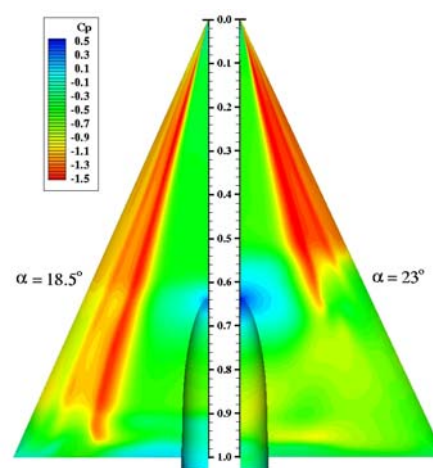
(a) EADS-MAS   (b) Glasgow   (c) NLR

Figure 29-9: Surface Pressure Coefficient Contours for Structured Codes, M = 0.85, Re = 6 x 10^6.

A comparison between the solutions for the Glasgow and NLR CFD solvers on a common grid was also performed. The turbulence models used by these two institutions are similar, with the difference mainly in the specification of the turbulence model diffusion coefficients [29-20]. The solutions obtained were very similar.

29.3.4.4   Influence of Time Accuracy

The comparison of surface pressure coefficient contours for the time averaged USAFA and KTH solutions shows an overall similar picture (see Figure 29-10). The USAFA solution shows a more pronounced shock upstream of the sting tip, which influences the interaction with the vortex. The KTH solution does not show such a distinct impact of the shock wave on the vortical system and presents a more diluted picture of the breakdown process. In general there are some differences in breakdown location and shock strength, however the behaviour of the breakdown location motion is very similar in both cases. Analyzing the pressure coefficient fluctuations on the vortex core axis for the KTH solution reveals that the main region of influence of the fore-sting shock movement is between $x/c_r = 0.54$ and $x/c_r = 0.72$ (see Figure 29-10 (b)), hereafter the fluctuations are due to the vortex breakdown unsteadiness. Time accurate behaviour of the shock and vortex breakdown movement is considered below.

(a) Comparison between USAFA and KTH Results

(b) Pressure Coefficient Distribution through Vortex Core for KTH Solution
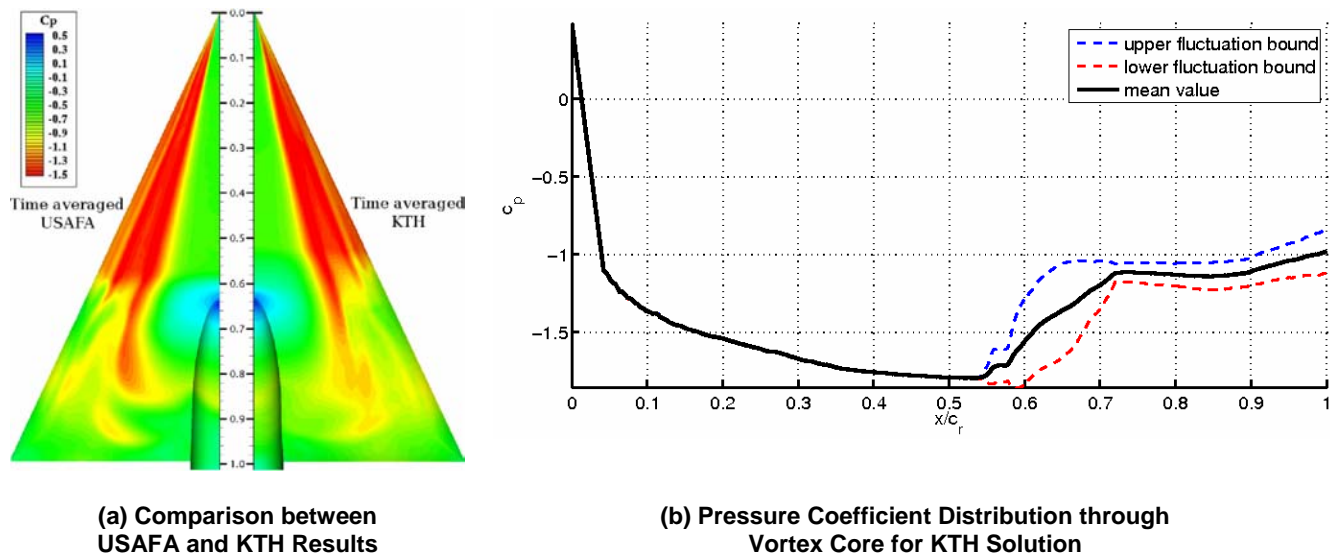
Figure 29-10: Time Averaged Surface Pressure Coefficient Contours for Unsteady Results, M = 0.85, Re = 6 x 10^6.

29.4   EVALUATION

29.4.1   Shock-Vortex Interaction – Analysis Framework

From the CFD results a shock ahead of the sting intersects the vortex system. It therefore seems possible that a shock/vortex interaction is important, particularly for higher angles of incidence. To consider this, the pressure in the freestream direction through the vortex cores for both angles of incidence was analysed. This is shown in Figure 29-11, with the calculated pressure ratios for each shock/vortex interaction location marked. For α = 18.5°, the interactions occur without vortex breakdown. It has been previously suggested that this is due

to the shock sitting above the vortex core [29-5]. However, from consideration of the vortex core properties it is found that there are three regions of adverse pressure gradient which will influence the vortex. These coincide with the two normal shocks at the symmetry plane and the trailing edge shock, as described above, and are clear from Figure 29-6. The pressure ratios for all three regions are less than 1.5 and, as shown, the primary vortex recovers after passing through each. Therefore, it may be suggested that these are weak interactions.
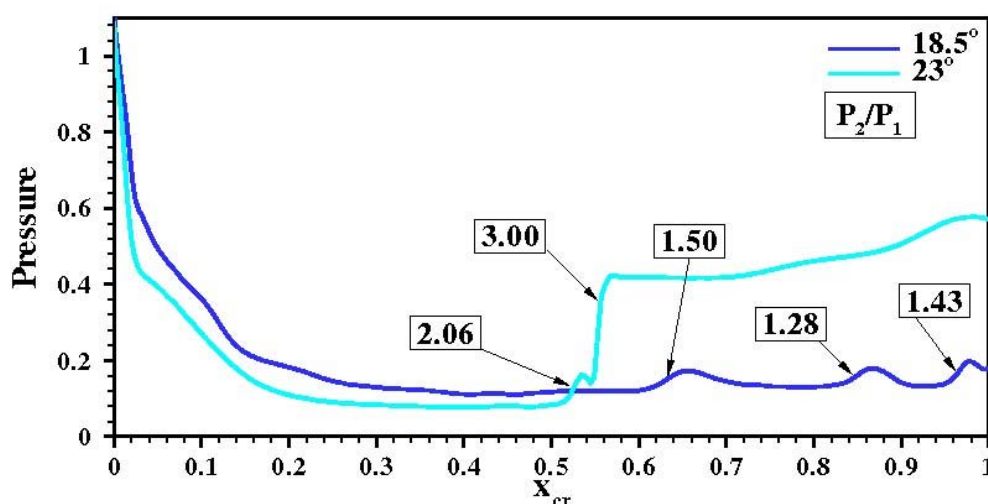
**Figure 29-11: Pressure Distribution (from the Glasgow Code) through Vortex Cores for
Both Angles of Incidence – the numbers on the plot signify the magnitudes
of the pressure ratios through the intersecting shocks).**

At $\alpha = 23°$, where breakdown occurs on the wing, it is clear that there are two regions of high adverse pressure gradient at the vortex core. The first coincides with the location of the normal shock upstream of the sting tip as shown at the symmetry plane in Figure 29-5 and also with the onset of vortex breakdown. Very close to this, the second, higher pressure gradient coincides with the occurrence of complete vortex breakdown. These pressure gradients have ratios of 2.00 and 2.36, respectively. It is likely that the first pressure increase is due to the effect of the normal shock at the symmetry plane on the vortex core, in a similar manner to the interaction at the lower incidence.

There are interactions between the shocks and vortex core for both angles of incidence, with a weaker interaction occurring for the lower incidence. It is suggested that there is a limiting behaviour below which the vortex can feel the effects of the shock and remain coherent. Above this limit, the interaction causes a considerable weakening of the vortex core, which results in vortex breakdown. In his comprehensive review, Deléry [29-22] demonstrated the importance of a number of parameters for vortex breakdown caused by shock/vortex interaction. These include the tangential or swirl velocity, U_θ, and the axial velocity of the vortex core, U_{axial}. He also proposed that the swirl ratio or the Rossby number may be used as a measure of the vortex intensity and, thus, the susceptibility of the vortex to shock induced breakdown. The Rossby number is a non-dimensional parameter, defined as the ratio of the axial and circumferential momentum in a vortex as defined by Equation 1. In this investigation, the maximum axial velocity at the vortex core and the maximum swirl velocity of the vortex are used. This relationship is the inverse of the axial swirl parameter [29-22], which is used as a breakdown criterion for a free-vortex.

$$Ro = \frac{U_{axial}}{U_{\theta}}$$ (1)

As a vortex passes through a normal shock, the tangential velocity is found to stay relatively constant while the axial velocity decreases, therefore reducing the Rossby number [29-23]. With the reduction in the Rossby number comes an increase in vortex intensity and, as a result, the susceptibility of the vortex to breakdown increases. A criterion for breakdown using the Rossby number has also been investigated by Spall et al. [29-24] and by Robinson et al. [29-25], who applied it to computational results on slender delta wings and determined that the limiting Rossby number occurs between 0.9 and 1.4 for most cases, with a stable vortex core occurring for values above 1.4. To consider this criterion, the Rossby number was calculated for both pre- and post-breakdown angles of incidence and the resulting graph is shown in Figure 29-12 with respect to streamwise location on the wing. Also noted on the plot are the critical Rossby numbers for vortex breakdown.
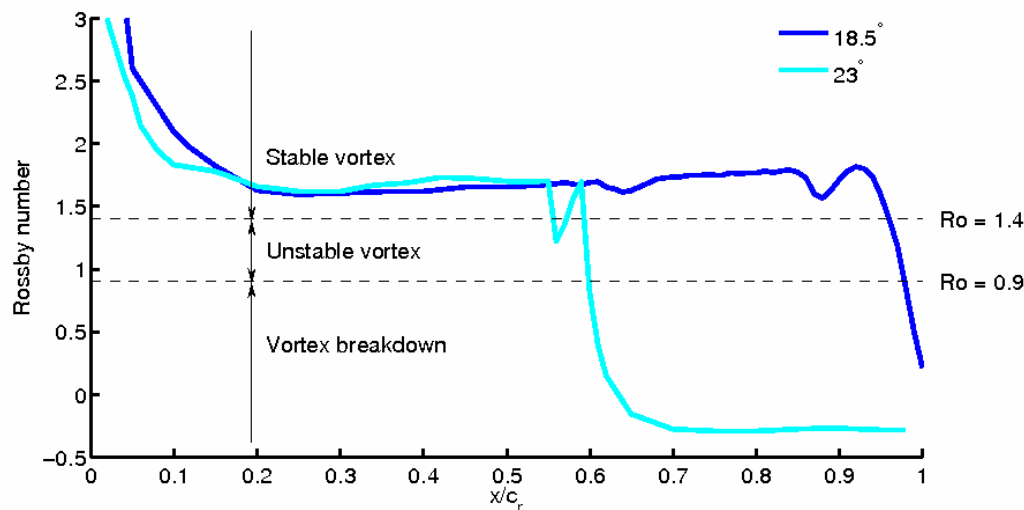
Figure 29-12: Rossby Number Distribution from the KTH Code against Root Chord Location for Pre- and Post-Breakdown Cases.

These results also show the influence of the shocks on the vortex behaviour. At $\alpha = 18.5°$, it is clear that weak interactions occur as the Rossby number decreases. However, this reduction is not significant which shows that the vortex is not sufficiently weakened by the shock. A recovery is witnessed downstream. At $\alpha = 23°$, a similar behaviour is noted where at $x/c_r = 0.58$ the vortex is affected by the normal shock. However, the reduction in Rossby number is greater than for $\alpha = 18.5°$ and the vortex becomes unstable. Vortex breakdown is then caused by a second shock at approximately $x/c_r = 0.62$ which has a greater effect on the already weakened vortex axial flow, and breakdown is almost immediate.

29.4.2   Quantitative Assessment

To investigate a limit for transonic delta wing vortices, the strength of the impinging shocks should be considered, pre- and post-breakdown. Unfortunately, little experimental data exists to allow the shock strength to be measured through the vortex core. However, the strength of the shocks incident on the surface of the wing may be considered to improve confidence in the computational solutions. Unfortunately, there are only

five data points from the NTF data, however, the presence of an increase in pressure between $x/c_r = 0.6$ and 0.8 for the 23.6° incidence and $x/c_r = 0.4$ and 0.6 for the 24.6° incidence is still clear. As the sting tip is located at approximately $x/c_r = 0.64$, these pressure jumps are most likely to be located close to the $x/c_r = 0.6$ streamwise location. Using this as a guide, an approximation to the shock strength at this location can be determined. The approximate values calculated are given in Table 29-2.

Table 29-2: Summary of Shock Strength from the Glasgow Code on Surface Conical Ray at Constant y/s = 0.3 for All Solutions at M = 0.85, Re = 6 x 10⁶ and α = 23° Compared to NASA NTF Data

Source	P_2/P_1
NASA NTF Experiment – 23.6°	1.16
NASA NTF Experiment – 24.6°	1.4673
CFD – 18.5°	1.2314
CFD – 23°	1.4695

Using the values in Table 29-2 as a guide, it is evident that there is a considerable difference in the calculated pressure changes at the sting tip location for the pre- and post-breakdown experimental results. The calculated pressure ratio for the post-breakdown case is roughly 25% larger than for the pre-breakdown case. Similar distributions were also obtained from the computational solutions for the pre- and post-breakdown cases and the shock strengths calculated are also stated in Table 29-2. From a comparison with the experimental data it is clear that the magnitude of the post-breakdown pressure ratio is very similar, however, the pre-breakdown ratio is larger. This means that overall the increase between the pre- and post-breakdown cases for the computational results is less. The larger pressure ratio of the computational results for the pre-breakdown case may have implications for the onset of breakdown. If the shock strength is over-predicted in the computational results, it is likely that breakdown would occur closer to the apex compared to the experimental results for a given vortex strength.

To consider the incidence at which vortex breakdown first occurs on the wing and relative strength of the shocks, additional calculations were performed for intermediate angles of incidence between 18.5° and 26° for the same flow conditions as before (M = 0.85 and Re = 6 x 10⁶). A summary of the important flow details are shown in Table 29-3. These details include whether vortex breakdown occurred, the maximum vortex core axial velocity, Mach number and the strengths and locations of the first impinging shock at each incidence. From the analysis, it was found that the 23° case was the only incidence to exhibit the double shock at vortex breakdown and so the combined shock strength is instead shown for comparison with the other results. More is said below about the shock pattern.

Table 29-3: Summary of Shock and Vortex Core Data for All Steady State Calculations Using the Glasgow Code at α = 18.5° – 26°, M = 0.85, Re = 6 x 10^6 ($\times$ Means No Breakdown and $\sqrt{}$ Means Breakdown)

α	VBD?	Max. U_{axial}	Max. M_{axial}	P_2/P_1	Shock x/c_r
18.5°	$\times$	1.74	1.76	1.5	0.62
19°	$\times$	1.76	1.80	1.67	0.64
20°	$\sqrt{}$	1.74	1.83	3.73	0.64
21°	$\sqrt{}$	1.74	1.86	4.87	0.64
22°	$\sqrt{}$	1.79	1.88	4.67	0.51
23°	$\sqrt{}$	1.80	1.92	5.25	0.55
24°	$\sqrt{}$	1.84	2.05	5.93	0.49
25°	$\sqrt{}$	1.84	2.10	5.64	0.47
26°	$\sqrt{}$	1.84	2.20	5.48	0.40

Before considering the onset of breakdown, it is important to note the behaviour of the flow variables with increasing incidence. It is clear from Table 29-3, that the predicted shock strength increases with incidence, which is in agreement with the experimental data in Table 29-2. The axial velocity and Mach number are also found to increase, however, the Rossby number was found to be constant at ≈1.7 for each incidence as described before. From the theory of supersonic flows, it is known that the strength of a shock is dependent on the upstream Mach number, thus for a higher axial flow, a stronger shock will occur. However, in this case the relationship does not appear to be linear. This is most likely to be due to changes in the shape of the shock in response to changes in the flow behaviour and the equilibrium conditions as the incidence is increased. This may also suggest that the behaviour of the vortex breakdown is also non-linear wth incidence.

Vortex breakdown first appears on the wing at α = 20°, which coincides with a significant increase in shock strength. At this point it may be assumed that the strength of the shock is high enough to cause a complete reorganisation of the flow behaviour. Thus, the shock strength limit for breakdown for these solutions may be given as 3.73. To determine a link between the vortex flow conditions, as described by the Rossby number, and the shock strength for breakdown to occur on the wing, further data, both experimental and computational, is needed.

To further consider the relation between the occurrence of breakdown, the vortex core behaviour and the predicted shock strength, the vortex core data for the EADS-MAS, NLR and time averaged USAFA results are considered in a similar manner. The pressure behaviour through the vortex core, with the pressure ratios marked, is shown in Figure 29-13. From this plot, it is clear that a similar behaviour occurs, with shocks intersecting the vortex core axis and vortex breakdown occurring. From the EADS-MAS and NLR solutions, the pressure ratios through the shocks are approximately 1.77 and 1.64, and 1.5 and 2.89, respectively. The USAFA time averaged

solution has only one shock region with a ratio of 4.5. However, from analysis of the instantaneous solutions, it was found that two shocks also exist at breakdown, which for the solution at a time step of $\tau = 16600$ correspond to 2.25 and 2.71.
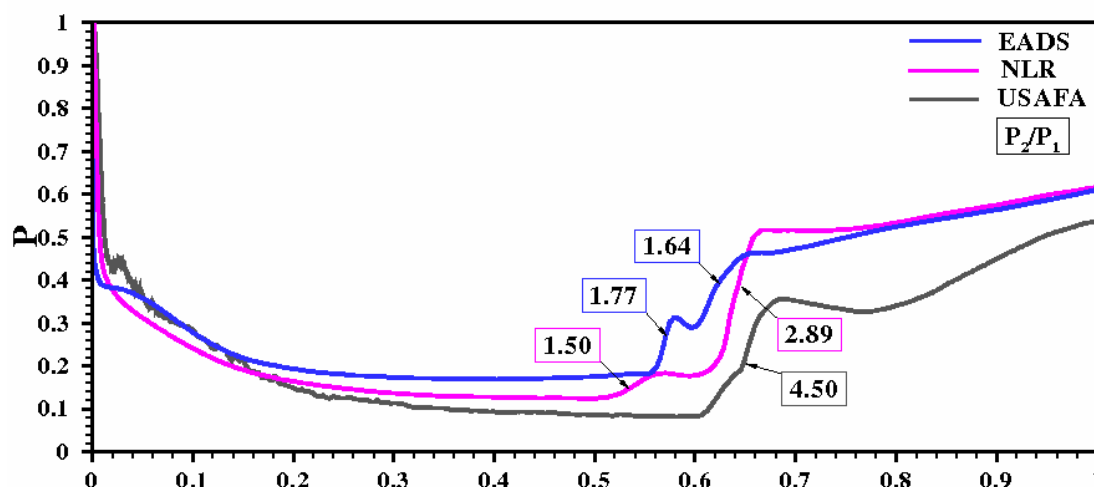
**Figure 29-13: Pressure Distribution through Vortex Cores for
EADS, NLR and USAFA (Time Averaged) Solutions.**

While the predicted strength of a shock can be dependent on such factors as grid refinement, turbulence model and discretisation, it is also apparent that there are corresponding differences in predicted maximum axial velocity through the vortex core, as summarised in Table 29-4. The current solution has predicted a maximum axial velocity which is the same as the USAFA solutions and higher than for the EADS-MAS and NLR solutions. As a result of this increase in axial velocity the Mach number upstream of the shock will increase, and the upstream pressure will reduce, resulting in a stronger shock to maintain equilibrium. However, it is evident that the Rossby number in each case is similar. This suggests that the shock strength predicted by the computational solutions is dependent on the vortex core behaviour predicted upstream. The axial flow behaviour is also dependent on the computational parameters mentioned above. However, despite the differences in flow solutions and computational set-up, the behaviour and effect of the shocks on the flow are the same.

Table 29-4: Summary of Maximum Axial Velocity, Shock Strength and Breakdown Location for All Solutions at α = 23°, M = 0.85 and Re = 6 x 10^6

	U_{axial}	M_{axial}	Ro	Vortex Core Shocks			Shock at y/s = 0.3 P_2/P_1	VBD x/c$_r$
				1st: P_2/P_1	2nd: P_2/P_1	Total: P_2/P_1		
EADS	1.50	–	1.67	1.77	1.64	2.55	1.4274	0.68
Glasgow	1.83	2.00	1.70	2.00	2.36	4.75	1.4695	0.64
NLR	1.60	–	1.74	1.50	2.89	4.33	1.5075	0.67
USAFA (time avg.)	1.80	2.03	1.67	–	–	4.50	1.4409	0.68
USAFA (instant.)	–	–	–	2.51	2.71	4.75	–	0.66
KTH (time avg.)	1.79	1.87	1.72	–	–	4.72	1.468	0.67

29.4.3   Validation of the Axial Flow Predictions

To consider the ability of the computational solutions to predict the axial flow upstream of breakdown, the PIV results obtained at DLR and described in Konrath et al. [29-14] were considered. These experiments were carried out for slightly different flow conditions, with a Mach number of M = 0.80 and Reynolds number of Re = 3 x 10^6. To compare with these results, a new set of calculations was performed by Glasgow, using the k-ω with P$_ω$ Enhancer turbulence model for M = 0.80 and Re = 2 x 10^6 at angles of incidence of α = 18.5° – 26°. Figure 29-14 shows a comparison of the cross-flow behaviour for a nominal incidence of α = 26°. The effect of the difference in Reynolds numbers should be negligible due to the sharp leading edge. In the experiment, it was found that vortex breakdown occurred between the x/c$_r$ = 0.6 and 0.7 streamwise stations. However, the computations predict breakdown further upstream at x/c$_r$ = 0.4. Therefore, to make a comparison of the pre-breakdown flow, the results were compared on planes which were a similar non-dimensional distance from the breakdown location, this corresponds to x/c$_r$ = 0.5 for the experiment and x/c$_r$ = 0.3 for the computational results assuming that the breakdown occurs close to the x/c$_r$ = 0.6 location.

PIV, α = 25.9°, Re = 3 x 10⁶   CFD α = 26°, Re = 2 x 10⁶
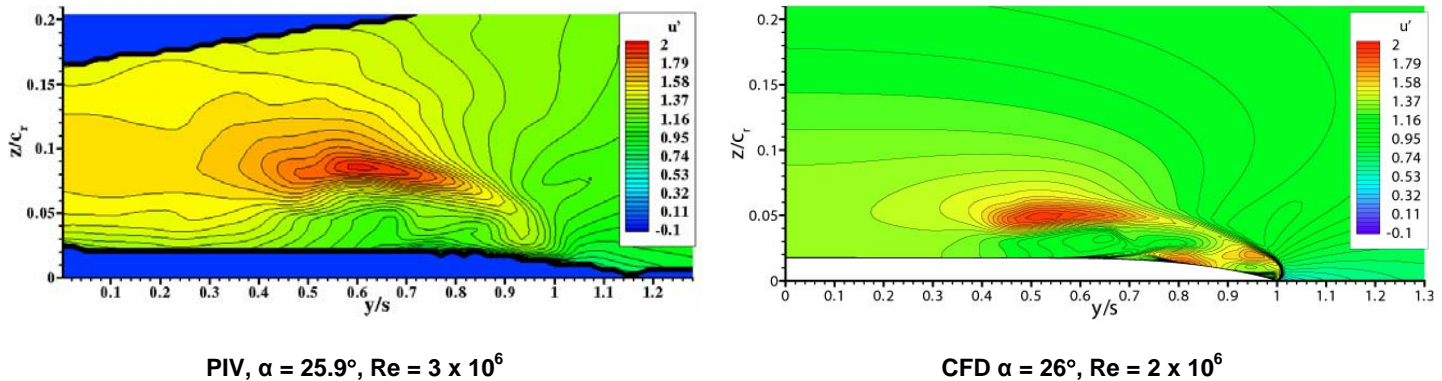
**Figure 29-14: Comparison between u Velocity Contours for Experimental
PIV and Computational Results for M = 0.80 on a Slice at x/c_r = 0.5.**

From the comparisons of the non-dimensional u velocity contours, a number of observations may be made. It is clear that the location of the vortex core is very different between the computational and experimental results, however this is likely to be due to the proximity of the computational slice to the apex of the wing as further downstream the vortex would lift further from the wing surface. However, the shape of the vortical system is the same, with a very elongated primary vortex in both sets of results. Considering the vortex core properties, from the experimental data at three pre-breakdown PIV planes, it was found that the u velocity corresponds to 1.962 at x/c_r = 0.5, 1.870 at x/c_r = 0.55, and 1.522 at x/c_r = 0.6. Although the maximum velocity found from the measurement planes is 1.962, it is likely that the actual maximum velocity will be larger. This is evident from Figure 29-15, which plots these three points along side the velocity behaviour of the computational results. The maximum u velocity for the computational results corresponds to $u = 1.88$, which is slightly lower than the maximum experimental value. Therefore, it is possible that the axial flow behaviour is under-predicted in the computational solutions.
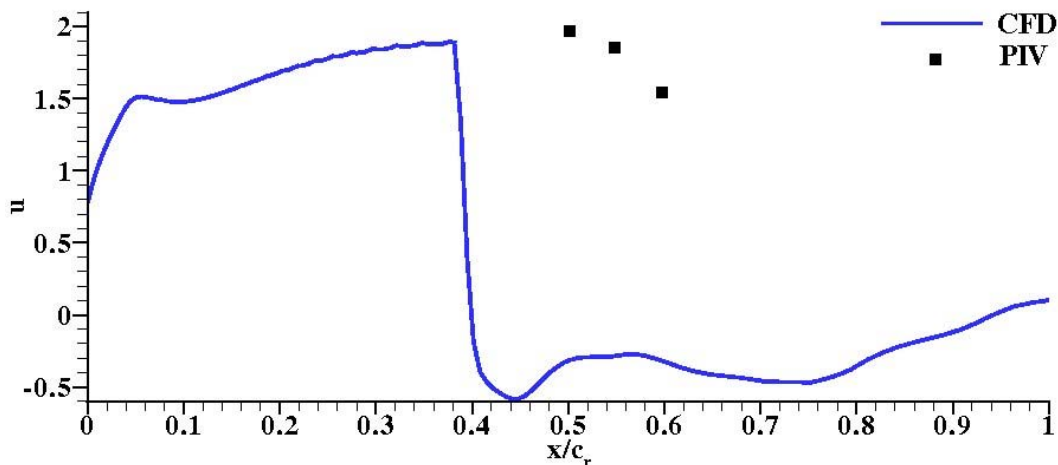
**Figure 29-15: u Velocity through Vortex Core for Computational Results
Compared to Experimental PIV Data for M = 0.80, α = 26°.**

29.4.4   Shock Behaviour in Unsteady Solutions

The analysis of all contributed RANS and the time-averaged DES computations reveals the presence of either one or two shocks upstream of the sting-wing intersection. To understand this discrepancy between the otherwise similar solutions, it is necessary to assess the time-dependent flowfield. In this section the DES computations performed at KTH have been evaluated. This analysis enables helps to explain the post-breakdown development of the main vortical structures, and also the complex interaction between vortex breakdown and the shock system ahead of the sting. Figure 29-16 shows the vortex breakdown position history for the last cycle of the KTH solution. The position of breakdown is defined here as the foremost chord-wise station where there is fully-reversed axial flow in the primary vortex. Flow details of the timesteps indicated by red dots in Figure 29-16 are shown in Figure 29-17.
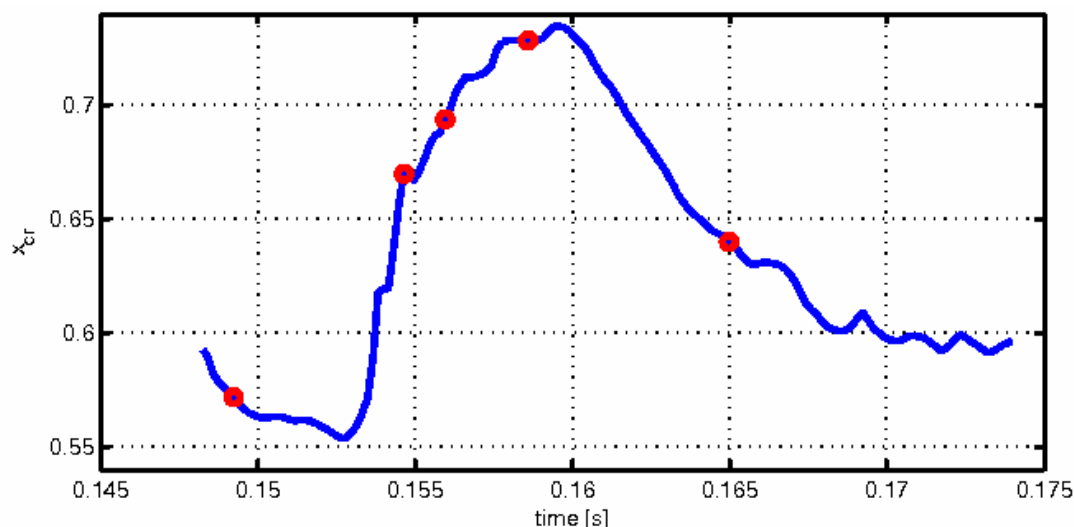
**Figure 29-16: Vortex Breakdown Position for the KTH Solution;
Timesteps Presented in Figure 29-17 are Designated with Red Dots.**

t = 0.1492s

t = 0.1547s

t = 0.1560s

t = 0.1586s

t = 0.1650s
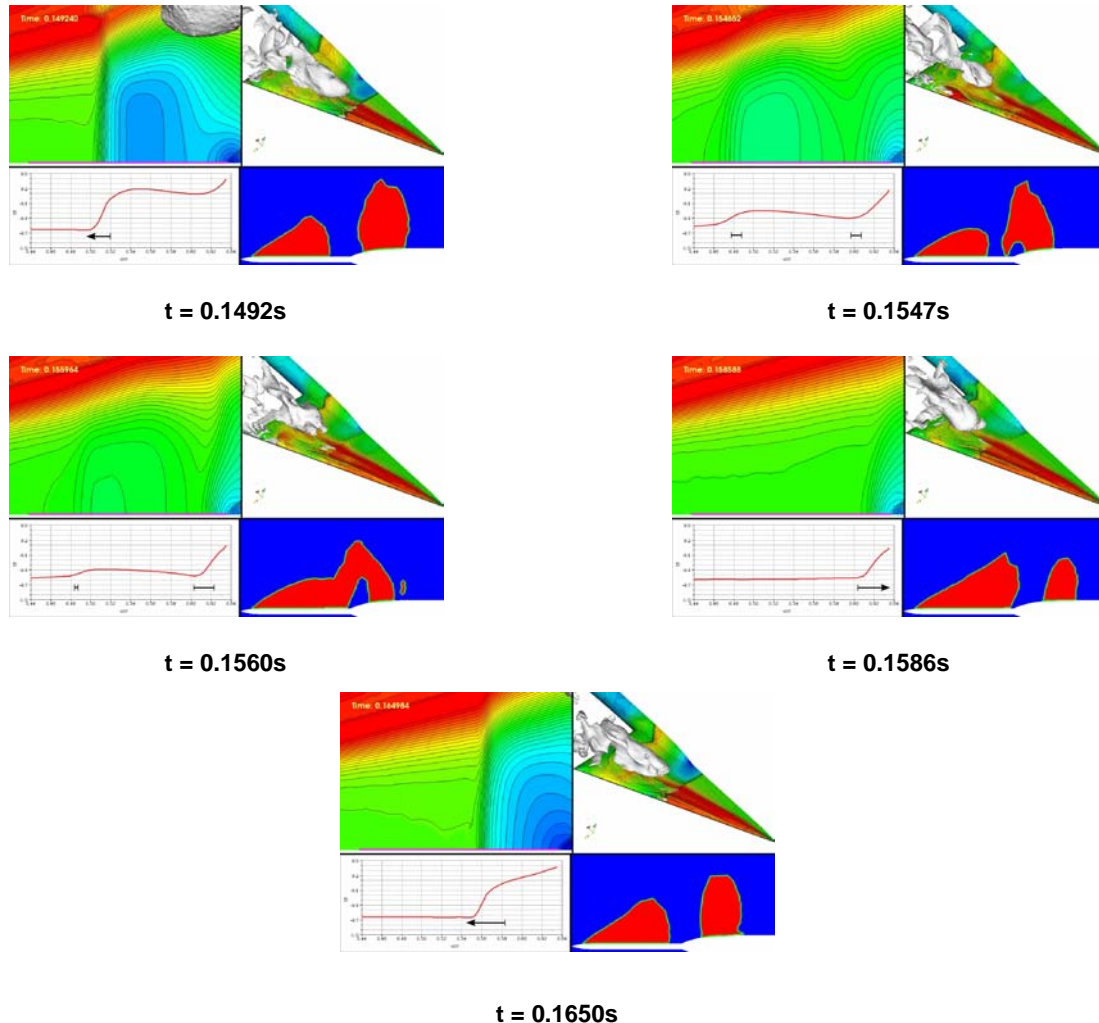
Figure 29-17: Sub-Frames Presenting Each in Clockwise Order, Starting from the Lower-Right Corner: Normal-View on Symmetry Plane Showing Mach Number Range from Subsonic (blue), Sonic (green) and Supersonic (red); Frontal-Isometric View of Half-Span Suction Side Showing Surface Pressure Coefficient and Reversed Flow Isosurface; Wall-Normal View on Suction Side in Front of Sting-Wing Intersection Showing Surface Pressure Coefficient; Pressure Coefficient at Intersection of Symmetry Plane and Wing Surface, Locations 0.44 and 0.635 – Also noted are the transient movement direction of the shock wave(s) and the relative strength.

It is apparent from Figure 29-16 that the downstream movement occurs relatively suddenly and the upstream recovery is more gradual. The USAFA DES predictions show a similar behaviour. Since the flowfield features several minor complex shock systems in the post-breakdown region, it is useful to constrain the analysis to a single plane. The reason for the different behavior of the downstream and upstream motion can be found from the flowfield at the symmetry plane.

At the earliest time a single shock wave is found to propagate upstream ahead of the sting tip at $x/c_r \approx 0.51$. A further supersonic region is present above the sting, aft of the sting tip (see Figure 29-17). In a subsequent

timestep the second shock region forms a supersonic bridge to the flat plate wing portion, right ahead of the sting tip, effectively resulting in a twin-shock fore-sting system. The first, now weaker shock having moved slightly more upstream than the aforementioned position at $x/c_r \approx 0.48$ and a second shock placed right in front of the sting-wing intersection at $x/c_r \approx 0.6$ (see Figure 29-17). Due to this peculiar arrangement, the vortex breakdown position moves abruptly from downstream of the (first) shock impinging on the vortex core, visible in Figure 29-17 downstream of the second shock. The relaying mechanism from the first to the second shock is what causes the abrupt downstream movement of the vortex breakdown position. When the two supersonic regions merge the downstream motion of the strong single shock still continues slowly towards the sting tip. A further downstream motion of the shock is halted by the presence of the sting tip. The furthermost downstream position of the vortex breakdown is reached at $x/c_r \approx 0.61$, when the bent field shock surface is weak enough to relieve the primary vortex core from the sudden pressure jump, see Figure 29-16. Now the vortex breakdown location starts to move upstream, following a discernible lag in the upstream movement of the shock wave. In contrast to the downstream movement, during the upstream movement the shock does not split in two. A gradual decrease in the strength of the single fore-sting shock is detectable, while simultaneously the size of the supersonic region on the sting increases. The next cycle starts only then, when the single fore-sting shock reaches its furthermost upstream position, which is coupled to a decrease of the shock strength. From the time-dependent solution it is possible to recognize disturbances in the region between the single fore-sting shock, the sting tip and the primary vortex. These disturbances propagate upstream from the sting tip and move towards the single shock. The frequencies of the upstream moving disturbances and the spiral motion of the disrupted vortex core are very similar. These disturbances, originating from the post-breakdown vortex filaments, could be the initial triggering mechanism behind the split-up of the single shock wave into two weaker ones.

29.4.5   Motion of Vortex Breakdown Location

Having considered the mechanisms which cause vortex breakdown to occur on the wing, it is possible to return to the issue of the discrepancies between the CFD and experimental results. It was found from the experimental data used in this study that vortex breakdown jumps abruptly from a location downstream of the trailing edge to a location upstream on the wing for a small increases in incidence. Indeed from the results summarised in Table 29-3, it is clear that the flow seems to go from full vortical flow over the whole wing surface to breakdown occurring close to the $x/c_r = 0.6$ location in a one degree increase.

From the plot in Figure 29-2 it is clear that the behaviour at the onset of vortex breakdown is qualitatively similar for both the CFD and experiment, however the angle at which this occurs varies. With further consideration of the literature it was found that there is a large spread of values for this critical angle. These are detailed in Table 29-5. It is quite clear from all these results that the critical onset angles for vortex breakdown over the wings for current CFD solutions are consistently earlier than for the majority of the experimental results.

Table 29-5: Critical Incidence for Transonic Vortex Breakdown to be Found on 65° Delta Wings

Source	*Type*	*Conditions*	$α_{cr}$
Elsenaar and Hoeijmakers [29-2]	exp.	$M = 0.85$, $Re = 9 \times 10^6$	23°
Houtmann and Bannink [29-20]	exp.	$M = 0.85$, $Re = 3.6 \times 10^6$	20°
Chu and Luckring [29-9]	exp.	$M = 0.799$, $Re = 6 \times 10^6$	26.6°
Chu and Luckring [29-9]	exp.	$M = 0.831$, $Re = 6 \times 10^6$	24.6°
Chu and Luckring [29-9]	exp.	$M = 0.851$, $Re = 6 \times 10^6$	24.6°
Chu and Luckring [29-9]	exp.	$M = 0.871$, $Re = 6 \times 10^6$	24.7°
Chu and Luckring [29-9]	exp.	$M = 0.9$, $Re = 6 \times 10^6$	22.6°
Chu and Luckring [29-9]	exp.	$M = 0.849$, $Re = 11.6 \times 10^6$	24°
Longo [29-3]	CFD	$M = 0.8$, Inviscid	25°
Glasgow	CFD	$M = 0.85$, $Re = 6 \times 10^6$	20°
EADS-MAS	CFD	$M = 0.85$, $Re = 6 \times 10^6$	21°

As shown, with an increase in incidence the strength of the shocks in the flow increases, most likely as a response to the increased flow acceleration over the wing surface. Similarly, the axial velocity in the vortex core increases and it has been shown that there is a critical relationship between these quantities which results in breakdown for a critical incidence. To change the angle at which vortex breakdown occurs, it will be necessary to have a change in either one of these parameters. For example, with an increase in vortex intensity and therefore a decrease in axial velocity or an increase in tangential velocity, the strength of the shock needed to cause breakdown will decrease and breakdown will occur earlier on the wing.

From the results detailed in the previous section, it is suggested that two factors are causing the early prediction of breakdown on the wing. These are an under-prediction of the axial velocity, which results in a vortex more susceptible to breakdown and an over-prediction of the strength of the shocks. From consideration of the effects of a number of flow parameters, it appears that these predictions are not greatly effected by grid structure, turbulence model, convergence or time accuracy. The effect of grid refinement was also considered, which also concluded that the overall refinement of the grid had little effect on the solution. However, this study did not consider localised refinement, particularly in the vortex core region. Despite continuing improvement in CFD codes, turbulence models and practises, prediction of the vortex core behaviour and axial flow is still a challenge. There have been a number of collaborations and investigations which have considered the vortical flows over delta wings, which have also generally predicted the flow behaviour well, however the axial velocity is almost always much lower than that found from experiments. This is also true for this case and may be attributed to the abilities of turbulence modelling and restrictions in grid refinement for the core region. To fully resolve the vortex core behaviour it would be necessary to have similar refinement as is applied to boundary layer regions. It is unclear at this time whether an improvement in vortex core axial velocity would alter the predicted strength of the shocks in the flow, however, if the shock strength remained constant, with an increase in axial velocity, it may be suggested that the angle of incidence at which breakdown occurred would increase.

29.5   CONCLUSIONS

The following conclusions are drawn:

- The sudden motion in breakdown location observed in experiments is due to a shock-vortex interaction.

- The CFD predictions of the breakdown movement are insensitive to the simulation details.

- The onset angle of the breakdown movement was predicted about 3 degrees earlier than the measurements. The tunnel interference could contribute to this and should be further investigated.

- The reason for this could be due to the prediction of the shock strength or axial flow in the vortex.

- More detailed measurements of surface pressures and flow field velocities are needed to evaluate this point.

29.6   ACKNOWLEDGEMENTS

29.7   REFERENCES

[29-1]   Jobe, C.E.: *Vortex Breakdown Location Over 65° Delta Wings – Empiricism and Experiment*, Aeronautical Journal, 108(1087):475-482, 2004.

[29-2]   Elsenaar, A. and Hoeijmakers, H.W.M.: *An Experimental Study of the Flow Over a Sharp-Edged Delta Wing at Subsonic and Transonic Speeds*, AGARD Conference Proceedings Vortex Flow Aerodynamics, pp. 15.1-15.19, 1991, AGARD-CP-494.

[29-3]   Longo, J.M.A.: *Compressible Inviscid Vortex Flow of a Sharp Edge Delta Wing*, AIAA Journal, 33(4):680-687, 1995.

[29-4]   Thomer, O., Schröder, W. and Krause, E.: *Normal Shock Vortex Interaction*, Proceedings of the RTO-AVT Symposium on "Advanced Flow Management: Part A – Vortex Flows and High Angle of Attack for Military Vehicles", RTO-MP-069(I), pp. 18.1-8.10, 2001, NATO RTO.

[29-5]   Donohoe, S.R. and Bannink, W.J.: *Surface Reflective Visualisations of Shock-Wave/Vortex Interactions Above a Delta Wing*, AIAA Journal, 35(10):1568-1573, 1997.

[29-6]   Elsenaar, A., Hjemberg, L., Bütefisch, K-A. and Bannink, W.J.: *The International Vortex Flow Experiment*, Validation of Computational Fluid Dynamics – AGARD-CP-437 Volume 1, pp. 9.1-9.23, 1988, AGARD.

[29-7]   Hummel, D. and Redeker, G.: *A New Vortex Flow Experiment for Computer Code Validation*, Proceedings of the RTO-AVT Symposium on "Advanced Flow Management: Part A – Vortex Flows and High Angle of Attack for Military Vehicles", RTO-MP-069(I), pp. 8.1-8.32, 2001, NATO RTO.

[29-8]   Hummel, D.: *Effects of Boundary Layer Formation on the Vortical Flow Above Slender Delta Wings*, RTO-MP-AVT-111, pp. 30.1-30.22, 2004, NATO.

[29-9] Chu, J. and Luckring, J.M.: *Experimental Surface Pressure Data Obtained on a 65° Delta Wing Across Reynolds Number and Mach Number Ranges: Volume 1 – Sharp Leading Edge*, NASA Technical Memorandum 4645, NASA Langley Research Centre, 1996.

[29-10] Chu, J. and Luckring, J.M.: *Experimental Surface Pressure Data Obtained on a 65° Delta Wing Across Reynolds Number and Mach Number Ranges: Volume 2 – Small Radius Leading Edge*, NASA Technical Memorandum 4645, NASA Langley Research Centre, 1996.

[29-11] Chu, J. and Luckring, J.M.: *Experimental Surface Pressure Data Obtained on a 65° Delta Wing Across Reynolds Number and Mach Number Ranges: Volume 3 – Medium Radius Leading Edge*, NASA Technical Memorandum 4645, NASA Langley Research Centre, 1996.

[29-12] Chu, J. and Luckring, J.M.: *Experimental Surface Pressure Data Obtained on a 65° Delta Wing Across Reynolds Number and Mach Number Ranges: Volume 4 – Large Radius Leading Edge*, NASA Technical Memorandum 4645, NASA Langley Research Centre, 1996.

[29-13] Konrath, R.L.: *Experimental Investigations on the VFE-2 Configuration at DLR, Germany*, RTO-TR-AVT-113, 2009.

[29-14] Kroll, N., Aumann, P., Bartelheimer, W., Bleecke, H., Eisfeld, B., Lieser, J., Heinrich, R., Kunt, M., Monsen, E., Raddatz, J., Reisch, U. and Roll, B.: *FLOWer Installation and User Handbook*, DLR Doc. No. MEGAFLOW-1001, 1998.

[29-15] Kok, J.C.: *Mathematical Physical Model of ENSOLV Version 3.20; A Flow Solver for 3D Euler/Navier-Stokes Equations in Arbitrary Multi-Block Domains*, NLR-CR-2000-620, Nationaal Lucht- en Ruimtevaartlaboratorium, NLR, 2000.

[29-16] Kok, J.C. and Prananta, B.B.: *User Guide of ENSOLV Version 5.01, A Flow Solver for 3D Euler/Navier-Stokes Equations in Arbitrary Multi-Block Domains with Aeroelastic Capabilities*, NLR-CR-2001-348, Nationaal Lucht- en Ruimtevaartlaboratorium, NLR, 2001.

[29-17] Badcock, K.J., Richards, B.E. and Woodgate, M.A.: *Elements of Computational Fluid Dynamics on Block Structured Grids using Implicit Solvers*, Progress in Aerospace Sciences, 36:351-392, 2000.

[29-18] Strang, W.Z., Tomaro, R.F. and Grismer, M.J.: *The Defining Methods of Cobalt-60 – A Parallel, Implicit, Unstructured Euler/Navier-Stokes Flow Solver*, AIAA Paper 1999-786, January 1999.

[29-19] Leonard, A.: *Energy Cascade in Large Eddy Simulation of Turbulent Fluid Flow*, Advances in Geophysics, 18A:237-248, 1974.

[29-20] Houtman, E.M. and Bannink, W.J.: *Experimental and Numerical Investigation of the Vortex Flow Over a Delta Wing at Transonic Speeds*, AGARD Conference Proceedings Vortex Flow Aerodynamics, pp. 5.1-5.11, 1991, AGARD-CP-494.

[29-21] Kok, J.C.: *Resolving the Dependence on Freestream Values for the k-ω Turbulence Model*, AIAA Journal, 38(7):1292-1294, 2000.

[29-22] Délery, J.M.: *Aspects of Vortex Breakdown*, Progress in Aerospace Sciences, 30(1):1-59, 1994.

[29-23] Kalkhoran, I.M. and Smart, M.K., *Aspects of Shock Wave-Induced Vortex Breakdown*, Progress in Aerospace Sciences, 36:63-95, 2000.

[29-24] Spall, R.E., Gatski, T.B. and Grosch, C.E.: *A Criterion for Vortex Breakdown*, Physics of Fluids, 30(11):3434-3440, 1987.

[29-25] Robinson, B.A., Barnett, R.M. and Agrawal, S.: *Simple Numerical Criterion for Vortex Breakdown*, AIAA Journal, 32(1):116-122, 1994.

Chapter 30 – NUMERICAL SOLUTIONS FOR THE VFE-2 CONFIGURATION ON UNSTRUCTURED GRIDS AT KTH, SWEDEN

by

Simone Crippa

30.1 INTRODUCTION

The flow over a sharp and blunt leading edged, slender delta wing is considered in this chapter under subsonic and transonic conditions. The range of Mach number presented here extends from 0.2 to 0.85 and the range of Reynolds number form 2 to 120 million. This investigation was undertaken as part of the 2nd International Vortex Flow Experiment (VFE-2), a facet of the NATO RTO AVT-113 Task Group, which was set up to consider the flow behaviour both experimentally and computationally over a specified delta wing of 65° sweep.

30.2 MODEL DESCRIPTION

The geometry proposed by Hummel and Redeker [30-16] for the VFE-2 project is that of a delta wing with a 65° leading-edge sweep angle (Λ). The initial wind tunnel campaign on which the facet is based on was performed by Chu and Luckring [30-3] in the National Transonic Facility (NTF), NASA Langley Research Center (LaRC). A remarkable feature of the wind tunnel model is the possibility to interchange the leading-edge section which is attached to the flat-plate central wing section. Three blunt leading-edge radii (r) and a sharp leading edge were originally tested. But for the AVT-113/VFE-2 project, only the sharp ($r/\overline{c} = 0$) and medium radius ($r/\overline{c} = 0.0015$) leading edge geometries were selected for numerical and further experimental evaluations.

30.3 COMPUTATIONAL METHOD

30.3.1 Solver

The flow solver Edge [30-7] is used throughout this study. Edge is an unstructured, edge-based, finite volume CFD code developed and maintained by the Swedish Defence Research Agency (FOI). KTH is one among several academic contributors to the development of the code. Time integration to steady state of the discretised Reynolds averaged Navier-Stokes (RANS) equations is achieved with an explicit three-stage Runge-Kutta scheme. For the spatial discretization, a second order accurate, central scheme with 4th order artificial dissipation set to 0.02 is used for all cases. To speed up convergence, implicit residual smoothing, local time stepping and four level agglomeration multigrid are used.

The turbulence model used for the closure of the RANS equations is the two-equation k-ω model by Hellsten [30-14] coupled to the explicit algebraic Reynolds stress model (EARSM) by Wallin and Johansson [30-30]. A strain-rate based (curvature corrected) modification to EARSM (CC-EARSM) coupled with the Hellsten k-ω model is also evaluated for single cases. The calculations are performed with the assumption of fully turbulent flow, with a free-stream turbulence intensity of 0.1%.

For the unsteady computations, the original Detached Eddy Simulation (DES) [30-27] model as implemented in Edge is used. Time integration is achieved through "dual time stepping", an implicit time marching technique with explicit sub-iterations.

30.3.2 Numerical Model and Boundary Conditions

The geometric description of the configuration is given analytically by Chu and Luckring [30-3]. A half-body, digital geometric definition is available through a Virtual Laboratory [30-20] set up and maintained by NASA LaRC. The origin of the right-handed, Cartesian coordinate system is at the apex of the delta wing with the x-coordinate pointing downstream (towards the sting), the z-coordinate being perpendicular to the flat plate section and the y-coordinate pointing in span-wise direction. The numerical geometry features a root chord (c_r) of 1m resulting in a mean aerodynamic chord ($\bar{c}$) of 2/3 m $\approx$ 0.667 m, which is hereafter used as reference length for the Reynolds number (R_{mac}). The numerical model for the various grids is the same, apart from the two different leading edge sections. The sting is represented exactly as in the wind tunnel model up to the position $x/c_r = 1.758$, as recommended by Chu and Luckring [30-3]. After this location, the sting is closed out using an elliptical revolution surface, which is continuous through the curvature at cut-off. The total length of the closure surface is five times the diameter of the sting at the cut-off position ($d/c_r = 0.165$), i.e. $x/c_r = 0.826$, see Figure 30-1. The farfield boundary is located at approx. $11 \cdot c_r$ from any wall, in all directions, resulting in a half-sphere farfield boundary with a radius of 12.5 m.
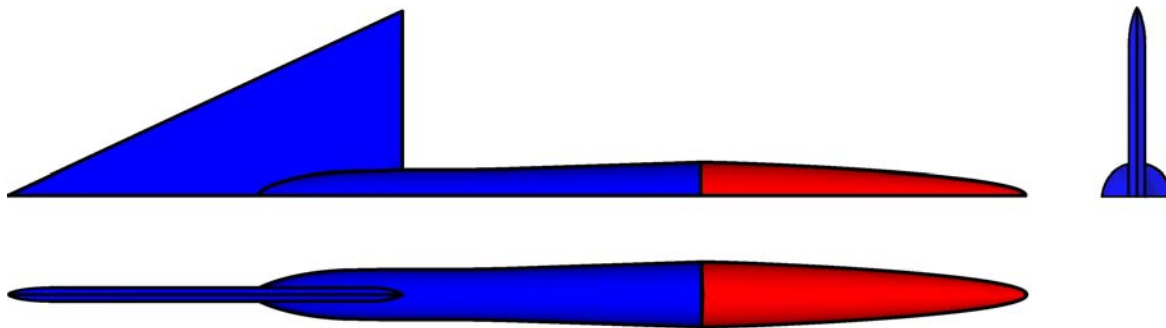
Figure 30-1: Three-View Sketch of Numerical Model – Exact NASA-NTF [30-3]
Geometry (in blue) and Sting Close-Off Surface (in red).

A common unstructured grid for the blunt leading-edge geometry is not available, thus for this study it is generated using a combination of the commercially available ANSYS ICEM CFD meshing package and the FOI-internal advancing-front grid generator TRITET [30-28]. The latter is the tool of choice for generating grids for Edge, as it is transparently interfaced to the solution based re-meshing and h-adaptation programs available within the Edge distribution. Although a common unstructured grid is available for the sharp leading edge model, for this work a topologically similar grid as for the blunt leading edge model is used also for the sharp leading edge computations.

Solution based adaptive grid refinement [30-29] is available in Edge and is used extensively throughout this study. Using a flow solution gained on a hybrid grid and a user-defined value for the selected adaptation sensor, the algorithm selects the cell edges to be subdivided and performs cell bisection for tetrahedral and prismatic elements. The prismatic cell elements are subdivided consistently in wall-normal direction to avoid hanging nodes and preserving the prismatic layer structure. This leads to further refinement of surface elements, whereby the additional points are projected to the interpolated location based on the neighbouring

original surface nodes. The algorithm can process only tetrahedral, pyramidal and prismatic volume elements. The available adaptation algorithm features three different vortex-capturing sensors [30-21] based on total pressure ratio, entropy loss or an eigenvalue analysis of the velocity gradient tensor, commonly called λ_2. It is also possible to refine several prismatic layers parallel to the wall for achieving a desired wall-normal non-dimensional cell spacing (y^+).

All grids feature a half-span representation of the delta wing model as described here, with a symmetric boundary condition applied on the symmetry plane. Furthermore, the boundary for the solid walls is of adiabatic, no-slip type for the viscous computations and of slip, wall-bounded type for the inviscid computations. On the farfield boundary a weak formulation characteristic condition is set.

Additional details of the numerical grids for the specific cases are given in the respective section.

30.4   SUBSONIC CASES

The results presented and discussed in this section allow for a deeper and more precise characterization of the unique double vortex system, which develops on the blunt leading edge delta wing at subsonic speeds.

Firstly, computational fluid dynamic (CFD) computations are presented for three Reynolds numbers (2, 6 and 60 million) at two angles of attack (18.5° and 23.0°) for a fixed Mach number of 0.4. Hereby the focus is laid on examining the angle of attack (AOA) dependence of the vortex separation onsets at a given Reynolds number. Secondly, a detailed flow topological analysis at and around the specific case at M = 0.4, α = 13.3°, R_{mac} = 3 x 10^6 is presented. For the flow topological interpretation, solutions at different Mach and Reynolds numbers are employed along with an inviscid case. Comparisons between computational results and experiments are presented with regard to surface pressure coefficient and surface flow patterns for the suction side of the delta wing.

30.4.1   Test Cases

The VFE-2 task group defined a matrix of computational cases based on realistic application problems and CFD development and evaluation needs. Each of the two main geometry configurations (sharp and blunt leading edge) are mainly used to study distinct effects. The conditions for the blunt leading edge geometry were chosen for studying primarily the transition from attached flow to semi-separated vortical flow up to separated dead-water flow. On the other hand, the sharp leading edge conditions were chosen for studying unsteady phenomena such as vortex breakdown and transonic vortex-shock interactions.

For the subsonic computations only the blunt leading edge cases are presented. With the initial case of interest being the M = 0.4, α = 18.5°, R_{mac} = 6 x 10^6 condition. From this condition, a lower and a higher R_{mac} are selected, respectively 2 and 60 million. The R_{mac} = 6 x 10^6 and R_{mac} = 60 x 10^6 wind tunnel data is available from the NTF campaign [30-3]. Unfortunately the R_{mac} = 2 x 10^6 data from the transonic wind tunnel in Göttingen (TWG) of the German-Dutch Wind tunnels (DNW) in Göttingen is not fully published yet, thus the data presented in Konrath et al. [30-17] is used for this comparison. The R_{mac} = 3 x 10^6 runs are available [30-17], [30-18],[30-19]; thus two additional conditions are chosen. One at R_{mac} = 3 x 10^6 for comparison to latest experimental data and another at R_{mac} = 120 x 10^6 to assess the effect of a further increase in Reynolds number.

30.4.1.1   Mid to High Incidence

To evaluate the coupling of angle of attack and Reynolds number, the initial condition are expanded to include also the α = 23.0° conditions. The cases for the AOA-Reynolds number dependency analysis are summarized

in Table 30-1. It is worth to note at this point that the initial VFE-2 test matrix is expanded here by the $R_{mac} = 60 \times 10^6$ cases.

Table 30-1: Test Cases for the AOA-Reynolds Number Dependency Analysis

α	M	R_{mac} $[\cdot 10^6]$
18.5°	0.40	2
18.5°	0.40	6
18.5°	0.40	60
23.0°	0.40	2
23.0°	0.40	6
23.0°	0.40	60

The free-stream conditions from the experimental campaign differ slightly from the VFE-2 computational matrix. The cases used for comparison are listed in Table 30-2.

Table 30-2: Experimental Cases Selected for Comparison (from Chu and Luckring [30-3])

Run number	Point number	α	M	R_{mac} $[\cdot 10^6]$
3	54	18.4°	0.400	6
21	424	18.3°	0.398	59.6
3	56	22.4°	0.400	6
21	426	22.4°	0.398	59.6

30.4.1.2   Low Incidence

At the establishment of the VFE-2 task group, one of the main cases of interest was the $\alpha = 13.3°$, $R_{mac} = 6 \times 10^6$, M = 0.4 condition for the blunt leading-edge configuration. This condition was selected since it exhibits the most distinctive trace of the inner vortex from the complete initial dataset (Chu and Luckring [30-3]). The availability of further, more detailed data from other experimental campaigns is mainly limited to lower Reynolds numbers. To harvest the most from the new experimental data, a shift of the computational efforts to lower Reynolds numbers was necessary. Thus a second set of conditions was chosen to tackle the flow topological description of the dual, co-rotating vortex system. Additionally to the M = 0.4 conditions, a further case is chosen at M = 0.2, $\alpha = 13°$, $R_{mac} = 2 \times 10^6$. Further analysis based on the solution of the Euler equations for the nominal conditions of $\alpha = 13.3°$ and M = 0.4, is helpful to assess the development of the flowfield in the theoretical inviscid assumption. The cases presented for this evaluation are listed in Table 30-3.

Table 30-3: Test Cases for the Flow Topology Study

α	13°	13.3°	13.3°	13.3°	13.3°	13.3°	13.3°
M	0.20	0.40	0.40	0.40	0.40	0.40	0.40
R_{mac} $[\cdot 10^6]$	2	2	3	6	60	120	- (inviscid)

30.4.2   Numerical Grids

Three similar numerical grids are employed within this study. Two hybrid grids consisting of tetrahedral volume elements and prismatic elements for the viscous layer resolution on an isotropic triangle-elements surface grid.

The main difference between the two hybrid grids is the targeted Reynolds number range (low or high) as well as the leading-edge resolution. The first hybrid grid is targeted for the cases with Reynolds number below and including 6 million (low R_{mac}), while the second hybrid grid for the 60 and 120 million cases (high R_{mac}). The third grid consists of purely tetrahedral elements in the volume and triangles on the surfaces. This grid is used for the inviscid computations and is generated by starting with the same surface mesh as the high Reynolds number mesh.

30.4.2.1   Low Reynolds Number Cases

The basic meshing strategy for these cases is to generate a suitable grid for the $R_{mac} = 6 \times 10^6$ case, in terms of first prismatic layer cell height, that can be subsequently used also for the lower Reynolds number cases. The surface discretization is given by isotropic triangular elements over the complete wing and sting. The first prismatic cell height needed to achieve y^+ target values around unity is found to be 1×10^{-6} m for the $R_{mac} = 6 \times 10^6$ case. The viscous layer discretization is realized with up to 32 prismatic layers with a total normal distance to the wall of 0.015 m. An optimal resolution of the viscous sublayer is achieved by setting a non-uniform expansion ratio of 1.17 near to the wall increasing up to 1.3 at the edge of the prismatic layers. The tetrahedral volume discretization is chosen coarse enough to yield first acceptable results. Subsequently, solution based refinement is employed for each case to achieve optimal results. For further details on the initial grid, please refer to Crippa and Rizzi [30-4]. The initial surface grid is visible in Figure 30-2.

| (a) Isometric View | (b) Side View of Apex | (c) Side View of Symmetry Plane |
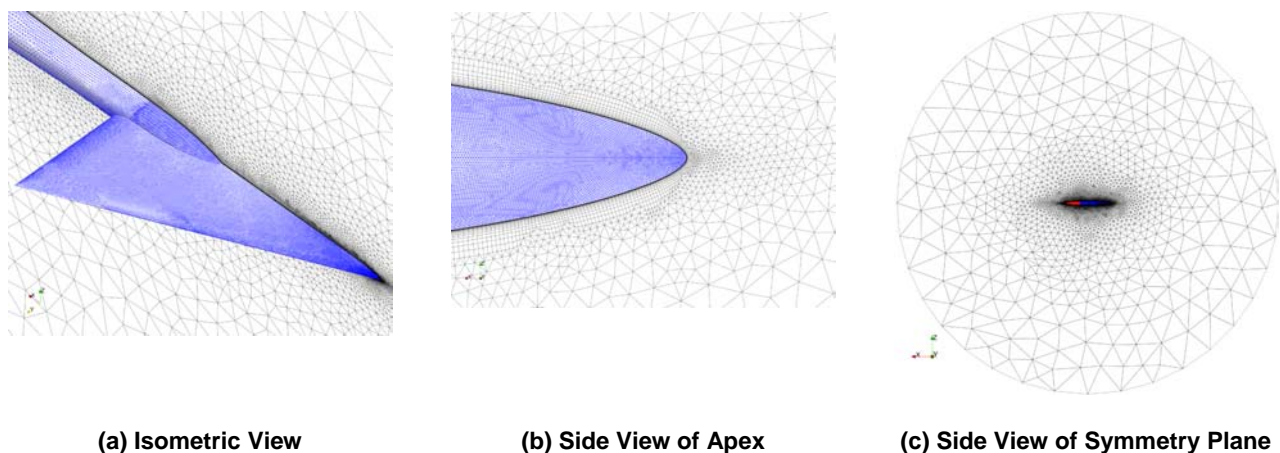
Figure 30-2: Initial Blunt Leading Edge Computational Grid for the $R_{mac} = 2 \times 10^6$ and $R_{mac} = 6 \times 10^6$ Cases.

For the solution based mesh refinement at each reference condition, the basic grid is refined using the λ_2 adaptation sensor. The adaptation above the main wing is mainly constrained to the tetrahedral elements by specifying a minimum edge length to be considered for adaptation. An example of the resulting adapted grid is given for the case $\alpha = 13.3°$, $M = 0.4$, $R_{mac} = 3 \times 10^6$. The comparison between the initial surface grid and the adapted grid on the suction side of the wing is shown in Figure 30-3 (a) and Figure 30-3 (b), while the additional tetrahedral cells above the wing are visible in Figure 30-3 (c) and Figure 30-3 (d).

(a) Top View, Initial Grid

(b) Top View, Twice Adapted Grid

(c) Isometric View of C$_p$ on Surface

(d) Front-Upper View of C$_p$ on Surface
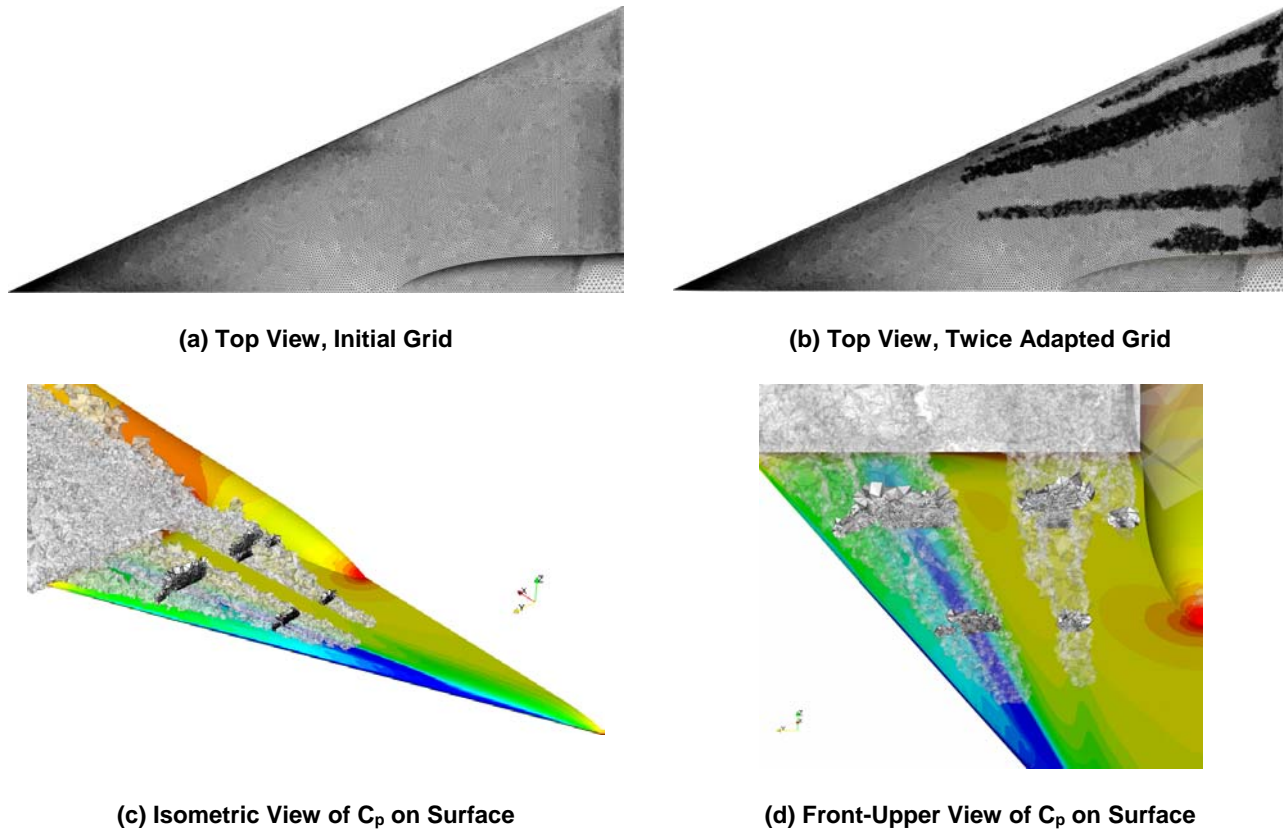
Figure 30-3: Comparison of Surface Elements on Suction Side and Additional Tetrahedral Elements after Second Solution-Based Adaptation for Case α = 13.3°, M = 0.4, R$_{mac}$ = 3 x 10^6.

The sensor threshold is set here to the minimum possible value, before several spurious regions are identified within the boundary layer. The additional elements as identified by the λ_2 sensor cluster around four main regions of vortical flow. The largest region of refinement is given by the leading-edge primary vortex. Between the path of the primary vortex and the leading edge it is also possible to discern the adaptation due to the identification of the secondary vortex. Next to the sting it is further possible to see the refinement of the horseshoe-vortex generated by the sting-wing intersection. The fourth identified region is due to an additional inboard vortex, co-rotating with the primary leading-edge vortex, and extensively described by several researchers [30-2],[30-18]. For this study, the correct resolution of this inboard vortex is crucial, but the λ_2 sensor fails here to localize a confined vortical region and thus to refine around the inner vortex upstream of $x/c_r \approx 0.49$. This failure is not due to the specified minimum edge length or the threshold value for the sensor being too high. The vortical motion of the horse-shoe vortex upstream of $x/c_r \approx 0.77$ is also not strong enough to trigger the adaptation sensor. The sizes for the initial grid, as well as the increase in nodes and elements due to the solution based refinement are summarized for each case in Table 30-4. The distribution of refined cells is very similar between the cases. This is mainly due to the relatively high selected sensor threshold value, which resulted in the adaptation algorithm to select and split cell edges beyond the strict region of influence of the main vortical structures. This, coupled to the flow topology for this configuration being similar, resulted in analogue adapted grids for all the different cases.

Table 30-4: Computational Grid Size for the Low R_{mac} Cases – Increase in Comparison to the Initial Grid is Given in Brackets; k = 10^3, M = 10^6 in the Table (Pyramidal elements are included in the total volume nodes counts)

Grid/Case	Total wall surface tri. elements	Prismatic volume cells	Tetrahedral volume cells	Total volume nodes
Initial	172 k	5.25 M	2.36 M	3.09 M
M=0.2, R_{mac}=$2 \cdot 10^6$	309 k (80%)	9.49 M (80%)	3.27 M (39%)	5.40 M (75%)
M=0.4, R_{mac}=$2 \cdot 10^6$	182 k (6%)	5.59 M (6%)	2.98 M (26%)	3.37 M (9%)
M=0.4, R_{mac}=$3 \cdot 10^6$	278 k (62%)	8.65 M (65%)	15.71 M (566%)	7.07 M (129%)
M=0.4, R_{mac}=$6 \cdot 10^6$	182 k (6%)	5.59 M (6%)	2.88 M (22%)	3.36 M (9%)

30.4.2.2   High Reynolds Number Cases

As for the numerical grid of the lower Reynolds number cases, the meshing program TRITET was used also here for producing the volume grid. The surface grid generation was performed again with ANSYS ICEM CFD. This meshing strategy allows for an optimal control of the main delta wing surface resolution. In this case it was modified to better resolve the region of primary separation, expected to shift downstream. This translates into a decrease of triangle density at the apex and an increase at the wing tip. The resolution of the leading edge downstream of $x/c_r = 0.7$ is increased by approx. a factor of three in comparison to the lower Reynolds number grid. The first cell height is 1 x 10^{-7} m, with the total extent of the 36 prismatic layers of 0.003 m, resulting in the non-uniform exponential expansion ratios normal to the wall of 1.21 near the wall and 1.35 at the edge of the prismatic layers.

For the $R_{mac} = 60$ x 10^6 case, two λ_2 sensor adaptation steps are performed, whereas the first solution-based adaptation for the 120 million R_{mac} case is aimed at achieving a satisfactory y^+ distribution. For this case only one adaptation step was then performed using the λ_2 sensor. See Table 30-5 for the grid size details.

Table 30-5: Computational Grid Size for the High R_{mac} Cases at M = 0.4 – Increase in Comparison to the Initial Grid is Given in Brackets; k = 10^3, M = 10^6 in the Table (Pyramidal elements are included in the total volume nodes counts)

Grid/Case	Total wall surface tri. elements	Prismatic volume cells	Tetrahedral volume cells	Total volume nodes
Initial	199 k	7.17 M	5.50 M	4.57 M
$60 \cdot 10^6$	289 k (45%)	10.38 M (45%)	16.61 M (202%)	8.08 M (77%)
$120 \cdot 10^6$	579 k (191%)	20.84 M (191%)	10.29 M (87%)	12.33 M (170%)

30.4.2.3   Inviscid Case

The same surface mesh as for the high Reynolds number case is used to generate a fully tetrahedral volume grid. The initial mesh is adapted twice using the same λ_2 sensor as for the RANS grids. The sizes of the numerical grids used for the inviscid computations are listed in Table 30-6.

Table 30-6: Computational Grid Size for the Inviscid Case at M = 0.4 – Increase in Comparison to the Initial Grid is Given in Brackets; k = 10^3, M = 10^6 in the Table

Grid	Total wall surface triangular elements	Tetrahedral volume cells	Total volume nodes
Initial	199 k	5.19 M	908 k
Adapted once	358 k (**80%**)	18.51 M (**257%**)	3.19 M (**251%**)
Adapted twice	375 k (**88%**)	23.97 M (**362%**)	4.14 M (**356%**)

30.4.3   Results and Discussion

The maximum and average y^+ values over the delta wing for some relevant cases are presented in Table 30-7.

Table 30-7: Wall-Normal Dimensionless Distance (y^+) on the Delta Wing Surface for the M = 0.4 Cases

$R_{mac} [\cdot 10^6]$	2	3	6	60	120
max y^+	0.44	0.48	0.898	0.648	1.65
mean y^+	0.069	0.096	0.179	0.148	0.41

30.4.3.1   Separation Onset Analysis

Grid size sensitivity is presented here only for case $\alpha = 18.5°$, M = 0.4, $R_{mac} = 6 \times 10^6$. Furthermore only one set of results is presented in this section from the turbulence model selection runs, relative to the comparison between the CC-EARSM and EARSM models for case $\alpha = 18.5°$, M = 0.4, $R_{mac} = 6 \times 10^6$.

30.4.3.1.1   18.5° Angle of Attack Cases

The increased prediction accuracy of CC-EARSM over EARSM expected for this type of vortical flows could not be confirmed. Up to $x/c_r = 0.4$, no difference between the two models could be observed in the pressure coefficient (C_p) plots, but after $x/c_r = 0.6$ the suction peak associated with the primary vortex is underrepresented by CC-EARSM, see Figure 30-4.

(a) x/c$_r$ = 0.4   (b) x/c$_r$ = 0.6   (c) x/c$_r$ = 0.8
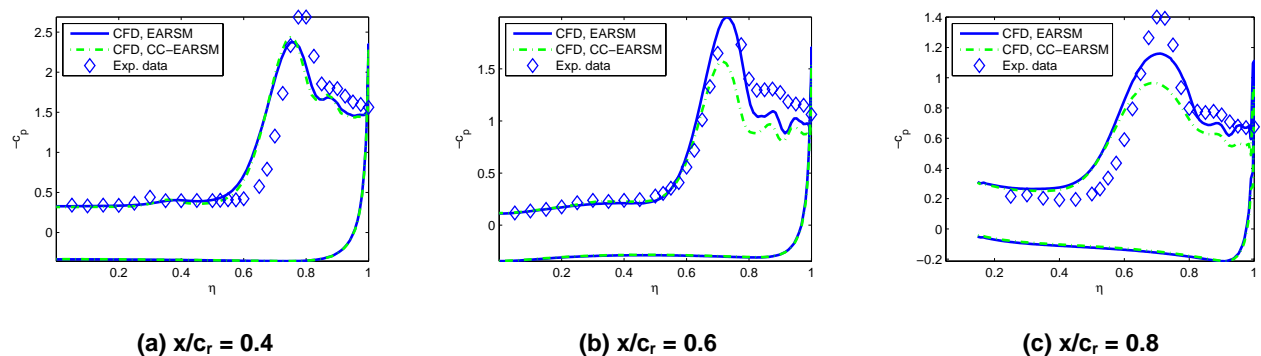
Figure 30-4: C$_p$ Plots for Different x/c$_r$ – Turbulence Model Comparison for Case α = 18.5°, M = 0.4, R$_{mac}$ = 6 x 10^6.

This is disappointing as CC-EARSM should alleviate the need for specific modifications [30-1] to the standard k-ω models, which in the original formulation are known to over-predict the eddy viscosity within vortex cores [30-12]. This led to CC-EARSM not being selected for further computations, but EARSM.

The typical residuals and force coefficients convergence behaviour shown in Figure 30-5 for case α = 18.5°, M = 0.4, R_{mac} = 6 x 10^6, did not differ substantially from the other cases.

| (a) Initial Grid | (b) Once Adapted Grid | (c) Twice Adapted Grid |
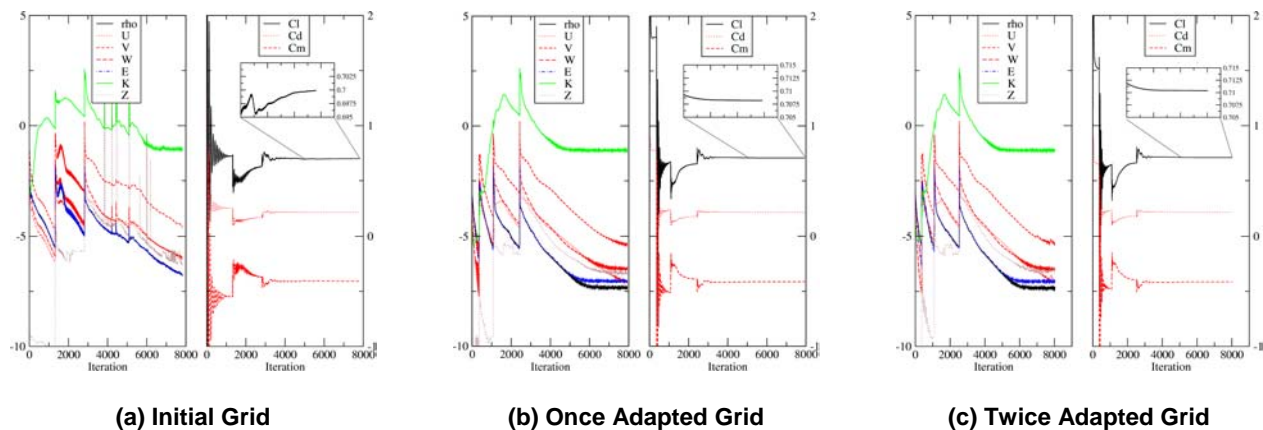
Figure 30-5: Convergence Behaviour for Case α = 18.5°, M = 0.4, R_{mac} = 6 x 10^6, Scaled Residuals (Logarithmic Scale) and Force Coefficients.

In Figure 30-5 we identify a significantly improved convergence behaviour between the initial and once adapted grid, but no substantial residual convergence gain between the once adapted and twice adapted grid. The increase of lift coefficient (C_L) from 0.7082 for the once adapted grid to 0.7104 for the twice adapted grid is attributed to the stronger primary vortex and thus lower pressure coefficient, see Figure 30-6.

| (a) x/c_r = 0.2 | (b) x/c_r = 0.4 | (c) x/c_r = 0.8 |
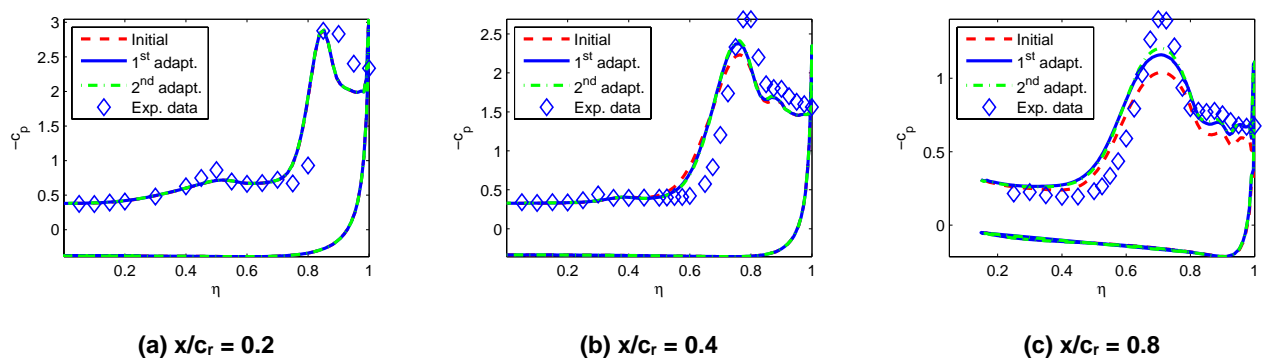
Figure 30-6: C_p Plots for Different x/c_r – Comparison of the Solution on the Initial Grid to Two Further Levels of Refinement and Experimental Data.

Since the main area of interest for this study is in the region of separation onset, the better resolution of the aft section given by the twice adapted grid does not justify the increased computational costs. Thus for the majority of the presented cases, only one adaptation step per case is applied to the initial mesh. If the presented results are achieved on a twice adapted mesh, then it is noted in the relative section. To better interpret the flow structures,

a detailed view of the apex region between approx. $x/c_r = 0.05$ and 0.5 for case $\alpha = 18.5°$, M = 0.4, $R_{mac} = 6 \times 10^6$ is shown in Figure 30-7.
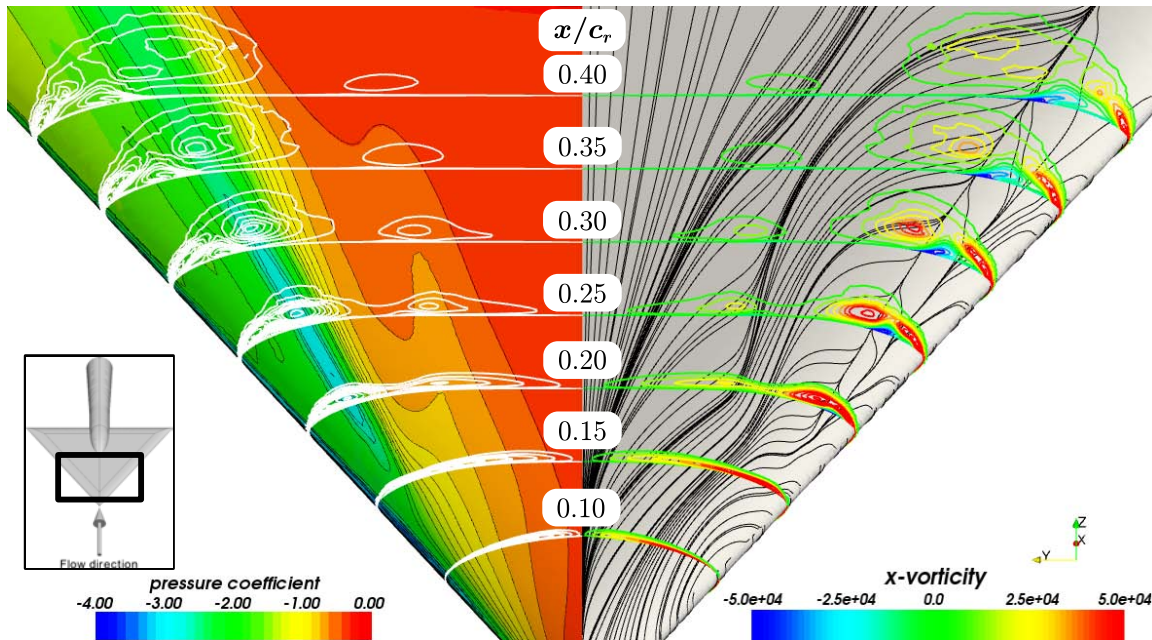
**Figure 30-7: Surface Pressure Coefficient, x-Vorticity Iso-Contours
and Skin Friction Lines for Case α = 18.5°, M = 0.4, R_{mac} = 6 x 10^6.**

In this figure the surface pressure coefficient is visualized on the left hand side and the skin friction lines on the right hand side. Furthermore, cuts through the flowfield, at constant x/c_r sections, show iso-contours of constant x-component of the vorticity vector. On the right hand side, the same contour curves are colored by the x-vorticity, where positive values indicate a left-handed rotation and negative values a right-handed rotation (in the depicted view). This enables to identify the primary vortex, which is formed at $x/c_r = 0.11$ and a co-rotating vortical structure located further inboard. This structure is dissipated quickly and according to the C_p footprint and the vorticity cuts, it is nearly vanished at $x/c_r = 0.4$.

For case $\alpha = 18.5°$, M = 0.4, $R_{mac} = 60 \times 10^6$ a similar phenomenon appears. For this case, the separation onset for both the outer primary vortex, as well as the inner primary vortex is shifted by $x/c_r \approx 5\%$ further downstream. Figure 30-8 depicts the same portion of the delta wing and is structured congruently to Figure 30-7. From this figure it is possible to further identify, based on the skin friction lines, the presence of an inner secondary vortex, developing at approx. $x/c_r = 0.32$.
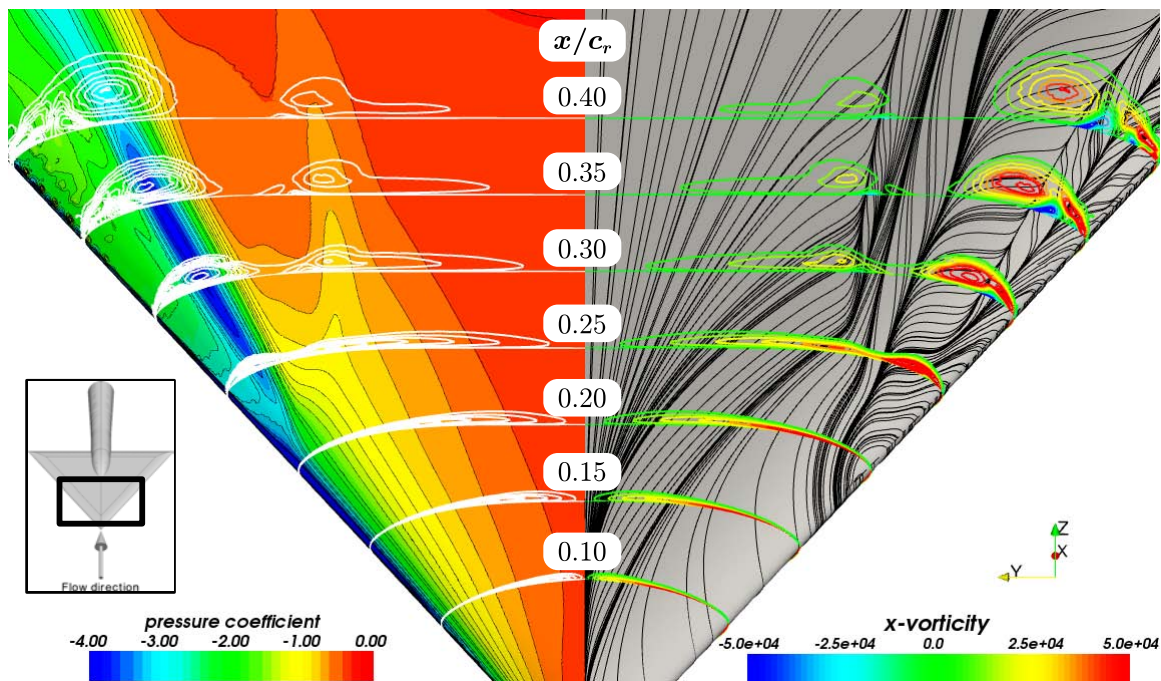
**Figure 30-8: Surface Pressure Coefficient, x-Vorticity Iso-Contours
and Skin Friction Lines for Case α = 18.5°, M = 0.4, R_{mac} = 60 x 10^6.**

The flow topology can be further characterized by identifying separation and attachment lines (SL, AL) of the primary and secondary vortices (PV, SV). The division into inner and outer vortical system (I, O) is added to the description nomenclature of Figure 30-9, e.g., OPVSL corresponds to the outer primary vortex separation line.
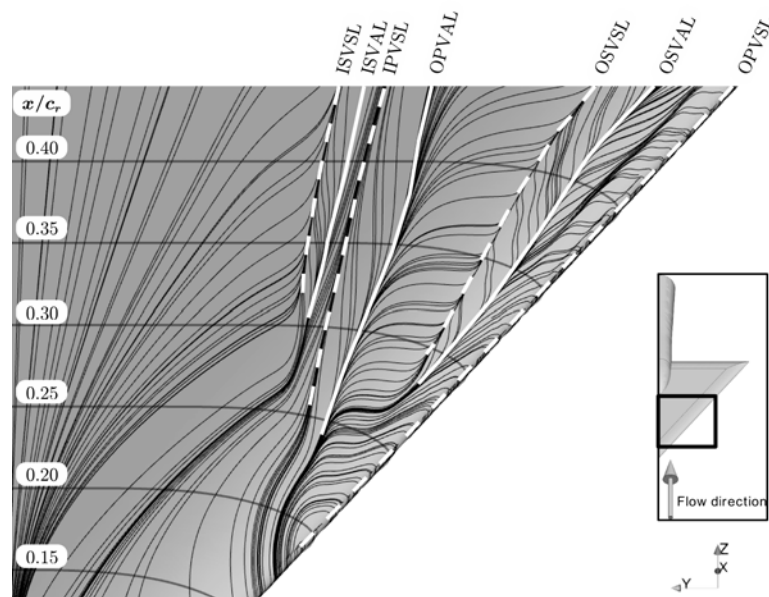
Figure 30-9: Skin Friction Lines and Topological Interpretation – **Case α = 18.5°, M = 0.4, R_{mac} = 60 x 10^6.**

Note that the inner primary vortex attachment line (IPVAL) is not visible in Figure 30-9, but with the help of spanwise velocity vector cuts (data not shown), it is possible to locate the IPVAL on the symmetry plane.

The pressure coefficient comparison between the computed case at $R_{mac} = 60 \times 10^6$ and experimental data shows good agreement, see Figure 30-10. This is mainly due to the small discrepancy between computed and experimental separation onset of the primary and inner vortices. The computations seem to over-predict the vortex strength, as visible on the C_p plot for $x/c_r = 0.95$, see Figure 30-10 (d).

| (a) x/c_r = 0.4 | (b) x/c_r = 0.6 | (c) x/c_r = 0.8 | (d) x/c_r = 0.95 |
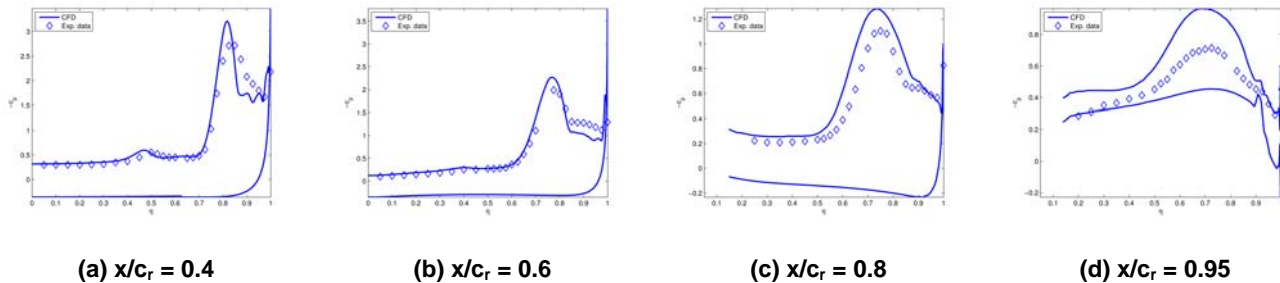
Figure 30-10: C_p Plots for Different x/c_r – Case $\alpha = 18.5°$, M = 0.4, $R_{mac} = 60 \times 10^6$.

30.4.3.1.2   23.0° Angle of Attack Cases

The sensitivity of the flowfield to the primary vortex separation location as shown for the $\alpha = 18.5°$ cases is expected to decrease when increasing the angle of attack. This is here the case, as visible in Figure 30-11, where for the $\alpha = 23.0°$ cases the outer primary vortex develops within a short distance from the apex, at about $x/c_r = 0.1$.
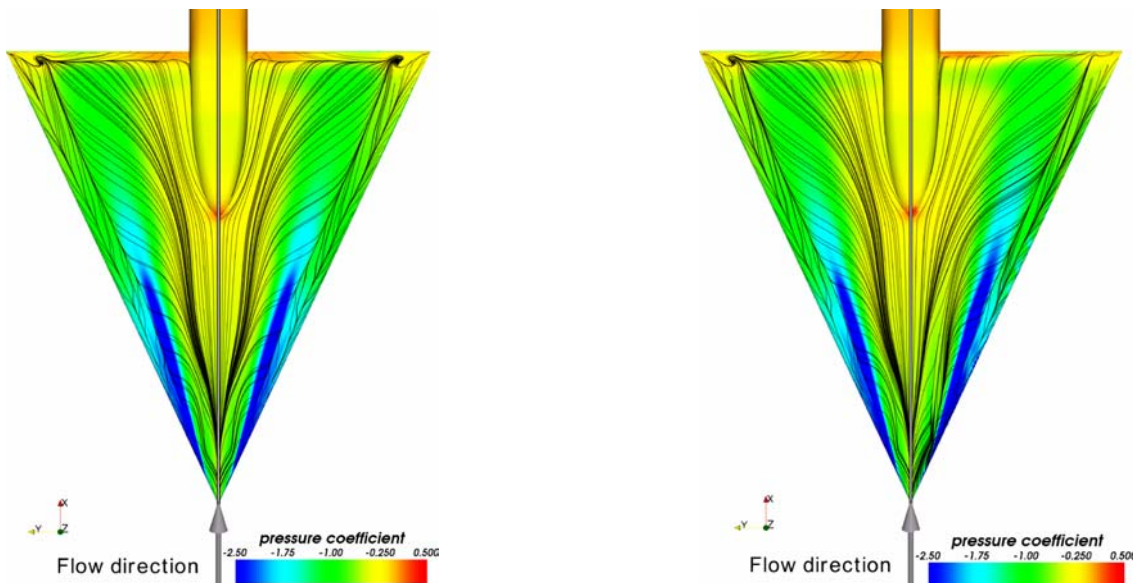
(a) Left Frame: $R_{mac} = 6 \times 10^6$; Right Frame: $R_{mac} = 2 \times 10^6$ **(b) Left Frame: $R_{mac} = 6 \times 10^6$; Right Frame: $R_{mac} = 60 \times 10^6$**

Figure 30-11: Surface Pressure Coefficient – View on the Suction Side, Perpendicular above the Flat Delta Wing Central Part; $\alpha = 23.3°$, M = 0.4.

The same viewpoint and visualization technique as for case α = 18.5°, M = 0.4, R_{mac} = 60 x 10^6 (Figure 30-8) can be used to identify a similar flow topology for case α = 23.0°, M = 0.4, R_{mac} = 60 x 10^6.
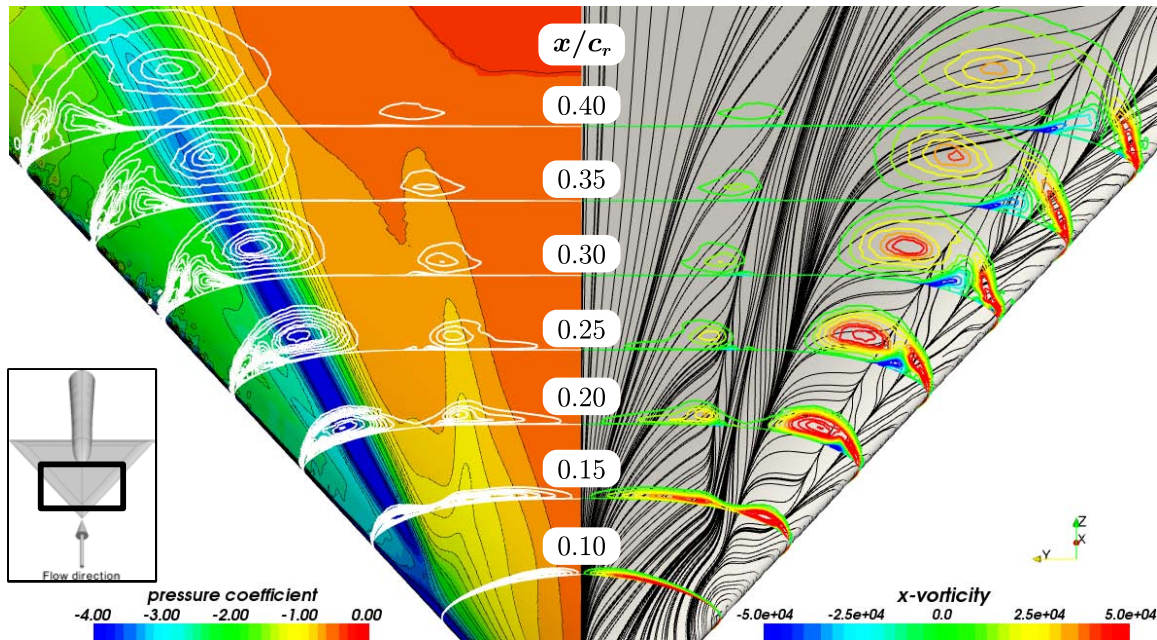
**Figure 30-12: Surface Pressure Coefficient, x-Vorticity Iso-Contours
and Skin Friction Lines for Case α = 23.3°, M = 0.4, R_{mac} = 60 x 10^6.**

Again, the skin friction pattern, combined with the iso-contours of x-vorticity at specific cuts reveals the presence of an inner primary and secondary vortex system. In contrast to case α = 18.5°, M = 0.4, R_{mac} = 60 x 10^6, here this system is dissipated relatively quickly and as soon as x/c_r = 0.3 the inner secondary attachment line detaches from the surface. This happens also for the inner secondary vortex separation line at x/c_r = 0.34. These observations are summarized in Figure 30-13 (a), where separation and attachment lines for both inner and outer vortical system are sketched.

(a) Skin Friction Lines and Topological Interpretation   **(b) Zonal Subdivision**

Figure 30-13: Skin Friction Lines and Topological Interpretation – α = 23.3°, M = 0.4, R_{mac} = 60 x 10^6.

For this AOA the CFD data is found to match best the experimental data, as can be seen in the C_p plots presented in Figure 30-14 for case α = 23.0°, M = 0.4, R_{mac} = 2 x 10^6, in Figure 30-15 for case α = 23.0°, M = 0.4, R_{mac} = 6 x 10^6 and in Figure 30-16 for case α = 23.0°, M = 0.4, R_{mac} = 60 x 10^6. At this incidence, as for the α = 18.5° case, the R_{mac} = 60 x 10^6 case matches best the experimental data.

(a) x/c$_r$ = 0.2   **(b) x/c$_r$ = 0.4**   **(c) x/c$_r$ = 0.6**   **(d) x/c$_r$ = 0.8**

Figure 30-14: C$_p$ Plots for Different x/c$_r$ – Case α = 23.3°, M = 0.4, R_{mac} = 2 x 10^6.

(a) x/c$_r$ = 0.2   **(b) x/c$_r$ = 0.4**   **(c) x/c$_r$ = 0.6**   **(d) x/c$_r$ = 0.8**

Figure 30-15: C$_p$ Plots for Different x/c$_r$ – Case α = 23.3°, M = 0.4, R_{mac} = 6 x 10^6.

(a) x/c_r = 0.2 **(b) x/c_r = 0.4** **(c) x/c_r = 0.6** **(d) x/c_r = 0.8**

Figure 30-16: C_p Plots for Different x/c_r – Case α = 23.3°, M = 0.4, R_{mac} = 60 x 10^6.

30.4.3.1.3 Conclusions

The location of primary vortex separation onset can be determined in two ways. A simple, graphical method, when fine-grained leading edge pressure measurements are not available, is to geometrically extend the location of the primary vortex core path upstream, to intersect the leading edge and mark this intersection as the separation onset. Another, more accurate, possibility is to evaluate the skin friction lines in the vicinity of the leading edge to identify the position, where convergence of two skin friction lines occurs first. This position determines the so-called squeeze-off separation onset location. For comparison, both methods are used here to determine the separation onset. The error of the vortex core prolongation method is minimal. For all cases, both methods give similar results. These are compared with experimental data and summarized in Figure 30-17. At the lowest Reynolds number and lowest incidence the agreement is worst. Going from the R_{mac} = 6 x 10^6 to the R_{mac} = 60 x 10^6 cases, the agreement increases. With the R_{mac} = 60 x 10^6 cases fitting best by considering the percental difference between CFD and experimental data.

(a) R_{mac} = 2 x 10^6 **(b) R_{mac} = 6 x 10^6** **(c) R_{mac} = 60 x 10^6**
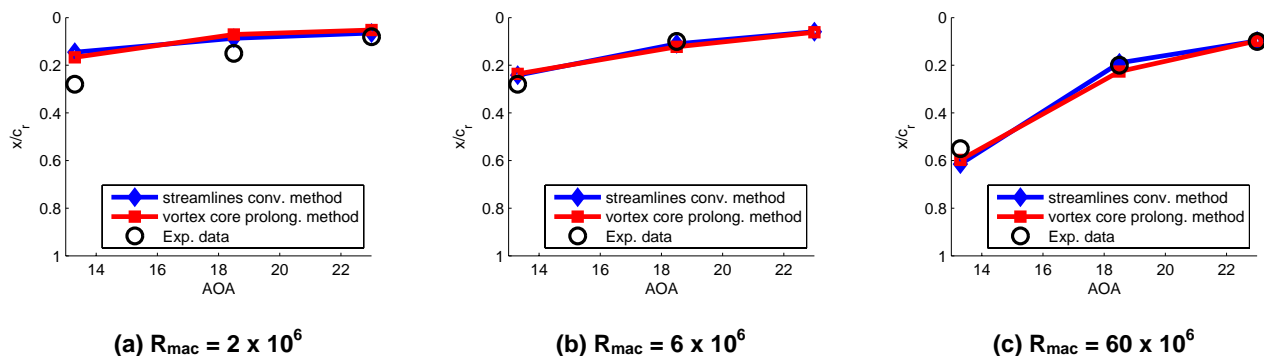
Figure 30-17: Outer Primary Vortex Separation Onset.

Since the separation onset of the inner primary vortex is not as clear for the α = 13.3° and all R_{mac} = 2 million cases, only the results for R_{mac} = 60 million and for the cases at higher AOA at R_{mac} = 6 million are presented in Figure 30-18. Comparison between computed and measured results is not possible here, due to unavailability of experimental data. The relatively constant distance between outer and inner primary vortex separation onset is an indication that these vortical systems are closely coupled.

(a) R$_{mac}$ = 6 x 10^6   **(b) R$_{mac}$ = 60 x 10^6**
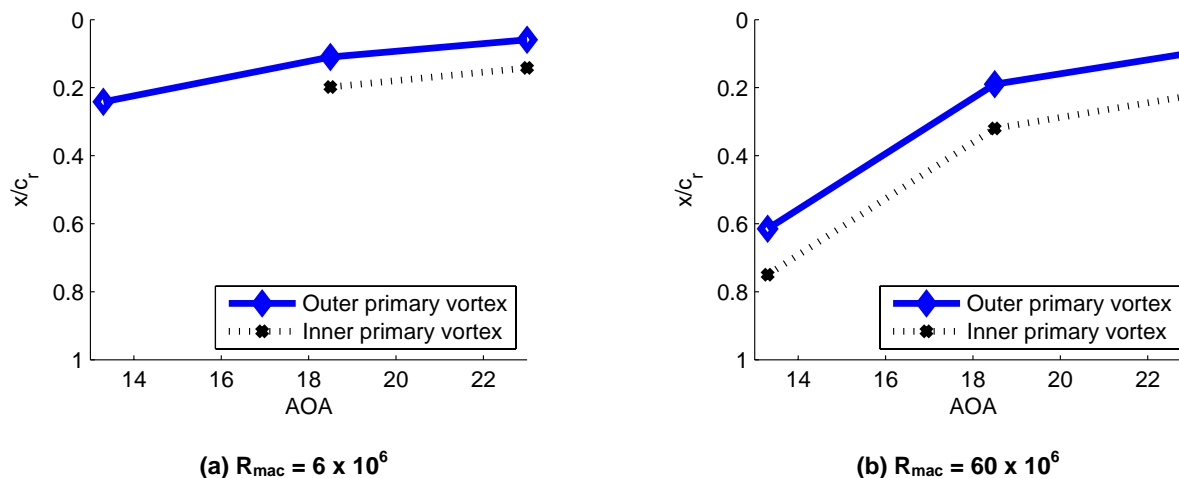
Figure 30-18: Inner and Outer Primary Vortex Separation Onset.

The predicted outer primary separation onset location is shown to match well the data from experimental investigations at high Reynolds numbers. This enables to gain certainty in the determination of the inner primary vortex separation, which is shown to correlate with the outer primary vortex separation and attachment. This is especially true for the high AOA, high R$_{mac}$ case (case α = 23.0°, M = 0.4, R$_{mac}$ = 60 x 10^6), where the coupling between outer primary vortex attachment line (onset and length) with the inner primary vortex separation line (onset and length) is clearly recognizable. The primary vortex attachment line (OPVAL in Figure 30-12) separates the diverging streamlines passing under the outer primary vortex on one side (pointing outboard, region "A" in Figure 30-13 (b)) and the streamlines being diverted towards the centreline on the other side (region "B" in Figure 30-13 (b)). The onset of the inner primary vortex (IPVSL in Figure 30-13 (a)) coincides where the streamlines diverted towards the centreline by the outer primary vortex hit for the first time the further upstream, inboard streamlines from the delta wing apex region ("C" in Figure 30-13 (b)). If the inner primary vortex strength is predicted well, the attached flow passing under the inner primary vortex core (coming from regions "D" and "E" in Figure 30-13 (b)) is accelerated sufficiently to trigger (inner) secondary separation. Where the outer primary vortex attachment on the surface is not present anymore (for case α = 23.0°, M = 0.4, R$_{mac}$ = 60 x 10^6 at x/c$_r$ = 0.30), the inner vortex starts to decrease in strength and shortly after (for case α = 23.0°, M = 0.4, R$_{mac}$ = 60 x 10^6 at x/c$_r$ = 0.34) the inner primary vortex separation stops.

Although the numerical results for the R$_{mac}$ = 6 x 10^6 cases do not match well the experimental data, the inner primary vortex separation mechanism described above can be recognized also here (e.g., case α = 18.5°, M = 0.4, R$_{mac}$ = 6 x 10^6). Both the outer primary vortex strength and the outer primary vortex attachment line extent are under-predicted. In this case the diversion of the streamlines from the outer primary vortex attachment line towards the centreline is not as strong as it is in reality. Thus the coincidence between these streamlines and the further inboard streamlines (for case α = 18.5°, M = 0.4, R$_{mac}$ = 6 x 10^6 at x/c$_r$ = 0.22) induces only a weak inner primary vortex, which does not trigger secondary separation. From the above discussion, it is clear that the numerical method used for this study is shown to perform best at the higher AOA of 23.0° and R$_{mac}$ of 60 million for resolving the double vortex system.

30.4.3.2   Flow Topological Analysis

This section contributes to the common effort to describe the flow phenomena for the co-rotating double-vortex system. This is done by highlighting the strengths and deficiencies encountered by steady CFD computations at low Reynolds numbers around the nominal angle of attack of 13.3°, and subsonic Mach number, M = 0.4.

For these free-stream conditions, the leading-edge normal AOA and Mach number are $\alpha_N = 29.22°$ and $M_N = 0.19$. Even though the classification by Eberle et al. [30-6] does not account for the effects of Reynolds number, it differentiates between sharp and blunt leading-edged, slender delta wings. The flow pattern to be expected for the considered case can be extracted from the α_N-M_N classification [30-6]. For the conditions as given above, the data point lies in the middle of the region denominated "development of vortex system". In this condition, a higher Reynolds number would shift the data point towards the fully attached flow region by delaying the separation onset; whereas a lower Reynolds number would eventually result in the appearance of fully developed vortices. The sensitivity of this case to small variations of Reynolds number, AOA and free-stream Mach number makes it a challenging case for computational methods. Thus the numerical exploration of a wide range of Reynolds numbers and a topological flow analysis are the main topics of this study.

30.4.3.2.1   Surface Pressure Coefficient

A comparison of computed surface pressure data to experimental pressure sensitive paint (PSP) data from Konrath et al. [30-17] is here only possible for the $R_{mac} = 3 \times 10^6$ case. This is presented in Figure 30-19 (to be compared against Figure 30-21(c)). The surface pressure coefficient plots of the delta wing suction side are presented in Figure 30-20 for the inviscid computation and in Figure 30-21 for the viscous computations.
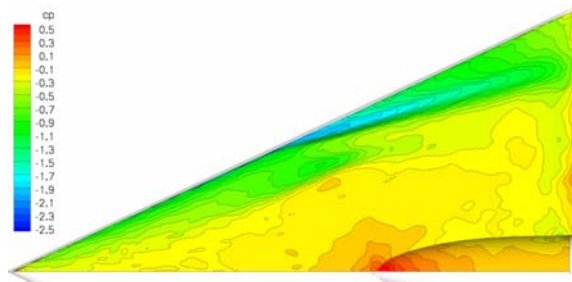
Figure 30-19: Experimental Pressure Coefficient Surface Plot for
α = 13.3°, M = 0.4, R$_{mac}$ = 3 x 10^6 Data Provided by DLR [30-17].
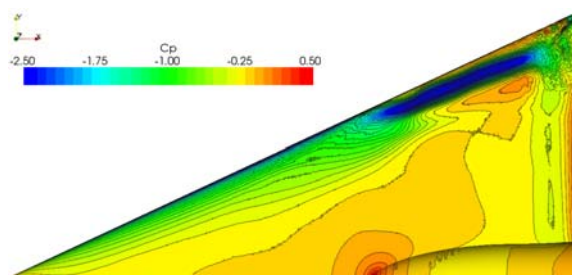
Figure 30-20: Surface Pressure Coefficient on Half-Span
Suction Side – CFD Result for the Inviscid Case.

(a) M = 0.2, R_{mac} = 2 x 10^6

(b) M = 0.4, R_{mac} = 2 x 10^6

(c) M = 0.4, R_{mac} = 3 x 10^6

(d) M = 0.4, R_{mac} = 6 x 10^6

(e) M = 0.4, R_{mac} = 60 x 10^6

(f) M = 0.4, R_{mac} = 120 x 10^6
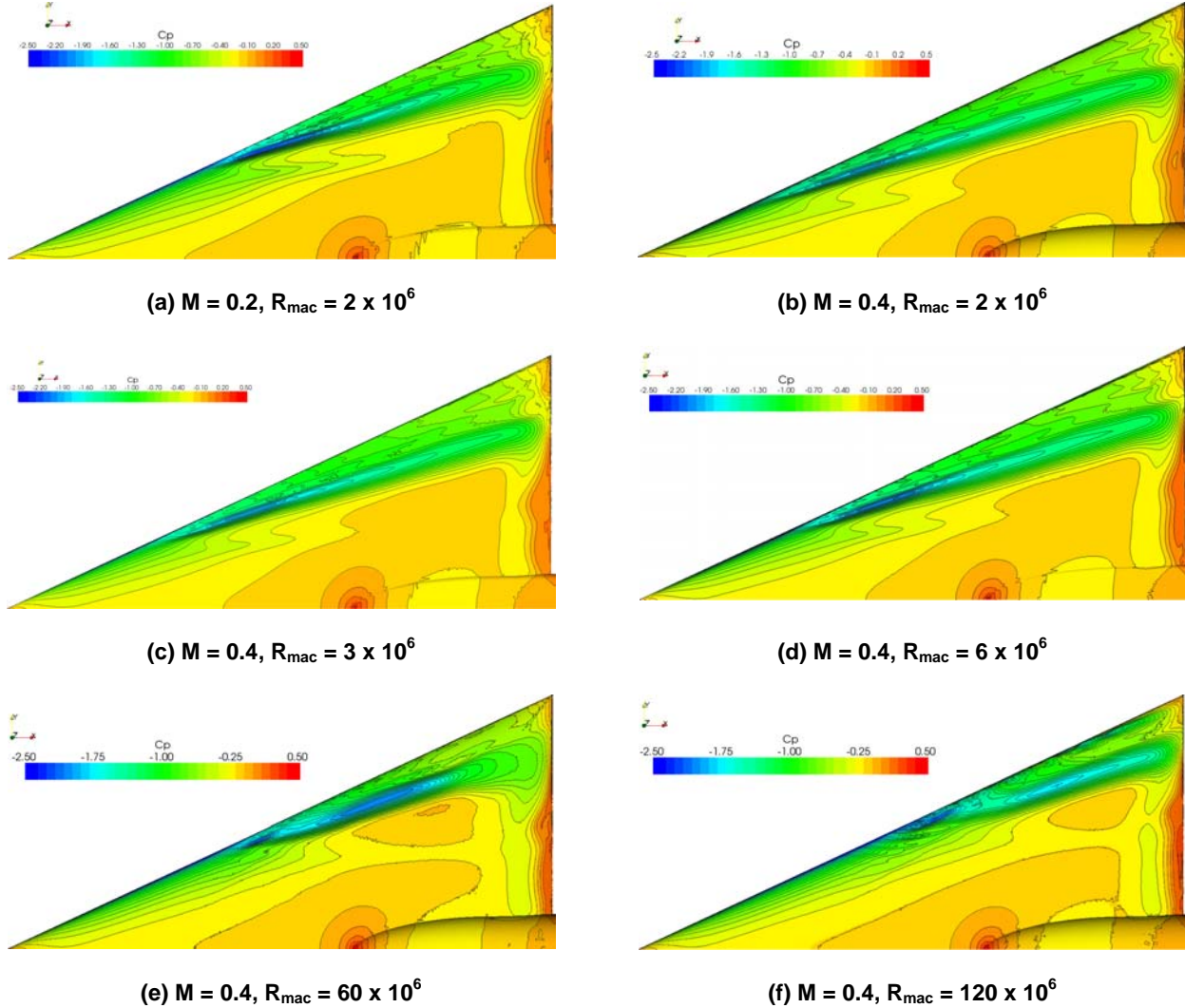
Figure 30-21: Surface Pressure Coefficient on Half-Span
Suction Side – CFD Results for the Viscous Cases.

The trends as described by Luckring [30-23] in respect to Reynolds number and compressibility dependence are also found when examining the computational results. The effect of an increase of Mach number on the upstream movement of primary separation onset is shown here from M = 0.2 to M = 0.4 (Figure 30-21(a) to Figure 30-21(b)). The opposite effect for an increase of Reynolds number, i.e. delay of primary separation onset, is clear when comparing Figure 30-21(b) to Figure 30-21(f).

The inviscid case features a substantially stronger primary vortex than the highest Reynolds number case. From analysis of the surface pressure data it forms at $x/c_r \approx 0.6$ and is located too far outboard. But the overall picture is as expected from an inviscid computation.

30.4.3.2.2   Span-Wise Pressure Coefficient

The half-span surface pressure coefficient graphs are presented here only for the cases with available experimental data and are normalized by the local semi-span to give the local non-dimensional semi-span (η). For all cases considered in this study, at $x/c_r = 0.2$ the computations agree with the experimental data in predicting fully attached flow. Thus the foremost available location from the experimental datasets ($x/c_r = 0.2$) is not presented hereafter.

The viscous computations are presented in Figure 30-22 to Figure 30-25, while the inviscid case is only compared to other viscous cases in Figure 30-26 and Figure 30-27.

(a) x/c_r = 0.4   **(b) x/c_r = 0.6**   **(c) x/c_r = 0.8**   **(d) x/c_r = 0.95**
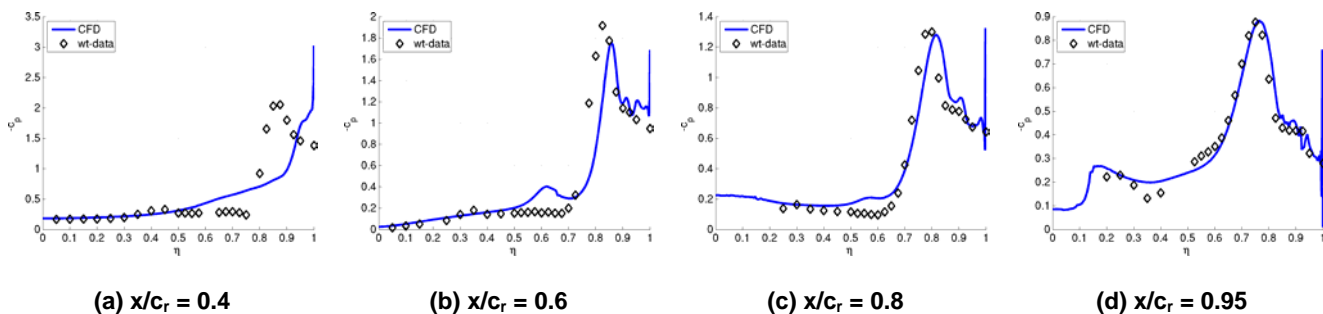
Figure 30-22: C_p Plots for Different x/c_r – Case α = 13°, M = 0.2, R_mac = 2 x 10^6
– Comparison between CFD Results and Experimental Data [30-17].

(a) x/c_r = 0.4   **(b) x/c_r = 0.6**   **(c) x/c_r = 0.8**   **(d) x/c_r = 0.95**
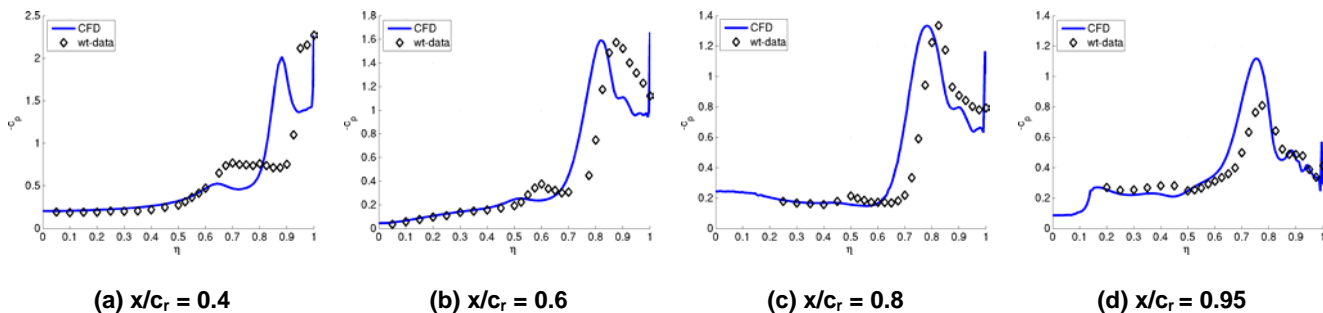
Figure 30-23: C_p Plots for Different x/c_r – Case α = 13.3°, M = 0.4, R_mac = 6 x 10^6
– Comparison between CFD Results and Experimental Data [30-3].

30.4.3.2.3   Effect of Turbulence Modelling

The only results presented in this section for the turbulence model comparison are between the CC-EARSM and EARSM models for the case $\alpha = 13.3°$, M = 0.4, $R_{mac} = 3 \times 10^6$, as the observed behaviour is similar for the other cases. Other examined turbulence models affected the location of primary vortex separation onset; in some cases positively as for the one-equation Spalart-Allmaras model and in other cases negatively as for the standard Wilcox k-ω model. None of the evaluated models correctly resolves the initial formation of the inner vortex. A motivation for the assessment of curvature corrected models is that a better resolution of the inner vortex was hoped for. Up to $x/c_r = 0.2$, no difference between the two models can be observed in the pressure coefficient (C_p) plots, but right after the formation of the primary vortex the main suction peak is

stronger, as expected from CC-EARSM, see Figure 30-24 (a) and Figure 30-24 (b). At $x/c_r = 0.8$ CC-EARSM shows a weaker primary suction peak and at $x/c_r = 0.95$ no major difference between the two models is seen in regards to primary suction peak. Although CC-EARSM initially performs as expected in regards to primary vortex strength, the inner vortex is under-predicted over the complete path. The difference to EARSM is only minor, but visible in Figure 30-24 (a), where at $\eta \approx 0.6$, it is possible to recognize the weaker inner vortex suction peak for the CC-EARSM case.

(a) $x/c_r = 0.4$ (b) $x/c_r = 0.6$ (c) $x/c_r = 0.8$ (d) $x/c_r = 0.95$
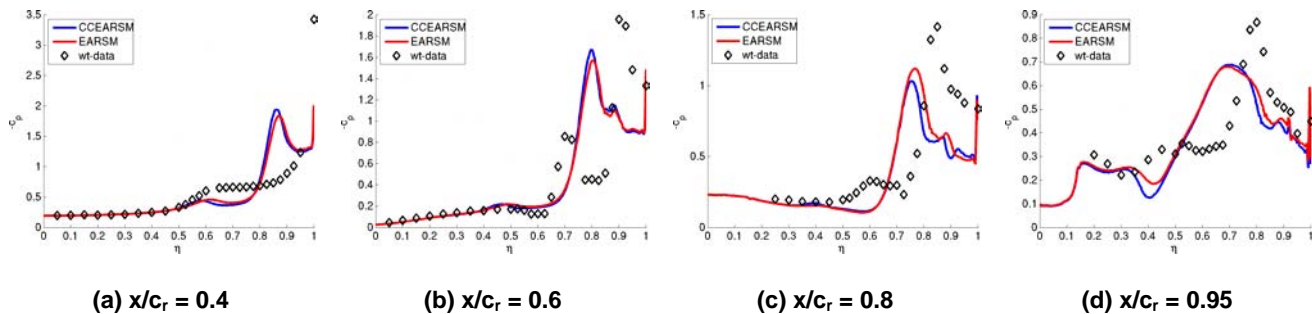
Figure 30-24: C_p Plots for Different x/c_r – Case α = 13.3°, M = 0.4, R_{mac} = 3 x 10^6
– Comparison between CFD Results and Experimental Data [30-3].

30.4.3.2.4   *Effect of Mesh Refinement*

The effect of solution-based mesh refinement on the solution accuracy is presented here only exemplary for the case $R_{mac} = 60 \times 10^6$. As displayed in Figure 30-25, a substantial improvement is found through the first adaptation step. A second adaptation does not result in an equally pronounced improvement over the majority of the wing. Only at $x/c_r = 0.95$ a difference is visible between the second and first adaptation step. This behaviour is found in all other evaluated cases, where a single adaptation step is sufficient.

(a) $x/c_r = 0.4$ (b) $x/c_r = 0.6$ (c) $x/c_r = 0.8$ (d) $x/c_r = 0.95$
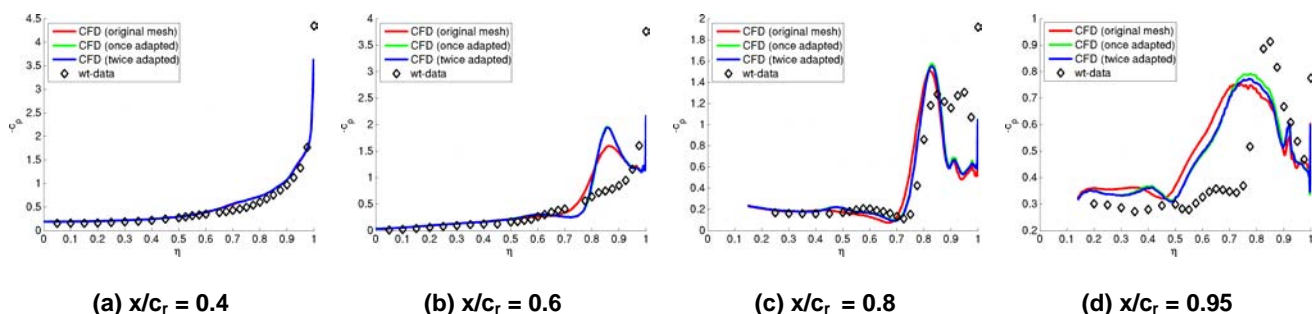
Figure 30-25: C_p Plots for Different x/c_r – Case α = 13.3°, M = 0.4, R_{mac} = 60 x 10^6
– Comparison between CFD Results and Experimental Data [30-17].

From the analysis of the available comparisons, it is obvious that the CFD computations consistently disagree with the experimental datasets in terms of separation onset of the primary leading-edge vortex. In all evaluated cases the separation onset of the primary vortex is predicted too far upstream, resulting in an inboard shift of the primary vortex suction peak in all sections downstream of separation onset. The typical over-prediction of secondary separation strength is also observed.

The inner vortical system is captured in all cases, but the location and strength are predicted wrongly. For the $\alpha = 13.3°$, M = 0.4, $R_{mac} = 2 \times 10^6$ case, the strength of the inner vortex is over-predicted in comparison to the experimental data (Figure 30-22). However, Figure 30-23 (a) to Figure 30-23 (c) and Figure 30-24 (a) to Figure 30-24 (c) present evidence of an under-prediction of inner vortex strength for the low Reynolds number, M = 0.4 cases. A feature that is missed consistently in all computational results is the span-wise extent of a low-pressure region just upstream of the primary leading-edge vortex separation onset, which extends from $\eta \approx 0.65$ to $\eta \approx 0.85$ (Figure 30-23 (a) and Figure 30-24 (a)). This difference is also discernible when comparing the experimental PSP data from Konrath et al. [30-17] in Figure 30-19 to the corresponding computed case in Figure 30-21 (c). None of the computed cases feature such an extended C_p plateau prior to leading-edge separation onset as experienced in the experimental campaigns.

The delaying effect of Reynolds number on the primary vortex separation onset is appreciated in Figure 30-26. A coupling between the primary vortex separation onset and the growth of inner vortex strength, as described by Crippa and Rizzi [30-4] and presented in previous sections, is observed in Figure 30-27. It is also possible to discern the presence of a weak suction peak in Figure 30-27 (d) at $\eta \approx 0.55$ for the inviscid case.

(a) $x/c_r = 0.3$ (b) $x/c_r = 0.5$ (c) $x/c_r = 0.6$ (d) $x/c_r = 0.8$
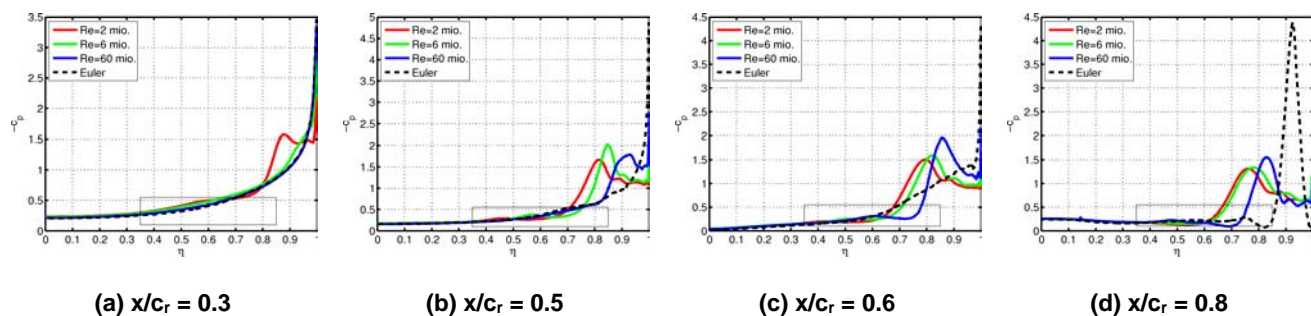
Figure 30-26: C_p Plots for Different x/c_r – Case $\alpha = 13.3°$, M = 0.4 – Comparison of
CFD Results for Different Reynolds Numbers and Inviscid Computation.

(a) $x/c_r = 0.3$ (b) $x/c_r = 0.5$ (c) $x/c_r = 0.6$ (d) $x/c_r = 0.8$
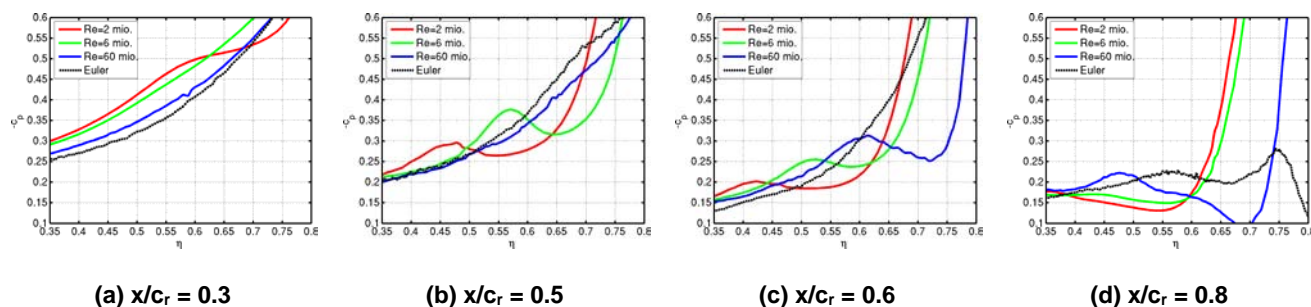
Figure 30-27: C_p Plots for Different x/c_r – Case $\alpha = 13.3°$, M = 0.4 – Comparison of CFD Results for
Different Reynolds Numbers and Inviscid Computation – Magnification on Inner Vortical Region.

30.4.3.2.5   Flow Topology

Despite the differences between the computational and the experimental results, the off-body vortical structures are analyzed to understand the formation of the inner vortex as well as its coupling to the primary leading-edge vortex formation. For this purpose the case at M = 0.2, $R_{mac} = 2 \times 10^6$ is presented hereafter, since it features the strongest inner vortex.

All the skin friction lines from the symmetry plane to the leading-edge secondary attachment line can be traced upstream to a very confined region at the apex, highlighted in Figure 30-28 (a) and presented Figure 30-28 (b). The attachment on the suction side from the symmetry plane at $x/c_r \approx 0.01$ at the half-saddle point C diverts the streamlines originating from the primary attachment line on the pressure side of the wing, see Figure 30-28 (b), where the centre-most skin friction line (St1) is parallel to the symmetry plane upstream of the attachment half-saddle point C. Downstream of the attachment half-saddle point C, St1 remains parallel to the streamlines emanating from C, see for example St2. This surface topology was found on all cases, whereby the location of C moves towards the apex as the Reynolds number increases.

(a) Complete Wing with Magnification Region at Apex

(b) Magnified Region, $x/c_r \approx 0 - 0.01$
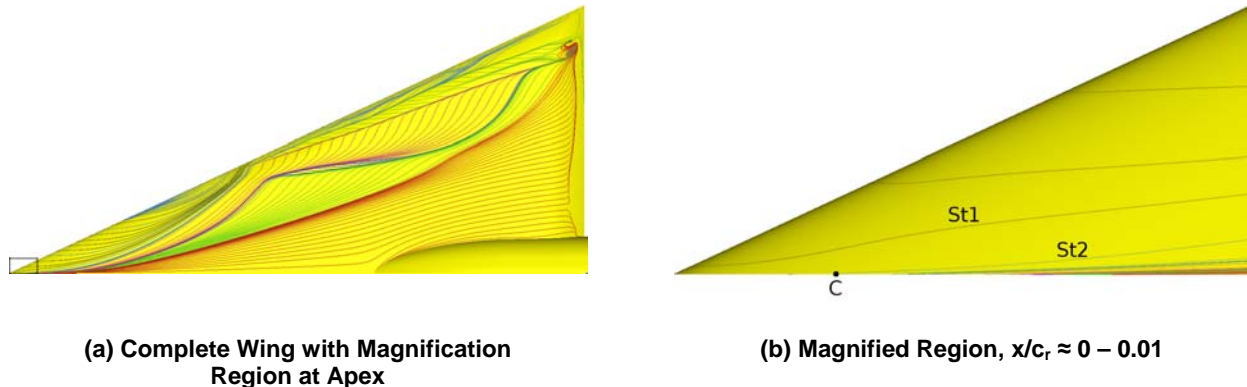
Figure 30-28: M = 0.2, R_{mac} = 2 x 10^6 – Color-Coded Skin Friction Lines on Suction Side.

The isometric view presented in Figure 30-29 (a) gives further insight in the off-body flow topology. From the trajectories at $x/c_r = 0.2$ it is possible to discern a weak vortical motion extending from the symmetry plane to $\eta \approx 0.5$ (Figure 30-29 (b)). The attachment line of this vortex is shown on the symmetry plane by the iso-line of zero wall-normal velocity. This vortical structure extends for this case from $x/c_r \approx 0.1$ to $x/c_r \approx 0.85$, where it merges with the primary leading-edge vortex. For this case, the onset of squeeze-off separation that leads to the formation of the leading-edge primary vortex happens at $x/c_r \approx 0.215$. This is downstream of the formation of the vortical structure near the centreline, the formation of which coincides with the foremost position of the iso-line of zero wall-normal velocity.

(a) Isometric View – Inner Vortex Attachment Line is Shown on the Symmetry Plane

(b) Frontal View of Trajectories Projected on Plane $x/c_r = 0.2$ and Surface Streamlines
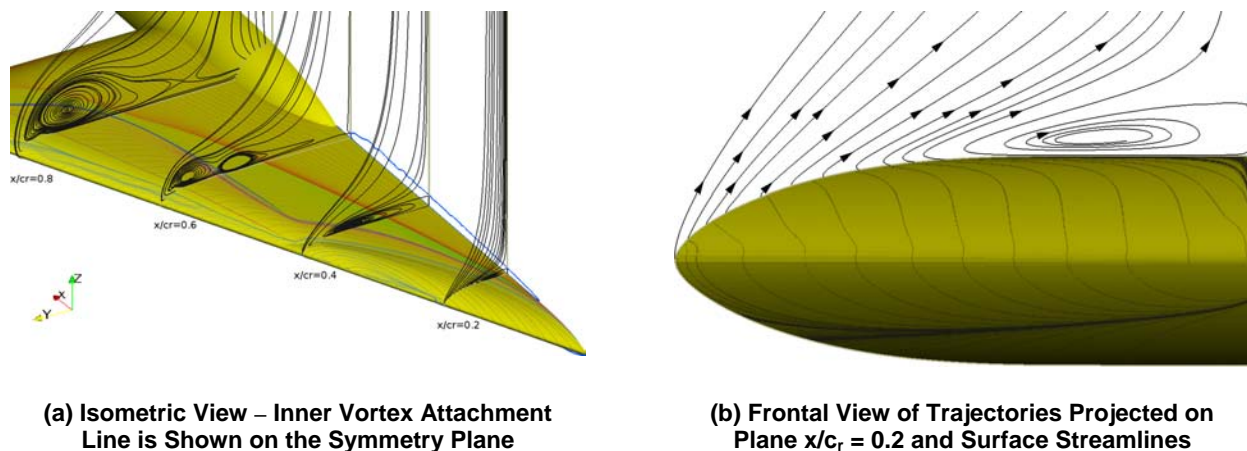
Figure 30-29: M = 0.2, R_{mac} = 2 x 10^6 – Skin Friction Lines and Field Lines of Force Projected on x/c_r Planes.

The presence of a thin vortical structure upstream of primary leading-edge separation onset is documented experimentally by Konrath et al. [30-18]. The PIV data for case $\alpha = 13.3°$, M = 0.4, R_{mac} = 3 x 10^6 at x/c_r = 0.35 is presented in Figure 30-30 (a) next to the computed case at the same conditions Figure 30-30 (b). Compared to the experimental data, the computations show a wider and flatter vortex. The span-wise extent of the computed vortex is approx. 75% of the local semi-span. A direct comparison to the experimental data is in this respect not possible since the PIV field does not reach the symmetry plane, but the vortex core location is visible. In the computations it is too far inboard by as much as 12% of the semi-span. However, the total surface-integrated vorticity is comparable between the computations and experiments. The observed discrepancy in location and extent of the apex vortex is believed to be the reason for the absence in the computations of the low-pressure plateau as presented in Section 30.4.3.2.2. A thicker, further outboard concentrated vortex could explain this C_p plateau.
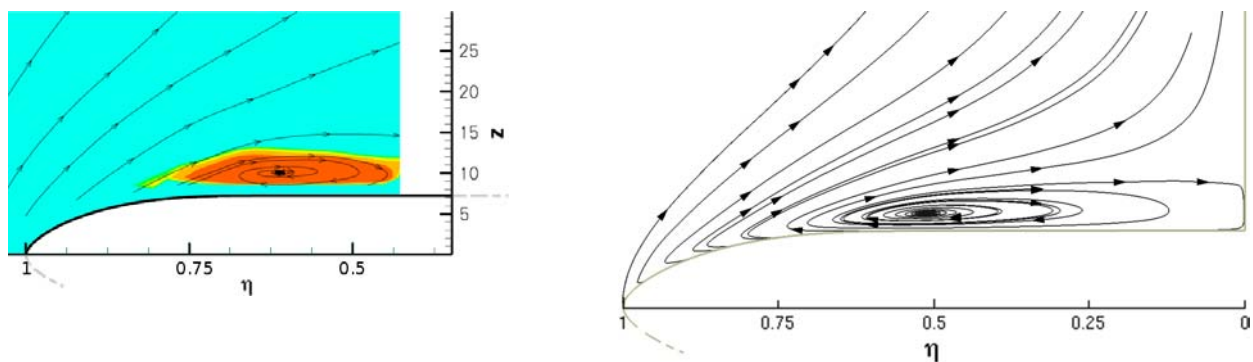
(a) Experimental Time-Averaged Vorticity Magnitude and Field Lines of Force – Data Provided by DLR [30-18]   **(b) Field Lines of Force for the CFD Results.**

Figure 30-30: $\alpha = 13.3°$, M = 0.4, R_{mac} = 3 x 10^6 – Cut Plane at x/c_r = 0.35.

The skin friction lines on the suction side of the wing presented in Figure 30-28 reveal a distinct separation line inboard of the primary vortex attachment line. This separation line extends from $x/c_r \approx 0.48$ to $x/c_r \approx 0.66$ and is difficult to classify without detailed off-body flow analysis. Through vorticity-colored cut-planes and interactive placement of streamlines, this separation line can be attributed to a secondary vortex. The formation of which is due to the very strong inner vortex. At higher incidences, this feature was already found numerically by Crippa and Rizzi [30-4], while at the lower incidences it is only documented experimentally at similar conditions by Furman and Breitsamter [30-11] (see Figure 30-31).
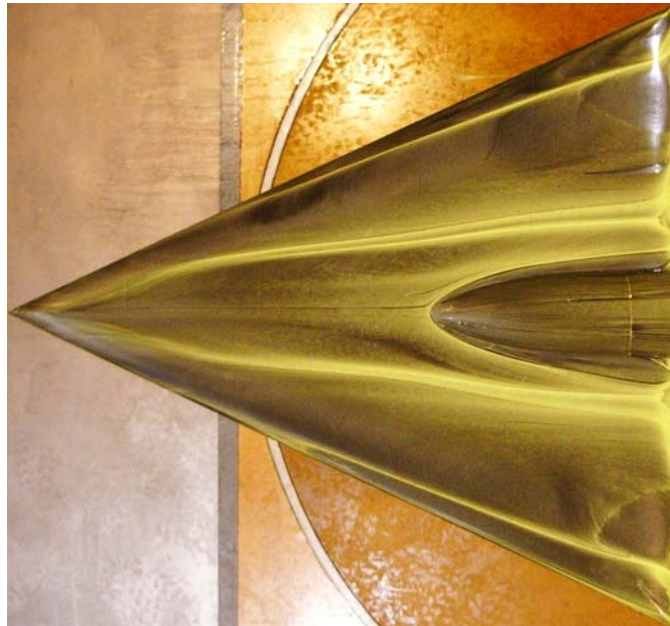
Figure 30-31: Oil-Flow Image of Blunt Leading-Edge Suction Side –
α = 13°, M = 0.14, R_{mac} = 2 x 10^6 (Reproduced with permission [30-11]).

In the experimental campaign, the extension of this inner separation line was coupled to an equally distinct inner attachment line, attributed to the inner vortex, originating in the apex region. The extent of the inner separation and attachment lines was found to span from $x/c_r \approx 0.27$ to the trailing edge and located inboard of $\eta = 0.5$. By further comparison of the oil-flow image data from Furman and Breitsamter [30-11] with the computed skin friction lines, it is apparent that the primary vortex separation onset is predicted computationally only \Delta $x/c_r \approx 0.05$ downstream of the experimental data. This good agreement is probably only due to the difference in freestream Mach number between 0.2 (CFD) and 0.14 (exp.) The higher Mach number for the computational case leads to an upstream shift of the primary vortex separation, and thus to a better agreement with the lower-Mach number experiments.

The inner vortical structure is not captured correctly, both in terms of the onset and of the downstream development. The first discrepancy can possibly be attributed to the assumption of fully turbulent flow in the computations and the second discrepancy to the dissipative effects on vortical structures of the chosen turbulence model.

The problematic of laminar-turbulent transition can be alleviated by computing at higher Reynolds numbers, where transition should take place earlier and thus the fully-turbulent assumption is more accurate. A better correlation to experimental data at higher Reynolds numbers was shown by Crippa and Rizzi [30-4] and presented in the previous sections. This is especially true for higher incidences, whereas at the lowest incidence of 13.3°, the computations still showed major discrepancies. The use of rotational (or curvature) corrections to the basic turbulence model does not show substantial improvements in the vortex strength prediction, which further indicates that the computational methods fail to predict the formation stage of the inner vortex, not its development.

To assess the importance of viscous effects, these can be numerically excluded by solving the Euler equations. With a proper choice of grid resolution and numerical dissipation, leading-edge separation can be achieved

even on the blunt geometry. Numerical simulations on this geometry using the Euler equations were last performed and published in the context of the International Vortex Flow Experiment on Euler Code Validation [30-8] (VFE-1). The main interest was then to study the application of Euler solvers also for the blunt leading-edge geometry, given appropriate corrections.

It is now intriguing to notice that the computations performed within this study, show evidence of the inner vortical structure upstream of primary leading-edge separation as already shown in the Section 30.4.3.2.2. Due to the very late primary leading-edge separation attainable in this case it is easier to analyze the flow structure between the apex and primary separation onset, where the inner vortex develops. The inviscid case shows a similar flow topology as all other viscous cases with a thin vortical structure starting in the apex region, which then concentrates outboard near the primary leading-edge vortex and looses strength (Figure 30-32 and Figure 30-33).

| (a) Top View of Suction Side | (b) Isometric View with Field Lines of Force Projected on x/c_r Planes and Attachment Line on Symmetry Plane |
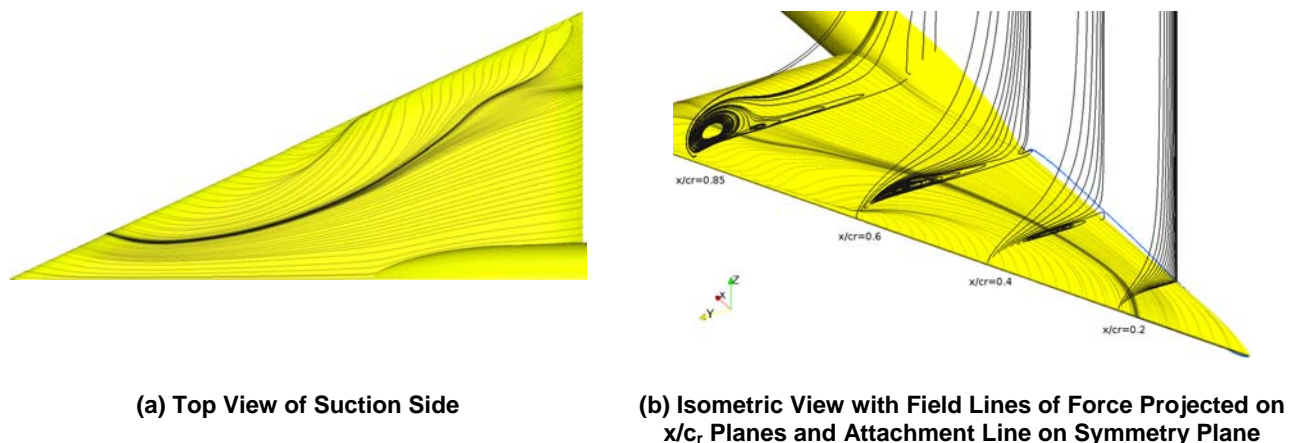
Figure 30-32: Inviscid Case – Skin Friction Lines.

In a plane upstream of the formation of the inner vortex (at $x/c_r \approx 0.1$), the field trajectories reveal fully-attached flow, see Figure 30-33 (a). Between inner vortex formation and primary vortex separation onset (at $x/c_r \approx 0.6$) the inner vortex is comparable in semi-span extent and thickness to the other viscous cases. Since the primary separation is stronger in the inviscid case, the inner vortex is absorbed faster, which results in a different picture at $x/c_r = 0.85$ than for the viscous cases.

| (a) $x/c_r = 0.15$ | (b) $x/c_r = 0.4$ | (c) $x/c_r = 0.85$ |
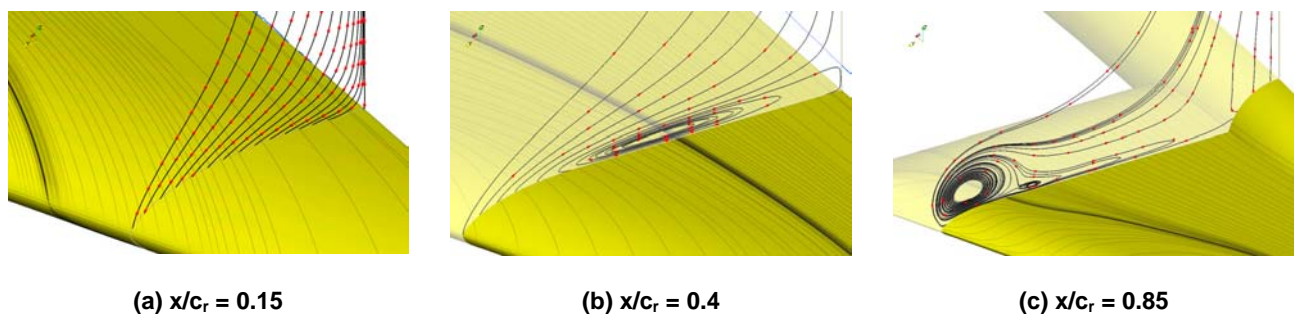
**Figure 30-33: Inviscid Case – Isometric Views of Skin Friction
Lines and Field Lines of Force Projected on x/c_r Planes.**

30.4.3.2.6   Conclusions

Summarizing the results from all cases, the wide, thin inner vortex observed to form very early in the apex region is easily found to attach on the symmetry plane. This may not be true for the experiments, where by comparing with available PIV data it is possible to deduce that the inner vortex is not only located further outboard, but is also stronger and more compact than in the numerical results. If the correct strength and location would be captured correctly by the computations, this could potentially result in the attachment line being shifted from the symmetry plane onto the wing, as shown by the low-speed, low-Reynolds number experiments.

Since the computations under-predict the strength of the inner vortex at its origin, the remaining development can't be matched either. This is consistent with the detailed analysis of the skin friction lines from the computations, where it is not possible to find a distinct convergence of skin friction lines that leads to the inner vortical flow formation. The only squeeze-off type of separations recognizable from the skin friction line analysis are due to the primary and secondary leading-edge vortices. As described by Délery [30-5], this is a common problem also for experimentally obtained oil-flow images at low incidences. The ultimate convergence of streamlines to form a visible separation line can occur far downstream of the saddle point of origin, in the computations an evident convergence does not happen for the inner vortex over the entire wing.

The inviscid case shows the potential to cast light from a different angle on the formation of the inner vortex. It has to be stressed here that due to the nature of inviscid vortical flow computations, it is possible to achieve a fully attached flow solution, or on the contrary a separation very near to the apex, depending on the resolution of the delta-wing surface or several numerical parameters. Given the same reference conditions, an inviscid computation can give very different results. This has been analysed and documented in the past years and the superiority of the RANS methods is proven. But nonetheless, through cautious and deliberate adjustment of the numerical parameters (on a given mesh) it is possible to trigger a pre-determined leading-edge separation position that emulates a desired flow structure. This has been done in this study and the results have to be analysed accordingly with caution, taking account of the restrictions.

In contrast to the general difference in primary (and secondary) leading-edge separation between viscous and inviscid computations, the inner vortical structure is predicted with striking similarity. Due to its mere presence also in the inviscid computations, it is possible to assume that the formation of the inner vortex may be independent of any additional viscous process modelled by the RANS equations. It is possible that for resolving this problem time-accurate computations might be necessary, since it is clear that both inviscid and viscous computations show essentially the same level of discrepancy to the experimental data. Similarly complex multi-vortex systems can be attributed by Gursul et al. [30-13] to the unsteady formation of vortical substructures growing from shear layer instabilities. In this case hybrid turbulence models, such as DES would fail to model the relevant flow physics and LES might be necessary. A detailed analysis of the PIV data by Konrath et al. [30-18],[30-19] reveals indeed also in the presented case the appearance of time-dependent sub-vortices upstream of primary separation onset, that after time-averaging form one vortex as presented Figure 30-30 (a).

30.5   TRANSONIC CASES

Several experimental investigations, e.g., by Elsenaar and Hoeijmakers [30-10], have determined that slender delta wings at transonic freestream conditions can experience a substantial motion of the vortex breakdown location due to a minimal variation of the incidence. The abrupt topological flow rearrangement is due to a non-linear shock-vortex interaction. The computational analysis and understanding of this phenomenon has been a major task within AVT-113/VFE-2, involving the combined efforts of several task group members [30-25]. The following sections will address as much as possible the contribution by KTH to this topic, even though some duplication of data is unavoidable for the sake of clarity.

30.5.1   Introduction

At transonic conditions, the occurrence of shock waves on delta wings at moderate to high angles of attack leads inevitably to shock-vortex interactions. For the majority of conditions, the shock waves are weak enough, or are located appropriately, to substantially have little influence on the vortex development. In these conditions a "classical" vortex breakdown is found at the trailing edge of the delta wing. These situation is found in the common VFE-2 cases of the sharp and blunt configuration at $\alpha = 18.5°$, $M = 0.85$, $R_{mac} = 6 \times 10^6$. Good correlation between computational and experimental results is not only found for this condition, but also for higher angles of attack, up to a certain critical value.

30.5.2   Test Case

The same numerical settings and physical modelling is used for the transonic cases as for other RANS computations. In this section, additionally to the RANS results, some unsteady results are presented, which are the results of a DES computation. For the only DES result presented in this section, 10760 time steps are performed with 100 explicit sub-iterations. The outer time step is set to 1.64×10^{-5}s, which corresponds to the non-dimensional value of 0.0048. Time-averaged DES results presented here are the results of averaging between the outer time steps 9550 and 10465.

The basic condition for the assessment of the transonic effects is $\alpha = 23.0°$, $M = 0.85$, $R_{mac} = 6 \times 10^6$ for the sharp leading edge configuration. At this condition, the experimental datasets show vortex breakdown to occur above the trailing edge, but several CFD investigations consistently predict vortex breakdown to occur at a chordwise position of approx. $x/c_r = 0.67$. The vortex breakdown is induced by one or two strong shock waves placed in front of the sting/wing intersection (at $x/c_r \approx 0.635$). For more details on the results of several task members, please refer to Chapter 29 of this report.

30.5.3   Numerical Grids

The numerical grid used for the investigations by KTH is specifically adapted to the main reference conditions. This is achieved by generating a RANS solution on an initial grid, and then by re-meshing it using TRITET and the RANS solution. This approach differs from the previously presented adaptation approach, as it is possible to achieve an improved, case-specific discretization, without increasing the cell count. In the adaptation approach, it is only possible to add cells to the domain. With the re-meshing approach, the original mesh is used as a back-bone to generate a new, partly skewed and refined mesh. One disadvantage of this approach is that it is not possible to re-mesh the surface grid, as it was generated with ANSYS ICEM CFD and the re-meshing procedure is performed with TRITET. Thus the surface discretization is not changed. The initial grid is presented in Figure 30-34, and the re-meshed volume grid for the main case $\alpha = 23.0°$, $M = 0.85$, $R_{mac} = 6 \times 10^6$ is presented in Figure 30-35.
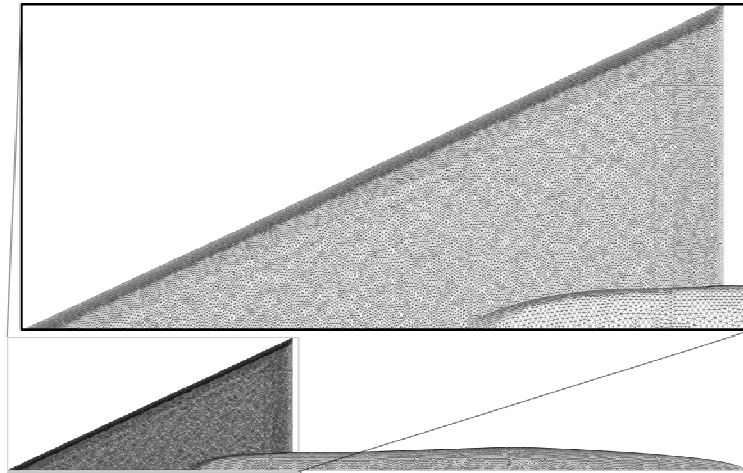
Figure 30-34: Upper Surface of the Initial Numerical Grid of the Sharp Leading Edge Geometry.
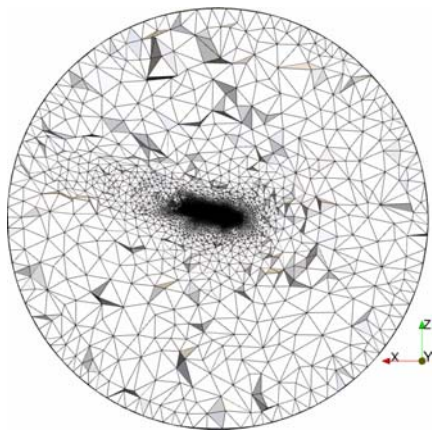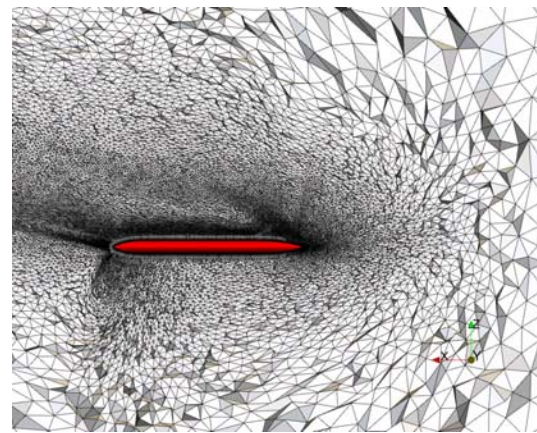
| (a) Global Side View | (b) Side View – $x/c_r \approx$ -0.2 – 1.2 |

Figure 30-35: Re-meshed Grid for Case α = 23.0°, M = 0.85,
R_{mac} = 6 x 10^6 – Mid-Span Cut Through Volume (η = 0.5).

Additionally to the sharp leading edge grids described above, two sting-less grids were produced for the sharp and blunt leading edge geometries. The walls of the sting-less grids are discretised exactly as the sting-fitted grids to ease a relative comparison. For a sideslip incidence analysis, the re-meshed grid is mirrored at the symmetry plane. The grid sizes are summarized in Table 30-8 and Table 30-9.

Table 30-8: Computational Grid Size for the Transonic, Sharp Leading Edge Cases –
Increase in Comparison to the Initial Grid is Given in Brackets; k = 10^3, M = 10^6 in
the Table (Pyramidal elements are included in the total volume nodes counts)

Grid/Case	Total wall surface tri. elements	Prismatic volume cells	Tetrahedral volume cells	Total volume nodes
Initial, with sting	106 k	3.58 M	5.03 M	2.67 M
Remeshed	106 k (-)	3.58 M (-)	7.19 M (**43%**)	3.02 M (**13%**)
Initial, no sting	101 k	4.05 M	3.55 M	2.67 M
Twice adapted	415 k (**311%**)	16.56 M (**309%**)	22.88 M (**545%**)	12.29 M (**360%**)

Table 30-9: Computational Grid Size for the Transonic, Blunt Leading Edge Cases –
Increase in Comparison to the Initial Grid is Given in Brackets; k = 10^3, M = 10^6 in
the Table (Pyramidal elements are included in the total volume nodes counts)

Grid/Case	Total wall surface tri. elements	Prismatic volume cells	Tetrahedral volume cells	Total volume nodes
Initial, with sting	169 k	5.25 M	2.36 M	3.09 M
Once adapted	191 k (**13%**)	6.13 M (**17%**)	3.46 M (**47%**)	3.73 M (**21%**)
Initial, no sting	137 k	4.39 M	2.37 M	2.64 M
Twice adapted	148 k (**8%**)	4.74 M (**8%**)	4.50 M (**90%**)	3.18 M (**20%**)

30.5.4   Comparison of Numerical Grids

Here we present the comparison in terms of relative solution accuracy between the initial grid and the re-meshed grid for the sharp configuration. A field cut-plane through the vortex core reveals in Figure 30-36 the improved resolution of flow details given by the re-meshed grid. Furthermore, the vortex core axial velocity and pressure ratio are presented in Figure 30-37. Here it is possible to recognize that the re-meshed grid, which is based on a RANS solution, shows the same solution accuracy also for another position of the shock/vortex interaction zone. The re-meshed grid was used also for the unsteady analysis.
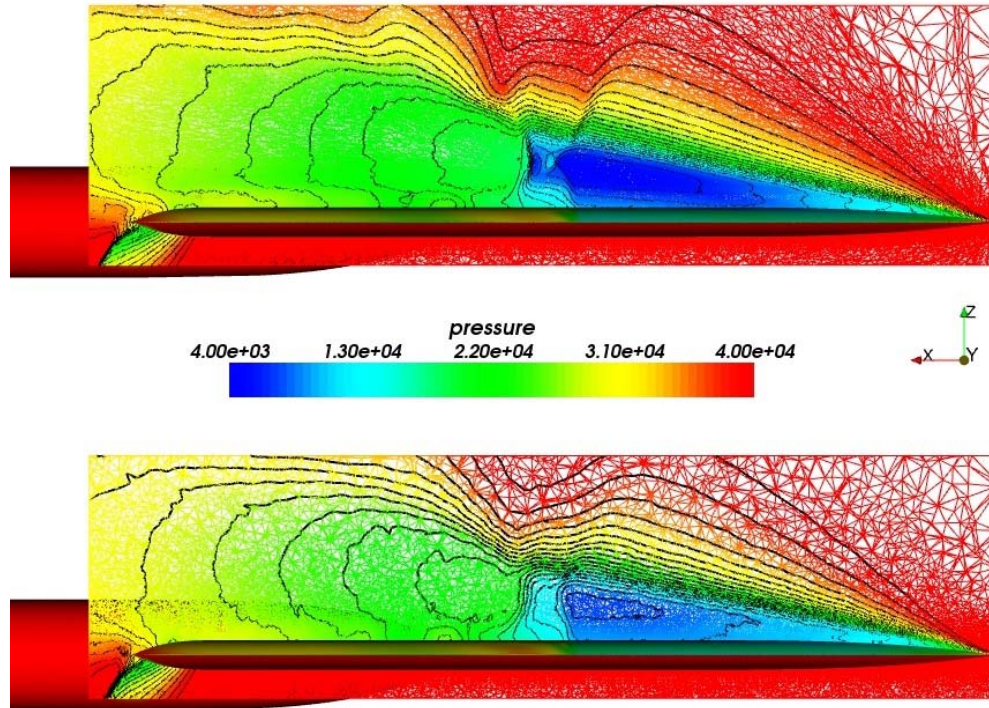
Figure 30-36: Constrained Volume Cut of the RANS Solution for Case α = 23.0°, M = 0.85,
R_{mac} = 6 x 10^6 – Upper Sub-Frame: Re-meshed Grid, Lower Sub-Frame: Initial Grid.
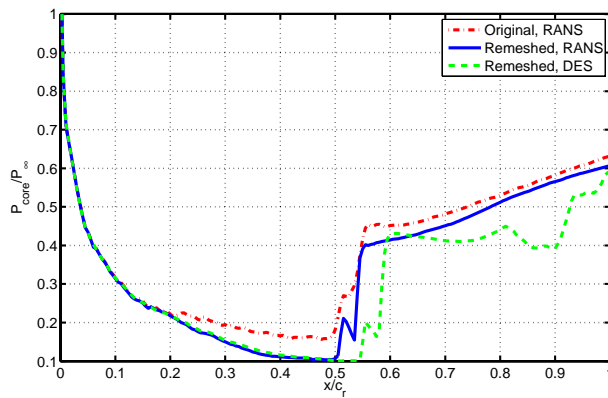
(a) Normalized Static Pressure in the Vortex Core
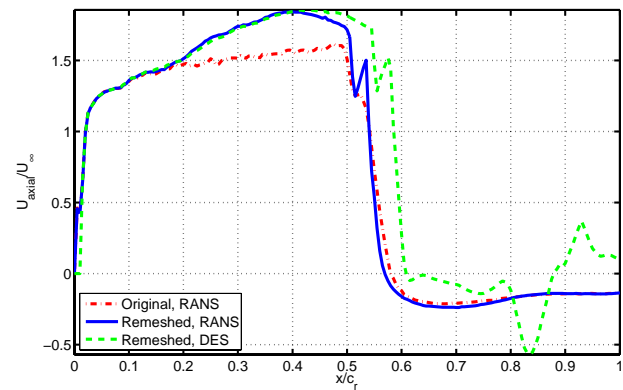
(b) Normalized Vortex Core Axial Velocity

Figure 30-37: Comparison between Re-meshed Grid and Initial Grid for Case α = 23.0°,
M = 0.85, R_{mac} = 6 x 10^6 – "DES" refers to the solution at a single time step.

30.5.5 Results

As previously described, this section is mainly focussed on presenting the contribution of KTH to the common task of understanding the sudden motion of the breakdown location. Possible factors of influence on the

discrepancy between computations and experiments are presented hereafter. A full discussion and analysis of this condition is presented in Chapter 29 of this report.

30.5.5.1   Sting Installation

It has been suggested within this task group and e.g. by Schiavetta et al. [30-26] that the shock upstream of the sting is caused by the installation of the sting onto the upper surface of the delta wing. This is in line with common knowledge, but the result of the following study reveals that the sting/wing intersection is not necessary the only reason for the occurrence of a mid-chord shock wave.

The RANS solutions for four different configurations at exactly the same conditions are presented here; sharp and blunt leading edge configuration, each with a sting-fitted and sting-less variant. The upper surface pressure coefficient plots are presented in Figure 30-38. Clearly in the case of the sharp leading edge geometry (Figure 30-38 (a)), the removal of the sting results only in a small difference in the location of the shock wave. The effect on the primary and secondary vortices is very similar. On the other hand, the removal of the sting on the blunt leading edge configuration (Figure 30-38 (b)) reveals a completely different picture. The shock wave is still present, but located approx. at $x/c_r = 0.72$, i.e. 20% of c_r further downstream than in presence of the sting. Since the shock wave is not only located further downstream, but it also is relatively weak, the vortex core can remain coherent up to approx. at $x/c_r = 0.72$. The conjectured cross-flow shock wave, outboard of the suction peak of the vortex core after $x/c_r = 0.72$ seems to join the trailing edge shock wave. The flow features and thus the surface pressure coefficient show a pattern which is very similar to the transonic, sharp leading edge experiments at this angle of attack. By considering the left-hand side of the Figure 30-38 (a) and Figure 30-38 (b), i.e. the difference being only the leading edge (sharp versus blunt), it is remarkable that the location, strength and effect on the vortex core are nearly identical.

(a) Sharp Leading Edge; Left Sub-Frame: Without Sting, Right Sub-Frame: With Sting

(b) Blunt Leading Edge; Left Sub-Frame: Without Sting, Right Sub-Frame: With Sting
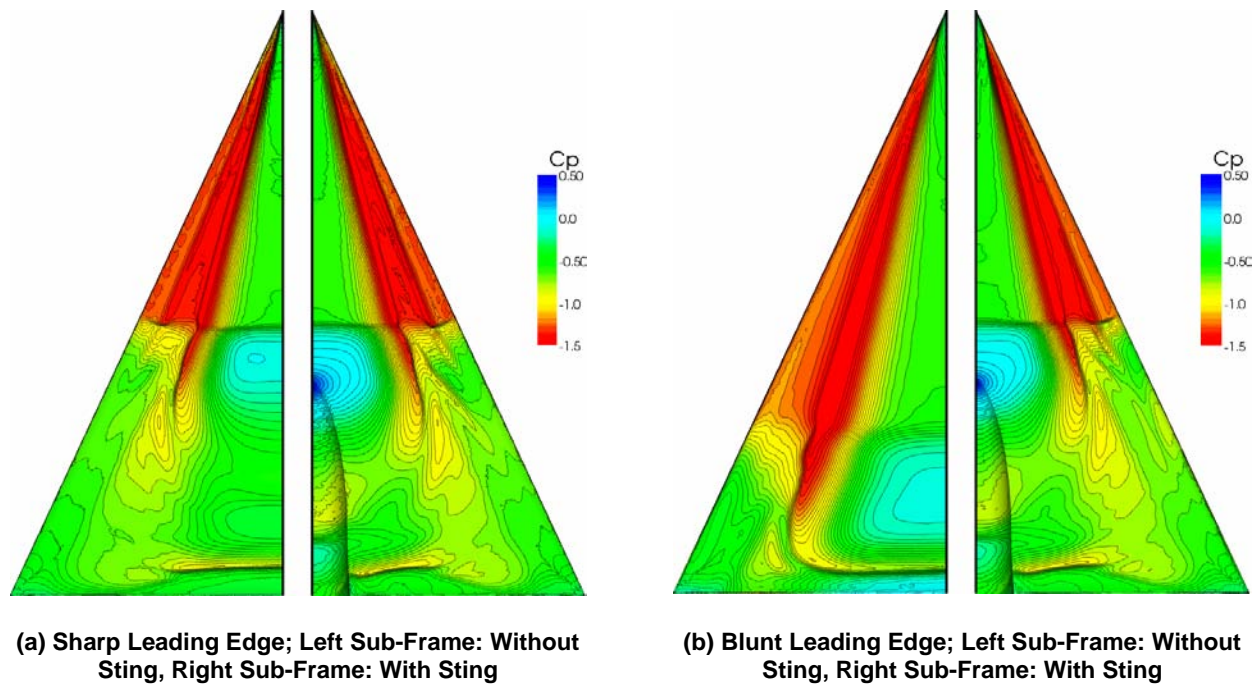
Figure 30-38: Comparison between Sting-Less and Sting-Fitted Solution for the Sharp and Blunt Geometries – RANS Solutions for Case α = 23.0°, M = 0.85, R_{mac} = 6 x 10^6.

To better study the difference between the four cases it is possible to derive from the CFD solution the Rossby number (Ro) by using a section-wise integration method by Robinson et al. [30-24]. The Rossby number can be used as a metric to determine the vortex intensity or strength. The Rossby number is computed as the ratio of the axial and circumferential momentum of a vortex. For further details on how to determine the Rossby number, refer to Robinson et al. [30-24]. A reduction in the Rossby number is equivalent to a weakening of the vortex core. Within a certain range the vortex becomes susceptible to further disturbances; this range is experimentally found by Robinson et al. [30-24] to lie between 0.9 and 1.4. A Rossby number below zero corresponds to flow reversal, but unrecoverable vortex breakdown happens below Ro = 0.9. The Rossby number between the apex and trailing edge of the four cases is presented in Figure 30-39.

(a) Sharp Leading Edge   **(b) Blunt Leading Edge**
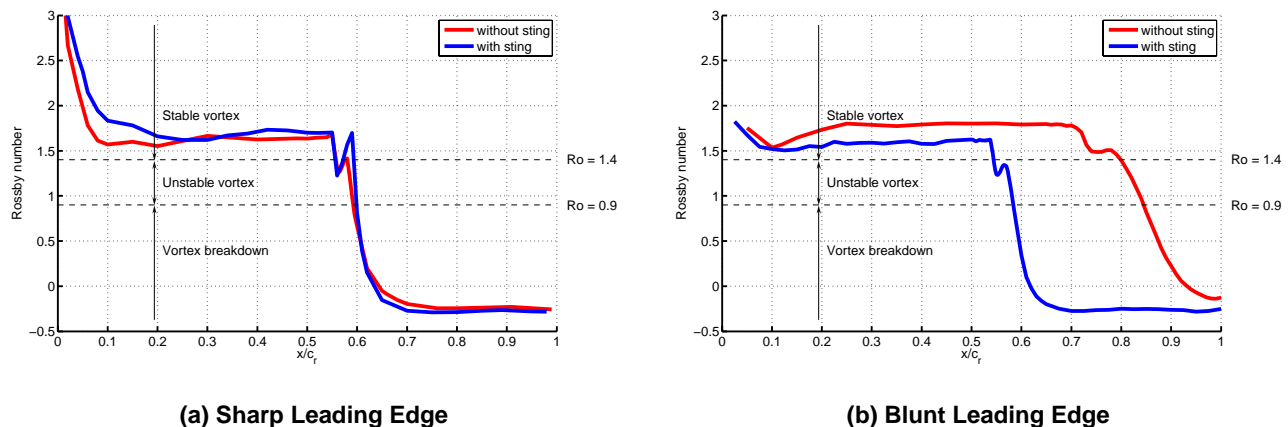
Figure 30-39: Rossby Number Comparison between Sting-Less and Sting-Fitted Solution for the Sharp and Blunt Geometries – RANS Solutions for Case α = 23.0°, M = 0.85, R_{mac} = 6 x 10^6.

In case of the sharp leading edge geometry (Figure 30-39 (a)), two local maxima are found around mid-chord. The location of the two peaks is virtually unchanged by the presence of the sting. The first peak corresponds to the first vortex core disturbance by the impinging shock wave, whereas the second peak corresponds to the start of full vortex breakdown. The Rossby number ahead of the first disturbance is similar, and thus also found to be independent of the presence of the sting.

When considering also the Rossby plot of the blunt leading edge geometries (Figure 30-39 (b)), some similarities to the sharp cases appear, but also some striking differences. Two subsequent peaks of Rossby number are found for both blunt leading edge configurations as for both sharp leading edge configurations. In case of the sting-less, blunt leading edge configuration, the Rossby number of upstream of vortex breakdown is markedly higher for the sting-less configuration. The stronger vortex for the blunt, sting-less configuration is able to withstand an abrupt breakdown at x/c_r = 0.72, and only at x/c_r = 0.8 the Rossby number slowly decrease to result in full flow reversal at x/c_r = 0.93. This smooth pattern in the Rossby number plot is only found for the blunt, sting-less configuration at these conditions, but it is very similar to the case α = 18.5°, M = 0.85, R_{mac} = 6 x 10^6 as shown in Chapter 29 and Schiavetta et al. [30-25].

By making a cross-figure comparison between Figure 30-39 (a) and Figure 30-39 (b) for the sting-fitted sharp and blunt configurations, it is possible to identify a similar location of the first disturbance, i.e. the location of the shock wave is similar. The Rossby number upstream of the shock wave is in the same range, thus the similarly strong shock wave reduces the strength of the vortex core by a similar amount. Indeed the lower peak of these two configurations is at Ro = 1.22 for the sharp leading edge case and Ro = 1.24 for the blunt leading edge case.

It has to be noted that Robinson et al. [30-24] derived the values for vortex core stability by using experimental data for subsonic conditions. Thus the breakdown mechanism follows the classical procedure and the Rossby number plots show a distinct, but gradual decrease at vortex breakdown. The presence of two local maxima in the Rossby plots is not documented by Robinson et al. [30-24] and is believed to be a unique feature of a shock-induced vortex breakdown.

30.5.5.2   Sideslip

A possible problem in an experimental campaign is that of a minimal sideslip angle due to unavoidable tolerances in the model support system. This is a possible explanation for the asymmetric PSP data measured by Konrath et al. [30-19]. Numerically it is thus interesting to check for sideslip angle dependency and assess any possible effect on the flowfield.

The pressure coefficient on the symmetry plane is presented in Figure 30-40 (a) for two symmetric ($\beta = 0°$) computations with different physical models, RANS and DES. It is interesting to note that the RANS solution for the symmetric condition agrees perfectly with the time-averaged DES solution in terms of shock location, but not in strength. Three additional results are presented for RANS computations of a full-body configuration at three different sideslip angles, $\beta = 0.1°$, $0.5°$, $1°$. The shock wave ahead of the sting/wing intersection is found to be very sensitive in respect to sideslip angle. An increase of the sideslip angle by a tenth degree results in an upstream movement of the shock wave of approx. $x/c_r = 8\%$. An additional increase to $\beta = 1°$ changes only little in the location of the shock wave. But at this sideslip angle, a new shock wave is present just ahead of the sting/wing intersection. The critical pressure coefficient for the given free-stream conditions is -0.302. The minimum C_p value for the $\beta = 1°$ case is located at $x/c_r \approx 0.6$ and reads -0.466. The upper surface pressure coefficient shown in Figure 30-40 (b) reveals the location and attitude of the two shock waves. With the clear presence of a sting-induced shock wave at $x/c_r \approx 0.6$, the further upstream located shock wave is conjectured not to be caused by the sting, but by a strong flow acceleration in the central part of the wing which is due to the starboard leading edge primary vortex. At a sideslip angle of $0°$, these two shock-inducing phenomena combine to induce only one shock wave located in between.
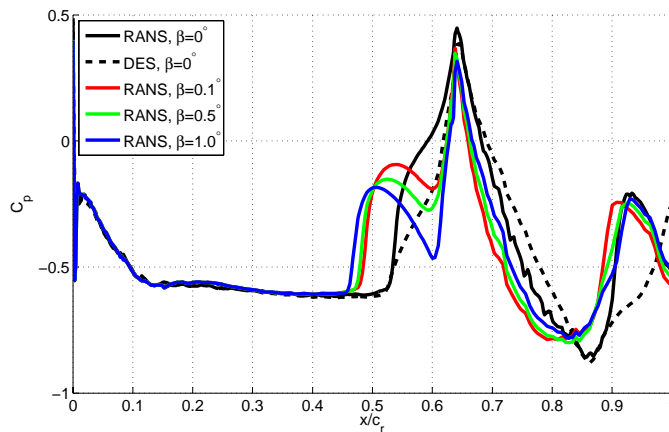
(a) C_p on the Delta Wing and Sting at the Intersection with the Symmetry Plane – "DES" refers to the time-averaged solution
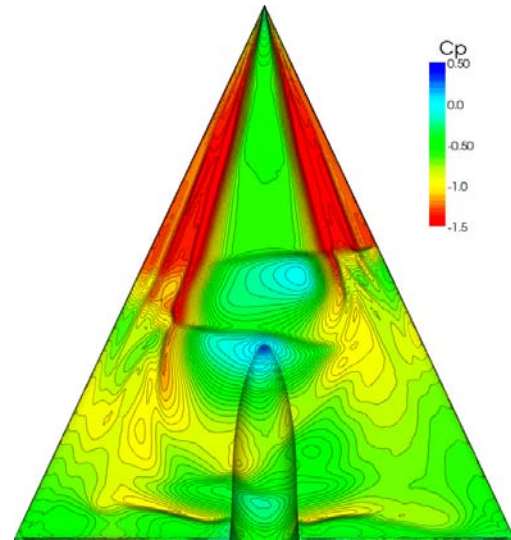
(b) C_p on Suction Side of Delta Wing – RANS Solution of Full-Body, Sharp Leading Edge Geometry at β = 1°

Figure 30-40: Effect of Sideslip Angle on Solution – CFD Solutions for Case α = 23.0°, M = 0.85, R_{mac} = 6 x 10^6 at Various Sideslip Angles (β).

The computations by Glasgow presented in Chapter 29 reveal for the symmetric configuration at the same free-stream condition the presence of two shock waves upstream of the sting/wing intersection. In light of this sideslip analysis it is here suggested that this might be due to the specific turbulence model used for the Glasgow analysis, i.e. the Wilcox k-ω with $P_ω$ enhancer model [30-1]. The modification to the Wilcox k-ω model is specifically targeted to decrease the dissipative nature of the original Wilcox k-ω model. This leads to stronger vortices. If the conjecture described above is correct, then an increase in vortex strength would lead to an increase in mass flow in the central wing section. Thus causing, as in the case of a sideslip angle of 1°, a split-up of the single shock wave seen in this study at β = 0° into two separate.

30.6   REFERENCES

[30-1]   Brandsma, J., Kok, J.C., Dol, H.S. and Elsenaar, A.: *Leading Edge Vortex Flow Computations and Comparison with DNW-HST Wind Tunnel Data*, Proceedings of the RTO/AVT Symposium on "Vortex Flows and High Angle of Attack", Loen, Norway, May 2001.

[30-2]   Chiba, K., Obayashi, S. and Nakahashi, K.: *CFD Visualization of Second Primary Vortex Structure on a 65-degree Delta Wing*, Proceedings of the 42nd AIAA Aerospace Sciences Meeting and Exhibit, Reno, NV, January 2004, AIAA-2004-1231.

[30-3]   Chu, J. and Luckring, J.M.: *Experimental Surface Pressure Data Obtained on 65° Delta Wing Across Reynolds Number and Mach Number Ranges*, Technical Report, NASA TM 4645, NASA Langley Research Center, Hampton, Virginia, 1996.

[30-4] Crippa, S. and Rizzi, A.: *Numerical Investigation of Reynolds Number Effects on a Blunt Leading-Edge Delta Wing*, Proceedings of the 24th Applied Aerodynamics Conference, San Francisco, CA, June 2006, AIAA-2006-3001.

[30-5] Délery, J.M.: *Physics of Vortical Flows*, Journal of Aircraft, 29(5):856-876, September – October 1992.

[30-6] Eberle, A., Rizzi, A. and Hirschel, E.H.: *Numerical Solutions of the Euler Equations for Steady Flow Problems*, Notes on Numerical Fluid Mechanics, Volume 34, Chapter 11, pp. 374-375, Vieweg, 1992.

[30-7] Eliasson, P.: *Edge, a Navier-Stokes Solver for Unstructured Grids*, Proceedings to Finite Volumes for Complex Applications III, pp. 527-534, 2002.

[30-8] Elsenaar, A. and Eriksson, G. editors: *International Vortex Flow Experiment on Euler Code Validation*, FFA, Flygtekniska Försökanstalten, October 1986.

[30-9] Elsenaar, A., Hjemberg, L., Bütefisch, K.-A. and Bannink, W.J.: *The International Vortex Flow Experiment*, Validation of Computational Fluid Dynamics – AGARD-CP-437, Volume 1, pp. 9.1-9.23, AGARD, 1988.

[30-10] Elsenaar, A. and Hoeijmakers, H.W.M.: *An Experimental Study of the Flow Over a Sharp-Edged Delta Wing at Subsonic and Transonic Speeds*, AGARD Conference Proceedings Vortex Flow Aerodynamics, pp. 15.1-15.19, AGARD-CP-494, July 1991.

[30-11] Furman, A. and Breitsamter, C.: *Investigation of Flow Phenomena on Generic Delta Wing*, Proceedings of the 25th International Congress of the Aeronautical Sciences, Hamburg, Germany, 2006, ICAS-2006-3.2.1.

[30-12] Gordnier, R.E.: *Computational Study of a Turbulent Delta-Wing Flowfield Using Two-Equation Turbulence Models*, Proceedings of the 27th AIAA Fluid Dynamics Conference, New Orleans, LA, June 1996.

[30-13] Gursul, I., Gordnier, R.E. and Visbal, M.R.: *Unsteady Aerodynamics of Non-Slender Delta Wings*, Progress in Aerospace Sciences, 41(7):515-557, October 2005.

[30-14] Hellsten, A.: *New Two-Equation Turbulence Model for Aerodynamics Applications*, PhD Thesis, Department of Mechanical Engineering, Helsinki University of Technology (Espoo, Finland), 2004.

[30-15] Hummel, D.: *The Second International Vortex Flow Experiment (VFE-2) – Objectives and First Results*, Proceedings of the 2nd International Symposium on "Integrating CFD and Experiments in Aerodynamics", pp. 1-12, Cranfield University (Shrivenham), UK, 2005.

[30-16] Hummel, D. and Redeker, G.: *A New Vortex Flow Experiment for Computer Code Validation*, Proceedings of the RTO/AVT Symposium on "Vortex Flow and High Angle of Attack Aerodynamics", Loen, Norway, May 2001, 2003.

[30-17] Konrath, R., Klein, C., Engler, R.H. and Otter, D.: *Analysis of PSP Results Obtained for the VFE-2 65° Delta Wing Configuration at Sub- and Transonic Speeds*, 44th AIAA Aerospace Sciences Meeting and Exhibit, 2006.

[30-18] Konrath, R., Schröder, A. and Kompenhans, J.: *Analysis of PIV Results Obtained for the VFE-2 65 Degree Delta Wing Configuration at Sub- and Transonic Speeds*, Proceedings of the 24th Applied Aerodynamics Conference, San Francisco, CA, 2006, AIAA-2006-3003.

[30-19] Konrath, R., Klein, C. and Schröder, A.: *PSP and PIV Investigations on the VFE-2 Configuration in Sub- and Transonic Flow*, Proceedings of the 46th AIAA Aerospace Sciences Meeting and Exhibit, Reno, NV, 2008, AIAA-2008-0379.

[30-20] Lamar, J.E., Cronin, C.K. and Scott, L.E.: *A Review of Steps Taken to Create an International Virtual Laboratory at NASA Langley for Aerodynamic Prediction and Comparison*, Progress in Aerospace Sciences, Volume 40, pp. 163-172, Elsevier Ltd., UK, 2004.

[30-21] Le Moigne, Y.: *Adaptive Mesh Refinement and Simulations of Unsteady Delta-Wing Aerodynamics*, Proceedings of the European Congress on "Computational Methods in Applied Sciences and Engineering", ECCOMAS, 2004.

[30-22] Luckring, J.M.: *Reynolds Number and Leading-Edge Bluntness Effects on a 65° Delta Wing*, Proceedings of the 40th AIAA Aerospace Sciences Meeting and Exhibit. Reno (NV), 2002.

[30-23] Luckring, J.M.: *Reynolds Number, Compressibility and Leading-Edge Bluntness Effects on Delta-Wing Aerodynamics*, Proceedings of the 24th International Congress of Aeronautical Sciences, 2004.

[30-24] Robinson, B.A., Barnett, R.M. and Agrawal, S.: *Simple Numerical Criterion for Vortex Breakdown*, AIAA Journal, Volume 32, No. 1, January 1994, Also presented as Paper 92-0057 at the AIAA 30th Aerospace and Sciences Exhibit.

[30-25] Schiavetta, L.A., Boelens, O.J., Crippa, S., Cummings, R.M., Fritz, W. and Badcock, K.J.: *Shock Effects on Delta Wing Vortex Breakdown*, Proceedings of the 46th AIAA Aerospace Sciences Meeting and Exhibit, Reno, NV, 2008, AIAA-2008-0395.

[30-26] Schiavetta, L.A., Boelens, O.J., Fritz, W. and Cummings, R.M.: *Sting Effects on Transonic Delta Wing Experiments*, Proceedings of the 3rd International Symposium on "Integrating CFD and Experiments in Aerodynamics", U.S. Air Force Academy, CO, USA.

[30-27] Spalart, P., Jou, W.H., Strelets, M. and Allmaras, S.R.: *Comments on the Feasibility of LES for Wings and on a Hybrid RANS/LES Approach*, Proceedings of the 1st AFSOR International Conference on "DNS/LES, Advances in DNS/LES", Greyden Press, 1998.

[30-28] Tysell, L.: *An Advancing Front Grid Generation System for 3D Unstructured Grids*, Proceedings of the 19th Congress of the International Council of the Aeronautical Sciences, ICAS-94-2.5.1, pp. 1552-1564, 1994.

[30-29] Tysell, L., Berglind, T. and Eneroth, P.: *Adaptive Grid Generation for 3D Unstructured Grids*, Proceedings of the 6th International Conference on "Numerical Grid Generation in Computational Field Simulation", pp. 391-400, 1998.

[30-30] Wallin, S. and Johansson, A.V.: *An Explicit and Algebraic Reynolds Stress Model for Incompressible and Compressible Turbulent Flows*, Journal of Fluid Mechanics, 403:89-132, 2000.

Chapter 31 – NUMERICAL SOLUTIONS FOR THE VFE-2 CONFIGURATION ON UNSTRUCTURED GRIDS AT DLR, GERMANY

by

Andreas Schütte and Heinrich Lüdeke

31.1   INTRODUCTION

The flow field around delta wing configurations with sharp leading edges is well known from former experimental and theoretical studies as well as the treatment of flow simulations using high fidelity numerical methods. Within the last years several experimental and numerical investigations are published focusing on the flow topology, Re- and Mach number effects as well as on transition behavior of the vortex dominated flow field around sharp leading edges. This is described in detail within publications of the US/European Vortex Flow Experiment [31-1]-[31-5]. The flow around a sharp leading edge delta wing is characterized by primary vortices initially separating directly at the apex even at small angles of attack. The shear layer rolls up to a pair of primary vortices over the wing. The secondary vortices occur due to the separation of the flow of the primary vortex interacting with the boundary layer on the wing surface, as depicted in Figure 31-1. The strength and position at the primary and secondary vortices are mainly influenced by the inflow velocity, angle of attack and the sweep angle of the delta wing [31-6] [31-7]. The vortex flow under turbulent flow conditions is fairly independent of the Reynolds number for sharp leading edge delta wings whereas under laminar flow conditions the Reynolds number affects the position and strength of the vortices as well as the vortex topology over the wing [31-8].
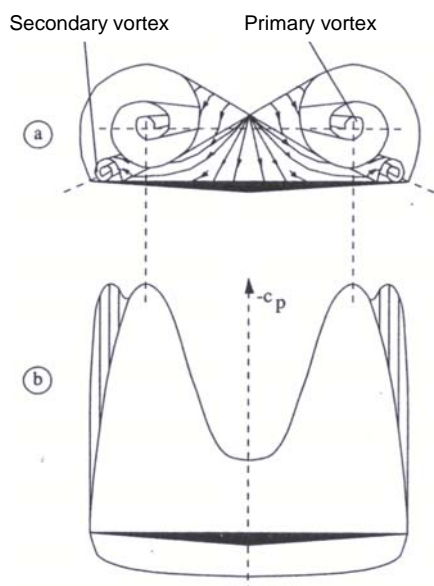
**Figure 31-1: Schematic View of the Flow over a Sharp Edged Delta Wing –
(a) Vortex Formation; (b) Pressure Distribution in a Cross Section [31-6].**

Recent and future fighter configurations are mainly delta wing configurations with rounded leading edges. The flow around delta wing configurations with rounded leading edges is still not entirely understood. Therefore a second Vortex Flow Experiment – VFE-2 with the RTO/AVT-113 was established, focusing on the flow around delta wing configurations with rounded leading edges [31-9]. Several experimental data sets were provided and generated within the RTO/AVT-113 task group regarding on a 65° swept delta wing with sharp and different rounded leading edges. The experimental data base is used to expand the knowledge about the flow topology and flow physics and to validate computational codes. This paper is focusing on the flow topology around the VFE-2 delta wing with medium rounded leading edges at different Reynolds numbers and angles of attack.

The motivation for using an unstructured grid approach is intended by the simulation of complex realistic fighter configurations especially by taking all control devices and storages into account. The presented investigation is intended as a test to predict the correct physics of the highly complex flow topology of delta wings with rounded leading edge by an unstructured code.

31.2   NUMERICAL APPROACH

31.2.1   CFD Solver TAU

The flowfield is predicted with the TAU-Code, a CFD tool developed by the DLR Institute of Aerodynamics and Flow Technology [31-10][31-12]. The TAU-Code solves the compressible, three-dimensional, time-accurate Reynolds-Averaged Navier-Stokes equations by using a finite volume formulation. The code is based on a hybrid unstructured-grid approach making use of the advantages of prismatic grids for the resolution of viscous shear layers near walls, and the flexibility in grid generation offered by unstructured grids. The grids used for simulations in this paper were created with the hybrid grid generator Centaur, developed by Centaur Soft [31-13]. A dual-grid approach is used in order to get a second-order cell-vertex based scheme. The TAU-Code consists of several different modules, among which are:

- The Preprocessor module, which uses the information of the initial grid to create a dual-grid and the coarser grids for multi-grid.

- The Solver module, which performs the flow calculations on the dual-grid.

- The Adaptation module, which refines and de-refines the grid in order to capture flow phenomena like vortex structures and shear layers near viscous boundaries, among others.

The Solver module contains several upwind schemes, as well as central schemes with artificial dissipation, which are used for the spatial discretization. For simulations of turbulent flows, various modifications of the one-equation Spalart-Allmaras and several two-equation turbulence models are implemented. For steady computations either an explicit Runge-Kutta type time-stepping or an implicit LU-SSOR-scheme are used in combination with the multi-grid technique to advance the solution in time. For time-accurate simulations an implicit dual-time stepping approach is used.

Several one- and two equation turbulence models are available for steady simulations. In the presented RANS-simulations the original one-equation Spalart-Allmaras (SA) [31-14] model and the two equations Wilcox k-ω model [31-15] are used which are briefly described in the following. The SA model defines the eddy viscosity field as:

$$\mu_t = \rho \nu_t = \rho \tilde{\nu} f_{v1}$$

with ρ as the density, ν_t as the turbulent kinematic viscosity and f_{v1} as a near wall-function that guarantees linearity of the turbulent transport quantity in the vicinity of walls. The distribution of the transport quantity $\tilde{\nu}$ is determined by the solution of a transport equation:

$$\frac{D(\rho\tilde{\nu})}{Dt} = \underbrace{c_{b1}\tilde{S}\rho\tilde{\nu}}_{P} - \underbrace{C_{w1}f_w\rho\left(\frac{\tilde{\nu}}{d}\right)^2}_{D} + \underbrace{\frac{\rho}{\sigma}\left\{\nabla[(\nu+\tilde{\nu})\nabla\tilde{\nu}] + c_{b2}(\nabla\tilde{\nu})^2\right\}}_{DF}$$

with d as the wall distance. This transport equation contains phenomenological models of production P, destruction D and diffusion DF which are described in the literature [31-14]. In the production term P a modified vorticity $\tilde{S}$ appears that maintains the linear behavior of the model near walls. The different model constants are determined by experimental data and analytical solutions and are well known for turbulent flow fields [31-14].

The k-ω model equations [31-15], including the cross-diffusion term C_D, are given by:

$$\frac{\partial\rho k}{\partial t} + \frac{\partial(\rho kV_j)}{\partial x_j} = P_k - \beta^*\rho\omega k + \frac{\partial}{\partial x_j}\left((\mu+\sigma_\omega\mu_t)\frac{\partial k}{\partial x_j}\right)$$

$$\frac{\partial\rho\omega}{\partial t} + \frac{\partial(\rho\omega V_j)}{\partial x_j} = P_k - \beta^*\rho\omega^2 + \frac{\partial}{\partial x_j}\left((\mu+\sigma_\omega\mu_t)\frac{\partial\omega}{\partial x_j}\right) + C_D$$

with ρ the density, $\tilde{V}$ the velocity vector, μ the molecular-viscosity coefficient, k the turbulent kinetic energy, ω the specific turbulent dissipation and $\mu_t = \rho k/\omega$ the eddy-viscosity coefficient. The production and cross-diffusion terms are given by Wilcox as well as the six closure coefficients: α_ω, β^*, β, σ_k, σ_ω and σ_d, also provided by Wilcox [31-15].

31.3   EXPERIMENTAL DATA

For the validation of the numerical simulation software, various wind-tunnel data sets are provided by NASA within the RTO/AVT-113 task group [31-16]. Additionally wind tunnel experiments were carried out with a 2/3 scaled wind tunnel model loaned by NASA to DLR [31-17]. These wind tunnel experiments consist of pressure distribution measurements using PSI pressure taps and PSP-"Pressure Sensitive Paint" [31-18] as well as measurements of the flow field via PIV – "Particle Image Velocimetry" [31-19]. Figure 31-2 shows the NASA wind tunnel model in the NTF wind tunnel at NASA Langley.
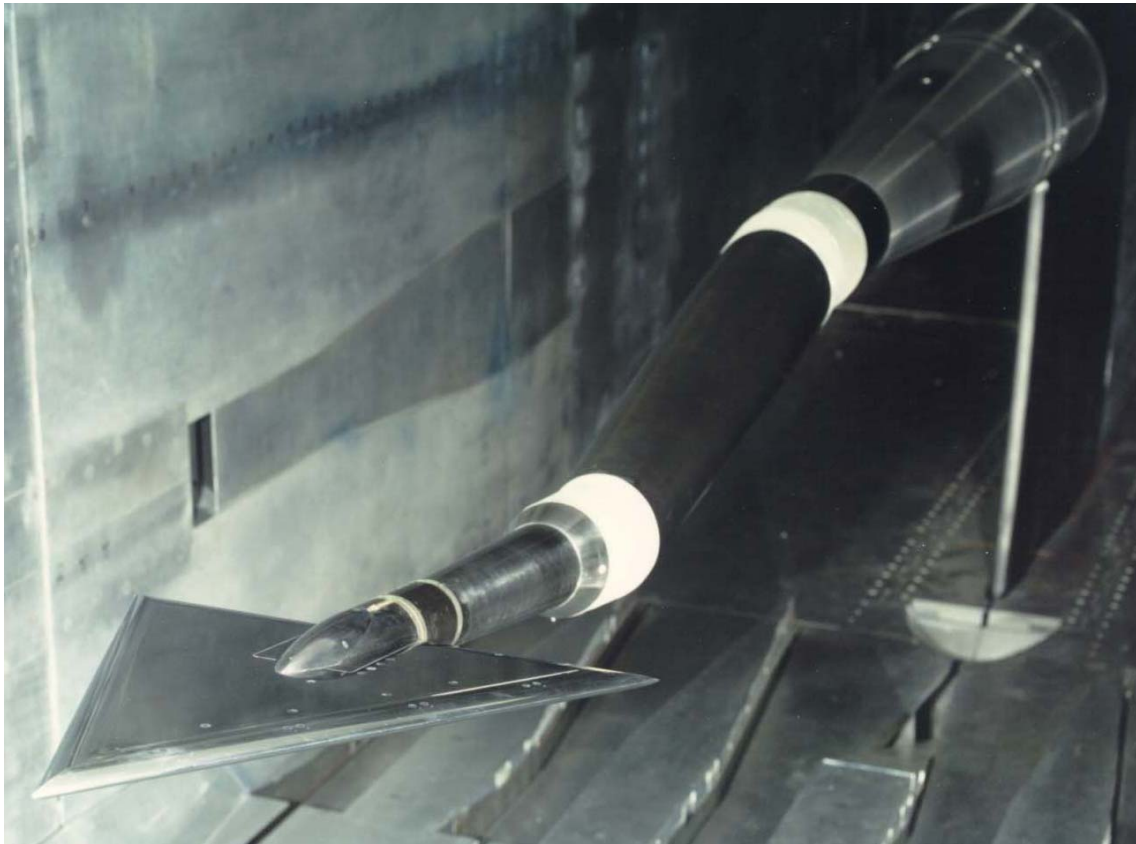
Figure 31-2: NASA 65° Delta Wing in the NTF-Wind Tunnel at NASA-Langley
Research Center. Source: J.M. Luckring, NASA Langley [31-16].

31.3.1   Flow Topology

For the validation of the RANS solver TAU, the results of the numerical simulations are compared against data collected from various experimental simulations. Figure 31-3 shows the pressure distribution over the delta wing with medium rounded leading edge radius. The measurement is done by using PSP at a Mach number of M = 0.4, an angle of attack of α = 13.3° and a Reynolds number of Re = 3 x 10^6. Two suction traces can be observed on the upper side of the delta wing. A weaker inner suction trace starting from the apex and a stronger outer suction trace initiates at approximately 50% chord length.
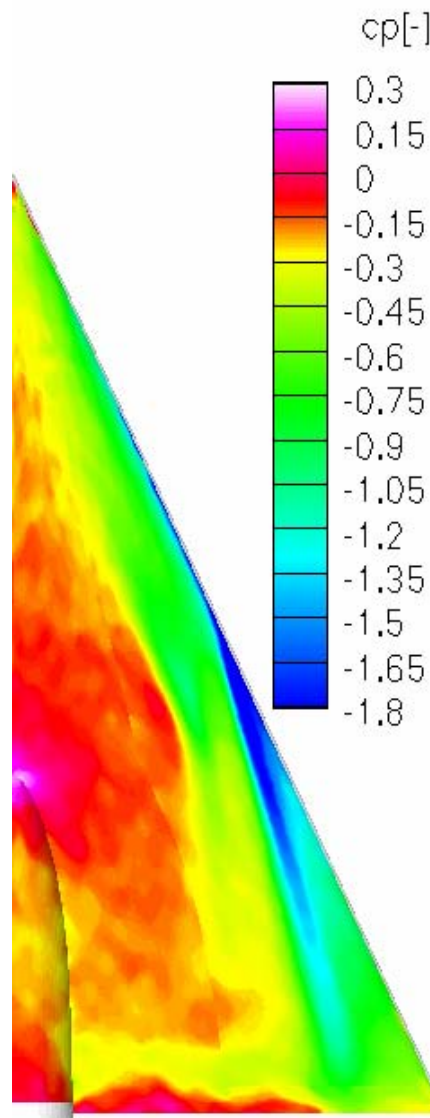
**Figure 31-3: Pressure Distribution on the Upper Side of the Wing Using
PSP-"Pressure Sensitive Paint" – M = 0.4, Re = 3 x 10^6, α = 13.3° [31-17].**

Figure 31-4 shows a PIV result under the same flow conditions described before. The measurement setup is shown in Figure 31-5. The PIV result in Figure 31-4 shows two vortices possessing the same rotational direction. The topology can be described as follows. Because of the leading edge geometry with rounded leading edges the wing tip can be assumed as a blunt body. The flow around the leading edge is initially attached. Further downstream the flow separates and the inner vortex is generated. Regarding the ratio between leading edge radius and wing span the leading edge is getting sharper relative to the downstream position. This leads eventually to a separation of the shear layer further downstream at the leading edge and the outer vortex is generated.
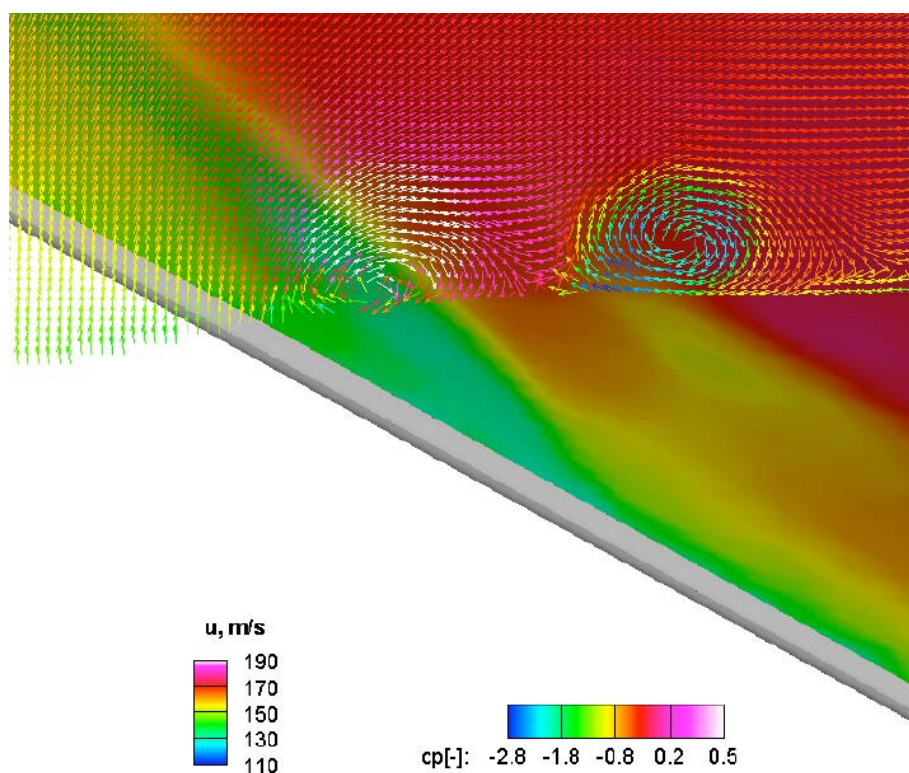
Figure 31-4: Pressure Distribution on the Upper Surface and PIV Measurement at x/c$_{ref}$ = 0.6 – M = 0.4, Re = 3 x 10^6, α = 13.3° [31-19].
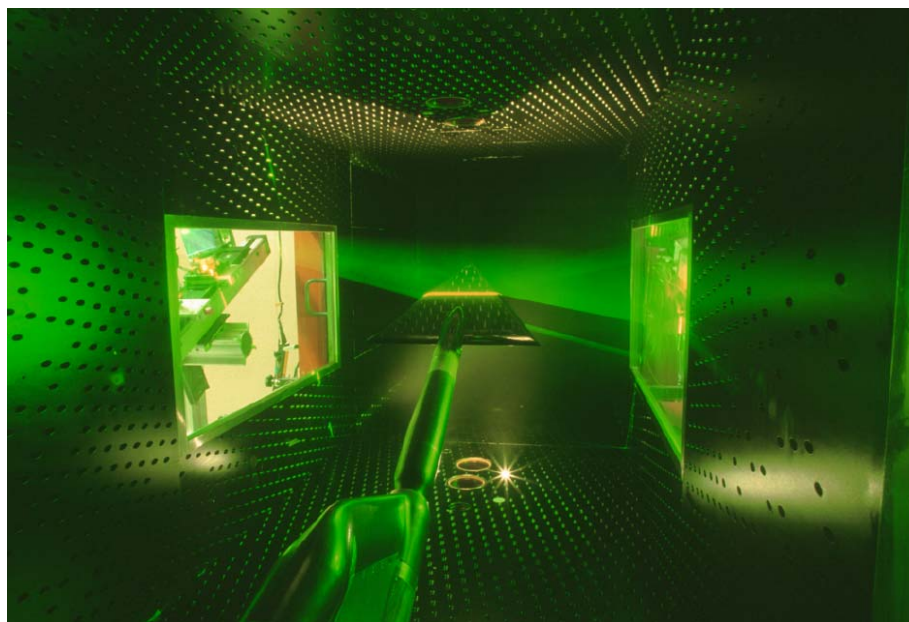
Figure 31-5: Model Setup for PIV Measurements in the TWG-"Transonic Wind Tunnel Göttingen". The laser light sheet can be observed at approximately 50% chord length [31-19].

31.4 NUMERICAL RESULTS

The capability to predict the flow topology with the TAU-Code shall be shown by the following numerical results. Furthermore Reynolds number and Mach number effects on the flow topology around the delta wing will be analyzed and discussed.

31.4.1 Computational Grid

In Figure 31-6 the grid topology of the computational model is depicted. For the numerical simulation a half configuration is used. The sting is modeled up to 30% chord length behind the trailing edge. Figure 31-7 shows a slice through the computational mesh at 90% chord length. For all calculations a pre-refined grid is used for which the area where the vortices occur is refined from the apex up to 10% chord length behind the trailing edge of the wing. The boundary layer is resolved by twenty prismatic layers which is sufficient since the flow is vortex dominated in the region of interest and an extensive resolution of the outer boundary layer is not necessary [31-20].
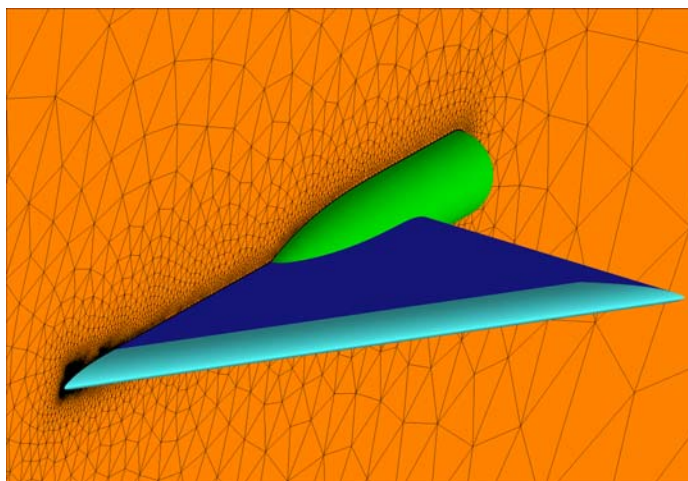
Figure 31-6: Numerical Model Topology and Computational Grid of the Symmetry Plane.
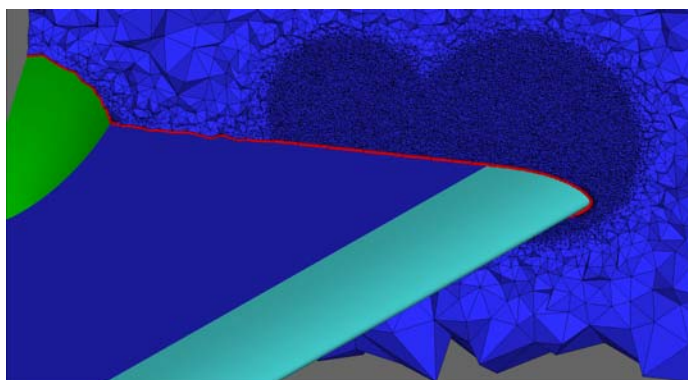
Figure 31-7: Slice through the Computational Grid Close to the Trailing Edge Regarding the Prismatic Layer in Red and the Pre-Refined Grid Area at the Outer Wing in Dark Blue.

For the RANS calculations the Wilcox k-ω turbulence model and the one equation Spalart-Allmaras turbulence model is used. For the time integration of the steady state simulations an implicit Backward Euler time-stepping scheme is chosen. For the RANS calculations a central classic and matrix dissipation scheme is used and fully turbulent flow is assumed for all calculations.

Figure 31-8 shows the simulation result at an angle of attack of $\alpha = 13.3°$ at a Reynolds number of 3×10^6. Comparing the flow topology with the PIV measurements in Figure 31-4 it can be observed that the two vortices are predicted correctly by the simulation. An inner vortex and an outer vortex occur rotating in the same direction.
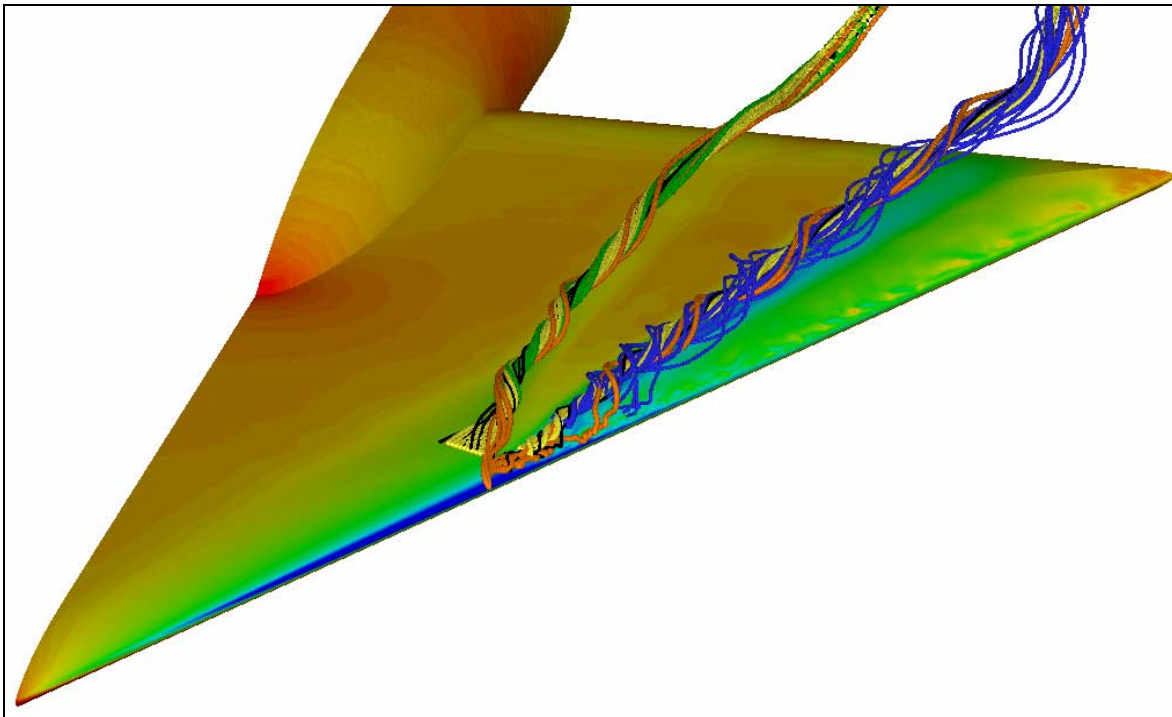
Figure 31-8: Flow Topology on the Upper Surface of the 65° Delta Wing with Medium Radius Leading-Edge. RANS calculation at M = 0.4, Re = 3 x 10^6, α = 13.3°.

31.4.2   Wilcox k-ω Calculations

Figure 31-9 and Figure 31-10 show a comparison of the pressure distributions between CFD calculation and PSP measurement. The free stream conditions are M = 0.4 at an angle of attack of $\alpha = 13.3°$. Figure 31-9 shows the surface pressure distribution at a Reynolds number of 2×10^6 while Figure 31-10 shows the pressure distribution at 3×10^6 Reynolds number.
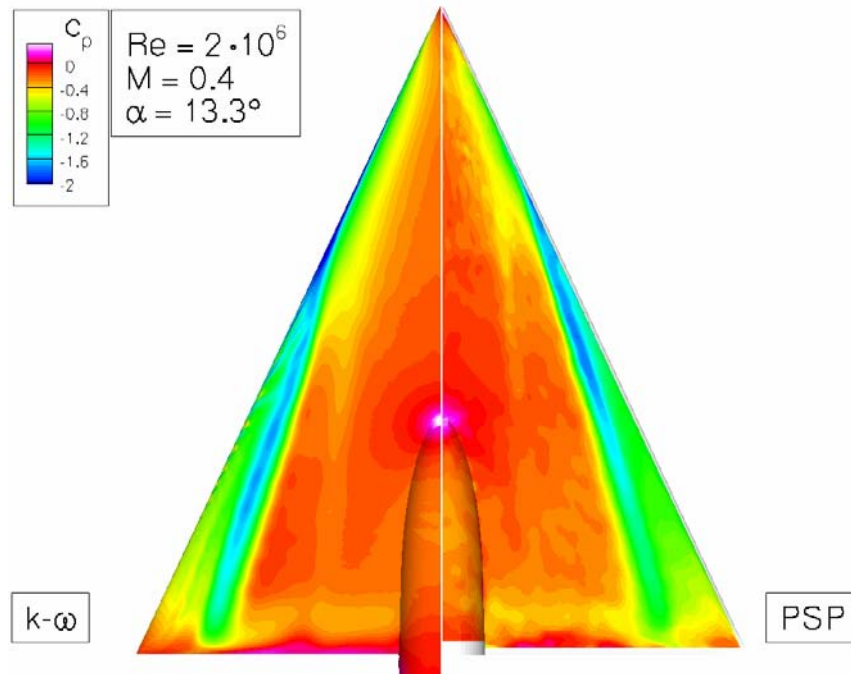
Figure 31-9: Comparison of Pressure Distribution at Angle of Attack α = 13.3° (Left: CFD Calculation Using the k-ω Turbulence Model; Right: PSP Measurement – M = 0.4, Re = 2 x 10^{6}).
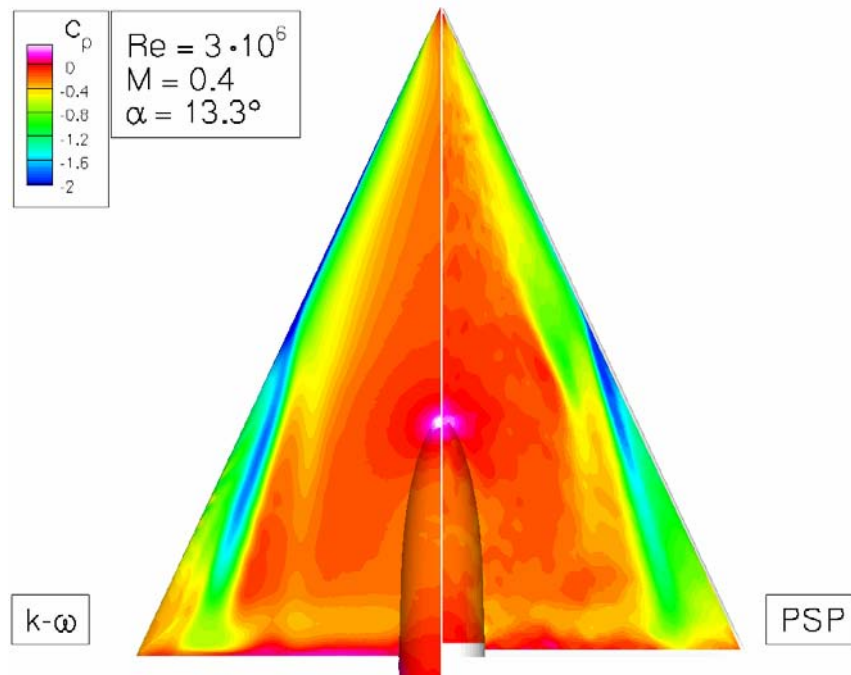
Figure 31-10: Comparison of Pressure Distribution at Angle of Attack α = 13.3° (Left: CFD Calculation Using the k-ω Turbulence Mode; Right: PSP Measurement – M = 0.4, Re = 3 x 10^{6}).

In both cases the two equation k-ω turbulence model is used. It is seen that for both Reynolds numbers the flow pattern of the inner and outer vortex is represented by the CFD calculation. Furthermore a Reynolds number effect is captured by the simulation. As in the experiment it is visible that the outer vortex is generated further downstream, enhancing with the Reynolds number and the suction pattern of the inner vortex affects the pressure distribution on the surface further towards the trailing edge. In the case of 2×10^6 Reynolds number it can be observed that the outer vortex occurs too far downstream in comparison with the experiment. In the case of 3×10^6 Reynolds number the location of the beginning of the outer vortex fits quite well with the experiment. For both Reynolds numbers the inner vortex occurs too far outboard. Concerning the strength of the inner and outer vortex it can be observed that in the 2×10^6 Reynolds number case the suction peak of the outer vortex is stronger than in the experiment whereas the suction pattern is going further towards the trailing edge. The same can be observed for the Reynolds number of 3×10^6. The strength of the inner vortex at 3×10^6 Reynolds number can be assumed to be under predicted by the simulation.

Taking a view on the quantities in Figure 31-11 and Figure 31-12 the results of the pressure distributions at five different stages x = const. planes are compared with the experiment taking from PSI pressure measurements. As discussed before the effect of the too far downstream generated outer vortex is visible in Figure 31-11 for a Reynolds number of 2×10^6. Whereas in the experiment at x = 0.4 the pressure distribution represents a vertical flow, the pressure distribution in the simulation is more or less attached at the leading edge.
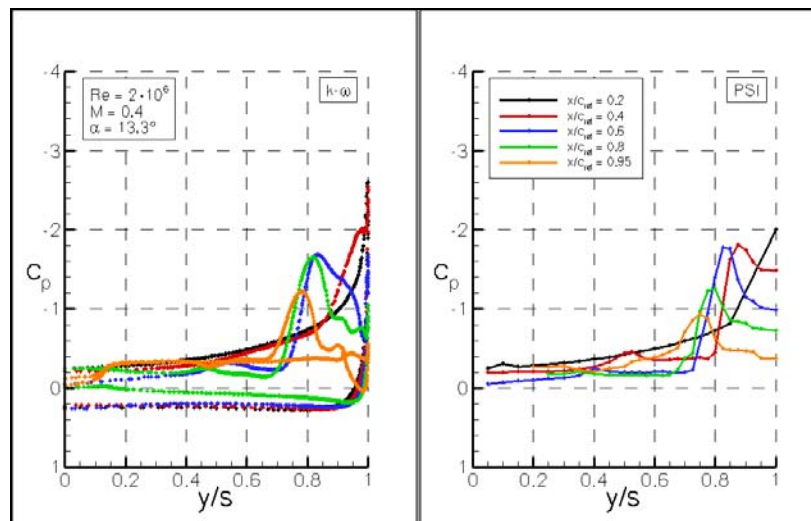
Figure 31-11: Comparison of Pressure Distribution at Angle of Attack α = 13.3°
(Left: PSI Measurement; Right: CFD Calculation Using the k-ω
Turbulence Model – M = 0.4, Re = 2 x 10^6).
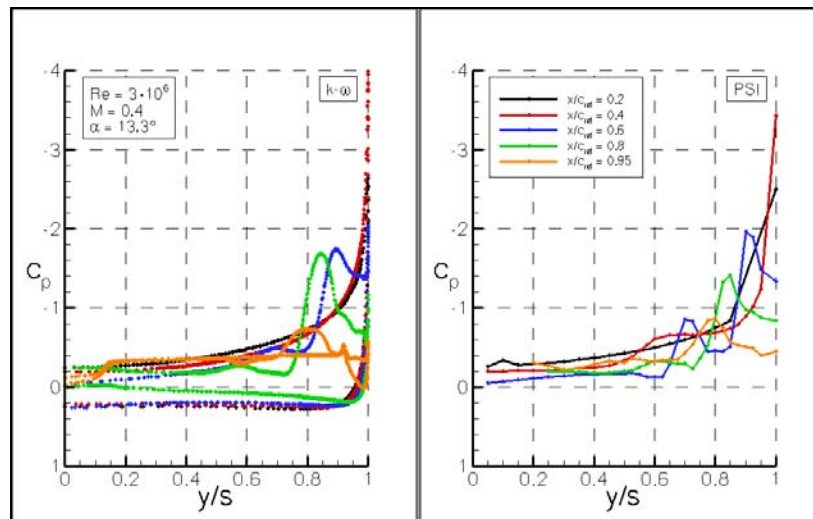
**Figure 31-12: Comparison of Pressure Distribution at Angle of Attack α = 13.3°
(Left: PSI Measurement; Right: CFD Calculation Using the k-ω
Turbulence Model – M = 0.4, Re = 3 x 10⁶).**

This results in higher suction peaks of the outer vortex further downstream in the simulation in comparison with the experiment, since the outer vortex is passing the x = const. stages further downstream within the simulation. For the 3 x 10^6 Reynolds number case in Figure 31-12 the flow in the experiment is attached till 40% chord length, while the suction peak at the leading is overpredicted in the simulation. The position of the outer vortex is predicted correctly by the simulation which can be observed by the correct positions of the spanwise suction peaks. For both cases the inner vortex suction peaks are predicted too weak independent of the downstream position. For both Reynolds number cases the inner vortex is represented too late in the pressure distribution. For both investigated Reynolds numbers the inner vortex can be detected by a small suction peak at 40% chord length in the experiment where as in the simulation the pressure distribution represents attached flow. Regarding the pattern of the pressure distribution towards the apex in Figure 31-9 and Figure 31-10 higher suction peaks can be observed in the experiment in comparison with the simulation. This might be a result of the weakness of the inner vortex because it occurs later than in the experiment or the vortex generating process starts later respectively.

31.4.3   Spalart-Allmaras Calculations

As identified above there are weaknesses concerning the use of the k-ω turbulence model. Because of this further investigations are carried out using the one equation Spalart-Allmaras (SA) turbulence model. In Figure 31-13 and Figure 31-14 the comparison between the measured pressure distribution with PSP on the right hand side and CFD simulation on left hand side is shown for two Reynolds numbers. It can be observed, that in comparison with the k-ω simulations the suction peaks of the inner and outer vortex in case auf the simulation using the Spalart-Allmaras turbulence model are much stronger. This fits significantly better with the experimental data for both Reynolds number cases (2 x 10^6 and 3 x 10^6). Whereas in the k-ω simulations the outer vortex is predicted for both Reynolds numbers further downstream than in the SA simulations the outer vortex is generated upstream of the experimental position. This causes the position of the inner vortex in the SA cases to be more inboard even though the suction peak of the inner vortex is predicted much better than using the k-ω turbulence model.
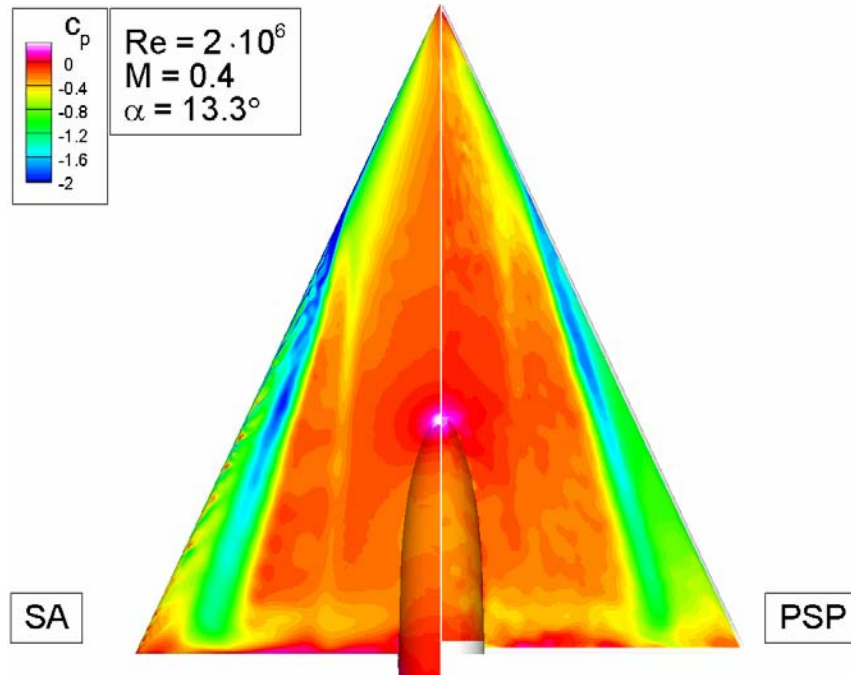
Figure 31-13: Comparison of Pressure Distribution at Angle of Attack α = 13.3° (Left: CFD Calculation Using the Spalart-Allmaras Turbulence Model: Right: PSP Measurement – M = 0.4, Re = 2 x 10^{6}).
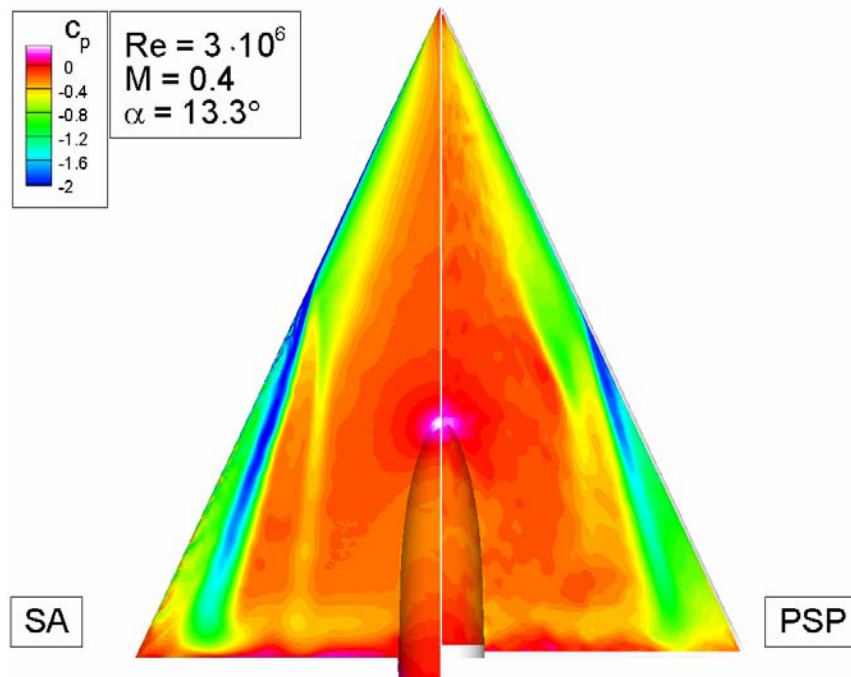
Figure 31-14: Comparison of Pressure Distribution at Angle of Attack α = 13.3° (Left: CFD Calculation Using the Spalart-Allmaras Turbulence Model; Right: PSP Measurement – M = 0.4, Re = 3 x 10^{6}).

This can be verified by looking at the results in Figure 31-15 and Figure 31-16. Similar to Figure 31-11 and Figure 31-12 the calculation results are compared with measured PSI data at several x = const. positions. The suction peak of the inner vortex is visible better predicted for the 3×10^6 Reynolds number case, see Figure 31-16 at $x/c_{ref} = 0.6$. But even for the SA turbulence model it is seen that the inner vortex occurs too far downstream comparing the pressure distribution at $x/c_{ref} = 0.4$ in Figure 31-16. For the 2×10^6 case in Figure 31-15 the inner vortex is generated at the correct position and can be observed in the pressure distribution at $x/c_{ref} = 0.4$ but stronger and more outboard than in the experiment. The overall results show a much better agreement with the experiment using the SA than the k-ω turbulence model.
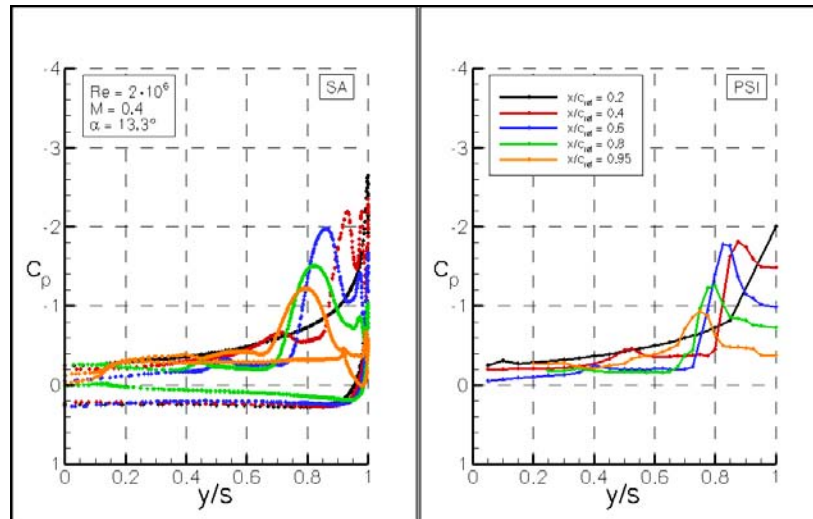
**Figure 31-15: Comparison of Pressure Distribution at Angle of Attack α = 13.3°
(Left: PSI Measurement; Right: CFD Calculation Using the Spalart-
Allmaras Turbulence Model – M = 0.4, Re = 2 x 10^6).**
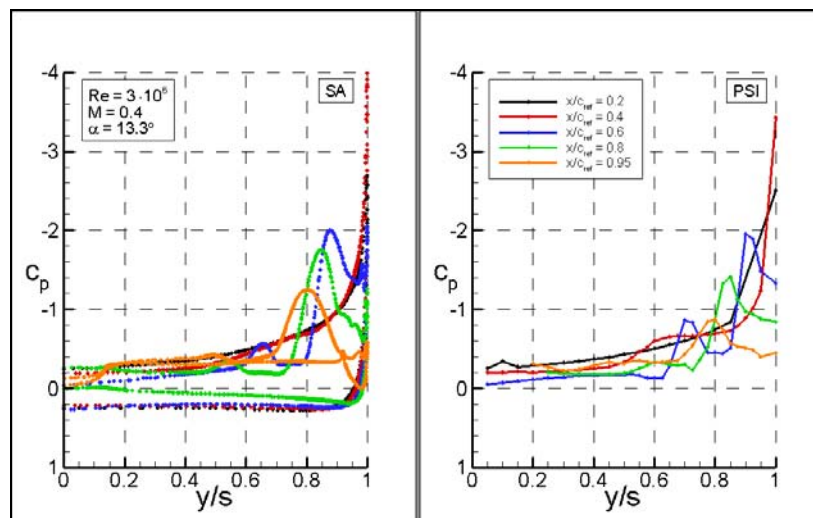
**Figure 31-16: Comparison of Pressure Distribution at Angle of Attack α = 13.3°
(Left: PSI Measurement; Right: CFD Calculation Using the Spalart-
Allmaras Turbulence Model – M = 0.4, Re = 3 x 10^6).**

31.4.4   Sensitivities

Within these section two main sensitivities influencing the flow topology on the upper surface of the delta wing will be discussed. These are the influence of the Reynolds number and the angle of attack. In Figure 31-17 the Reynolds number effect is shown. Three different simulations at Re = 1 x 10^6, 2 x 10^6 and 3 x 10^6 are depicted. For all three simulations the k-ω turbulence model is used. The effect of the Reynolds number matches with former observations. By increasing the Reynolds number the outer and inner vortex occurs further downstream and the suction peak of the inner vortex is shifted consequently towards the trailing edge.
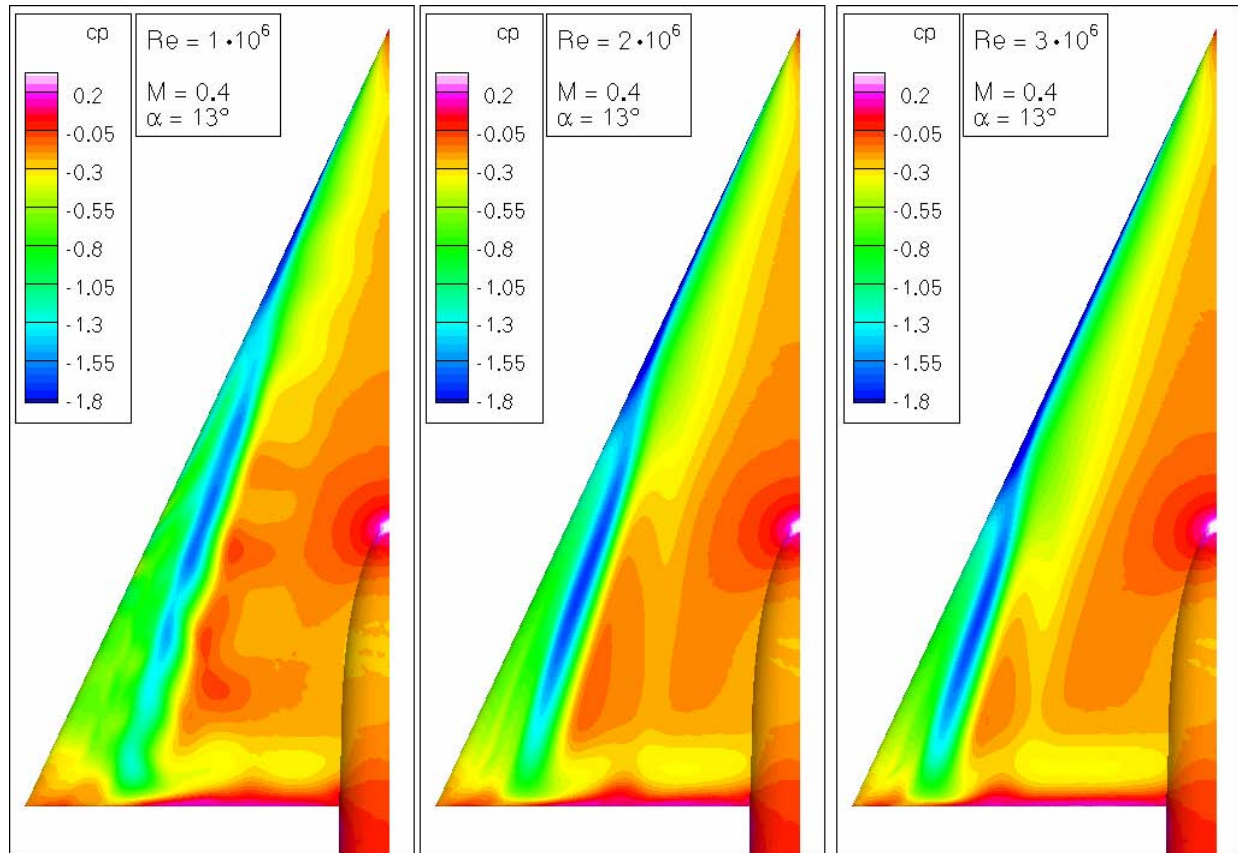
Figure 31-17: CFD Simulation with the DLR TAU-Code. Comparison of pressure distribution at an angle of attack of α = 13.0° – M = 0.4 and three different Reynolds numbers.

Figure 31-18 shows the effect of the angle of attack on the upper side pressure distribution of the delta wing. On the left hand side the simulation at an angle of attack of $\alpha = 13.3°$ is shown and on the right hand side the result at $\alpha = 13.0°$. Both simulations are done by using the Spalart-Allmaras turbulence model. This small difference of $\Delta\alpha = 0.3°$ results in significant differences of the vortex locations. By enhancing α the inner and outer vortex are generated further upstream and the location of the inner vortex moves inboard. This is visible even better in Figure 31-19 comparing the suction peaks of the inner vortex at $x/c_{ref} = 0.6$.
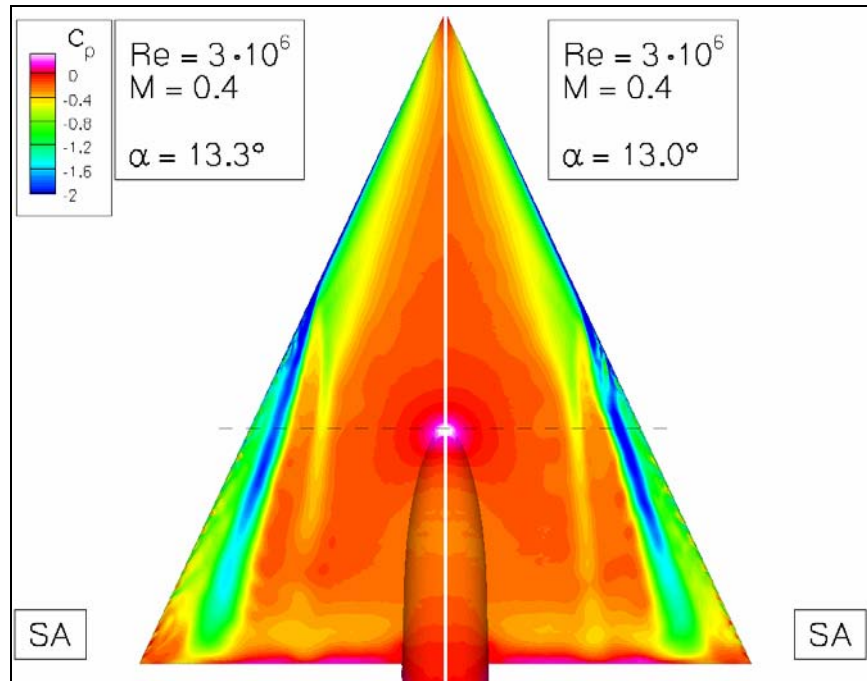
Figure 31-18: Comparison of Surface Pressure Distribution at an Angle of Attack of α = 13.3° and α = 13.0°. CFD calculation using the Spalart-Allmaras turbulence model – M = 0.4, Re = 3 x 10⁶.
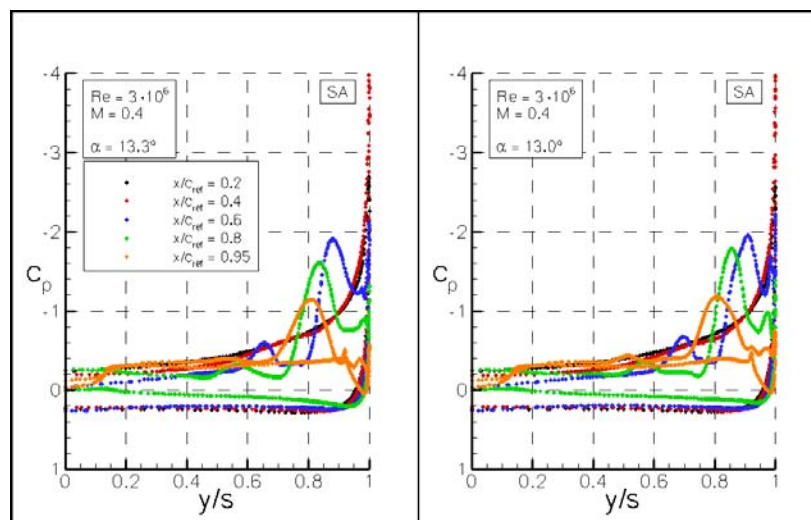
Figure 31-19: Comparison of Pressure Distribution at Slices x = const at an Angle of Attack of α = 13.3° and α = 13.0°. CFD calculation using the Spalart-Allmaras turbulence model – M = 0.4, Re = 3 x 10⁶.

31.4.5   Flow Physics

The flow topology on the upper wing surface of the delta wing and the mechanism of the generation of the inner and outer vortex will be discussed in the following section. Figure 31-20 shows the surface friction lines

for the 3×10^6 Reynolds number case at an angle of attack of $\alpha = 13.3°$. Figure 31-20 shows the same calculation, already discussed for Figure 31-14 and Figure 31-16. The red dashed lines assign the trajectories of the vortices on the upper wing side. The most central one is the inner primary vortex, the next one outboard is the outer primary vortex and finally the secondary vortex of the outer primary vortex is visible near the leading edge. Furthermore the attachment lines of the primary outer vortex as well as the separation lines of the inner and outer primary vortex and the secondary vortex are depicted.
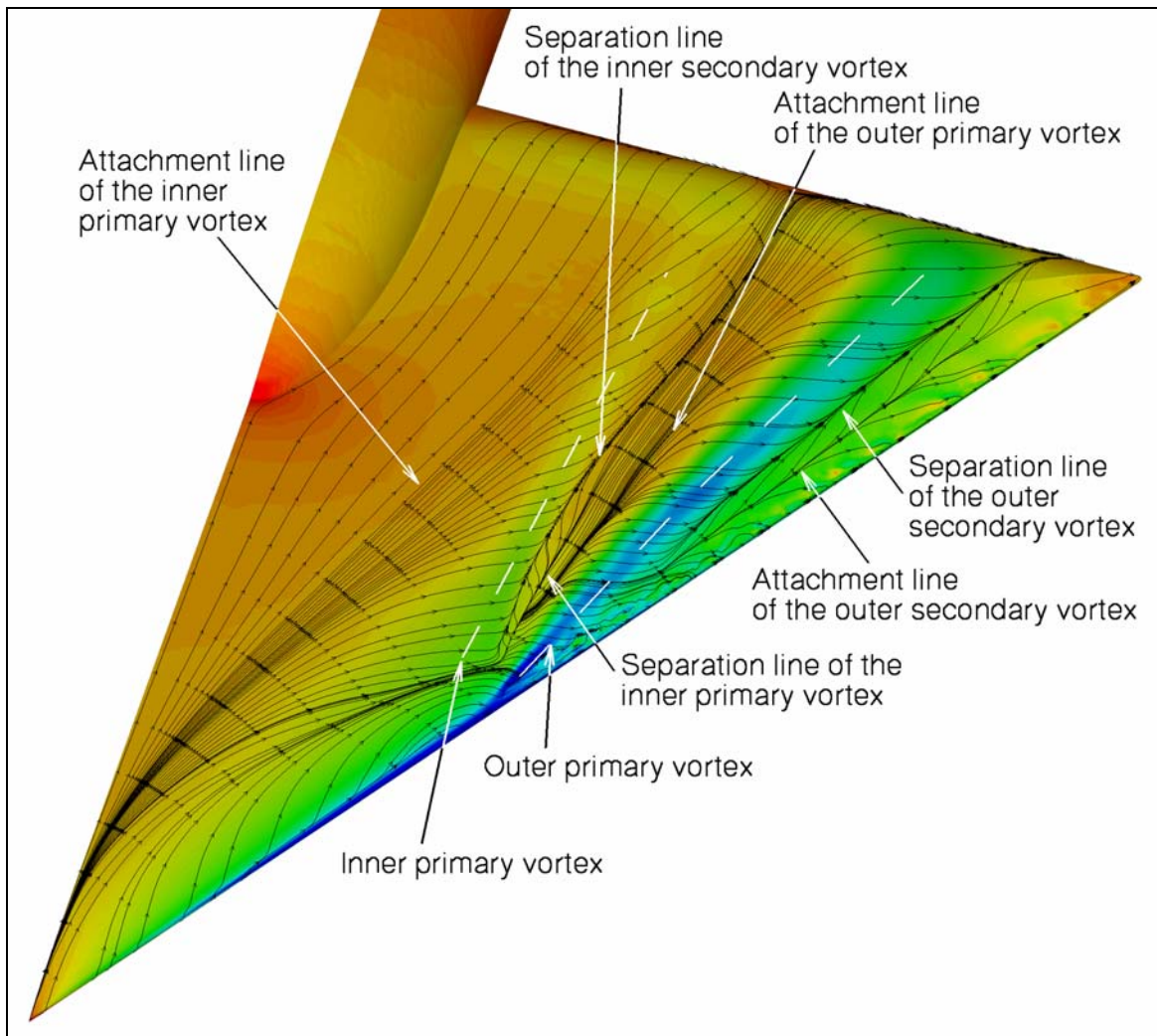
Figure 31-20: Friction Lines and Pressure Distribution on the Upper Surface
of the Delta Wing. TAU calculation at M = 0.4, Re = 3 x 10^6, α = 13.3°.

Regarding the pressure distributions in Figure 31-20 as well as the results discussed before it is assumed that the flow around the leading edge is attached from the apex to the point were the inner vortex is generated. Looking at the pressure distribution in Figure 31-16 there is only a suction peak at the leading edge $x/c_{ref} = 0.2$ and no bump in the more inboard pressure distribution which is an advice for a vortical flow. It can be observed from the friction lines at the apex in Figure 31-20 that the flow is diverted outboard towards the

leading edge. Looking at the pressure distribution at $x/c_{ref} = 0.4$ in Figure 31-16 it can be observed from the experiments that the flow at the leading edge is still attached but there is a suction peak at $y/s = 0.65$ which indicates the onset of the inner vortex. This can be observed as well in the simulation results at $x/c_{ref} = 0.4$ and $y/s = 0.7$ but much weaker than in the experiment. This indicates that the inner vortex occurs first and afterwards the outer primary vortex.

In Figure 31-21 the vorticity distribution in x = const. slices are shown. An initial layer of high vorticity generated from the apex close to the boundary layer can be observed. This layer is getting thicker while moving downstream and turning outboard. Finally this high vorticity layer is the origin of the inner vortex. This is also visible by streamlines released from different positions within the boundary layer and close to the wall as seen in Figure 31-22.
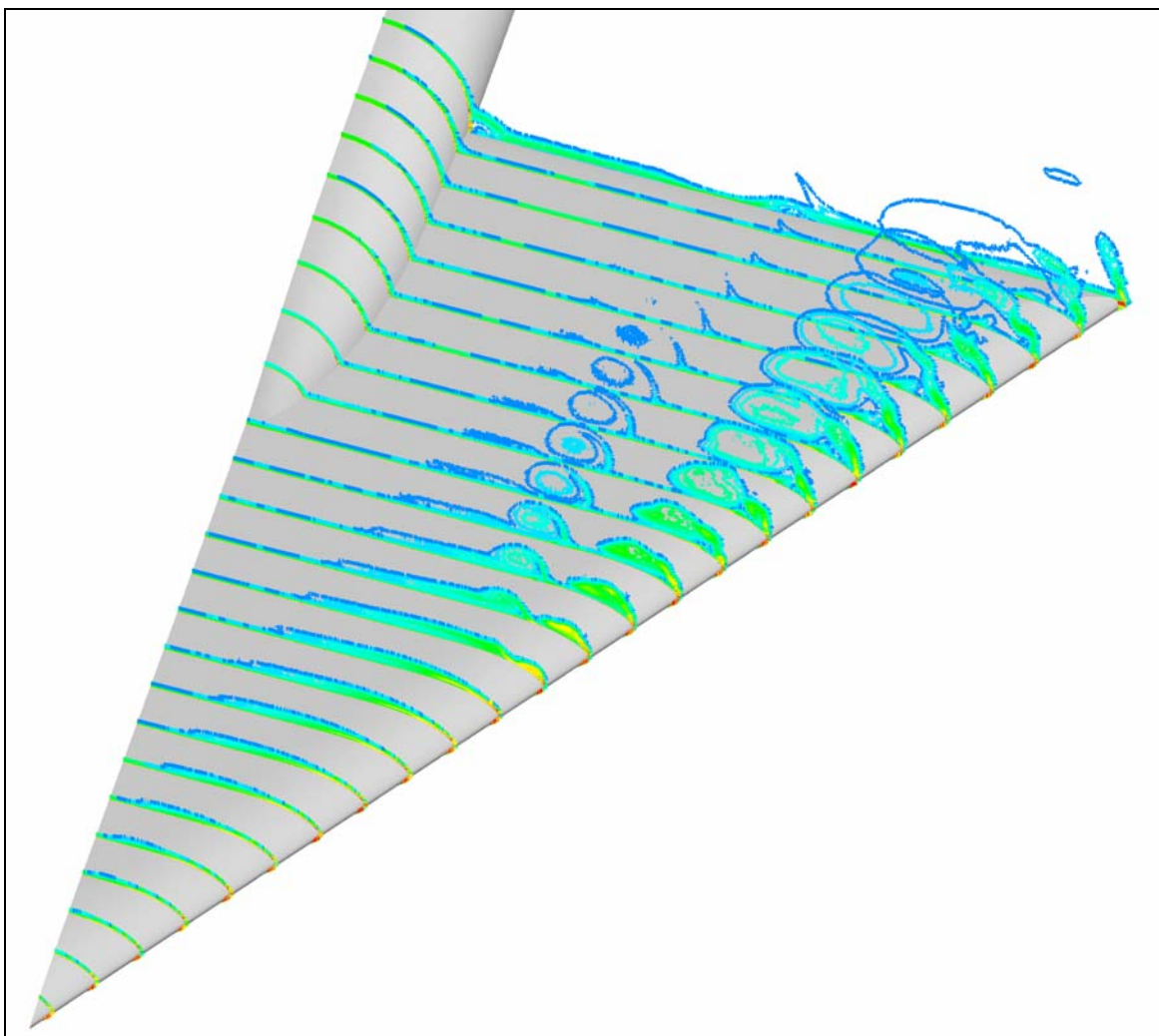
**Figure 31-21: Vorticity Slices on the Upper Surface of the Delta
Wing. TAU calculation at M = 0.4, Re = 3 x 10^6, α = 13.3°.**
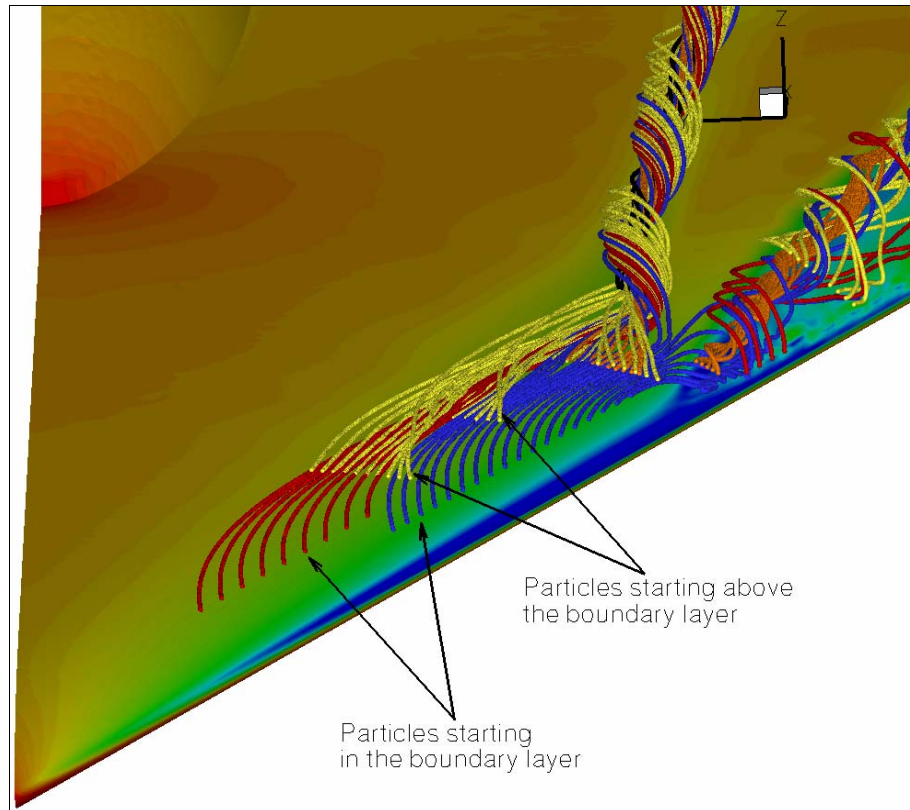
Figure 31-22: Streamlines and Pressure Distribution on the Upper Surface
of the Delta Wing. TAU calculation at M = 0.4, Re = 3 x 10^6, α = 13.3°.

The red and blue traces start within the boundary layer flow. The flow is attached and strongly diverted outboard. It will finally feed the inner and outer primary vortex depending on the starting position. The yellow particles are starting out of the boundary layer within the high vorticity layer described before. These streamlines have a vorticity and generate a kind of vortex far upstream from the point where the outer vortex occurs.

Figure 31-23 supports this flow topology description by regarding the flow opposite to the free stream direction. It can be expected finally, that the inner vortex gets so much vorticity induced by the upstream vorticity layer where it hits the surface at the position where the outer primary vortex is generated, that it suddenly grows up in wall normal direction. The mechanism that forms the inner primary vortex might be directly related to the formation of the outer primary vortex. As seen in Figure 31-21 to Figure 31-23 the thin vorticity layer that represents the first stage of the inner primary vortex rolls up at the point where the outer primary vortex is generated. This behavior can be induced by the vorticity of the outer primary vortex.
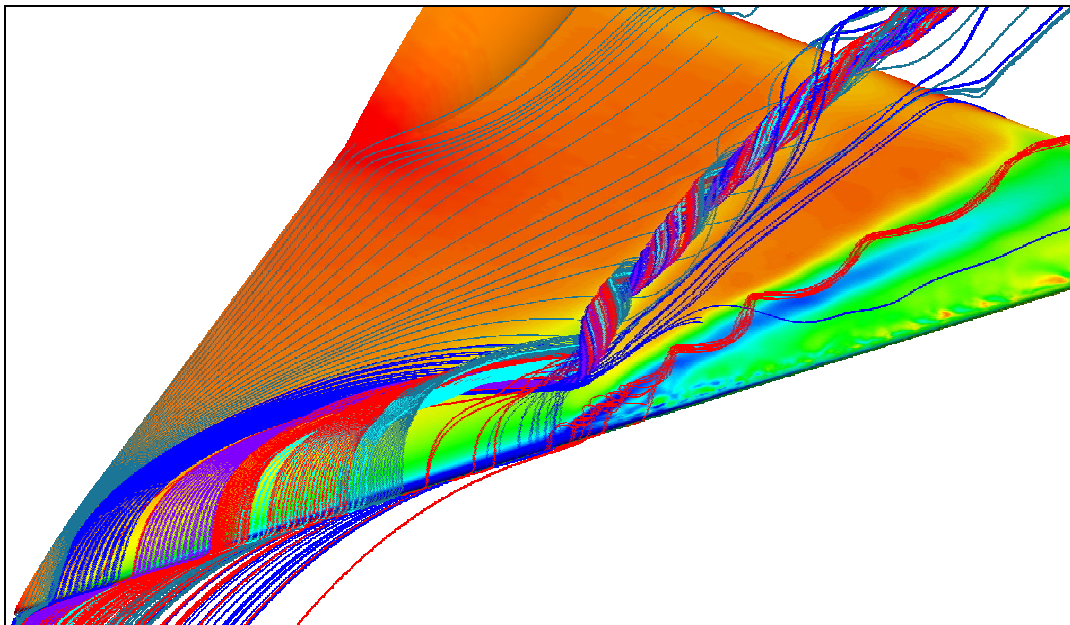
**Figure 31-23: Streamlines and Pressure Distribution on the Upper Surface
of the Delta Wing. TAU calculation at M = 0.4, Re = 3 x 10^6, α = 13.3°.**
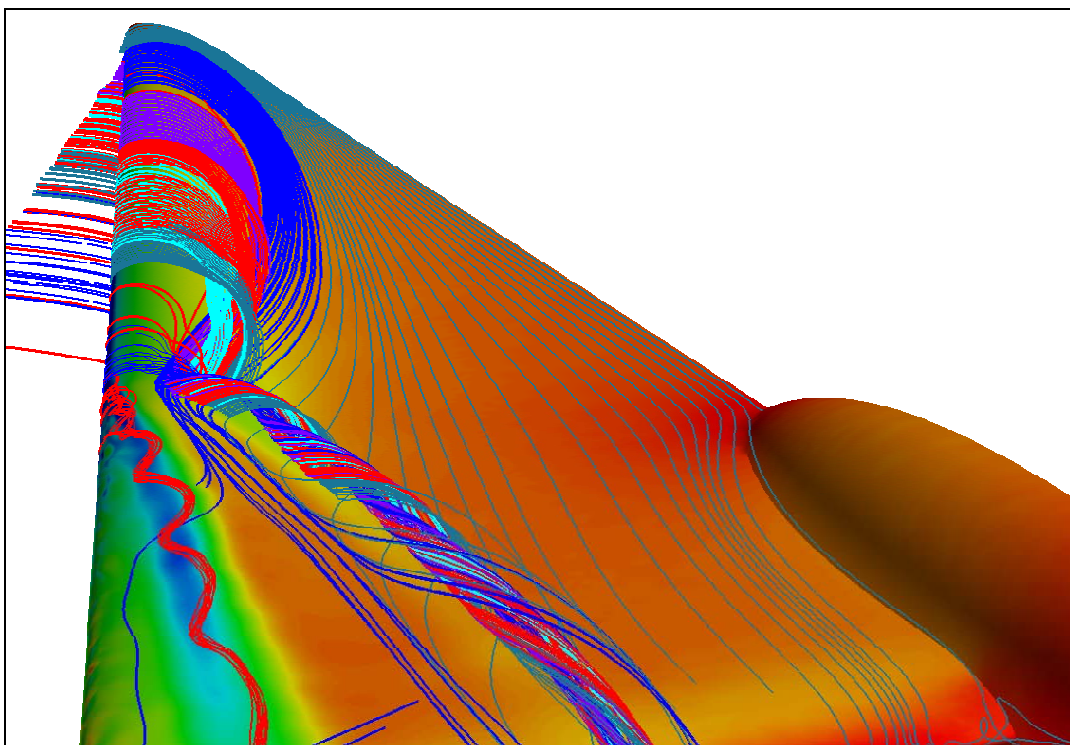
**Figure 31-24: Streamlines and Pressure Distribution on the Upper Surface
of the Delta Wing. TAU calculation at M = 0.4, Re = 3 x 10^6, α = 13.3°.**

31.5   CONCLUSIONS

Results of CFD simulations using the DLR TAU-Code around a 65° delta wing with rounded leading edges at an angle of attack of $\alpha = 13.3°$ are presented in this chapter. The test case was chosen as an example for a complex flow topology with two primary vortices, an inner- and an outer one, instead of one vortex for the standard delta wing configuration with sharp leading edges. The DLR TAU-Code is a cell-vertex finite volume code using hybrid unstructured meshes. By means of simulations at the investigated angle of attack of 13.3° and at several different Reynolds numbers it is shown that the overall flow topology which is proven to be complex and sensitive with respect to various parameters can be predicted by this Code.

As demonstrated by the results a small increase of the angle of attack moves the position of the inner and outer vortex significantly more upstream. The main features of the flow field are carried out quite well by using the Spalart-Allmaras turbulence model. Nevertheless the inner vortex caused a weaker suction peak on the upper side of the delta wing and the outer vortex is generated too far upstream for this model approach. On the other hand the vortex is predicted further downstream than in the experiment by the Wilcox k-ω turbulence model. This model is furthermore very sensitive on the choice of the angle of attack. The influence of additional experimental boundary conditions like the wind tunnel walls are not taken into account within the presented investigations.

Although there are slight differences between the computed pressure distribution and the experimental data, several specific numerical and physical sensitivities are carried out. The influence of the turbulence model is taken into account by using two RANS models, the two equation Wilcox k-ω turbulence model and the one equation Spalart-Allmaras turbulence model. Influences of the Reynolds number and small changes in the incidence angle have been verified.

For all simulations fully turbulent flow is assumed which might be an inadequate simplification since it is not known from experiments whether or where transition occurs. Partly laminar flow at the leading edge may cause different separation behavior of the investigated vortices. This could lead to an earlier and stronger occurrence of the inner vortex. The generation of the outer vortex would be different as well in that case.

Finally the mechanisms of generating two primary vortices under the investigated flow conditions are discussed by means of the numerical simulation. It is shown that the inner vortex is generated out of a vorticity layer moving downstream and outboard towards the trailing edge, generating the inner vortex. It is also shown, that the inner vortex occurs earlier than the outer vortex.

31.6   REFERENCES

[31-1]   Drougge, G.: *The International Vortex Flow Experiment for Computer Code Validation*, ICAS-Proceedings 1988, Vol. 1, pp. XXXV-XLI.

[31-2]   Elsenaar, A., Hjelmberg, L., Bütefisch, K.-A. and Bannink, W.J.: *The International Vortex Flow Experiment*, AGARD-CP-437 (1988), Vol. 1, pp. 9-1 to 9-23.

[31-3]   Wagner, B., Hitzel, S., Schmatz, M.A., Schwarz, W., Hilgenstock, A. and Scherr, S.: *Status of CFD Validation on the Vortex Flow Experiment*, AGARD-CP-437 (1988), Vol. 1, pp. 10-1 to 10-10.

[31-4]   Hoeijmakers, H.W.M.: *Modeling and Numerical Simulation of Vortex Flow in Aerodynamics*, AGARD-CP-494 (1991), pp. 1-1 to 1-46.

[31-5]   Luckring, J.M.: *Recent Progress in Computational Vortex-Flow Aerodynamics*, AGARD-CP-494 (1991), pp. 6-1 to 6-21.

[31-6]   Hummel, D.: *Zur Umströmung scharfkantiger schlanker Deltaflügel bei großen Anstellwinkeln*, Z. Flugwiss, 15 (1967), 376-385.

[31-7]   Hummel, D.: *Experimentelle Untersuchung der Strömung auf der Saugseite eines Deltaflügels*, Z. Flugwiss, 13 (1965), 247-252.

[31-8]   Hummel, D.: *Effects of Boundary Layer Formation on the Vortical Flow Above Slender Delta Wings*, Proceedings of the I MECH E Part G Journal of Aerospace Engineering, Volume 220, Number 6, 2006, pp. 559-568(10).

[31-9]   Hummel, D. and Redeker, G.: *A New Vortex Flow Experiment for Computer Code Validation*, RTO-AVT Symposium on "Vortex Flow and High Angle of Attack", Loen, Norway, 07-11.05.2001.

[31-10] Galle, M., Gerhold, T. and Evans, J.: *Technical Documentation of the DLR TAU-Code*, DLR-IB 233-97/A43 1997.

[31-11] Gerhold, T., Galle, M., Friedrich, O. and Evans, J.: *Calculation of Complex Three-Dimensional Configurations Employing the DLR TAU-Code*, AIAA-97-0167, 1997.

[31-12] Gerhold, T: *Overview of the Hybrid RANS Code TAU*, in N. Kroll, J. Fassbender (Eds.) MEGAFLOW – Numerical Flow Simulations for Aircraft, NNFM Vol. 89, Berlin, 2005, pp. 81-92.

[31-13] Centaur Soft: http://www.Centaursoft.com.

[31-14] Spalart, P.R. and Allmaras, S.R.: *A One-Equation Turbulence Model for Aerodynamic Flows*, AIAA-Paper 92-0439, 1992.

[31-15] Wilcox, D.C.: *Reassessment of the Scale Determining Equation for Advanced Turbulence Models*, AIAA-Journal, Vol. 26, No. 11, pp. 1299-1310, 1988.

[31-16] Chu, J. and Luckring, J.M.: *Experimental Surface Pressure Data Obtained on 65° Delta Wing Across Reynolds Number and Mach Number Ranges*, NASA Technical Memorandum 4645, Vol. 1-4, 1996.

[31-17] Konrath, R., Klein, C., Engler, R.H. and Otter, D.: *Analysis of PSP Results Obtained for the VFE-2 65° Delta Wing Configuration at Sub- and Transonic Speeds*, 44th AIAA Aerospace Sciences Meeting and Exhibit 9-12 January 2006, AIAA Paper No. 2006-60-592, Reno, Nevada.

[31-18] Klein, C., Sachs, W.E., Henne, U., Engler, R.H., Wiedemann, A. and Konrath, R.: *Development of PSP Technique for Application on the VFE-2 65° Delta Wing Configuration*, 44th AIAA Aerospace Sciences Meeting and Exhibit 9-12 January 2006, AIAA Paper No. 2006-59-624, Reno, Nevada.

[31-19] Konrath, R., Schröder, A. and Kompenhans, J.: *Analysis of PIV Results Obtained for the VFE-2 65° Delta Wing Configuration at Sub- and Transonic Speeds*, 24th Applied Aerodynamics Conference 5-8 June 2006, AIAA Paper No. 2006-3003, San Francisco, California.

[31-20] Boelens, O.J., Görtz, S., Morton, S., Fritz, W. and Lamar, J.E.: *Description of the F-16XL Geometry and Computational Grids Used in CAWAPI*, 45th AIAA Aerospace Science Meeting and Exhibit, 8-11 January 2007, AIAA Paper No. 2007-488, Reno, Nevada.

Chapter 32 – NUMERICAL SOLUTIONS FOR THE VFE-2 CONFIGURATION ON UNSTRUCTURED GRIDS AT USAFA, UNITED STATES

by

Russell M. Cummings and Andreas Schütte

The numerical simulation of the flow for the VFE-2 configuration with rounded leading edges is presented. For the numerical simulation the Cobalt Code was used, which uses a cell-centered unstructured hybrid mesh approach. Several numerical results are presented for the steady RANS equations as well as for DES and DDES hybrid approaches. Within this paper the focus is related to the dual primary vortex flow topology, especially the sensitivity of the flow to angle of attack and Reynolds number effects. Reasonable results are obtained with both steady RANS and SA-DDES simulations. The results are compared and verified by experimental data, including surface pressure and pressure sensitive paint results. The impact of transition on the resulting flow field is also assessed, and recommendations for improving future simulations are made.

32.1 NOMENCLATURE

a	=	Speed of sound
b_{loc}	=	Local span
$\bar{c}$	=	Mean aerodynamic chord, $= 2c_r/3$
c_r, c_{ref}	=	Root chord of the wing (reference length)
C_p	=	Pressure coefficient, $\equiv (p - p_\infty)/q_\infty$
k	=	Thermal conductivity
p	=	Static pressure
q	=	Dynamic pressure, $\equiv \rho V^2/2$
M	=	Mach number, $\equiv V/a$
R_{mac}	=	Reynolds number, $\equiv V_\infty \bar{c}/\nu_\infty$
s	=	Local semi span, $= b_{loc}/2$
V	=	Velocity (with x, y, z components of u, v, w)
x, y, z	=	Chordwise, spanwise, and vertical coordinates ($x = 0$ at the apex, $y = 0$ at the centerline)
α	=	Angle of attack, deg
μ	=	Viscosity
ν	=	Kinematic viscosity, $\equiv \mu/\rho$
ρ	=	Density
∞	=	Freestream conditions
PSI	=	Measurements using pressure sensors
PSP	=	Pressure sensitive paint

32.2   INTRODUCTION

The flow field around delta wing configurations with sharp leading edges is well known, as are approaches to simulating the flow using high fidelity numerical methods. Within recent years several experimental and numerical investigations have been published focusing on the flow topology, Reynolds and Mach number effects, as well as on transition behavior of the vortex dominated flow field around sharp leading-edge delta wings. This is described in detail within publications from the US/European Vortex Flow Experiment 1 [32-1]-[32-5]. The flow around a sharp leading-edge delta wing is characterized by primary vortices initially separating directly at the apex, even at fairly low angles of attack. The shear layer rolls up to form a pair of primary vortices over the wing, with the shear layer formed along the leading edge continuously feeding the vortex down the length of the wing. The secondary vortices occur due to the interaction of the flow induced by the primary vortex interacting with the boundary layer on the upper wing surface, as seen in Figure 32-1. The strength and position of the primary and secondary vortices are mainly influenced by the freestream velocity, angle of attack, as well as on the sweep angle of the delta wing [32-6],[32-7]. The vortex flow under turbulent flow conditions is fairly independent of the Reynolds number for sharp leading-edge delta wings, whereas under laminar flow conditions the Reynolds number effects the position and strength of the vortices as well as the vortex topology over the wing [32-8].
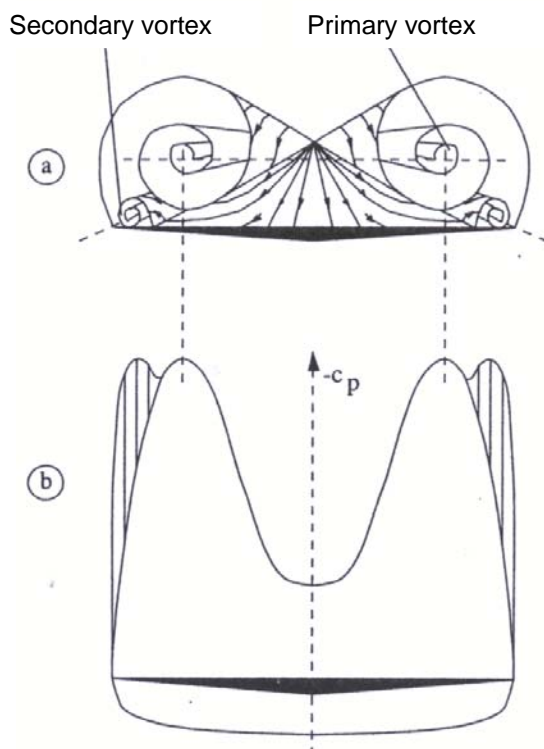
Figure 32-1: Schematic View of the Flow over a Sharp Leading Edge Delta Wing [32-7]:
(a) Vortex Formation; (b) Pressure Distribution in a Cross Flow Plane.

However, the flow around delta wing configurations with rounded leading edges is still not entirely understood. Therefore the Second International Vortex Flow Experiment – VFE 2 – was established focusing on the flow

around delta wing configurations with rounded leading edges [32-9]. Several experimental data sets were provided and generated within the NATO RTO/AVT-113 task group for a 65° swept delta wing with sharp and various blunt/rounded leading edges. The rounded leading edge shapes include low, medium, and high leading-edge radii. The experimental data base is used to expand the knowledge about the flow topology and flow physics and to verify and validate computational codes. This paper focuses on the flow topology around the VFE-2 delta wing with medium rounded leading edges at different Reynolds numbers and angles of attack using various turbulence models, especially RANS and hybrid models such as DES and DDES. The overall goal is to understand more fully the flow topology for these non-sharp leading-edge delta wings.

Previous numerical studies on the VFE-2 delta wings have been limited, with Londenberg [32-10] showing results for the sharp leading-edge delta wing under transonic conditions and Chiba and Obayashi [32-11] performing calculations of the dual primary vortices that form on the medium radius leading edge. The topology of the dual primary vortices is especially interesting, and formed the basis for the majority of papers in two special sessions at the 46th AIAA Aerospace Sciences Meeting and Exhibit in 2008.

32.3   NUMERICAL APPROACH

32.3.1   CFD Solver Cobalt

In this section a brief description of the numerical method is provided. Full details of the computational scheme are presented by Strang et al. [32-12] Solutions for all configurations were computed with the commercial version of Cobalt developed by Cobalt Solutions, LLC. Cobalt solves the unsteady, three-dimensional, compressible Navier-Stokes equations on a hybrid unstructured grid. The code has several choices of turbulence models, including Spalart-Allmaras (SA), Spalart-Allmaras with Rotation Corrections (SARC), and Menter's Shear Stress Transport (SST) RANS models, as well as Detached-Eddy Simulation (DES) and Delayed Detached-Eddy Simulation (DDES) versions of SA, SARC, and SST. All simulations were computed on unstructured meshes with prisms in the boundary layer and tetrahedra elsewhere. The computational meshes were generated with the grid generator Centaur from Centaur-Soft [32-13].

32.3.2   Turbulence Models

For simulation of turbulent flows, the governing equations are suitably averaged, yielding turbulent stresses that require a turbulence model. A Boussinesq approximation is invoked in the momentum equations and the turbulent eddy viscosity (μ_t) is used to relate the stresses to the strain rate. The turbulent heat flux is also modeled using a gradient-transport hypothesis, requiring specification of a turbulent thermal conductivity (k_t). The Reynolds analogy is applied and the turbulent heat flux is modeled using a constant turbulent Prandtl number of 0.9. Using turbulent eddy viscosity and turbulent conductivity, the variable, μ, is replaced by ($\mu + \mu_t$) and k is replaced by ($k + k_t$) in the governing equations.

32.3.2.1   Spalart-Allmaras Turbulence Model (SA)

The Spalart-Allmaras [32-14] one equation model (SA) solves a single partial differential equation for a working variable $\tilde{\nu}$ which is related to the turbulent viscosity. The differential equation is derived by "using empiricism and arguments of dimensional analysis, Galilean invariance and selected dependence on the molecular viscosity" [32-14]. The model includes a wall destruction term that reduces the turbulent viscosity in the laminar sublayer. The model takes the form:

$$\frac{D\tilde{v}}{Dt} = c_{b1}\tilde{S}\tilde{v} - c_{w1}f_w\left[\frac{\tilde{v}}{d}\right]^2 + \frac{1}{\sigma}\left[\nabla\cdot\left((v+\tilde{v})\nabla\tilde{v}\right) + c_{b2}\left(\nabla\tilde{v}\right)^2\right]$$

The turbulent kinematic viscosity is obtained from:

$$v_t = \frac{\mu_t}{\rho} = \tilde{v}f_{v1} \qquad\qquad f_{v1} = \frac{\chi^3}{\chi^3 + c_{v1}^3} \qquad\qquad \chi = \frac{\tilde{v}}{v}$$

where S is the magnitude of the vorticity given by:

$$S = |\omega| = \left|\nabla\times\left(u\hat{i} + v\hat{j} + w\hat{k}\right)\right|$$

and the modified vorticity is:

$$\tilde{S} = S + \frac{\tilde{v}}{\kappa^2 d^2}f_{v2} \qquad\qquad f_{v2} = 1 - \frac{\chi}{1 + \chi f_{v1}}$$

where d is the distance to the closest wall. The wall destruction function f_w is:

$$f_w = g\left[\frac{1 + c_{w3}^6}{g^6 + c_{w3}^6}\right]^{\frac{1}{6}}$$

and

$$g = r + c_{w2}\left(r^6 - r\right) \qquad\qquad r \equiv \frac{\tilde{v}}{\tilde{S}\kappa^2 d^2}$$

The turbulent viscosity is obtained from the turbulent kinematic viscosity by $\mu_t = \rho v_t$. The model coefficients are given in Table 32-1.

Table 32-1: Spalart-Allmaras Turbulence Model Coefficients

$c_{b1} = 0.1355$	$c_{b2} = 0.622$	$c_{v1} = 7.1$
$\kappa = 0.41$		$\sigma = 2/3$
$c_{w1} = c_{b1}/\kappa^2$ $+ \left(1 + c_{b2}\right)/\sigma$	$c_{w2} = 0.3$	$c_{w3} = 2$

32.3.2.2 Spalart-Allmaras Turbulence Model with Rotation Correction (SARC)

The turbulence model correction for rotating flows is based on concepts first proposed by Spalart and Shur [32-15] as well as Knight and Saffman [32-16]. The approach is, "based on tracking the direction of the principal axes of the strain tensor and, thus, is both Galilean invariant and usable in a simple model" [32-17]. The only difference between SARC and SA is that in the SARC model the production term in the eddy viscosity transport equation is multiplied by the rotation factor f_{r1}:

$$f_{r1}\left(r^*, \tilde{r}\right) = \left(1 + c_{r1}\right) \frac{2r^*}{1 + r^*} \left[1 - c_{r3} \tan^{-1}\left(c_{r2}\tilde{r}\right)\right] - c_{r1}$$

If the variables and their derivatives are defined with respect to the rotating reference frame (rotating at rate Ω), the non-dimensional quantities r^* and $\tilde{r}$ are given by:

$$r^* = S / \omega$$

$$\tilde{r} = 2\omega_{ik} S_{jk} \left[\frac{DS_{ij}}{Dt} + \left(\varepsilon_{jmn} S_{in}\right)\Omega_m\right] / D^4$$

where:

$$S_{ij} = 0.5\left(\frac{\partial u_i}{\partial x_j} + \frac{\partial u_j}{\partial x_i}\right)$$

$$\omega_{ij} = 0.5\left[\left(\frac{\partial u_i}{\partial x_j} - \frac{\partial u_j}{\partial x_i}\right) + 2\varepsilon_{mji}\Omega_m\right]$$

and the constants are $c_{r1} = 1.0$, $c_{r2} = 12$, and $c_{r3} = 1.0$ (see Ref. [32-17] for details).

32.3.2.3 Detached-Eddy Simulation (DES)

The Detached-Eddy Simulation (DES) method was proposed by Spalart et al. [32-18] and was originally based on the Spalart-Allmaras one equation RANS turbulence model (detailed above). The wall destruction term presented above is proportional to $\left(\tilde{v} / d\right)^2$, where d is the distance to the wall. When this term is balanced with the production term, the eddy viscosity becomes proportional to $\hat{S}d^2$, where $\hat{S}$ is the local strain rate. The Smagorinski Large-Eddy Simulation (LES) model varies its sub-grid scale (SGS) turbulent viscosity with the local strain rate, and the grid spacing: $v_{SGS} \propto \hat{S}\Delta^2$, where $\Delta = \max\left(\Delta x, \Delta y, \Delta z\right)$. If d is replaced with Δ in the wall destruction term, the SA model will act as a Smagorinski LES model.

To exhibit both RANS and LES behavior, d in the SA model is replaced by:

$$\tilde{d} = \min\left(d, c_{DES}\Delta\right)$$

When $d << \Delta$, the model acts in a RANS mode and when $d >> \Delta$ the model acts in a Smagorinski LES mode. Therefore the model switches into LES mode when the grid is locally refined.

DES was implemented in an unstructured grid method by Forsythe et al. [32-19]. They determined that the DES constant should be $c_{DES} = 0.65$, consistent with the structured grid implementation of Spalart et al. [32-18] when the grid spacing, Δ, was taken to be the longest distance between the cell center and all of the neighboring cell centers.

32.3.2.4   Delayed Detached-Eddy Simulation (DDES)

Delayed Detached-Eddy Simulation (DDES) [32-20] corrects one of the problems exhibited by DES, namely that the switch between the RANS turbulence model and LES was controlled by the grid spacing. While correct grid spacing could solve this problem for many flows [32-21], in cases where the separation is quite shallow (such as a separation bubble over an airfoil), the model often switched in a non-physical manner. To correct this problem, DDES has a switch based on the location of the outer edge of the boundary layer, so that RANS is used within the boundary layer and LES is used outside of the boundary layer. Early results using DDES have shown that the model works very well for flows that are massively or shallowly separated.

32.4   EXPERIMENTAL DATA

For the verification and validation of the numerical simulations, various wind-tunnel data have been provided by NASA within the RTO/AVT-113 task group [32-22]. Additionally, several wind tunnel experiments were done with a 2/3-scaled wind tunnel model loaned by NASA to DLR [32-23]. These wind tunnel experiments consist of pressure distribution measurements using pressure taps and Pressure Sensitive Paint (PSP) [32-24], as well as measurements of the flow field via Particle Image Velocimetry (PIV) [32-25]. Figure 32-2 shows the NASA wind tunnel model in the National Transonic Facility wind tunnel at NASA Langley Research Center. With this model a variety of tests focusing on Reynolds number and Mach number effects were completed. The Reynolds number range is from 6 x 10^6 to 120 x 10^6 at a Mach number of 0.85, and across a Mach number range of 0.4 to 0.9 at Reynolds numbers of 6 x 10^6, 60 x 10^6 and 120 x 10^6. Normal force and pitching moment coefficient data for these Reynolds number and Mach number ranges are also available. These NASA data were given to the task group for code validation since the beginning of the project. Specifically for the purposes of the AVT-113 task group, DLR measurements with the 2/3-scaled NASA Low-Turbulence Pressure Tunnel (LTPT) model were obtained. Several test campaigns delivered surface pressure data and flow field data for increasing knowledge of the behavior of the rounded leading-edge delta wing configuration. Furthermore, the data were given to the task group for computer code validation. Figure 32-3 shows the pressure distribution over the delta wing measured with PSP, Figure 32-4 shows the setup in the Transonic Wind Tunnel in Göttingen to provide the PIV measurements, and Figure 32-5 shows an example of a PIV flow field measurement.

Figure 32-2: NASA 65° Delta Wing in the NTF Wind Tunnel at NASA Langley Research Center [32-22].
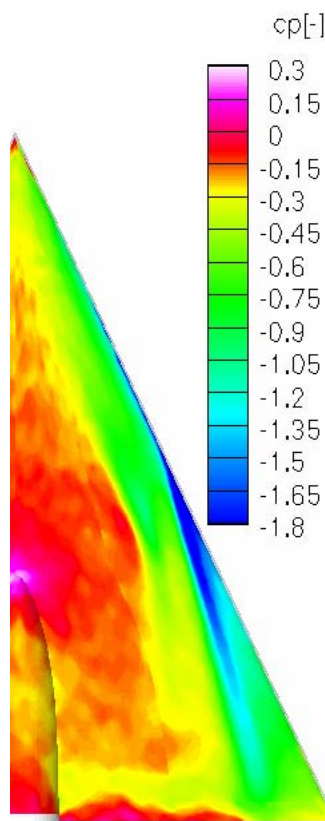
**Figure 32-3: Pressure Distribution on the Upper Side of the Wing Using PSP
(Pressure Sensitive Paint) – M = 0.4, R_{mac} = 3 x 10^6, α = 14° [32-23][32-24].**
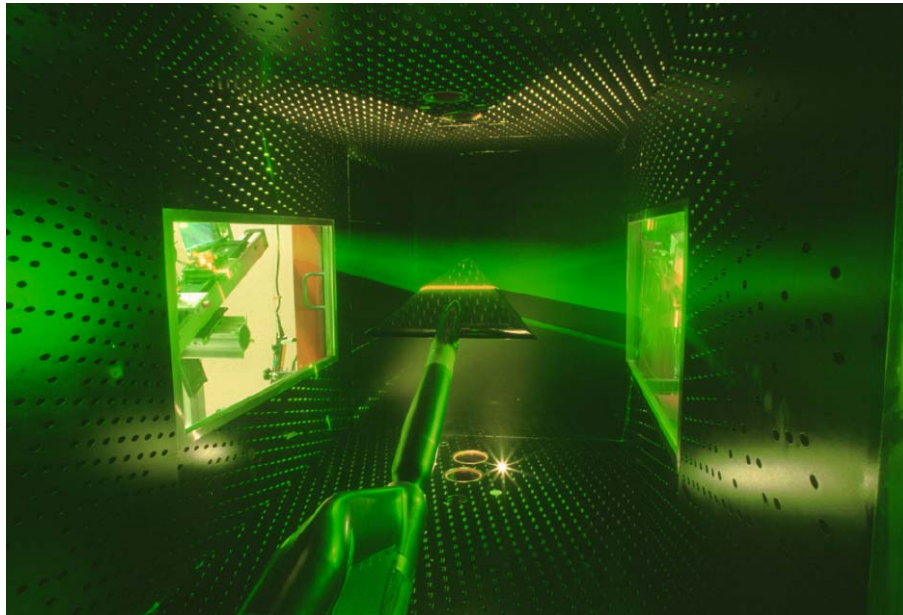
**Figure 32-4: Model Setup for PIV Measurements in the Transonic Wind Tunnel Göttingen (TWG).
The laser light sheet can be observed at approximately 50% chord length [32-25].**
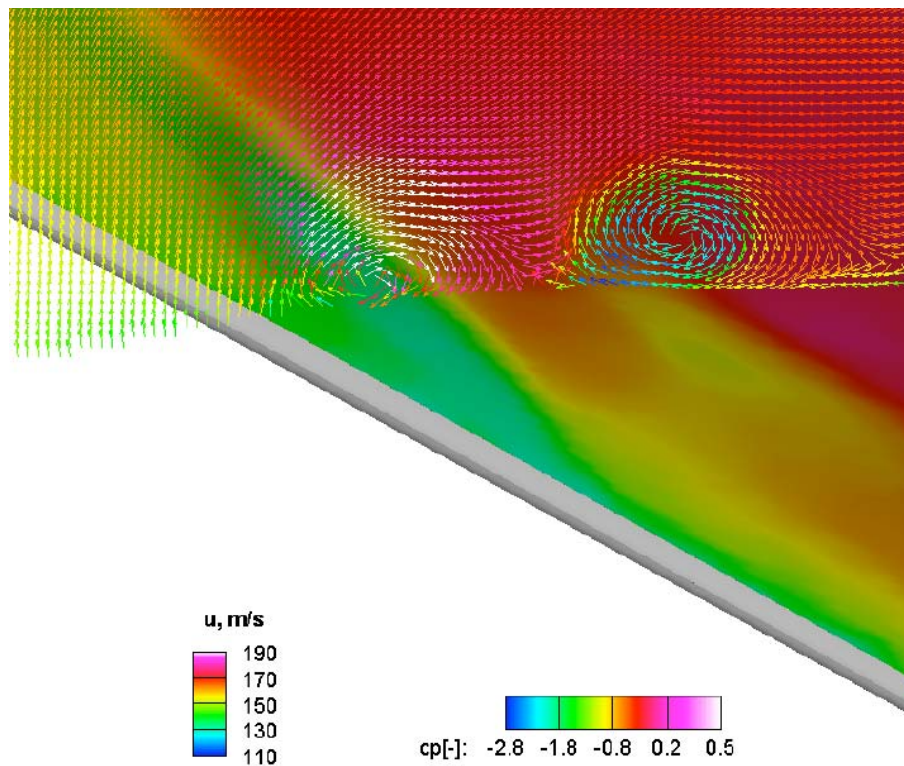
**Figure 32-5: Pressure Distribution on the Upper Surface and PIV Measurement at x/c_{ref} = 0.6 for M = 0.4,
R_{mac} = 3 x 10^6 and α = 14° [32-25]. PIV measurement shows the double primary vortex system.**

32.5   NUMERICAL RESULTS AND DISCUSSION

32.5.1   Rounded Leading Edge Flowfield

From the experimental results for the medium rounded leading edge it can be observed that the flow topology over the delta wing is completely different when compared to the flow around the sharp leading-edge configuration. Comparing the flow topology for the sharp leading edge depicted in Figure 32-1, the round leading edge generates two primary vortices rotating in the same direction on the upper wing surface (a weaker inner vortex which is apparently generated first and a stronger outer vortex), as shown in Figure 32-5.

The location, strength, and starting point of the primary vortices on the upper wing surface vary with Mach number, Reynolds number, and angle of attack. In general, however, the same basic flow topology occurs for all flow conditions. In the following section the numerical capabilities for simulating the flow around the medium rounded leading-edge delta wing will be discussed. Furthermore, the flow physics leading to the described specific flow topology will be discussed and analyzed by use of the computational simulations.

32.5.2   RANS Simulations

In the following section the Reynolds-Averaged Navier-Stokes (RANS) simulation results will be presented. The simulations were done on an IBM P690 system at the Arctic Region Supercomputer Center (ARSC). For all RANS calculations 256 processors were used in parallel. Figure 32-6 and Figure 32-7 show the computational unstructured grid. Figure 32-6 shows the grid resolution on the surface especially in the vicinity of the rounded leading edge. A slice through the mesh at a position x = constant shows the 15 prismatic layers resolving the flow in the boundary layer as well as the field distribution in the spanwise direction. To resolve the flow field on the wing the mesh is pre-refined with a field source in the area where the vortex flow is assumed. The overall grid contains approximately 26×10^6 cells or 6×10^6 grid points. Figure 32-7 shows the grid distribution at five x = constant cut planes to show the refinement over the chord of the delta wing. Based on our experience this level of grid density is sufficient for accurate prediction of delta wing flows using either RANS or hybrid turbulence models [32-26].
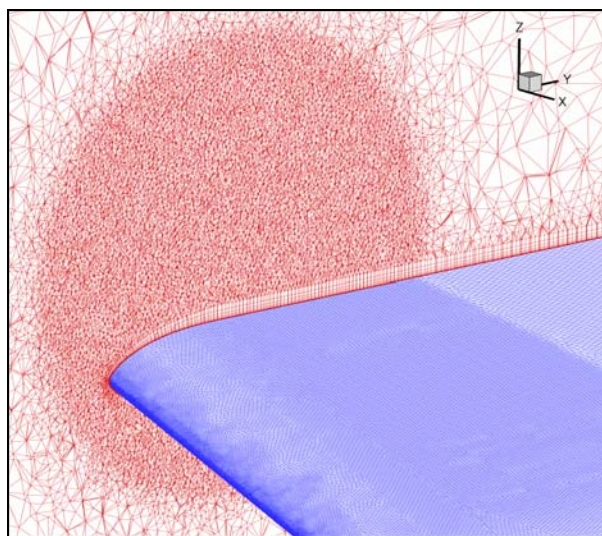
Figure 32-6: Slice through the Computational Unstructured Grid. Fifteen prismatic layers to resolve the boundary layer flow and a field source to resolve the vortex flow over the wing.
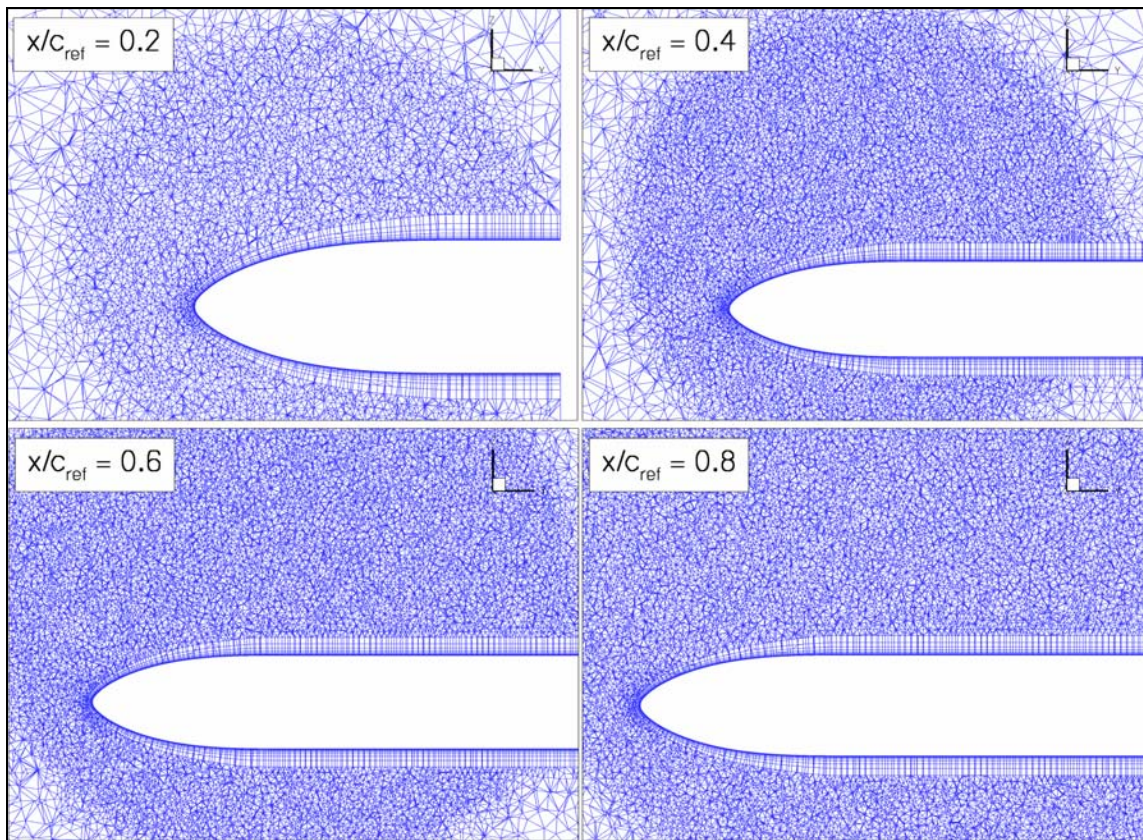
**Figure 32-7: Slice through the Computational Unstructured
Grid at Four Different x = Constant Positions.**

In Figure 32-8 and Figure 32-9 the pressure distributions over the upper wing surface at an angle of attack of 13.3° for two different Reynolds numbers (2×10^6 and 3×10^6) are depicted. On the right side the PSP wind tunnel measurements are shown, and on the left side the CFD simulations using the Spalart-Allmaras turbulence model are shown. For both cases the overall flow topology is given correctly by the CFD calculation. The footprint of the inner and outer vortex is predicted by the simulation. One major difference is seen regarding the outer vortex at $R_{mac} = 2 \times 10^6$. The strength of the outer vortex is predicted too weak by the CFD simulation and too far upstream. For the case of $R_{mac} = 3 \times 10^6$ the outer vortex also occurs too far upstream, which causes the inner vortex to occur too far outboard. Furthermore, it can be observed that by increasing the Reynolds number the outer vortex occurs further downstream and the vortex is stronger, causing a higher suction peak on the surface; the inner vortex is getting stronger as well. The same Reynolds number effect can be observed by increasing the Reynolds number to 4.5×10^6 as depicted in Figure 32-10. The outer vortex is generated further downstream and the effect of the inner vortex on the surface pressure distribution is far more downstream towards the trailing edge.

**Figure 32-8: Pressure Distribution on the Upper Surface of the Wing – Comparison
of CFD Calculation and PSP Measurement for R_{mac} = 2 x 10^6, M = 0.4 and α = 13.3°.**

**Figure 32-9: Pressure Distribution on the Upper Surface of the Wing – Comparison
of CFD Calculation and PSP Measurement for R_{mac} = 3 x 10^6, M = 0.4 and α = 13.3°.**
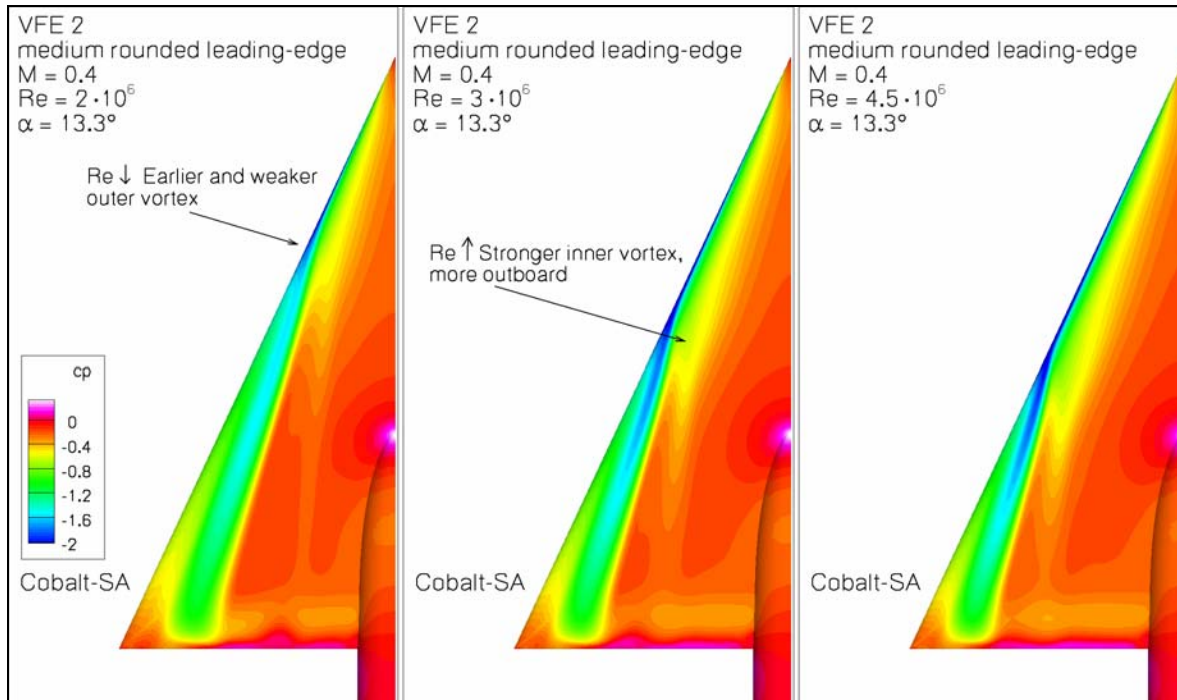
Figure 32-10: Pressure Distribution on the Upper Surface of the Wing – Comparison
of CFD Simulations at Different Reynolds Numbers for M = 0.4 and α = 13.3°.

The discussion to this point has focused on the quality of the CFD results; we will now take a look at the results quantitatively. In Figure 32-11 and Figure 32-12 the related PSI pressure tap distributions at five x = constant positions are depicted. On the left side the experimental PSI pressure tap data are shown, and on the right side the CFD simulations are shown. While the correct qualitative representation of the flow topology is made by the CFD simulation, there are some differences in the pressure levels. For a Reynolds number of 2×10^6 (Figure 32-11), the flow is initially attached around the leading edge and over the span at 20% chord length. The suction peak directly at the leading edge is predicted too high by the CFD simulation (note, however, that the experimental data points are fairly widely spaced compared with the CFD cell size). The suction peak of the outer vortex at 40% and 60% chord length is represented too weak by the simulation as mentioned previously. The distribution at the other positions at 80% and 95% are predicted a bit too strong. The spanwise position of the outer vortex is given correctly by the CFD simulation. The strength of the suction peak of the inner vortex at 40% chord length is represented quite well by the simulation but too far outboard. The position and strength of the inner vortex depends on the position of its origin as well as on the strength and position of the outer vortex making this especially difficult to compute since it is based on the prediction of separation near the apex of the wing. Also, there might be transition effects for this case, which will be discussed later on.
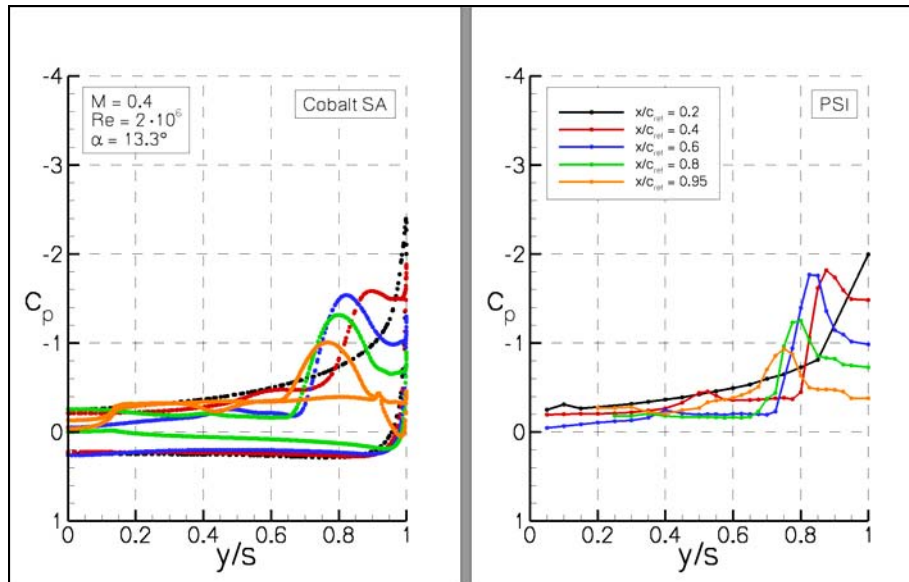
Figure 32-11: Pressure Distribution at Positions x = Const. – Comparison of Experiment and CFD Calculation for R_{mac} = 2 x 10^6, M = 0.4 and α = 13.3°.
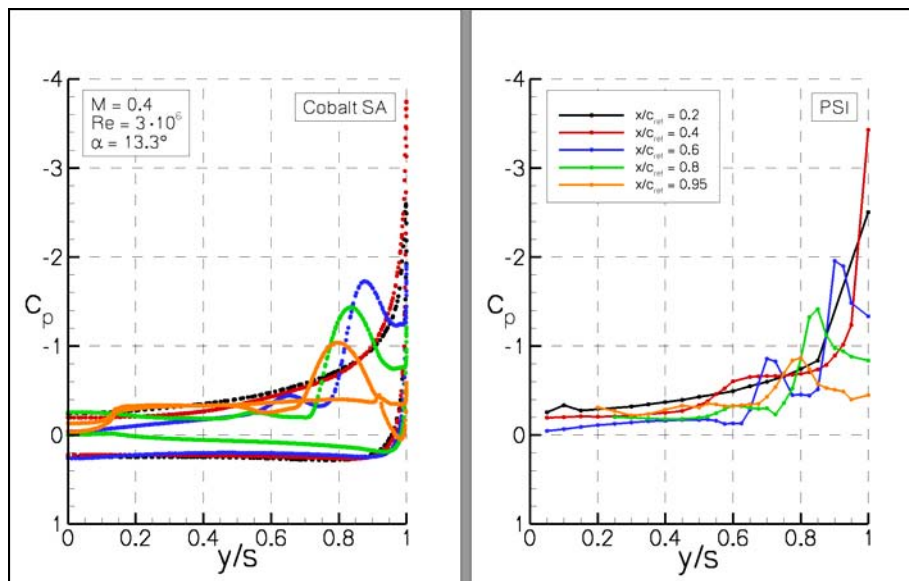
Figure 32-12: Pressure Distribution at Positions x = Const. – Comparison of Experiment and CFD Calculation for R_{mac} = 3 x 10^6, M = 0.4 and α = 13.3°.

In Figure 32-12 the situation at a Reynolds number of 3 x 10^6 is depicted. As mentioned before, enhancing the Reynolds number leads to a generation of the outer vortex further downstream. The flow around the leading edge is attached over the whole span up to 40% chord length. The suction peak at the leading edge at 20% chord length is predicted correctly when compared with the experiment whereas the suction peak at 40% is

predicted too high. The inner vortex occurs more upstream in the experiment as identified by the suction peak at 65% span wise position approximately. In the simulation there is no suction peak observed at this position. At 60% chord length the inner vortex suction peak can be observed, but it is weaker and further inboard as compared with the experiment. One reason for a weaker and more inboard suction peak of the outer vortex at 60% chord length might be related to the fact that the inner vortex in this case is generated too far upstream at the leading edge in comparison to the experiment. This can also be observed in Figure 32-9. The suction peak of the outer vortex is predicted too high at 80% and 95% chord length in the same way as in the case at a Reynolds number of 2×10^6. However the vortex occurs more upstream, although the span wise position is given correctly at 80% and 95% chord length. But this could be more or less fortuitous because the balance of the vortex strength between the inner and the outer vortex is very sensitive to several factors which will be discussed later on.

Due to the fact that there are several differences between the experiment and the simulation, some sensitivity factors that may influence the numerical solution should be discussed. These factors are, among others, the selected turbulence model, the angle of attack and Reynolds number effects. Finally, the effect of transition is a factor which could influence the flow topology. Even if it is not correct to compare CFD simulations with experimental results under different conditions, it should show that small changes in the flow field variables could have a large effect on the flow topology. Particularly we are not taking the wind tunnel surroundings into account within the CFD, which could have a big influence on the flow conditions [32-26]. In the following discussion some of these sensitivities will be discussed.

The Reynolds number effect was discussed previously. In Figure 32-13 the results at Reynolds numbers of 3×10^6 and 4.5×10^6 are compared. As described before, if we increase the Reynolds number the outer vortex occurs further downstream. Comparing the PSP results at Reynolds number 3×10^6 with the CFD solution at 4.5×10^6 in Figure 32-14 and Figure 32-15 it can be observed that the pressure distribution of the outer vortex fits better with the experiment than in the case of 3×10^6 Reynolds number. The outer vortex is generated at nearly the same position as in the experiment as seen in Figure 32-14. Figure 32-15 shows an even better agreement compared with the quantitative results. The suction peak of the outer vortex at 60% chord fits well with the experiment. Nevertheless, the inner vortex is too weak as well as in the direct comparison with the 3×10^6 Reynolds number simulation. But the location of the inner vortex in case 4.5×10^6 is more inboard and occurs further downstream which fits better with the experiment at 3×10^6. These results should show how sensitive the flow topology is to small Reynolds number changes.
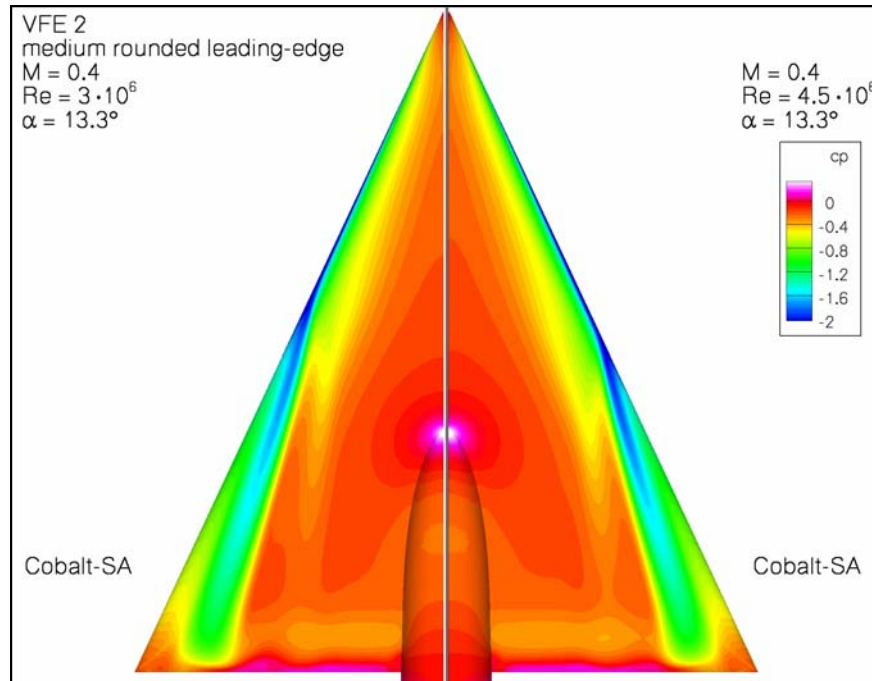
**Figure 32-13: Computed Pressure Distribution on the Upper Surface of the
Wing for R_{mac} = 3 x 10^6 (left) and 4.5 x 10^6 (right) at M = 0.4 and α = 13.3°.**
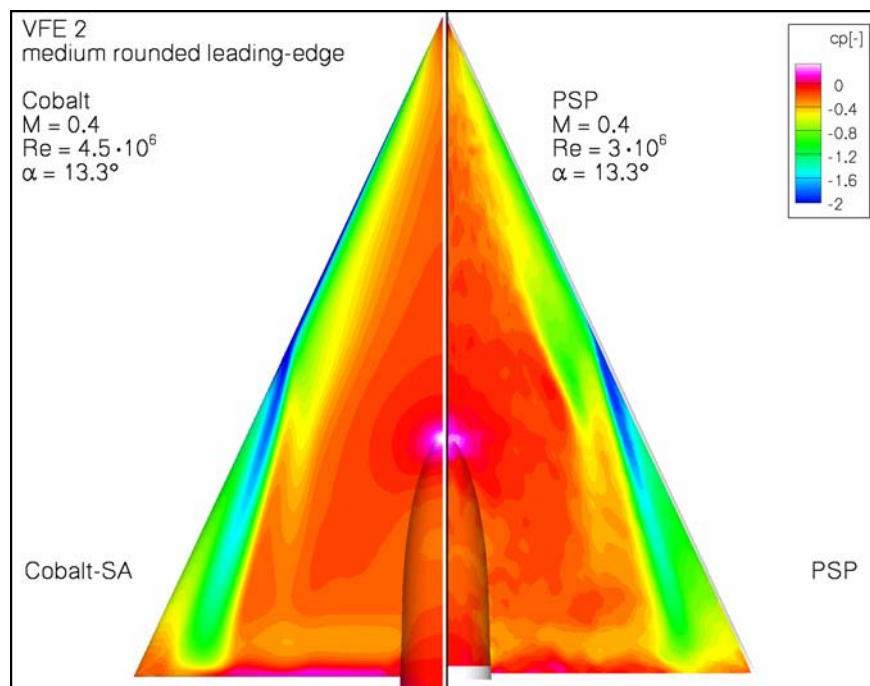
**Figure 32-14: Pressure Distribution on the Upper Surface of the Wing – Comparison of CFD
Calculation (R_{mac} = 4.5 x 10^6) and PSP Measurement (R_{mac} = 3 x 10^6) for M = 0.4 and α = 13.3°.**
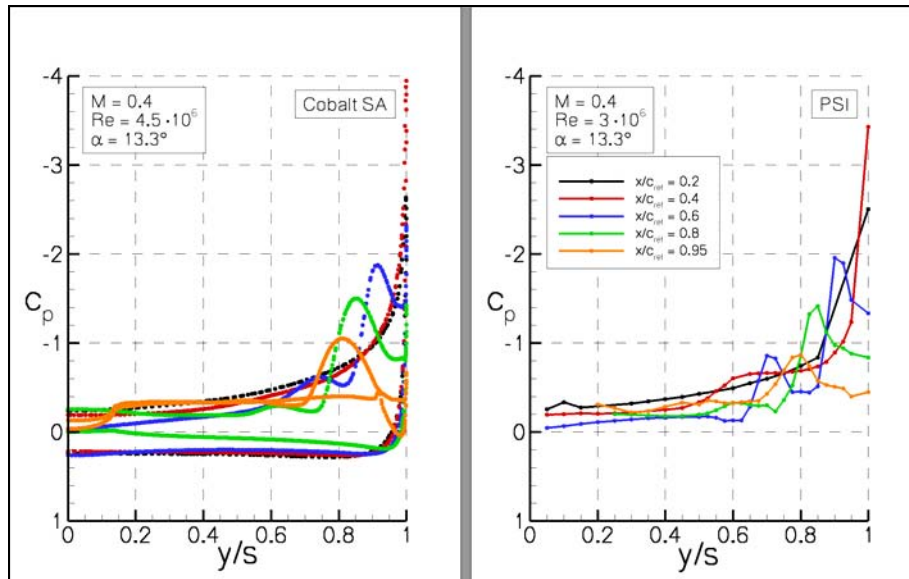
Figure 32-15: Pressure Distribution at Positions x = Const. – Comparison of CFD Calculation
(R_{mac} = 4.5 x 10^6) and Experiment (R_{mac} = 3 x 10^6) for M = 0.4 and α = 13.3°.

The simulations in Figure 32-16 at a Reynolds number of R_{mac} = 6 x 10^6 should give an example of the angle of attack effect on the flow topology over the wing. Compared to the Reynolds number effect, the effect of increasing the angle of attack yields the opposite result. Increasing the angle of attack causes the generation of the outer vortex to move upstream; the same thing happens to the inner vortex. Due to the outer vortex location and enhanced strength, the inner vortex is pushed further inboard. Figure 32-17, Figure 32-18, and Figure 32-19 show the comparison between PSI data on the left hand side and CFD calculation on the right hand side. For the experimental data, the spanwise data at y/s = 0.675 is quite sparse, which should be kept in mind while making comparisons. Comparing Figure 32-17 and Figure 32-18 for α = 13.3° and 18.4°, it can be observed in the experimental data that the suction peak of the inner vortex stays constant for increasing the angle of attack, even though the suction peak of the outer vortex grows. The same can be observed in the numerical simulation, but far more downstream. The outer vortex seems to occur too far downstream in the simulation. This leads to the fact that the suction peak of the inner vortex can be observed at x/c_{ref} = 0.8 for the angle of attack of α = 13.3° and at x/c_{ref} = 0.4 for the angle of attack of α = 18.4°. As with the other simulations discussed before, the strength of the inner vortex is given too weak by the simulation. Finally, the simulation at α = 23° fits quite well with the experiment since the flow topology is well established and less sensitive at this higher angle of attack, as shown in Figure 32-19.
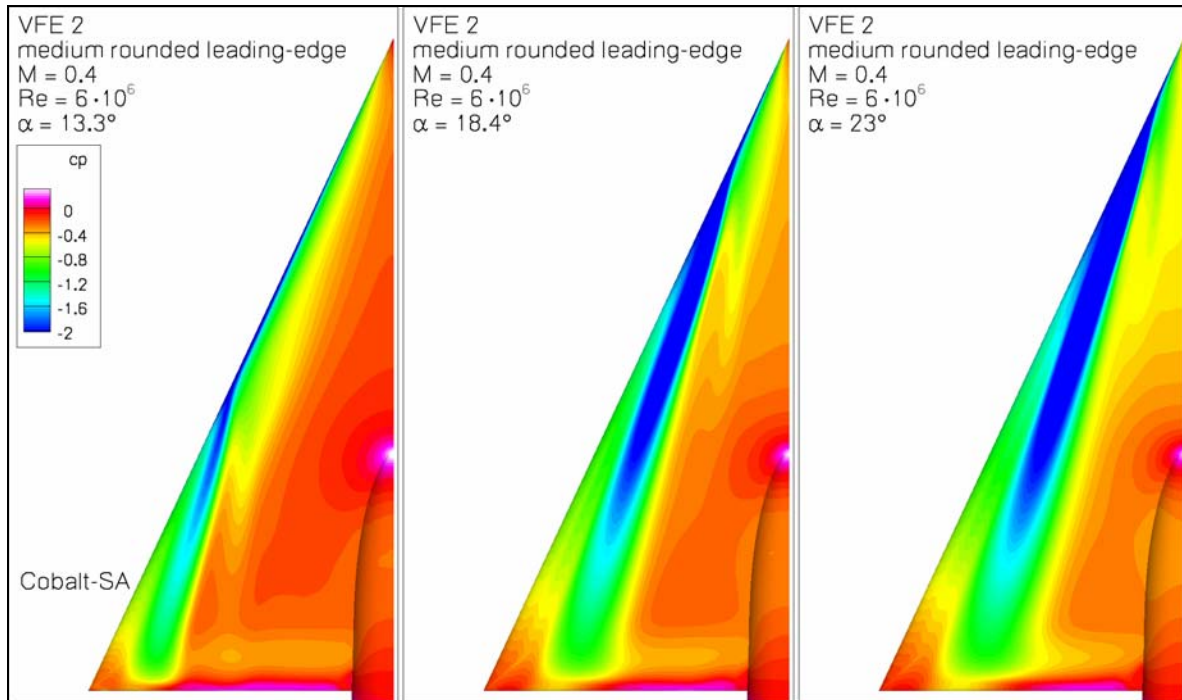
**Figure 32-16: Pressure Distribution on the Upper Surface of the Wing – Comparison
of CFD Simulations at Different Angles of Attack for $R_{mac} = 6 \times 10^6$ and M = 0.4.**
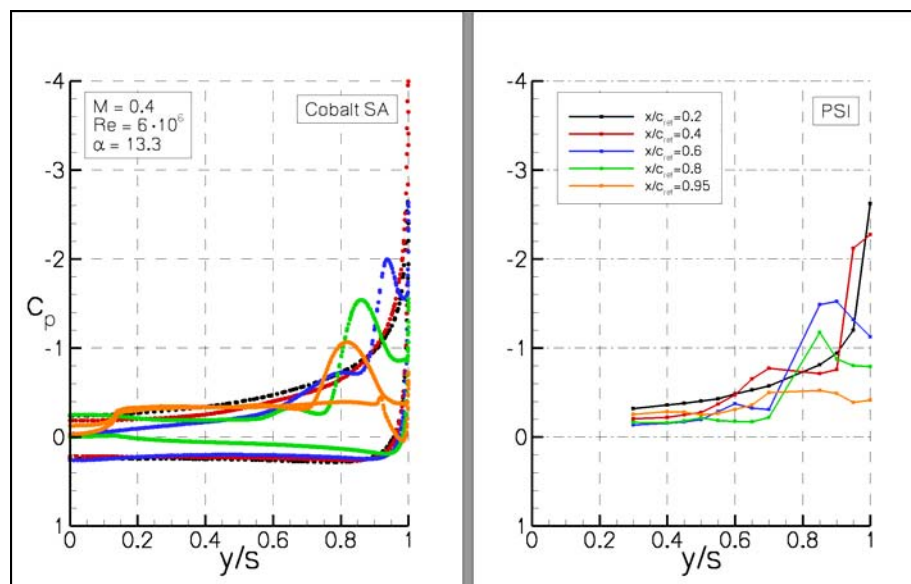
**Figure 32-17: Pressure Distribution at Positions x = Const. – Comparison of CFD
Calculation ($R_{mac} = 6 \times 10^6$) and Experiment ($R_{mac} = 6 \times 10^6$) for M = 0.4 and α = 13.3°.**
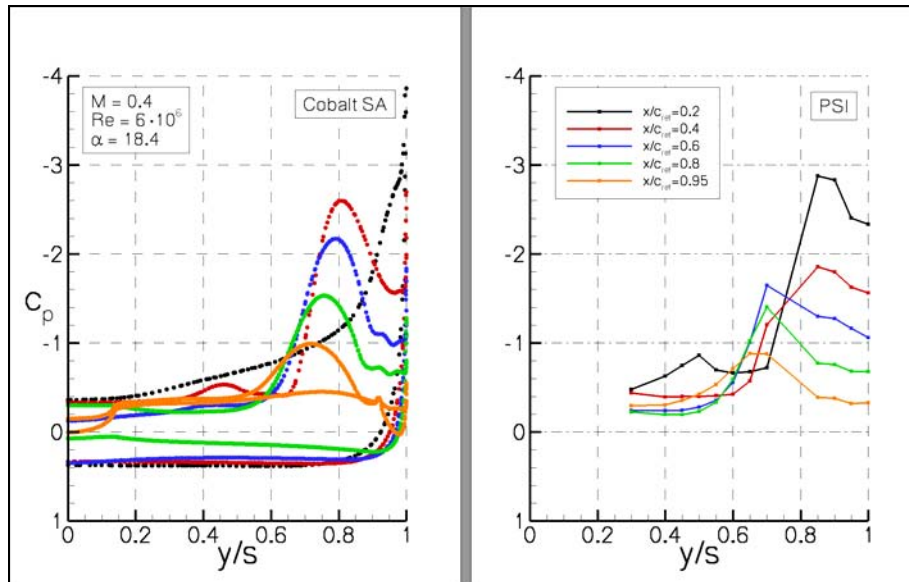
**Figure 32-18: Pressure Distribution at Positions x = Const. – Comparison of CFD
Calculation (R_{mac} = 6 x 10^6) and Experiment (R_{mac} = 6 x 10^6) for M = 0.4 and α = 18.4°.**
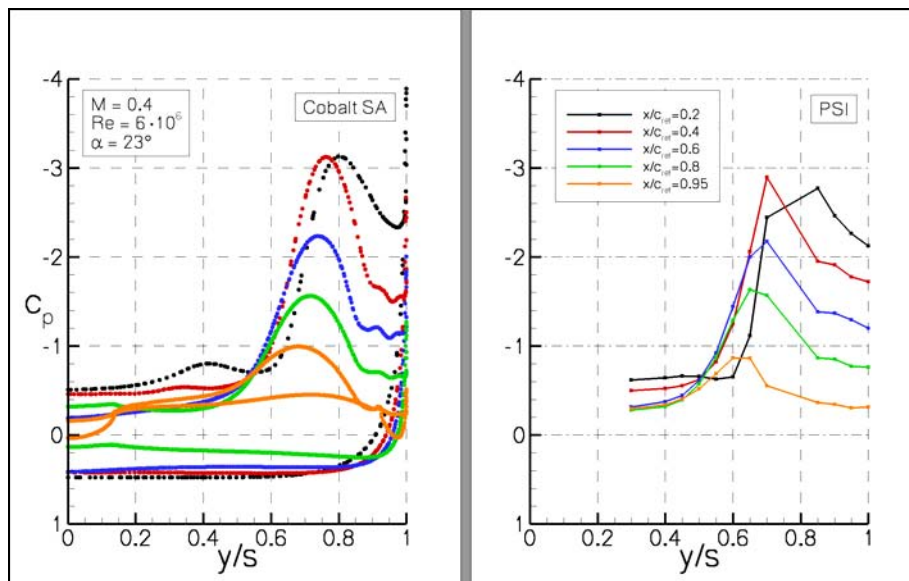
**Figure 32-19: Pressure Distribution at Positions x = Const. – Comparison of CFD
Calculation (R_{mac} = 6 x 10^6) and Experiment (R_{mac} = 6 x 10^6) for M = 0.4 and α = 23°.**

In nearly all computational simulations the inner vortex is predicted too weak and the question arises as to which boundary condition influences the generation of the inner vortex. For the final RANS simulation the production of turbulence is set to zero up to 10% of the centerline chord. Even though a real transition line is much more complicated on the delta wing surface, this transition line should show if there is an influence. Figure 32-20

shows the comparison of the pressure distribution between the case with and without transition. Besides the bending of the contour lines at the apex, no significant change in the overall pressure distribution can be observed. Regarding the pressure distribution in Figure 32-21, it can be observed that there is an effect of transition at 20% chord length. But there is no influence on the flow topology further downstream. The transition setting probably leads to a thicker boundary layer at the apex but is not influencing the generation of the inner vortex significantly. Furthermore, the implementation of the non-slip boundary condition in a region of high surface curvature might have an influence on the transition behavior and should be investigated.
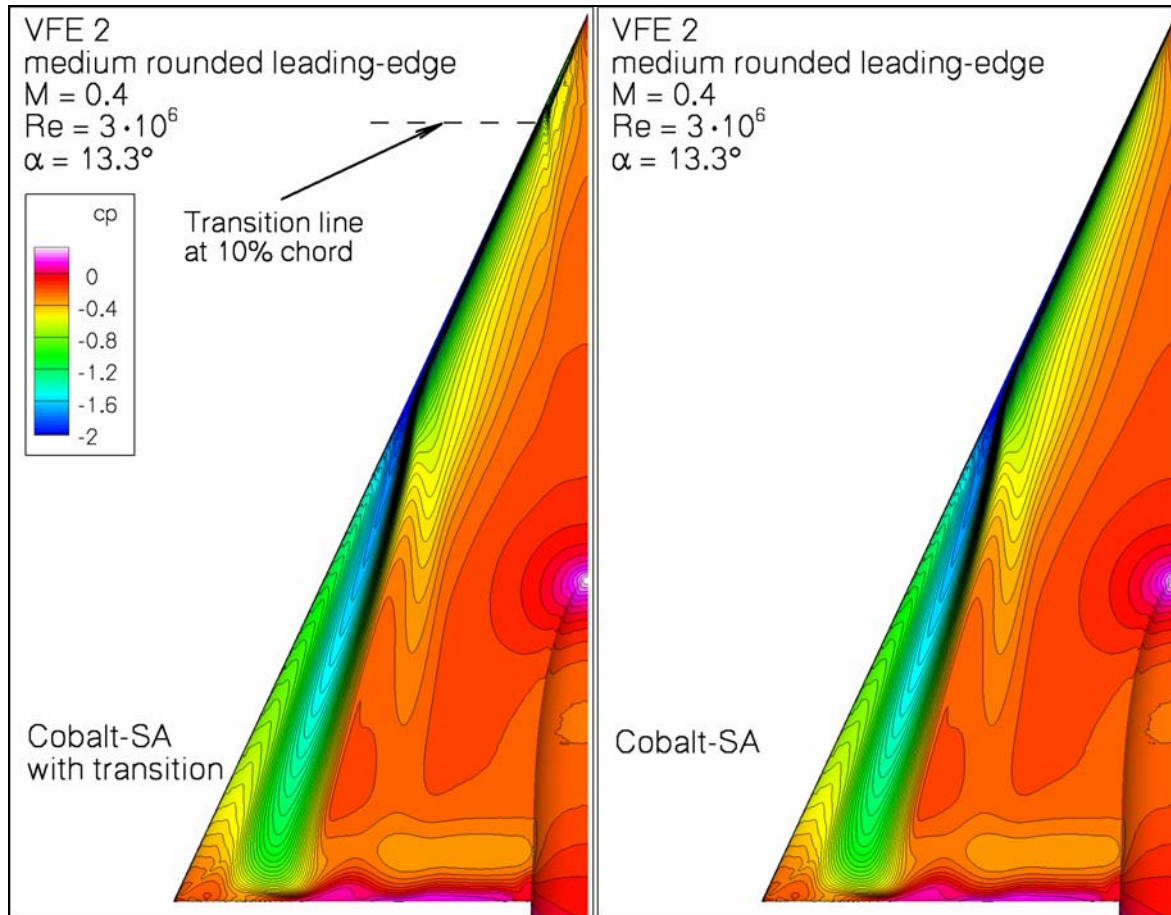
**Figure 32-20: Pressure Distribution on the Upper Surface of the Wing – Comparison of
CFD Calculation (R_{mac} = 3 x 10^{6}) With and Without Transition Line for M = 0.4 and α = 13.3°.**
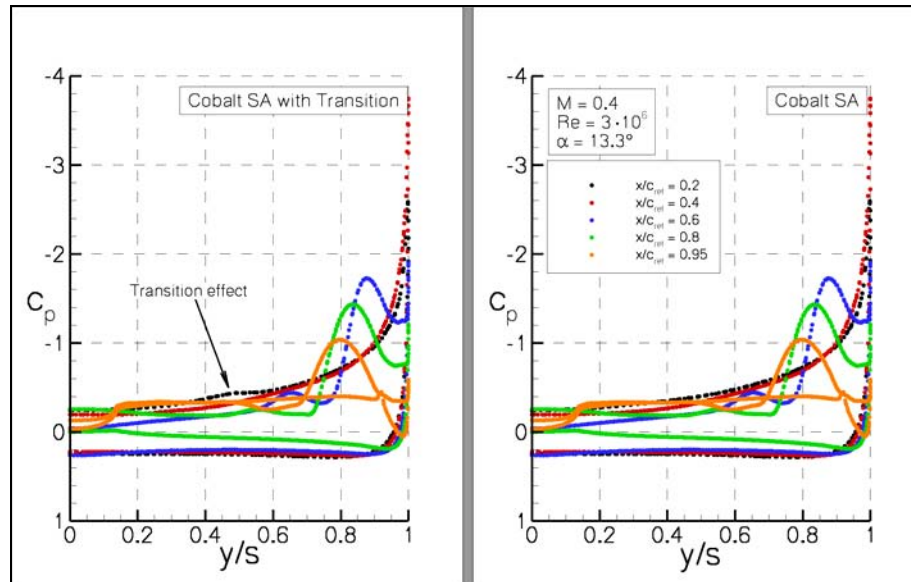
**Figure 32-21: Pressure Distribution at Positions x = Const. – Comparison of CFD
Calculation (R_{mac} = 3 x 10^6) With and Without Transition for M = 0.4 and α = 13.3°.**

32.5.3   DES and DDES Simulations

The use of Detached-Eddy Simulation (DES) has traditionally been reserved for massively separated, or at the very least, unsteady flow fields. Steady vortical flows are often well predicted with modern RANS turbulence models and often do not require the use of DES. The unusual nature of the flow around the blunt leading edge delta wing, however, makes the use of DES a possible candidate for flow prediction in this case. The shallow nature of the flow features on the front half of the wing (as seen in Figure 32-5), can give DES a difficult challenge, since flow features close to a surface can be poorly predicted with traditional DES, so Delayed Detached-Eddy Simulation (DDES) will also be used to simulate this flow.

The first simulation using DES is with the SA model with a Rotation Correction (SARC-DES). SARC has been shown to work well for vortical flows in conjunction with DES [32-26]. Surface pressures using SARC-DES are compared with experimental PSP measurements in Figure 32-22. The numerical simulation shows the inner and outer primary vortices forming too far upstream, and the outer vortex shows signs of unusual behaviour as the vortex wanders inboard and outboard as it convects toward the trailing edge. There is no evidence that the solution is unsteady except near the trailing edge, which does not explain the vortex wandering. Figure 32-23 shows a comparison of surface pressures with the PSI data, and the early formation of the vortices is confirmed. By 20% of the chord, the inner and outer vortices have formed, contrary to the experimental data which shows only early signs of the formation of the inner vortex at this chordwise station. Because the vortices form too early, the downstream position of both the inner and outer vortices is too far outboard, and the inner vortex is too weak when compared with the experimental data.
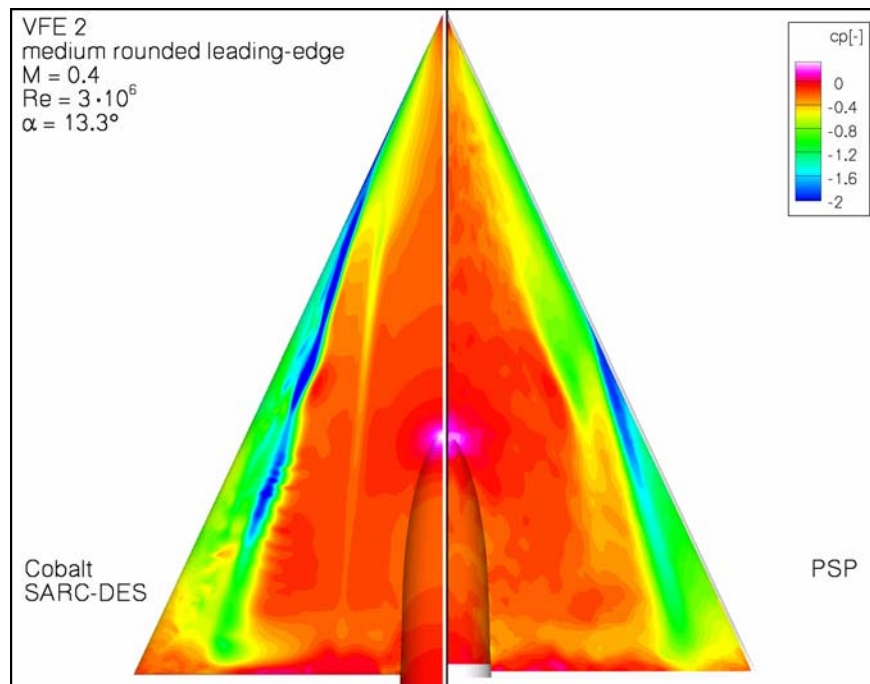
Figure 32-22: Pressure Distribution on the Upper Surface of the Wing – Comparison of CFD Calculation (SARC-DES) and PSP Measurement for R_{mac} = 3 x 10^6, M = 0.4 and α = 13.3°.
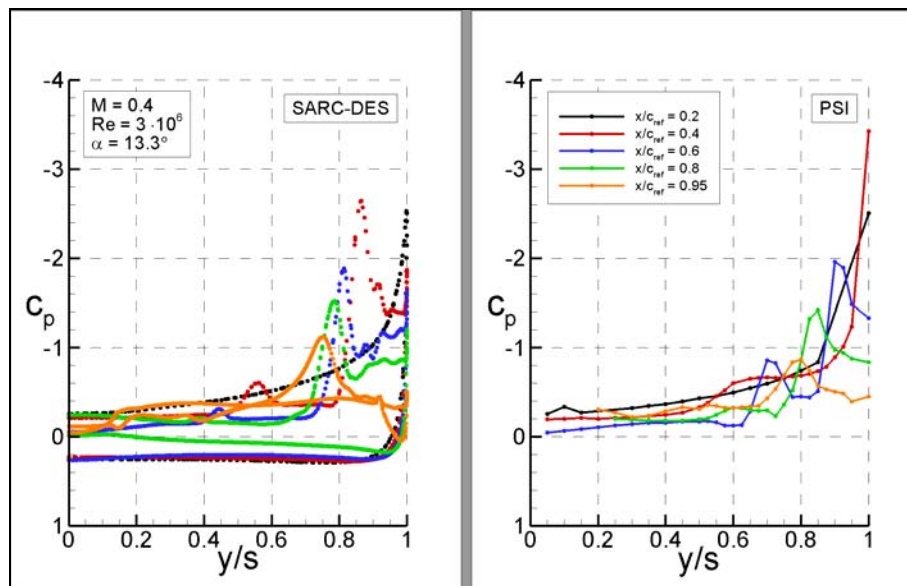
Figure 32-23: Pressure Distribution at Positions x = Const. – Comparison of CFD Calculation (SARC-DES) and Experiment for R_{mac} = 3 x 10^6, M = 0.4 and α = 13.3°.

Due to the shallow nature of the vortices (especially the inner vortex), it was decided to try DDES on this configuration in conjunction with SARC, as shown in Figure 32-24 and Figure 32-25. While the surface pressure map for SARC-DDES shown in Figure 32-24 is much better than the SARC-DES prediction in

Figure 32-22, the remainder of the prediction is in fact very similar to the SARC-DES prediction. The vortices again form too early (as shown in both Figure 32-24 and Figure 32-25) and the position and strength of the vortices are not greatly improved over the SARC-DES simulation.
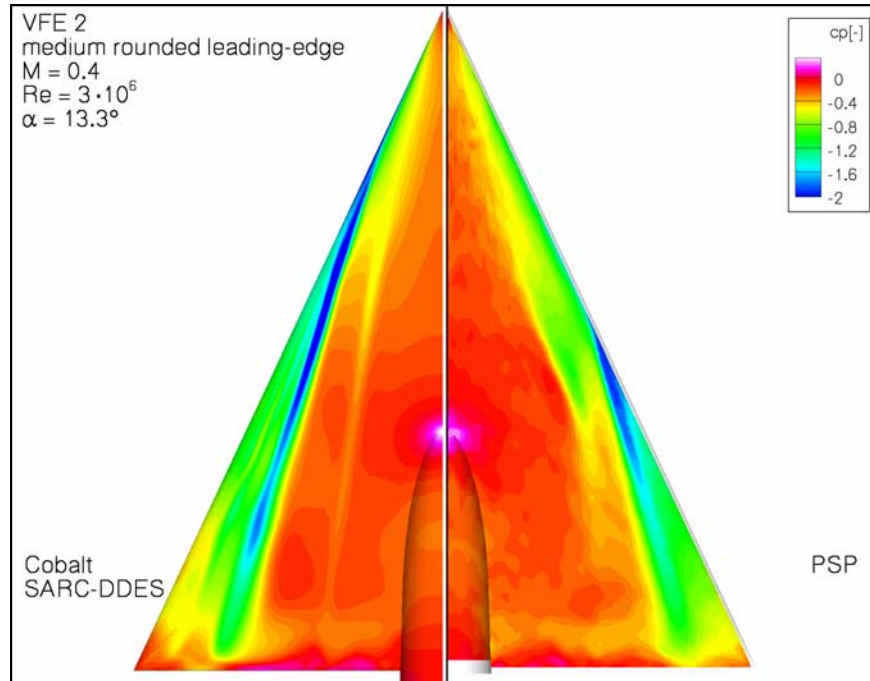
Figure 32-24: Pressure Distribution on the Upper Surface of the Wing – Comparison of CFD Calculation (SARC-DDES) and PSP Measurement for R_{mac} = 3 x 10^6, M = 0.4 and α = 13.3°.
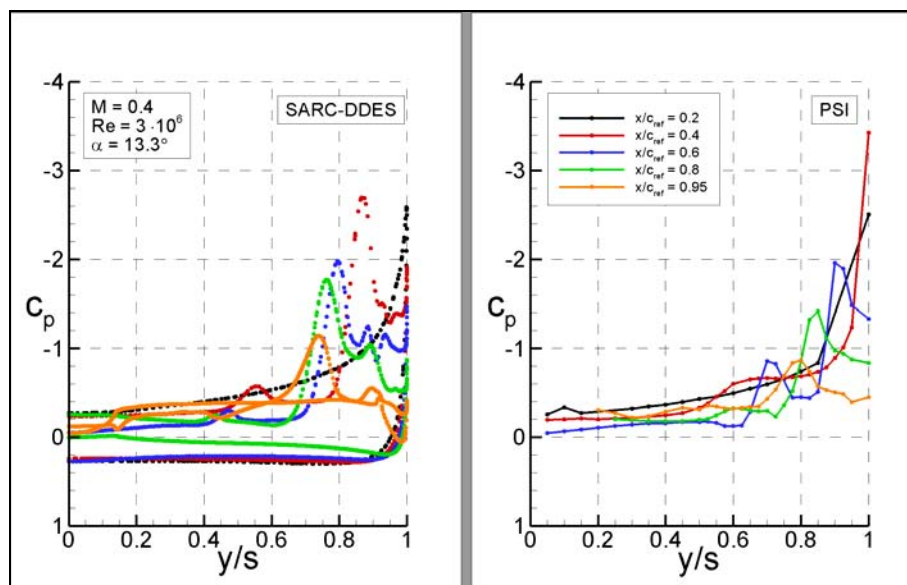
Figure 32-25: Pressure Distribution at Positions x = Const. – Comparison of CFD Calculation (SARC-DDES) and Experiment for R_{mac} = 3 x 10^6, M = 0.4 and α = 13.3°.

Since the previous applications of DES and DDES were not as successful as hoped, a further simulation was performed using the basic Spalart-Allmaras turbulence model (SA) in conjunction with DES (labelled SA-DES). The surface pressure map and pressure comparisons with experimental data are presented in Figure 32-26 and Figure 32-27, respectively. The surface pressure map in Figure 32-26 shows signs of the vortex wandering similar to the SARC-DES simulation in Figure 32-22. However, the surface pressures are in better agreement with the experimental data than the previous simulations. Specifically, Figure 32-27 shows that there is no significant vortex generation at $x/c_{ref} = 0.2$, although a region of decreased pressure is evident near $y/s = 0.4$, which is very similar to the experimental trend. Also, by $x/c_{ref} = 0.6$, both an inner and outer vortex have formed, although the secondary vortex near the leading edge is different than the experiment, and the location of the outer vortex is also incorrectly predicted. The inner and outer vortex positions are consistent as the flow convects downstream, with small differences in vortex strength and position noted.
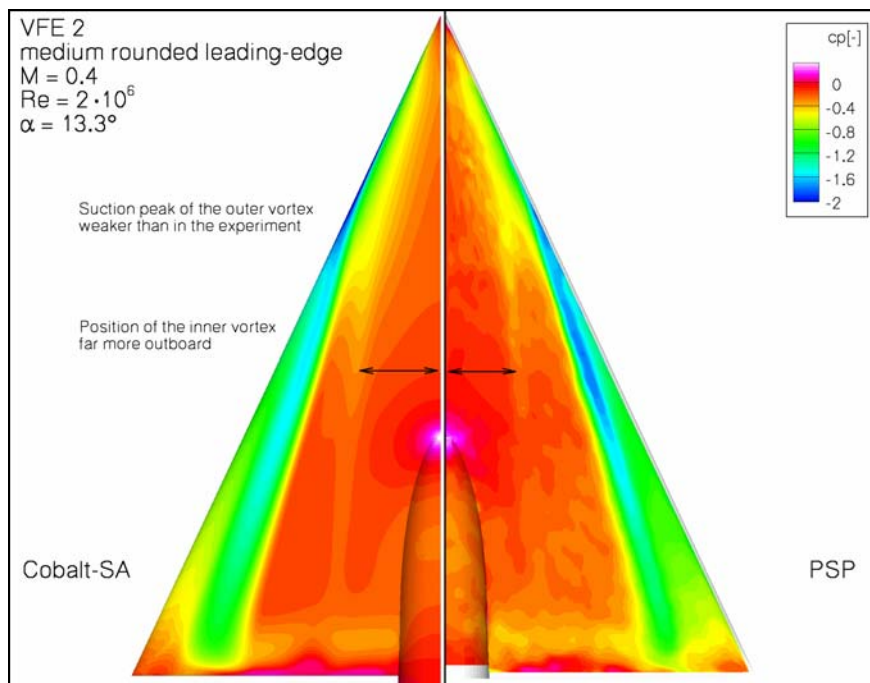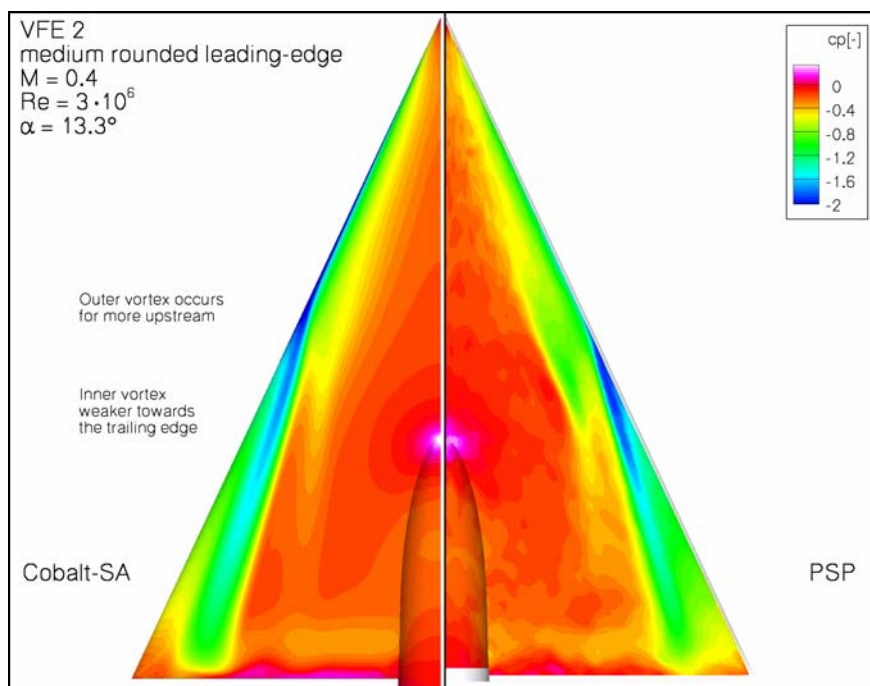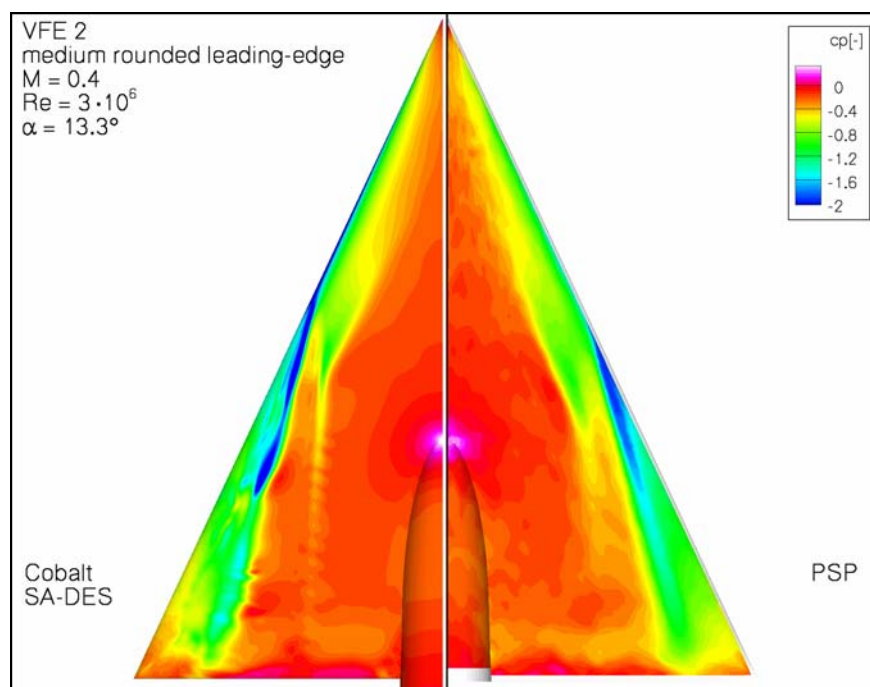

**Figure 32-26: Pressure Distribution on the Upper Surface of the Wing – Comparison of CFD
Calculation (SA-DES) and PSP Measurement for $R_{mac} = 3 \times 10^6$, M = 0.4 and α = 13.3°.**
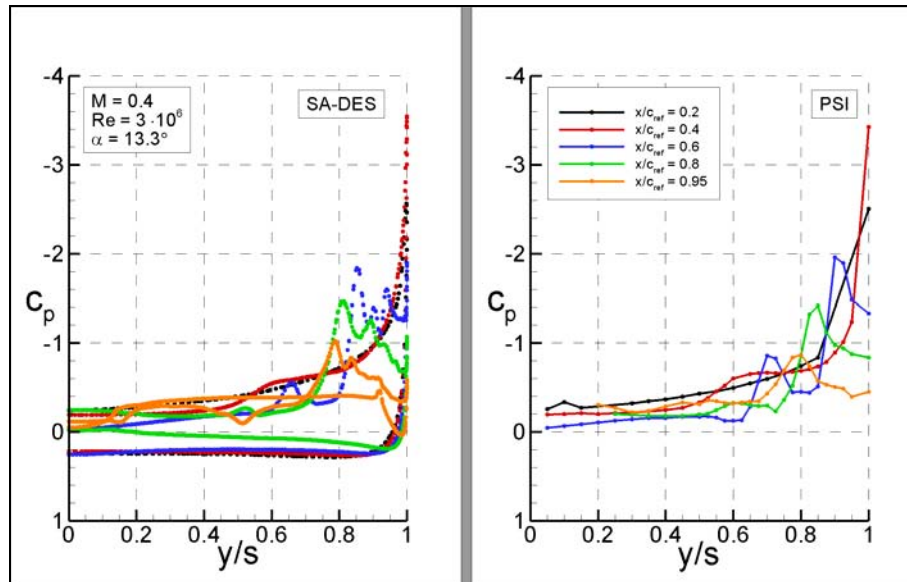
**Figure 32-27: Pressure Distribution at Positions x = Const. – Comparison of CFD
Calculation (SA-DES) and Experiment for R_{mac} = 3 x 10^6, M = 0.4 and α = 13.3°.**

The improvement shown by the SA-DES solution, coupled with the relative success of the SARC-DDES solution when compared with SARC-DES, led to a final simulation using SA-DDES. The surface pressure map for this case is shown in Figure 32-28, while the pressure comparison with experimental data is shown in Figure 32-29. The simulated flow field using SA-DDES is significantly improved over any of the other previous hybrid turbulence model simulations. The formation of the inner and outer vortices matches the experimental data quite well, and the position and strength of the vortices is as close to the experiment as with the other simulations presented. While the suction peak seems higher than the experimental data, the experimental pressure taps were fairly widely spaced in this region, making it difficult to determine the precise suction peak magnitude and location from the experiment. The main differences between the predictions and experimental data lie near the trailing edge of the delta wing, however the simulations showed that the vortices were unsteady in this region, and a sufficiently high time averaging may improve the predictions in this region. The SA-DDES model probably has performed the best because of the ability of DDES to properly transition from RANS to LES without being influenced by the local grid refinement, coupled with the relatively poor performance of SARC in the leading-edge region of the delta wing, where large flow curvature exists that is not associated with vortices.
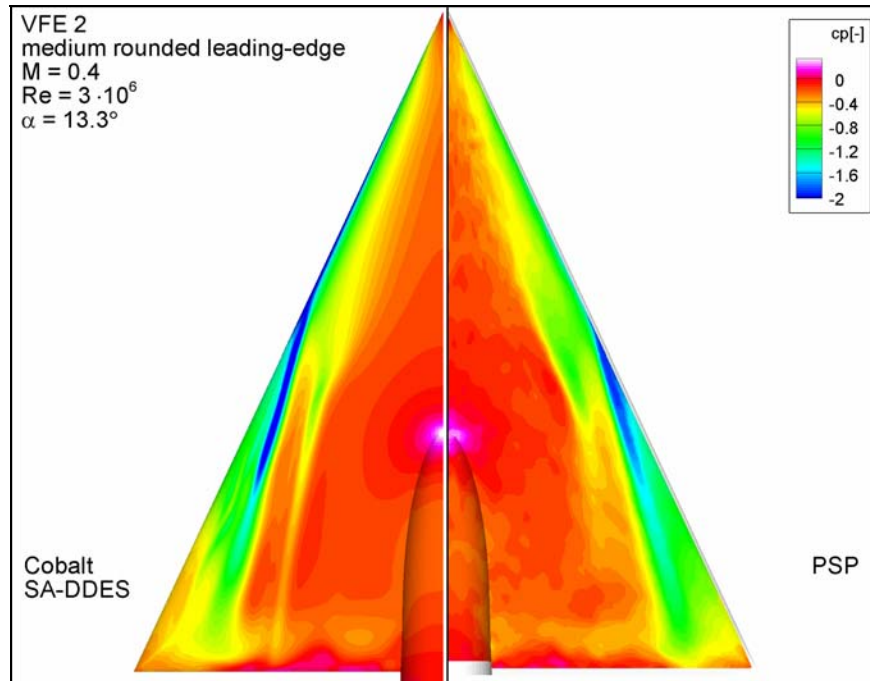
**Figure 32-28: Pressure Distribution on the Upper Surface of the Wing – Comparison of CFD
Calculation (SA-DDES) and PSP Measurement for $R_{mac} = 3 \times 10^6$, M = 0.4 and α = 13.3°.**
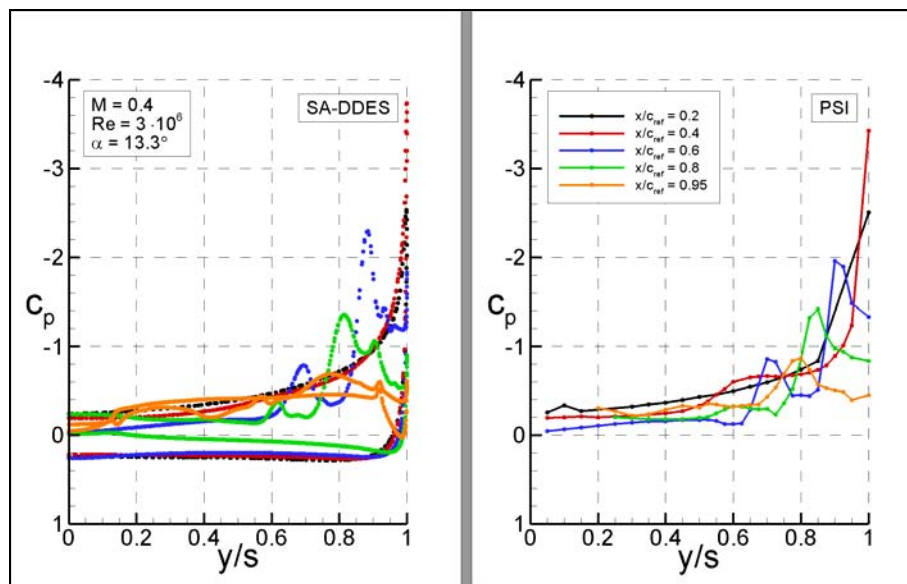
**Figure 32-29: Pressure Distribution at Positions x = Const. – Comparison of CFD
Calculation (SA-DDES) and Experiment for $R_{mac} = 3 \times 10^6$, M = 0.4 and α = 13.3°.**

32.5.4   Discussion of Flow Topology

The rounded leading-edge delta wing yields an interesting and complex flow topology which is only marginally understood at this time. While the experimental results shown in Figure 32-5 are helpful in understanding the flow, the necessary limitations of the experiments (such as the number of axial locations where PIV measurements were made) make it difficult to fully understand the flow field. The experimental predictions, in conjunction with the numerical simulations, can begin to form a fuller picture of the flow.

Figure 32-30 and Figure 32-31 show the SA-DDES solution of the flow field with surface pressure maps, x-vorticity contours, and streamlines. Figure 32-32 shows the skin friction lines for the flow, which adds another layer of information for understanding what is happening with this configuration. The x-vorticity contours in Figure 32-30 show that a region of vorticity near the surface of the delta wing exists at $x/c_{ref} = 0.2$. This is the same region that was noted upstream of the formation of the inner and outer vortices in previous simulations using RANS and SA-DES. Examination of the flow in the region of vorticity at $x/c_{ref} = 0.2$ has shown that there is no reversed flow present, and no noticeable boundary layer separation has taken place. Further investigation into the boundary layer profile at $x/c_{ref} = 0.2$ might aid in a fuller understanding of the flow topology. At $x/c_{ref} = 0.4$ the two primary vortices have clearly formed, but it is not obvious which vortex formed first and how the formation of the vortices is impacted by the upstream low pressure/higher vorticity region. Figure 32-31 shows the streamlines created by releasing particles near the surface along the leading edge of the delta wing. Flow around the apex and near the centerline of the wing stays attached along the entire length of the wing, but after a short distance along the leading edge a shear layer forms that eventually rolls up into the inner vortex. Between these two flows there is a region where flow near the surface travels under the shear layer and passes toward the leading edge. There is a critical point along the leading edge where the separating flow no longer feeds the inner vortex, but rather begins to feed the outer vortex. Since the inner vortex is no longer being fed vorticity from the leading edge shear layer, it does not continue to grow in size or strength as it convects downstream. The outer vortex, however, continues to gain vorticity from the shear layer and grows in size and strength down the remainder of the delta wing length.
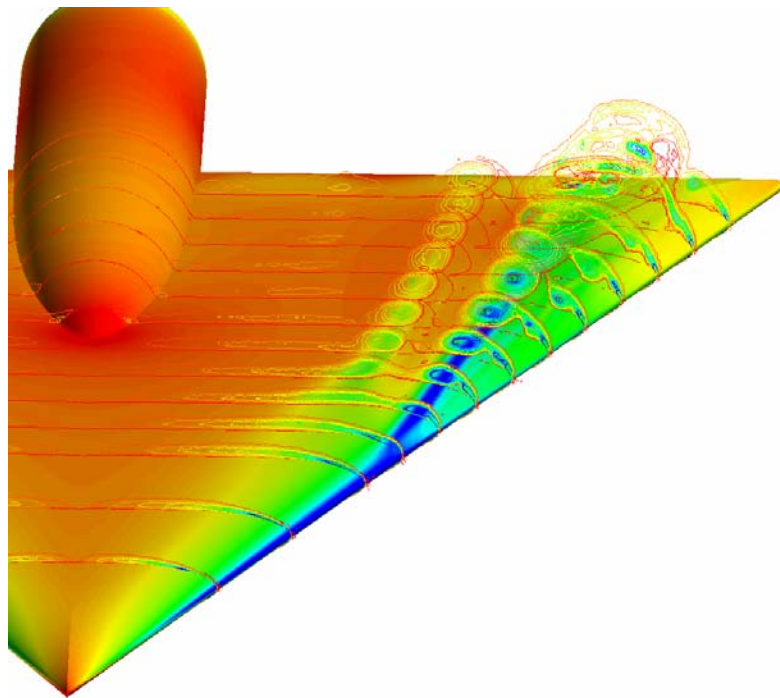
**Figure 32-30: Surface Pressure Distribution and x-Vorticity at
Positions x = Const. for R_{mac} = 3 x 10^6, M = 0.4 and α = 13.3°.**
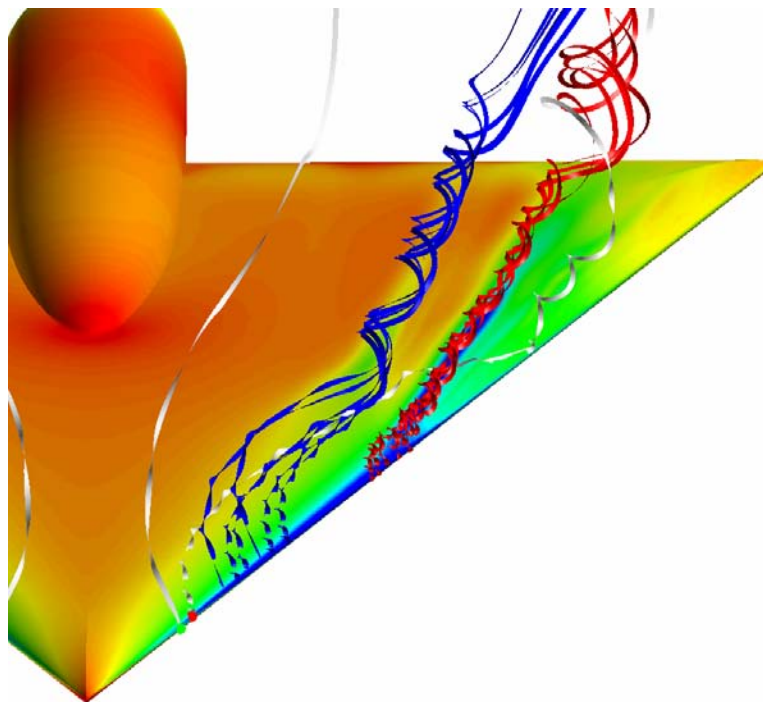
Figure 32-31: Surface Pressure Distribution and Streamlines for R_{mac} = 3 x 10^6, M = 0.4 and α = 13.3°.
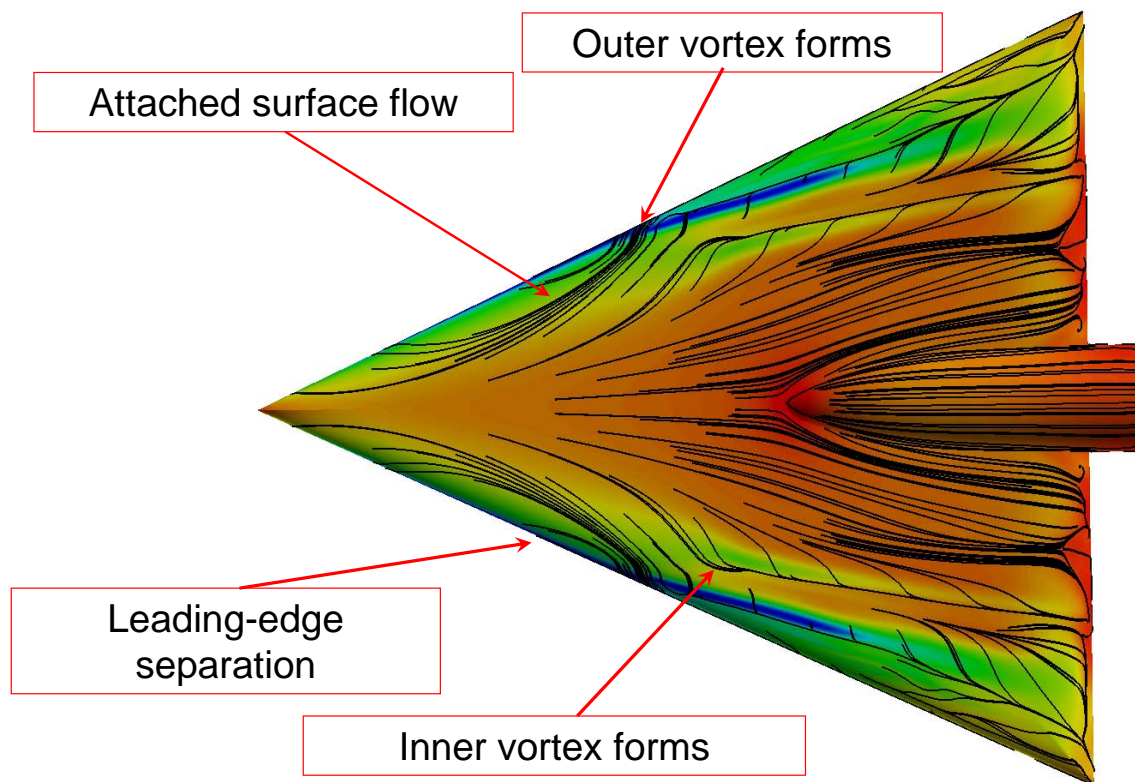
Figure 32-32: Skin Friction Lines and Surface Pressure Distribution – R_{mac} = 3 x 10^6, M = 0.4 and α = 13.3°.

The combined information from Figure 32-30 and Figure 32-31, coupled with the skin friction lines of Figure 32-32, shows a more comprehensive picture of the formation of the dual primary vortex system. A separation line is evident along the leading edge, but it does not extend to the apex of the wing. This coincides with the attached flow along the centerline of the wing. Once the separation line forms, a shear layer convects over the upper surface of the delta wing. A region of flow near the wing surface, corresponding to the region of lower pressure/higher vorticity mentioned above, is diverted outboard to the location where the outer primary vortex is formed. The outboard flow is possibly caused by the rotation of the shear layer that is flowing above this region; the shear layer eventually rolls up into the inner primary vortex. It is possible that the surface flow which is forced outboard is the cause of the critical point where the outer primary vortex is formed, although more detailed investigation is warranted to more fully understand this complex flow region.

32.6   CONCLUSIONS

In this paper the results of CFD calculation with the unstructured Cobalt code are presented. Numerical simulations for flow around a rounded leading-edge delta wing with 65° of sweep are performed using RANS, DES, and DDES turbulence models. Comparisons with available experimental data, including surface pressures, pressure sensitive paint, and particle image velocimetry, show that a reasonable simulation of this flow field can be made with RANS turbulence models, although the SA-DDES model showed promise for gaining a fuller understanding of the flow field. As usual, researchers should use the level of modeling that is appropriate for the level of detail required for a given application; the expense and computer resources required for hybrid turbulence models may not be warranted for every application.

The numerical simulations have led to an increased understanding of the flow field for the round leading-edge delta wing, especially for the formation of the dual primary vortex system. A proposed mechanism for the formation of the dual primary vortex system is given based on various surface and off-surface flow visualizations. A complex flow topology exists due to the rounded leading edge, including an initial shear layer that induces flow underneath the formation of the inner vortex that eventually causes the inner vortex to be cut off from the shear layer. This leads to the formation of the outer primary vortex, while the inner primary vortex is cut off from the shear layer and stops growing in size or strength.

Designers of various aircraft that might use rounded leading edges on highly swept wings (such as UCAVs) will have to more fully understand the complexities of the dual primary vortex system, and how the vortex system is influenced by sweep angle, leading edge radius, and freestream conditions (such as Reynolds number, Mach number, and angle of attack).

32.7   ACKNOWLEDGEMENTS

32.8   REFERENCES

[32-1]   Drougge, G.: *The International Vortex Flow Experiment for Computer Code Validation*, ICAS Proceedings, Vol. 1, 1988, pp. 35-41.

[32-2]   Elsenaar, A., Hjelmberg, L., Bütefisch, K.-A. and Bannink, W.J.: *The International Vortex Flow Experiment*, AGARD-CP-437, Vol. 1, 1988, pp. 9-1 to 9-23.

[32-3]   Wagner, B., Hitzel, S., Schmatz, M.A., Schwarz, W., Hilgenstock, A. and Scherr, S.: *Status of CFD Validation on the Vortex Flow Experiment*, AGARD-CP-437, Vol. 1, 1988, pp. 10-1 to 10-10.

[32-4]   Hoeijmakers, H.W.M.: *Modelling and Numerical Simulation of Vortex Flow in Aerodynamics*, AGARD-CP-494, 1991, pp. 1-1 to 1-46.

[32-5]   Luckring, J.M.: *Recent Progress in Computational Vortex-Flow Aerodynamics*, AGARD-CP-494, 1991, pp. 6-1 to 6-21.

[32-6]   Hummel, D.: *Zur Umströmung scharfkantiger schlanker Deltaflügel bei großen Anstellwinkeln*, Z. Flugwiss, Vol. 15, 1967, pp. 376-385.

[32-7]   Hummel, D.: *Experimentelle Untersuchung der Strömung auf der Saugseite eines Deltaflügels*, Z. Flugwiss, Vol. 13, 1965, pp. 247-252.

[32-8]   Hummel, D.: *Effects of Boundary Layer Formation on the Vortical Flow Above Slender Delta Wings*, Journal of Aerospace Engineering, Vol. 220, No. 6, 2006, pp. 559-568.

[32-9]   Hummel, D. and Redeker, G.: *A New Vortex Flow Experiment for Computer Code Validation*, RTO-AVT Symposium on "Vortex Flow and High Angle of Attack", Loen Norway, May 7-11, 2001.

[32-10] Londenberg, W.K.: *Transonic Navier-Stokes Calculations about a 65 deg Delta Wing*, NASA CR 4635, November 1994.

[32-11] Chiba, K. and Obayashi, S.: *CFD Visualization of Second Primary Vortex Structure on a 65-Degree Delta Wing*, AIAA Paper 2004-1231, January 2004.

[32-12] Strang, W.Z., Tomaro, R.F. and Grismer, M.J.: *The Defining Methods of Cobalt: A Parallel, Implicit, Unstructured Euler/Navier-Stokes Flow Solver*, AIAA Paper 99-0786, January 1999.

[32-13] Centaur Soft: http://www.Centaursoft.com.

[32-14] Spalart, P.R. and Allmaras, S.R.: *A One Equation Turbulence Model for Aerodynamic Flows*, La Recherche Aerospatiale, Vol. 1, 1994, pp. 5-21.

[32-15] Spalart, P.R. and Shur, M.L.: *On the Sensitization of Turbulence Models to Rotation and Curvature*, Aerospace Science and Technology, Vol. 1, No. 5, 1997, pp. 297-302.

[32-16] Knight, D.D. and Saffman, P.C.: *Turbulence Model Predictions for Flows with Significant Mean Streamline Curvature*, AIAA Paper 78-0258, January 1978.

[32-17] Shur, M.L., Strelets, M.K., Travin, A.K. and Spalart, P.R.: *Turbulence Modeling in Rotating and Curved Channels: Assessing the Spalart-Shur Correction*, AIAA Journal, Vol. 38, No. 5, 2000, pp. 784-792.

[32-18] Spalart, P.R., Jou, W-H., Strelets M. and Allmaras, S.R.: *Comments on the Feasibility of LES for Wings, and on a Hybrid RANS/LES Approach*, Advances in DNS/LES, 1st AFOSR Int. Conf. on DNS/LES, August 4-8, 1997, Greyden Press, Columbus OH.

[32-19] Forsythe, J.R., Hoffmann, K.A. and Dieteker, F.F.: *Detached-Eddy Simulation of a Supersonic Axisymmetric Base Flow with an Unstructured Flow Solver*, AIAA Paper 2000-2410, June 2000.

[32-20] Spalart, P.R., Deck, S., Shur, M.L., Squires, K.D., Strelets, M.K. and Travin, A.: *A New Version of Detached-Eddy Simulation, Resistant to Ambiguous Grid Densities*, Theoretical and Computational Fluid Dynamics, Vol. 20, 2006, pp. 181-195.

[32-21] Spalart, P.R.: *Young Person's Guide to Detached-Eddy Simulation Grids*, NASA CR 2001-211032, July 2001.

[32-22] Chu, J. and Luckring, J.M.: *Experimental Surface Pressure Data Obtained on 65° Delta Wing Across Reynolds Number and Mach Number Ranges*, NASA TM 4645, Vols. 1-4, 1996.

[32-23] Konrath, R., Klein, C., Engler, R.H. and Otter, D.: *Analysis of PSP Results Obtained for the VFE-2 65° Delta Wing Configuration at Sub- and Transonic Speeds*, AIAA Paper 2006-0060, January 2006.

[32-24] Klein, C., Sachs, W.E., Henne, U., Engler, R.H., Wiedemann, A. and Konrath, R.: *Development of PSP Technique for Application on the VFE-2 65° Delta Wing Configuration*, AIAA Paper 2006-0059, January 2006.

[32-25] Konrath, R., Schröder, A. and Kompenhans, J.: *Analysis of PIV Results Obtained for the VFE-2 65°
Delta Wing Configuration at Sub- and Transonic Speeds*, AIAA Paper 2006-3003, June 2006.

[32-26] Mitchell, A.M., Morton, S.A., Forsythe, J.R. and Cummings, R.M.: *Analysis of Delta-Wing
Substructures Using Detached-Eddy Simulation*, AIAA Journal, Vol. 44. No. 5, 2006, pp. 964-972.

Chapter 33 – SEMI-EMPIRICAL PREDICTION OF VORTEX ONSET ON THE VFE-2 CONFIGURATION

by

Raj K. Nangia

ABSTRACT

This paper, via the initiative of the RTO-AVT Task Group AVT-113, is concerned with the VFE-2 theoretical and experimental activities on a series of 65° delta wings with different leading edge bluntness (sharp, small, medium and large radius). Experimental results have included independent sweeps of Mach and Reynolds number in the NTF wind tunnel.

Onset of vortical flow is predicted on the basis of semi-empirical attained leading edge thrust considerations. The approach based originally on Carlson's work at NASA, also incorporates centre section and wing tip modifications of the sheared wing concept according to Kuchemann.

Flow is assumed to be attached in regions with predicted LE suctions below the criteria developed from 2-D suction limits. Where the predicted LE suctions are above the criteria, the flow is assumed to be separated and this allows the determination of onset of vortical flow that is handled, using Polhamus LE suction analogy.

The method has been applied to all VFE-2 configurations. Results are compared with experimental data from NASA and ONERA Tests. Good agreement has been obtained for small and medium radius LE.

The vortex onset information together with a knowledge of forces, moments and loadings provides an understanding for either exploitation or avoidance in the wider design perspective. This is an important motivation.

33.1   NOMENCLATURE

AR or A	Aspect Ratio
B = 2 s	Wing span
c	Local Wing Chord (streamwise x direction)
$c_{av} = c_{ref} = S/b$	Mean Geometric Chord
$\bar{c} = c_{bar}$	Mean Aerodynamic Chord
c_n	Normal chord, effective, see Figure 33-23
c_r	Root chord
c_t	Tip chord (0 for deltas)
C_A = Axial force/(q S)	Axial Force Coefficient
C_{AL}	Local Axial Force Coefficient
C_D or C_{Di}	Lift-induced Drag Force/(q S), Lift-induced Drag Coefficient
C_{DL}	Local Lift-induced Drag Coefficient

CG	Centre of Gravity
C_L = Lift Force/(q S)	Lift Coefficient
C_{LL}	Local Lift Coefficient
C_{TL}	Local Thrust Coefficient, normal to LE
C_p	Coefficient of Pressure
C_{pcrit}	Sonic C_p
C_{plim}	Limiting C_p
C_{pvac}	Vacuum limit on C_p
c_t = LE	Thrust in chordwise direction, in certain figures due to Carlson, e.g. Figure 33-13
$c_{t,n}$ = C_{TL}	Coefficient of LE Thrust, normal to LE
dt	Parameter for delay in onset of flow separation due to thickness
$k = \pi A\, C_{Di} / C_L^2$	Lift Induced Drag Factor
$K_T = C_{plim}/C_{pvac}$	Thrust Factor
LE, TE	Leading Edge, Trailing Edge
M	Mach Number
M_n	Mach Number normal to LE
$q = 0.5\, \rho\, V^2$	Dynamic Pressure, ρ Air Density
$r = r_{le}$	LE radius in streamwise direction
r_n	LE radius normal to LE
Re	Reynolds Number, based on c_{av}
$R_n = R_{mac}$	Reynolds Number, based on mean aerodynamic chord as used by Luckring, 6 million and 60 million
R_n	Reynolds Number, based on c_n (chord normal to LE), used only in Sections 33.3.2 and 33.3.3, and Figure 33-16 – Figure 33-23
s, S	Semi-span, Wing Area respectively
t	Local maximum thickness along chord
t_n	Local maximum thickness in direction, normal to LE
t/c	Local thickness/chord ratio at a spanwise station
x,y,z	Orthogonal co-ordinates
x_m	Position of maximum thickness along chord
x_v,y_v	Position of vortex onset
V	Free-stream Velocity
α	AoA, Alpha, Angle of Attack
α_{BD}	AoA, Alpha, Angle of Attack for Vortex Breakdown onset at Trailing Edge
ß	Sideslip angle
γ	Ratio of specific heat constants for flow medium, γ = 1.4 for air
Λ	LE Sweep Angle
$\eta = y/s$	Non-dimensional spanwise distance

33.2   INTRODUCTION AND BACKGROUND

For highly manoeuvrable or advanced aircraft, manned / unmanned, it is imperative to understand the onset of wing vortex flows and their breakdown and the prospects of controlling them [33-1]. The applications are to military and civil type wings featuring moderate to high sweep.

An understanding of vortex flows in symmetric and asymmetric flow is required from the viewpoint of control and also, for example, the design of LE / TE devices**.** We need qualitative and quantitative information on vortex flows, e.g. forces, moments and loadings so as to either exploit them or avoid them, e.g. by using camber and twist. This design perspective is an important motivation from our viewpoint.

The challenge seen here is to predict forces and moments on a wing-body (deltas and swept tapered wings, cambered, rounded LE) operating in symmetric or asymmetric conditions throughout a full α range with Mach and Reynolds number effects. Furthermore, a quick turn-around is needed to cope with many geometric and flow variables.

The RTO-AVT has been interested in vortex flows and a recent task group, involving several countries and researchers, was the AVT-080 [33-2]. Our part of the work for that group was reported for wider circulation in Refs. [33-2], [33-3].

This Paper is motivated via the initiative of the RTO-AVT Task group AVT-113. One of the tasks (VFE-2) is concerned with theoretical and experimental activities on a series of 65° delta wings with differing LE bluntness, initiated by Luckring at NASA LaRC [33-4]-[33-6].

The NASA delta wing (Figure 33-1) with one sharp and three rounded leading edge geometries (Figure 33-2) has been tested at the NASA Langley NTF facility (Figure 33-3) at various Mach and Reynolds number combinations. Recently the model was tested in the DNW Transonic Wind Tunnel (TWG) at DLR Goettingen, in the low speed facilities at ONERA Lille and also in the Turkish facilities at Ankara. The model has non-standard aerofoil sections. Figure 33-4 shows the effective semi-span t/c and r/c distributions.

(a) Model Installed in NTF   (b) Instrumentation Layout
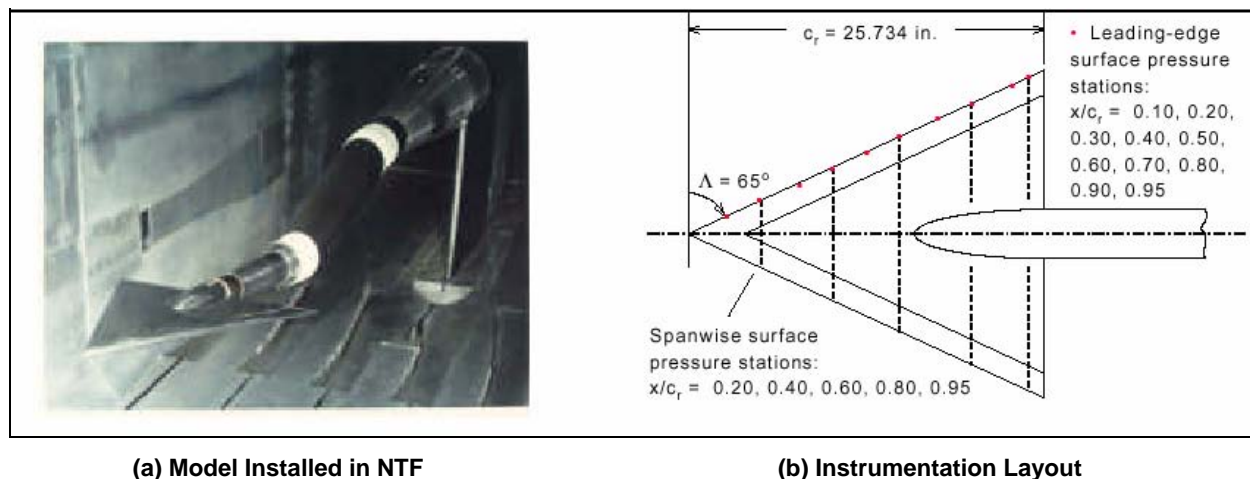
Figure 33-1: NTF 65° Delta Wing (Luckring).
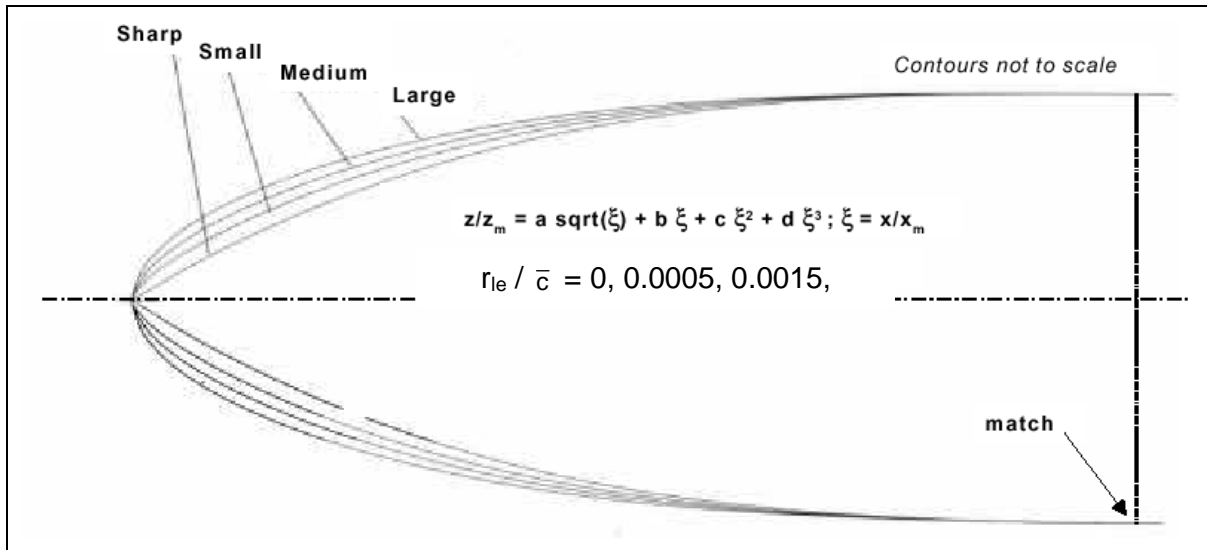
Figure 33-2: Streamwise Leading-Edge Contours for NTF Delta Wings (Luckring).
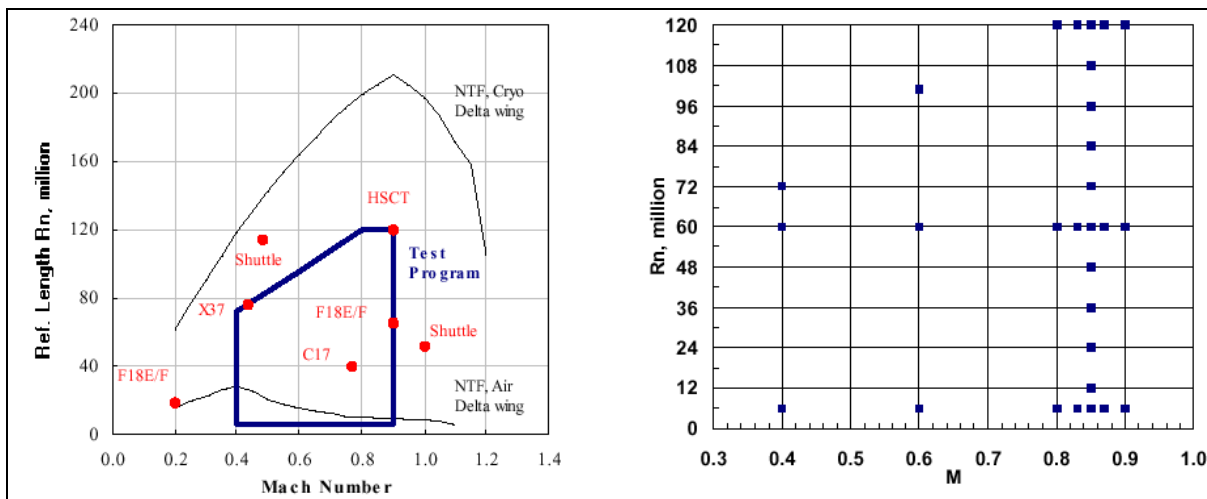
(a) NTF Envelopes and Aircraft Operation   **(b) Representative Delta-Wing Test Matrix**

Figure 33-3: Reynolds Number and Mach Number Conditions (NASA LaRC, Luckring).
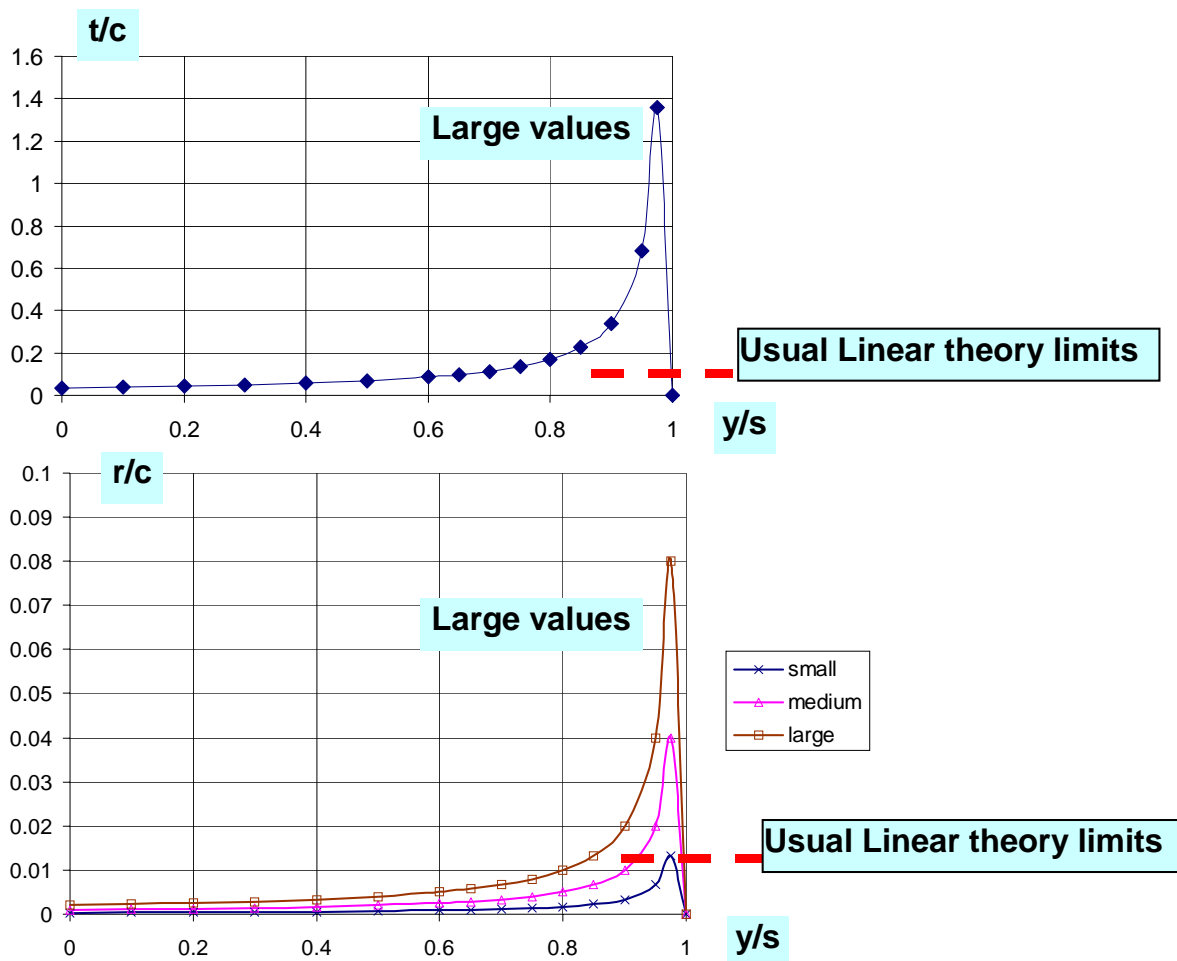
Figure 33-4: Delta Wing, t/c and r/c Variations with y/s for Rounded Edge Models.

From the NASA results (Luckring, Refs. [33-4]-[33-6], all wings), Figure 33-5-Figure 33-8 depict the position of onset of vortical flow, x_v measured from the wing apex, as a function of angle of attack (AoA or α), Mach number and Reynolds number (2 settings, R_{mac} = 6 million & 60 million, based on mean aerodynamic chord). The model geometries and results are reviewed and discussed in more detail in Section 33.4.

R_{mac} = 6 million

R_{mac} = 60 million
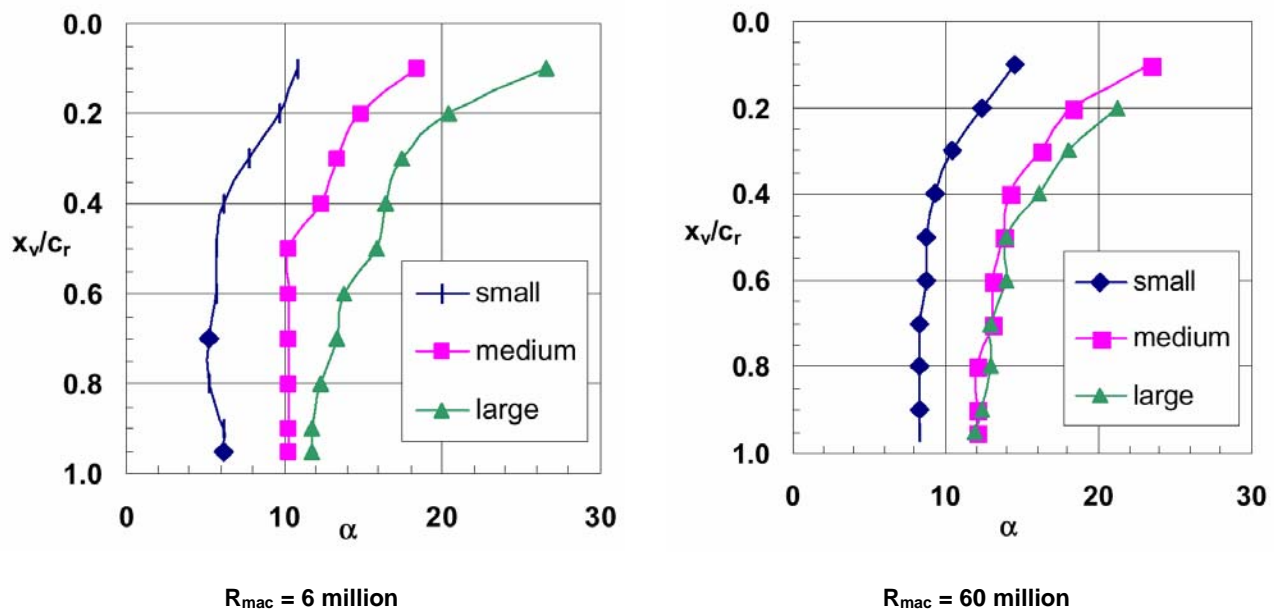
Figure 33-5: Models with Small, Medium and Large Roundness, Flow Separation
(LE Vortex) Onset and Movement, Effect of R_{mac}, Mach 0.4.

AIAA-2004-0765
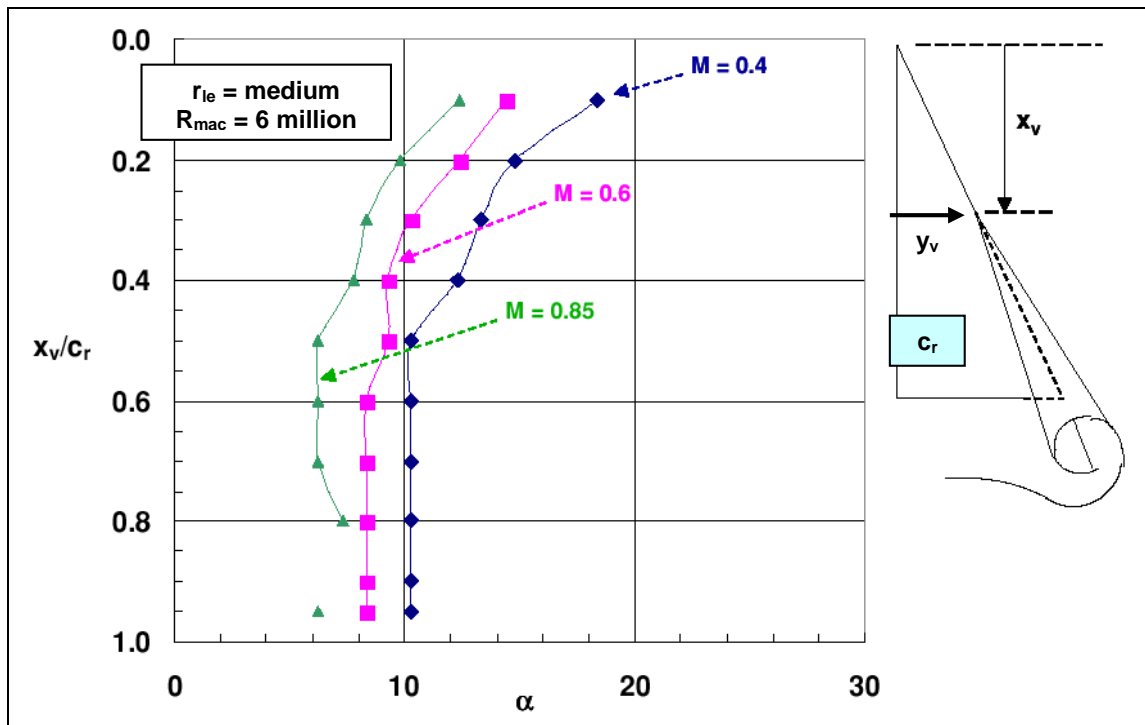
Figure 33-6: Model with Medium Round LE, Flow Separation Onset and Movement,
Effect of Compressibility, Mach 0.4, 0.6 & 0.85, R_{mac} = 6 Million.
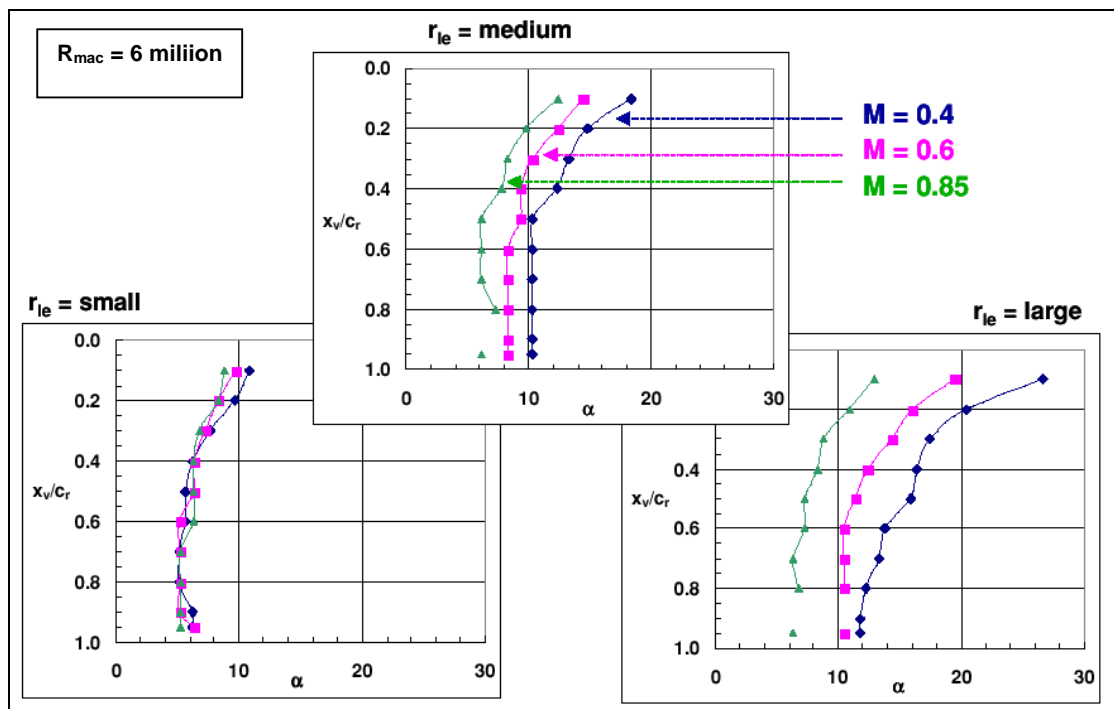
**Figure 33-7: Models with Small, Medium and Large Roundness LE, Flow Separation Onset
and Movement, Effect of Compressibility, Mach 0.4, 0.6 & 0.85, R_{mac} = 6 Million.**
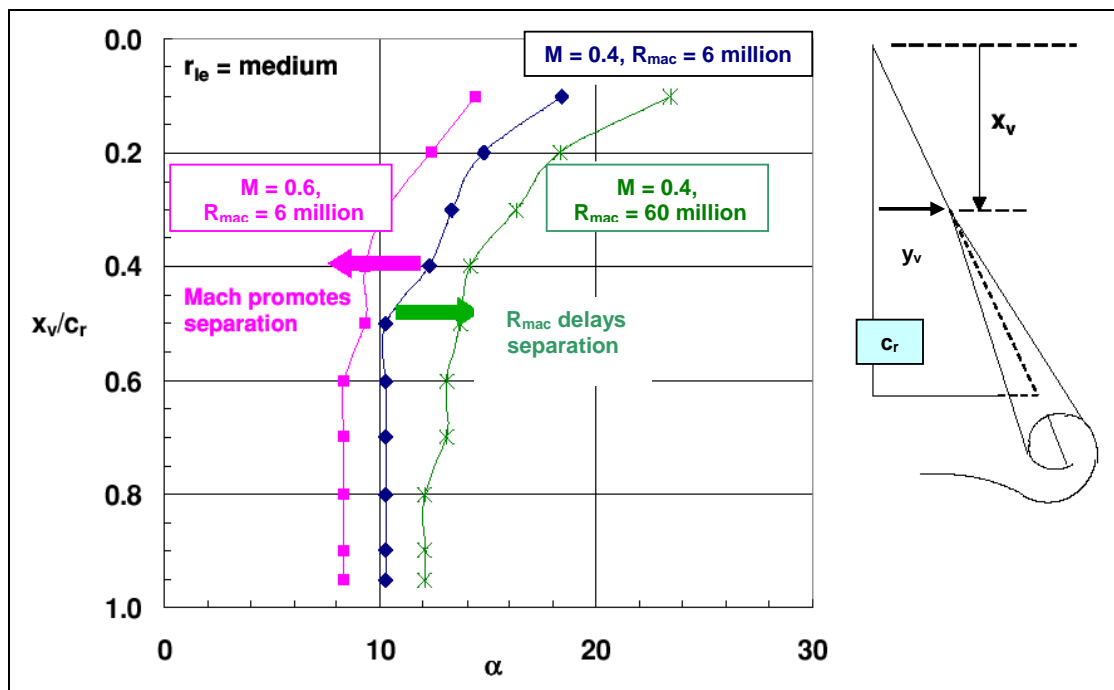
**Figure 33-8: Model with Medium LE, Flow Separation Onset and Movement, Effect
of Compressibility and R, Mach 0.4 & 0.6, R_{mac} = 6 Million & 60 Million.**

Towards a first order perspective at low speeds, it is interesting to reflect on Figure 33-9 from Ref. [33-2] (developed from Refs. [33-7]-[33-8]) to give an idea of the vortex flows domains. It would appear that vortex breakdown would begin to occur at the TE at about 17.5° AoA, at least for sharp LE. At higher Mach numbers, this will occur at lower AoA.
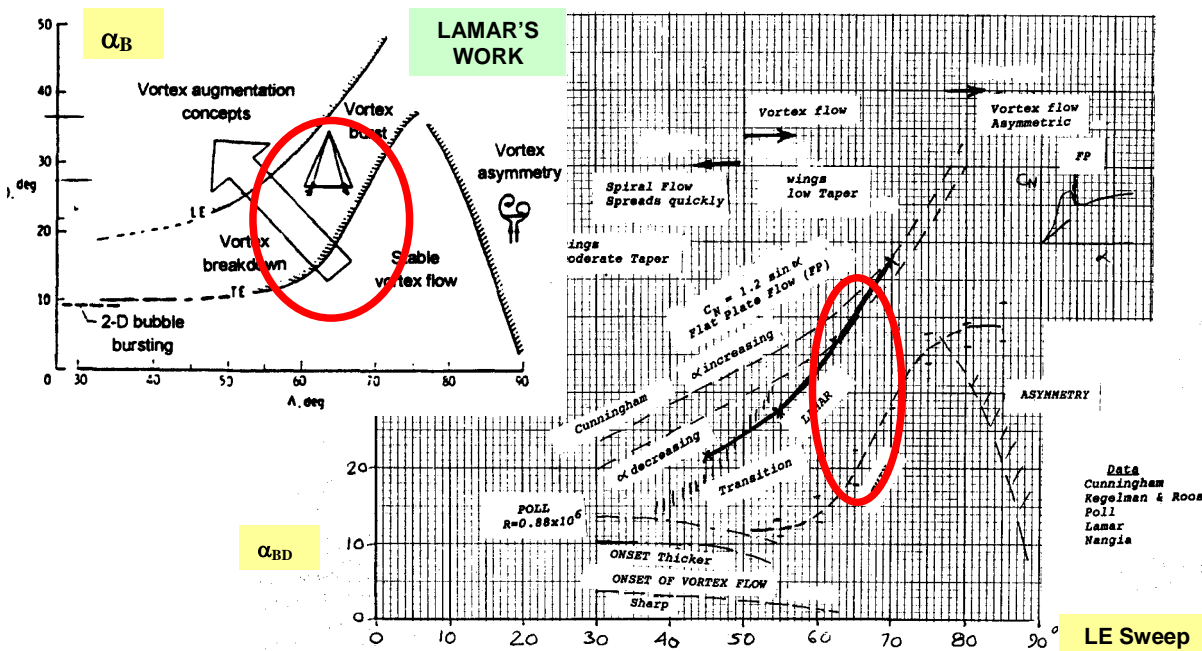
Figure 33-9: Extended Qualification of Vortex Flow Onset,
Breakdown and Control, Starting from Lamar's Work.

The onset of the vortical flow will be predicted in this document, using the semi-empirical approach developed by Nangia from the publications of Carlson, Kuchemann, Polhamus and others [33-9]-[33-16].

33.3   PREDICTION APPROACH

We have developed, since the 80's, a theoretical approach based typically on Refs. [33-9]-[33-10]. The method uses an inviscid, subsonic lifting surface theory coupled with semi-empirical "attained" thrust and vortex effects depending upon Mach, Reynolds number and aerofoil geometry (based initially on NASA LaRC work, Carlson and others (Refs. [33-11]-[33-16]) and further developed by Nangia. The method is capable of tackling symmetric and asymmetric flows. Confidence in the basic method has been built up over the years in analysis and design modes (e.g. Refs. [33-17]-[33-18]).

For a given Mach number and wing geometry, the inviscid theory (surface-singularity (panel) method or a thin lifting surface / vortex lattice, or even an Euler) produces the idealized (attached) flow loads, moments and C_p distribution over the whole wing. To a first order, within the limitations of the inviscid approach assumptions, the forces and moments correspond to the "infinite" Reynolds number case. In general, the LE thrust predicted by such codes correlates well with practical situations at low incidences. However, at the higher incidences, the LE thrust attained becomes a reducing proportion of the idealized thrust (flow partly separates). The experience

is also that the thicker wings have wider regions of attached flow, than thinner wings. Sharp LE wings cannot sustain LE suction.

This brings in the need for attained thrust techniques to analyse / predict practical situations with finite Reynolds number effects. The underlying idea is to "scale back" the attained thrust as a function of flow and geometry parameters.

33.3.1   General Approach

With reference to Figure 33-10-Figure 33-11, there are three main features of the attained thrust technique. Essentially the approach works between 2-D and 3-D to predict the forces and moments with attained thrust. The main features are:

a) Prediction of 3-D inviscid aerodynamic characteristics;

b) Evaluation of limits e.g. C_{plim} with Mach and Reynolds number constraints from 2-D considerations;

c) Estimation of the effect of aerofoil parameters; and

d) Using simple sweep theory to connect 2-D and 3-D.

A staged process can be highlighted in the following steps:

1) Define the geometry of the wing. In the present work this is a simple delta planform of root chord c_r. The tip chord c_t is zero. Estimate the aerofoil LE geometry variations on the wing as a function of spanwise co-ordinate y/s. We need LE radius/chord ratio (r/c), thickness/chord ratio (t/c) and position of Maximum thickness along chord (x_m/c).

2) At the given freestream Mach number M, apply an inviscid solver e.g. lifting surface / vortex lattice approach to predict the attached flow aerodynamic characteristics including chordwise loadings and spanwise loadings of Normal and Axial forces (C_{NL} & C_{AL}). For a planar wing, the scaling with AoA effects is simple: C_{NL} increases directly with AoA and C_{AL} is function of AoA squared. From the C_{AL} loadings, we can determine LE suction C_{TL} (c_t , Carlson) along the wing LE. The lift and drag (C_{LL} and C_{DL}) loadings can be obtained with appropriate resolution of the normal and axial loadings.

3) The linear theory attached flow results in Step 2, essentially correspond to 100% LE suction. For wings of "sufficient" LE sweep, we can derive 0% LE suction results simply by using the Polhamus LE suction analogy i.e. turning the LE suction upwards by 90° to give a non-linear vortex lift (combining 2-D & 3-D geometry). The results for 0% LE suction, including the non-linear lift, correspond to a sharp LE wing. The two solutions for 100% and 0% LE suction essentially form the "tram-lines" for the application of attained thrust solutions for other combinations of LE roundness. The 0% LE suction result implies that vortex appears all along the LE at all AoA (either side of AoA = 0°).

4) For wings with "non-sharp" i.e. rounded LE, the onset of vortical flow is delayed. This delay depends on several parameters including Mach number, Reynolds number and Aerofoil geometry parameters (established in Step 1). The "attained thrust" approach (based initially on NASA LaRC work) is applied, together with an adaptation of the Polhamus analogy to "non-attained" thrust. This is discussed in the next Sections 33.3.2 and 33.3.3.

5) If further analysis towards prediction of vortex breakdown is required, then this step, using Lan's method needs to be included. In this report, however, we do not consider this.

**1. Definition of
Swept, Cambered Thin
Wing Geometry,
Aerofoil Geometry**

**2. At given Mach number, apply an Inviscid Solver
Lifting Surface / vortex Lattice
Symmetric & Asymmetric situations**

**3. Determine values for 100% LE Suction
Polhamus Analogy for Swept Sharp LE to
derive 0% LE suction results
"tram lines" Obtained**

**4. Apply Semi-Empirical "Attained" Thrust
Approach, using
Mach & Reynolds No. & Aerofoil Geometry
Predict Onset of Vortical Flow & Progression**

**Polhamus Analogy on "non-attained" thrust
(sufficiently Swept Edges)
Vortex Development**

**5. Check for Vortex Strength Distribution
along Span**

**If required, apply
Lan's Method
Vortex Breakdown onset criteria**

**Figure 33-10: Different Stages in Evaluation Method Incorporating Attained Thrust, LE Suction
Analogy and Vortex Breakdown Empiricisms, Symmetric and Asymmetric Situations.**
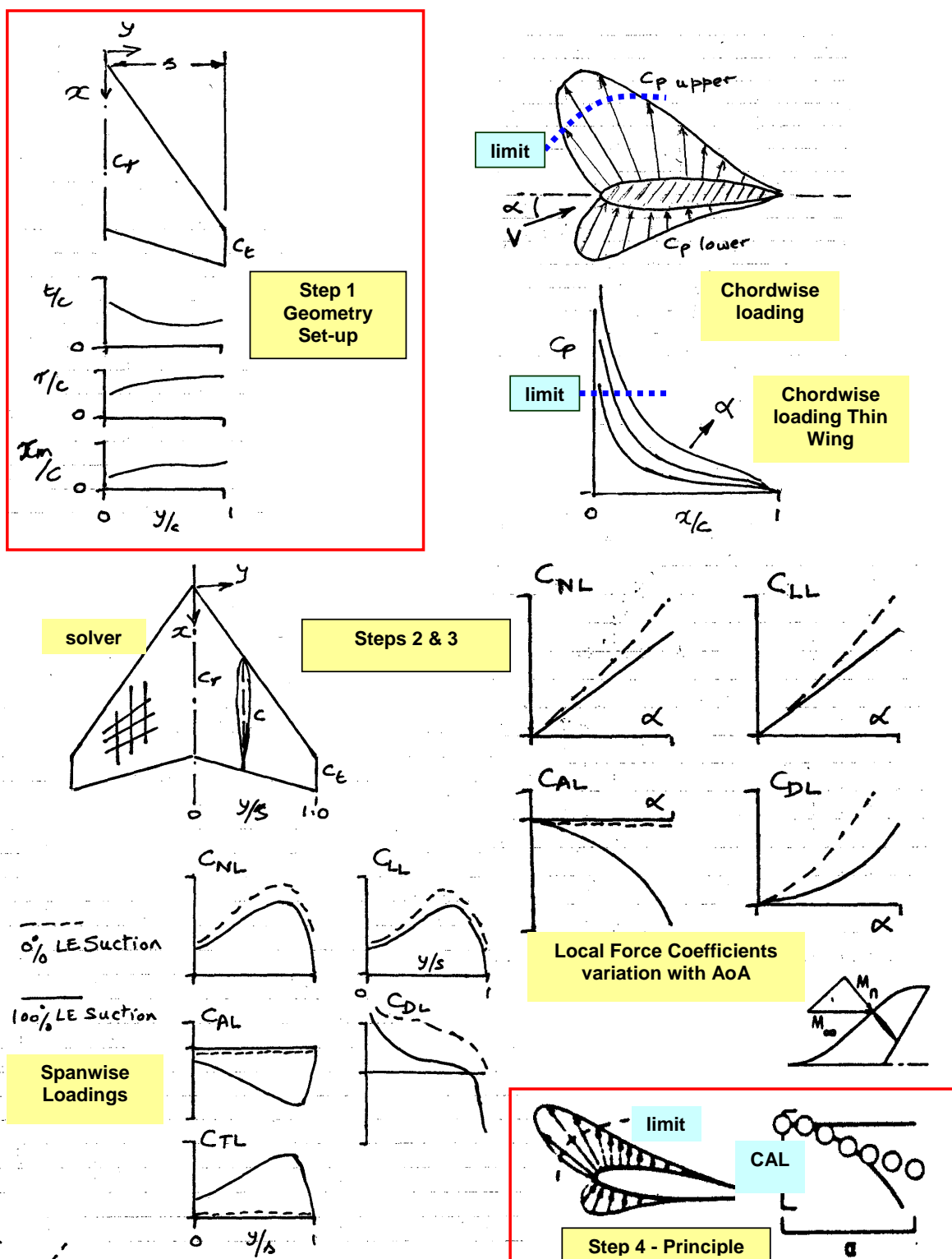
Figure 33-11: Key Features and Various Steps of the
Attained Thrust Prediction Method (Carlson et al).

33.3.2   Analysis of Sectional LE Thrust (Based on Carlson's Work)

The inviscid linear lifting surface theory at the given Mach number leads to the description of maximum suction $C_{TL}(y)$ along the LE (Steps 1 – 2 above). In general, at all AoA beyond the LE attachment condition, it is implied that C_p at the LE will be infinite (negative) and the strength of this will vary with AoA. We know that in physical flow this is unrealistic and a limiting value of C_p i.e. C_{plim}, needs to be introduced as sketched in Figure 33-11.

The considerations for C_{plim} are:

- C_p cannot be less than the vacuum limit $C_{pvac} = -2\,\gamma\,/M_n{}^2$, where M_n is the Mach number normal to the wing LE.

- Effects on $-C_{plim}$ are related to Mach, Reynolds number and the aerofoil parameters. These are conveniently described by curve-fit formulae using C_{pvac} (based on LaRC work and updated by Nangia).

A factor $K_T = C_{plim}/C_{pvac}$ (i.e. relating C_{plim} to C_{pvac}) needs to be determined. The correlations can be built into a prediction method for 3-D wings. At any spanwise station (y/s), the onset of flow separation is predicted when K_T is less than 1.0. Curtailing K_T implies lower magnitudes of C_{TL} and C_{AL} (axial force coefficient).

Figure 33-12 shows the C_{plim} , Mach number and sweep angle Λ relationships. C_{plim} is infinite at M = 0. It is conveniently expressed in terms of the vacuum limit $C_{pvac} = -2\gamma/(M_n{}^2)$, with $M_n = M\cos\Lambda$. Note that $C_{plim} = C_{pvac} = -1.0$ signifies vacuum and $C_{plim} = C_{pcrit}$ implies $M_n = 1.0$ i.e. sonic flow.
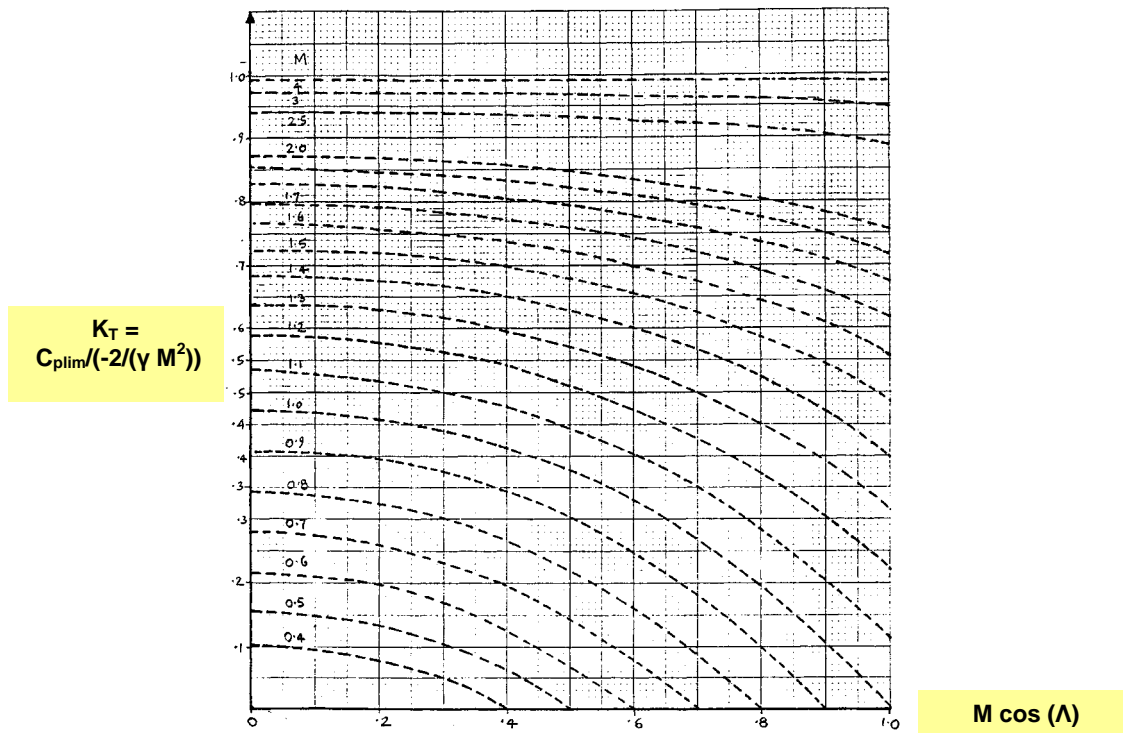
Figure 33-12: C_{plim} and Mach Number Relationships.

A typical C_p distribution for a symmetrical aerofoil section at a moderate AoA is illustrated in Figure 33-13. Integration of C_p values leads to local normal force coefficient C_{NL} and local thrust coefficient C_{TL} (c_n and c_t respectively in Carlson's notation). With AoA increasing, linear theory does not place any bounds on the magnitude of suction pressure, which therefore can become much greater than -C_{pcrit} and any practically realizable value (-C_{pvac}). This can therefore severely limit the attainment of real thrust forces and adversely affect the prediction of aerodynamic properties, e.g. onset of flow separation, drag, lift and pitching moment.
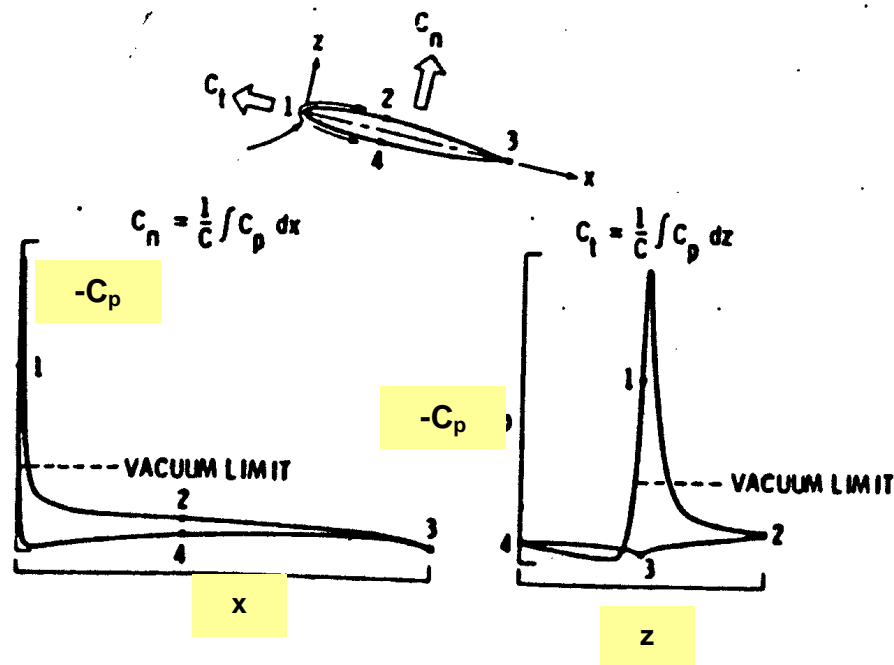
Figure 33-13: Typical Theoretical C_p Distributions and Local Force Coefficients c_t and c_n (Carlson).

The crux of the attained suction approach is to see how C_{plim} varies with suction level predicted on the basis of linear theory, flow parameters (Mach and Reynolds number) and geometry parameters of the aerofoil (r/c, t/c and position of maximum thickness x_m/c). The three-dimensional effects can be inserted via sweep theory. A Polhamus type approach allows the unattained part of the suction to be resolved into a non-linear force.

The prediction method needs, as a core, the attached flow properties (linear part) to develop the non-linear properties by adapting Polhamus LE suction analogy.

As mentioned in Section 33.3.2, for a sharp LE "uncambered" thin wing, all of the LE suction force is essentially "unattained" and this is "rotated" upwards giving rise to non-linear lift. This behaviour begins at 0° AoA.

Now, if the leading edge is not sharp then the flow "hangs on" and flow separation onset is delayed. The delay depends on:

1) The level of local LE suction;

2) The "local" aerofoil properties; and

3) The local Reynolds / Mach number combination.

This then becomes a function of y/s and helps in tracking the onset of flow separation and its development. On an aft swept wing with rounded LE, the flow separation begins from the wing tip area and travels inboard as AoA increases.

For an uncambered wing, at a given AoA, a rounded LE wing will have less total lift (linear + nonlinear) than that for a sharp LE wing.

In Carlson's approach, a series of 2-D aerofoils, Figure 33-14, were used to evaluate the 2-D limitations. The aerofoil thickness parameter (t/c) varied from 0.06 to 0.18. The aerofoil radius parameter (r/c) varied from 0.0012 to 0.0288. Maximum thickness of the aerofoil family was located at mid-chord.
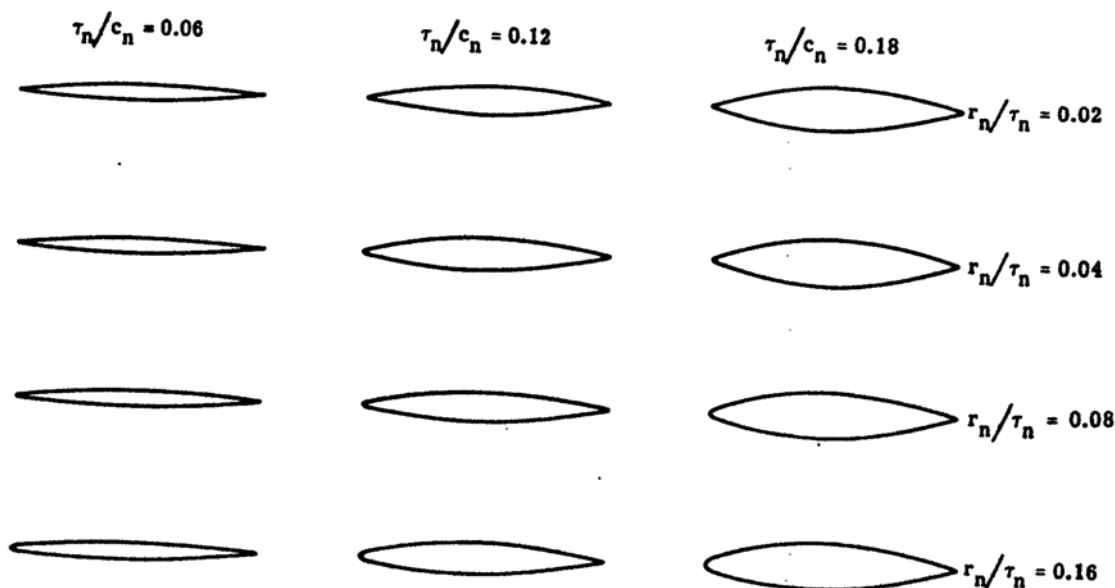
Figure 33-14: Family of Aerofoil Sections, Differing t/c,
Maximum Thickness t_{max} at Mid-Chord (Carlson).

As the AoA increases or the Mach number increases, the magnitude of C_p reaches C_{pcrit} and then goes beyond C_{plim}, Figure 33-15. This allows the determination of factor K_T relating thrust with (given M) and without the vacuum limit (M = 0).
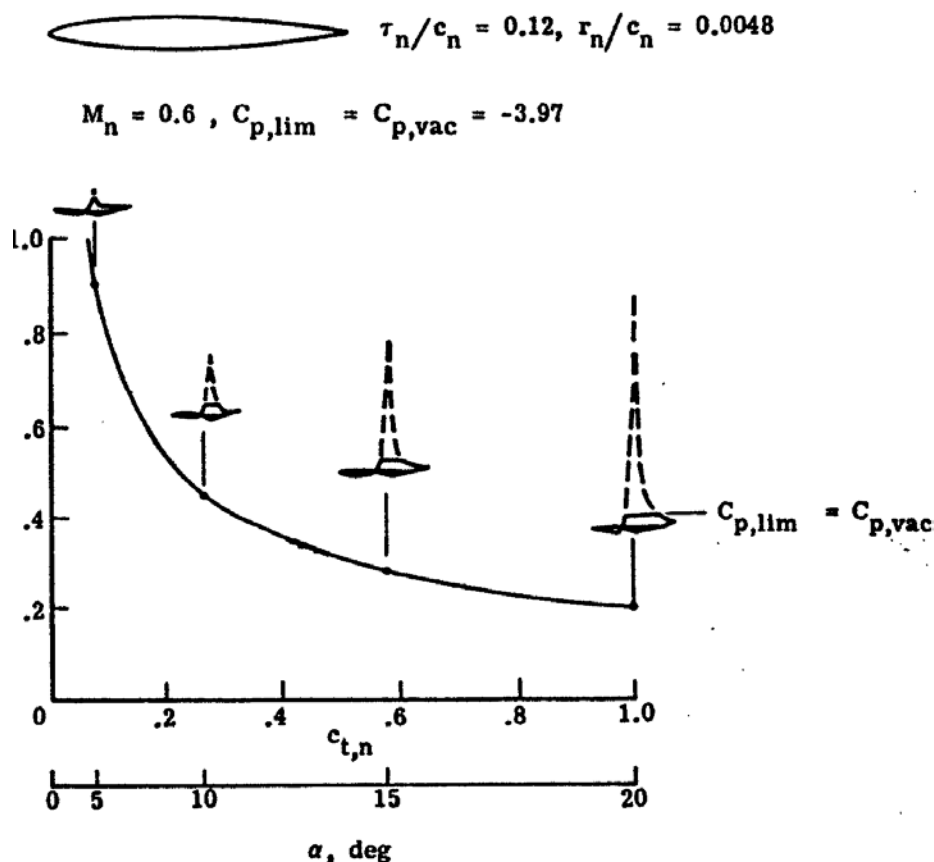
Figure 33-15: An Example of K_T Variation for AoA Increasing, Vacuum Limit (Carlson).

33.3.2.1 Mach and Reynolds Number Effects on C_{plim} or K_T

The values of C_{plim} and K_T are also subject to Reynolds number effects within two boundaries of:

1) K_T approaching 1.0 as Reynolds number approaches infinity; and

2) K_T will tend to vanish as Reynolds number approaches zero.

On the basis of experimental evidence, C_{plim} has been determined by Carlson et al, as a function of flow parameters normal to the leading edge: Mach number, M_n, and Reynolds number, R_n, see Figure 33-16. Figure 33-17 and Figure 33-18 illustrate two different curve fitted forms with parameter e_m (either 0 or an alternative value as in Figure 33-17).
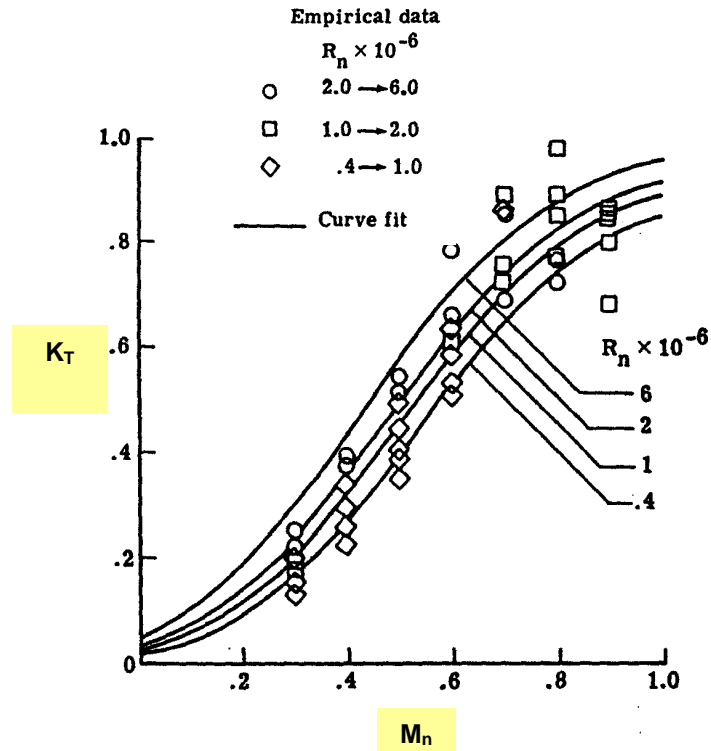
Figure 33-16: Dependence of K_T on Normal Mach Number and Normal Reynolds Number, Experiment and Theory ($e_m = 0$, see Figure 33-17) (Carlson).

$$C_{p,lim} = \frac{-2}{\gamma M_n^2} \left[\frac{R_n \times 10^{-6}}{R_n \times 10^{-6} + 10^e} \right]^E$$

$$E = .05 + .35(1-M_n)^2$$

$$e = 4 - 3M_n + 4\underbrace{(1-M_n)^{15}}_{e_m}$$
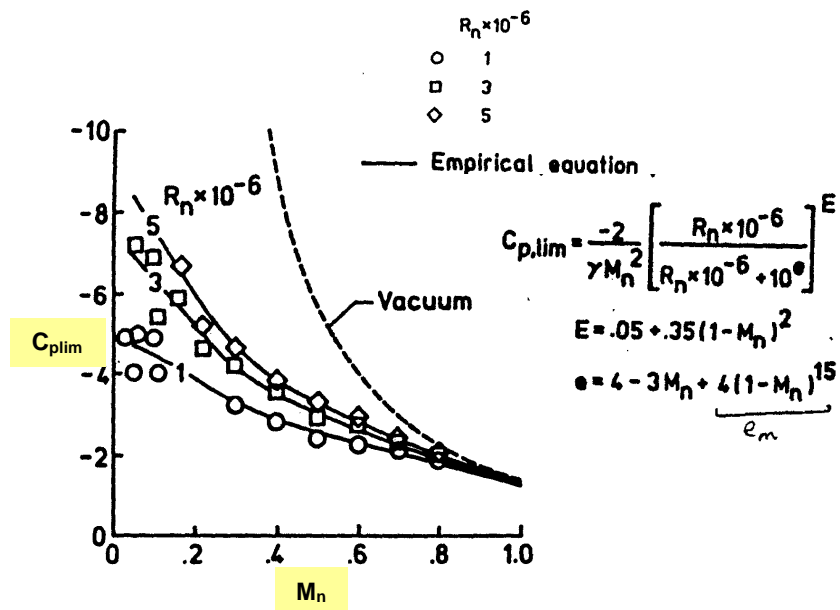
Figure 33-17: C_{plim} Variation with Normal Mach and Normal Reynolds Number, Experiment and Theory (e_m Finite as Defined) (Carlson).
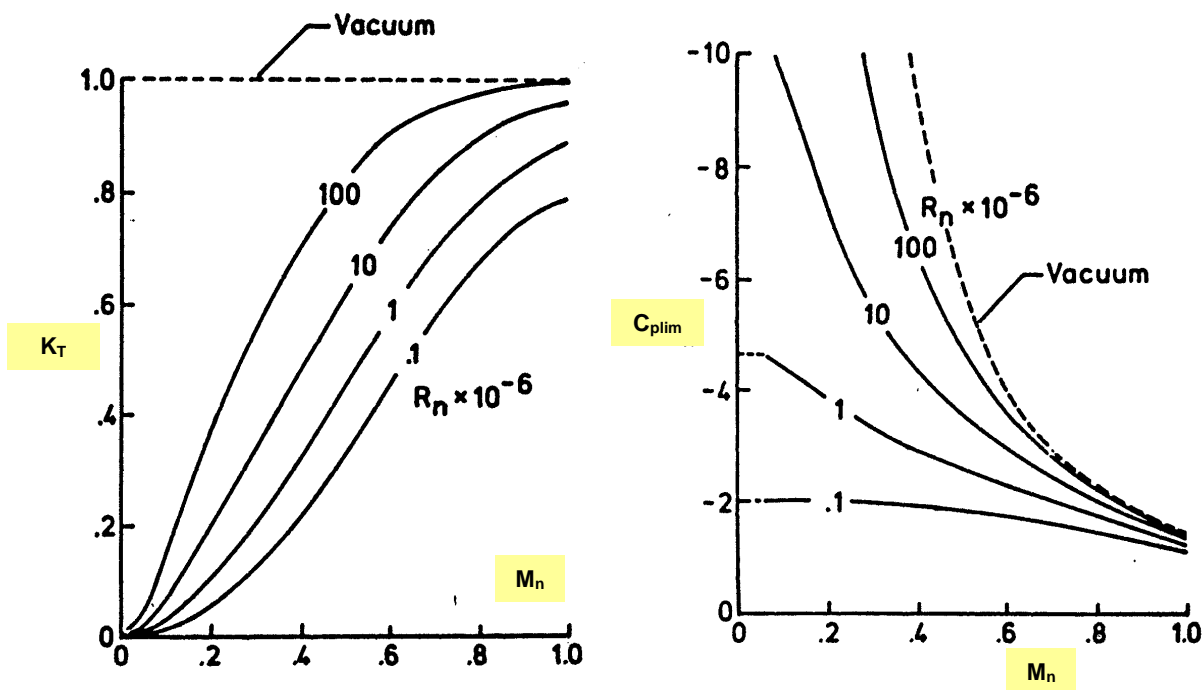
Figure 33-18: Variation of K_T and C_{plim} as Given by Carlson's Formula (e_m Finite as in Figure 33-17).

C_{plim} is also likely to be affected by the 3-D nature of the flow. For example, spanwise flow on the upper surface of a swept wing may relieve the adverse pressure gradient on certain areas (root of an aft-swept wing and the tip of a forward-swept wing). This can lead to achieving a higher C_{plim} over such areas.

General experience using Carlson's expressions incorporated into a vortex lattice lifting surface theory is that C_{plim} is under-estimated at the lower Mach numbers.

This led to further consideration by Nangia of available data for the extraction of C_{plim}. As a result, possible updates were produced for C_{plim} for R_n between 10^5 and 10^{10}. Figure 33-19-Figure 33-21 show the updates.
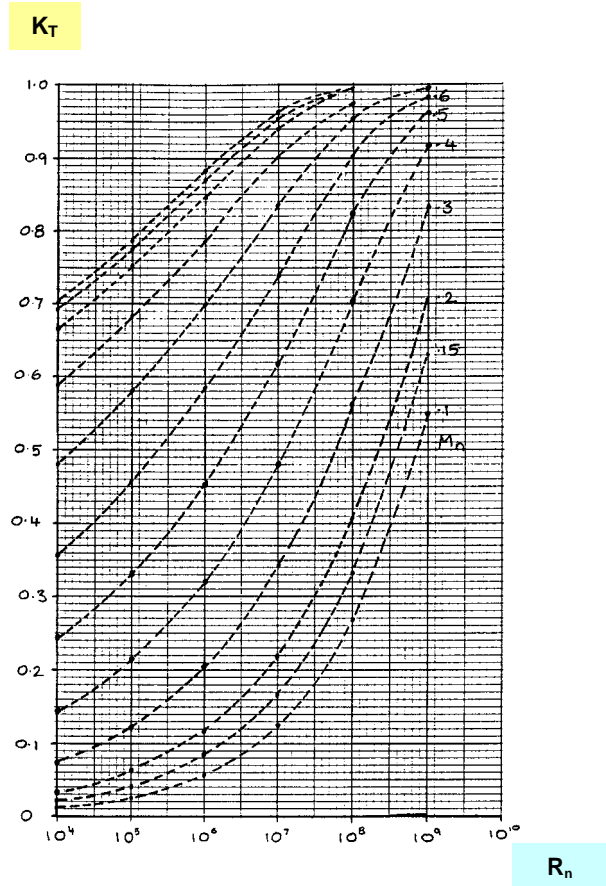
Figure 33-19: Variation of K_T with R_n, $e_m = 0$ (Carlson).
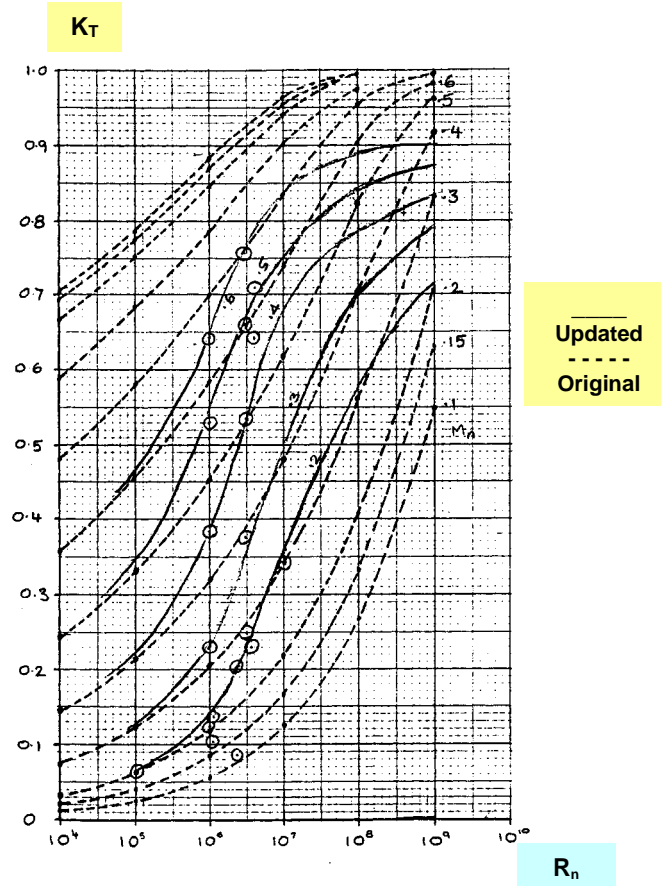
Figure 33-20: Updated Variation of K_T, R_n Varies between 10^4 and 10^{10}.
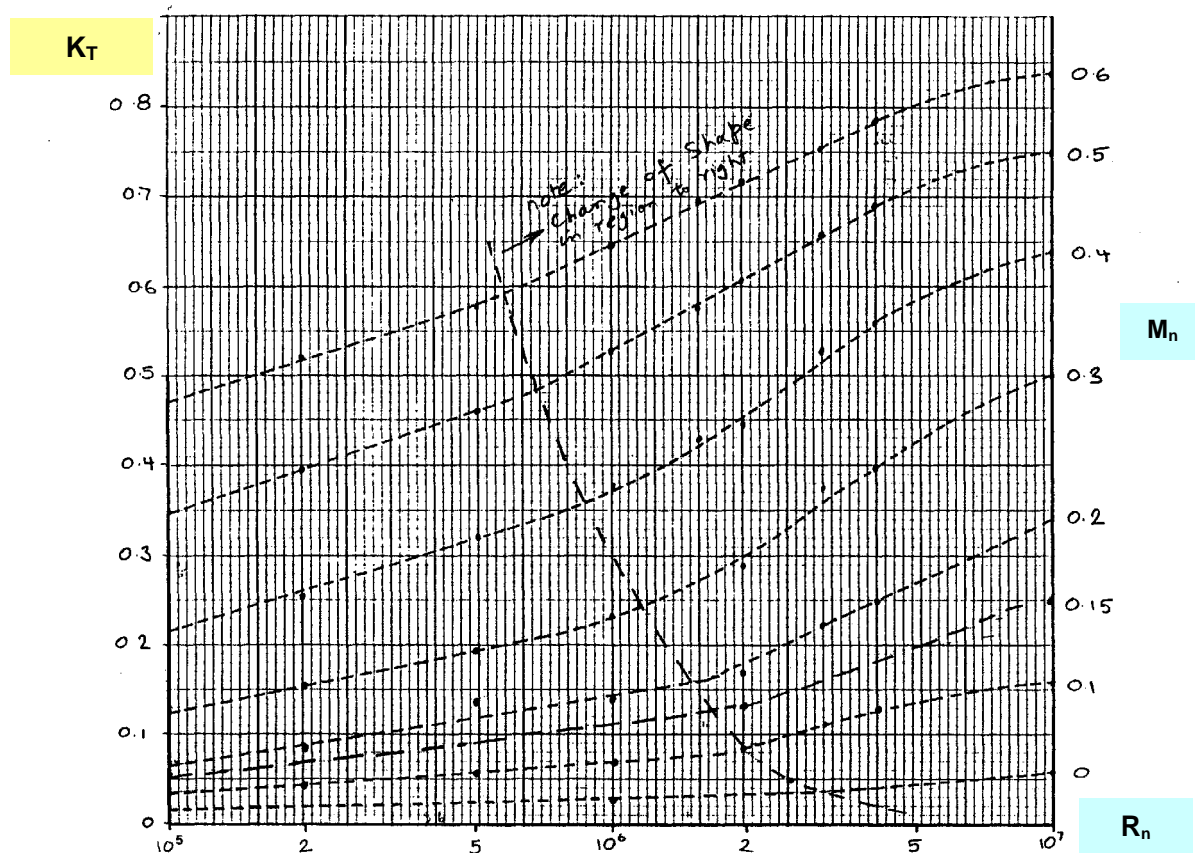
Figure 33-21: More Detail of Updated Variation of K_T, R_n Varies between 10^5 and 10^7.

33.3.2.2   Aerofoil Geometry Effects on C_{plim} and K_T

Following Carlson, K_T can be related to the aerofoil parameters as shown in Figure 33-22. The definition of normal aerofoil parameters (subscript n) follows from Figure 33-23 focussing on 3-D sweep relationships for a given planform.
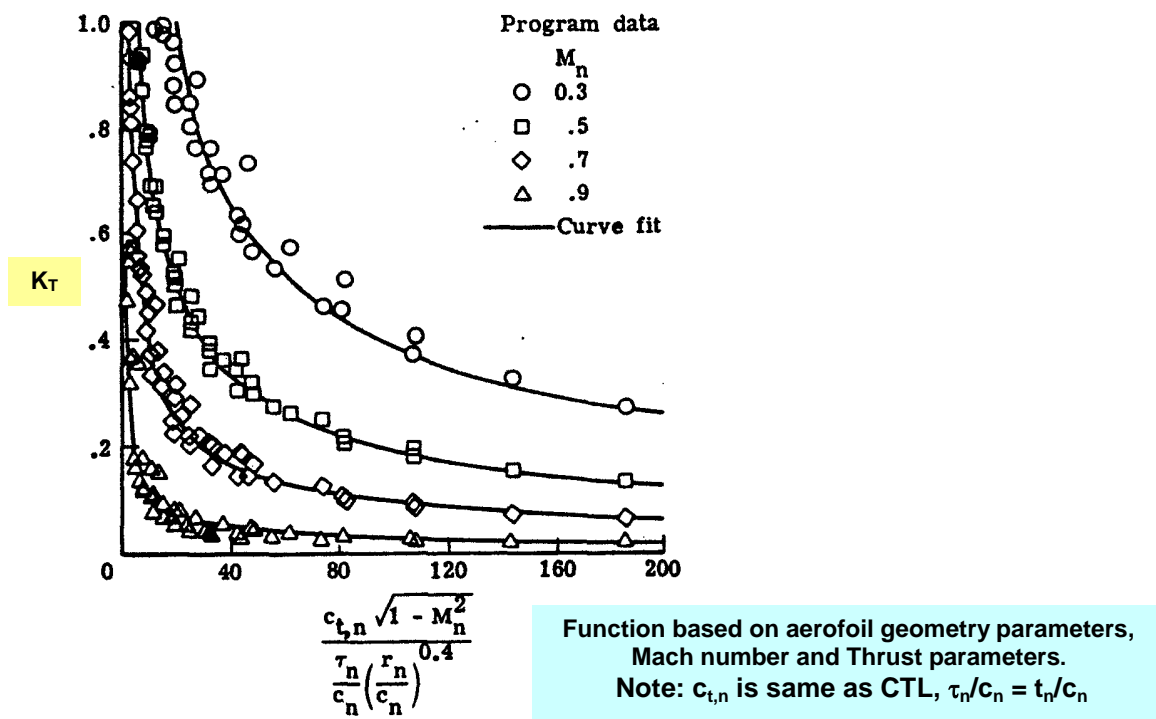
**Figure 33-22: Dependence of Thrust Factor K_T on Normal Aerofoil
Parameters and Normal Mach Number (see also Figure 33-23).**
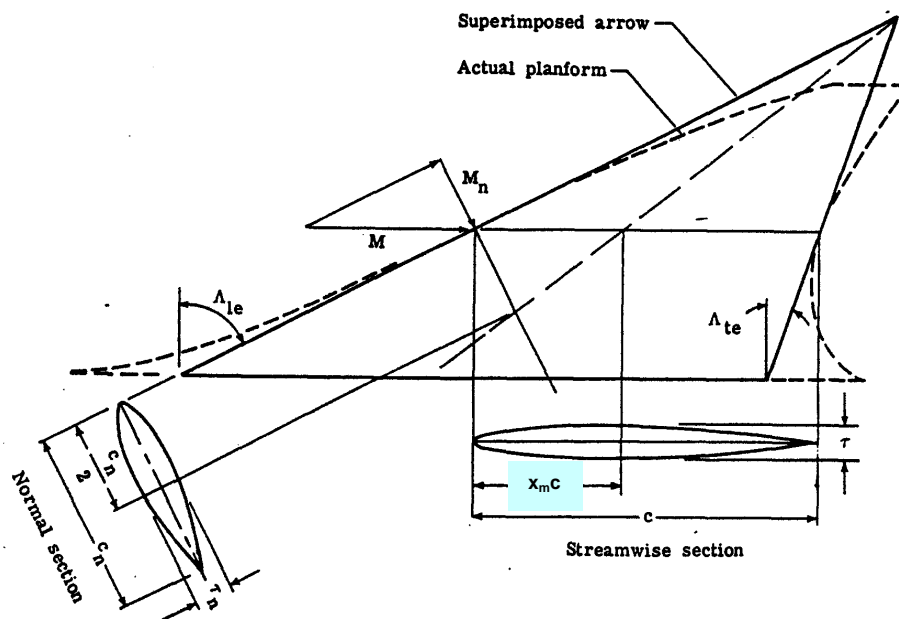
**Figure 33-23: Sweep Theory and Definition of Normal Aerofoil
Sections from Streamwise Sections of 3-D Wings.**

33.3.3 LE Thrust Considerations for Swept 3-D Wings

The main steps are:

- The 2-D Considerations according to Section 33.3.2 are applied in the normal direction (n) of a swept wing (sheared wing part), Figure 33-23.

- The unusual 2-D cross-sections with flat upper and lower surface are transformed into "effective" aerofoils (normal to the LE) with assumed position of half chord.

- The ideal maximum C_{TL} distribution is modified for the root region and the tip region of the 3-D wing according to Kuchemann (Figure 33-24-Figure 33-27), resulting in a factor P_L (y/s), Figure 33-28.
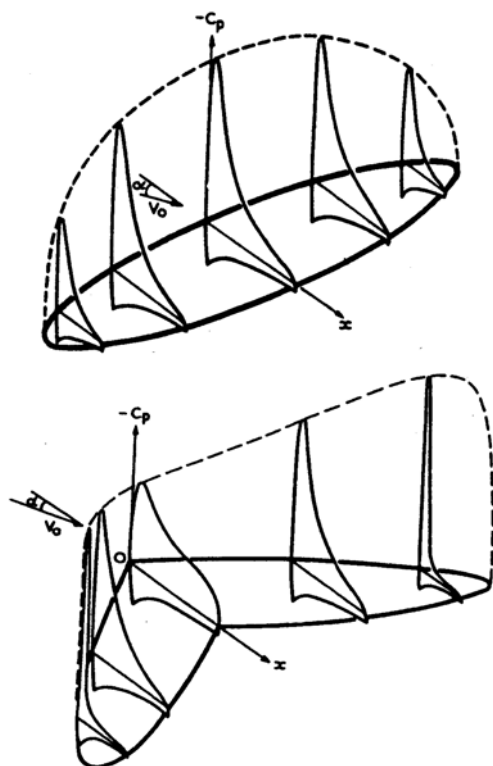
Figure 33-24: Pressure Distributions over Unswept and Swept Wings (Kuchemann).

Section pressure distribution for swept back wings as influencing boundary layer flow.
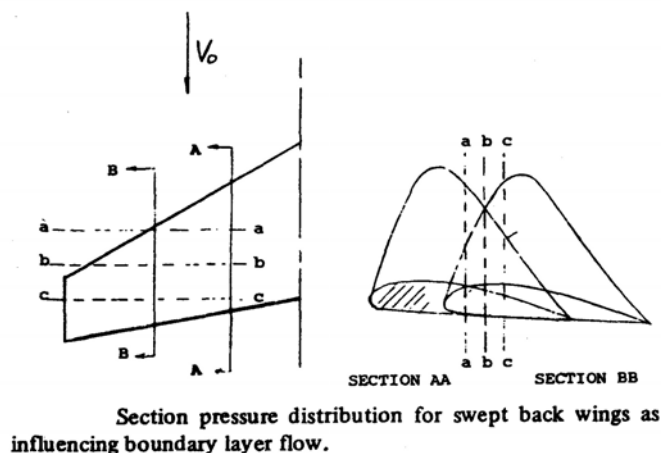
Figure 33-25: Spanwise Flow and Alleviation of Gradients on Aft-Swept Wings.
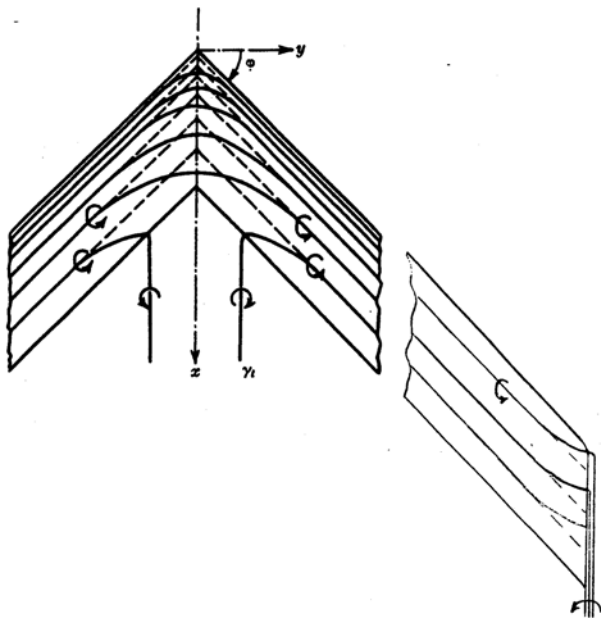
Figure 33-26: Vortex Lines Near the Centre and Tip of a Plane Swept Wing.
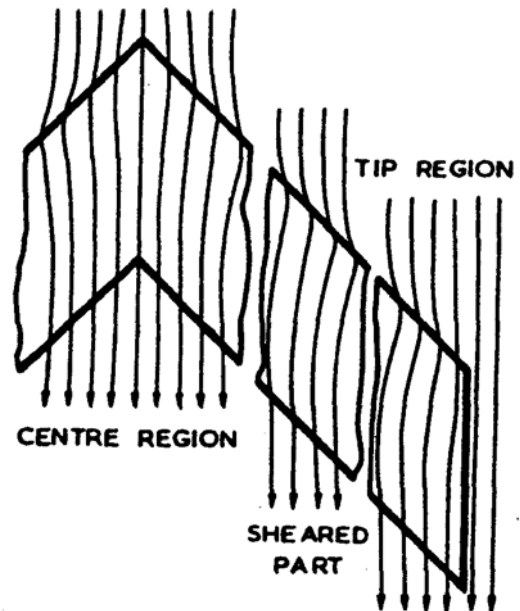
Figure 33-27: Streamlines Straightening at Wing Root and at Tip.
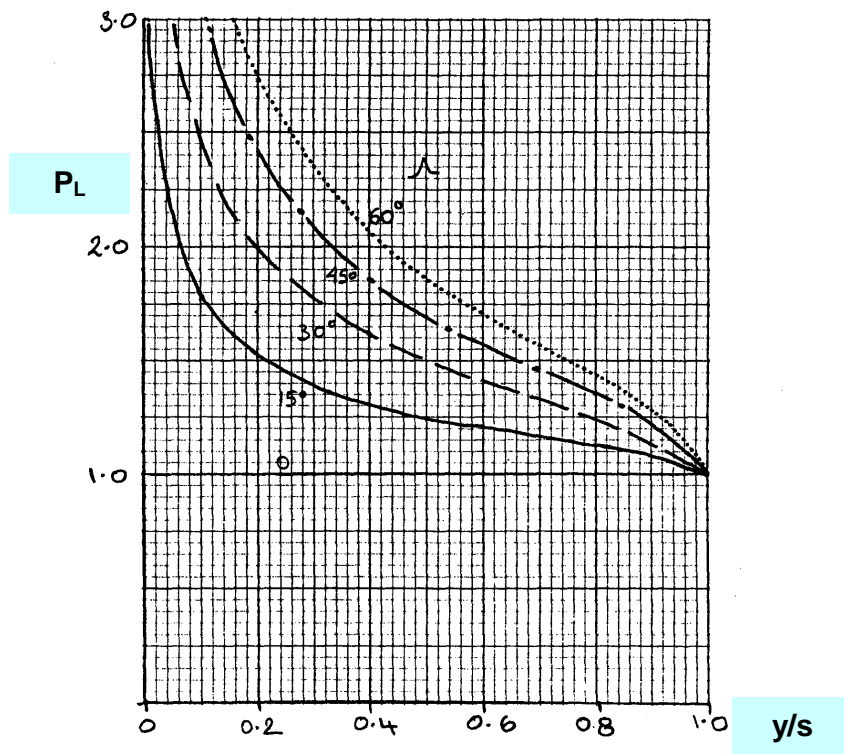
Figure 33-28: Typical Variation of P_L.

33.3.3.1 C_{plim} on 3-D Wings

This feature was neglected by Carlson. On a 3-D wing, C_{plim} near the leading edge of a swept wing is subject to boundary layer and varying pressure gradients along the wing-span, Figure 33-23. This may in some cases alleviate adverse interaction effects and thus imply higher C_{plim} values being attained over certain areas of the wing. In essence, the boundary layer flow acts in a manner similar to the use of suction for preventing separation and allows the wing section to develop a higher local lift coefficient than would be measured in 2-D flow. As shown in Figure 33-25 (based on Kuchemann, [33-16]), spanwise and chordwise pressure gradients interact as a result of wing sweep. Consider, on a swept-back wing, two chordwise pressure distributions (spanwise stations AA and BB) and y-z plane cuts at streamwise locations a, b and c. From a to b to c along AA, negative pressure (suction) tends to return to the freestream value. From a to b to c along BB, suction increases. Between a and b on AA the pressure remains more negative than between a and b on BB. There is no spanwise pressure differential between AA and BB at b. Between b and c on BB the suction increases whereas between b and c on AA suction decreases in magnitude. This mechanism causes the flow to move in the spanwise direction. Further, in the absence of a fuselage, the boundary layer is thinner near the wing root than at the wing tip of an aft-swept wing.

Kuchemann and others have shown that on swept-back wings, Figure 33-24 and Figure 33-26, the LE singularity strength and pressure gradients at the wing root are weaker than those at the mid semi-span of the wing. Near the wing-tip, LE singularity strength and pressure gradients are stronger than those at the mid-semi-span of the wing. The behaviour is reversed for forward-swept wings.

The curved streamlines typical of sheared-wing flow can persist neither into the center of the wing nor up to the wing tip. As sketched in Figure 33-27, the streamlines are straightened out in both regions.

After a great deal of analysis on a series of wings (unpublished work), it was found convenient to incorporate 3-D planform effects on C_{plim} by introducing a factor P_L (y/s):

$$C_{plim} \text{ (3-D)} = P_L \text{ (y/s)} \times C_{plim} \text{ (2-D)}.$$

A typical variation of P_L (y/s) for swept-back wings is given in Figure 33-28. Alternative forms for P_L (y/s) can be devised and a few of these have been studied. The current computer programmes allow the choice of using factor P_L (y/s) as needed.

33.3.3.2 Modelling Delay in Flow Separation Onset Due to Model Thickness

In view of the models unusual thickness distribution especially near the wing-tip, we may also need to include an additional feature to simulate the AoA delay in flow separation onset. This would appear to be a function of compressibility, LE radius and, or (possibly) the thickness terms at the tip region. We do not yet have a sufficiently convincing technique to include this term. The simplest technique for the present types of wing is to add on this term as a function of compressibility and LE radius thickness term:

$$\Delta(AoA) = dt° \times \sqrt{(1-M \times M)} \times (r/\bar{c})^2, \text{ where dt is a suitable constant}$$

This function could be stronger at lower Mach numbers. Alternative proposals in terms of t/c near the wing tip are possible. The main inference is that further analyses using higher order approaches and correlations need to be obtained throughout the Mach number range. Experiments on VFE-2 will help.

33.3.4 Summarising the Process for Determining the Position of the Onset of Vortical Flow

For a given configuration geometry, AoA, Mach number and Reynolds number:

- Perform a linear solution by a Vortex / doublet lattice method and determine C_{TLmax} (or c_{tmax}, Carlson) distribution, modified for root and tip region (Kuchemann).

- Determine the local K_T thrust factor for given values of C_{TLmax}, Mach number, Reynolds number, Aerofoil section parameters normal to LE from the universal diagram (Figure 33-22).

- Compare maximum LE thrust C_{TLmax} and attainable LE thrust C_{TL} (attained) = K_T x C_{TLmax}, as a function of spanwise dimension. We note that if $C_{TL} = C_{TLmax}$ then the flow is attached. For $C_{TL} < C_{TLmax}$, the flow is separated.

- As in Polhamus's work, any reduction in axial force is turned by 90° and added to the lift. This corresponds to non-linear lift.
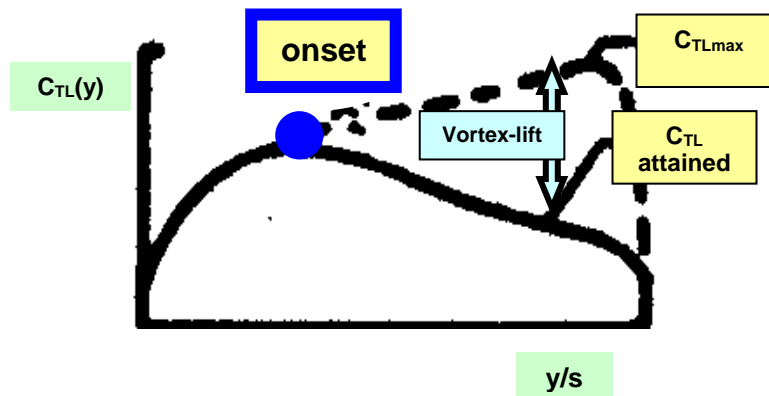
Figure 33-29: Determination of the Separation Onset.

33.3.5 Remarks

The application of the theory has a bearing on several issues e.g.:

- The unconventional aerofoils of the present delta wings might lead to improvements / modifications of the Carlson curve-fit formulae.

- The effects of Reynolds number on the $-C_{plim}$ reduction might also be different for the present unconventional aerofoils.

- Other inferences / criteria from the present approach to explain the differences for the large radius rounded LE configuration.

There are however issues such as non-standard aerofoil thickness distributions and Mach 0.85 application that need further understanding and verification. This can be enhanced by using higher-order solvers. In particular, an Euler solver could be used as a core solver along with the attained thrust approach. The thrust coefficient C_{TL} variations would then be based on the Euler results.

From a practical perspective, simple linear theory has limitations in modelling configuration associated details, e.g. fuselage, nacelles, etc. Such limitations could be handled more easily with an Euler method.

33.4   COMPARISONS WITH VFE-2 EXPERIMENTS

33.4.1   Modelling Detail from NASA LaRC Work Programme on 65° Delta

Figure 33-1-Figure 33-4 from Refs. [33-4]-[33-6], refer to the 65° delta wing model and the NTF wind tunnel facilities. Geometric details of the model are given together with tunnel operating ranges in terms of Mach and Reynolds number.

For application of the theoretical techniques, the salient particulars of the NASA model are:

Root chord of 2.1445 ft, aerodynamic chord, $\bar{c}_r$ = 1.4297 ft, Wing Area S = 2.1445 ft^2, AR = 1.8652.

In the NTF, independent Mach and Reynolds number sweeps/variations were carried out at Mach 0.4, 0.6 and 0.85. Reynolds number R_{mac}, varied between 6 & 60 million based on the mean aerodynamic chord $\bar{c}$ of the delta.

Four representative Leading Edges with different LE radii (sharp, small, medium and large) were used by Luckring, Figure 33-5. The corresponding LE radius distributions varied from sharp to smooth.

Model & LE	$r_{le}/\bar{c}$	$t/\bar{c}$
Config. with sharp LE	0.0	0.051
Config. with small round LE	0.0005	0.051
Config. with medium round LE	0.0015	0.051
Config. with large round LE	0.0030	0.051

Essentially, all the models featured non-standard aerofoils because of large flat areas, joined with strongly curved LE and TE regions. Figure 33-4 showed the effective t/c and r/c distributions along the semi-span. Both these quantities are extremely large towards the wing-tip even with the small round LE. In most practical highly swept-back wing configurations, the bounds of t/c and r/c values are much lower. For example, supersonic configurations usually have t/c of the order of 2.5 to 3.5% along the span.

It also follows that t/s (s is local semi-span at a given x) is very large in the apex region. The edge angle is correspondingly fairly large and the sharpness of the LE may not dominate the characteristic flow in the apex region.

This poses special problems for assessments using simpler theory as some of the implicit empiricisms do not encompass very large local t/c, t/s and r/c values. Also most of the theoretical assumptions imply "standard" aerofoil shapes.

33.4.2   Results from Luckring's Papers on Vortex Flow Onset (Figure 33-5 – Figure 33-8 of Section 33.2)

As mentioned in Section 33.2, for the different wings, Luckring presented a series of parametric results for the onset of flow separation (LE vortex) in Figure 33-5 – Figure 33-8. Mach and Reynolds number have been varied. It is useful to provide some further detail here. This is also further discussed in a separate Chapter.

For models with different rounded LE, Figure 33-5 shows the effect of R_{mac} = 6 & 60 million, on flow separation (LE vortex) onset and movement with respect to AoA. Note that the rounded edge delays the vortex onset. Onset occurs at higher AoA as Reynolds number increases.

For the model with medium rounded LE, Figure 33-6 shows the effect of compressibility (M = 0.4, 0.6 & 0.85) at Reynolds number (R_{mac} = 6 million) on flow separation (LE vortex) onset and movement with respect to AoA. Note that decreasing Mach number delays vortex onset. As Reynolds number increases, onset occurs at higher AoA.

For models with different rounded LE, Figure 33-7 shows the effect of compressibility (M = 0.4, 0.6 & 0.85) at Reynolds number R_{mac} = 6 million, on flow separation (LE vortex) onset and movement with respect to AoA. Note that the decreasing Mach number delays vortex onset. The delays are higher with roundness increasing. For the small LE roundness, there appears to be very little effect due to compressibility.

For the model with medium rounded LE, Figure 33-8 summarises the effect of compressibility (M = 0.4, 0.6 & 0.85) at R_{mac} = 6 & 60 million. This confirms the general inference that increasing Mach number promotes flow separation and increasing Reynolds number delays the separations.

33.4.3   Results and Comparisons

Using the current theoretical approach, we have predictions for the onset of vortical flow (wing-tip) on the various models and these have been compared with results available from Luckring's experiments.

Figure 33-30 refers to the Reynolds number R_{mac} = 6 million case, as a function of compressibility (Mach 0.4, 0.65 & 0.8) for models with different roundness. Theory and experiment results are shown separately prior to super-imposition. Note that agreement is very good at all Mach numbers for the small roundness wings. As roundness increases, the correlation is still within about 2° AoA at lower Mach numbers. The correlation improves as Mach number increases.
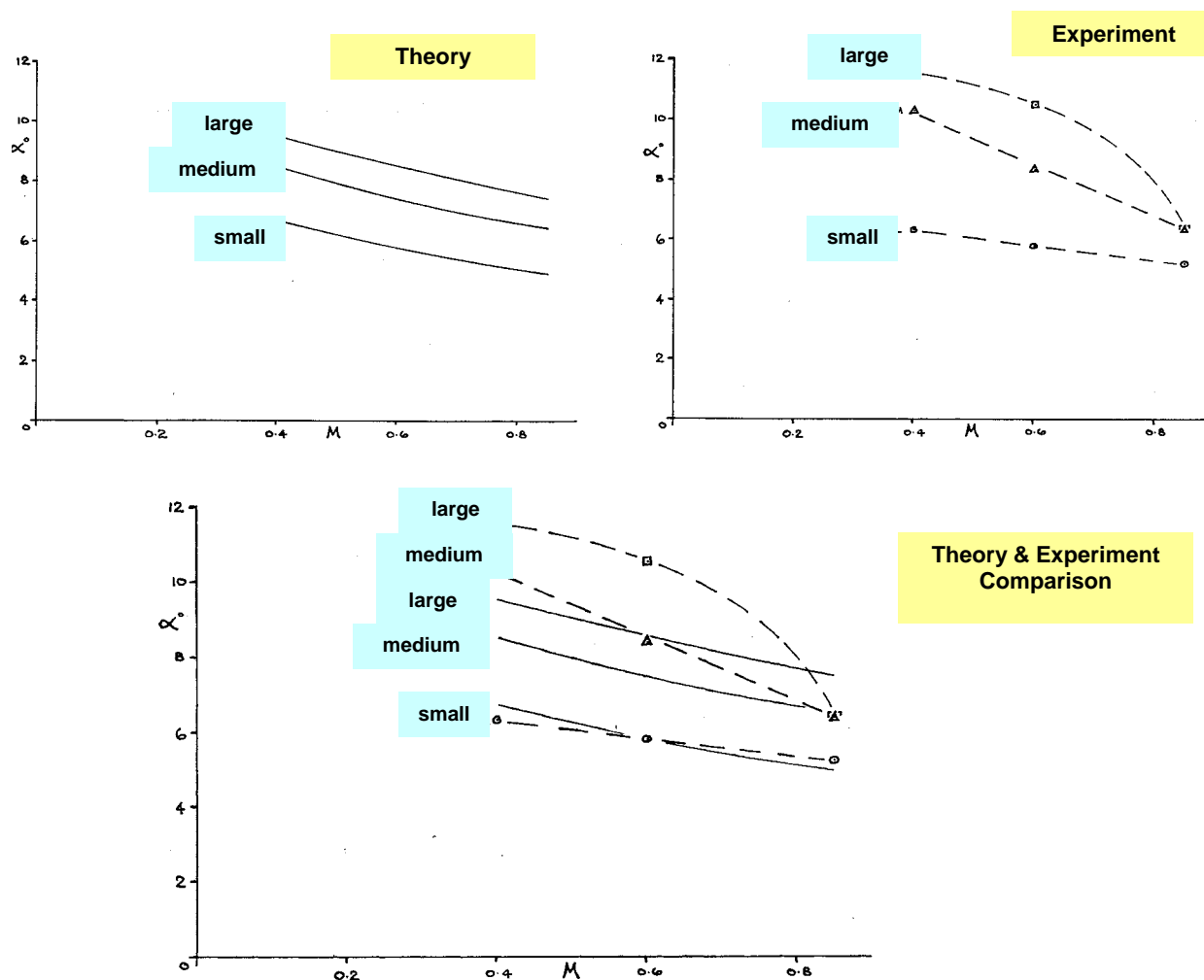
**Figure 33-30: Onset of Separation at Wing-Tip, Theory and Expt.
Small, Medium and Large Roundness Models, R_{mac} = 6 Million.**

The results also suggest that there is a need for a delay term of the order of $2° – 3°$ for the higher roundness wings. It may be that vortical flow over the blunt edges arises inboard of the actual geometrical LE. This will then depart from the assumptions implied in the predictive approach.

For the small roundness model at Reynolds number R_{mac} = 6 million, Figure 33-31 shows the development of the onset of separation along the span (y/s scale) for Mach 0.4, 0.65 and 0.85. Note that y/s = 1.0 corresponds to x/c_r of 1.0. The agreement between theory and experiment is excellent over the wing span.
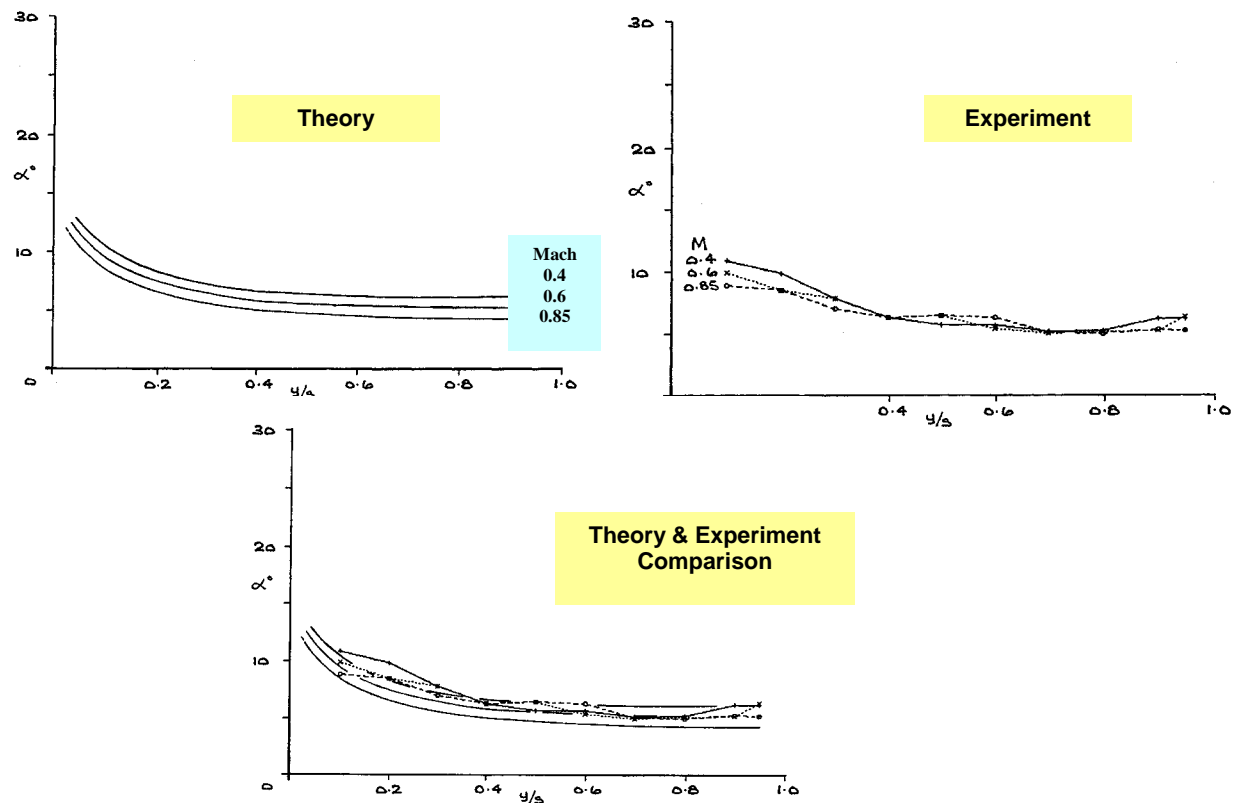
Figure 33-31: Development of Onset of Separation along Wing, Theory and Experiment, Small Roundness Model, R_{mac} = 6 Million, Mach Varies.

For the medium roundness model at Reynolds number R_{mac} = 6 million, Figure 33-32 refers to the development of the onset of separation along the span. Mach number values are: 0.4, 0.65 and 0.85. The agreement between theory and experiment is excellent at Mach 0.85. At Mach 0.6, the correlation is between about 1° AoA at the tip to about 2° in AoA at 0.2 y/s. At Mach 0.4, the correlation is between about 2° AoA at the tip to about 3° in AoA at 0.2 y/s.
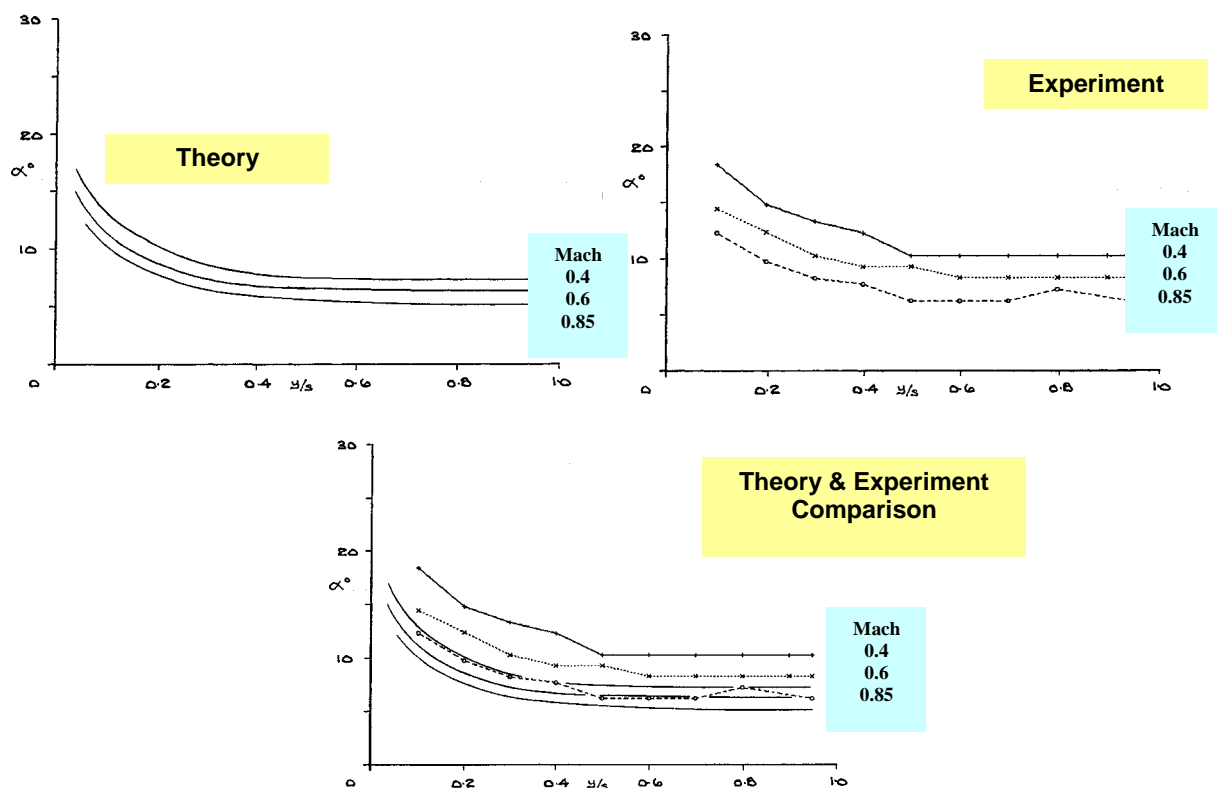
**Figure 33-32: Development of Onset of Separation along Wing, Theory
and Experiment, Medium Roundness, R_{mac} = 6 Million, Mach Varies.**

For the large roundness model at Reynolds number R_{mac} = 6 million, Figure 33-33 refers to the development of the onset of separation along the span. Mach number values are: 0.4, 0.65 and 0.85. The agreement between theory and experiment is excellent at Mach 0.85. At Mach 0.6, the correlation is between about 3° AoA at the tip to about 5° in AoA at 0.2 y/s. At Mach 0.4, the correlation is between about 4° AoA at the tip to about 8° in AoA at 0.2 y/s.
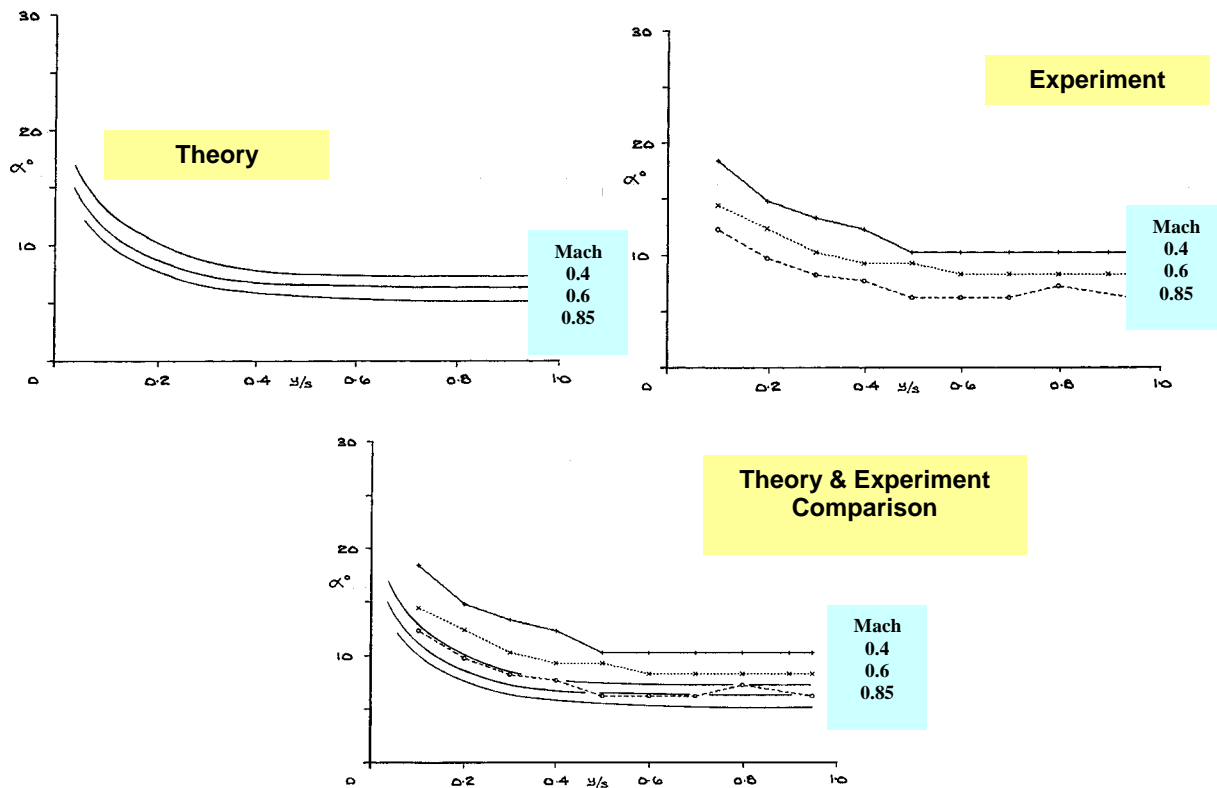
Figure 33-33: Development of Onset of Separation along Wing, Theory
and Experiment, Large Roundness, R_{mac} = 6 Million, Mach Varies.

For Reynolds number R_{mac} = 6 million and Mach 0.4, Figure 33-34 refers to the development of the onset of separation along the span of the models with different rounded LE. For the small radius model, the agreement between theory and experiment is excellent over the whole span.
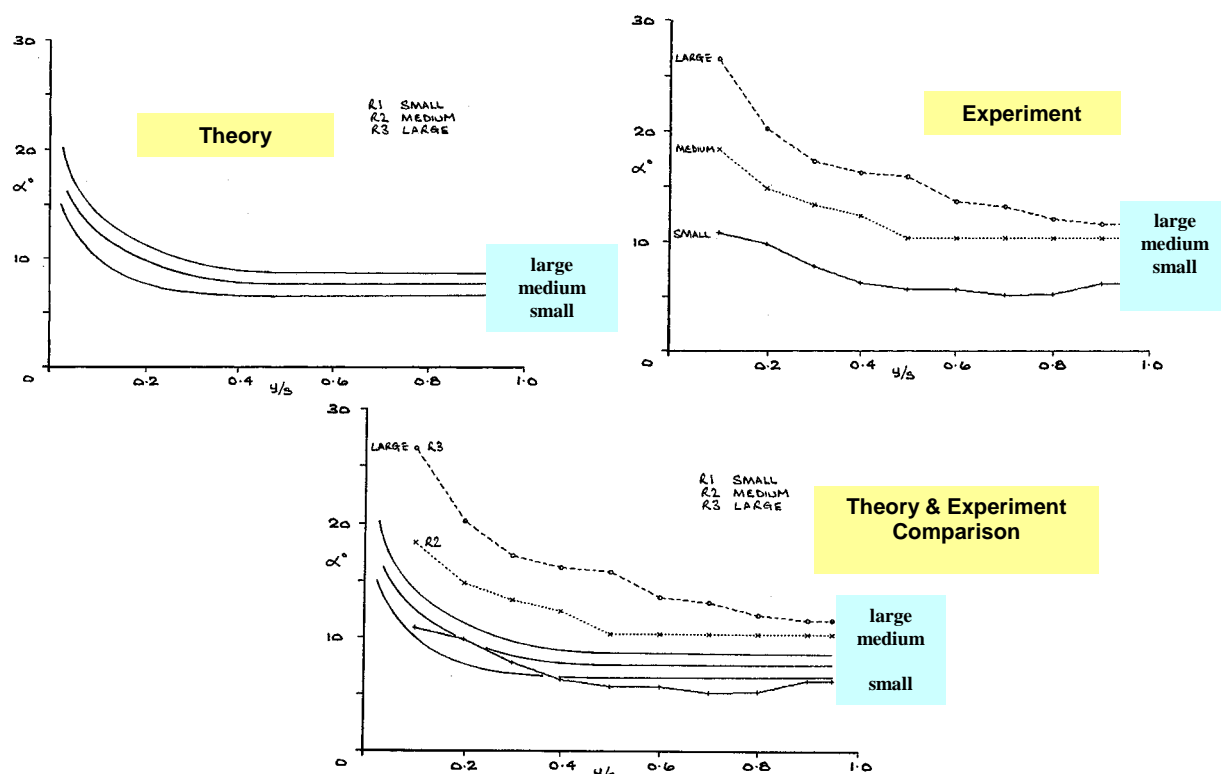
Figure 33-34: Development of Onset of Separation along Wing, Theory, Mach 0.4,
R_{mac} = 6 Million, Small, Medium and Large Roundness Models.

For Reynolds number R_{mac} = 60 million and Mach 0.4, Figure 33-35 refers to the development of the onset of separation along the span of the models with different roundness. For the small radius model, the agreement between theory and experiment is excellent over the whole span.
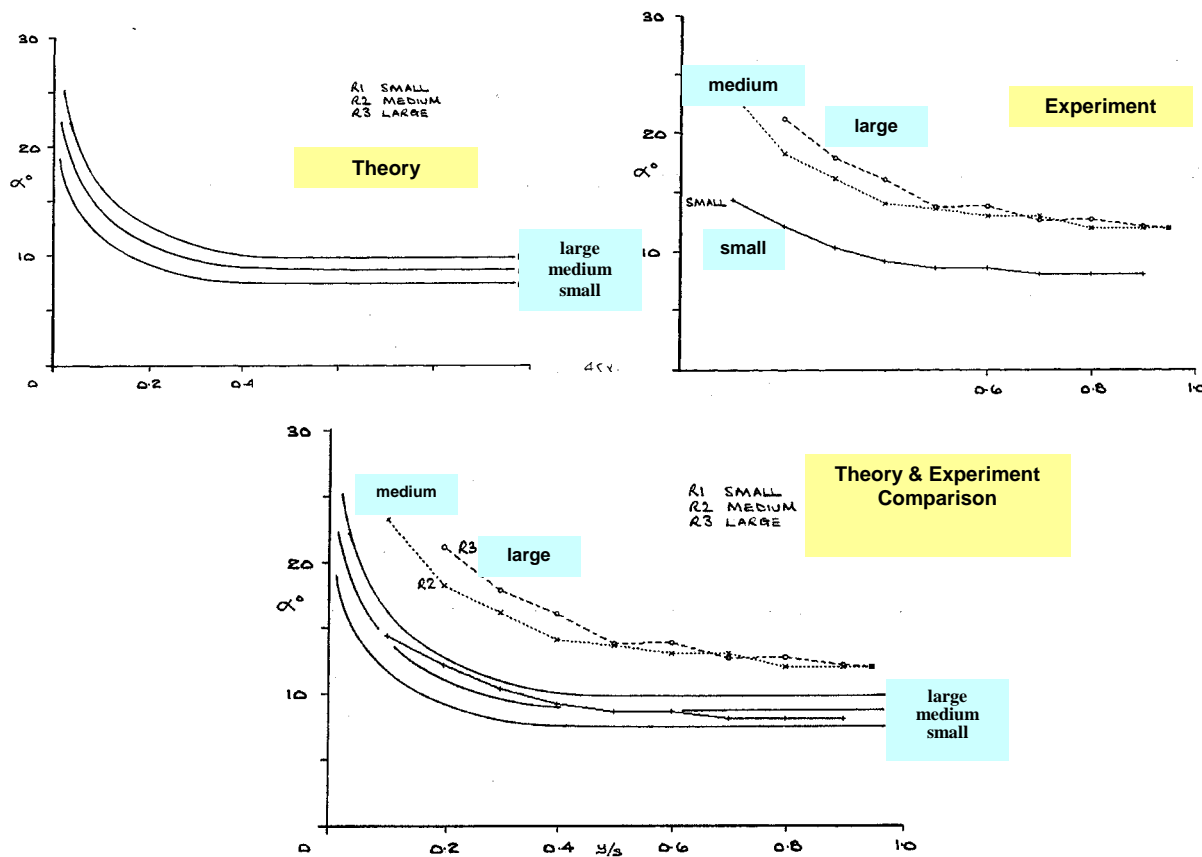
Figure 33-35: Development of Onset of Separation along Wing, Theory, Mach 0.4,
R_{mac} = 60 Million, Small, Medium and Large Roundness Models.

33.5   CONCLUDING REMARKS

This paper is motivated via the initiative of the RTO-AVT Task group AVT-113. This task group has followed on from the previous AVT-080 group. One of the tasks, VFE-2, is concerned with theoretical and experimental activities on a series of 65° delta wings with different LE bluntness. These were initially tested by Luckring at NASA LaRC. This paper is concerned with the prediction of flow separation onset for VFE-2.

The models used by Luckring have been described. These featured somewhat unusual non-standard aerofoils and some of the local parameters and curvatures were very much larger than those expected on practical wings. Nevertheless useful experimental results for the onset of vortical flow were available with independent sweeps of Mach and Reynolds number (NTF-WT).

Details of the Attained suction approach have been given. It starts with a Subsonic lifting surface theory and incorporates Mach and Reynolds number and Attained thrust and Vortex Effects.

Results obtained for various wings have been compared with Luckring data. These show encouraging correlation for wings with small and medium radii. For the large radii LE, the correlations were "best" at the

higher Mach number. The large roundness model wing implies perhaps a different interpretation from the experimental data – separation may be appreciably inboard of the LE.

It must be remembered that we are predicting onset of flow separation. Vortex formation (as observed in experiments) could be delayed!

The challenge is there for developers to improve on the empiricisms. Further development can be envisaged on many aspects. Moderate sweep wings are of current interest e.g. on UCAVs.

The present work has allowed an understanding of the directions in which the empiricism can be improved e.g. using an Euler solver as the core solver.

33.6   ACKNOWLEDGEMENTS

33.7   REFERENCES

[33-1]   Nangia, R.K. and Miller, A.S.: *Vortex Flow Dilemmas & Control on Wing Planforms for High Speeds*, RTO-AVT Symposium on "Advanced Flow Management, Vortex Flows & High Angle of Attack", Loen, Norway, May 2001, Meeting Proceedings RTO-MP-069 (I), SYA 9-1 to 9-14, 2003.

[33-2]   AVT-080 Report. Published by RTO & Springer Verlag, 2007.

[33-3]   Nangia, R.K.: *Applying Vortex Breakdown Empiricisms to Predict Aerodynamic Characteristics in Symmetric & Asymmetric Situations*, AIAA Paper 2003-3945, 2003.

[33-4]   Luckring, J.M.: *Reynolds Number and Leading-Edge Bluntness Effects on a 65° Delta Wing*, AIAA Paper 2002-0419, 2002.

[33-5]   Luckring, J.M.: *Transonic Reynolds Number and Leading-Edge Bluntness Effects on a 65° Delta Wing*, AIAA Paper 2003-0753, 2003.

[33-6]   Luckring, J.M.: *Compressibility and Leading-Edge Bluntness Effects for a 65° Delta Wing*, AIAA Paper 2004-0765, 2004.

[33-7]   Lamar, J.E.: *Some Recent Applications of the Suction Analogy to Vortex-Lift Estimates*, NASA-TM-X-72785, 1972.

[33-8]   Lamar, J.E. and Campbell. J.F.: *Recent Studies at NASA Langley of Vortical Flows with Neighbouring Surfaces*, AGARD-CP-342, 10-1 to 10-27, 1983.

[33-9] Carlson, H.W. and Mack, R.J.: *Studies of Leading-Edge Thrust Phenomena*, J. Aircraft., Vol. 17, No. 12, pp. 890-897, 1980.

[33-10] Carlson, H.W., Shrout, B.L. and Darden, C.M.: *Wing Design with Attainable Leading-Edge Thrust Considerations*, J. Aircraft, Vol. 22, No. 3, pp. 244-248, 1985.

[33-11] Polhamus, E.C.: *Predictions of Vortex-Lift Characteristics by a Leading-Edge Suction Analogy*, J. Aircraft., Vol. 8, No. 4, pp. 193-199, 1971.

[33-12] Polhamus, E.C.: *Charts for Predicting the Subsonic Vortex-Lift Characteristics of Arrow, Delta, and Diamond Wings*, NASA TN-D-6243, April 1971.

[33-13] Lan, C.E. and Hsu, C.H.: *Effects of Vortex Breakdown on Longitudinal and Lateral Aerodynamics of Slender Wings by the Suction Analogy*, AIAA Paper 82-1385, 1982.

[33-14] Lan, C.E.: *Theoretical Prediction of Wing Rocking*, AGARD-CP-386, pp. 32-1 to 32-13, 1985.

[33-15] Tseng, J.B. and Lan, C.E.: *Calculation of Aerodynamic Characteristics of Airplane Configurations at High Angle of Attack*, NASA CR-4182, 1988.

[33-16] Kuchemann, D.: *The Aerodynamic Design of Aircraft*, Pergamon Press, Oxford, 1978.

[33-17] Nangia, R.K.: *The Design of Manoeuvrable Wings using Panel Methods, Attained Thrust & Euler Codes*, ICAS-92, China, 1992.

[33-18] Nangia, R.K. and Palmer, M.E.: *A Comparative Study of Four UCAV Wing Layouts – High-Speed Aero Performance & Stability Considerations*, ICAS – 2006-1.7, Germany, September 2006.

Chapter 34 – LESSONS LEARNED FROM THE NUMERICAL INVESTIGATIONS ON THE VFE-2 CONFIGURATION

by

Willy Fritz[1] and Russell M. Cummings[2]

The Second International Vortex Flow Experiment provided a variety of experimental data for a 65° delta wing with sharp and blunt/rounded leading edges. Flow measurements including forces and moments, surface pressures, Pressure Sensitive Paint measurements, and off-surface flow variables from Particle Image Velocimetry were made available for comparisons with computational simulations. A number of test cases were chosen for simulation by seven numerical groups, and a summary of their results is presented here. The ability of computational fluid dynamics to predict such flow features as the dual primary vortex system found on the blunt leading edge configuration and a shock/vortex interaction for the sharp leading edge are assessed. While computational simulation has made great strides in recent years, there are still areas where further improvement can be made, including in turbulence modeling, transition modeling, and the ability to accurately compute unsteady flows.

34.1   NOMENCLATURE

A	=	wing aspect ratio, $\equiv b^2 / S$
a	=	speed of sound
b	=	wing span
C_p	=	pressure coefficient, $\equiv (p - p_\infty)/q_\infty$
c_f	=	local skin friction coefficient, $\equiv \tau / q_\infty$
c_{mac}	=	mean aerodynamic chord, $= 2c_r / 3$ (also c_{bar})
c_r	=	root chord (also c)
d	=	sting diameter
M	=	Mach number, $\equiv V / a$
p	=	pressure
q	=	dynamic pressure, $\equiv \rho V^2 / 2 = \gamma p M^2 / 2$
Re	=	Reynolds number based on mean aerodynamic chord, $\equiv V_\infty c_{mac} / \upsilon$
r_{le}	=	leading edge radius
S	=	wing planform area
t	=	wing maximum thickness
V	=	velocity
x	=	longitudinal dimension ($x = 0$ at apex of wing)

---

[1] Senior Development Engineer, Aerodynamics & Methods.

[2] Professor of Aeronautics, Department of Aeronautics.

x_v	=	position of vortex origin
α	=	angle of attack, deg
γ	=	ratio of specific heats
η	=	normalized local half span of the wing $\equiv 2y/b$
Λ	=	wing leading edge sweep angle, deg
λ	=	wing taper ratio, $\equiv c_t / c_r$
ρ	=	density
τ	=	shear stress
υ	=	kinematic viscosity
∞	=	free stream condition

DLR	=	German Aerospace Center / Germany
EADS	=	European Aeronautic Defence and Space Company / Germany
KTH	=	Royal Institute of Technology / Sweden
NASA	=	National Aeronautics and Space Administration / United States
NLR	=	National Aerospace Laboratory / Netherlands
UG	=	University of Glasgow / UK
USAFA	=	US Air Force Academy / United States

34.2   INTRODUCTION

The Second International Vortex Flow Experiment (VFE-2) is the outgrowth of a very successful First International Vortex Flow Experiment (VFE-1) program that took place from 1984 through 1986 [34-1]. VFE-1 was an experimental program that was undertaken to provide experimental data for the rapidly improving computational fluid dynamics (CFD) capabilities of the time. Euler calculations for delta wings in the early 1980s had progressed to such a state that improved experiments would be necessary to provide CFD simulations with important data for validation and verification of predictions. The VFE-1 configuration (see Figure 34-1) was a 65° sweep leading-edge clipped delta wing with a sharp leading edge and a fuselage. The experiments recorded surface pressures at three chord wise locations, as well as force measurements and flow field visualization. The results of VFE-1 were summarized in [34-2], and later reviews were made of the state-of-the-art in Euler code simulations in [34-3], [34-4]. Even for sharp leading edge delta wings with fixed primary separation, the Euler codes were not well suited to calculate the pressure distributions properly since the secondary vortex separation was not simulated by the inviscid equations.

Aspect ratio   A = 1.378
Taper ratio   λ = 0.15
Leading edge sweep   Λ = 65°
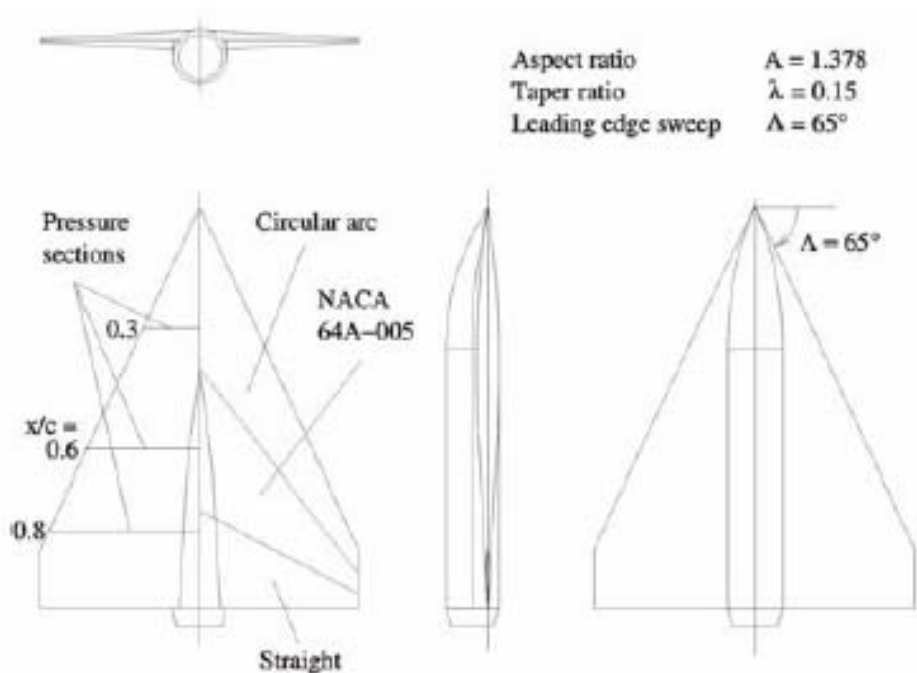
Figure 34-1: Configuration of the First International Vortex Flow Experiment (VFE-1); Ref. [34-1].

Since the mid 1980s it has become commonplace to simulate delta wing flows using the Navier-Stokes equations. Initially Reynolds-Averaged Navier-Stokes (RANS) simulations were performed, first with algebraic turbulence models, and later with 1- and 2-equation turbulence models [34-5]. In recent years, hybrid turbulence models have also been applied to the flow around delta wings with good success [34-6]. RANS simulations were able to predict secondary (and even tertiary) vortex separation, but issues with turbulence models often led to poor prediction of the surface pressures, especially the location and strength of the secondary vortices. This led to a need for improved experimental data for delta wings, and improved computational simulation methods, especially improvements in turbulence models.

In order to validate the results of Navier-Stokes calculations, new and more detailed experimental data are required, which led to a Second International Vortex Flow Experiment (VFE-2, see Ref. [34-7] and Chapter 17). The configuration for VFE-2 was chosen to create distinct flow regimes, including:

1) Attached flow without vortex formation, $0° \leq \alpha \leq 4°$

2) Separated vortical flow without vortex breakdown, $4° \leq \alpha \leq 20°$

3) Separated vortical flow with vortex breakdown, $20° \leq \alpha \leq 40°$

4) Separated deadwater flow, $40° \leq \alpha \leq 90°$

A delta wing with a leading edge sweep of 65° was chosen for the experiments with a flat plate inner portion in combination with interchangeable leading edges. Four leading edge configurations were chosen: a sharp leading edge, and three rounded leading edges of varying radii. The configuration, shown in Figure 34-2, had been initially tested at NASA Langley Research Center (Ref. [34-9] and Chapter 18), and additional experiments have been conducted at a variety of locations, including DLR in Germany (see Chapter 19), ONERA in France

(Chapter 20), TU Munich (Chapter 21), The University of Glasgow (Chapter 22), and Tübitak in Turkey (Chapter 23). The objectives for the VFE-2 experiments include (Ref. [34-8] and Chapter 17):

1) Investigations of laminar/turbulent transition on delta wings.

2) Detailed pressure distribution measurements, especially in the region of the onset of flow separation for configurations with rounded leading edges.

3) Boundary layer measurements including distributions of the components of velocity, vorticity, turbulent energy, and eddy viscosity.

4) Determination of the wall shear stress and detection of the secondary and tertiary separation lines.

5) Flow field measurements in the primary and secondary vortices including the distributions of the components of velocity, vorticity, turbulent energy, and eddy viscosity.

6) Investigations on the vortex breakdown flow field for delta wings with sharp and rounded leading edges including the surface pressure fluctuations caused by the spiral mode of vortex breakdown.
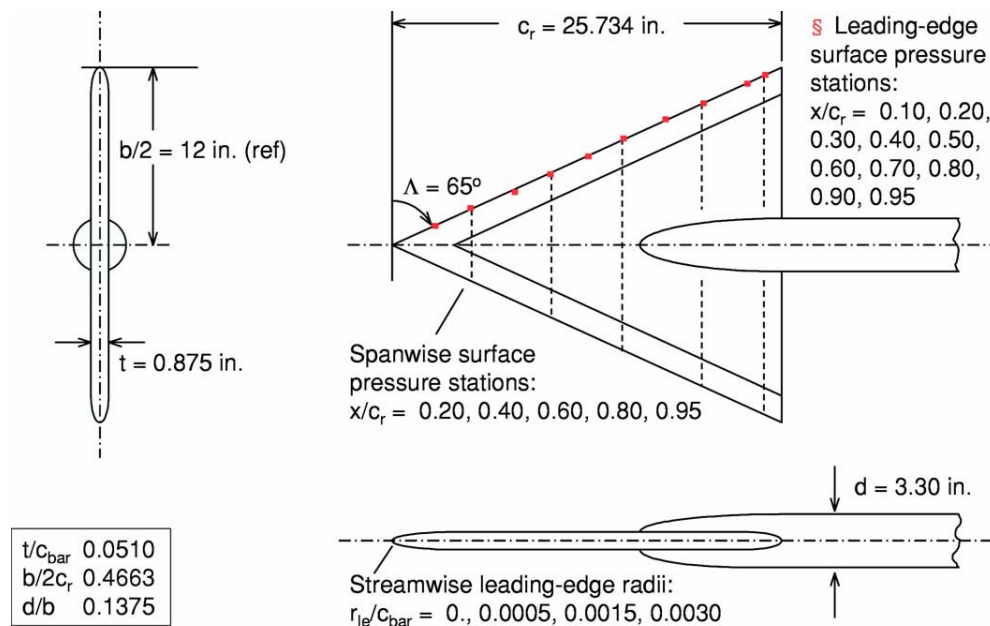
Figure 34-2: Configuration of the Second International Vortex Flow Experiment (VFE-2); Ref. [34-9].

Limited previous numerical simulations have been conducted to match the NASA Langley Research Center VFE-2 experiments. Londenberg performed simulations for a sharp leading edge transonic case in 1994 (in conjunction with the original wind tunnel tests) (Ref. [34-10]). Also, Chiba and Obayashi showed simulations of the dual primary vortex system for the rounded leading edge configuration [34-11]. The interesting topology of the dual primary vortex system led to the majority of numerical simulations for VFE-2. VFE-2 was formed as a Task Group (AVT-113) under the NATO Research and Technology Organization's Applied Vehicle Technology Panel. Numerical simulations were performed by participants from seven organizations in six countries (Germany, The Netherlands, Sweden, Turkey, United Kingdom, and United States). The majority of this paper serves as a summary for the numerical predictions that were presented in a special session at the AIAA 46th Aerospace Sciences Meeting, including in Refs. [34-12] through [34-17].

34.3   GOALS FOR THE VFE-2 NUMERICAL SOLUTIONS

Since the quantity of data and tested flow conditions for VFE-2 was quite large ([34-18] and Chapter 24), the CFD simulations were chosen to concentrate on about thirty specific flow/geometry combinations (see Appendix 34-1). Of these, a specific subset was chosen as representative of the various simulations, including:

1) Onset of vortical flow:

    a)   Sharp leading edge: Separated flow

    b)   Medium radius leading edge: Partly attached, partly separated flow

2) Separated flow without vortex breakdown:

    a)   Sharp leading edge

    b)   Medium radius leading edge

3) Separated flow with vortex breakdown:

    a)   Sharp leading edge

    b)   Medium radius leading edge

4) Transonic flow with vortex breakdown

This led to comparisons for the cases shown in Table 34-1 that will be presented in this review.

Table 34-1: CFD Cases Chosen for Summary Comparison

Case No.	Leading Edge*	Mach No., M_∞	Angle of Attack, α (deg)	Reynolds Number, Re
4.5	MRLE	0.4	13	3×10^6
5	MRLE	0.4	13	6×10^6
14	MRLE	0.4	18	6×10^6
15	SLE	0.4	18	6×10^6
24	SLE	0.4	23	6×10^6
27	SLE	0.85	23	6×10^6

*MRLE: Medium Radius Leading Edge; SLE: Sharp Leading Edge

34.4   ROUNDED LEADING EDGE FLOW TOPOLOGY

The rounded leading edge delta wing was the primary configuration chosen for study because the early wind tunnel experiments at NASA Langley Research Center had shown unusual flow features. Specifically, two primary, co-rotating, vortices were seen which were dramatically different than the vortex system found for delta wings with sharp leading edges. Sharp leading edge delta wings have primary vortices that roll up from the shear layer that separates along the sharp edge from the apex of the delta wing (see Figure 34-3). These vortices produce secondary vortices on the upper surface that form due to boundary layer separation from the

outboard flow induced by the primary vortices. Because the separation location is fixed, the flow is only mildly sensitive to Reynolds number, but flow properties also vary with angle of attack and Mach number. Rounded (or blunt) leading edge delta wings have quite different flow fields, however. Specifically, because the separation location is not fixed, the flow exhibits a displaced vortex origin that varies strongly with angle of attack, Mach number, Reynolds number, and leading-edge radius. In addition, a dual primary vortex structure develops for these flows (see Figure 34-4).
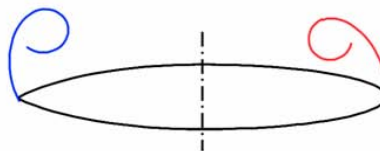
**Figure 34-3: Comparison of Vortical Flow Features for Sharp and
Rounded Leading Edge Delta Wings; Ref. [34-9] and Chapter 18.**
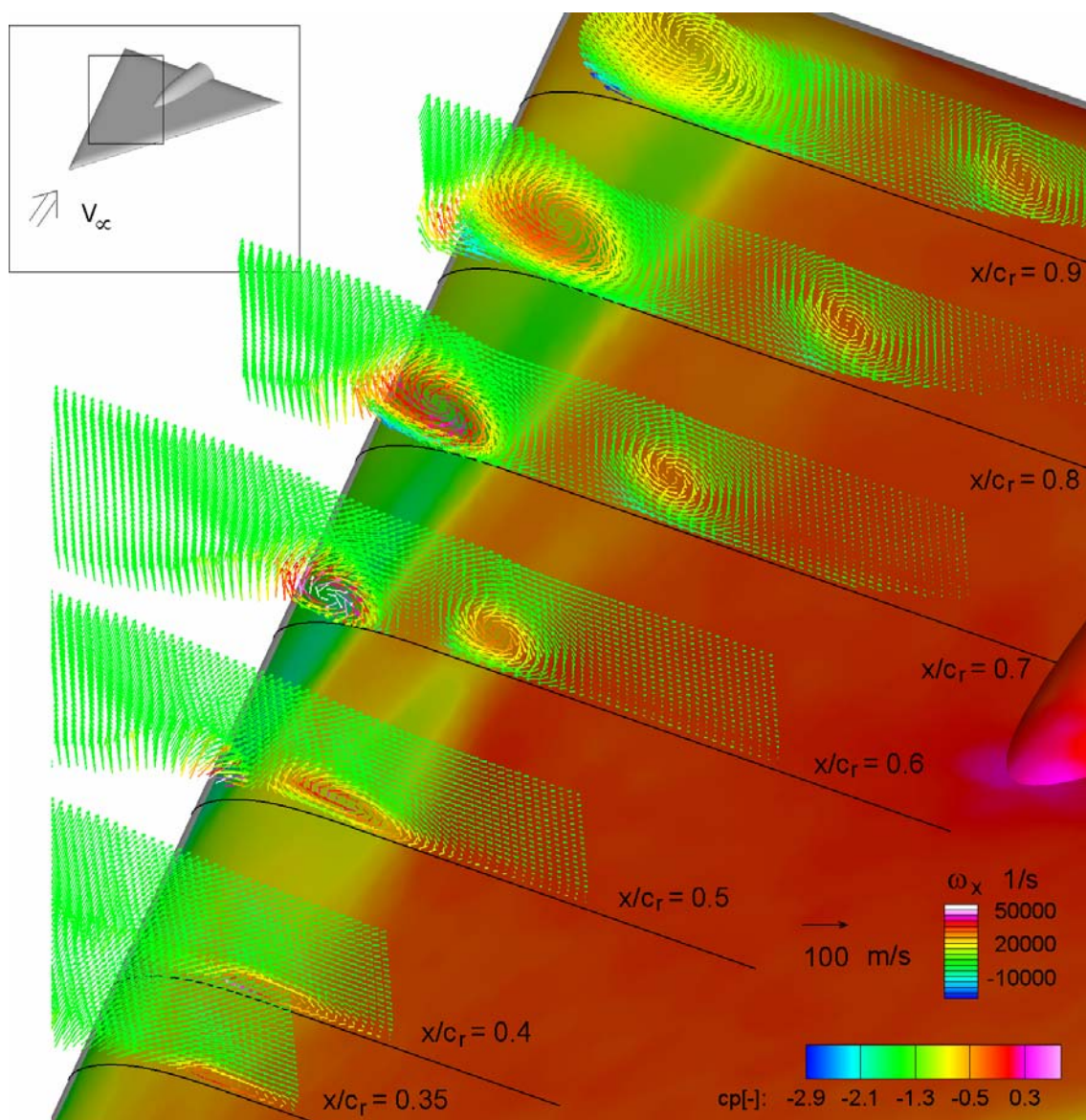
**Figure 34-4: Dual Primary Vortex System for MRLE Delta Wing with PIV
and PSP, M = 0.4, Re = 3 x 10⁶, α = 13°; Ref. [34-19] and Chapter 19.**

34.5   COMPUTER CODES AND TURBULENCE MODELS

One of the important aspects of the VFE-2 working group was to determine the abilities and capabilities of modern CFD Navier-Stokes codes and turbulence models to properly simulate the flows found in the wind tunnel experiments. A group of researchers from seven organizations in six countries simulated various combinations of the test cases, and results for those simulations will be summarized and discussed here. Table 34-2 shows the organizations, codes, and turbulence models used in the following simulations. Refs. [34-12] through [34-17] and Chapters 25 through 32 should be referred to for details about the particular codes, grids, and turbulence models.

Table 34-2: Organization, Codes, and Turbulence Models for CFD Simulations

Organization	Grid Type	Grid Size	Code	Turbulence Models
EADS	Block Structured	$\sim$10 x 10^6	FLOWer	Wilcox k-ω
KTH	Unstructured, adapted	up to 7 x 10^6	EDGE	EARSM + Hellsten k-ω
NLR	Block Structured	$\sim$4 x 10^6	ENFLO	TNT k-ω + vorticity correction
TAI	Block Structured	$\sim$2 x 10^6	TAI-xFlowg	SA
UG	Block Structured	$\sim$7 x 10^6	PM3D	TNT k-ω + vorticity correction
DLR	Unstructured	$\sim$16 x 10^6	Tau	SA, Wilcox k-ω
USAFA	Unstructured	$\sim$26 x 10^6	Cobalt	SA and SA-DES

34.6   RESULTS AND DISCUSSIONS

Various solutions for the six cases described in Table 34-1 will be presented and compared in this section. The goal is not to show comparisons of every solution, rather to show a representative set of comparisons so that appropriate conclusions can be drawn about the state of the art in simulating these complex flow fields.

34.6.1   Case 4.5: MRLE, M = 0.40, α = 13°, Re = 3 x 10^6

This case was a cryptic test case for a very long time. As Figure 34-5 shows, there are the footprints of two vortices in the surface pressure distribution. Besides the classical main leading edge vortex, which begins at a certain distance from the apex of the wing due to the rounded leading edges, there is also a second primary vortex more inboard. The stream traces show that both vortices have the same sense of rotation. The inner vortex is formed by a flow separation in the front region of the wing, which rolls up into a longitudinal vortex. (By their torsion the 3-D volume ribbons also indicate the local vorticity).
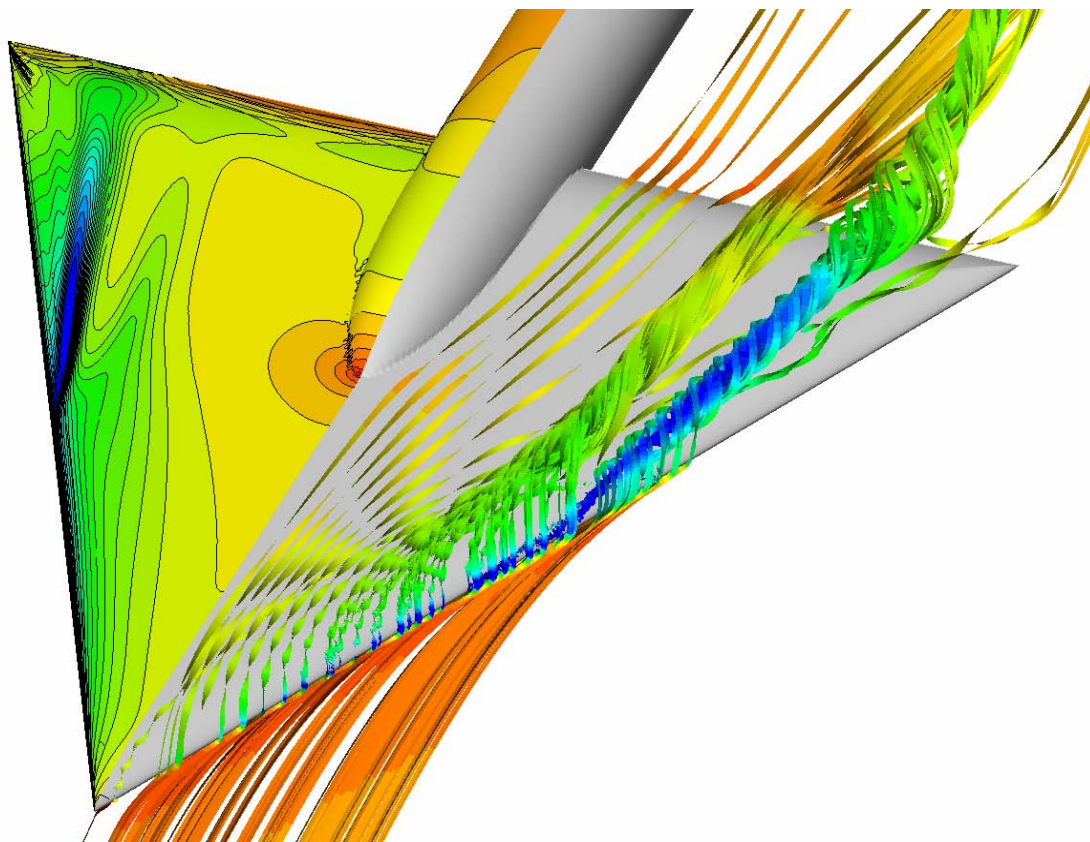
**Figure 34-5: Flow Features for Case 4.5: MRLE, M = 0.40, α = 13°, Re = 3 x 10^{6} (Surface Pressure
Contours and Streamtraces by 3-D Volume Ribbons, Colored by Local C_p Values).**

A detailed discussion of this complicated flow field is given in the individual chapters of the contributors, and in the Refs. [34-12]-[34-17], [34-19]. In order for the numerical solutions to provide quantitatively correct results, it is important that the onset of the main primary separation is fairly well predicted. A more up- or downstream position of this separation point will lead to large differences in the surface pressure distribution, in addition to other aspects of the flow field. A second challenge for the numerical methods is the separation in the forward region of the wing, which leads to the inner vortex. The strength and the position of the inner vortex affect the second suction peak in the surface pressure distribution. The strength of this inner vortex (and the effect on the surface pressure distribution) depends very much on the position of the leading edge separation. As soon as this leading edge vortex has reached certain strength, the inner vortex is no longer fed, since it is separated from the shear layer coming from the leading edge. From this longitudinal position (and downstream), the inner vortex weakens and finally dissipates. If the predicted formation point for the inner vortex is too much upstream, leading edge separation produces a very weak inner vortex which dissipates very early. All these details are, of course, strongly affected by the grid resolution, the quality of the turbulence model, and also the transition location (due to the round leading edge).

Figure 34-6 shows a comparison of different numerical surface pressure contours with those of the PSP experiment of DLR (Ref. [34-19] and Chapter 19). The dashed horizontal line indicates the onset of the main primary separation in the experiment. The prediction of this vortex onset is the main difference between the different numerical solutions. The EADS-solutions has this separation point slightly behind, but very close to,

the experimental separation point. The other solutions show a slightly more upstream position (DLR, TAI, and USAFA) or a considerable more upstream position (KTH). Except for the TAI-solution. All other solutions show the footprint of the inner vortex. Possibly the TAI-grid with 2 million grid points is not fine enough to resolve this flow feature. As can also be seen, none of the solutions exactly match the experimental surface pressure pattern.
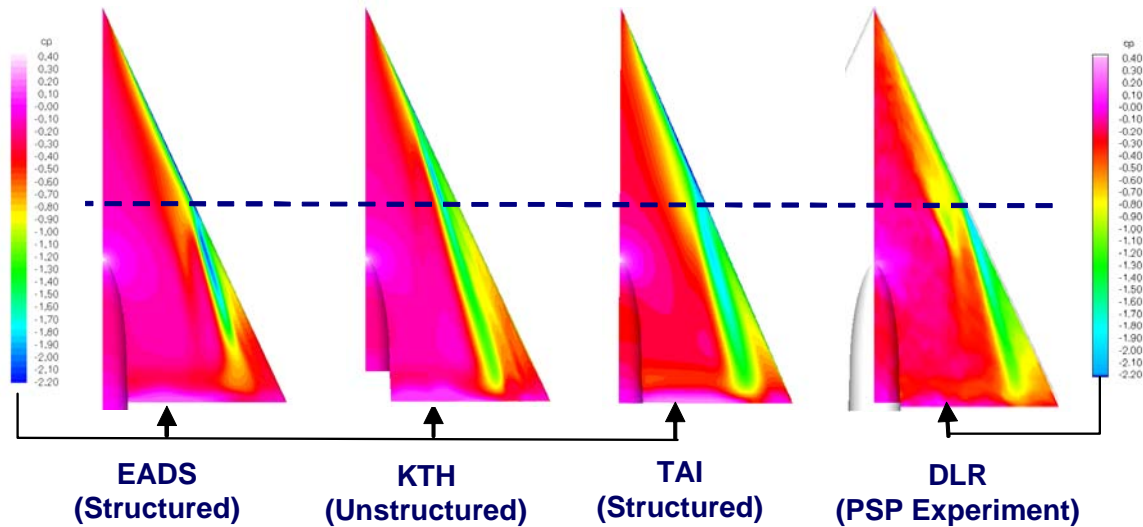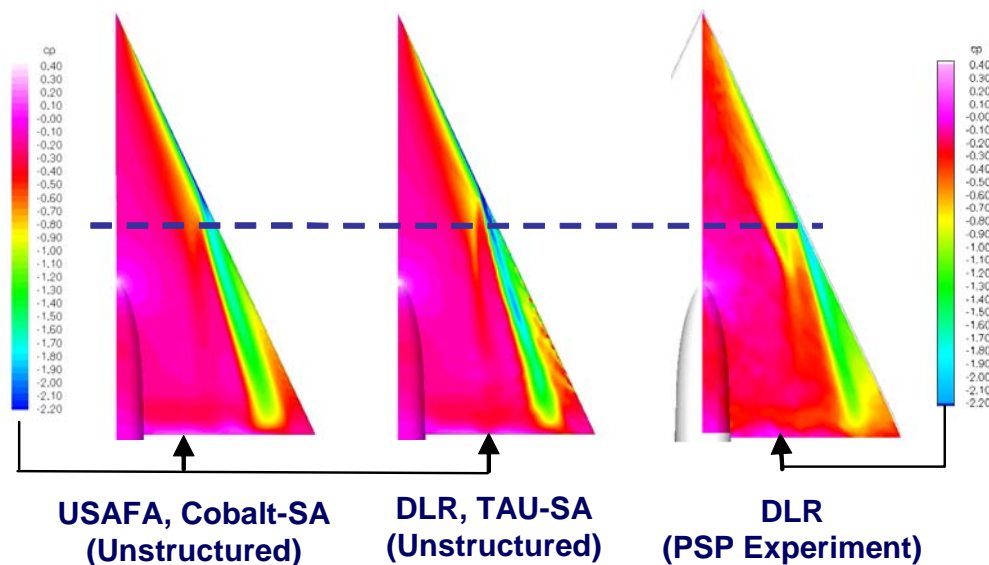
**Figure 34-6: Surface Pressure Maps and Onset of Leading-Edge
Vortex for Case 4.5: MRLE, M = 0.40, α = 13°, Re = 3 x 10^6.**

A more detailed comparison of the surface pressure distribution is given in Figure 34-7. At the first cross section shown ($x/c_r = 0.2$), where no leading edge separation occurs, all the numerical pressure distributions are identical and agree with the experimental data. There is a similar situation at $x/c_r = 0.4$; four of the five numerical pressure distributions still show no leading edge separation and thus are identical and agree very well with the experimental data. The KTH solution already shows the effect of a primary vortex and differs from the other solutions. The experimental pressure distribution in this section already shows an effect of the beginning of the inner vortex. This effect can slightly be seen in the KTH solution.

$x/c_r=0.2$

$x/c_r=0.4$

$x/c_r=0.6$

$x/c_r=0.8$

$x/c_r=0.95$

**Figure 34-7: Comparison of Surface Pressures and Experimental Data
(Ref. [34-19]) for Case 4.5: MRLE, M = 0.40, α = 13°, Re = 3 x 10^{6}.**

At $x/c_r = 0.6$, all solutions and the experimental data clearly show a primary vortex. There are differences in the position and the magnitude of the leeward suction peak due to this primary vortex. These differences can be related to the onset of the primary leading edge separation. The more upstream this separation occurs, the more inboard the suction peak moves due to the primary vortex at this cross section. The experimental data also show very clearly the effect of the second, inner vortex. As already mentioned above, the foot print of this second vortex is not present in the TAI solution. In the KTH solution, this inner vortex is due to the early leading edge separation which is too weak at this cross section. The other three solutions show the effect of this inner vortex. The EADS solution shows this second peak at the correct span wise position. The DLR and USAFA solutions show that the outer primary vortex is already more inboard when compared with the experiment, and the inner suction peak is consequently also more inboard. But in all of these three solutions the inner vortex is too weak when compared to the experiment.

In the cross section $x/_{cr}$ = 0.8 the various results are very similar. The more upstream the leading edge separation occurs, the more inboard the primary vortex is positioned (in the DLR and USAFA solution this can be detected at the position of the inboard pressure gradient). The footprint of the inner vortex has become very weak and those solutions which showed the inner vortex in the cross section x/c_r = 0.6 also show the decrease of this vortex.

At the last cross section, x/c_r = 0.95, the experimental pressure distribution shows a weak primary vortex. This cross section is situated in the region of high surface curvature where the geometry changes from the flat plate to the sharp leading edge. This leads to a significant deceleration of the axial flow. Additionally, all other upstream effects have accumulated in this section. Therefore, the prediction of the flow characteristics in this section is very difficult. This can be seen in the numerical pressure distributions, which scatter from under prediction to over prediction of the suction peak.

Figure 34-8 shows a comparison of the numerical prediction of the skin friction magnitude for this test case. The skin friction distributions are consistent with the surface pressure distributions shown in Figure 34-7. They show more clearly the position and the compactness of the main primary vortex, as well as the inner vortex. The maximum values at the peak of the main primary vortex are very similar. This indicates that the grid resolution in the boundary region is very similar in the different grids.
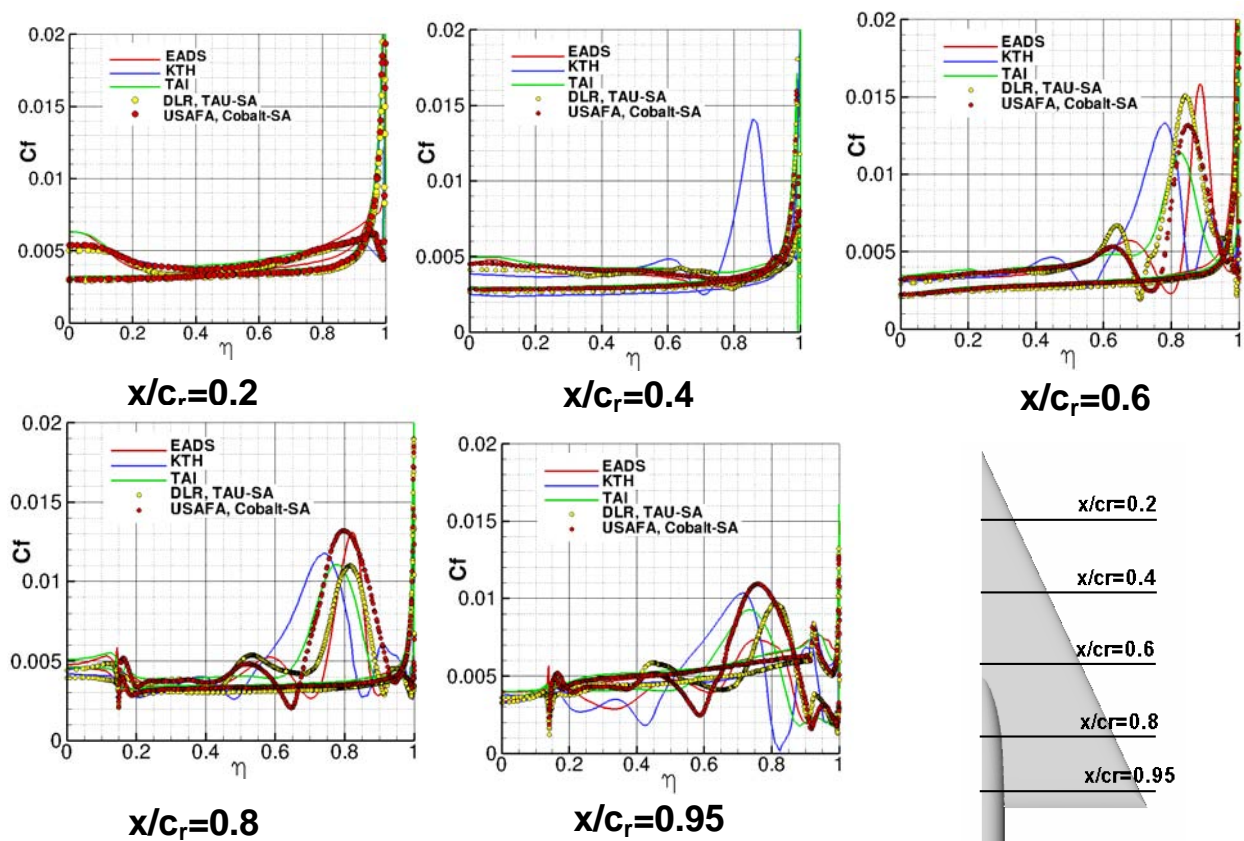
Figure 34-8: Comparison of Computed Surface Skin Friction
Data for Case 4.5: MRLE, M = 0.40, α = 13°, Re = 3 x 10^6.

The different surface grids which have been used for this test case are given in Figure 34-9. From these surface grids it can be concluded that the TAI grid is possibly not fine enough for a resolution of the inner vortex. Because of the isotropic surface triangulation, the unstructured grids also have high grid density in the axial direction. The structured grids are both conical grids.

EADS   **KTH**   **TAI**

USAFA   **DLR**
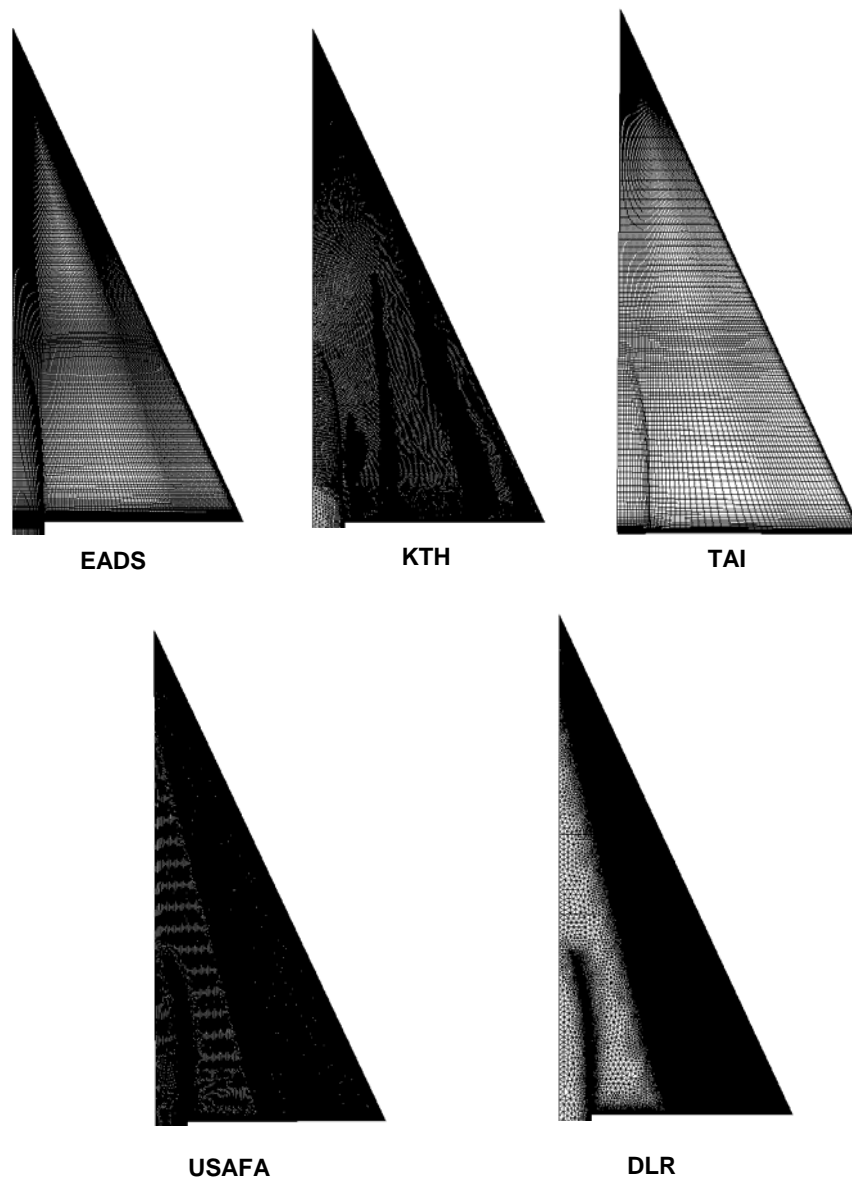
Figure 34-9: Surface Grid Density Comparison for Various Predictions.

34.6.2   Case 5: MRLE, M = 0.40, α = 13°, Re = 6 x 10^6

This test case is very similar to Case 4.5 above, but in the experiments two very important differences have been observed. Due to the higher Reynolds number, the leading edge separation is delayed to a more downstream

position. Also due to the higher Reynolds number, the inner vortex is now much weaker when compared with the test case above. The LPTP experimental data from NASA (Ref. [34-9]) are used for comparison with the numerical predictions.

The surface pressure contours of three different typical solutions are presented in Figure 34-10. The horizontal dashed lines mark the onset of the leading edge separation in the different numerical solutions. In the experiment, the onset of the leading edge vortex is somewhere upstream of the cross section $x/c_r = 0.6$. There are very clear differences in the prediction of this leading edge separation. In the EADS solution it occurs more downstream (slightly behind $x/c_r = 0.6$), in the KTH-solution the separation is too much upstream (close to $x/c_r = 0.2$) and in the TAI-solution separation is at $x/c_r = 0.5$. Footprints of the inner vortex are weakly present in the KTH solution and very weakly present in the EADS solution.

**EADS
(Structured)**　　**KTH
(Unstructured)**　　**TAI
(Structured)**　　**NASA
(Experiment)**
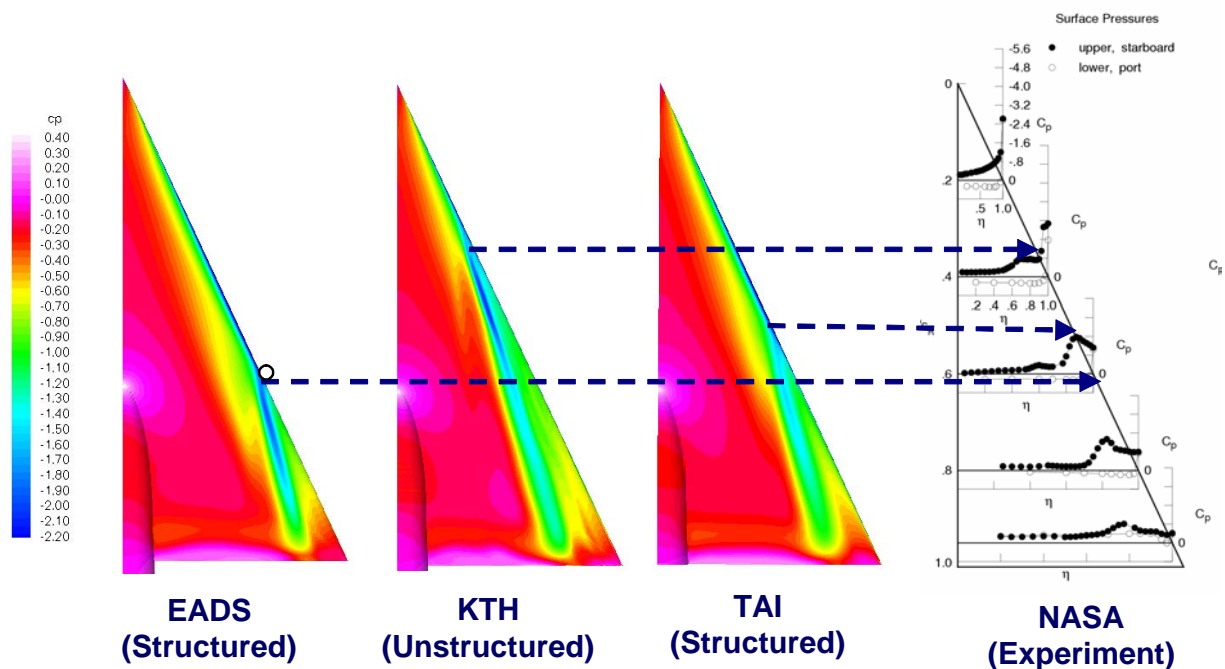
**Figure 34-10: Surface Pressure Maps and Onset of Leading-Edge
Vortex for Case 5: MRLE, M = 0.40, α = 13°, Re = 6 x 10^6.**

Figure 34-11 shows the comparison of the surface pressure distributions for this test case. In the experimental pressure distribution there is only a considerable effect of the inner separation at the cross section $x/c_r = 0.4$, and at $x/c_r = 0.6$ only the effect of a very weak inner vortex can be observed. So for this test case the inner vortex plays only a minor role. The three solutions can be characterized as follows:

- Too early leading edge separation (KTH);

- Too late leading edge separation (EADS); and

- Leading edge separation very close to the experiment (TAI).
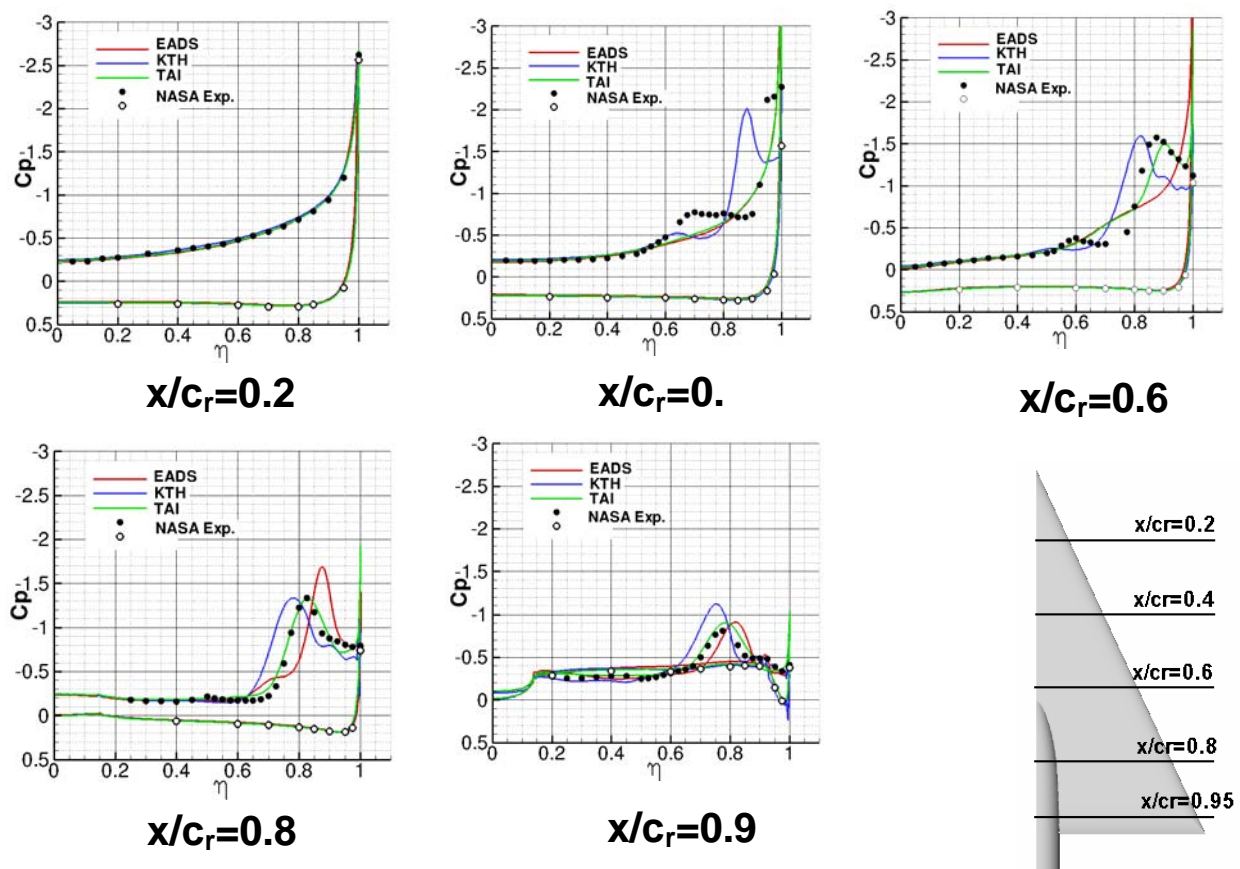
**Figure 34-11: Comparison of Surface Pressures and Experimental Data
(Ref. [34-9]) for Case 5: MRLE, M = 0.40, α = 13°, Re = 6 x 10^{6}.**

The different surface pressure distributions are consequences of these effects. The more upstream leading edge separation (KTH) leads to a more inboard position of the leeward suction peak. A more delayed separation (EADS) gives a more inboard position. The TAI solution with the leading edge separation very close to the experimental value shows the correct position of the suction peak and matches the experimental data quite well.

There are surely several effects or sensitivities which may influence the onset of this leading edge separation. One effect may be the unknown position of boundary layer transition. (All numerical simulations have been done in fully turbulent mode). In order to asses the effect of transition, a calculation with prescribed transition was performed at EADS. The result is presented in Figure 34-12.

Transiton   **No Transition**
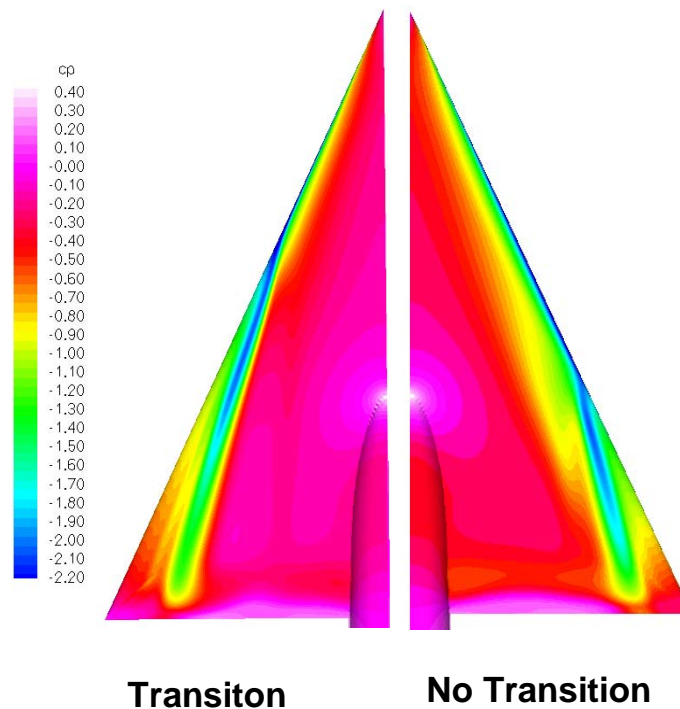
**Figure 34-12: Impact of Transition on Surface Flow for Case 5
(EADS-Solution, see Chapter 25): MRLE, M = 0.40, α = 13°, Re = 6 x 10^6.**

The transition was specified along a conical line close to the wing leading edge on the upper side of the wing. The distance of this conical section from the leading edge was $\Delta y = 0.006 * b_{local}$. During the calculation the effect of transition is realized by forcing zero production of turbulence within the laminar region. As Figure 34-12 demonstrates, there is a considerable effect on the solution. Up to now it has not been quite clear whether this is a real physical effect, or whether the turbulence model produces too much eddy viscosity around the leading edge, which must be corrected. But in any case this calculation shows that the numerical solution is very sensitive to small variations in the eddy viscosity distribution.

An assessment of the effect of the Reynolds number on the leading edge separation is given in Figure 34-13. From the experiments [34-9] it is known that increasing Reynolds number delays the primary separation location. This effect is not uniform in the different solutions. The EADS solution probably shows a too strong delay, the KTH solution shows no clear effect, and the TAI solution shows a reasonable effect of increasing Reynolds number.
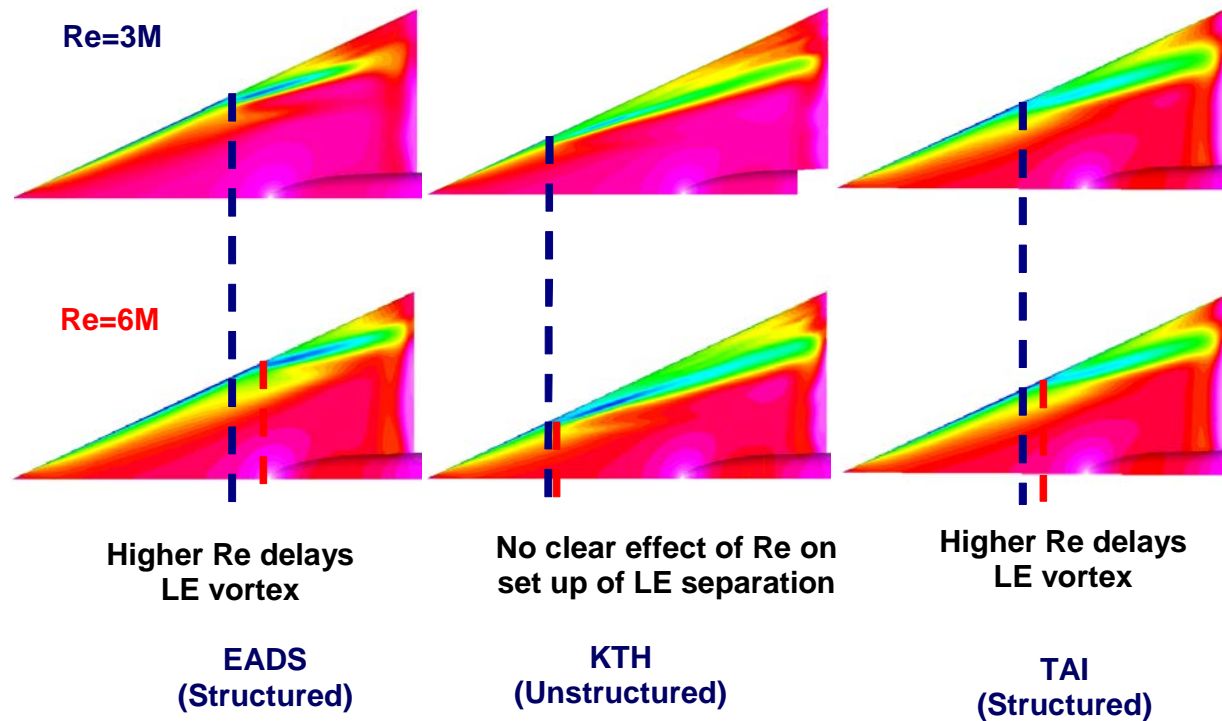
**Figure 34-13: Effect of Reynolds Number on Surface Flows
for Case 5: MRLE, M = 0.40, α = 13°, Re = 6 x 10^6.**

34.6.3   Case 14: MRLE, M = 0.40, α = 18°, Re = 6 x 10^6

The next test case is again the round leading edge geometry, but at a higher angle of attack. The leading edge separation now moves close to the wing apex and the inner vortex has no considerable effect. A fully developed primary vortex without vortex break down should be expected for this case. The vortical flow structure is shown in Figure 34-14, as shown by the EADS solution.
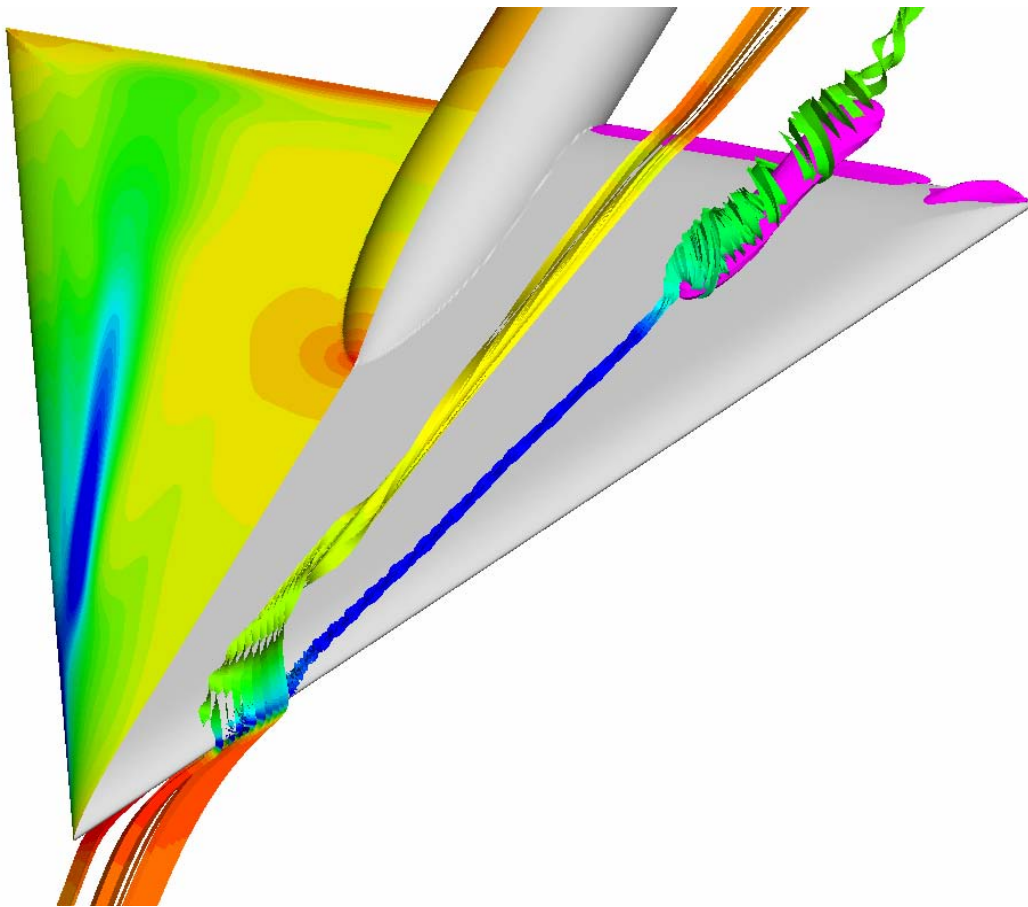
Figure 34-14: Flow Features for Case 14: MRLE, M = 0.40, α = 18°, Re = 6 x 10^6.

In Figure 34-14 the vortical flow structure is visualized again by 3-D volume ribbons. There is a separation at the apex region of the wing which rolls up into a small inner vortex. But this inner vortex only has a small impact on the pressure distribution in the apex region. The leading edge separation now begins very close to the wing apex. The core of the leading edge vortex remains very compact until $x/c_r = 0.8$. At this position the core forms a small bubble until to the rear end of the wing where the core becomes compact again. The pink colored bubble in the figure is an iso-surface of zero axial velocity. Inside the bubble the axial velocity is negative and outside it is positive. Negative axial velocity in the vortex core is a criterion for vortex breakdown, which means that the calculation shows a very weak vortex breakdown. In general for a 65° swept delta wing, vortex breakdown is expected at $\alpha = 21°$, but the geometry has a highly curved trailing edge region, which induces an additional increase in pressure. This may lead to an earlier vortex breakdown.

Figure 34-15 shows the surface pressure contours for different numerical solutions. The differences in the onset of the leading edge separation are now much smaller and the pressure contours look more similar as in the previous cases. Three solutions (EADS, KTH, DLR) indicate the above mentioned vortex breakdown at the rear end of the wing. In the experimental pressure distributions (NASA LTPT experiments [34-9]) there is a rather compact suction peak up to $x/c_r = 0.8$. At $x/c_r = 0.95$, there is still a vortical flow structure, but the suction peak is smeared out. This may indicate a very weak vortex breakdown at the rear end of the wing (due to the high curvature of the trailing edge).

**EADS
(Structured)**

**KTH
(Unstructured)**

**TAI
(Structured)**

**NASA
(Experiment)**

**USAFA, Cobalt-SA
(Unstructured)**

**DLR, TAU-kω
(Unstructured)**

**NASA
(Experiment)**
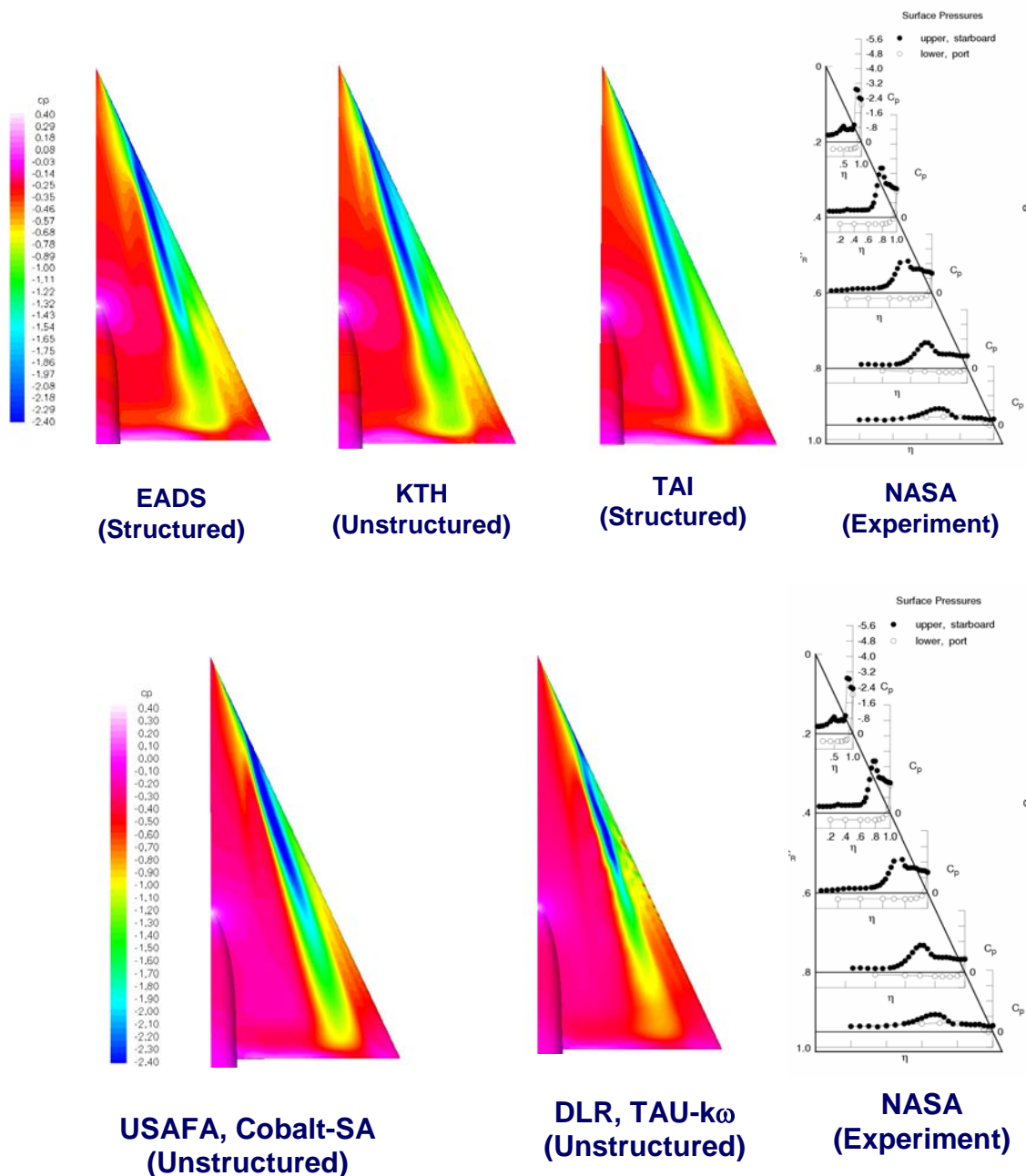
Figure 34-15: Surface Pressure Maps for Case 14: MRLE, M = 0.40, α = 18°, Re = 6 x 10⁶.

The surface pressure distributions now agree much better compared to the previous cases (Figure 34-16). Essential differences are at $x/c_r = 0.2$. The KTH solution already clearly shows a primary vortex, but slightly more inboard compared to the experiment. All other solutions do not yet show a primary vortex. This indicates that the KTH solution has the leading edge separation a little bit too early (but very close to the experiment) and that the other solutions have the leading edge separation later when compared with the experiment.
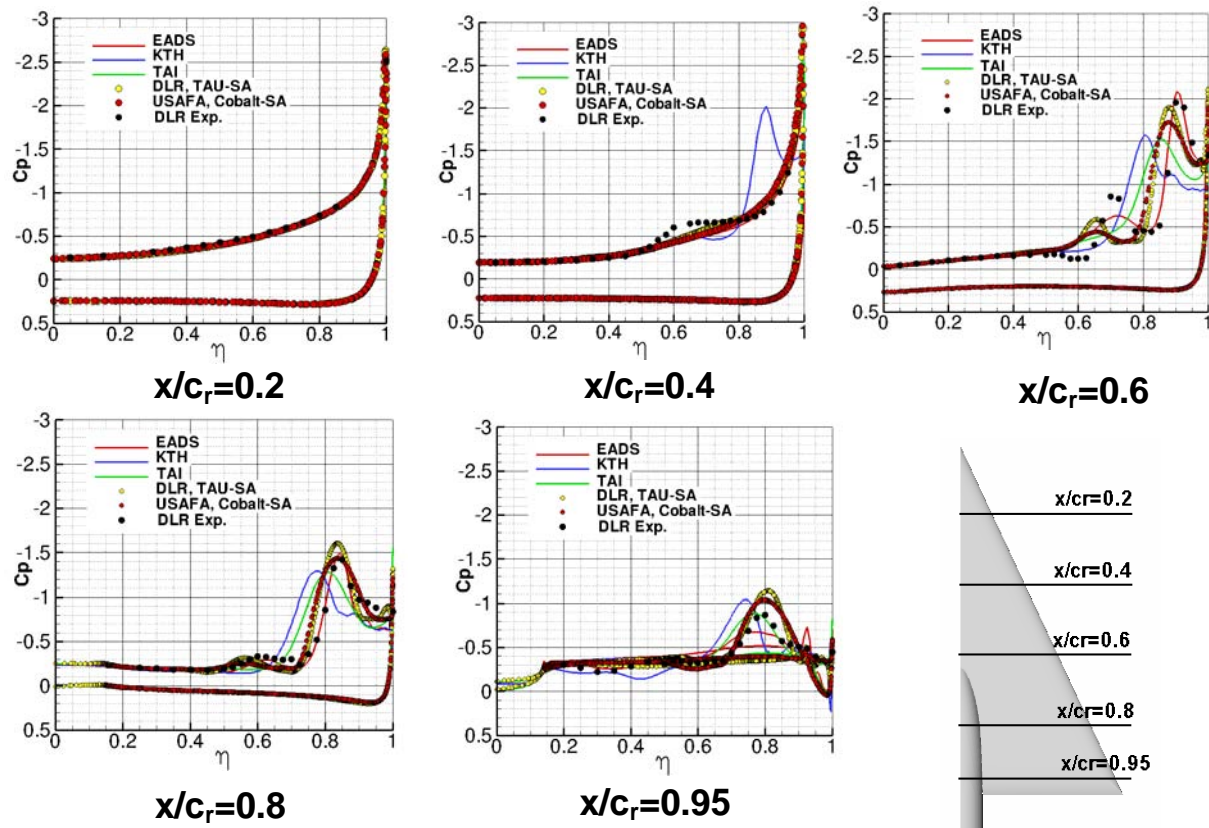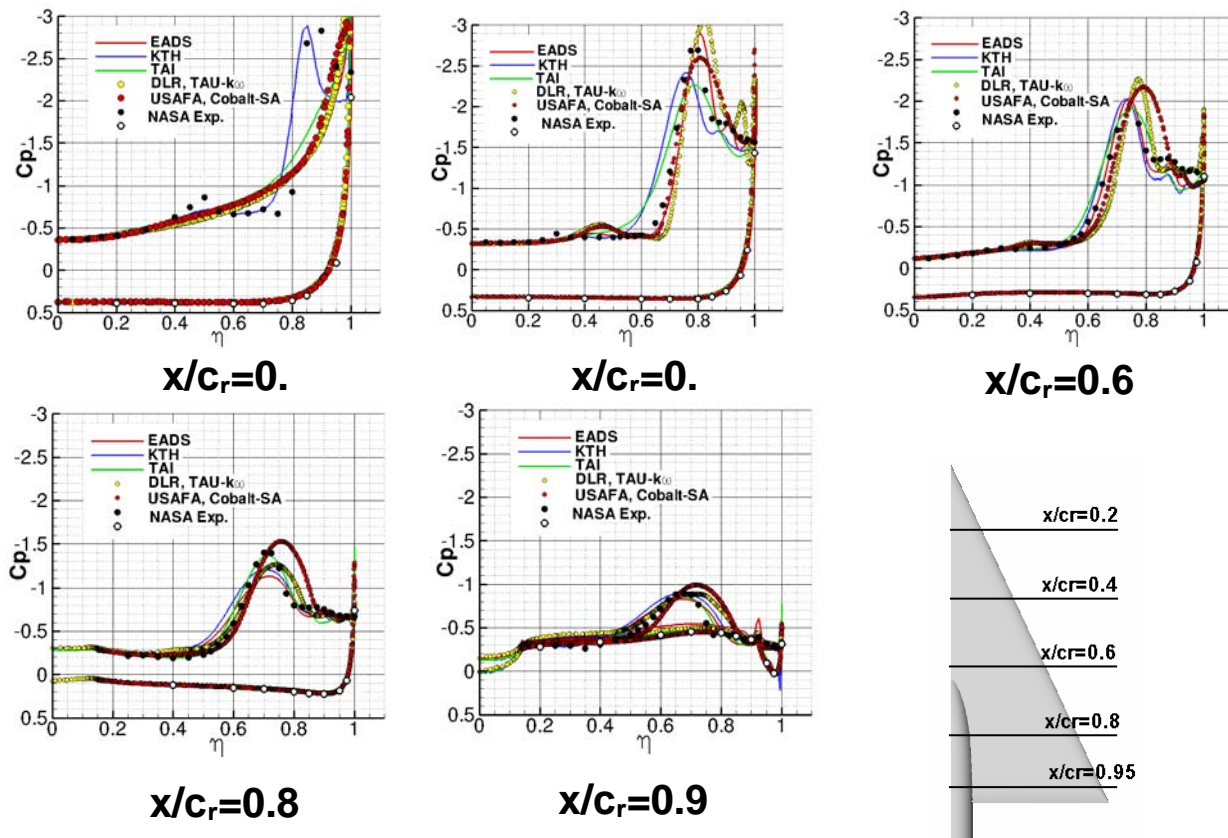
**Figure 34-16: Comparison of Surface Pressures and Experimental Data
(Ref. [34-9]) for Case 14: MRLE, M = 0.40, α = 18°, Re = 6 x 10⁶.**

At $x/c_r = 0.4$ and $x/c_r = 0.6$ all solutions show the correct flow features. There is a dominating primary vortex and the effect of a secondary vortex (between the leading edge and suction peak). Differences between the different solutions occur mainly in over- or under-prediction of the effects of the secondary vortex and in over- or under-prediction of the main suction peak. These may be effects of the different turbulence models and of the different grid resolutions. At $x/c_r = 0.8$ the EADS, DLR, and KTH solutions are under-predicting the main suction peak and smearing it out. The reason, therefore, may be the above mentioned spread of the vortex core. At the cross section $x/c_r = 0.95$ the EADS solution with its weak vortex breakdown matches quite well to the experimental data. This indicates that the above mentioned weak vortex breakdown due to the high curvature of the rear end of the wing is also present in the experiment.

34.6.4 Case 15: SLE, M = 0.40, α = 18°, Re = 6 x 10⁶

In this test case the leading edge separation is fixed by the sharp leading edge and the primary vortex formation begins at the wing apex. A well developed primary vortex without vortex breakdown should be expected for this test case. In Figure 34-17 three different solutions for this test case are presented. The solutions all look very similar and all again indicate vortex breakdown over the rear end of the wing (see above section for details).

EADS
(Structured)

KTH
(Unstructured)

NLR
(Structured)

NASA
(Experiment)
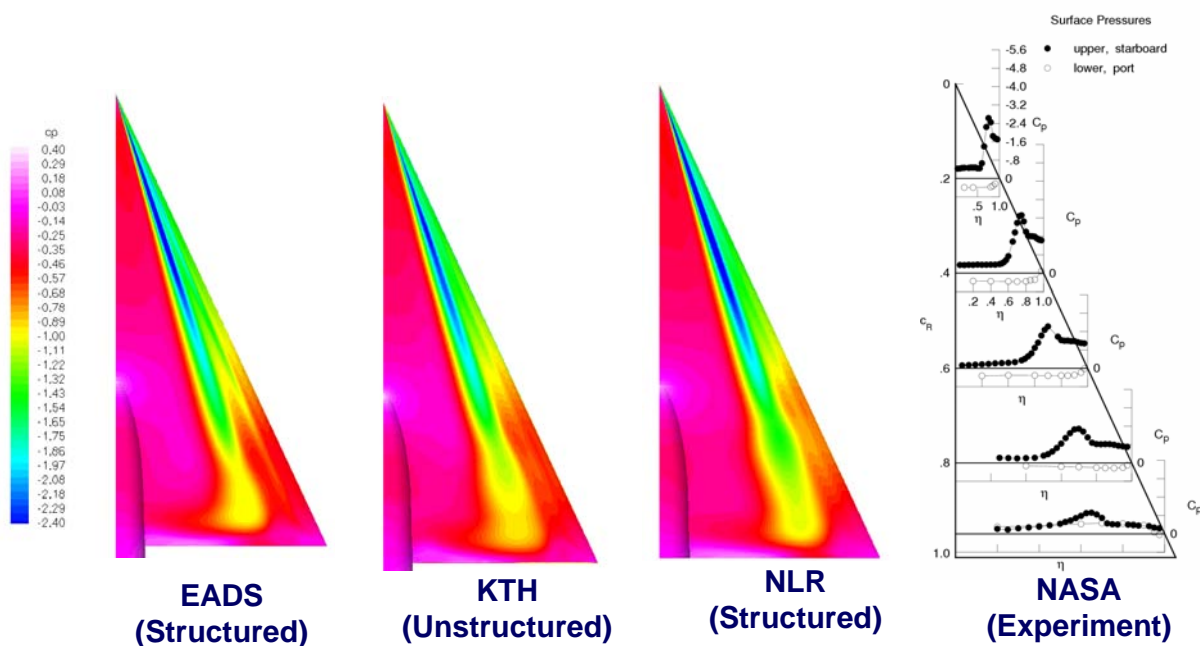
Figure 34-17: Surface Pressure Maps for Case 15: SLE, M = 0.40, α = 18°, Re = 6 x 10^6.

The agreement of the surface pressure distributions up to the cross section $x/c_r = 0.6$ is very good, as shown in Figure 34-18. Differences between the predictions and experiment mainly occur in the level of the maximum suction peak and in the region of the secondary vortex; this is commonly related to the turbulence model. In the cross section $x/c_r = 0.8$, all solutions indicate a less compact suction peak. This can again be related to the spreading of the vortex core in the calculations. In the last cross section the experiment shows a rather compact suction peak (unlike in the previous case), whereas in all calculations the suction peak is smeared out.

x/c$_r$=0.2   x/c$_r$=0.4   x/c$_r$=0.6

x/c$_r$=0.8   x/c$_r$=0.95
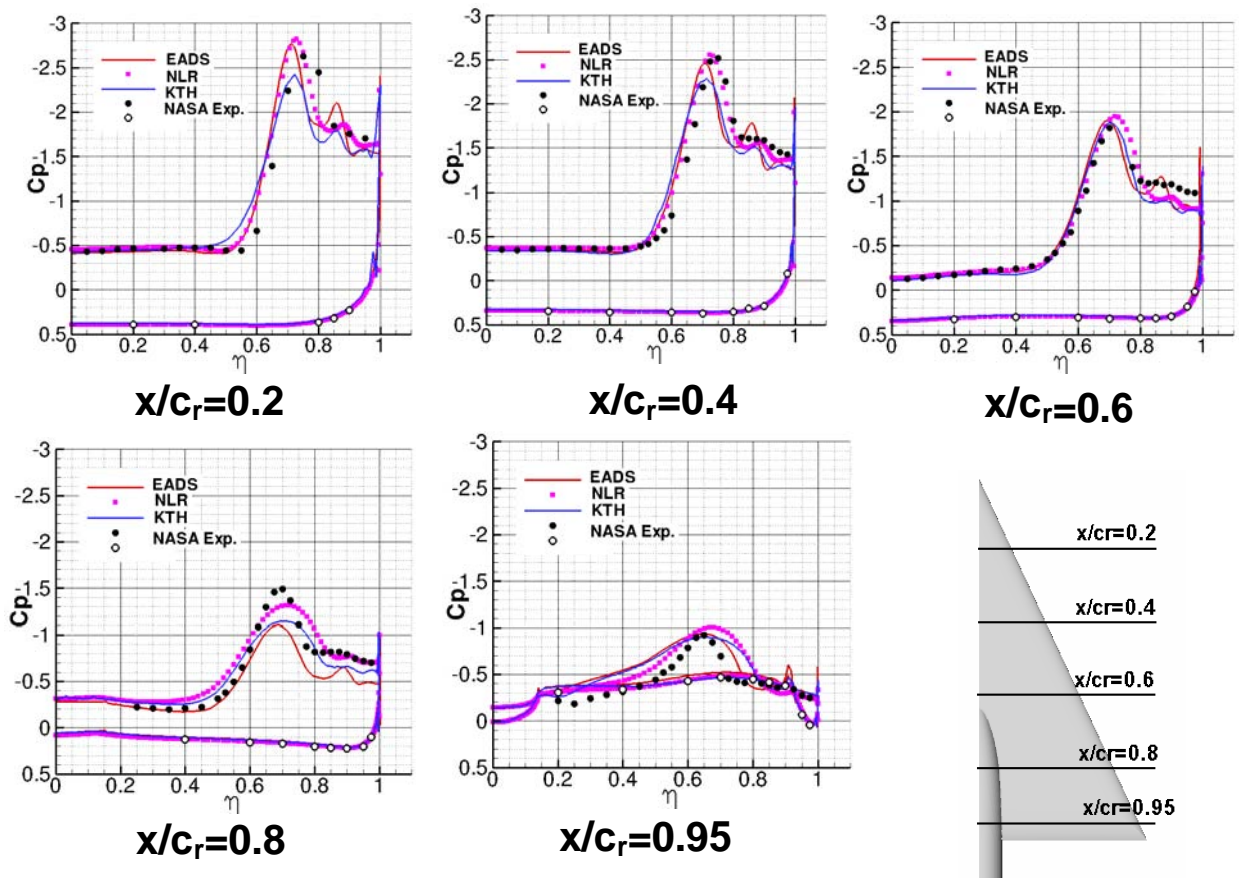
Figure 34-18: Comparison of Surface Pressures and Experimental Data
(Ref. [34-9]) for Case 15: SLE, M = 0.40, α = 18°, Re = 6 x 10^{6}.

34.6.5   Case 24: SLE, M = 0.40, α = 23°, Re = 6 x 10^{6}

This is again a case where the onset of the leading edge separation is fixed by the sharp leading edge and begins at the wing apex. Unlike Case 15, vortex breakdown is also present in the experiment. Figure 34-19 shows the surface pressure map and the vortical flow structure for this test case using the EADS solution as an example. The 3-D volume ribbons along the vortex core are again colored according to the local C_p values. There is a very compact vortex core up to about x/c$_r$ = 0.6. Then the vortex widens and sidesteps the region with negative axial velocity (which is again indicated by the pink bubble in the figure). This region with negative axial velocity has a small radius but the axial extension is rather large. The widening of the vortex core results in a reduced rotation of the vortex, and by this the leeward suction peak in the surface pressure distribution is cut back, as can be seen in the surface pressure contours on the left hand side of Figure 34-19. From the rather long bubble with negative axial velocities in Figure 34-19 it can be assumed that the axial velocities in the vortex core are under-predicted in the different numerical methods. As different numerical methods with different turbulence models and different grids have been used for the calculations, the results seem to not be an issue of grid resolution. Also, different turbulence models do not affect the prediction a great deal. In fact it seems that the turbulence models still have a difficulty with respect to vortical flow.
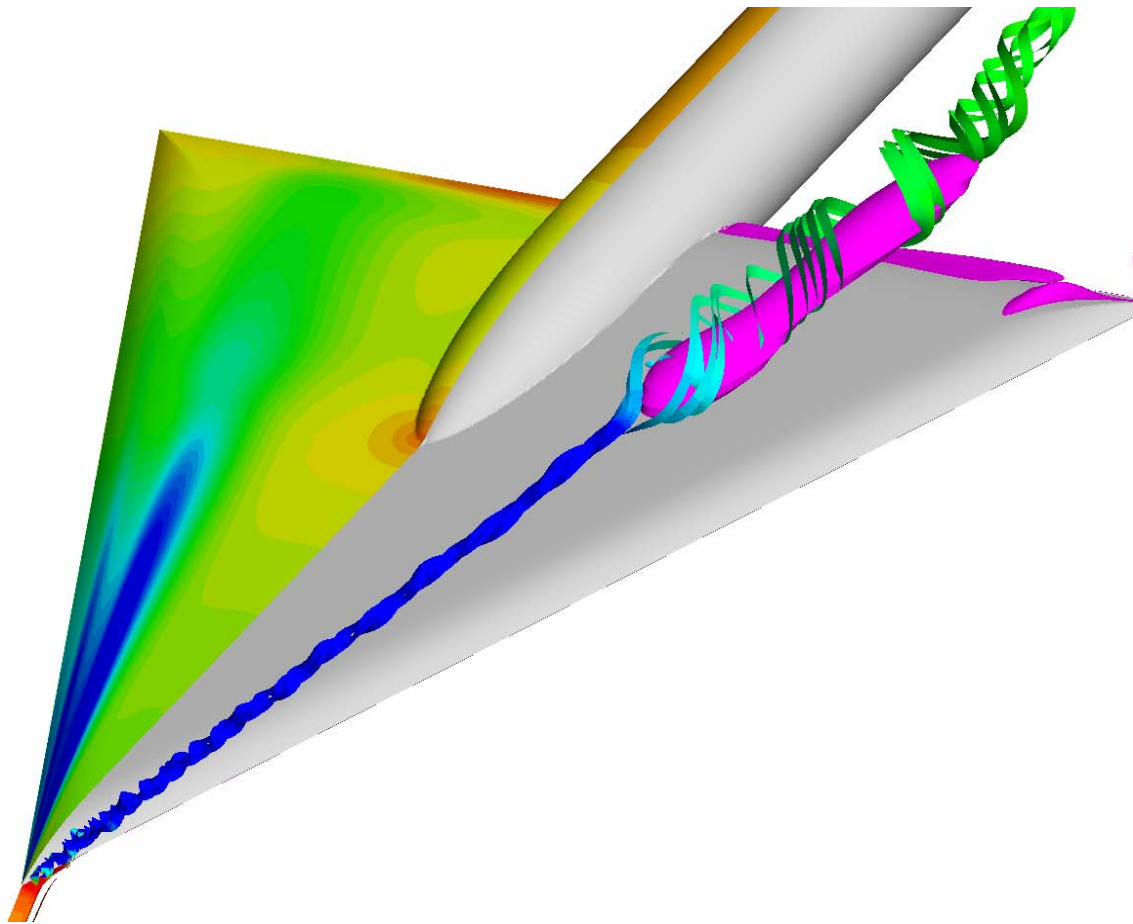
Figure 34-19: Flow Features for Case 24: SLE, M = 0.40, α = 23°, Re = 6 x 10⁶.

The comparison of the surface pressure contours for this test case is presented in Figure 34-20. Compared to the last test case (Figure 34-17), the structure is very similar, but the rapid decay of the leeward suction peak now begins farther upstream. This decay of the suction peak is due to the above mentioned widening of the vortex core and indicates the beginning of vortex breakdown in the numerical solutions. The onset point of this vortex breakdown is at about $x/c_r = 0.6$ in all numerical solutions. The EADS and KTH solutions are very similar and show a rather quick decay of the suction peak along the rear part of the wing, whereas the NLR solution shows a slower decay of this suction peak. In the experimental pressure distributions at $x/c_r = 0.6$ there is still a compact vortex present and the onset of vortex breakdown is somewhere near $x/c_r = 0.8$ (at the last cross section, the experimental pressure distribution shows clearly vortex breakdown; at $x/c_r = 0.8$ there is still a recognizable vortical flow structure, but the suction peak is less compact as in the upstream sections).
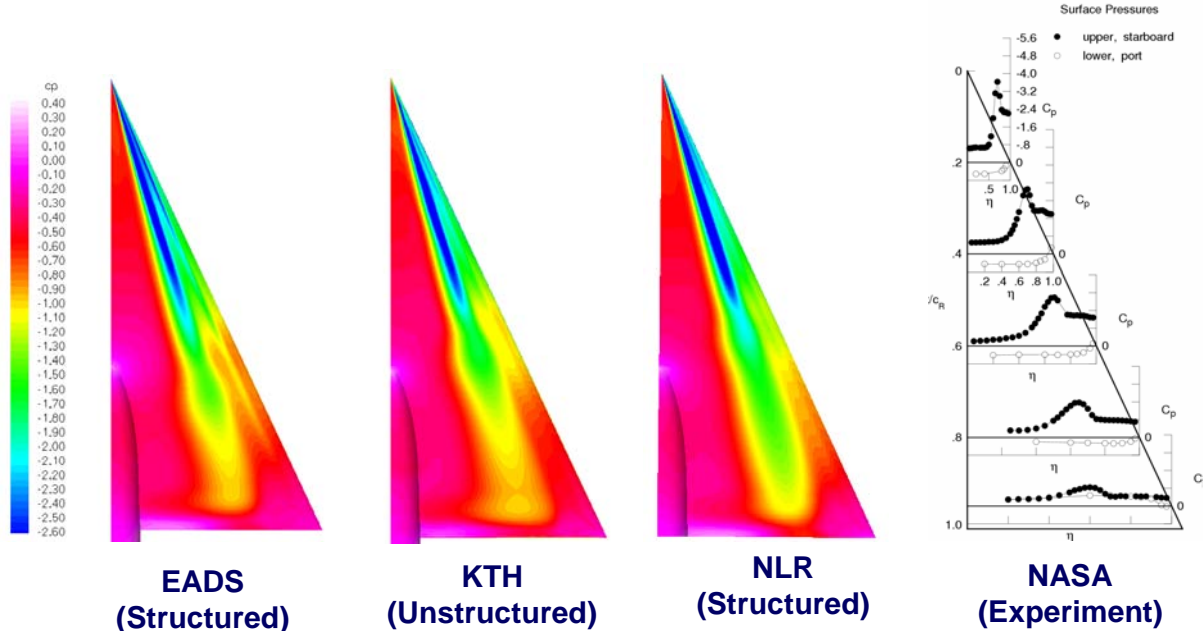
Figure 34-20: Surface Pressure Maps for Case 24: SLE, M = 0.40, α = 23°, Re = 6 x 10^6.

The differences between experimental and numerical data can be seen in more details in the pressure comparisons shown in Figure 34-21. In the two most upstream cross sections the numerical solutions match the main flow features (effects of primary and secondary vortices) quite well. The differences are again in the levels of the main suction peak and in the details in the region of the secondary vortex. From $x/c_r = 0.6$ the agreement with the experimental pressure distribution is less good. All numerical solutions show a less compact and smeared out vortex compared to the experimental data. This may be related to the above mentioned widening of the vortex core, which may lead to a more upstream onset of vortex breakdown in the numerical calculations.

x/c_r=0.2   **x/c_r=0.4**   **x/c_r=0.6**

x/c_r=0.8   **x/c_r=0.95**
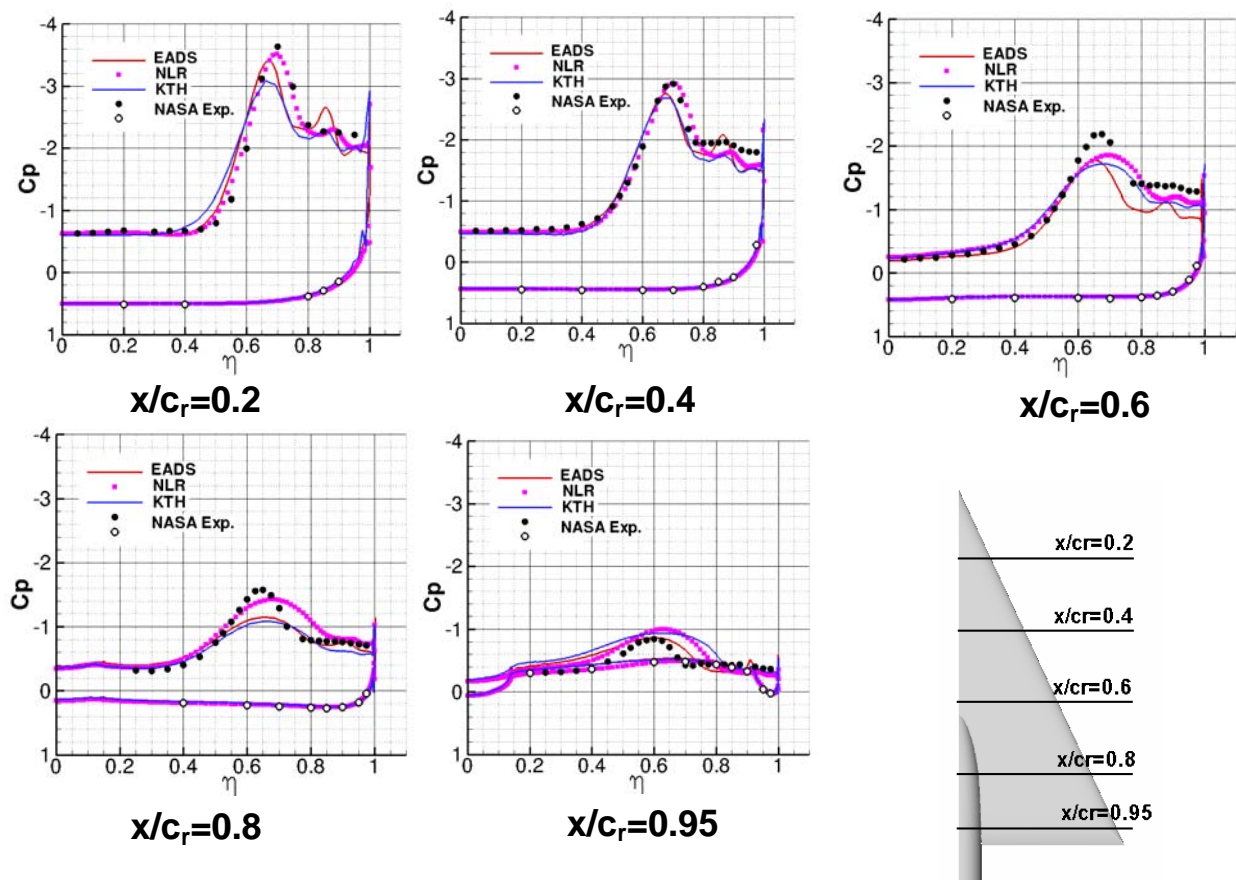
**Figure 34-21: Comparison of Surface Pressures and Experimental Data
(Ref. [34-9]) for Case 24: SLE, M = 0.40, α = 23°, Re = 6 x 10^6.**

34.6.6   Case 27: SLE, M = 0.85, α = 23°, Re = 6 x 10^6

The last test case finally is a transonic one at high incidence. In the subsonic region (M = 0.4) it was seen in the experiments that vortex breakdown begins at about α = 21° at the rear end of the wing, and then continuously moves upstream with increasing angle of attack. In the transonic region however, the onset of vortex breakdown took place suddenly somewhere in the middle of the wing. The reason found for this sudden onset of breakdown is a shock/vortex interaction, which is triggering the breakdown. An impression of the surface shock structure and the 3-D vortical structure is given in Figure 34-22 (a detailed discussion of this test case is given in Ref. [34-14]).
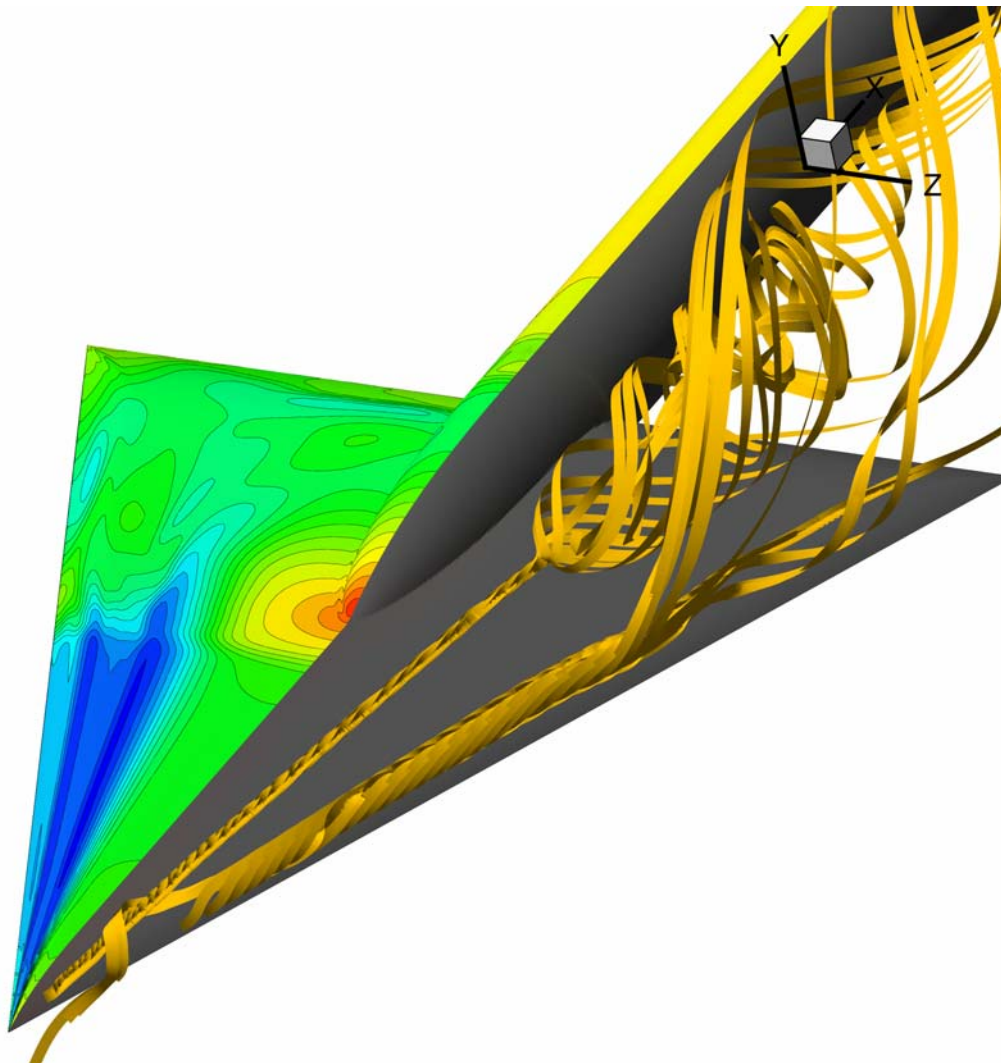
Figure 34-22: Flow Features for Case 25: SLE, M = 0.85, α = 23°, Re = 6 x 10^6.

Figure 34-22 shows the surface pressure contours (left hand side) and 3-D volume ribbons along the core of the primary and secondary vortex (right hand side). The surface pressure contours show a very clear vortex structure on the forward part of the wing, consisting of a primary and a secondary vortex. At $x/c_r \approx 0.5$ there is a shock. Downstream of the shock the vortical flow structure vanishes very rapidly and a more dead water type pressure distribution develops. The visualization of the core of the primary vortex indicates a very compact vortex core upstream of the shock. Even across the shock this vortex core remains very compact. However, a very short distance downstream of the shock a sudden, very strong breakdown of the primary vortex occurs. The secondary vortex also seems to have vortex breakdown, but exactly at the shock position.

Figure 34-23 shows the surface pressure contours of four different numerical solutions together with the experimental data [34-9]. There are three very similar solutions (EADS, KTH, NLR) which all show the above mentioned vortex structure, the shock which is followed by vortex breakdown, and finally the dead water type flow over the rear part of the wing. However, the TAI solution looks completely different. The suction peak is

more smeared out and there is no significant effect of a secondary vortex. There is only a very weak shock, which is farther downstream, and the vortical structure is maintained downstream of the shock. This solution is more similar to the experimental data, which also indicates a vortical flow structure over the rear end of the wing.

EADS (Structured)   **KTH (Unstructured)**   **NLR (Structured)**   **TAI (Structured)**   **NASA Experiment**
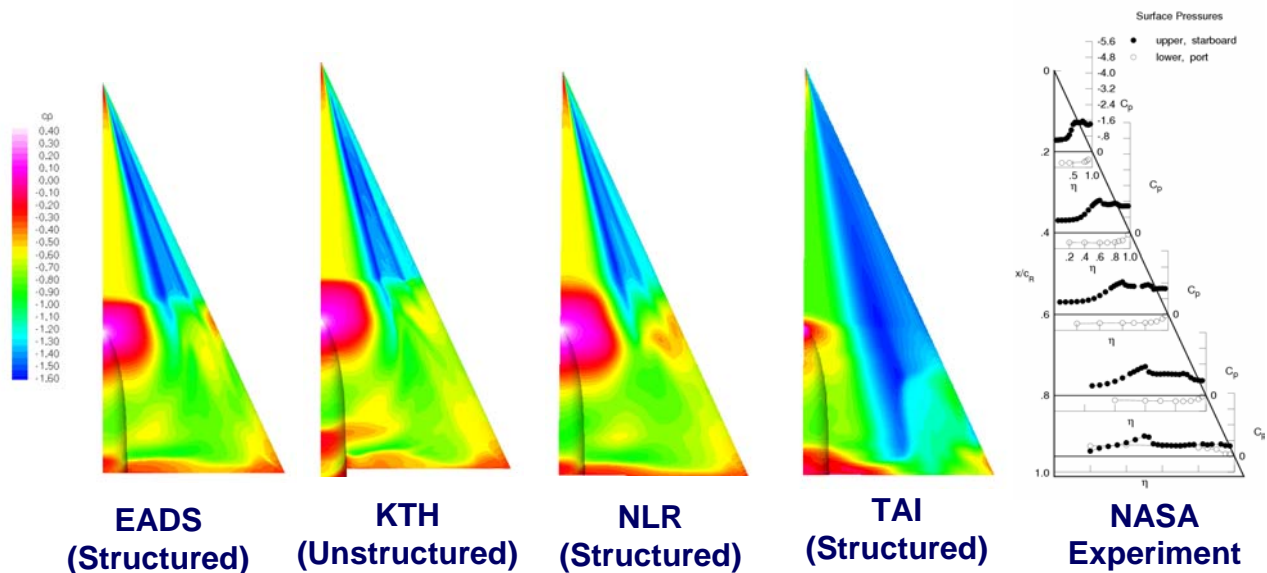
Figure 34-23: Surface Pressure Maps for Case 25: SLE, M = 0.85, α = 23°, Re = 6 x 10^6.

The surface pressure distributions in Figure 34-24 underline the differences between the two classes of solutions. Upstream of the shock (at $x/c_r = 0.2$ and $x/c_r = 0.4$) the numerical results of EADS, NLR, and KTH are identical and match the experimental data. The TAI solution shows a lower suction peak, a much smoother inboard pressure gradient, and no significant effect of a secondary vortex. This indicates weaker vortices in the TAI solution compared to the experiment and to the other solutions.
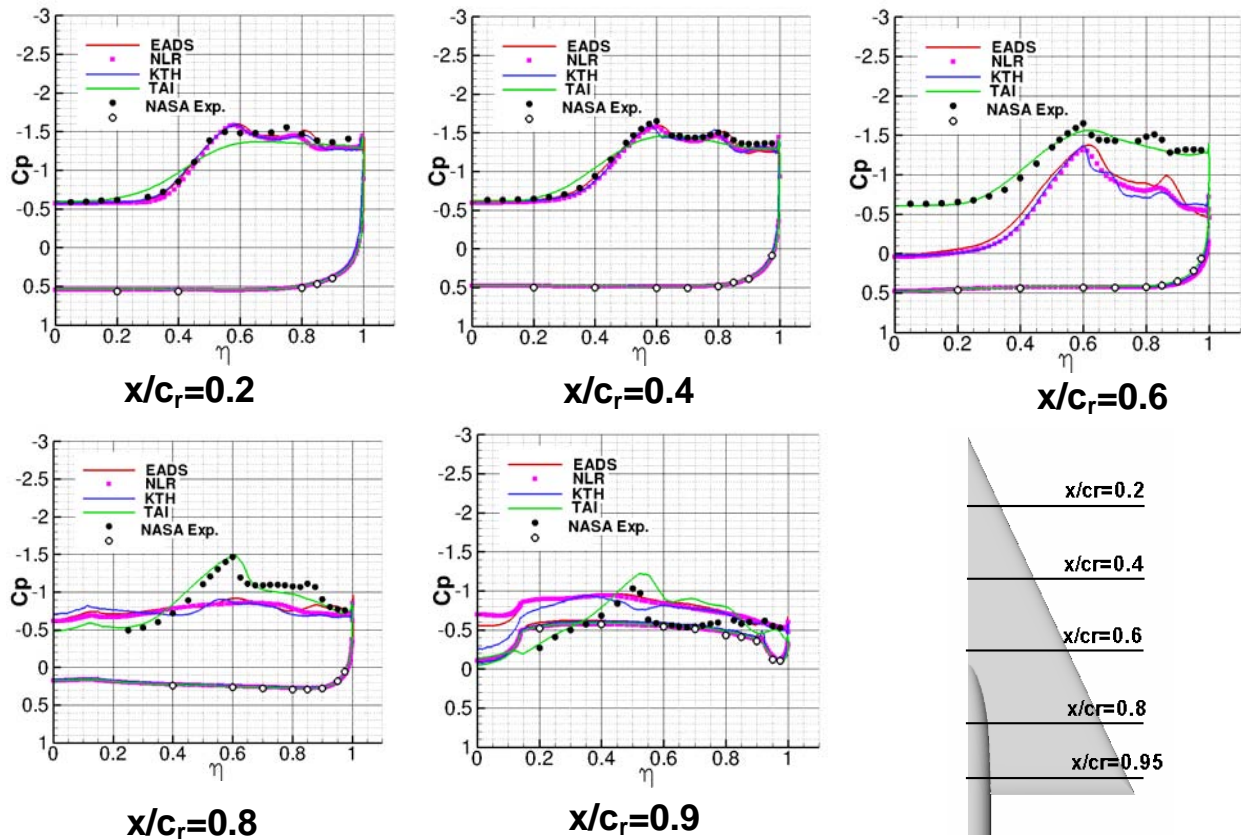
**Figure 34-24: Comparison of Surface Pressures and Experimental Data
(Ref. [34-9]) for Case 25: SLE, M = 0.85, α = 23°, Re = 6 x 10^6.**

At $x/c_r = 0.6$ the TAI solution does not yet show the effect of a shock, as is also shown in the experiment. Because of the weaker upstream shock, the agreement of the TAI solution at the inboard part of the wing is better than the other solutions. The suction peaks of primary and secondary vortex are however under-predicted. The other three solutions are again very similar and they all show the pressure jump due to the shock at $x/c_r \approx 0.5$. Because of these reasons the solutions do not match the experimental data, but they still show a vortical structure. In the cross sections $x/c_r = 0.8$ and $x/c_r = 0.95$ the solutions of EADS, NLR, and KTH all show a dead water type pressure distribution without any vortical structure, whereas the TAI solution fits the experimental data very well.

The main problem of this test case is the position of the shock. In the EADS, NLR, and KTH solutions the shock is too far upstream and too strong compared to the experiment. Because of this the vortical flow field downstream of the shock is destroyed and the experimental data cannot be matched. In Ref. [34-14], where this test case is discussed very intensively, it was seen that the problem of the forward upstream shock position is not affected by grid resolution or by different turbulence models. Even time-averaged DES simulations have shown the same problem. It was however also seen that this test case is very sensitive to small changes in the angle of incidence, as it is shown in Figure 34-25.
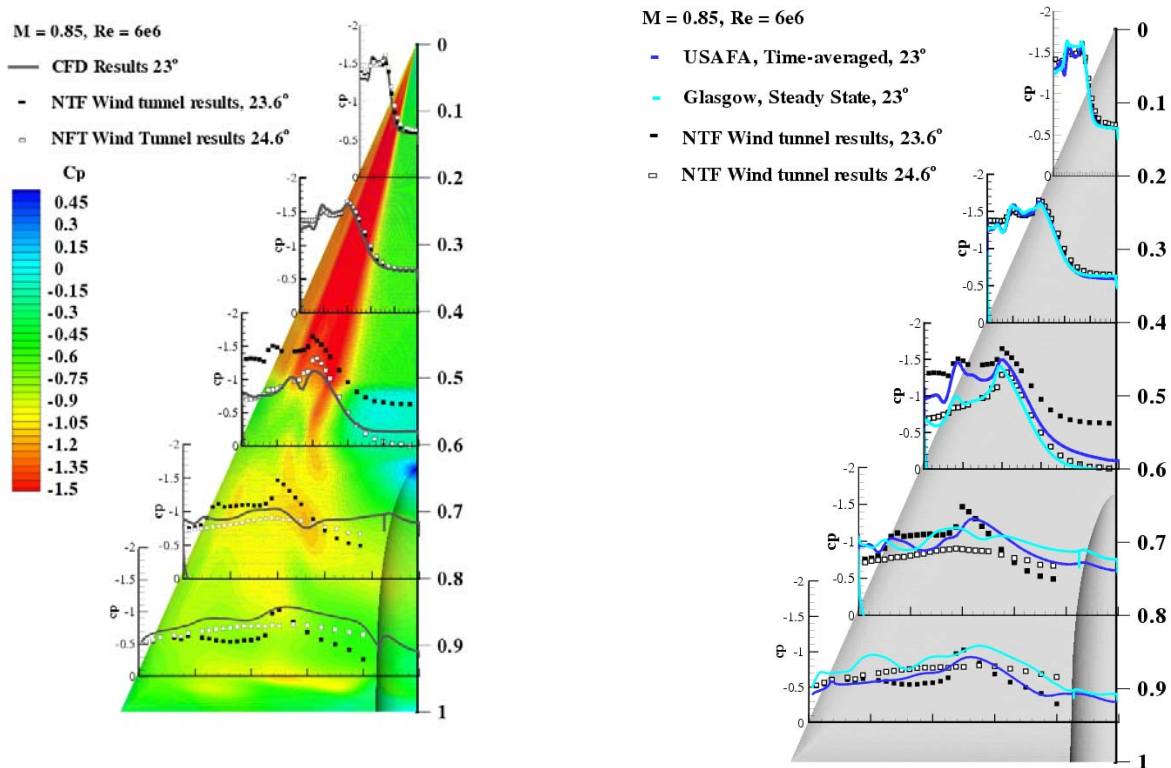
**Figure 34-25: Comparison of Surface Pressures and Experimental Data
(Ref. [34-9]) for Case 25: SLE, M = 0.85, α = 23°, Re = 6 x 10^{6}.**

Figure 34-25 shows on the left hand side the result of the University of Glasgow (UG) using a structured grid. It shows the same pattern as the three above mentioned solutions: an upstream position of the shock and dead water type flow downstream of the shock. The right hand side of Figure 34-25 shows the UG results together with the time-averaged DES results of USAFA. Also presented are experimental results [34-9] for α = 23.6° and α = 24.6°. This comparison shows that even the time-averaged DES results show the upstream shock with its consequences on breakdown. It also shows that if the experimental data from a higher angle of attack are taken for comparison, the agreement with the numerical data is very good and thus demonstrates the high sensitivity of the shock position to small changes in the angle of attack.

Figure 34-26 shows a detailed comparison between the EADS surface pressure contours (representative for the other numerical solutions), the surface pressure contours of the TAI solution and the experimental pressure distribution. The pressure gradients now appear more clearly. In the EADS solution there is a strong shock at $x/c_r \approx 0.5$, the dead water type of flow downstream of the shock, and a terminating shock at the inner part of the wing. It also shows a very significant secondary vortex which also interacts with the shock. The TAI solution shows a much weaker and more smeared out single vortex in the forward part of the wing. This weaker and less compact vortex obviously induces a weaker and more upstream positioned shock. The suction peak is only slightly reduced across this shock. More downstream, at $x/c_r \approx 0.8$, a second weak shock wave builds up from the wing leading edge towards the suction peak. When reaching the suction peak, this shock wave makes a 90° angle and becomes a weak cross flow shock, which finally merges with the terminating shock close to the trailing edge. This shock formation can also be concluded from the experimental pressure distribution. There is a

considerable pressure increase at the outer part of the wing between the last two wing sections. This indicates this second weak shock. The experimental pressure distributions at $x/c_r = 0.8$ and $x/c_r = 0.95$ also give an indication of a weak cross flow shock. This analysis indicates that in the five "common" solutions the axial velocities upstream of the shock are possibly too high and thus a too strong shock at a too much upstream position builds up. One reason therefore may be that a too strong (primary or secondary) vortex induces too high axial velocities in these numerical solutions.

EADS

TAI

**NASA
Experiment**
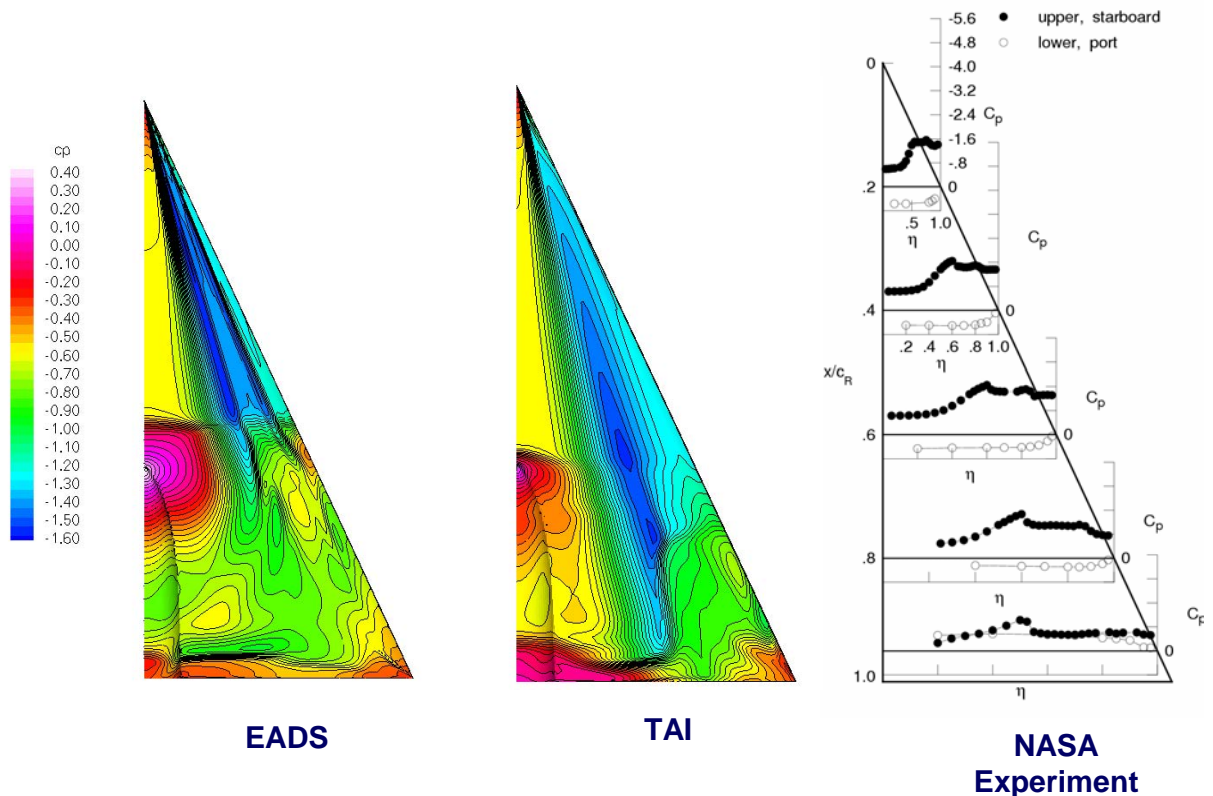
Figure 34-26: Surface Pressure Maps for Case 25: SLE, M = 0.85, α = 23°, Re = 6 x 10^6.

Figure 34-27 finally shows a comparison of the skin friction magnitude of four different solutions. There are again the three "common" solutions (EADS, NLR, and KTH) and the TAI solution. The three "common" solutions show very clearly the effect of a primary and a secondary vortex. It is remarkable that the maximum skin friction at the secondary vortex has nearly the same magnitude as that of the primary vortex. This confirms the strong rotation of the secondary vortex, which could already be observed in the surface pressure contours (see Figure 34-23). The TAI solution shows no effect of a secondary vortex and also the primary vortex is less compact compared with the other solutions. This may be an additional indication that too compact vortices upstream of the shock may be the reason for a shock that is too strong and too much upstream in the other solutions.

x/c_r=0.2

x/c_r=0.4

x/c_r=0.6

x/c_r=0.8
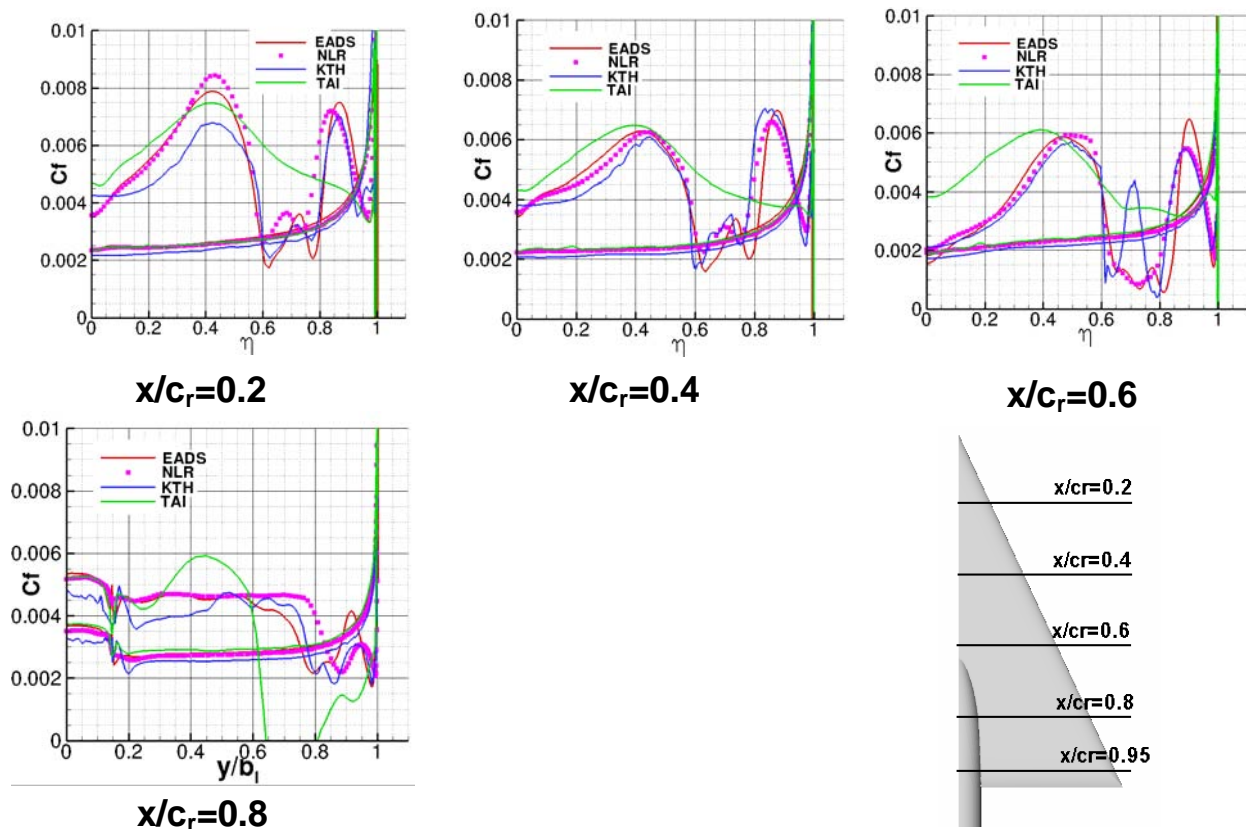
**Figure 34-27: Comparison of Skin Friction Predictions
for Case 25: SLE, M = 0.85, α = 23°, Re = 6 x 10⁶.**

34.7   CONCLUSIONS AND RECOMMENDATIONS

From the comparisons of the different solutions for the different test cases the following conclusions and recommendations are drawn and given:

- The subsonic SLE test cases show the best agreement between the different numerical results and between numerical results and experiment. But even for these test cases with clearly defined leading edge separation the correct prediction of vortex break down is still a very difficult task. In all the numerical simulations presented here, vortex break down occurred at earlier angles of attack compared to the experiment. This may be due to an under-prediction of the axial velocity in the vortex core. Either there is still a deficit of the existing turbulence models for a proper treatment of vortical flow, or RANS methods are overstrained and DES methods are required for the correct prediction of vortex break down.

- In the transonic region there is the tendency that the shock position is predicted too much upstream and by this vortex break down is also predicted earlier as in the experiment. On the other hand vortex break down due to shock/vortex interaction is very sensitive to small changes in the angle of attack, which rises the question about the accuracy of the experimental data in such cases (is there an uncertainty or error band about the nominal angle of attack).

- For the test cases with round leading edge, the prediction of the onset of the primary leading edge is the most essential problem. The position of this separation point can be predicted too much upstream

or too much downstream or (by accident?) at the correct position. Depending on this, the agreement between numerical and experimental results can be very good or less good. One uncertainty parameter which was found for these test cases is the unknown transition, which can have a strong effect on the solution. So transition modeling should be further promoted. Another difficulty is the effect of the Reynolds number at delta wings with round leading edges. This effect also can be under- or over-predicted.

Summarizing it can be stated, that not for all test cases the experimental surface pressure distributions could be matched satisfactorily, but anyhow detailed numerical flow analysis gave an essential insight into some complex flow structures (double vortex system at round LE, shock vortex interaction in transonic flow) and the numerical calculations helped to design the PIV experiments.

34.8   ACKNOWLEDGEMENTS

34.9   REFERENCES

[34-1]   Drougge, G.: *The International Vortex Flow Experiment for Computer Code Validation*, ICAS Proceedings, 1988, Vol. 1, pp. 35-41.

[34-2]   Elsenaar, A., Hjelmberg, L., Bütefisch, K.-A. and Bannink, W.J.: *The International Vortex Flow Experiment*, AGARD-CP-437, Vol. 1, 1988, pp. 9-1 to 9-23.

[34-3]   Wagner, B., Hitzel, S., Schmatz, M.A., Schwarz, W., Hilgenstock, A. and Scherr, S.: *Status of CFD Validation on the Vortex Flow Experiment*, AGARD-CP-437, Vol. 1, 1988, pp. 10-1 to 10-10.

[34-4]   Hoeijmakers, H.W.M.: *Modelling and Numerical Simulation of Vortex Flow in Aerodynamics*, AGARD-CP-494, 1991, pp. 1-1 to 1-46.

[34-5]   Ekaterinaris, J.A. and Schiff, L.B.: *Numerical Simulation of Incidence and Sweep Effects on Delta Wing Vortex Breakdown*, Journal of Aircraft, Vol. 31, No. 5, 1994, pp. 1043-1049.

[34-6]   Mitchell, A.M., Morton, S.A., Forsythe, J.R. and Cummings, R.M.: *Analysis of Delta-Wing Vortical Substructures Using Detached-Eddy Simulation*, AIAA Journal, Vol. 44, No. 5, 2006, pp. 964-972.

[34-7]   Hummel, D. and Redeker, G.: *A New Vortex Flow Experiment for Computer Code Validation*, RTO AVT Symposium on "Vortex Flow and High Angle of Attack Aerodynamics", Loen Norway, RTO-MP-069, 2003, pp. 8-1 to 8-31.

[34-8]   Hummel, D.: *The Second International Vortex Flow Experiment (VFE-2): Objective and First Results*, 2nd International Symposium on "Integrating CFD and Experiments in Aerodynamics", Cranfield University, 2005.

[34-9]   Chu, J. and Luckring, J.M.: *Experimental Surface Pressure Data Obtained on 65° Delta Wing Across Reynolds Number and Mach Number Ranges*, NASA TM 4645, 1996.

[34-10] Londenberg, W.K.: *Transonic Navier-Stokes Calculations about a 65 Degree Delta Wing*, NASA-CR-4635, November 1994.

[34-11] Chiba, K. and Obayashi, S.: *CFD Visualization of Second Primary Vortex Structure on a 65-Degree Delta Wing*, AIAA Paper 2004-1231, January 2004.

[34-12] Fritz, W.: *Numerical Simulation of the Peculiar Subsonic Flow-Field about the VFE-2 Delta-Wing with Rounded Leading-Edge*, AIAA Paper 2008-0393, January 2008.

[34-13] Gürdamar, E.: *Influence of Grid Resolution on the Accuracy of High Angle of Attack Delta Wing Simulations*, AIAA Paper 2008-0394, January 2008.

[34-14] Schiavetta, L., Boelens, O.J., Crippa, S., Cummings, R.M., Fritz, W. and Badcock, K.J.: *Shock Effects on Delta Wing Vortex Breakdown*, AIAA Paper 2008-0395, January 2008.

[34-15] Cummings, R.M. and Schütte, A.: *Detached-Eddy Simulation of the Vortical Flowfield about the VFE-2 Delta Wing*, AIAA Paper 2008-0396, January 2008.

[34-16] Crippa, S.: *Steady, Subsonic CFD Analysis of the VFE-2 Configuration and Comparison to Wind Tunnel Data*, AIAA Paper 2008-0397, January 2008.

[34-17] Schütte, A. and Lüdeke, H.: *Numerical Investigations on the VFE-2 Rounded Leading Edge Configuration using the Unstructured DLR TAU Code*, AIAA Paper 2008-0398, January 2008.

[34-18] Luckring, J.: *What was Learned from the New VFE-2 Experiments*, AIAA Paper 2008-0383, January 2008.

[34-19] Konrath, R., Schröder, A. and Kompenhans, J.: *Analysis of PIV Results Obtained for the VFE-2 65° Delta Wing Configuration at Sub- and Transonic Speeds*, AIAA Paper 2006-3003, June 2006.

Appendix 34-1

This is a full listing of the cases considered for the VFE-2 numerical simulation project. The cases in bold were considered to be important for the subsonic analysis, while Cases 18 and 27 were important to the transonic analysis.

Table 34-A1: Full List of the Cases Considered within VFE-2 Numerical Simulations

Case No.	Old Case No.	α (deg.)	Leading Edge	M_∞	$Re_{\bar{c}}$ (millions)
1	None	13.3	RLE	0.2	1
2	None	13.3	RLE	0.2	2
3	None	13.3	SLE	0.2	2
4	**12**	**13.3**	**RLE**	**0.4**	**2**
4.5	**None**	**13.3**	**RLE**	**0.4**	**3**
5	**11**	**13.3**	**RLE**	**0.4**	**6**
6	**9**	**13.3**	**SLE**	**0.4**	**6**
7	None	13.3	RLE	0.85	2
8	None	13.3	RLE	0.85	6
9	None	13.3	SLE	0.85	6
10	None	18.5	RLE	0.2	1
11	None	18.5	RLE	0.2	2
12	None	18.5	SLE	0.2	2
13	**6**	**18.5**	**RLE**	**0.4**	**2**
14	**5**	**18.5**	**RLE**	**0.4**	**6**
15	**1**	**18.5**	**SLE**	**0.4**	**6**
16	8	18.5	RLE	0.85	2
17	7	18.5	RLE	0.85	6
18	3	18.5	SLE	0.85	6
19	None	23.0	RLE	0.2	1
20	None	23.0	RLE	0.2	2
21	None	23.0	SLE	0.2	2
22	**18**	**23.0**	**RLE**	**0.4**	**2**
23	**17**	**23.0**	**RLE**	**0.4**	**6**
24	**13**	**23.0**	**SLE**	**0.4**	**6**
25	20	23.0	RLE	0.85	2
26	19	23.0	RLE	0.85	6
27	15	23.0	SLE	0.85	6

Chapter 35 – FINAL RESULTS OF THE INTERNATIONAL VORTEX FLOW EXPERIMENT – RESUMÉ AND OUTLOOK

by

Dietrich Hummel *(Retired)*

35.1   SUMMARY

At the end of the RTO-phase of the Second International Vortex Flow Experiment (VFE-2) the up to now achieved experimental and numerical results on the vortical flow about a delta wing with sharp and blunt leading edges are summarized, and special attention is called to the present status of knowledge. Some problems, which could not be solved within VFE-2, are also mentioned and the needs for further investigations are stressed in an outlook.

35.2   INTRODUCTION

The Second International Vortex Flow Experiment (VFE-2) has been carried out on a flat plate delta wing according to Figure 35-1 with interchangeable leading edges, one sharp and three blunt ones [35-1], [35-2]. The experimental and numerical investigations were mainly concentrated on the medium radius blunt leading edge (MRLE) configuration and on the sharp leading edge (SLE) case for comparison [35-3], see Chapter 17.

$c_R = 25.734$ in

$b/2 = 12$ in.

$\Lambda = 65°$

$t = 0.875$ in.

Spanwise surface pressure stations
$x/c_R = 0.20, 0.40, 0.60, 0.80, 0.95$

$t/c_R = 0.0340$

$b/2c_R = 0.4663$

$d/b = 0.1375$

$d = 3.30$ in.

Streamwise leading-edge radii:
$r_{LE}/\overline{c} = 0, 0.0005, 0.0015, 0.0030$
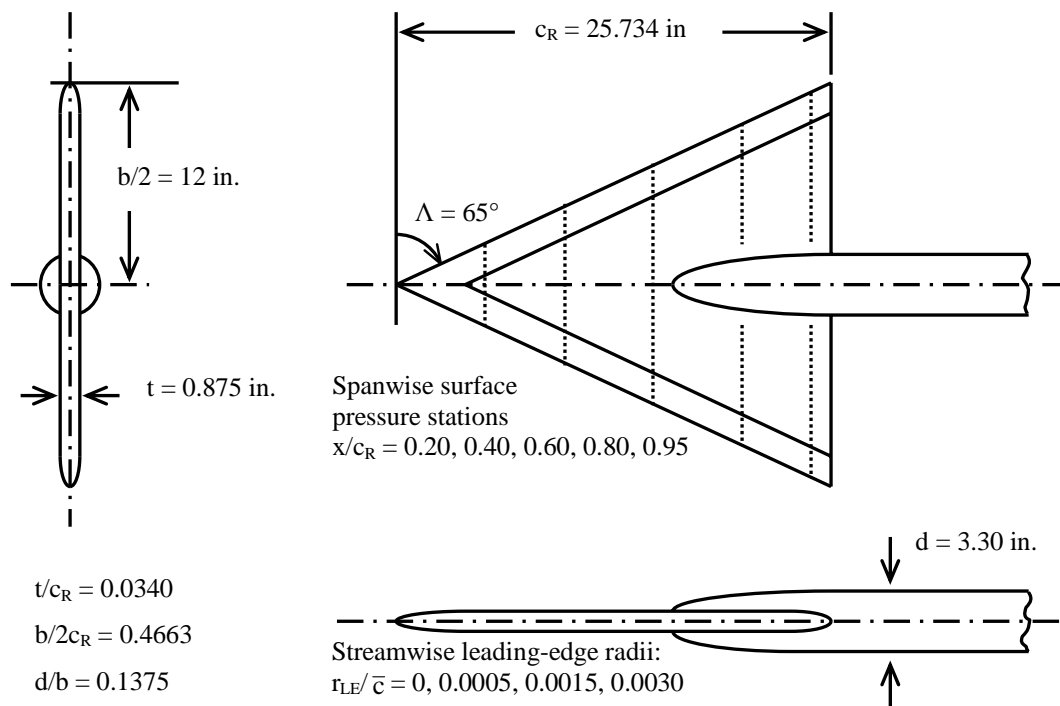
Figure 35-1: VFE-2 Configuration: NASA Delta Wing $\Lambda = 65°$ According to [35-1].

The geometry of the VFE-2 configuration looks very simple, but the details of the shape indicate some geometric properties, which have to be noticed:

i)   In the apex region the ratio of local thickness to half-span d/b_{loc} reaches considerable values and this means that a thickness distribution is present there, which may cause local flow separations. This applies for sharp and for blunt leading edges.

ii) For blunt leading edges the curvature radius r_{LE} is constant along the leading edge. Therefore the ratio r_{LE}/b_{loc} reduces along the leading edge from the apex of the wing towards the trailing edge. This means that the leading edge becomes sharper downstream, and this again favours flow separations.

In the subsequent discussion of the results of the VFE-2 these geometric peculiarities have to be born in mind. A special configuration has been investigated both experimentally and numerically. From the results many conclusions about the aerodynamic behaviour of slender bodies with rounded leading edges may be drawn, but not all aerodynamic problems related to blunt bodies with low aspect ratio are covered properly by the VFE-2 data sets.

35.3   FULLY SEPARATED FLOW WITHOUT VORTEX BREAKDOWN

In this section the results for the VFE-2 configuration at *angle of attack α = 18°* are discussed. For sharp and medium radius rounded leading edge the flow is fully separated along the whole leading edge. This is the standard case of a vortical flow around this configuration.

35.3.1   Overall Forces and Moments

The experiments at NASA [35-4], ONERA and TUBITAK-SAGE [35-6], see Chapters 18, 20, 23 and 24, have shown, that there exist only minor differences between the SLE and the MRLE configuration concerning the normal force coefficient as indicated in Figure 35-2. However, the centre of pressure of the blunt-edged wing is located slightly more forward compared to the sharp-edged wing [35-9] and in addition the blunt-edged wing produces a larger forward facing axial force than the sharp-edged wing due to the suction area in the leading edge region, see Figure 35-2.
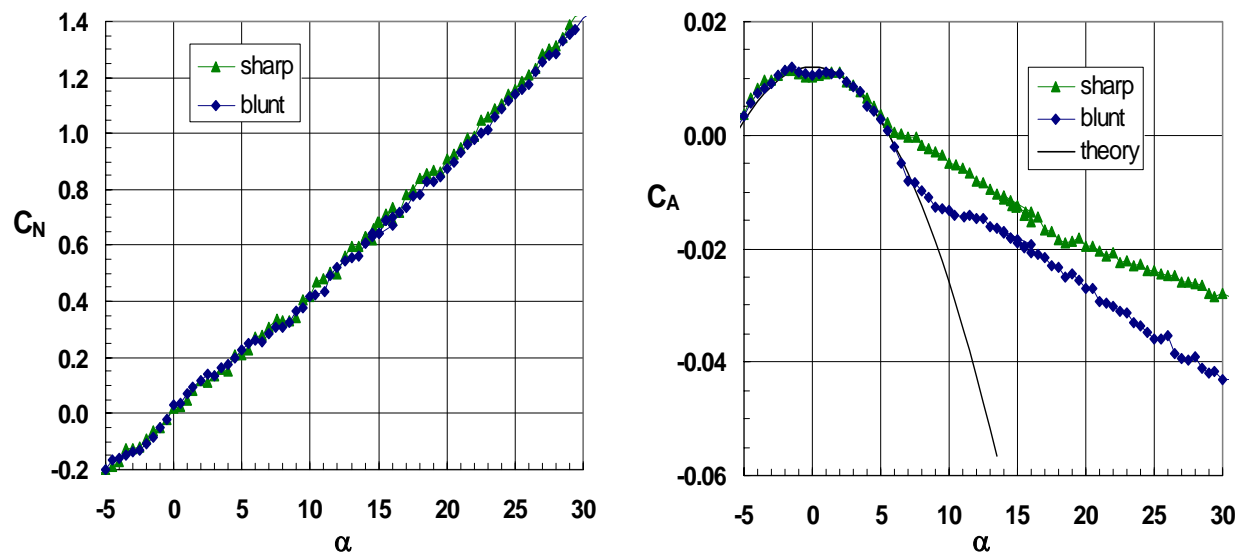
**Figure 35-2: Effect of Bluntness on Experimental Normal and Axial Force Coefficients for
the VFE-2 Configuration with Sharp (SLE) and Medium Radius Rounded Leading Edge
(MRLE) at M = 0.1, R_{mac} = 1 x 10^6. Results from ONERA L1 [[35-6] and Chapter 20].**

35.3.2 Pressure Distributions

All CFD codes available within VFE-2 have been applied to the most simple case of fully developed vortical flow at $\alpha = 18°$. Some results for SLE [35-11], [35-15], see Chapter 25, 30 and 34, are shown in Figure 35-3 and Figure 35-4. In general the experimental data are covered properly by the numerical solutions, but in the region of maximum suction and in the secondary vortex area some deviations are visible, which might be due to different turbulence models used.

Figure 35-3: Surface Pressure Distribution on the VFE-2 Configuration with Sharp Leading Edges (SLE) at M = 0.40, α = 18°, Re = 6 x 10^6 [[35-17] and Chapter 34].

Figure 35-4: Comparison of Calculated Surface Pressures with Experimental Data for the VFE-2 Configuration with Sharp Leading Edges (SLE) at M = 0.40, α = 18°, Re = 6 x 10^6 [[35-17] and Chapter 34].
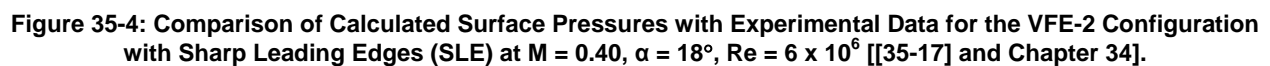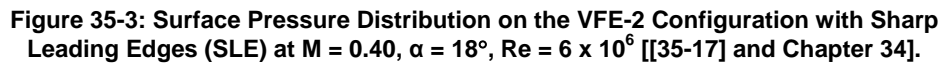
Corresponding results for the medium radius rounded leading edge (MRLE) configuration [35-11], [35-12], [35-14], [35-15], [35-16], see Chapters 25, 28, 30, 31 and 32, are presented in Figure 35-5 and Figure 35-6. Also for this configuration reasonable agreement between the experiments and the various numerical results turned out, but again the question of correct turbulence modeling remains.
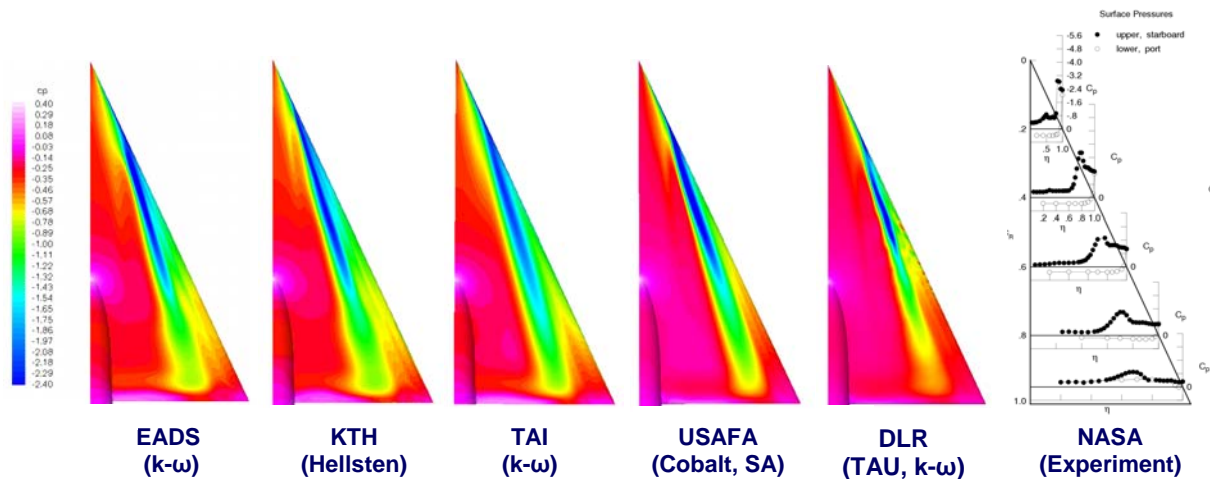
Figure 35-5: Surface Pressure Distribution on the VFE-2 Configuration with Medium Radius Rounded Leading Edges (MRLE) at M = 0.40, α = 18°, Re = 6 x 10^6 [[35-17] and Chapter 34].
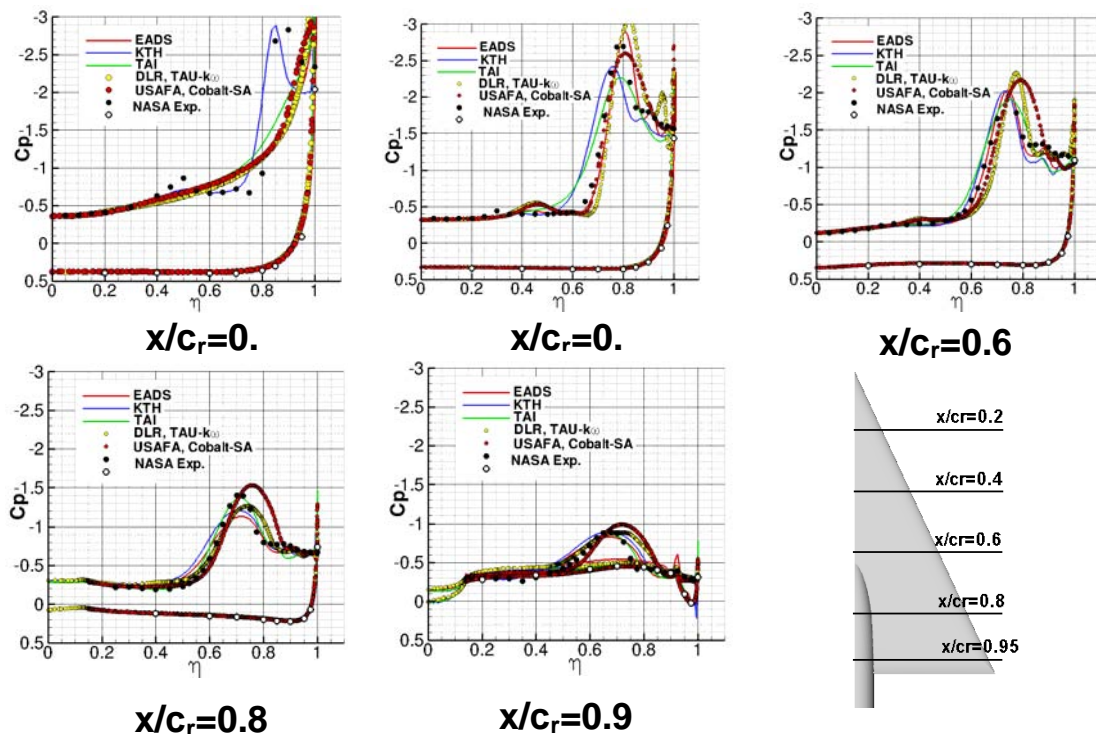
Figure 35-6: Comparison of Calculated Surface Pressures with Experimental Data for the VFE-2 Configuration with Medium Radius Rounded Leading Edges (MRLE) at M = 0.40, α = 18°, Re = 6 x 10^6 [[35-17] and Chapter 34].

35.3.3   Viscous Flow Details

For turbulent flow in solutions of the Reynolds-averaged Navier-Stokes equations a turbulence model has to be applied, which provides additional viscous damping in the boundary layers as well as in the viscous regions of the primary and secondary vortices. The pressure distribution on the upper surface of the wing is very sensitive to correct modelling of the viscous regions of the flow field, and therefore different turbulence models lead to differences in the pressure distributions. Only the correct prediction of the secondary separation line and of the structure of the secondary vortex lead to the right lateral and vertical position of the primary vortex and hence to the correct suction peak in the pressure distribution. Looking into more details of such calculations, the distributions of the total pressure and of the eddy viscosity in the flow field show large differences for different turbulence models.

Within VFE-2 so far all calculations have been carried out for fully turbulent boundary layers and regions with laminar boundary layers have not been taken into account. Attempts have been undertaken to answer the following questions:

- Which turbulence model is best suited for the calculation of vortical flows? Within VFE-2 the experimental part has been treated in detail by HWA, but the numerical part is still open.

- Where is the transition line laminar/turbulent located on the wing? IR and TSP investigations have been carried out within VFE-2, but the evaluations are difficult and they have not yet been finished. Vortical flow calculations for prescribed regions of laminar and turbulent boundary layer have not yet been completed, and the stability analysis of the result for an improvement of the prescription is still open.

Both problems will be discussed subsequently.

35.3.3.1   Flow Field Measurements

In almost all experimental contributions to VFE-2 the time-averaged flow field has been measured using PIV, [35-5], [35-6], [35-7], see Chapters 19, 20, 21. An example is shown in Figure 35-7. The fully developed vortical flow is indicated for both cases, and there are only minor differences concerning the position of the primary vortex relative to the wing.
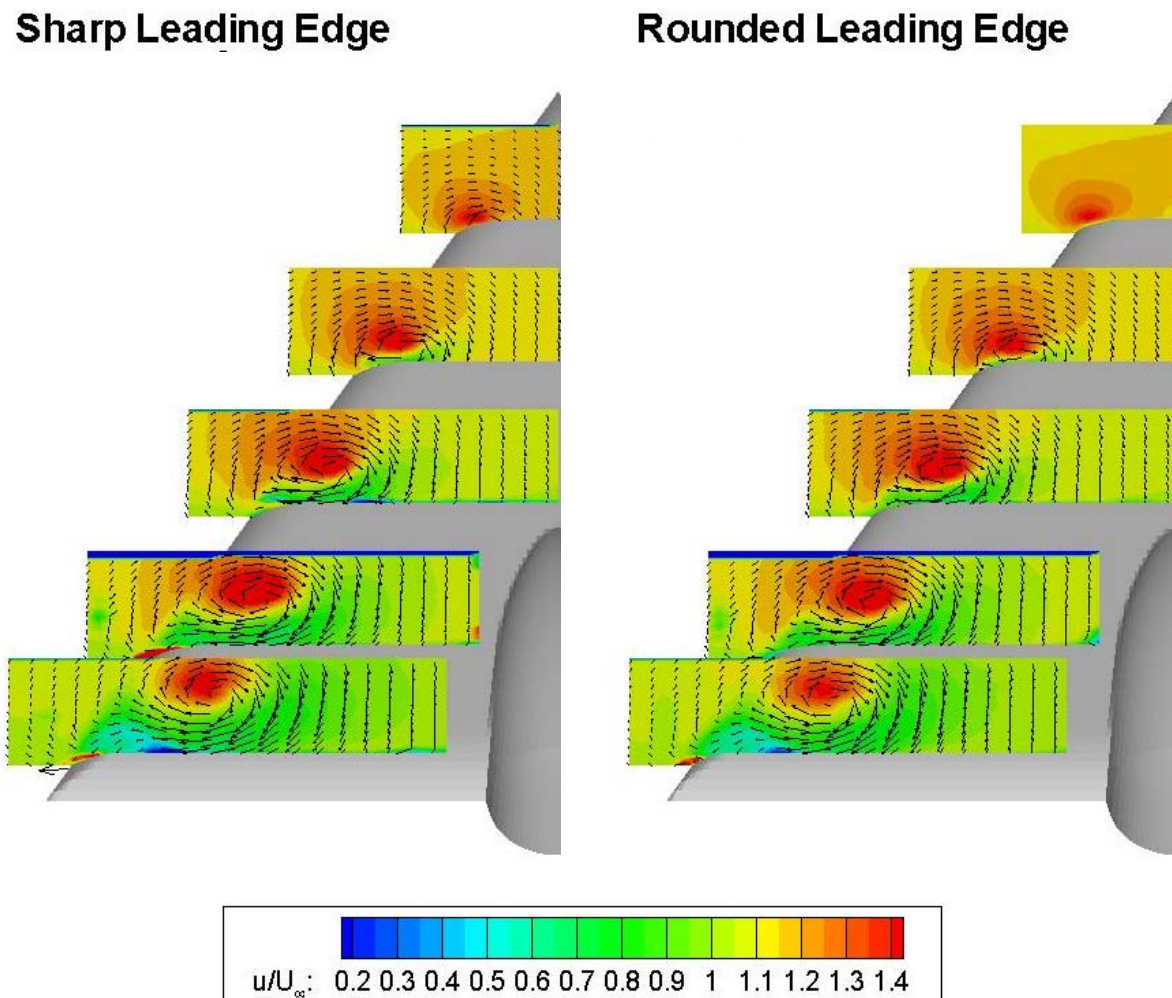
**Figure 35-7: Flow Field around the VFE-2 Configuration with Sharp (SLE) and Medium
Radius Rounded (MRLE) Leading Edges at M ≈ 0.1, R_{mac} = 1 x 10^6, α = 18°. PIV
results for the time-averaged velocity in various cross sections [35-7].**

In order to provide experimental data for comparison with numerical flow solutions using various turbulence models, the flow field has been measured by Hot-Wire Anemometry (HWA) at TU Munich [35-7], see Chapter 21, and the complete field of the velocity fluctuations u', v', w' is now available. Again there are only minor differences between the measurements for sharp (SLE) and for medium radius rounded (MRLE) leading edges. Therefore as an example Figure 35-8 shows the measured fluctuations of the u-component of the velocity u_{rms}/U_∞ as well as $\overline{u'w'}/U_\infty^2$ in the cross section plane at x/c = 0.6 for the configuration with sharp leading edges (SLE) only. From the full measured field of the fluctuations u', v', w' the distributions of the turbulent kinetic energy and of the eddy viscosity in the flow field can be determined, and corresponding evaluations of the experiments are still under way.
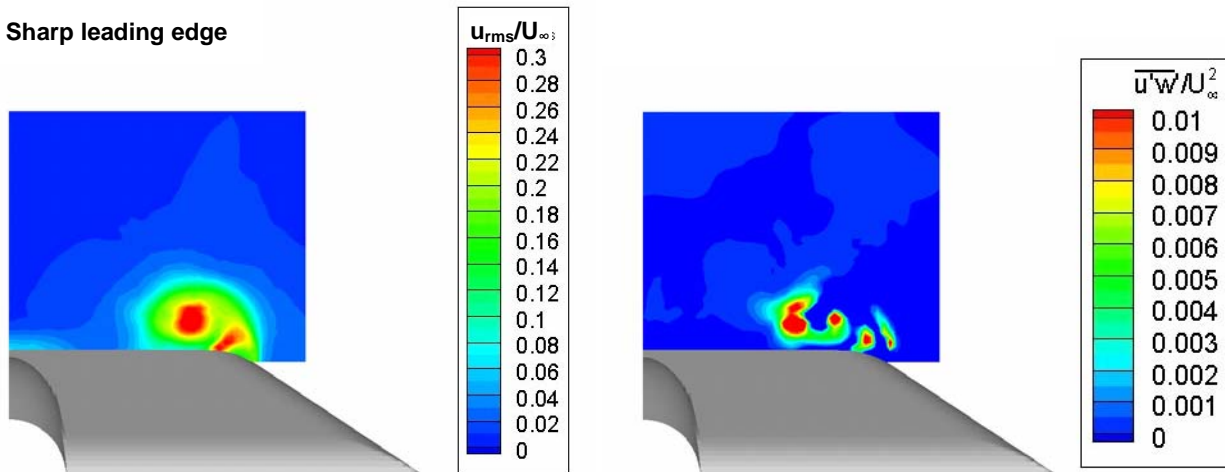
Figure 35-8: Flow Field around the VFE-2 Configuration with Sharp Leading Edges (SLE)
at M ≈ 0.1, $R_{mac} = 1 \times 10^6$, α = 18° – HWA Results from TU Munich [35-7] for the
Velocity Fluctuations u_{rms}/U_∞ and $\overline{u'w'}/U_\infty^2$ in the Plane at x/c = 0.6.

The unsteadiness of the flow can also be evaluated from these experiments by determining the power spectrum density distribution of any fluctuating flow quantity as function of the frequency at any position in the flow field. An example of this kind is shown in Figure 35-9 for the sharp leading edge (SLE) configuration. In the left-hand graph the distribution of the fluctuations of the u-component of the velocity u_{rms}/U_∞ is given, and the location near the vortex centre is indicated, for which the power spectrum density distribution for the velocity component u/U_∞ is shown on the right-hand side. In this turbulent flow near the vortex centre a large variety of frequencies is present with distinctly high values at low frequencies.
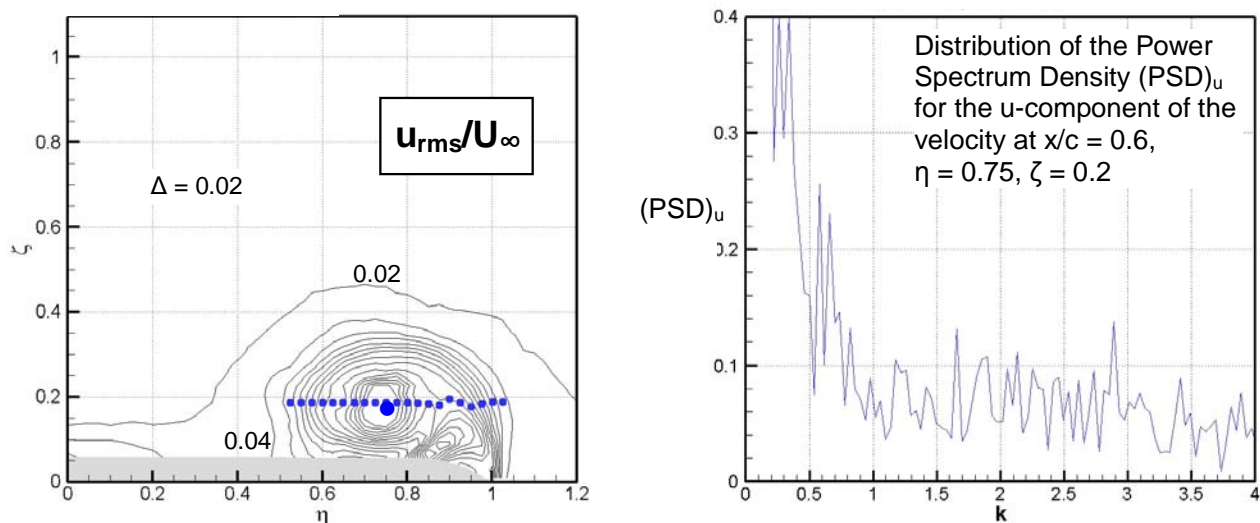
Figure 35-9: Flow Field around the VFE-2 Configuration with Sharp Leading Edges (SLE) at M ≈ 0.1, $R_{mac} = 1 \times 10^6$,
α = 18° – Power Spectrum Density (PSD)$_u$ for the u-Component of the Velocity as Function of the Reduced
Frequency k at x/c = 0.6, η = 0.75, ζ = 0.2 According to HWA at TU Munich [35-7].

In order to find the best suited turbulence model for vortical flow simulations the results of these unsteady flow field measurements will be used for comparisons with numerical calculations. Unfortunately, however, it was only possible to carry out these experiments for incompressible flow ($M \approx 0.1$) and for a very low Reynolds number ($R_{mac} = 1 \times 10^6$), and this causes serious problems on the numerical side, since the convergence rate of the various computer codes is very low. Up to now no comparisons have been performed, and the numerical part of this task is still open.

35.3.3.2   Laminar/Turbulent Transition

The laminar/turbulent transition within the upper surface boundary layer of a delta wing is poorly known even for the simplest case of a sharp leading edge configuration. Following the flow separation at the leading edge the vortical flow reattaches on the upper surface of the wing. This is demonstrated in Figure 35-10 by oilflow patterns taken long ago by the author on the upper surface of the VFE-1 delta wing configuration [35-3] at $M \approx 0.1$, $\alpha = 10°$ for two different Reynolds numbers. The reattachment line (a) is clearly indicated for both Reynolds numbers. Underneath the primary vortex the flow is directed outboard and an acceleration takes place until the surface pressure minimum is reached. Further outboard the pressure increase towards the leading edge leads to a secondary separation and to the formation of a secondary vortex underneath the primary vortex. At very low Reynolds numbers the reattached boundary layer flow is laminar everywhere (see $R_{mac} = 0.42 \times 10^6$), and this leads to an early secondary separation (sl) in a quite large distance from the leading edge. At a higher Reynolds number, however, in the rear part of the wing transition laminar/turbulent may occur due to increased distance from the apex and underneath the primary vortex the adverse pressure gradient towards the leading edge causes also transition laminar/turbulent prior to the secondary separation. Since turbulent boundary layers stay longer attached, the secondary separation line is then shifted towards the leading edge if the separating boundary layer has undergone transition. This phenomenon can be recognized in Figure 35-10 for $R_{mac} = 0.93 \times 10^6$. The kink in the secondary separation line is located at $x/c_r \approx 0.3$. For $x/c_r \leq 0.3$ a laminar boundary layer separates, whereas for $x/c_r \geq 0.3$ the separating boundary layer is turbulent.
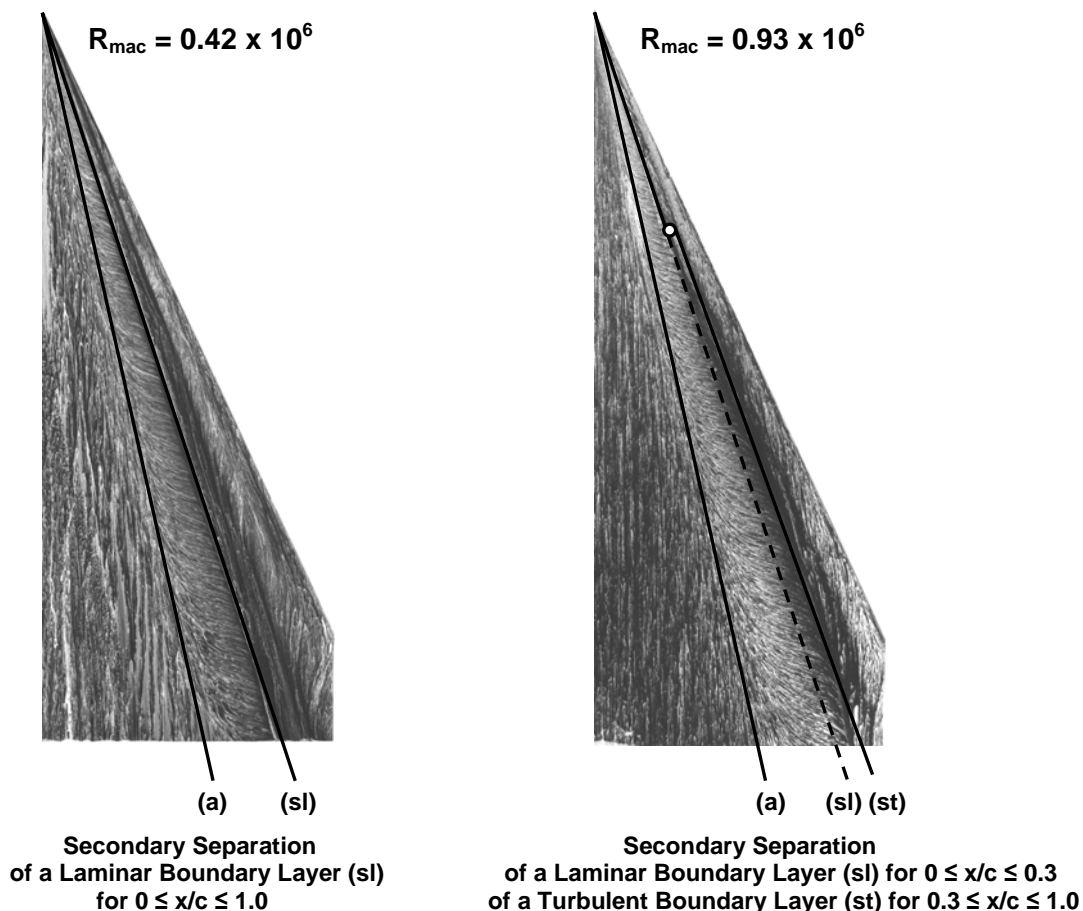
**Figure 35-10: Surface Oilflow Patterns on the Upper Surface of the Sharp-Edged VFE-1 Cropped
Delta Wing (Leading Edge Sweep Λ = 65°) at M = 0.12, α = 10° for Different Reynolds Numbers.**

On the wing surface there exists a transition line, which connects all transition points and which starts at the kink in the separation line. It is important to note that this transition line is not known. Up to now no systematic investigations have been carried out to determine the regions of laminar and of turbulent flow on a sharp edged delta wing. If a method would come up to predict these regions, we would not be able to validate it due to lack of experimental data. On the other hand CFD calculations are presently carried out either for fully laminar or for fully turbulent flow. For very high Reynolds numbers the laminar flow part near the apex of the wing is very small, and calculations for fully turbulent flow are justified in this case. For moderate and low Reynolds numbers, however, in CFD calculations the laminar front part should be taken into account properly and this could be done using an experimentally determined transition location.

For wings with rounded leading edges the primary flow separation is no longer enforced by the leading edge shape. The primary flow separation takes place somewhere in the leading edge region, but the separation line is no longer fixed to the leading edge. Its position depends on the status of the lower surface boundary layer being either laminar or turbulent. This means that the lower surface boundary layer status at the leading edge effects the formation of the primary vortex on the upper surface of the wing. Underneath the primary vortices the upper surface boundary layer formation virtually takes place according to the principles described so far for the sharp leading edge case.

Within VFE-2 attempts have been undertaken to determine the laminar/turbulent transition experimentally, see Chapters 19 and 23. If Temperature Sensitive Paint (TSP) and Infrared Techniques (IR) are used, the position of the temperature jump at transition has to be determined. Unfortunately underneath the primary vortex a considerable temperature distribution is generated on the wing surface due to compressibility effects even for nearly incompressible flow, which has to be separated from the artificially generated temperature distribution caused by the heated or cooled wind tunnel model. Evaluations of this kind are complicated and final results of these experiments are not yet available.

On the numerical side calculations have been started within VFE-2 to produce a solution for the RANS equations for a prescribed distribution of laminar and turbulent boundary layer regions on the wing, which could be chosen according to available experimental results. On the basis of a converged numerical solution a point by point stability analysis should then justify or modify the prescribed transition line on the wing. Unfortunately these investigations could not be finished within the RTO phase of VFE-2.

At the end of the RTO phase of VFE-2 the experimental and the numerical determination of the laminar/ turbulent transition are still open and further investigations on this subject are necessary. The existing attempts will be continued and new investigations are encouraged to be carried out within the subsequent open phase of VFE-2 in the years to come.

35.4   FULLY SEPARATED FLOW WITH VORTEX BREAKDOWN

In this section the results for the VFE-2 configuration at *angle of attack α = 23°* are discussed. In this case the flow is fully separated and vortex breakdown takes place in the rear part of the wing. Today it is common understanding that the flow past slender delta wings at large angles of attack becomes unsteady even for fixed wings. This means that for large angles of attack and steady boundary conditions only unsteady solutions of the governing equations do exist. The spiral-type vortex breakdown is well predicted by numerical solutions of the Navier-Stokes equations [[35-17] and Chapters 25 and 34], see Figure 35-11. The instantaneous vortex axis spirals in space against the sense of rotation of the primary vortex and this spiral turns around with respect to time in the sense of rotation of the primary vortex, and in the centre of the spiralling motion a region of reversed flow is present. Correspondingly all quantities of the flow field show oscillations.
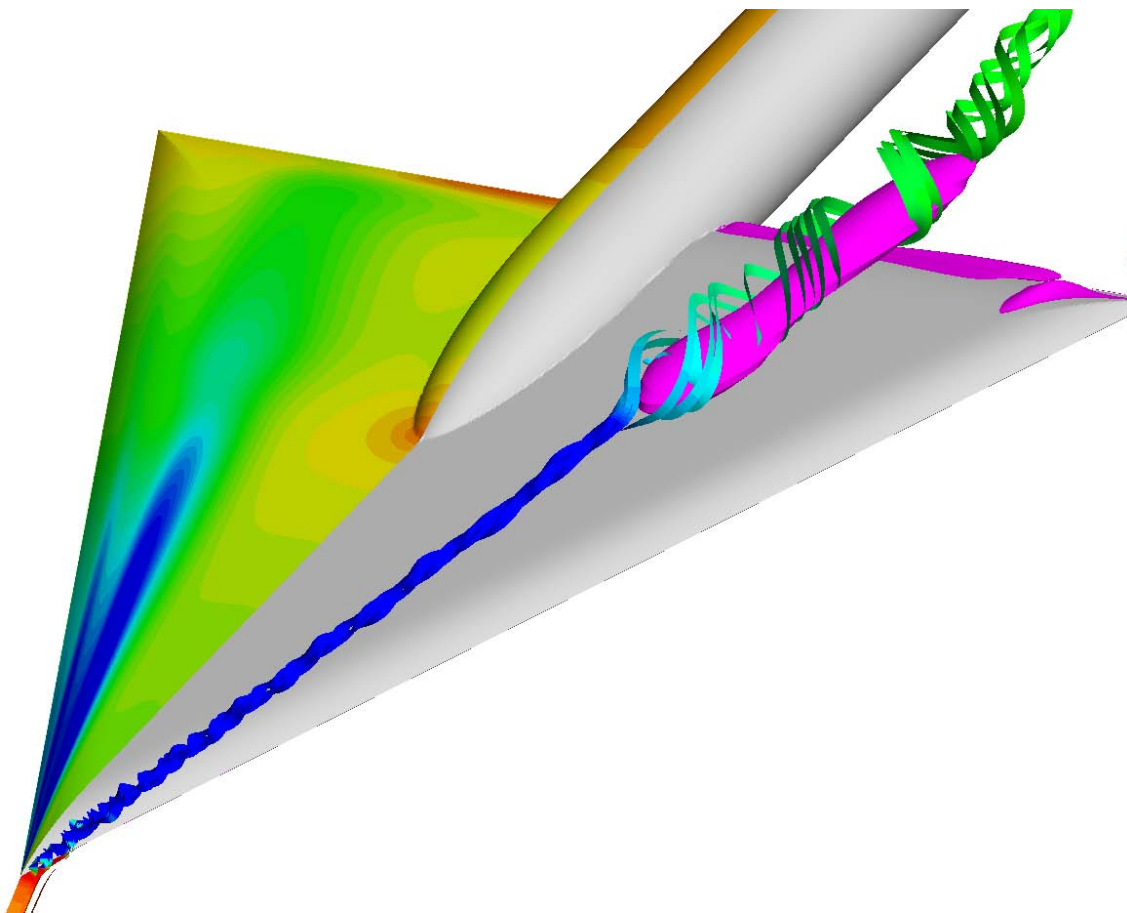
Figure 35-11: Numerical Simulation of the Flow around the VFE-2 Configuration with Sharp Leading Edge (SLE) for M = 0.4, R_{mac} = 6 x 10^6, α = 23° [[35-17] and Chapters 25 and 34]. Surface pressure distribution (left) and flow field (right).

35.4.1   Subsonic Flow Investigations

35.4.1.1   Surface Pressure Fluctuations

In new experiments on the VFE-2 configuration unsteady pressure distribution measurements have been carried out [[35-7] and Chapter 21] in order to provide data on the oscillations including the governing frequencies for comparison with numerical results. As an example, for the configuration with medium radius rounded leading edges (MRLE) Figure 35-12 shows the surface pressure fluctuations $(C_p)_{rms}$ in four cross sections on the wing, and for a certain station in each of these distributions the amplitude spectrum $(SD)_{cp}$ of the pressure fluctuations as a function of the reduced frequency $k = f\,\bar{c}\,/U_\infty$ is given. The high values of the fluctuations around $k \approx 1.3$ in the last section are caused by the spiral motion of vortex breakdown.
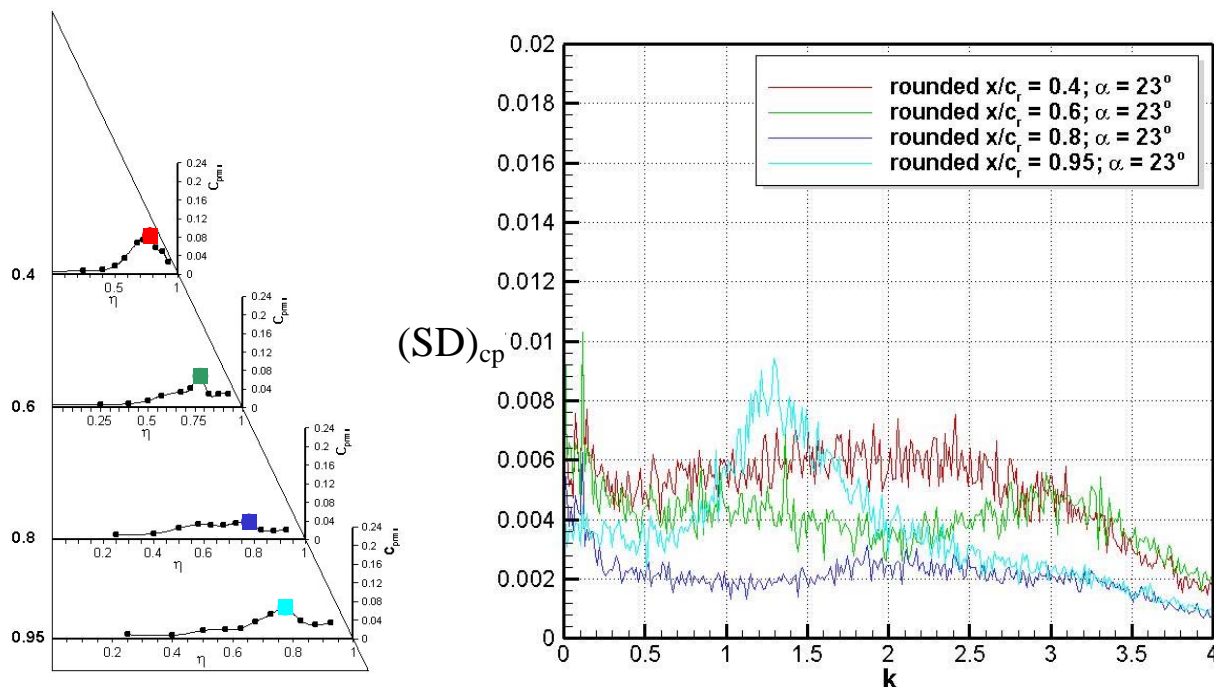
Figure 35-12: Flow Field around the VFE-2 Configuration with Medium Radius Rounded Leading Edges (MRLE) at M = 0.14, R_{mac} = 2 x 10^6, α = 23°. Surface pressure fluctuations $(C_p)_{rms}$ and spectrum density $(SD)_{cp}$ for certain stations in four cross sections according to the measurements at TU Munich [[35-7] and Chapter 21].

35.4.1.2   Unsteady Flow Field

Flow field measurement in various cross sections have also been carried out for α = 23° at TU Munich [[35-7] and Chapter 21]. In these cross sections the time-averaged flow field has been measured by means of PIV investigations and the complete unsteady flow field has been determined using the HWA technique. For the configuration with medium radius rounded leading edge (MRLE) Figure 35-13 shows the unsteadiness of the flow field with vortex breakdown in the cross section at x/c = 0.8. The annular form of the area with high fluctuations is typical for the spiral mode of vortex breakdown, and further analysis of these data will lead to experimental results for the frequency of the spiral mode of vortex breakdown. Evaluations of this kind are presently under way.
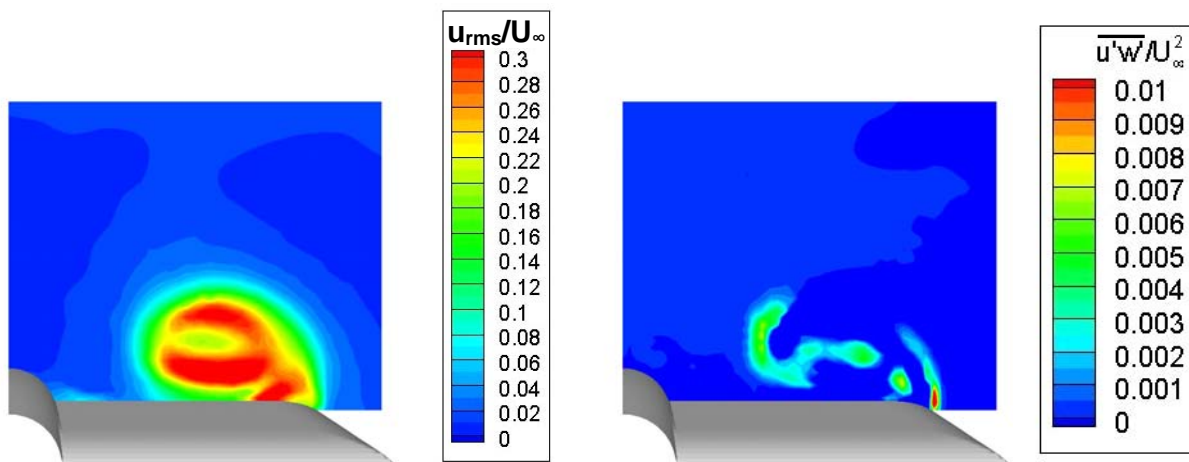
Figure 35-13: Flow Field around the VFE-2 Configuration with Medium Radius Rounded Leading Edges (MRLE) at M ≈ 0.1, R_{mac} = 1 x 10^6, α = 23°. HWA results from TU Munich [[35-7] and Chapter 21] for the velocity fluctuations u_{rms}/U_∞ and $\overline{u'w'}/U_\infty^2$ in the cross section at x/c = 0.8.

Unfortunately these measurements could only be carried out for incompressible flow (M ≈ 0.1) and for very low Reynolds numbers (R_{mac} = 1 x 10^6). In comparisons with flow simulations these conditions cause serious problems on the numerical side, since the convergence rate of the various computer codes is very low. Up to now no comparisons have been performed, and the numerical part of this task is still open.

35.4.1.3   Time-Averaged Surface Pressure Distributions

For comparison with numerical results experimental surface pressure distribution data are available from the NASA measurements [35-1]. Since the vortical flow with vortex breakdown is unsteady, numerical simulations have to be carried out time-accurate, but in the subsequent comparison with experimental data again time-averaged quantities are used. A comparison of this kind is shown in Figure 35-14 for the sharp leading edge (SLE) VFE-2 configuration [[35-17] and Chapter 34]. All numerical simulations predict the onset of vortex breakdown at about x/c_r = 0.6, whereas in the experiments vortex breakdown occurs more downstream. In addition the gradient of the reduction of suction towards the trailing edge is different for the shown numerical solutions. A more detailed comparison of the numerical solutions with the experimental data is presented in Figure 35-15. In the two most upstream cross sections the numerical solutions match the main flow features quite well and the differences are found in the levels of the main suction peak and in the details of the secondary vortex region. However, for $x/c_r \geq 0.6$ some discrepancies are visible. All numerical solutions show a less compact and smeared out vortex as compared to the experimental data.

**EADS
(Structured)**

**KTH
(Unstructured)**

**NLR
(Structured)**

**NASA
(Experiment)**
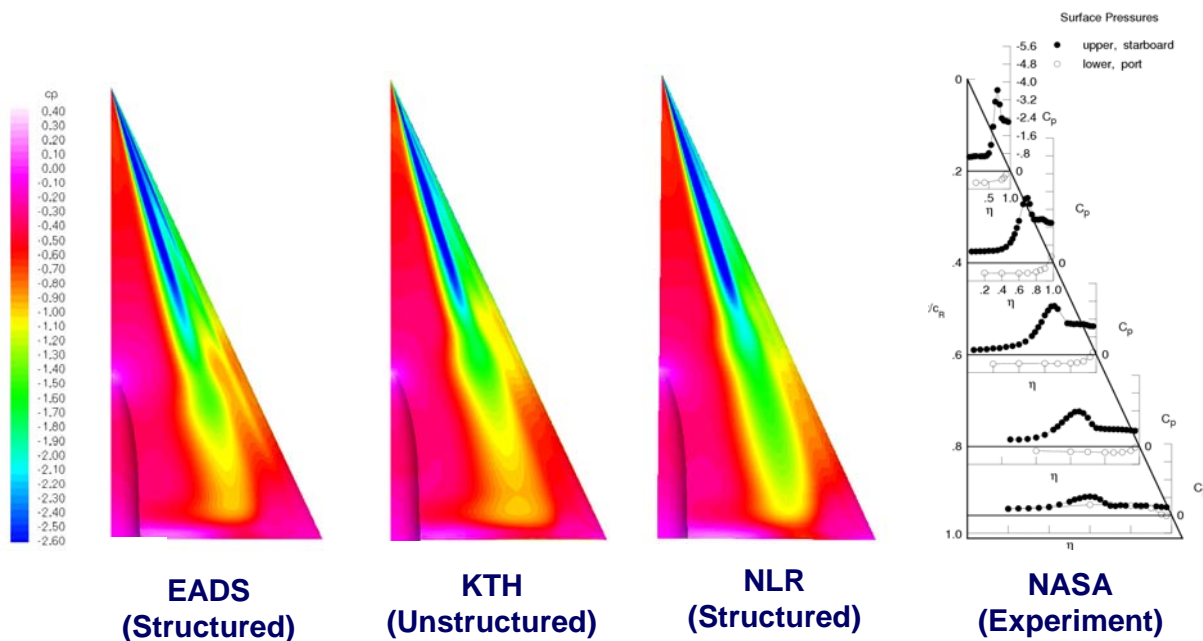
**Figure 35-14: Surface Pressure Distribution on the VFE-2 Configuration with Sharp
Leading Edges (SLE) at M = 0.40, α = 23°, Re = 6 x 10^6 [[35-17] and Chapter 34].**

x/c$_r$=0.2

x/c$_r$=0.4

x/c$_r$=0.6

x/c$_r$=0.8

x/c$_r$=0.95
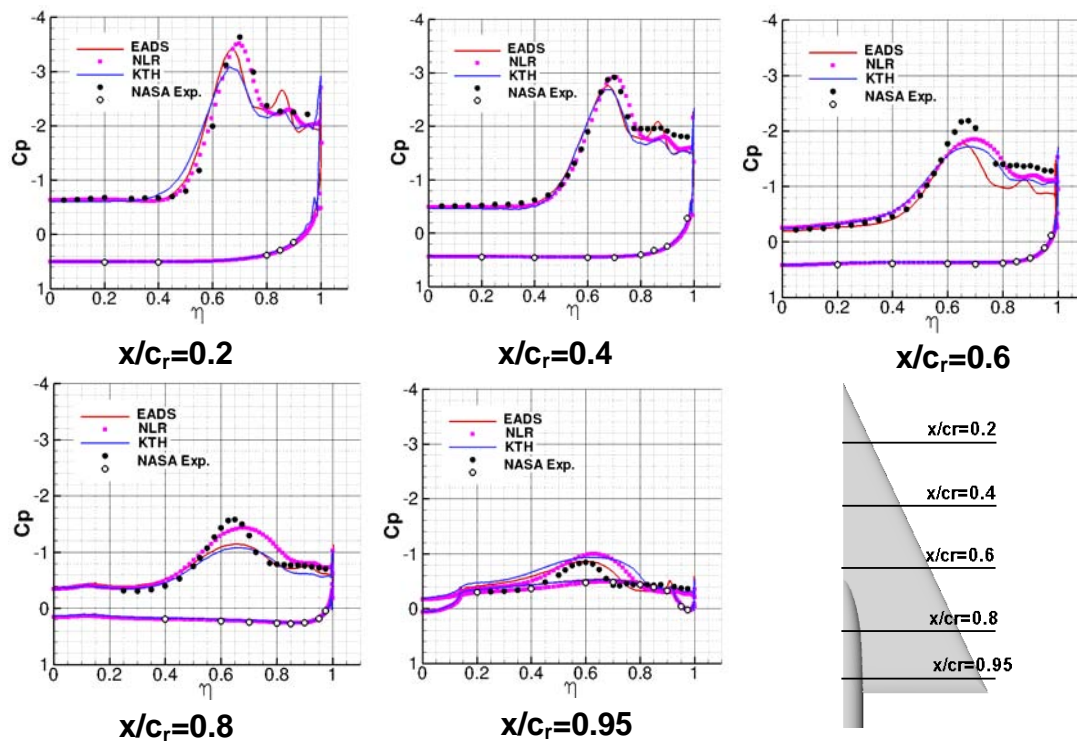
**Figure 35-15: Comparison of Calculated Surface Pressures with Experimental Data for the VFE-2 Configuration
with Medium Radius Rounded Leading Edges (MRLE) at M = 0.40, α = 23°, Re = 6 x 10^6 [[35-17] and Chapter 34].**

35.4.2   Transonic Flow Investigations

35.4.2.1   Experimental Results

For high angles of attack the wind tunnel investigations showed a large effect of Mach number on the vortex breakdown position and hence on the pressure distribution. This is demonstrated in Figure 35-16 for the VFE-2 configuration at $\alpha = 25°$, $R_{mac} = 2 \times 10^6$ and two different Mach numbers. In both cases only moderate differences exist between the results for sharp and blunt leading edges. At the lower Mach number $M = 0.4$ (left-hand part) no supersonic zones and no shock waves do exist for $\alpha = 25°$. At this angle of attack vortex breakdown would certainly be ahead of $x/c = 0.8$, although the precise breakdown location is in general difficult to discern from subcritical surface pressure information. At constant angle of attack and with the increase to a transonic Mach number, however, a distinct change of the pressure distribution on the wing can be taken from the results for $M = 0.8$ (right-hand part). At this transonic Mach number a local supersonic zone with a shock wave is formed in the vicinity of the sting mount. The adverse pressure jump in the shock wave causes additional unsteadiness in the vortical flow field, and most likely shifts vortex breakdown upstream.
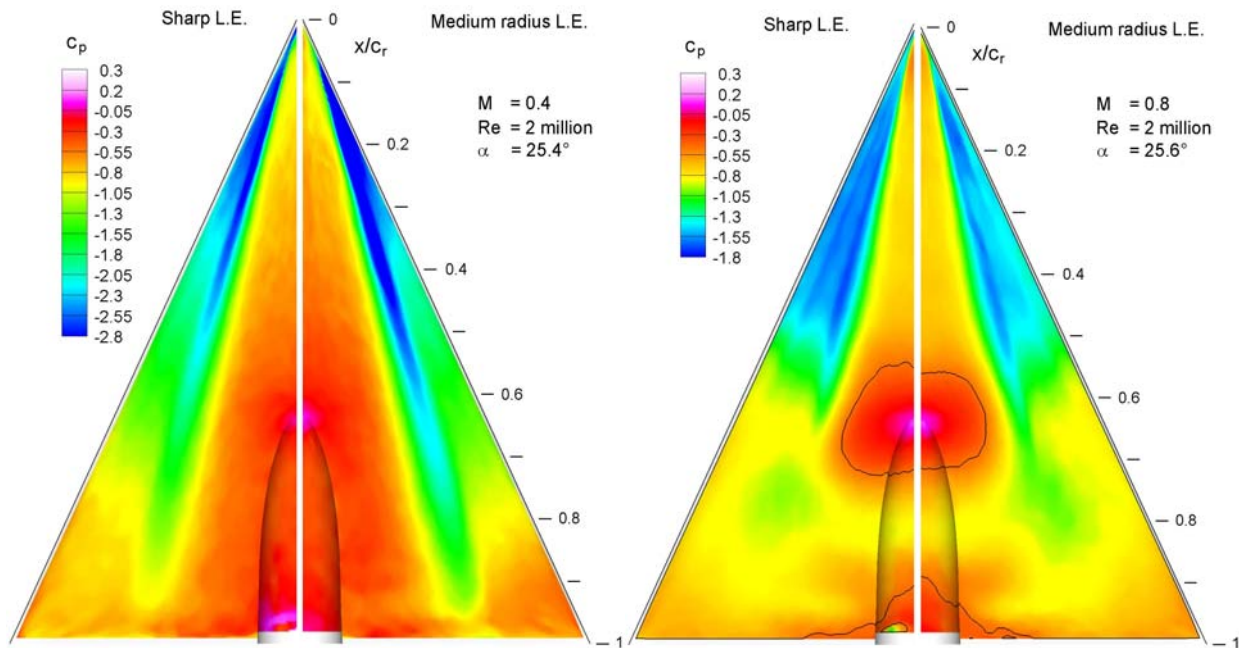
Figure 35-16: Pressure Distributions on the VFE-2 Configuration with Sharp and Medium Radius Rounded Leading Edges (MRLE) at $R_{mac} = 2 \times 10^6$ and $\alpha = 25°$ for Two Mach Numbers According to the PSP Experiments at DLR Goettingen [[35-5] and Chapter 19]. The black line indicates the sonic pressure coefficient.

35.4.2.2   Numerical Results

The surface pressure distributions according to four different numerical solutions together with the experimental data [35-1] are shown in Figure 35-17. There are three very similar solutions by EADS, NLR and KTH, see Chapters 25, 27 and 30. The TAI solution, see Chapter 28, however, is distinctly different, but it is more similar to the experimental data. In the front part at $x/c_r = 0.2$ and $x/c_r = 0.4$ the numerical results of EADS, NLR and KTH are identical and they match the experimental data, whereas in the TAI solution the

initial primary vortex is obviously weaker. At $x/c_r = 0.6$ neither in the experiments nor in the TAI solution a shock has been passed in the flow field, and therefore the TAI solution nicely coincides with the experimental data. The other three solutions are again very similar and they all show the pressure jump due to the shock already at $x/c_r \approx 0.5$. Therefore these solutions do not match the experimental data at $x/c_r = 0.6$, but they still indicate some vortical structure there. In the cross sections $x/c_r = 0.8$ and $x/c_r = 0.95$ the solutions of EADS, NLR, and KTH all show a dead water type pressure distribution without any vortical structure, whereas the TAI solution indicates a vortical structure, which fits the experimental data very well.
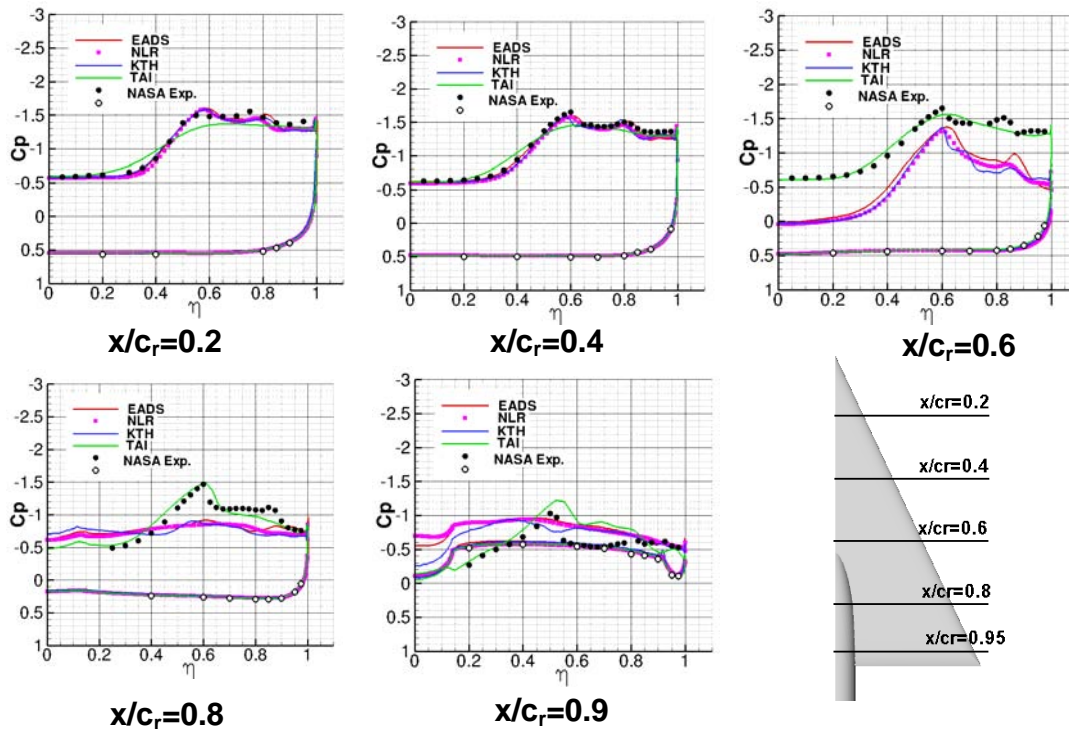
**Figure 35-17: Comparison of Calculated Surface Pressures with Experimental
Data for the VFE-2 Configuration with Sharp Leading Edges (SLE)
at M = 0.85, α = 23°, Re = 6 x 10^6 [[35-17] and Chapter 34].**

A closer look into the surface pressure distributions is shown in Figure 35-18. In the EADS solution, which is representative also for the two other solutions, a strong shock occurs at $x/c_r \approx 0.5$, a dead water type flow is indicated downstream of the shock, and a terminating shock is present at the inner part of the wing. In addition a very significant secondary vortex turns out, which also interacts with the shock. The TAI solution shows a much weaker and more smeared out single vortex in the forward part of the wing, which produces obviously a weaker and more downstream positioned shock. The suction peak is only slightly reduced across this shock. More downstream, at $x/c_r \approx 0.8$, a second weak shock wave builds up from the wing leading edge towards the suction peak. When reaching the suction peak, this shock wave turns at 90° angle and becomes a weak cross flow shock, which finally merges with the terminating shock close to the trailing edge. This result for the shock formation can also be concluded from the experimental pressure distribution, since the measurements at $x/c_r = 0.8$ and $x/c_r = 0.95$ also give an indication of a weak cross flow shock.

EADS   **TAI**   **NASA
Experiment**
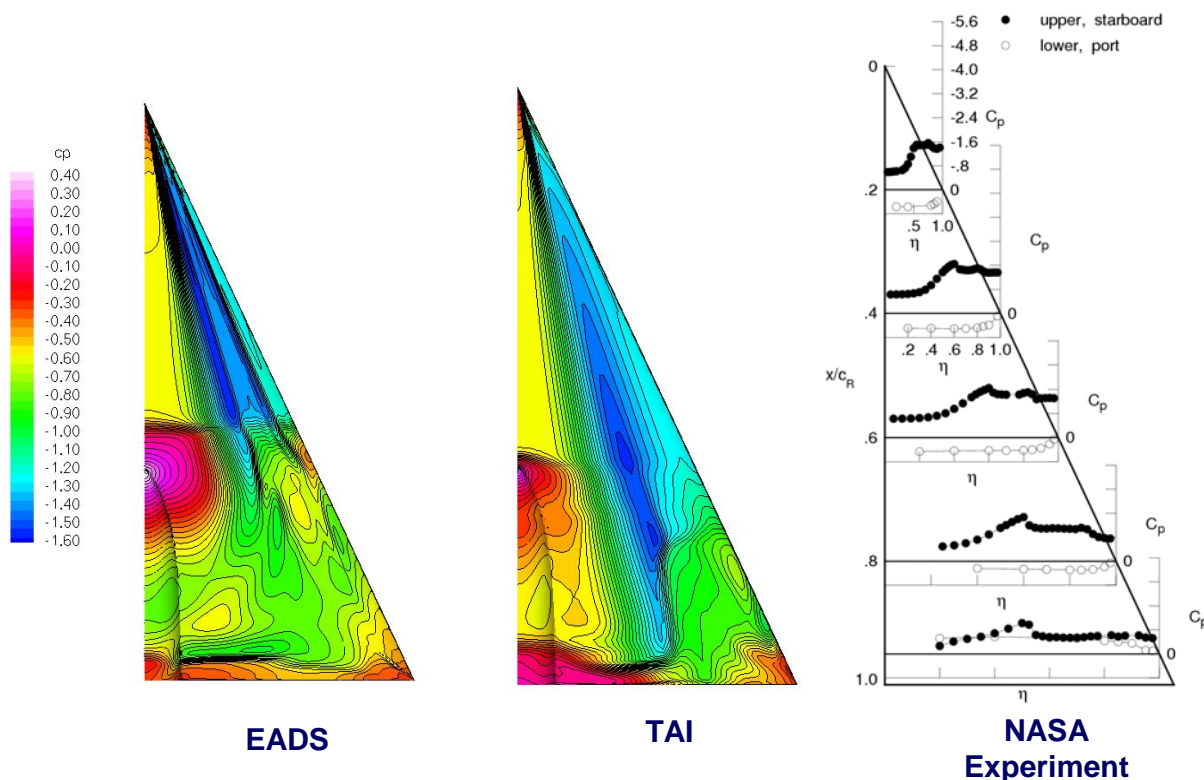
**Figure 35-18: Surface Pressure Maps on the VFE-2 Configuration with Sharp Leading
Edges (SLE) at M = 0.85, α = 23°, Re = 6 x 10^6 [[35-17] and Chapter 34].**

In transonic flow the upstream shift of the vortex breakdown position is caused by shock waves. Within
VFE-2 this phenomenon has been studied intensively by joint numerical investigations [35-13], see Chapter
29. For the VFE-2 configuration the sting mount might be regarded to be responsible for the occurrence of this
shock, but numerical investigations at KTH, see Chapter 30, have indicated that such shocks occur also for the
clean wing without a sting mount and furthermore in transonic flow an unsteady shock system may be present.
The numerical results according to Figure 35-18 show shock shapes, which have never seen before in
experimental results. Therefore new measurements should be carried out related to shock formation and
vortex breakdown onset as well as concerning their mutual interference. On the other hand the available
numerical tools should be checked for the correct prediction of the shock shape and its position in the vortical
flow field, since the present investigations have shown that numerical surface pressure distributions fit
experimental data only if the shocks are covered properly.

35.5   PARTLY SEPARATED VORTICAL FLOW

In this section the results for the VFE-2 medium radius rounded leading edge (MRLE) configuration at *angle
of attack α = 13°* are discussed. In this case partly separated flow is present on the upper surface of the wing
[35-1] as sketched in Figure 35-19 according to [35-17]. This is the most challenging flow situation both
experimentally and numerically. A semi-empirical attempt [35-10] for the prediction of the distance x_V of the
separation onset has been carried out, see Chapter 33, but the more detailed findings within VFE-2 and the
remaining problems are discussed subsequently.
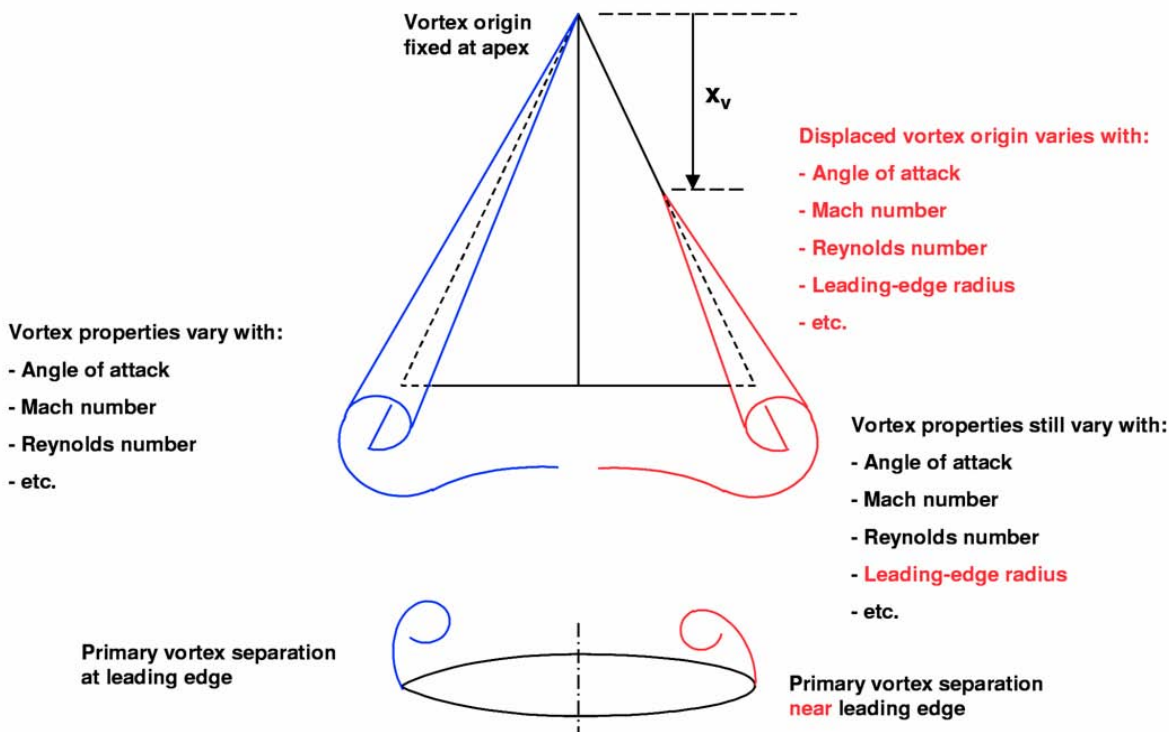
**Figure 35-19: Comparison of Vortical Flow Features for Sharp and Blunt
Leading Edge Delta Wings According to [35-1], taken from [35-17].**

35.5.1   Overall Forces and Moments

The effect of leading-edge bluntness on the normal force and pitching moment coefficients for the VFE-2 configuration is presented in Figure 35-20 from measurements taken in the NASA Langley NTF at a Mach number of 0.4 and a Reynolds number of 6 million. At low angles of attack both wings develop the same normal force. The blunt leading edge wing has attached flow at these conditions, and any leading-edge vortex separation effects for the sharp-edged wing are very small at these low angles of attack. Over the rest of the angle of attack range investigated the blunt leading edge wing develops less normal force than the sharp-edged wing. The blunt leading edge weakens the leading edge vortex resulting in reduced vortex-induced normal force. Pitching moments show the blunt-edged wing has a more forward center of pressure, compared to the sharp-edged wing, over the range of conditions investigated. The vortex flow physics associated with these effects may be taken from the following discussions.
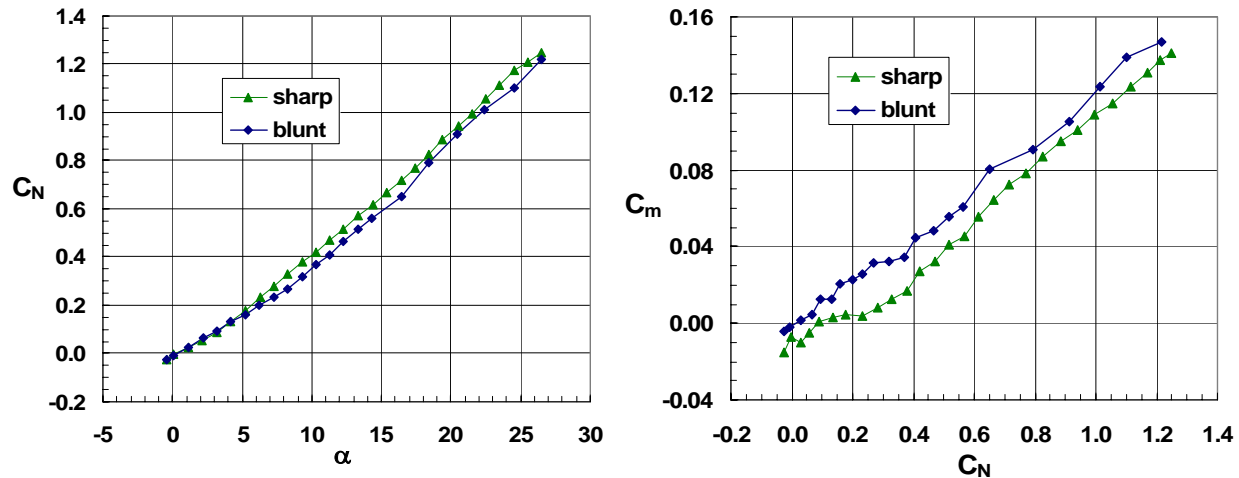
**Figure 35-20: Effect of Bluntness on Experimental Normal Force and Pitching Moment Coefficients
for the VFE-2 Configuration with Sharp (SLE) and Medium Radius Rounded Leading Edges
(MRLE) at M = 0.4, R_{mac} = 6 x 10⁶. Results from NASA Langley NTF [35-1].**

35.5.2   Pressure Distributions

The experimental pressure distribution on the VFE-2 configuration with medium radius rounded leading edges (MRLE) at Mach number M = 0.4 and Reynolds number R_{mac} = 3 million at an angle of attack α = 13° [35-5], see Chapter 19, is shown in Figure 35-21. On the left-hand side the pressure distributions according to PSI experiments from pressure tabs are shown. In the region of attached flow near the apex of the wing high suction occurs at the leading edge. Further downstream an inner suction peak develops followed by an even higher outer suction peak, which replaces the original leading edge suction. Towards the trailing edge of the wing the outer suction peak is still maintained, whereas the inner suction peak reduces more and more and finally disappears. The PSP results on the right-hand side show these features in the same way. The full view of the pressure distribution on the configuration is given in the coloured figure in the centre of Figure 35-21. It shows the onset of the strong outer suction peak to be located at about x/c_r = 0.45 and undoubtedly this suction peak is related to the primary vortex of the separated flow. In order to clarify the flow structures related to the inner suction peak, 3D PIV investigation have been carried out. Figure 35-22 shows the result for the flow field in various cross-sectional planes [35-5], see Chapter 19, in comparison with the numerical result. The surface pressure distribution from the PSP investigations according to Figure 35-21 is repeated in colours for the right half of the wing in the left-hand figure. The outer suction peak underneath the primary vortex is marked by the green area and the one underneath a second, inner vortex can be identified by a yellow band. Two vortices with the same sense of rotation are clearly indicated in the rear part of the wing. Around x/c_r = 0.7 the size of both vortices is about the same as predicted by the CFD results shown in the right-hand figure. More downstream the outer vortex becomes the stronger one, whereas the inner vortex decays. The experimental results are in excellent agreement with the numerical findings [35-11], see Chapter 25, as shown in the right-hand figure.

Figure 35-21: Experimental Pressure Distribution on the VFE-2 Configuration with Medium Radius Rounded Leading Edges (MRLE) for M = 0.4, R_{mac} = 3 x 10^6, α = 13° [[35-5] and Chapter 19].
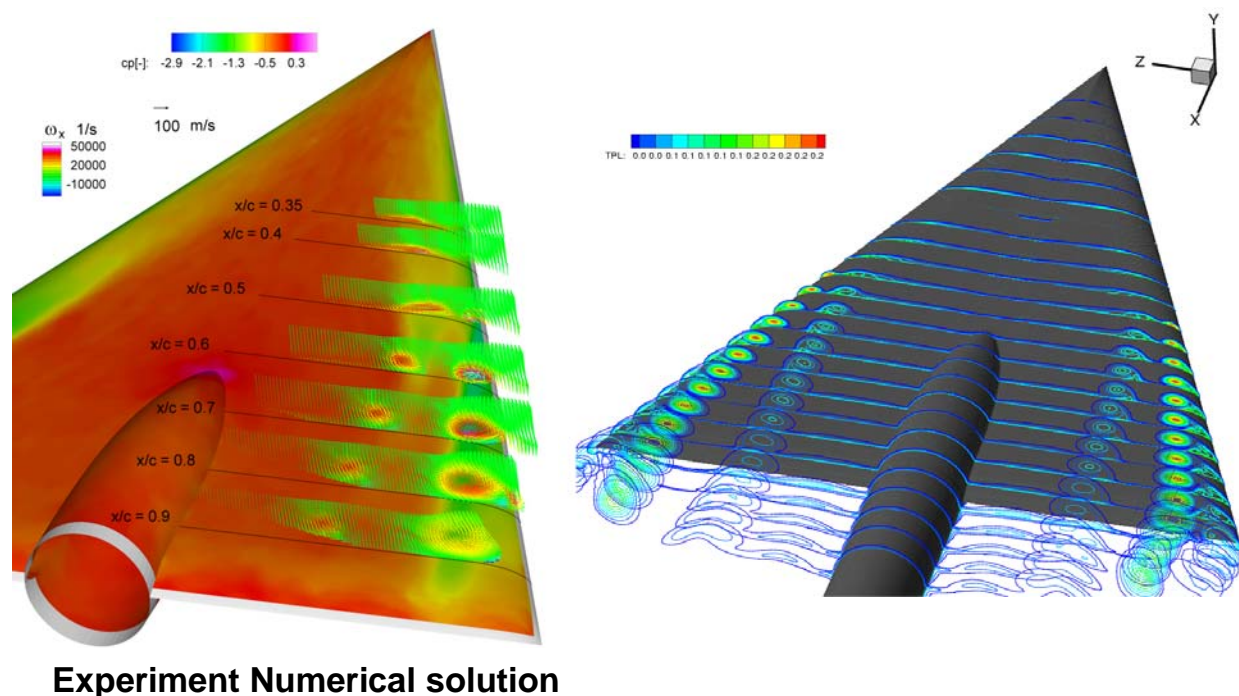
Figure 35-22: Pressure (Surface Color), Velocity (Vectors) and Vorticity (Vector Color) Distributions above the VFE-2 Configuration with Medium Radius Rounded Leading Edges (MRLE) for M = 0.4, R_{mac} = 3 x 10^6, α = 13°. Comparison of the PSP and PIV measurements (left) with the numerical solution (right).

After the encouraging first numerical results [35-11], see Chapter 25, almost all available CFD codes have been applied to the experimentally documented flow case $M = 0.4$, $R_{mac} = 3 \times 10^6$, $\alpha = 13°$. The result for the comparison of different numerical pressure maps with the experimental result of DLR [35-17], see Chapter 34, is shown in Figure 35-23. The dashed horizontal line indicates the onset of the main primary separation in the experiment. The prediction of this vortex onset is the main difference between the various numerical solutions. The EADS-solution [35-11] has this onset point slightly behind, but very close to the experimental onset point. The other solutions show a slightly more upstream position (DLR [35-16], TAI [35-12], and USAFA [35-14]) or a considerable more upstream position (KTH [35-15]) of the onset point. Except for the TAI-solution all other results show the footprint of the inner vortex. Possibly the TAI-grid with 2 million grid points is not fine enough to resolve this flow feature. As can also be seen, none of the solutions exactly matches the experimental surface pressure pattern.
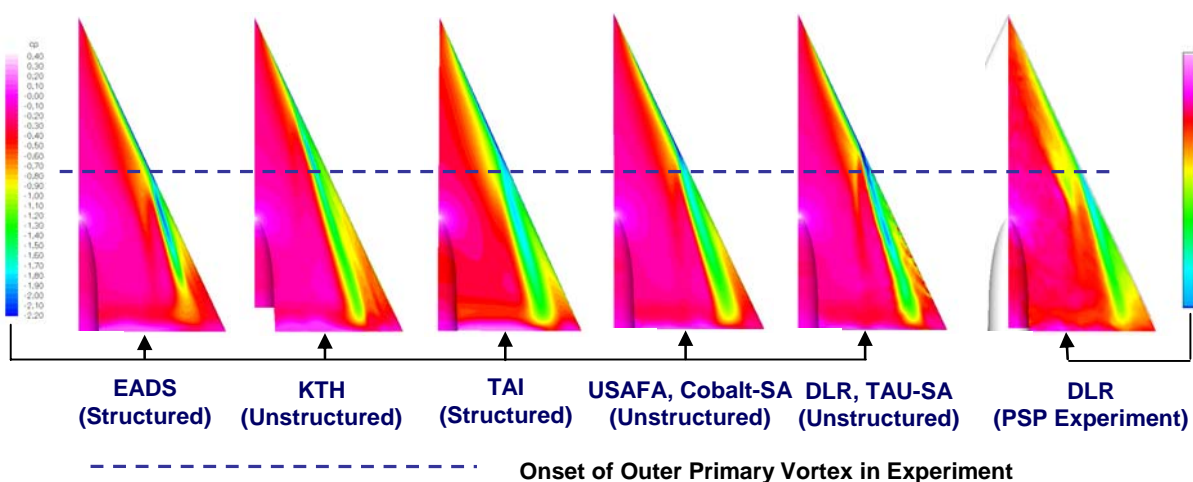
Figure 35-23: Surface Pressure Distribution on the VFE-2 Configuration with Medium Radius Leading Edges (MRLE) at M = 0.40, α = 13°, Re = 3 x 10^6 [[35-17] and Chapter 34].

A more detailed comparison of the surface pressure distribution is given in Figure 35-24. At the first shown cross section at $x/c_r = 0.2$, where no leading edge separation occurs, all numerical pressure distributions are identical and agree well with the experimental data. At $x/c_r = 0.4$ the same applies for four of the five numerical pressure distributions, but the KTH solution [35-15] already shows the formation of a primary vortex. In addition the experimental pressure distribution in this section indicates the beginning of an inner vortex formation, and this effect can also slightly be seen in the KTH solution. At $x/c_r = 0.6$, all solutions as well as the experimental data clearly show a primary vortex, but there are differences in the position and the magnitude of the corresponding suction peak. These differences can be related to the onset of the primary leading edge separation. The more upstream this separation is prescribed, the more inboard located is the suction peak due to the primary vortex. The experimental data also show very clearly the effect of the second, inner vortex. Its foot print is not present in the TAI solution [35-12] and it is hard to identify in the KTH solution [35-15], but the other three solutions [35-12], [35-14], [35-16] clearly indicate the effect of the inner vortex. The EADS solution [35-11] shows this second peak at the correct spanwise position. In the DLR [35-16] and USAFA [35-14] solutions the outer primary vortex is already more inboard as compared with the experiment, and consequently the inner suction peak is also more inboard located. However, in all these three solutions the inner vortex is too weak in comparison with the experiment. In the last cross sections at $x/c_r = 0.8$ and 0.95 the various results are very similar. The more upstream the leading edge separation has

been predicted, the more inboard located is the outer primary vortex. The footprint of the inner vortex has become very weak, and those solutions, which showed the inner vortex in the cross section at $x/c_r = 0.6$ also show the decrease of this vortex.
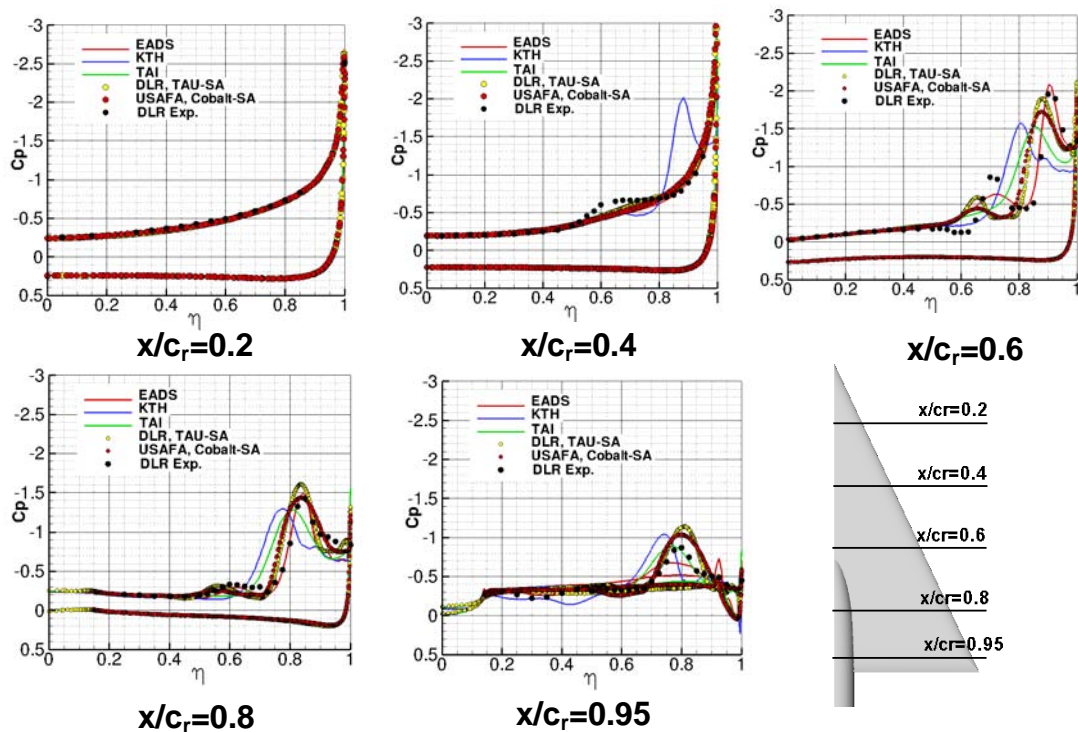
Figure 35-24: Comparison of Calculated Surface Pressures with Experimental Data for the VFE-2 Configuration with Medium Radius Rounded Leading Edges (MRLE) at M = 0.40, α = 13°, Re = 3 x 10^6 [[35-17] and Chapter 34].

35.5.3   Effects of Angle of Attack

Experimental pressure distributions for various angles of attack [35-5], see Chapter 19, are shown in Figure 35-25. Up to α = 11.2° only the inner primary vortex exists, and the corresponding suction on the wing surface reaches considerable values near the trailing edge. With increasing angle of attack the outer primary vortex is formed in the rear part of the configuration and its onset point moves upstream with increasing angle of attack. The strength of the inner primary vortex increases up to the region of the onset of the outer primary vortex, but then decreases suddenly downstream towards the trailing edge. This is due to the fact that the vorticity shed from the leading edge is now fed into the outer primary vortex, and this leads to the considerable reduction of the strength of the inner primary vortex. Another effect can also be recognized from Figure 35-25. In that region where an outer primary vortex already exists, the weakened inner primary vortex moves inboard [35-9].
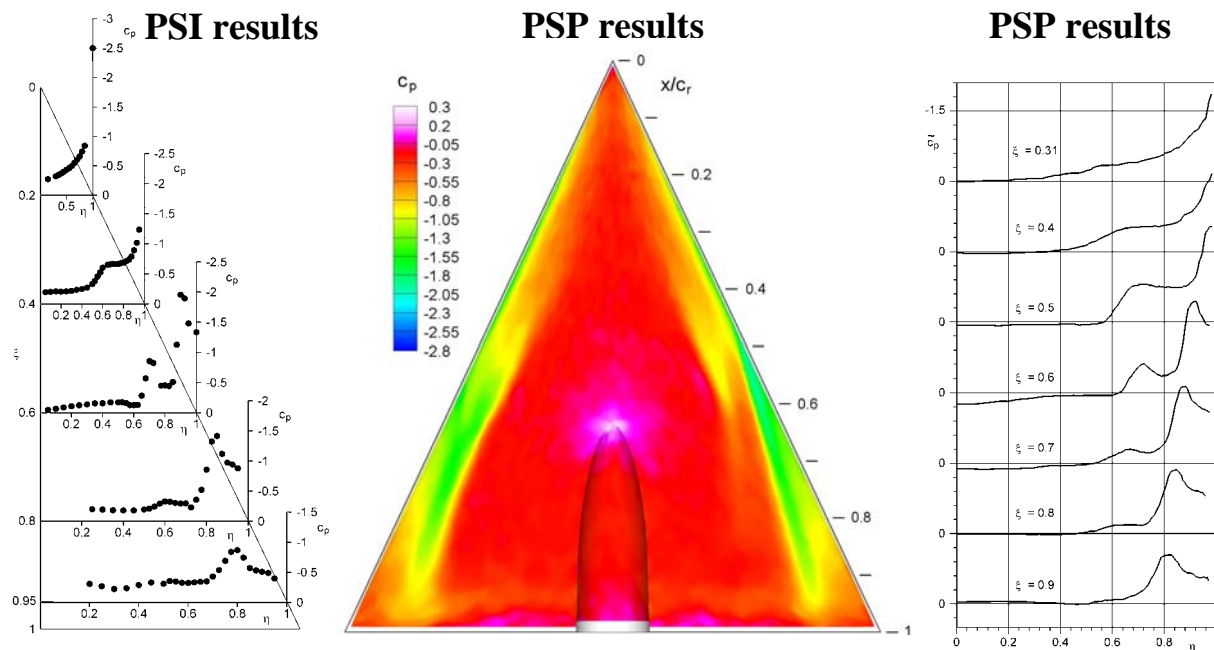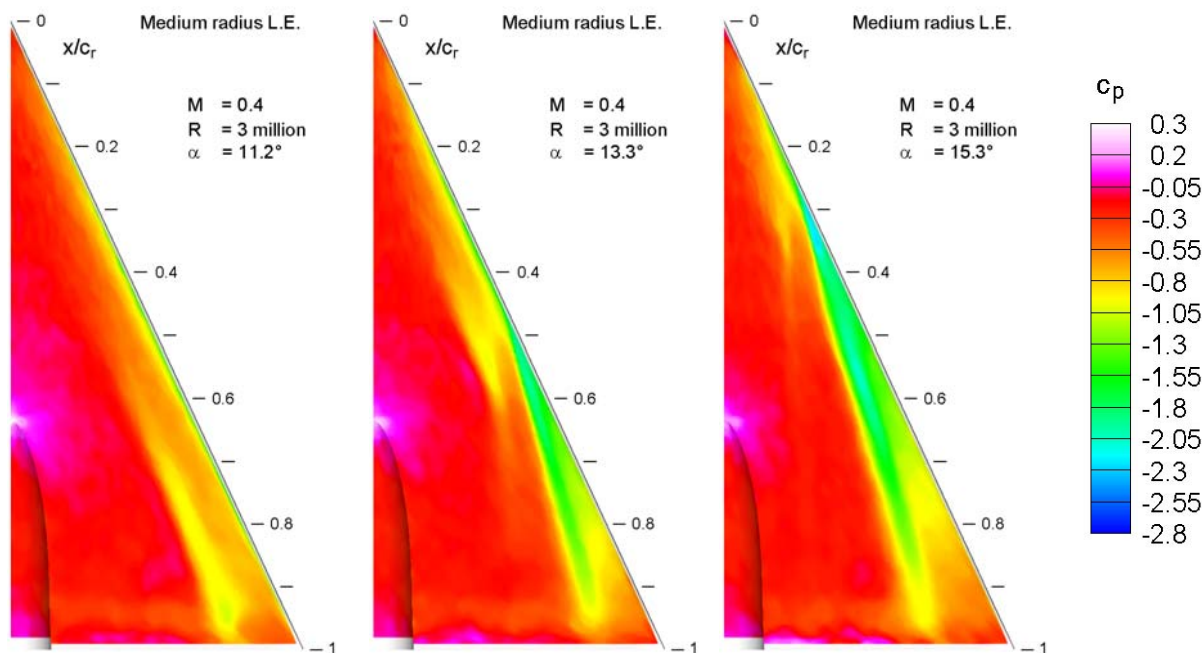
Figure 35-25: Pressure Distributions on the VFE-2 Configuration with Medium Radius Rounded Leading Edges (MRLE) for M = 0.4, R_{mac} = 3 x 10^6 at Various Angles of Attack [[35-5] and Chapter 19].

35.5.4   Effects of Reynolds Number

The vortex formation strongly depends on the Reynolds number [35-5], see Chapter 19. An example is shown in Figure 35-26. With decreasing Reynolds number the onset of the outer primary vortex moves upstream and its strength increases, whereas the inner primary vortex is weakened and its position moves distinctly inboard. Thus, a reduction in Reynolds number has an analogous effect as an increase of the angle of attack according to Figure 35-25, but nevertheless the reasons for this upstream movement of the onset of the outer primary vortex are different for both cases. With increasing angle of attack the adverse pressure gradients on the upper surface of the wing increase as well, and this leads to the upstream movement of the onset of the outer primary vortex. If the angle of attack is unchanged, however, the adverse pressure gradients remain at the same level, but with decreasing Reynolds number the viscous flow is no longer able to stay attached, and this leads again to an upstream movement of the onset of the outer primary vortex [35-9].
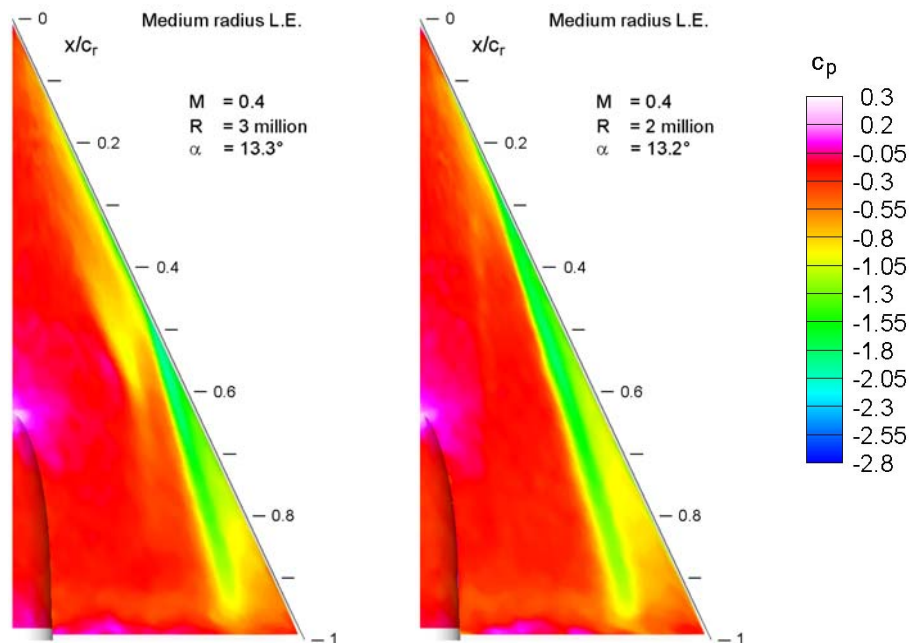
Figure 35-26: Pressure Distributions on the VFE-2 Configuration with Medium Radius Rounded Leading Edges (MRLE) for M = 0.4, α = 13° at Different Reynolds Numbers [[35-5] and Chapter 19].

35.5.5   Effects of Mach Number

In contrasting a subsonic and a transonic Mach number condition, the principal vortex topology remains unchanged, but some compressibility effects can be recognized. In transonic flow the formation of the outer primary vortex starts earlier [35-5], see Chapter 19. Figure 35-27 shows the pressure distributions at α = 13° and $R_{mac} = 2 \times 10^6$ for two different Mach numbers. At the higher Mach number the onset of the outer primary vortex has moved slightly upstream and its axis is distinctly shifted inboard. For M = 0.8 an inner primary vortex has no longer been found. If it exists at all in transonic flow, this vortex must be very weak [35-9].
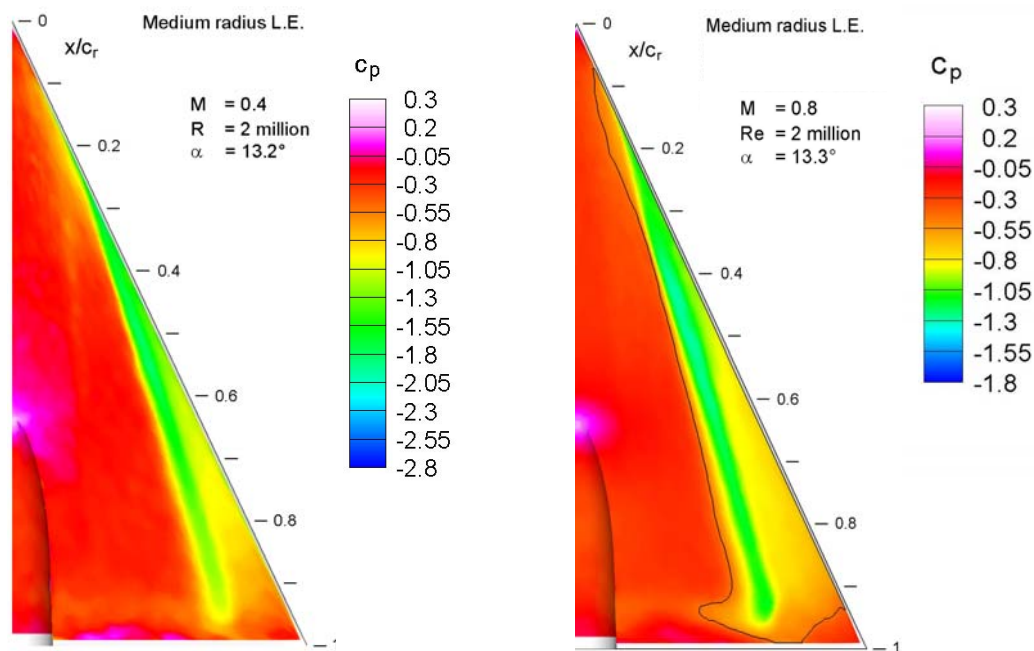
Figure 35-27: Pressure Distributions on the VFE-2 Configuration with Medium Radius Rounded Leading Edges (MRLE) at R_{mac} = 2 x 10^6 and α = 13° for Different Mach Numbers [[35-5] and Chapter 19]. The black line indicates the sonic pressure coefficient.

35.5.6 Understanding of the Flow Physics

Based on the experimental results obtained within the VFE-2 the onset of a vortical flow on the present delta wing with medium radius rounded leading edge can be summarized as follows: at α = 13° the first flow separation takes place in the front part of the wing, where the body is relatively thick. At its very beginning the separated flow region is located close to the body surface, but further downstream a concentrated inner primary vortex is formed quite rapidly. Along the blunt leading edge the curvature radius of the leading edge remains constant, whereas the local half span increases downstream. This means in other words that the leading edge becomes relatively sharper (r_{LE} /b_{loc}) towards the trailing edge of the wing. Correspondingly the suction at the leading edge increases downstream, and finally new flow separations take place in the outer portion of the rear part of the wing, forming an outer primary vortex there. In the region of the onset of this outer primary vortex, strong interference with the already existing inner primary vortex takes place. The dominant part of vorticity, shed from the leading edge, is now fed into the outer primary vortex, whereas the feeding of the inner vortex with vorticity is reduced. Therefore the inner primary vortex decays downstream due to dominating viscous effects.

Unfortunately within VFE-2 not all details of the onset of vortical flow in the front part of the configuration could be investigated experimentally because of geometric constraints of the PIV setup in the wind tunnel, see Chapter 19. However, an important experimental result of the variation of angle of attack, of Reynolds number and of Mach number as described in the previous sections is the fact, that during all movements of the location of the outer primary vortex onset point the two co-rotating vortices were originally connected. The inner primary vortex is present at first, then the outer primary vortex starts, and after its formation the two vortices separate from each other, the outer one increasing in strength and the inner one moving inboard and decaying

downstream through viscous effects. Further experimental investigations of these details may be expected from Glasgow University [35-8], see Chapter 22, where a new wind tunnel model of the VFE-2 configuration came into operation just at the end of the RTO phase of VFE-2.

Due to the encouraging agreement between the experimental and the calculated results related to the two co-rotating primary vortices, see Chapters 25 and 34, further studies of the details of the vortex formation may also be carried out through an analysis of numerical solutions. However, caution is necessary in such an attempt, since the CFD codes themselves are presently not fully validated. Figure 35-28 and Figure 35-29 show latest calculated results on a structured grid by EADS Munich and on an unstructured grid by DLR Braunschweig, and from these numerical results some conclusions may be drawn, which are summarized subsequently and sketched in Figure 35-30.
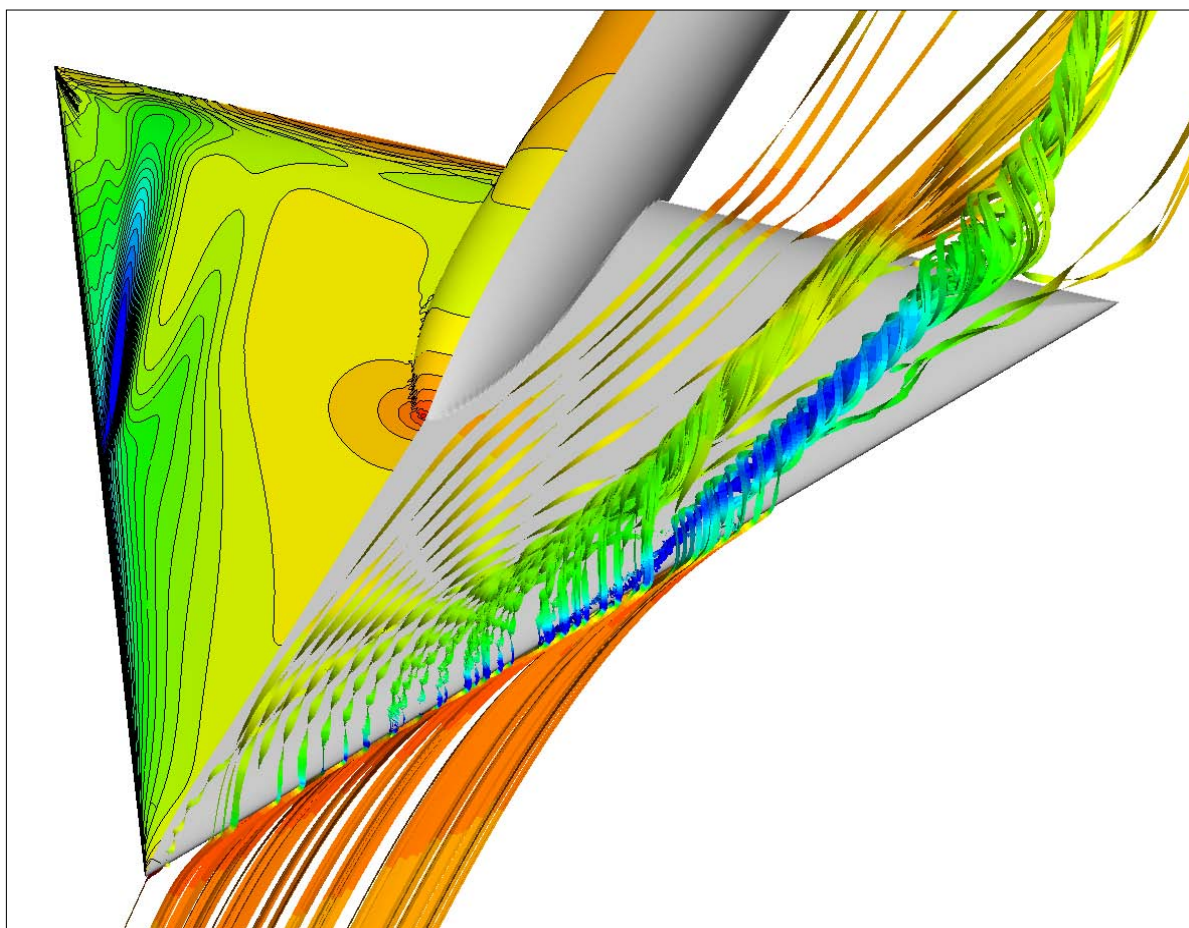
Figure 35-28: Numerical Solution on a Structured Grid for the Flow around the VFE-2 Configuration with Medium Radius Rounded Leading Edges at M = 0.4, R_{mac} = 3 x 10^6, α = 13.3°. Pressure distribution (left) and streamlines in the flow field (right) [[35-11] and Chapter 25].
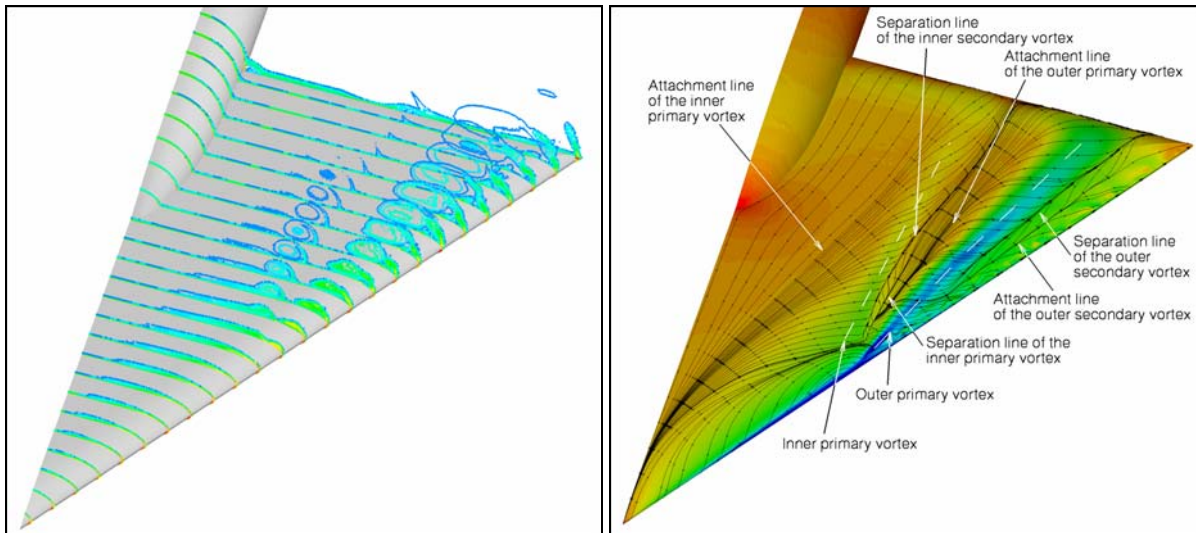
Figure 35-29: Numerical Solution on an Unstructured Grid for the Flow around the VFE-2 Configuration with Medium Radius Rounded Leading Edges at M = 0.4, R_{mac} = 3 x 10^6, α = 13.3°. Distribution of axial vorticity (left) and upper surface friction lines (right) [[35-16] and Chapter 31].
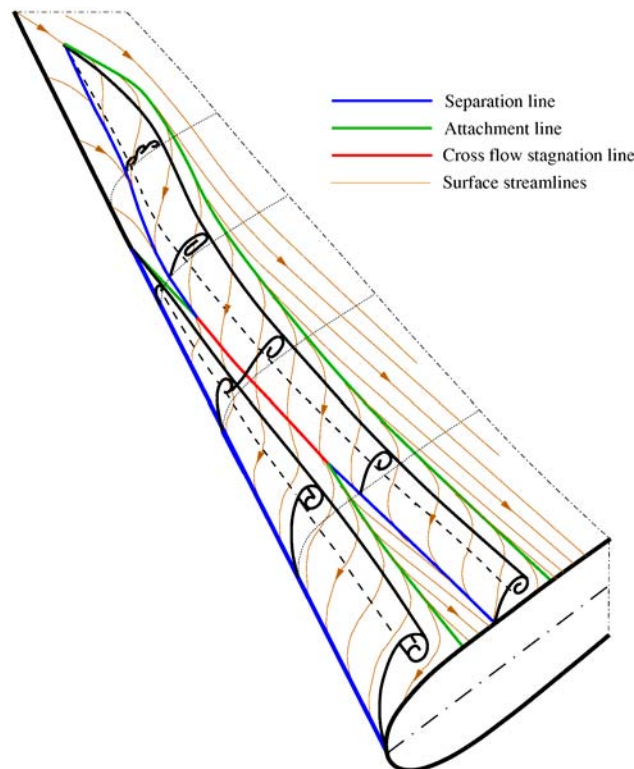
Figure 35-30: Schematic View of the Vortex Formation on the VFE-2 Configuration with Medium Radius Rounded Leading Edge (MRLE) at M = 0.4, R_{mac} = 3 x 10^6, α = 13.3°. According to the Numerical Solutions of EADS [Chapter 25] and DLR [Chapter 31]. (Region between the onset of the outer primary vortex and the separation of the two primary vortices enlarged, secondary vortices omitted).

The first separation due to the thickness distribution of the configuration takes place near the wing apex. The corresponding separation and attachment lines are located far inboard, and according to experimental results [35-5], see Chapter 19, the separated region is thin and broad. According to Figure 35-29 (left) vorticity is distributed over the whole separated region [35-16], see Chapter 31, and a concentrated vortex is not yet present. Underneath the attached flow around the leading edge the primary separation develops and a tiny vortex is formed, marked in both numerical solutions in blue, see Figure 35-28 and Figure 35-29 (right). Due to this small primary vortex the already existing inner flow separation is now set in a new order. The vorticity suddenly concentrates and the inner separation takes the form of an inner primary vortex in the same region where also the outer primary vortex is established. As long as the strength of the outer primary vortex is smaller than that of the inner primary vortex, an attachment line related to the outer vortex and a separation line related to the inner vortex do exist separately. Due to the increasing strength of the outer primary vortex the two lines join and form a cross flow stagnation point, which leaves the wing surface, and correspondingly the outer primary vortex becomes double branched as sketched in Figure 35-30 and the two vortices are connected. More downstream the outer primary vortex becomes dominant. Therefore the free stagnation point in the cross flow between the two vortices approaches the wing again and on the surface it splits up into a separation line corresponding to the inner primary vortex and into an attachment line corresponding to the outer primary vortex. Both vortices are now separated from each other. In this discussion on the conjecturable flow behaviour the secondary vortices related to both primary vortices have not been taken into account, but they could be included into the topology according to Figure 35-30 quite easily.

In future numerical calculations the CFD codes should be validated using the existing experimental data, and if the results are reliable the schematic view of the vortex formation according to Figure 35-30 should be checked, and if necessary corrections should be applied.

35.6   CONCLUSIONS AND OUTLOOK

In the present chapter the results of the Second International Vortex Flow Experiment (VFE-2) have been summarized. The original experimental NASA data base has been considerably enlarged. Significant details of the vortical flow have now been measured. This was accomplished through 15 new wind tunnel experiments coordinated among four countries. A focus was established on two of the leading edges (sharp and medium bluntness) from the NASA experiments, and four new wind tunnel models were fabricated to support the new testing. Surface and off-body measurements, for both steady and fluctuating quantities, have been accumulated using a wide variety of test techniques as well as three-component forces and moments.

The experimental campaigns confirm the multiple-vortex structure of blunt leading edge vortex separation, and considerably more details of this flow are now available through the use of the Pressure Sensitive Paint (PSP) technique. Detailed flow field measurements by Particle Image Velocimetry (PIV) provided new insight into the vortical structure, and surface and off-body fluctuating measurements by Hot-Wire Anemometry (HWA) showed the turbulent structure of these flows.

Within VFE-2 the available CFD codes have been applied to the vortical flow around a relatively simple delta wing configuration with sharp and rounded leading edges. Numerical calculations have been carried out on structured and unstructured grids. The CFD codes have been validated using the experimental data, and the numerical results have been used as guidelines for the set-up of the wind tunnel experiments. Moreover in the final RTO-phase of VFE-2 the numerical results played an important role in the understanding of the flow physics, since the lack of experimental details in some flow regions could be replaced by numerical results. Therefore the present state of knowledge is the outcome of a proper combination of experiments and numerics.

The scientific work of the VFE-2 facet of the RTO AVT-113 Task Group has been carried out from 2003 to 2007 [35-3] as outlined in Chapter 17, and the achieved status of knowledge is described in the present Final Report. As shown in this Chapter 35 many results could be documented, but some problems are still unsolved. Therefore, at the end of the RTO-phase of VFE-2 the scientific program is not terminated. As with VFE-1, the scientific work will continue in the next decade. Many problems have not been solved completely or have even been started, and others have not yet been looked at within the framework of the present Task Group. Therefore new experiments will be carried out worldwide in a new open phase of VFE-2. The configuration under consideration is relatively simple and described analytically, and therefore new wind tunnel models can be built quite easily. Numerical calculations will go on as well, and better results as well as new solutions will be achieved.

The results according to this Final Report will be the starting point for future investigations. In the present resuming Chapter 35 the achievements as well as the unsolved problems have been summarized. On this basis an outlook for the needs of further investigations may be given here.

On the experimental side the needs are:

- Measurements on the boundary layer status laminar/turbulent for the VFE-2 configuration with sharp and rounded leading edges. Fully developed vortical flow without vortex breakdown at $\alpha = 18°$ should be the starting point, and later also partly separated vortical flow at $\alpha = 13°$ could be added. The already existing experimental results will be further evaluated, but there is an urgent need for new measurements.

- Experimental investigations on the shock formation in transonic fully developed vortical flow $\alpha = 23°$ for the VFE-2 configuration with sharp and medium radius rounded leading edges. Subject should be the mutual interference between the terminating and the cross flow shocks on the one hand and vortex breakdown on the other.

- New measurements on the partly separated vortical flow at $\alpha = 13°$. Up to now the structure of the initial flow separation due to the thickness distribution near the apex of the configuration, see Figure 35-30, is unknown. Numerical simulations [35-16] have shown vorticity distributions without a dominating concentrated vortex in this area, see Figure 35-29 and Chapter 31, whereas experiments [35-5] indicate some weak longitudinal vortices in this area, see Figure 35-30 and Chapter 19.

On the numerical side the needs are

- New calculations related to the fully developed vortical flow without vortex breakdown at $\alpha = 18°$ for the VFE-2 configuration with sharp and medium radius rounded leading edges in incompressible flow and at very low Reynolds numbers. Converged solutions should be achieved for various turbulence models, and in comparisons with the available results from Hot-Wire-Anemometry (HWA) [35-7], see Chapter 21, the best suitable turbulence model for calculations of vortical flows should be found.

- Attempts should be made to predict the laminar/turbulent transition in fully developed vortical flows without vortex breakdown at $\alpha = 18°$. Starting point could be the sharp edged VFE-2 configuration. For this purpose two steps would be helpful

    - Calculation of the vortical flow for prescribed laminar and turbulent boundary layer regions on the wing as a guess. A converged solution should be achieved. As input experimental results could be used.

    - Point by point stability analysis of the calculated flow field. Based on the results corresponding modification of the original laminar/turbulent transition guess.

- For partly separated vortical flow at α = 13° the CFD codes should be further validated using the already available or new experimental data. The vortical flow field in the vicinity of the onset point of the outer primary vortex should be analysed in detail in order to check the validity of the schematic view presented in Figure 35-30.

The first RTO-phase of the Second International Vortex Flow Experiment (VFE-2) has been terminated in 2008 by the present Final Report. A second open phase of VFE-2 starts now in 2008. The scientific community is invited to join this project and to start new investigations. Information on the ongoing research may be taken from the new website www.dlr.de/as/vfe-2.

35.7   REFERENCES

[35-1]   Chu, J. and Luckring, J.M.: *Experimental Surface Pressure Data Obtained on 65° Delta Wing Across Reynolds Number and Mach Number Ranges*, NASA TM 4645 (1996).

[35-2]   Hummel, D. and Redeker, G.: *A New Vortex Flow Experiment for Computer Code Validation*, RTO AVT Symposium "Vortex Flow and High Angle of Attack Aerodynamics", Loen, Norway, 7-11 May 2001, Meeting Proceedings RTO-MP-069 (I), SYA 8-1 to 8-31, 2003.

[35-3]   Hummel, D.: *Review of the Second International Vortex Flow Experiment (VFE-2)*, AIAA Paper 2008-0377, 2008.

[35-4]   Luckring, J.M.: *Initial Experiments and Analysis of Vortex Flow on Blunt Edged Delta Wings*, AIAA Paper 2008-0378, 2008.

[35-5]   Konrath, R., Klein, Ch. and Schröder, A.: *PSP and PIV Investigations on the VFE-2 Configuration in Sub- and Transonic Flow*, AIAA Paper 2008-0379, 2008.

[35-6]   Le Roy, J.F., Rodriguez, O. and Kurun, S.: *Experimental and CFD Contribution to Delta Wing Vortical Flow Understanding*, AIAA Paper 2008-0380, 2008.

[35-7]   Furman, A. and Breitsamter, Ch.: *Turbulent and Unsteady Flow Characteristics of Delta Wing Vortex Systems*, AIAA Paper 2008-0381, 2008.

[35-8]   Coton, F., Mat, S. and Galbraith, R.: *Low Speed Wind Tunnel Characterization of the VFE-2 Wing*, AIAA Paper 2008-0382, 2008.

[35-9]   Luckring, J.M. and Hummel, D.: *What was Learned from the New VFE-2 Experiments*, AIAA Paper 2008-0383, 2008.

[35-10] Nangia, R.K.: *Semi-Empirical Prediction of Vortex Onset and Progression on 65° Delta Wings*, RTO-AVT-113, VFE-2 Facet, AIAA Paper 2008-0384, 2008.

[35-11] Fritz, W.: *Numerical Simulation of the Peculiar Subsonic Flow-Field about the VFE-2 Delta Wing with Rounded Leading Edge*, AIAA Paper 2008-0393, 2008.

[35-12] Gürdamar, E., Ortakaya, Y., Kaya, S. and Korkem, B.: *Some Factors Influencing the Vortical Flow Structures on Delta Wings*, AIAA Paper 2008-0394, 2008.

[35-13] Schiavetta, L.A., Boelens, O.J., Crippa, S., Cummings, R.M., Fritz, W. and Badcock, K.J.: *Shock Effects on Delta Wing Vortex Breakdown*, AIAA Paper 2008-0395, 2008.

[35-14] Cummings, R.M. and Schütte, A.: *Detached-Eddy Simulation of the Vortical Flowfield about the VFE-2 Delta Wing*, AIAA Paper 2008-0396, 2008.

[35-15] Crippa, S. and Rizzi, A.: *Steady, Subsonic CFD Analysis of the VFE-2 Configuration and Comparison to Wind Tunnel Data*, AIAA Paper 2008-0397, 2008.

[35-16] Schütte, A. and Lüdeke, H.: *Numerical Investigations on the VFE-2 65-degree Rounded Leading Edge Delta Wing Using the Unstructured DLR-TAU-Code*, AIAA Paper 2008-0398, 2008.

[35-17] Fritz, W. and Cummings, R.M.: *What was Learned from the Numerical Simulations for the VFE-2*, AIAA Paper 2008-0399, 2008.

Chapter 36 – SUMMARY OF THE SYNERGISTIC EFFECTS OBTAINED BY THE PRESENT STUDY OF VORTICAL FLOWS

by

John E. Lamar *(Retired)* **and Dietrich Hummel** *(Retired)*

36.1 SUMMARY

This chapter identifies the benefits that occurred to the AVT-113 task group members and the resulting progress made to two separate vortical flow proposals for task group status being combined into one. Both of these proposals dealt with multiple-vortices, and though they shared different focuses, the general topic, as well as the specific features of this flow, made it of great interest to each sub-task or facet member. The joint meetings increased our overall understanding of vortical flow and the synergistic benefits are summarized in terms of experimental and computational data, virtual laboratory usage, dissemination of results, and career development.

36.2 INTRODUCTION

This chapter identifies the benefits that occurred to members of the AVT-113 task group as a result of two separate vortical flow proposals for task group status – contained in [36-1], [36-2] – being combined into one. Though these proposals had different focuses, the general topic, as well as the specific features of the flow, made our joint meetings of great interest to each sub-task or facet member; moreover, these gatherings increased our overall understanding of the grand variety of multiple vortices that can occur over a wing. Each meeting was a seminar in itself and the official ten meetings, plus those held in advance under the Exploratory Team AVT/ ET-026, provided directions for the next steps. Highlights of the synergy that took place are given next.

36.3 SYNERGY

The synergistic benefits are a direct result of sharing together at semi-annual official, as well as unofficial, meetings, and by e-mail or telephone, plus jointly working common problems and writing up the results. They are separated for discussion below into the general categories dealing with data, its communication, and the careers influenced.

36.3.1 Experimental and Computational Data

Data presentations and the following discussions by participating members gave an early insight of the novel vortical flow features that were measured or predicted for the F-16XL aircraft or the 65° delta-wing model at a variety of test conditions.

However, before we could get to the point of discussing the data, there was a need to share geometry/grids data or a wind-tunnel model among the international participants. This need led to a sharing of the process learned by one facet with the other. In particular, since the experimental data existed for the CAWAPI facet, the immediate focus for this facet was on securing a suitable geometry and grids that could be used by the members and to work the ITAR agreements with the European participating organizations. In the VFE-2 facet

the geometry of the delta-wing model was not subject to ITAR restrictions, as it was analytically described, and therefore new wind tunnel models could be fabricated quite easily. However, the immediate focus of the VFE-2 facet was the transfer of a NASA model to the DLR for use in an upcoming wind-tunnel campaign, and this transfer required again international agreements similar to those in the CAWAPI facet.

Another part of the task-group synergy is that some members of the CAWAPI facet ended up contributing solutions to the VFE-2 facet as well, along with those who only generated solutions for the VFE-2 facet. In particular, O.J. Boelens, primarily a CAWAPI member, located an existing structured-grid solution at the NLR for the 65° sharp-edged delta-wing configuration and this was one of the first utilized by that facet [36-3].

Also, W. Fritz, initially only a CAWAPI facet member, played an important role within the VFE-2 facet. He supported the DLR-Goettingen PIV wind-tunnel tests of the VFE-2 facet with an initial CFD flow solution [36-4]. This guided the experimentalists to investigate the details of the primary vortex separation in the appropriate region of the flow field, where two co-rotating vortices, an inner and an outer one, have been found. This success was the origin of a close cooperation between the experimental and the numerical part of VFE-2 [36-5].

Another task group synergy took place in the opposite direction. In the CAWAPI facet the flow around the F-16XL aircraft turned out to be very complex, and a large number of vortical flow regions have been found in the numerical solutions. During the final interpretation of the results the expertise of members of the VFE-2 facet was very helpful.

36.3.2   Virtual Laboratory Usage

Chapter 2 of this report details the planned and actual usage of a virtual laboratory (VL) to speed the information being generated by members and to facilitate comparisons. Since the details are already given, the synergistic effect to note is that the CAWAPI facet hardware and software system, being developed and in place, was also in the process of being adapted/modified for use by the VFE-2 facet.

36.3.3   Dissemination of Results

Dissemination of the AVT-113 results was always key to what this task group would do and even early on, as well as stated in the TAP, plans were laid for communicating what was being learned through various venues.

36.3.3.1   Conferences

Since the CAWAPI facet did not need to generate new experimental data to commence its work, this facet was able to conclude its limited CFD scope on the order of a year earlier than that of the VFE-2 facet. As a result, the CAWAPI facet was able to report out its results at two special sessions of the AIAA Aerospace Sciences Meeting (ASM) in January 2007, and the session chairmen came from the VFE-2 facet. Similarly, the VFE-2 facet reported out its results at two special sessions of the ASM in January 2008 and used CAWAPI facet members as session chairmen.

36.3.3.2   Journal Articles

The thirteen papers presented by the CAWAPI facet members at the AIAA ASM have been combined into six articles, plus one editorial, for publication in the AIAA Journal of Aircraft as a Special Section. Publication is expected in late 2008 or early 2009. The fifteen papers presented by VFE-2 facet members at the AIAA ASM

are targeted for publication in the AIAA Journal at some future date. They chose the AIAA Journal because it was better suited to their more fundamental topic. This journal would also allow them to discuss the topic without having to combine or shorten articles and could even be published in one or more issue, depending on the amount of information selected.

36.3.4   Career Development

Task group participation by doctoral students from the University of Glasgow (GBR), the Royal Institute of Technology (KTH) in Stockholm (SWE), the Technical Universities of Braunschweig and Munich (DEU) not only greatly assisted the work of the group but also provided these young engineers with opportunities to be exposed to senior people and prospective employers on a regular basis. Consequently, the results are that:

- Six doctoral theses by members/regular-invited-guests have utilized all or a portion of their task-group work as a basis and some of them have already been published (S. Goertz [36-6], A. Jirasek [36-7], L. Schiavetta [36-8] and S. Crippa [36-9]).

- Two National Research Council post-doctoral fellowship at USAFA were awarded (S. Goertz [2005] and A. Jirasek [2008]).

- Two permanent careers started (S. Goertz [2006] and S. Crippa [2008]).

In addition, task group members already employed by USAFA and DLR-Braunschweig have participated in reciprocal sabbaticals for their mutual benefit and career enhancement.

36.4   CONCLUDING REMARKS

This task group succeeded in accomplishing its assigned tasks and benefited by the combined strength of two differently focused groups of people, one in a difficult CFD application to a complex airplane and the other more fundamental. The energy, determination of each sub-group or facet, and the reported progress at the semi-annual meetings/seminars were examples of cooperation as each facet encouraged the other. Moreover, the cooperation between the AVT-113 co-chairmen was especially cordial and helpful. The results of synergy within the group were particularly noted in the handling of the experimental and computational data, virtual laboratory usage, dissemination of results, and career development.

36.5   REFERENCES

[36-1]   Lamar, J.E.: *Cranked Arrow Wing (F-16XL-1) Flight Flow Physics with CFD Predictions at Subsonic and Transonic Speeds*, Presented at RTO AVT Symposium on "Advanced Flow Management; Part A – Vortex Flow and High Angle of Attack", Paper Number 44, in Loen, Norway, during May 7-11, 2001, Meeting Proceedings RTO-MP-069 (I), SYA 44-1 to 44-20, 2003.

[36-2]   Hummel, D. and Redeker, G.: *A New Vortex Flow Experiment for Computer Code Validation*, Presented at RTO AVT Symposium on "Advanced Flow Management; Part A – Vortex Flow and High Angle of Attack", Paper Number 8, in Loen, Norway, during May 7-11, 2001, Meeting Proceedings RTO-MP-069 (I), SYA 8-1 to 8-31, 2003.

[36-3]   Boelens, O.J.: *Numerical Solutions for the VFE-2 Configuration on Structured Grids at NLR, The Netherlands*, Chapter 27, RTO-TR-AVT-113 Final Report, 2009.

[36-4]   Fritz, W.: *Numerical Simulation of the Peculiar Subsonic Flow-Field about the VFE-2 Delta Wing with Rounded Leading Edge*, AIAA Paper 2008-0393, 2008.

[36-5]   Hummel, D.: *Final Results of the International Vortex Flow Experiment – Resumé and Outlook*, Chapter 35, RTO-TR-AVT-113 Final Report, 2009.

[36-6]   Goertz, S.: *Realistic Simulations of Delta Wing Aerodynamics Using Novel CFD Methods*, Ph.D. Thesis, KTH, Aeronautics and Vehicle Engineering, Stockholm, Sweden, February 2005.

[36-7]   Jirásek, A.: *Vortex Generator Modeling and its Application to Optimal Control of Airflow in Inlet*, Ph.D. Thesis, KTH, Aeronautics and Vehicle Engineering, Stockholm, Sweden, October 2006.

[36-8]   Schiavetta, L.A.: *Evaluation of URANS and DES Predictions of Vortical Flows Over Slender Delta Wings*, Ph.D. Thesis, University of Glasgow, February 2007.

[36-9]   Crippa, S.: *Advances in Vortical Flow Prediction Methods for Design of Delta-Wing Aircraft*, Ph.D. Thesis, KTH, Aeronautics and Vehicle Engineering, Stockholm, Sweden, June 2008.

Chapter 37 – CONCLUSIONS AND RECOMMENDATIONS

by

John E. Lamar *(Retired)* **and Dietrich Hummel** *(Retired)*

37.1 SUMMARY

This chapter provides a brief wrap-up of the task group report and focuses on the overall conclusions and recommendations for future work for the CAWAPI and VFE-2 facets beyond the task group. The overall conclusion is that the Technology Readiness Level (TRL) of CFD solvers has been improved in predicting the flow-physics of vortex-dominated flows during the work of the task group, by having flight and wind-tunnel data available for comparison. Moreover, like all good scientific studies, this task group has identified flight conditions on the F-16XL airplane or wind-tunnel test conditions for a specific leading-edge radius on the 65° delta-wing model where the TRL still needs to be increased.

37.2 INTRODUCTION

From the preceding chapters, as well as the TAP and TOR, each facet of this task group dealt with questions that needed answers. For the CAWAPI facet, it was how well did CFD, in particular unstructured grid solvers, predict the flight data. For the VFE-2 facet, there were at least two questions: one dealt with could new experiment data be generated beyond that published to provide additional, fundamental insight into the flow around the 65° delta wing, especially with a medium radius rounded leading-edge; and the second dealt with how well could these measured data sets be predicted. Some of these answers appear in the lesson learned chapters [37-1] to [37-4] of this report and the results are summarized here.

37.3 CONCLUSIONS

37.3.1 CAWAPI Facet

As reported in [37-5], the F-16XL-1 aircraft had been successfully modelled in a structured grid solver. However, for the CAWAPI study, there was a need to use an improved geometrical description and to satisfy the needs of both the structured and unstructured grid communities with a common surface-grid. This was accomplished and reported in [37-6]. The solutions generated by the unstructured grid solvers are reported in [37-7] to [37-14] and join those generated with the structured grid solvers reported in [37-15] to [37-17]. The basic message here is that complex aircraft, having many of the surface details modelled, can be successfully computed over a range of vortex-flow-dominated fight conditions with both unstructured and structured grid solvers. Moreover, the Technology Readiness Level (TRL) has been increased and best practices identified for the solvers employed in this study. One surprise occurred at the transonic flight condition, low α, where none of the CFD solvers predict well the C_ps over the middle third of the inboard wing or on the outer panel, yet there was good C_p agreement across the wing among all the solvers. Thus, we still have the unanswered question: Why should this be so?

37.3.2   VFE-2 Facet

Within Second International Vortex Flow Experiment (VFE-2) the original experimental NASA data base has been considerably enlarged. Four new wind tunnel models were fabricated and 15 new wind tunnel experiments were coordinated among four countries. A focus was established on two of the leading edges (sharp and medium bluntness) from the NASA experiments, and significant details of the vortical flow have been measured. The experimental campaigns confirmed the multiple-vortex structure of blunt leading edge vortex separation, and considerably more details of this flow are now available through the use of the Pressure Sensitive Paint (PSP) technique. Detailed flow field measurements by Particle Image Velocimetry (PIV) provided new insight into the vortical structure, and surface and off-body fluctuating measurements by Hot-Wire Anemometry (HWA) showed the turbulent structure of these flows.

Within VFE-2, the available CFD codes have been applied to the vortical flow around the relatively simple delta wing configuration with sharp and rounded leading edges. Numerical calculations have been carried out on structured and unstructured grids. The CFD codes have been validated using the experimental data, and the numerical results have been used as guidelines for the set-up of the wind tunnel experiments. Moreover in the final RTO-phase of VFE-2 the numerical results played an important role in the understanding of the flow physics, since the lack of experimental details in some flow regions could be replaced by numerical results. Therefore the present state of knowledge is the outcome of a proper combination of experiments and numerics.

The status of knowledge achieved by the VFE-2 facet of the RTO AVT-113 Task Group is described and many results documented in [37-4]. However, some problems have not been solved completely, some have not yet been addressed, and others were outside the scope of the present Task Group. Therefore new experiments will be carried out worldwide in a new open phase of VFE-2. The configuration under consideration is relatively simple and described analytically, and therefore new wind tunnel models can be built quite easily. Numerical calculations will go on as well to aid in the study.

37.4   RECOMMENDATIONS

37.4.1   CAWAPI Facet

The basic recommendation is to resolve the C_p predictive disagreement for the transonic, low α flight condition. Another item of note is whether acceptable vortical-flow dominated flow-physics results can be generated with simplifications of the complex aircraft geometry. Both of these items are subject to further study.

37.4.2   VFE-2 Facet

At the end of the RTO-phase of VFE-2 the scientific program is not terminated. As with VFE-1, the scientific work will continue in the next decade. Recommendations for future experimental investigations are:

- New measurements on the boundary layer status laminar/turbulent for the VFE-2 configuration with sharp and rounded leading edges.

- Experimental investigations on the mutual interference between the terminating and the cross flow shocks in transonic fully developed vortical flow with vortex breakdown for the VFE-2 configuration with sharp and medium radius rounded leading edges.

- New measurements on the partly separated vortical flow in order to check the final view of the flow structure as described in Figure 35-30 [37-4].

For the numerical side the recommendations are:

- New calculations related to the fully developed vortical flow without vortex breakdown for the VFE-2 configuration with sharp and medium radius rounded leading edges in incompressible flow and at very low Reynolds numbers in order to check the suitability of the various turbulence models.

- Prediction of the laminar/turbulent transition in fully developed vortical flows without vortex breakdown, starting with the sharp edged VFE-2 configuration.

- Further validation of the CFD codes for partly separated vortical flow at $\alpha = 13°$. The vortical flow field in the vicinity of the onset point of the outer primary vortex should be analysed in detail in order to check the validity of the schematic view presented in Figure 35-30 [37-4].

The RTO-phase of the Second International Vortex Flow Experiment (VFE-2) has been concluded and is documented in the present Final Report. An open phase of VFE-2 begins in 2008 and the scientific community is invited to join this project and to start new investigations.

37.5   REFERENCES

[37-1]   Rizzi, A., Jirásek, A., Lamar, J.E., Badcock, K.J., Boelens, O.J. and Crippa, S.: *What was Learned from the Numerical Investigations on the CAWAPI Configuration*, Chapter 16, RTO-TR-AVT-113 Final Report, 2009.

[37-2]   Luckring, J.M., and Hummel, D.: *What was Learned from the Experimental Investigations on the VFE-2 Configuration*, Chapter 24, RTO-TR-AVT-113 Final Report, 2009.

[37-3]   Fritz, W; and Cummings, R.M.: *What was Learned from the Numerical Investigations on the VFE-2 Configuration*, Chapter 34, RTO-TR-AVT-113 Final Report, 2009.

[37-4]   Hummel, D.: *Final Results of the International Vortex Flow Experiment – Resumé and Outlook*, Chapter 35, RTO-TR-AVT-113 Final Report, 2009.

[37-5]   Lamar, J.E., Obara, C.J., Fisher, B.D. and Fisher, D.F.: *Flight, Wind-Tunnel, and Computational Fluid Dynamics Comparison for Cranked Arrow Wing (F-16XL-1) at Subsonic and Transonic Speeds*, NASA/TP-2001-210629, February 2001.

[37-6]   Boelens, O.J., Görtz, S., Morton, S., Fritz, W. and Lamar, J.E.: *F-16XL Geometry and Grids*, Chapter 4, RTO-TR-AVT-113 Final Report, 2009.

[37-7]   Fritz, W.: *Numerical Solutions for the CAWAPI Configuration on Unstructured Grids at EADS-M, Germany*, Chapter 8, RTO-TR-AVT-113 Final Report, 2009.

[37-8]   Morton, S., McDaniels, D.R. and Cummings, R.M.: *Numerical Solutions for the CAWAPI Configuration on Unstructured Grids at USAFA*, United States, Chapter 9, RTO-TR-AVT-113 Final Report, 2009.

[37-9]   Görtz, S. and Jirásek, A.: *Numerical Solutions for the CAWAPI Configuration on Unstructured Grids at KTH/FOI – Part I*, Sweden, Chapter 10, RTO-TR-AVT-113 Final Report, 2009.

[37-10] Jirásek, A. and Rizzi, A.: *Numerical Solutions for the CAWAPI Configuration on Unstructured Grids at KTH/FOI – Part II*, Sweden, Chapter 11, RTO-TR-AVT-113 Final Report, 2009.

[37-11] Michal, T., Oser, M., Mani, M. and Roos, F: *Numerical Solutions for the CAWAPI Configuration on Unstructured Grids at Boeing-St. Louis, United States*, Chapter 12, RTO-TR-AVT-113 Final Report, 2009.

[37-12] Davis, M., Reed, C. and Yagle, P.: *Numerical Solutions for the CAWAPI Configuration on Unstructured Grids at Lockheed-Martin, United States*, Chapter 13, RTO-TR-AVT-113 Final Report, 2009.

[37-13] Karman, S., Mitchell, B., Sawyer, S. and Whitt, J.: *Numerical Solutions for the CAWAPI Configuration on Unstructured Grids at UT-Sim Center, United States*, Chapter 14, RTO-TR-AVT-113 Final Report, 2009.

[37-14] Lamar, J.E. and Abdol-Hamid, K.: *Numerical Solutions for the CAWAPI Configuration on Unstructured Grids at NASA Langley Res. Cntr., United States*, Chapter 15, RTO-TR-AVT-113 Final Report, 2009.

[37-15] Boelens, O.J., Spekreijse, S., Sytsma, H. and de Cock, K.: *Numerical Solutions for the CAWAPI Configuration on Structured Grids at NLR, The Netherlands*, Chapter 5, RTO-TR-AVT-113 Final Report, 2009.

[37-16] Badcock, K.J.: *Numerical Solutions for the CAWAPI Configuration on Structured Grids at University of Glasgow/Liverpool University, United Kingdom*, Chapter 6, RTO-TR-AVT-113 Final Report, 2009.

[37-17] Abdol-Hamid, K., Elmiligui, A. and Massey, S.: *Numerical Solutions for the CAWAPI Configuration on Structured Grids at NASA Langley Res. Cntr., United States*, Chapter 7, RTO-TR-AVT-113 Final Report, 2009.

Appendix 1 – LIST OF THE MEMBERS
OF THE TASK GROUP AVT-113

(Postal and email addresses while acting as Task Group member)

Name and Full Postal Address	Email Address	CAWAPI Facet Numer./Exper.	VFE-2 Facet Numer./Exper.
Lamar, Dr. John E. NASA Langley Research Center Mail Stop 499 Hampton, VA 23681-2199 USA	john.e.lamar@nasa.gov	Co-chairman CAWAPI	
		Numer./Exper.	
Hummel, Prof. Dr.-Ing. Dietrich Institut für Stroemungsmechanik TU Braunschweig Bienroder Weg 3 D-38106 Braunschweig Germany	d.hummel@tu-bs.de	Co-chairman VFE-2	
Hirsch, Prof. Charles VrijeUniversiteit Brussel Pleinlaan, 2 1050 Brussels Belgium	charles.hirsch@numeca.be	Panel Mentor	
◊Abdol-Hamid, Dr. Khaled S. NASA Langley Research Center Mail Stop 499 Hampton, VA 23681-2199 USA	khaled.s.abdol-hamid@nasa.gov	Numerical	
Arthur, Dr. Malcolm Terence Aerodynamics Integration Dept. QinetiQ, Cody, Ively Road Farnborough, Hampshire GU14 0LX United Kingdom	mtarthur@qinetiq.com		Numerical
Badcock, Prof. Dr. Ken J. Department of Engineering The University of Liverpool Brownlow Hill, Liverpool L69 3GH United Kingdom	k.j.badcock@liverpool.ac.uk	Numerical	Numerical

---

◊ Contributor/Co-author

Name and Full Postal Address	Email Address	CAWAPI Facet Numer./Exper.	VFE-2 Facet Numer./Exper.
Bin Mat, Mr. Shabudin The University of Glasgow Dept. of Aerospace Engineering Glasgow G12 8QQ United Kingdom	smat@eng.gla.ac.uk		Experimental
Boelens, Mr. Okko J. Aerospace Vehicles Division Dept. of Flight Physics and Loads National Aerosp. Laboratory NLR 2 Anthony Fokkerweg 1059 BM Amsterdam The Netherlands	boelens@nlr.nl	Numerical	Numerical
Breitsamter, Dr.-Ing. Christian Lehrstuhl für Aerodynamik TU München Boltzmannstr. 15 D-85748 Garching Germany	christian.breitsamter@ aer.mw.tum.de		Experimental
Coton, Prof. Frank N. The University of Glasgow Dept. of Aerospace Engineering Glasgow G12 8QQ United Kingdom	f.coton@aero.gla.ac.uk		Experimental
Crippa, Mr. Simone Royal Inst. of Technology (KTH) Aeron. and Vehicle Engineering Division of Aerodynamics Teknikringen 8 SE-10044 Stockholm Sweden	crippa@kth.se		Numerical
*Cronin, Catherine K. NASA Langley Research Center Mail Stop 125 Hampton, VA 23681-2199 USA	catherine.k.cronin@nasa.gov	Virtual Laboratory	Virtual Laboratory
Cummings, Prof. Russell M. US Air Force Academy Department of Aeronautics 2354 Fairchild Drive, Suite 6H27 Colorado Springs, CO 80840-6222 USA	russ.cummings@usafa.edu	Numerical	Numerical

* Guest Participant

Name and Full Postal Address	Email Address	CAWAPI Facet Numer./Exper.	VFE-2 Facet Numer./Exper.
Davis, Dr. M. Bruce Lockheed Martin Aeronautics P.O. Box 748, Mail Zone 9333 Ft. Worth, TX 76101 USA	myron.b.davis@lmco.com	Numerical	
◊de Cock, Mr. Koen M.J. Aerospace Vehicles Division Dept. of Flight Physics and Loads National Aerosp. Laboratory NLR 2 Anthony Fokkerweg 1059 BM Amsterdam The Netherlands	cock@nlr.nl	Numerical	
◊Elmiligui, Dr. Alaa A. Analytical Services & Materials, Inc. Hampton, VA 23666 USA	alaa.a.elmiligui@nasa.gov	Numerical	
Fritz, Mr. Willy Senior Development Engineer EADS – Military Air Systems Rechliner Straße D-85077 Manching Germany	willy.fritz@eads.com	Numerical	Numerical
*Furman, Andrej Lehrstuhl für Aerodynamik TU München Boltzmannstr. 15 D-85748 Garching Germany	andrej.furman@ aer.mw.tum.de		Experimental
Galbraith, Prof. Roderick The University of Glasgow Dept. of Aerospace Engineering Glasgow G12 8QQ United Kingdom	roddy@aero.gla.ac.uk		Experimental
*Görtz, Dr. Stefan Royal Inst. of Technology (KTH) Aeron. and Vehicle Engineering Division of Aerodynamics Teknikringen 8 SE-10044 Stockholm Sweden	goertz@kth.se	Numerical	

◊ Contributor/Co-author

* Guest Participant

Name and Full Postal Address	Email Address	CAWAPI Facet Numer./Exper.	VFE-2 Facet Numer./Exper.
Groot, Dr. Klaus de Institut für Aerodynamik und Strömungstechnik DLR Braunschweig Lilienthalplatz 7 D-38108 Braunschweig Germany	klaus.degroot@dlr.de		Experimental
*Gürdamar, Emre Turkish Aircraft Industries TUSAS Ziyabey Cad.3 sok.No:16 06520 Balgat, Ankara Turkey	egurdamar@tai.com.tr		Numerical
Jirásek, Dr. Adam FOI Gullfossgatan 6 SE-164 90 Stockholm Sweden	adam.jirasek@foi.se	Numerical	
Karman, Dr. Steve L., Jr. Research Professor UT SimCenter at Chattanooga 701 East M.L. King Blvd Chattanooga, TN 37403 USA	steve-karman@utc.edu	Numerical	
*Kaya, Serpil Turkish Aircraft Industries TUSAS Ziyabey Cad.3 sok.No:16 06520 Balgat, Ankara Turkey	serkaya@tai.com.tr		Numerical
Klein, Dr. Christian Institut für Aerodynamik und Strömungstechnik DLR Göttingen Bunsenstr. 10 D-37073 Göttingen Germany	christian.klein@dlr.de		Experimental
Konrath, Dr. Robert Institut für Aerodynamik und Strömungstechnik DLR Goettingen Bunsenstr. 10 D-37073 Göttingen Germany	robert.konrath@dlr.de		Experimental

---

* Guest Participant

Name and Full Postal Address	Email Address	CAWAPI Facet Numer./Exper.	VFE-2 Facet Numer./Exper.
Korkem, Mr. Bulent Turkish Aircraft Industries TUSAS Ziyabey Cad.3 sok.No:16 06520 Balgat, Ankara Turkey	bkorkem@tai.com.tr		Numerical
Kurun, Mr. Suleyman Aerodynamic Division TUBITAK-SAGE, P.K. 16 06261 Mamak, Ankara Turkey	skurun@sage.tubitak.gov.tr		Experimental
Le Roy, Dr. Jean-François ONERA – Centre de Lille 5, Boulevard Painleve F-59045 Lille France	jean-francois.le_roy@onera.fr		Numerical
◊Luckring, Dr. James M. NASA Langley Research Center Mail Stop 499 Hampton, VA 23681-2199 USA	james.m.luckring@nasa.gov		Experimental
*Lüdeke, Dr. Heinrich DLR Braunschweig Lilienthalplatz 7 D-38108 Braunschweig Germany	heinrich.luedeke@dlr.de		Numerical
◊Mani, Dr. Mortaza Boeing Phantom Works P.O. Box 516 MC-S306-4030 St. Louis, MO 63166 USA	mori.mani@boeing.com	Numerical	
◊Massey, Dr. Steven J. NASA Langley Research Center Mail Stop 340 Hampton, VA 23681-2199 USA	steven.j.massey@nasa.gov	Numerical	

◊ Contributor/Co-author

* Guest Participant

Name and Full Postal Address	Email Address	CAWAPI Facet Numer./Exper.	VFE-2 Facet Numer./Exper.
◊McDaniels, Mr. David R. US Air Force Academy Department of Aeronautics 2354 Fairchild Drive, Suite 6H27 Colorado Springs, CO 80840-6222 USA	david.mcdaniels@usafa.edu	Numerical	
Michal, Dr. Todd R. Boeing Phantom Works P.O. Box 516 MC-S306-4030 St. Louis, MO 63166 USA	todd.r.michal@boeing.com	Numerical	
◊Mitchell, Mr. Brent UT SimCenter at Chattanooga 701 East M.L. King Blvd Chattanooga, TN 37403 USA	brent-mitchell@utc.edu	Numerical	
Morton, Prof. Dr. Scott HQ USAFA/DFAN 2354 Fairchild Drive, Suite 6H27 Colorado Springs, CO 80840-6222 USA	scott.morton@usafa.af.mil	Numerical	
‡Nangia, Dr. Raj K. Nangia Aero Associates Maggs House, 78 Queen's Road Clifton, Bristol BS8 1QX United Kingdom	nangia@blueyonder.co.uk		Invited Consultant
◊Obara, Mr. Clifford J. NASA Langley Research Center Mail Stop 237 Hampton, VA 23681-2199 USA	clifford.j.obara@nasa.gov	Experimental	
*Ortakaya, Yüksel Turkish Aircraft Industries TUSAS Ziyabey Cad.3 sok.No:16 06520 Balgat, Ankara Turkey	yortakaya@tai.com.tr		Numerical

◊ Contributor/Co-author

‡ Invited Consultant

* Guest Participant

Name and Full Postal Address	Email Address	CAWAPI Facet Numer./Exper.	VFE-2 Facet Numer./Exper.
◊Oser, Mr. Matt P.O. Box 516 MC-S064-2920 The Boeing Company St. Louis, MO 63166 USA	matt.oser@boeing.com	Numerical	
◊Reed, Mr. Christopher L. Lockheed Martin Aeronautics P.O. Box 748, Mail Zone 9333 Ft. Worth, TX 76101 USA	christopher.l.reed@lmco.com	Numerical	
◊Riou, Jacques ONERA/DAAP/MHL 8, Rue des Vertugadins F-92190 Meudon France	jacques.riou@onera.fr		Numerical
Rizzi, Prof. Dr. Arthur Royal Inst. of Technology (KTH) Aeron. and Vehicle Engineering Division of Aerodynamics Teknikringen 8 SE-10044 Stockholm Sweden	rizzi@kth.se	Numerical	Numerical
Rodriguez, Dr. Ovide ONERA – Centre de Lille 5, Boulevard Painleve F-59045 Lille France	ovide.rodriguez@onera.fr		Experimental
◊Roos, Mr. Frederick W. Boeing Phantom Works P.O. Box 516 MC-S306-4030 St. Louis, MO 63166 USA	frederick.w.roos@boeing.com	Numerical	
◊Sawyer, Mr. Shane UT SimCenter at Chattanooga 701 East M.L. King Blvd Chattanooga, TN 37403 USA	shane-sawyer@utc.edu	Numerical	

◊ Contributor/Co-author

Name and Full Postal Address	Email Address	CAWAPI Facet Numer./Exper.	VFE-2 Facet Numer./Exper.
Schiavetta, Ms. Lucy A. The University of Glasgow Dept. of Aerospace Engineering Glasgow G12 8QQ United Kingdom	lschiave@aero.gla.ac.uk		Numerical
Schröder, Dr. Andreas Institut für Aerodynamik und Strömungstechnik DLR Göttingen Bunsenstr. 10 D-37073 Göttingen Germany	andreas.schroeder@dlr.de		Experimental
Schütte, Dipl.-Ing. Andreas DLR Braunschweig Lilienthalplatz 7 D-38108 Braunschweig Germany	andreas.schuette@dlr.de		Numerical
◊Spekreijse, Mr. Stephanus P. Aerospace Vehicles Division Dept. of Flight Physics and Loads National Aerosp. Laboratory NLR 2 Anthony Fokkerweg 1059 BM Amsterdam The Netherlands	spekreijse@nlr.nl	Numerical	
◊Sytsma, Mr. Harmen A. Aerospace Vehicles Division Dept. of Flight Physics and Loads National Aerosp. Laboratory NLR 2 Anthony Fokkerweg 1059 BM Amsterdam The Netherlands	sytsma@nlr.nl	Numerical	
◊Whitt, Mr. Justin UT SimCenter at Chattanooga 701 East M.L. King Blvd Chattanooga, TN 37403 USA	justin-whitt@utc.edu	Numerical	
◊Yagle, Mr. Patrick J. Lockheed Martin Aeronautics P.O. Box 748, Mail Zone 9333 Ft. Worth, TX 76101 USA	patrick.j.yagle@lmco.com	Numerical	

◊ Contributor/Co-author

Appendix 2 – CAWAP EXPERIMENTAL DATA – NASA/TP-2001-210629/SUPPLEMENT

by

John E. Lamar (*Retired*)

A2.1 SUMMARY

Flight surface flow data of various types for the F-16XL-1 aircraft, employed in the Cranked Arrow Wing Aerodynamics Project (CAWAP), are available.

A2.2 INTRODUCTION

The CAWAP flight data are unclassified and unrestricted and also available for purchase. This is unusual for such a modern fighter but was accomplished because the aircraft was on loan to NASA from the US Air Force. Moreover, all the research flights were conducted with the intent that the flight flow physics data be unrestricted, even available over the web with a customized search engine.

The data are published on a separate CD cited as [3-7] in Chapter 3 and which is a supplement to [3-2] of that chapter. The supplement provides:

1) Tabular data of the Flight Conditions from Table 5;

2) Boundary layer data from Table 12 for three flights in multiple formats;

3) Skin-friction data – *xmgr* format – used to generate Figure 26;

4) Surface pressure data with a listing of the parameters; and

5) Tuft-images from three cameras in two formats.

This CD may be purchased from:

NASA STI Help Desk
NASA Center for AeroSpace Information
7115 Standard Drive
Hanover, MD 21076-1320
USA

A2.3 CONCLUSIONS

The flight data of surface pressures and flow-fields patterns, along with available boundary-layer profiles and skin friction data, may be obtained on a CD.

Appendix 3.1 – EXPERIMENTAL RESULTS FROM NASA LANGLEY

by

James M. Luckring[1]

A3.1.1   SUMMARY

In this Appendix, sample data are provided in support of Chapter 18. Links and references are also provided.

A3.1.2   PRESSURE MEASUREMENTS

Data from the National Transonic Facility (NTF) have been published in references 1 to 4. These reports include both summary plots and data tabulations and can be accessed through the NASA report server link http://ntrs.nasa.gov/search.jsp, for example, by searching with the report number NASA TM-4645.

For AVT-113, considerable attention was placed upon a condition exhibiting part-span leading-edge vortex separation that included dual co-rotating vortices. These results corresponded to $M = 0.4$, $R_{mac} = 6 \times 10^6$, $\alpha = 13.3°$ for the medium bluntness leading edge, and are presented in Figure 18-8 of Chapter 18. These pressure data can be found in Reference 3 and are also presented in Table A3.1-1.

---

[1] Senior Research Engineer, NASA Langley Research Center, Hampton VA, USA.

Table A3.1-1: NTF Delta Wing Surface Pressure Coefficients.
Medium leading-edge bluntness, M = 0.4, R_{mac} = 6 x 10^6, α = 13.3°

2y/b \ x/c$_R$	0.1	0.2	0.3	0.4	0.5	0.6	0.7	0.8	0.9	0.95
0.050		-0.2285		-0.1942		-0.0349				
0.100		-0.2299		-0.1875		-0.0578				
0.150		-0.2636		-0.1928		-0.0763				
0.200		-0.2757		-0.1912		-0.0964				-0.2711
0.250				-0.2048		-0.1103		-0.1780		-0.2519
0.300		-0.3175		-0.2029		-0.1363		-0.1670		-0.2549
0.350				-0.2072		-0.1476		-0.1632		-0.2686
0.400		-0.3591		-0.2209		-0.1572		-0.1578		-0.2822
0.450		-0.3812		-0.2481		-0.1721		-0.1783		-0.2818
0.500		-0.4055		-0.2753		-0.1935		-0.2143		-0.2484
0.525				-0.3141		-0.2240		-0.1987		-0.2540
0.550		-0.4308		-0.3674		-0.2845		-0.1860		-0.2670
0.575				-0.4144		-0.3428		-0.1728		-0.2926
0.600		-0.4829		-0.4734		-0.3756		-0.1730		-0.3111
0.625						-0.3373		-0.1711		-0.3352
0.650		-0.5266		-0.6529		-0.3226		-0.1681		-0.3605
0.675				-0.7393		-0.3028		-0.1820		-0.3989
0.700		-0.5741		-0.7711		-0.3081		-0.2190		-0.4983
0.725				-0.7516				-0.3345		-0.6339
0.750		-0.6343		-0.7479				-0.5914		-0.7634
0.775				-0.7398		-0.4496		-0.9427		-0.8086
0.800		-0.7103		-0.7612		-0.7490		-1.2245		
0.825				-0.7389		-1.1767		-1.3358		-0.6424
0.850		-0.8101		-0.7145		-1.4874		-1.1747		-0.5218
0.875				-0.7153		-1.5737		-0.9304		-0.4876
0.900		-0.9404		-0.7552		-1.5235		-0.8751		-0.4869
0.925				-1.1008		-1.4016		-0.8423		-0.4780
0.950		-1.1972		-2.1184		-1.3167		-0.8030		-0.3879
0.975				-2.1575		-1.2297		-0.7806		-0.3375
1.000	-1.4583	-2.6237	-3.5857	-2.2709	-1.5979	-1.1227	-0.9577	-0.7932		-0.4124

(a) Upper Surface

2y/b \ x/c$_R$	0.1	0.2	0.3	0.4	0.5	0.6	0.7	0.8	0.9	0.95
0.200		0.2609		0.2355		0.2368				-0.2897
0.400		0.2613		0.2503		0.2118		0.0642		-0.3359
0.600		0.2753		0.2530		0.2196		0.0942		-0.3318
0.700		0.2925		0.2642		0.2232		0.1058		-0.3628
0.800		0.2925		0.2773		0.2399		0.1335		-0.3925
0.850		0.2687		0.2841		0.2531		0.1539		-0.4007
0.900				0.2620		0.2508		0.1798		-0.3976
0.950		0.0777		0.1640		0.2085		0.1882		-0.1463
0.975				-0.0375		0.0818		0.1416		0.0097
1.000		-2.5640		-1.5652		-1.0384		-0.7393		-0.3794

(b) Lower Surface

A3.1.3 FORCE MEASUREMENTS

Limited data from the Low Turbulence Pressure Tunnel (LTPT) have been published in reference 5. Further links to these data are unavailable at time of this publication.

An analysis of compressibility effects on normal force coefficient for the medium bluntness leading edge with data from both LTPT and NTF was presented in reference 5 and can be found in Figure 18-14 of Chapter 18. A tabulation of these normal force coefficients is presented in Table A3.1-2.

Table A3.1-2: Normal Force Measurements from LTPT and NTF Experiments. Medium bluntness leading edge.

LTPT $M = 0.2$, $R_{mac} = 8 \times 10^6$		NTF $M = 0.4$, $R_{mac} = 6 \times 10^6$		NTF $M = 0.6$, $R_{mac} = 6 \times 10^6$	
α	C_N	α	C_N	α	C_N
-2.2	-0.078	-0.4	-0.023	-0.4	-0.033
-1.0	-0.042	0.1	-0.008	0	-0.017
0.0	0.000	1.1	0.028	1.1	0.029
1.0	0.021	2.2	0.065	2.1	0.061
2.1	0.063	3.2	0.092	3.2	0.100
3.2	0.089	4.2	0.132	4.2	0.138
4.2	0.115	5.2	0.160	5.2	0.170
5.4	0.147	6.2	0.199	6.3	0.206
6.4	0.180	7.3	0.234	7.3	0.244
7.5	0.208	8.3	0.268	8.3	0.287
8.5	0.251	9.3	0.318	9.3	0.344
9.7	0.289	10.3	0.368	10.3	0.395
10.6	0.343	11.3	0.409	11.3	0.453
11.8	0.394	12.3	0.466	12.4	0.511
12.8	0.441	13.3	0.517	13.4	0.568
14.0	0.501	14.3	0.563	14.4	0.616
15.0	0.542	16.4	0.649	16.5	0.721
16.1	0.578	18.4	0.793	18.5	0.830
17.3	0.632	20.4	0.911	20.5	0.937
18.3	0.681	22.4	1.013	22.5	1.042
19.5	0.736	24.5	1.102	24.6	1.146
20.6	0.798	26.5	1.217	26.6	1.263
21.7	0.856				

A3.1.4 REFERENCES

[A3.1-1] Chu, J. and Luckring, J.M.: *Experimental Surface Pressure Data Obtained on 65° Delta Wing Across Reynolds Number and Mach Number Ranges, Volume 1 – Sharp Leading Edge*, NASA TM-4645, February 1996.

[A3.1-2] Chu, J. and Luckring, J.M.: *Experimental Surface Pressure Data Obtained on 65° Delta Wing Across Reynolds Number and Mach Number Ranges, Volume 2 – Small Leading Edge*, NASA TM-4645, February 1996.

[A3.1-3] Chu, J. and Luckring, J.M.: *Experimental Surface Pressure Data Obtained on 65° Delta Wing Across Reynolds Number and Mach Number Ranges, Volume 3 – Medium Leading Edge*, NASA TM-4645, February 1996.

[A3.1-4] Chu, J. and Luckring, J.M.: *Experimental Surface Pressure Data Obtained on 65° Delta Wing Across Reynolds Number and Mach Number Ranges, Volume 4 – Large Leading Edge*, NASA TM-4645, February 1996.

[A3.1-5] Luckring, J.M.: *Initial Experiments and Analysis of Vortex Flow on Blunt Edged Delta Wings*, AIAA Paper 2008-0378, 2008.

Appendix 3.2 – EXPERIMENTAL RESULTS FROM DLR GÖTTINGEN

by

Robert Konrath

This Appendix is related to Chapter 19 and contains a description of the electronically available data set (test case 4.5) which was obtained on NASA's ¾ scale 65° delta wing model (VFE-2 model No. 1) with medium radius leading edges in the transonic wind tunnel in Göttingen (DNW-TWG) at a Mach number of M = 0.4, a mean aerodynamic chord based Reynolds number of R_{mac} = 3 million and an angle of attack of α = 13.3°. The data is written in an ASCII format using a TecPlot® readable header. Not available data points are marked in the files with 999.999.

A3.2.1 SURFACE PRESSURE DISTRIBUTIONS

Measured with Pressure Sensitive Paint

C_p distributions on the pressure and suction side

File: Tecplot 360 Layout psp.lay (Original data set see psp_rleM04R3A13.plt)

Obtained by PSI Modules

C_p distributions at the chord stations x/c_r = 0.2, 0.4, 0.6, 0.8 and 0.95

File: Tecplot 360 Layout psi.lay (Original data set see psi_rleM04R3A13.plt)

A3.2.2 FLOW VELOCITY VECTOR FIELDS

Measured with Particle Image Velocimetry (Stereo-PIV)

3d velocity vectors in planes perpendicular to the model axis at the chord stations x/c_r = 0.35, 0.4, 0.5, 0.6, 0.7, 0.8 and 0.9.

Files: Tecplot 360 Layout piv.lay

(Original data set see: piv35_rleM04R3A13.plt

piv40_rleM04R3A13.plt

piv50_rleM04R3A13.plt

piv60_rleM04R3A13.plt

piv70_rleM04R3A13.plt

piv80_rleM04R3A13.plt

piv90_rleM04R3A13.plt

The exact values of the Mach and Reynolds number are given in the header of the file psi_rleM04R3A13.plt.

Appendix 3.3 – EXPERIMENTAL RESULTS FROM TU MUNICH

by

Andrej Furman[1] and Christian Breitsamter[2]

In this chapter further results are added for angles of attack which are not discussed in detail in this report but were tested within the TU Munich investigations for the Vortex Flow Experiment 2 (VFE-2) project. These results include:

- Oil flow visualisation using black pigment at $\alpha = 13°$, $18°$ and $23°$ for $R_{mac} = 1 \times 10^6$, $M = 0.07$ are shown in Figure A3.3-1 and at $\alpha = 10°$, $12°$, $13°$, $14°$, $16°$, $18°$, $20°$, $21°$, $22°$, $23°$, $24°$, $25°$, $26°$, $27°$, $28°$, $29°$ and $30°$ for $R_{mac} = 2 \times 10^6$, $M = 0.14$ in Figure A3.3-2 to Figure A3.3-7.

- Steady pressure distributions are presented at $\alpha = 0°$, $5°$, $10°$, $12°$, $13°$, $14°$, $16°$, $18°$, $20°$, $21°$, $22°$, $23°$, $24°$, $25°$, $26°$, $27°$, $28°$, $29°$ and $30°$ for $R_{mac} = 1 \times 10^6$, $M = 0.07$ in Figure A3.3-8 to Figure A3.3-13 and for $R_{mac} = 2 \times 10^6$, $M = 0.14$ in Figure A3.3-14 to Figure A3.3-19.

- Pressure fluctuation intensities are shown at $\alpha = 0°$, $5°$, $10°$, $12°$, $13°$, $14°$, $16°$, $18°$, $20°$, $21°$, $22°$, $23°$, $24°$, $25°$, $26°$, $27°$, $28°$, $29°$ and $30°$ for $R_{mac} = 1 \times 10^6$, $M = 0.07$ in Figure A3.3-20 to Figure A3.3-25 and for $R_{mac} = 2 \times 10^6$, $M = 0.14$ Figure A3.3-26 to Figure A3.3-31, see Chapter 21.

---

[1] Dipl.-Ing.

[2] PD Dr.-Ing. habil.

a) α = 13°

b) α = 18°

c) α = 23°

Figure A3.3-1: Surface Oil Flow Visualisation at $R_{mac} = 1 \times 10^6$ and M = 0.07 for Sharp (left) and Rounded (right) Leading Edges – α = 13°, α = 18°, α = 23°.

a) α = 13°

b) α = 18°

c) α = 23°
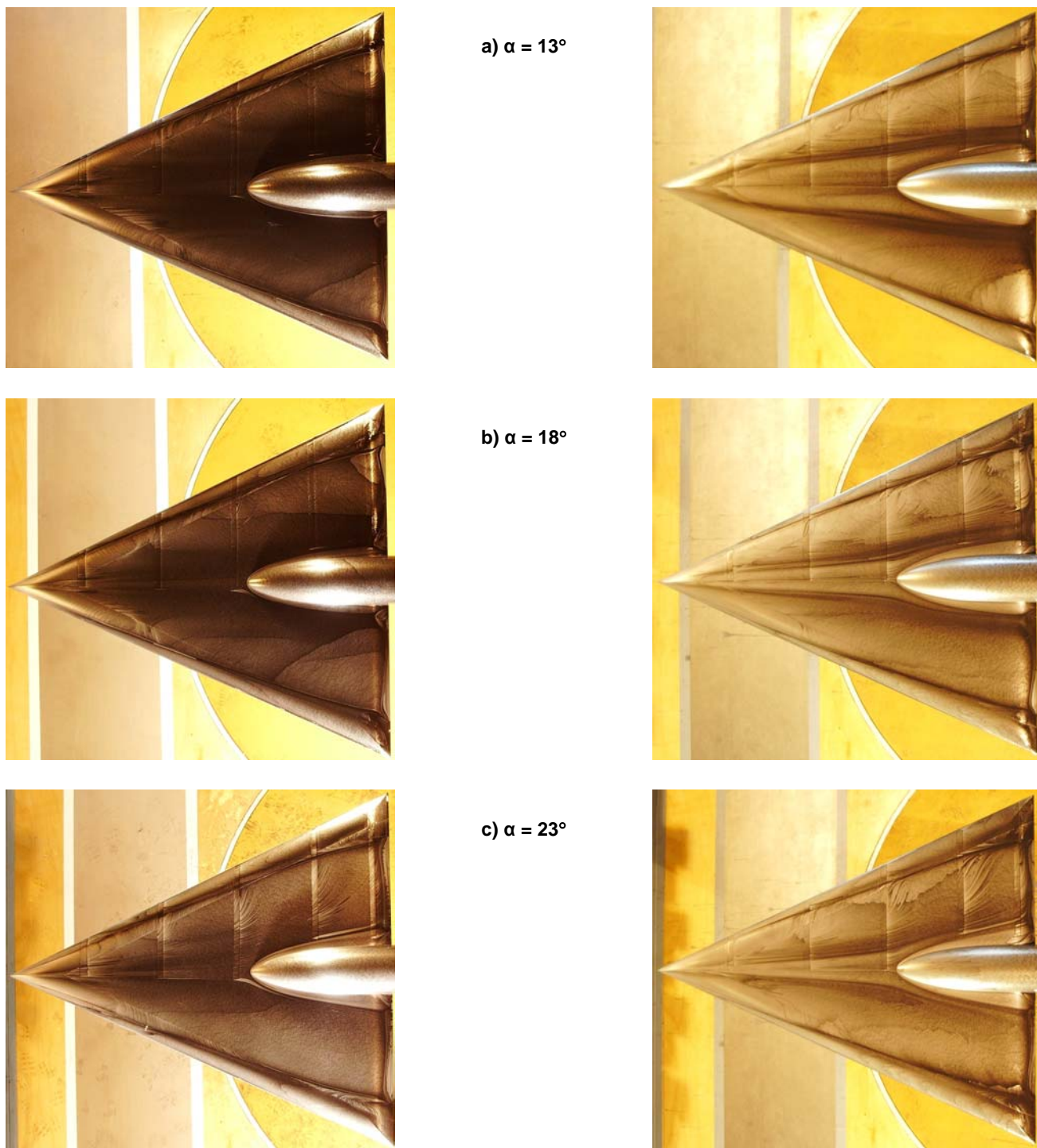
Figure A3.3-2: Surface Oil Flow Visualisation at $R_{mac} = 2 \times 10^6$ and M = 0.14 for Sharp (left) and Rounded (right) Leading Edges – α = 13°, α = 18°, α = 23°.

a) α = 10°

b) α = 12°

c) α = 20°

Figure A3.3-3: Surface Oil Flow Visualisation at R$_{mac}$ = 2 x 10^6 and M = 0.14 for Sharp (left) and Rounded (right) Leading Edges – α = 10°, α = 12°, α = 20°.

a) α = 16°

b) α = 20°

c) α = 21°
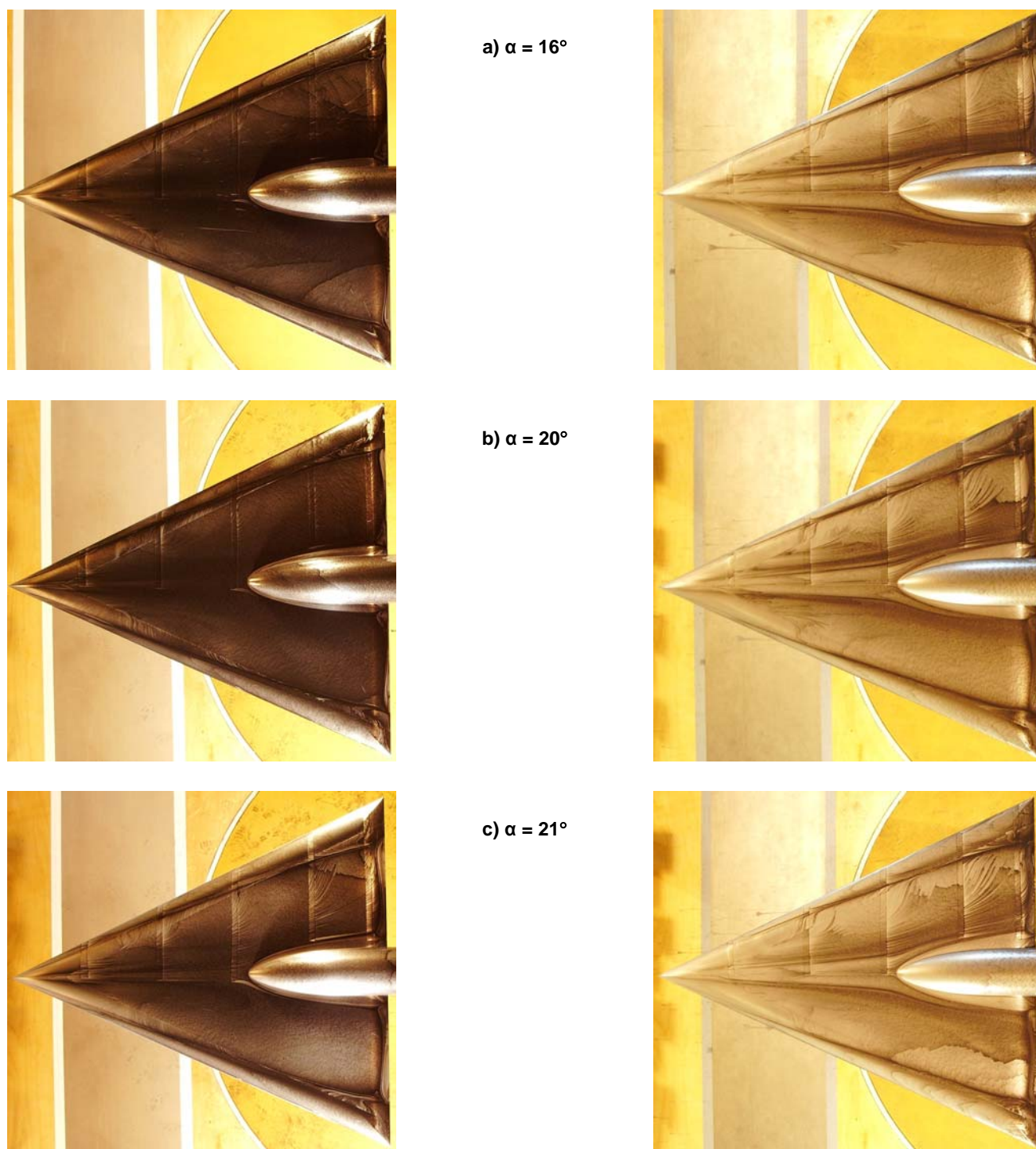
Figure A3.3-4: Surface Oil Flow Visualisation at $R_{mac} = 2 \times 10^6$ and M = 0.14 for Sharp (left) and Rounded (right) Leading Edges – α = 16°, α = 20°, α = 21°.

a) α = 22°

b) α = 24°

c) α = 25°

Figure A3.3-5: Surface Oil Flow Visualisation at R_{mac} = 2 x 10^6 and M = 0.14 for Sharp (left) and Rounded (right) Leading Edges – α = 22°, α = 24°, α = 25°.

a) α = 26°

b) α = 27°

c) α = 28°
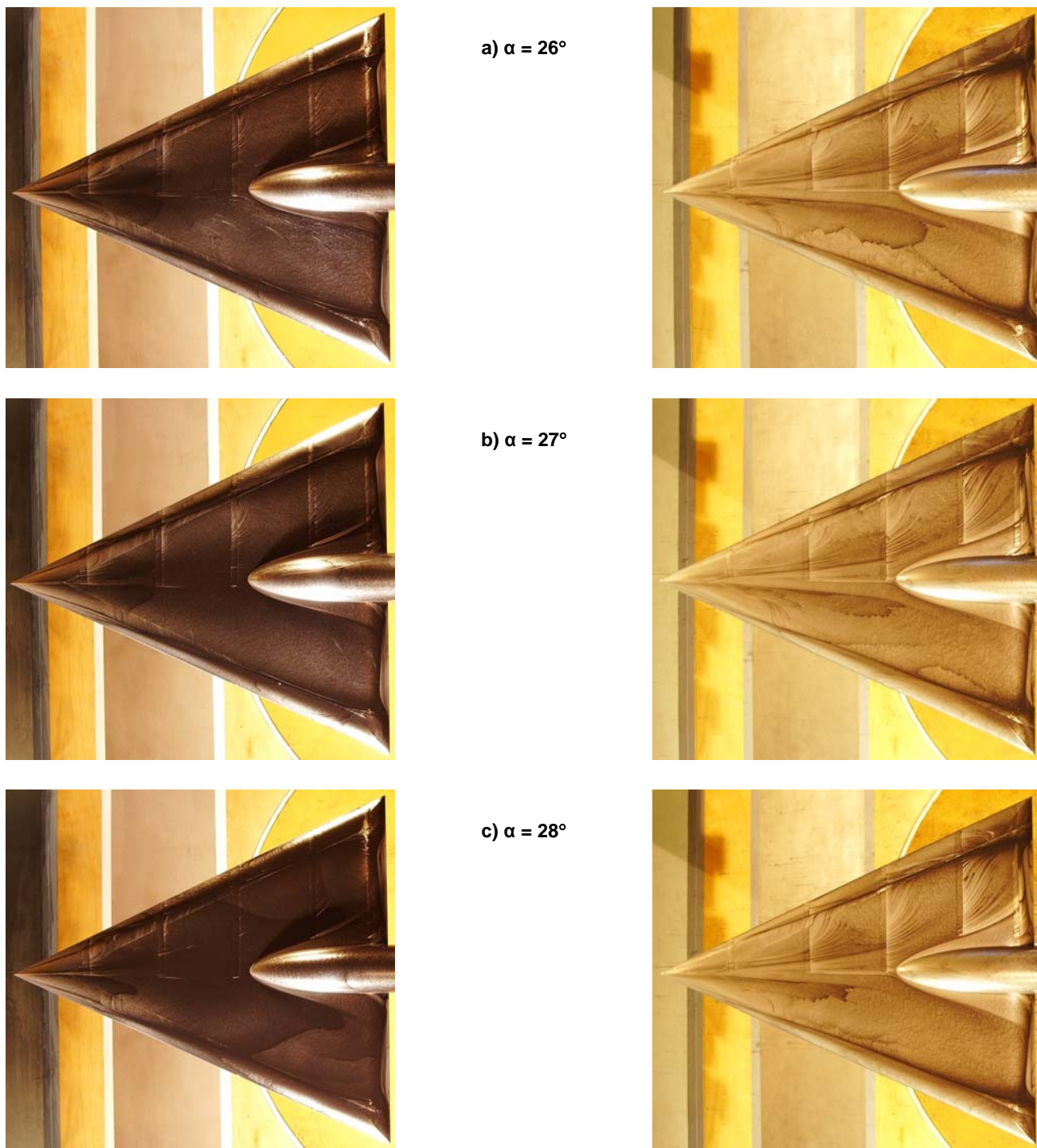
Figure A3.3-6: Surface Oil Flow Visualisation at R_{mac} = 2 x 10^6 and M = 0.14 for Sharp (left) and Rounded (right) Leading Edges – α = 26°, α = 27°, α = 28°.

a) α = 29°

b) α = 30°

Figure A3.3-7: Surface Oil Flow Visualisation at $R_{mac} = 2 \times 10^6$ and M = 0.14 for Sharp (left) and Rounded (right) Leading Edges – α = 29°, α = 30°.
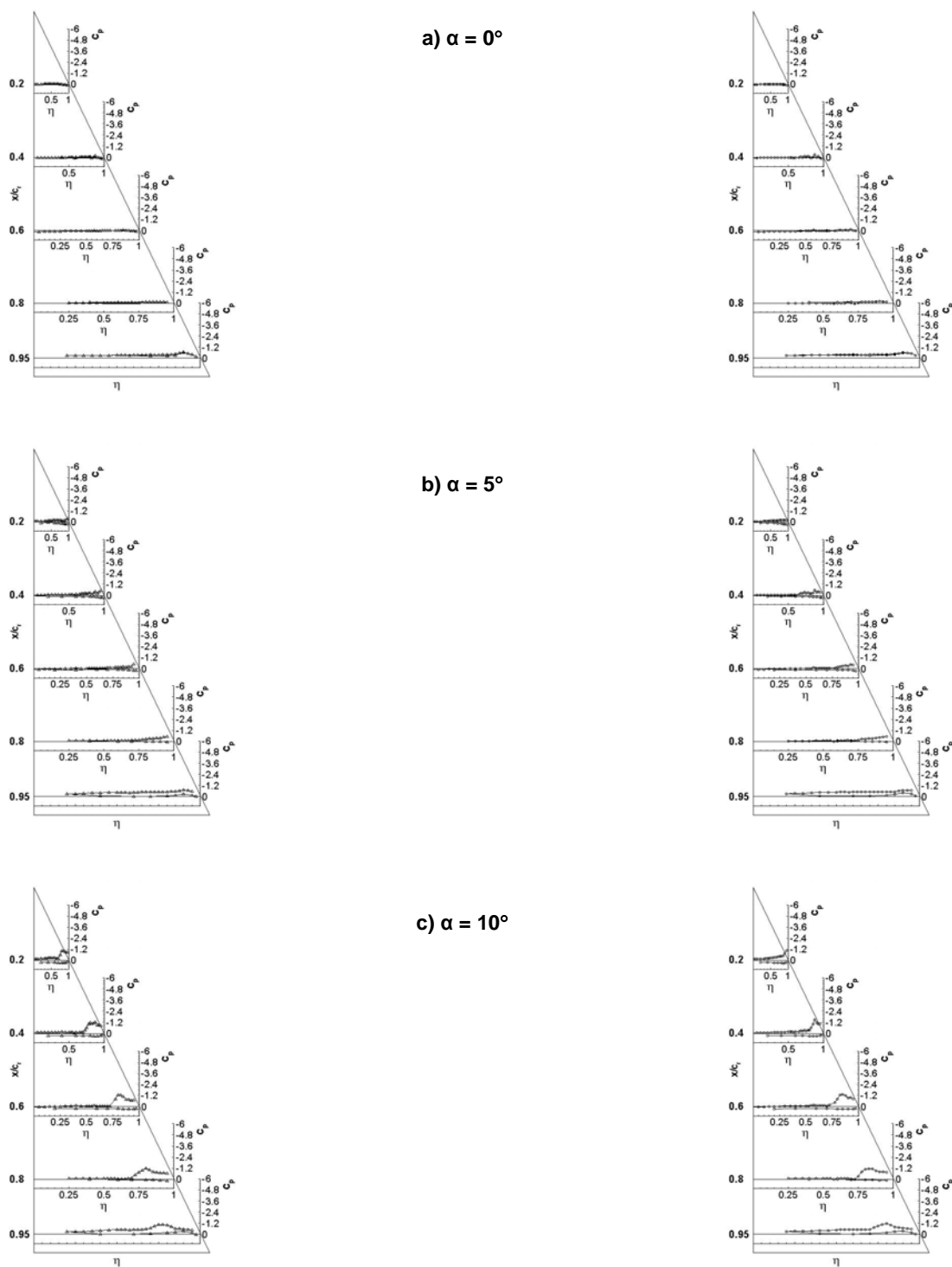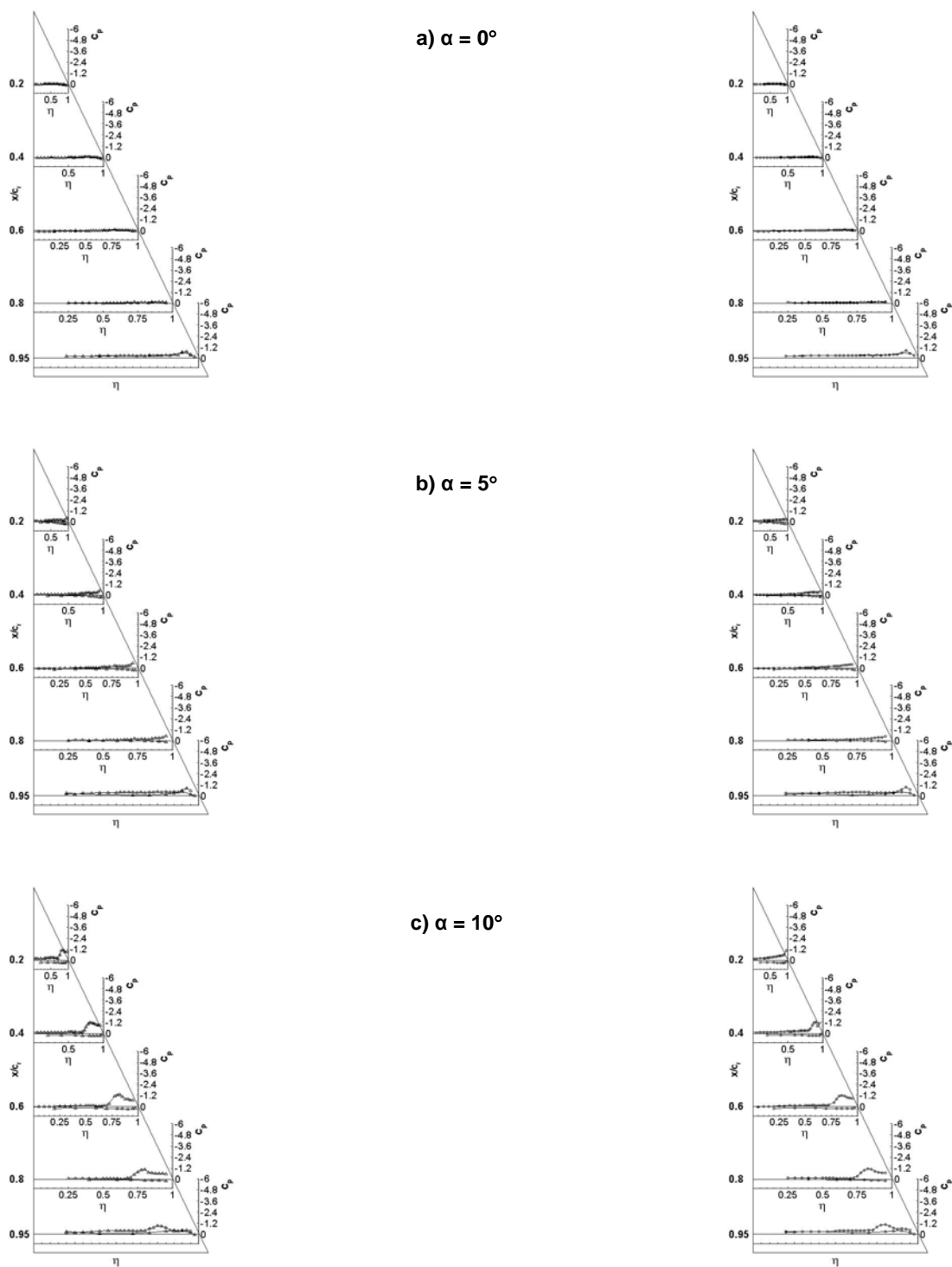
Figure A3.3-8: Steady Pressure Distribution at $R_{mac} = 1 \times 10^6$ and M = 0.07 for Sharp (left) and Rounded (right) Leading Edges – $\alpha = 0°$, $\alpha = 5°$, $\alpha = 10°$.

a) α = 12°

b) α = 14°

c) α = 16°
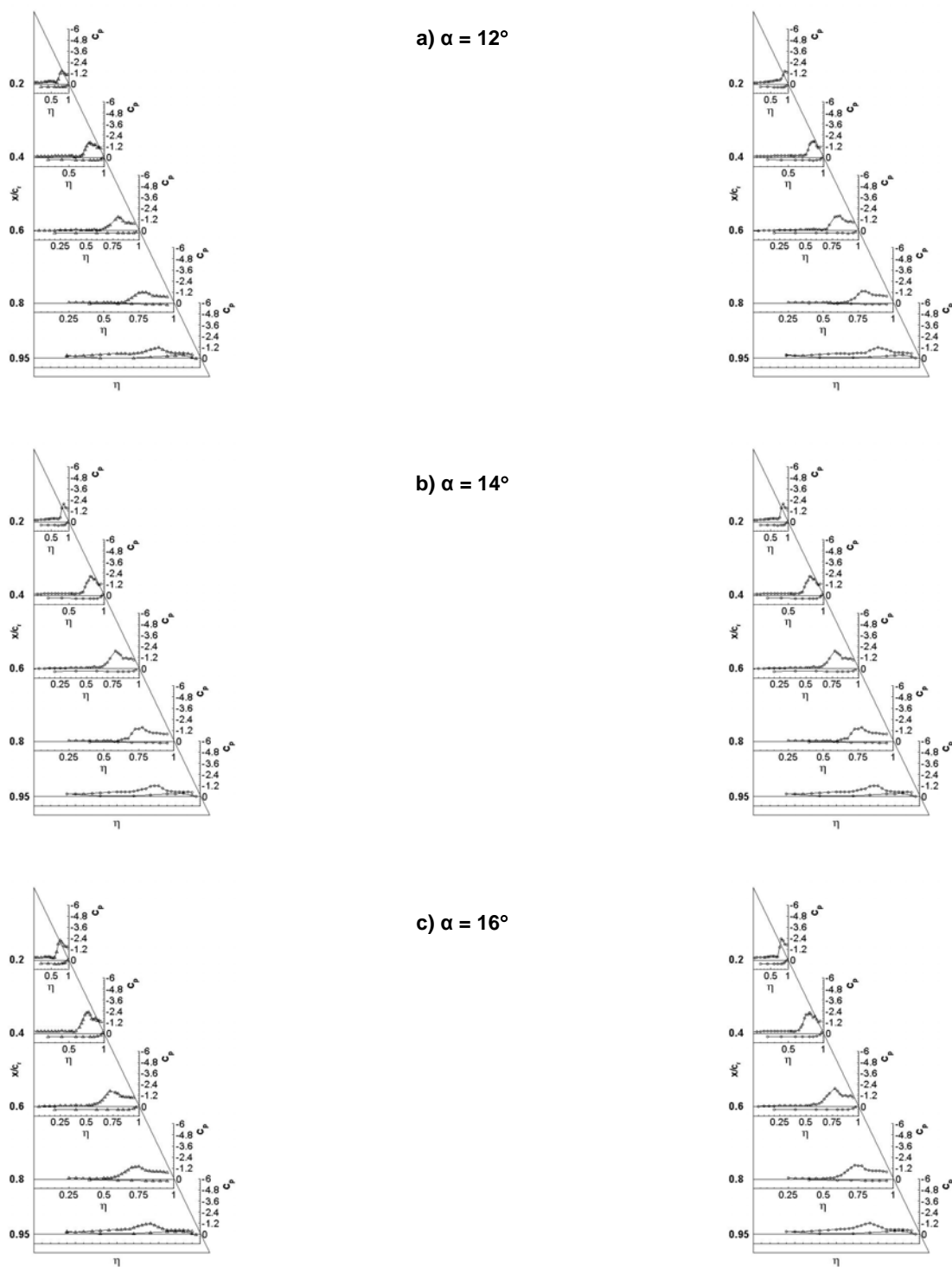
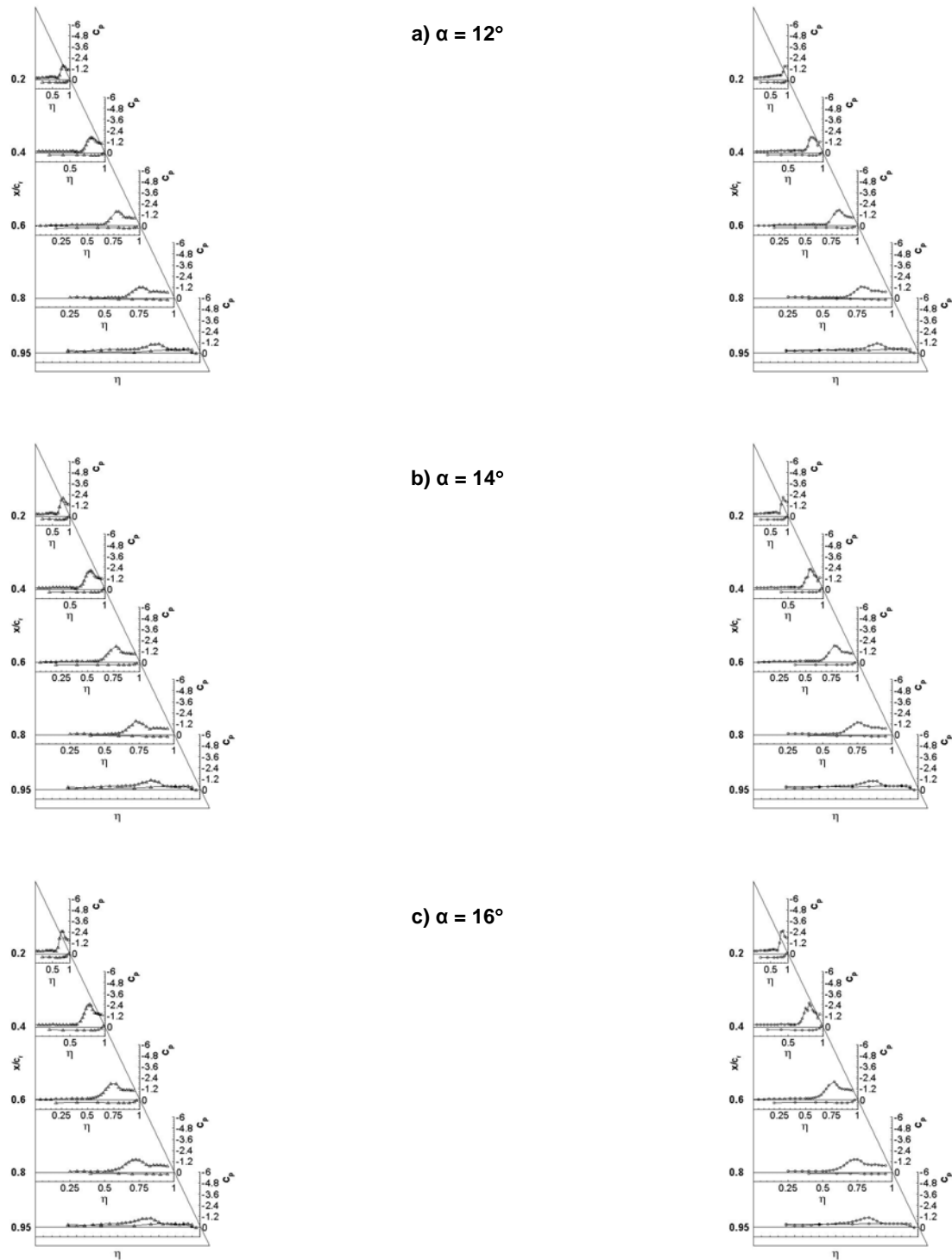**Figure A3.3-9: Steady Pressure Distribution at R_{mac} = 1 x 10^6 and M = 0.07 for Sharp (left) and Rounded (right) Leading Edges – α = 12°, α = 14°, α = 16°.**
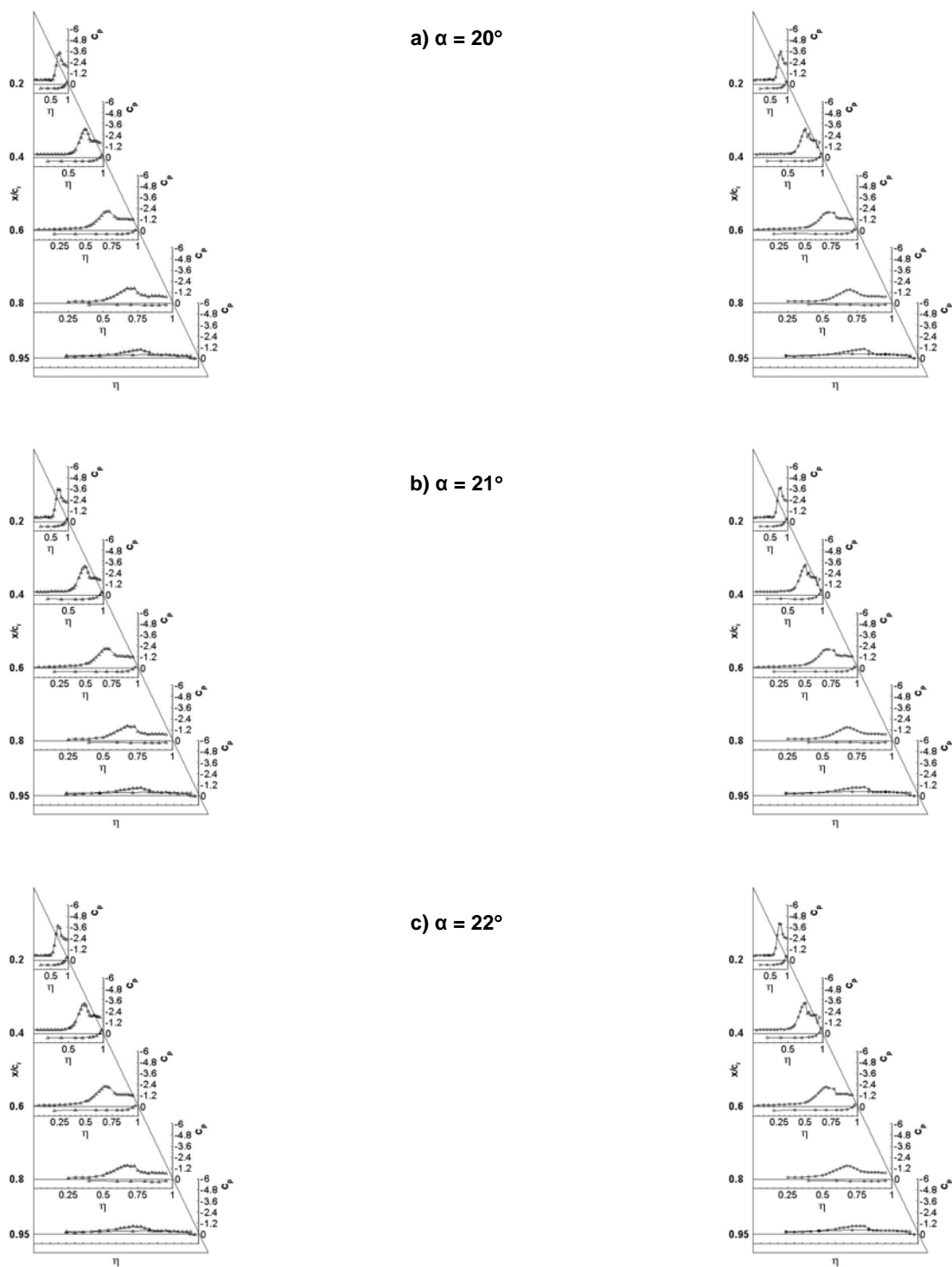
a) α = 20°

b) α = 21°

c) α = 22°
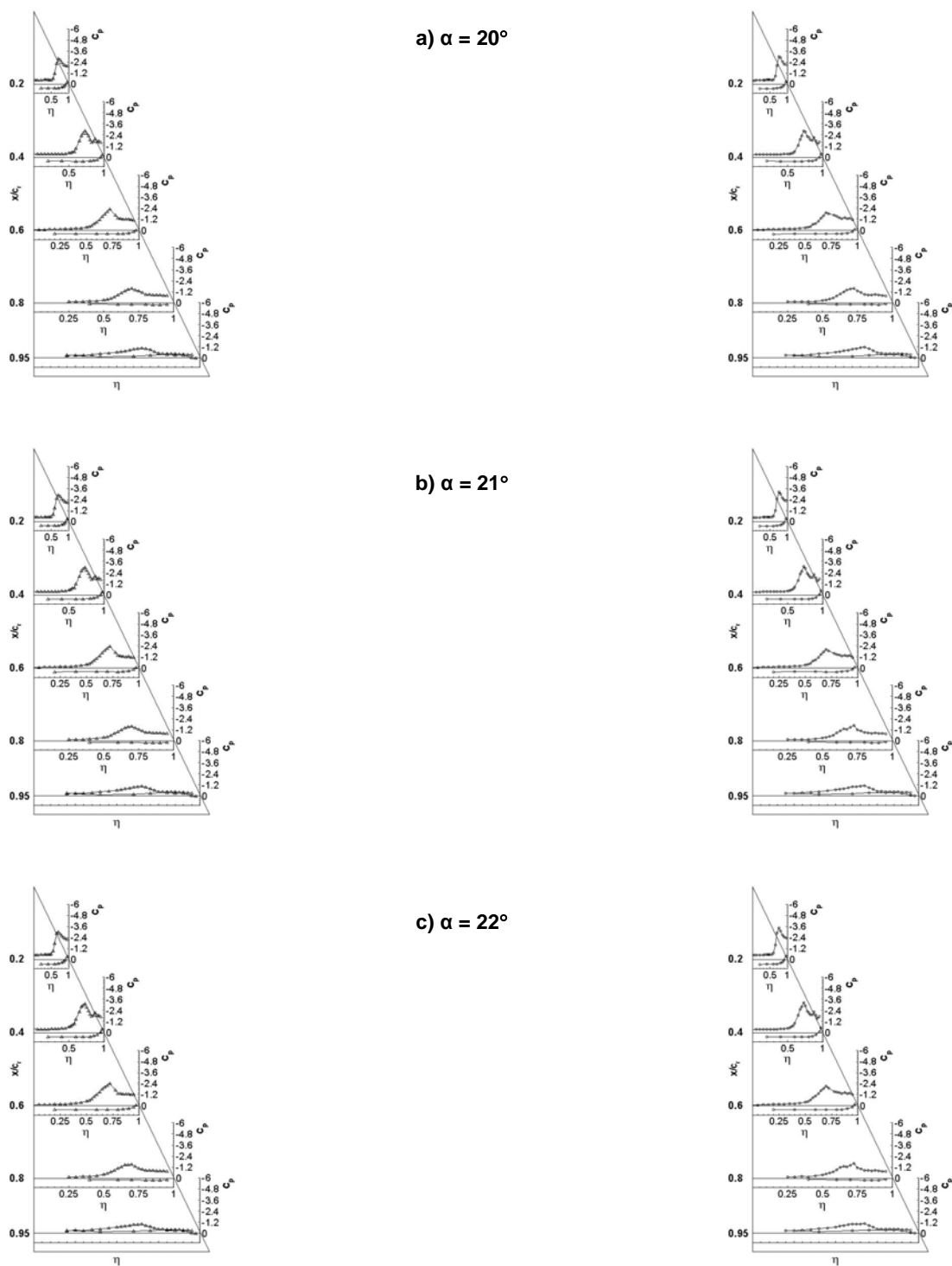
Figure A3.3-10: Steady Pressure Distribution at R_{mac} = 1 x 10^6 and M = 0.07 for
Sharp (left) and Rounded (right) Leading Edges – α = 20°, α = 21°, α = 22°.

a) α = 24°

b) α = 25°
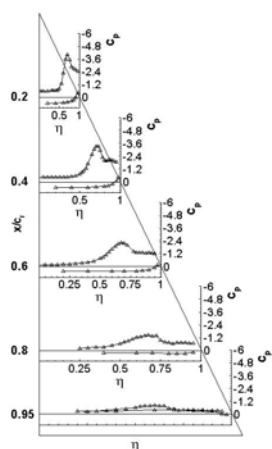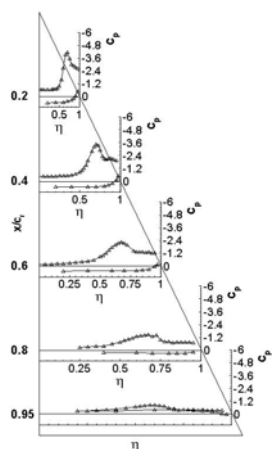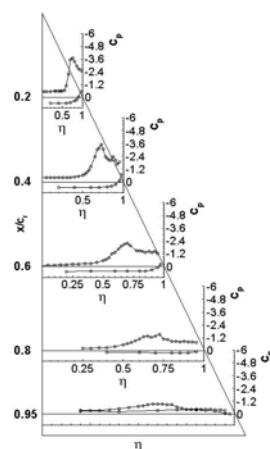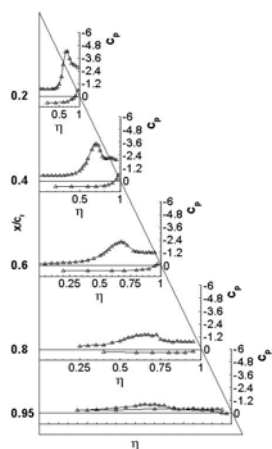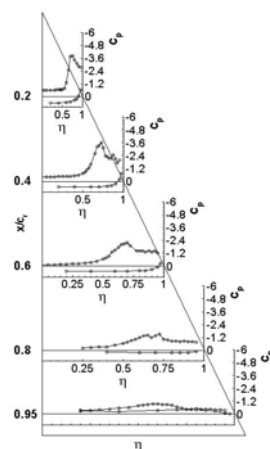
c) α = 26°
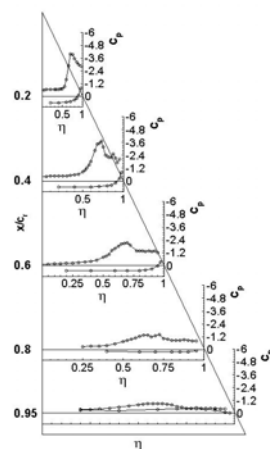
Figure A3.3-11: Steady Pressure Distribution at R_{mac} = 1 x 10^6 and M = 0.07 for Sharp (left) and Rounded (right) Leading Edges – α = 24°, α = 25°, α = 26°.
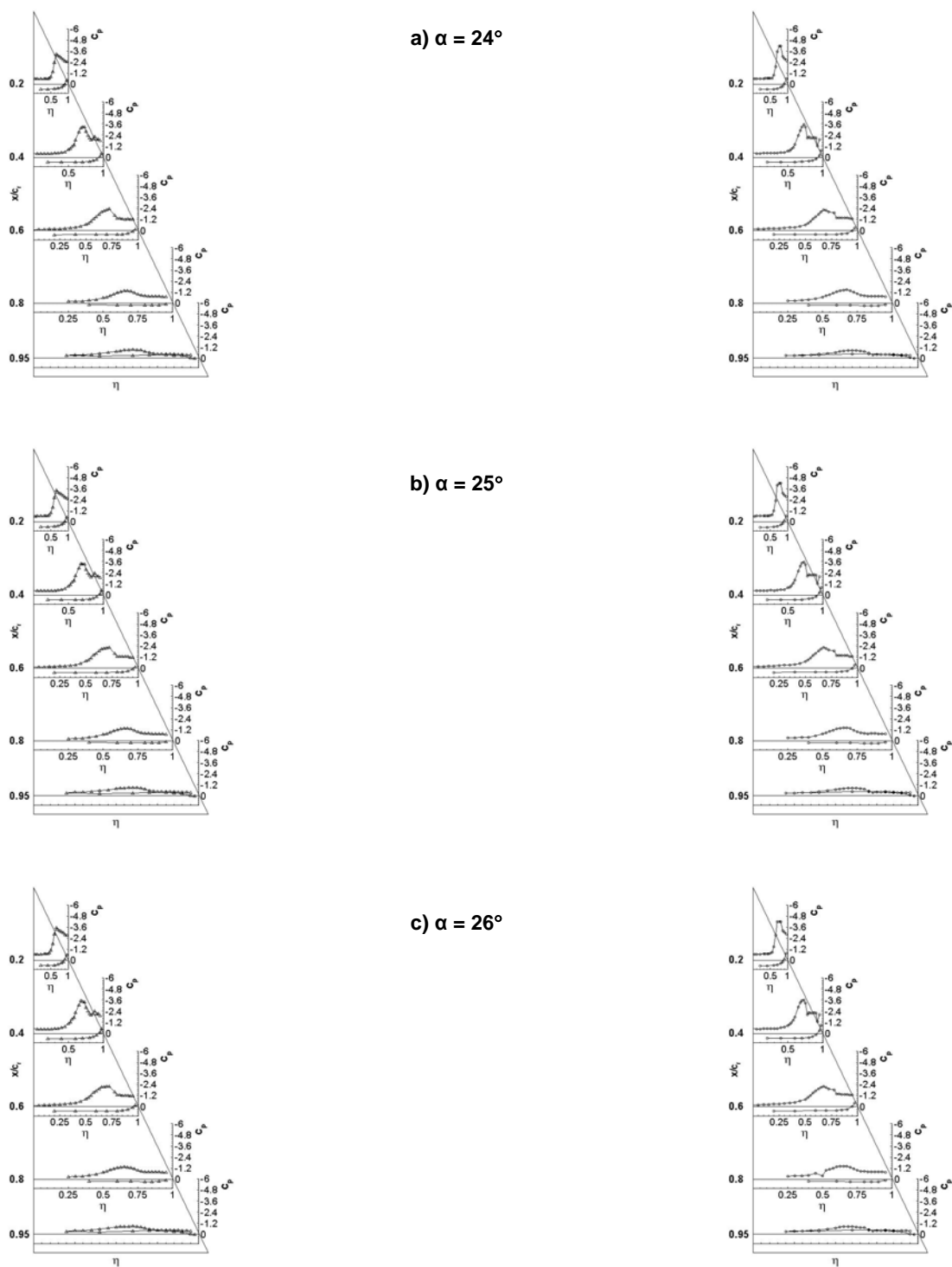
a) α = 27°

b) α = 28°

c) α = 29°

Figure A3.3-12: Steady Pressure Distribution at $R_{mac} = 1 \times 10^6$ and M = 0.07 for Sharp (left) and Rounded (right) Leading Edges – α = 27°, α = 28°, α = 29°.

a) α = 30°
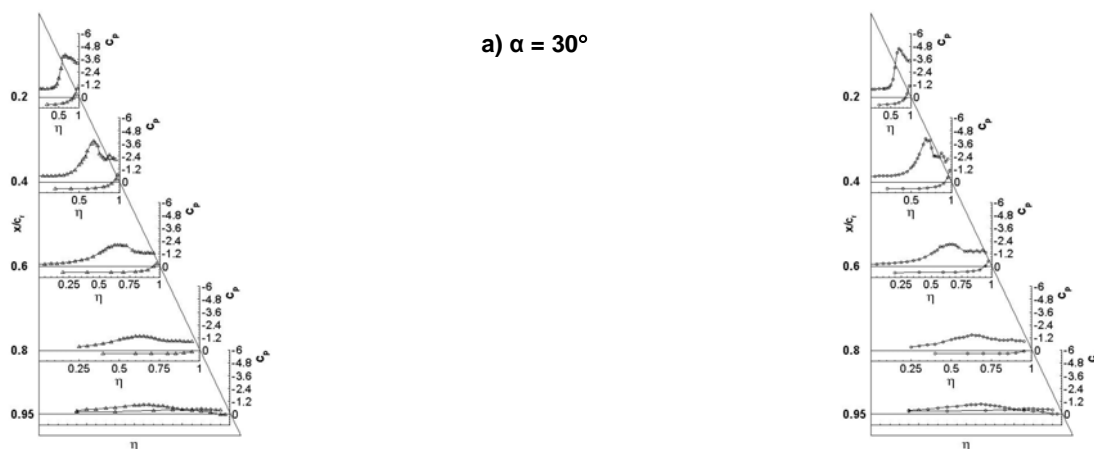
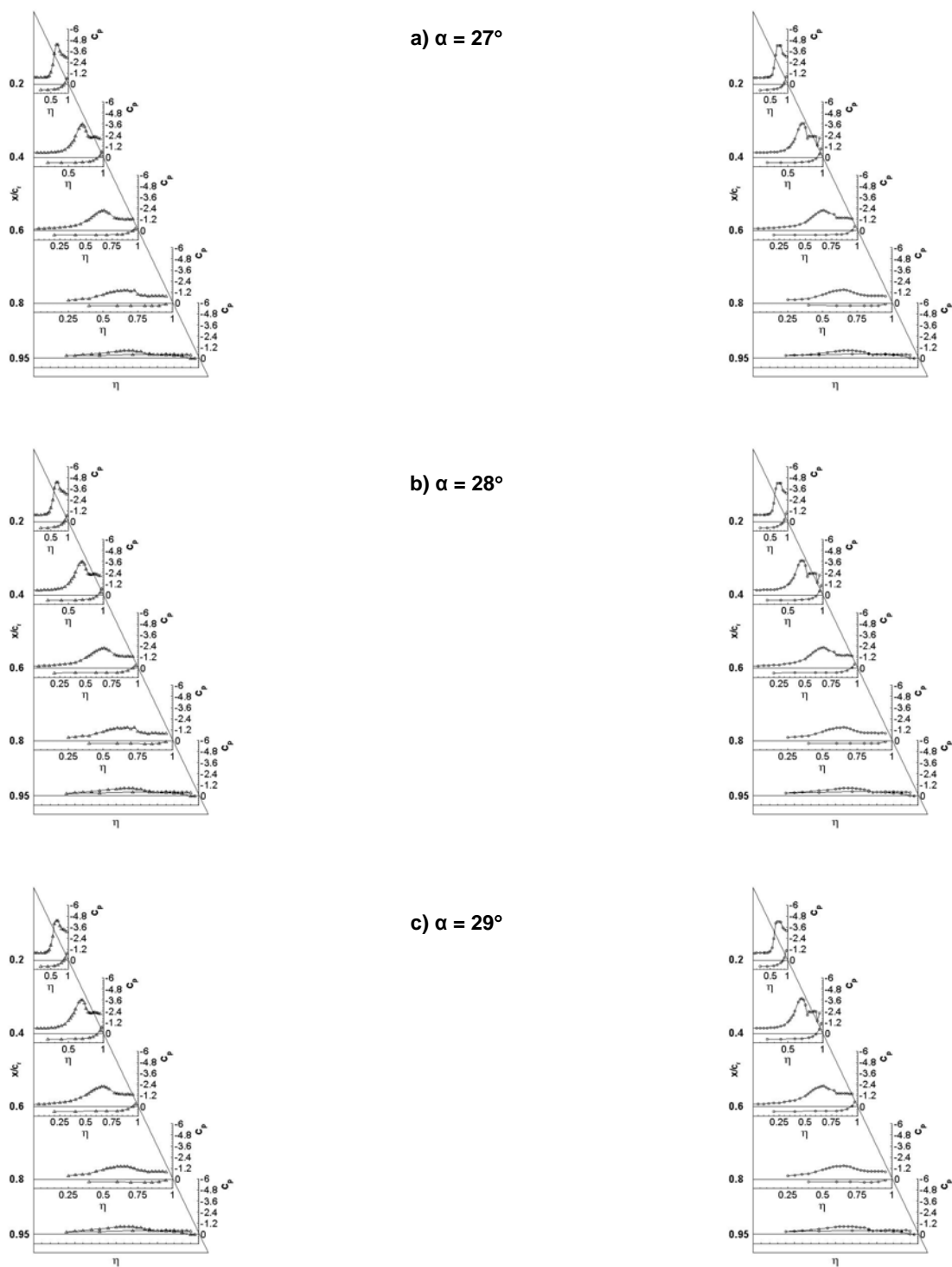**Figure A3.3-13: Steady Pressure Distribution at $R_{mac} = 1 \times 10^6$ and M = 0.07 for Sharp (left) and Rounded (right) Leading Edges – α = 30°.**

a) α = 0°

b) α = 5°

c) α = 10°

Figure A3.3-14: Steady Pressure Distribution at R_{mac} = 2 x 10^6 and M = 0.14 for Sharp (left) and Rounded (right) Leading Edges – α = 0°, α = 5°, α = 10°.

a) α = 12°

b) α = 14°

c) α = 16°

Figure A3.3-15: Steady Pressure Distribution at $R_{mac} = 2 \times 10^6$ and M = 0.14 for Sharp (left) and Rounded (right) Leading Edges – α = 12°, α = 14°, α = 16°.
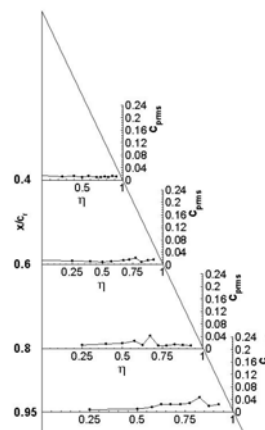
a) α = 20°

b) α = 21°

c) α = 22°

Figure A3.3-16: Steady Pressure Distribution at $R_{mac} = 2 \times 10^6$ and M = 0.14 for Sharp (left) and Rounded (right) Leading Edges – α = 20°, α = 21°, α = 22°.

a) α = 24°

b) α = 25°

c) α = 26°

Figure A3.3-17: Steady Pressure Distribution at R_{mac} = 2 x 10^6 and M = 0.14 for Sharp (left) and Rounded (right) Leading Edges – α = 24°, α = 25°, α = 26°.
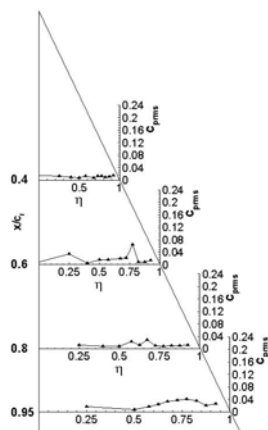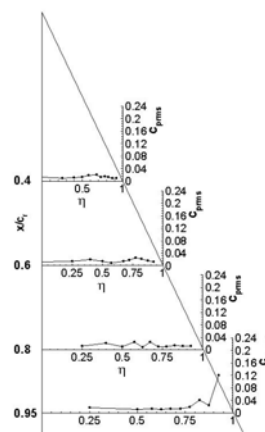
a) α = 27°

b) α = 28°

c) α = 29°

Figure A3.3-18: Steady Pressure Distribution at $R_{mac} = 2 \times 10^6$ and M = 0.14 for Sharp (left) and Rounded (right) Leading Edges – α = 27°, α = 28°, α = 29°.
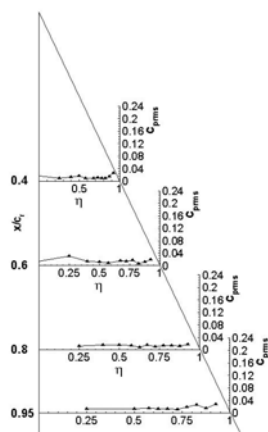
a) α = 30°
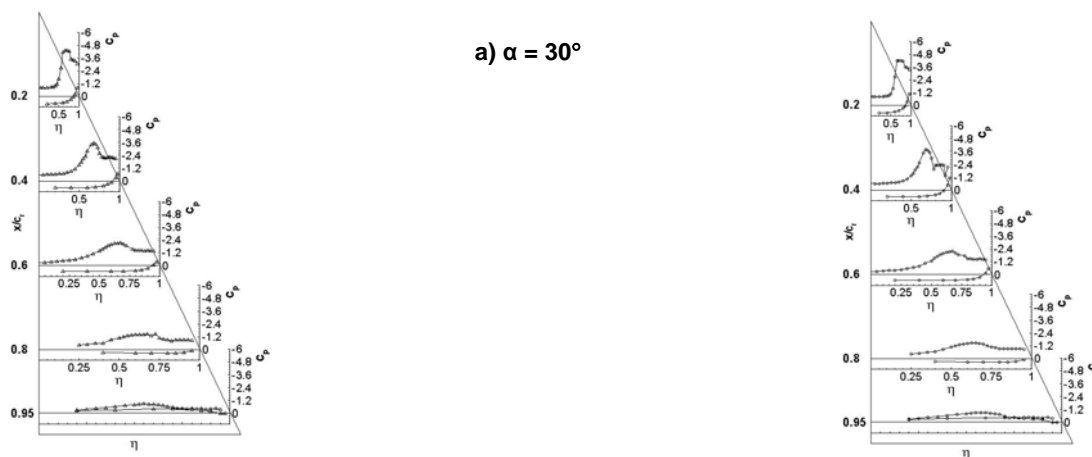
Figure A3.3-19: Steady Pressure Distribution at $R_{mac} = 2 \times 10^6$ and M = 0.14
for Sharp (left) and Rounded (right) Leading Edges – α = 30°.

a) α = 0°

b) α = 5°

c) α = 10°

Figure A3.3-20: Pressure Fluctuation Intensity at R_{mac} = 1 x 10^6 and M = 0.07 for Sharp (left) and Rounded (right) Leading Edges – α = 0°, α = 5°, α = 10°.

a) α = 12°

b) α = 14°

c) α = 16°
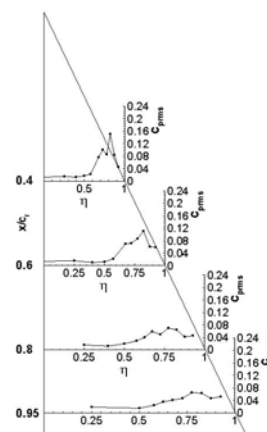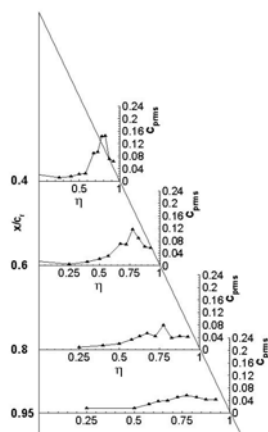
Figure A3.3-21: Pressure Fluctuation Intensity at R_{mac} = 1 x 10^6 and M = 0.07 for Sharp (left) and Rounded (right) Leading Edges – α = 12°, α = 14°, α = 16°.
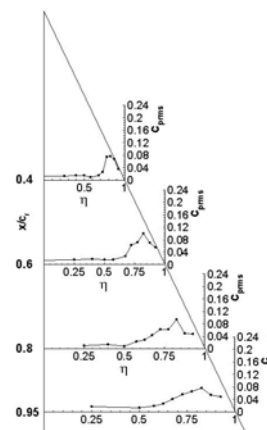
a) α = 20°

b) α = 21°

c) α = 22°

Figure A3.3-22: Pressure Fluctuation Intensity at R_{mac} = 1 x 10^6 and M = 0.07 for Sharp (left) and Rounded (right) Leading Edges – α = 20°, α = 21°, α = 22°.
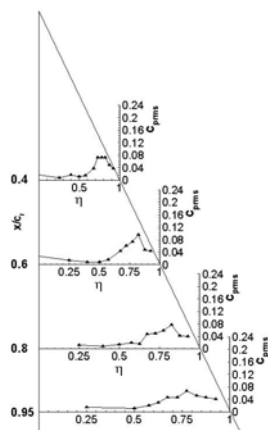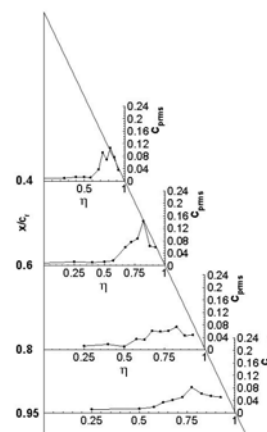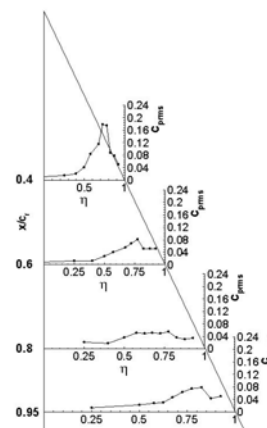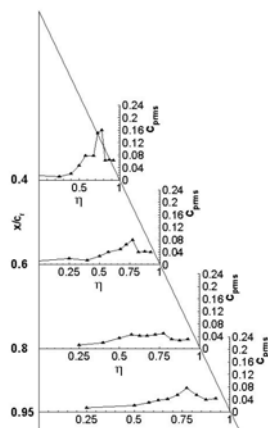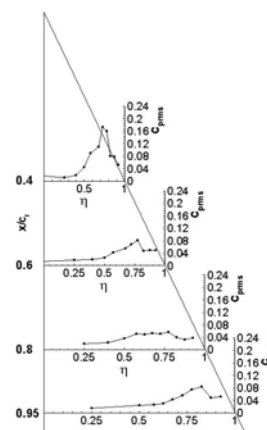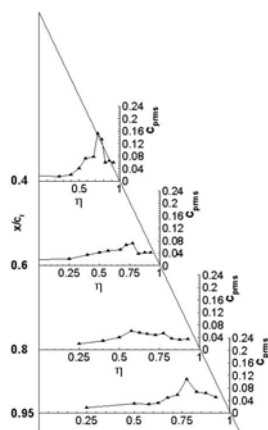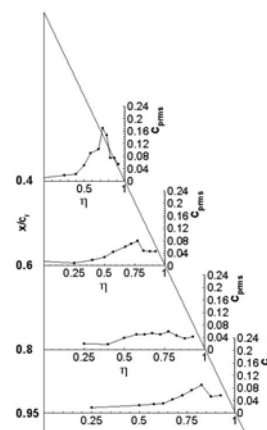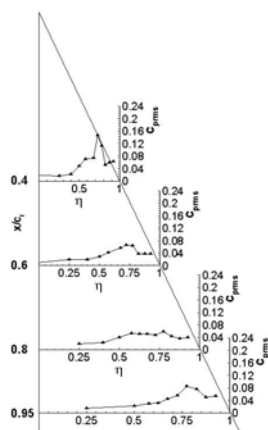
Figure A3.3-23: Pressure Fluctuation Intensity at R_{mac} = 1 x 10^6 and M = 0.07 for Sharp (left) and Rounded (right) Leading Edges – α = 24°, α = 25°, α = 26°.
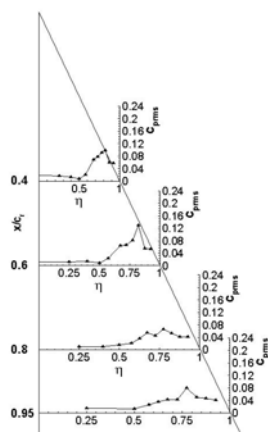
a) α = 27°

b) α = 28°

c) α = 29°
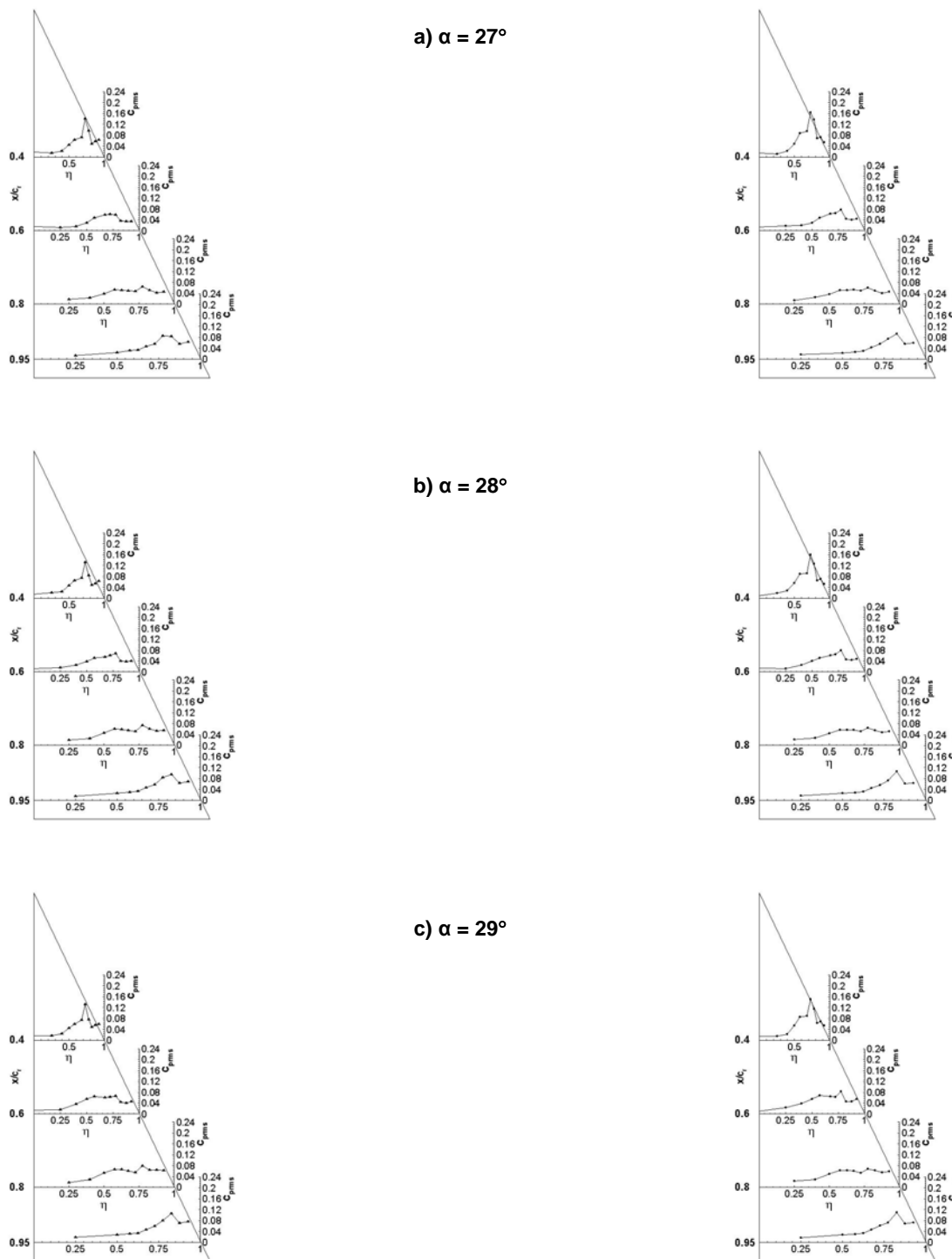
Figure A3.3-24: Pressure Fluctuation Intensity at R_{mac} = 1 x 10^6 and M = 0.07 for Sharp (left) and Rounded (right) Leading Edges – α = 27°, α = 28°, α = 29°.

a) α = 30°
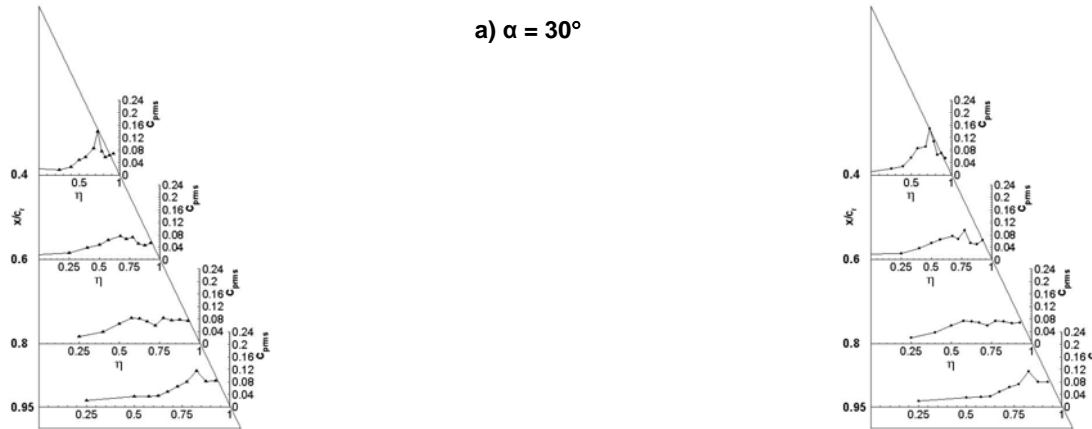
Figure A3.3-25: Pressure Fluctuation Intensity at R_{mac} = 1 x 10^6 and M = 0.07 for Sharp (left) and Rounded (right) Leading Edges – α = 30°.

a) α = 0°

b) α = 5°

c) α = 10°

Figure A3.3-26: Pressure Fluctuation Intensity at R_{mac} = 2 x 10^6 and M = 0.14 for Sharp (left) and Rounded (right) Leading Edges – α = 0°, α = 5°, α = 10°.

Figure A3.3-27: Pressure Fluctuation Intensity at R_{mac} = 2 x 10^6 and M = 0.14 for Sharp (left) and Rounded (right) Leading Edges – α = 12°, α = 14°, α = 16°.
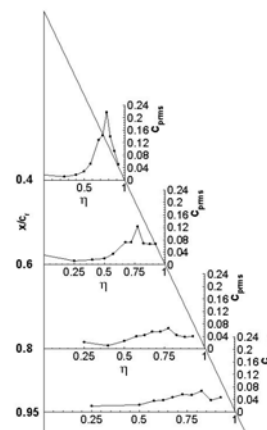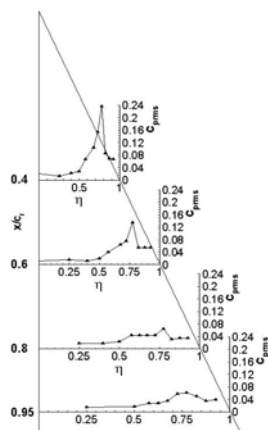
a) α = 20°

b) α = 21°

c) α = 22°

Figure A3.3-28: Pressure Fluctuation Intensity at R$_{mac}$ = 2 x 10^6 and M = 0.14 for Sharp (left) and Rounded (right) Leading Edges – α = 20°, α = 21°, α = 22°.
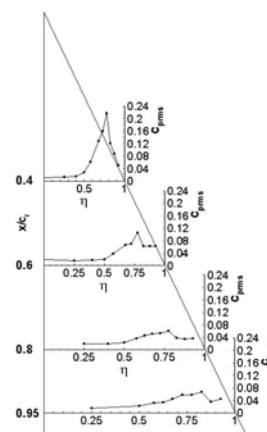
a) α = 24°

b) α = 25°

c) α = 26°

Figure A3.3-29: Pressure Fluctuation Intensity at R_{mac} = 2 x 10^6 and M = 0.14 for Sharp (left) and Rounded (right) Leading Edges – α = 24°, α = 25°, α = 26°.
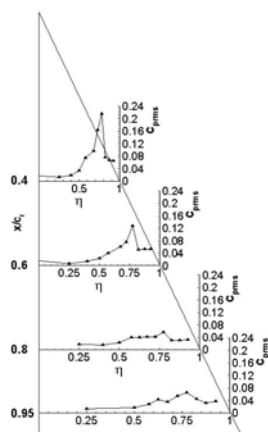
a) α = 27°

b) α = 28°

c) α = 29°

Figure A3.3-30: Pressure Fluctuation Intensity at R_{mac} = 2 x 10^6 and M = 0.14 for Sharp (left) and Rounded (right) Leading Edges – α = 27°, α = 28°, α = 29°.

a) α = 30°

Figure A3.3-31: Pressure Fluctuation Intensity at $R_{mac} = 2 \times 10^6$ and M = 0.14 for Sharp (left) and Rounded (right) Leading Edges – α = 30°.

Copyright © 2008 by C. Breitsamter and A. Furman. Published by RTO with permission.

Appendix 3.4 – EXPERIMENTAL RESULTS FROM ONERA

by

Ovide Rodriguez

Chapter 20 is the ONERA experimental contribution to VFE-2 within AVT-113. The present appendix provides the numerical data files for all the results described in Chapter 20.

A3.4.1   STRUCTURE OF THE DATA

A3.4.1.1   General Configuration and Test Conditions

- Medium and sharp leading edges
- $M = 0.133$
- $Re_{mac} = 1$ million

A3.4.1.2   Specific Test Conditions

- Solid walls
- $-4° \leq \alpha \leq 40°$
- Model 1
  - Contents
    - Surface pressure distribution from PSI modules
    - Upper surface C_p distribution at chord station $\xi = 0.2, 0.4, 0.6, 0.8$
      > File: Model_1_medium_upper
    - Upper and lower surface C_p distributions at $\xi = 0.2, 0.4, 0.6, 0.8, 0.95$
      > File: Model_1_sharp_upper
      > File: Model_1_sharp_lower
- Solid walls
- $-9° \leq \alpha \leq 40°$
- Models 4 and 5
  - Contents:
    - Forces from a balance: C_N, C_A, C_m
    - Upper and lower pressure distribution from PSI modules (reduced number of taps)
      > File: Models_4and5_solid_walls

- Open jet tunnel

- $0° < \alpha < 34°$

- Models 4 and 5

  - Contents:

    - Forces from a balance: C_N, C_A, C_m

    - Upper and lower pressure distribution from PSI modules (reduced number of taps)

            File: Models_4and5_open_jet_tunnel

- Solid walls

- $\alpha = 24.7°$

- Models 4 and 5

  - Contents:

    - Velocity vectors fields measured with Particle Image Velocity (Stereo PIV)

    - 3D velocity vectors in planes perpendicular to model axis at $\xi = 0.3, 0.4, 0.5, 0.6, 0.7$

            Files: s_p03, s_p04, s_p05, s_p06, s_p07
                    m_p03, m_p04, m_p05, m_p06, m_p07

    - Velocity vectors fields measured with 2 components PIV in a plan parallel to the upper surface

            Files: 2c_sharp
                    2c_medium

A more detailed description of the structure of PIV data is available in file piv_read_me.

Appendix 3.5 – EXPERIMENTAL RESULTS FROM UNIVERSITY OF GLASGOW

by

Frank N. Coton, Shabudin Bin Mat, Roderick A.McD. Galbraith

This appendix is related to Chapter 22. It contains flow visualisation and force and moment data measured on the VFE-2 configurations at the University of Glasgow. In the case of flow visualisation, the images are presented as a time series of the developing flow. The final image in each series represents the point at which the flow pattern on the wing stopped changing. Flow visualisation data are presented for the medium-radius edged wing at Reynolds numbers of 1×10^6 and 2×10^6 and for the sharp-edged wing at a Reynolds number of 2×10^6. For both wings, data are presented at angles of attack 13.3°, 18.5° and 23°. Force and moment data are presented as time averaged, uncorrected data with the exception of one case where the time series measured by the data collection system is provided to indicate the unsteadiness of the loads.

A3.5.1   FLOW VISUALISATION DATA

A3.5.1.1   Angle of Attack, α = 13.3°
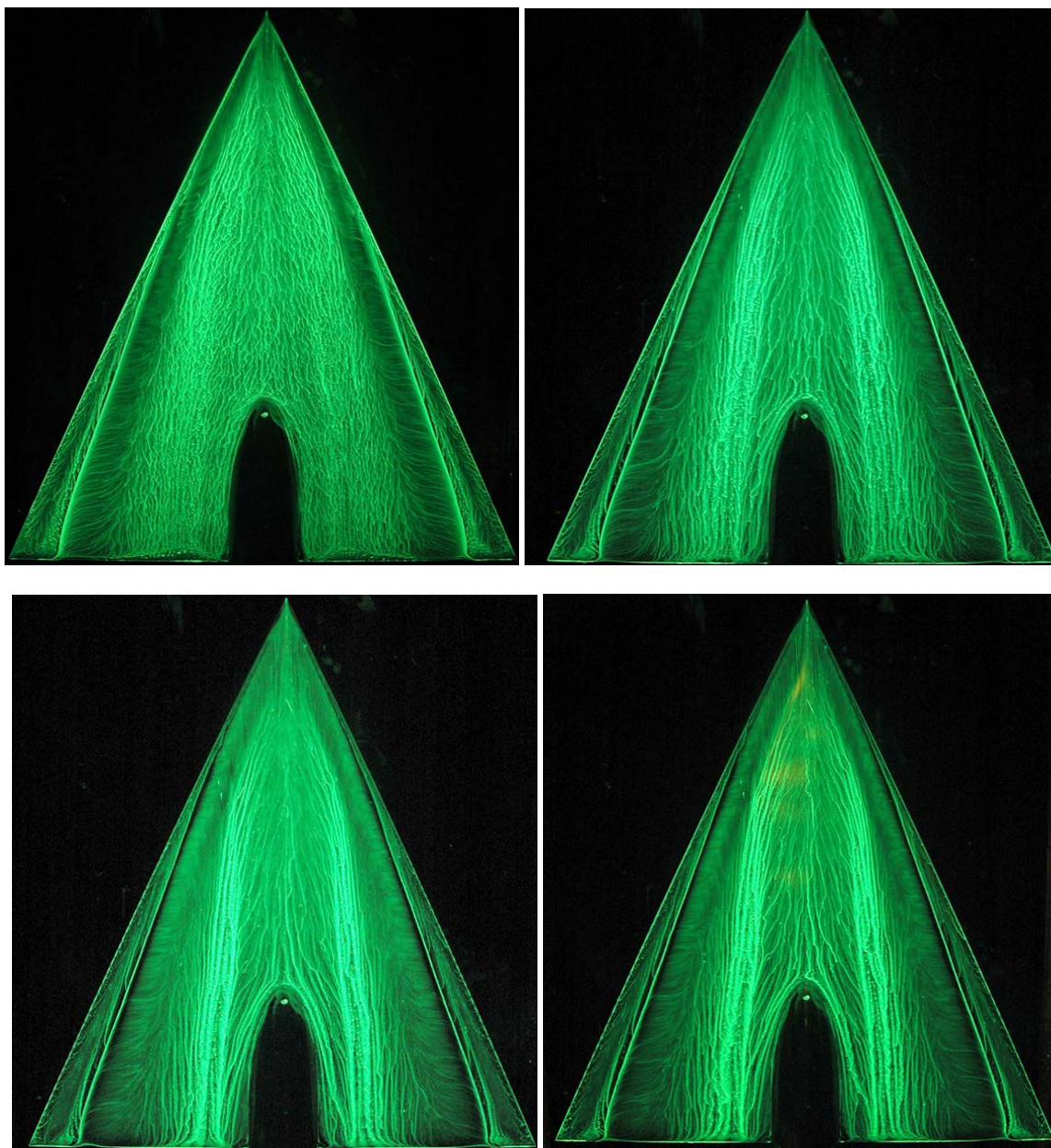
**Figure A3.5-1: Development of the Flow Topology on the
Medium-Radius Wing at α = 13.3° and R_{mac} = 1 x 10^6.**
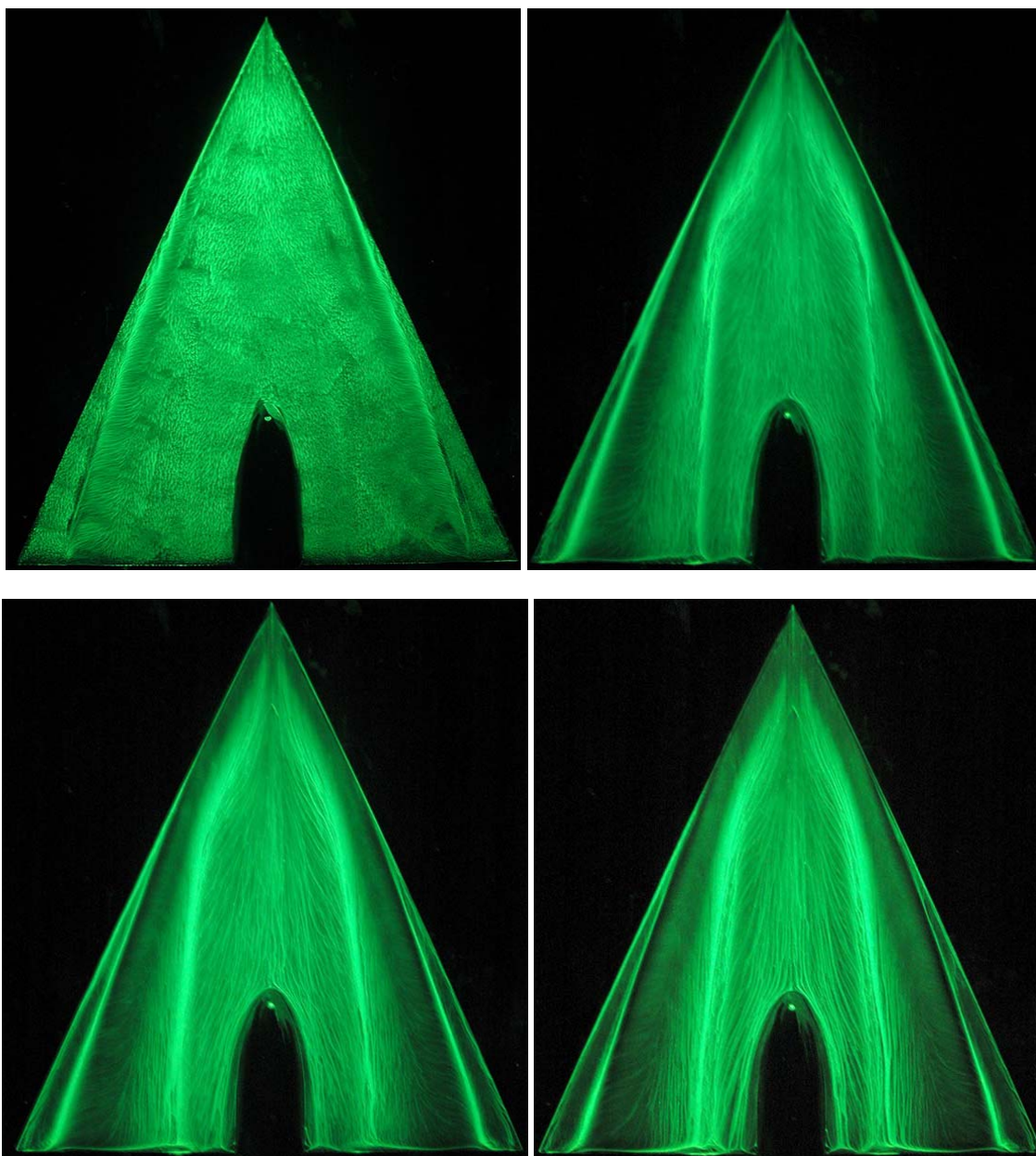
**Figure A3.5-2: Development of the Flow Topology on the
Medium-Radius Wing at α = 13.3° and R_{mac} = 2 x 10^6.**
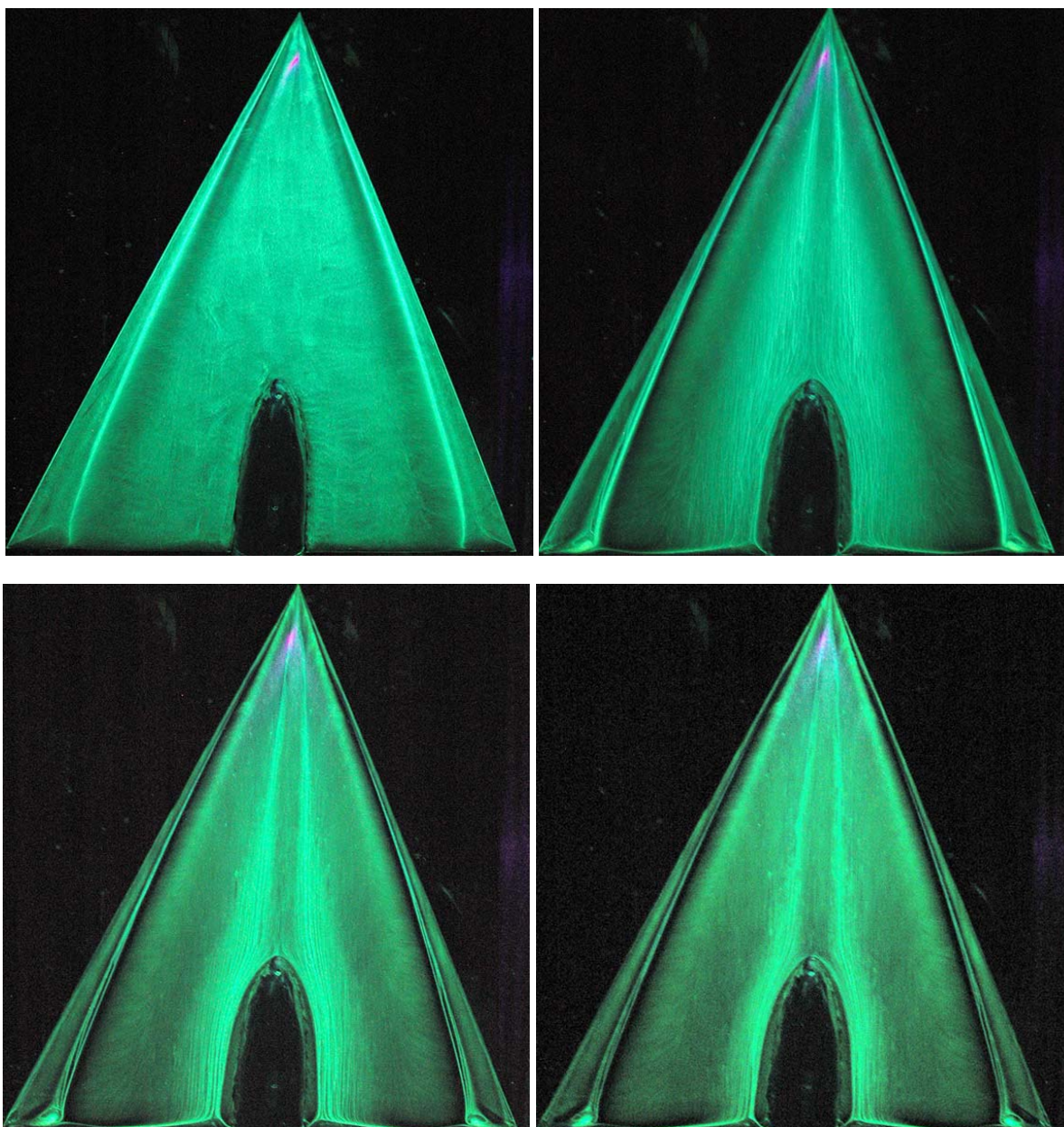
Figure A3.5-3: Development of the Flow Topology on the
Sharp-Edged Wing at α = 13.3° and R_{mac} = 2 x 10^6.

A3.5.1.2 Angle of Attack, α = 18.5°
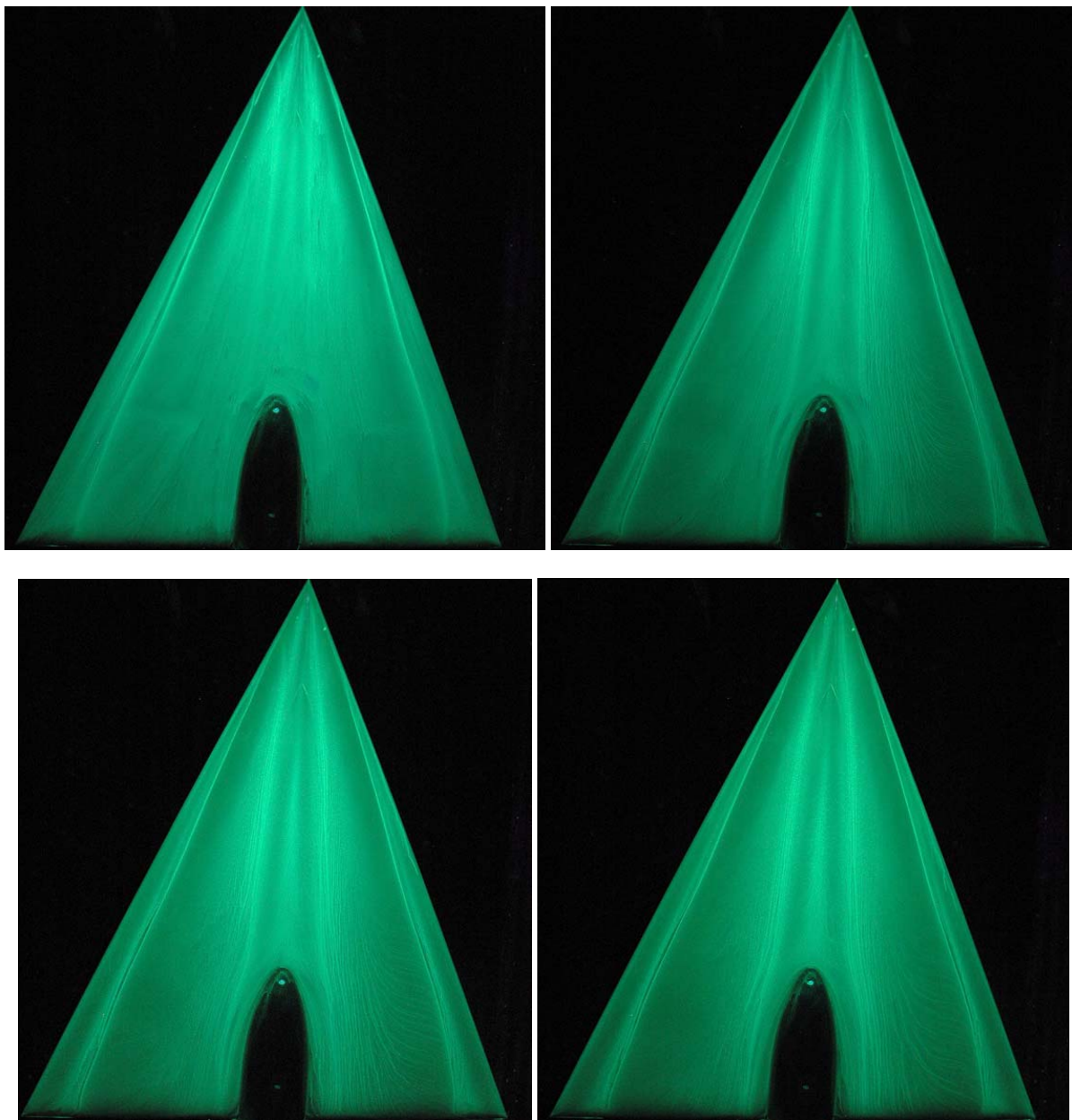
**Figure A3.5-4: Development of the Flow Topology on the
Medium-Radius Wing at α = 18.5° and R_{mac} = 1 x 10^6.**
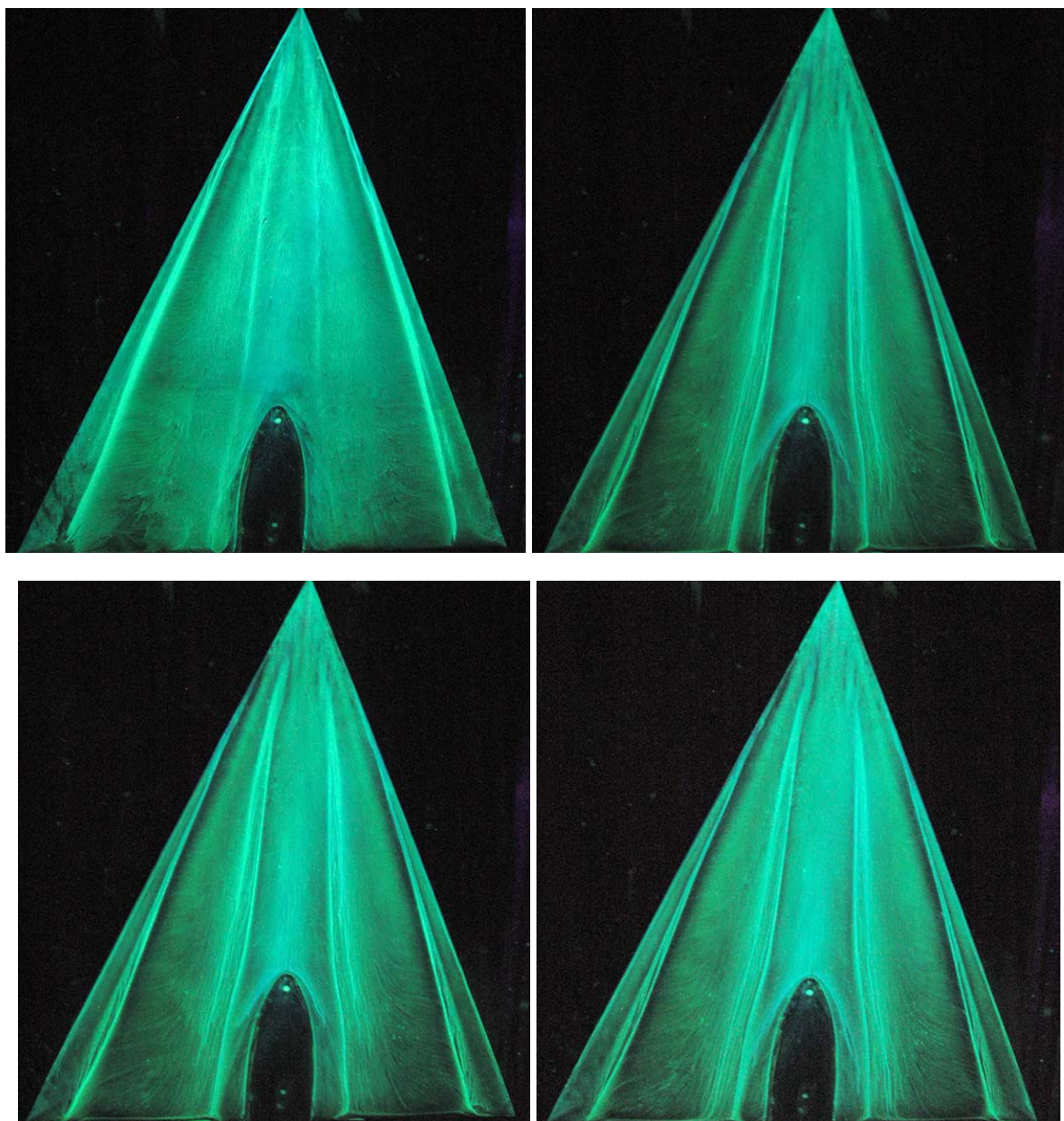
Figure A3.5-5: Development of the Flow Topology on the
Medium-Radius Wing at α = 18.5° and R_{mac} = 2 x 10^6.
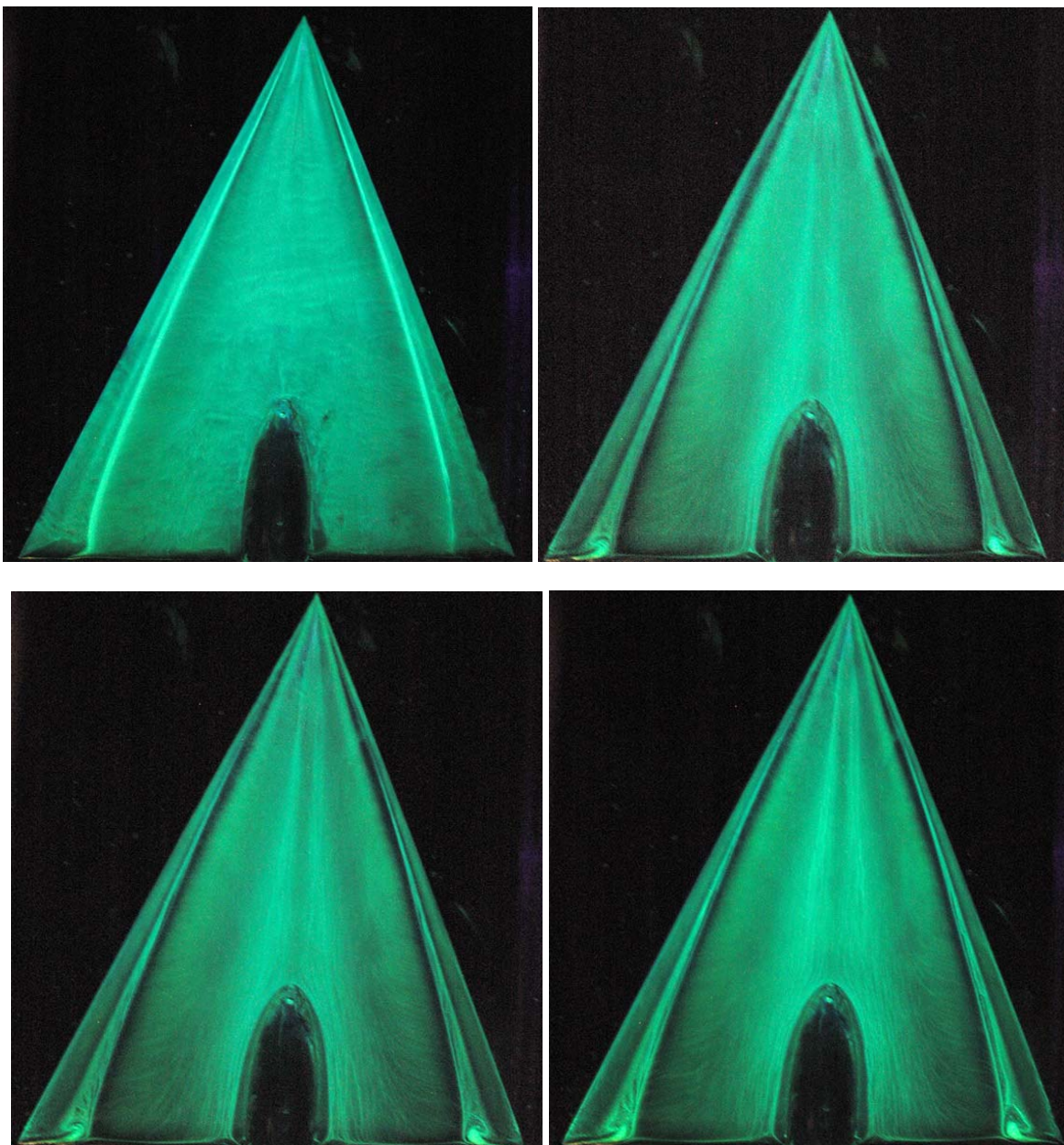
**Figure A3.5-6: Development of the Flow Topology on the
Sharp-Edged Wing at α = 18.5° and R$_{mac}$ = 2 x 10^6.**

A3.5.1.3 Angle of Attack, α = 23°
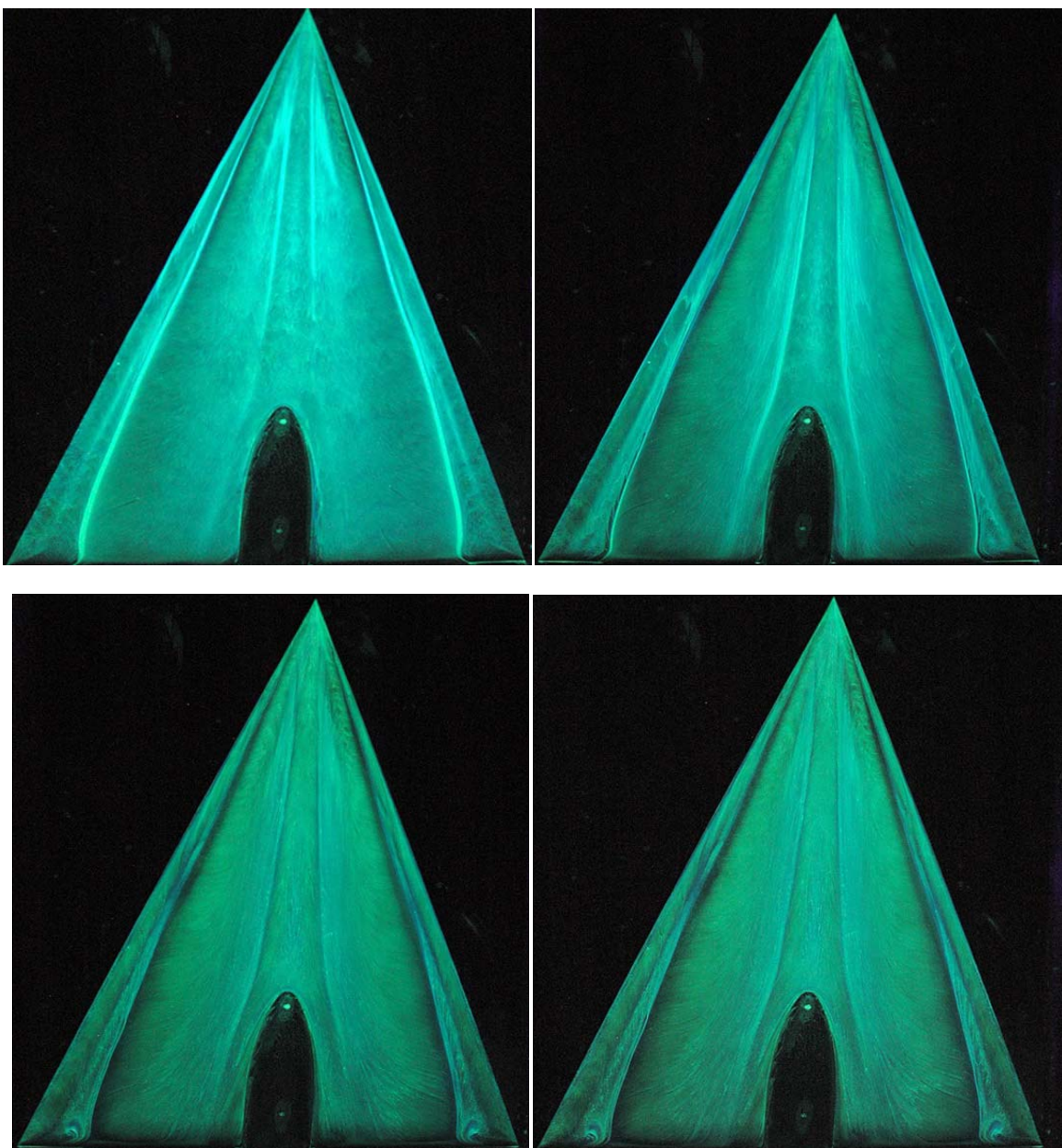
Figure A3.5-7: Development of the Flow Topology on the Medium-Radius Wing at α = 23° and R_{mac} = 1 x 10^6.
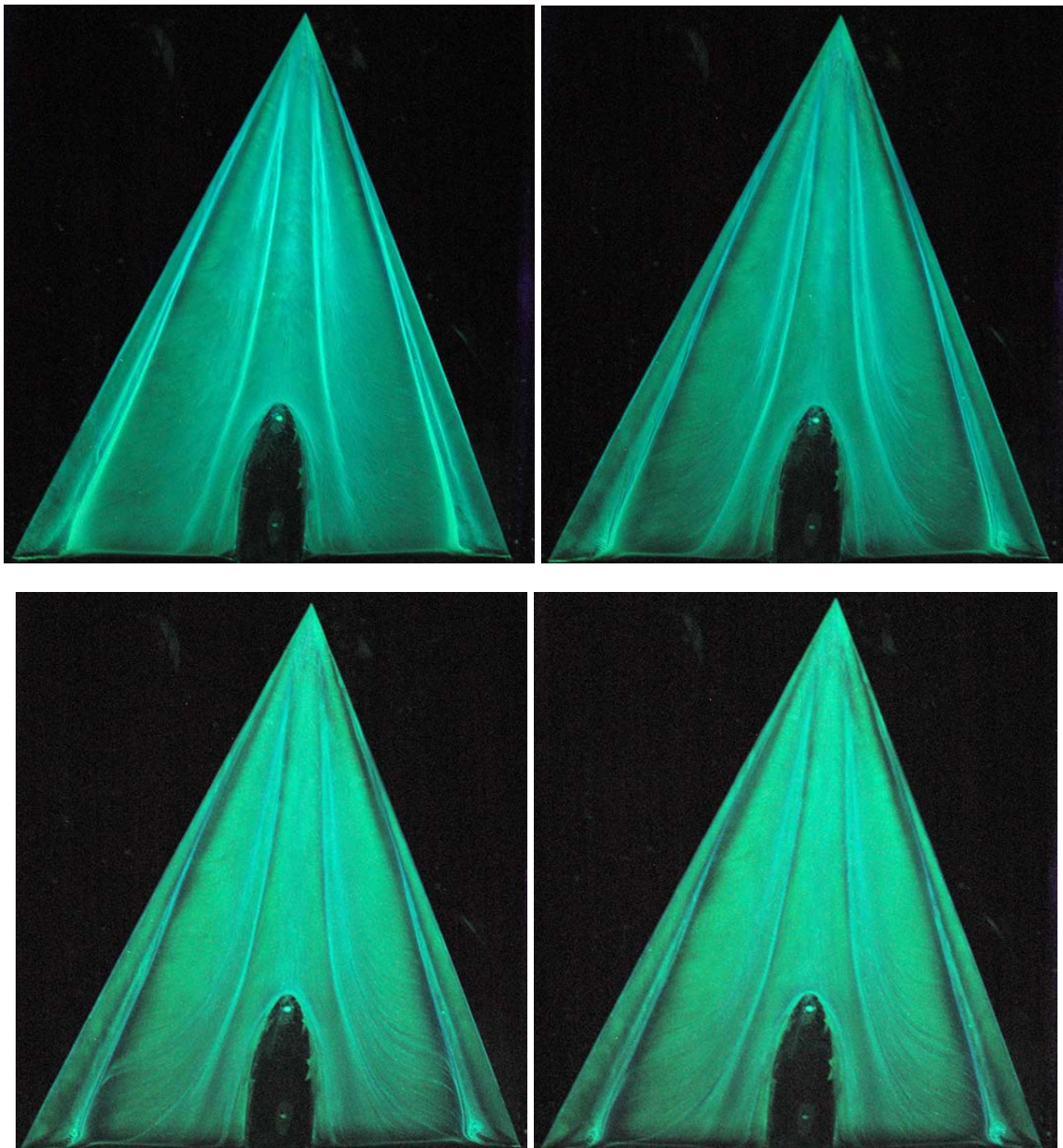
**Figure A3.5-8: Development of the Flow Topology on the
Medium-Radius Wing at α = 23° and R_{mac} = 2 x 10^6.**
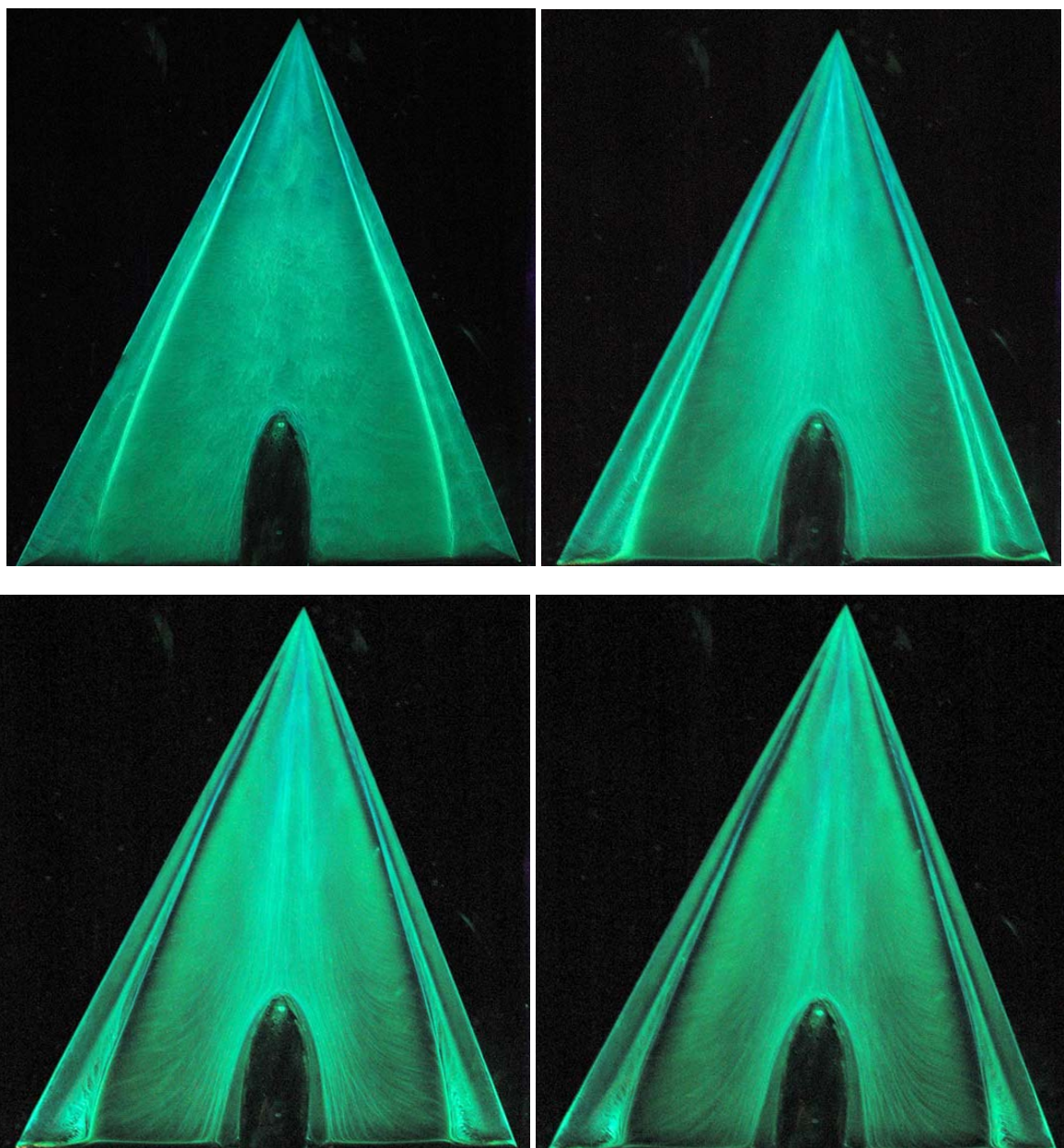
Figure A3.5-9: Development of the Flow Topology on the Sharp-Edged Wing at α = 23° and R_{mac} = 2 x 10^6.

A3.5.2 STEADY FORCE AND MOMENT COEFFICIENTS FOR VFE-2 WING CONFIGURATIONS

A3.5.2.1 Medium Radius Wing

Table A3.5-1: Time Averaged Force and Moment Coefficients for Medium Radius Wing

α	$R_{mac} = 1 \times 10^6$			$R_{mac} = 2 \times 10^6$		
	C_N	C_A	C_M	C_N	C_A	C_M
13.3	0.58145916	0.1839282	-0.07577118	0.5559778	0.1545126	-0.07538
15.5	0.683607	0.2162924	-0.101998	0.6401042	0.175724	-0.096514
17	0.770599	0.24486	-0.11098	0.7279008	0.2170232	-0.110004
18.5	0.8438178	0.274565	-0.136166	0.7854936	0.2130722	-0.134712
20	0.9037188	0.2856268	-0.157664	0.898526	0.224118	-0.143176
22	1.0040172	0.3260496	-0.191636	1.01905402	0.2446008	-0.164536
23	1.0437962	0.335031	-0.197492	1.0113132	0.2382516	-0.164536
25	1.1878362	0.3662968	-0.211364	1.1948814	0.2558062	-0.190192

A3.5.2.2 Sharp Edged Wing

Table A3.5-2: Time Averaged Force and Moment Coefficients for Sharp Edged Wing, $R_{mac} = 2 \times 10^6$

α	C_N	C_A	C_M
13.3	0.548833	0.169993	-0.09728
18.5	0.833557	0.229252	-0.15045
23	1.074284	0.263991	-0.19924

A3.5.3 UNSTEADY FORCE AND MOMENT COEFFICIENTS

The table below contains load cell data collected at 8 kHz for a period of one twentieth of a second for the case of the medium radius wing at an angle of attack of 13.3 degrees and a Reynolds number of two million. These data are provided as an example of the collected unsteady force and moment coefficient data. A typical case would have data for one second collected at 8 kHz.

Table A3.5-3: Force and Moment Coefficients Measured at 8 kHz
for the Medium Radius Wing at α = 13.3° and R_{mac} = 2 x 10^6

C_N	C_A	C_M
0.575462793	0.153392346	-0.073024953
0.574921315	0.161820315	-0.073413899
0.57463121	0.169522981	-0.073577726
0.574645172	0.174901823	-0.073718008
0.574963049	0.178849965	-0.073753473
0.575169958	0.181357061	-0.073877574
0.575504919	0.182138592	-0.073920856
0.575537574	0.181164069	-0.074051668
0.576007128	0.178772827	-0.074026958
0.576417623	0.176208647	-0.073950701
0.576520059	0.173054847	-0.074144378
0.576478355	0.169749397	-0.074362115
0.576317903	0.165671502	-0.074656416
0.576152818	0.162258473	-0.07493719
0.57563797	0.15836924	-0.075476412
0.574753758	0.155853641	-0.07605552
0.573374845	0.152556055	-0.07691698
0.571780041	0.149002432	-0.077903778
0.570157735	0.145187982	-0.078920559
0.569010664	0.141153301	-0.079794731
0.568608124	0.137827612	-0.080162042
0.56886449	0.135330869	-0.080277732
0.569574285	0.134652626	-0.080115308
0.570573067	0.136112111	-0.079839454
0.571828457	0.138896235	-0.079450135
0.573202086	0.142464904	-0.078984744
0.574545547	0.146565495	-0.078550629
0.575764368	0.15079958	-0.078179634
0.576681547	0.15394866	-0.077912024
0.577498262	0.156614648	-0.077776532
0.578153236	0.15776421	-0.077608663
0.578489163	0.15616389	-0.077667027
0.578301258	0.153742297	-0.077940998
0.57728052	0.150111198	-0.078603069
0.575719057	0.145823046	-0.079538249
0.573968895	0.140344738	-0.080568691
0.572512151	0.13540977	-0.081483368
0.570974339	0.129780552	-0.082389829
0.569552932	0.125467262	-0.083221173

C_N	C_A	C_M
0.568213844	0.122512567	-0.084076142
0.566966403	0.122203409	-0.084884921
0.56599105	0.123589998	-0.085523638
0.565459747	0.127101575	-0.085954321
0.565491543	0.133397049	-0.08610065
0.566271292	0.140918229	-0.085934337
0.567143203	0.148385762	-0.085623618
0.568188384	0.156685075	-0.085274506
0.568872051	0.164302997	-0.085059378
0.569104356	0.17258053	-0.085056122
0.569059361	0.179536887	-0.085209056
0.568712822	0.184599261	-0.085464847
0.568423689	0.187969686	-0.085756626
0.567828621	0.190242597	-0.086137616
0.566877145	0.189701471	-0.086649664
0.565540192	0.188490994	-0.08734007
0.5640686	0.183806393	-0.088049431
0.562696285	0.177724117	-0.088806426
0.561378089	0.170639647	-0.089405659
0.560663429	0.163351717	-0.089797897
0.560974857	0.15563054	-0.089606657
0.561942296	0.147954402	-0.089149405
0.563672899	0.14206993	-0.088420928
0.565431657	0.138843334	-0.087678678
0.566837619	0.138357685	-0.087033267
0.568316742	0.140461471	-0.086481556
0.569410215	0.145032631	-0.086027148
0.570900421	0.151620166	-0.085421593
0.572620024	0.158755467	-0.084732634
0.574093953	0.16651571	-0.084102585
0.575183774	0.172939034	-0.083650086
0.575946584	0.178997378	-0.083427784
0.576293131	0.183721691	-0.083399331
0.576067412	0.187237411	-0.083643553
0.575621713	0.188098432	-0.083998424
0.574903113	0.187858705	-0.084425856
0.57391721	0.186185094	-0.085036964
0.573067998	0.183591813	-0.085611172
0.572385396	0.17975513	-0.086019586
0.571919455	0.176096418	-0.086400016
0.57142686	0.171731131	-0.086712348
0.57112464	0.168027464	-0.086928648

C_N	C_A	C_M
0.571252032	0.164434307	-0.086895071
0.572033264	0.160947174	-0.086498403
0.57306098	0.157572732	-0.08596064
0.574243666	0.155126025	-0.085344601
0.575544992	0.15294632	-0.08465246
0.576625525	0.151829692	-0.084072201
0.578128476	0.151548777	-0.083327566
0.580213189	0.152018731	-0.082223867
0.582516878	0.15373273	-0.08110727
0.584691718	0.15670841	-0.079957935
0.585939656	0.161183199	-0.07935832
0.585737337	0.166417397	-0.079426185
0.584347041	0.172607382	-0.080143272
0.582270591	0.17783424	-0.081141711
0.580234633	0.182599569	-0.082233906
0.578236354	0.186661589	-0.083225672
0.576235205	0.189042468	-0.084284233
0.574026887	0.190659468	-0.085480401
0.571752961	0.191343147	-0.086693484
0.569657766	0.190733932	-0.087865248
0.567908775	0.189321071	-0.088845877
0.566439455	0.187898621	-0.089668886
0.565211097	0.186906165	-0.090419364
0.564217426	0.186282799	-0.09100231
0.564086824	0.186999191	-0.091165972
0.5645562	0.188382447	-0.091026662
0.565555605	0.19054996	-0.09060321
0.566306816	0.193528088	-0.09032175
0.566642858	0.196324214	-0.09015225
0.566356731	0.199145009	-0.090329855
0.566317413	0.199830898	-0.090350119
0.566710638	0.198954145	-0.090200713
0.567408243	0.197115294	-0.089848512
0.568078832	0.193025252	-0.089509835
0.568187954	0.187350185	-0.089470907
0.567879491	0.180119712	-0.089708044
0.567561194	0.172073691	-0.089917439
0.567223676	0.164182167	-0.090169326
0.567098355	0.157332617	-0.090297471
0.567212661	0.152903945	-0.09036995
0.567544923	0.151207316	-0.090250733
0.568179208	0.151671765	-0.090044343

C_N	C_A	C_M
0.568841852	0.154264327	-0.089823989
0.569293083	0.157145426	-0.089743178
0.569682703	0.161570079	-0.089612119
0.56972353	0.167193382	-0.089673409
0.569688841	0.174305545	-0.089838039
0.569358894	0.180463514	-0.090118923
0.568622979	0.185026164	-0.090604785
0.567598796	0.188379256	-0.091219733
0.566372929	0.19037563	-0.091903398
0.564981117	0.192086372	-0.092654225
0.563705408	0.192969942	-0.093313363
0.562852497	0.191872641	-0.093790953
0.562421465	0.188737437	-0.093973771
0.562166556	0.184839511	-0.094116524
0.562136678	0.181426865	-0.094064168
0.562032253	0.176844583	-0.094098288
0.561764299	0.172128975	-0.094198839
0.561594921	0.168438507	-0.094168504
0.561454793	0.165601151	-0.094205406
0.561546444	0.163325711	-0.094158174
0.561390054	0.16114531	-0.094155032
0.560862638	0.159464026	-0.094274278
0.56016022	0.158744258	-0.094531116
0.559257718	0.158011745	-0.09485659
0.558409961	0.1568717	-0.095122073
0.557813498	0.156927269	-0.095260727
0.557206286	0.157767378	-0.095372549
0.556514081	0.159030599	-0.09556012
0.555670033	0.162089917	-0.095938953
0.554566324	0.164957153	-0.096334961
0.553657689	0.168227938	-0.096648681
0.552805629	0.173079702	-0.096917723
0.552078996	0.178595171	-0.097123425
0.551391996	0.184516805	-0.097325577
0.550934692	0.190124601	-0.097330238
0.551049033	0.195913522	-0.097143779
0.551577143	0.201786963	-0.096666629
0.552468892	0.206348239	-0.096038233
0.553166034	0.209041015	-0.095491476
0.553595381	0.209496129	-0.095112489
0.553472224	0.20819807	-0.094963506
0.553194364	0.204192648	-0.094794604

C_N	C_A	C_M
0.55314756	0.197459588	-0.094606733
0.553358633	0.188548486	-0.094190601
0.553552994	0.177528498	-0.093815211
0.554094777	0.165706726	-0.093263942
0.554950029	0.15339805	-0.092635709
0.556301218	0.142132509	-0.091740388
0.558165142	0.13241816	-0.090520833
0.560009189	0.125116366	-0.089360431
0.561520497	0.120904629	-0.088433672
0.562631204	0.120394831	-0.087677044
0.56361619	0.122156602	-0.087000613
0.564433935	0.126037482	-0.086392723
0.565362414	0.1309679	-0.085696383
0.566225776	0.138027476	-0.085033425
0.566862476	0.144340116	-0.084566392
0.567348379	0.148622122	-0.084093925
0.56771394	0.152113392	-0.083698363
0.567769133	0.15414373	-0.083475428
0.567498512	0.15463522	-0.083302232
0.566936311	0.154304999	-0.083259508
0.566550908	0.153534304	-0.083094133
0.566249015	0.151990336	-0.082951193
0.566162759	0.1503763	-0.082585114
0.565980896	0.149425528	-0.082267422
0.565669961	0.147941328	-0.081998801
0.565303294	0.147217331	-0.08169318
0.565194151	0.146762023	-0.081273625
0.56578578	0.146712945	-0.080516297
0.56682351	0.147465937	-0.079549868
0.568278047	0.147506688	-0.07829119
0.569959336	0.146627031	-0.076918215
0.571396158	0.144701189	-0.075685125
0.57272045	0.143866983	-0.074557926
0.57384628	0.14249418	-0.073498646
0.574353847	0.139951777	-0.072784449
0.574534339	0.137447456	-0.072284834
0.574233623	0.135606806	-0.072012347
0.573539219	0.135748726	-0.0719066
0.572296595	0.136602453	-0.072143409
0.571001817	0.138273705	-0.072439416
0.569724187	0.140241172	-0.072775798
0.568624087	0.14364747	-0.072990065

C_N	C_A	C_M
0.567574402	0.147490828	-0.073244069
0.566577972	0.151045205	-0.073438443
0.565580895	0.15406996	-0.073633039
0.564940881	0.15790308	-0.073679767
0.564683937	0.160668765	-0.073532737
0.564758947	0.162787904	-0.073250665
0.565296377	0.162623091	-0.072685745
0.566464385	0.159841946	-0.071867324
0.568432197	0.15541926	-0.070563145
0.571183231	0.15009536	-0.068928134
0.574147254	0.143953649	-0.067152831
0.576751073	0.137134183	-0.065526794
0.579213737	0.129281077	-0.064004973
0.580787036	0.120504333	-0.062916468
0.582260965	0.111463461	-0.0618621
0.583380174	0.103281377	-0.061068888
0.584184999	0.094922908	-0.060352944
0.58439429	0.086839576	-0.059954269
0.584199331	0.080834647	-0.05969472
0.583590983	0.076213171	-0.059741946
0.582679061	0.073551795	-0.059893828
0.581420526	0.07367935	-0.060237347
0.580274339	0.07551431	-0.060491664
0.579183608	0.080119473	-0.060717759
0.578289871	0.086055201	-0.060876642
0.577338374	0.093004318	-0.060999296
0.576076864	0.101024025	-0.06131097
0.574577551	0.109205639	-0.061791703
0.572910273	0.117959405	-0.062422727
0.571440938	0.126677476	-0.062888441
0.570430039	0.133826903	-0.063155173
0.570130101	0.140200659	-0.063095356
0.570025236	0.146127972	-0.06285542
0.56974586	0.152748788	-0.062752712
0.56929732	0.158692611	-0.062702828
0.568835181	0.163943679	-0.062610895
0.568840959	0.168169086	-0.062347641
0.56912484	0.170250095	-0.061910978
0.569436623	0.171169866	-0.061525475
0.569492993	0.169774089	-0.061154737
0.569519955	0.168307822	-0.060896858
0.569296572	0.166853838	-0.060765893

C_N	C_A	C_M
0.569484515	0.164583881	-0.060606603
0.570323211	0.163482354	-0.060070054
0.571668549	0.162840586	-0.059375494
0.57332208	0.163435508	-0.058590862
0.575136497	0.165580586	-0.057643729
0.577384953	0.168300365	-0.056542828
0.579300801	0.171717184	-0.055659047
0.580737097	0.174728151	-0.055001287
0.581598996	0.178261711	-0.054617572
0.582050292	0.181002294	-0.054441302
0.582249446	0.182946836	-0.054392315
0.582404615	0.182926217	-0.054414141
0.582944208	0.180377421	-0.05424134
0.583323832	0.176487509	-0.054132873
0.58367477	0.172466031	-0.054054889
0.583767162	0.168214956	-0.054188689
0.583420906	0.163783455	-0.054462561
0.582808133	0.15925793	-0.054936147
0.581997898	0.154316264	-0.055477018
0.580855806	0.148820672	-0.056136668
0.579633294	0.143966535	-0.056788306
0.578345689	0.140183717	-0.057473136
0.576991442	0.137411339	-0.058094008
0.57567992	0.136264062	-0.058742397
0.574403817	0.136851783	-0.05938946
0.573046204	0.138083689	-0.06002902
0.571445683	0.139867381	-0.06082408
0.569518278	0.142787283	-0.061670328
0.567351829	0.145260092	-0.062768016
0.565080264	0.147713945	-0.063886234
0.562627459	0.15004295	-0.065128229
0.559733459	0.152054582	-0.066511305
0.556644697	0.153774838	-0.067976113
0.553329782	0.155479665	-0.069554596
0.550305324	0.157396643	-0.070920634
0.547432151	0.15942315	-0.072193562
0.545255027	0.162641336	-0.073130818
0.543284745	0.16648812	-0.073914701
0.541575048	0.17048926	-0.074599449
0.54005902	0.174814404	-0.075284416
0.538918774	0.177139862	-0.075762892
0.538591436	0.178220195	-0.075977293

C_N	C_A	C_M
0.538712392	0.177037739	-0.075964855
0.539002361	0.174415477	-0.075899385
0.539512644	0.170138676	-0.075608508
0.540138805	0.166565419	-0.075324435
0.541072856	0.162769683	-0.074950172
0.542327198	0.159921689	-0.07443069
0.543567608	0.158258796	-0.073885929
0.544739085	0.156375312	-0.073457405
0.54559155	0.155687222	-0.073190215
0.546420442	0.156622733	-0.072967927
0.547123749	0.15888171	-0.07280934
0.548127688	0.160683182	-0.072629319
0.548977826	0.162031731	-0.07242937
0.54974736	0.16248325	-0.072318842
0.550472238	0.16211005	-0.072181976
0.551212278	0.161628604	-0.072086211
0.55255792	0.161154058	-0.071700638
0.554213751	0.161144298	-0.071044317
0.555668031	0.161303531	-0.070554928
0.55700562	0.161284459	-0.070059108
0.557533079	0.162291275	-0.069923571
0.557419221	0.161899295	-0.069997435
0.557600507	0.160444664	-0.069938267
0.55793329	0.156845413	-0.069769683
0.559022693	0.151426546	-0.069284018
0.560533722	0.144916017	-0.06852008
0.562489579	0.137882095	-0.067531565
0.56442114	0.131476846	-0.066490178
0.56595802	0.125993651	-0.065615859
0.567052819	0.122519845	-0.064981615
0.567219809	0.12103451	-0.064800206
0.566675934	0.120207781	-0.064945658
0.565193903	0.12028865	-0.065516316
0.563449215	0.120084329	-0.066187065
0.561388691	0.121353758	-0.067033858
0.559706026	0.122346662	-0.067673558
0.557840624	0.122971031	-0.068438156
0.556079994	0.12387958	-0.069182449
0.554199641	0.125336108	-0.070019693
0.552188873	0.126375147	-0.07090632
0.549889437	0.128517991	-0.072036298
0.547747606	0.131798869	-0.073004879

C_N	C_A	C_M
0.545270281	0.136292862	-0.074191721
0.542602073	0.141042957	-0.075474786
0.539736447	0.14550579	-0.076840833
0.537090749	0.149820161	-0.078095292
0.535195218	0.153895931	-0.079035666
0.534365337	0.157535796	-0.07940455
0.533931454	0.160685661	-0.079426417
0.534097975	0.163074509	-0.079226215
0.534437198	0.164480739	-0.079069171
0.534918467	0.163650367	-0.078872747
0.535656468	0.160431786	-0.07854636
0.536711045	0.154743125	-0.078141391
0.538119717	0.147076417	-0.077557706
0.539637666	0.138517724	-0.07695184
0.541256182	0.12926644	-0.076213951
0.542970055	0.120826336	-0.075428374
0.54483204	0.113492595	-0.074633576
0.546435486	0.11009196	-0.073888186
0.547687708	0.109352462	-0.073336607
0.548929862	0.111519675	-0.072774092
0.550437467	0.1159698	-0.072126633
0.551844198	0.122544876	-0.071530311
0.552982926	0.129635225	-0.07103678
0.554150523	0.137124032	-0.070528597
0.555096618	0.142272123	-0.070213679
0.556240439	0.146228956	-0.069814894
0.557717821	0.148028407	-0.0691982
0.559699701	0.148872173	-0.068309901
0.561719029	0.148250089	-0.067418331
0.563939295	0.147435247	-0.06635958
0.566011213	0.145305398	-0.065407915
0.5676085	0.142984056	-0.064598204
0.568735278	0.140814828	-0.064042679
0.568897375	0.139162953	-0.063941997
0.568742479	0.137914322	-0.064001639
0.568289369	0.137844562	-0.06417957
0.567851633	0.138868021	-0.064398864
0.567084467	0.141074682	-0.064752266
0.56586586	0.144199235	-0.065317496
0.564141512	0.147324072	-0.066138297
0.56209787	0.150901385	-0.067218108
0.559867806	0.154698454	-0.068310623

C_N	C_A	C_M
0.557878885	0.157017653	-0.069232528
0.556031165	0.158111269	-0.070018025
0.554378442	0.158476159	-0.070803089
0.552563145	0.159371476	-0.071654367
0.550732507	0.159638109	-0.072562303
0.548440222	0.159339944	-0.073638441
0.546585009	0.158636561	-0.074477403
0.545201856	0.157710369	-0.075159332
0.544078641	0.157065963	-0.075742345
0.543242242	0.156952203	-0.07618065
0.542580939	0.156861261	-0.076579279
0.541893964	0.156239102	-0.077006886
0.541379076	0.155367011	-0.07738018
0.540831977	0.155768656	-0.077688068
0.540201821	0.155785938	-0.078070392
0.539501644	0.155198077	-0.078373652
0.538341668	0.154100019	-0.078957807
0.537025557	0.152735915	-0.07962089
0.535803209	0.150430804	-0.08022029
0.535066153	0.148155261	-0.0806073
0.534854729	0.145129932	-0.080778087
0.534983001	0.141039287	-0.080744869
0.535479469	0.137466763	-0.080493235
0.536404046	0.134322776	-0.080074354
0.537544264	0.132360571	-0.07953039
0.538979284	0.13179727	-0.078967941
0.540641504	0.132967374	-0.078307346
0.542037732	0.136990416	-0.077667264
0.543039007	0.142641493	-0.077291918
0.543559384	0.149420179	-0.077061488
0.543808571	0.157012081	-0.077016797
0.543959925	0.164667384	-0.076923359
0.544166546	0.17284084	-0.076785545
0.54460499	0.179433918	-0.076546916
0.544975782	0.183092244	-0.076309639
0.54565241	0.185048491	-0.07596653
0.546564716	0.184568641	-0.075438647
0.547643143	0.181218159	-0.074924259
0.548965623	0.177314941	-0.074253854
0.549867247	0.171543317	-0.073763371
0.55055402	0.166190946	-0.073398147
0.551040017	0.161223013	-0.073102001

C_N	C_A	C_M
0.551797434	0.157227272	-0.072734048
0.552451476	0.154948861	-0.072402289
0.553337043	0.155879392	-0.072002701
0.554349361	0.159292189	-0.07145801
0.555283102	0.164597011	-0.071018257
0.556275045	0.171435165	-0.070435498
0.55716193	0.178451522	-0.069971214
0.557552366	0.185436827	-0.069692667
0.55713614	0.190592076	-0.069854407
0.556123028	0.193495346	-0.070317589
0.554974094	0.194521997	-0.070816527
0.554091107	0.192244306	-0.071197207
0.553327631	0.190357236	-0.071501213
0.552156168	0.187139341	-0.072011206
0.550663293	0.184045509	-0.072667301
0.549187842	0.180446726	-0.073363411
0.54795468	0.177892289	-0.073904785
0.546807029	0.176262159	-0.074386674
0.545676829	0.175191794	-0.074908878
0.544644289	0.174474176	-0.075300206
0.54371192	0.173105652	-0.075657156
0.543348465	0.171458	-0.075710485
0.542993931	0.169425012	-0.075791576
0.542250714	0.166584901	-0.07605238
0.541322761	0.163073463	-0.076422315
0.540324206	0.159342718	-0.076713245
0.539587304	0.156729249	-0.077002032
0.539075338	0.154324743	-0.077095414
0.538730464	0.152996418	-0.077136971
0.538317633	0.151798478	-0.077196802
0.537971444	0.152203579	-0.077239507
0.537762067	0.153831484	-0.077246089
0.537718335	0.157163504	-0.077120175
0.537655325	0.161321086	-0.077037085
0.537541501	0.166171419	-0.077012746
0.537498699	0.170723542	-0.076887221
0.538046443	0.174512812	-0.076512469
0.538903799	0.176696186	-0.075948675
0.539832946	0.17609845	-0.075364413
0.540768637	0.173507288	-0.074776719
0.541983794	0.167765865	-0.074112544
0.543850487	0.160788423	-0.07306991

C_N	C_A	C_M
0.545782649	0.151818223	-0.071993826
0.548170205	0.141391266	-0.070703885
0.550447266	0.131072998	-0.069436816
0.552898197	0.122365038	-0.068130889
0.555234084	0.115392809	-0.066931719
0.557005306	0.111485558	-0.066050624
0.558488891	0.109851923	-0.065331378
0.559768766	0.110467565	-0.064683005
0.561144135	0.112813914	-0.063986897
0.56240954	0.117150169	-0.063314307
0.563630235	0.122445187	-0.062713574
0.564244933	0.129601541	-0.062419215
0.564284097	0.135563108	-0.062399287
0.564027158	0.140973806	-0.062496203
0.563701819	0.145433897	-0.062595128
0.563707231	0.147916934	-0.062559178
0.563896588	0.149507843	-0.062495484
0.563947124	0.148891088	-0.062355018
0.563887392	0.147820368	-0.062400845
0.563332079	0.145389159	-0.062631737
0.562355515	0.14254841	-0.063042991
0.561085141	0.139493635	-0.063668204
0.55993562	0.138161483	-0.064216558
0.55911565	0.137875961	-0.064549848
0.55877338	0.139058061	-0.064642402
0.5586836	0.142452738	-0.064526078
0.559012271	0.146975933	-0.064312736
0.559334115	0.151488062	-0.064086461
0.559592319	0.155937075	-0.063794378
0.55974691	0.159225764	-0.063619628
0.560067066	0.161325539	-0.063377268
0.56009839	0.163277042	-0.063264441
0.559950477	0.164181226	-0.063274444
0.55964862	0.16468693	-0.063378201
0.559082329	0.165425719	-0.063582679
0.558179664	0.165166515	-0.064087097
0.556921169	0.16528923	-0.064754797
0.555450778	0.165301937	-0.065562179
0.554114142	0.165226764	-0.066139006
0.552789001	0.165494474	-0.066840538
0.551488185	0.164956151	-0.067497369

Appendix 3.6 – STRUCTURED GRIDS FROM EADS-MAS, GERMANY

by

Willy Fritz

A3.6.1   GEOMETRY

The test geometry is a delta wing with constant thickness, sharp trailing edge and different types of leading edges (sharp leading edge, small range leading edge radius, medium range leading edge radius and long range leading edge radius). The leading edge sweep angel is 65°. At the rear end of the wing there is a cylindrical sting which is blended by a fairing to the wing surface.
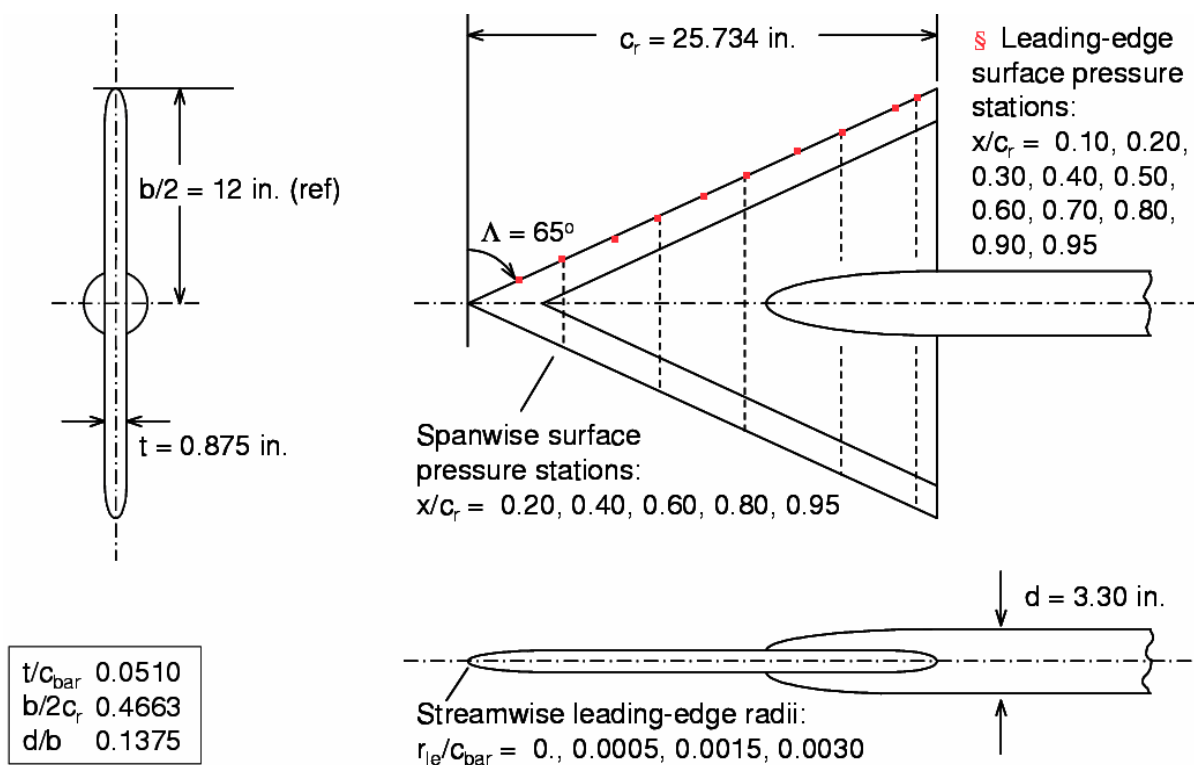

Figure A3.6-1: Geometry of VFE-2 Delta Wing.

Wing, sting-fairing and sting are analytically defined and this definition can be found in the NASA TM 465 (1996) "Julio Chu and James M. Luckring: Experimental Surface Pressure Data Obtained on 65° Delta Wing Across Reynolds Number and Mach Number Ranges, Volume 3: Medium Range Leading Edge". This report is on the NASA-LaRC techreports server http://techreports.larc.nasa.gov/ltrs/html available. To get the report and other publications concerning this delta wing type in the search-letters "Luckring Delta Wing".

A3.6.2   COMPUTATIONAL GRID

The computational grid is a so called conical grid having a singular line from the apex of the wing towards the upstream far field boundary. In the plane of symmetry, the grid wraps as a C-Mesh around the apex of the wing, in the cross sections x = const. the grid is of O-Type. The grid has been generated using a 3-D hyperbolic grid generator. The hyperbolic partial differential equations specify orthogonality and volume control. To avoid an intersection of the grid lines in concave corners (sting fairing) numerical dissipation is added to the equations.

The sting is included in the surface definition of the wing. This means, that the wing-sting intersection is not always mapped as an exact line in the grid. From the wing trailing edge, the sting is kept as a cylindrical body with constant cross section down to the far field boundary.

Figure A3.6-2 gives a total view of the 3-D grid structure. Figure A3.6-3 shows the grid in the plane of symmetry as well as the wing surface grid and the grid in the wake region. The conical grid (same number of grid points in each cross section x = const.) yields a very fine resolution of the apex of the wing.
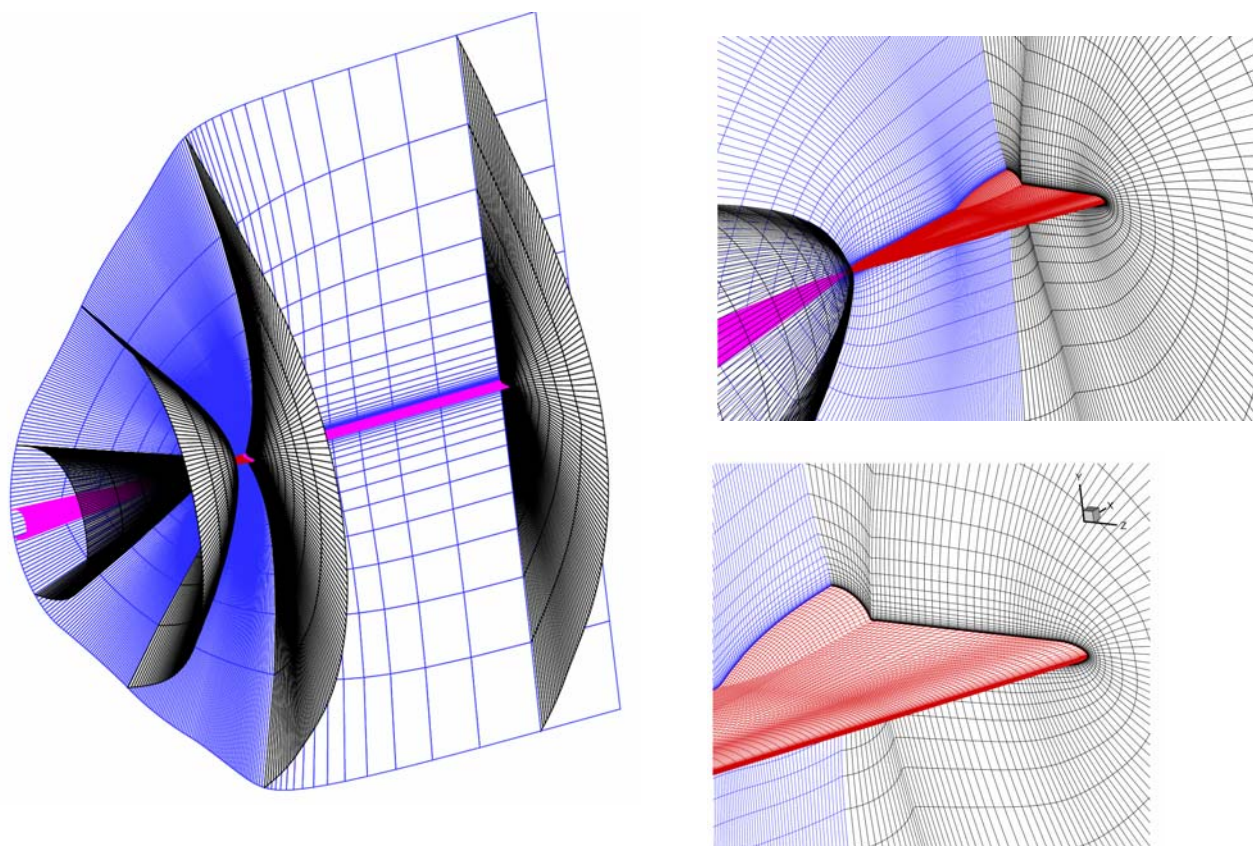

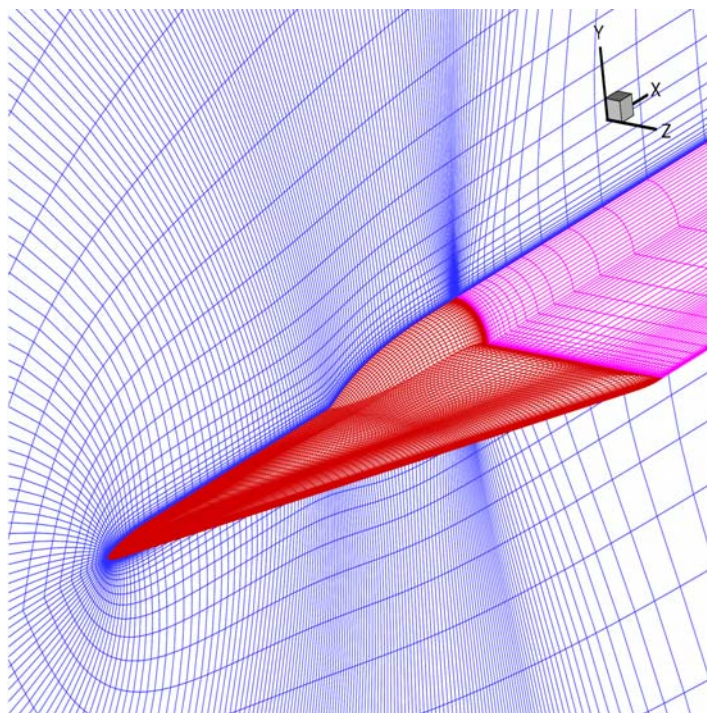**Figure A3.6-2: 3-D Grid Structure.**

Figure A3.6-3: Grid in Plane of Symmetry.

Figure A3.6-4 shows the grid structure behind the wing. The O-mesh orientation of the last wing section is kept towards the far field boundary.
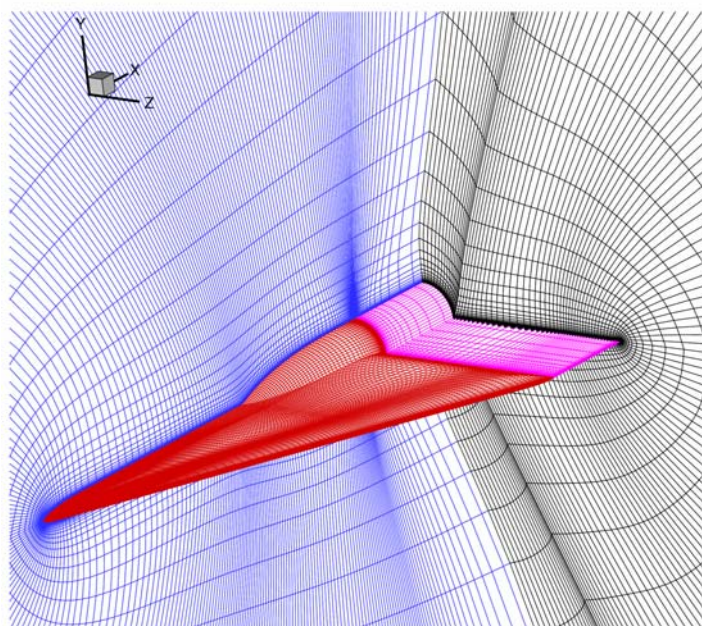

Figure A3.6-4: Grid Structure in Wake Region.

Figure A3.6-5 finally shows the grid lines around the leading edge. Due to the hyperbolic grid generation, the grid lines are nearly orthogonal around the leading edge.
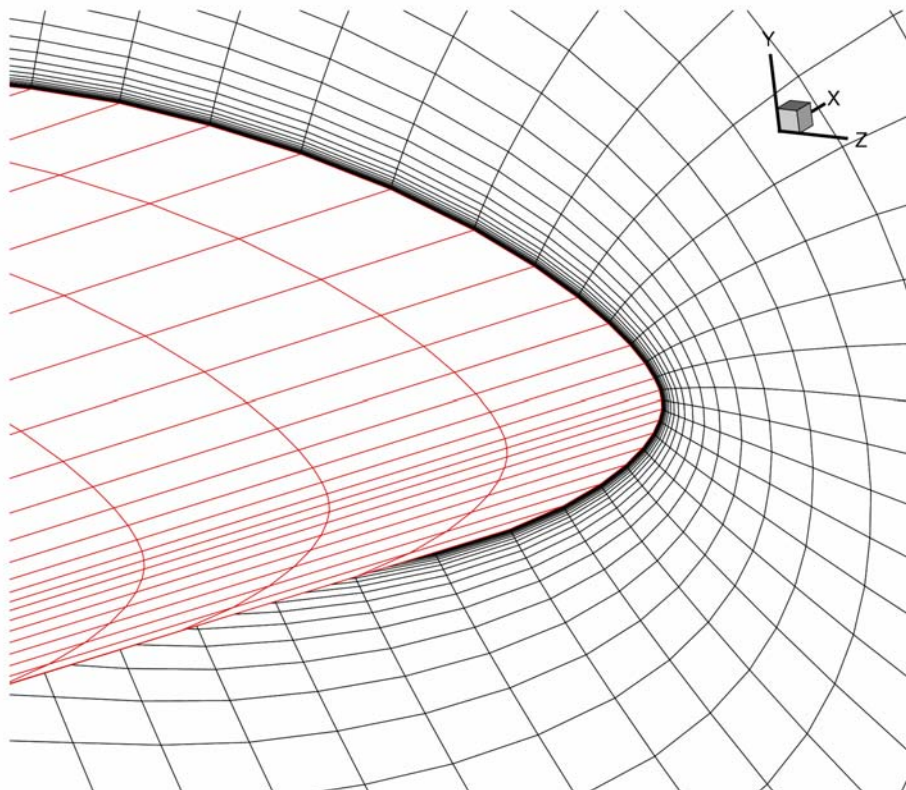

Figure A3.6-5: Grid around Leading Edge (only each second line is shown).

Two different grids have been generated fort he VFE-2 configuration:

> Grid 1: 321*257*129 Points in i-, k- und j-direction.
> Grid 2: 161*129*97 Points in i-, j- und k-direction.

This yields 10,642,113 points for grid 1 and 2,014,593 points for grid 2. The index directions are defined as follows:

> i-direction: in stream wise direction, starting from the wing apex.
> j-direction: from wing surface towards the far field.
> k-direction: in span wise direction, beginning at the upper plane of symmetry and ending at the lower plane of symmetry.

Both grids cover only one half of the wing. The grids are so called single block grids. That means that the index space is one contiguous topological region. (Of course the grids can be subdivided into multiple blocks for parallel computations). Grid 1 is suitable for 5-level multi grid and grid 2 allows 4 level multi grid.

A3.6.3 AVAILABILITY OF THE GRIDS

Both grids are available as (compressed) ASCII-files as mono block grids. The grid data sets have been written by the following FORTRAN statements:

```
c
c
      write(21,'(a)') '$$  nblock  nlevel  icoord'
      write(21,'(4(i5,2x))') nblock,nlevel,icoord
c
      write(21,'(a,i5,a,i5)') '$$  block no.',nblck,' level no.',nlevel
      write(21,'(a)') '$$  physical block dimensions:'
      write(21,'(a)') '$$     i      j      k    iwidth'
      write(21,'(4(i5,2x))') il,jl,kl,iwidth
      write(21,'(a)') '$$  coordinates:'
      write(21,'(a)') '$$      x                y                z'
c
        do k =1,kl
          do j = 1,jl
            do i=1,il
               write(21,'(3(e18.11, 1x))') x(i,j,k),y(i,j,k),z(i,j,k)
            end do
          end do
        end do
C
```
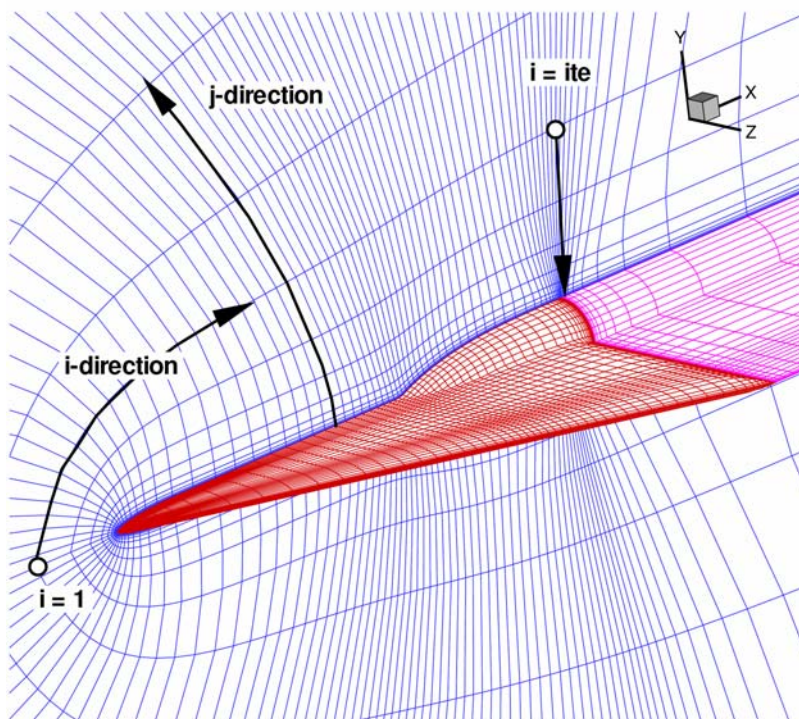

Figure A3.6-6: Index Directions i and j.

The coordinates are written within a multiple DO-Loop. The indices I, j and k are as described above Figure A3.6-6 and their orientation can be seen in the Figure A3.6-6, Figure A3.6-7 and Figure A3.6-8. These figures also show the orientation of the coordinate system. The origin is located in the apex of the wing.
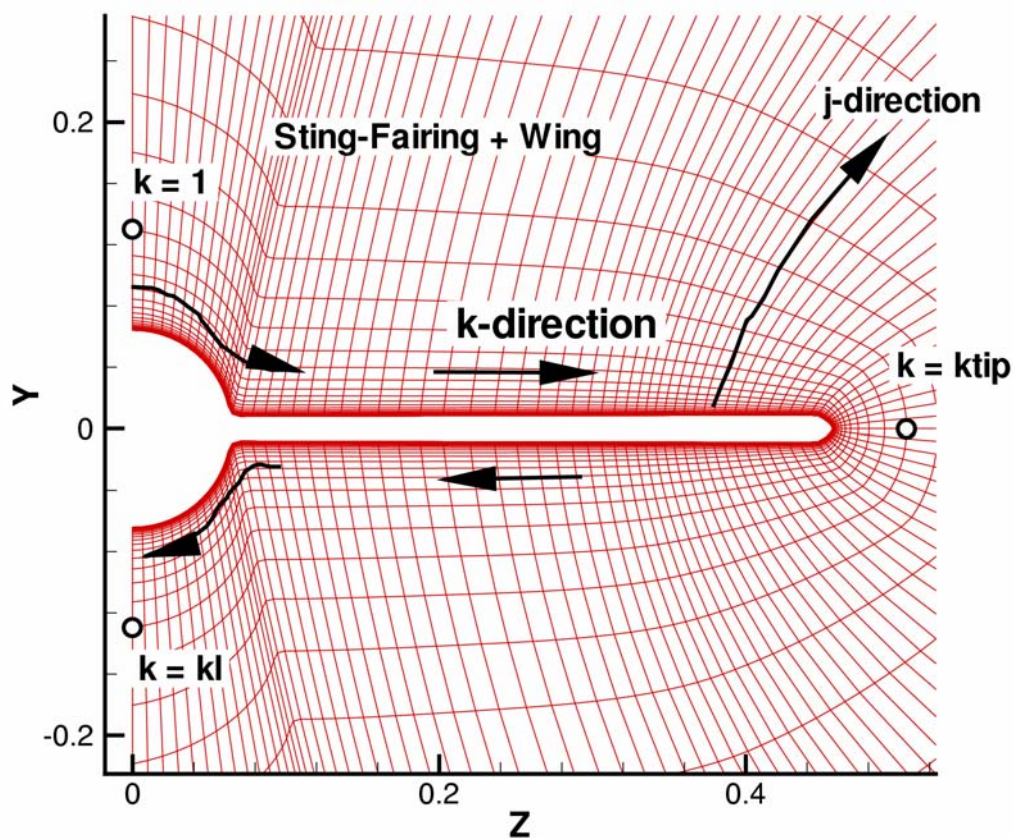

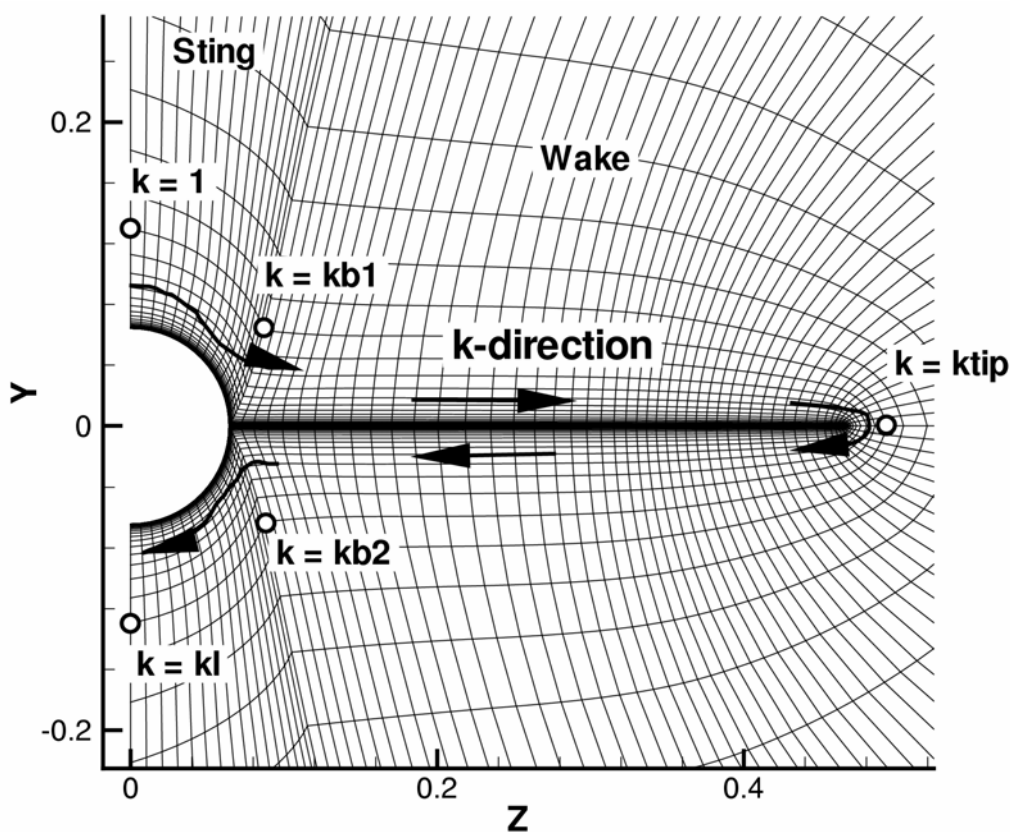**Figure A3.6-7: Index k in the Wing Region.**

Figure A3.6-8: Orientation of Index k in the Wake Region.

The index I starts at the apex of the wing and runs in stream-wise direction towards the downstream far field (i = il). The wing trailing edge is located at i = ite. In the fine grid there is il = 321 and ite = 257, in grid 2 il = 161 and ite = 129.

The index k runs o-shaped around the configuration. From k = 1 to k = kl there is a solid wall as boundary condition. The location of the leading edge is ktip. In grid 1 kl = 257 and in grid 2 kl = 129. The index ktip is 129 in the fine grid and 65 in the medium grid.

In the wake region, there is a solid wall from k = 1 to k = kb1 and from k = kb2 to k = kl (sting). From k = kb1 over ktip to k = kb2 there is an internal cut in the flow field. For the fine grid (grid 1) kb1 = 33, and kb2 = 225, and in grid 2 kb1 = 17 and kb2 = 113.

The coordinates of all grids have been normalized with the wing root chord. This gives the following reference values:

c_r = 1.0
c_{mac} = 0.6667 (Mean Aerodynamic Chord)
$b/2$ = 0.4663 (Halfspan)
S = 0.23315 (Area of one half of the Wing)

As reference point fort he pitching moment xm = 0.5625 was used at EADS-MAS.

A3.6.4   SOME EADS RESULTS USING THE GRIDS

Following there are some results, which were obtained at EADS with these grids. All calculations were carried out using the DLR flow solver FLOWer 116.15 with the Wilcox k-ω turbulence model without transition setting.

Figure A3.6-9 shows the surface pressure contours in the medium grid for the DLR-test case (M = 0.4, Re = 3 million, α = 13°) without transition setting. There is a weak footprint of the second vortex. The main leading edge separation begins a little bit too late (this can be manipulated by setting transition.
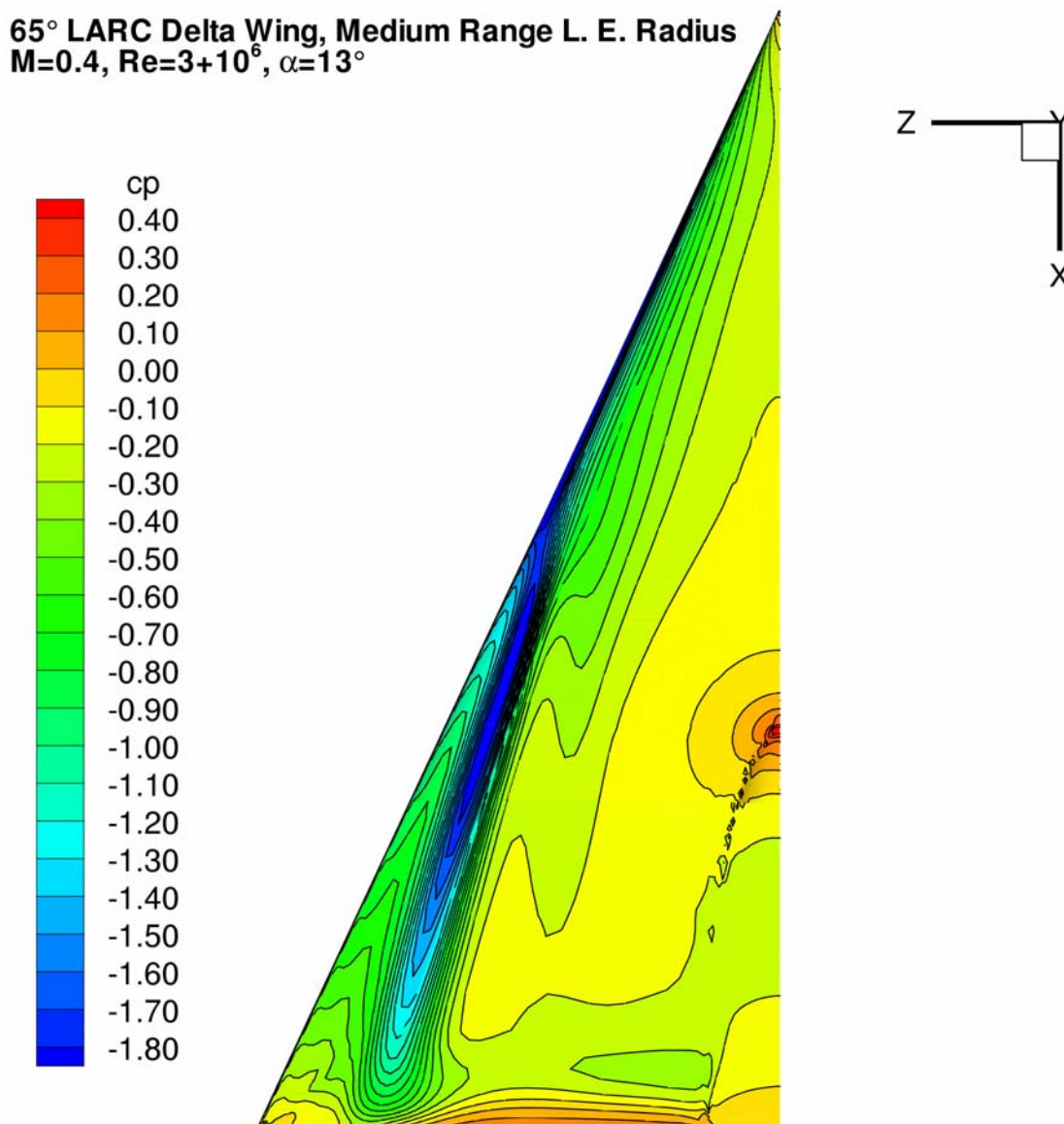

Figure A3.6-9: Surface Pressure Contours in Medium Grid.

Figure A3.6-10 shows the surface pressure contours for the same test case in the medium grid. The effect of the second vortex can be seen very clearly. But again the setup of the leading edge vortex separation is delayed compared to the experiment.
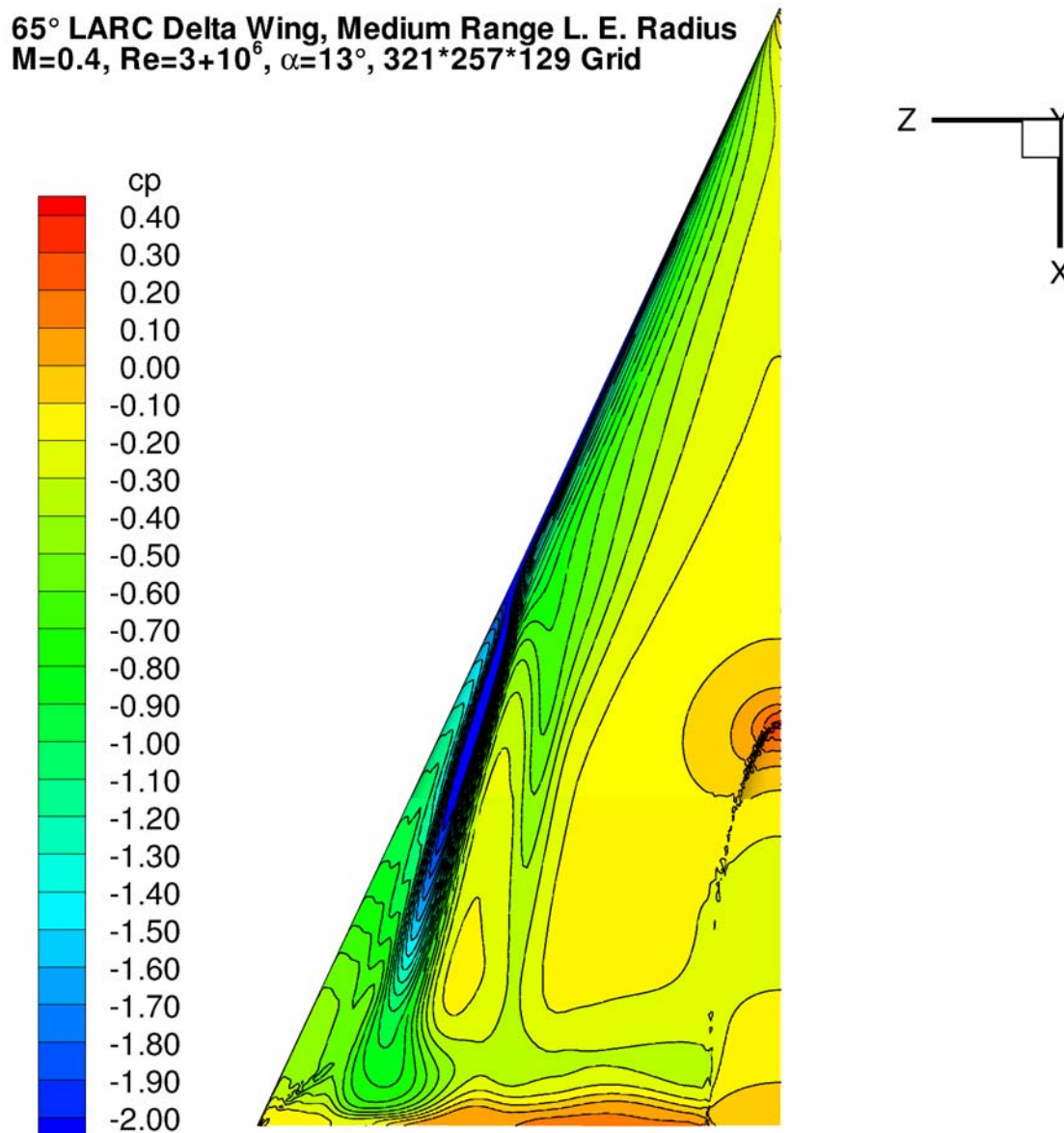

Figure A3.6-10: Pressure Contours in the Fine Grid.

Appendix 3.7 – UNSTRUCTURED GRID GEOMETRY AND DESCRIPTION

by

Andreas Schütte

A3.7.1 GEOMETRY

The test geometry is a delta wing with constant thickness, sharp trailing edge and different types of leading edges (sharp leading edge, small range leading edge radius, medium range leading edge radius and long range leading edge radius). The leading edge sweep angel is 65°. At the rear end of the wing is a cylindrical sting which is mounted by a fairing to the wing surface.
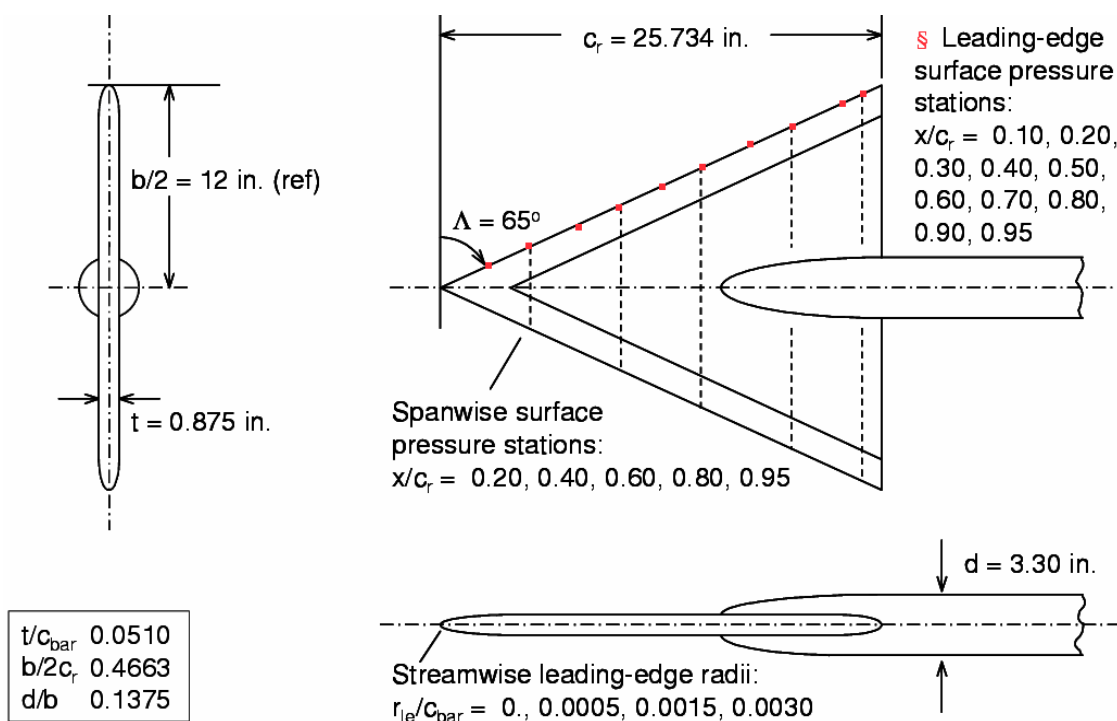

Figure A3.7-1: Geometry of VFE-2 Delta Wing.

Wing, sting-fairing and sting are analytically defined. This definition can be found in the NASA TM 465 (1996) "Julio Chu and James M. Luckring: Experimental Surface Pressure Data Obtained on 65° Delta Wing Across Reynolds Number and Mach Number Ranges, Volume 3: Medium Range Leading Edge". This report can be found on the NASA-LaRC techreports server http://techreports.larc.nasa.gov/ltrs/html available. To get the report and other publications concerning this delta wing type, take a lock into the search-letters "Luckring Delta Wing".

A3.7.2   DLR TAU-CODE AND COBALT GRID GENERATION DESCRIPTION

The difference between the computational grid for the DLR TAU-Code and Cobalt is the number of prism layers in the Cobalt grid to resolve the flow in the boundary layer and the resolution in the field, compare Figure A3.7-2 and Figure A3.7-3 with Figure A3.7-5 and Figure A3.7-6. For the cell centered code Cobalt the grid is sufficient with a coarser distribution than necessary for the cell vertex code TAU.

Table A3.7-1: Computational Grid Parameters

Code	Points	Elements	Prism Layers	First Spacing
DLR TAU-Code	12.8×10^6	51×10^6	20	0.005
Cobalt	6.1×10^6	26×10^6	15	0.005

Both grids are pre-refined grids with an initial value of 0.5 mm at the leading edge for the surface cells and tetrahedras. The influence radius for this leading edge source is 3 mm. The field is refined with tetrahedrons of 3mm for the Cobalt and 2mm for the TAU grid respectively, see Figure A3.7-4.

The grid surface topology is located under \TR-AVT-113-Appendix-3.7-Files\$TR-AVT-113-APPENDIX 3-7-Download-IGES-File.iges.
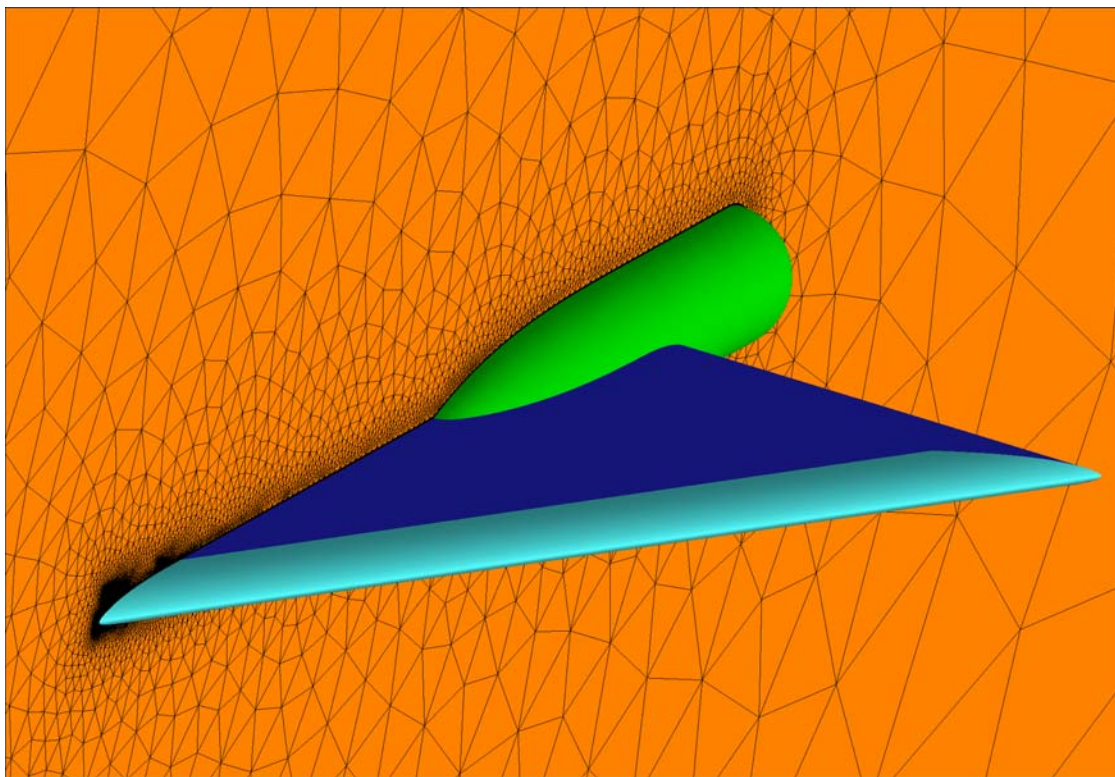

Figure A3.7-2: TAU Grid – Surface Topology and Discretization of the Symmetry Plane.
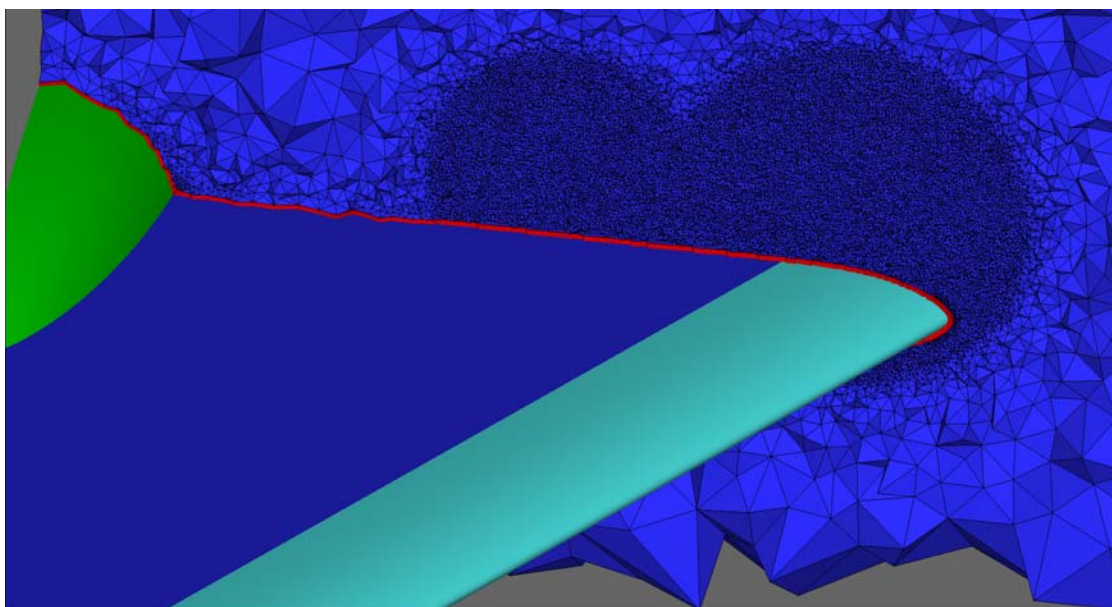
Figure A3.7-3: TAU Grid – Prism Layer and Pre-Refined Tetrahedral Grid at 80% Chord Length.
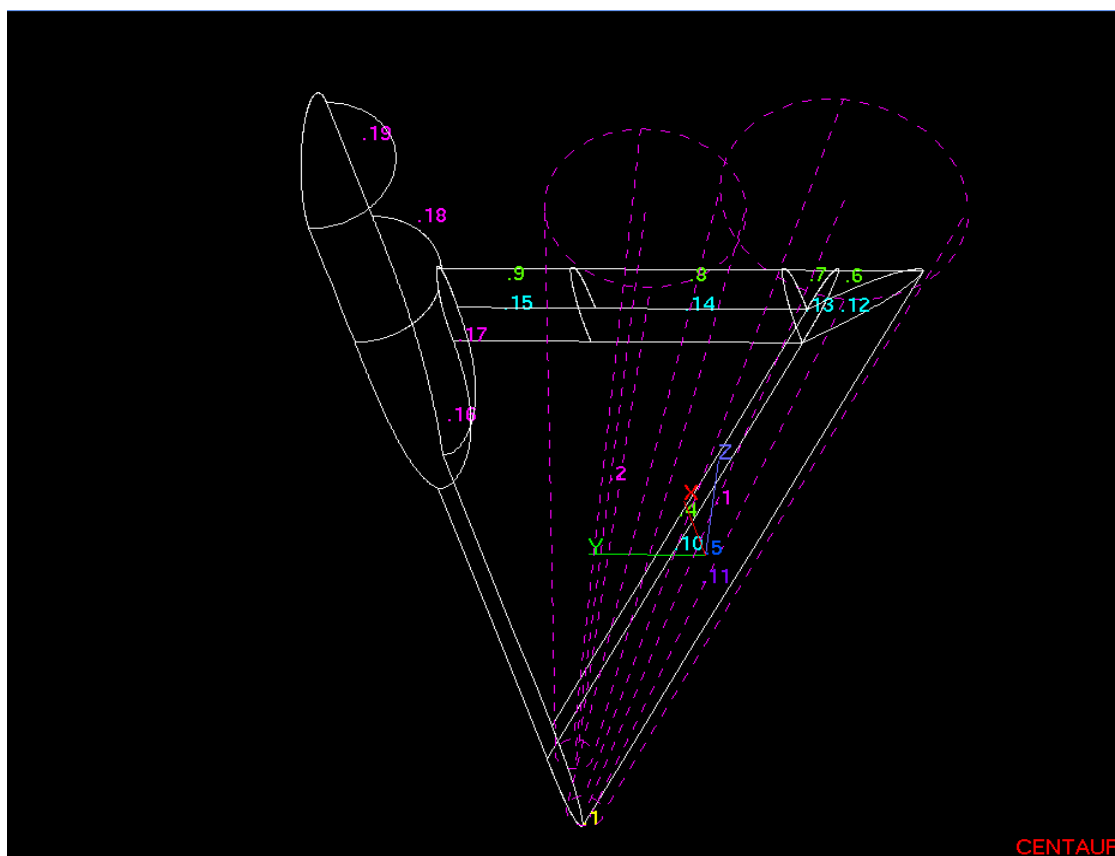

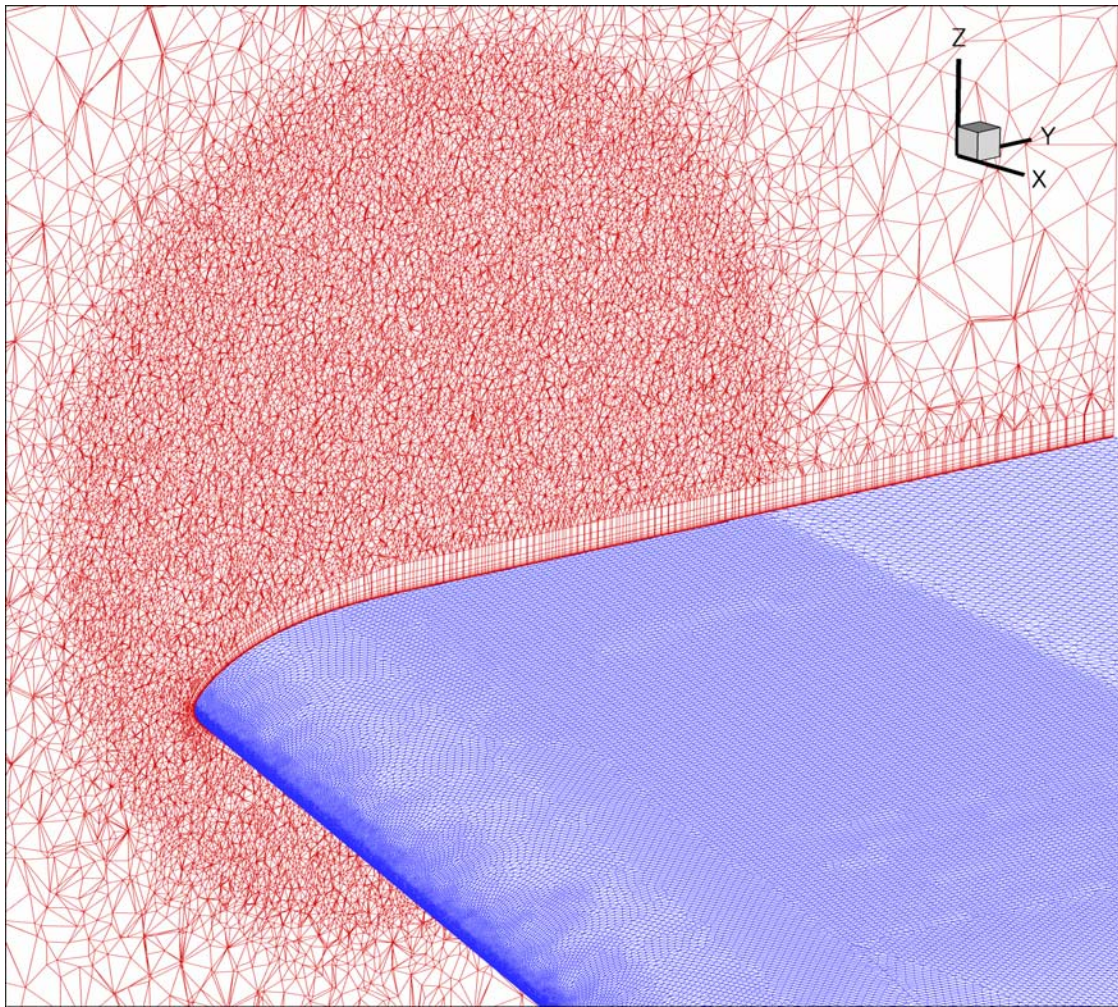**Figure A3.7-4: Source Topology for the Tetrahedral Field Sources.**

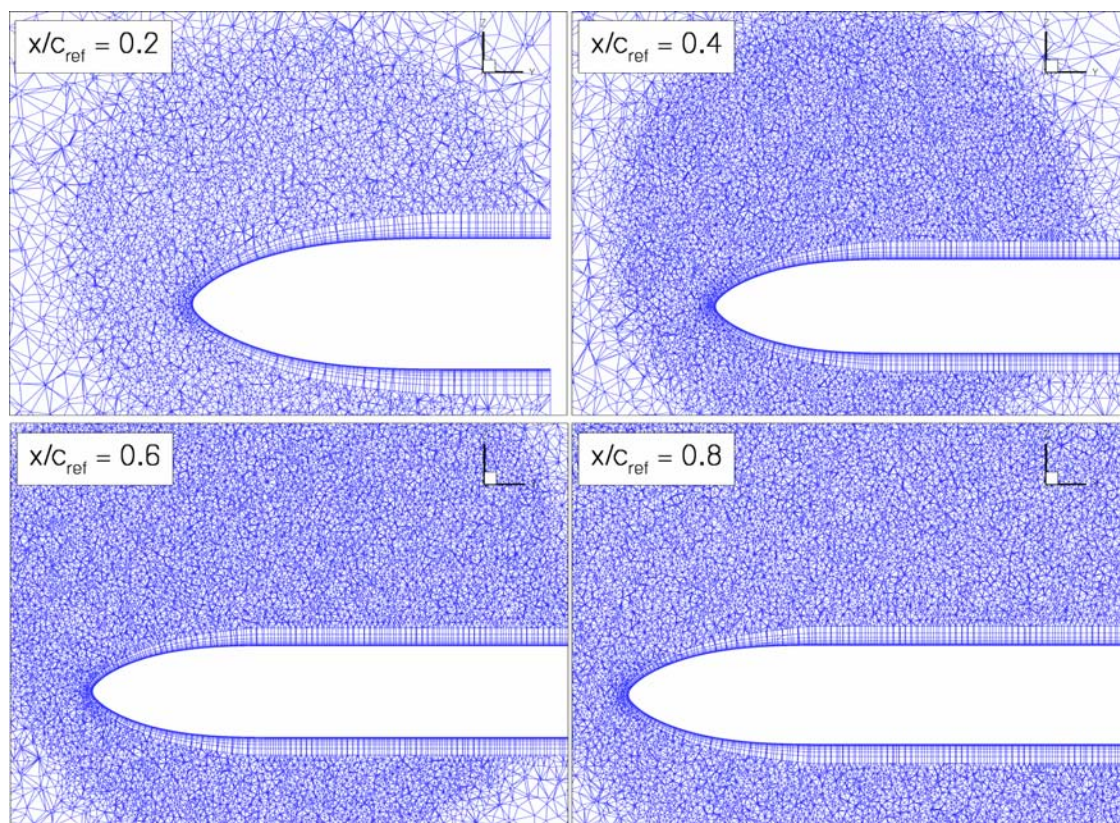**Figure A3.7-5: Cobalt Grid – Prism Layer and Pre-Refined Tetrahedral Grid.**

Figure A3.7-6: Cobalt Grid – Prism Layer and Pre-Refined Tetrahedrals.

REPORT DOCUMENTATION PAGE

1. Recipient's Reference	2. Originator's References	3. Further Reference	4. Security Classification of Document
	RTO-TR-AVT-113 AC/323(AVT-113)TP/246	ISBN 978-92-837-0073-9	UNCLASSIFIED/ UNLIMITED

5. Originator	Research and Technology Organisation North Atlantic Treaty Organisation BP 25, F-92201 Neuilly-sur-Seine Cedex, France

6. Title	Understanding and Modeling Vortical Flows to Improve the Technology Readiness Level for Military Aircraft

7. Presented at/Sponsored by	Summary Report of Task Group AVT-113.

8. Author(s)/Editor(s)	9. Date
Multiple	October 2009

10. Author's/Editor's Address	11. Pages
Multiple	1104

12. Distribution Statement	There are no restrictions on the distribution of this document. Information about the availability of this and other RTO unclassified publications is given on the back cover.

13. Keywords/Descriptors

Aerodynamic characteristics	Flight control	Unsteady flow
Aerodynamics	Flow control	Vortex dynamics
Algorithms	Flow distribution	Vortex interactions and control
Computerized simulation	Flow visualization	Vortical flows
Control surfaces	Mathematical models	Vortices
Delta wings	Methodology	Wings
Equations of motion		

14. Abstract

The charter and goal for Task Group AVT-113 is expressed in its title: "Understanding and Modeling Vortical Flows to Improve the Technology Readiness Level for Military Aircraft". To that end new experiments and complimentary computational solutions were obtained on a simple 65° delta wing model and new computations were obtained on a complete fighter aircraft (F-16XL) for which flight measurements existed. Studying the resulting vortical flows from these two scale- and shape-perspectives together has provided insight and led to an increased understanding of the dominant flow physics which exists on- and off-the-surface, or in- and out-of-the-boundary-layer. Researchers from Belgium, the Czech Republic, France, Germany, Italy, Slovenia, Sweden, The Netherlands, Turkey, the United Kingdom and the United States of America – representing the commitment of air-frame manufacturers, government laboratories and universities – contributed to the work of this task group.

BP 25
F-92201 NEUILLY-SUR-SEINE CEDEX • FRANCE
Télécopie 0(1)55.61.22.99 • E-mail mailbox@rta.nato.int

DIFFUSION DES PUBLICATIONS

RTO NON CLASSIFIEES

Les publications de l'AGARD et de la RTO peuvent parfois être obtenues auprès des centres nationaux de distribution indiqués ci-dessous. Si vous souhaitez recevoir toutes les publications de la RTO, ou simplement celles qui concernent certains Panels, vous pouvez demander d'être inclus soit à titre personnel, soit au nom de votre organisation, sur la liste d'envoi.

Les publications de la RTO et de l'AGARD sont également en vente auprès des agences de vente indiquées ci-dessous.

Les demandes de documents RTO ou AGARD doivent comporter la dénomination « RTO » ou « AGARD » selon le cas, suivi du numéro de série. Des informations analogues, telles que le titre est la date de publication sont souhaitables.

Si vous souhaitez recevoir une notification électronique de la disponibilité des rapports de la RTO au fur et à mesure de leur publication, vous pouvez consulter notre site Web (www.rto.nato.int) et vous abonner à ce service.

CENTRES DE DIFFUSION NATIONAUX

ALLEMAGNE
Streitkräfteamt / Abteilung III
Fachinformationszentrum der Bundeswehr (FIZBw)
Gorch-Fock-Straße 7, D-53229 Bonn

BELGIQUE
Royal High Institute for Defence – KHID/IRSD/RHID
Management of Scientific & Technological Research
for Defence, National RTO Coordinator
Royal Military Academy – Campus Renaissance
Renaissancelaan 30, 1000 Bruxelles

CANADA
DSIGRD2 – Bibliothécaire des ressources du savoir
R et D pour la défense Canada
Ministère de la Défense nationale
305, rue Rideau, 9e étage
Ottawa, Ontario K1A 0K2

DANEMARK
Danish Acquisition and Logistics Organization (DALO)
Lautrupbjerg 1-5, 2750 Ballerup

ESPAGNE
SDG TECEN / DGAM
C/ Arturo Soria 289
Madrid 28033

ETATS-UNIS
NASA Center for AeroSpace Information (CASI)
7115 Standard Drive
Hanover, MD 21076-1320

FRANCE
O.N.E.R.A. (ISP)
29, Avenue de la Division Leclerc
BP 72, 92322 Châtillon Cedex

GRECE (Correspondant)
Defence Industry & Research General
Directorate, Research Directorate
Fakinos Base Camp, S.T.G. 1020
Holargos, Athens

HONGRIE
Department for Scientific Analysis
Institute of Military Technology
Ministry of Defence
P O Box 26
H-1525 Budapest

ITALIE
General Secretariat of Defence and
National Armaments Directorate
5th Department – Technological
Research
Via XX Settembre 123
00187 Roma

LUXEMBOURG
Voir Belgique

NORVEGE
Norwegian Defence Research
Establishment
Attn: Biblioteket
P.O. Box 25
NO-2007 Kjeller

PAYS-BAS
Royal Netherlands Military
Academy Library
P.O. Box 90.002
4800 PA Breda

POLOGNE
Centralny Ośrodek Naukowej
Informacji Wojskowej
Al. Jerozolimskie 97
00-909 Warszawa

PORTUGAL
Estado Maior da Força Aérea
SDFA – Centro de Documentação
Alfragide
P-2720 Amadora

REPUBLIQUE TCHEQUE
LOM PRAHA s. p.
o. z. VTÚLaPVO
Mladoboleslavská 944
PO Box 18
197 21 Praha 9

ROUMANIE
Romanian National Distribution
Centre
Armaments Department
9-11, Drumul Taberei Street
Sector 6
061353, Bucharest

ROYAUME-UNI
Dstl Knowledge and Information
Services
Building 247
Porton Down
Salisbury SP4 0JQ

SLOVAQUIE
Akadémia ozbrojených síl
M.R. Štefánika, Distribučné a
informačné stredisko RTO
Demanova 393, P.O.Box 45
031 19 Liptovský Mikuláš

SLOVENIE
Ministry of Defence
Central Registry for EU and
NATO
Vojkova 55
1000 Ljubljana

TURQUIE
Milli Savunma Bakanlığı (MSB)
ARGE ve Teknoloji Dairesi
Başkanlığı
06650 Bakanliklar
Ankara

AGENCES DE VENTE

NASA Center for AeroSpace
Information (CASI)
7115 Standard Drive
Hanover, MD 21076-1320
ETATS-UNIS

The British Library Document
Supply Centre
Boston Spa, Wetherby
West Yorkshire LS23 7BQ
ROYAUME-UNI

Canada Institute for Scientific and
Technical Information (CISTI)
National Research Council Acquisitions
Montreal Road, Building M-55
Ottawa K1A 0S2, CANADA

Les demandes de documents RTO ou AGARD doivent comporter la dénomination « RTO » ou « AGARD » selon le cas, suivie du numéro de série (par exemple AGARD-AG-315). Des informations analogues, telles que le titre et la date de publication sont souhaitables. Des références bibliographiques complètes ainsi que des résumés des publications RTO et AGARD figurent dans les journaux suivants :

Scientific and Technical Aerospace Reports (STAR)
STAR peut être consulté en ligne au localisateur de ressources
uniformes (URL) suivant: http://www.sti.nasa.gov/Pubs/star/Star.html
STAR est édité par CASI dans le cadre du programme
NASA d'information scientifique et technique (STI)
STI Program Office, MS 157A
NASA Langley Research Center
Hampton, Virginia 23681-0001
ETATS-UNIS

Government Reports Announcements & Index (GRA&I)
publié par le National Technical Information Service
Springfield
Virginia 2216
ETATS-UNIS
(accessible également en mode interactif dans la base de
données bibliographiques en ligne du NTIS, et sur CD-ROM)

AGARD & RTO publications are sometimes available from the National Distribution Centres listed below. If you wish to receive all RTO reports, or just those relating to one or more specific RTO Panels, they may be willing to include you (or your Organisation) in their distribution.

RTO and AGARD reports may also be purchased from the Sales Agencies listed below.

Requests for RTO or AGARD documents should include the word 'RTO' or 'AGARD', as appropriate, followed by the serial number. Collateral information such as title and publication date is desirable.

If you wish to receive electronic notification of RTO reports as they are published, please visit our website (www.rto.nato.int) from where you can register for this service.

NATIONAL DISTRIBUTION CENTRES

BELGIUM
Royal High Institute for Defence – KHID/IRSD/RHID
Management of Scientific & Technological Research
  for Defence, National RTO Coordinator
Royal Military Academy – Campus Renaissance
Renaissancelaan 30
1000 Brussels

CANADA
DRDKIM2 – Knowledge Resources Librarian
Defence R&D Canada
Department of National Defence
305 Rideau Street, 9th Floor
Ottawa, Ontario K1A 0K2

CZECH REPUBLIC
LOM PRAHA s. p.
o. z. VTÚLaPVO
Mladoboleslavská 944
PO Box 18
197 21 Praha 9

DENMARK
Danish Acquisition and Logistics Organization (DALO)
Lautrupbjerg 1-5
2750 Ballerup

FRANCE
O.N.E.R.A. (ISP)
29, Avenue de la Division Leclerc
BP 72, 92322 Châtillon Cedex

GERMANY
Streitkräfteamt / Abteilung III
Fachinformationszentrum der Bundeswehr (FIZBw)
Gorch-Fock-Straße 7
D-53229 Bonn

GREECE (Point of Contact)
Defence Industry & Research General Directorate
Research Directorate, Fakinos Base Camp
S.T.G. 1020
Holargos, Athens

HUNGARY
Department for Scientific Analysis
Institute of Military Technology
Ministry of Defence
P O Box 26
H-1525 Budapest

ITALY
General Secretariat of Defence and
  National Armaments Directorate
5th Department – Technological
  Research
Via XX Settembre 123
00187 Roma

LUXEMBOURG
See Belgium

NETHERLANDS
Royal Netherlands Military
  Academy Library
P.O. Box 90.002
4800 PA Breda

NORWAY
Norwegian Defence Research
  Establishment
Attn: Biblioteket
P.O. Box 25
NO-2007 Kjeller

POLAND
Centralny Ośrodek Naukowej
  Informacji Wojskowej
Al. Jerozolimskie 97
00-909 Warszawa

PORTUGAL
Estado Maior da Força Aérea
SDFA – Centro de Documentação
Alfragide
P-2720 Amadora

ROMANIA
Romanian National Distribution
  Centre
Armaments Department
9-11, Drumul Taberei Street
Sector 6, 061353, Bucharest

SLOVAKIA
Akadémia ozbrojených síl
M.R. Štefánika, Distribučné a
  informačné stredisko RTO
Demanova 393, P.O.Box 45
031 19 Liptovský Mikuláš

SLOVENIA
Ministry of Defence
Central Registry for EU & NATO
Vojkova 55
1000 Ljubljana

SPAIN
SDG TECEN / DGAM
C/ Arturo Soria 289
Madrid 28033

TURKEY
Milli Savunma Bakanlığı (MSB)
ARGE ve Teknoloji Dairesi
  Başkanlığı
06650 Bakanliklar – Ankara

UNITED KINGDOM
Dstl Knowledge and Information
  Services
Building 247
Porton Down
Salisbury SP4 0JQ

UNITED STATES
NASA Center for AeroSpace
  Information (CASI)
7115 Standard Drive
Hanover, MD 21076-1320

SALES AGENCIES

NASA Center for AeroSpace
  Information (CASI)
7115 Standard Drive
Hanover, MD 21076-1320
UNITED STATES

The British Library Document
  Supply Centre
Boston Spa, Wetherby
West Yorkshire LS23 7BQ
UNITED KINGDOM

Canada Institute for Scientific and
  Technical Information (CISTI)
National Research Council Acquisitions
Montreal Road, Building M-55
Ottawa K1A 0S2, CANADA

Requests for RTO or AGARD documents should include the word 'RTO' or 'AGARD', as appropriate, followed by the serial number (for example AGARD-AG-315). Collateral information such as title and publication date is desirable. Full bibliographical references and abstracts of RTO and AGARD publications are given in the following journals:

Scientific and Technical Aerospace Reports (STAR)
STAR is available on-line at the following uniform resource
locator: http://www.sti.nasa.gov/Pubs/star/Star.html
STAR is published by CASI for the NASA Scientific
  and Technical Information (STI) Program
STI Program Office, MS 157A
NASA Langley Research Center
Hampton, Virginia 23681-0001
UNITED STATES

Government Reports Announcements & Index (GRA&I)
published by the National Technical Information Service
Springfield
Virginia 2216
UNITED STATES
(also available online in the NTIS Bibliographic Database
or on CD-ROM)